Lecture Notes in Electrical Engineering 1118

Sanjay Yadav
Yogendra Arya
Nor Asiah Muhamad
Karim Sebaa *Editors*

Energy Power and Automation Engineering

Select Proceedings of the International Conference, ICEPAE 2023

Springer

Lecture Notes in Electrical Engineering

Volume 1118

The book series *Lecture Notes in Electrical Engineering* (LNEE) publishes the latest developments in Electrical Engineering—quickly, informally and in high quality. While original research reported in proceedings and monographs has traditionally formed the core of LNEE, we also encourage authors to submit books devoted to supporting student education and professional training in the various fields and applications areas of electrical engineering. The series cover classical and emerging topics concerning:

- Communication Engineering, Information Theory and Networks
- Electronics Engineering and Microelectronics
- Signal, Image and Speech Processing
- Wireless and Mobile Communication
- Circuits and Systems
- Energy Systems, Power Electronics and Electrical Machines
- Electro-optical Engineering
- Instrumentation Engineering
- Avionics Engineering
- Control Systems
- Internet-of-Things and Cybersecurity
- Biomedical Devices, MEMS and NEMS

For general information about this book series, comments or suggestions, please contact leontina.dicecco@springer.com.

To submit a proposal or request further information, please contact the Publishing Editor in your country:

China

Jasmine Dou, Editor (jasmine.dou@springer.com)

India, Japan, Rest of Asia

Swati Meherishi, Editorial Director (Swati.Meherishi@springer.com)

Southeast Asia, Australia, New Zealand

Ramesh Nath Premnath, Editor (ramesh.premnath@springernature.com)

USA, Canada

Michael Luby, Senior Editor (michael.luby@springer.com)

All other Countries

Leontina Di Cecco, Senior Editor (leontina.dicecco@springer.com)

**** This series is indexed by EI Compendex and Scopus databases. ****

Sanjay Yadav · Yogendra Arya ·
Nor Asiah Muhamad · Karim Sebaa
Editors

Energy Power and Automation Engineering

Select Proceedings of the International Conference, ICEPAE 2023

Springer

Editors
Sanjay Yadav
Former Head Physico-Mechanical
Metrology Division
CSIR-National Physical Laboratory
New Delhi, Delhi, India

Nor Asiah Muhamad
Electrical and Electronic Engineering
Department
Universiti Teknologi Brunei
Bandar Seri Begawan, Brunei Darussalam

Yogendra Arya
J.C. Bose University of Science
and Technology, YMCA
Faridabad, Haryana, India

Karim Sebaa
University of Medea
Médéa, Algeria

ISSN 1876-1100 ISSN 1876-1119 (electronic)
Lecture Notes in Electrical Engineering
ISBN 978-981-99-8877-8 ISBN 978-981-99-8878-5 (eBook)
https://doi.org/10.1007/978-981-99-8878-5

This Springer imprint is published by the registered company Springer Nature Singapore Pte Ltd.
The registered company address is: 152 Beach Road, #21-01/04 Gateway East, Singapore 189721, Singapore

Paper in this product is recyclable.

Committee Member

Conference General Chair

Prof. Bo Zhao, Zhejiang University of Water Resources and Electric Power, China
Prof. Guohai Liu, Jiangsu University, China
Prof. Fushuan Wen, Zhejiang University, China
Prof. Chong Kok Keong, Universiti Tunku Abdul Rahman, Malaysia.

Technical Program Committee Chair

Prof. Jinfeng Gao, Zhejiang Sci-Tech University, China
Prof. Karim Sebaa, University of Médéa, Algeria
Prof. Zhou Wu, Chongqing University, China.

Organizing Committee Chair

Prof. Yunxia Luo, Zhejiang University of Water Resources and Electric Power, China
Prof. Congli Mei, Zhejiang University of Water Resources and Electric Power, China.

Publication Chair

Prof. Dr. Sanjay Yadav, Formerly with CSIR-National Physical Laboratory, India
Prof. Nor Asiah Muhamad, Universiti Teknologi Brunei, Malaysia
Dr. Vladimir Vukovic, Teesside University, UK.

Technical Program Committee

Prof. Qingshan She, Hangzhou Dianzi University, China
Prof. Xiaofu Ji, Jiangnan University, China
Prof. Jinhui Zhao, Zhejiang University of Water Resources and Electric Power, China
Prof. Haibao Huang, Sun Yat-Sen University, China
Prof. Jing Zhou, Xi'an Shiyou University, China
Prof. Wenshao Bu, Henan University of Science and Technology, China
Prof. Yujun Zhang, University of Science and Technology of China, China
Prof. Baoling Cai, Xi'an Thermal Power Research Institute Co., Ltd., China
Prof. Dinesh Birla, Rajasthan Technical University, India
Prof. Longbo Ma, Zhejiang University of Water Resources and Electric Power, China
Prof. Ling Wang, China Jiliang University, China
Prof. Jianjun Bo, Hangzhou Dianzi University, China
Prof. Jianning Li, Hangzhou Dianzi University, China
Prof. Syed Abdul Rahman Kashif, University of Engineering and Technology, Pakistan
Prof. Abu, Zaharin Ahmad University Malaysia Pahang, Malaysia
Prof. Zhiqiang Wang, Shandong University, China
Prof. Jiwa Abdullah, Universiti Tun Hussein Onn Malaysia, Malaysia
Prof. Yichen Jiang, Dalian University of Technology, ChinaS
Prof. Mandhir K Verma, GL BAJAJ Group of Institutions, India
Dr. Pooya Lotfabadi, Eastern Mediterranean University (EMU), North Cyprus
Dr. Rock Keey Liew, Universiti Malaysia Terengganu, Malaysia
Dr. Vladimir Vukovic, Teesside University, UK
Senior Engineer Tesfaye Abebe Geleta, Chung Yuan Christian University, Taiwan, China
Mr. Caiquan Wen, China Southern Power Grid, China.

Organizing Committee

Prof. Jianping Cai, Zhejiang University of Water Resources and Electric Power, China
Prof. Xiushan Wu, Zhejiang University of Water Resources and Electric Power, China
Prof. Ouguan Xu, Zhejiang University of Water Resources and Electric Power, China
Prof. Jinhui Zhao, Zhejiang University of Water Resources and Electric Power, China
Prof. Mariana Dumitrescu, University Dunarea de Jos Galati, Romania
Prof. Khalil El-Hami, University of Hassan 1st, Morocco
Prof. Osiris Canciglieri Junior, Pontifical Catholic University of Paraná, Brazil
Prof. Zakaria Boumerzoug, University of Biskra, Algeria
Prof. Haruki MATSUURA, Kanagawa University, Japan
Prof. Fangfang Jian, Henan University of Science and Technology, China

Prof. Wei Yao, Zhejiang University of Water Resources and Electric Power, China
Prof. Qiuzhen Yan, Zhejiang University of Water Resources and Electric Power, China
Prof. Tao Peng, Zhejiang University of Water Resources and Electric Power, China
Prof. Ranran Wang, Shandong Agricultural University, China
Lecturer Chuanhui Zhu, Zhejiang University of Water Resources and Electric Power, China
Lecturer Dong Guo, Zhejiang University of Water Resources and Electric Power, China
Lecturer Qiyao Yang, Zhejiang University of Water Resources and Electric Power, China
Lecturer Guoqin Zhang, Zhejiang University of Water Resources and Electric Power, China.

Preface

Titled with *Lecture Notes in Electrical Engineering* and available on latest research progress of electrical engineering, this paper volume gathers a bunch of papers collected from *2023 4th International Conference on Energy Power and Automation Engineering (ICEPAE 2023)*, held in hybrid mode at Zhejiang University of Water Resources and Electric Power (Nanxun Campus), China, during June 9–11, 2023.

The Conference, attended by more than 130 delegates around the globe, was hosted by Yan He, Director of the International Cooperation and Exchange Office of Zhejiang University of Water Resources and Electric Power, and Dr. Chuanhui Zhu. In the opening ceremony speech, Bo Zhao, Vice President of Zhejiang University of Water Resources and Electric Power, expressed his heartfelt thanks and sincere welcome to all academicians, experts and scholars who spared their precious time to attend the Conference. In the keynote speech part, Professor Guohai Liu from Jiangsu University, China, Professor Jinfeng Gao from Zhejiang Sci-Tech University, China, Professor Jinfeng Liu from University of Alberta, Canada, and other keynote speakers made wonderful academic reports on international frontier hot spots. Apart from keynote speeches, oral and poster presentation part were also held and displayed by various scholars, leading to a warm atmosphere of academic discussion.

We received a number of research article submissions in the Conference. After rigorous review by related top experts and review rebuttal process, various excellent papers were accepted and included in this paper volume. These papers cover mainly three parts of the conference: 1. Energy Conversion and Utilization and Thermal Power Engineering, 2. Mechanical Manufacturing and Electrical Automation Control and 3. Mechatronics and Remote Sensing Signal Monitoring. The research works of this volume can promote the development of energy power and automation engineering and thereby enhance scientific information interchange between scholars from top universities, research centers and high-tech enterprises working all around the world.

Featuring the most cutting-edge research directions and achievements related to energy power and automation engineering, this conference provided the most comprehensive research in the related fields and a more comprehensive understanding of the latest results of cross research in this field. Meanwhile, it also helped researchers and engineers to understand the research frontier, as well as discover the solutions to engineering problems.

We would like to acknowledge the authors for their contributions and the reviewers for their time to review the submissions rigorously. We are thankful to all the committee members and advisors of this volume. Finally, this volume presents some of the latest researches in the fields of energy power and automation engineering and is believed to be beneficial to develop relevant subjects. We hope that it will serve as a reference for researchers and practitioners in academia and industry related to energy power and automation engineering.

The Committee of ICEPAE 2023

New Delhi, India — Sanjay Yadav
Faridabad, India — Yogendra Arya
Bandar Seri Begawan, Brunei Darussalam — Nor Asiah Muhamad
Médéa, Algeria — Karim Sebaa

Contents

About the Editors

Sanjay Yadav obtained his master's degree in science (M.Sc.) in 1985 and his Ph.D. degree in Physics in 1990. Presently, he is working as Editor-in-Chief (EIC) of the MAPAN: The *Journal of Metrology Society of India.* He is also Vice President of the Metrology Society of India (MS), New Delhi, as well as Vice President of the Ultrasonic Society of India (USI), New Delhi. He is Former Chief Scientist and Head of the Physico Mechanical Metrology Division of NPL and also Former Professor at the Faculty of Physical Sciences, Academy of Scientific and Innovative Research (AcSIR), HRDG, Ghaziabad. He has taught "Advanced Measurement Techniques and Metrology" courses, taken practical classes and supervised graduate, master and Ph.D. students since 2011. He is Recipient of several awards and scholarships of National and international repute. He has significantly contributed to the field of pressure metrology, biomedical instrumentation, ultrasonic transducers and instrumentation systems. His current research interests include research and developmental activities in physicomechanical measurements; establishment, realization, maintenance and up-gradation of national pressure and vacuum standards; dissemination of national practical pressure scale to users through apex level calibration, training and consultancy services; inter-laboratory comparisons, proficiency testing program and key comparisons; implementation of quality system in the laboratory as per ISO/IEC 17025 standard and finite element analysis (FEA) and Monte Carlo simulations for pressure balances. He has published more than 450 research papers in national and international journals of repute and conferences, 20 books, 14 patents and copyrights, supervised eight PhDs (another five in waiting) and drafted several projects, scientific and technical reports, documents and policy papers.

Yogendra Arya is currently an Associate Professor at J.C. Bose University of Science and Technology, YMCA, India. He has published more than 50 research papers in reputed International journals. He received the "MSIT Best Faculty Award" in 2018 and "MSIT Certificate of Excellence in Research" in 2018 and 2019. He has been placed among the "Top 2% of Researchers in the World" for 2019, 2020, 2021 and 2022 by Stanford University, USA/Elsevier. He is Regular Reviewer of leading journals. He has Google Scholar citations of 3000-plus and h-index of 34. He has

received the "Best Associate Editor Award 2021, 2022 and 2023" from the *Journal of Electrical Engineering and Technology*. He is Associate Editor of a few SCIE journals. He is Fellow of IETE, Senior Member of IEEE, AMIE(I) and Life Member of ISTE. His major areas of research interest include AI techniques, optimization techniques, fuzzy control, control systems, AGC/LFC in smart grids, energy storage systems and renewable energy systems.

Nor Asiah Muhamad received a bachelor's degree in electrical and electronic engineering from Universiti Teknologi PETRONAS, Malaysia, in 2002, a master's degree in electrical power engineering from the University of South Australia, in 2006, and a Ph.D. degree from the University of New South Wales, Australia, in 2009. She was Researcher and Senior Lecturer with the Faculty of Electrical Engineering, Institute of High Voltage and High Current (IVAT), Universiti Teknologi Malaysia. She is currently serving as Senior Assistant Professor for Universiti Teknologi Brunei. She also acts as Associate Professor with the School of Electrical and Electronic Engineering, Universiti Sains Malaysia. Her research interests include power system equipment monitoring, in particular insulation diagnosis and the development of new systems for condition monitoring. Besides, she also works in energy efficiency and integration for domestic and industrial areas in Malaysia. She has two books, over 60 papers and 74 conference papers to her credit.

Karim Sebaa received his Electrical Engineering Degree and Magister in High Voltage and Power Systems from Ecole Nationale Polytechnique, Algiers, Algeria in 1998 and 2000, respectively. From September 2007 to March 2009, he was Visiting Student at Suplélec French. Since 2003, he has joined the University of Medea, Algeria, where presently he is currently Full Professor of Power Systems. His research interests include power system dynamics, distribution power systems and green energy penetration into power systems. He has authored and co-authored more than 30 technical papers comprising of journals and conference proceedings. He also has contributed to articles for many conferences and journals published by IEEE, Elsevier and others.

Energy Conversion and Utilization and Thermal Power Engineering

Analysis of the Thermal–Hydraulic Characteristics of Supercritical CO_2/Kr Mixtures in the Straight-Channel Printed Circuit Heat Exchanger

Ya-Nan Ma and Peng Hu

Abstract The supercritical carbon dioxide recompression Brayton cycle (SCO_2RBC) has attracted much attention as one of the most promising thermal power conversion systems. As the component with the largest volume and quantity in the cycle, the heat exchanger has a crucial impact on the cycle efficiency. Printed circuit heat exchanger (PCHE) is widely utilized as regenerator and precooler in the Brayton cycle. CO_2/krypton has shown great potential for development as the working fluid of Brayton cycle. In this work, PCHE is analyzed as the high-temperature regenerator for Brayton cycle with CO_2/krypton mixtures as the heat transfer fluid in both hot and cold channels. Thermal properties of CO_2/Kr vary with temperature, and mass fraction of Kr is explored. The thermal–hydraulic characteristics of S-CO_2/Kr mixture flow in straight-channel PCHE are investigated. The effects of krypton mass fraction, channel diameter, and Reynolds number on heat transfer and friction features are discussed via numerical analysis. The results show that the Nusselt number of cold and hot channel increases by 1.09 and 0.87% when the molar fraction of krypton varies from 0 to 0.25 while the change of Fanning friction factor can be neglected. The channel diameter and Reynolds number have important effects on the thermal–hydraulic performance of cold and hot channels. New correlations are developed for the flow and heat transfer performance of CO_2/krypton (mass fraction 0.75/0.25) PCHEs with errors of less than ± 5%.

Keywords Supercritical Brayton cycle · CO_2-based mixtures · Printed circuit heat exchanger · Thermal–hydraulic characteristics

Y.-N. Ma · P. Hu (✉)
Department of Thermal Science and Energy Engineering, University of Science and Technology of China, Hefei 230027, China
e-mail: hupeng@ustc.edu.cn

Y.-N. Ma
e-mail: mynnym@mail.ustc.edu.cn

S. Yadav et al. (eds.), *Energy Power and Automation Engineering*, Lecture Notes in Electrical Engineering 1118, https://doi.org/10.1007/978-981-99-8878-5_1

1 Introduction

Compared to traditional thermal power conversion systems, the supercritical CO_2 Brayton cycle (SCO_2BC) has higher efficiency, more compact structure and lower cost [1]. The bulk and efficiency advantage of the SCO_2 Brayton cycle come from the fact that CO_2 behaves almost like an incompressible fluid with high density, high thermal conductivity, low viscosity, and high diffusion coefficient near its critical point (30.98 °C and 7.38 MPa) [2]. The critical point acts as a limitation of the lowest operating condition of the cycle. The critical point of CO_2 can be regulated by mixing with other gases, thus changing the minimum operating conditions of the Brayton cycle. Using CO_2-based binary mixtures as the working fluids is a way to improve the performance of the Brayton cycle [3–5]. Ma et al. [5] carried out thermo-economic analysis and multi-objective optimization on SBC with CO_2-based mixtures. It was shown that compared with the SCO_2BC, the supercritical CO_2/krypton (Kr) cycle had a large increase in cycle efficiency but less cost increase. The supercritical CO_2/Kr Brayton cycle shows better thermodynamic performance than SCO_2BC and has great potential for development.

Printed circuit heat exchanger (PCHE) is widely utilized as regenerator and precooler in the Brayton cycle because of its compact structure, high efficiency, high temperature and pressure resistance, and other advantages [6]. At present, most researches on the thermal–hydraulic characteristics in PCHE focus on the structure, operating conditions [7, 8], and working fluid [9, 10]. Zhou et al. [11] took CO_2/propane mixture as the working fluid of Brayton cycle. The thermal and hydraulic characteristics of CO_2/propane mixtures with different concentrations in straight-channel PCHE were investigated by numerical analysis. It can be found that CO_2/propane mixture as a heat transfer fluid has lower pressure drop and higher heat transfer coefficients. In our previous work [5], CO_2/Kr has shown great potential for development as the working fluid of SBC. There is a lack of research and correlations on the supercritical CO_2/Kr (S-CO_2/Kr) mixture flow in PCHE. In this work, the thermal–hydraulic characteristics of S-CO_2/Kr mixture flow in straight-channel PCHE are investigated and compared. The effects of the mass fraction of Kr, the geometric parameters of the channel, and Reynolds number on the thermal–hydraulic performances of PCHE are shown in the numerical analysis. Based on the numerical results, correlations for Nusselt number and Fanning friction factor on Reynolds number are proposed, respectively. The following are the main originality of this paper:

1. PCHE is analyzed as the high-temperature regenerator (HTR) for supercritical Brayton cycle with outlet pressure up to 20 MPa and inlet temperature up to 700 K.
2. The study is carried out for S-CO_2/Kr mixture as the working fluid in both hot and cold channels.
3. The global Fanning friction factor and Nusselt number correlations are proposed. This study provides guidance for the design of PCHE and its application in the Brayton cycle.

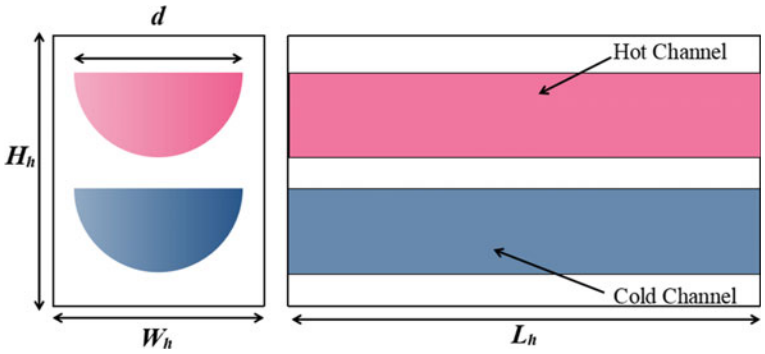

Fig. 1 Schematic diagram of PCHE geometric model

Table 1 Computational domain size parameters

Parameters	Symbol	Size (mm)
Channel diameter	d	1.4–2
Height of the heat exchanger unit	H_h	3.2
Length of the channel	L_h	200
Width of the heat exchanger unit	W_h	2.5

2 Model and Numerical Method

2.1 Physical Model and Boundary Condition

The physical model of PCHE is shown in Fig. 1. A double-channel straight PCHE units are chosen for numerical simulation because PCHE consists of a large number of heat exchanger units arranged periodically. Table 1 shows the geometric size parameters of PCHE. The setting of model parameters refers to Refs. [11, 12], which is the commonly used size of heat transfer unit of straight-channel PCHE at present. The solid material is Inconel 617 alloy with constant physical properties. Ansys Fluent 19.0 is utilized for numerical simulation in this work. The structured mesh of geometric model is generated by Ansys ICEM. The velocity inlet boundary conditions and the pressure outlet boundary conditions are adopted at inlet and outlet of the cold and hot channels. Supercritical CO_2/Kr is used as the working fluid for both channels.

2.2 Mathematical Model

The heat transfer coefficient h of the fluid can be defined as follows:

$$h = \frac{q_w}{T_b - T_w} \tag{1}$$

where T_w is the area weight average wall temperature, and T_b is the mass weighted average bulk temperature. The hydraulic diameter of the channel D_h can be calculated by

$$D_h = \frac{\pi d}{2(\pi/2 + 1)} \tag{2}$$

The Reynolds number and Prandtl number are determined as:

$$\mathrm{Re} = \frac{\rho v D_h}{\mu} = \frac{G D_h}{\mu} \tag{3}$$

$$\mathrm{Pr} = \frac{\mu c_p}{\lambda} \tag{4}$$

where dynamic viscosity μ, thermal conductivity λ, density ρ, and specific heat capacity c_p are based on bulk temperature T_b. v represents the velocity of the fluid.

The Nusselt number is calculated by

$$\mathrm{Nu} = \frac{h \cdot D_h}{\lambda} \tag{5}$$

The accelerated pressure drop, the frictional pressure drop, and Fanning friction factor f of the channel can be expressed from Eqs. (6) to (8), and the subscripts in and out mean inlet and outlet.

$$\Delta P_{ac} = \rho_{out} v_{out}^2 - \rho_{in} v_{in}^2 \tag{6}$$

$$\Delta P_f = \Delta P - \Delta P_{ac} \tag{7}$$

$$f = \frac{\Delta P_f \cdot D_h}{2 L \rho v^2} \tag{8}$$

2.3 Working Fluid Selection

Krypton is selected to mix with CO_2 in this study due to its great potential for application in the Brayton cycle shown in previous studies. The variation curves of the critical temperature and pressure of the CO_2/Kr mixtures with the increase of Kr mass fraction are shown in Fig. 2. According to the analysis in Ref. [5], the critical temperature of the working fluid was 5 K higher than the ambient temperature. The

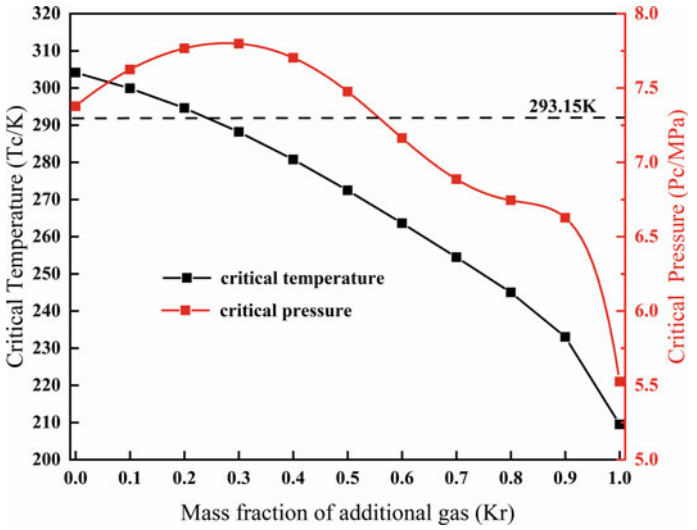

Fig. 2 Critical pressure and temperature of the CO_2/Kr mixtures with different mass fraction of Kr

study is conducted under the assumption that ambient temperature value is higher than 288 K. Therefore, the mass fraction of Kr is studied in the range of 0–0.25.

3 Results and Discussions

3.1 Influence of Mass Fraction of Kr on Flow and Heat Transfer Characteristics

The trends of thermal properties changing with temperature in the range of 400–600 K are shown in Fig. 3. The density ρ and the viscosity μ increase as the mass fraction of Kr increases which means better compressibility. The specific heat capacity c_p and thermal conductivity λ decrease with the increasing mass fraction of Kr. As the temperature increases, the thermal conductivity increases linearly which means greater heat transfer performance of working fluids.

The inlet temperatures of the cold and hot fluids are 480 K and 700 K, respectively. The outlet pressure of the hot and cold channel is kept at 8.2 and 20 MPa. Figure 4 shows the Nusselt and friction factor variation of straight-channel PCHE with the mass fraction of Kr for hot and cold working fluid. When the mass fraction of Kr changes from 0 to 0.25, the Nusselt number of hot and cold channels increases by 1.06% and 0.87%, respectively, the friction factor increases first and then decreases, and the numerical change is very small. This result can be attributed to the decrease of thermal conductivity and specific heat and the increase of density of the working

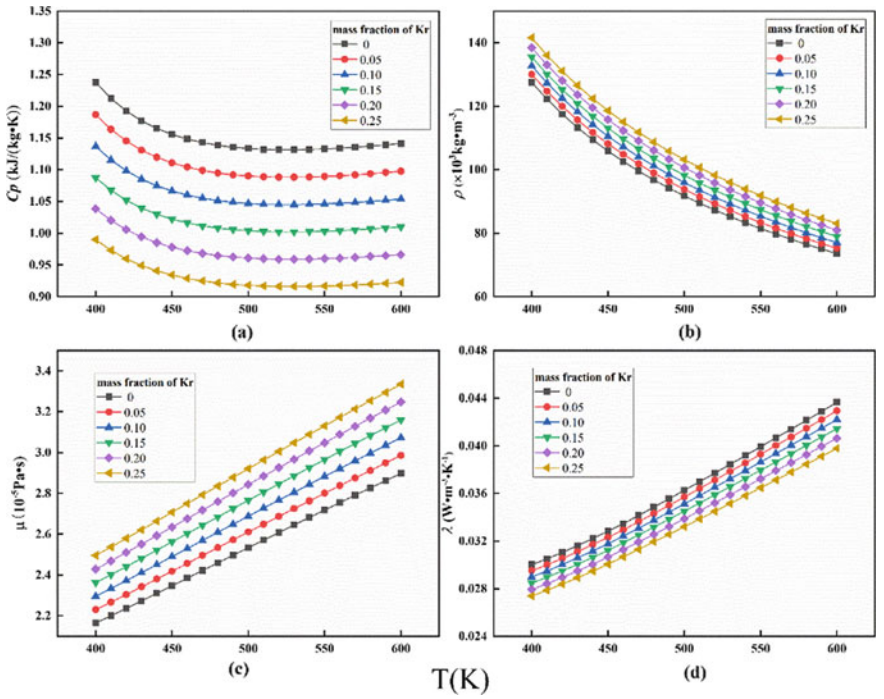

Fig. 3 Thermal properties of CO_2/Kr vary with temperature and mass fraction of Kr

fluid due to the addition of Kr. The reduction of specific heat makes the heat transfer decrease, but the thermal conductivity also decreases, so the Nusselt number shows an upward trend. With the addition of Kr, the heat transfer performance of PCHE is slightly enhanced. Taking Nusselt number as the heat transfer evaluation standard, the addition of Kr is beneficial to the heat transfer efficiency.

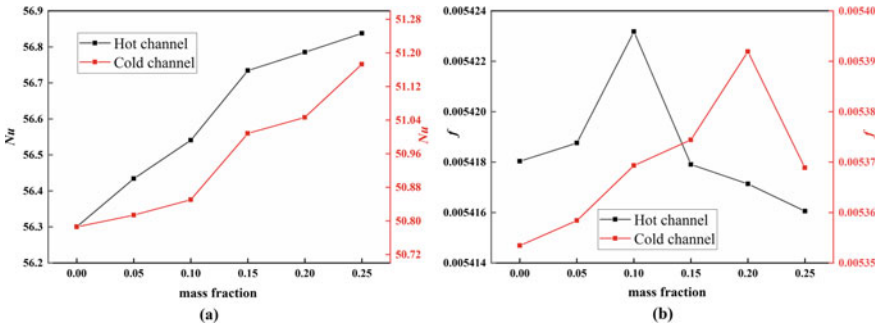

Fig. 4 **a** Nusselt number, **b** fraction factor of fluid versus the mass fraction of Kr

3.2 Influence of Channel Diameter and Reynolds Number on Flow and Heat Transfer Characteristics

The geometric models of four different channel diameters are established, respectively, 1.4, 1.6, 1.8, and 2 mm, while $H_h/2$ and $(W_h - d)$ are kept constant. Using CO_2/Kr mixture with mass fraction of 0.75/0.25 as the working fluid, the inlet mass flow rate of cold and hot working fluids is adjusted so that the corresponding inlet Reynolds number is 5500, 11,000, 16,500, 22,000, and 27,500, respectively. In Fig. 5a, as the Re increases, the Nusselt number generally shows a trend of linear growth. Because when the Reynolds number increases, the fluid velocity increases, the boundary layer thickness becomes thinner, and the heat transfer is enhanced. Figure 5a shows that the increase in channel diameter will reduce Nusselt number, thus negatively affecting the growth of heat transfer efficiency. It can be seen from Fig. 5b that the increase of Re reduces the friction factor and the increase of channel diameter has a positive impact on the flow in the channel. When the diameter of the channel increases, the heat transfer area increases, which promotes the heat transfer. However, the increase of channel diameter will lead to the decrease of velocity, resulting in the decrease of fluid turbulence intensity and fluid disturbance, which will reduce the flow loss but inhibit the heat transfer. When Reynolds number increases, the effect of velocity on friction factor is more significant than that of frictional pressure drop. Therefore, the friction factor gradually decreases with the increase of Reynolds number. When Re is 22,000, the diameter of the hot channel is from 1.4 to 2 mm, and the Nusselt number is reduced by 7.36% while the friction factor is reduced by 8.33%. Larger heat exchangers will result in less pressure loss to some extent increase in cycle efficiency.

3.3 Correlations for Flow and Heat Transfer

Based on the numerical simulation at three hot channel inlet temperatures of 650, 700, and 750 K, the new correlations for Nusselt number and Fanning friction factor are fitted. Figure 6 shows the accuracy of the developed correlations which are shown in Table 2. Nusselt number is positively correlated with Reynolds number, while friction factor is opposite. Higher Reynolds number is instrumental in improving thermal–hydraulic characteristics of PCHE. The prediction deviations of the correlations for Nu_h, f_h, Nu_c, and f_c are less than 2%, 5%, 3%, and 2%, respectively, indicating that the correlations have high accuracy and can be used to predict the flow heat transfer characteristics of supercritical CO_2/Kr fluid with mass fraction ratio of 0.75/0.25 in the PCHE within the Reynolds number range of 5500–27,500.

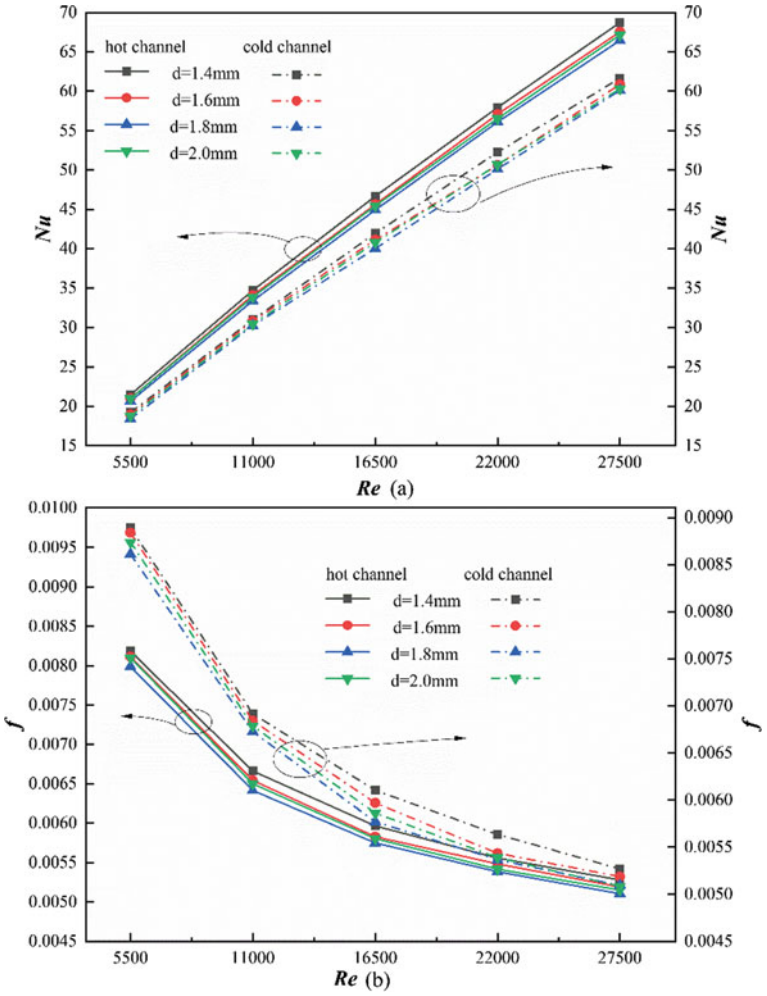

Fig. 5 **a** Nusselt number, **b** fraction factor of fluid versus channel diameters in straight channel for various Reynolds numbers

4 Conclusion

In this work, a straight double-channel PCHE numerical model is established. The thermal and hydraulic characteristics of S-CO_2/Kr mixture flow in straight-channel PCHE are investigated; finally, the correlations for Nusselt number and Fanning friction factor are proposed. The conclusions are obtained as below:

(1) The Nusselt number slightly increases, and the friction factor increases first and then decreases with the increase of the mass fraction of Kr. There is a slightly enhancement in heat transfer of the heat exchanger with the addition of Kr. It

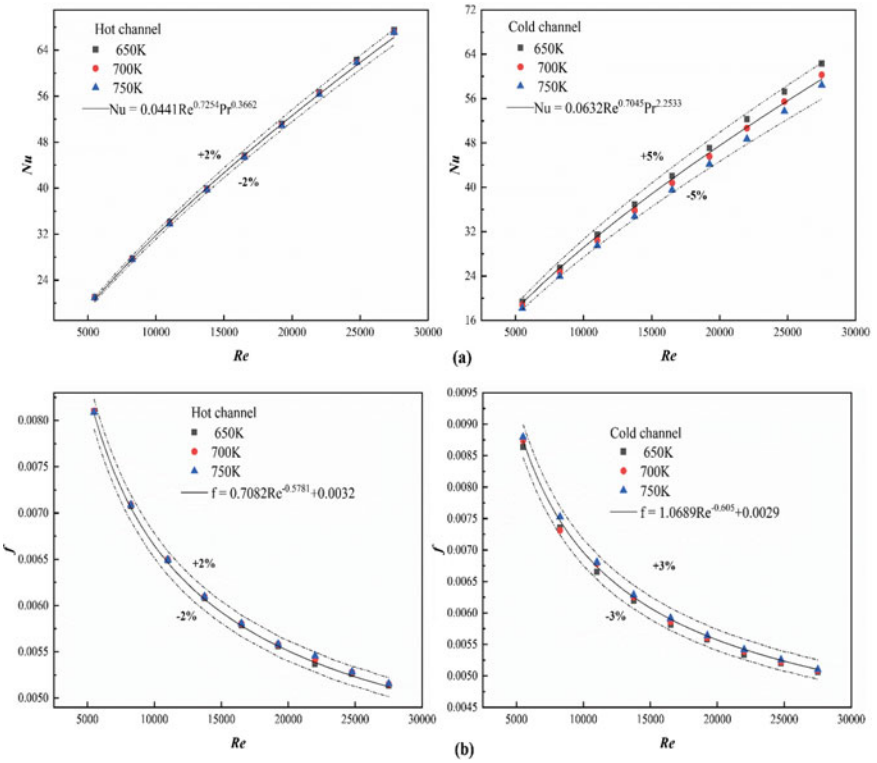

Fig. 6 Comparison of **a** Nusselt number correlation, **b** Fanning friction factor correlation of supercritical CO_2/Kr with numerical simulation data

Table 2 Nusselt and friction factor correlations for hot and cold channel

Case	Nusselt number	Fanning friction factor
Hot channel (500 K < T_b < 700 K)	$Nu_h = 0.0441Re^{0.7254}\,Pr^{0.3662}$ (0.75 < Pr < 0.9)	$f_h = 0.7082Re^{-0.5781} + 0.0032$
Cold channel (480 K < T_b < 600 K)	$Nu_c = 0.0632Re^{0.7045}\,Pr^{2.2533}$ (0.75 < Pr < 0.9)	$f_c = 1.0689Re^{-0.605} + 0.0029$

shows that using CO_2/Kr as working fluid has a positive effect on the efficiency of heat exchanger compared with CO_2 as working fluid.

(2) Larger channel diameter is beneficial to reduce channel pressure loss but not conducive to heat transfer. The Nusselt number increases while the friction factor decreases with the increase of Reynolds number, and the flow and heat transfer characteristics of the fluid are improved.

(3) New correlations for Nusselt number and Fanning friction factor are proposed to predict the heat transfer and flow characteristics of CO_2/Kr mixtures with the mass fraction of 0.75/0.25. The maximum prediction deviation of the correlations is less than $\pm$ 5%. The correlations can be used to predict the flow heat transfer characteristics of supercritical CO_2/Kr fluid in the PCHE within a certain range of Reynolds number.

Flow and heat transfer characteristics are the basis of PCHE thermal design. The regenerator numerical analysis can be combined with the S-CO_2/Kr Brayton cycle analysis to select appropriate mass flow rate and geometry sizes. Based on the numerical simulation results, new criterion correlations are proposed with a wide Reynolds number, which provides a reference for PCHE application in S-CO_2/Kr cycle and simplifying experiments.

Acknowledgements This work is supported by the National Natural Science Foundation of China (Grant No.: 52176171).

References

1. Wu P, Ma Y, Gao C et al (2020) A review of research and development of supercritical carbon dioxide Brayton cycle technology in nuclear engineering applications. Nucl Eng Des 368:110767
2. Guo JQ, Li MJ, Xu JL et al (2019) Thermodynamic performance analysis of different supercritical Brayton cycles using CO_2-based binary mixtures in the molten salt solar power tower systems. Energy 173:785–798
3. Jeong WS, Yong HJ (2013) Performance of supercritical Brayton cycle using CO_2-based binary mixture at varying critical points for SFR applications. Nucl Eng Des 262(9):12–20
4. Hu L, Chen DQ, Huang YP et al (2015) Investigation on the performance of the supercritical Brayton cycle with CO_2-based binary mixture as working fluid for an energy transportation system of a nuclear reactor. Energy 89:874–886
5. Ma YN, Hu P, Jia CQ et al (2023) Thermo-economic analysis and multi-objective optimization of supercritical Brayton cycles with CO_2-based mixtures. Appl Therm Eng 219:119492
6. Wang Q, Xu B, Huang X et al (2022) Heat transfer and flow characteristics of straight-type PCHEs with rectangular channels of different widths. Nucl Eng Des 391:111734
7. Mylavarapu SK, Sun X, Figley J et al (2008) Investigation of printed circuit heat exchangers for VHTRs. In: International topical meeting on high temperature reactor technology, pp 33–40
8. Ma T, Li L, Xu XY et al (2015) Study on local thermal–hydraulic performance and optimization of zigzag-type printed circuit heat exchanger at high temperature. Energy Convers Manage 104(11):55–66
9. Chen M, Sun X, Christensen RN et al (2016) Pressure drop and heat transfer characteristics of a high-temperature printed circuit heat exchanger. Appl Therm Eng 108:1409–1417
10. Kim IH, No HC (2013) Thermal–hydraulic physical models for a printed circuit heat exchanger covering He, He–CO_2 mixture, and water fluids using experimental data and CFD. Exp Therm Fluid Sci 48:213–221
11. Zhou Y, Yin D, Guo X et al (2022) Numerical analysis of the thermal and hydraulic characteristics of CO_2/propane mixtures in printed circuit heat exchangers. Int J Heat Mass Transf 185:122434

12. Meshram A, Jaiswal AK, Khivsara SD et al (2016) Modeling and analysis of a printed circuit heat exchanger for supercritical CO_2 power cycle applications. Appl Therm Eng 109:861–870

Hydrogen Fuel Cells Lifetime Prediction Based on Multi-layer Perceptron

Xiaokai Zhou and Qinyu Liu

Abstract Hydrogen fuel cells lifetime is essential for vehicles utilization and machines, which has been concerned by existing researchers. However, existing prediction is based on mathematical calculation and leaks the parameters of other situations including using situation and cells surroundings. This paper presents a novel approach to predict the lifetime of hydrogen fuel cells using a multi-layer perceptron (MLP) model by measuring the cell voltages. The lifetime of hydrogen fuel cells is a critical factor in their successful application and deployment. In this work, a MLP model is utilized to predict the lifetime of hydrogen fuel cells based on various input parameters including temperature, voltage and current information. The model is trained and tested on a dataset of experimental results from a laboratory-scale hydrogen fuel cell. The results demonstrate that the proposed MLP model is able to accurately predict the lifetime of hydrogen fuel cells with a mean absolute error of 0.17 years. This approach is promising for the development of hydrogen fuel cell technology and could be used to optimize the design and operation of fuel cells.

Keywords Hydrogen fuel · Lifetime prediction · Multi-layer perceptron · Parameter control · Cell voltage

1 Introduction

Hydrogen starts from the anode plate negative electrode of the hydrogen fuel cell, and through the action of the catalyst platinum in the polymer electrolysis membrane, the two electrons in the hydrogen molecule are separated, and the hydrogen ion protons that have lost electrons pass through the proton exchange membrane and reach the positive electrode of the cathode plate of the hydrogen fuel cell.

Hydrogen fuel cells are a form of renewable energy technology that has been widely used in physical researches, which is a type of energy storage and conversion

X. Zhou (✉) · Q. Liu
School of Mechanical, Electronic and Control Engineering, Beijing Jiaotong University, Beijing, China
e-mail: 21221093@bjtu.edu.cn

S. Yadav et al. (eds.), *Energy Power and Automation Engineering*, Lecture Notes in Electrical Engineering 1118, https://doi.org/10.1007/978-981-99-8878-5_2

device that utilizes a chemical reaction between hydrogen and oxygen to produce electricity [1]. Hydrogen fuel cells have been utilized in a variety of applications including powering vehicles, providing backup power for buildings and providing energy for portable devices. Hydrogen fuel cells are essential for developing physical energy and improve the physical environments.

Hydrogen fuel cells are considered to be one of the most efficient and cleanest forms of energy in current social productions. Hydrogen fuel cells are considered to be up to fifty percentage utilization ratio and compare with traditional coal or gas engines, which cause low energy transfer and emit serious air pollutants [2]. Indeed, hydrogen fuel cells are also non-flammable and a safer option than gasoline or diesel. The components of a hydrogen fuel cell include a fuel cell stack, a fuel cell membrane, a catalyst and an electrolyte [3]. The fuel cell stack is composed of a series of fuel cells arranged in a stack. The fuel cells use a chemical reaction between hydrogen and oxygen to produce electricity [4].

The lifetime of a fuel cell is affected by a number of factors including temperature, humidity, pressure and the amount of power the fuel cell is producing. The lifetime of a fuel cell is also affected by the materials used to construct the fuel cell and the inner structure of the fuel cell [5]. Materials platinum can decrease the usage time and cause the fuel cell to degrade. The inner structure of the fuel cell can also affect lifetime [6]. Specifically, a fuel cell with a higher power output will degrade represent more faster than with a lower power output.

Generally, the lifetime of a fuel cell is estimated to be between five and ten years. However, it is extremely depending on the operating environment, the materials used in the fuel cell and the inner structure of the fuel cell. Regular maintenance and monitoring of the fuel cell can assist to extend usage lifetime [7].

Additionally, hydrogen fuel cells are a promising form of renewable energy technology that can offer numerous advantages over traditional forms of energy generation. Hydrogen fuel cells are clean and efficient with emitting no air pollutants and consuming less energy than traditional fuels. Hydrogen fuel cells are relatively cost-effective [8]. The cost of producing energy from hydrogen fuel cells is comparable to other forms of renewable energy and is rapidly decreasing as technology improves. This makes them an attractive option for businesses and households that are looking to reduce their energy costs [9].

Multi-layer perceptron (MLP) is a type of artificial neural network that can be utilized for predicting the lifetime of hydrogen fuel cells. MLP is trained by utilizing a supervised learning algorithm to analyze a set of input data and predict the output results. In the case of predicting the lifetime of a hydrogen fuel cell, the input data can include factors including the temperature, humidity, pressure and power output of the fuel cell [10]. The output of the MLP is a predicted lifetime for the fuel cell. MLP have been used to predict the lifetime of hydrogen fuel cells in a variety of applications.

Existing studies have shown that MLP can accurately predict the lifetime of a fuel cell when trained on a dataset of input factors. This is especially useful for applications in which the lifetime of a fuel cell is critical in industrial and automotive

Table 1 Primary symbols explanations

Symbols	Descriptions
I	Input dataset
T	Target parameters
β	MLP model weight parameters
R	Prediction results set
τ	Prediction years set

applications [11]. However, the accuracy of the MLP-based lifetime prediction is highly dependent on the quality of the input data.

Therefore, it is important to ensure that the input data is correct and update the date. Additionally, the MLP should be regularly retrained on new data to ensure that it is able to accurately predict the lifetime of a fuel cell. The reminder of this paper including the introduction about primary symbols, the general framework of proposed model, experimental results analysis and conclusion.

2 Primary Symbols Description

Table 1 demonstrates the primary symbols that is used in this article and explain the meaning of used symbols.

3 Model Framework

In this section, we introduce the general framework of proposed model and describe the primary parameters that the model concerns.

3.1 Primary Input Parameter Introduction

A hydrogen fuel cell is an energy conversion device in which the electronic chemical energy of the fuel is converted into electricity. Similar to batteries, it is also an electronic chemical power generation device, so it is called a fuel cell. The corresponding fuel cell that uses hydrogen as fuel is a hydrogen fuel cell. It can be understood as the reverse reaction of water electrolysis into hydrogen and oxygen. As a result, the reaction process is both clean and efficient. Because it is not limited by the thermal efficiency of about 42% of the Carnot cycle used by conventional engines. The efficiency of hydrogen fuel cells can easily reach more than 60%. In this section, we illustrate the three input parameters including temperature, voltage pressure and

power output of the cell representing as I1, I2 and I3, respectively. The target parameters include the prediction usage lifetime and signed lifetime for theoretical calculation represent as T1 and T2, respectively. The multi-layers perceptron are utilized to determine the difference of the prediction weights, which can greatly influence the prediction results. Therefore, much more iterations and training processes are extremely required.

3.2 System Framework

Initially, Fig. 1 demonstrates the general framework of proposed model with three layers of multi-layer perceptron.

Data pre-processing is the initial step is to pre-process the input data, which involves normalizing and scaling the data so that it can be used by the MLP.

Model selection is to select an appropriate model for the MLP. This involves selecting the number of layers and the type of activation functions to be used.

Training the MLP can be trained by utilizing a supervised learning algorithm. The algorithm is used to analyze the input factors and determine which factors have the most influence toward the output lifetime.

Testing the MLP is last procedure to simulate and ensure that the proposed model is accurately predicting the output lifetime. The procedure is typically done by comparing the predicted lifetimes of the MLP with actual lifetimes.

4 Experimental Results and Analysis

In this section, we initially introduce the compared algorithm about cell lifetime prediction and demonstrate the comparison results.

4.1 Introduction of Comparison Algorithm

Artificial neural networks (ANN) is a type of machine learning algorithm that is model after the biological neural networks in the human brain. They are composed of interconnected artificial neurons units that are organized into layers and are capable of learning from data and making decisions. ANN have been used in a variety of applications including computer vision, natural language processing and robotics. ANN are also able to learn complex nonlinear relationships and can be used for both supervised and unsupervised learning tasks.

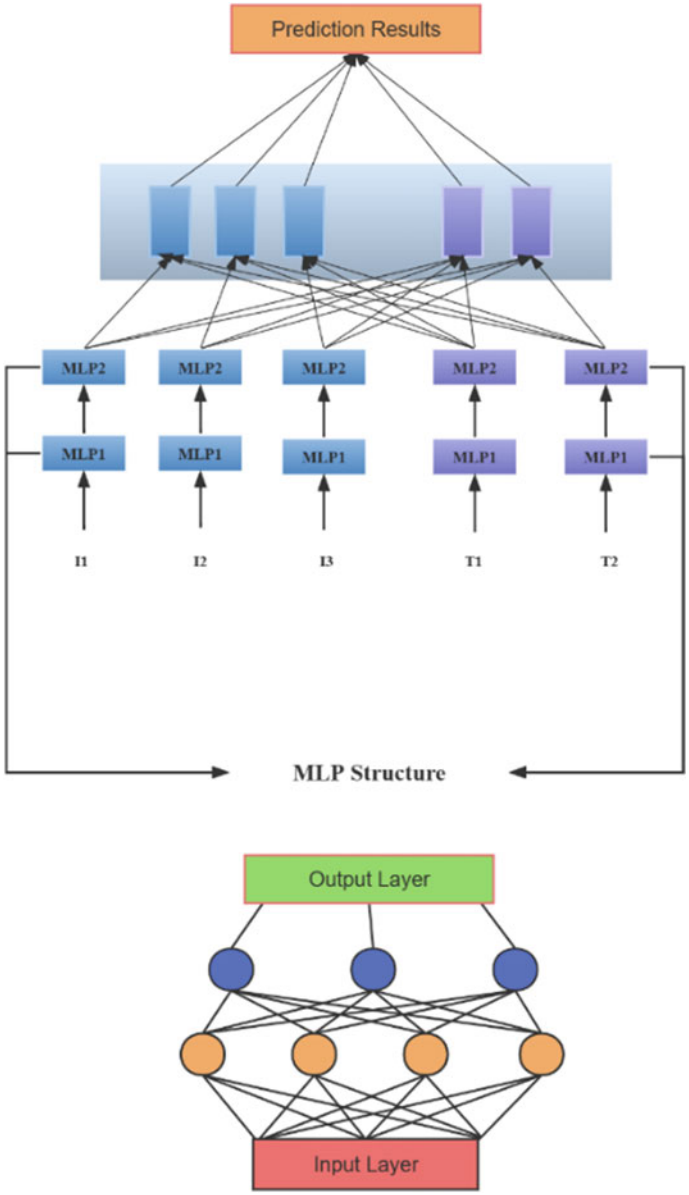

Fig. 1 Model framework demonstration

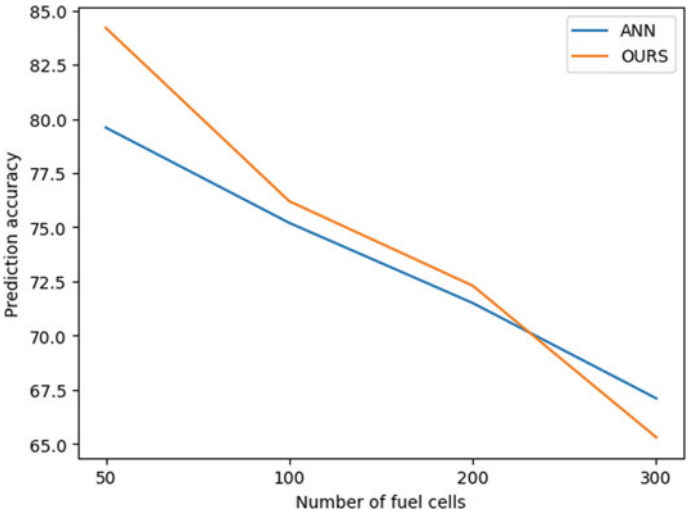

Fig. 2 System prediction result comparison results

4.2 Experimental Results and Analysis

Figure 2 demonstrates the comparison results about our proposed model and ANN model, we can conclude that our proposed model can obtain better prediction accuracy with the low levels of input data with current ANN model. Higher accuracy indicates the higher performance of prediction system.

We simulate our model in dataset from average performance forecast of hydrogen fuel cell systems in industrial big data. Figure 3 shows the prediction voltage and real voltage values.

Indeed, the system response time is another essential evaluation indicator for cell lifetime prediction, which means long-term prediction system requires the continuous prediction results to precisely estimate the lifetime of fuel cells. Therefore, short response time presents the practicability of prediction model. Table 2 demonstrates the response time comparison results.

From simulation and comparison evaluations, we can conclude that our proposed method can effectively achieve hydrogen fuel cells prediction with acceptable accuracy and computation costs. The accuracy indicates that our model can realize the prediction with 75% accuracy ratio when the amount of input cells is less than 100, which can apply in most physical situations.

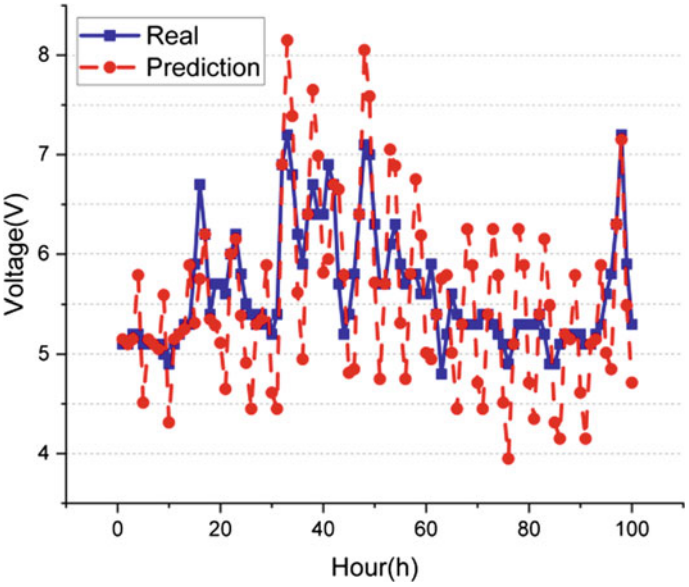

Fig. 3 Prediction voltage results

Table 2 Response time comparison results

Number of fuel cells	ANN (s)	Ours (s)
50	5.1	7.5
100	10.3	15.2
200	20.2	30.4
400	40.7	60.1
800	85.4	132.8

5 Conclusion and Future Improvements

In conclusion, our proposed model is trained using a supervised learning algorithm and requires a dataset of input factors and corresponding output lifetimes. Once the multi-layer perceptron is trained, it is subsequently utilized to predict the output lifetime of a fuel cell based on the input factors. From our experimental results, our accuracy of the MLP-based lifetime prediction is higher than existing prediction methods. As for future improvements, we could utilize large amount of data and retrain the proposed model to obtain the precise results. Indeed, the complexity of proposed model is almost relied on the layers of MLP, and the balance between computation cost and prediction accuracy is essential for the future investigations.

References

1. Lin R-H, Xi X-N, Wang P-N, Wu B-D, Tian S-M (2018) Review on hydrogen fuel cell condition monitoring and prediction methods. Int J Hydrogen Energy
2. Quan S, Wang Y-X, Xiao X, He H, Sun F (2021) Disturbance prediction-based enhanced stochastic model predictive control for hydrogen supply and circulating of vehicular fuel cells. Energy Convers Manag
3. Fu Z, Chen Q, Zhang L, Fan J, Zhang H, Deng Z (2021) Research on energy management strategy of fuel cell power generation system based on Grey–Markov chain power prediction. Energy Rep 7(Supplement 1)
4. Long B, Wu K, Li P, Li M (2022) A novel remaining useful life prediction method for hydrogen fuel cells based on the gated recurrent unit neural network. Appl Sci
5. Huang D-W, Qi D-Q, Yu N (2016) Capacity allocation of hydrogen production and fuel cells in wind farm based on stochastic prediction error. In: International conference on energy development and environmental protection (EDEP 2016)
6. Shi Y, Xiao J, Quan S, Pan M, Zhang L (2009) Fractal model for prediction of effective hydrogen diffusivity of gas diffusion layer in proton exchange membrane fuel cell. Int J Hydrogen Energy
7. Zhang B, Pang L, Shen X, Gao Y (2016) Measurement and prediction of detonation cell size in binary fuel blends of methane/hydrogen mixtures. Fuel
8. Hydrogen; researchers from Russian Academy of Science detail new studies and findings in the area of hydrogen (lifetime prediction for the hydrogen-air fuel cells). Chemicals & Chemistry (2015)
9. Pei P, Chen D, Wu Z, Ren P (2019) Nonlinear methods for evaluating and online predicting the lifetime of fuel cells. Appl Energy
10. Lin X, Wang Z, Wu J (2020) Energy management strategy based on velocity prediction using back propagation neural network for a plug-in fuel cell electric vehicle. Int J Energy Res
11. Hu X, Zou C, Tang X, Liu T, Hu L (2020) Cost-optimal energy management of hybrid electric vehicles using fuel cell/battery health-aware predictive control. IEEE Trans Power Electron

Lattice Boltzmann Simulation of Droplet Growth Processes in Flow Channel of Proton Exchange Membrane Fuel Cell

Jiadong Liao, Guogang Yang, Shian Li, Qiuwan Shen, Ziheng Jiang, and Hao Wang

Abstract Liquid water transport is an important issue for water management in proton exchange membrane fuel cells (PEMFC). The lattice Boltzmann method (LBM) with multi-relaxation time (MRT) is presented to simulate the droplet growth process in the flow channel during the operation of PEMFC. The effects of different flow channel heights, contact angles of the flow channel surface, and the size, distribution and distance of liquid pores are considered. By analyzing the droplet shape changes and the detachment time, it is found that lower flow channel height and larger contact angle are favorable for droplet detachment, and the detached droplet mass is smaller. When two liquid pores are present, the droplet interaction hinders the droplet detachment, especially when the diameter of both pores is 35 μm, a liquid film is formed on the flow channel surface, and the droplet can be detached only by increasing the distance between the two pores.

Keywords Proton exchange membrane fuel cell · Flow channel · Droplet growth · Lattice Boltzmann method

1 Introduction

In the context of climate change and fossil energy shortages, proton exchange membrane fuel cells (PEMFC) has become the most promising energy conversion devices due to their rapid response to various loads, non-emission of environmental pollutants and high energy density [1]. Water management has always been a hot topic for researchers. The two-phase flow of gas and water in the flow channel is an important element of water management. Water is produced in the cathodic catalytic layer and transported to the flow channel through the pores in the gas diffusion layer (GDL). If the liquid water is not discharged in time, it will accumulate in the flow channel, and more pores on the GDL surface will be covered, affecting the gas supply

J. Liao · G. Yang (✉) · S. Li · Q. Shen · Z. Jiang · H. Wang
Marine Engineering College, Dalian Maritime University, Dalian 116000, Liaoning, China
e-mail: yanggg@dlmu.edu.cn

S. Yadav et al. (eds.), *Energy Power and Automation Engineering*, Lecture Notes in Electrical Engineering 1118, https://doi.org/10.1007/978-981-99-8878-5_4

and reducing the performance of PEMFC. Some research advances have been made on the problem of gas–water two-phase flow in flow channel.

Deng et al. [2] used numerical methods to simulate the motion of a single droplet in a flow channel and showed that higher surface contact angles and air velocities can accelerate droplet flow. Hou et al. [3] investigated the effect of size and distance of two droplets in the flow channel on the flow and found that large size droplets in the front position and close distance of two droplets can promote droplet aggregation and enhance droplet discharge from the flow channel. Moslemi et al. [4] considered the influence of temperature on droplet motion and found that the higher the temperature in the flow channel, the greater the droplet movement speed. Choi et al. [5] studied the effect of flow channel height and showed that the higher the height, the smaller the pressure difference in the flow channel, which is conducive to the uniform distribution of gas in the GDL, but the outlet is prone to water accumulation. All the above studies are without considering the case of liquid pores, where droplets exist directly on the flow channel surface. However, the study of the droplet formation process is equally important. The size of the droplet flowing out of the liquid pore affects the droplet flow status. Han et al. [6] analyzed the growth and interaction of two droplets on the surface of a flow channel and discovered that an increase in the gas flow rate and the distance between the liquid pores can prevent droplet aggregation and enhance droplet removal. Hao and Cheng [7] examined the impact of flow channel surface wettability and gas flow rate on droplet detachment size and discharge time and proposed a model that can predict droplet detachment size. The research on droplet growth in flow channels is still rare, and the variables considered are not comprehensive enough. The impact of flow channel height has not yet been discovered.

Through the literature research, it has been found that scholars tend to use numerical simulation methods to investigate two-phase flow in flow channels, because they do not require high cost and can observe the droplet dynamic behavior in detail. Among various numerical models, the lattice Boltzmann method (LBM) is easy to program, has high computational efficiency, and has advantages in dealing with dynamic changes at the phase interface, and its application in the two-phase flow simulation of flow channels is gradually increasing [2–4, 8].

In this work, the LBM with multi-relaxation time (MRT) that reflects the real physical properties of the fluid is established to simulate the droplet growth process in the flow channel. The effects of the surface contact angle, the flow channel height, and the size, distribution and distance of the two liquid pores on the droplet growth and separation are investigated, which provide more insight into the droplet dynamics behavior in the flow channel.

2 Model Formulation

2.1 Lattice Boltzmann Method

The flow channel belongs to a macro-scale, in which the simulation of gas–liquid two-phase flow needs to consider a large gas–liquid density ratio, it can challenge the stability of the model. The MRT–LBM is used to enhance the stability of the model in this paper, and its distribution function evolution equation is as follows:

$$f_\alpha(x + c_\alpha \Delta t, t + \Delta t) = f_\alpha(x,t) - \Lambda_{\alpha\beta}\left(f_\beta - f_\beta^{\mathrm{eq}}\right)\big|_{(x,t)} + \Delta t\left(S_\alpha - 0.5\Lambda_{\alpha\beta}S_\beta\right)\big|_{(x,t)} \tag{1}$$

The distribution function f and the equilibrium distribution function f^{eq} are transformed into matrix space from velocity space by the orthogonal matrix M:

$$m = M \cdot f \tag{2}$$

$$m^{\mathrm{eq}} = M \cdot f^{\mathrm{eq}} \tag{3}$$

$$m^{\mathrm{eq}} = \rho\big(1, -2 + 3|v|^2, 1 - 3|v|^2, v_x, -v_x, v_y, -v_y, v_x^2 - v_y^2, v_x v_y\big)^{\mathrm{T}} \tag{4}$$

where ρ is the fluid macroscopic density and v is macroscopic velocity, the calculation equations are given in Eqs. (5) and (6), respectively.

$$\rho_\sigma = \sum_\alpha f_{\sigma,\alpha} \tag{5}$$

$$v = \frac{\sum_\sigma \left(\sum_\alpha f_{\sigma,\alpha} c_\alpha + \frac{F_\sigma}{2}\delta_{\mathrm{t}}\right)}{\sum_\sigma \rho_\sigma} \tag{6}$$

where F_σ is the force on the fluid, divided into flow–flow and flow–solid forces, the equations are

$$F_{\sigma,\mathrm{int}}(x) = -G_{\sigma\sigma}\psi_\sigma(x)\sum_\alpha w\big(|c_\alpha|^2\big)\psi_\sigma(x + c_\alpha \Delta t)c_\alpha - G_{\sigma\bar{\sigma}}\psi_\sigma(x)\sum_\alpha w\big(|c_\alpha|^2\big)\psi_{\bar{\sigma}}(x + c_\alpha \Delta t)c_\alpha \tag{7}$$

$$F_{\sigma,\mathrm{ads}}(x) = -G_{\sigma w}\psi_\sigma(x)\sum_\alpha w\big(|c_\alpha|^2\big)\psi_\sigma(x)s(x + c_\alpha \Delta t)c_\alpha \tag{8}$$

$$\psi_\sigma = \begin{cases} \sqrt{2\left(\kappa p_{\mathrm{EOS}} - \rho_1 c_{\mathrm{s}}^2\right)/G_{11}}, & \sigma = 1 \\ \rho_2, & \sigma = 2 \end{cases} \tag{9}$$

where κ is used to regulate the gas–liquid interface thickness, which is related to the model stability. p_{EOS} is the water component pressure, obtained from the Peng–Robinson state equation.

Equation (1) is transformed through the spatial matrix to Eq. (10).

$$m' = m - \Lambda(m - m^{\mathrm{eq}}) + \Delta t\left(I - \frac{\Lambda}{2}\right)S + \Delta t C \tag{10}$$

where I is the unit matrix, S and C are the source terms, Λ is the diagonal matrix, and the expressions are as follows [9]:

$$\Lambda = \mathrm{diag}\left(\tau_\rho^{-1}, \tau_{\mathrm{e}}^{-1}, \tau_\varsigma^{-1}, \tau_j^{-1}, \tau_{\mathrm{q}}^{-1}, \tau_j^{-1}, \tau_{\mathrm{q}}^{-1}, \tau_\upsilon^{-1}, \tau_\upsilon^{-1}\right) \tag{11}$$

$$S = \begin{bmatrix} 0 \\ 6\left(v_x F_x + v_y F_y\right) + \frac{12\sigma|F|^2}{\psi^2 \delta_{\mathrm{t}}(\tau_{\mathrm{e}} - 0.5)} \\ -6\left(v_x F_x + v_y F_y\right) - \frac{12\sigma|F|^2}{\psi^2 \delta_{\mathrm{t}}(\tau_\varsigma - 0.5)} \\ F_x \\ -F_x \\ F_y \\ -F_y \\ 2\left(v_x F_x - v_y F_y\right) \\ \left(v_x F_y + v_y F_x\right) \end{bmatrix} \quad C = \begin{bmatrix} 0 \\ 1.5\tau_{\mathrm{e}}^{-1}\left(Q_{xx} + Q_{yy}\right) \\ -1.5\tau_\varsigma^{-1}\left(Q_{xx} + Q_{yy}\right) \\ 0 \\ 0 \\ 0 \\ 0 \\ -\tau_\upsilon^{-1}\left(Q_{xx} - Q_{yy}\right) \\ -\tau_\upsilon^{-1} Q_{xy} \end{bmatrix} \tag{12}$$

$$Q = \gamma \frac{G_{11}}{2} \psi(x,t) \left[\sum_{\alpha=1}^{8} w\left(|e_\alpha|^2\right)[\psi_1(x + e_\alpha, t) - \psi_1(x,t)] e_\alpha e_\alpha\right] \tag{13}$$

where σ is adopted for thermodynamic consistency adjustment. γ is adopted for surface tension adjustment. Finally, the matrix space is transformed to the velocity space to obtain the new distribution function:

$$f' = M^{-1} m' \tag{14}$$

The specific values of the parameters in the model have been mentioned by the authors in previous work, please refer to Ref. [8].

2.2 Model Validation

To verify whether the model can achieve real fluid properties, the model is tested for high density viscosity ratio, thermodynamic consistency, independent adjustment of surface tension, Laplace's law, and contact angle test, which verified the accuracy of the model, the specific results of which are presented in the authors' previous work [8].

3 Results and Discussion

3.1 The Effect of Different Flow Channel Heights

Figure 1a–c present the droplet growth and detachment process at different flow channel heights. The flow channel length is 800 μm, the liquid pore is 300 μm away from the air inlet, the air velocity is 4 m/s, the water flow velocity is 0.08 m/s, and the operating temperature of PEMFC is 80 °C. It is observed that when the flow channel height of 200 μm, the droplet detaches from the liquid pore at 1.30 ms and forms a single droplet with a small droplet size. However, the droplet detachment times are 2.8 ms and 4.90 ms for the flow channel heights of 250 μm and 300 μm, respectively, and the droplet size increases. This is because when the droplet grows to a certain height, the contact surface with air increases, and the larger air force can overcome the flow–flow force, the water band connecting the droplet breaks, and the droplet detaches. The smaller the flow channel height, the stronger the air force on the droplet, the sooner it detaches.

The droplet detachment time and mass variation curves for different channel heights are given in Fig. 1d. It can be seen that the droplet detachment time and the detached droplet mass increase with the increase of the flow channel height, and the increase amplitude increases. The detachment time and droplet mass increase by 1.5 ms and 2.079×10^{-3} kg when the flow channel height increases from 200 to 250 μm, and by 2.1 ms and 3.074×10^{-3} kg when the flow channel height increases from 250 to 300 μm.

3.2 The Effect of Different Surface Contact Angles

Figure 2a–c present the droplet growth and detachment process under different contact angles of the flow channel surface. The smaller the contact angle, the longer the droplet is connected to the pore before detaching, this is due to the larger flow–solid forces. As the contact angle decreases, the droplet tends to develop a liquid film on the surface, the resistance to flow increases, and the flow rate becomes slower. With the continuous input of water in the liquid pore, the droplet gradually becomes

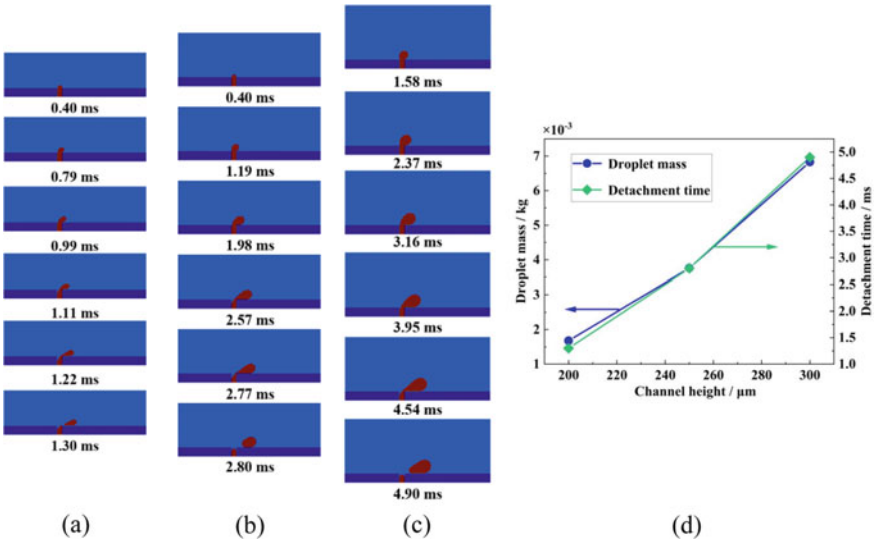

Fig. 1 Droplet growth and detachment processes in different flow channel heights: **a** 200 μm, **b** 250 μm, **c** 300 μm and **d** droplet detachment time and mass

larger, and the air force increases until it is larger than the sum of flow–solid force and flow–flow force at the connection between the droplet and the pore, the connection is broken, and the droplet is detached. The detachment times corresponding to the cases of 120°, 140°, and 160° contact angles are 3.71 ms, 2.96 ms, and 2.80 ms, respectively.

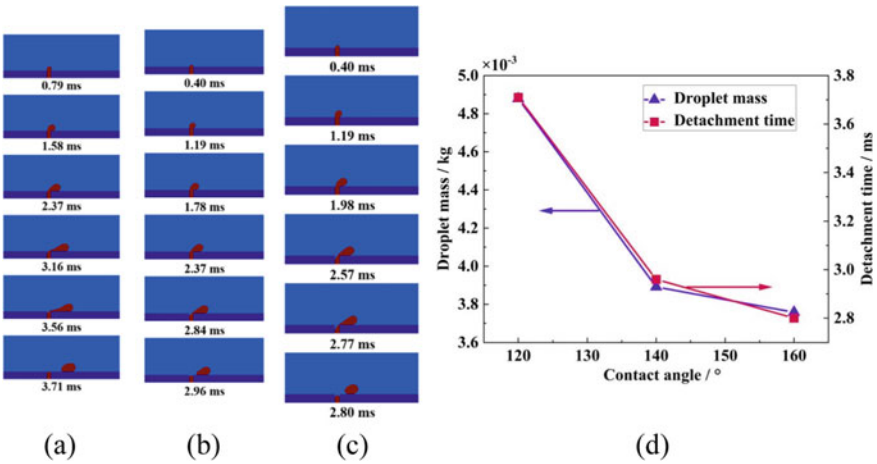

Fig. 2 The processes of droplet growth and detachment for different surface contact angles: **a** 120°, **b** 140°, **c** 160° and **d** droplet detachment time and mass

Figure 2d exhibits the droplet detachment time and mass variation curves for different contact angles. The droplet detachment time and mass decrease greatly when the contact angle increases from 120° to 140°, which is 0.75 ms, 0.988 × 10^{-3} kg, respectively. The increase in contact angle from 140° to 160° results in a slow decrease in droplet detachment time and mass of 0.16 ms and 0.133 × 10^{-3} kg, respectively. The earlier the droplets are detached, the smaller the mass and the easier the droplets are to exit the flow channel.

3.3 Effect of Different Pore Sizes and Distribution

The growth and detachment processes of droplets in the presence of two liquid pores are given in Fig. 3. The diameter of the left pore is D_1, the diameter of the right pore is D_2, and the distance between the two pores is S. From Fig. 3a–c, it can be seen that the droplet of the first pore detaches and coalesces with the droplet of the second pore at 3.48 ms for $D_1 = D_2 = 25$ μm, which is significantly longer than the droplet detachment time (2.80 ms) for one liquid pore. Until 3.56 ms, the coalesced droplets detached. At $D_1 = 25$ μm and $D_2 = 35$ μm, the first droplet detaches at 3.59 ms. The two coalesced droplets detach at 3.71 ms. When $D_1 = 35$ μm, $D_2 = 25$ μm, the droplets of the two pores coalesce at 2.37 ms, then a liquid film is developed on the flow channel surface, and the droplets cannot detach. Figure 3a, d show two cases with the same pore size, respectively, the former pore size is both 25 μm and the latter pore size is both 35 μm. It is obvious that the increase in pore size hinders the detachment of droplets and tends to develop a liquid film on the flow channel surface, which will affect the transfer of gas into the GDL. Figure 3d, e show the two pores at different distances. It can be seen that after increasing the distance to 180 μm, the first droplet detaches at 3.08 ms and subsequently coalesces with the second pore and detaches at 3.20 ms.

4 Conclusions

MRT–LBM is adopted to simulate the droplet growth process in the PEMFC flow channel and investigated the effects of flow channel height, surface contact angle, and liquid pore size and distribution, respectively. The results show that as the flow channel height decreases, the droplets are more easily detached, and the mass of detached droplets is smaller under the larger air force. The surface contact angle increases from 120 to 160°, the droplet detachment time decreases by 0.91 ms, and the mass decreases by 1.121 × 10^{-3} kg. When there are two liquid pores, the droplet interaction hinders the droplet detachment. When the large pore is in front ($D_1 =$ 35 μm) or both pores are large ($D_1 = D_2 = 35$ μm), a liquid film is developed on the flow channel surface, and the droplet can be detached by increasing the distance between the two pores.

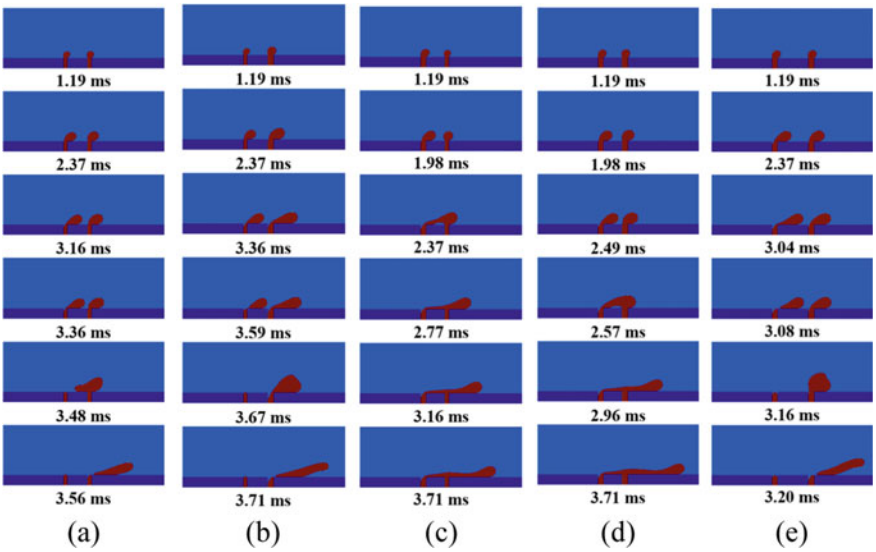

Fig. 3 The processes of droplet growth and detachment in the flow channel for different pore sizes and distributions: **a** $D_1 = D_2 = 25\ \mu m$, $S = 120\ \mu m$; **b** $D_1 = 25\ \mu m$, $D_2 = 35\ \mu m$, $S = 120\ \mu m$; **c** $D_1 = 35\ \mu m$, $D_2 = 25\ \mu m$, $S = 120\ \mu m$; **d** $D_1 = D_2 = 35\ \mu m$, $S = 120\ \mu m$; **e** $D_1 = D_2 = 35\ \mu m$, $S = 180\ \mu m$

Acknowledgements This research work is funded by the National Natural Science Foundation of China, grant number No. 52001045 and No. 51779025; Science and Technology Innovation Foundation of Dalian, China, grant number No. 2021JJ11CG004; Laboratory of Transport Pollution Control and Monitoring Technology, grant number No. Z2209-030.

References

1. Chen L, Chen Y, Tao WQ (2023) Schroeder's paradox in proton exchange membrane fuel cells: a review. Renew Sustain Energy Rev 173:113050
2. Deng H, Jiao K, Hou YZ, Park JW, Du Q (2019) A lattice Boltzmann model for multi-component two-phase gas-liquid flow with realistic fluid properties. Int J Heat Mass Transf 128:536–549
3. Hou YZ, Deng H, Du Q, Jiao K (2018) Multi-component multi-phase lattice Boltzmann modeling of droplet coalescence in flow channel of fuel cell. J Power Sources 393:83–91
4. Moslemi M, Javaherdeh K, Ashorynejad HR (2022) Temperature effect on moving water droplets at the channel of PEMFC by multi-component multiphase lattice Boltzmann method. J Appl Comput Mech 159:1–16
5. Choi K, Kim H, Moon S (2011) Numerical studies on the geometrical characterization of serpentine flow-field for efficient PEMFC. Int J Hydrogen Energy 36:1613–1627
6. Han B, Yu J, Meng H (2012) Lattice Boltzmann simulations of liquid droplets development and interaction in a gas channel of a proton exchange membrane fuel cell. J Power Sources 202:175–183
7. Hao L, Cheng P (2009) Lattice Boltzmann simulations of liquid droplet dynamic behavior on a hydrophobic surface of a gas flow channel. J Power Sources 190:435–446

8. Liao JD, Yang GG, Li SA, Shen QW, Jiang ZH, Wang H, Li Z (2022) Study of droplet flow characteristics on a wetting gradient surface in a proton exchange membrane fuel cell channel using lattice Boltzmann method. J Power Sources 529:231245
9. Li Q, Luo KH (2013) Achieving tunable surface tension in the pseudopotential lattice Boltzmann modeling of multiphase flows. Phys Rev E 88:053307

Deviation Control and Fast Drilling Technologies in the Carboniferous Strata of Junggar Basin

Hongshan Zhao, Min Zeng, and Jingyang Xi

Abstract The Carboniferous strata deep in Junggar basin have great exploration potential. The previous drilling practice showed that its geological conditions are very complicated, such as poor drillability and difficult deviation control, which severely influence drilling speed and increase downhole risk, so research on deviation control and fast drilling technologies was conducted to accelerate the exploration and development of Carboniferous strata. Technical difficulties and deviation causes of Carboniferous strata in Junggar basin were analyzed and summarized. Through analyzing their technical advantages and adaptability, it was presented that gas drilling, compound drilling with impregnated diamond bit and turbodrill and automatic vertical drilling were three effective drilling technologies for deviation control and fast drilling in the Carboniferous strata. Through comparatively analyzing the deviation correction ability of tapered drill string assembly, single stabilizer pendulum assembly and double stabilizer pendulum assembly with trend angle of deviation, the deviation correction ability of three assemblies were significantly decreased along with WOB increasing, and the deviation control ability of single stabilizer pendulum assembly was best when WOB was bigger, while the deviation correction ability of double stabilizer pendulum assembly was best when WOB was smaller. All the technical solutions have important guiding for drilling in the Carboniferous strata of Junggar basin.

Keywords Deviation control and fast drilling · Gas drilling · Automatic vertical drilling · Compound drilling · Design of anti-deviation BHA

H. Zhao (✉) · J. Xi
Drilling Technology Research Institute, Sinopec Shengli Oilfield Service Corporation, 827# Beiyi Road, Dongying City, Shandong Province, China
e-mail: zhaohongshan2002@126.com

J. Xi
e-mail: xijy23.ossl@sinopec.com

M. Zeng
Petroleum Development Center Co. Ltd., Sinopec Shengli Oilfield Company, 89# Liaocheng Road, Dongying City, Shandong Province, China
e-mail: t-zengmin.slyt@sinopec.com

S. Yadav et al. (eds.), *Energy Power and Automation Engineering*, Lecture Notes in Electrical Engineering 1118, https://doi.org/10.1007/978-981-99-8878-5_5

1 Introduction

Because the Carboniferous strata of Junggar basin have great exploration potential, many oil and gas fields such as Sx oilfield, Dx gasfield, Wcw oilfield have been discovered in the strata, and several deep exploration wells such as Wc-1 well and Y-2 well have been deployed successively in recent years.

According to the analysis of adjacent wells drilled, the geological conditions of the Carboniferous strata are extremely complex, and some factors such as high rock strength, strong abradability, poor drillability and prominent well deviation have seriously affected the drilling speed and increased the downhole risk, which has become the main technical bottleneck restricting the deep Carboniferous exploration wells.

In view of the geological characteristics and technical difficulties of Carboniferous strata, the anti-deviation mechanism of new drilling technologies, such as gas drilling, compound drilling with impregnated diamond bit and turbodrill, and automatic vertical drilling, was studied, and the comparison and analysis of several commonly used anti-deviation bottom hole assembly (BHA) were carried out by using the index of "well deviation trend angle," which had an important guiding significance for the deviation control and fast drilling of Carboniferous strata in the future.

2 Analysis of Drilling Difficulties in the Carboniferous Strata

2.1 Difficulties of Deviation Control and Fast Drilling

The Carboniferous strata of Junggar basin are dominated by igneous rocks with multiple types and complex lithology, which are widely distributed in the western uplift, Luliang uplift, central uplift and eastern uplift in the basin. Based on the analysis of the drilled data, the following technical difficulties exist in the deviation control and fast drilling of the formation:

- Igneous rock has high hardness and poor drillability. According to the core test results of Wc-1 well, its cone bit drillability level is as high as 7.6 ~ 8.5, and the rock hardness is 2500 ~ 2900 MPa. In addition, there are volcanic breccia and sandy gravel in local strata. It not only limits the use of PDC bits, but also makes the cone bit prone to skip and break teeth. As the drilling continues, the bit damage is gradually intensified, and the rate of penetration (ROP) is also sharply reduced. According to statistics, the ROP of igneous rocks in Wc-1 well is only 0.74 m/h, and the average drill bit footage is less than 40 m.

- Well deviation problem is prominent. During drilling in the Carboniferous strata of Wc-1 well, well deviation had been increasing continuously, with a maximum deviation of 12.82°/5143 m. The pendulum drill, pendulum + screw drill and torsion impact drill were used successively, which had not achieved good drilling results. Due to the increase of well deviation, the use of drilling parameters is limited, which is also the main reason for the low ROP.
- The thickness of igneous rock is very large. According to the previous drilling data, the thickness of igneous rock in Wc-1 well of Wulungu area is 692 m, that in Lu3 well of Luliang uplift is 922 m, that in Cai30 well of Wcw area is 1126 m, and that in Hs-3 well of western uplift is estimated to be more than 3200 m.

2.2 Causes of Well Deviation During Drilling

The causes of well deviation in the Carboniferous strata of Junggar basin are as follows:

- The stratum inclination is high in many areas. For example, the inclination of complex strata such as Tugulu anticline and Horgus anticline is between 30 and 70°. The inclination of Ashley area is expected to be above 60° due to the influence of the Tianshan orogeny.
- In Piedmont area, it is easy to tilt the borehole toward the direction of formation stress release due to strong tectonic movement. In addition, strong tectonic movement resulted in a large number of faults and fault zones, when drilling in these fault zones, the bit is prone to slip along the fracture surface, which causes well deviation.
- The drillability of igneous rocks is quite different and the fractures are developed, which is easy to make the borehole extend along the direction of good drillability.

3 New Drilling Technologies Suitable for the Carboniferous Strata

3.1 Gas Drilling Technology

As a special under-balanced drilling technology, gas drilling has significant technical advantages in improving ROP, shortening drilling cycle, reducing drilling cost, protecting and discovering oil and gas fields, etc. [1, 2].

Db-1 well in Xinjiang Oilfield is a vertical wildcat well deployed in Luliang uplift of Junggar Basin. Gas drilling was applied in the igneous rocks of 3365–3924.56 m interval of Φ215.9 mm borehole, with a footage of 559.56 m and an average ROP of 5.26 m/h, which was 4.28 times faster than that (1.23 m/h) of adjacent intervals

when drilling with drilling fluid [3]. This indicates that gas drilling can be performed in the Carboniferous igneous rocks to increase ROP.

Well deviation has always been a prominent problem encountered during gas drilling. Considering downhole safety and other factors, there is little use of stabilizer to adjust the performance of BHA to achieve anti-deviation, so there is no effective anti-deviation technical means for gas drilling.

According to statistics, about 30% of the gas drilling wells have deviated beyond the standard or seriously exceeded the standard. By studying the cause of well deviation in gas drilling, it is pointed out that formation anisotropy, formation inclination, borehole enlargement rate, BHA structure and weight on bit (WOB) are the main factors, and corresponding anti-deviation measures for gas drilling were put forward as follows:

Deviation Control by Air Hammer Gas Drilling

Air hammer drilling is a drilling technology which uses high pressure gas medium to transfer energy to achieve high-frequency (800–1900 times/min) impact rock breaking. Compared with conventional drilling methods, it can improve the ROP in hard brittle and high abrasive formation, and at the same time, it can achieve good anti-deviation effect [4, 5].

During air hammer gas drilling, because the WOB applied is small (10 ~ 30 kN) and the rotational speed is low (20 ~ 30 r/min), it has the characteristics of low WOB and low rotational speed and plays a unique role in anti-deviation, and well deviation can be basically controlled within 2°. As shown in Fig. 1, variation of well deviation during air hammer drilling in Well Hs-101 is given.

Deviation Control by Pendulum Drill

The pendulum drill is used to prevent well deviation by restricting the lateral deflection force on the bit with the pendulum force generated by the gravity of the drill string under the centralizer.

Compared with drilling fluid drilling, because there is no loss of collar buoyancy in gas drilling, the pendulum force is greater, and pendulum drill is more effective in gas drilling.

At present, a special centralizer for gas drilling has been developed. The entrance shape of its diversion groove is optimized by fluid numerical simulation technology. It can ensure that debris from any direction and angle enter the diversion groove smoothly, and will not stay and accumulate at the centralizer, which can effectively solve the problems during drilling with conventional centralizer.

Automatic Vertical Gas Drilling Technology

Based on the principles of aerodynamics and fluid–solid coupling, a split-flow automatic vertical drilling tool for gas drilling is designed by using the reaction force of the gas split-flow jet to adjust the lateral force of drill bit [6].

It can realize the automatic induction and correction of well deviation and achieve the purpose of vertical drilling. Its structure is relatively simple, and if developed

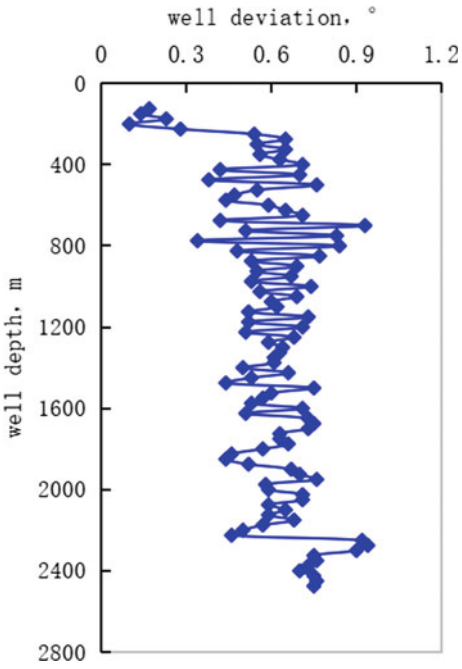

Fig. 1 Variation of well deviation during air hammer drilling in Well Hs-101

and tested successfully, the problem of deviation control and fast drilling during gas drilling can be solved.

3.2 Compound Drilling Technology with Impregnated Diamond Bit and Turbodrill

Field test results show that the compound drilling technology with impregnated diamond bit + turbodrill has the function of deviation control and fast drilling when drilling in the high-steep structure formation. It can greatly increase the ROP or drilling rate of a trip in deep hard-to-drill formations [7, 8].

Compared with screw drill, turbodrill drill has a soft characteristics of high rotational speed and low torque, and its rotational speed can be more than 5 times that of common screw drills. As it works smoothly, drill damage caused by downhole vibration can be reduced and bit life can be prolonged.

Impregnated diamond bit is a self-sharpening drill bit which mainly crushes rock by grinding. The diamond has high wear resistance and is suitable for igneous strata with poor drillability.

Moreover, compared with cone bits, impregnated diamond bit requires the characteristics of low WOB, high rotational speed and low power energy, which are well matched with the output characteristics of turbodrills. Combined with top drive

compound drilling, not only deviation control, but also high ROP and drilling footage can be obtained.

In view of the characteristics of high hardness and poor drillability in Carboniferous igneous strata, when gas drilling cannot continue due to the large amount of water produced from formation and unstable wellbore, compound drilling with impregnated diamond bit and turbodrill is another effective technology to increase the drilling speed in poor drillability and high abrasiveness formation.

For example, compound drilling with impregnated diamond bit and turbodrill was applied in the Carboniferous igneous rocks of 3350.50–3537.00 m interval of Φ215.9 mm borehole in Hs-3 well, with a footage of 186.50 m and an average ROP of 1.71 m/h, which were, respectively, 292% and 130.1% higher than the tricone bits, and the well deviation was always controlled within 1° during drilling.

3.3 Automatic Vertical Drilling Technology

Automatic vertical drilling technology is a downhole intelligent drilling system with mechanical, electrical and hydraulic integrated closed-loop control system, which can realize active deviation correction and keep the borehole vertical. It can release WOB, improve ROP and ensure good borehole quality, and is also an effective drilling technology to realize the deviation control and fast drilling in the Carboniferous formation of Junggar basin.

At present, the automatic vertical drilling system in the world is mainly represented by Verti-Trak system of Baker-Hughes Company and Power-V system of Schlumberger Company. For example, Verti-Trak vertical drilling system was applied in the 3606–3690 m interval of Φ215.9 mm borehole of H-1 well, Junggar basin, and good application results were achieved. The well deviation was corrected successfully from 5.3 to 0.4°, and the average ROP was 0.78 m/h, which was 25.8% higher than that of conventional drilling.

Geosteering and Logging Research Institute of Sinopec has also developed strap-down automatic vertical drilling system suitable for Φ311.2 mm and Φ215.9 mm borehole [9, 10]. As shown in Fig. 2, it is composed of a strap-down stabilization platform and a deviation control and correction mechanism. Under the control of the strap-down stabilization platform, by driving the deviation control and correction mechanism to manipulate the passing-by drilling fluid, a piston pushes the pad toward the borehole wall and a lateral force on the BHA is formed to effectively and correct deviation.

Through field tests and improvements of more than 20 wells, its reliability and life have been verified in the field and gradually become stable. For example, the strap-down vertical drilling system was applied in the 2436–2610.79 m interval of Φ311.2 mm borehole of As-1 well in Guizhou Province. The strata drilled were Permian basalt. During drilling, the well deviation was successfully corrected from 6.25 to 0.25°. The average ROP was 1.02 m/h, and the average footage was 87.4 m, which were, respectively, increased by 25.9% and 18.3% compared with conventional

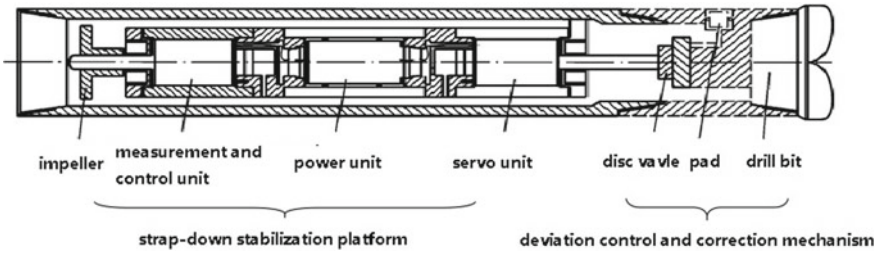

Fig. 2 Sketch diagram of the structure of strap-down vertical drilling system

Table 1 Comparison of drilling results before and after the application of vertical drilling system

Stratum	Well depth (m)	Bit type	Bit footage (m)	ROP (m/h)	WOB (kN)	Variation of well deviation (°)	Drilling mode
Longtan	2230.34–2303.35	HJT537GK	73.01	1.04	200–220	4.9 → 5.1	Conventional drilling
	2303.35–2420.88	HJT537GK	117.53	1.02	200–220	5.1 → 6.01	
Maokou	2420.88–2436	HJT537GK	15.12	0.60	200–220	6.01 → 6.25	
	2436–2518.37	HJT537GK	82.37	1.02	180–220	6.25 → 2.22	Vertical drilling
	2518.37–2610.79	HJT537GK	92.42	1.03	180–200	2.22 → 0.25	Vertical drilling
	2610.79–2684.69	HJT537GK	73.9	0.81	160–180	0.25 → 0.62	Conventional drilling
	2684.69–2709	HJT617G	24.31	0.90	160–180	0.62 → 0.73	

drilling. As shown in Table 1, the drilling results before and after the application of strap-down vertical drilling system were compared.

4 Comparison of Deviation-Reducing Ability of Different Conventional Bottom Hole Assemblies

At present, when designing anti-deviation BHA and optimizing drilling parameters, technicians on drilling site usually take "maximum bit lateral force" (e.g., pendulum BHA) or "minimum bit tilt angle" (e.g., packed hole BHA) as evaluation indexes, not only ignoring the anisotropy of drill bit and formation, but also considering the influence of bit lateral force and bit tilt angle on drilling trend in isolation.

The index of "deviation tendency angle" is based on a bit-rock interaction model, and comprehensively considers the features of drilling bits, the anisotropy of rock, bit lateral force and bit tilt angle [11, 12]. Therefore, the comparison and analysis of deviation-reducing ability of several conventional bottom hole assemblies (tower BHA, single stabilizer and double stabilizer pendulum BHA) by using the index of

"deviation tendency angle" can help field technicians select the appropriate BHA and drilling parameters according to actual formation conditions.

The BHA to be analyzed are as follows: Φ215.9 mm drill bit + Φ177.8 mm drill collar × 2 + (Φ214 mm stabilizer) + Φ177.8 mm drill collar × 1 + (Φ214 mm stabilizer) + Φ165.1 mm drill collar × 3 + Φ127 mm drill pipe, in which the number of stabilizers selected and their placement position are different for different bottom hole assemblies. Other parameters: the anisotropy indices of drill bit and formation are 0.3 and 0.95, respectively, the well enlargement rate is 3%, the well deviation at the bottom is 4°, and the drilling fluid density is 1.10 g/cm^3.

As shown in Fig. 3, the deviation-reducing ability of three conventional anti-deviation bottom hole assemblies under different WOB is compared. It can be seen that the deviation-reducing ability of three anti-deviation assemblies is relatively sensitive to WOB. As WOB increases, the deviation-reducing ability rapidly decreases, and even transforms into the effect of increasing deviation. Taking the tower BHA as an example, when WOB is 20, 80, 120 and 160 kN, the deviation tendency angle is − 0.7, − 0.07, 0 and 0.03°, respectively. It shows that when WOB exceeds 120 kN, the tower BHA no longer has the deviation-reducing ability.

In addition, it can be seen from the diagram that the deviation-reducing ability of three assemblies is different under different WOB. When WOB exceeds 100 kN, the deviation-reducing ability of single stabilizer pendulum BHA is strong, while when WOB is less than 100 kN, the deviation-reducing ability of double stabilizer pendulum BHA is the best.

In summary, for the new drilling technologies such as gas drilling and compound drilling with impregnated diamond bit and turbodrill, when designing the BHA, the wellbore stability, the natural deviation ability in the lower formation, the bit type and drilling parameters selected should be fully considered to optimize the appropriate BHA and achieve the deviation control and fast drilling of Carboniferous strata during drilling.

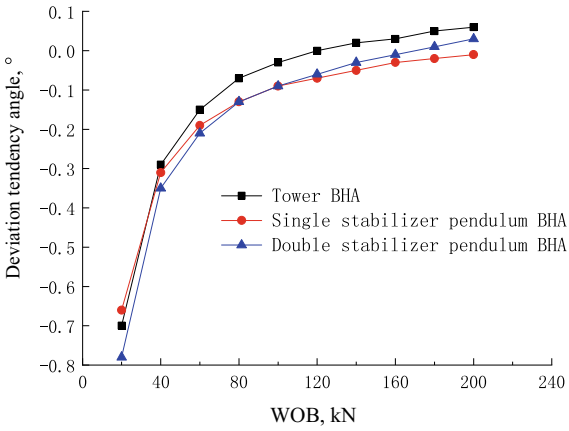

Fig. 3 Comparison of deviation-reducing ability of several conventional bottom hole assemblies

5 Conclusions and Suggestions

(1) In view of the technical problems such as poor drillability and prominent well deviation in the deep Carboniferous formation of Junggar Basin, gas drilling, compound drilling with impregnated diamond bit and turbodrill and automatic vertical drilling are currently three new effective drilling technologies, which can achieve the deviation control and fast drilling of Carboniferous strata.
(2) By comparing the deviation-reducing ability of three conventional assemblies under different WOB, their deviation-reducing ability decreases significantly with the increase of WOB, when WOB is big, the deviation-reducing ability of single stabilizer pendulum BHA is strong, while when WOB is low, the deviation-reducing ability of double stabilizer pendulum BHA is the best.
(3) It is suggested that in the future, the new drilling technologies such as gas drilling and compound drilling should fully consider the wellbore stability, the natural deviation ability in the lower formation, the bit type and drilling parameters to optimize the appropriate BHA, so as to achieve the purpose of deviation control and fast drilling during drilling.

Acknowledgements This study was funded by China Petroleum and Chemical Corporation (P21077-6). This support is gratefully acknowledged by the authors, who are also grateful to the reviewers of this paper for their detailed comments.

References

1. Lu DY, Wang CS, Deng K, Shi YZ, Yang JQ (2020) Practice and understanding of gas drilling in huge thick gravel layer in Tarim oilfield BZ block. Drill Prod Technol 43:8–11
2. Dong SM (2017) Research and application of valve type continuous circulation gas drilling technology. Drill Prod Technol 40:15–16
3. Zhao BZ, Gao LX, Qin LJ (2008) Experiment of air drilling in Dibei-1 well and its result. Oil Drill Prod Technol 30:8–11
4. Niu HB, Feng GT, Zhao HS, Yu HY (2018) Application of air hammer drilling technology in the igneous strata of Well Hashan 101. Oil Drill Prod Technol 40:164–168
5. Ge PF, Ma QT, Guo M (2013) Application of air hammer drilling technology in continental wells of Yuanba block. China Petrol Mach 41:9–12
6. Zhao JH (2008) The design of a lateral jet type automatic vertical gas drilling tool. Petrol Drill Techn 38:15–19
7. Wang SC, Wang WT, Yu S (2016) Combination of turbodrill and impregnated diamond bit to enhance ROP in drilling of wells in piedmont zone, Tarim Basin. Oil Drill Prod Technol 38:156–159
8. Jiang JB, Sun X, Zhao GS, Dong WZ, Wang JC, Wang HW (2011) Technology of deviation control and drilling fast by decelerating turbine in super-deep wells. J China Univ Petrol 35:68–71
9. Wu XX, Duan SJ, Wang QM, Zhang HQ, Zuo YQ, Deng R, Jing XF (2023) Application analysis of rotating and pushing type automatic vertical drilling tool. Mech Eng 21:115–117
10. Sun F, Lv GY, Ma QM (2011) A strap-down automatic vertical drilling system. Acta Petrol Sin 32:360–363

11. Shi YC, Guan ZC, Zhao HS, Huang GL (2017) A new method for build-up rate prediction of bottom-hole assembly in well drilling. J China Univ Petrol 85–89
12. Shi YC, Guan ZC, Xia Y, Ma GJ (2004) Optimizing the design of bottom-hole assembly in deviation control by the trend angle of deviation. Petrol Drill Techn 32:10–12

Study on Dielectric Characteristics of Composite Based on Functional Design

Chen Chen, Hao Liao, Jiaxiao Yan, Yunjie Fang, Chenghui Lin, and Wenbin Zeng

Abstract In recent years, with the rapid development of ultra-high-voltage AC and DC transmission technology, the problem of electric field equalization and regulation of high-voltage electrical equipment has become increasingly prominent. Due to the fact that the conductivity and dielectric constant of nonlinear insulating materials can vary with the intensity of the electric field, they have excellent effects on homogenizing the distribution of the electric field and inhibiting the accumulation of electric charges. Using them to manufacture insulation for high-voltage electrical equipment is expected to improve the reliability and structural compactness of products, ensure the stable operation of the power grid, and solve the problem of uneven voltage distribution. The purpose of this thesis is to explore a composite dielectric material with high dielectric properties and good processability. Using $BaTiO_3$ powder as functional phases, epoxy resin (EP) as matrix phase, a solution blending method was used to prepare $BaTiO_3$/EP composite materials to investigate for its dielectric characteristics.

Keywords Dielectric characteristics · Epoxy resin · Inorganic filler phase

1 Introduction

When spacecraft is operating in space, due to the impact of external environments such as radiation and extreme temperatures, a large amount of electric charges can accumulate on the surface and deep layers of materials. When electric charge accumulates to a certain extent, it will generate a very strong electrostatic field, which can induce different forms of pulse discharge, leading to circuit board breakdown, making the instrument unable to operate normally, seriously affecting the operation of sensitive components on spacecraft, and making it unreliable. Therefore, the study of the charging mechanism, dielectric properties, and protective technology of

C. Chen (✉) · H. Liao · J. Yan · Y. Fang · C. Lin · W. Zeng
School of Electronical Engineering, Zhejiang University of Water Resources and Electric Power, Hangzhou, China
e-mail: cc@zjweu.edu.cn

S. Yadav et al. (eds.), *Energy Power and Automation Engineering*, Lecture Notes in Electrical Engineering 1118, https://doi.org/10.1007/978-981-99-8878-5_6

dielectric materials has become a hot topic in recent years, and the study of composite dielectric materials with better performance has also been a key and difficult point to be overcome in aerospace technology [1].

Epoxy resin (EP) has excellent electrical insulation, adhesion, and high strength, making it a common material for circuit boards, making it important in many industries. In order to release the space charge accumulated inside the spacecraft more quickly, material modification technology can be used to achieve this requirement, namely, to study its nonlinear conductivity performance. Through literature review, it is found that there is currently very little research on the modification of space dielectric materials to achieve charged protection technology. Moreover, it is not perfect to solve the problem of uneven voltage distribution of insulation equipment or components in high-voltage power systems by adding zinc oxide to improve the conductivity of epoxy resin [2]. Boron nitride should also be co-doped to improve its electrical insulation and thermal stability [3]. The use of material modification technology allows for faster release of space charges accumulated within the spacecraft, thereby enabling it to withstand uneven voltages well, thereby greatly improving the performance of insulating materials.

The distribution of electric fields borne by insulating equipment or components in high-voltage power transmission and transformation systems is often extremely uneven. For example, the insulation portion of cable terminals, the high-voltage end portion of various insulators, and other materials with nonlinear electrical parameters can have their conductivity or dielectric constant adaptively changed with the spatial electric field, thereby achieving the effect of intelligently improving the uniformity of the spatial electric field distribution of insulating media. It can be used to alleviate the high electric field locally concentrated in high-voltage equipment [4–9]. The polymer nanocomposites studied by Toyata Group have opened up a new level in the field of inorganic nanomaterials. The preparation of polymer inorganic nanocomposites using fillers from inorganic nanomaterials has a wide range of applications in automotive, aerospace, construction, and electronic industries due to its unique properties [10, 11]. The constitutive equation of epoxy resin was derived from rheological experiments. Although it also belongs to the range of empirical models, the parameters have clear physical significance, which can better reveal the rheological properties of polymer materials. Polymer nanocomposites refer to materials composed of fillers that are nano-sized in at least one dimension by introducing them into a polymer matrix in a certain way [12]. Through a detailed understanding of the current research situation at home and abroad, this design adds nanomaterials to organic polymer compounds, making the polymer material modified into a nonlinear composite conductivity material, which has excellent nonlinear conductivity characteristics and solves the problem caused by uneven voltage distribution. At the same time, its ability to withstand voltage is also improved, and it also maintains good mechanical properties and thermal stability.

In this study, using the high dielectric inorganic filler phase $BaTiO_3$ as functional phases, epoxy resin (EP) as matrix phase, a solution blending method was used to prepare the composite materials to investigate for its dielectric characteristics. The

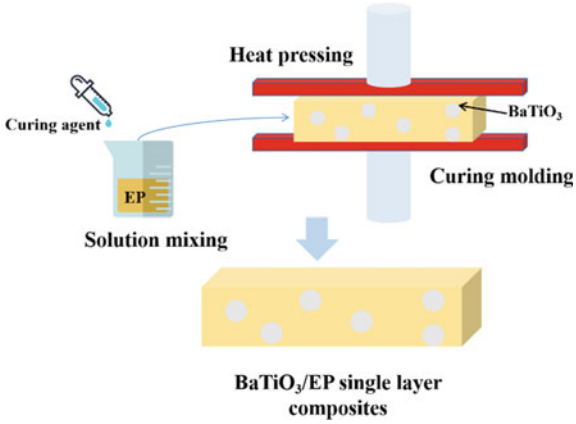

Fig. 1 Schematic diagram of preparation process

$BaTiO_3$/EP single layer composites obtained corresponding dielectric constant of 5.3 and dielectric loss of 0.02 at different volume fraction.

2 Experimental Section

2.1 Preparation of $BaTiO_3$/EP Single Layer Composites

The above-mentioned specific preparation process is shown in Fig. 1.

As shown in the preparation process in Fig. 1, the purchased $BaTiO_3$ NP is first mixed with a silane coupling agent in alcohol, and then subjected to ultrasonic dispersion, centrifugation, and heating drying to obtain surface modified nano-fillers. Then, the EP is weighed into a beaker, and the surface modified $BaTiO_3$ NP is weighed according to the volume fractions of 1.5 vol.%, 3 vol.%, and 4.5 vol.%, respectively, and added to the beaker. Then, a mechanical stirrer is used to stir at 80 °C for 2 h to completely dissolve $BaTiO_3$ NP. Dissolve and evenly disperse $BaTiO_3$ NP, add curing agent MTHHPA, and then place the beaker in a vacuum oven and stir for 0.5 h. Finally, take out the beaker, use a syringe to push the composite material into the preheated mold, and use a flat vulcanizer to heat and cure. The curing process is carried out in stages at 80 °C/2 h + 100 °C/2 h + 120 °C/6 h.

2.2 Characterization and Performance Testing

Using X-ray diffraction (XRD) and Cu Kα to detect the phase composition of the thin film at 40 kV and 40 mA. The surface and cross-sectional morphology of composites were observed using field emission scanning electron microscopy (FESEM).

For the measurement of dielectric parameters, aluminum electrodes (25 mm diameter) are deposited on both sides of composites, and the relative dielectric constant, conductivity and dielectric loss tangent values are obtained by using a broadband Impedance analyzer at room temperature in the frequency range of 10 Hz ~ 1 MHz. For the breakdown performance test, more than 10 samples were selected from each group and subjected to a breakdown electric field strength test.

3 Results and Discussion

3.1 Characterization of $BaTiO_3$/EP Single Layer Composites

As shown in Fig. 2, the abscissa 2θ of the atlas is the diffraction angle, representing the diffraction direction, also known as the position of the peak. The ordinate is the peak intensity, which is the diffraction intensity. The abscissa and ordinate correspond to the corresponding characteristic plane, from which phase analysis is performed. In Fig. 2, for the epoxy resin material, a peak with relatively high intensity of diffraction peak can be clearly seen when the abscissa angle is about 15°. For $BaTiO_3$ high dielectric filled phases, their characteristic diffraction peaks can be found at corresponding angles. For the composite media involved in this article, they are all pure phases, without the introduction of other phases [13, 14].

As can be seen from Fig. 3, the cross-section morphology of pure epoxy resin is river like, with certain ductile deformation, and the cross-section of composite medium is brittle deformation. The cross-section of the composite medium has no bubbles, obvious voids or cracks, and the cross-section is relatively smooth, indicating that the powder is evenly dispersed in the composite medium and there is no obvious agglomeration phenomenon inside. The original structure of the matrix has not been damaged, and the composite material still retains the flexibility of the original polymer matrix.

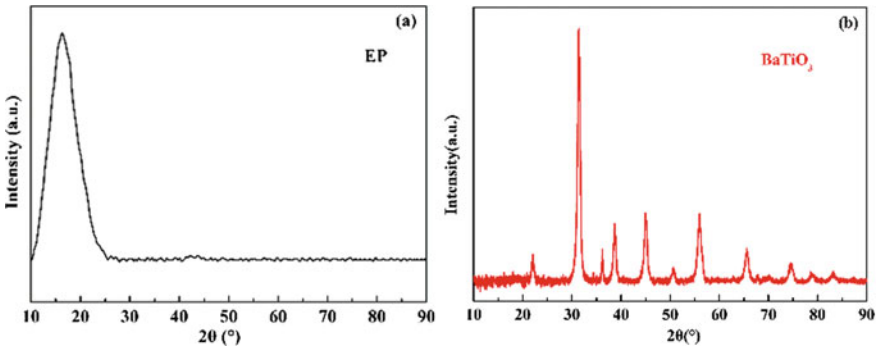

Fig. 2 XRD patterns of $BaTiO_3$/EP composites

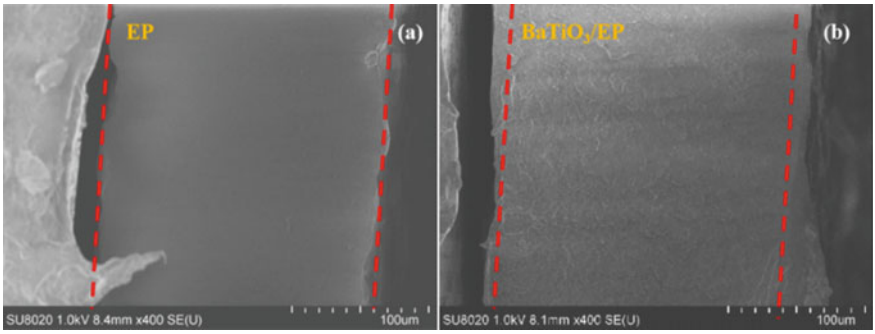

Fig. 3 SEM spectra of $BaTiO_3$/EP composites

3.2 Dielectric Characteristics of $BaTiO_3$/EP Single Layer Composites

The dielectric constant of the $BaTiO_3$/EP single layer composites at different frequency can be seen from Fig. 4. As the volume fraction increases, the dielectric constant of the composite material will also increase. The dielectric constant of the pure epoxy resin material is about 3.84 at a frequency of 10 Hz. When the volume fraction of $BaTiO_3$ NPs is 4.5 vol.%, the dielectric constant of the composite material increases to 5.28 at a frequency of 10 Hz. The increased dielectric constant of the former one may be attributed to the interfacial polarization between the inorganic layer and polymer layer [15, 16], it also means that the addition of high dielectric inorganic filler phases can effectively improve the dielectric constant of epoxy resin composites.

Figure 5 shows the dielectric loss of the $BaTiO_3$/EP single layer composites at different frequency states. With the introduction of $BaTiO_3$, the dielectric loss of composite materials has achieved a trend of first decreasing and then increasing in the lower frequency range. The reduced dielectric loss means that the introduction of $BaTiO_3$ at a low filling ratio can inhibit the dielectric loss of the epoxy resin itself within a certain range, while the increased dielectric loss is due to the fact that with the increase of the filling ratio, BT tends to form agglomeration within the composite, which increases the overall conductivity loss of the composite [17, 18].

Figure 6 shows the variation curve of the electrical conductivity of the thin film with frequency at room temperature. As can be seen from Fig. 6, with the increase of frequency, the conductivity of the thin film also increases, indicating that the conductivity of the composite thin film presents a strong frequency dependence. The logarithm of AC conductivity and the logarithm of frequency have an approximate linear relationship, which to some extent indicates that the insulation performance of the composite thin film is good.

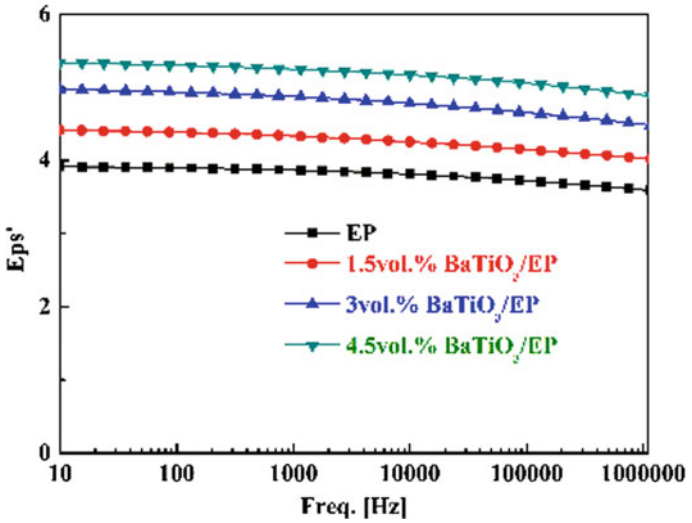

Fig. 4 Frequency-dependent changes of the dielectric constant of $BaTiO_3$/EP composites

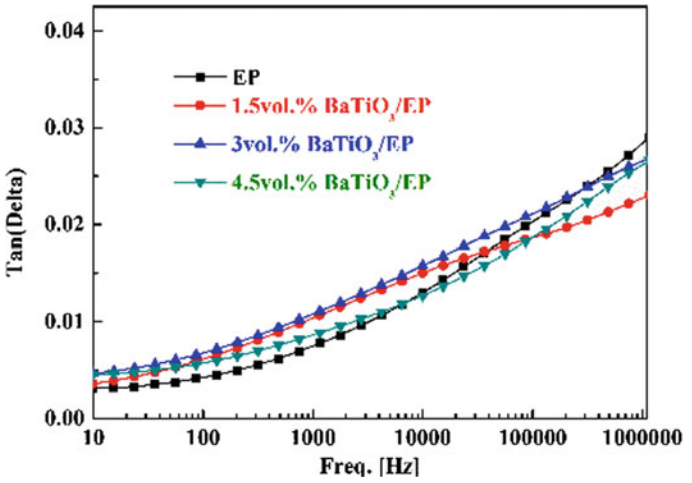

Fig. 5 Frequency-dependent changes of the dielectric loss of $BaTiO_3$/EP composites

4 Breakdown Characteristics of $BaTiO_3$/EP Single Layer Composites

Using two parameters to describe the breakdown strength [19, 20], as shown in Table 1,

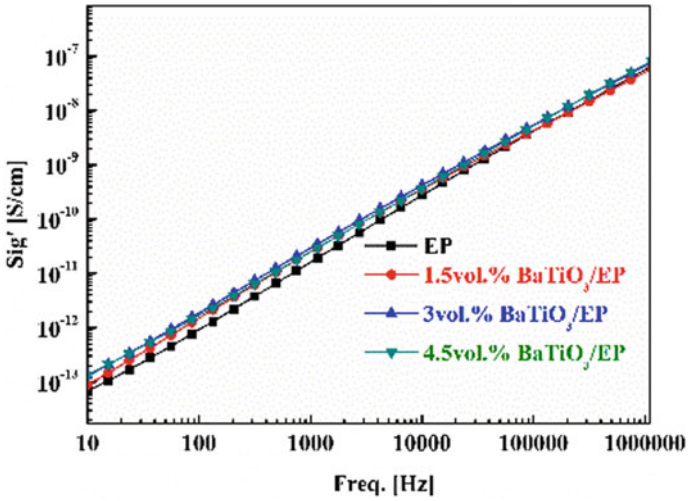

Fig. 6 Frequency-dependent changes of the conductivity of $BaTiO_3$/EP composites

$$P(E) = 1 - \exp\left(-(E/E_0)^{\beta_0}\right) \tag{1}$$

where $P(E)$ is the cumulative probability of failure, E is the breakdown strength, β_0 is a shape parameter, E_0 is the breakdown field strength when $P(E) = 63.28\%$, which can be used to compare the breakdown strength of the same material at different temperatures. The linear regression equation obtained by taking the logarithmic deformation of equation is

$$\ln(-\ln(1 - P(E))) = \beta_0(\ln E - \ln E_0) \tag{2}$$

$\ln(-\ln(1 - P(E)))$ and $\ln E$ are plotted in Fig. 7. It can be found that with the introduction of $BaTiO_3$, the breakdown field strength of the composite exhibits a trend of first increasing and then decreasing, which means that a certain volume fraction of doping can affect the breakdown characteristics of the epoxy resin material itself to a certain extent.

Table 1 Linear fitting results and Weibull parameters of $BaTiO_3$/EP composites

Sample	Linear fitting results			S	Weibull parameters	
	Slope	$\ln(-\ln(1 - P(E)))$	R		β_0	E_0
EP	6.54	− 27.09	0.80	1.09	6.54	62.9
1.5 vol.%	6.05	− 31.87	0.98	0.27	6.05	193.9
3 vol.%	9.80	− 48.97	0.94	0.80	9.80	147.9
4.5 vol.%	2.88	− 13.59	0.86	0.43	2.88	112.0

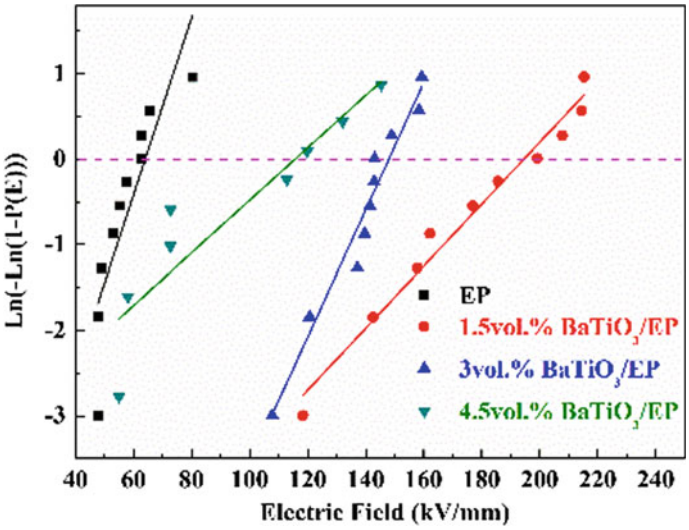

Fig. 7 The breakdown characteristics of $BaTiO_3$/EP composites

5 Conclusion

The application prospects of polymer composite materials with excellent mechanical properties, light weight, low cost, and easy processing are broad. This study uses high dielectric inorganic filler phase $BaTiO_3$ as the functional phase and epoxy resin (EP) as the matrix phase to prepare composite materials using solution blending method and study their dielectric properties. The research results indicate that a certain volume fraction of filling can improve the dielectric constant and breakdown field strength of $BaTiO_3$/EP composite materials. For example, when the volume fraction is 4.5 vol.%, the dielectric constant of the composite material is 5.3, and the breakdown field strength is 110 kV/mm. Good insulation performance will be beneficial for the application of EP in the field of high-temperature insulation materials.

Acknowledgements The work was supported in part by the Zhejiang University Student Innovation and Entrepreneurship Training Plan Project No. S202211481059. The National Natural Science Foundation of China under Grant No. 61975189, in part by the Zhejiang Provincial Natural Science Foundation of China under Grant No. LZY22E030003, Grant No. LD21F050001, and Grant No. Y21F040001. The Key Research Project by Department of Water Resources of Zhejiang Province under Grant No. RA2101, the Key Research and Development Project of Zhejiang Province under Grant No. 2021C03019.

References

1. Guney MS, Tepe Y (2016) Classification and assessment of energy storage systems. Renew Sustain Energy Rev 75:1187–1197
2. Liu C, Li F, Ma LP, Cheng HM (2010) Advanced materials for energy storage. Adv Mater 22:28–62
3. Panwar NL, Kaushik SC, Kothari S (2011) Role of renewable energy sources in environmental protection: a review. Renew Sustain Energy Rev 15:1513–1524
4. Wang YF, Cui J, Yuan QB, Niu YJ, Bai YY, Wang H (2015) Significantly enhanced breakdown strength and energy density in sandwich-structured barium titanate/poly(vinylidene fluoride) nanocomposites. Adv Mater 27:6658–6663
5. Liu FH, Li Q, Cui J, Li ZY, Yang G, Liu Y, Dong LJ, Xiong CX, Wang H, Wang Q (2017) High-energy-density dielectric polymer nanocomposites with trilayered architecture. Adv Funct Mater 27:1606292
6. Prateek, Thakur VK, Gupta RK (2016) Recent progress on ferroelectric polymer-based nanocomposites for high energy density capacitors: synthesis, dielectric properties, and future aspects. Chem Rev 116:4260–4317
7. Guo MF, Jiang JY, Shen ZH, Lin YH, Nan CW, Shen Y (2019) High-energy-density ferroelectric polymer nanocomposites for capacitive energy storage: enhanced breakdown strength and improved discharge efficiency. Mater Today 29:49–67
8. Jiang JY, Zhang X, Dan ZK, Ma J, Lin YH, Li M, Nan CW, Shen Y (2017) Tuning phase composition of polymer nanocomposites toward high energy density and high discharge efficiency by nonequilibrium processing. ACS Appl Mater Interfaces 9:29717–29731
9. Zhou Y, Li Q, Dang B, Yang Y, Shao T, Li H, Hu J, Zeng R, He JL, Wang Q (2018) A scalable, high-throughput, and environmentally begin approach to polymer dielectrics exhibiting significantly improved capacitive performance at high temperatures. Adv Mater 30:1805672
10. Azizi A, Gadinski MR, Li Q, AlSaud MA, Wang JJ, Wang Y, Wang B, Liu FH, Chen LQ, Alem N, Wang Q (2017) High-performance polymers sandwiched with chemical vapor deposited hexagonal boron nitrides as scalable high-temperature dielectric materials. Adv Mater 29:1701864
11. Shi YM, Li HN, Li LJ (2015) Recent advances in controlled synthesis of two-dimensional transition metal dichalcogenides via vapour deposition techniques. Chem Soc Rev 44:2744–2756
12. Fernández-Sánchez ME, Barbier S, Whitehead J, Béalle G, Michel A, Latorre-Ossa H, Rey C, Fouassier L, Claperon A, Brullé L, Girard E, Servant N, Rio-Frio T, Marie H, Lesieur S, Housset C, Gennisson JL, Tanter M, Ménager C, Fre S, Robine S, Farge E (2015) Mechanical induction of the tumorigenic β-catenin pathway by tumour growth pressure. Nature 523:92–95
13. Kikutani S, Nakajima K, Nagasato C, Tsuji Y, Miyatake A, Matsuda Y (2016) Thylakoid luminal θ-carbonic anhydrase critical for growth and photosynthesis in the marine diatom *Phaeodactylum tricornutum*. Proc Natl Acad Sci U S A 113:9828–9833
14. Kim KK, Hsu A, Jia XT, Kim SM, Shi YM, Hofmann M, Nezich D, Rodriguez-Nieva JF, Dresselhaus M, Palacios T, Kong J (2012) Synthesis of monolayer hexagonal boron nitride on Cu foil using chemical vapor deposition. Nano Lett 12:161–166
15. Zhang Y, Zhang CH, Feng Y, Zhang TD, Chen QG, Chi QG, Liu LZ, Wang X, Lei QQ (2019) Energy storage enhancement of P(VDF-TrFE-CFE)-based composites with double-shell structured BZCT nanofibers of parallel and orthogonal configurations. Nano Energy 66:104195
16. Xie YC, Yu YY, Feng YF, Jiang WR, Zhang ZC (2017) Fabrication of stretchable nanocomposites with high energy density and low loss from cross-linked PVDF filled with poly(dopamine) encapsulated $BaTiO_3$. ACS Appl Mater Interfaces 9:2995–3005
17. Wang YF, Cui J, Yuan QB, Niu YJ, Bai YY, Wang H (2015) Significantly enhanced breakdown strength and energy density in sandwich-structured barium titanate/poly(vinylidene fluoride) nanocomposites. Adv Mater 27:6657

18. Li Q, Zhang GZ, Liu FH, Han K, Gadinski MR, Xiong CX, Wang Q (2014) Solution-processed ferroelectric terpolymer nanocomposites with high breakdown strength and energy density utilizing boron nitride nanosheets. Energy Environ Sci 8:922–931
19. Pan ZB, Yao LM, Ge GL, Shen B, Zhai JW (2018) High performance capacitors based on $NaNbO_3$ nanowires/poly(vinylidene fluoride) nanocomposites. J Mater Chem A 6:14614–14622
20. Zhang X, Shen Y, Zhang QH, Gu L, Hu YH, Du JW, Lin YH, Nan CW (2014) Ultrahigh energy density of polymer nanocomposites containing $BaTiO_3$@TiO_2 nanofibers by atomic scale interface engineering. Adv Mater 27:819–824

Optimal Operation of CHP Units and Thermal Storage Electric Heating Considering Wind Power Consumption

Gaoqiang Qu, Chengchen Li, Shiqin Wang, Zhaoxi Wang, Zifa Liu, Qingping Zhang, and Peng Wan

Abstract In the background of "dual carbon," as the scale of wind turbines connected to the grid becomes larger, the grid needs to improve the capacity of wind power consumption. At the same time, considering the weak peaking capacity of combined heat and power (CHP) units during the winter heating period in northern regions due to the problem of "heat-determined electricity," a large amount of abandoned wind is generated. In order to limit the wind abandonment and carbon emission, this paper introduces the wind abandonment penalty and carbon trading mechanism and establishes the system operation model with the optimal system operation cost.

Keywords Regenerative electric heating · CHP unit · Wind power consumption · Carbon trading scheme

1 Introduction

Wind power generation belongs to clean energy [1, 2]. Due to its advantages of wide distribution and renewable, the scale of wind turbines connected to the power grid has been increasing [3]. At the same time, due to the large thermal load at night during the heating period in the north, the problem of "fixing power by heat" exists in the thermoelectric units [4], which results in the compression of wind power consumption space in the low period at night. Therefore, it is of great significance to improve the operating characteristics of CHP units, realize thermoelectric decoupling, and reduce the wind abandonment and carbon emission of power system [5].

G. Qu (✉) · Z. Wang · Q. Zhang · P. Wan
State Grid Ningxia Electric Power Co.Ltd, Yinchuan 750001, China
e-mail: qgq300@163.com

C. Li · S. Wang · Z. Liu
School of Electrical and Electronic Engineering, North China Electric Power University, Beijing 102206, China

S. Yadav et al. (eds.), *Energy Power and Automation Engineering*, Lecture Notes in Electrical Engineering 1118, https://doi.org/10.1007/978-981-99-8878-5_7

At present, a large number of scholars have carried out research on the consumption of heating and wind power. In terms of wind power consumption, the literature [6] considers the factor of peak regulation period in the wind power model to increase the local consumption capacity of wind power. The literature [7] considers the wind power factor in the peak-regulating right trading model and proposes a power market model involving wind power to further promote the consumption of wind power. The literature [8, 9] established a heat storage system model, introduced control links to adjust energy storage, and improved the consumption rate of wind power. In terms of improving unit characteristics, the literature [10] improves the problem of "fixing power by heat" by adding heat storage device on the far side and improves the wind abandon absorption by guiding the system on the load side through time-of-use electricity price. The literature [11] established a system model including CHP unit and electric boiler and established a linear model of electric heating characteristics. In terms of regenerative electric heating operation, the literature [12] uses electric boilers to increase the power load of the system and improve the Internet space of wind power. The literature [13] proposes to install regenerative electric heating at the end of the power grid to make use of wind power abandonment. The literature [14] dynamically simulates the heating process of the regenerative device and establishes the relationship between energy utilization rate and heat release of the regenerative device, which is conducive to the establishment of the mathematical model of regenerative electric heating.

Most of the current studies only consider the role of CHP units, heat storage units, and electric boilers in absorbing wind power, rarely consider the combined operation of CHP units and regenerative electric heating, and do not consider the impact of carbon emission mechanism and wind abandonment penalty on system operation. Therefore, this paper establishes a joint optimization operation model of CHP units and regenerative electric heating, which considers carbon trading mechanism [15] and wind abandonment penalty, which can effectively improve the wind power consumption while reducing the system operation cost. The feasibility and superiority of the proposed model are verified through the analysis of numerical examples.

2 CHP Unit and Regenerative Electric Heating Combined Operation System Structure

Wind turbines, coal-fired thermal power units, and CHP units can provide electric energy. While providing electric energy, CHP units use steam generated by turbo-generator to provide thermal power to users, which has a higher energy utilization rate than traditional thermal power units. As a clean energy, wind power generation can reduce carbon emissions of the system, but it has the characteristics of anti-peak regulation. The combined operation of wind power and regenerative electric heating can improve the stability of the power system.

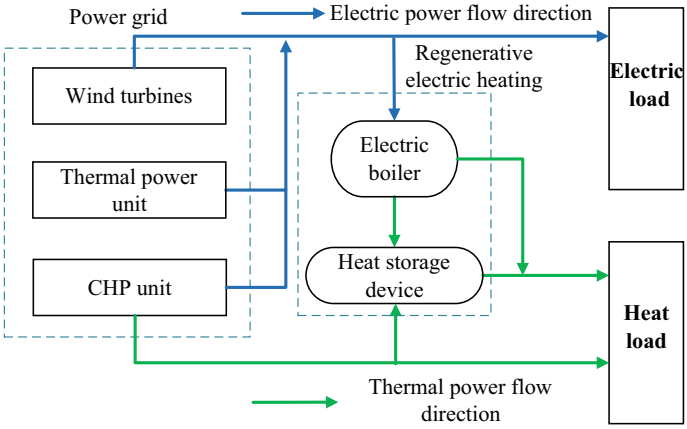

Fig. 1 System operation structure diagram

As a common regenerative electric heating equipment [16], regenerative electric boiler can be divided into two parts, namely direct heat electric boiler and regenerative device. The heat storage device stores heat in the off-peak hours and releases heat in the peak hours, which reduces the output of the CHP unit and improves the economic benefits of the system. As a kind of adjustable load, regenerative electric heating decouples the thermoelectricity produced by thermal power plant, which is conducive to peak regulation of power grid and heat network and improves the absorption rate of new energy. Based on the objective function of minimization of operation cost, this paper considers the wind abandoning penalty and carbon trading mechanism and considers environmental benefits while pursuing economic benefits. The combined operation system structure of CHP unit and regenerative electric heating considering wind power consumption is shown in Fig. 1.

3 Model of Electric-Thermal System Equipment

3.1 Model of Wind Turbine

Wind turbines convert captured wind energy into electricity, whose output power has reverse peak regulation and uncertainty. The output power of the wind turbine is related to the wind speed, as shown in Eq. (1).

$$P_{\mathrm{WT}}(t) = \begin{cases} 0 & , v(t) < v_{\mathrm{CI}} \text{ or } v(t) > v_{\mathrm{CO}} \\ P_{\mathrm{R}} \frac{v(t)-v_{\mathrm{CI}}}{v_{\mathrm{R}}-v_{\mathrm{CI}}} & , v_{\mathrm{CI}} \le v(t) < v_{\mathrm{R}} \\ P_{\mathrm{R}} & , v_{\mathrm{R}} \le v(t) < v_{\mathrm{CO}} \end{cases} \tag{1}$$

Here, P_R is the rated output power of wind power; $P_{WT}(t)$ and $v(t)$ are, respectively, wind power output and wind speed at time t; v_{CI}, v_{CO}, and v_R are, respectively, the wind speed in time t, cut out wind speed, and rated wind speed.

Existing studies show that wind speed follows Weibull distribution [17], and its probability distribution is as follows:

$$f(v) = \frac{k}{c}\left(\frac{v}{c}\right)^{k-1} \exp\left[-\left(\frac{v}{c}\right)^{k}\right] \tag{2}$$

Here, k and c are shape and scale parameters of Weibull distribution, respectively.

3.2 Thermal Power Unit

In this paper, the coal-burning pure condensing unit is used, and its operation mode is steam Rankine cycle. Only electrical power is output during unit operation. The generation cost of thermal power F_G includes the generation fuel cost F_{G1} and start–stop cost F_{G2}, as shown in Formula (3).

$$F_G = F_{G1} + F_{G2} \tag{3}$$

In the formula, the formulas of F_{G1} and F_{G2} are shown in Formula (4) and Formula (5), respectively. Among them, the power generation fuel cost of thermal power unit is expressed in the quadratic form of its power generation, and the formula is shown in Eq. (4).

$$F_{G1} = \sum_{t=1}^{T}\sum_{i=1}^{N}\left(a_i P_{G,i,t}^2 + b_i P_{G,i,t} + c_i\right) \tag{4}$$

Here, F_G is the power generation cost of thermal power unit; T and N, respectively, represent the total operation period and the number of thermal power units in operation. $P_{G,i,t}$ is the output power of the i-th thermal power unit at time t; a_i, b_i, and c_i is the generation cost coefficient of thermal power unit.

$$F_{G2} = \sum_{t=1}^{T}\sum_{i=1}^{N}\left[u_{i,t}\left(1 - u_{i,t}\right)C_i\right] \tag{5}$$

Here, $u_{i,t}$ is the start–stop state of the i-th thermal power unit at time t; C_i is the start–stop cost of the i-th thermal power unit.

3.3 CHP Unit

The thermoelectric ratio of the backpressure CHP unit is fixed, and the electrical output is fixed after the heat load is determined. Compared with the back pressure CHP unit, the extraction steam CHP unit uses steam as the heat source and determines the amount of steam extracted according to the need of heat production. The thermoelectric ratio can be adjusted, and the system has better flexibility. Therefore, in this paper, the extraction CHP unit is used, and its operating characteristics are shown in Fig. 2.

In order to ensure the thermal load demand of the extraction CHP unit, it is not necessary to consider the start–stop cost of the unit. The fuel cost of the CHP unit is shown in Formula (6).

$$F_{\mathrm{C}} = \sum_{t=1}^{T} \sum_{i=1}^{K} \left(a_{i,0} P_{e,i,t}^2 + b_{i,0} P_{e,i,t} + c_{i,0} P_{h,i,t} P_{e,i,t} + d_{i,0} P_{h,i,t}^2 + e_{i,0} P_{h,i,t} + f_{i,0} \right) \tag{6}$$

Here, K is the total number of CHP units; $a_{i,0}$, $b_{i,0}$, $c_{i,0}$, $d_{i,0}$, $e_{i,0}$, and $f_{i,0}$ is the coal consumption coefficient of CHP; $P_{e,i,t}$ and $P_{h,i,t}$, respectively, represent the generating power and heating power at time t of extraction type CHP unit i.

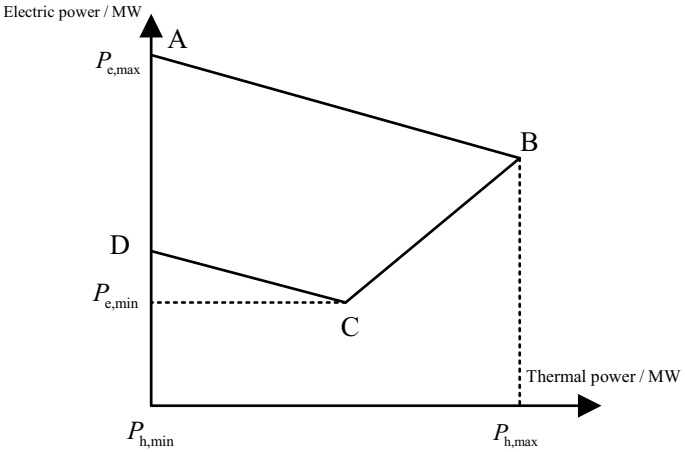

Fig. 2 Thermoelectric relationship of extraction CHP unit

3.4 Regenerative Electric Heating

Despite the randomness of wind power, wind power output is generally large at night, when the grid is in the trough period, resulting in the phenomenon of wind curtailment. Regenerative electric heating uses the "wind curtailment" electricity at night to store the heat generated and release it in the daytime peak hours, which not only improves the economic benefits of the system, but also further expands the consumption space of wind power. In this paper, regenerative electric heating mainly refers to regenerative electric boiler, including electric boiler and heat storage device.

Electric Boiler. The electric boiler provides heat supply through electric power, which is safe and reliable in operation. Its energy conversion efficiency is high, and the energy loss is reduced. At the same time, compared with coal-fired heating, electric boilers have better environmental benefits. The output of CHP units can be further reduced and coal consumption reduced by using wind abandoned electricity for heating at night by electric boilers. The mathematical model of the electric boiler is shown in Eq. (7).

$$P_{h,\mathrm{EB},t} = \eta_{\mathrm{EB}} P_{\mathrm{EB},t} \tag{7}$$

Here, η_{EB} is the thermoelectric conversion efficiency of electric boiler; $P_{h,\mathrm{EB},t}$ and $P_{\mathrm{EB},t}$ are, respectively, the output thermal power and input electric power of the electric boiler at time t.

Heat Storage Device. The electric boiler with heat storage device has a stronger capacity of heating regulation, which breaks the mode of "fixing electricity by heat" and plays the role of thermoelectric decoupling. According to the different ways of heat storage, the regenerative electric heating can be divided into water heat storage, solid heat storage, and phase change heat storage. The mathematical model of the heat storage device can be expressed in Eq. (8).

$$S_{\mathrm{H},t} = (1-\delta) S_{\mathrm{H},t-1} \left(P_{h,\mathrm{H_{in}},t} \eta_{\mathrm{H_{in}},t} - \frac{P_{h,\mathrm{H_{out}},t}}{\eta_{\mathrm{H_{out}},t}} \right) \Delta t \tag{8}$$

Here, $S_{\mathrm{H},t}$ is heat storage capacity at time t; δ is heat dissipation loss rate; $P_{h,\mathrm{H_{out}},t}$ and $P_{h,\mathrm{H_{in}},t}$ are the heat release and heat storage power of the heat storage device at time t, respectively; $\eta_{\mathrm{H_{out}},t}$ and $\eta_{\mathrm{H_{in}},t}$ are, respectively, the heat release and heat storage efficiency of the heat storage device at time t.

4 The Optimal Operation Model of Regenerative Electric Heating and CHP Unit Considering Wind Power Consumption

4.1 Objective Function

In this paper, a joint optimization system of CHP unit and regenerative electric heating is proposed to improve the thermoelectric decoupling capacity of the system, and wind abandonment penalty is considered to further increase the consumption rate of wind power. At the same time, the carbon trading mechanism has been introduced to limit the coal consumption of CHP units and thermal power units, which is conducive to increasing the output of regenerative electric heating and reducing carbon emissions. In this paper, the minimum operation cost of the system is taken as the objective function, that is, the optimal economy of the system operation. The objective function is shown in Eq. (9).

$$F = \min\left(F_G + F_C + F_{\text{wind}} + F_{\text{co}_2}\right) \tag{9}$$

Here, F_{G} is the operating cost of thermal power unit, as shown in Eq. (3); F_C is the operating cost of CHP unit, as shown in Eq. (6); F_{wind} and F_{CO_2} are wind curtailment penalty cost and carbon trading cost, respectively.

(1) Abandon wind punishment

In addition to economy, the goal of system operation should be to reduce air abandonment volume. Therefore, this paper considers the penalty cost of wind abandonment, which is shown in Eq. (10).

$$F_{\text{wind}} = \sum_{j=1}^{M}\sum_{t=1}^{T}\alpha_j\left(P_{\text{SW},t,j} - P_{\text{W},t,j}\right) \tag{10}$$

Here, α_j is the unit wind abandon cost of wind turbine j; $P_{\text{SW},t,j}$ and $P_{\text{W},t,j}$ are the predicted power and generating power at time t of wind turbine j, respectively.

(2) Carbon emission cost

The carbon emissions of the model proposed in this paper mainly come from thermal power units and CHP units, and the carbon emission allocation of the system at time t is shown in Eq. (11).

$$E^* = \beta_{\text{e}}^*\left(\sum_{t=1}^{T}\sum_{i=1}^{N}P_{\text{G},i,t} + \sum_{t=1}^{T}\sum_{i=1}^{K}P_{e,i,t}\right) \tag{11}$$

Here, E^* is the system's free carbon emission quota; β_{e}^* is the free carbon quota per unit of electricity.

The calculation method of actual carbon emission E_a is basically consistent with Eq. (11), but different in the value of carbon emission coefficient. Carbon trading costs are shown in Eq. (12).

$$F_{co_2} = k_C\left(E_a - E^*\right) \tag{12}$$

Here, k_C is the price of carbon trading market.

4.2 Constraints

The normal operation of the system also needs to meet the electrical balance, thermal balance, and operation constraints of each unit and equipment.

(1) Electrical equilibrium constraint

$$\sum_{i=1}^{N} P_{G,i,t} + \sum_{i=1}^{K} P_{e,i,t} + \sum_{j=1}^{M} P_{W,t,j} = P_{e,\text{Load},t} + P_{EB,t} \tag{13}$$

Here, $P_{e,\text{Load},t}$ is the electric load at time t.

(2) Thermal equilibrium constraint

$$\sum_{i=1}^{K} P_{h,i,t} + P_{h,\text{Hout},t} + P_{h,EB,t} = P_{h,\text{Load},t} \tag{14}$$

Here, $P_{h,\text{Load},t}$ is the heat load at time t.

(3) Constraints on thermal power units

The upper and lower limits of unit output are shown in Eq. (15).

$$P_{G,i}^{\min} \le P_{G,i,t} \le P_{G,i}^{\max} \tag{15}$$

The upper and lower limits of unit output are shown in Eq. (16).

$$-\Delta r_{i,\text{ down}} \le P_{G,i,t} - P_{G,i,t-1} \le \Delta r_{i,\text{ up}} \tag{16}$$

Here, $P_{G,i}^{\max}$ and $P_{G,i}^{\min}$ are the maximum and minimum output values of thermal power unit i, respectively; $\Delta r_{i,\text{ up}}$ and $\Delta r_{i,\text{ down}}$ are climbing and downclimbing restrictions of thermal power unit i, respectively. The output and climb limits of CHP units are similar to those of thermal power units.

(4) Constraints on wind turbines

$$0 \le P_{\mathrm{W},t,j} \le P_{\mathrm{W},j}^{\max} \tag{17}$$

Here, $P_{\mathrm{W},j}^{\max}$ is the upper limit of j output of wind turbine.

(5) Constraints of regenerative electric boiler

The constraint of electric boiler is shown in Eq. (18).

$$0 \le P_{\mathrm{EB},t} \le P_{\mathrm{EB}}^{\max} \tag{18}$$

Here, $P_{\mathrm{EB}}^{\max}$ is the maximum electric power of the electric boiler at time t.

The constraints of the heat storage device are shown in Eq. (19).

$$\begin{cases} S_{\mathrm{H,\ min}} \le S_{\mathrm{H},t} \le S_{\mathrm{H,\ max}} \\ 0 \le P_{h,\mathrm{H_{in}},t} \le \eta_{\mathrm{H_{in}},t} S_{\mathrm{H,n}} \\ 0 \le P_{h,\mathrm{H_{out}},t} \le \eta_{\mathrm{H_{out}},t} S_{\mathrm{H,n}} \\ P_{h,\mathrm{H_{in}},t} P_{h,\mathrm{H_{out}},t} = 0 \end{cases} \tag{19}$$

Here, $S_{\mathrm{H,\ min}}$ and $S_{\mathrm{H,\ max}}$ are divided into the minimum and maximum capacities of the heat storage device in normal operation; $S_{\mathrm{H,n}}$ is the rated capacity of the heat storage device.

5 Example Analysis

5.1 Basic Data

In this paper, the winter heating in a northern region is taken as the background. The system is equipped with six pumping steam CHP units and three thermal power units. Among them, the rated electric power of the CHP unit is 300 MW and the rated heating power is 400 MW. The other specific parameters are detailed in the reference [18]. In this paper, day-ahead scheduling is used, with a scheduling cycle of 24 h and a unit scheduling time of 1 h. The parameters of regenerative electric heating are shown in Table 1, and the real-time electricity price is shown in Table 2.

Table 1 Regenerative electric heating parameters

Device attribute	Parameter
Heating power/MW	40
Heat storage/GJ	550
Maximum heat storage temperature/°C	750
Thermal efficiency	95%

Table 2 Real-time tariff

Time	Time period	Electricity price/yuan/kWh
8:00–11:00 18:00–21:00	Peak load period	0.699
7:00–8:00 11:00–18:00	Medium load period	0.548
21:00–7:00	Low load period	0.279

In order to integrate operation cost, wind power consumption, and carbon trading cost, four operation optimization scenarios are proposed in this paper.

Scenario 1: Without carbon trading mechanism, only CHP unit heating is considered, not regenerative electric heating.

Scenario 2: The thermal power output of the CHP unit and the electric boiler meets the thermal load without considering the carbon trading scheme.

Scenario 3: Without considering the carbon trading mechanism, add the heat storage device, and the combined thermal power output of the CHP unit and the regenerative electric heating meets the heat load.

Scenario 4: The model proposed in this paper is adopted, that is, the carbon trading mechanism is taken into account, and the heat load is borne by the joint operation of the CHP unit and the regenerative electric heating.

5.2 Calculation Result

In this paper, the YALMIP toolbox of MATLAB is used to compile and call the solver GUROBI, and the running results under different scenarios are shown in Table 3.

Table 3 shows the results of four optimized operation scenarios. Scenario 2 considers the output of electric boiler on the basis of scenario 1, which can reduce the nighttime output of CHP units, increase the nighttime electrical load demand, and improve the wind power consumption rate. Therefore, scenario 2 has better operating costs and curtailment rate than scenario 1. Scenario 3 adds a heat storage device based on Scenario 2. Compared with the reduction of operating cost and curtailment

Table 3 Optimize the comparison of run scenario results

Running scenario	Wind power consumption / MWh	Carbon trading cost/Ten thousand yuan	Running cost/Ten thousand yuan	Wind abandonment rate/%
1	98.20	0	103.29	84.89
2	186.21	0	92.36	71.35
3	411.23	0	71.21	36.73
4	554.29	2.54	55.40	14.72

rate in scenario 2 and scenario 1, the reduction rate of operating cost in scenario 3 is larger. The reason is that the addition of a heat storage device can not only reduce the output of CHP units at night, but also further reduce the output of CHP units by heat release in the daytime. Due to the existence of peak-valley electricity price, the electricity consumption in the daytime peak hours is reduced, while the consumption of electricity and wind power in the night trough hours is increased, and the operation cost is greatly reduced.

Scenario 4 adds a carbon trading mechanism on the basis of Scenario 3. Although the carbon trading cost of 25,400 yuan is generated, the overall operating cost decreases. After considering the carbon trading mechanism, the system still takes the minimum operation cost as the objective function, so it needs to reduce carbon emissions and reduce the cost of the carbon trading mechanism. Therefore, the system needs to increase the output of regenerative electric heating to reduce the thermal power output of CHP units, so as to reduce the coal consumption of the system. Scenario 4 increases the output of the heat storage device while reducing carbon emissions and further reduces the wind abandonment rate and reduces the cost of wind abandonment by using the characteristics of "peak cutting and valley filling" of regenerative electric heating. Figures 3, 4, 5 and 6 shows the thermal power balance of each scenario.

Figures 3, 4, 5 and 6 shows the comparative analysis of the treatment of CHP units in four scenarios. As can be seen from Fig. 3, when there is no regenerative electric heating involved in heating, the output of CHP units reaches its trough between 8:00 and 17:00 in a day, and the output of CHP units at night is higher. In Fig. 4, electric boiler is added on the basis of CHP unit heating, but CHP unit still maintains

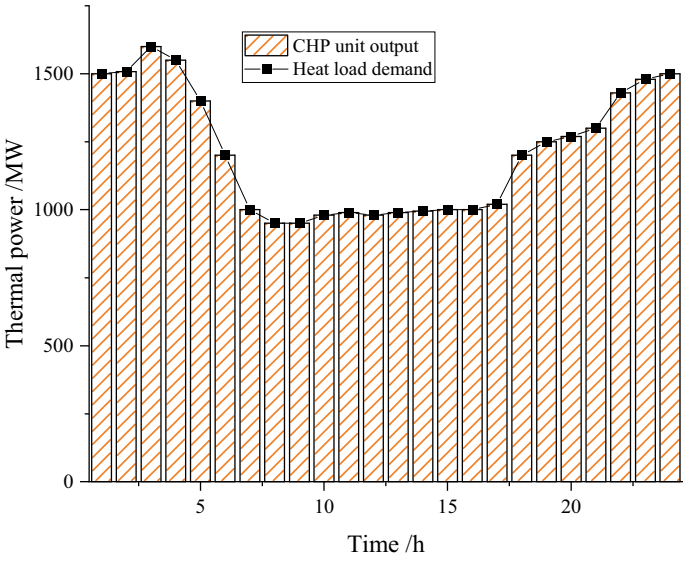

Fig. 3 Thermal power balance diagram for scenario 1

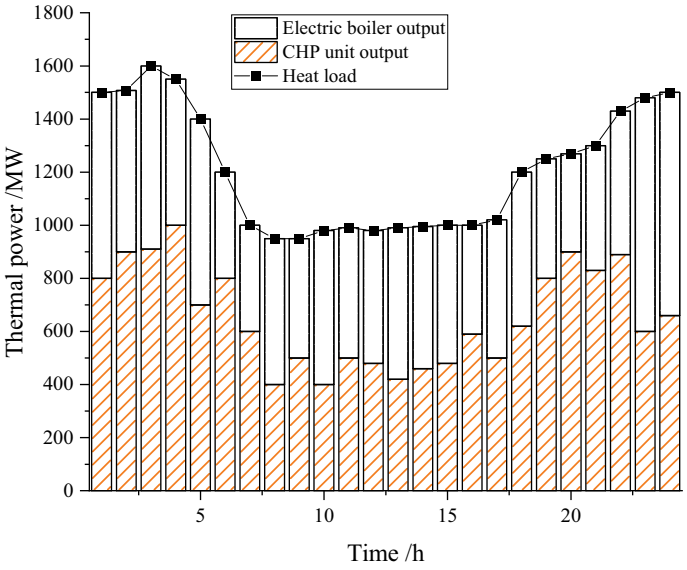

Fig. 4 Thermal power balance diagram for scenario 2

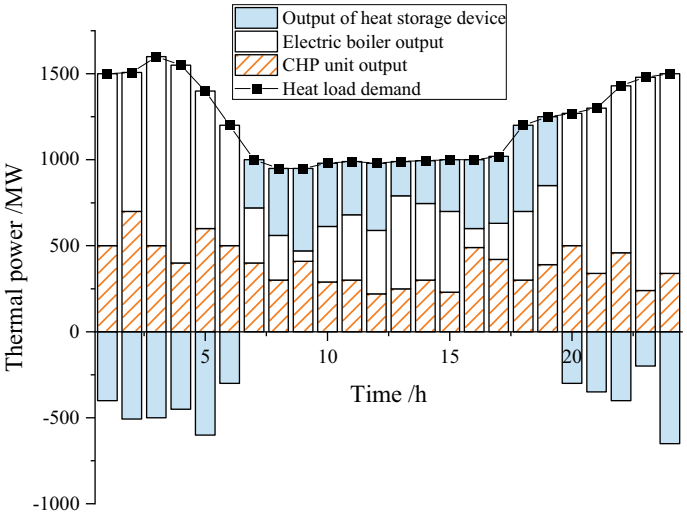

Fig. 5 Thermal power balance diagram for scenario 3

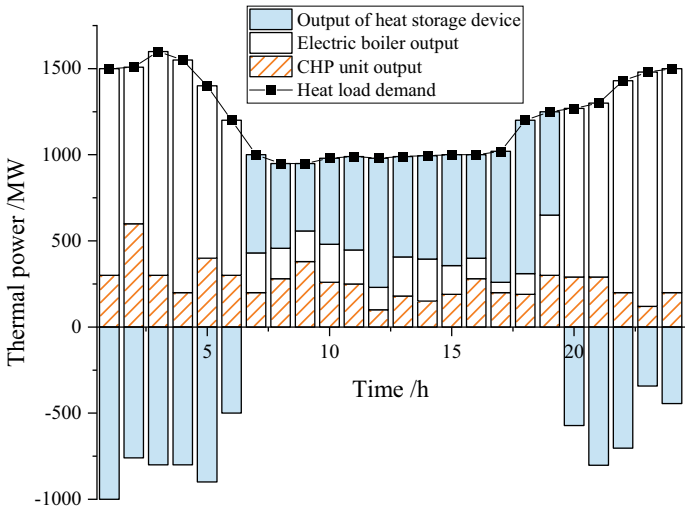

Fig. 6 Thermal power balance diagram for scenario 4

high output; In Fig. 5, a heat storage device is added on the basis of scenario 2, which effectively reduces the output of CHP units and correspondingly reduces the wind power discard volume. In Fig. 6, the carbon trading mechanism is added, which further increases the output proportion of the heat storage device and further increases the wind power grid space. Compared with the scenario without the implicit heat device, the wind abandonment situation is significantly improved.

6 Conclusion

As more wind turbines are connected to the grid, the problem of wind curtailment is exacerbated by the "heat-to-power" problem of CHP units in the north. This paper presents a combined operation model of CHP unit and regenerative electric heating considering wind power absorption. On this basis, the carbon emission and air abandonment volume are further restricted by introducing the wind abandonment penalty and carbon trading mechanism and verified by simulation examples. The analysis of numerical examples shows that.

(1) The combined operation system of wind turbine, CHP unit, and regenerative electric heating can greatly reduce the wind abandonment rate and increase the wind power consumption. At the same time, the regenerative electric heating can play the role of "peak cutting and valley filling" and reduce the operating cost of the system.

(2) Through the introduction of carbon trading mechanism, the output power of CHP units can be reduced while the output of regenerative electric heating is increased, which can reduce the coal consumption of the system and improve the economic benefits of the system.

The combined operation model considering wind power consumption and carbon trading mechanism proposed in this paper can well guarantee the economic and environmental benefits of the system, which is conducive to the "thermoelectric decoupling" of CHP units in northern China, and further improve the wind power consumption capacity of the power system.

Acknowledgements This research is financially supported by Natural Science Foundation of Ningxia under grant 2022AAC03614, and the authors thank the reviewers for their constructive suggestions.

References

1. Liu L, Liu J, Ye Y et al (2023) Ultra-short-term wind power forecasting based on deep Bayesian model with uncertainty. Renew Energy 205:598–607. https://doi.org/10.1016/J.RENENE.2023.01.038
2. Odoi-Yorke F, Adu TF, Ampimah BC et al (2023) Techno-economic assessment of a utility-scale wind power plant in Ghana. Energy Convers Manage X 18:100375. https://doi.org/10.1016/j.ecmx.2023.100375
3. Zhang Z, Kuang L, Zhao Y et al (2023) Numerical investigation of the aerodynamic and wake characteristics of a floating twin-rotor wind turbine under surge motion. Energy Convers Manage 283:116957. https://doi.org/10.1016/j.enconman.2023.116957
4. Dorotić H, Pukšec T, Schneider DR et al (2021) Evaluation of district heating with regard to individual systems–Importance of carbon and cost allocation in cogeneration units. Energy 221:119905. https://doi.org/10.1016/j.energy.2021.119905
5. Panowski M, Zarzycki R, Kobyłecki R (2021) Conversion of steam power plant into cogeneration unit—case study. Energy 231:120872. https://doi.org/10.1016/j.energy.2021.120872
6. Yuan W, Xin W, Su C et al (2022) Cross-regional integrated transmission of wind power and pumped-storage hydropower considering the peak shaving demands of multiple power grids. Renew Energy 190:1112–1126. https://doi.org/10.1016/j.renene.2021.10.046
7. Jiang Y, Zhang Y (2017) Peak regulation right trading between wind farm and thermal unit for second accommodation of wind power. Electric Power Autom Equip 37(11):14–21(in Chinese). https://doi.org/10.16081/j.issn.1006-6047.2017.11.003
8. Chen L, Xu F, Wang X et al (2015) Implementation and effect of thermal storage in improving wind power accommodation. Proc CSEE 35(17):4283–4290. https://doi.org/10.13334/j.0258-8013.pcsee.2015.17.001
9. He H, Guo J, Wang Y (2019) Research on multi-objective optimization strategy for ice storage air conditioning system for distribution network wind power consumption. Power Syst Protection Control 47(23):181–188. https://doi.org/10.19783/j.cnki.pspc.191092
10. Luo Y, Qiu S (2021) A wind power consumption model of CHP with thermal energy storage based on demand response. Acta Energiae Solaris Sinica 42(2):90–96. https://doi.org/10.19912/j.0254-0096.tynxb.2018-0887

11. Ge W, Gao M, Zhang Y et al (2019) Optimal economic dispatch of integrated energy system based on electric boiler for wind power accommodation. Southern Power Syst Technol 13(8):59–66. https://doi.org/10.13648/j.cnki.issn1674-0629.2019.08.009
12. Chen X, Kang C, O'Malley M et al (2015) Increasing the flexibility of combined heat and power for wind power integration in China: modeling and implications. IEEE Trans Power Syst 30(4):1848–1857. https://doi.org/10.1109/TPWRS.2014.2356723
13. Ding M, Liu X, Xie J et al (2017) Research on heat and electricity coordinated dispatch model of multi-area for improving wind power accommodation ability. Proc CSEE 37(14):4079–4088+4287 (in Chinese). https://doi.org/10.13334/j.0258-8013.pcsee.160598
14. Wang X, He Z, Xu C et al (2019) Dynamic simulations on simultaneous charging/discharging process of water thermocline storage tank. Proc CSEE 39(20):5989–5998. https://doi.org/10.13334/j.0258-8013.pcsee.190027
15. Wang L, Dong H, Lin J et al (2022) Multi-objective optimal scheduling model with IGDT method of integrated energy system considering ladder-type carbon trading mechanism. Int J Electr Power Energy Syst 143:108386. https://doi.org/10.1016/j.ijepes.2022.108386
16. Tang ZW, Hu MD, Zhang XF et al (2019) Structural optimization and numerical simulation of a high temperature phase change thermal storage electric boiler. J Beijing Univ Technol 45(12):1261–1268
17. Wang W, Qin C, Zhang J et al (2022) Correlation analysis of three-parameter Weibull distribution parameters with wind energy characteristics in a semi-urban environment. Energy Rep 8:8480–8498. https://doi.org/10.1016/j.egyr.2022.06.043
18. Yang LJ, Liang XR, Wang XR et al (2020) Combined heat and power economic dispatching considering peak regulation right trading to improve secondary accommodation capability of wind power. Power Syst Technol 44(05):1872–1880. https://doi.org/10.13335/j.1000-3673.pst.2019.0932

Study on the Effect of Inorganic Fiber on the Energy Storage Characteristics of Sandwich Composite Films

Yang Cui, Guang Liu, and Chang Hai Zhang

Abstract Polymer-based composite dielectrics are expected to be widely used as key materials for thin film capacitors in fields such as pulsed power supplies and high-power energy storage systems due to their excellent breakdown performance and excellent flexibility. This work uses PVDF polymers as a matrix and introduces PMMA to reduce dielectric loss. Inorganic fibers with different structures were designed and filled into the intermediate layer of the sandwich structure, with polymers selected as outer layers on both sides to maintain flexibility. It was found that the addition of Ag particles can effectively improve the polarization strength of the composite film, but the breakdown characteristics also deteriorate. However, the addition of the Al_2O_3 shell layer can effectively alleviate the problem of breakdown degradation and reduce ferroelectric losses. Finally, ABA Film has the best energy storage characteristics, with a discharge energy storage density of 5.98 J/cm^2, and a charge–discharge efficiency of not less than 65.4%.

Keywords Core shell structure · Sandwich film · Energy storage density

1 Introduction

Dielectric capacitors exhibit advantages such as high voltage, extremely high power density, ultra-long service life, and high reliability, making them important in the fields of new energy, power transmission and transformation engineering, and electromagnetic weapons [1]. The energy storage density of dielectric capacitors is closely

Y. Cui (✉) · G. Liu
School of Electrical Engineering, Zhejiang University of Water Resources and Electric Power, Nanxun Campus, Hangzhou, China
e-mail: cuiy@zjweu.edu.cn

C. H. Zhang
School of Electrical and Electronic Engineering, Harbin University of Science and Technology, Harbin, China

S. Yadav et al. (eds.), *Energy Power and Automation Engineering*, Lecture Notes in Electrical Engineering 1118, https://doi.org/10.1007/978-981-99-8878-5_8

related to their dielectric constant (ε_r, polarization strength) and applied electric field (E_b, breakdown strength). Using high dielectric inorganic phase doping to improve the energy storage characteristics of polymer-based composite dielectrics is the most common method.

In the early days, researchers used high dielectric ferroelectric ceramic nanoparticles to increase the dielectric constant of composite dielectrics and improve their energy storage capacity. Dang et al. [2] found that the size of nanoparticles has an impact on the dielectric of composite dielectrics, which is related to interface polarization and the crystalline phase of nanoparticles. However, nanoparticles need to reach a certain amount of filling to significantly increase the dielectric constant, which can cause a serious decline in the dielectric breakdown strength. To alleviate the above problems, nanofibers were introduced into the polymer matrix. Zhang et al. [3] have found that nanofibers can generate large dipole moments, while their size advantage reduces the occurrence of agglomeration, which can effectively enhance the dielectric constant and energy storage density of composite dielectric. To achieve uniform filling phase dispersion and small electric field distortion, core–shell structured nanofibers have been extensively studied [4–8]. In addition, sandwich or multilayer structures have also been proven to maintain high breakdown strength [4]. The multi-layer structure design can not only adjust the electric field distribution in the dielectric at the macro-level but also combine the advantages of each layer [9], for example, using a composite dielectric containing 1 vol.% $BaTiO_3$ as the "hard layer" as the central layer to ensure high effective breakdown strength, and selecting a composite dielectric containing 10–50 vol.% $BaTiO_3$ as the "soft layer" for the outer layer to provide a high relative dielectric constant [4]. Based on the above research, it can be found that how to utilize the micro- and macro-interfaces is a key issue in improving the energy storage density of dielectric materials.

In this work, three types of inorganic fibers, namely single-phase inorganic fibers (BFs), two-phase doped inorganic fibers (BA Fs), and core–shell three-phase inorganic fibers (ABA Fs), were prepared and introduced into the intermediate layer of the sandwich structure. In addition, in order to alleviate the ferroelectric hysteresis loss of the PVDF matrix, a low-loss linear PMMA was blended with it to obtain a new polymer matrix. Based on this, three kinds of polymer-based sandwich structure films were prepared, and the influence of inorganic fiber structure on the energy storage characteristics of sandwich composite films was studied. It was found that the polarization intensity of the sandwich film filled with BA Fs was the highest under the same electric field, but the residual polarization was also large. Through the buffering of the shell layer, the applied electric field and residual polarization of the sandwich film have been positively improved, which enables the sandwich film to obtain a large energy storage density under a relatively higher electric field.

2 Experimental Section

2.1 Material

In this work, the ferroelectric polymer used is polyvinylidene fluoride produced by Shanghai Sannaifu New Material Technology Co., Ltd. The organic solvent used for dissolving polymers is N, N-dimethylformamide (DMF) produced by Chemical Reagents Co., Ltd. of China National Pharmaceutical Group. PMMA, $Al(NO_3)_3{\cdot}9H_2O$, $Ba(OH)_2{\cdot}8H_2O$, $Ca(OH)_2$, $C_{16}H_{36}O_4Ti$, $AgNO_3$, $NH_3{\cdot}H_2O$, $N_2H_4{\cdot}H_2O$, C_2H_6O, CH_3-COOH, $C_5H_8O_2$, and N, N-dimethylformamide (DMF) were purchased from Sinopharm Chemical Reagent Co. Ltd. $C_{20}H_{28}O_8Zr$, polyvinylpyrrolidone (PVP, K90), and tris(hydroxymethyl)aminomethane (tris) were purchased from Aladdin.

2.2 Preparation of Inorganic Filling Phase

The inorganic fibers used in this work include $Ba_{0.85}Ca_{0.15}Zr_{0.1}Ti_{0.9}O_3$ fiber (BCZT) abbreviated as B Fs, Ag particle doped B Fs abbreviated as BA Fs, and Al_2O_3 coated BA Fs core–shell fibers abbreviated as ABA Fs. The above inorganic fibers can be obtained by the method in previous work 1 [10].

2.3 Thin Film Preparation

The preparation methods of the PMMA/PVDF blend polymer layer and the inorganic fiber doped composite polymer layer prepared in this work can be obtained through the method in previous work 2 [11]. In this work, a blend polymer of 15% PMMA/PVDF was used as the outer layer in the sandwich structure. The composite polymer obtained by filling 3 vol.% inorganic fibers into a 15% PMMA/PVDF polymeric matrix serves as a sandwich intermediate layer. Finally, three thin films were successfully prepared, with 15% PMMA/PVDF-3 vol.% B Fs/15% PMMA/PVDF-15% PMMA/ PVDF abbreviated as B Film, 15% PMMA/PVDF-3 vol.% BA Fs/15% PMMA/PVDF-15% PMMA/PVDF abbreviated as BA Film, and 15% PMMA/PVDF-3 vol.% ABA Fs/15% PMMA/ PVDF-15% PMMA/PVDF abbreviated as ABA Film. The specific preparation process is shown in Fig. 1.

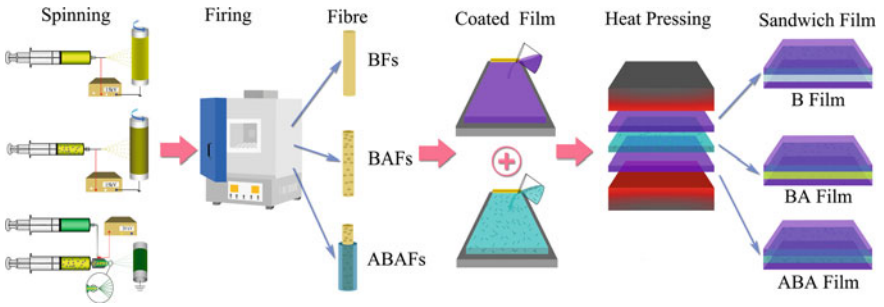

Fig. 1 Flow chart of preparation of inorganic fibers and sandwich films

3 Results and Discussion

In this work, in order to determine the composite phase of the sandwich film prepared, it was first characterized by XRD, as shown in Fig. 2. As can be seen from the figure, an amorphous peak appeared at $2\theta = 15°–20°$ in the three thin films B Film, BA Film, and ABA Film, which was the characteristic peak formed after PMMA and PVDF were blended. The characteristic peak of $\theta = 20.1°$ is the PVDF characteristic peak [10, 11]. In addition, the characteristic peak of BCZT (indicated by the green dotted line) appeared in the three films, which is due to the BCZT phase contained in the inorganic fibers B Fs, BA Fs, and ABA Fs. The characteristic peak of Ag (indicated by the blue dotted line) appeared at $\theta = 38.1°$ in BA Film and ABA Film, and the characteristic peak of Ag in BA Film was stronger than that in ABA Film [11]. This is because the shell of ABA Fs is amorphous Al_2O_3 (indicated by the orange arrow), which weakens the characteristic peak of Ag. In addition to the above characteristic peaks, no other miscellaneous peaks were found, indicating that the polymer matrix and inorganic fiber phases were physically composite, and no chemical reaction occurred.

As a ferroelectric polymer, PVDF has a higher dielectric constant than ordinary polymers, but also a high dielectric loss, as shown in reference 11. In order to alleviate the problem of high loss, 15% PMMA was introduced into the polymer matrix in this work. From Fig. 3, it can be observed that due to the presence of intermediate inorganic fibers and the addition of multi-layer interfaces, the dielectric constant of sandwich structure composite films has not significantly decreased. The dielectric levels of the three thin films are basically consistent. However, the dielectric loss has been significantly suppressed due to the addition of PMMA, especially in the low-frequency region, which is basically less than 0.06 in the range of 10^0–10^5 Hz. This is beneficial to the later suppression of hysteresis losses at high fields. In addition, due to the selection of pure polymers on both sides of the sandwich structure composite film, the overall conductivity basically remains at a relatively low level. From the above results, it is found that the structure of inorganic fibers has a relatively small impact on the polarization of sandwich composite films under low electric fields.

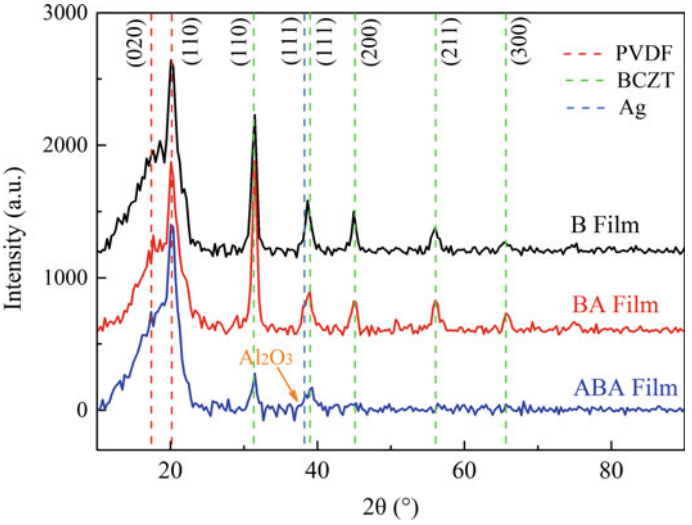

Fig. 2 XRD patterns of sandwich films

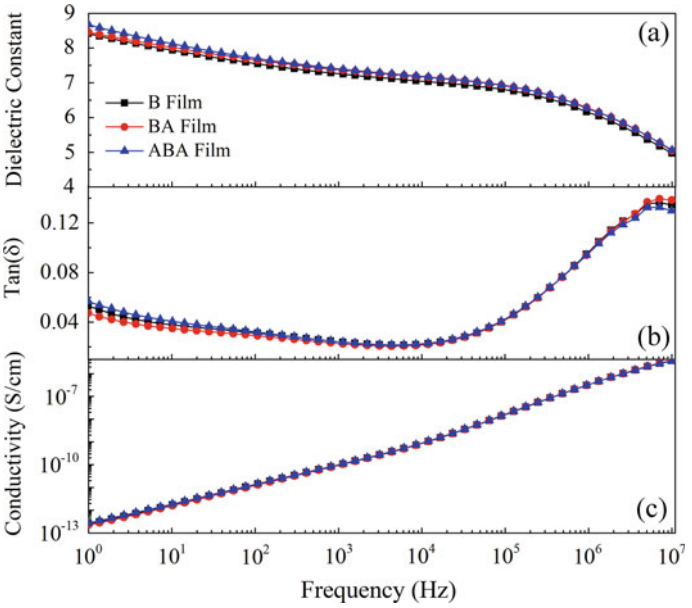

Fig. 3 **a** Dielectric constant, **b** dielectric loss tangent, (c) conductivity of sandwich film

In order to better study the influence of inorganic fiber structure on the polarization and breakdown characteristics of sandwich composite films under high field conditions, D–E curve tests were conducted on three types of films: B Film, BA Film, and ABA Film, as shown in Fig. 4. From Fig. 4a, it can be seen that under the same electric field conditions, the film filled with BA Fs has the maximum polarization (D_{max}) and remnant polarization (D_r), due to the addition of conductive Ag. The film filled with ABA Fs having an Al_2O_3 shell layer has lower D_{max} and D_r than the film filled with BA Fs, where the composite film filled with B Fs has the smallest D_{max} and D_r. This is due to the dielectric gradient effect of inorganic fiber structures. Wrapping a layer of Al_2O_3 with a dielectric constant similar to that of the matrix on the surface of high dielectric B Fs or BA Fs can reduce the MWS interfacial polarization in the composite. It is particularly worth noting that composite films with Al_2O_3 shells under the same conditions still have a lower D_r when polarized at higher electric fields, which is beneficial to improving the breakdown strength of the composite films. This also means that once the electric field is removed, the stored energy can be more fully released [12, 13]. As shown in Fig. 4b, it is obvious that the addition of an inorganic fiber Al_2O_3 shell effectively enhances the breakdown strength of ABA Film, which makes it have the highest D_{max}.

In order to more clearly analyze the impact of inorganic fiber structure on polarization, Fig. 5 shows a comparison diagram of D_{max} and D_r under different electric fields. From Fig. 5a, b, it is found that in the entire electric field range, the D_{max} and D_r of BA Film are the highest, while the D_{max} and D_r of B Film are the lowest. And the D_{max} and D_r of each composite film increase with the increase of the electric field. D_{max}–D_r is an important parameter representing the effective potential shift. As shown in Fig. 6, the D_{max}–D_r of B Film is 2.21 μC/cm^2, with the addition of Ag particles, the D_{max}–D_r of BA Film increases to 4.25 μC/cm^2. The addition of an Al_2O_3 shell further increases the D_{max}–D_r value of ABA Film (4.56 μC/cm^2). According to the formula $D = \varepsilon_0\varepsilon_r E$, this may be due to the contributions of ε_r and E_b. ABA Film has a relatively high ε_r and E_b, resulting in the highest D_{max}–D_r, which is powerful for achieving high discharging energy density and charge–discharge efficiency.

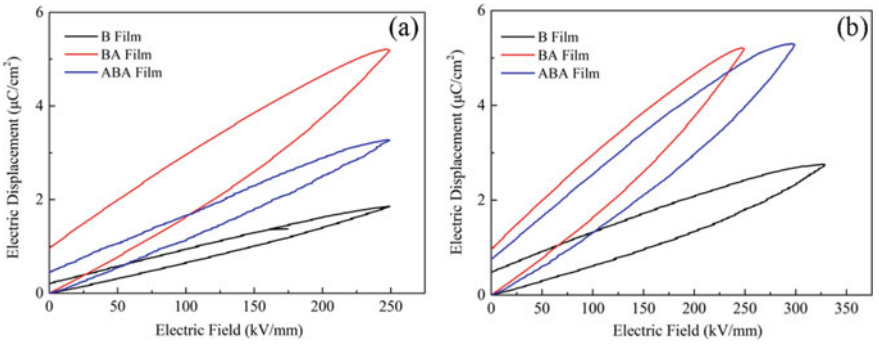

Fig. 4 D-E curve of sandwich films. **a** At the same electric field, **b** at the maximum electric field

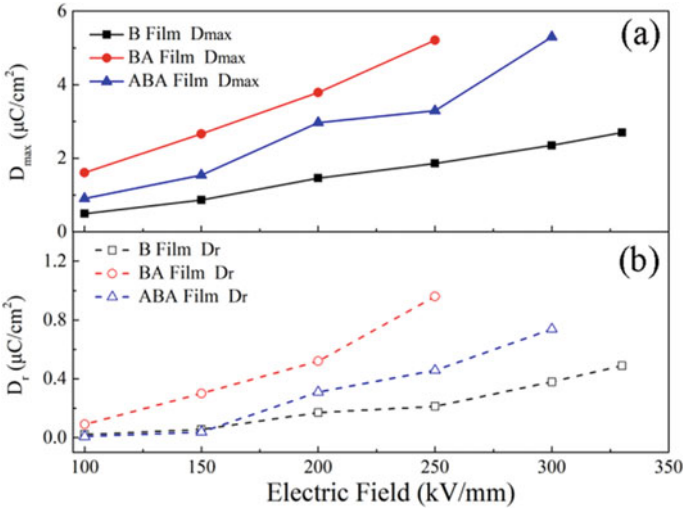

Fig. 5 **a** D_{max} and **b** D_r curves under different electric fields

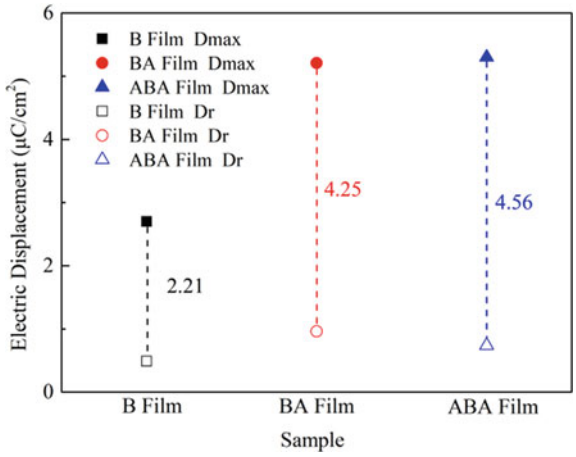

Fig. 6 D_{max}–D_r curves of sandwich films

The energy storage characteristics of the sandwich films are shown in the Fig. 7. Due to the advantage of D_{max} of BA Film, it achieves the maximum charging energy density (7.36 J/cm^2) under the same electric field. However, excessive D_r results in large energy loss, significantly weakening the advantage of discharging energy density (4.72 J/cm^2), and a sharp downward trend in charging–discharging efficiency. The breakdown electric field of B Film is the largest, but due to the minimum polarization intensity, its charging energy density (5.25 J/cm^2) and discharging energy density (3.25 J/cm^2) are both poor, but the charging–discharging efficiency has a relatively

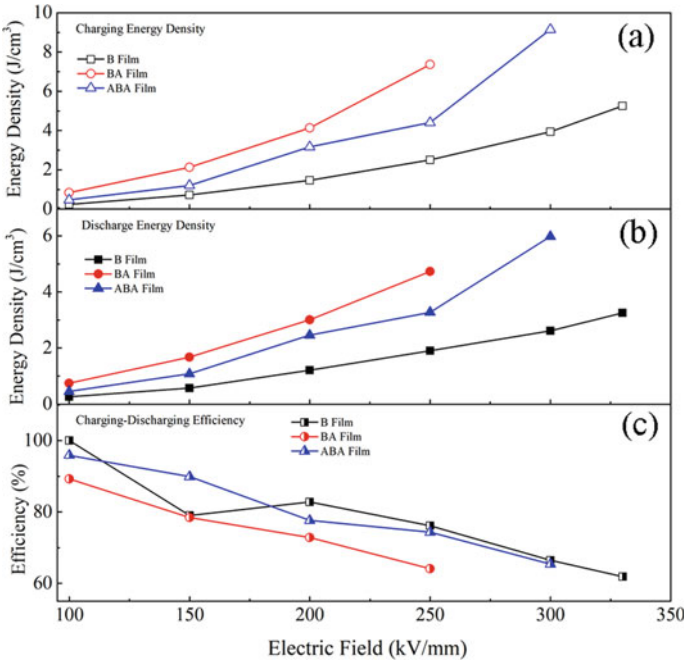

Fig. 7 Energy storage characteristics of sandwich films. **a** Charging energy density, **b** discharge energy density, **c** charging–discharging efficiency

slow downward trend. Due to its relatively good breakdown electric field and polarization strength, ABA Film achieves the maximum charging energy density (9.14 J/cm^2) and discharging energy density (5.98 J/cm^2) under the maximum electric field, while the relative decline in charge–discharge efficiency is relatively flat, basically maintaining at 65.4% or above. Therefore, ABA Film has the best comprehensive energy storage characteristics.

4 Conclusion

In this work, three types of inorganic fibers were prepared and filled into the intermediate layer of the sandwich structure. The polymer matrix is selected as 15% PMMA/PVDF. The study found that the addition of Ag particles can effectively improve the polarization strength of BA Film, but at the same time cause a decrease in the breakdown field strength, resulting in a poor discharge energy storage density (4.72 J/cm^2). The addition of an Al_2O_3 shell layer effectively alleviated the breakdown field strength and ferroelectric losses of ABA Film, resulting in a discharge energy storage density of 5.98 J/cm^2 and a charge–discharge efficiency of no less than 65.4% for ABA Film.

Acknowledgements This research was supported by the Joint Funds of the Zhejiang Provincial Natural Science Foundation of China under Grant No. LZY22E030003, the National Natural Science Found at ion of China under Grant No.52007042, the Natural Science Foundation of Heilongjiang Province Joint Guide Project Grant LH2020E091. This research was supported by funded by the Nanxun Scholars Funding Program.

References

1. Feng Q, Zhong S, Pei J, Zhao Y, Zhang D, Liu D, Zhang Y, Dang Z (2022) Chem Rev 122:3820–3878
2. Fan B, Zha J, Wang D, Zhao J, Dang Z (2012) Appl Phys Lett 100:2228
3. Zhang H, Marwat M, Xie B, Ashtar M, Liu K, Zhu Y, Zhang L, Fan P, Samart C, Ye Z (2019) ACS Appl Mater Interfaces 12:1–37
4. Luo H, Zhou X, Ellingford C, Zhang Y, Chen S, Zhou K, Zhang D, Bowen C, Wan C (2019) Chem Soc Rev 48:4424–4465
5. Guan L, Weng L, Zhang X, Wu Z, Li Q, Liu L (2020) J Mater Sci 55:15238–15251
6. Xu J, Fu C, Chu H, Wu X, Tan Z, Qian J, Li W, Song Z, Ran X, Nie W (2020) Sci Rep 10:17084
7. Rahimabady M, Mirshekarloo M, Yao K, Lu L (2013) Phys Chem Chem Phys 15:16242
8. Yang K, Huang X, He J, Jiang P (2015) Adv Mater Interfaces 2:1500361
9. Li H, Liu F, Fan B, Ai D, Peng Z, Wang Q (2018) Small Methods 2:1700399
10. Cui Y, Wang X, Zhang T, Zhang C, Chi Q (2019) RSC Adv B 33229–33237
11. Cui Y, Zhang T, Feng Y, Zhang C, Zhang Q, Zhang Y, Chen Q, Chen X, Lei Q (2019) Compos Part B Eng 177:107429
12. Xie Y, Jiang W, Fu T, Liu J, Zhang Z, Wang S (2018) ACS Appl Mater Interfaces 10:29038–29047
13. Pan Z, Yao L, Zhai J, Fu D, Shen B, Wang H (2017) ACS Appl Mater Interfaces 9:4024–4033

Nonlinear Dynamic Modelling for the Novel Inverse-Pendulum Wave Energy Converter with a Constant-Pressure Hydraulic Power Take-off

Xuhui Yue, Guanchen Liu, Junjie Yang, Jiaying Liu, and Qijuan Chen

Abstract Novel inverse-pendulum wave energy converter (NIPWEC) is an optional oscillating wave surge converter. It utilizes an adjustable internal mass to realize the wave–structure interaction system resonance and the efficient power generation. Several references have researched on its performance via wave flume tests or numerical simulations. However, the NIPWEC structure with a constant-pressure hydraulic power take-off (CPHPTO) has not been systematic investigated. This paper aims at the dynamic modelling and performance assessment of the NIPWEC with a CPHPTO. At first, a wave-to-wire nonlinear state space model (SSM) is constructed. Then, the SSM correctness is verified by comparing simulation results to the existing experimental/simulation data. Finally, the response curve analysis and performance assessment are implemented against different electric loads. Results show that the CPHPTO efficiency, output active power and wave-to-wire efficiency could all be weakened under the excessive resistance, vice versa. Besides, both the inductive and capacitive components possess the capability of reducing the values of the above three variables. According to the simulated efficiency values, NIPWEC can obtain the wave-to-wire efficiency of 0.4, when it is at a resonant state. In the future, we will further investigate the influence of different designed parameters on the NIPWEC operating performance based on the SSM.

Keywords Wave energy · Inverse pendulum · Constant-pressure hydraulic power take-off · Dynamic modelling · Response curve · Performance assessment

X. Yue (✉) · G. Liu · J. Yang · J. Liu
PowerChina HuaDong Engineering Corporation Limited, Hangzhou 311122, China
e-mail: yue_xh@hdec.com

Huachen Electric Power Control Corporation Limited, Hangzhou 311122, China

Q. Chen
Ministry of Education Key Laboratory of Transients in Hydraulic Machinery, Wuhan University, Wuhan 430072, China

S. Yadav et al. (eds.), *Energy Power and Automation Engineering*, Lecture Notes in Electrical Engineering 1118, https://doi.org/10.1007/978-981-99-8878-5_9

1 Introduction

Wave energy is one kind of marine renewable energy with great potential. More than 1000 prototypes for wave energy conversion have been proposed by researchers all around the world [1]. Wave energy converters (WECs) can be divided into four categories, i.e. point absorbers, oscillating wave columns, attenuator-type WECs and terminator-type WECs [2]. Wherein, terminators are oriented perpendicular to the wave propagation direction. They include duck-like devices, oscillating wave surge converters (OWSCs) and overtopping devices, etc., in formal. OWSCs are widely concerned by scholars. Diverse OWSC structures are proffered, containing cylinders, flaps or flaps with vanes, etc., to harvest wave energy. Besides, hydraulic power take-offs (HPTOs) or hydro-turbines are adopted by OWSCs as the power equipment, in order to drive generators to rotate and generate electricity.

As an optional OWSC, the novel inverse-pendulum WEC (NIPWEC) was first presented by Cai et al. [3–5]. The main difference between the NIPWEC and other terminators is that it owns an adjustable internal mass. Hence, NIPWEC natural period can be regulated to be consistent with the characteristic wave period of irregular waves, which leads to the wave–structure interaction system resonance and efficient power generation. Ouyang et al. [6] investigated the NIPWEC with a mechanical power take-off. In their study, a wave-to-wire dynamic model was established for the time-domain characteristic analysis.

This paper focuses on the NIPWEC structure with a constant-pressure HPTO (CPHPTO), as shown in Fig. 1, aiming at nonlinear dynamic modelling and performance assessment. The principle of the NIPWEC with a CPHPTO is as follows. Firstly, a gear-and-rack mechanism converts the inverse-pendulum swing into the reciprocating motion of the piston rods of two hydraulic rams (HRs). Then, two HRs generate high-pressure oil and push the rectified oil into the main circuit through four check valves (CVs). Afterwards, a high-pressure accumulator (HPA) weakens oil pressure fluctuations at the main circuit inlet and smooths the main circuit flow rate. Finally, the filtered oil enters a variable axial piston motor (VAPM) and drives it as well as the coaxially connected permanent magnet synchronous generator (PMSG) to generate electricity. In addition, a mass-position-adjusting mechanism is able to tune the internal mass vertical position, in order to keep the NIPWEC nature period consistent with the characteristic wave period. A flow control valve (FCV) is arranged between HPA and VAPM, in order to adjust the oil flow rate as well as the VAPM hydraulic power. A relief valve (RV) is utilized for discharging the redundant oil directly to a low-pressure reservoir (LPR) for the safety of the main circuit.

Sections are arranged as bellow. Section 2 expounds the dynamic modelling procedure. Section 3 explains parameter settings for simulation. Section 4 implements the model validation, response curve analysis and performance assessment. Conclusions are summarized in Sect. 5.

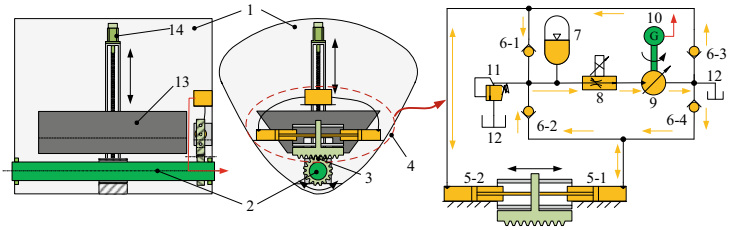

1. an inverse pendulum; 2. a supporting shaft; 3. a gear-and-rack mechanism; 4. a CPHPTO; 5. two HRs; 6. 4 CVs; 7. a HPA; 8. a FCV; 9. a VAPM; 10. a PMSG; 11. a RV; 12. a LPR; 13. an internal mass; 14. a mass-position-adjusting mechanism.

Fig. 1 Sketch of the NIPWEC structure

2 Nonlinear Dynamic Modelling Of NIPWEC

2.1 Inverse Pendulum

Inverse pendulum is the key device to capture ocean wave energy. Force analysis of the inverse pendulum is illustrated in Fig. 2. Inverse pendulum is restricted on the supporting shaft and swings driven by the wave excitation moment in the pitch direction. Its dynamic model can be described by the following Cummins' equation [7].

$$\begin{aligned}&(J_{P+M}(l_M(t)) + J_{55\infty})\ddot{\theta}(t) + \int_0^t K(t-\tau)\dot{\theta}(\tau)\mathrm{d}\tau \\ &\quad + (F_B l_B - G_P l_P - G_M l_M(t))\sin\theta(t) \\ &= M_E(t) + M_{\mathrm{PTO}}(t) + M_{\mathrm{end}}(t)\end{aligned} \tag{1}$$

Here, J_{P+M} is the total moment of inertia, $J_{55\infty}$ the added mass at the wave frequency of $+\infty$, $K(t)$ the impulse response function, l_B, l_P or $l_M(t)$ the distance between R and B, P or M. Herein, $l_M(t)$ can be adjusted according to sea states, for the sake of resonance power generation.

2.2 CPHPTO

CPHPTO transmits mechanical power from the inverse pendulum to the PMSG. In this process, the HRs, HPA, FCV and VAPM are the vital components for energy conversion and power smoothing. Their dynamic models are introduced separately.

HRs. Based on oil compressibility, HR model can be described by:

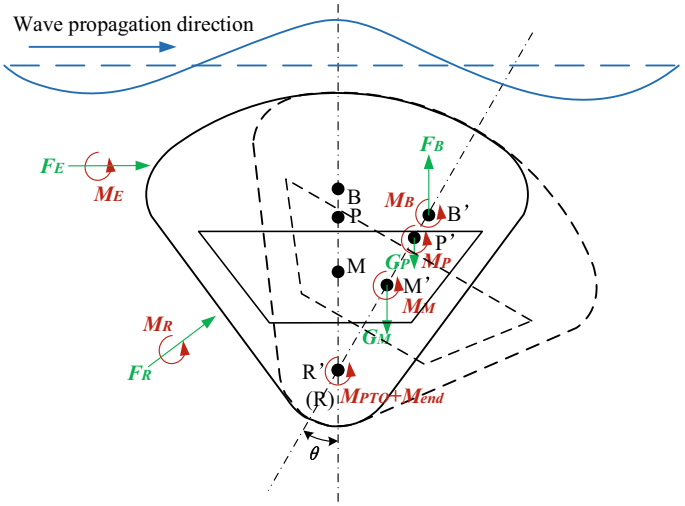

Fig. 2 Force analysis of the inverse pendulum. In this figure, R represents the rotation centre, M the mass centre of the internal mass, P the mass centre of the pendulum hull, B the buoyancy centre. F_E means the wave excitation force, F_R the radiation force, G_M the gravity force of the internal mass, G_P the gravity force of the pendulum hull, F_B the buoyancy force. M_E, M_R, M_M, M_P and M_B are the corresponding moments against R. M_{PTO} is the PTO moment, M_{end} the end-stop moment to avoid the swing angle θ exceeding its limits

$$\begin{cases} M_{\text{PTO}}(t) = r_g\left[-(p_1 - p_2)s_c - F_f\right] \\ M_{\text{end}}(t) = r_g F_{\text{end}} \\ \frac{V_1}{\beta}\dot{p}_1 = s_c\dot{x} - q_1 - q_2 - \frac{C_{ec}}{\mu}p_1 \\ \frac{V_2}{\beta}\dot{p}_2 = -s_c\dot{x} - q_3 - q_4 - \frac{C_{ec}}{\mu}p_2 \end{cases} \tag{2}$$

Here, r_g means the gear reference diameter, p_1 and p_2 the oil pressures in two rodless chambers, s_c the piston effective area, F_f the HR friction force, F_{end} the end-stop force, V_1 and V_2 the volumes of two rodless chambers, β the oil effective bulk elastic modulus, $x = r_g\theta$ the translational displacement of the rack or piston, q_1, q_2, q_3 and q_4 the flow rates passing through four check valves, C_{ec} the HR external leakage coefficient, μ the oil dynamic viscosity. Herein, V_1 and V_2 can be represented as follows:

$$\begin{cases} V_1 = s_c(\frac{x_s}{2} - x) + V_d \\ V_2 = s_c(\frac{x_s}{2} + x) + V_d \end{cases} \tag{3}$$

Here, x_s signifies the piston rod stroke, V_d the rodless chamber dead volume.

HPA. HPA owns two working modes, i.e. the normal working mode and fully discharged mode. In the normal working mode, there is enough oil inside the HPA.

HPA possesses the capability of smoothing the oil pressure and flow rate of the main circuit by charging and discharging oil. In contrast, there is no oil inside, when HPA is fully discharged. At this moment, HPA is unable to work normally, which leads to the huge fluctuations of pressure and flow rate. Model considering pressure bound [8] is used for depicting the aforementioned two working modes.

FCV. FCV is composed of a pressure compensation valve and a throttle valve. Its flow rate–pressure difference characteristic can be depicted by a 6-order state space model (SSM) [9]. In this paper, we propose the following empirical formula to reflect the above characteristic instead.

$$q_{\mathrm{fcv}} = \begin{cases} q_{\mathrm{set}}\left\{\left(1-\mathrm{erf}\left(1.85\times\frac{|\Delta p_{\mathrm{fcv}}|}{\Delta p_{\min}}\right)\right)\frac{\sqrt{|\Delta p_{\mathrm{fcv}}|}}{\sqrt{\Delta p_{\min}}}+\mathrm{erf}\left(1.85\times\frac{|\Delta p_{\mathrm{fcv}}|}{\Delta p_{\min}}\right)\right. \\ \left.\left[1+k_{\mathrm{fcv}}\left(\frac{\sqrt{|\Delta p_{\mathrm{fcv}}|}}{\sqrt{\Delta p_{\min}}}-1\right)\exp\left(1-\left(\frac{|\Delta p_{\mathrm{fcv}}|}{\Delta p_{\min}}\right)^{\delta_{\mathrm{fcv}}}\right)\right]\right\} & \Delta p_{\mathrm{fcv}}\geq 0 \\ -q_{\mathrm{set2}}\frac{\sqrt{|\Delta p_{\mathrm{fcv}}|}}{\sqrt{\Delta p_{\min}}} & \Delta p_{fcv}<0 \end{cases} \tag{4}$$

Here, q_{fcv} refers to the oil flow rate passing through the FCV, $q_{\mathrm{set}}/q_{\mathrm{set2}}$ the preset forward/backward flow rate, erf(•) the error function utilized for the transition of the two parts of a flow rate–pressure difference characteristic curve, Δp_{fcv} the oil pressure difference between the inlet and outlet, $\Delta p_{\min}$ the minimum working pressure difference, k_{fcv} and δ_{fcv} the two corrective coefficients. The simulated and experimental flow rate–pressure difference characteristic curves are compared in Fig. 3. Results show that the empirical formula can successfully emulate the transition section of increasing first and then decreasing, compared with the 6-order SSM. Besides, empirical formula is analytical and does not need to be calculated numerically. Hence, the empirical formula is an alternative modelling method, if we are not interested in the FCV transient response.

VAPM. VAPM dynamic model can be expressed as:

$$\begin{cases} J\dot{\omega}_m = x_m D_m \Delta p_m - B_m\omega_m - M_g - M_{\mathrm{loss}} \\ q_m = q_{\mathrm{loss}} + x_m D_m \omega_m \end{cases} \tag{5}$$

Here, J signifies the output shaft moment of inertia, ω_m the motor angular velocity, x_m the fractional motor displacement, D_m the maximum motor displacement, Δp_m the oil pressure difference between the inlet and outlet, B_m the output shaft damping, M_g the PMSG moment, M_{loss} the VAPM moment loss, q_m the oil flow rate entering VAPM, q_{loss} the VAPM flow rate loss. Herein, M_{loss} and q_{loss} is depicted by improved Jeong's model [8], which preserves the high accuracy of Jeong's model [10] and widens the fitting range of Jeong's model to the shaft speed of 0 rpm.

Other Components. RV model [see Eq. (6)] is constructed based on the flow rate–pressure difference characteristic curve of a direct acting RV without regard to the spool friction.

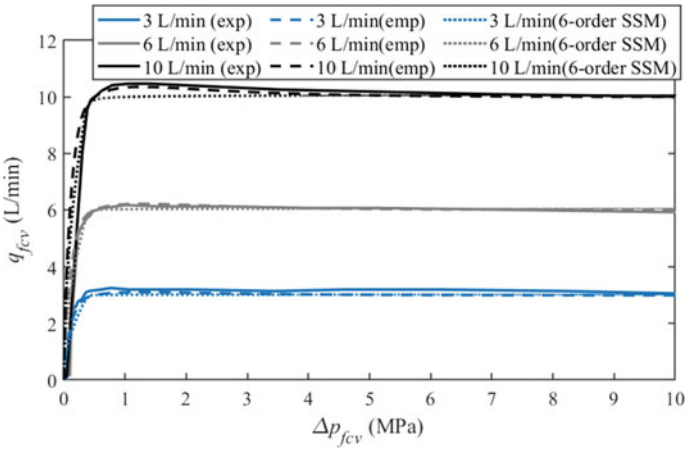

Fig. 3 Comparison of the simulated and experimental flow rate–pressure difference characteristic curves for a FCV. Herein, "exp" means experimental results, "emp" empirical formula. Moreover, the experimental data and the results for "6-order SSM" are all collected from Ref. [9]

$$q_{\mathrm{rv}} = \begin{cases} k_{\mathrm{rv}}(p_a - p_b - p_{\mathrm{rvset}}) & p_a - p_b > p_{\mathrm{rvset}} \\ 0 & p_a - p_b \le p_{\mathrm{rvset}} \end{cases} \tag{6}$$

Here, q_{rv} means the oil flow rate passing through RV, k_{rv} the slope of the flow rate–pressure difference characteristic curve, p_a/p_b the oil pressure at HPA/LPR, p_{rvset} the preset opening pressure. In addition, the models of the CVs, PMSG and LPR are all established according to Ref. [8].

2.3 *Wave-to-Wire Nonlinear SSM of the NIPWEC with a CPHPTO*

Define state variables $y_1 = \theta$, $y_2 = \dot{\theta}$, $y_3 = p_1$, $y_4 = p_2$, $y_5 = p_a$, $y_6 = p_b$, $y_7 = V_b$, $y_8 = p_m$, $y_9 = \omega_m$, $y_{10} = i_d$, $y_{11} = i_q$ and $y_{11+k} = \left[\boldsymbol{y_r}\right]_k$. Wherein, V_b means the LPR gas volume, p_m the oil pressure at the VAPM inlet, i_d/i_q the PMSG d/q-axis current, $\boldsymbol{y_r}$ the state vector for the SSM approximation of $I = \int_0^t K(t-\tau)\dot{\theta}(\tau)\mathrm{d}\tau$ in Eq. (1), k=1 − N (N is the dimension of $\boldsymbol{y_r}$). Based on Sects. 2.1 and 2.2, a NIPWEC SSM can be successfully established by introducing the above state variables.

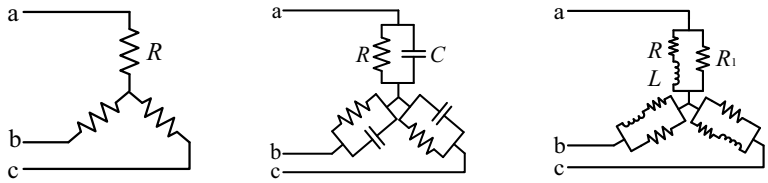

(a) Resistive load (b) Capacitive load (c) Inductive load

Fig. 4 Three general types of electric loads. Herein, R and R_1 denotes the resistance of resistors, C the capacitance of capacitors, L the inductance of inductors

3 Parameter Settings

3.1 Irregular Waves

The NIPWEC SSM was simulated at the irregular waves of JONSWAP spectrum, whose energy period T_e=6 s and significant wave height H_s=1.5 m. Herein, the internal mass position is adjusted to a suitable place, i.e. l_M=1.2 m, to make sure that the NIPWEC natural period is consistent with T_e. At this moment, wave–structure interaction system stands in the resonate state.

3.2 Electric Loads

Three general types of electric loads, i.e. the resistive, capacitive and inductive loads, were adopted for simulation. As shown in Fig. 4, the three load types are all three-phase symmetrical and connected in the form of Y. Resistive load is represented by a resistor at each phase. Meanwhile, capacitive load is described by a resistor and a capacitor connected in parallel at each phase. In addition, a resistor coupled with an inductor in series refers to an inductive load. Since NIPWEC is simulated as a current source, a resistor of the large resistance R_1 ($R_1 = 10R$) is added to the inductive load in parallel at each phase, in order to ensure the smooth implementation of the simulation.

3.3 Simulation Platform and Solver

Simulation was implemented in MATLAB/Simulink. Simulation type in Powergui is set as “Continuous”. In addition, ode45 with a tolerance of 5E-3 is adopted as the SSM solver.

4 Results and Discussion

4.1 Model Validation

Simulation results of the PTO moment M_{PTO}, PTO absorbed power P_{PTO} and output active power P_{out} are shown in Fig. 5a, b. It can be seen that M_{PTO} curve presents the profile of a square wave with the synchronously changed positive and negative amplitudes. Besides, the square-wave period is consistent with the ocean-wave period. In terms of power, P_{PTO} curve appears a mound shape. Its value adjusts from 0 to peak and then to 0 every half ocean-wave period. Moreover, P_{out} is obviously stable without severe oscillations due to power smoothing. All these characteristics are verified by the experimental results (Fig. 5c, d) from Ref. [11]. The similar simulation results can also be seen in Refs. [12, 13].

In addition, the time-averaged power and efficiency against different loads are calculated and displayed in Table 1. It can be seen that the power values of each link sequentially decrease from wave energy absorption to electricity generation.

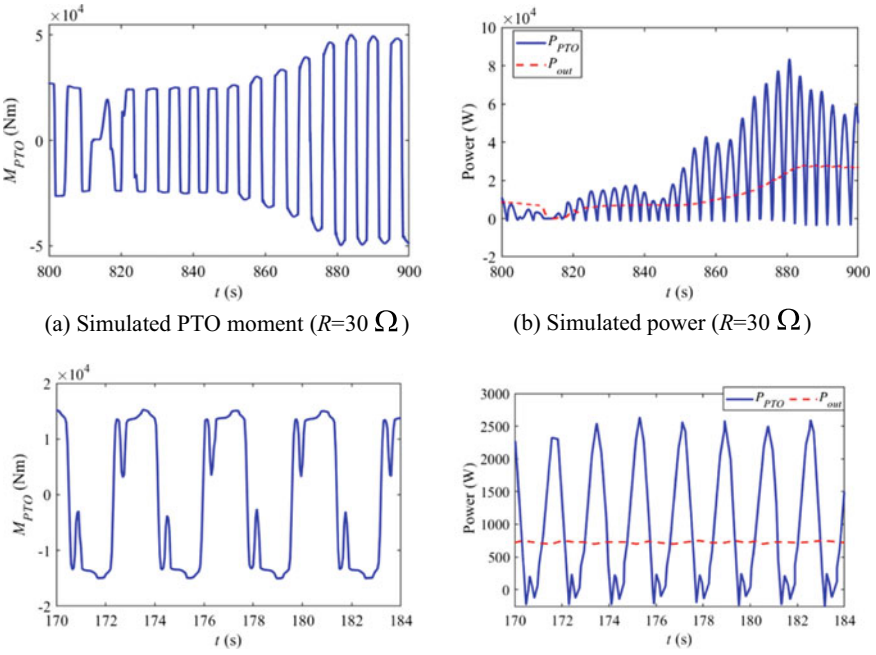

(a) Simulated PTO moment (R=30 Ω)

(b) Simulated power (R=30 Ω)

(c) Experimental results of the PTO moment [11]

(d) Experimental results of the power [11]

Fig. 5 Model validation for the NIPWEC SSM. Herein, experimental results of a raft-type WEC are introduced for comparison, since the raft-type WEC and NIPWEC have the similar working principles and the analogous CPHPTO

Table 1 Time-averaged power and efficiency against different loads

Load setting	$\overline{P}_{\mathrm{PTO}}$ (W)	$\overline{P}_a$ (W)	$\overline{P}_m$ (W)	$\overline{P}_{\mathrm{out}}$ (W)	$\overline{Q}_{\mathrm{out}}$ (Var)	CWR	η_{PTO}	η_{WW}
R=10 Ω	18466	17232	10076	8709	0	0.558	0.472	0.263
R=20 Ω	18127	17105	14240	12416	0	0.547	0.685	0.375
R=30 Ω	16655	15767	15391	13249	0	0.503	0.795	0.400
R=40 Ω	15574	14747	14740	12456	0	0.470	0.800	0.376
R=50 Ω	14630	13848	13763	11390	0	0.442	0.779	0.344
R=90 Ω	12486	11695	11165	8449	0	0.377	0.677	0.255
R=30 Ω, C=1.667E−4 F	18201	17146	13074	11235	− 35199	0.550	0.617	0.339
R=30 Ω, L=0.15 H	11809	11001	6367	3502	4050	0.357	0.297	0.106

Note $\overline{P}_{\mathrm{PTO}}$ is the time-averaged PTO absorbed power, $\overline{P}_a/\overline{P}_m$ the time-averaged hydraulic power at the HPA/VAPM, $\overline{P}_{\mathrm{out}}/\overline{Q}_{\mathrm{out}}$ the time-averaged output active/reactive power, CWR the capture width ratio, η_{PTO} the PTO efficiency, η_{WW} the wave-to-wire efficiency ($\eta_e = \mathrm{CWR}^*\eta_{\mathrm{PTO}}$)

Additionally, the NIPWEC capture width ratio (CWR) spreads between 0.357 and 0.558, which is confirmed by the statistical CWRs of the fixed OWSCs. The fixed-OWSC CWR can reach 0.72, according to Ref. [14]. In reality, CWR of a NIPWEC prototype can achieve 0.38 nowadays, according to flume test in irregular waves [4]. Meanwhile, the PTO efficiency η_{PTO} is mainly distributed in the range of 0.6–0.8, which basically matches the existing PTO efficiency range, i.e. 0.57–0.8, obtained via experiments or simulations [11, 15]. A few cases below 0.6 is caused by the long-term RV overflow or the inductive load (Figs. 6 and 7a–b).

In summary, simulation results of the NIPWEC SSM are reliable.

4.2 Response Curve Analysis and Performance Assessment

Time-domain response curves against different loads are shown in Figs. 6 and 7. The corresponding time-averaged power and efficiency have been displayed in Table 1. The findings are as follows.

1. Too small resistance, e.g. $R = 10$ Ω, leads to the oversized CPHPTO damping, which causes the excessive p_a and the longstanding RV overflow. Therefore, η_{PTO} is weakened. On the contrary, if resistance is too large, e.g. $R = 90$ Ω, CPHPTO damping and p_a will significantly decrease. At this moment, the possibility that HPA stays in a fully discharged mode greatly increases, which results in a η_{PTO} decline. In addition, CWR also descends, since inverse pendulum possesses lower energy capture ability along with resistance increasing. As a whole resistance adjustment has the greater impact on η_{PTO} than CWR, η_{PTO}, $\overline{P}_{\mathrm{out}}$ and η_{WW} could all be cut down under the excessive resistance, vice versa. Herein, $R = 30$ Ω

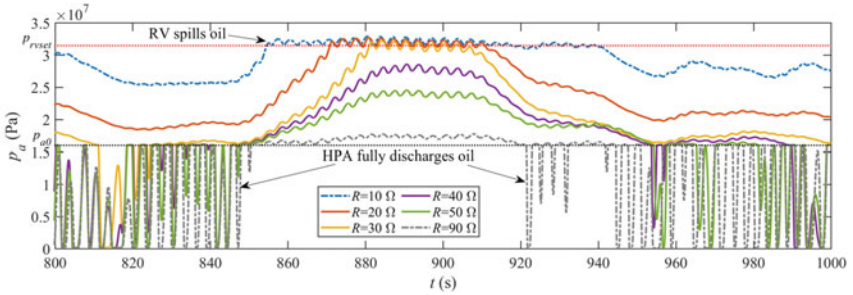

(a) Oil pressure at the HPA oil inlet.

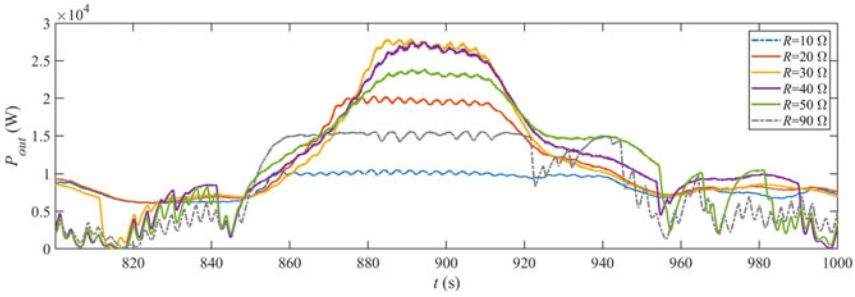

(b) Output active power.

Fig. 6 Time-domain response curves of the NIPWEC against different R

is the optimal resistance, which corresponds to the relatively higher η_{PTO}/CWR and the maximum $\eta_{\mathrm{WW}} = 0.4$.

2. Inductive component makes the HPA fully discharged mode longer, which results in a η_{PTO} decline. Besides, it can also reduce the inverse-pendulum energy capture ability. Moreover, capacitive component increases the overflow duration, which also leads to a η_{PTO} reduction. Overall, both inductive and capacitive components are able to weaken η_{PTO}, $\overline{P}_{\mathrm{out}}$ and η_{WW}.
3. Both inductive and capacitive components can generate a large amount of output reactive power Q_{out}. The reactive power against the inductive component is positive, whilst that is negative for the capacitive component.

5 Conclusions

This paper proposed a wave-to-wire nonlinear SSM of the NIPWEC with a CPHPTO. During the modelling process, an empirical formula was presented to describe the FCV flow rate–pressure difference characteristic. Then, the SSM correctness was verified via the comparison between simulation results and the experimental/simulation data from other references. In the end, the response curve analysis and

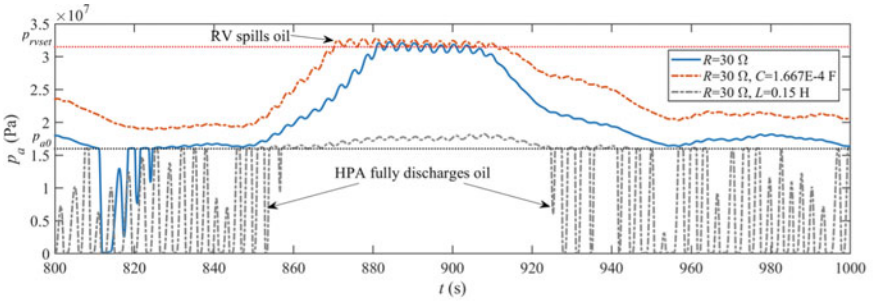

(a) Oil pressure at the HPA oil inlet.

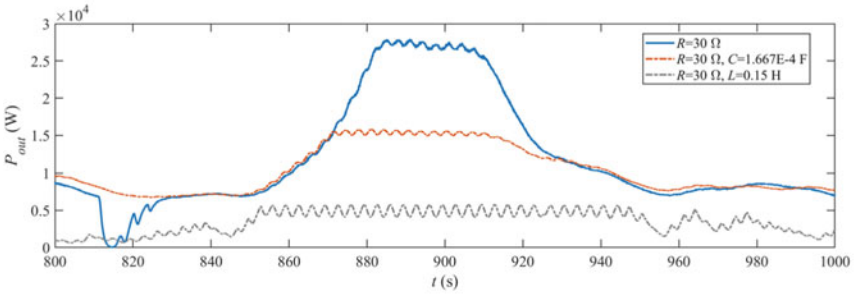

(b) Output active power.

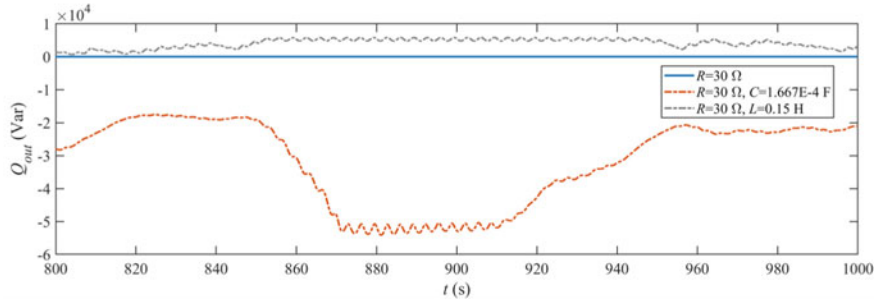

(c) Output reactive power.

Fig. 7 Time-domain response curves of the NIPWEC against different load types

performance assessment for the NIPWEC were conducted against different electric loads, via a series of SSM simulations. The main conclusions are presented as below.

1. The simulated profiles of the PTO moment and power are consistent with the experimental data. Besides, the sequential power decrease from wave energy absorption to electricity generation is nicely reflected. Moreover, the simulated CWRs and PTO efficiency are trustworthy.
2. The PTO efficiency, time-averaged output active power and wave-to-wire efficiency could all be weakened under the excessive resistance, vice versa. In addition, both the inductive and capacitive components of loads are able to cut

down values of the aforementioned three variables. Based on the simulated efficiency values, the CWR of 0.558, the PTO efficiency of 0.8 and the wave-to-wire efficiency of 0.4 can be achieved, when the NIPWEC is at a resonant state.

In the future, the influence of different designed parameters on the NIPWEC operating performance will be further studied via the SSM.

Acknowledgments This work is supported by the National Natural Science Foundation of China (Grant No. 52179088) and the Science and Technology Project of Enterprise (Grant No. ZKY2023-HCDK-02-01).

References

1. López I, Andreu J, Ceballos S, De Alegría IM, Kortabarria I (2013) Review of wave energy technologies and the necessary power-equipment. Renew Sustain Energy Rev 27:413–434. https://doi.org/10.1016/j.rser.2013.07.009
2. Guo B, Ringwood JV (2021) Geometric optimisation of wave energy conversion devices: a survey. Appl Energy 297:117100. https://doi.org/10.1016/j.apenergy.2021.117100
3. Cai Y, Huo Y, Liu J, Shi X, Liu Y (2021) U.S. Patent Application No. 17/382,911. https://patents.glgoo.top/patent/US20210355905A1/en
4. Cai Y, Shi X, Huo Y, Liu Y (2022) Experimental study on a pitching wave energy converter with adjustable natural period. Ocean Eng 261:112128. https://doi.org/10.1016/j.oceaneng.2022.112128
5. Cai Y, Huo Y, Shi X, Liu Y (2022) Numerical and experimental research on a resonance-based wave energy converter. Energy Convers Manage 269:116152. https://doi.org/10.1016/j.enconman.2022.116152
6. Ouyang Z, Zheng Y, Yue X, Chen Q (2023) Wave-to-wire dynamic modeling and time-domain characteristic analysis for the Novel inverse-pendulum wave energy converter. J Ocean Technol 42(02):94–104. https://doi.org/10.3969/j.issn.1003-2029.2023.02.012(inChinese)
7. Cummins WE (1962) The impulse response function and ship motions. Schiffstechnik 47:101–109. https://readpaper.com/paper/2153978658
8. Yue X, Chen Q, Wang Z, Geng D, Yan D, Jiang W, Wang W (2019) A novel nonlinear state space model for the hydraulic power take-off of a wave energy converter. Energy 180:465–479. https://doi.org/10.1016/j.energy.2019.05.095
9. Geng D, Zheng Y, Chen Q, Yue X, Yan D (2021) Novel hydraulic mechanism-based output power regulation for the wave energy converter. Appl Ocean Res 110:102587. https://doi.org/10.1016/j.apor.2021.102587
10. Jeong HS, Kim HE (2007) A novel performance model given by the physical dimensions of hydraulic axial piston motors: experimental analysis. J Mech Sci Technol 21:630–641. https://doi.org/10.1007/BF03026968
11. Liu C, Hu M, Gao W, Chen J, Zeng Y, Wei D, Bao G et al (2021) A high-precise model for the hydraulic power take-off of a raft-type wave energy converter. Energy 215:119107. https://doi.org/10.1016/j.energy.2020.119107
12. Penalba M, Ringwood JV (2019) A high-fidelity wave-to-wire model for wave energy converters. Renew Energy 134:367–378. https://doi.org/10.1016/j.renene.2018.11.040
13. Cargo CJ, Hillis AJ, Plummer AR (2016) Strategies for active tuning of wave energy converter hydraulic power take-off mechanisms. Renew Energy 94:32–47. https://doi.org/10.1016/j.renene.2016.03.007

14. Babarit A (2015) A database of capture width ratio of wave energy converters. Renew Energy 80:610–628. https://doi.org/10.1016/j.renene.2015.02.049
15. Lasa J, Antolin JC, Angulo C, Estensoro P, Santos M, Ricci P (2012) Design, construction and testing of a hydraulic power take-off for wave energy converters. Energies 5(6):2030–2052. https://doi.org/10.3390/en5062030

Spectral Properties of GaAs Cell Under the Space Irradiation

Yutao Zhang, Xiaying Meng, Jian Liu, Lingxuan Zhu, Yi Liao, and Yunze Gao

Abstract GaAs solar cell is the most important source of energy of satellite to maintain the steady working. Irradiation of electron and ozone will affect the performance of the GaAs solar cell. This paper is focused on the variety of spectral properties of GaAs cell under space irradiation. The surface structure is constructed according to the interaction between the solar surface and irradiation electron and atomic oxygen. Then the effect of erosion of structured surface on the spectral properties of GaAs cell is discussed. The variety of the spectral with the change of parameters of rough surface is investigated, which can be a good candidate for satellite design.

Keywords GaAs cell · Space irradiation · Spectral properties · Satellite

1 Introduction

Satellite plays an important role in our life, such as communication, remote observation, meteorological observation, etc. [1, 2]. Solar cell is the most important part of the whole satellite, which provides the energy for satellite to maintain the steady working [3]. GaAs cell is widely used in the satellite for its high optoelectronic conversion efficiency [4–6]. Plenty of efforts have been put into the design and optimization of GaAs cell, in which many kinds of structured surface are utilized to increase the conversion efficiency [7, 8].

The performance of solar cell tends to be degraded with the operation due to the space irradiation [9]. The electron and atomic oxygen are the most two prominent irradiation particles resulting in the degraded performance of solar cell around low orbit [10]. The electron and atomic oxygen particles with high-speed bombard on the surface of solar cell and interact with the atom of protecting layer of GaAs cell

Y. Zhang · X. Meng · J. Liu · L. Zhu · Y. Liao (✉)
National Key Laboratory of Scattering and Radiation, Shanghai Radio Equipment Research Institute, Shanghai 200438, China
e-mail: lygc21@163.com

Y. Gao
Xi'an Aerospace Yuan Dongli Engineering Co., Ltd, Xi'an 710100, China

S. Yadav et al. (eds.), *Energy Power and Automation Engineering*, Lecture Notes in Electrical Engineering 1118, https://doi.org/10.1007/978-981-99-8878-5_10

[11]. The atoms of protecting layer are disorderly stripped from the surface of GaAs cell. The primary surface structure would be changed, and the spectral properties are consequently degraded [12]. As a result of disordered stripping of atoms of protecting layer, the surface of GaAs cell tends to be a rough surface, whose roughness is obviously relative to the densities of electron and atomic oxygen, as well as the speed of irradiation particles [13].

Generally speaking, the surface structure of solar cell is seriously designed to possess the best spectral absorption and optoelectronic conversion within the working wavelength band. As the surface is eroded to rough surface, the spectral absorption is decreased, and the photocurrent of solar cell is reduced. In the worst case, the energy supply is not enough to maintain the equipment to normally operate. Great efforts have been put into the investigation of the effects of space irradiation on the satellite [14, 15]. Zhu et al. investigated the damage effects of LEO atomic oxygen environment on solar cell circuit and the erosion of atomic oxygen was obviously found in the solar cell [16]. Xu and Tang simulated the spectral properties of rough surface of different materials of satellite. It was found that the reflectance was gradually enhanced as the roughness was increased [17]. Up to now, the most investigations on the effects of electron and atomic oxygen irradiation on the spectral properties of space solar cell are centered on the experiment of space materials under irradiation. Few research about the simulation of spectral properties of solar cell under space irradiation is reported.

This paper is focused on the spectral properties of GaAs single-junction solar cell in the space environment. The structured surface is firstly optimized to possess the excellent spectral absorption within operating band. Then the rough surface is constructed according to the electron and atomic oxygen irradiation. Consequently, the spectral properties of solar cell are simulated by FDTD method and compared to analyze the effect of space irradiation.

2 Simulation Model

The structured surface is schematically shown in Fig. 1. The planar structured surface is considered for GaAs solar cell. The Ag film of thickness d_6 is employed as back electrode. The $Al_{0.3}Ga_{0.7}As$ film of thickness d_5 is contacted as n-type material on Ag film. The intrinsic GaAs film of thickness d_4 is deposited on $Al_{0.3}Ga_{0.7}As$ film. The p-type $Al_{0.8}Ga_{0.2}As$ film of thickness d_3 is deposited on GaAs film. Finally, the anti-reflection coating (ARC) consisted of TiO_2 film of thickness d_2 and SiO_2 film of thickness d_1 is deposited on the top of solar cell to suppress the reflection. The normal incident solar light propagates along the negative z-direction. As the irradiation is considered, the SiO_2 film is eroded to be rough surface, as shown in Fig. 1.

The optical properties of the materials used in GaAs solar cell are given in Fig. 2. The real part and imaginary part of refractive index of materials of GaAs cell are presented in Fig. 2a, b, respectively. The refractive index of GaAs, SiO_2, TiO_2, and Ag are obtained from Palik [18]. The properties of $Al_{0.8}Ga_{0.2}As$ and $Al_{0.3}Ga_{0.7}As$ are

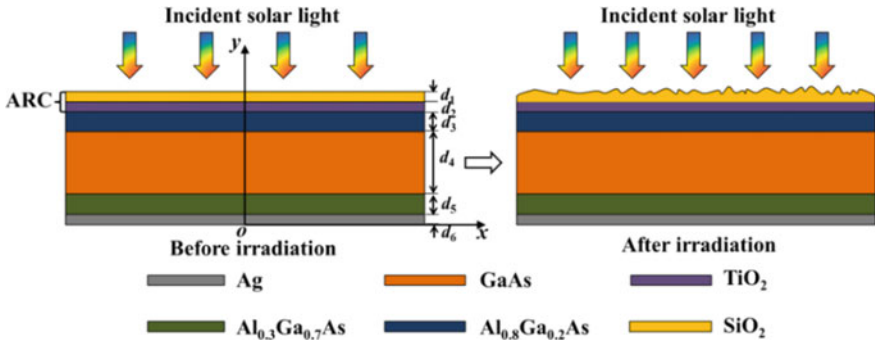

Fig. 1 Schematic diagram of structured surface of GaAs solar cell before irradiation and after irradiation

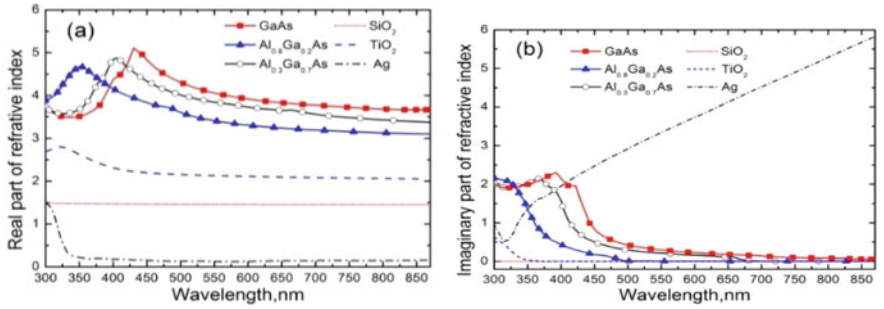

Fig. 2 Optical properties of materials used in GaAs solar cell, **a** real part of refractive index, **b** imaginary part of refractive index

obtained from Aspnes [19]. The optical properties are employed by FDTD algorithm to simulate the spectral properties of GaAs solar cell. The periodic boundary condition is applied along x- and y-directions, while the perfectly matched layer (PML) is applied in z-direction in the simulation.

3 Results and Discussion

The spectral properties of the GaAs solar cell are simulated by FDTD method and the geometry parameters are optimized. As shown in Fig. 3a, the total spectral absorption and the absorption of each layer within the wavelength band of 300–870 nm, which is same as operating band of GaAs cell, are presented. The incident solar light is mainly absorbed by the GaAs layer and p-type $Al_{0.8}Ga_{0.2}As$ due to their wonderful optical properties and enough thickness. This is benefit for the energy utilization, because the photons absorbed by GaAs layer, p-type $Al_{0.8}Ga_{0.2}As$ layer, and n-type

$Al_{0.3}Ga_{0.7}As$ layer can generate effective electron–hole pairs to convert to electric energy. The incident light within wavelength band of 300–400 nm is partly reflected due to the saltation of refractive index of material at the SiO_2/air interface. The light within wavelength band of 400–800 nm is almost completely absorbed. The absorption of the rest layers below GaAs layer is negligible. The standard spectral of solar irradiation in space, which is named AM 0, is shown in Fig. 3b. The green part indicates the energy within the wavelength band of 300–870 nm, which can be utilized by GaAs cell and converted to electric energy. According to spectral of AM 0, the average absorption of GaAs is calculated as

$$\alpha_a = \frac{\int_\lambda \alpha_{(\lambda)} I_{(\lambda)} \mathrm{d}\lambda}{\int_\lambda \alpha_{(\lambda)} \mathrm{d}\lambda} \tag{1}$$

where $\alpha_{(\lambda)}$ is the spectral absorption. $I_{(\lambda)}$ is for AM 0 emissions [20]. The average value of total absorption of GaAs cell within wavelength band of 300–870 nm obtained from Eq. (1) can reach as high as 0.957, while the average absorption of GaAs layer is 0.848. The average absorptions of p-type $Al_{0.8}Ga_{0.2}As$ layer and n-type $Al_{0.3}Ga_{0.7}As$ layer are 0.094 and 0.004, respectively. The total effective absorption, which contains the absorption of GaAs layer, $Al_{0.8}Ga_{0.2}As$ layer, and $Al_{0.3}Ga_{0.7}As$, is 0.946. Thus, the excellent absorption of GaAs cell is realized to benefit the photoelectric conversion.

By assuming that each photon absorbed by GaAs layer, p-type $Al_{0.8}Ga_{0.2}As$ layer, and n-type $Al_{0.3}Ga_{0.7}As$ layer can generate an electron–hole pair, the optical generation can be expressed as

$$G_{\mathrm{opt}}(r) = \int_{300\,\mathrm{nm}}^{\lambda_g} \frac{\varepsilon'' |E(r,\lambda)|^2}{2\hbar} I(\lambda) \mathrm{d}\lambda \tag{2}$$

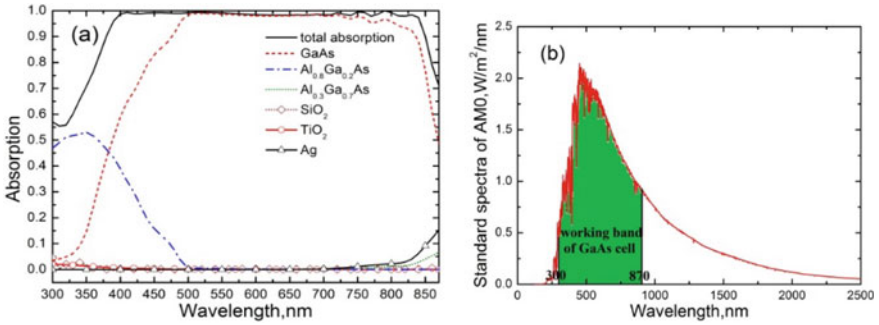

Fig. 3 Spectral absorption of the GaAs solar cell and standard spectra of AM 0, **a** absorption of GaAs cell, **b** standard spectra of AM 0

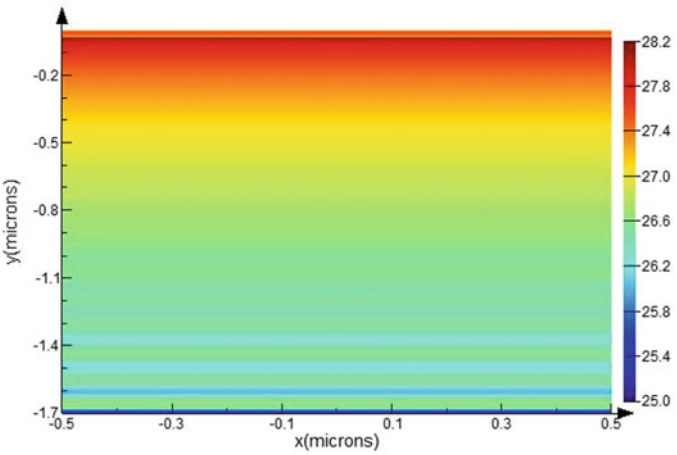

Fig. 4 Optical generation rate of the GaAs solar cell

where E is the electric field, ε'' is the imaginary part of the permittivity of the semiconductor material, $\hbar$ is the reduced Planck constant, and λ_g is the cut-off wavelength corresponding to the band gap of the semiconductor. According to Eq. (2), the optical generation distribution is calculated and presented in Fig. 4. As the light propagates in the solar cell, the energy is rapidly absorbed, and the energy arrives at the n-type $Al_{0.3}Ga_{0.7}As$ is quite low. Hence, the optical generation is mainly located at the p-type $Al_{0.8}Ga_{0.2}As$ layer and the upper part of GaAs layer.

Generally speaking, the erosion of space irradiation could be dozens of nanometers. To ensure enough protecting film, the thickness of 120 μm of SiO_2 film is practically applied in the industry. The spectral properties of such a solar cell are presented and compared to the spectral performance of the solar cell with the thickness of 94 nm of SiO_2 film, as shown in Fig. 5. The absorption of the solar cell with the thickness of 120 μm of SiO_2 film is slightly smaller than the absorption of solar cell with the thickness of 94 nm of SiO_2 film. To evaluate the performance difference, the average values of absorption of the solar cell with two different thicknesses of SiO_2 film are calculated according to Eq. (1), as listed in Table 1. It can be found that the total absorption and the intrinsic absorption of GaAs layer are both slightly reduced, as the thickness of SiO_2 protecting layer is increased to 120 μm. Despite the reduction of absorption performance, the detriment of space irradiation of atomic oxygen and electron can be effectively prevented to ensure the normal operation of solar cell.

As the satellite operates in the space, the surface of solar cell is eroded to be the rough surface. The rough surface is generally described by the root mean square (RMS) of roughness and correlation length L_c. The RMS and correlation length of rough surface of solar cell in space are closely relative to irradiation flux of electron and atomic oxygen. The rough surface induced by irradiation is presented in Fig. 6.

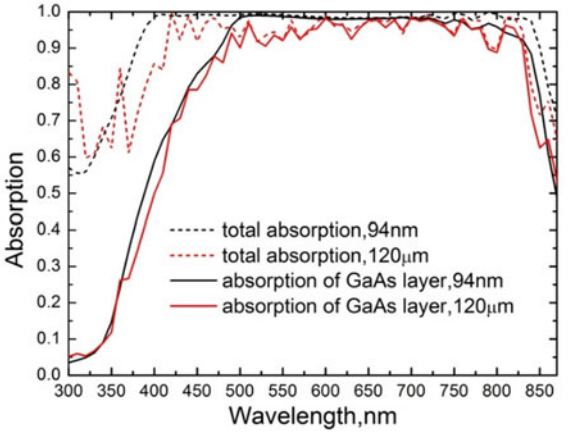

Fig. 5 Comparison of spectral properties of the solar cells to the thicknesses of SiO_2 film 94 nm and 120 μm

Table 1 Average absorption of the solar cell with different thicknesses of SiO_2 film

Thickness of SiO_2 film	94 nm	120 μm
Total absorption	0.957	0.919
Absorption of GaAs layer	0.848	0.816

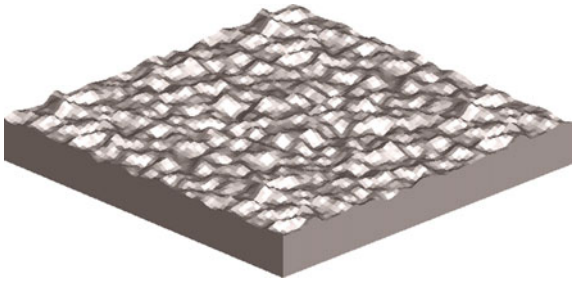

Fig. 6 Rough surface induced by irradiation of electron and atomic oxygen

The spectral properties of the solar cell with rough surface are calculated and presented in Fig. 7. In order to ensure the enough thickness of protecting SiO_2 film, the thickness of 5 μm of SiO_2 film is employed in the GaAs cell. According to the experimental results in the reported literature, the RMS of protecting film of GaAs cell is 31 nm. Thus, the RMS of 31 nm of SiO_2 film protecting layer is considered in the GaAs cell, while the different correlation lengths are respectively employed. As shown in Fig. 7a, the spectral absorptions of GaAs cells with different correlation lengths are presented. It is found that the absorption is obviously reduced as the cell surface is eroded to be rough surface. However, the change of absorption of the GaAs cell with the rough protecting layer is almost negligible. The average absorption is calculated according to Eq. (1) and given in Fig. 7b. The average absorption is obviously decreased from 0.92 to 0.818 as the flat surface is eroded to rough surface with the correlation length of 250 nm. With the further increasing of correlation

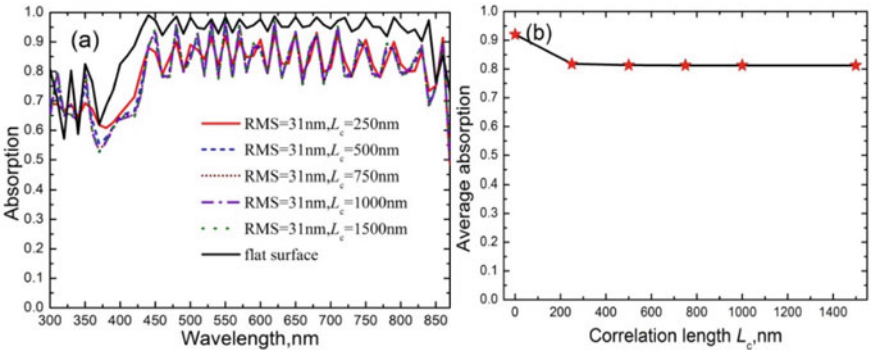

Fig. 7 Absorption properties of rough surface with different correlation lengths, **a** spectral absorption, **b** average absorption

length, the change of the average absorption is negligible. The average absorption tends to be a constant of 0.812. This is due to that the designed matching of refractive indices at the SiO_2/air interface is damaged by the space irradiation.

4 Conclusion

The effect of space irradiation on the spectral properties is considered in the GaAs space solar cell. The anti-reflection coating is designed firstly for the GaAs cell with the solar cell materials. Then the space irradiation is introduced, and the rough surface is discussed. The rough surface is induced due to the erosion of space irradiation on the surface of GaAs cell. Consequently, the mismatch of refractive indices is brought out and the absorption within the working band of GaAs cell is reduced. The average absorption would be reduced by 11.1%.

Acknowledgements The authors thank the Natural Science Foundation of Shanghai (Grant No. 20ZR1455100), the Natural Science Foundation of Shanghai (Grant No. 20ZR 1454800), and the National Natural Science Foundation of China (Grant No. U22B2045) for their support.

References

1. Liu L (2021) The optimization of satellite orbit for space-VLBI observation. Res Astron Astrophys 21(2):037
2. Lou RC, Sanchez Esguevillas AJ, Ia B et al (2008) IPv6 networks over DVB-RCS satellite systems. Int J Satellite Commun Netw 26:45–56
3. Sheng Z, Liang R (2016) Heteroscedastic linear reliability evaluation for solar cell degradation testing. In: IEEE international conference on industrial engineering and engineering management, Indonesia, pp 890–893

4. Strobl G, Dietrich R, Hilgarth J et al (2003) Advanced Gainp/Ga(In)As/Ge triple junction space solar cells. In: Proceedings of 3rd World Conference on Photovoltaic Energy Conversion, Osaka, pp 658–661
5. Yamaguchi M, Takamoto T, Araki K et al (2005) Multi-junction III-V solar cells current status and future potential. Sol Energy 79(1):78–85
6. King R, Fetzer C, Law DC et al (2006) Advanced III-V multi-junction cells for space. In: Conference record of the 2006 IEEE, World conference on photovoltaic energy conversion, Waikoloa, pp 1757–1762
7. Peng Y, Gong S, Liu K, Yao M (2020) Nano-sphere surface arrays based on GaAs solar cells. J Semicond 41:012701
8. Zhang M, Ning T, Chen J et al (2019) Improvement on the interface properties of p-GaAs/n-InP heterojunction for wafer bonded four-junction solar cells. J Mater Technol 35:330–333
9. Rochy A, Marjila B, Onohara K et al (2020) Numerical simulation of GaAs solar cell aging under electron and proton irradiation. IEEE J Photovoltaics 6(9):1774–1782
10. Li T, Jiang L, Feng W et al (2009) The effects of space atomic oxygen erosion on epoxy and silicone adhesives in LEO spacecraft. Spacecraft Environ Eng 26(3):222–224
11. Silverman EM (1996) Space environmental effects on spacecraft LEO materials selection guide. NASA, Washington, DC
12. Ondoh T, Marubashi K (2000) Science of space environment. IOS Press, Amsterdam, pp 181–187
13. Sun C (2007) An investigation on the space charged particle environmental effects of the cover-glass for solar cell. Harbin Institute of Technology.
14. Ali N, Ali TA, Rafat NH (2019) Impact of proton and electron irradiation-induced defects on the dark current of GaAs solar cells. IEEE J Photovoltaics 9(6):1661–1667
15. Xin G, Zhan-Zu F, Xin-Yu C et al (2014) Performance evaluation and prediction of single-junction and triple-junction GaAs solar cells induced by electron and proton irradiations. IEEE Trans Nucl Sci 61(4):1838–1842
16. Zhu L, Qiao M, Zeng Y et al (2019) Atomic oxygen effect analysis and experimental study of LEO satellite solar cell circuit. Spacecraft Eng 28(1):137–142
17. Xu B, Tang Y (2020) Influence of exterior materials roughness variation on satellite spectrum reddening effect. Chin J Space Sci 40(1):86–92
18. Palik ED (1985) Handbook of optical constants of solids. Academic Press, New York
19. Aspnes DE, Kelso SM, Logan RA et al (1986) Optical properties of AlxGa1-xAs. J Appl Phys 60(2):754–767
20. Website for NREL's AM 0 Standard Dataset. Reference solar spectral irradiance: air mass 0 (2015) Available at: http://rredc.nrel.gov/solar/spectra/am1.5. Accessed 18 Nov 2015

Control Method of High-power Flywheel Energy Storage System Based on Position Sensorless Algorithm

Zeming Zeng, Congzhe Gao, and Dahui Zhang

Abstract In this paper, a direct arcsine method based on motor-side voltage is proposed to estimate rotor position and speed. However, under high power, the inductive voltage drop of the flywheel motor is larger, and the motor-side voltage has a larger phase difference with the counter-electromotive force of the motor. By analyzing the operating state of the voltage circle during flywheel charging and discharging at high power, the angle is compensated, so that the angle can be corrected. This paper also gives the control method for charging and discharging the flywheel energy storage system based on the speed-free algorithm. Finally, experiments are carried out on real hardware to verify the correctness and effectiveness of the control method of flywheel energy storage system based on the speed sensorless algorithm.

Keywords Flywheel · Sensorless · Charge and discharge control

1 Introduction

The flywheel energy storage converts electrical energy into mechanical energy in the process of charging, while the discharge converts mechanical energy into electrical energy and feeds it back to the grid. Due to its advantages of simple structure, less loss, reliable operation, and high efficiency, permanent magnet synchronous motor has become one of the main forms of motor in flywheel energy storage system [1]. However, when the permanent magnet synchronous motor is controlled, sensors need to be installed on the rotor to detect the position and speed of the rotor, which will undoubtedly increase the hardware cost, and the output signal is also vulnerable to electromagnetic interference, such as high frequency. Therefore, various sensorless technologies are widely used in the control of permanent magnet synchronous motor.

The literature [2] provides an overview of the control of permanent magnet synchronous motors without speed sensors, and the current control methods can

Z. Zeng · C. Gao (✉) · D. Zhang
Beijing Institute of Technology, Beijing, China
e-mail: gcz_fly@163.com

S. Yadav et al. (eds.), *Energy Power and Automation Engineering*, Lecture Notes in Electrical Engineering 1118, https://doi.org/10.1007/978-981-99-8878-5_11

be divided into two broad categories: (1) One category is mainly applicable to the control of low speeds, including the high frequency injection method and so on. This method is more complex for signal processing and the dynamic performance is not ideal. (2) The other category is based on mathematical models to extract the rotor position as well as the speed by various algorithms. These methods can be subdivided into open-loop and closed-loop algorithms. The open-loop algorithms include direct calculation method, inverse potential integration method, etc. The closed-loop algorithms mainly include the sliding-mode observer, Kalman filter method, etc.

In this paper, a direct calculation method based on the arcsine method of the machine terminal voltage is proposed to estimate the rotor position and speed. The method is computationally small and has a fast response time. Since the flywheel energy storage system requires high-power operation, when the inductive voltage drop of the motor increases, resulting in a large phase difference between the motor terminal voltage and the motor counter-electromotive force, the angle is compensated and corrected at high power, so that the active power can be boosted. The current closed-loop control with simulated angle is used for open-loop start-up, and switched to the speed-free algorithm control in this paper after the speed reaches the set value. And the charging and discharging experiments of flywheel energy storage system are carried out to verify the effectiveness of the flywheel energy storage system control of the algorithm.

2 Direct Calculation Method Based on High-power Angle Compensation

2.1 Arcsine Calculation

The direct arcsine calculation method has less computation and faster response speed, and it can estimate the rotor information position more accurately at low speed. This method requires reading back the three-phase voltages u_a, u_b, u_c from the flywheel, low-pass filtering, and extracting and normalizing the magnitudes after filtering. The normalization formula is shown in formula (1).

$$F_x = \frac{u_X}{k\sqrt{u_a^2 + u_b^2 + u_c^2}}, X = a, b, c \tag{1}$$

F_x is the value after normalization, and k is a constant, $k = \sqrt{\frac{2}{3}}$.

After normalizing the three-phase voltage, as shown in Fig. 1, it is divided into six parts in one fundamental period as shown in the following method. Where yellow, green, and red are the three-phase waveforms F_a, F_b, F_c, respectively.

We find the angles in each of the six regions and finally stitch it together to get a final angle θ_{af}. The calculation formulas for the six regions are shown in formula

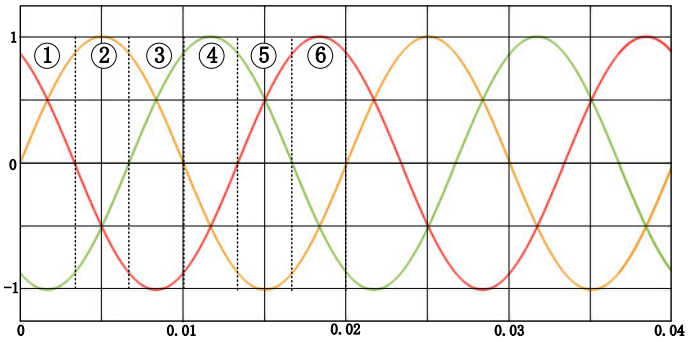

Fig. 1 Three-phase voltage waveform after normalization

(2).

$$\begin{cases} 1: & F_b < 0 \text{ and } F_c < 0, \theta_{af} = -\arcsin(F_c) + \pi/3 \\ 3: & F_a > 0 \text{ and } F_b > 0, \theta_{af} = \arcsin(F_b) + 2\pi/3 \\ 4: & F_a < 0 \text{ and } F_c < 0, \theta_{af} = -\arcsin(F_a) + \pi \\ 5: & F_b > 0 \text{ and } F_c > 0, \theta_{af} = \arcsin(F_c) + 4\pi/3 \\ 6: & F_a < 0 \text{ and } F_b < 0, \theta_{af} = -\arcsin(F_c) + 5\pi/3 \end{cases} \tag{2}$$

The angle θ_{af} is obtained after splicing, and the angular velocity ω_{af} is obtained after differentiation, as shown in Eq. (3). Afterwards, ω_{af} is adjusted by PI to obtain ω.

$$\omega_{af} = \frac{\mathrm{d}\theta_{af}}{\mathrm{d}t} \tag{3}$$

After that, the angle θ_1 can be obtained by integrating by ω. As shown in Eq. (4).

$$\theta 1 = \int \omega \mathrm{d}t \tag{4}$$

The three-phase voltage is collected back after adding a low-pass filtering link, which will make the motor at high frequencies when the voltage will produce hysteresis, resulting in the angle will also produce hysteresis, so the filtering compensation angle $\Delta\theta_1$ needs to be added. Where $\Delta\theta_1$ is related to the frequency of the three-phase voltage and current of the motor, and is a fixed value that can be obtained by checking the table.

2.2 Angle Compensation During High-power Charging and Discharging of Flywheel

The above method is calculated by using the voltage U_m at the machine end, the method in the case of low power and small current, the inductive voltage drop U_L of the motor is small according to Eq. (5), which can approximate the voltage at the machine end to the moto's counter-electromotive force E. However, when the flywheel is running at high power and high current, the voltage drop of the motor is larger, the voltage at the machine end and the motor's counter-electromotive force will have phase difference, so compensation is needed. If not compensated, it will lead to abc three phases can not fully correspond to the dq axis, a lot of energy are done reactive power consumption, resulting in active power up, the power factor is low.

$$U_m = U_L + E \tag{5}$$

$$U_L = \omega_e L_m I_m \tag{6}$$

$$E = \omega_m K \tag{7}$$

$$\Delta\theta 2 = K_a \mathrm{I}_m \tag{8}$$

Formula (6) is the calculation formula of inductance voltage. Where ωe is the electrical angle, ω_m is the mechanical angle, the motor counter-electromotive force and motor speed are linearly related, K is the counter-electromotive force coefficient. Formula (7) is the formula for calculating motor counter-electromotive force. L_m is the motor inductance, and I_m is the motor current. As the motor power rises, the motor current rises with it, creating a greater phase difference. Therefore, the angle is positively related to the current magnitude and K_a is the current coefficient of the compensation angle. The compensation formula for the compensation angle $\Delta\theta_2$ is shown in Formula (8).

Finally, the power factor of the high-power flywheel system is the maximum when the angle θ_m is used for the current closed-loop control. θ_m angle is calculated as shown in Formula (9). The control block diagram of the overall speed-free algorithm is shown in Fig. 2.

$$\theta_m = \theta_1 + \Delta\theta_1 + \Delta\theta_2 \tag{9}$$

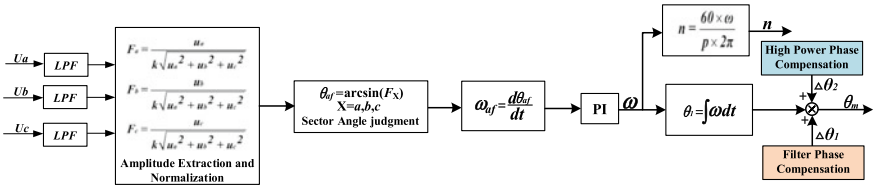

Fig. 2 Overall speed sensorless algorithm control block diagram

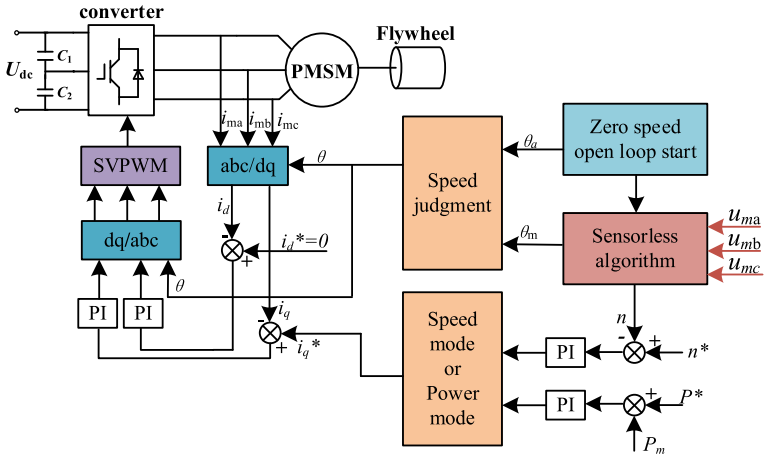

Fig. 3 The charging and discharging control block diagram

3 Flywheel Start and Charge and Discharge Control

The motor is started at zero speed with an open-loop start using current loop control with analog angle, and after the speed rises to the set speed value, it switches to the speed-free algorithm control in this paper. The current inner loop control is used and the outer loop is either speed outer loop or power outer loop, which can be switched for control. The charging and discharging control block diagram is shown in Fig. 3.

4 Experimental Results and Analysis

The hardware structure circuit diagram of flywheel energy storage system is shown in Fig. 4. It consists of a grid-side converter, a machine-side converter, an LC filter, a permanent magnet synchronous motor, and a flywheel. The grid-side converter controls the DC bus voltage and the machine-side converter controls the motor speed and the overall power. The voltage on the grid-side is 750 V.

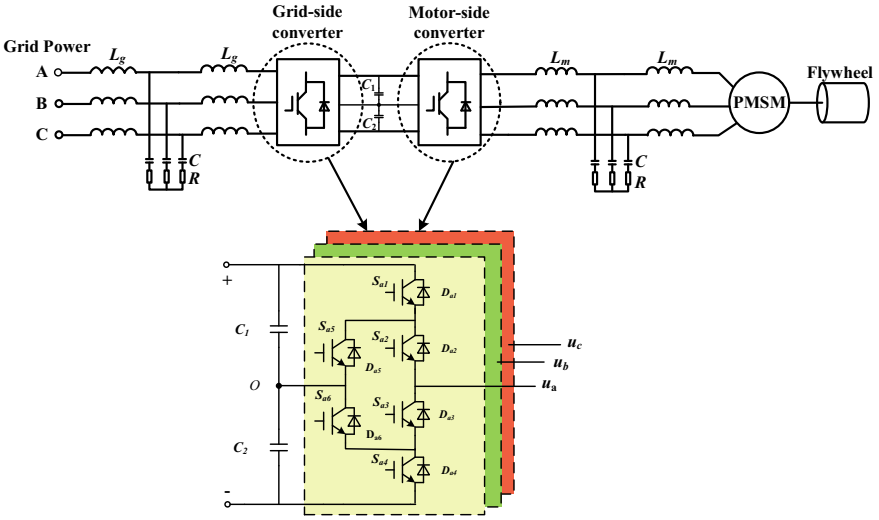

Fig. 4 Hardware structure circuit diagram of flywheel energy storage system

Table 1 Parameters of PMSM

Parameters	Value
Rated speed (r/min)	6000
Stator inductance (mH)	120
Pole-pairs	3
Inertia (kg m^2)	510

The parameters of the permanent magnet synchronous motor are shown in Table 1. The experimental hardware circuit and flywheel are shown in Fig. 5. The flywheel can run up to 500 kw of power.

As shown in Fig. 6, the angle extracted by the speed-free algorithm can be seen to be relatively smooth. Finally, the algorithm is used to run to the rated speed of 6000 rpm. Figure 7 shows the voltage and current waveforms when the flywheel is running at high power, where red is the motor-side current, green is the motor-side voltage, and blue is the grid-side current. Figure 7a shows the waveform before the high-power angle is compensated, which can also be speed regulated, but it can be seen that the net-side current is only 110 A, and the power factor is relatively low. Figure 7b shows the waveform after the angle compensation, which can be seen that the net-side current increases and the power factor is improved with the same speed and current of the motor.

Figure 8 shows the voltage-current waveforms of the flywheel operating at full power. Figure 8a shows the waveform when the flywheel is charged at 500 kw and Figure 8b shows the waveform when the flywheel is discharged at 500 kw. It can be seen that it operates well under this algorithm.

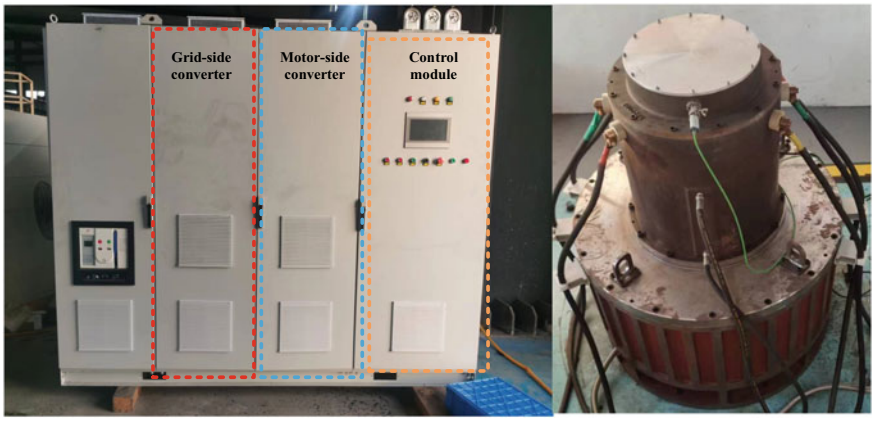

Fig. 5 Hardware physical diagram

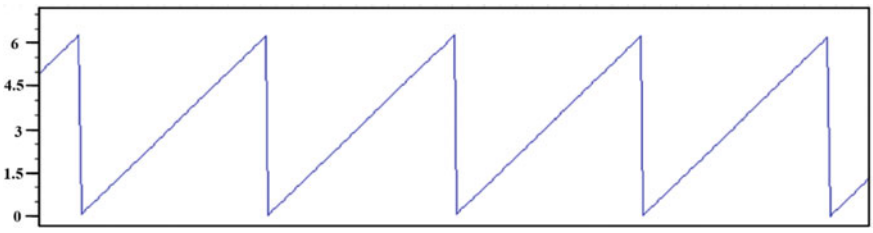

Fig. 6 Actual angle waveform

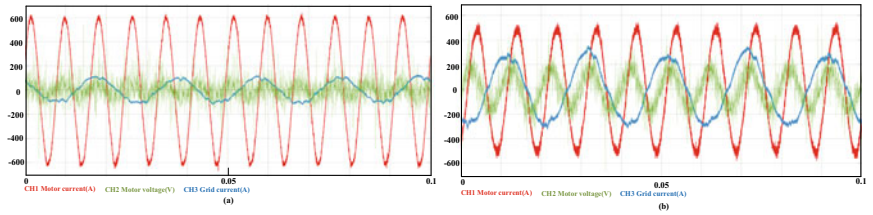

Fig. 7 Voltage and current waveforms during flywheel operation

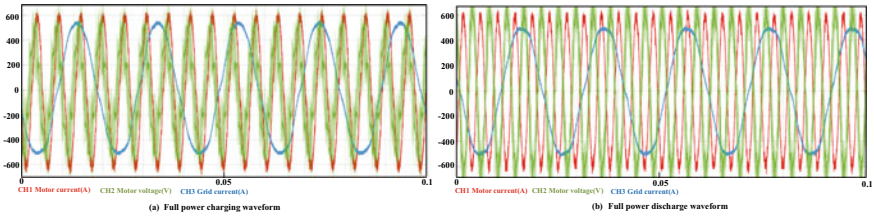

Fig. 8 Waveform at full power operation

5 Conclusion

In this paper, for high-power flywheel energy storage motor control, an inverse sine calculation method based on the voltage at the end of the machine is proposed, and angular compensation can be performed at high power, which makes its power factor improved. The charging and discharging control block diagram of the motor based on this algorithm is drawn. The voltage of the DC bus is stabilized and controlled by the grid-side converter, while the machine-side converter performs the control of motor speed and overall system power charging and discharging. The relevant experiments are conducted through the hardware platform, and their experimental results also verify the feasibility of the algorithm.

References

1. Liu W, Zhou L, Tang X et al (2014) Research on FESS control based on the improved sliding-mode observer. Proc CSEE 34(1):71–78
2. Zhou T, Jiang Q (2021) Overview of sensorless control technology for full speed range permanent magnet synchronous motors. Electron Technol 34(4):11
3. Shao Y, Guo L, Cai G et al (2022) Research on fast power smoothing control strategy for wind power generation system with flywheel energy storage. Sichuan Power Technol 45(5):14–19
4. Zhang ZS, Wang CC, Zhou ML et al (2020) Parameters compensation of permanent magnet synchronous motor in flux-weakening region for rail transit. IEEE Trans Power Electron 35(11):12509–12521
5. Zhuang X, Wen X, Zhao F (2010) Wide-speed-range sensorless control of Interior PMSM based on MRAS. In: 2010 international conference on electrical machines and systems, IEEE
6. Consoli A, Raciti A (1991) Analysis of permanent magnet synchronous motors. IEEE Trans Ind Appl 27(2):350–354
7. Jin L, Wang F, Yang Q et al (2018) Typical deep learning model and training method for performance analysis of permanent magnet synchronous motor. Trans China Electrotechnical Soc 33:41–48
8. Zhang J, Liu Q, Gui Z et al (2022) Charge-discharge composite control strategy and application research of flywheel energy storage system. J Inner Mongolia Univ Technol Nat Sci Edn 41(5):451–457
9. Yuan JQ, Li YL, Li BT et al (2012) A novel bidirectional DC-DC converter with robust control scheme for flywheel energy storage system. Adv Mater Res 383–390:3545–3551
10. Saleh K, Sumner M (2022) Sensorless control of a PMSM drive post an open circuit failure based on 3D-SVPWM technique. IEEJ Trans Electr Electron Eng 7:17

Analysis of the Effect of Pressure on the Flow Characteristics of Pulverized Coal in a Pipe Based on Surface Energy Theory

Zhifeng Kang and Zhihai Cheng

Abstract The surface energy of coal powder has a significant impact on its tribological properties. Due to the presence of surface energy, free molecules in the air will undergo physical adsorption on the surface of coal powder, resulting in changes in surface structure. Pressure has a significant impact on the physical adsorption and surface structure of coal powder, thereby altering its flow characteristics. Establish a model for pneumatic conveying in the pipeline between the outlet of the coal mill and the boiler burner, and use CFD software Fluent to numerically simulate the movement of coal powder in the pipeline. In numerical simulation, the effects of different pressure levels on the velocity of coal powder at the outlet of the pipeline were studied under the same inlet and outlet pressure difference. The simulation results showed that within the pressure level range of this study, the velocity of coal powder at the outlet of the pipeline increased as the pressure decreased. Based on the analysis of surface energy theory, it can be concluded that as the pressure level decreases, the surface energy of coal powder decreases, the adsorption capacity of coal powder decreases, the interaction force between coal powder decreases, the friction loss of coal powder in the pipeline decreases, and the flow characteristics of coal powder enhance.

Keywords Coal powder · Surface energy · Physical adsorption · Pressure · Flow properties

1 Introduction

The uneven distribution of gas powder in the furnace of thermal power plants is mainly determined by the mobility of coal powder. The fluidity of pulverized coal consists of two parts: flow characteristics and jet characteristics. Flow characteristics mainly refer to the performance of pulverized coal transported outside the blast

Z. Kang · Z. Cheng (✉)
Shanghai University of Electric Power, Shanghai, China
e-mail: 1270474435@qq.com

S. Yadav et al. (eds.), *Energy Power and Automation Engineering*, Lecture Notes in Electrical Engineering 1118, https://doi.org/10.1007/978-981-99-8878-5_12

furnace, such as pipeline transport and stacking [1]. The foreign research fields of powder flow characteristics are mainly focused on food and pharmaceutical industries, and the research direction is mainly focused on the innovation of flowability testing methods, and there are few systematic studies on the flow characteristics of pulverized coal. The domestic research status of systematic research on powders started late [2]. Previously, scholars at home and abroad studied the flow characteristics of pulverized coal mostly in pulverized coal bunkers, and seldom involved in the study of flow characteristics in the gas–solid two-phase flow in pulverized coal pipeline transportation process, and the former mostly used the rest angle method, Carr index method [3], HR, JENIKE shear experiment, and other methods to evaluate the flowability of pulverized coal [4]; the former studied the research of pulverized coal particle size and pulverized coal moisture content on the flow characteristics, but did not investigate the underlying causes affecting the flow characteristics [5]. Few studies have involved the effect of pressure on the flow characteristics of pulverized coal, and all reactions occurring between pulverized coal and the external environment start from the surface of pulverized coal, then the pressure as well as the energy on the surface of pulverized coal is bound to be the key to study these reactions, and the previous studies on this aspect are not so in-depth.

The essential reason for the effect of pressure on the flow characteristics of pulverized coal is still that the pressure change changes the surface energy of pulverized coal. The pressure change around the pulverized coal affects the "quality" of the surface energy, which affects the adsorption capacity per unit area [6]. The unbalanced force on the surface molecules of pulverized coal makes pulverized coal produce surface energy, and the surface energy of pulverized coal is the root cause of adsorption and agglomeration of pulverized coal particles. Therefore, it is very critical to study the surface energy of pulverized coal for the flow characteristics of transport in pulverized coal pipeline, and it has very important research significance.

2 Research Methodology

2.1 Research Idea

This study focuses on the flow characteristics of pulverized coal in the pipeline, the change of adsorption layer on the surface of pulverized coal is affected by the pressure on the surface of pulverized coal, so set up the experimental program according to the numerical simulation of the change of flow rate of pulverized coal pipeline at different pressure levels, the numerical simulation, the differential pressure between the import and export of the pipeline is the driving force of the flow of pulverized coal, interfering with the simulation results, so the same group of simulated pipeline is set up with the same differential pressure between the import and export, different

pressure levels. The simulation results are analyzed, the results are derived, and the results are experimentally verified and studied and discussed to form a scientific and reliable conclusion.

2.2 Numerical Simulation

Fluent was used to numerically simulate the movement of pulverized coal in the outlet pipe of the coal mill [7]. The effect of pressure on the movement of pulverized coal in the pipe was studied by setting different groups of variables and comparing and analyzing the flow rate of pulverized coal at the outlet of different groups of pipes [8]. The ANSYS FLUENT pre-processing software SCDM was used to establish a geometric model of the pulverizer system feeding pipeline. In this study, a 1:1 3D geometric model was established based on the actual structure and dimensions of the pulverized coal pipeline given in the boiler drawing of Tangzhai power plant in Guizhou, taking the coal mill outlet direction as the x-direction, the back wall direction as the y-direction, and the height direction as the z-direction. The calculation area includes the area pipeline from the coal mill outlet to the burner inlet section. The calculation model is divided into the mesh of the geometric model by the method of Fluent meshing, and the total number of meshes generated by the simulation is 1055792 with a mesh quality of 0.65. This set of meshes not only ensures the conditions of high precision, but also has relatively good applicability. Air is blown vertically upward from the coal mill outlet into the powder feeding duct at a certain rate, and the numerical simulation is calculated using a three-dimensional model. The solid properties refer to the physical properties of the pulverized coal particles, the gas phase is air, the dynamic viscosity and the density are taken according to the physical properties of dry air, the pressure is 101325 Pa, the acceleration of gravity is 9.8 m/s^2, and the velocity of the particles at the inlet of the mill is taken as 2 m/s. The time step of the unsteady state calculation is 2×10^{-2} s.

As shown in Fig. 1, the pulverized coal piping model is built by using the data of BBD4360 double-inlet and double-outlet mill direct blow pulverization system F coal mill outlet piping of Huadian Guizhou Tangzhai Power Plant 2 × 600 MW—HG-1900/25.4-WM10 boiler, which has four pipes of different lengths and different arrangements. Fluent set up the ducts with the initial air velocity of 2 m/s, pulverized coal volume of 3 kg/s, pulverized coal density of 500 kg/m^3, air temperature of 80 °C, duct inlet pressure of 3200 pa, duct outlet pressure of 1000 pa, pulverized coal particle size of 50 microns, based on the pressure, Fluent model and experimental data are set with reference to the actual operating data of the power plant, which is relatively reliable and scientific. It is one of the most widely used fluid calculation methods. The turbulence model is selected as standard k-e, and the near-wall surface is selected as standard wall function; the discrete phase model interaction is selected as interaction with continuous phase; the numerical simulation method is selected as finite volume

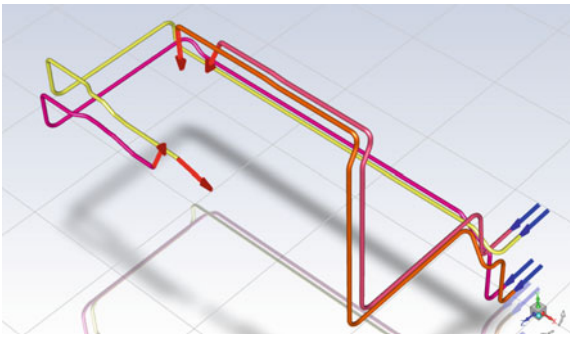

Fig. 1 Four sets of pipeline models used in numerical simulation

method, which has the advantage of showing accurate integral conservation even in the case of coarse grid; The discrete format first-order windward format [9], relaxation factors 0.7, 0.8, 0.8, 1, 0.5.

3 Results

The study of pressure influence on the outlet flow rate of pulverized coal pipeline was numerically simulated by setting four experimental groups of inlet pressure/outlet pressure of 2700/2000, 2200/1500, 1700/1000, 1200/500 pa for 700 pa differential pressure in Fluent; the same mill #1, #2, #3, #4 four pipelines for numerical simulation.

As shown in Fig. 3, according to the 1 # exits velocity Fluent simulation results: as shown in Fig. 3 pipe exit velocity in the range of 14–17 m/s. When the pressure difference is certain, the pipe exit velocity increases as the inlet and outlet pressure levels decrease. In the line graph, the slope of the line is basically constant or the slope becomes smaller, indicating that the relationship between the coal powder pipeline outlet flow velocity and pressure level change in the region outside the pressure level range of this study may be positively or negatively correlated, and this study only discusses the experiments in the specific pressure level range.

In Fig. 4, velocity clouds, *P* represents the pipe inlet pressure of this experimental group, all four clouds are at the same pipe outlet location, due to the very small difference in pipeline flow velocity at the four pressure levels, a relatively small velocity domain is set, the velocity range of 17–21 m/s, it can be seen that as the pressure level of the pipe decreases, the flow velocity out of the bend at the exit of the same pipe becomes greater and greater.

In order to verify the results of the numerical simulation, the actual operation of the coal mill at the power plant site was experimented. Under the stable operation data of each power plant, the coal volume of the coal mill was kept constant and the temperature of the coal mill pipeline was kept constant, four sets of different coal powder pipeline inlet pressure/outlet pressure experiments were set up, and the

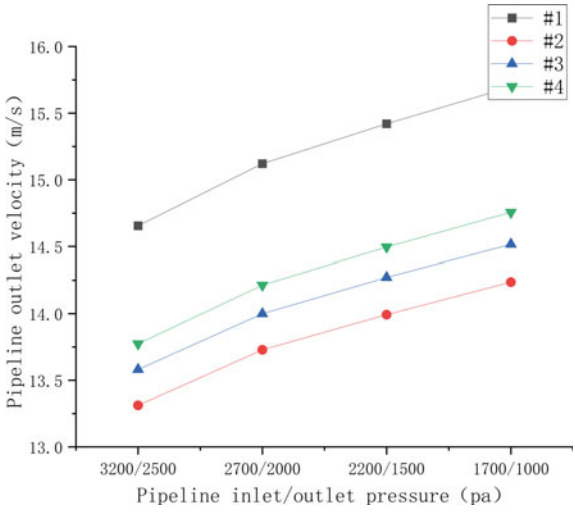

Fig. 2 Relationship between flow rate and pressure at the outlet of coal powder pipe in the experiment

experimental data results are shown in Fig. 2. With the decrease of the pressure level in the pipeline, the coal powder pipeline outlet flow rate also increased gradually, which is the same as the data change pattern in the numerical simulation to verify the correctness of the numerical simulation results.

4 Discussion

To study the reasons for this from the surface energy perspective:

(1) The effect of pressure on the adsorption on the surface of pulverized coal. Previous studies have shown that the higher the pressure, the greater the adsorption of coal dust on the gas [10]. Other studies have shown that the adsorption of gases increases with the increase in pressure [11]. The adsorption energy characterizes the stability of the adsorption system and can reflect the change in the total surface energy before and after the occurrence of adsorption [12]. Many studies have shown that the adsorption of methane on coal surfaces is mainly physical and is caused mainly by Van der Waals forces between methane molecules and coal molecules [13].

(2) Mechanism of pressure influence on adsorption process. For coal with a certain degree of metamorphism, the higher the gas pressure on the coal surface, the more gas flows into the various pores of the coal powder, the easier the gas adsorption on the coal surface, the smaller the surface energy of the coal, the coal powder expands and becomes larger [14], and physical deformation occurs, and the amount of gas adsorption on the coal surface increases with the increase

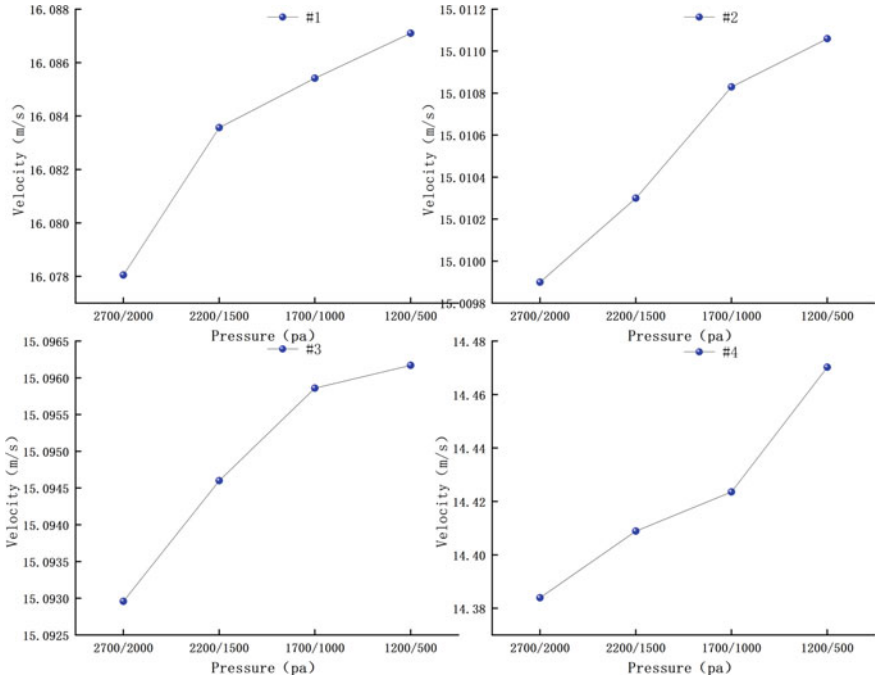

Fig. 3 Pipeline pressure #1, #2, #3, #4 and outlet velocity of pulverized coal pipeline at 700 pa pressure difference

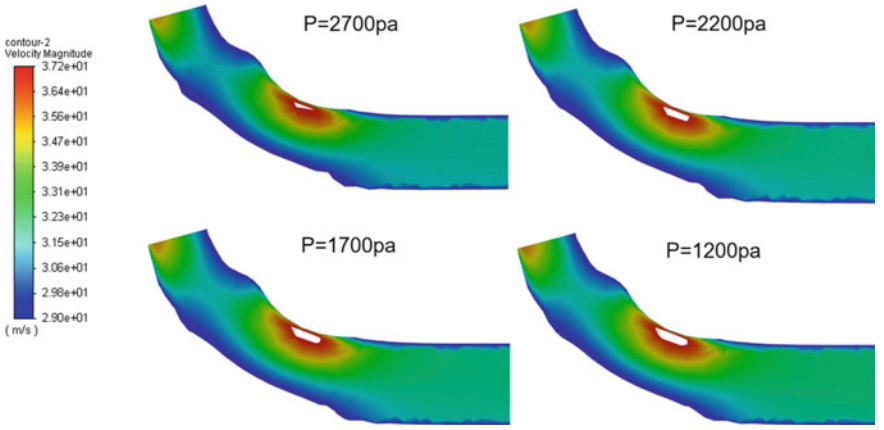

Fig. 4 Velocity cloud 17–21 m/s of #3 pipe outlet section at different pressure levels

of the gas pressure applied, i.e., at a certain temperature, the adsorption of coal is proportional to the pressure. The increase in adsorbed gas pressure causes adsorption and gas buildup.

(3) As the external gas pressure becomes smaller, the attraction ability of coal dust to gas molecules is weaker, and some gas molecules on the surface of coal dust and in the pores desorb away from coal dust into free state gas molecules, and the adsorption amount on the surface of coal dust decreases, while the whole of coal dust and adsorption layer is in contraction deformation, and the number of collisions between coal dust in the same pipe space decreases; the interaction force between coal dust and coal dust is weakened. The interaction force between pulverized coal and pulverized coal is weakened, which leads to the reduction of collision loss energy between pulverized coal, thus reducing the collision friction loss between pulverized coal. The velocity of pulverized coal at the outlet of the pipe increases.

Surface energy is the root cause of pulverized coal adsorption, using the physical adsorption on the surface of pulverized coal to study the pneumatic transport process of pulverized coal, and exploring the deep mechanism of the amount of adsorption on the surface of pulverized coal on the flow characteristics of pulverized coal in the pipe, can provide a reliable solution for the uneven flow rate of the gas-powder mixture at the exit of the burner in the furnace of thermal power plants; for the actual operation of the power plant to adjust the combustion and solve the uneven heat distribution inside the boiler, can improve the capability of thermal power plants for deep peaking.

5 Conclusion

In the range of pressure levels in this study, the following conclusions are drawn:

1. As the ambient pressure level decreases, the higher energy molecules adsorbed on the surface and in the pores of pulverized coal start to leave the surface of pulverized coal and leave the adsorption layer; the adsorption equilibrium of the adsorption layer on the surface of pulverized coal moves toward desorption, and the adsorption amount on the surface of pulverized coal decreases;
2. Pressure level decreases, the adsorption amount on the surface of pulverized coal decreases, and the pulverized coal gas–solid as a whole is in the stage of contraction and deformation;
3. The pressure level decreases, the force between pulverized coal decreases, and under the dual influence of the contraction and deformation of pulverized coal and the decrease of pulverized coal interaction force, the friction between pulverized coal decreases and the flow characteristics are enhanced, which is beneficial to the transport of pulverized coal in the pipeline.

References

1. Zhang W, Qi C, Zhang J, Ma C (2012) Correlation between the powder flow ability and coal quality of pulverized coal for a blast furnace. J Chin J Eng 34(4):430–436. https://doi.org/10.13374/j.issn1001-053x.2012.04.013
2. Xi H, Guo X, Liu H (2012) Measurement of flowability of coal powders and research methods. J CIESC J 63(2):433–440. https://doi.org/10.3969/j.issn.0438-1157.2012.02.014
3. Qi C, Feng G, Yu C (2016) Research on flowability of pulverized coal injection based on Carr index method. J Exp Technol Manag 33(08):54–58. https://doi.org/10.16791/j.cnki.sjg.2016.08.014
4. Fan B, Yao L, Song K et al (2014) Flowability of pulverized coal under different consolidation stress. J Combust Sci Technol 20(05):418–422. https://doi.org/10.11715/rskxjs.R201403047
5. Xie X, Shen X, Tang X et al (2008) Study on some factors impacting flowability of pulverized coal. J Mei T'an Hsueh Pao (J Chin Coal Soc) 33. https://doi.org/10.3321/j.issn:0253-9993.2008.01.019
6. Gao Z, Ma D, Chen Y et al (2020) Effect of water content on adsorption/desorption of methane of different macroscopic lithotypes. J Coal Sci Technol 48(8):97–105. https://doi.org/10.13199/j.cnki.cst.2020.08.012
7. Pei Y, Xiong Y, Zhou H (2015) Numerical simulation on high-pressure dense-phase pneumatic conveying of pulverized coal in vertical elbow. J Chin Soc Power Eng 35(09):760–767. https://doi.org/10.3969/j.issn.1674-7607.2015.09.012
8. Liu Y, Su Z, Fang H et al (2010) Review on CBM desorption/adsorption mechanism. J Well Testing 19(6):37–44. https://doi.org/10.3969/j.issn.1004-4388.2010.06.007
9. Ge X, Sun J, Li Y et al (2020) Numerical simulation of silt erosion characteristics of an injector of Pelton turbine. J Hydraul Eng 51(12):1486–1494. https://doi.org/10.13243/j.cnki.slxb.20200430
10. Zhang Y, Han Z, Xue H et al (2019) Impact factors on gas adsorption and desorption of typical mining area in Southwest China. J Coal Eng 51(06):18–23. https://doi.org/10.11799/ce201906004
11. Zhang L (2019) Analysis on influencing factors of coal adsorption performance. J Coal Sci Technol Mag 40(02):26–28. https://doi.org/10.3969/j.issn.1008-3731.2019.02.009
12. Xue C, Gao P, Wang G et al (2022) Interface structure and stability of Al/Fe_2O_3 nano-thermite: a periodic DFT study. J Chin J Energ Mater 30(03):197–203. https://doi.org/10.11943/CJEM2021224
13. Huang B, Zhao R, Xu H, Deng J (2019) Adsorption of methylene blue on bituminous coal: adsorption mechanism and molecular simulation. J ACS Omega 4(9):14032–14039. https://doi.org/10.1021/acsomega.9b01812
14. Sakurovs R, He L, Melnichenko YB et al (2012) Pore size distribution and accessible pore size distribution in bituminous coals. Int J Coal Geol 100:51–64. https://doi.org/10.1016/j.coal.2012.06.005

Risk Assessment and Early Warning Model for Water Conservancy Projects Based on IoT and Big Data

Xiuqian Yang and Jing Zhao

Abstract The conventional risk assessment methods for water conservancy projects mainly rely on calculating project risk values to achieve risk assessment. However, there is usually a lack of consistency testing of risk values, resulting in poor assessment. Therefore, a water conservancy project risk assessment and warning model based on the Internet of Things and big data is proposed. Analyze project risk characteristics, extract key influencing factors, and construct a risk assessment system. Calculate the weight values of evaluation indicators through the judgment matrix and test their consistency. By using the KNN algorithm, the risk assessment level is combined with the risk assessment level to achieve the evaluation and early warning of engineering projects. The experimental results show that when this method is used for engineering project risk assessment, the error between the evaluation score and the expert score is small, and the average value of the evaluation error is below 0.5, ensuring the accuracy of the assessment.

Keywords Internet of Things · Dig data · Water conservancy projects · Risk assessment · Risk warning

1 Introduction

Due to various factors, such as construction scale, construction cycle, and construction responsibility, water conservancy engineering projects are often unstable during the construction process. These unstable factors may lead to risks in the project, failure to complete on time, and affect the effectiveness of the project construction. In order to effectively explore the unstable factors that affect the construction quality

X. Yang
School of Information Engineering, Guangxi Vocational College of Water Resources and Electric Power, Nanning 530023, Guangxi, China

J. Zhao (✉)
School of Hydraulic Engineering, Guangxi Vocational College of Water Resources and Electric Power, Nanning 530023, Guangxi, China
e-mail: 17102225@qq.com

S. Yadav et al. (eds.), *Energy Power and Automation Engineering*, Lecture Notes in Electrical Engineering 1118, https://doi.org/10.1007/978-981-99-8878-5_13

of engineering projects, it is necessary to conduct a risk assessment of the engineering project and provide early warning based on the assessment results. There are three main factors affecting the construction quality of engineering projects, namely, human factors, construction factors, and supervision factors. The human factor refers to the construction personnel making wrong estimation of the project construction level, which leads to the mismatch between the subsequent decision and the actual project level and negatively affects the project construction effect. The construction factor refers to the fact that the project is limited by the mistakes made by the construction personnel during the construction process. The construction factor refers to the construction risks associated with the project, which are affected by differences in construction methods, construction cycles, and materials used in construction. The supervision factor refers to the lack of effective supervision of the project quality at a later stage after the completion of the project, which leads to safety problems and affects the operation of the project. Therefore, in order to effectively avoid the above, it is necessary to effectively explore the risks arising during the construction of the project so as to achieve risk identification and assessment.

Artamonov et al. [1] proposed a forming neural network algorithm to achieve the assessment and early warning of chemical production risks. In the process of chemical production, neural network technology was applied to construct a functional evaluation mathematical model. Multiple experimental samples were selected to train the constructed model, and the training results were directly transmitted to the neural network through a single hidden layer. Through the prediction of real data in chemical production in the model, risk factors in the production process were evaluated, and effective risk warning was achieved. However, the weight of risk assessment indicators was not calculated during the model construction process, resulting in significant errors in the evaluation results. Zhang et al. [2] constructed an agricultural flood disaster risk assessment model, combining local geographic, meteorological, and socio-economic data to construct flood disaster risk assessment indicators. Use the entropy weight method to calculate the weight of indicators and construct a risk assessment indicator system. By analyzing the sensitivity of evaluation indicators and obtaining risk assessment values, a scientific and effective risk warning strategy can be developed to provide data support for water conservancy project risk assessment. However, in the weight calculation process, due to the incomplete setting of evaluation indicators, the accuracy of the calculation results is not high. A water conservancy engineering risk assessment and warning model based on the Internet of Things and big data is proposed to address the above issues. For risk identification of engineering projects, it is necessary to first identify the source of risk, then analyze and explore the main factors that affect project safety, and compare the degree of impact of different factors on the risk of the project, in order to clarify the risk assessment indicators [3]. This can be achieved by analyzing the construction data of the project and finding rules. For risk assessment of engineering projects, appropriate evaluation indicators can be selected based on identifying the main risk factors, and an evaluation system can be constructed by analyzing the importance of evaluation indicators. The importance of evaluation indicators can generally be achieved by calculating weight values. Using mathematical model establishment

method or difference coefficient method, calculate the weight values of different evaluation indicators and sort the results. Using the ranking results of evaluation index weights as the main benchmark for the construction of the evaluation system, thus completing the construction of the evaluation system. The risk warning work of construction projects needs to be carried out on the basis of risk assessment, combined with the results of risk assessment, to construct a risk assessment level related to the degree of warning. By matching the risk value of each project with the evaluation level one by one, the projects with higher risk levels are those that require early warning. Then, combined with real-time warning technology, timely warning can be carried out in the project management center to ensure the construction effect of the project and provide security for the safety issues of the engineering project.

2 Construction of a Risk Assessment System for Water Conservancy Projects

In order to evaluate the risks in the construction process of water conservancy projects, this article first analyzes the risk characteristics of engineering projects. And select appropriate evaluation indicators based on the main influencing factors to construct a risk evaluation system.

Water conservancy engineering usually has the following characteristics: strong professionalism, large project scale (with many sub projects), long construction cycle, and high construction difficulty [4, 5]. According to the above risk characteristics, combined with the actual operation data of water conservancy projects, based on fuzzy analytic hierarchy process, six construction risks, including financial risk, construction risk, operational risk, legal policy risk, political risk, and force majeure, are selected as the first level indicators for evaluation, and an evaluation system is established, as shown in Table 1.

As can be seen from Table 1, the engineering risk evaluation system mainly includes risk categories, such as financial risk, construction risk, operation risk, legal policy risk, political risk, and force majeure, among which, the main risks in financial risk include availability of funds, interest rate risk financing cost risk, financing cost risk, inflation risk; construction risk mainly includes design change, demolition, low technical level, construction schedule overrun, construction cost overruns, project quality, construction safety, contractor default; operational risk mainly includes operational quality, operating income shortfall, operational cost overrun; legal and policy risk mainly includes law or policy changes, tax adjustment; political risk mainly includes government credit, asset collection; force majeure risk mainly includes natural environment risk and other force majeure risk. According to the engineering risk assessment system, calculate the weights of each evaluation index, and evaluate the engineering risk value based on the ranking results of the weight values.

Table 1 Risk assessment system for water resources projects

Risk category	Major risks	Risk interpretation
Financial risks	Availability of funds C1	Availability of construction funds on time
	Interest rate risk C2	Increase in financing costs due to changes in interest rates
	Financing cost risk C3	Actual financing cost is higher than the bid price level
	Inflation risk C 4	Costs greater than forecast due to large inflation rate forecast error
Construction risk	Design changes C5	Risk of cost increases due to design changes
	Demolition and relocation C6	Failure to complete demolition and resettlement on time affects the project schedule
	Low level of technology/ technology C7	Risk of cost overruns or project delays due to low technology/technology level
	Overrun of construction period C8	Risk of cost increases due to overrun of construction period
	Construction cost overrun C9	Construction cost overruns due to internal and external factors
	Project quality C10	Rework due to substandard construction quality, etc
	Construction safety C11	Personal safety of construction personnel and property safety of construction site, etc
	Contractor's breach of contract C12	A series of risks caused by the default of the general construction contractor
Operational risk	Operation quality C13	Quality problems caused by the operation process
	Insufficient operation revenue C14	Risk of lower than expected operating income
	Operation cost overrun C15	Operating cost overruns due to low management level of the project company
Legal and policy risk	Law or policy change C16	Project cost increases due to changes in laws, regulations, and other policies. Increase in project costs due to changes in laws, regulations, and other policies
	Tax adjustment C17	Increase or decrease in total costs due to changes in tax policies
Political risk	Government credit C18	Risk of failure to perform contract terms due to government default
	Asset expropriation C19	Expropriation of assets due to changes in government plans and policies or nationalization
Force majeure	Natural environmental risks C20	Natural disasters such as earthquakes, floods, rainstorms, etc
	Other force majeure C21	Force majeure risks other than natural environmental risks

3 Calculation of Risk Assessment Indicator Weights

Use Analytic Hierarchy Process to construct a judgment matrix for indicators and calculate their weights.

Firstly, assume that the judgment matrix composed of evaluation indicators at the same evaluation level is $A = \{a_{ij}\}$, where a_{ij} represents the ratio of the importance of element i to element j in this matrix. Assuming the corresponding weight values of the evaluation indicators, the formula for calculating the weights can be obtained as shown below.

$$w_i = \frac{\left(\prod_{j=1} a_{ij}\right)^{1/n}}{\sum_{j=1}^{i} a_{ij}} \tag{1}$$

where n represents the total number of elements in the judgement matrix. Pair the 21 evaluation indicators mentioned above to establish an evaluation matrix, calculate the weight values of the indicators, and normalize them to calculate the maximum eigenvalue of each judgment matrix. The calculation formula is shown below.

$$\lambda_{\max} = 1/n \sum_{i=1}^{n} \frac{A \cdot w_i}{n} \tag{2}$$

The higher the scale value, the higher the difference in importance between the two evaluation elements in the judgment matrix. In this regard, this paper specifies the scale values and the corresponding meanings for the judgment matrix constructed. The interpretation of the corresponding values of the judgment matrix scale is shown in Table 2.

As can be seen from Table 2, the judgment matrix constructed includes mainly five scaled values and four intermediate values of importance judgments, in order to ensure that the judgment matrix constructed above has a certain degree of reliability, this paper chooses to use the indicator CI to test the consistency of the matrix

Table 2 Interpretation of the corresponding values of the judgment matrix scales

Scale value	Explanation of the corresponding meaning
1	If the scale value is 1, then the two factors are equally important compared to each other
3	If the scale value is 3, then the former is slightly more important than the latter
5	If the scale is 5, then the former factor is significantly more important than the latter
7	If the scale is 7, then the former is more important than the latter
9	If the scale value is 9, then the former is more important than the latter when comparing the two factors
2, 4, 6, 8	A scale of 2, 4, 6, 8 represents the middle value of the above importance judgments

constructed above, and the specific expression is shown below.

$$\mathrm{CI} = \frac{\lambda_{\max} - n}{n - 1} \tag{3}$$

The maximum eigenvalue of the judgment matrix obtained above is substituted into Formula (3) to calculate the corresponding consistency value. The feasibility of the matrix can be tested through the above steps, and the consistency meets the requirements, which can be used as the weight value.

4 Construction of a Risk Assessment and Early Warning Model for Water Conservancy Projects Based on IoT and Big Data

This paper constructs an assessment and early warning model for the risk of water conservancy projects by combining the results of the above constructed assessment system with the calculation of index weight values. The risk assessment and early warning process for engineering projects is shown in Fig. 1.

According to the risk assessment flowchart shown in Fig. 1, this article completes the risk assessment of engineering projects by matching the comprehensive evaluation values with the evaluation level. For high-risk projects, use KNN algorithm for real-time warning. The early warning process is shown in Fig. 2.

From Fig. 2, the overall flow of the KNN algorithm can be seen, in order to provide early warning of risk evaluation results, it is also necessary to classify the risk evaluation results into evaluation levels. In order to quantify the evaluation results obtained from different projects, a unified evaluation level system is used to clarify the degree of risk corresponding to different projects and to realize risk early warning. In this regard, this paper combines the risk level calculation formula to classify the importance of the evaluation results, the specific calculation formula is shown below.

$$\begin{cases} C = Q * R = [h_1, h_2, h_3, h_4, h_5] \\ E = C * P^{\mathrm{T}} \end{cases} \tag{4}$$

where C represents the comprehensive evaluation result of the project at the target level, P represents the evaluation weight vector value corresponding to each level of evaluation index, and E represents the comprehensive evaluation level of the project. Match the risk assessment scores of different projects with the evaluation level to clarify the severity of project risks. If the project reaches a serious and extreme serious risk level, early warning is needed, thus completing the risk assessment and early warning model of water conservancy projects based on the Internet of Things and big data.

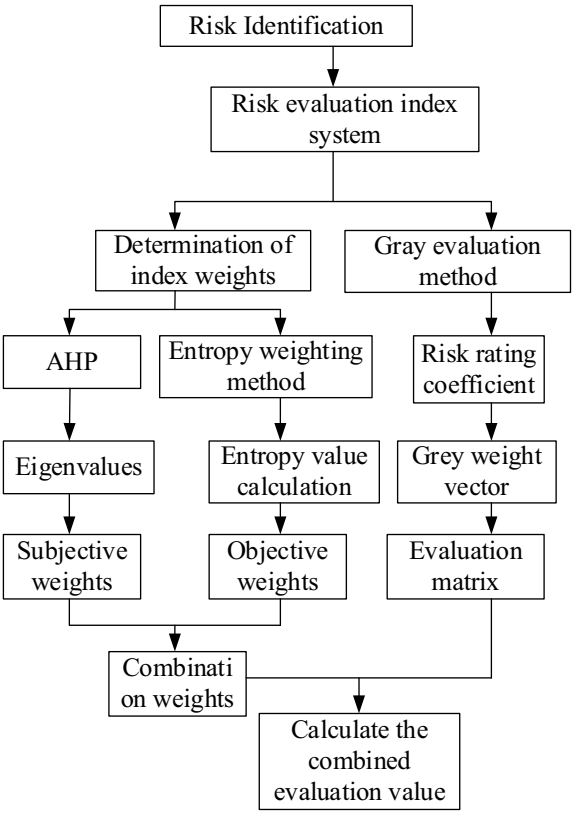

Fig. 1 Model risk assessment and early warning process

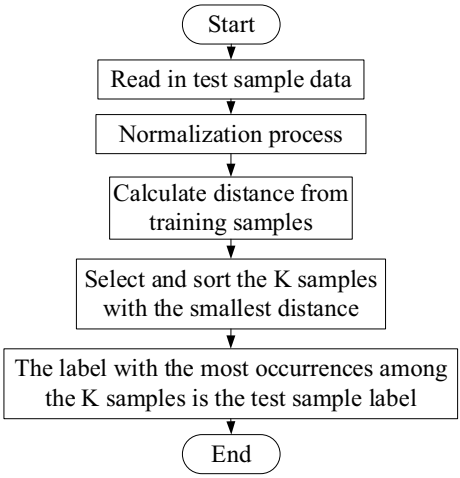

Fig. 2 Flowchart of the KNN algorithm

Table 3 Assignment of expert levels

Evaluation indicators	Project sub-project number		
	01	02	03
C1	2.5	3.5	2.5
C2	2.0	1.5	2.0
C3	1.0	1.0	1.5
C4	2.0	2.0	2.0
C5	3.5	2.5	3.5
C6	1.5	2.0	1.5
C7	2.5	1.5	1.5
C8	2.5	2.0	2.5
C9	2.0	1.5	2.0
C10	2.5	1.5	2.0

5 Experiments and Analysis

5.1 Experimental Preparation

Experimental verification of the actual evaluation effectiveness of the method is proposed in this paper. Select the engineering project risk assessment and warning model based on combination assignment and the engineering project risk assessment and warning model based on decision tree as the comparison method. This experiment selected a large-scale hydropower station construction project. The construction cycle of the entire project is planned to be 60 months, and the entire project will take 62 months. In order to ensure the reliability of the experimental results, the comparison standard selected for this experiment is expert scoring. By comparing the evaluation scores obtained by different methods with expert scores, the evaluation effect is obtained. The expert risk rating results are shown in Table 3.

As can be seen from Table 3, in order to facilitate discussion and analysis, three sub-projects were selected for risk evaluation, with 10 risk evaluation indicators under each sub-project.

5.2 Analysis of Test Results

The comparison standard selected for this experiment is the evaluation accuracy of different evaluation methods, and the specific measure is the scoring error value between the evaluation scores obtained by different evaluation methods and the expert evaluation scores, and the results of the comparison of assessment score errors are shown specifically in Fig. 3.

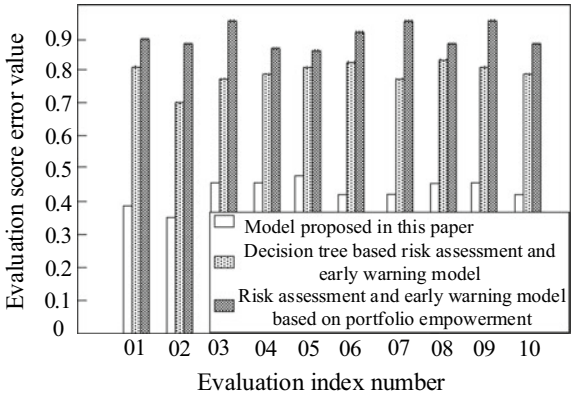

Fig. 3 Comparison results of evaluation score errors

From the content of Fig. 3, it can be seen that the numerical comparison shows that the error between the evaluation scores and the expert scores obtained by the IoT and Big Data-based risk assessment method proposed in this paper is significantly smaller, with the average value of the evaluation error being below 0.5. The error between the evaluation results of the two conventional methods and the expert scores is significantly larger, and the maximum evaluation error is close to 1.0, which can prove that the method in this paper occupies a greater advantage in evaluation accuracy.

6 Concluding Remarks

In this paper, a new engineering project risk evaluation and early warning method is proposed by combining IOT technology for the problem that conventional engineering project risk evaluation is not ideal. By analyzing the risk characteristics of engineering projects, suitable risk evaluation indicators are selected and an evaluation system is constructed. And the weight value corresponding to each indicator in the system is calculated by constructing a judgment matrix, thereby quantifying and analyzing the degree of connection between each indicator and the evaluation object. In future research work, the evaluation index system needs to be refined and the evaluation process further sub-optimized.

References

1. Artamonov AA, Bogdanova LM, Nagibin SY et al (2021) Mathematical model of chemical process prediction for industrial safety risk assessment. Procedia Comput Sci 190(1):107–114
2. Zhang LY, Yang WT (2022) Risk assessment of agricultural flood disaster based on WGA operator-entropy weight method. Chin J Agricult Resour Reg Plann 43(8):180–188

3. Simonsen LC, Slaba TC (2021) Improving astronaut cancer risk assessment from space radiation with an ensemble model framework. Life Sci Space Res 31(11):14–28
4. Zhong Z, Qw A, Sh A et al (2022) Source-specific risk assessment for cadmium in wheat and maize: Towards an enrichment model for China—ScienceDirect. J Environ Sci 125(3):723–734
5. Ye HZ, Hao W, Huang FY (2022) Communication scheduling algorithm of Aol and sample extrusion aware. Comput Simul 39(6):192–196, 458

Preparation and Performance of Solid Oxide Fuel Cell Connector

Xuhan Li and Kening Sun

Abstract Lanthanum chromate ($LaCrO_3$) is a kind of ceramic bonding material in common use at present, in order to improve the phenomenon of poor sintering activity and conductivity, this article doped lanthanum chromate ($LaCrO_3$)-based materials with different elements and ratios to improve their performance. A series of $La_{0.8}Ca_{0.2}Cr_{1-x}Cu_xO_3$ ($x = 0.0, 0.1, 0.2, 0.3, 0.4, 0.5$) perovskite-type oxides were prepared by sol–gel method using $LaCrO_3$-based materials modified by Ca–Cu doping. After doping, the material has a series of advantages, such as coefficient of thermal expansion matching with electrolyte, and good chemical compatibility with other parts of the battery, good chemical stability in the reduction atmosphere, and high conductivity in the air and the reduction atmosphere, at 800 °C, the maximum conductivity of $La_{0.8}Ca_{0.2}Cr_{1-x}Cu_xO_3$ is 22.1 s cm^{-1} in air and 12.31 s cm^{-1} in H_2.

Keywords Connector · $LaCrO_3$ · Performance · Doping

1 Introduction

Solid oxide fuel cells (SOFCs) are a new type of energy conversion device, which can directly convert chemical energy into electrical energy. It has the advantages of simple system design, high energy efficiency, environmental friendliness, large-scale flexibility, and long life span, and is widely recognized as the green energy of the twenty-first century [1, 2]. SOFC is an all-solid structure. The key materials include electrolyte, cathode, anode, connecting material, and sealing material. The main function of electrolytes is to transport oxygen ions or protons, and the main function of electrodes is to conduct electrons and provide electrochemical reaction sites. The connecting material is mainly used for connecting the cathode and anode of adjacent batteries to form a battery stack [3, 4].

X. Li · K. Sun (✉)
School of Chemistry and Chemical Engineering, Beijing Institute of Technology, Beijing 100081, People's Republic of China
e-mail: 3020135344@qq.com

S. Yadav et al. (eds.), *Energy Power and Automation Engineering*, Lecture Notes in Electrical Engineering 1118, https://doi.org/10.1007/978-981-99-8878-5_14

If a single battery is used, there is a fatal drawback, which is that the output power is bound to be very low. So, we need to use battery packs, which means connecting multiple single batteries in series [5]. A connector needs to be added between the anode and cathode of two batteries. The function of the connecting material mainly includes two aspects: on the one hand, it should be separated physically to prevent the contact between the air electrode and the fuel gas and the contact between the fuel gas electrode and the oxidizing atmosphere; on the other hand, it acts as an electrical connection between one battery anode and another battery cathode [6, 7]. Therefore, the material requirements of the connection material are the most stringent. The successful development of competitive and inexpensive joining materials is critical to the eventual commercialization of SOFC. In general, a material that can become a good connector must have good conductivity, be dense enough to hinder the mixture of fuel and oxidant, and match the coefficient of thermal expansion of adjacent components (TEC), to reduce mechanical stress [8]. $LaCrO_3$-based materials are commonly used as ceramic linker materials, belonging to perovskite-type (ABO_3) composite oxides, which have the following excellent properties: (1) high electronic conductivity in oxidation and reduction atmosphere; (2) the compatibility of phase, microstructure, and thermal expansion with other components of fuel cell is good, which can meet the requirements of high temperature and corrosion resistance [9]. However, the main disadvantages of $LaCrO_3$ are its high melting point, difficulty in obtaining fully dense products, and poor sintering in air. In order to improve sintering ability and electrical conductivity, basic metals at La point or transition metals at Cr point have been studied [10–12].

In this work, $La_{0.8}Ca_{0.2}Cr_{1-x}Cu_xO_3 (x = 0.0, 0.1, 0.2, 0.3, 0.4, 0.5)$ doped with Cu and Ca was prepared by sol–gel method and Pechini citric acid method and sintered in air. The phase composition of the sintered powders was analyzed by X-ray diffraction (XRD). The coefficient of thermal expansion and electrical conductivity of the sintered powders were measured by thermal dilatometer and four-probe technique. The microstructures of the scanning electron microscope and sintered materials were observed by SEM, and the effects of different doping elements on the properties of the materials were studied.

2 Experimental

A series of $La_{0.8}Ca_{0.2}Cr_{1-x}Cu_xO_3 (x = 0.0, 0.1, 0.2, 0.3, 0.4, 0.5)$ perovskite powders doped with Ca and Cu (LCCCx, $0 \leq x \leq 0.5$) were prepared by sol–gel method. $La(NO_3)_3 \cdot 6H_2O$, anhydrous $CaCl_2$, $Cr(NO_3)_3 \cdot 9H_2O$ and $Cu(NO_3)_3 \cdot 3H_2O$ were stoichiometry and dissolved in deionized water. Citric acid was added to the solution, and the molar ratio of citric acid to total metal ions was 1.5:1. Then add ammonia to adjust the PH of the solution to 7. The PH-adjusted mixture is heated at 80 °C and stirred until most of the water in the solution evaporates to form a blue, transparent gel. It was then dried in an oven at 150 °C for 10 h in an air atmosphere to obtain a black dry gel precursor. To remove any residual carbon, the precursor was calcined

in a muffle furnace at 1000 °C for 5 h to obtain a brown-to-black powder (the color deepens with increasing Cu doping), La0.8Ca0.2Cr1–xCuxO$_3$ powder.

Using Brucker's D8 Advance X-ray powder diffractometer (XRD), at 40 kV and 20 mA, the samples were scanned by Cu–Kα Ray ($\lambda = 1.54051$å) at a scanning speed of 10° min^{-1} in the range of 10°–90° and characterized by phase structure analysis. The limiting slit is 1°, the transmitting slit is 1°, the receiving slit is 0.3°, and the sampling interval is 0.02°. The electrical conductivity of the samples was measured in the range of 300–800 °C by four-probe method in the air and hydrogen atmosphere, respectively, and the interval of 50 °C was measured once. The resistance of the sample was measured by the four-wire resistance mode of the digital multimeter, and the voltage between the two voltage lines was measured by the digital multimeter, the resistance value R between the sample voltage lines can be obtained. The conductivity of the sample can be calculated by the formula $\sigma = \mathrm{L/Sr}$. Where σ is the conductivity of the sample in units of S cm^{-1}, L is the length between the two voltage probes, and *S* is the cross-sectional area of the sample. The thermal expansion curve (TEC) was measured in the temperature range of 30–1000 °C by using a thermal expansion instrument. The microstructure of the prepared material and the micro-size and micro-morphology of the surface and cross-section of the joint material after co-firing with the anode support were observed by scanning electron microscope scanning electron microscope (SEM).

3 Result Analysis

This section mainly discusses various tests, characterization, and result analysis.

3.1 X-ray Diffraction a Series of LCCC$_x$ Powders Were Prepared by Sol–gel Method

The XRD patterns of LCCCx powders calcined at 1000 °C are shown in Fig. 1. As can be seen from the diagram, each proportion of the powder presents a distinct perovskite structure. However, when the doping amount of Cu is more than 0.3, a small number of impurity peaks appear. The software analysis shows that the impurity peaks are some copper compounds, which is because Cu is not completely doped into LCCCx powder during calcination, instead, other compounds form, which precipitate from the perovskite lattice during calcination.

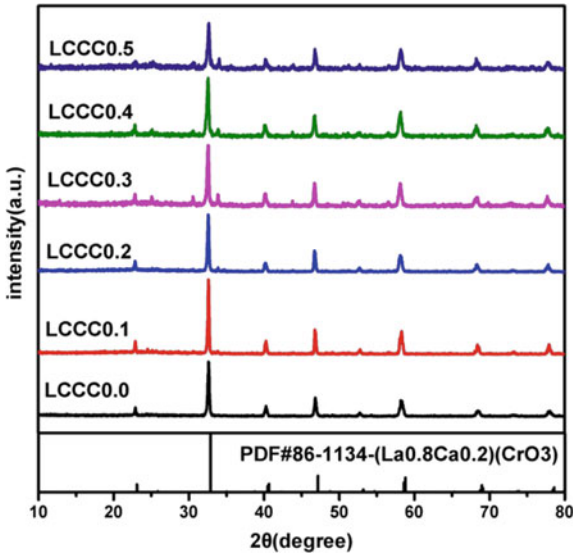

Fig. 1 XRD patterns of $La_{0.8}Ca_{0.2}Cr_{1-x}Cu_xO_3$ powder and comparison to PDF standard card

3.2 Scanning Electron Microscope (SEM) Characterization

The $LCCC_x$ powder was characterized by scanning electron microscopy powder was characterized by scanning electron microscope (SEM), to observe its morphological characteristics, as shown in Fig. 2. At the same time, $LCCC_x$ powder was prepared into screen-printing paste, which was coated on the anode support by screen-printing and sintered, and then characterized by scanning electron microscope scanning electron microscopy (SEM), as shown in Fig. 3. It can be seen from the figure that the particle size of $LCCC_x$ powder is relatively uniform, and the comparison of the surface electron microscope photographs of the powders with different proportions coated on the anode support after high temperature sintering by screen printing technology shows that, in addition to the undoped Cu and the powders with high doping content show poor sintered compactness, the other doped powders have good overall compactness. The reason is that when the Cu doping ratio is too high, the excess Cu is not completely doped into the $LCCC_x$ powder and precipitates, forming some other compounds, the impurity produced during sintering affects the densification degree of the junction surface. However, the overall results show that doping Cu into lanthanum chromate-based materials can improve the sintering activity to a certain extent, which is helpful to the sintering of materials to achieve higher density [13].

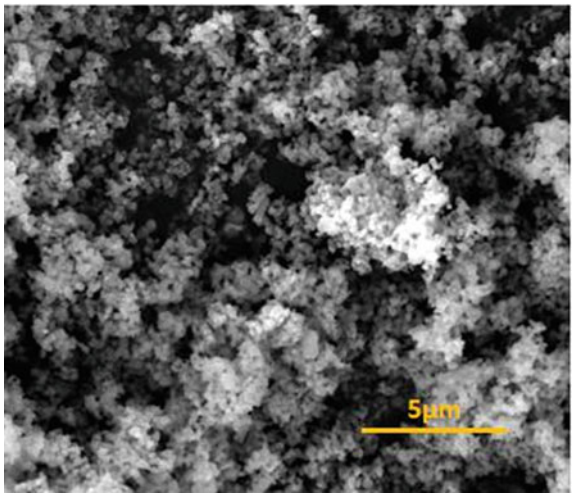

Fig. 2 SEM image of $La_{0.8}Ca_{0.2}Cr_{1-x}Cu_xO_3$ powder

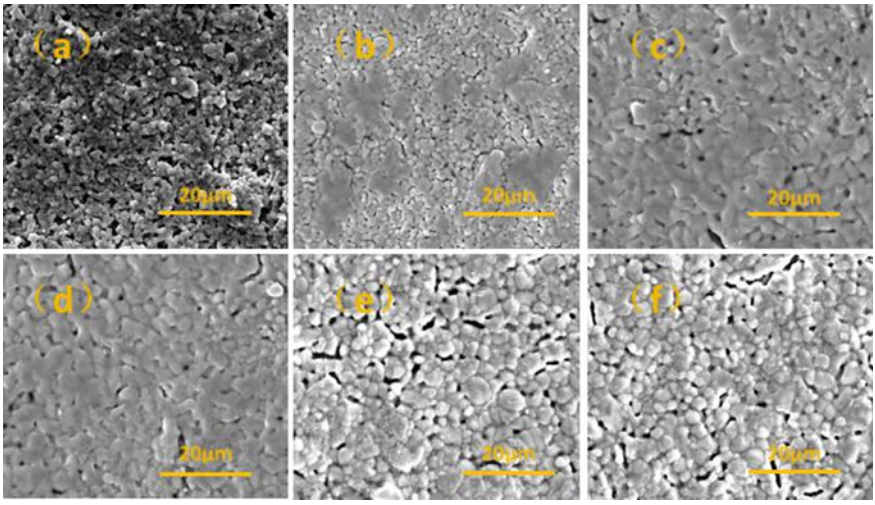

Fig. 3 SEM image of the doping ratios of $La_{0.8}Ca_{0.2}Cr_{1-x}Cu_xO_3$ powders after screen-printing sintering were, **a** 0.0, **b** 0.1, **c** 0.2, **d** 0.3, **e** 0.4, and **f** 0.5, respectively

3.3 Electrical Conductivity

Doping Cu with lanthanum chromate material will have an impact on conductivity. This article studies the changes in conductivity. Measure the conductivity of $LCCC_x$ under reduction and air conditions. Figure 4 shows the variation curve of $LCCC_x$ powder conductivity with temperature under air conditions. As shown in the figure, with the increase of temperature, the conductivity of the sample increases, and the

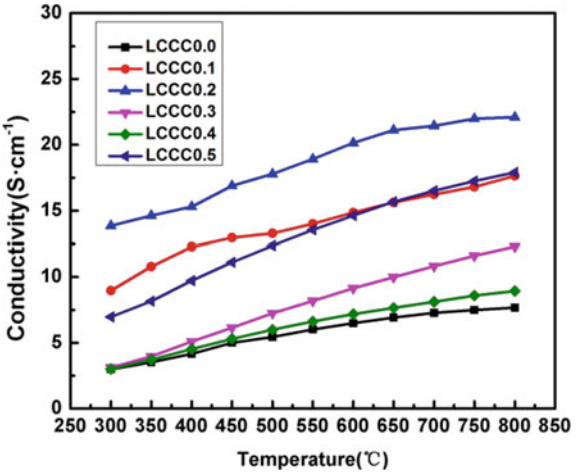

Fig. 4 $La_{0.8}Ca_{0.2}Cr_{1-x}Cu_xO_3$ conductivity in air atmosphere

more Cu doping, the conductivity curve of the sample shows a trend of first increasing and then decreasing [14]. However, the conductivity increases when the doping ratio of Cu is 0.5. According to the XRD analysis shown above, this is because some Cu precipitates in $LCCC_{0.5}$, which leads to the increase of conductivity. At 800 °C, the conductivity of $LCCC_{0.2}$ is the highest, up to 22.1 s cm^{-1}. The results show that the conductivity of lanthanum chromate-based materials is obviously improved after doping Cu, and the conductivity of lanthanum chromate-based materials is increased in a certain range.

The temperature dependence of conductivity of $LCCC_x$ samples in hydrogen atmosphere is shown in Fig. 5. Figure 5a is a function of conductivity with temperature in hydrogen and Fig. 5b is a curve of conductivity with Cu doping in hydrogen. As shown in the figure, under hydrogen conditions, the higher the temperature, the higher the conductivity of lanthanum chromate. In a reducing atmosphere, the conductivity of lanthanum chromate can be greatly improved by doping Cu. At the temperature of 800 °C, the conductivity of the samples without Cu doping is only 4.08 s cm^{-1} in the reduction atmosphere, but after Cu doping, the conductivity of the samples can reach more than ten s cm^{-1}. The electrical conductivity of Cu increased from 0 to 0.5 at first and then decreased in reducing atmosphere, and the electrical conductivity of $LCCC_{0.2}$ was the highest (12.31 s cm^{-1}).

Therefore, not only the increase of electrical conductivity was obviously improved by Cu doping in air atmosphere, but also the electrical conductivity of the samples changed from $LCCC_0$ 4.08 s cm^{-1} to $LCCC_{0.2}$ 12.31 s cm^{-1} in hydrogen atmosphere, the electrical conductivity is greatly improved. The reasonable conductivity of $LCCC_x$ in a dual atmosphere makes it a suitable connector material for flat tube solid oxide fuel cell.

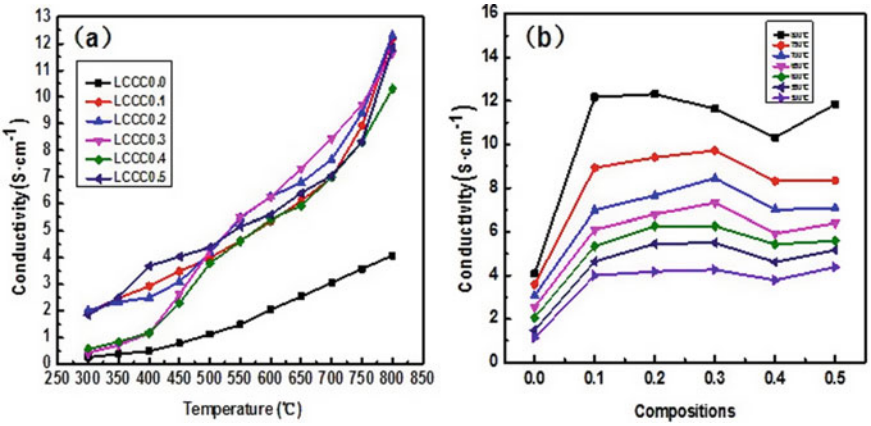

Fig. 5 $La_{0.8}Ca_{0.2}Cr_{1-x}Cu_xO_3$ conductivity in hydrogen atmosphere: **a** change with temperature; **b** change with Cu doping amount

3.4 Study on Chemical Compatibility with Anode Powder and Electrolyte

Because the connector material is in contact with the anode material NiO and the electrolyte material YSZ, in order to confirm the chemical compatibility of the connector with the anode and the electrolyte, the $LCCC_x$ powder was mixed with NiO and 8 mol% YSZ, respectively, at the mass ratio of 1:1, and then sintered at 1400 °C for 5 h.

Figure 6 shows the XRD spectra of the mixture of LCCCx and NIO, as well as a comparison to the XRD spectra of the mixture of NIO. Figure 7 shows the XRD spectra of $LCCC_x$ and YSZ mixture, and the comparison of the XRD patterns of the mixture with YSZ. From the observed XRD peak, there is no obvious formation of the second phase. So, under the normal calcination and working conditions of solid oxide fuel cell, the connector material $LCCC_x$ does not react with other components of the cell. The XRD spectrum of the calcined sample did not show any additional diffraction peaks, indicating that a second phase was not formed. Therefore, $LCCC_x$ is a cyclically stable connecting material.

3.5 Thermal Shrinkage and Coefficient of Thermal Expansion

The length of LCCCx strip samples was measured before and after calcination at 1400 °C. The thermal shrinkage of the $LCCC_x$ samples doped with Cu was all about 12%, the thermal shrinkage of the samples without Cu doping was only 5.77%.

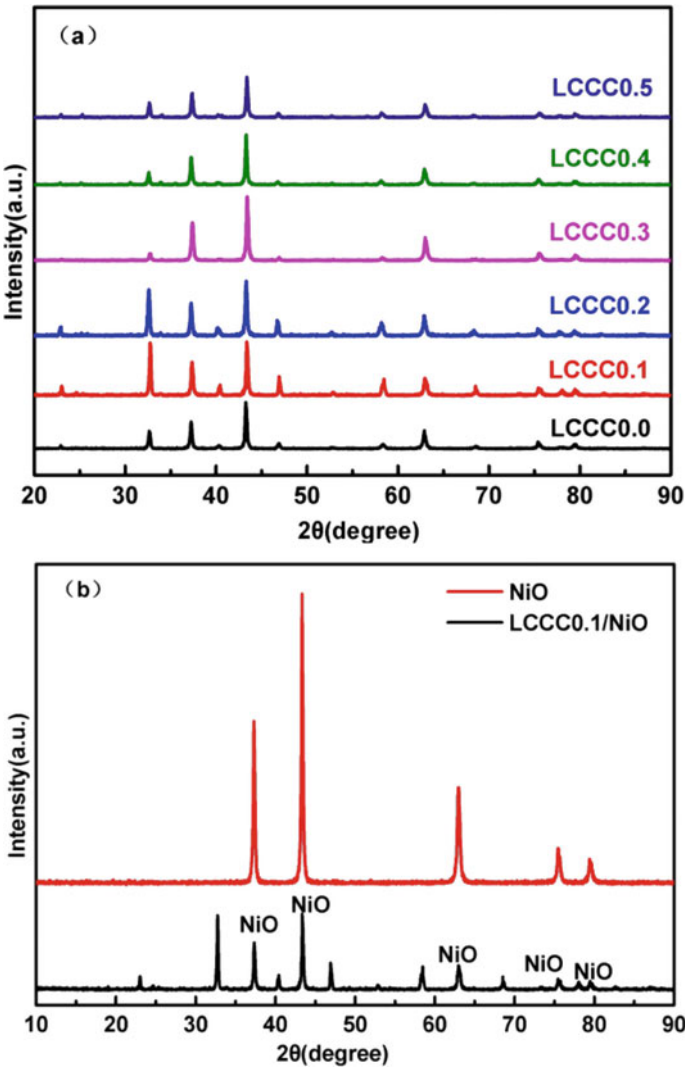

Fig. 6 **a** XRD patterns of the mixture of $LCCC_x$ with NiO (50:50 wt%) after 5 h of calcination at 1400 °C; **b** XRD comparisons of the mixture with NiO

At programmed temperature, the coefficient of thermal expansion of the connector material $LCCC_x$ was characterized by a thermal dilatometer and compared to other parts of the commonly used solid oxide fuel cell [15]. Between 30 °C and 1000 °C, the coefficient of thermal expansion of $LCCC_x$ closely matched the coefficient of thermal expansion of 8 mol% YSZ (10.6×10^{-6} K^{-1}), as shown in Fig. 7b. The TEC of $LCCC_0$ was 11.13×10^{-6} K^{-1}, still close to YSZ. The TEC of $LCCC_{0.1}$ is 10.58×10^{-6} K^{-1}, which is very similar to that of YSZ. The coefficients of thermal

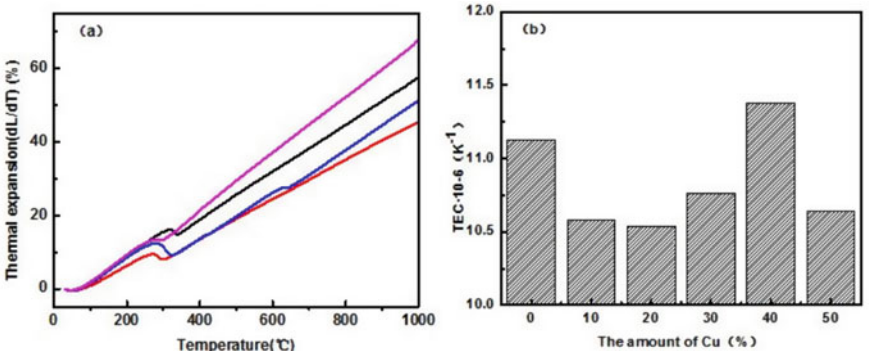

Fig. 7 **a** shows the thermal expansion curve of $La_{0.8}Ca_{0.2}Cr_{1-x}Cu_xO_3$ and **b** shows the thermal expansion curve of $La_{0.8}Ca_{0.2}Cr_{1-x}Cu_xO_3$ and the coefficient of thermal expansion curve (TEC) of $La_{0.8}Ca_{0.2}Cr_{1-x}Cu_xO_3$

expansion of $LCCC_{0.2}$–$LCCC_{0.5}$ were 10.54×10^{-6}, 10.76×10^{-6}, 11.38×10^{-6}, 10.64×10^{-6} K^{-1}, respectively, which were close to YSZ's TEC. It can be seen from the figure that Cu doping has a certain effect on TEC of lanthanum chromate, that is, with the increase of Cu doping amount, the coefficient of thermal expansion first decreases and then increases [16]. However, $LCCC_{0.5}$ contains impurities, which are different from their coefficient of thermal expansion and lead to the bending of the sample during the heating process, thus causing the difference in the coefficient of thermal expansion.

In addition, lanthanum chromate-based materials will change from orthorhombic system to trapezohexahedron, when the temperature rises to about 250–300 °C. Therefore, this phase transition process may occur during the heating of $LCCC_x$ samples. As shown in Fig. 7, it is obvious that there is an inflection point in the thermal expansion curve at about 300 °C. Although the material undergoes a phase transition around 300 °C, this does not affect the life of the solid oxide fuel cell, as the material is very close to YSZ's TEC [17, 18].

3.6 Study on the Stability in Reducing Atmosphere

The prepared $LCCC_x$ powder was placed in a tube furnace at 800 °C, and hydrogen was introduced into it to reduce it in hydrogen atmosphere for 10 h, then its XRD was tested. The XRD of reduced $LCCC_x$ powder is shown in Fig. 8. As can be seen from the diagram, there is no new impurity formation after 10 h of reduction, and $LCCC_x$ can keep a good perovskite structure. As a result, the $LCCC_x$ is stable for the duration of the solid oxide fuel cell, extending the battery's life to some extent [19].

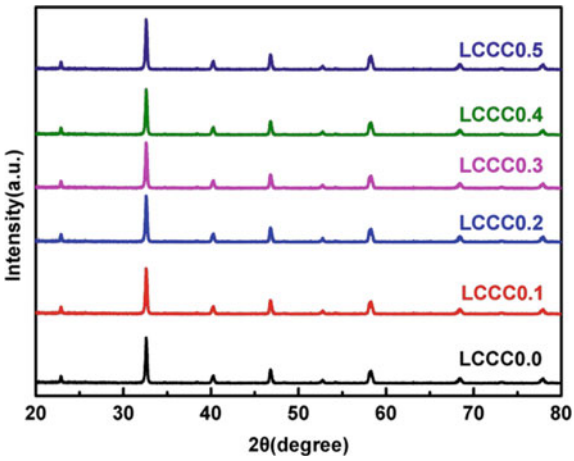

Fig. 8 XRD patterns of $La_{0.8}Ca_{0.2}Cr_{1-x}Cu_xO_3$ powders after 10 h reduction at 800 °C in hydrogen

4 Conclusion

A series of Ca and Cu doped lanthanum chromate ($La_{0.8}Ca_{0.2}Cr_{1-x}Cu_xO_3$($x = 0.0$, 0.1, 0.2, 0.3, 0.4, 0.5) ceramic perovskite powders were synthesized by sol–gel method, a series of characterizations were carried out. From the results, it can be seen that under air conditions, as Cu doping increases, the conductivity of the sample first increases and then decreases. But, when the atmosphere switches to hydrogen gas, the amount of Cu doping increases, and the conductivity first increases, then decreases. When the doping amount is increased again, the conductivity will increase. The electrical conductivity of $La_{0.8}Ca_{0.2}Cr_{0.8}Cu_{0.2}O_3$ is 22.1 s cm^{-1} at 800 °C in air atmosphere, and the electrical conductivity of $La_{0.8}Ca_{0.2}Cr_{0.8}Cu_{0.2}O_3$ increases greatly in hydrogen atmosphere, the conductivity of $La_{0.8}Ca_{0.2}Cr_{0.8}Cu_{0.2}O_3$ at 800 °C is 12.31 s cm^{-1}. The coefficient of thermal expansion of $La_{0.8}Ca_{0.2}Cr_{1-x}Cu_xO_3$($x =$ 0.0, 0.1, 0.2, 0.3, 0.4, 0.5) is very close to the coefficient of thermal expansion of YSZ, and the coefficient of thermal expansion increases with the increase of Cu doping amount, in addition, the stability of the powder at high temperature (800 °C) and in reducing atmosphere was good, which met the requirements of the solid oxide fuel cell connector materials, and the powder had good chemical compatibility with NiO and YSZ, under high temperature conditions, it does not react with NiO and YSZ. Therefore, the properties of $La_{0.8}Ca_{0.2}Cr_{1-x}Cu_xO_3$($x = 0.0$, 0.1, 0.2, 0.3, 0.4, 0.5) powder are good, especially $La_{0.8}Ca_{0.2}Cr_{0.8}Cu_{0.2}O_3$ powder, very suitable for use as connector material.

References

1. Neelima M, Banerjee A, Gupta A, Omar S, Balani K (2015) Progress in material selection for solid oxide fuel cell technology: a review. Prog Mater Sci 72:141–337. https://doi.org/10.1016/j.pmatsci.2015.01.001
2. Grove WRXXIV (1966) On voltaic series and the combination of gases by platinum. Lond Edinb Dublin Philos Mag J Sci 14:127–130. https://doi.org/10.1080/14786443908649684
3. Gaugain J (1853) Note sur les signes electriques attribues au mouvement de la chaleur. CR Hebd Seances Acad Sci 37:82–84.https://doi.org/10.1016/S0035-3159(99)80026-9
4. Haber F, Moser A (1905) Das Generatorgas und das Kohlenelement. Z Elektrochem 11:593–609. https://doi.org/10.1002/bbpc.19050113603
5. Akashi T, Maruyama T, Goto T (2003) Transport of lanthanum ion and hole in $LaCrO_3$ determined by electrical conductivity measurements. Solid State Ionics 164:177–183. https://doi.org/10.1016/j.ssi.2003.08.050
6. Steele B (1995) Interfacial reactions associated with ceramic ion transport membranes. Solid State Ionics 75:157–165. https://doi.org/10.1016/0167-2738(94)00182-R
7. Lee GY, Song RH, Kim JH, Peck DH, Lim TH, Shul YG, Shin DR (2006) Properties of Cu, Ni, and V doped-$LaCrO_3$ interconnect materials prepared by pechini, ultrasonic spray pyrolysis and glycine nitrate processes for SOFC. J Electroceram 17:723–727. https://doi.org/10.1007/s10832-006-0473-1
8. Hilpert K, Steinbrech RW, Boroomand F, Wessel E, Meschke F, Zuev A, Teller O, Nickel H, Singheiser L (2003) Defect formation and mechanical stability of perovskites based on $LaCrO_3$ for solid oxide fuel cells (SOFC). J Eur Ceram Soc 23:3009–3020. https://doi.org/10.1016/S0955-2219(03)00097-9
9. Fabbri E, Pergolesi D, Traversa E (2010) Ionic conductivity in oxide heterostructures: the role of interfaces. Sci Technol Adv Mater 11:054503. https://doi.org/10.1088/1468-6996/11/5/054503
10. Barriocanal JG, Calzada AR, Arco MV, Sefrioui Z, Santamaria J (2008) Colossal ionic conductivity at interfaces of epitaxial ZrO_2: $Y_2O_3/SrTiO_3$ heterostructures. Science 321:676–680. https://doi.org/10.1126/science.1156393
11. Tarancón A (2009) Strategies for lowering solid oxide fuel cells operating temperature. Energies 2:1130–1150. https://doi.org/10.3390/en20401130
12. Guo X, Matei I, Lee JS, Maier J (2007) Ion conduction across nanosized CaF_2/BaF_2 multilayer heterostructures. Appl Phys Lett 91:103102. https://doi.org/10.1063/1.2779254
13. Zhu B (2009) Solid oxide fuel cell (SOFC) technical challenges and solutions from nano-aspects. Int J Energy Res 33:1126–1137. https://doi.org/10.1002/er.1600
14. Zhu B, Raza R, Abbas G, Singh M (2011) An electrolyte-free fuel cell constructed from one homogenous layer with mixed conductivity. Adv Funct Mater 21:2465–2469. https://doi.org/10.1002/adfm.201002471
15. Singhal SC (2002) Solid oxide fuel cells for stationary, mobile, and military applications. Solid State Ionics 152:405–410. https://doi.org/10.1016/S0167-2738(02)00349-1
16. Huang K, Singhal SC (2013) Cathode-supported tubular solid oxide fuel cell technology: a critical review. J Power Sources 237:84–97. https://doi.org/10.1016/j.jpowsour.2013.03.001
17. Kim JH, Song RH, Song KS, Hyun HS, Shin DR, Yokokawa H (2003) Fabrication and characteristics of anode-supported flat-tube solid oxide fuel cell. J Power Sources 122:138–143. https://doi.org/10.1016/S0378-7753(03)00431-2
18. Zhu WZ, Deevi SC (2003) Development of interconnect materials for solid oxide fuel cells. Mater Sci Eng A 348:227–243. https://doi.org/10.1016/S0921-5093(02)00736-0
19. Yang Z, Weil KS, Paxton DM, Stevenson JW (2003) Selection and evaluation of heat-resistant alloys for SOFC interconnect applications. J Electrochem Soc 150:A1188-1210. https://doi.org/10.1149/1.1595659

Study of Obstruction Rate in Confined Spaces on the Behavior and Overpressure Characteristics of LPG Deflagration Flame

Jianfeng Gao, Yanan Han, Yang Wu, Xiaojun Shao, and Bingjian Ai

Abstract Experiments were conducted with a self-designed small-scale oil and gas explosion device and studied the effect of flat-type obstacles with different obstruction rates on LPG deflagration behavior and overpressure characteristics and deflagration pressure relief phenomenon in a narrow space. The results showed that the appearance of peak breaking pressure was largely independent of the arrangement of the barrier. Throughout the explosion process, the pressure at the ignition port gradually increases as the obstruction rate decreases, while the pressure at the vent decreases as the obstruction rate decreases. The peak of the negative pressure generated during the explosion similarly decreases as the obstruction rate decreases. And the arrangement with a reduced obstruction rate has a suppressive effect on flame propagation, while the arrangement with an increased obstruction rate will have an accelerating effect on flame propagation.

Keywords LPG · Explosion · Obstacle · Obstruction rate

J. Gao (✉) · Y. Han · Y. Wu · X. Shao · B. Ai
School of Petrochemical Engineering and Environment, Zhejiang Ocean University, Zhoushan 316022, China
e-mail: gaojf309@126.com

J. Gao
National and Local Joint Engineering Research Center of Harbor Oil and Gas Storage and Transportation Technology, Zhoushan 316022, China

Zhejiang Key Laboratory of Petrochemical Environmental Pollution Control, Zhejiang Ocean University, Zhoushan 316022, China

Y. Wu · X. Shao · B. Ai
School of Naval Architecture and Maritime, Zhejiang Ocean University, Zhoushan, China

S. Yadav et al. (eds.), *Energy Power and Automation Engineering*, Lecture Notes in Electrical Engineering 1118, https://doi.org/10.1007/978-981-99-8878-5_15

1 Introduction

Oil and natural gas are both indispensable energy materials for industry, national defense, and residential life, as well as typical flammable and explosive materials. With the increase in oil and gas storage and transportation facilities, the number of oil and gas pipelines laid is growing rapidly, posing a huge safety hazard to production safety. As the medium of storage and transportation is crude oil, light oil, liquefied gas, and other flammable, explosive, and volatile, and easy to the electrostatic gathering of fluids, some also contain toxic substances. Once the system accident, the leakage of oil and gas is very easy to fire, and explosion, resulting in casualties and property damage of vicious disasters. The development pattern of oil and gas deflagration is closely related to the geometric conditions of space. Accident investigation shows that a significant portion of oil and gas deflagration accidents occur in underground pipe trenches, pits, oil/gas pipelines, storage tank ventilation pipes, and other facilities in the narrow space. Qingdao, Shandong, 11–22 accident in 2013, Kaohsiung, Taiwan, 8–1 accident in 2014 and 2021 occurred in the 6–13 Hubei Shiyan natural gas explosion accident and other major gas explosion accidents are closely related to the special space structure of the narrow space [1]. Due to structural or functional needs, long and narrow spaces in actual projects often contain different types of obstacles, such as various types of equipment and facilities, section abrupt reduction structures, etc. Therefore, from the perspective of safety production, it is important to study oil and gas combustion and explosion experiments in confined spaces with obstacles.

To study the influence of obstacles in confined spaces on the explosive combustion of oil and gas, domestic and international scholars have conducted many experimental studies. Different concentrations and different types of oil and gas mixtures will be composed of different deflagration media. Gao et al. [2] proposed that the overpressure generated during the explosion does not always increase with the increase in oil and gas concentration. At the same time, Li et al. [3] also believe that other conditions are the same, the overpressure value generated in the deflagration will increase and then decrease with the concentration of oil and gas mixture. But, when the deflagration medium is in the presence of obstacles to the disturbance, the explosion of the overpressure value will also increase significantly. The shape of the obstacles also has an important effect on the degree of explosive combustion. Patel et al. [4] built an experimental model with three obstacle plates in a straight pipe and found that the explosion pressure of a premixed gas of methane and air increased dramatically after ignition. And through experimental studies, Xu et al. [5] found that triangular obstacles can successfully accelerate flames by creating continuously varying flow areas and stable double vortex flow. Successively, Li et al. [6] conducted experimental studies for trapezoidal, circular, square, and rectangular shapes of obstacles and found that all these obstacles have a great impact on the overpressure and flame propagation generated by the explosion. And Valiev et al. [7] showed that symmetrical cylindrical obstacles increase the turbulence effect of the flow field more than flat ones. The increase in the number of obstacles can make the premixed oil and

gas deflagration more intense. By increasing the number of obstacles, Xiao et al. [8] found that the difference in the effect of obstacle shape on overpressure was amplified. And as the number of obstacles increases, the contribution of triangular obstacles to overpressure becomes progressively more pronounced. And Li et al. [9] proposed that as the number of obstacles increases, the maximum distance of flame front propagation from the ignition end increases, but the time to reach the farthest distance decreases. Obstacle obstruction rate also affects explosive combustion. Wang et al. [10] found experimentally that the peak overpressure caused by the obstruction increases with the rate of obstruction.

The above scholars focus on the combustion medium, the shape of the obstacle, the number and the rate of blockage, and other effects on the explosion characteristics of oil and gas, while the obstacle blockage rate gradient on the impact of oil and gas deflagration is relatively little research. Based on this paper, a study of the change in LPG deflagration flame behavior and overpressure characteristics of the same obstacle discharged by a column in a narrow space with changing blockage rate to form a height gradient is carried out.

2 Experimental Setup

This experiment investigates the overpressure characteristics under obstacle perturbation by building a self-designed small oil and gas explosion device. Equipment includes self-designed small explosive pipe (pipe length 1000 mm, section side length 100 mm) and a variety of small obstacles, Mikrotron high-speed camera, CY 301 digital pressure sensor, gas explosion dynamic data acquisition system, KTGD-B adjustable igniter, GMI PS200 portable gas concentration detector, LPG-O2, LZB-6WBF rotor flow meter, PVC film, self-circulation system, data acquisition computer, etc. The experimental schematic is shown in Fig. 1 (for the first set of experiments):

The size of the obstacles selected for the experiment was 1000 mm × 100 mm (length × width), and the heights were 20 mm, 30 mm, and 40 mm, constituting an obstruction rate of 20%, 30%, and 40%, respectively. The fixed position of the obstacle is 200 mm, 500 mm, and 800 mm from the ignition source, respectively. The experiment was designed for 3 working conditions, and the order of obstacle arrangement was (from ignition to opening) 30 mm, 30 mm, 30 mm, noted as Case 1; 40 mm, 30 mm, 20 mm, noted as Case 2; 20 mm, 30 mm, 40 mm, noted as Case 3.

After putting the obstacle into the pipe and installing the equipment, seal the opening on the left side of the pipe with film to prevent oil and gas leakage. Then the premixed gas is charged by the partial pressure method and the self-circulation system is turned on. After the experimental system is stable, turn on the data acquisition system and high-speed camera. Then ignite the premixed gas with an igniter, check the site's safety after the explosion, and save the data. 6–10 valid experiments were performed for each group to reduce the error. Each experiment requires the

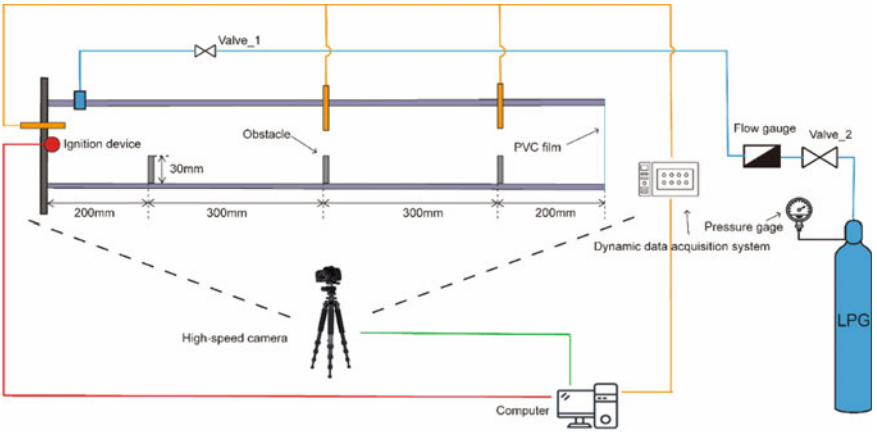

Fig. 1 Experimental schematic

acquisition of pressure and flame images, including pressure monitoring points 3, for the ignition port, intermediate position, and vent.

3 Experimental Results

3.1 Effect of Obstacle Blockage Rate Gradient Arrangement on Flame Behavior

Figure 2 shows the flame images obtained under Case 1, Case 2, and Case 3 working conditions. In contrast, the structure of the flame is similar for the three operating conditions, when the flame does not reach the obstacle. The flame structure of the process goes through a hemispherical phase and a finger-shaped phase, and its flame propagation velocity is related to the laminar combustion velocity, and the presence of obstacles downstream has no effect. As the flame reaches the first obstacle, the presence of the obstacle causes the front surface of the flame to begin to become sharp and begin to stretch to varying degrees depending on the size of the blockage rate of the first obstacle. After the flame passed the first obstacle, a counterclockwise flame vortex of different sizes appeared to the left of the first obstacle due to the effect of the obstacle. This vortex is most evident in Case 2 and is caused by the larger blockage rate of the 40 mm obstacle. The phenomenon when the flame passes the second obstacle is similar to the above process. When the flame reaches the third obstacle, the acceleration of the flame by Case 3 is more pronounced due to the different blockage rates. As the flames continued to advance, they quickly filled the entire pipe and rushed out of the vent on the left side of the pipe. From the whole process of the explosion, the 1st, 2nd, and 3rd groups of experiments from

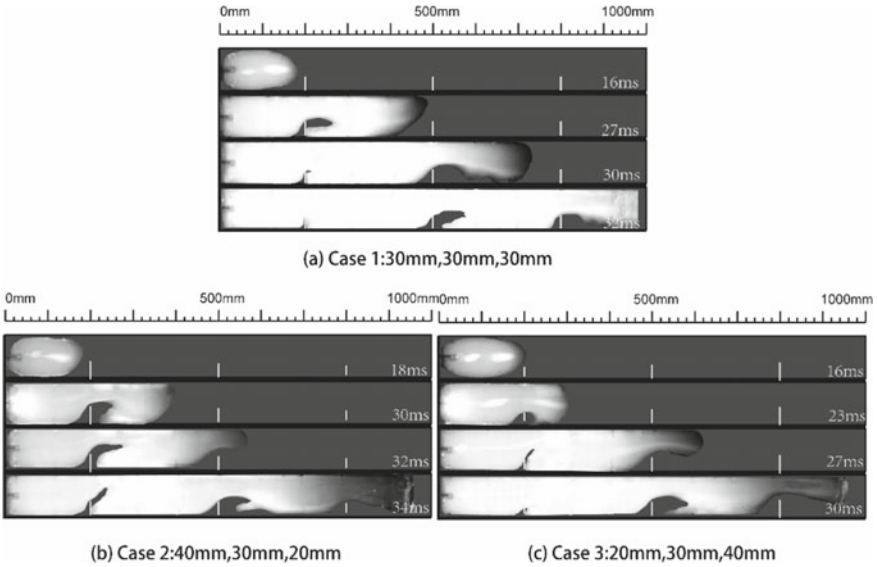

Fig. 2 Flame images under three working conditions

the beginning of the ignition to the flame filled the entire pipe used in the time of 32 ms, 34 ms, and 30 ms, respectively. With Case 1 as the control group, the barrier arrangement of Case 2 had an inhibitory effect on flame propagation. This is because the area near the ignition port placed a blockage rate of a large obstacle, where the flame is inhibited by the larger, so in the process of propagation of energy decay faster and slower. The obstacle arrangement of Case 3 has an accelerating effect on flame propagation. This is because, at the beginning of the explosion, the fuel is fully burned here due to the presence of smaller blockage rate obstacles, after which it encounters obstacles with increasing blockage rate step by step, allowing the flame to accelerate through at a faster rate.

3.2 Effect of Obstruction Rate Gradient Arrangement on Peak Explosion Overpressure

Figure 3 shows the pressure curves obtained for Case 1, Case 2, and Case 3 operating conditions. Where inlet indicates the pressure at the ignition port, mid indicates the pressure in the middle of the pipe, and outlet indicates the pressure at the explosion vent. For all three operating conditions, the pressure profile shows three distinct peaks: (1) Pv stands for "film-breaking pressure", which is the pressure generated by the PVC film at the outlet of the pipe, all three plots capture this pressure more clearly, and the order of appearance of the peak is in chronological order for the vent, the middle, and the ignition port. This is because at the beginning of the ignition,

the fuel is not fully burned and the pressure generated is small, but the speed of the pressure wave can reach 1000–3000 m/s. Therefore, the pressure wave first reaches the left side of the pipe burst location, then, the film breaks and reflects in the pipe, following this consequence. And it can be seen from the images that the magnitude of the breaking pressure is not significantly affected by the arrangement of the barrier. (2) Pmax indicates the peak pressure during the entire explosion. It can be seen from the three diagrams that the ignition port is at the maximum pressure, followed by the middle, the minimum pressure at the explosion vent, which is consistent with the actual. In comparison, Case 3 has the highest ignition port pressure, which is due to the smaller obstruction rate of 20 mm obstacle, so the fuel reacts with air more fully and burns more vigorously here. And 20, 30, and 40 mm obstacles rise in a gradient, each obstacle has a certain reflection effect on the pressure wave, and the superposition of multiple reflected waves drives the sudden change in pressure; Case 2 pressure at the vent is the largest, which is due to the 40 mm obstacle placed near the ignition port, the pressure through the larger blockage rate of the obstacle to forming a compression wave will produce a certain degree of compression and reflection. After encountering the obstruction rate decrease step by step, the obstruction of the pressure wave is weak and the pressure loss is smaller, so that the pressure measured here is larger than the other 2 groups of experiments. (3) Pneg is a negative pressure, this negative pressure is generated because, after the peak of the explosion, the fuel inside the pipe will consume oxygen and the gas inside the pipe to the outside of the pipe to form a brief "vacuum" inside the pipe. As can be seen from the three graphs, this negative pressure is the largest for Case 2, the second largest for Case 1, and the smallest for Case 3. This is because the larger blockage rate of Case 2 at the ignition port allows the pressure wave to accelerate through, pushing the unburned gas toward the exit. Therefore, the flame burns fully after the 40 mm obstacle, consuming a large amount of air in the pipe and making the gas in the pipe be discharged quickly outside the outlet. The obstruction rate of 20 mm at the outlet is smaller than the other two types, which has less influence on the outward gas discharge rate of the tube, so the "vacuum" pressure generated is larger.

4 Conclusion

After the experiment, the following conclusions were obtained:

(1) The order of the peak pressure of the rupture of the membrane in chronological order of appearance of the vent, the middle, and the ignition port. And the pressure peak is largely independent of the arrangement of the obstacle. The entire explosion process, the ignition port at the maximum pressure, followed by the middle, the minimum pressure at the explosion vent.

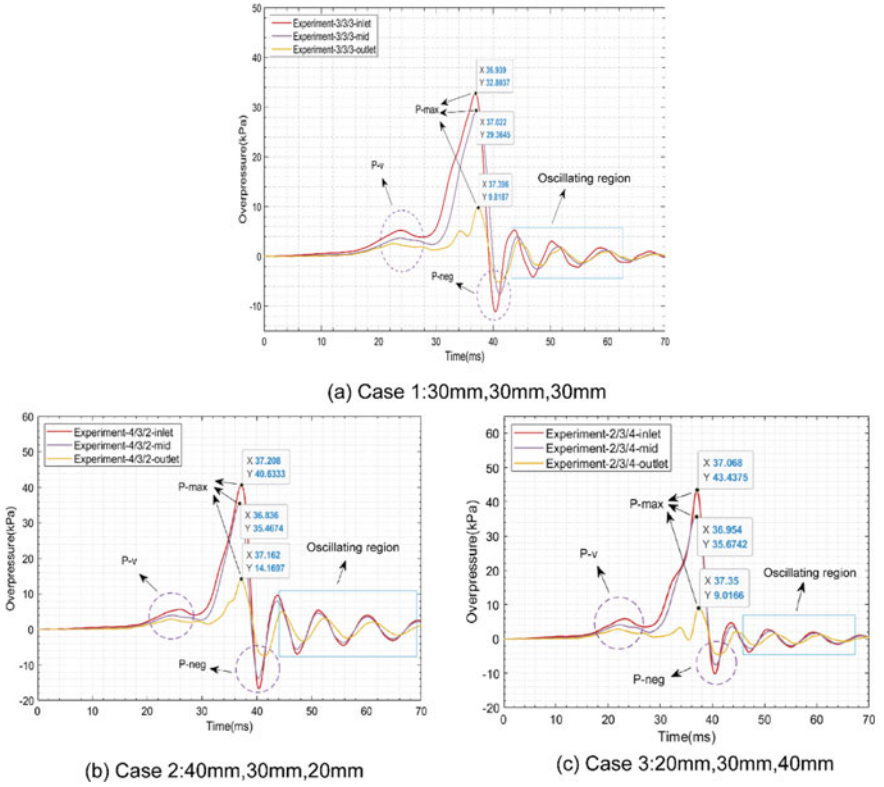

Fig. 3 Pressure curves under three working conditions

(2) A comparison of the three operating conditions shows that Case 3 has the highest pressure at the ignition port and Case 2 has the highest pressure at the explosion vent. The negative pressure during the explosion: Case 2 is the largest, Case 1 is the second, and Case 3 is the smallest.
(3) Using the Case 1 experiment as the control group, the obstacle arrangement of Case 2 had an inhibitory effect on flame propagation, and the obstacle arrangement of Case 3 had an accelerating effect on flame propagation.

Acknowledgements This research was funded by THE BASIC PUBLIC WELFARE RESEARCH PROJECT OF ZHEJIANG PROVINCE, grant number LGF22E040002.

References

1. Lu MC, Xiao H, Zuo B (2017) Research on the prevention of Sinopec pipeline leakage and explosion based on "11.22" in Qingdao. J Technol Vision 149–154. https://doi.org/10.19694/j.cnki.issn2095-2457.2017.34.099
2. Gao J, He X, Qiu Y, Mao J (2019) Experimental and numerical simulation of oil and gas explosion in crude oil pipelines. J Oil Gas Storage Transp 38(01):71–75. https://kns.cnki.net/kcms/detail/13.1093.TE.20180629.1516.004.html
3. Li GQ, Wu J, Wang SM, Bai J, Wu DJ, Qi S (2021) Effects of gas concentration and obstacle location on overpressure and flame propagation characteristics of hydrocarbon fuel-air explosion in a semi-confined pipe [Article]. J Fuel 285:13, Article 119268. https://doi.org/10.1016/j.fuel.2020.119268
4. Patel SNDH, Jarvis S, Ibrahim SS, Hargrave GK (2002) An experimental and numerical investigation of premixed flame deflagration in a semiconfined explosion chamber. J Proc Combust Inst 29(2):1849–1854. https://doi.org/10.1016/S1540-7489(02)80224-3
5. Xu QM, Chen GH, Zhang Q, Su S (2022) Numerical simulation study and dimensional analysis of hydrogen explosion characteristics in a closed rectangular duct with obstacles. Int J Hydrogen Energy 47(92):39288–39301. https://doi.org/10.1016/j.ijhydene.2022.09.091
6. Li GQ, Du Y, Bai J, Wu J, Li MY, Wu XS, Zhu L (2020) The influence of flat barrier channel shape on the propagation characteristics of oil and gas explosions. J Chem Eng 71(04):1912–1921. https://kns.cnki.net/kcms/detail/11.1946.TQ.20200103.1313.004.html
7. Valiev D, Bychkov V, Akkerman VY, Law CK, Eriksson L-E (2010) Flame acceleration in channels with obstacles in the deflagration-to-detonation transition. Combust Flame 157(5):1012–1021. https://doi.org/10.1016/j.combustflame.2009.12.021
8. Xiao G, Wang S, Mi H, Khan F (2022) Analysis of obstacle shape on gas explosion characteristics. Process Saf Environ Prot 161:78–87. https://doi.org/10.1016/j.psep.2022.03.019
9. Li GQ, Du Y, Qi S, Wang SM, Zhang PL, Wei SH, Li M (2018) Effect of obstacle location and oil and gas concentration on oil and gas pressure relief explosion characteristics. J Chem Eng 69(05):2327–2336. https://kns.cnki.net/kcms/detail/11.1946.TQ.20171227.1458.006.html
10. Wang Q, Luo X, Li Q, Rui S, Wang C, Zhang A (2022) Explosion venting of hydrogen-air mixture in an obstructed rectangular tube. Fuel 310:122473. https://doi.org/10.1016/j.fuel.2021.122473

Economic Analysis of the Energy Storage Systems for Frequency Regulation

Lidong Guo, Yi Peng, Weiwei Li, Hai Yu, Tianchen Gu, and Kaiwei Wang

Abstract Energy storage system is expected to be the crucial component of the future new power system. Besides the capacity service, the energy storage system can also provide frequency support to the power system with high penetration of renewable power. This paper firstly discusses the economic features for the various energy storage systems for frequency regulation. And then, based on the pros and cons of the existing energy storage systems, the paper proposes the constructure of the hybrid energy storage systems that can achieve promising frequency regulation effect.

Keywords Hybrid energy storage systems (HESSs) · Grid frequency regulation · Levelized cost of storage (LCOS) · Energy storage

1 Introduction

To decrease the carbon emission, large-scale renewable energy sources (RESs) are gradually replacing the traditional synchronous generators to dominate the behaviors of the power system. Since the RESs are connected to the grid through the

L. Guo (✉) · Y. Peng · W. Li · H. Yu · T. Gu · K. Wang
Petrochina Shenzhen New Energy Research Institute, Shanghai, China
e-mail: paulguo@petrochina.com.cn

Y. Peng
e-mail: pengyi69@petrochina.com.cn

W. Li
e-mail: leeww@petrochina.com.cn

H. Yu
e-mail: yuhaine@petrochina.com.cn

T. Gu
e-mail: tianchen.gu@petrochina.com.cn

K. Wang
e-mail: wangkw23@petrochina.com.cn

S. Yadav et al. (eds.), *Energy Power and Automation Engineering*, Lecture Notes in Electrical Engineering 1118, https://doi.org/10.1007/978-981-99-8878-5_16

power electronic interface, they cannot provide the inertia and frequency support to the power system as the synchronous generators [1]. Moreover, the fluctuation and intermittency of the renewable power further deteriorate the stability and security of the power systems [2, 3]. In this context, as a typical RES-leading system, the frequency stability of the grid is facing severe challenge [4].

The implement of large-scale energy storage systems (ESSs) that can provide frequency support to the grid is listed as one of the key solutions to enhance the frequency stability of the power systems [5]. Existing researches have validated that hybrid energy storage systems (HESSs) that constructed by two or more storage devices can achieve better frequency support effect comparing to the traditional ESS [6]. Reference [7] analyzes the HESSs constructed by the battery and supercapacitor. Based on that, reference [8] proposes the energy management methods for the HESSs combining the battery and supercapacitor. Reference [9] discusses the HESSs consisted by the superconducting flywheel energy storage system and large-capacity battery hybrid energy storage system to the wind power plants, and thus enables to depress the fluctuation of output wind power and provide extra frequency support to the grid. Reference [10] proposes a structure of HESSs composed of utilizing hydro energy storage, battery, and fuel cell. Reference [11] claims that the selection of the HESS for a power system should highly depend on the local conditions.

This paper analyzes the cost and the potential economic benefit of various energy storages that can provide frequency regulation, and then, discusses the constructure of the hybrid energy storage system from the view of the economic and frequency regulation effect.

2 Cost and the Potential Economic Benefit of the Energy Storage

This section economically compares the different energy storages via their levelized cost and discusses the potential applications for various storages on the frequency regulation of power system.

2.1 Definition of the Levelized Cost of Storage

The power generation cost converted into kilowatt-hour in the whole life cycle of energy storage system is called Levelized Cost of Storage (LCOS) [12]. The computation formula of LCOS is the following:

$$\mathrm{LCOS} = \frac{\mathrm{C_{invest}} + \sum_n^N \frac{C_{\mathrm{m\&o}}}{(1+d)^n} + \sum_n^N \frac{C_{\mathrm{charge}}}{(1+d)^n} + \sum_n^N \frac{C_{\mathrm{tax}}}{(1+d)^n} + \frac{C_{\mathrm{end}}}{(1+d)^{\mathrm{Tba}+1}}}{\sum_n^N \frac{Q_{\mathrm{dis}}}{(1+d')^n}} \quad (1)$$

where d is discount rate; n is time of specific operating year; N is service life of this energy storage technology; C_{invest} is initial investment cost; $C_{\text{m\&o}}$ is the cost of operation and maintenance; C_{charge} is the charging cost of the energy storage; C_{tax} is taxable amount of energy storage projects; C_{end} is the scrap cost; Q_{dis} is the total discharge or total capacity during the investment period.

2.2 *LCOS of Various Energy Storage Systems Providing Frequency Regulation*

By collecting the real-world datum of different energy storages, Figs. 1 and 2 present the probability of minimal LCOS and the corresponding mean LCOS for the ESS that can provide primary and secondary frequency regulation serves, respectively.

As we can see in Fig. 1, the supercapacitor, flywheel energy storage (FES), and lithium-ion battery can provide the primary frequency regulation due to their fast charging/discharging feature. From the view of LCOS, battery shows the better potential for the wide applications in the future.

According to the above discussion, we can conclude the potential of the storages for the future applications of the various energy storage systems for frequency regulation in Table 1.

To sum up, economically speaking, the lithium-ion battery is supposed to be the most common energy storage for power system frequency regulation in the future.

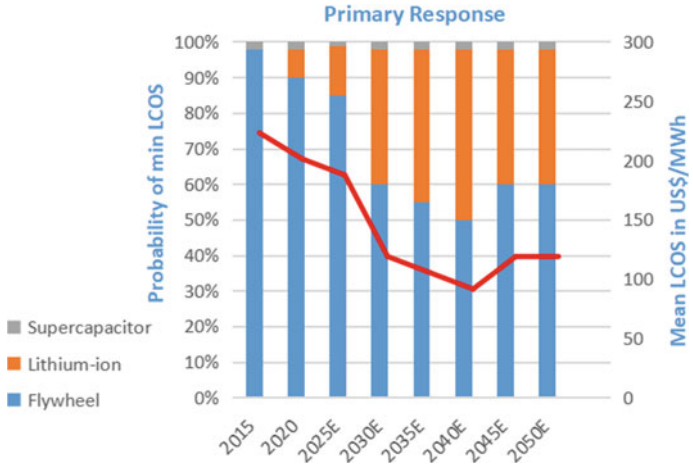

Fig. 1 Minimal LCOS probability of energy storages for primary frequency regulation

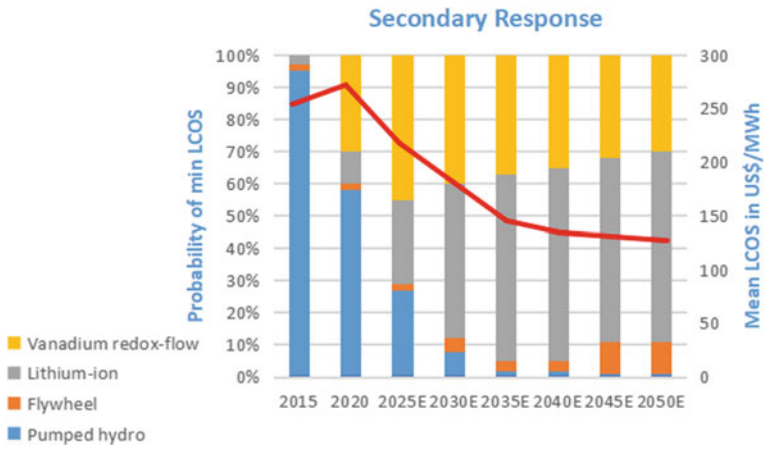

Fig. 2 Minimal LCOS probability of energy storages for secondary frequency regulation

Table 1 The current situation and the potential of the energy storage applications for power system frequency regulation

Frequency regulation	Current proportion	Developing potential
Primary frequency regulation	Lithium-ion, flywheel	Lithium-ion > flywheel
Secondary frequency regulation	Lithium-ion	Lithium-ion > liquid flow

3 Potential HESS for Frequency Regulation

According to Sect. 2, lithium-ion battery can be the most suitable energy storage to provide the frequency regulation of the power system from economic view. This section further explains the dynamic features of the lithium-ion battery and providing the suggestions for constructing the HESS combined the battery with other storage to further improve the frequency regulation effect.

3.1 Battery Energy Storage System

Battery is one of the most common energy storage systems. Because of its flexible operation mode and fast charging and discharging speed, it can respond quickly to the frequency deviation of the power system [13], so it is suitable for providing frequency support. In a battery energy storage system, the internal units cooperate with each other, centrally and uniformly adjust the state of charge (SoC) between the units and release energy according to the different needs of the grid to maintain the power balance of the grid.

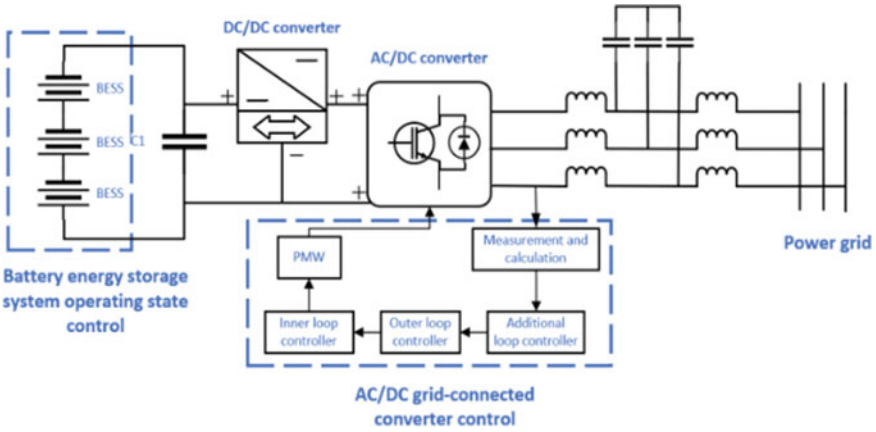

Fig. 3 Frequency modulation principle of battery energy storage

The structure and working principle of the battery are shown in Fig. 3. As shown in Fig. 3, the battery energy storage system is connected to the grid through an AC/DC converter to realize flexible charging and discharging. The AC/DC converter can act as an active rectifier, while the DC/DC converter acts as a charger.

The main disadvantage of the battery is the frequent adjustment of its state of charge (SoC). Once the SoC is lower than 20% of the battery capacity or higher than 80% of the battery capacity, the internal resistance of the battery will deviate from the normal value [14], which will lead to unexpected reactive power dissipation, thus leading to an increase in the internal temperature of the battery. In this case, the working life of the battery will be shortened, which increases the operating cost and reduces the reliability of ESS. HESS, which is composed of battery and other energy storage devices, can prolong the working life of battery and become a better choice to provide frequency support to the grid.

3.2 HESSs Consists of Batteries and Supercapacitors

Supercapacitor is characterized as the high energy density that allows the fast response to the frequency variation of the power system within tens to hundreds of milliseconds. The main drawback of the supercapacitor is the relatively high cost. The combination of the battery and supercapacitor can effectively prolong the working life of the battery by reducing the times of adjusting the SOC of the battery, and therefore saves the cost of the supercapacitor.

3.3 HESSs Consists of Battery and Flywheel

Flywheel energy storage system can effectively mitigate the impact of fluctuation and intermittence of renewable energy. Therefore, the flywheel is very suitable for fertile wind fields. The main shortcoming of the flywheel energy storage system is the limited capacity of energy, which is hard to meet the energy requirement for the frequency regulation of the system. The combination of flywheel and battery can effectively improve the frequency regulation effect by balancing the response speed and lasting time.

4 Conclusion

In this paper, through the calculation and analysis of LOCS, it is concluded that lithium-ion battery is the most economic energy storage device for frequency regulation and has the great potential to be widely used in the future power system. By considering the shortcoming of the lithium-ion battery, two kinds of hybrid energy storage systems are proposed to achieve the best frequency regulation effect with the lowest cost.

References

1. Hu X, Fan H, Li T, Meng Z, Luo P, Zhou H (2022) Stability analysis and parameter configuration of parallel virtual generators in microgrid. Energy Rep 8(Supplement 10):866–873. ISSN 2352-4847
2. El-Bahay MH, Lotfy ME, El-Hameed MA (2022) Computational methods to mitigate the effect of high penetration of renewable energy sources on power system frequency regulation: a review. Arch Comput Methods Eng. https://doi.org/10.1007/s11831-022-09813-9
3. Moustakas K, Loizidou M, Rehan M, Nizami AS (2020) A review of recent developments in renewable and sustainable energy systems: key challenges and future perspectives. Renew Sustain Energy Rev 119:109418. ISSN 1364-0321
4. Bevrani H, Ghosh A, Ledwich G (2010) Renewable energy sources and frequency regulation: survey and new perspectives. IET Renew Power Gener 4(5):438–457. https://doi.org/10.1049/iet-rpg.2009.0049
5. Molina MG (2017) Energy storage and power electronics technologies: a strong combination to empower the transformation to the smart grid. Proc IEEE 105(11):2191–2219. https://doi.org/10.1109/JPROC.2017.2702627
6. Yang P, Nehorai A (2014) Joint optimization of hybrid energy storage and generation with renewable energy. IEEE Trans Smart Grid 5(4):1566–1574. https://doi.org/10.1109/TSG.2014.2313724
7. Del Granado PC, Pang Z, Wallace SW (2016) Synergy of smart grids and hybrid distributed generation on the value of energy storage. Appl Energy 170:476–488. ISSN 0306–2619
8. Ju C, Wang P, Goel L, Xu Y (2018) A two-layer energy management system for microgrids with hybrid energy storage considering degradation. IEEE Trans Smart Grid 9(6):6047–6057. https://doi.org/10.1109/TSG.2017.2703126

9. Lee H, Shin BY, Han S, Jung S, Park B, Jang G (2012) Compensation for the power fluctuation of the large scale wind farm using hybrid energy storage applications. IEEE Trans Appl Supercond 22(3):5701904–5701904, Art. 5701904. https://doi.org/10.1109/TASC.2011.2180881
10. Suberu MY, Mustafa MW, Bashir N (2014) Energy storage systems for renewable energy power sector integration and mitigation of intermittency. Renew Sustain Energy Rev 35:499–514. ISSN 1364-0321
11. Aneke M, Wang M (2016) Energy storage technologies and real life applications—a state of the art review. Appl Energy 179:350–377. ISSN 0306-2619
12. Schmidt O, Melchior S, Hawkes A, Staffell I (2019) Projecting the future levelized cost of electricity storage technologies. Joule 3(1):81–100. ISSN 2542-4351
13. Cai Y, Qi D (2022) A distributed VSG control method for a battery energy storage system with a cascaded H-bridge in a grid-connected mode. Glob Energy Interconnection 5(4):343–352. ISSN 2096-5117
14. Zhuotong L, Yi Z, Yun J, Fang F (2022) Rule-based dual planning strategy of hybrid battery energy storage system. IFAC-PapersOnLine 55(9):495–500. ISSN 2405-8963

Construction of Heat Load Demand Quantitative Model for Clean Heating

Weiqi Zhang and Baosheng Chen

Abstract This paper fully considers the flexible response ability of thermal load and the potential of clean energy consumption, builds a quantitative model of thermal load demand for clean energy consumption, and takes a clean heating demonstration project as an example to analyze the economy of the waste air heat storage heating system. An example shows that its economic benefits can be greatly improved under this quantitative model.

Keywords Demand quantification · Electric heating load

1 Introduction

Heating is the largest energy consumption area, and heating accounts for about 50% of global final energy consumption. From the perspective of global energy consumption, the use of clean energy is becoming an important development trend. Renewable energy heating accounts for about 10% of global heating. The use of heating energy will become an important factor in restricting energy security, environmental governance, and ensuring social sustainable development [1].

In the current market environment where the rate of wind and light abandonment of new energy in the "three north" and other places in China is high, effective use of spot goods, increase of power generation, and increase of benefits are effective means for new energy enterprises to increase benefits. New energy spot trading can effectively reduce the wind and light rejection rate of new energy through market mechanism construction without increasing hardware investment. In addition, the traditional demand-side response resources have the potential to absorb clean energy. In addition to the traditional power load, the thermal demand response is also of scheduling value to the power system in the context of the deepening degree of electrothermal coupling. Therefore, taking full account of the flexible response capacity of thermal load and

W. Zhang (✉) · B. Chen
State Grid Ningxia Electric Power Co., Ltd., Economic and Technological Research Institute, Ningxia, China
e-mail: 1027383287@qq.com

S. Yadav et al. (eds.), *Energy Power and Automation Engineering*, Lecture Notes in Electrical Engineering 1118, https://doi.org/10.1007/978-981-99-8878-5_17

the potential of clean energy consumption, and building a spot power transaction oriented to clean energy consumption will be an important development direction of future power market transactions, and preliminary exploratory research has been carried out at home and abroad [2].

In recent years, the Chinese government has actively promoted the development and utilization of clean energy and formulated a series of policies and regulations to support the consumption of clean energy. While increasing the supply of clean energy, various forms of new energy supply technologies, such as combined heat and power, have also developed rapidly. In response to the current situation of new energy curtailment in areas such as the "Three North" region, many domestic enterprises and institutions have begun to explore the application of electricity spot trading to increase the utilization of clean energy. Among them, the Energy Internet Research Institute of Tsinghua University has achieved certain results in the field of clean energy trading. The Institute has realized the dual goals of clean energy consumption and energy conservation and emissions reduction by building an electricity market trading platform for clean energy consumption [3].

In addition, to further increase the consumption rate of clean energy, various fields in China are actively conducting research. For example, in the industrial field, multiple technologies have been applied to the recovery and utilization of heat energy to achieve efficient energy utilization by converting waste heat into electricity or direct heating. At the same time, many domestic enterprises are also developing smart heating systems to improve the flexibility of thermal load and the consumption rate of clean energy by establishing a heating management platform based on cloud computing, the Internet of Things, big data, and other technologies. In addition, multiple research institutions in China are actively exploring energy-saving technologies and management models for heating networks to improve the energy efficiency and clean energy utilization rate of heating systems in cities.

In summary, with the rapid development of clean energy and policy support, various sectors in China have begun to explore multiple pathways and methods for clean energy consumption. In the future, we have reason to believe that with continuous technological innovation and the improvement of market mechanisms, clean energy will become an important driving force for the development of China's energy industry and make greater contributions to promoting energy revolution and building a beautiful China.

In foreign countries, for the cost-risk-assessment of thermal load response, the literature [5] uses Markov chain Monte Carlo method to model the dynamic of thermal load, proposes a risk assessment method of thermal load, and verifies it. Literature [6] establishes a nonlinear model of multi-ring heat network based on graph theory and hydraulic calculation model, uses Newton method to solve the model, and judges the fault state of the system according to the actual heat gain of users or the indoor temperature of users, forming a risk assessment method considering heat load. For the response regulation strategy of thermal load, many studies have been carried out abroad mainly for the response optimization regulation of thermal load after participating in the market. Literature [7] and others put forward a structural framework of thermal load aggregation, and on this basis studied the

optimal regulation strategy of thermal load response when participating in market regulation in the form of thermal load aggregator in the day-ahead market, realizing the minimization of energy costs and the flexibility planning of thermal load. The detailed population model of independent housing in Finland and the day-ahead market data of Nord Pool's Elspot are used for simulation verification. Literature [8] proposes a two-stage stochastic programming model for the flexible demand response of heat storage devices, which realizes the flexible thermal load demand response of the two heat storage forms of building material heat storage and hot water heat storage. For the research on thermal load—green energy trading mechanism and trading variety design, the document [9] continuously improves the renewable energy incentive policy, improves the mode of renewable energy participating in the electricity market, studies and proposes the electricity market 2.0, and improves the electricity market to adapt to the high proportion of new energy access. Literature [10] proposes corresponding micro-grid power market schemes for different scenarios combined with blockchain to solve the mutual aid transaction of local communities and meet the self-sufficiency of local power generation and consumption. In view of the business model of grid-thermal control platform, the literature [11] summarizes the research status of foreign countries using thermal load to absorb green new energy. The United States has developed rapidly in this field in recent years, and the installed capacity of cogeneration has accounted for about 7% of the total installed capacity of the United States. Japan's energy consumption is mainly a district heating system with electricity-heat system as the heat source. In Europe, the EU's cogeneration power generation has accounted for 9% of its total power generation (among which Denmark, Finland, and the Netherlands have reached more than 30%). However, many studies have remained on the development of cogeneration units, without combining the electricity-heat consumption method with the market, and without a clear business model oriented to the bilateral spot market, so that the demand, willingness, and value of both parties cannot be accurately grasped. As a result, power plants and users cannot trust each other, and the large-scale promotion of the electricity-heat consumption mode is hindered.

2 Construction of Demand Quantification Model

Electric heating load forecasting model:

$$P = P_B + P_W$$

where P is total electrical heating load requirement, P_B is primary electrical heating. P_W is an electrical heating load component which is sensitive to weather factors.

$$P_B(t) = \left[\sum_{t=1}^{24}(Cair\rho airNSH + \partial KA)(T_{\text{in}}(t) - T_{\text{out}}(t)) - Q_{\text{in}e} - Q_{\text{in}h}\right]/\eta_h$$

where, *Cair* is the specific heat capacity of air; *ρair* is the air density; *N* is air quantity, *S* is housing area, *H* is room height, Q_{ine} is electric equipment; Q_{inh} is the heat value of human body; ∂ is the temperature differential correction coefficient; *K* is the heat transfer coefficient of the housing. Tin (*t*) is the room temperature at *t*, T_{out} (*t*) is the outside temperature at *t*, T_{out} (*t*) is the outside temperature at *t*, and η_h is the energy transfer efficiency.

To increase the precision of electric heating load prediction, taking into account the effect of humidity on electrical heating load, the electric heating load prediction was revised by regression analysis, and the following equation was obtained:

$$P_W = \max\left(\frac{\Delta S_H}{23.10}, \frac{\Delta S_T}{39.43}\right) / \min\left(\frac{\Delta S_H}{23.10}, \frac{\Delta S_T}{39.43}\right)$$

where: ΔS_H is the sensitivity of electric heating load at the corresponding humidity, ΔS_T is the sensitivity of electric heating load at the corresponding temperature *T*.

Output model of regenerative electric heating equipment:

$$Q_h(t) = \eta_h \times P_h(t)$$

where, $P_h(t)$ is the power consumption of the thermal storage electrical heating installation. In this paper, the conversion efficiency of solid heat storage electric heating is 95–98%.

Most of the solid heat storage materials are MgO, which can be heated up to 800 °C, relationship between the common storage and temperature is common:

$$S_{in} = cm(T_2 - T_1), \ T_2 \leq 800\ ^\circ\mathrm{C}$$

where: c is MgO specific thermal capacity; M is MgO weight; T1 is the temperature prior to the thermal storage of MgO; T2 is the thermal storage temperature of MgO. Among them, the relation of heat storage capacity and heating time is as follows:

$$S_{HS}(t) = (1 - \eta_{HS})S_{HS}(t-1) + (S_{in}(t) - S_{out}(t))$$

$$S_{in}(t) = Q_{in}(t)\eta_{in}$$

$$S_{out}(t) = Q_{out}(t)\eta_{out}$$

Here: S_{HS} (*t*) is the heat storage capacity of the thermal energy in the time *t*, η_{HS} is the heat storage loss ratio, and S_{out} (*t*) is the heat release; Q_{in} (*t*) is the heat storage power at *t*, and *Q*out (*t*) is the heat release power at *t*, η_{in}, η_{out} is the efficiency of heat storage and heat release of the heat storage tank.

Thermal storage electric heating meets the requirement of "big customers directly purchasing electricity." By negotiating directly with the wind farm, the discarded wind power is bought at the agreed price. The network charges only the transport

and distribution costs, and the remainder is bought from the network at the time of use. The economic evaluation model of regenerative electric heating is presented in the formula.

$$P_{\text{sum}} = C_{jp} \sum_{i=1}^{n} Q_{\text{hot}}^{i} + C_{\text{hot}} S - P_{\text{pay.s}} - P_{\text{pay.r}}$$

where, S is the heating zone for regenerative electrical heating; C_{hot} is the heating charge; C_{jp} is the unit price for saving energy and reducing emissions; $P_{\text{pay.s}}$ Static investment cost means that the initial investment cost and the retirement residual value are allocated to N years' service life; $P_{\text{pay.r}}$ for the operating cost, the operating cost means the cost equivalent to the energy consumed by the regenerative electric boiler in the entire heating period.

3 Example Analysis

Based on an example of clean heating, this paper analyzes the economic performance of the waste air thermal storage heating system.

(1) Conditions for heating. The heating time is 181 days, the heating area is 200,000 m^2, the heating cost is 20.375 yuan/m_2, and the cost of energy saving and emission reduction allowance is O.
(2) Regenerative electrical heating system parameters. The regenerative electrical feeding system is composed of 9 electric boilers; Electrothermal conversion efficiency 95%; Heat loss of 5% of pipeline network; Static investment cost: 1 million, $N = 20$, initial investment of 22.5 million, remaining value 2.5 million;
(3) Additional parameters. The total installed capacity of the approved wind farm is 400 MW; the power transmission and distribution cost of the grid company corresponds to the Charge of 0.11 yuan/kWh.

There are two kinds of operating modes in the thermal storage electric heating system: full power heating at low time and full time heating mode with heat storage. The economical operating mode in the wind-down period, i.e., it starts when the wind farm abandons the wind. In the case of shortage of wind power, the power grid can be bought to satisfy the heating requirement (Fig. 1).

Different operating modes of regenerative electric heating system have different energy consumption. Because of the uncertainty of the abandonment of wind power, it is impossible to satisfy the demand of the thermal storage electric heating system. The power consumption of the thermal storage electrical heating system is illustrated in the diagram.

In these two modes, the thermal storage electric heating system directly buys and discards wind energy. Finally, the economic efficiency of the entire heating cycle is demonstrated. During the entire heating period, the total economic loss was

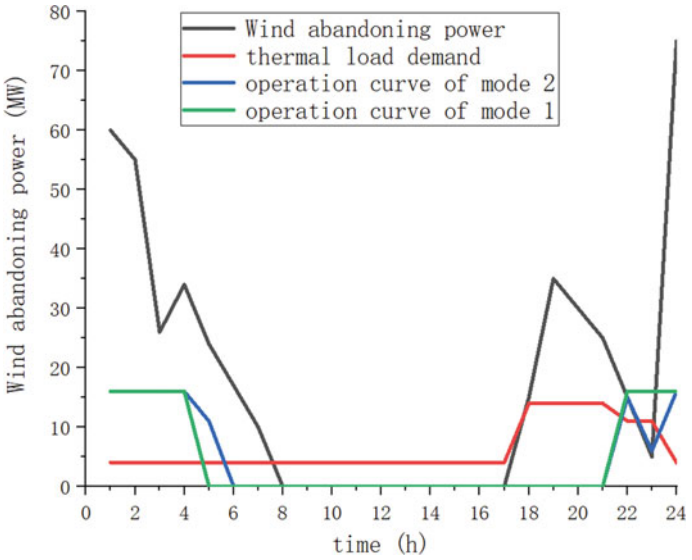

Fig. 1 Operating state diagram of regenerative electrical heating system

4.9493 million RMB and 5.1902 million RMB. It is mainly caused by the high cost of operation of electric power and the lack of relevant environmental subsidies. In the electricity market environment, the thermal storage electric heating system can further reduce operating costs and increase overall revenue through negotiation with the wind farm to lower the agreed price of wind power. For Mode 1, due to the low amount of power required to abandon the wind, even if the contract price for the abandonment of wind power is zero, the thermal storage electric heating system will suffer a loss. As for the second mode, as the power price is gradually lowered, the heat storage electric heating system is becoming profitable. When the contract price is set at 0.014 RMB/KW/h, the thermal storage electric heating system reaches its equilibrium point.

Gradually improving the power market will make it possible to take full responsibility for the operation of the electric heating system. In the case of 100% wind abandonment, the price of power is 0.045 yuan/kWh to break even. Given the state's concern about fog and thunder, the regenerative electric heating will be popularized, the energy conservation and emission reduction of the regenerative electric heating will be subsidized, and the economic efficiency will be greatly increased.

4 Conclusion and Suggestion

The power, thermal, and demand-side load combined absorption control technology studied in this paper has improved the rapid absorption capacity of the grid for intermittent renewable energy such as clean energy. In view of the above research, the following suggestions are put forward:

Establish the electricity heating price mechanism linked by the plant and the network, set up the electricity heating trading varieties by pre-listing or government guidance, and further reduce the electricity heating trading price. In the initial stage, wind power and other new energy will be the main energy source. In the later stage, the part above the minimum operation mode of thermal power units in the valley will enter the market and carry out transactions with electric heating users. The price shall not be higher than the marginal cost of the main thermal power units. Continue to implement the peak-valley electricity price policy on the user side, guide users to avoid peaks and valleys, increase the power load in the valley section, further reduce wind abandonment, and improve the utilization efficiency of thermal power units in the valley section. Combine the user categories of electric heating and retain the residential, general industrial, and commercial electric heating categories. Except for residential electric heating users (including schools, nursing homes, welfare homes, village committees, and other users who implement residential electric heating tariffs), other users are considered as general industrial and commercial heating users.

References

1. Duenas P, Julián Barquin, Reneses J (2012) Strategic management of multi-year natural gas contracts in electricity markets. IEEE Trans Power Syst 27(2):771–779
2. Mathiesen BV, Lund H (2009) Comparative analyses of seven technologies to facilitate the integration of fluctuating renewable energy sources. IET Renew Power Gener 3(2):190–204
3. Lv Q, Jiang H, Chen T et al (2014) Thermal power plant wind power consumption scheme based on electric boiler and its national economic evaluation. Power Syst Automa 38(1):2–12
4. Yu Jing, Sun Hongbin, Shen Xinwei. Joint optimal operation strategy of wind power and thermal power unit considering heat storage device [J] Power Automation Equipment, 2017, 37 (6): 139–145
5. Chen S, Xin H, Wang T et al (2016) Robust optimization model for combined heating dispatching of wind power and thermal storage electric boiler. Power Constr 37(1):103–109
6. Shariatkhah M-H, Haghifam M-R, Mohesn P-M et al (2015) Modelling the reliability of multi-carrier energy systems considering dynamic behavior of thermal loads. Energy Build 103:375–383
7. Hassine IB, Eicker U (2013) Impact of load structure variation and solar thermal energy integration on an existing district heating network. Appl Therm Eng 50(2):1437–1446
8. Alahäivälä A et al (2017) A control framework for the utilization of heating load flexibility in a day-ahead market. Electric Power Syst Res 145:44–54
9. Good N, Karangelos E, Navarro-Espinosa A, Mancarella P (2015) Optimization under uncertainty of thermal storage-based flexible demand response with quantification of residential users' discomfort. IEEE Trans Smart Grid 6(5):2333–2342

10. Federal Ministry for Economic Affairs and Energy (2015) An electricity market for Germany's energy transition. Federal Ministry for Economic Affairs and Energy, Berlin
11. Green J, Newman P (2017) Citizen utilities: the emerging power paradigm. Energy Policy 105:283–293

Conditional Value at Risk Model of New Power System Reserve Assessment Considering Primary Energy Supply Risk

Shuiping Zhang, Lian Tu, Qinwei Duan, Zhu Chao, Xuchen Tang, Xingxing Wanyan, and Xiaoting Chen

Abstract To deal with the difficulty of assessing the reserve demand of the new power system caused by the strong randomness in the new power system, a reserve assessment method of the new power system considering the primary energy supply risk is proposed. Based on conditional value at risk theory, this method constructs a reserve evaluation model by quantifying the risk of loss of load and current of renewable energy, which overrides the shortcuts of traditional statistical methods that cannot consider the coupling characteristics of time period. Based on the actual case in Guangdong, the effective management of power balance and new energy consumption risk of standby time-sharing assessment is verified, and the evaluation method for the reserve assessment of the new power system considering the risk of primary energy supply is provided with both reliability and economy.

Keywords Alternate assessments · CVaR · Spot market · Primary energy supply

1 Introduction

With the advancement of intermittent renewable energy sources, such as wind and solar power in the electricity system, the role of controllable power sources like coal and gas has shifted, leading to increased demands for reliability and flexibility in power system operations. Relying on traditional methods of reserving proves insufficient to meet the operational requirements of modern power systems [1].

This challenge is reflected in two aspects: First, with the increasing complexity of the power system operation risk mechanism, it becomes difficult to reserve

S. Zhang · L. Tu · Q. Duan · Z. Chao · X. Tang
Electric Power Dispatching Control Center of Guangdong Power Grid Co., Ltd., Guangzhou, Guangdong, China

X. Wanyan · X. Chen (✉)
Beijing Tsintergy Technology Co., Ltd., Guangzhou Branch, Guangzhou, Guangdong, China
e-mail: chenxt@tsintergy.com

S. Yadav et al. (eds.), *Energy Power and Automation Engineering*, Lecture Notes in Electrical Engineering 1118, https://doi.org/10.1007/978-981-99-8878-5_18

reliable reserve capacity. Second, traditional reserve evaluation methods have economic disadvantages that are amplified in the power system with high renewables penetration [2].

For the reserve evaluation method considering the uncertainty of primary energy supply, the existing research ideas mainly include the following four categories: (1) statistical method [3]. However, such methods are limited in their ability to consider the time-coupling characteristics of power systems. (2) Two-stage method [4, 5]. This method is unable to balance control costs and actual losses, and easy to ignore high-risk small probability events. (3) Robust optimization method [6, 7], which requires that the system unit combination scheme can meet the output of new energy under the most unfavorable condition of the system. However, the robust optimization method often suffers from overly conservative solutions. (4) The risk method has been improved in the above method. The comprehensive quantitative modeling of the occurrence probability and risk event loss is established in the objective function. References [8–10] introduced the value at risk theory to take the risk of power system load loss and wind and light abandonment into account in the reserve evaluation method. However, existing research mainly focuses on the uncertainty of wind power output and neglects other important factors that affect the reserve demand of power systems.

This paper analyzes the uncertainty factors and mechanisms influencing primary energy supply in new power systems. The specific contributions of this paper are as follows:

1. The study analyzes the impact mechanisms of various primary energy supply risks on the power system and constructs a multi-level reserve evaluation model based on the conditional value at risk theory. The model includes operational and spinning reserves and provides a quantitative approach for evaluating reserve capacity reasonably while considering multiple complex risks.
2. By setting the risk preference parameters, this paper quantifies the time-varying risks associated with load loss and wind and light abandonment. While effectively managing the power balance risk considering time coupling, the time-sharing effectiveness, and economy of reserve assessment are improved and increase the level of new energy consumption.

2 Risk Impact Analysis of Primary Energy Supply

2.1 Influence of Uncertainty of Primary Energy Supply on Power Supply Adequacy

Uncertainty of New Energy Output. After the large-scale access of new energy to the grid, the system is faced with bilateral randomness, weak fluctuation regularity of new energy, large random disturbance amplitude, and long period [10, 11], which puts forward higher requirements for the availability of the system. The uncertainty

surrounding new energy sources means that extreme conditions can cause power system blackouts, resulting in incalculable losses. For example, the rotating blackout in California in 2020 [12], and the UK blackout in August 2019 [13].

Multi-energy System Coupling Risk. In the context of the energy Internet [14, 15], the risk of cross system transmission caused by multi-energy coupling will inevitably exist [16].

For example, the power outage in Taiwan in August 2017 and the extreme cold weather power outage in Texas in the United States in 2021 were caused by the fact that the long-term planning and operation optimization results of the reserve capacity ignored the risk of fault transmission across the energy system [16, 17].

2.2 Influence of Uncertainty of Primary Energy Supply on Flexible Resource Demand of New Power System

The flexibility demand of the new power system mainly comes from the random fluctuation of wind/photovoltaic power generation and the random variations of rigid load. The random fluctuation of net load (the difference between load and new energy output) increases significantly.

3 Multi-level Reserve Assessment Model Considering Primary Energy Supply Risk

This paper establishes a risk-averse multilevel reserve evaluation model for new power systems considering the uncertainty of primary energy supply. The evaluation model construction process is shown in Fig. 1. The objective of the model is to minimize the operation cost of the power system operation and the risk of system load loss.

3.1 Quantitative Method of Primary Energy Supply Uncertainty in New Power System

Uncertainty Modeling Method of New Energy Output. This paper generates new energy risk scenario data through the risk scenario module, which can obtain the predicted output values of various typical scenarios and periods of new energy units.

Uncertainty Modeling Method for Coal-Fired Gas Generating Units. The main reasons for the uncertainty of coal-fired and gas-fired units can be divided into the

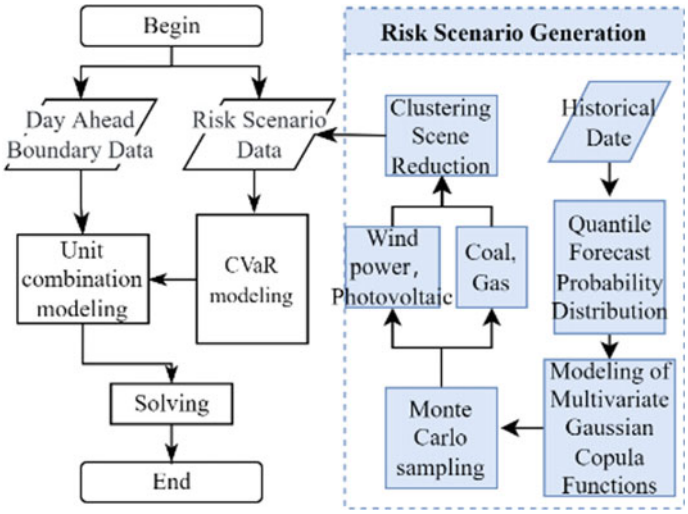

Fig. 1 Flow chart of reserve assessment method

following three categories: primary energy shortage, equipment failure, and risk spread across the system.

3.2 Multi-level Reserve Assessment Model

Objective Function. The objective function is to minimize the power system operation cost and the risk of power system load loss in the dispatching cycle. The power system operation cost includes the start-up cost of units, the operation cost of units, and the penalty cost of security constraint overrun.

$$\begin{aligned}
&\min(1-\beta)\cdot F^{\text{cost}}+\beta\cdot F^{\text{risk}}\\
&F^{\text{cost}}=\sum_{t}\sum_{i}\left(C_i^U\cdot y_{i,t}+C_i\left(p_{i,t}\right)\cdot p_{i,t}\right)+\sum_{t}\sum_{c}M^{c}\cdot\left(S_{c,t}^{+}+S_{c,t}^{-}\right),\\
&F^{\text{risk}}=\sum_{t}M^{\text{lost},w}\cdot\xi_t^{\text{VaR},\alpha,w}+\sum_{t}M^{\text{lost},l}\cdot\xi_t^{\text{VaR},\alpha,l}
\end{aligned}\tag{1}$$

where, i is the subscript of the conventional power unit, w denotes the subscript of the new energy unit. Additionally, l is the subscript of the load, t signifies the subscript of the dispatch period, s is the subscript of the risk scenario, and F^{cost} refers to the total cost of system operation in the dispatch period t. The risk of power system load loss within the dispatching period t is given by F^{risk}. Here, β serves as the risk preference coefficient, with $\beta > 0$ indicating risk aversion; this paper only considers

this situation. $M^{\text{lost},l}$ is the risk value of load loss, and $M^{\text{lost},w}$ is the risk value of wind and solar abandonment.

In the power system operation cost function, $p_{i,t}$ denotes the output decision variable of unit i in the period t, the unit is MW, $y_{i,t}$ is the start-up binary decision variable for unit i in the period t (1 indicates start-up, otherwise 0); C_i^U represents the start-up cost of the unit i, and $C_i\left(p_{i,t}\right)$ signifies the generation cost curve of the unit i.

In the system load loss risk function, $\xi_t^{\text{VaR},\alpha,w}$ stands for the condition risk value of wind and light abandonment in the period t when the confidence degree is α, and $\xi_t^{\text{VaR},\alpha,l}$ corresponds to the load loss condition risk value in the period t, given a confidence level of α.

Prediction Scenario Operational Constraints. The unit combination model includes thermal power unit output constraints, new energy output constraints, system load balance constraints, network security constraints, and multi-level reserve constraints.

(1) Output constraints of thermal power units

$$\begin{aligned} &g_{i,t} \times P_i^{\min} \le p_{i,t} \le g_{i,t} \times P_i^{\max}, \\ &\phi_k(\overrightarrow{r}) = (2\pi)^{2/3} \exp\left(\mathrm{i}\overrightarrow{k} \cdot \overrightarrow{r}\right), \\ &A^{(3/2)} = A^{(+)} - A^{(-)} \quad (I = \tfrac{3}{2}) \end{aligned} \tag{2}$$

where, $g_{i,t}$ is the 0/1 operating state decision variable of the unit i in the period t $P_i^{\max}$ and $P_i^{\min}$ are the maximum and minimum technical output of the unit i in the period t, respectively.

The output of the unit must meet the requirements of the ramp rate. In the period t, the ramp constraint of each unit i can be described as:

$$\begin{aligned} &p_{i,t-1} - p_{i,t} \le \Delta P_i^D \times \left(1 - z_{i,t}\right) + z_{i,t} \times P_i^{\min}, \\ &p_{i,t} - p_{i,t-1} \le \Delta P_i^{\mathrm{U}} \times \left(1 - y_{i,t}\right) + y_{i,t} \times P_i^{\min} \end{aligned} \tag{3}$$

In the formula, ΔP_i^{U} represents the maximum ramp rate when the unit is operating within its normal output range; ΔP_i^{D} represents the maximum value of the downhill climbing rate when the operating unit is within the normal output range.

(2) Minimal continuous start-stop time constraints of thermal power units

Due to the physical properties of thermal power units and operational requirements, the minimum continuous start-stop time constraint can be described as:

$$T_{i,t}^D - (g_{i,t} - g_{i,t-1})T_D \ge 0, \quad T_{i,t}^U - (g_{i,t-1} - g_{i,t})T_U \ge 0 \tag{4}$$

Among them, T_U, T_D are the minimum continuous start-up time and minimum continuous shutdown time of the unit; $T_{i,t}^U$ represents the time that the unit i has been continuously started during the period t, and $T_{i,t}^D$ donates the time that the unit i has been continuously shut down during the period t. $T_{i,t}^U$, $T_{i,t}^D$ expressed $g_{i,t}$ as:

$$T_{i,t}^U = \sum_{k=t-T_U}^{t-1} g_{i,k},\ T_{i,t}^D = \sum_{k=t-T_D}^{t-1} (1 - g_{i,k}) \tag{5}$$

(3) Maximum start-stop times constraint of thermal power unit

Defined $y_{i,t}$ as the binary decision variable of whether the unit i is switched to the start state during the period t; the binary decision variable $z_{i,t}$ is defined to indicate whether the unit i is switched to the shutdown state during the period t; $y_{i,t}$ and $z_{i,t}$ satisfy the following conditions:

$$y_{i,t} = \begin{cases} 1 \text{ iff } g_{i,t} = 1 \& g_{i,t-1} = 0 \\ 0 \qquad \text{otherwise} \end{cases} \quad z_{i,t} = \begin{cases} 1 \text{ iff } g_{i,t} = 0 \,\&\, g_{i,t-1} = 1 \\ 0 \qquad \text{otherwise} \end{cases} \tag{6}$$

The limit of starting and stopping times of corresponding unit i can be expressed as follows:

$$\sum_{t=1}^{T} y_{i,t} \le y_i^{\max}, \quad \sum_{t=1}^{T} z_{i,t} \le z_i^{\max} \tag{7}$$

Among them, $y_i^{\max}$,$z_i^{\max}$ are the maximum start-up and shutdown times of the unit i, respectively. The analytical expression of $y_{i,t}$, $z_{i,t}$ is as follows:

$$y_{i,t} - z_{i,t} = g_{i,t} - g_{i,t-1}, \quad 0 \le y_{i,t} + z_{i,t} \le 1 \tag{8}$$

(4) Output constraint of new energy

$$p_{w,t} = P_{w,t}^{DA} \tag{9}$$

In the formula, $p_{w,t}$ presents the planned output of the new energy unit w in the period t; $P_{w,t}^{DA}$ is the short-term power forecast of the new energy unit w in the period t.

(5) System load balancing constraint

$$\sum_i p_{i,t} + \sum_w p_{w,t} = D_t \tag{10}$$

where, D_t donates prediction system load in the period t.

(6) Hierarchical reserve constraints

$$\begin{aligned} R_t^{\mathrm{Up,Thermal}} &= \sum_i \left(g_{i,t} \cdot P_i^{\max} - p_{i,t}\right),\ R_t^{\mathrm{Dn,Thermal}} = \sum_i \left(p_{i,t} - g_{i,t} \cdot P_i^{\min}\right) \\ R_t^{\mathrm{SpinUp,Thermal}} &= \sum_i \min\left(g_{i,t} \cdot P_i^{\max} - p_{i,t}, \Delta P_i^{\mathrm{U}}\right), \\ R_t^{\mathrm{SpinDn,Thermal}} &= \sum_i \min\left(p_{i,t} - g_{i,t} \cdot P_i^{\min}, \Delta P_i^{D}\right) \end{aligned} \tag{11}$$

In the formula, $R_t^{\mathrm{Up,Thermal}}$,$R_t^{\mathrm{Dn,Thermal}}$ are the operating reserves provided by the thermal power unit during the period t, and $R_t^{\mathrm{SpinUp,Thermal}}$, $R_t^{\mathrm{SpinDn,Thermal}}$ are the spinning reserves provided by the thermal power unit during the period t.

(7) Section tidal current constraint

In the period t, the tidal current constraints of all sections c can be described as:

$$\begin{aligned} P_c^{\min} &\le \sum_{i=1}^{N} G_{c-i} P_{i,t} + \sum_{j=1}^{N_T} G_{c-j} T_{j,t} - \sum_{k=1}^{K} G_{c-k} D_{k,t} - S_{c,t}^{+} + S_{c,t}^{-} \\ \sum_{i=1}^{N} G_{c-i} P_{i,t} &+ \sum_{j=1}^{N_T} G_{c-j} T_{j,t} - \sum_{k=1}^{K} G_{c-k} D_{k,t} - S_{c,t}^{+} + S_{c,t}^{-} \le P_c^{\max} \end{aligned} \tag{12}$$

where, $P_c^{\min}$, $P_c^{\max}$ respectively represent the minimum and maximum value of the tidal current transmission of the section c; G_{c-i} donates the transfer distribution factor of the generator output power of the node of the unit i on the section c; G_{c-j} represents the transfer distribution factor of the generator output power of the node of the tie line j on the section c; G_{c-k} stands for the transfer distribution factor of the generator output power of node k on the section c; $S_{c,t}^{+}$, $S_{c,t}^{-}$ represent the forward and reverse flow slack variables of the section c.

Risk modeling of lost load and wind and light abandonment

(1) Lost load risk modeling

Let $\lambda_{t,s}^{l}$ represent the part where the power load loss is greater than $\xi_t^{\mathrm{VaR},\alpha,l}$ in each scenario, then the condition risk value of the load loss of the power system $V_t^{\mathrm{aR},\alpha,l}$ can be expressed as:

$$\xi_t^{\mathrm{VaR},\alpha,l} = V_t^{\mathrm{aR},\alpha,l} + s^{-1} \cdot (1-\alpha)^{-1} \cdot \sum_s \tau_s \cdot \lambda_{t,s}^{l}, \quad \lambda_{t,s}^{l} \ge \sum_l d_{l,t,s} - V_t^{\mathrm{aR},\alpha,l} \ge 0 \tag{13}$$

Let $\lambda_{t,s}^{w}$ represent the part where the power load loss is greater than $V_t^{aR,\alpha,w}$ in each scenario, then the condition risk value of the power system abandonment of wind and light $\xi_t^{VaR,\alpha,w}$ can be expressed as:

$$\xi_t^{\mathrm{VaR},\alpha,w} = V_t^{\mathrm{aR},\alpha,w} + s^{-1} \cdot (1-\alpha)^{-1} \sum_s \tau_s \cdot \lambda_{t,s}^{w}, \lambda_{t,s}^{w} \geq \sum_w p_{w,t,s}^{c} - V_t^{\mathrm{aR},\alpha,w} \geq 0 \tag{14}$$

Among them, α is the confidence degree, τ_s indicates the probability of the scene s, $p_{w,t,s}^{c}$ refers to the amount of wind and light curtailment, and $d_{l,t,s}$ is the load shedding variable.

(2) Lost load constraint

Wind and solar curtailment and load shedding do not occur at the same time in the same scenario. Defined $w_{s,t}$ as binary decision variable of whether the new energy units in the scene s have the phenomenon of abandoning wind and light during the period t. Defined $l_{s,t}$ as the binary decision variable of whether the load shedding phenomenon occurs in the scene s during the period t.

$$w_{s,t} + l_{s,t} \leq 1, 0 < d_{l,t,s} < l_{s,t} \cdot d_{l,t,s}^{\max}, \quad 0 < d_{l,t,s} < l_{s,t} \cdot d_{l,t,s}^{\max} \tag{15}$$

where, $d_{l,t,s}^{\max}$ is the upper limit of the load l that can be shed during the period t in the scene s, and $p_{w,t,s}^{c,\max}$ is the predicted output of new energy w in the period t in the scene s.

(3) Lost load calculation method

$$\sum_i p_{i,t,s} + \sum_w \left(p_{w,t,s}^{DA} - p_{w,t,s}^{c}\right) = D_t - \sum_l d_{l,t,s} \tag{16}$$

In the formula, $p_{i,t,s}$ is the output power of the thermal power unit i in the period t under the risk scenario s; $p_{w,t,s}^{c}$ represents the amount of wind and light curtailment of the new energy unit w in the period t under the risk scenario s; $d_{l,t,s}$ stands for the load shedding power of the load l during the period t in the risk scenario s. $p_{w,t,s}^{DA}$ donates the upper limit of the actual discharge capacity of the new energy unit w in the period t under the risk scenario s.

(4) Output constraints of thermal power units in risk scenarios

$$g_{i,t} \cdot P_{i,t,s}^{\min} \leq p_{i,t,s} \leq P_{i,t,s}^{\max} \cdot g_{i,t} \tag{17}$$

In the formula above, $P_{i,t,s}^{\max}$, $P_{i,t,s}^{\min}$ are the upper and lower limits of the discharge capacity of the thermal power unit i in the risk scenario s during the period t, which is affected by the uncertainty of coal and gas supply.

At the same time, the output of the thermal power unit in the risk scenario satisfies the climbing constraints shown in the formula (35) and (36).

$$\begin{aligned} p_{i,t,s} - p_{i,t-1,s} &\le \Delta P_i^{\mathrm{U}}\left(1 - y_{i,t}\right) + y_{i,t} \times P_i^{\min}, \\ p_{i,t-1,s} - p_{i,t,s} &\le \Delta P_i^{D}\left(1 - z_{i,t}\right) + z_{i,t} \times P_i^{\min} \end{aligned} \tag{18}$$

4 Case Analysis

This paper selects the typical daily data of Guangdong provincial power grid in August and uses the method proposed above to evaluate the multi-level reserve. The comparison of the typical day-ahead forecast load and actual load curve is shown in Fig. 2. The bidding space of the day-ahead dispatch on a typical day is shown in Fig. 3.

This paper assumes that only coal-fired and gas-fired units can provide system adequacy. This paper simulates the installed proportion of new energy in Guangdong in 2030. The proportion of various unit capacities is shown in Table 1, in which the new energy capacity accounts for 20.2%.

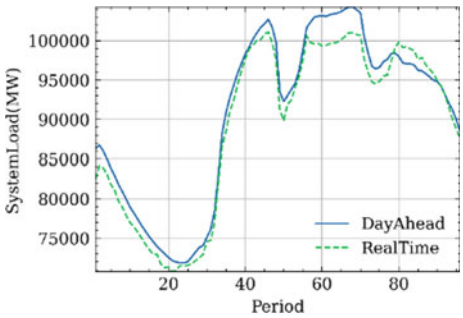

Fig. 2 Comparison of forecasting and actual system load curve in day-ahead dispatch

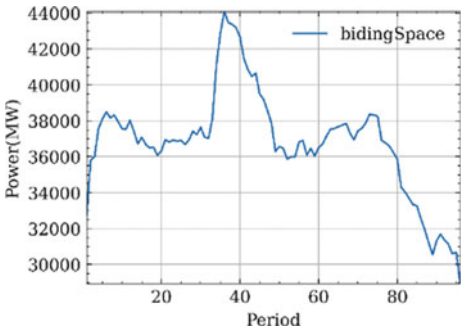

Fig. 3 Bidding space curve

Table 1 Proportion of each type of unit capacity

Unit type	Number of units	Capacity/MW	Capacity ratio/%
Coal	111	64,662	48.93
Gas	88	20,858	15.78
Nuclear power	13	11,550	8.74
Hydropower	19	972	0.74
Pumped storage	30	7420	5.62
Wind power	216	19,298	14.60
Photovoltaic	48	7387	5.59

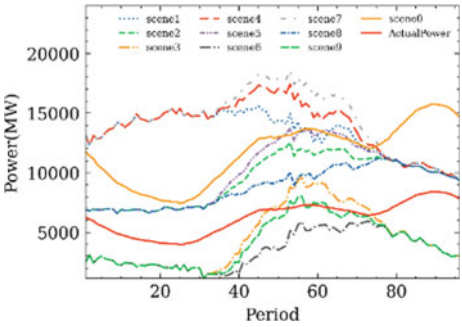

Fig. 4 Renewable outputs under simulated scenarios

4.1 Risk Scenario Description

The day-ahead forecast output curve of new energy units is shown in Fig. 4. Through historical data analysis and Monte Carlo sampling, nine risk scenarios are obtained through scenario clustering, as shown in scenes 1–9 of Fig. 4. The actual output value of new energy is shown in "ActualPower" of Fig. 4.

To simulate the uncertainty of traditional primary energy supply, output range limitations and start-stop restriction scenarios were simulated separately for coal-fired and gas-fired units, which, combined with 9 typical scenarios of new energy, resulted in 27 risk scenario data. The probability distribution of the 27 risk scenarios is shown in Fig. 5.

4.2 Validity Analysis of Reserve Assessment Results

This section will compare the effectiveness and economy of the conventional reserve assessment method with our proposed method. The conventional reserve margin is determined using a linear deterministic reserve assessment method.

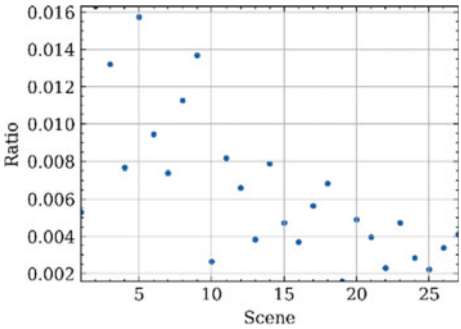

Fig. 5 Supply risks of primary energy resources under simulated scenarios

Conventional methods tend to over-reserve in some periods, resulting in a certain amount of wind and solar abandonment in real-time, while some periods experience a certain amount of load shedding due to insufficient reserve capacity. However, this method provides a more accurate and effective time-sharing reserve capacity, and the evaluation results are shown in Table 2.

The decision result of spinning reserve in this method comes from the demand for load balancing across scenarios for the climbing ability of the system. When the risk preference coefficient is taken as 0.9, 0.6, and 0.3 respectively, the positive spinning reserve provided by the system is shown in Fig. 6. Taking the 36-time period as an example, under the 90% confidence level of the net load demand under the forecast scenario, the spinning reserve capacity meets the power regulation demand from the benchmark scenario with more than 90% to the next period under each risk scenario, which is greater than 8677.66mw. The spinning reserve evaluation result is 8340.60mw.

Table 2 Comparison of load loss and renewable curtailment by each reserve evaluation methods

	Actual lost load (MW)	The actual total amount of wind and solar curtailment (MW)
Routine reserve assessment method	132	1692
Reserve assessment considering only the risk of new energy output	0	2498
Reserve assessment considering the cross-risk transmission of coal and gas (risk weight 0.9)	43	136

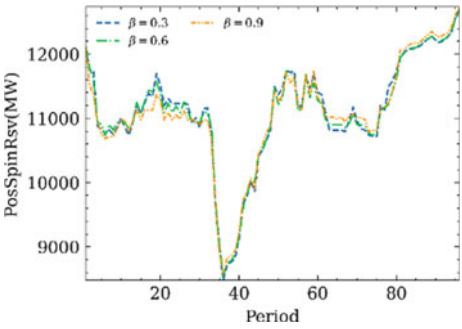

Fig. 6 Spin-reserve curve with different risk weights

4.3 Reserve Assessment Results Under Different Risk Preferences

Risk trends

The degree of confidence $\alpha = 0.9$. When the risk preference coefficients β take 0.999, 0.9, 0.8, 0.6, 0.4, and 0.2 respectively, the changes of value at risk and power generation cost are shown in Fig. 7. As the value of β approaches 1, risk aversion intensifies, leading to a monotonic decline in risk value and a concurrent monotonic escalation in power generation cost.

When the risk preference coefficients β are set to 0.999, 0.9, 0.8, 0.6, 0.4, and 0.2, the risk values of wind and light abandonment for each period are shown in Fig. 8, and the load shedding risk value distribution is depicted in Fig. 9. When the confidence level exceeds 0.9, the load shedding risk ceases to occur, reaching a saturated state.

Reserve decision result

When the risk preference coefficients are taken, the positive and backup situations that the system can provide are shown in Fig. 10. As the risk preference coefficient increases, the reserve decision results tend to be conservative, but still retain time difference and accuracy: during the 18–28 time period with the risk of wind and light abandonment, the model reduces the reservation to reduce the wind and light

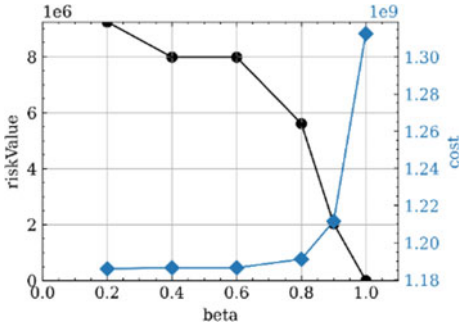

Fig. 7 Risk value and generation cost with different risk weights

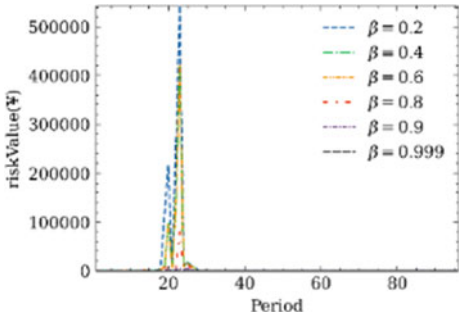

Fig. 8 Risk of renewable curtailment with different risk weights

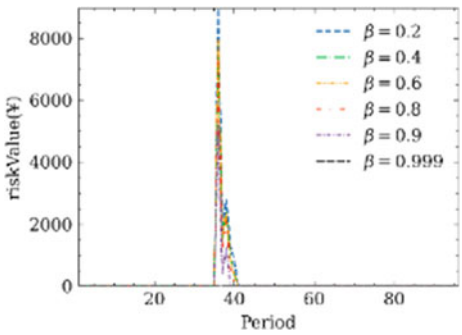

Fig. 9 Risk of load loss with different risk weights

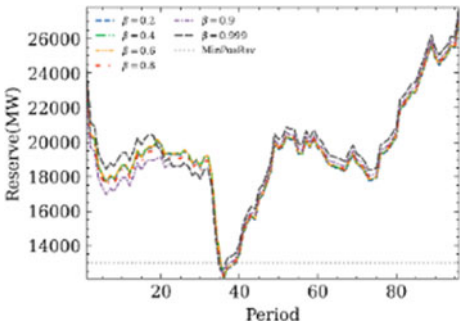

Fig. 10 Positive reserve curve with different risk weights

abandonment in real-time operating scenarios; During the 36 to 41 period with a risk of loss of load, the model reduces the risk of real-time loss of the load by increasing reserves.

5 Conclusions

Based on the conditional value at risk theory, this paper proposes a multi-level reserve evaluation method that takes into account the risks quantification of loss of load and wind and solar curtailment, providing an effective and economical quantitative basis for reserve decisions in the new power system considering primary energy supply risks. According to the impact of the uncertainty of primary energy supply such as wind, solar, coal, and gas on the power balance, a quantitative model is established, and a reserve evaluation model based on minimizing conditional value at risk is constructed to balance the risk of load loss, wind and solar curtailment, and system operation cost, to improve the effectiveness of time-sharing reserve capacity reservation.

To sum up, this paper discusses the assessment of reserve and spinning reserve considering cross scenario risk. The spinning reserve obtained by this method is the reserve demand taking into account the regulation rate of cross scenario risk. If this method is used to assess the ramp capacity coupled between periods, the results will tend to be conservative. According to the analysis and quantification of the independence and coupling between risk scenarios, how to develop resource demand assessment methods will be the focus of this paper in the future.

Acknowledgements Guangdong Provincial Power Company Science and Technology Project 036000KK52210008 (GDKJXM20200713).

References

1. Yang X, Luo J, Yu C et al (2020) Review of power system reserve configuration and optimization for large-scale renewable energy integration. Electr Power Eng Technol 39(1):10–20
2. Liu S, Yang Y, Yang Z et al. A method for reserve capacity determination and its cost allocation considering stochastic characteristics of renewable energy. Autom Electr Power Syst 1–9
3. Ma Y, Xin LI, Liu J et al (2020) Multi-scenario optimal dispatch considering temporal-spatial correlation of wind farms. Electr Power Autom Equip 40(2):55–65
4. Xing C, Xi X, He T et al (2022) Rolling optimization method of reserve capacity considering wind power frequency control. Electr Power Construct 43(2):117–125
5. Tao S, Hong Y, Zhang T et al (2021) Stochastic optimal scheduling considering multiple flexible reserve resources on both source and load sides. Electr Power Construct 42(12):39–48
6. Zhang Z, Zhou M, Zhu L et al (2022) Robust optimal operation method of wind farms synergetic participation in generation-reserve in power systems. Power Syst Technol 46(4):1316–1325
7. Li X, Wang W, Wang H et al (2020) Robust optimized operation strategy for cross-region flexibility with bilateral uncertainty of load source. High Voltage Eng 46(5):1538–1549
8. Li Y, Zhou M, Li G (2019) A day-ahead flexible dispatch method for power system with wind power considering correlation. Renew Energy Resour 37(4):564–572
9. Zhang G, Li F (2020) Day-ahead optimal scheduling of power system considering comprehensive flexibility of source-load-storage. Electr Power Autom Equip 40(12):159–167
10. Zhang G, Li F (2022) Two-stage optimal dispatch for wind power integrated power system considering operational risk and reserve availability. Power Syst Protect Control 50(11):139–148

11. Niu W, Wu C, Xue G et al (2022) Research on development path of Jiangsu's electric power market under new electric power system. Guangdong Electr Power 35(3):1–10
12. Hu Q, Ding H, Chen X et al (2020) Analysis on rotating power outage in California, USA in 2020 and its enlightenment to power grid of China. Electr Power Autom Equip 44(24):11–18
13. Hu Y, Xue S, Zhang H et al (2021) Cause analysis and enlightenment of global blackouts in the past 30 years. Electr Power 54(10):204–210
14. Zhuang Z, Hongli Z, Cong W (2022) Research on optimization of "source-net-charge-storage" operation of regional energy internet. Renew Energy Resour 40(2):238–246
15. Wu K, Wang J, Li W et al (2019) Research on the operation mode of new generation electric power system for the future energy internet. Proceedings of the CSEE 39(4):966–979
16. Hou Y, Ding Y, Bao M et al (2022) Analysis of Texas blackout from the perspective of electricity-gas coupling and its enlightenment to the development of China's new power system. Proc CSEE
17. Zhong H, Zhang G, Cheng T et al (2022) Analysis and enlightenment of extremely cold weather power outage in Texas, U.S. in 2021. Autom Electr Power Syst 46(6):1–9

Numerical Simulation of Coal Seam Floor Under Multi-field Coupling

Hao Li and Chunhui Yang

Abstract This article presents a THM (Thermal–Hydrological–Mechanical) coupling model for the temperature field, seepage field, and stress field of rock masses. The study investigates the inherent effects of various structural rock masses when subjected to the coupling of tectonic stress field, rock mass temperature field, and groundwater seepage field. Firstly, the connected THM model's governing equation was formulated by integrating the equations related to solid deformation, seepage control differential, mechanics, and heat transfer. Secondly, the coupling model is built by setting boundary conditions. Finally, the model was numerically simulated using COMSOL Multiphysics. The results showed that under the coupling effect of stress seepage temperature, there is almost no effect on the geothermal in the promoting process of the production, whereas the seepage field has a great influence on the temperature distribution, and the temperature contour will move toward the seepage velocity. The faster the seepage velocity is, the greater the influence on the geothermal gradient is, and the more obvious the influence on the temperature distribution.

Keywords floor water inrush · THM coupling model · Numerical simulation · Temperature

1 Introduction

Under the special conditions of deep rock mass, the problem of floor water inrush caused by deep engineering disturbance is a major hidden danger of coal mine safety production in China [1]. In the evolution process of water inrush disaster, mining activities form the dynamic load of surrounding rock fiber mass. The coupling induction of THM of fractured rock mass under dynamic load change is the key to the emerging of water channel in rock strata. Based on Biot's consolidation theory and

H. Li (✉) · C. Yang
College of Energy and Mining Engineering, Shandong University of Science and Technology, Qingdao 266590, Shandong, China
e-mail: 2903434746@qq.com

S. Yadav et al. (eds.), *Energy Power and Automation Engineering*, Lecture Notes in Electrical Engineering 1118, https://doi.org/10.1007/978-981-99-8878-5_19

different assumptions, foreign scholars have proposed different mechanical models of THM coupling process [2]. Based on the small deformation and thermoelastic linear theory of porous materials, Chinese scholars have derived a set of relatively complete THM coupling equations [3], established a thermal-fluid–solid coupling mathematical model, and numerically solved it [4]. In the study of nonlinear seepage of fault water inrush, Zhao et al. [5] proposed a nonlinear seepage-stress coupling model. Zhang et al. [6] used COMSOL software to calculate the three-dimensional model of fluid-thermal coupling in Panxi Coal Mine, which included the parameters of monoclinic fault zone. The calculation results show that the cracks and seepage in the rock fiber mass will lead to the fluctuation of the temperature field of the rock fiber mass. Bian et al. [7] used FLAC3D numerical simulation software, from the perspective of the coupling effect of stress, displacement, seepage, and failure zone, the law of water inrush from coal seam floor under different conditions of fault morphology and confined water pressure was analyzed. Li et al. [8] conducted numerical simulation and experimental verification on the variation law of each physical field during the deformation and failure of coal and rock under load.

At present, many scholars have studied the prediction of water inrush of floor caused by coal seam mining from the view of theory, modeling, experiment, and measurement, and obtained the relevant control criteria of water inrush [9]. There are relatively few studies on the coupling of multi-field interaction in deep rock mass environment, especially the evolution pattern of temperature field under multi-field coupling conditions. Therefore, the paper will use numerical simulation software to simulate and analyze on the basis of theoretical research.

2 Governing Equations of Coupled THM Model

2.1 Fluid Solid Coupling Solid Deformation Equation

Under planar conditions, the equilibrium conditions for force expressed in tensor form are:

$$-\nabla \cdot [\sigma] = F \tag{1}$$

where $[\sigma]$ is the stress tensor; F is a force vector that includes fluid pressure gradient and other stresses.

2.2 Differential Equation for Seepage Control

According to the law of conservation of mass, the fluid flow equation is

$$\frac{\partial(\phi\rho_1)}{\partial t} + \nabla\phi\rho_1 V_1 = Q \tag{2}$$

where ϕ is the porosity of the rock mass, ρ_1 is the fluid density, t represents time, V_1 is the fluid velocity vector field, and Q is the source-sink of the fluid.

$$V_1 = -\frac{k}{\mu_1}(\nabla P - \rho_1 g) \tag{3}$$

where k is the permeability of the rock mass, μ_1 is the hydrodynamic cohesive soil viscosity, P is the interstitial pressure, and g is the gravitational acceleration.

Combining the above three equations is the stress seepage coupling control equation.

3 Model Establishment

3.1 Geometric Modeling

Simplify the model based on the actual mining geological conditions and comprehensive rock column chart of Anju Coal Mine, and only consider the rock layers within a certain range near the coal seam roof and floor that needs to be calculated. For the convenience of simulation calculation, on the basis of meeting the actual geological conditions, reasonable composite should be carried out for rock layers with similar physical properties, and treated as single rock layers [10]. Based on the actual occurrence of coal seams, the coal seam is set as a level coal seam in based model, with a strike length of 253 m, and the working face is arranged along the strike. The direction of coal seam mining is X-axis, and the gravity direction is Y-axis. The overlying strata of the coal seam are divided into three layers, with sandstone of 45 m, mudstone of 30 m, and sandstone of 15 m from top to bottom. The coal seam is 3 m long, and the lower layer of the coal seam is allocated to 4 layers, with mudstone 4.2 m, sandstone 50.3 m, mudstone 35 m, and water-bearing limestone 5.7 m from top to bottom.

3.2 Model Parameter Settings

The mechanical and physical parameters of various rock formations in the model are defined using material parameters in the software, as illustrated in Table 1. After setting up and characterizing the geometric modeling and the physical property of each rock burst, it is necessary to network the model. In order to reduce computational complexity whereas guaranteeing a certain degree of precision, the unit estimate of the lattice is chosen at the standard level.

Table 1 Material parameters of numerical simulation model

Number	Nature of ground	Density (kg/m^3)	Bulk modulus(GPa)	Shear modulus (GPa)	Permeability (m^2)	Porosity
1	Sandstone	2660	9.896	8.051	1e-14	0.05
2	Sudstone	2524	8.730	4.264	2e-14	0.12
3	Sandstone	2660	9.896	8.051	1e-14	0.05
4	Coal	1400	5.455	1.295	6e-14	0.20
5	Mudstone	2480	8.730	4.264	2e-14	0.12
6	Sandstone	2660	9.896	8.051	1e-14	0.05
7	Mudstone	2480	8.730	4.264	2e-14	0.12
8	Water-bearing Limestone	2620	10.417	5.952	1e-13	0.25

3.3 Boundary Conditions

Based on the geology situation and geothermal data of Anju Coal Mine, the gravity of the overlying stratum of the coal stratum is equivalent to a boundary load of 22 MPa. The gravity effect is activated by the model's self weight in the software, and the floor and left and right sides of the model are respectively constrained by fixed and roller supports. The overall temperature of the model is set at 37 °C, with upper and lower boundary temperatures of 47.32 and 51.7 °C, respectively.

4 Numerical Calculation and Analysis

4.1 Temperature Distribution at Different Driving Distances

After calculation, the temperature distribution under different propulsion distances is obtained, as shown in Fig. 1.

As shown in Fig. 1, as the progress of mining production, the temperature field near the coal seam will be redistributed. Due to the destruction of the original rock stress state, the stress in the rock of the mining zone will be redistributed. Stress concentration will occur close to the open-cutting and working face, accompanied with the generation and development of cracks, and the continuous heat exchange process. The temperature of the top and bottom of the coal bed gradually approaches the temperature of the rock mass medium, and the heat reaches an equilibrium state within the given range, thus the distribution of temperature field in the original vertical direction gradually changed. In addition, this temperature change is only in the direction of advancement, which only occurs near the temperature near the mining site. However, in the relatively far vertical direction, the temperature of the

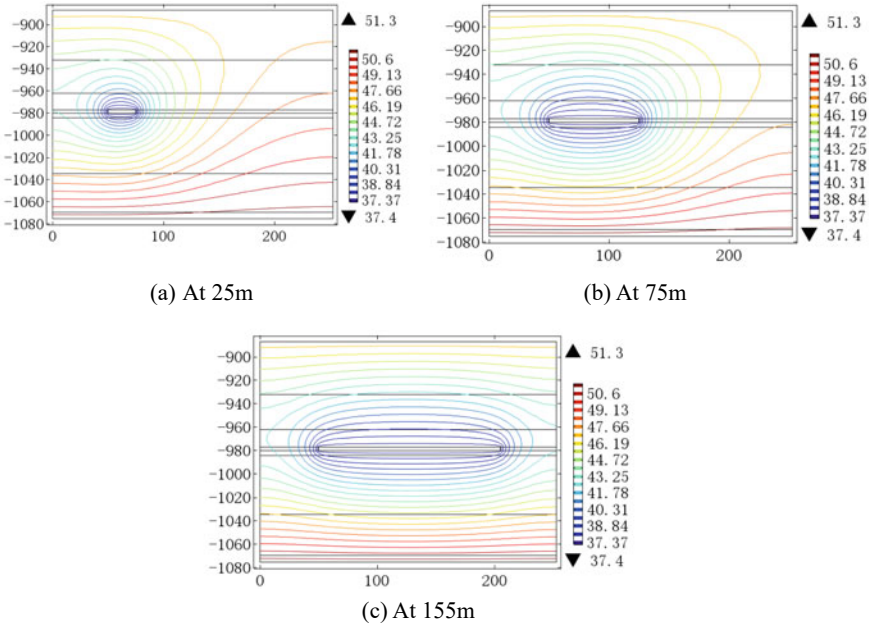

(a) At 25m (b) At 75m

(c) At 155m

Fig. 1 Contour map of temperature distribution in advance of working face

entire rock layer does not change much, which means that there is almost no effect on the temperature gradient in the promoting process of the production.

4.2 Effect of Seepage on Temperature Distribution

According to the research plan, in order to facilitate the study of the effect of seepage on temperature distribution, the seepage velocity is amplified. The specific plan is to enlarge the seepage velocity by 10–100 times to calculate the temperature distribution, as shown in Fig. 2.

It can be seen from Fig. 2 that with the increase of seepage velocity, the original temperature field of the embracing rock is redistributed under the influence of the seepage field with upward velocity, and the heat exchange balance zone is shifted to the direction of seepage velocity, so the isotherm is shifted upward.

Figure 3 shows the temperature change of the coal seam floor at the same depth under the influence of seepage velocity. It is evident from the figure that when the seepage velocity is amplified by 10 times and by 100 times, the maximum temperature difference can reach 3 °C.

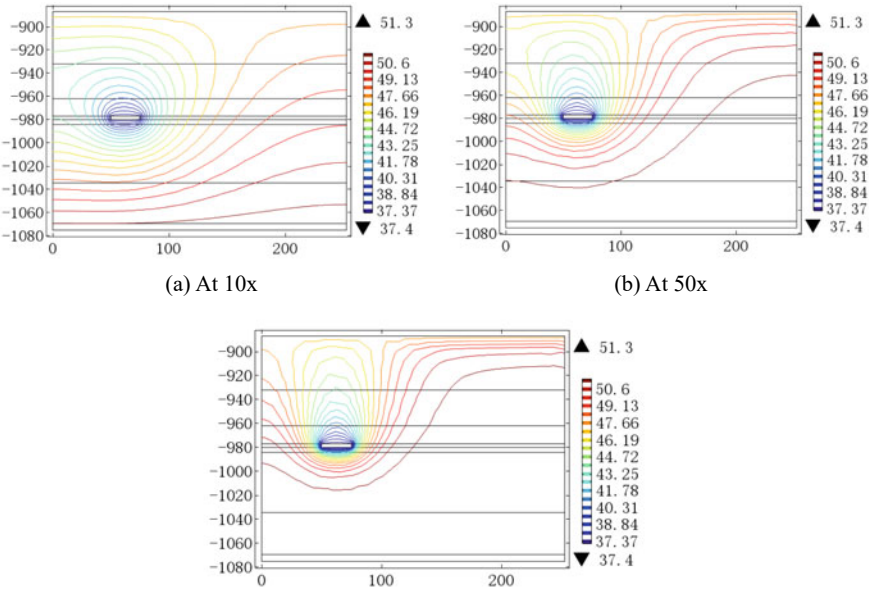

(a) At 10x

(b) At 50x

(c) At 100x

Fig. 2 Isogram of temperature distribution at different magnification of seepage velocity

Fig. 3 Temperature distribution curve at 50 m from the upper boundary of the direct bottom under different seepage velocities

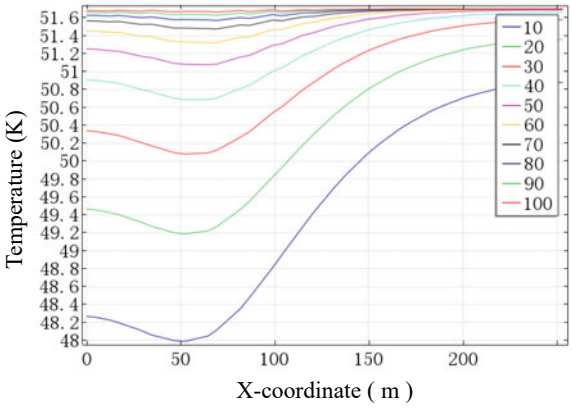

5 Conclusion

(1) Under the coupling effect of stress seepage temperature, different footage only affects the temperature distribution near the stope and has little effect on the geothermal gradient in the promoting process of the production.

(2) The seepage field has a great influence on the temperature distribution. The seepage field will affect the geothermal gradient, and the heat exchange balance zone will shift to the seepage velocity direction, which will eventually cause the temperature contour to move within the heading of seepage velocity. The faster the seepage velocity is, the greater the influence on the geothermal gradient is, and the more obvious the influence on the temperature distribution is. Therefore, the seepage field is the main factor affecting the geothermal distribution.

References

1. Liu WT, Zhao JY, Ding XY (2018) Study on the model of temperature-nonlinear seepage-stress coupling of fault water inrush. J Coal Mine Safety 49(11):59–62+68. https://doi.org/10.13347/j.cnki.mkaq.2018.11.013
2. Noorishad J, Tsang CF, Witherspoon PA (1984) Coupled thermal-hydraulic-mechanical phenomena in saturated fractured porous rocks: numerical approach. J Geophys Res 89(B12):10365–10373. https://doi.org/10.1029/jb089ib12p10365
3. Zhu WC, Wei CH, Tian J (2009) Thermal-fluid-mechanical coupling model in rock failure process and its primary study. J Geomech 30(12):3851–3857. https://doi.org/10.16285/j.rsm.2009.12.017
4. Zhang J, Yang T, Wang B et al (2017) Prediction and analysis of roof water outburst in shallow coal layers under gully runoff mining. J Coal Mine Safety 34(5):868–875. https://doi.org/10.13545/j.cnki.jmse.2017.05.007
5. Zhao J, Liu CY, Li JW (2017) Characteristics of overburden failure and mine pressure behavior of shallow coal seam working face in gully area. J Coal Sci Technol 45(1):34–40. https://doi.org/10.13199/j.cnki.cst.2017.01.006
6. Zhang SG, Li ZJ, Xu YH (2011) Three-dimensional numerical simulation analysis of flow-heat coupled heat transfer in crack rock mass. J Geomech 32(8):2507–2511. https://doi.org/10.16285/j.rsm.2011.08.022
7. Bian K, Li SY, Liu B (2022) Study on water outburst law of floor in coal layers mining with fault on confined water. J Coal Mine Safety 53(6):169–177. https://doi.org/10.13347/j.cnki.mkaq.2022.06.027
8. Li X, Li H, Yang Z (2020) Temperature-stress-electromagnetic multi-physical field coupling mechanism of deformation and cracking of composite coal rock. J Coal 45(5):1764–1772. https://doi.org/10.13225/j.cnki.jccs.2019.0525
9. Song Z Q, Hao J, Tang J (2013) Predictive control theory of fault water inrush. J Coal 38(9):1511–1515. https://doi.org/10.13225/j.cnki.jccs.2013.09.011
10. Li JF, Liu SX (2018) Numerical simulation software for safety evaluation of coal mining above confined water based on COMSOL and its application. J Coal Econ Inner Mong 267(22):5–6. https://doi.org/10.13487/j.cnki.imce.013180

Research on Control Technology of Ship Hybrid Propulsion System

Minggang Li and Jing Chen

Abstract Generally speaking, gas turbines have the advantages of light weight, small size, high power, and fast response, but also have the disadvantage of high fuel consumption, while diesel engines have the opposite. Due to the complementary characteristics of these two types of prime movers, in order to maximize the power potential of diesel engines, it is necessary to study the electromechanical compatibility of the combined propulsion system by considering the combined drive technology of diesel engines and gas turbines.

Keywords Gas turbine · Diesel engine · Combined drive · Matching research

1 Introduction

The combined drive of a diesel engine and a gas turbine is essentially a hybrid propulsion technology, with the power source coming from both the gas turbine and the propulsion motor. In hybrid systems, the motor can be used as both a generator and an electric motor [1].

The propulsion system adopts dual shaft propulsion, and the gas turbine and propulsion motor are connected in parallel through a gearbox to drive the propeller. The propulsion motor is controlled by a four quadrant frequency converter and can extract or feedback electrical energy from the distribution network [2]. The power distribution network is powered by lithium battery pack and diesel generator set to supply power for propulsion system and daily load of ships. The basic architecture is shown in Fig. 1.

M. Li (✉) · J. Chen
Wuhan Institute of Marine Electric Propulsion, Wuhan, China
e-mail: 18040510963@163.com

S. Yadav et al. (eds.), *Energy Power and Automation Engineering*, Lecture Notes in Electrical Engineering 1118, https://doi.org/10.1007/978-981-99-8878-5_20

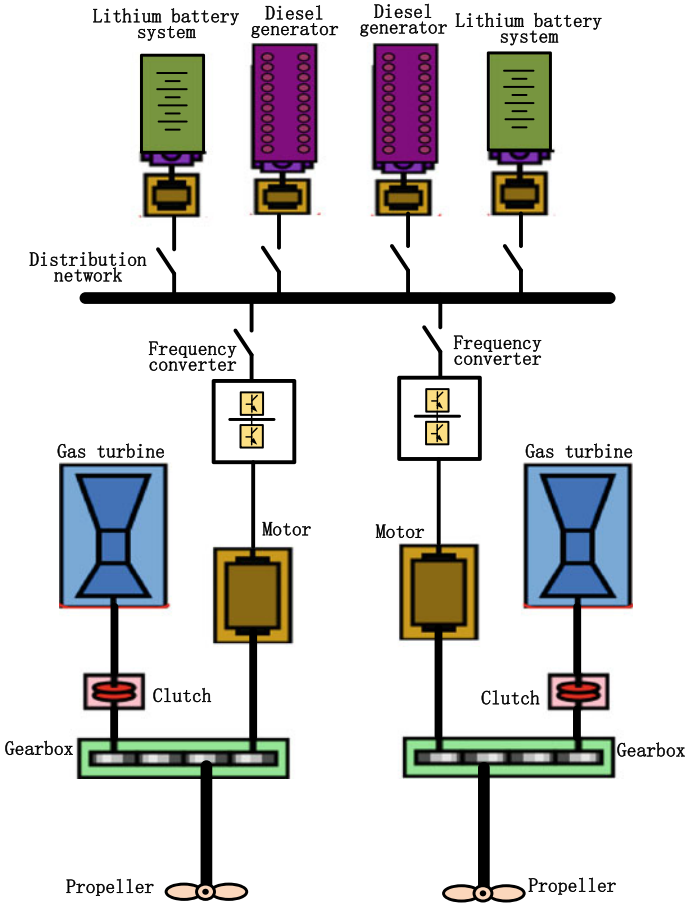

Fig. 1 Schematic diagram of the joint propulsion system

2 System Operating Mode

2.1 Gas Turbine Propulsion Mode

In this mode, the propulsion power of the ship is supplied by a gas turbine, and the operation is exactly the same as that of a gas turbine direct propulsion ship. The frequency converter stops and is disconnected from the distribution network, and the motor and gearbox are disengaged through a clutch. The energy flow mode is shown in Fig. 2.

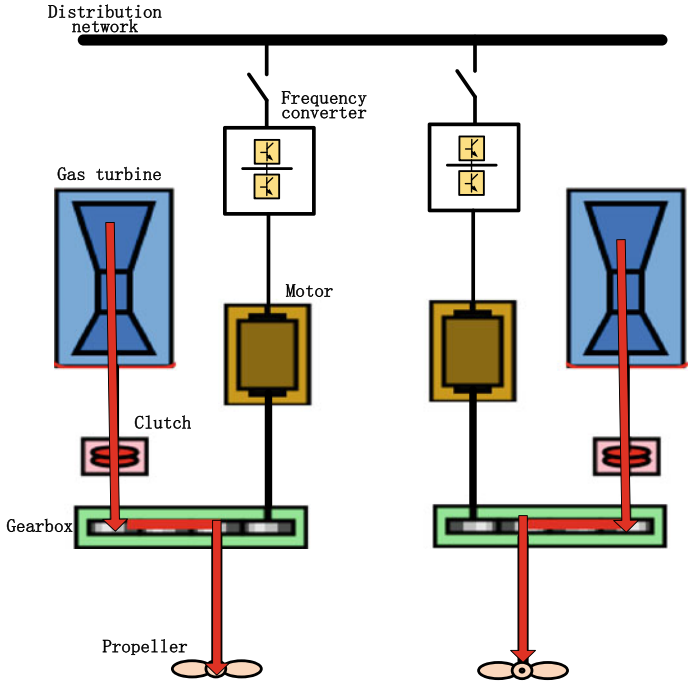

Fig. 2 Gas turbine direct push mode

2.2 PTI Propulsion Mode

In this mode, the gas turbine to propel at full speed, while the motor drives the propeller through the power distribution network to increase propulsion power and achieve high-speed navigation. The energy flow mode is shown in Fig. 3.

2.3 PTO Propulsion Mode

In this mode, the motor as a shaft generator feeds the energy back to the power grid through the frequency converter to provide power for the load of the distribution network. This working condition generally works at medium and low speed. At this time, the propulsion load provided by the gas turbine to the propeller is small, which can make the gas turbine still have good fuel efficiency under the condition of small propulsion power. The energy flow mode is shown in Fig. 4.

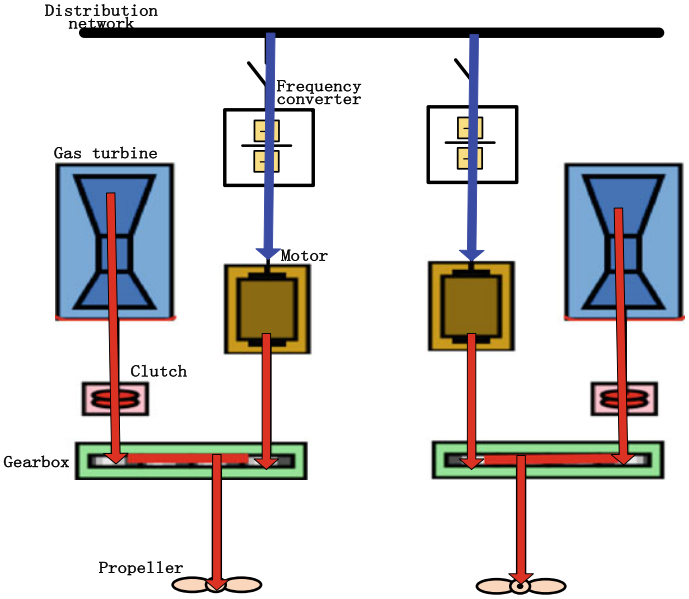

Fig. 3 PTI propulsion mode

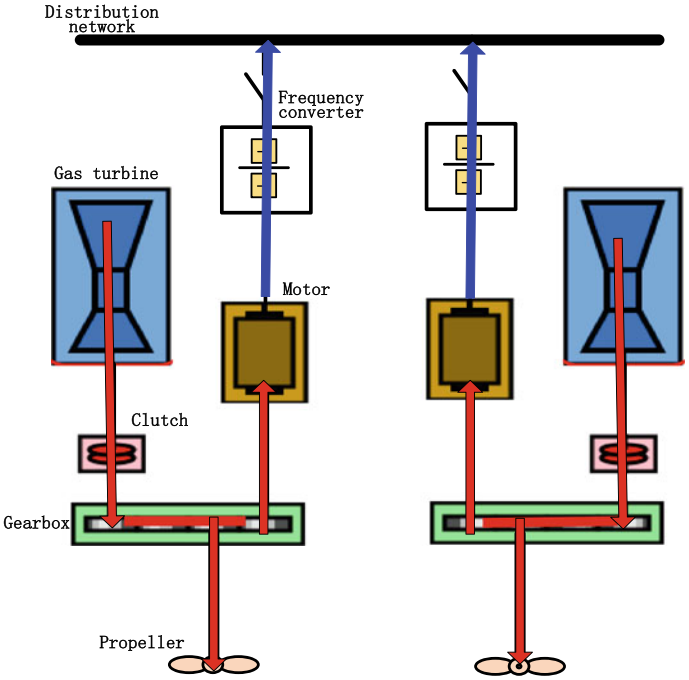

Fig. 4 PTO propulsion mode

2.4 PTH Propulsion Mode

After the battery pack passes through the DC/DC conversion device, the DC load switch and fuse are used to connect to the DC bus. The DC load switch and fuse are used to connect the main push unit and inverter lamp power unit to the DC bus. Fu11 ~ fu2b are DC fuses with overcurrent and short-circuit protection functions. DC fuses at all levels cooperate to realize short-circuit selective protection. Qs11 ~ qs2b are DC load switches without short-circuit segmentation ability, forming a mechanical breakpoint between battery unit and DC bus, which is convenient for equipment maintenance. The energy flow mode is shown in Fig. 5.

3 Electromechanical Control Technology of Joint Propulsion System

The diesel electric fuel combined power system includes two propulsion modes: mechanical propulsion and electric propulsion, and their control strategies are different. Traditional mechanical propulsion ships generally use simple power open-loop control, which directly determines the throttle opening of the prime mover

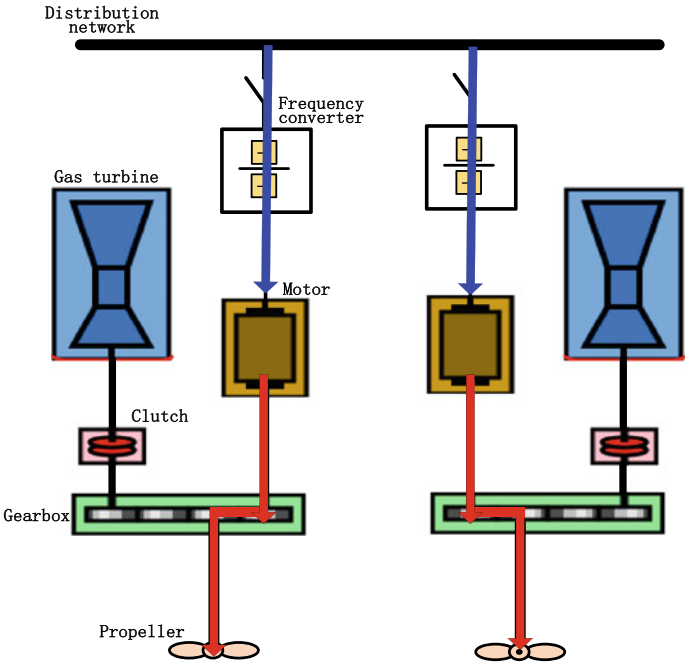

Fig. 5 PTO propulsion mode

based on the ship's gear position. After actual navigation tests of the ship, the corresponding relationship between each gear position and throttle opening is determined to achieve the expected navigation speed. The main reason for choosing this control method is that the throttle of the prime mover should not be adjusted frequently to avoid reducing the service life of the equipment. The electric propulsion system, due to its flexible motor control, can adopt speed closed-loop control to achieve precise control of ship navigation speed [3, 4].

Using MATLAB/Simulink simulation software, based on the mathematical models of various mechanical and electrical components, and using the tools provided by the simulation software in the component model library, a gas turbine (speed regulation) model, a parallel gearbox model, a load model, and a controller model were established. The dynamic characteristics of the system were comprehensively simulated, and different control strategies were compared and analyzed [5].

4 Electromechanical Control Technology of Joint Propulsion System

According to the research purpose, some models of certain subsystems in the system have been simplified to a certain extent, ignoring or shielding intermediate parameters that have little impact on the research problem. The models of each subsystem are as follows:

4.1 Gas Turbine and Governor Model

Due to the fact that this report mainly considers the dynamic performance of the main parameters such as speed and torque under various operating conditions of the joint propulsion system, the gas turbine and the installed speed controller are modeled as a whole and appropriately simplified. According to the interrelationships between its various components, it can be decomposed into a module structure as shown in Fig. 6.

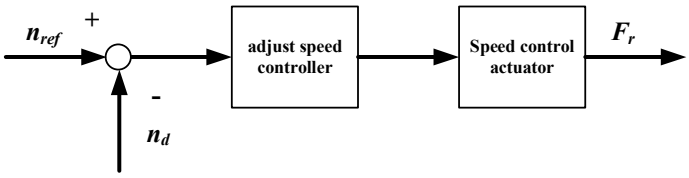

Fig. 6 Control structure of gas turbine governor

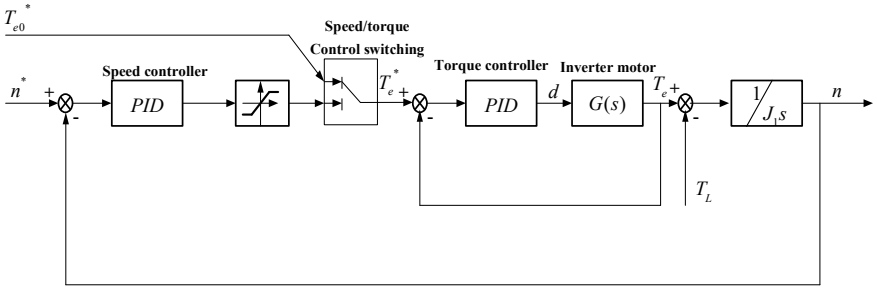

Fig. 7 Control block diagram of frequency converter drive motor

4.2 Propulsion Motor and Control Model

The propulsion motor is controlled by a bidirectional frequency converter, and the propulsion motor and bidirectional frequency converter are modeled as a whole and appropriately simplified. The control block diagram is shown in Fig. 7.

4.3 Transmission System Model

The transmission relationship structure diagram of the parallel gearbox is shown in Fig. 8.

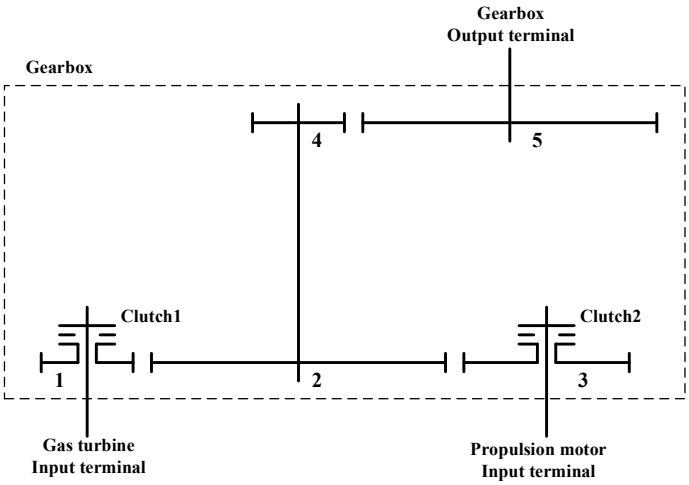

Fig. 8 Structure diagram of parallel gearbox transmission relationship

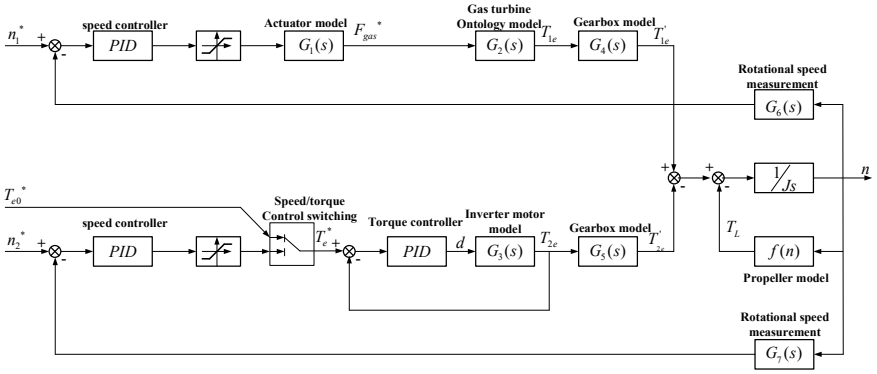

Fig. 9 Block diagram of parallel control system

4.4 Parallel Controller Model

The parallel controller is used to control the switching of working modes between gas turbines and propulsion motors and can control load distribution by changing the set speed of the gas turbine or propulsion motor. The control block diagram is shown in Fig. 9.

5 Simulation Result

Based on MATLAB/Simulink, modeling of the control system of the joint propulsion system was carried out, and simulation analysis was conducted on the startup and switching processes of various working conditions of the joint propulsion system. Typical simulation results are as follows:

The operation of process is as follows: At 0 s, the gas turbine and propulsion motor are respectively started. After 88 s, the gas turbine reaches idle speed ~ 2200 rpm, and the propulsion motor reaches rated speed 1100 rpm after 88 s; At 100 s, the gas turbine is connected to the exhaust, driving the propeller to run while also driving the ship's operation. At 300 s, the propulsion motor is connected and discharged, and the gas turbine and propulsion motor are jointly propelled (PTI). At 500 s, the gas turbine and propulsion motor are adjusted to the rated speed, and the system operates at full power; 650 and 700 s are the disturbance and recovery times of the propeller load of 105Nm. At 800 s, the gas turbine decelerates and unloads, and exits at 832 s. At this time, the propulsion motor is in direct propulsion mode (PTH).

After the propulsion motor is connected, the working mode is switched from gas turbine propulsion mode to PTI propulsion mode. Both the gas turbine and propulsion motor use speed control for joint propulsion, and the output power/torque is distributed according to the maximum power/torque that can be output by the two

in the joint propulsion mode. The power distribution ratio is about 4:1, and the torque distribution ratio is about 2:1. During the deceleration process of the gas turbine, the output torque rapidly decreases, and the output torque of the propulsion motor increases. After the gas turbine is disconnected, the propulsion motor advances independently. At this time, due to torque limitations, the propulsion motor cannot operate at the rated speed.

During the deceleration process of the gas turbine, the output torque rapidly decreases, and the output torque of the propulsion motor increases. After the gas turbine is disconnected, the propulsion motor advances independently. At this time, due to torque limitations, the propulsion motor cannot operate at the rated speed. Due to the large mass of the ship and the large inertia of rotating components such as gearboxes and propellers, the increase and decrease in speed take a long time.

According to the simulation results, it can be seen that the gas turbine is connected at idle speed. Due to the constant pitch of the propeller, the idle speed of the gas turbine is still very high after being decelerated by the gearbox. Moreover, because the ship has just started, the inlet ratio is small, the ship resistance is high, and the load torque of the propeller is high. The output speed of the gas turbine decreases significantly, and there is a significant fluctuation in the output torque, which is close to the rated torque of the gas turbine. For this simulation result, it is recommended not to use a gas turbine for direct starting when using a fixed pitch propeller.

6 Conclusion

Firstly, the mathematical models of the main components of the nuclear fuel combined propulsion system were analyzed, and simulation models of each component and control system were established; simulation analysis was conducted on the switching operating conditions of the system, and it was found that when using a fixed pitch propeller, the torque fluctuation of the propulsion motor during low speed startup of the ship was smaller than that of the gas turbine during idle startup.

References

1. Research on modeling methods for gas turbines and their combined cycle units. North China Electric Power Technology, pp 67–70
2. Zhang C, Jia B (2020) Design and optimization control simulation of ship hybrid electric propulsion system. Ship Sci Technol 42(15):134–139
3. Liu J, Zhao T, Qiu A et al (2016) Research on the “diesel electric” parallel control technology in the booster mode of marine diesel electric hybrid power system. Ship Sci Technol 38(S1):123–126
4. Zhu A, Dai R (2022) Research on vector control system for ship electric propulsion. Ship Electr Technol 42(07):33–36. https://doi.org/10.13632/j.meee.2022.07.015
5. Li H, Wang C, Guo H et al (2020) Simulation research on ship propulsion motor motion control system. Ship Sci Technol 42(13):114–119

Optimization Methodologies for Uncertainty Characterization with Large-Scale Renewables Integration

Miao Wang, Zeke Li, Bo Sun, Haiwei Fan, Xin Hu, and Linglong Ding

Abstract The increasing penetration of renewable sources into the power grid brings uncertainty of active power on both the generation side and demand side also increases significantly. Power grid dispatching needs to be transformed from deterministic optimization to uncertain optimization. The scenario-based, stochastic programming, and robust optimization methods are optimization methods that can be used to characterize the uncertainty of renewable energy generation and improve power grid dispatching. This paper utilizes three methods to characterize the uncertainty of renewable output and employs a series of techniques to convert these methods into optimization that can be directly handled by existing solvers. An evaluation of each method is provided at the end.

Keywords Renewables integration · Stochastic optimization · Robust optimization

M. Wang
China Electric Power Research Institute, Beijing 100192, China

Z. Li · H. Fan · L. Ding
State Grid Fujian Electric Power Co. LTD, Fuzhou 350003, China

B. Sun · X. Hu (✉)
State Key Laboratory of Advanced Electromagnetic Engineering and Technology, School of Electrical and Electronic Engineering, Huazhong University of Science and Technology, Wuhan 430074, China
e-mail: 272957772@qq.com

S. Yadav et al. (eds.), *Energy Power and Automation Engineering*, Lecture Notes in Electrical Engineering 1118, https://doi.org/10.1007/978-981-99-8878-5_21

1 Introduction

The increasing penetration of renewable energy into the power grid brings uncertainty on both the generation side and demand side [1]. Renewable energy is of intermittent and stochastic nature with high volatility and unpredictability. They can be influenced by seasonal factors over a long-term period, as well as weather conditions on a short-term scale. As a result, the random nature of these distributed power sources poses significant challenges to the operation of the power system. To effectively deal with uncertainty, it is important to identify the uncertain parameters and select the appropriate methodology to address them. Power grid dispatching requires a change from deterministic optimization to uncertain optimization. This paper summarizes current optimization methods and provides 4 main approaches to addressing uncertainty of Security Constrained Unit Commitment (SCUC).

(1) Reserve plays a crucial role in enabling the power grid to withstand disruptions such as equipment failures and fluctuating loads while maintaining a balance between power generation. Reserve can be characterized by its response speed (ramp speed and start-up time), response duration, frequency of use, direction of regulation (up or down), and type of control (e.g., control center activation, automatic control, etc.). For instance, European grid operator, ELIA divides reserve capacity into three categories based on response time: primary reserves, secondary reserves, and tertiary reserves (the latter being major solutions for balancing imbalances and congestion) [2]. NERL categorizes reserves as non-accident reserves and accident reserves [3]. Increasing reserve requirements can enhance the system's ability to resist uncertain risks. The frequency is within a specified range, and chain accidents or large area power failures are prevented. However, this approach has a drawback as it cannot accurately model system operation uncertainties, and costs are usually high.
(2) Stochastic programming is capable of modeling random failures such as unit and line outages, as well as inaccuracies in load forecasting. Monte Carlo simulation provides an accurate representation of uncertainty. However, a significant drawback is that it requires an extensive amount of computation.
(3) Fuzzy programming utilizes the fuzzy MIP algorithm to model system uncertainties as fuzzy constraints, which can be resolved efficiently and have the potential for widespread applications.
(4) Robust optimization method substitutes the exact probability distribution of random variables with the uncertainty set and conducts unit commitment of the system under the "worst-case" scenario through optimization methods. As a result, this approach is more consistent with practical engineering requirements.

Based on this, this paper puts forward models for characterizing the uncertainty of renewable energy output and incorporating the variability of renewables into the optimization model. These are discussed from the perspectives of uncertainty characterization, modeling, and solution in Section II. The optimization model methods used in global markets are outlined in Section III, while Section IV offers a discussion of the topic.

2 Optimization Methodologies that Characterize Uncertainty with Large-Scale Renewables Integration

To resolve the uncertainty, it is crucial to identify the uncertain parameters and determine the appropriate methodology to address them. The paper proposes optimization methodologies that accurately characterize uncertainty when integrating large-scale renewables. These methodologies are divided into four distinct categories.

2.1 Deterministic Methodology for Reserve Optimization

The method known as the 3 δ method is a deterministic approach that incorporates integrating renewables prediction uncertainty into the unit commitment. This approach sets the reserve requirement as a multiple (λ times, typically 3) of the difference between the standard deviation of demand and the standard deviation of the renewables forecast (wind power and photovoltaic) [4, 5], as shown in formulas (1) and (2).

$$r_d = \lambda * \sigma_d^t \tag{1}$$

$$\sigma_d^t = \sqrt{\left(\sigma_\ell^t\right)^2 + \left(\sigma_u^t\right)^2} \tag{2}$$

In the formula, r_d is the reserve requirement, $\sigma_d^t \cdot \sigma_\ell^t \cdot \sigma_u^t$ are standard deviation of the total demand, load forecast error, and renewables.

The 3 δ method aims to address extreme prediction errors by allocating enough reserve capacity to mitigate potential imbalances caused by renewable power forecast errors. This deterministic approach is a variation of the traditional security constraint unit commitment (SCUC), which treats wind and photovoltaic power generation scenarios similarly to generation and transmission emergencies. A more generalized version of the 3 δ method has been proposed in Ref. [6], which identifies a set of extreme scenarios based on network constraints that fall outside the range of 3 confidence intervals. However, this semi-fixed approach ignores the probability or severity of system contingencies and simply acquires the reserve capacity as total wind power generation and installed capacity increase. Consequently, its effectiveness may be limited in practical system.

2.2 Scenario-Based Stochastic Optimization

The scenario-based optimization method is designed to account for the variability of wind power output by utilizing a range of potential scenarios for wind power and

photovoltaic output. Through conversion of the uncertain dispatching problem into a deterministic problem with multiple scenarios, an optimal objective expectation is achieved through statistical analysis. Stochastic model follows a two-stage process: unit commitment and dispatching. The unit commitment stage is not affected by the scenarios, while dispatching is dependent on scenario-specific information [7]. If the dispatching fails to meet the requirements, bender cuts are created and added to the main problem to modify the unit commitment.

There are two primary approaches to generating scenarios: (1) The Monte Carlo method, which uses predicted probability distribution functions (PDFs) to simulate random time series. (2) The construction of a scene tree structure.

The effective utilization of wind and solar power forecast data is essential for power grid dispatching. This paper presents a comprehensive approach to address the unpredictability of wind power using probability distribution functions (PDFs) within a predetermined scenario set. The PDFs are derived from preprocessed data to represent the probability of different wind and solar power scenarios. These scenarios are then converted into discrete sets with assigned probability weights, which form the basis for conducting SCUC (Security Constrained Unit Commitment) models that can be applied to power grid dispatching. The process involves the following four steps:

Step 1: Utilize the wind power uncertainty model to generate different scenarios of wind power output. The uncertainty model for wind power would mainly take into account the prediction bias arising from limited wind power prediction accuracy, the actual wind power output is represented as (3):

$$W_a^t = W_f^t + \varepsilon_w^t \tag{3}$$

This equation represents wind power forecasting model, where: W_a^t represents the actual wind power output. W_f^t represents forecast wind power output for day-ahead operation. ε_w^t denotes the bias in the wind power forecast. The bias follows a normal distribution with a mean of 0 and variance of $(\sigma_w^t)^2$.

The formula (4) is utilized to calculate the standard deviation of this normal distribution.

$$\sigma_w^t = \frac{1}{5} W_f^t + \frac{1}{50} W_I \tag{4}$$

For the reliability of the forecast, 200 scenarios are generated as Fig. 1 shows.

Step 2: Calculate the geometric distance between each pair of scenarios s and s' from the set of wind power scenarios **S**. Calculate the sum of probability distances between each scenario and the remaining scenarios, then select the scenario d that has the minimum probability distance with the remaining scenarios.

Step 3: Replace scenario d with scenario r in **S**, where r is the scenario in **S** that is geometric closest to d. After adding the probability of d to the probability of r, scenario d is eliminated and new set of scenarios $\mathbf{S}'$ is formed.

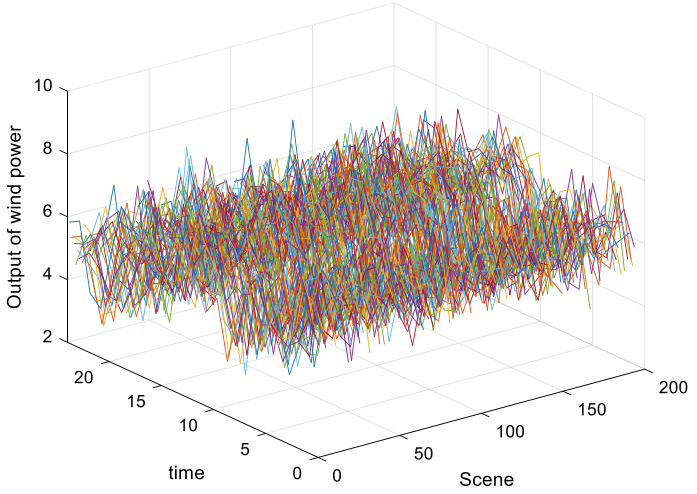

Fig. 1 200 wind power scenarios

Step 4: Check if the number of remaining scenarios in $\mathbf{S}'$ meets the requirement. If not, repeat Steps 1–3; if the number of scenarios in $\mathbf{S}'$ is already within the desired range, the scenario reduction is finished.

Figure 2 displays the five wind power scenarios after scenario reduction, while the likelihood of each of the five scenarios is presented in Fig. 3. The actual wind power output is illustrated in Fig. 4.

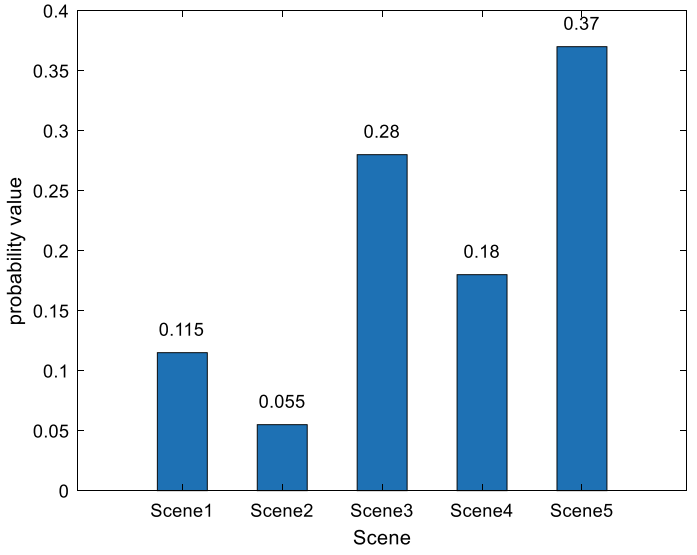

Fig. 2 5 wind power scenarios after scenario reduction

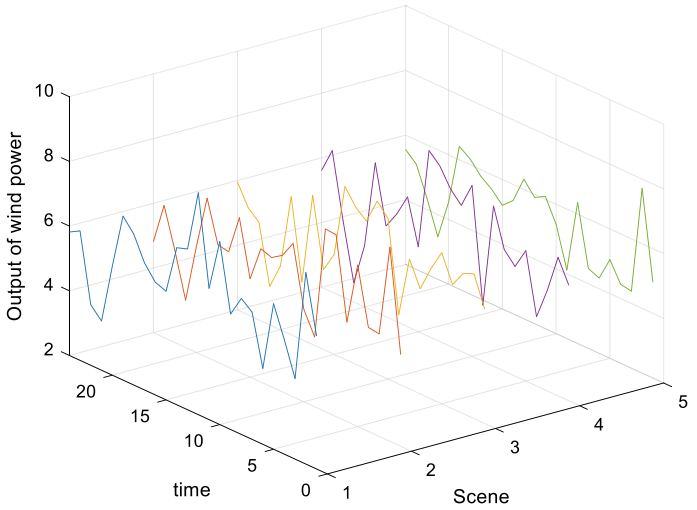

Fig. 3 The probability of the 5 scenarios

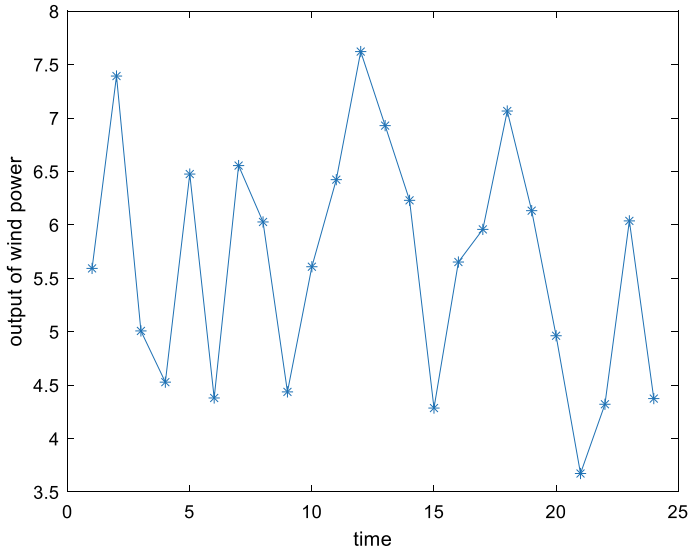

Fig. 4 Actual output of wind power

2.3 Chance-Constrained Optimization Method

The chance-constrained optimization method also uses the probability distribution of wind power output for modeling. This method converts the constraints containing renewable output variables of the optimization into probabilistic constraints and

makes them meet the operation requirements under certain confidence probability so as to ignore small probability events, which improves the economy of system operation [8, 9]. Due to the introduction of probabilistic constraints, the difficulty of solving chance-constrained optimization model is to transform it into deterministic optimization. Three main methods are proposed to solve chance-constrained optimization problems: scenario-based method [10], sample average approximation [11], and robust optimization method [12].

The optimization model with multiple fuzziness constraints is presented as (5).

$$\begin{aligned} &\min \quad h(y) \\ &\text{s.t.} \quad r(y,\zeta) \le 0 \end{aligned} \tag{5}$$

In the formula, y renders the vector of decision variable, ζ renders parameters vector of fuzziness, $h(y)$ is objection function, and $r(y,\zeta)$ renders constraint.

If constraint function $g(y,\zeta)$ has polynomial form, it can be presented as (6) shows:

$$r(y,\zeta) = f_1(y)\zeta_1 + f_2(y)\zeta_2 + \cdots + f_k(y)\zeta_k + f_0(y) \tag{6}$$

If ζ_k is fuzziness parameters in trapezoidal form, $(\zeta_{k1}, \zeta_{k2}, \zeta_{k3}, \zeta_{k4}), k = 1, 2, \ldots, N$; $\zeta_{k1}, \zeta_{k2}, \zeta_{k3}, \zeta_{k4}$ render subordinating parameters.

To clarify the explicit equivalence, define two functions as (7) shows:

$$\begin{aligned} f_k^-(y) &= \begin{cases} 0, & f_k(y) \ge 0 \\ -f_k(y), & f_k(y) < 0 \end{cases} \\ f_k^+(y) &= \begin{cases} f_k(y), & f_k(y) \ge 0 \\ 0, & f_k(y) < 0 \end{cases} \end{aligned} \tag{7}$$

If $f(y) = 1$, then $f_k^+(y) = 1$ and $f_k^-(y) = 0$; if $f(y) = -1$, then $f_k^+(y) = 0$ and $f_k^-(y) = 1$.

If credibility confidence $\alpha \ge 0.5$, , equivalence class of chance constraints is presented as (8):

$$\begin{aligned} &(2-2\alpha)\sum_{k=1}^{t}\left[\zeta_{k3} f_k^+(x) - \zeta_{k2} f_k^-(x)\right] + (2\alpha - 1) \\ &\times \sum_{k=1}^{t}\left[\zeta_{k4} f_k^+(x) - \zeta_{k1} f_k^-(x)\right] + f_0(x) \le 0 \end{aligned} \tag{8}$$

Fuzziness parameters by trapezoidal function in each scheduling period are presented as (9) shows:

$$\mu(P_{\mathrm{F}}) = \begin{cases} \frac{P_{\mathrm{F4}} - P_{\mathrm{F}}}{P_{\mathrm{F4}} - P_{\mathrm{F3}}}, & P_{\mathrm{F3}} < P_{\mathrm{F}} \leq P_{\mathrm{F4}} \\ 1, & P_{\mathrm{F2}} \leq P_{\mathrm{F}} \leq P_{\mathrm{F3}} \\ \frac{P_{\mathrm{F}} - P_{\mathrm{F1}}}{P_{\mathrm{F2}} - P_{\mathrm{F1}}}, & P_{\mathrm{F1}} \leq P_{\mathrm{F}} < P_{\mathrm{F2}} \\ 0, & \text{others} \end{cases} \tag{9}$$

$\mu(P_{\mathrm{F}})$ is the membership function; P_{F1}—P_{F4} is the membership parameter, determining the shape of the membership function.

P_{F1}—P_{F4} are determined based on predicted values P_{fc} as (10) shows:

$$P_{\mathrm{Fk}} = w_k P_{\mathrm{fc}}, \quad k = 1, 2, 3, 4 \tag{10}$$

$P_{\mathrm{Wc},t}$ is prediction value of wind power; w_k is weight coefficient ranging from 0 to 1. Weight coefficient is set according to empirical value of intermittent renewable supply and demand of load.

Quartet of trapezoidal fuzziness parameters are as (11) follows:

$$\tilde{P}_F = (wP_{\mathrm{F1}}, wP_{\mathrm{F2}}, wP_{\mathrm{F3}}, wP_{\mathrm{F4}}) = P_{\mathrm{forcast}}(\mu w_1, \mu w_2, \mu w_3, \mu w_4) \tag{11}$$

If $\mu w_2 = \mu w_3 = 1$, then $P_{F2} = P_{F3} = P_{fc}$, that is, the fuzziness parameter is a triangular function. Trapezoidal and triangular fuzziness parameter functions are shown in Fig. 5.

Following the fuzzy decision process described earlier, the opportunity constraints are translated into equivalent crisp sets. More information on the implementation of SCUC can be found in the literature [13].

The scenario-based method approximates the chance constraint program by using a dataset with N scenarios. The optimal solution is feasible for all N scenarios. However, both the optimal objective value and the optimal solution depend on the

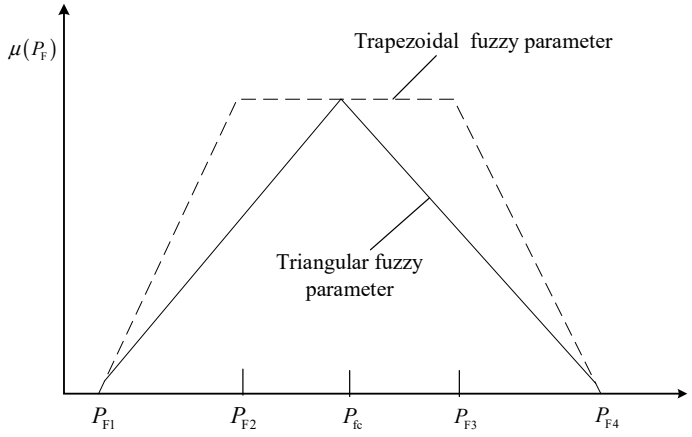

Fig. 5 Trapezoidal and triangular fuzziness parameter functions

random sample, thus scenario-based method has a strong dependence on the sample selected. To address this issue, most papers utilize prior assurance using the scenario-based method and verify posterior feasibility of the solution through Monte Carlo simulation. Sample average approximation (SAA) converts probabilistic constraints into a series of scenarios. Unlike the scenario-based optimization method, SAA introduces binary variables to indicate whether the sample scenario meets the original constraints. By using SAA to handle opportunity constraints, one can approximate the frequency of a sample scenario satisfying the original constraints. The solution obtained from the SAA algorithm indicates a high probability of satisfying constraints within the feasible region. On the other hand, the solution from the scenario-based method only guarantees feasibility of the optimal solution, but may not necessarily meet all the properties guaranteed by constraints. The SAA model is as (12) and (13) shows:

$$\min_{x,Y} c^T x + \frac{1}{N} \sum_{i=1}^{N} c^T Y \hat{\xi}_i \tag{12}$$

$$\text{s.t.} A(Y)\hat{\xi}_i \leq b(x) \tag{13}$$

The Sample Average Approximation (SAA) method involves utilizing statistical techniques to estimate the expectation and variance of the objective function and constraints. This enables the transformation of chance-constrained optimization into a deterministic optimization that possesses equivalent statistical properties. An important feature of SAA is that it can yield highly accurate results through the use of just a small number of scenarios.

2.4 Robust Optimization

Conventional deterministic optimization methods can be employed to solve Mixed Integer Linear Programming; however, the optimality of the solution hinges heavily upon the accuracy of the forecast. In practical operations, various stochastic factors exist that make it challenging to guarantee the accuracy of the forecast. As a result, deterministic optimization models often tend to produce solutions that are too "risky," emphasizing the need to account for uncertainty in the models. There are different ways to represent the sets of uncertainty that characterize the problem, for instance through scenarios or bounded ranges. In this case, the uncertainty set U is constructed in the form of a box-shaped set to accommodate fluctuations within the range of photovoltaic power output and load power, as described in Eq. (14).

$$U = \begin{cases} u = [u_{PV}(t), u_L(t)]^{\mathrm{T}} \in \mathbb{R}^{(N_T)\times 2}, t = 1, 2, \ldots, N_T \\ u_{PV}(t) \in \left[\hat{u}_{PV}(t) - \Delta u_{PV}^{\max}(t), \hat{u}_{PV}(t) + \Delta u_{PV}^{\max}(t)\right] \\ u_L(t) \in \left[\hat{u}_L(t) - \Delta u_L^{\max}(t), \hat{u}_L(t) + \Delta u_L^{\max}(t)\right] \end{cases} \tag{14}$$

In the formula, $u_L(t)$ and $u_{PV}(t)$ denote variables of photovoltaic output and load power with uncertainty, and $\Delta u_{PV}^{\max}(t)$ and $\Delta u_L^{\max}(t)$ represent the maximum allowable fluctuation deviation of photovoltaic output and load, respectively. The purpose of the two-stage robust optimization model is to find the optimal dispatch plan with the best economy when uncertain variable u changes toward the worst-case scenario within the uncertain set "U," which has the following form as (15):

$$\begin{aligned} &\max_{u\in U}\ \min_{y\in\Omega(u)}\ c^T y(t) \\ &\text{s.t.}\quad \begin{aligned} &\mathrm{A}y(t)\geq b \\ &I_u y(t)=\hat{u}(t) \end{aligned} \end{aligned} \tag{15}$$

In the above equation, $y(t) = (y_1(t), y_2(t), \ldots, y_i(t))^T$ "A" corresponds to the coefficient matrix of variables under unit constraints, and "b" is the corresponding constant column vector and the equality constraint is the system balance constraint. Optimization variables are u and y. For each given uncertain variable u, the inner minimization problem is equivalent to the objective function of the deterministic dispatch, which is to minimize operating costs. $\Omega(u)$ represents feasible domain for the optimization variable y given u. The specific expression is as (16) follows:

$$\boldsymbol{\Omega}(\mathbf{u}) = \left\{ y \middle| \begin{matrix} A\mathbf{y} \geq b \rightarrow \boldsymbol{\gamma} \\ \mathbf{I}_{\mathrm{u}}\mathbf{y} = u \rightarrow \boldsymbol{\pi} \end{matrix} \right\} \tag{16}$$

Given a fixed uncertain variable u, the inner minimization is a linear problem. According to the strong duality theory and the equivalence relationship of Eq. (16), it can be transformed into a max form under the given u. Then, it can be merged with the outer layer max problem to obtain the dual problem as (17) follows:

$$\begin{cases} \max_{\mathbf{u}\in\mathbf{U},\boldsymbol{\gamma},\boldsymbol{\pi}}\ \mathbf{d}^{\mathrm{T}}\boldsymbol{\gamma} + \mathbf{u}^{\mathrm{T}}\boldsymbol{\pi} \\ \text{s.t. } \mathbf{D}^{\mathrm{T}}\boldsymbol{\gamma} + \mathbf{I}_{\mathrm{u}}^{\mathrm{T}}\boldsymbol{\pi} \leq \mathbf{c} \\ \boldsymbol{\gamma} \geq 0,\ \boldsymbol{\pi} \geq 0 \end{cases} \tag{17}$$

The equation includes a bilinear term $\mathbf{u}^{\mathrm{T}}\boldsymbol{\pi}$. The optimal solution u^* for the dual problem represents a pole of the uncertainty set U. When Eq. (17) achieves its maximum value, the uncertain variable u should lie on the boundary of the fluctuation interval described in Eq. (14). This can be expressed mathematically as shown in Eq. (18).

$$\mathbf{U} := \begin{cases} \mathbf{u} = [u_{\mathrm{PV}}(t), u_{\mathrm{L}}(t)]^{\mathrm{T}} \in \mathbb{R}^{(N_{\mathrm{T}})\times 2}, \quad t = 1, 2 \ldots N_{\mathrm{T}}| \\ u_{\mathrm{PV}}(t) = \hat{u}_{\mathrm{PV}}(t) - B_{\mathrm{PV}}(t)\Delta u_{\mathrm{PV}}^{\max}(t) \\ \sum_{t=1}^{N_{\mathrm{T}}} B_{\mathrm{PV}}(t) \le \Gamma_{\mathrm{PV}} \\ u_{\mathrm{L}}(t) = \hat{u}_{\mathrm{L}}(t) + B_{\mathrm{L}}(t)\Delta u_{\mathrm{L}}^{\max}(t) \\ \sum_{t=1}^{N_{\mathrm{T}}} B_{\mathrm{L}}(t) \le \Gamma_{\mathrm{L}} \end{cases} \tag{18}$$

In the equation, is a binary variable, and represents whether the corresponding uncertain variable falls on the upper or lower bound of the fluctuation interval. Γ_{L} is the "uncertainty adjustment parameters" for the photovoltaic power and load power respectively, used to adjust the level of conservatism in the optimal solution. They take integer values ranging from 0 to N_{T}, representing the total number of periods when the photovoltaic power and load power reach the minimum or maximum value described by Eq. (18) in the fluctuation interval. The larger the value, the more conservative the solution, and vice versa. After substituting the expression of the uncertain variable into equation, there will be a product of binary variable and continuous variable. Linearization is achieved through the introduction of auxiliary variables and constraints, as shown.

In this equation, the variable $B = [B_{\mathrm{PV}}(t), B_{\mathrm{L}}(t)]^{T}$ is binary and indicates whether an uncertain variable falls on the upper or lower bound of its fluctuation interval. Parameters Γ_{PV} and Γ_{L} are called "uncertainty adjustment parameters" for photovoltaic power and load power, respectively. They adjust the level of conservatism in the optimal solution and take integer values from 0 to N_{T}. This value represents the number of periods when the power reaches its minimum or maximum level, as described by Eq. (18). The larger the value of these parameters, the more conservative the solution, and vice versa. After substituting the expression of the uncertain variable in Eq. (18) into Eq. (17), a product of binary variable and continuous variable emerges. To linearize the equation, auxiliary variables and constraints are introduced, as shown in Eq. (19).

$$\begin{cases} \max_{\mathbf{B},\mathbf{B}',\boldsymbol{\gamma},\boldsymbol{\pi}} \mathbf{d}^{\mathrm{T}}\boldsymbol{\gamma} + \hat{\mathbf{u}}^{\mathrm{T}}\boldsymbol{\pi} + \Delta\mathbf{u}^{\mathrm{T}}\mathbf{B}' \\ \text{s.t. } \mathbf{D}^{\mathrm{T}}\boldsymbol{\gamma} + \mathbf{I}_{\mathrm{u}}^{\mathrm{T}}\boldsymbol{\pi} \le \mathbf{c} \\ 0 \le \mathbf{B}' \le \overline{\boldsymbol{\pi}}\mathbf{B} \\ \boldsymbol{\pi} - \overline{\boldsymbol{\pi}}(1 - \mathbf{B}) \le \mathbf{B}' \le \boldsymbol{\pi} \\ \sum_{t=1}^{N_{\mathrm{T}}} B_{\mathrm{PV}} \le \Gamma_{\mathrm{PV}} \\ \sum_{t=1}^{N_{\mathrm{T}}} B_{\mathrm{L}} \le \Gamma_{\mathrm{L}} \end{cases} \tag{19}$$

The uncertainty adjustment parameters Γ_{L} and Γ_{PV} are set to 12 and 6 respectively, indicating that load power can take the maximum value in the prediction interval for up to 12 time periods, and photovoltaic output can take the minimum value in the prediction interval for up to 6 time periods, while the remaining periods assume the

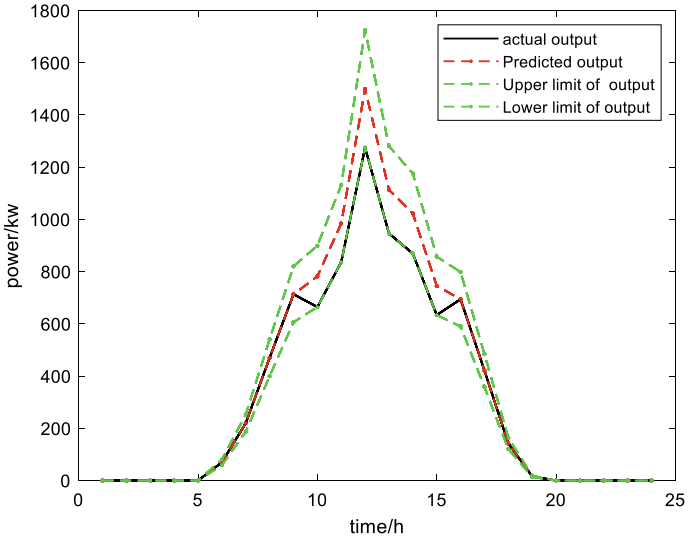

Fig. 6 Predicted/actual photovoltaic output curve

predicted value, as Figs. 6 and 7 show. The uncertainty deviation for load power and photovoltaic output is assumed to be 10% and 15% respectively, based on reference [14]. Using model (19) for optimization, with specific parameter settings referenced in the literature [15], the area surrounded by the green line represents the fluctuation region of the uncertain set, and the red line represents the predicted value. The black line is the actual result after optimization. Taking the boundary at these moments corresponds to the worst-case scenario in the optimization process. After the aforementioned derivation and transformation, the robust model is finally decoupled into a mixed-integer linear form.

3 Methods Used by Markets Around the World in Day-Ahead Scheduling of Reserve

This section illustrates the methods adopted by markets worldwide for day-ahead SCUC, as summarized in Table 1. Table 1 suggests that deterministic methods are generally preferred over more precise models. To ensure adherence to constraints, certain markets, such as CAISO, MISO, NYISO, and ISO-NE add extract partial scenarios to SCUC.

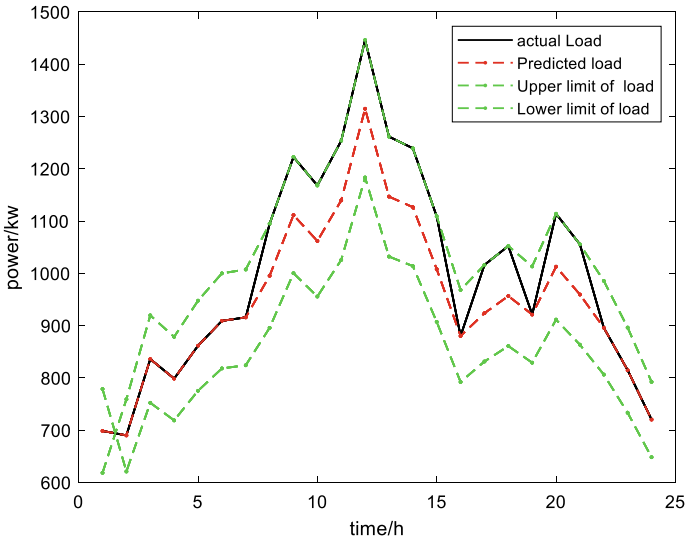

Fig. 7 Predicted/actual load curve

Table 1 Markets around the world in day-ahead scheduling

Market	Unit commitment	Types of reserve	Response time	Forecast
PJM [16]	Reliability-based	Demand response and asynchronous reserve	10 min	External suppliers
CAISO [17]	SCUC	Synchronous and asynchronous reserve	10 min	External suppliers
MISO [18]	SCUC	Demand response and asynchronous reserve	10 min	Make own prediction
NYISO [19]	SCUC	Synchronous and asynchronous reserve	10 and 30 min	External suppliers
ERCOT [20]	Reliability-based	Demand response and asynchronous reserve	10 and 30 min	External suppliers
ISO-NE [21]	SCUC	Synchronous and asynchronous reserve	10 and 30min	External suppliers

On the other hand, Chile employs probabilistic models to analyze alternative models. In the ERCOT market, centralized unit commitment is not mandatory, and market players in the advance market make their own decisions. Typically, wind generation projections are obtained from external sources, such as PJM, CAISO, NYISO, ISO-NE, and ERCOT. MISO creates independent forecasts using external weather data sources. In Chile, each wind farm generates its own forecast.

4 Conclusion

This article employs three methods to characterize the unpredictability of uncertain renewable output, transforming the original uncertain optimization into a deterministic optimization.

(1) The scenario-based method is effective in describing the characteristics of renewable output through various scenarios. However, it can lead to dimension disaster in its application process, which means that the number of scenarios can quickly become unmanageable.
(2) The optimization method based on chance constraints can cover various risk events that may occur in the power system. However, it cannot cover events with small probabilities due to economic considerations. These events may be high-risk and threaten the security of the power grid.
(3) The robust optimization method can deal with the worst situation in the power system and is independent of probability distribution, which improves reliability with less economic benefits.

In summary, each method has its strengths and limitations, and the appropriate method should be chosen depending on the specific situation and objectives.

Acknowledgements This work was supported by the State Grid Corporation of China Science and Technology Project under Grant No.5108-202255040A-1-1-ZN.

References

1. Chen X, Liu Y, Wang Q, Lv J, Wen J, Chen X, McElroy MB (2021) Pathway toward carbon-neutral electrical systems in China by mid-century with negative CO_2 abatement costs informed by high-resolution modelling. Joule 5(10):2715–2741
2. ELIA. Procedure for constitution of strategic reserve (2017)
3. NERL. Operating reserves and variable generation (2011)
4. Black M, Strbac G (2007) Value of bulk energy storage for managing wind power fluctuations. IEEE Trans Energy Convers 22(1):197–205. https://doi.org/10.1109/TEC.2006.889619
5. Holttinen H et al (2013) Steps for a complete wind integration study. In: 2013 46th Hawaii international conference on system sciences, pp 2261–2270. https://doi.org/10.1109/HICSS.2013.497
6. Kalantari A, Galiana FD (2015) Generalized sigma approach to unit commitment with uncertain wind power generation. Int J Electr Power Energy Syst 65:367–374. ISSN 0142-0615
7. Uçkun C, Botterud A, Birge JR (2016) An improved stochastic unit commitment formulation to accommodate wind uncertainty. IEEE Trans Power Syst 31(4):2507–2517. https://doi.org/10.1109/TPWRS.2015.2461014
8. Kalantari, Restrepo JF, Galiana FD (2013) Security-constrained unit commitment with uncertain wind generation: the loadability set approach. IEEE Trans Power Syst 28(2):1787–1796. https://doi.org/10.1109/TPWRS.2012.2230029
9. Wu Y, Wang C, Lou S (2017) Peak load regulating operation and optimization in power systems with large-scale wind power and considering coupling relation between wind power and Load. Autom Electr Power Syst 41(21):163–169

10. Modarresi MS et al (2019) Scenario-based economic dispatch with tunable risk levels in high-renewable power systems. IEEE Trans Power Syst 34(6):5103–5114. https://doi.org/10.1109/TPWRS.2018.2874464
11. Geng X, Xie L (2019) Data-driven decision making in power systems with probabilistic guarantees: theory and applications of chance-constrained optimization. Ann. Rev. Control 47:341–363. ISSN 1367-5788. https://doi.org/10.1016/j.arcontrol.2019.05.005
12. Ming H, Xie L, Campi MC, Garatti S, Kumar PR (2019) Scenario-based economic dispatch with uncertain demand response. IEEE Trans. Smart Grid 10(2):1858–1868. https://doi.org/10.1109/TSG.2017.2778688
13. Hu X, Li Z, Lv Y, Fan H, Li L, Ding L, Chen X (2023) Optimization methodologies for reserve with large-scale renewables integration. In: 2nd International conference on energy utilization and automation, Sanya (online), China
14. China Electricity Council (2013) NB/T 32011–2013 Technical requirement of power forecasting system for PV power station. National Energy Administration of China, Beijing (in Chinese)
15. Liu Y, Guo L, Wang C (2018) Two-stage robust optimization economic dispatch method for microgrid. Proc Chin Soc Electr Eng 38(14):4013–4022+4307. https://doi.org/10.13334/j.0258-8013.pcsee.170500
16. PJM (2020) PJM Manual 18: capacity market: prepared by capacity market & demand response operations. Revision: 45. 28 May 2020
17. CAISO (2022) Business practice manual for market operations
18. MISO (2020) Energy and operating reserve markets business practices manual
19. NYISO (2019) Manual 11 day-ahead scheduling manual
20. Independent Market Monitor for ERCOT (2021) 2020 State of the market report for the ERCOT Electricity Markets
21. ISO-NE (2022) Day-ahead energy market—commitment, scheduling, and dispatch

Quantitative Research on Energy-Saving Benefits of Different Integration Methods of Vehicle–Grid

Jia Zhao, Peng Liu, Peng Ge, Yifang Zhu, Haifeng Fang, and Shu Wang

Abstract The National High Technology Research and development Program in the "10th Five-Year Plan" 863 plan proposed a major scientific and technological project of "electric vehicles," and the electric vehicle technology system has been continuously improved. Especially after the goal of carbon peaking and carbon neutrality is put forward, the interaction between transportation and energy is further enhanced, and the integration of electric vehicles and the power grid has become an increasingly normal state. This research focuses on the energy-saving benefits of the integrated development of electric vehicles and power grids. By constructing a quantitative model, we explore the best technical path for the synergy between the two to achieve the greatest energy-saving benefits and provide a basis for large-scale demonstration applications of vehicle–grid integration.

Keywords Electric vehicle · Power grid · Integration · Energy saving · Quantitative model

1 Introduction

Electric vehicles (EVs) develop rapidly under the two-wheel drive of industrial policy and market. By June 2022, the cumulative sales volume of EVs has exceeded 10 million. The development of electric vehicle is not only the urgent requirement of green and low carbon development of automobile industry, but also the urgent requirement of constructing clean energy system and sustainable transportation system. By May 2022, there are 102 pilot demonstration projects of vehicle network integration

J. Zhao · P. Ge · Y. Zhu · H. Fang (✉)
China Automotive Technology and Research Center, Dongli District, Tianjin, China
e-mail: fanghaifeng@catarc.ac.cn

S. Wang
Chang'an University, Shangyuan Road, Weiyang District, Xi'an, China

P. Liu
Automotive Data of China Co., Ltd., Dongli District, Tianjin, China

S. Yadav et al. (eds.), *Energy Power and Automation Engineering*, Lecture Notes in Electrical Engineering 1118, https://doi.org/10.1007/978-981-99-8878-5_22

in the world, and only one in China [1]. How to make full use of positive interaction between electric vehicles and electric power system is a major topic of China energy transition and development of smart grid. From the perspective of energy-saving potential, this paper studies the energy-saving potential of the integrated development mode of electric vehicles and power grid.

2 Application Scenarios and Energy-Saving Potential Analysis

2.1 Analysis of Application Scenarios of Vehicle–Grid Integration

At present, the basic key scenarios for the integrated development of electric vehicles and power grids mainly include peak cutting and valley filling, new energy consumption and demand response.

Peak shaving and valley filling reduce the peak load of the power grid, increase the low valley load, smooth the load curve and stabilize the operation of the power grid. The charge and discharge process of EVs is controlled by the energy management system, so that EVs as distributed energy storage devices charge in the low load of the system and discharge in reverse to the grid system at the peak, which could improve the "peak–valley difference" of the load curve of the power system, play the role of "peak cutting and valley filling" and improve the economy of power grid operation.

New energy consumption refers to the systematic problems involving power supply, power grid and electricity load. By 2020, the curtailment rate should be controlled at about 5%, the curtailment rate of photovoltaic power generation should be less than 5%, and the water energy utilization rate should also reach more than 95%. However, renewable energy output has relatively large randomness and fluctuation. The vehicle–grid integration could effectively promote energy conservation.

Demand response is changing users' electricity demand through changes in price signals, which provides a new direction to solve the problem of large-scale renewable energy consumption under the background of new power system construction. In recent years, there are many researches on wind power generation dispatch focusing on demand side response.

2.2 Review on Energy-Saving Potential of Vehicle Network Integration

EVs is a key scenario for the integration development of vehicle network. Based on this scenario, scholars have studied the potential energy-saving benefits of disorderly

charging, orderly charging and orderly charging and discharging, and demonstrated the necessity of vehicle–grid integration mode.

Disordered charging of EVs is random, which probably further increases the peak–valley difference of power grid load on the basis of the current peak–valley difference. It is not conducive to energy conservation. Many domestic and foreign scholars have demonstrated that disordered charging is difficult to achieve the consumption of new energy by using a variety of model methods [2–4].

The orderly charging mode that can regulate the charging behavior of electric vehicles in one direction stabilizes the fluctuations caused by large-scale wind and solar power generation access and optimizes the peak–valley difference of the power grid [5–7], so as to achieve the minimum power generation consumption of thermal power and nuclear power [8–10].

In the orderly charging and discharging mode, the interaction between electric vehicles and the power grid is dynamically regulated in both directions, which not only expands the system's capacity to consume new energy sources such as wind power [11, 12], but also reduces the energy consumption of conventional electric power generation [13] and maximizes the energy-saving potential in this mode.

3 Modeling the Energy Efficiency of Vehicle–Grid Integration

3.1 Calculation Model of Charging Energy Load Benefit for Unordered Charging

Monte Carlo method is used to calculate the daily charging load of a vehicle, and then the total charging load is calculated by stacking. By dividing a day into 24 periods, i.e., 1-h interval for each period. As shown in Eq. (1), where N is the number of EVs. j is the charging time, P is the charging load.

$$P_j = \sum_{n=1}^{N} P_{nj} \tag{1}$$

Objective Function. The energy efficiency benefits of the ordered charging are modeled for maximizing the use of renewable energy generation and for reducing the peak load of charging stations as an objective function.

The part of the new energy output exceeding the charging load at every moment is defined as the absorption degree of new energy power generation, as shown in Eq. (2), where P_{curtail} is the discarded amount of new energy, P_{volt} is charging power, and P_{ev} is the charging power of EVs.

$$P_{\text{curtail}}(i) = \begin{cases} 0, & P_{\text{volt}}(i) < P_{\text{ev}}(i) \\ P_{\text{volt}}(i) - P_{\text{ev}}(i), & P_{\text{volt}}(i) \geq P_{\text{ev}}(i) \end{cases} \tag{2}$$

It is necessary to minimize the sum of the discarded amount of new energy at every moment of the day, which is taken as the objective function, as shown in Eq. (3), where Δt_i is the time period length.

$$f_1 = \min\left\{\sum_{i=1}^{n} P_{\text{curtail}}(i) \cdot \Delta t_i\right\} \tag{3}$$

When new energy power generation meets the demand of EVs charging, charging stations do not need to purchase electricity from the grid, vice versa, as shown in Eq. (4), where P_{grid} is purchasing load.

$$P_{\text{grid}}(i) = \begin{cases} 0, & P_{\text{ev}}(i) < P_{\text{volt}}(i) \\ P_{\text{ev}}(i) - P_{\text{volt}}(i), & P_{\text{ev}}(i) \geq P_{\text{volt}}(i) \end{cases} \tag{4}$$

The smaller the peak value of the charging station, the smaller the negative impact of charging on it, the objective function is shown in Eq. (5), where P_{peak} is peak load of charging stations.

$$f_2 = \min\left\{P_{\text{peak}}\right\}, \quad P_{\text{peak}} = \max P_{\text{grid}} \tag{5}$$

For the above two objective functions, the direct decision variable is the price difference, while the indirect decision variable is the optimized starting charging time of the charging vehicle. Since the decision variables are the same and the objective function values influence each other, the multi-objective optimization problem is transformed into single-objective optimization in this paper, and the linear-weighted summation algorithm is adopted to calculate the comprehensive optimal of the two. As shown in Eq. (6), ω is the weight coefficients of the objective function, and $\omega_1 + \omega_2 = 1$. $f_{1,\max}$ and $f_{2,\max}$ are the maximum values of objective function (3) and (5), respectively.

$$f_3 = \min\left\{\omega_1 \cdot \frac{f_1}{f_{1,\max}} + \omega_2 \cdot \frac{f_2}{f_{2,\max}}\right\} \tag{6}$$

Constraint Condition. It is assumed that the total EVs charging load remains unchanged before and after. Meanwhile, the number of electric vehicles being charged at any time should not exceed the total number of charging piles in the charging station, and the load of the charging station should not exceed the distribution capacity of the transformer of the charging station at any time. For the guided charging price, the charging price difference of the guided peak–valley period, peak–normal period and the peaceful period should be guaranteed to be a positive number, and the guided charging period should only have three attributes: peak, flat and valley.

The constraints of the model are obtained as shown in Eq. (7), where $P_{ev}^{*}(i)$ is the charging power of electric vehicles at moment after optimization, P_{sum} is the total charging load of electric vehicles in a day, N_{pile} is the total number of charging piles in the station, P_{max} is the rated power distribution capacity of the transformer in the charging station.

$$\sum_{i=1}^{N} P_{ev}(i) = \sum_{i=1}^{N} P_{ev}^{*}(i) = P_{sum}, N_i^{*} \le N_{pile}, P_{grid}(i) \le P_{max}, \quad i \in \{1, 2, 3\} \quad (7)$$

4 Sections, Subsections and Subsubsections

4.1 Setting the Parameters of the Energy Efficiency Potential Assessment Model

B city is selected as a typical demonstration object to analyze the energy-saving benefits of orderly charging and discharge. Coal-fired units are taken as traditional energy, wind power and photovoltaic power as renewable energy, and it is assumed that all electric vehicle users can participate in the charging and discharging decision-making model.

All the inputs to the example model are as follows: for the traditional energy, the carbon emissions of coal-fired units are calculated by whole life cycle theory to depend mainly on coal combustion (2.75% for coal production, 0.32% for coalfield gas, 3.48% for coal transport, 91.66% for coal combustion and 1.80% for power plant desulphurization). The traditional energy carbon emission intensity is 0.997 kg/kWh. Through multiple surveys, the carbon trading price in the carbon market is assumed to be 74.6 yuan/t. As for renewable energy generation, by 2020, China's solar projects have generated 260.5 billion kWh and wind power projects have generated 466.5 billion kWh, with a total of 727 billion kWh generated by renewable energy.

The annual solar power generation of B city is 620 million kWh, and the wind power generation is 370 million kWh. The annual new energy power generation reaches 990 million kWh in total. In 2020, the national average wind and light abandonment rates will be 3% and 2%, respectively, totaling about 19.2 billion kWh. Moreover, the renewable energy abandonment rate of B city is the same as the national rate of wind and light abandonment, totaling about 0.235 billion kWh.

The annual total amount of wind power and solar power generation of B city is predicted through the typical output curve. The wind power output model adopts Weibull distribution, and the solar power output model conforms the normal distribution curve. Thus, the daily power abandonment curves of wind power and solar power in B city are shown in Figs. 1 and 2.

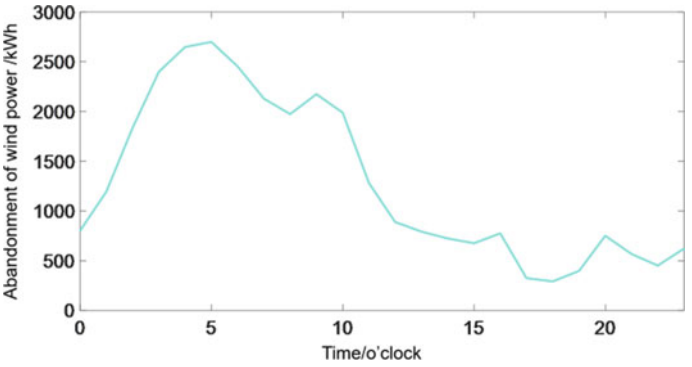

Fig. 1 Average historical data of the daily power abandonment curves of wind power

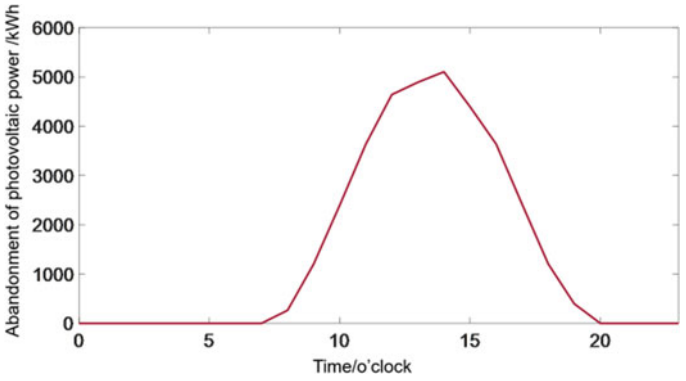

Fig. 2 Average historical data of the daily power abandonment curves of solar power

The basic electricity load curve of B city is referenced to the load statistics of 2020 from the National Energy Administration. In this project, the 118-node distribution system is adopted to simulate the power distribution network structure of B city, and then, the load profile of B city at each time period is equally distributed to each node as the base electricity load of each node in B city.

In addition, for other parameters, it is assumed that the battery capacity of electric vehicles is all referred to "BYD E6," and the battery capacity is 82.5 kWh. The minimum and maximum values of the initial SOC of electric vehicles are 0.2 and 1, respectively. The earliest time for electric vehicles to access and leave the grid is set at 13:00 and 13:00 on the second day, respectively. The total optimization time is 24 h, and the optimization interval is 1 h ($M = 24$; $\Delta T = 1$ h). The output parameter of the example is the decision variable, which is the charging and discharging decision of the electric vehicle in each period.

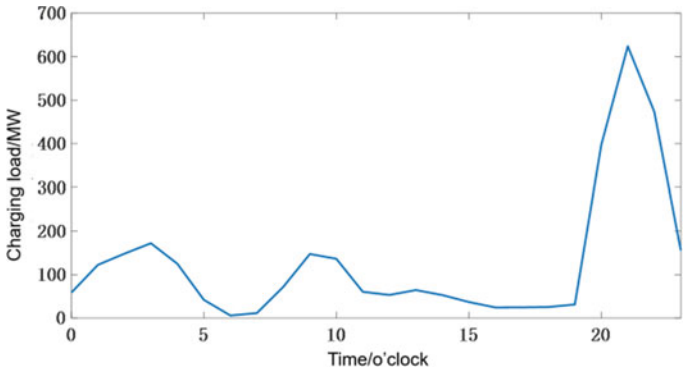

Fig. 3 B City EV daily charging load

By 2020, the number of electric vehicles in B city will be about 400,000, and it is assumed that the model and parameters of the probability distribution of electric vehicles are connected to the grid and charged satisfy. In addition, the EV starting SOC is assumed to conform to a Gaussian distribution with a mean of 0.3 and a variance of 0.1. The electric vehicle charging power is 30 kW, and then, Monte Carlo sampling is used to sample the probability distribution of the charging start time to obtain the daily electric vehicle charging load curve in B city. The daily charging load curve of electric vehicles in B city is shown in Fig. 3.

4.2 Potential Calculation of Energy-Saving Benefit in Typical Cities

The use of sections to divide the text of the paper is optional and left as a decision for the author. Where the author wishes to divide the paper into sections, the formatting shown in Table 2 should be used. Table 1 shows the results of the energy-saving benefits of disordered charging, ordered charging and discharging strategies for B city in 2020, China in 2020 and 2030.

The results show that the orderly charging and discharging behavior of electric vehicles can significantly reduce the amount of new energy abandoned and effectively improve the new energy utilization at charging stations. As can be seen from the table, B city achieves full dissipation of the new energy waste in 2020, which is mainly due to the low new energy share of the city with a low volume of electricity abandoned and a high number of electric vehicles. Compared to the results of the nationwide orderly charging and discharging strategies in 2020, only 13.7 billion kWh of new energy power abandonment is dissipated due to the low number of electric vehicles nationwide and the total electric vehicle charging load being lower than the new energy power abandonment in 2020.

Table 1 Energy-saving results of different charging and discharging strategies

Comparison of optimization effect	Unorderly charging	Orderly charging	Orderly charging and discharging
New energy power abandonment of B city in 2020 (100 million kWh)	9.9	0	0
New energy power abandonment of China in 2020 (100 million kWh)	192	55	55
New energy power abandonment of China in 2030 (100 million kWh)	376	0	0

Table 2 Analysis results of energy efficiency sensitivity of orderly and discharging strategies

Users participation (%)	2020 (100 millions kWh)	2030 (100 millions kWh)
5	6.85	53.2
10	13.7	106
20	27.4	213
30	41.1	319
40	54.8	376
60	82.2	376
80	109.6	376
100	137	376

In 2030, orderly charging and orderly charging and discharging scheduling in China will realize full absorption of new energy as shown in Table 1.

This is mainly due to the rapid growth of the production and marketing scale of electric vehicles, and a large number of electric vehicles will be connected to the power grid in 2030. Therefore, the absorption of new energy power generation can be better realized and the maximum utilization of new energy power generation can be realized.

At the same time, this paper will also conduct a sensitivity analysis on Chinese user participation in 2030, and user participation = (the number of users participating in orderly charging or discharge)/the total number of electric vehicle users.

According to Table 2, there is a linear growth relationship between user engagement and energy saving in 2020. This is because the charging load of electric vehicles in 2020 is much lower than the new energy power abandonment. Therefore, when more users participate in dispatching, the absorption of new energy power and energy saving will increase linearly.

However, the macro-sensitivity analysis of the user participation in 2030 shows that when the user participation is not less than 40%, all the new energy power abandonment can be absorbed, saving 37.6 billion kWh of electric energy. When the

user participation is less than 40%, the corresponding power saving will gradually decrease as fewer users participate in the scheduling.

5 Conclusion

This paper summarizes the domestic and foreign research results on the social and economic benefits of vehicle network integration and analyzes the charging load prediction method of electric vehicle driving behavior. Based on the combination of wind and light energy, this paper studies the quantification of energy-saving benefits of vehicle network integration by taking B city as a typical example. This paper constructs the calculation model of energy-saving load benefit of the electric vehicle when it is orderly charging and orderly charging and discharging by combining the characteristics of electric vehicle user charging and new energy power generation. The paper constructs an objective function for renewable energy generation to achieve the goal of promoting local consumption of charging loads and maximizing the use of renewable energy generation. In addition, when the new energy generation is insufficient, electricity is purchased from the grid to make up for the load difference, and the peak–normal–valley attribute of the charging period is guided and the charging time of the charging vehicle is optimized. The experimental results confirm that the orderly charging and discharging behavior of electric vehicles can significantly reduce the new energy power abandonment and improve the utilization rate of new energy of charging stations effectively. Moreover, when the number of users participating in dispatching increases, the new energy absorbed increases linearly with the electric energy saved.

References

1. V2G Hub. https://www.v2g-hub.com/insights#graphs
2. Wang R, Wang P, Xiao G (2016) Two-stage mechanism for massive electric vehicle charging involving renewable energy. IEEE Trans Veh Technol 65(6):4159–4171
3. Hou JC, Hu QF, Tan ZF (2016) Multi-objective optimization model of wind power-electric vehicle collaborative scheduling based on demand response. Electr Power Automat Equip 36(7):22–27
4. Chen K, Ma Z, Zhou S (2020) A two-stage multi-objective orderly charging strategy for electric vehicles. Power Syst Protect Control 48(1):65–72
5. Ge SY, Guo JH, Liu H (2014) Effect of orderly charging of electric vehicles on power grid load curve considering demand-side response and regional wind-power output. Power Grid Technol 38(7):1806–1811
6. Yang H, Yang S, Xu Y (2015) Electric vehicle route optimization considering time-of-use electricity price by learnable partheno-genetic algorithm. IEEE Trans Smart Grid 6(2):657–666
7. Wei DJ, Zhang CH, Sun B (2015) Multi-objective optimal charging and discharging scheduling for electric vehicles based on time-of-use tariff. Power Grid Technol 38(11):2972–2977
8. Chen DJ, Gong QW, Zhang ML (2011) Multi-objective optimization of wind farm scheduling considering energy and environmental benefits. Proc CSEE 31(13):10–17

9. Yang YM (2017) Research and thinking on comprehensive energy consumption and development direction of electric vehicle. China Mark 06:39–40+ 48
10. Yu DY, Huang HL, Lei M, Li X, Zhang B, Han XS (2012) Analysis of carbon emission reduction benefits of electric vehicle charging and wind power cooperative dispatching. Automat Electr Power Syst 36(10):14–18
11. Liu DQ, Wang YN, Yuan XF (2017) Cooperative dispatch of large-scale electric vehicles with wind-thermal power generating system. Trans China Electrotech Soc 32(3):18–26
12. Yang LH, Xu Z (2011) Application of electric vehicles in Danish power system with large-scale wind power. Automat Electr Power Syst 35(14):43–47
13. Zhang N, Tang Z (2018) Multi-objective optimization strategy considering the cooperative dispatching of electric vehicles and wind power under V2G. Electr Meas Instrum 55(12):54–59 + 87

Collaborative Optimization Method for Integrated Energy of Campus Cluster Based on Improved Particle Swarm Optimization

Jie Xu and Jianli Yang

Abstract In order to fully adapt to the natural endowment and load distribution of the region and facilitate the overall arrangement of energy supply and consumption activities in a specific range, the integrated energy system of the park is generally established based on the differences in the construction and operation of energy supply facilities in the park. At present, many studies have been carried out on the optimal scheduling of the integrated energy system in the park. In view of the uncertain energy Internet in the park, the coupling relationship exists between the energy flow and the equipment in the park. In this paper, the particle swarm optimization is easy to fall into local optima. The particle swarm optimization algorithm is improved, and the adaptive mutation mechanism is integrated into the adaptive mutation particle swarm algorithm. The effectiveness of the new algorithm is verified by the simulation results using MATLAB software. Through the simulation analysis of the park, it can be concluded that different constraint operation strategies have a certain impact on the optimization of the park energy Internet. By improving the alternate direction of variable step, the optimal operation scheme of the system is obtained, which not only ensures the economy of the integrated energy system in the park, but also takes into account the flexible and stable operation of the distribution network.

Keywords Park energy management · Multi-regional collaboration · Integrated energy allocation · Particle swarm optimization

1 Introduction

With the increase of the number of parks in the region and the access of a large number of energy supply equipment, especially distributed energy and various energy supply units in the park, the multi-agent and distributed characteristics of the system are

J. Xu (✉) · J. Yang
Ningbo Power Supply Company of State Grid Zhejiang Electric Power Co. Ltd., Ningbo 315000, Zhejiang, China
e-mail: tspdhsd@163.com

S. Yadav et al. (eds.), *Energy Power and Automation Engineering*, Lecture Notes in Electrical Engineering 1118, https://doi.org/10.1007/978-981-99-8878-5_23

becoming more and more obvious. The disadvantage of poor information protection has been unable to meet the application needs [1]. It is urgent to study an optimization algorithm with less information traffic, fast solution speed, and strong confidentiality. In the current energy market, different types of energy suppliers belong to different stakeholders, and the pursuit of interests of each park may be different. Thus, it is impossible to fully share information with each other. There are information barriers [2]. In the case of limited information exchange, how to take into account the interests of all subjects and ensure the overall economy and stability of the system has become a bottleneck, restricting the further development of IES (integrated Energy System) [3].

In Ref. [4], considering the uncertainty of the internal source and load of the integrated energy system, a two-stage iterative optimization model is proposed to optimize the controllable equipment in the system. A simulation verification is carried out by taking a region in the UK as an example. In Ref. [5], a network model including power and heat supply is established based on the energy hub, and an equilibrium constraint solving method is proposed to solve the model. The optimal power flow and optimal heat flow under the network constraints of the physical system are obtained. Reference [6] also considers the uncertainty of renewable energy, such as wind power and photovoltaic power. It proposes an optimal dispatching method based on chance constrained programming to solve the problem and verifies the feasibility of the method on the IEEE30-bus system.

In this paper, under the background of the park energy Internet, considering the uncertainty of the integrated energy synergy of the park group in the park energy Internet system, the improved particle swarm optimization algorithm is used to solve the optimal scheduling of the park. Firstly, the comprehensive energy model of the park group is established. According to the uncertainty set of data and the equivalent transformation theory, an improved algorithm with slack variables is adopted to overcome the shortcomings of the traditional particle swarm optimization. Then, the optimization model is established to deal with the uncertainty according to the objective function and constraints.

2 Coordinated Dispatching Model of Integrated Energy in the Industrial Park Group

Due to the complex coupling in the park, the dynamic performance of other equipment is ignored. According to the optimization results, the dynamic performance of the whole system is improved by optimizing the upstream equipment in the system in the strategy [7]. The structural optimization strategy is shown in Fig. 1.

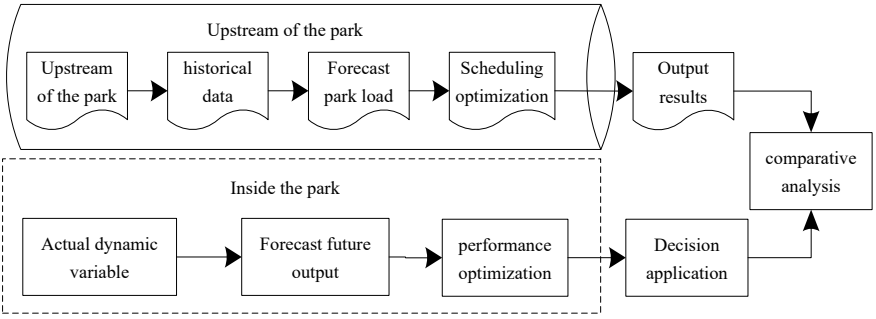

Fig. 1 Optimization of energy structure in the park

Through rolling prediction and rolling optimization, the impact of randomness and volatility of renewable energy output and users can be effectively reduced as far as possible. Under the background of optimal system economy, we should determine the steady-state output value of each energy in the park, play the optimal utility of the park, and realize the best energy matching between various energy sources and loads [8].

3 Scheduling Optimization Strategy Based on the Particle Swarm Optimization

For the optimization problem with constraints, the most common method is to transform the constraints into penalty function terms, thus transforming the problem into an unconstrained problem. However, the selection of the penalty factor has strong subjectivity. Too large penalty factor will lead to "premature" of the optimal solution, otherwise it is not conducive to the direction of the feasible solution. Therefore, it is necessary to determine the appropriate penalty factor with the help of past experience or repeated trials. The core idea of the dual fitness function is to regard the constraint condition as an additional fitness function of the particle, as shown in Formula (1).

$$\mathrm{fix}(x) = V_{(t)} = \sum_{i=1}^{n} \min(\alpha_1, \beta_1) \cdot |x| \tag{1}$$

In Eq. (1), $\mathrm{fix}(x)$ is the minimum power generation of the generation end in time period x; $V_{(t)}$ is the parameter of the generation end; $\min(\alpha_1, \beta_1)$ is the upper and lower limits of the constraint load; and $|x|$ is the park consumption constrained by equality [9].

According to the separation comparison rule, the quality of a particle is determined by the two fitness functions, as shown in Formula (2).

$$\begin{cases} Q_i = \frac{t_i}{\max t_j} \cdot \sqrt{\alpha_1} \\ Q_j = \frac{t_i+1}{\max t_j - 1} \cdot \sqrt{\beta_1} \end{cases} \tag{2}$$

In Eq. (2), Q_i, Q_j is the initial and final values of energy consumption, and t_i, t_j is the maximum and minimum number of iterations.

If the minimization problem is solved, there are two different particles x_1, y_1 in the population, and the separation comparison rule is as follows:

(1) When both particles are feasible solutions, $V_t^{(x_1)}$ and $V_t^{(y_1)}$ are equal to zero, comparing the objective function values of the particles, the particle with smaller objective function value is better;
(2) When both particles are infeasible solutions, $V_t^{(x_1)}$ and $V_t^{(y_1)}$ are greater than zero. The constraint function values between particles are compared, and the particle with smaller constraint function value is better;
(3) When the feasibility of two particles is different, assuming that the particle x_1 is a feasible solution and y_1 is an infeasible solution, the feasible solution particle x_1 is determined to be a better particle [10].

The algorithm flow is displayed in Fig. 2.

(1) Initialize isoparameters, generate a population composed of particles, and initialize the position and velocity of particles.
(2) Calculate all individual fitness values within the population according to the objective function.
(3) Calculate the optimal population fitness value $f(pg)$ and record the optimal position.
(4) Determine the initial particle consumption.
(5) Calculate the jump probability under the current state.
(6) A certain alternative value is determined according to the roulette strategy. Update the particle position according to Formula (2).
(7) Calculate the fitness value of each particle, confirm, and update the particle and population according to the separation and comparison rules.

4 Analysis of Algorithm Performance Measurement

4.1 Simulation Settings

The simulation environment refers to [11]. With 24 h as the planning period, 1 h as a planning period, a total of 24 periods, and then the MATLAB is used for simulation. To verify the superiority of the improved algorithm compared to the conventional particle swarm algorithm, the two algorithms are configured with similar iteration parameters in advance to optimize the same iteration problem, and the optimization results are observed.

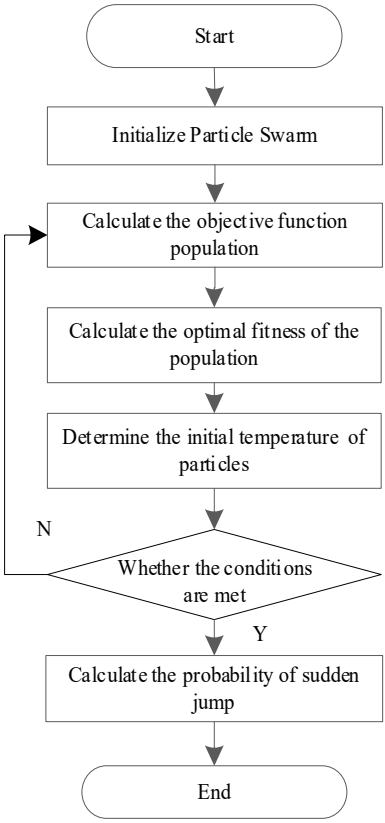

Fig. 2 Flow of the energy optimization algorithm

Multi-objective optimization algorithms mainly focus on two aspects: convergence and diversity. The convergence index γ and diversity index Δ are introduced to evaluate the performance of the algorithm. The smaller the index value is, the better the performance is. The average value of the minimum distance between the solution obtained by the algorithm and the corresponding point on the Pareto optimal front is the convergence index, which is:

$$\lambda = \sum_{i=1}^{n} \frac{\phi^2 t}{|\theta|} \tag{3}$$

In Eq. (3), λ is the Pareto optimal frontier point, ϕ is the number of populations, and θ is the number of iterations.

The non-inferior solutions calculated by the algorithm are orderly distributed in the objective space according to the value of a certain objective function, and the diversity index is as follows.

Table 1 Simulation test parameters

Index	Parameter
Particle swarm size	150
Maximum number of iterations	200
Minimum number of iterations	100
Particle inertia weight	0.85
Acceleration	1.17

$$\Delta\varpi_n = \sum_t \frac{\phi_t^i \cdot f_{(x)}}{\phi_{t-1}^j \cdot \left| f_{(x-1)} \right|} \tag{4}$$

In Eq. (4), $\Delta\varpi_n$ is the average Euclidean distance between the boundary solution obtained by the algorithm on the nth target and the extreme solution of the nth target on the Pareto optimal front.

The algorithm parameters are set as shown in Table 1.

4.2 Analysis of Test Results

The superiority of the improved particle swarm algorithm in this paper enables both of them to search the optimal solution for the optimal path generation in Ref. [11] at the same time. The iterative curve can be obtained, as displayed in Fig. 3.

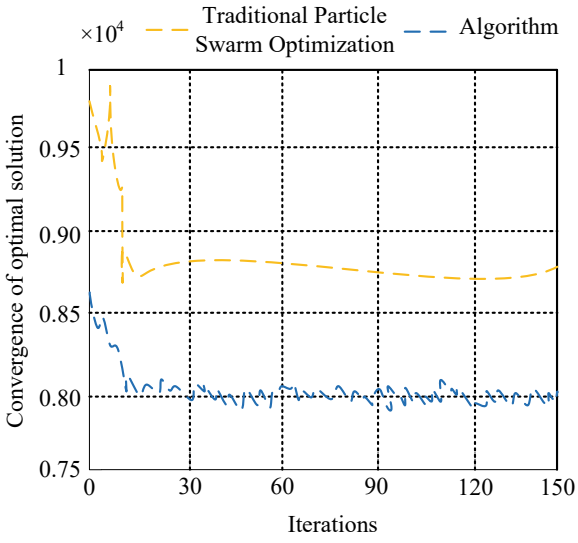

Fig. 3 Iteration curve of the convergence test

Table 2 Comparison results of algorithm accuracy

Comparison items	Parameter	Calculated value
Traditional particle swarm optimization	Mean value	0.024
	Variance	0.0017
Algorithm	Mean value	0.005
	Variance	0.0009

For the function test of Ref. [11] and Pareto real front, the test results are indicated in Table 2.

By analyzing the diversity index in the table and comparing to other traditional function tests, the optimized algorithm in this paper has better performance.

5 Conclusion

In this paper, the overall structure of the integrated energy system of the industrial park group is established. The integrated energy operation model of the industrial park group is established from small to large. Based on the regional adjustment design particle swarm optimization algorithm, the optimal operation strategy of the system is obtained. The output of each energy supply equipment in the system is obtained. The effectiveness and dynamic response ability of the algorithm are verified by the simulation example. The results verify that the proposed algorithm is optimized, and the test results are good. The non-inferior solutions obtained by the algorithm test are basically distributed on the Pareto front, and the convergence index and diversity index of the algorithm are good.

In future work, the weak robust optimization method will be applied to model the uncertainty of energy, which can get better economy, but the stability of the weak robust optimization model is not considered. In the future, new technologies can be applied to optimize the energy Internet system in the park according to the development of the times so as to achieve better economy.

References

1. Liu J, Zhang Y, Yu Y (2020) Fixed-time leader-follower consensus of networked nonlinear systems via event/self-triggered control. IEEE Trans Neural Netw Learn Syst (99)
2. Ning X (2019) Multi-agent consensus algorithm-based optimal power dispatch for islanded multi-microgrids. Processes 7(10):679–682
3. Liu Z, Yi Y, Yang J (2020) Optimal planning and operation of dispatchable active power resources for islanded multi-microgrids under decentralised collaborative dispatch framework. IET Gener Transm Distrib 14(3):408–422
4. Zhou X, Ai Q, Yousif M (2019) Two kinds of decentralized robust economic dispatch framework combined distribution network and multi-microgrids. Appl Energy 253:113588

5. Wang J, Li K-J, Javid Z, Sun Y (2019) Distributed optimal coordinated operation for distribution system with the integration of residential microgrids. Appl Sci 9(10):2136
6. Li P, Sheng W, Duan Q (2020) A Lyapunov optimization-based energy management strategy for energy hub with energy router. IEEE Trans Smart Grid 11(6):4860–4870
7. Xu D, Wu Q, Zhou B (2020) Distributed multi-energy operation of coupled electricity, heating, and natural gas networks. IEEE Trans Sustain Energy 11(4):2457–2469
8. Wang F, Zhou L, Ren H (2018) Multiobjective optimization model of source-load-storage synergetic dispatch for a building energy management system based on TOU price demand response. IEEE Trans Ind Appl 54(2):1017–1028
9. Zhong Y, Xie D, Zhai S (2018) Day-ahead hierarchical steady state optimal operation for integrated energy system based on energy hub. Energies 11(10):2765
10. Wang J, Zhong H, Ma Z (2017) Review and prospect of integrated demand response in the multi-energy system. Appl Energy 202:772–782
11. Zhang L, Kuang J, Sun B (2020) A two-stage operation optimization method of integrated energy systems with demand response and energy storage. Energy 208

Thermal Management of Batteries with Nano Phase Change Material Emulsion as Cooling Medium

Zhaoyang Deng, Xuliang Xie, Yanliang Shi, and Luyang Zhang

Abstract This paper mainly discusses the 5C high discharge rate, OP28E phase change emulsion was used instead of water as the cooling medium to cool the battery pack. Taking 18,650 battery as the research object, the 6s4p battery was analyzed by ANSYS FLUENT. The comparison of cooling capacity and power consumption between water and OP28E emulsion with different concentrations was analyzed, and the influence of coolant flow rate was analyzed. The results show that 10% OP28E emulsion was better than water.

Keywords Battery thermal management · Nano phase change material emulsion · Simulation · Li-ion battery

1 Introduction

With the continuous development of society, electric vehicles have become a common choice in people's daily life, and more and more researches about electric vehicle have been conducted. The battery life and safety largely determine the performance of electric vehicles. On the issue of how to guarantee the life and performance of power batteries, the control of power battery temperature has become the focus of research [1]. In recent years, lithium-ion battery is widely used because of its no memory life and long cycle life. Lithium-ion battery operating environment temperature in the range of 20°–45° is more appropriate, while the temperature difference between the battery for less than 5°, to maintain the temperature consistency between the single battery, this can maintain the best performance and the longest service life, otherwise it may cause local degradation of the battery pack, or even cause thermal runaway [2]. Therefore, controlling the working temperature and the difference in temperature of battery within the reasonable temperature scope is the key to settle the safety matter of battery. Battery thermal management system can be divided into active cooling system and passive cooling system according to the cooling method.

Z. Deng · X. Xie (✉) · Y. Shi · L. Zhang
School of Energy and Electrical Engineering, Chang'an University, Xi'an, Shaanxi, China
e-mail: Xiexl@chd.edu.cn

S. Yadav et al. (eds.), *Energy Power and Automation Engineering*, Lecture Notes in Electrical Engineering 1118, https://doi.org/10.1007/978-981-99-8878-5_24

The difference lies in whether additional energy is consumed to control the battery temperature. Passive cooling system only relies on its own structure heat dissipation, more energy saving but limited heat dissipation effect, active cooling system has better heat dissipation/heating effect, but needs to consume extra work. At present, battery pack cooling methods mainly include air, liquid, phase change material, heat pipe, and so on. Air cooling has disadvantages such as insufficient cooling and poor temperature uniformity. The cooling structure of the phase change material is simple and temperature uniformity is good, but thermal conductivity of it is not sufficient. Heat pipe cooling is effective and does not require additional power, but the related research is still in the initial stage and the applicability is not enough. In recent years, the research of liquid cooling plate structure is increasing and liquid cooling has good thermal conductivity. Cai [3] proposed a parallel non-equal-length DC channel liquid cooling plate structure scheme, and designed the non-equal-length flow channel coolant from inside to outside in order to return in advance, which can slow down the flow of coolant to the outer flow channel and make the cooling effect more obvious. Gao [4] proposed a liquid cooling channel with GCD (gradient channel design), where cooling tube is divided into two sections in flow direction. The results show that in this structure, the arrangement of large channels in the front and four small channels at the rear increases the flow-solid contact area. With the continuous development of nanotechnology in recent years, phase change material emulsions are prepared by spitting phase change materials into fluid with the action of emulsifiers, resulting in superior accumulation energy capacity than water [5]. In particular, when their droplets shrink down to the nano scale, usually 20–500 nm [6], nano emulsions can be obtained with good dispersion stability [7]. The phase change material has a higher specific heat capacity than water due to its latent heat effect [8, 9]. So far, the application of phase change material emulsions in thermal management of batteries is seldom studied.

In this paper, nano phase change emulsion is used to replace water as the cooling medium for batteries thermal management. The CFD simulation method was used to analyze the influence of different coolant selection and coolant flow rate affects the temperature of a battery pack.

2 Simulation Model and Mesh Division

2.1 Material Selection

18,650 Li-ion battery is widely used at present, where 18 means the battery diameter is 18 mm, 65 means the battery height is 65 mm, 0 means the cylindrical battery, and its capacity is generally in 1200–3600 mAh, and its specific thermal physical parameters are shown in Table 1.

Table 1 18,650 battery properties

Density	Specific heat	Thermal conductivity	
		X, *Y* direction	*Z* direction
2765 kg/m^3	1300 J/kg K	1.07W/m K	19.03W/m K

Table 2 Thermo-physical properties of fluids

Material	c_p (J/kg K)	k (W/m K)	ρ (kg/m^3)	μ (mPa s)
Water	4180	0.6	998	1
10%OP28E	3930–9580	0.58–0.65	972	0.9–2.1
20%OP28E	3840–19,430	0.52–0.58	957	1.8–5.1

A common PCM (OP28E) was scattered in water to create 10% and 20% nano emulsions of OP28E. Water and OP28E phase change emulsion are selected as coolants for usage, respectively. Obviously, water is a pure liquid while the emulsion is a solid–liquid mixture in which OP28E is dispersed in water through an emulsifier. Nevertheless, PCM emulsions can still be considered as Newtonian fluids when the volume concentration of PCM is below 30% as described by Delgado [10] (the maximum volume concentration of PCM in this study is 20%). Since phase change processes exist in phase change emulsions, the variable specific heat capacity is used in this paper to simulate phase changes process. The relevant material thermal properties of OP28E [11] were shown in Table 2. Its specific heat curve with time is similar to a normal distribution, the maximum value is reached at 301–303 K (melting temperature of OP28E).

2.2 Physical Model

For complexity of the simulation, the cylindrical battery lug part is ignored as shown in Fig. 1a, where the cylinder battery is regarded as the heat source. Battery heat production is taken away by the fluid through the three vertical cooling channels embedded in the upper and lower copper cold plates. The reverse flow way is chosen as the flow pattern as shown in (b). The relevant dimensions are shown in (c) and (d). The influence of different coolant flow rates and different coolant types on the battery temperature uniformity and temperature rise is studied to provide strong foundation for the optimization and design of the thermal management system.

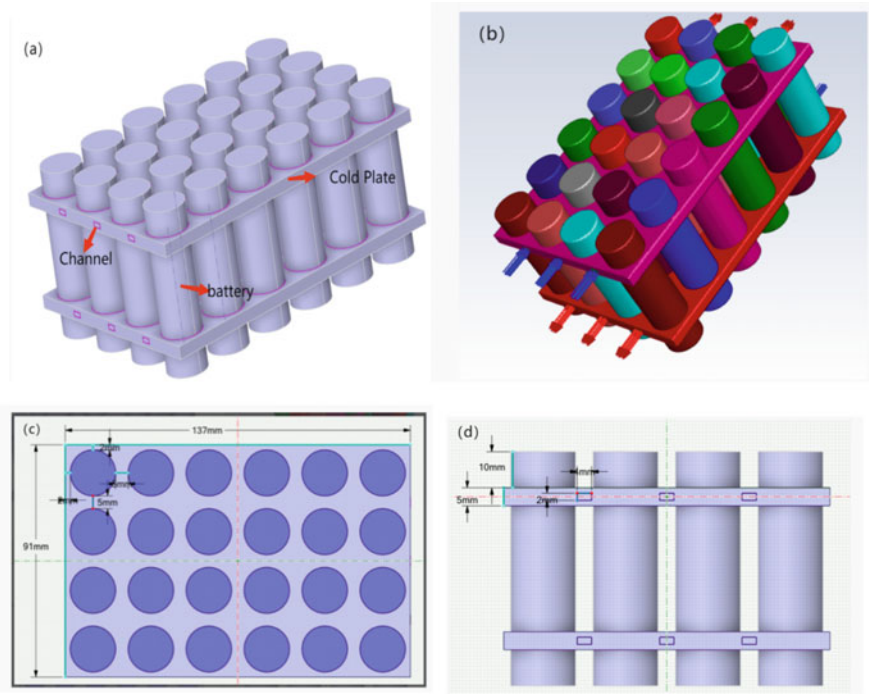

(a) Model diagrams; (b) Reverse flow; (c) Vertical view; (d) Side view

Fig. 1 Physical model of the battery pack

2.3 *Battery Heat Generation Model*

Bernardi started from both the entropic reaction of the cell and the internal resistance, assuming that the heat source of the cell is uniform and stable, thus proposing a typical formula for the heat generation rate, which is expressed as shown in Eq. (1).

$$q = \frac{I}{V}\left[(U_{\mathrm{oc}} - U) + T\frac{\partial U_{\mathrm{oc}}}{\partial T}\right] \tag{1}$$

where q is heat liberation rate, I is discharge current, V is the volume of the battery, U_{oc} is the open-circuit voltage, U is the battery working voltage, T is temperature, $\frac{\partial U_{\mathrm{oc}}}{\partial T}$ is the coefficient affected by temperature.

2.4 Liquid-Cooled Models

The cooling effect is investigated with different coolant. The energy, momentum, and continuity equation are calculated with Eqs. (2)–(4).

$$\frac{\partial}{\partial t}\left(\rho_c C_{p,c} T_c\right) + \nabla \cdot \left(\rho_c C_{p,c} \vec{V} T_c\right) = -\nabla \cdot (k_c \nabla T_c) \tag{2}$$

$$\frac{\partial_{\rho_c}}{\partial_t} + \nabla \cdot \left(\rho_c \vec{V} \vec{V}\right) = -\nabla p \tag{3}$$

$$\frac{\partial_{\rho_c}}{\partial_t} + \nabla \cdot \left(\rho_c \vec{V}\right) = 0 \tag{4}$$

where ρ_c is the coolant density, $C_{p,c}$ is the specific heat of coolant, T_c is coolant temperature, $\vec{V}$ is the velocity vector of fluid in the cooling plate, k_c is the thermal conductivity, p is pressure.

2.5 Grid Division

In the simulation of this paper, the initial ambient temperature is set to 300 K, and the battery is discharged at 5C discharge rate, assuming that the whole system does not have any heat exchange with the outside world, the fluid region is locally encrypted, three boundary layers are divided into the inner wall of the passage, and the body mesh is generated by polyhedra, the total number of meshes is 555,018, the overall mesh diagram is shown in Fig. 2. At the same time, in order to study the effect of different flow rates of coolant on the temperature field, the flow rate selected is 0.1–0.5 m/s. Re is less than 2300, regardless of whether the coolant is water or OP28E, so the momentum equation is set to laminar flow for simulation.

3 Results and Discussion

3.1 Effect of Different Coolant Choices on Battery Pack Temperature

Comparison of Cooling Performance When Different Coolant Flow Rates Are the Same

Three coolants were selected for comparison, namely, water, 10% OP28E nano emulsion, and 20% OP28E nano emulsion. The environment temperature, initial battery temperature, coolant inlet temperature are all 300 K. The inlet flow rate is 0.1 m/s.

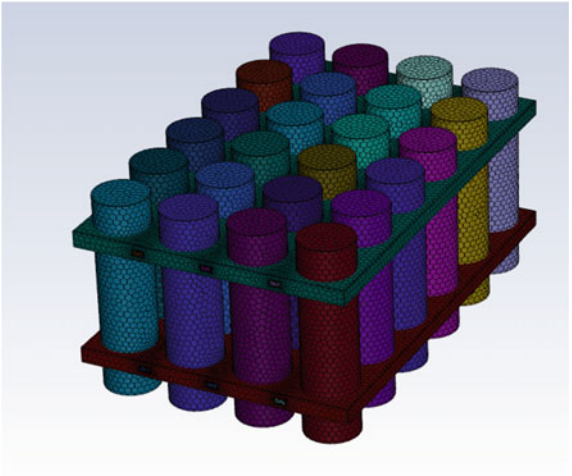

Fig. 2 Liquid cooling system integral grid

The maximum temperature, the maximum temperature difference with time obtained from the simulation are shown in Fig. 3.

From Fig. 3, it can be seen that contrasted with water, the cooling performance of 10% and 20% OP28E is better due to the existence of phase change process, and the maximum temperature and temperature difference are both lower than water. The cooling performance of 20% OP28E is slightly stronger than that of 10% OP28E.

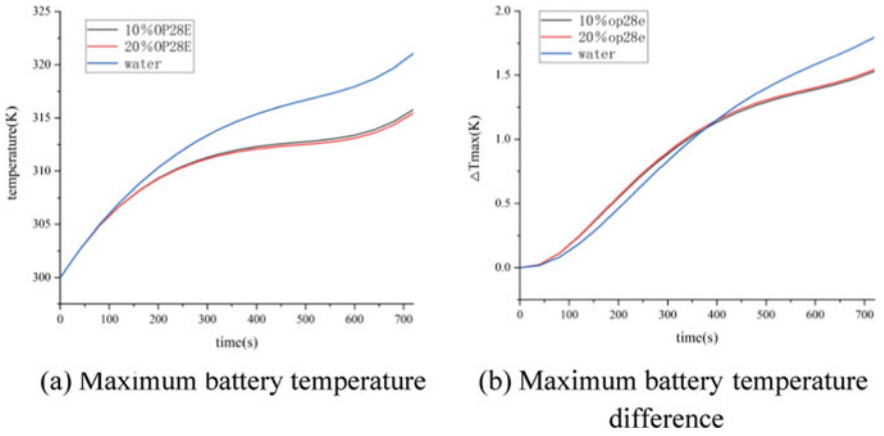

Fig. 3 The effect of different coolant on the battery

Comparison of Cooling Performance When Different Coolants Consume the Same Amount of Energy

Because of the higher viscosity of nano phase change emulsion, the pressure drop is higher when flowing, and the energy consumption will also be increased, at the flow rate of 0.1 m/s, the pressure drop of water is 71.22 Pa, 10% OP28E is 106.11 Pa, and the pressure drop of 20% OP28E is 244.10 Pa. Therefore, this paper combines the energy consumption and cooling effect to make a comprehensive evaluation of the three fluids and compare the cooling performance of the same three fluids under the same energy consumption, and the simulation results are shown in Fig. 4.

From Fig. 4, we can see that at the same flow rate, although nano phase change emulsion energy consumption is larger than water, but at the same pressure drop ($\triangle P = 400$ Pa), comparing the maximum temperature of the cell, the nano phase change emulsion still has advantages compared to water, and among them, 10% OP28E emulsion has the best cooling performance, so we finally choose 10% OP28E emulsion as the coolant.

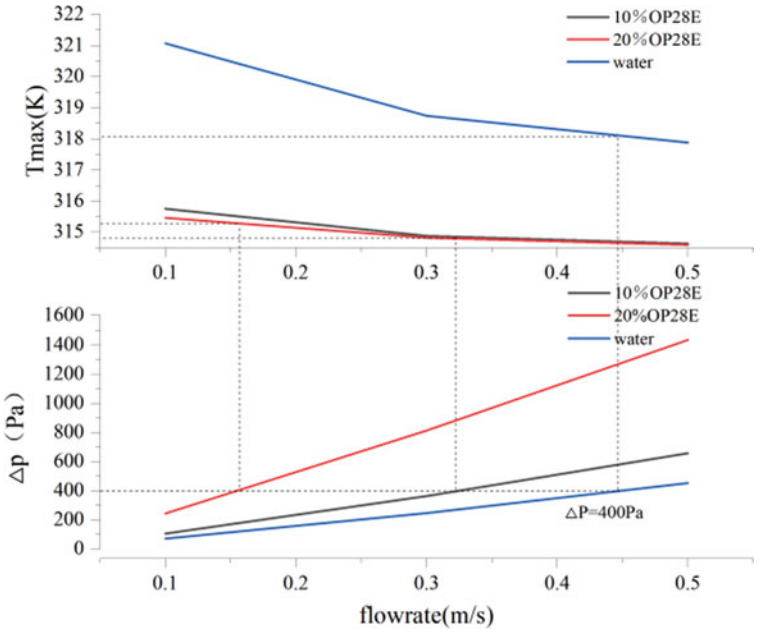

Fig. 4 Comparison of the maximum temperature of different coolants

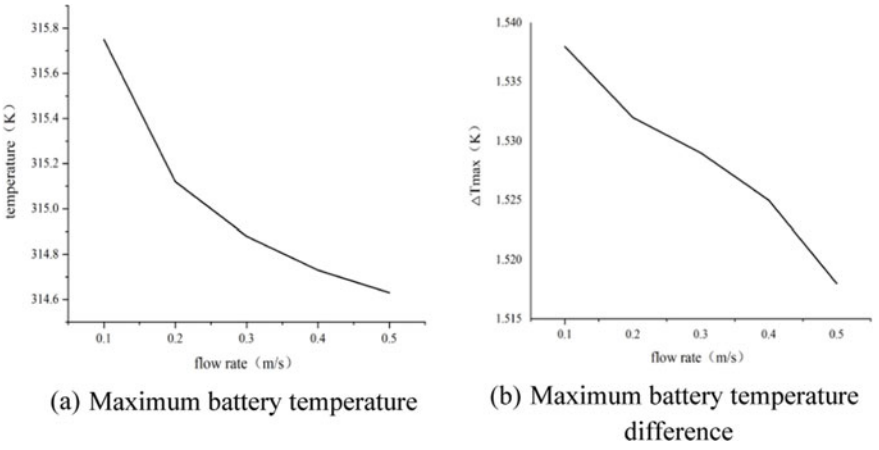

(a) Maximum battery temperature

(b) Maximum battery temperature difference

Fig. 5 The effect of different flow rate

3.2 Effect of Different Coolant Flow Rates on Battery Pack Temperature

The effect of the coolant flow rate on the battery pack temperature is equally important. In general, increasing coolant flow improves heat exchange rate and thus cooling performance. The ambient temperature, initial battery temperature, and coolant inlet temperature are all 300 K, the inlet flow rate is 0.1–0.5 m/s. 10% OP28E emulsion is used as the coolant for simulation. Battery maximum temperature, maximum temperature difference obtained by simulation along with the flow rate are shown in Fig. 5.

The maximum temperature keeps decreasing as the flow rate keeps increasing as shown in Fig. 5a, but the higher the flow rate, the slower the descent. The maximum temperature difference keeps decreasing as the flow rate keeps increasing, but the overall decrease is not very obvious as shown in Fig. 5b.

4 Conclusion

In this paper, a new thermal management scheme using OP28E nano phase change emulsion instead of water as the cooling medium is studied to satisfy the heat dissipation requirements at 5C discharge multiplier. FLUENT software was used to analyze the influence of different coolant selection and coolant flow rate on the temperature rise of battery. The research's conclusions are as follows:

(1) Flow rate is identical time, the cooling effect of OP28E nano phase change emulsion is stronger than water, although the high viscosity of the former results in high pressure drop, the cooling effect is still stronger than water at the same pressure drop, in which 10% OP28E emulsion is the best.
(2) Increasing the flow rate of coolant can improve the maximum temperature and temperature difference, but improvement effect is not obvious after the flow rate reaches a certain level.

References

1. Dong T, Peng P, Cao WK, Wang YW, Cen JW, Guo J (2019) Study on thermal management and safety of lithium-ion batteries. New Energy Prog 7(01):50–59. https://kns.cnki.net/kcms/detail/44.1698.TK.20190304.1718.010.html
2. Zhu X, Wang Z (2020) A review of research on thermal runaway and safety management of lithium-ion power batteries. J Mech Eng 56(14):91–118. https://doi.org/10.19535/j.1001-1579.2023.02.022
3. Cai L, Wei M et al (2021) Simulation of power battery cooling performance based on DC channel liquid cooling plate. J Automot Saf Energy Conserv 12(03):380–385. https://kns.cnki.net/kcms2/article/abstract?v=3uoqIhG8C44YLTlOAiTRKibYlV5Vjs7iy_Rpms2pqwbFRRUtoUImHS7c9Wo6yPGJiPgGId508yOJ6Iei9WKVdp2iju3n-FEe&uniplatform=NZKPT
4. Gao R, Fan Z (2022) A gradient channel-based novel design of liquid-cooled battery thermal management system for thermal uniformity improvement. J Energy Storage 48:2352–152X. https://doi.org/10.1016/j.est.2022.104014
5. Wang F, Lin W, Ling Z (2019) A comprehensive review on phase change material emulsions: fabrication, characteristics, and heat transfer performance. Sol Energy Mater Sol Cells 191:218–34. https://doi.org/10.1016/j.solmat.2018.11.016
6. Pey CM, Maestro A, Solé I, González C (2006) Optimization of nano-emulsions prepared by low-energy emulsification methods at constant temperature using a factorial design study. Colloids Surf A Physicochem Eng Aspects 288(1–3):144–50. https://doi.org/10.1016/j.colsurfa.2006.02.026
7. Agresti F, Fedele L, Rossi S, Cabaleiro D, Bobbo S et al (2019) Nano-encapsulated PCM emulsions prepared by a solvent-assisted method for solar applications. Solar Energy Mater Solar Cells 194:268–275. https://doi.org/10.1016/j.solmat.2019.02.021
8. Yu Q, Tchuenbou-Magaia F, Al-Duri B, Zhang Z, Ding Y (2018) Thermo-mechanical analysis of microcapsules containing phase change materials for cold storage. Appl Energy 211:1190–1202. https://doi.org/10.1016/j.apenergy.2017.12.021
9. Mikkola V, Puupponen S, Saari K, Ala-Nissila T (2017) Thermal properties and convective heat transfer of phase changing paraffin nanofluids. Int J Therm Sci 117:163–71. https://doi.org/10.1016/j.ijthermalsci.2017.03.024
10. Delgado M, Lázaro A, Mazo J (2012) Review on phase change material emulsions and microencapsulated phase change material slurries: materials, heat transfer studies and applications. Renew Sustain Energy Rev 16:253–273. https://doi.org/10.1016/j.rser.2011.07.152
11. Wang F, Cao J, Ling Z, Zhang Z (2020) Experimental and simulative investigations on a phase change material nano-emulsion-based liquid cooling thermal management system for a lithium-ion battery pack. Energy. https://doi.org/10.1016/j.energy.2020.118215

Application of Hydrogen Reburning Technology in Low Nitrogen Combustion in 660 MW Coal-Fired Boilers

Hufei Zhou, Fangqin Li, Xiaolei Zhang, Haoyang Li, and Jianxing Ren

Abstract Coal-fired boilers are one of the main sources of NO_x emissions, and controlling the generation and emission of nitrogen oxides is a hot issue of general concern in today's society. Hydrogen has the characteristics of "zero pollution", by analyzing the nature of hydrogen combustion, according to the principle of reburning, hydrogen is used as a reburning fuel in a 660 MW coal-fired boiler, and an embodiment scheme for hydrogen reburning to reduce NO_x generation is proposed. Through theoretical analysis and calculation, the technical parameters of hydrogen reburning are obtained, which effectively improves the denitration efficiency, and NO_x can be reduced by about 30%, which plays a positive guiding role for the application of hydrogen reburning in coal-fired boilers.

Keywords Hydrogen reburning · Low nitrogen combustion · NO_x

1 Introduction

The emission of pollutants from coal burning in China is relatively serious, especially the emission of NO_x. As early as the early twenty-first century, the proportion of NO_x emission in all pollutants reached 67%, 80% of which comes from the combustion of pulverized coal [1]. Therefore, as the main source of pollutants in coal-fired boilers, the control of nitrogen oxides is urgent.

H. Zhou (✉) · F. Li · H. Li · J. Ren
College of Energy and Mechanical Engineering, Shanghai University of Electric Power, Shanghai, China
e-mail: 1403172449@qq.com

X. Zhang
Department of Chemical and Process Engineering, University of Strathclyde, Glasgow, UK

S. Yadav et al. (eds.), *Energy Power and Automation Engineering*, Lecture Notes in Electrical Engineering 1118, https://doi.org/10.1007/978-981-99-8878-5_25

Low NO_x emission technologies include low NO_x burners, air stage combustion, flue gas recirculation, fuel stage combustion technology, etc. Fractional fuel combustion technology, also known as reburning technology, has the advantages of low cost of transformation, high efficiency of nitrogen removal, low possibility of furnace slagging and high temperature corrosion, thus it is a very effective way of nitrogen removal.

With the increasingly prominent problem of energy shortage, hydrogen, as a high energy density gas that does not directly produce CO_2, SO_2, soot, and other pollutants in the process of its utilization, is regarded as a clean fuel with the most potential for development at present [2]. Hydrogen has a certain reducibility to NO_x, and does not contain N element to cause secondary pollution. Hydrogen is used as the reburning fuel, and is directly injected into the furnace for reburning combustion according to certain requirements. The intermediate product of hydrogen mixed combustion is used to reduce NO_x and generate N_2, so as to achieve the purpose of reducing the NO_x emission in the boiler furnace.

2 Physicochemical Properties and Combustion Characteristics of Hydrogen

The physical and chemical properties of hydrogen are shown in Table 1 [3]. Hydrogen has a small molecular mass but a large heat per unit mass. The diffusion coefficient of hydrogen in air is 0.61 cm^2/s (1 atm, 20 °C), and the flame propagation velocity is 2.75 m/s^{-1}, this is much larger than most hydrocarbon gas fuels, such as natural gas, oil, and methane. If released in the air, it can quickly spread out and reach a burning concentration. The minimum ignition energy of hydrogen in air is only 0.02 MJ, and the quenching distance is 0.64 mm. Compared to abovementioned hydrocarbon fuels, hydrogen is much smaller. It has strong ignition property and improved combustion thermal efficiency, and it is not easy to quench. Hydrogen is more prone to spontaneous combustion, and is usually grounded during transport to prevent combustion caused by static electricity. The hydrogen explosion limit is 4–75 V%. If the pipeline equipment is not strictly controlled, the hydrogen will leak and explode. Therefore, the safety of the pipeline or equipment during hydrogen transportation needs to be strictly controlled.

Table 1 Physical and chemical properties of hydrogen

Project name	Hydrogen	Project name	Hydrogen
Molecular mass	2.1588	Diffusion coefficient in air ($cm^2\ s^{-1}$)	0.61
Density ($g\ L^{-1}$)	0.089	Explosion limit (V%)	4–75
Boiling point (°C)	− 252.8	Flame propagation velocity ($m\ s^{-1}$)	2.75
Gas–liquid volume ratio ($L\ L^{-1}$)	974	Heat of vaporization ($kJ\ kg^{-1}$)	305
Low calorific value ($MJ\ m^{-3}$)	12.8	Ignition temperature (°C)	582 (Air) 450 (O_2)
Minimum ignition energy in air (mJ)	0.02	Flame temperature (°C)	2045 (Air) 2660 (O_2)
Specific heat capacity ($kJ\ kg^{-1}\ K^{-1}$)	10.21	Quenching distance (mm)	0.64

3 Principle and Influencing Factors of Hydrogen Reburning

3.1 Reburning Principle

Reburning NO_x reduction technology is to inject the reburning fuel by the nozzle added between the main combustion zone and the burnout zone, and then the nitrogen oxide generated in the main combustion zone and the reducing intermediate products such as CHi, NHi, HCN generated by the combustion reaction of the reburning fuel in the furnace will undergo reduction reaction to produce N_2, so as to reduce the NO_x emission. Finally, appropriate burnout air is added in the burnout area to make it burn out completely.

Considering that reburning fuels, such as natural gas and biomass, reduce nitrogen oxides by combining with reducing substances, such as intermediate products CHi and NHi, the main reaction process is $CH_4 + O \rightarrow CH_3 + NO \rightarrow HCN + O \rightarrow NH + H \rightarrow N + NO \rightarrow N_2$. Similarly, in biomass gas reburning technology, CH_4, CO, H_2, and other substances and unfinished combustion products CO, H_2, C, CnHm react with NO_x generated in the main combustion zone to generate N_2 for denitration treatment [4].

According to the combustion characteristics, physical and chemical properties and reburning mechanism of hydrogen, hydrogen is a kind of clean fuel, easy to burn, and reductive to most metal oxides. When reacting with NO, reducing substances such as NHi and HNO are generated, which have the same reducing property as methane. The reaction is $2NO + 2H_2 \rightarrow N_2 + 2H_2O$, and its main denitration reactions are listed in Eqs. (1)–(3) [5]:

$$H + NO + M \rightleftharpoons HNO + M \text{ (is the intermediate product)} \quad (1)$$

$$HNO + H \rightleftharpoons NH + OH \quad (2)$$

$$NH + NO \rightleftharpoons N_2 \quad (3)$$

3.2 *Factors Affecting the Formation of NO_x*

The factors affecting hydrogen reburning are roughly the same as gas reburning fuel. The main influencing factors include reburning zone temperature, reburning fuel amount, excess air coefficient, and reburning zone residence time. The residence time of the reburning zone is 0.6 s–1.1 s, which is suitable [6]. Too short residence time will lead to insufficient reduction and insignificant NO_x reduction efficiency. Too long residence time will not increase NO_x reduction, but reduce fuel combustion efficiency. The excess air coefficient in the reburning zone is 0.85–0.9. When the excess air coefficient is too small, the reducing intermediates such as NHi and HCN produced by combustion will enter the burnout zone and be oxidized to generate NO. When the excess air coefficient is too large, the reducibility of the reburning zone is weakened, and the intermediate NHi and HCN used to reduce NO_x are reduced, which is not conducive to the reduction of NO_x. The temperature of most reburning fuels is more appropriate at 1250 °C. Too low temperature will lead to insufficient reduction of NO_x and cannot achieve a better denitration rate. As the temperature continues to rise, some reburning fuel reduction NO_x will reach the extreme value, and the burnout zone will generate a large number of thermal NO_x in the oxygen-rich environment, ultimately leading to the increase of NO_x emissions.

4 Implementation of Hydrogen Reburning Technology for 660 MW Coal-Fired Boiler

4.1 *Boiler Overview*

The study subjects were a 660 MW quadrate tangential pulverized coal boiler with subcritical pressure primary intermediate reheat control cycle drum furnace. The combustion mode with four corners and swinging pulverized coal nozzle are adopted. The furnace section is 16.44 m deep, 19.558 m wide, and 57 m high. The four corners of the burner are arranged in circular shape. The primary air nozzle is 6 layers. There are 24 nozzles in total. Secondary air 7 layers, a total of 28 nozzles; Burnout air 2 layers, total of 8 nozzles. The area of the primary air nozzle is 0.6 m × 0.6 m, and

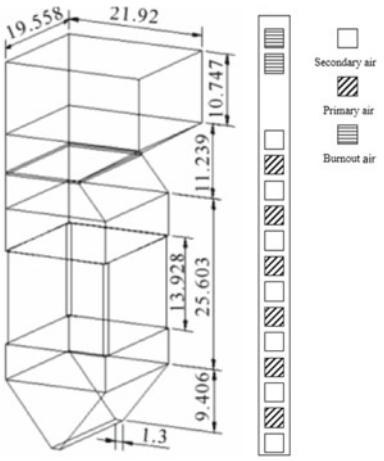

Fig. 1 Furnace structure and burner nozzle layout before modification, unit m

the area of the secondary air nozzle is 0.6 m × 0.75 m. Primary air and secondary air nozzle interval arrangement. The burnout air area is 0.6 m × 0.75 m. The Furnace structure and burner nozzle layout before modification is shown in Fig. 1. The effect of inhibiting NO_x generation in the furnace is mainly studied, so the influence of superheater on the upper part of the furnace is ignored [7]. The boiler main design parameters and combustion system parameters are shown in Table 2. The industrial analysis and element analysis of coal are shown in Table 3.

4.2 Implementation Plan of Hydrogen Reburning

The principle of reburning technology is shown on the left in Fig. 2, the hydrogen nozzle is located at the four corners of the combustion zone, above the main combustion zone and below the burnout zone, so as to ensure sufficient residence time of hydrogen and achieve better denitrification effect. The injection Angle is consistent with the primary air Angle to ensure the cutting round burning of the boiler [8]. The calorific value of hydrogen is relatively high. In order to reduce the influence of hydrogen on combustion, the area of hydrogen nozzle should be reduced by reducing the height of the nozzle, which is about 0.6 m × 0.1 m. First of all, fuel and air accounting for 70–95% of the total heat of the boiler is injected into the main combustion zone, and the excess air coefficient is greater than 1, and hydrogen fuel and air accounting for 5–30% of the total heat of the boiler is injected into the reburning zone, and the excess air coefficient is less than 1, the excess air in the burnout area is greater than 1. The application on the actual 660 MW coal-fired boiler is shown on the right in Fig. 2.

Table 2 Boiler main design parameters and combustion system parameters

Project name	Numerical value	Project name	Numerical value
Main steam flow (t h^{-1})	1969.7	Reheat steam temperature (°C)	543
Reheat steam flow (t h^{-1})	1733.4	Water supply pressure (MPa)	21
Main steam pressure (MPa)	18.1	Water supply temperature (°C)	275
Main steam temperature (°C)	540	Fuel consumption (t h^{-1})	299.783
Reheat steam pressure (MPa)	3.9	Boiler efficiency (%)	93
Primary air velocity (m s^{-1})	24.09	Secondary air velocity (m s^{-1})	55.40
Primary air temperature (°C)	298	Secondary air temperature (°C)	308
Burnout air velocity (m s^{-1})	49.69	Furnace outlet smoke temperature (full load) (°C)	1135
Burnout air temperature (°C)	308	NO_x mass concentration at furnace outlet (full load) (mg m^{-3})	298

Table 3 The proximate and ultimate analysis results of the coal

Industrial analysis w_{ar} (%)				Elemental analysis w_{daf} (%)					Low calorific value (kJ kg^{-1})
M	A	V	FC	C	H	O	N	S	
15	22.95	25.44	36.61	77.90	5.30	13.91	13.91	13.91	18,645

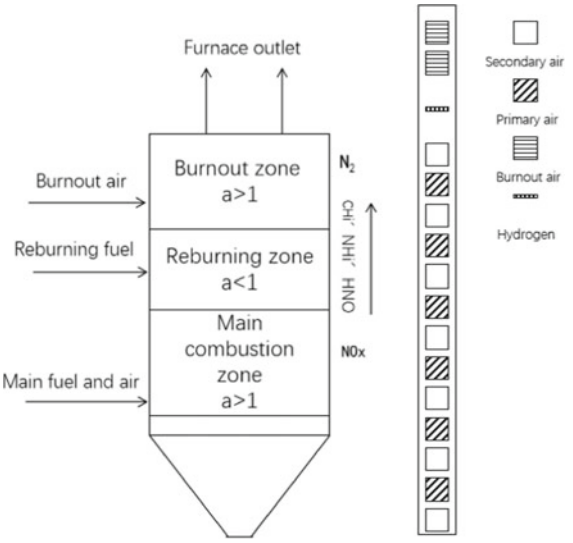

Fig. 2 Principle of reburning technology and burner nozzle layout after modification

4.3 Effect of Hydrogen Reburning on NO_x Formation

According to the design parameters of coal-fired boilers, coal consumption is shown in Eq. (4):

$$B_{\text{coal}} = \frac{Q_{yx}}{Q_{\text{net,ar}} \times \eta} \tag{4}$$

where: B_{coal} is the consumption of coal during pure coal combustion, kg/h; Q_{yx} is the heat absorption per hour of steam in the boiler, kJ/h; $Q_{\text{net,ar}}$ is the low calorific value of pulverized coal, kJ/kg; η is the boiler thermal efficiency, %.

In the process of hydrogen reburning, hydrogen replaces part of pulverized coal for combustion in the furnace. Under full load, according to the heat contained in the unit mass of the reburning fuel, it can be calculated that the flow rate of hydrogen is about 12.13 m^3/s. Four spouts are arranged in total, and the flow rate of a single spout is about 3.03 m^3/s. The formula is as follows [9]:

$$q_H = \frac{B_{\text{coal}} \times Q_{\text{net,ar}} \times \beta}{3600 \times Q_H} \tag{5}$$

where, q_H is hydrogen flow, m^3/s; β is hydrogen reburning ratio; Take 10%. Q_H is the energy released by burning hydrogen per unit volume at a certain temperature, kJ/m^3.

Under the reburning condition, the required coal consumption is:

$$B_0 = B_{\text{coal}} \times (1 - \beta) \tag{6}$$

where, B_0 is the coal consumption required for hydrogen reburning, kg/h.

The theoretical amount of air consumed by pulverized coal combustion is:

$$V^0 = B_0 \times (0.0889 \times (C_{\text{ar}} + 0.375 \times S_{\text{ar}}) + 0.265 \times H_{\text{ar}} - 0.0333 \times O_{\text{ar}}) \tag{7}$$

where, V^0 is the theoretical air amount consumed by pulverized coal combustion, Nm^3/s; C_{ar}, S_{ar}, H_{ar}, O_{ar} are received base element analysis of the designed coal, respectively, %.

Hydrogen combustion equation is $H_2 + 0.5O_2 \rightarrow H_2O$. Then 0.5 mol oxygen is needed to complete the combustion of 1 mol hydrogen. Under standard conditions, the theoretical and actual air amount consumed by hydrogen combustion is:

$$V_H^0 = 1000 \times \left(3.222 \times 0.5 \times 22.4 \times 10^{-3}\right)^{-1} \times (0.21)^{-1} \tag{8}$$

$$V_L = \left(V^0 + V_H^0\right)\alpha \tag{9}$$

where, V_H^0 is the theoretical amount of air consumed by hydrogen combustion. V_L is the actual amount of air consumed by hydrogen reburning, m^3/s; α is the excess air coefficient; Take 1.2.

The inlet velocity of the reignition nozzle is [10]:

$$V_a = \frac{q_H}{4 \times S_b} \tag{10}$$

where, V_a is the injection velocity of reburning fuel, m^3/s; S_b is the area of the reburning fuel nozzle, m^2.

The theoretical and actual smoke volume during fuel combustion are shown in Eqs. (11) and (12), respectively:

$$\begin{aligned} Vy_0 = {} & 1.866(C_{\text{ar}} + 0.375S_{\text{ar}}) \times 100^{-1} + 0.79V^0 + 0.8N_{\text{ar}} \times 100^{-1} \\ & + 0.111H_{\text{ar}} + 0.0124M_{\text{ar}} + 0.016V^0 + 1.24G_{\text{wh}} \end{aligned} \tag{11}$$

$$V_y = Vy_0 + (a-1)V^0 + 0.0161(a-1)V^0 \tag{12}$$

where, Vy_0 is the theoretical smoke volume, G_{wh} is the amount of steam consumed during atomizing fuel, kg/kg. V_y is the smoke volume generated by fuel, Nm^3/kg.

The amount of nitrogen oxides generated by fuel combustion can be calculated as follows [11]:

$$G_{\text{NO}_x} = 1.63B(\varepsilon \cdot n + 10 - 6V_y \cdot C_{\text{NO}_x}) \tag{13}$$

where, G_{NO_x} is the amount of nitrogen oxide (NO_2 meter) generated by fuel combustion, kg; B is coal consumption, kg; ε is the conversion rate of combustion nitrogen to fuel type NO (%), which is 25–50% ($n \geq 0.4\%$) for coal-burning layer furnaces and 20–25% for pulverized coal furnaces; n is the content of nitrogen in fuel (%); C_{NO_x} is the thermal NO concentration, mg/Nm^3, usually 93.8 mg/Nm^3. The analysis results are shown in Table 4.

Table 4 Hydrogen reburning parameters at full load

Project name	Hydrogen	Project name	Hydrogen
Excess air coefficient	1.25	Reburn fuel injection velocity (m^3/s)	50.54
Boiler efficiency (%)	92.2	Reburning nozzle size (m)	0.6 × 0.1
Reburning ratio (%)	10	Reburning zone temperature (°C)	1250
Pulverized coal consumption (kg/h)	2.7×10^5	Furnace outlet smoke temperature (°C)	1137
Hydrogen flow rate (m^3/s)	12.13	NO_x content in furnace outlet ($mg\ m^{-3}$)	208.6

Hydrogen reburning, resulting in the increase of water vapor in the furnace flue gas, heat capacity, that is, the increase of the heat released by the flue gas per reduction of 1 °C, that is, when the soda, air in the absorption of the same amount of heat in the same situation caused by the temperature reduction of flue gas, so the boiler with the increase of water shows the characteristics of heat release lag. Therefore, the phenomenon of smoke exhaust temperature will rise. Through theoretical analysis and reference to relevant literature, the implementation of hydrogen reburning technology in coal-fired boilers can reduce NO_x by about 30%.

5 Conclusion

(1) According to the reburning principle, through the analysis of the physical and chemical properties of hydrogen, hydrogen is a clean fuel that can be used as a reburning fuel to control the generation and emission of NO_x in coal-fired boilers.
(2) For the implementation of hydrogen reburning in 660 MW coal-fired boiler, the implementation plan is proposed through theoretical analysis and calculation, and the technical parameters of hydrogen reburning are determined. The denitration efficiency is high when the reburning zone of coal-fired boiler furnace stays 0.6–1.1 s, the excess air coefficient is 0.85–0.9, the temperature is about 1250 °C, the reburning nozzle area is 0.6 m × 0.1 m, the reburning ratio is 10%, the hydrogen flow rate is 12.13 m^3/s, and the hydrogen injection speed is 50.54 m^3/s. It can reduce NO_x by about 30%.
(3) Hydrogen reburning has a wide application prospect, but the process of combustion in the furnace during hydrogen reburning is complicated, the theoretical analysis is not mature, and the reburning experiment or numerical simulation needs to be further improved and strengthened.

Acknowledgements This work was partially funded by Shanghai Science and Technology Project (21DZ1207203).

References

1. Lin Q, Pan WG, Li MD (2004) Status quo and development tendency of combustion technique with NO_x reduction by reburning. J Gen Equip 06:346–349+ 358. https://doi.org/10.3969/j.issn.1671-086X.2004.06.006
2. Zhao QX, Wang ZY, Deng SF et al (2022) Hydrogen combustion technology and progress. J Sci Technol Eng 22(36):15870–15880. https://doi.org/10.3969/j.issn.1671-1815.2022.36.003
3. Xu D, Liu Y, Li ZY et al (2021) A cost-efficiency review of hydrogen energy exploitation. J Oil Gas New Energy 33(2):50–56. https://doi.org/10.3969/j.issn.2097-0021.2021.01.011

4. Zhang XT, Duan FY, Huang Y, Wang AJ (2020) Numerical simulation on biomass gas re-burning in a 660 MW coal-fired boiler. J Thermal Power Gen 49(03):38–44. https://doi.org/10.19666/j.rlfd.201911175
5. Glarborg P, Kristensen PG, Dam Johansen K et al (2000) Nitric oxide reduction by non-hydrocarbon fuels. Implications for reburning with gasification gases. J Energy Fuels 14(4):828–838. https://doi.org/10.1021/ef990186r
6. Wang PT, Wang NJ, Liang X, Niu F (2019) Denitration mechanism and engineering application progress of gas fuel reburning. J Clean Coal Technol 25(06):51–60. https://doi.org/10.13226/j.issn.1006-6772.19011401
7. Liu SJ, Lu XA, Cheng ST et al (2020) Numerical simulation of mixed combustion of biomass gas in a quadrangle tangential power station boiler. J Energy Conserv 39(12):45–48. https://doi.org/10.3969/j.issn.1004-7948.2020.12.013
8. Ma XL (2018) Feasibility study on NO_x reduction by biomass gas reburning. J Sci Technol Innov Herald 15(20):93–94 + 96. https://doi.org/10.16660/j.cnki.1674-098X.2018.20.093
9. Liu X, Ren JX, Li FQ, Li KJ (2023) Numerical simulation of effect of primary air mixed with hydrogen and oxygen on furnace temperature of coal-fired boiler. J Therm Power Eng 38(01):156–163. https://doi.org/10.16146/j.cnki.rndlgc.2023.01.019
10. Zhang WD (2021) Research on pollutant emissions of biomass gas re-burning in a 600 MW coal-fired boiler. D. North China University of Water Resources and Electric Power. Zhengzhou, Henan Province. https://doi.org/10.27144/d.cnki.ghbsc.2021.000206
11. Ruan Q, He WJ, Jiao JJ (2017) Exploration on the calculation method of NO_x source intensity in environmental impact assessment of metallurgical lime shaft kiln production line. J Low Carbon World 34:5–6. https://doi.org/10.16844/j.cnki.cn10-1007/tk.2017.34.003

Study on the Optimization of Grinding Efficiency in Gold Mine Concentrator

Guangsheng Li, Xingfu Zhu, Xiangwei Qin, Mingming Cai, and Chao Xu

Abstract Through the investigation of the mill grading process of the concentrator, the operation concentration is determined, analyze the feeding and drainage of the ball mill, feed, overflow and sand return, and understand the problems of various operations, production status of various processes and units in the mill grading process, and evaluate the reasons of 10% of + 0.6 mm content of the selected material. Through the optimization of process parameters, adjusting the amount of grinding and grading supplement, the grinding concentration and grading concentration are reasonably controlled, and the particle size composition of operation products is optimized. Through the optimization of equipment parameters, the size of hydrocyclone overflow core and sand settling nozzle are adjusted to optimize the classification effect. Through the optimization of grinding efficiency, the content of + 0.6 mm was reduced from 10% to less than 1%, and the content of − 0.074 mm increased from 45 to 50%; the recovery rate increased from 93.17 to 93.41%, increasing by 0.24%.

Keywords Gold mine · Concentrator · Optimization of grinding efficiency

1 Introduction

The purpose of grinding is to make all or most of the useful components in the ore to achieve the separation of monomer, and at the same time to avoid the phenomenon of "overgrinding" as far as possible, and to achieve the particle size of the selection operation, so as to create conditions for the effective recovery of the useful components in the ore. The quality of the selection index depends on the quality of the grinding products to a large extent. If the fineness of the grinding products is not enough, and the mineral particles do not achieve sufficient monomer separation from each other, then the selection index will not be too high. If the mud produced by grinding,

G. Li · X. Zhu · X. Qin (✉) · M. Cai · C. Xu
Metallurgical Laboratory Branch of Shandong Gold Mining Technology Co., Ltd., Shandong 261441, Laizhou, China
e-mail: 287506806@qq.com

S. Yadav et al. (eds.), *Energy Power and Automation Engineering*, Lecture Notes in Electrical Engineering 1118, https://doi.org/10.1007/978-981-99-8878-5_26

regardless of the dressing method can not be effectively recovered. Grinding operation also depends on the economic indicators of mineral processing. Grinding is an operation with the most power consumption in concentrator. Improving the grinding operation, improving the product quality of the mill, reducing the grinding cost, and improving the productivity of the mill can not only improve the concentrate quality and metal recovery rate. Moreover, it is of great significance to reduce the total cost of beneficiation and improve the productivity of the concentrator [1, 2].

Hydrocyclone is a classification equipment that uses centrifugal force to achieve ore settlement. It has large processing capacity and high grading efficiency. It is mostly used for the second section of closed grinding classification. The main components are cylinder, feed pipe, overflow pipe, overflow pipe, and sand settling mouth [3, 4].

2 Selecator Process

The design processing capacity of the concentrator is 3000 t/d. The crushing process is adopted, and the final particle size of the crushing product is P80 = 10 mm. The grinding grading process adopts two sections of two closed circuit grinding grading process, and one section of grinding grading process is divided into two series. Each series adopts one MQG2.7 × 3.6 m wet lattice ball mill and one 2FLGφ2.0 m high weir double screw grading machine to form the closed circuit grinding grading system. The grader overflow grades through the 710 mm cyclone, and the cyclone sinks the sand into a MQY2.7 × 3.6 m wet overflow ball mill to form a two-section closed circuit mill, and the cyclone overflows into the flotation operation. The flotation operation adopts one coarse, two sweeping, and two selective process. The flotation tailings are preferentially used for underground filling, and the excess tailings pond is stored. The flotation gold concentrate is transported to the gold smelter by concentrated pressure filter.

3 Inspection of Grinding Ore Grading Process

3.1 Preparation Work Before the Process Inspection

In order to ensure the smooth development of the process investigation and ensure that all the samples are representative, strict preparations are carried out before the process examination. Organize mill grading process, determine 12 sampling points; confirm sampling time at 9:00 am and finish sampling time at 2:00 PM, with sampling times of 11 times; formulate sampling plan, clarify sampling requirements, and train sampling personnel on sampling technology and sampling requirements [5, 6].

3.2 Process Investigation Results

Production Situation Records

As can be seen from Table 1, during the sampling period, the 1# ball mill treated 63.7 t/h and the 2# ball mill treated 64.1t/h.

Sample Concentration at the Sampling Point

As can be seen from Table 2, one section of grinding ball mill, that is, the moisture of the crushing final product is about 6%; the discharge concentration of 1# ball mill is 71.2%, in the normal range; the discharge concentration of 2# ball mill is 68.5%; and the discharge concentration of 3# ball mill is 69.1%, which basically meets the requirements. The overflow concentration of 1# grading machine is 64.7%, and sand return concentration is 79.2%; 60.0%, and sand return concentration is 78.1%; the overflow concentration and sand return concentration of grading machine are consistent with the empirical value. Rofeed concentration is 62.8%, high; overflow concentration is 52.2%, high; sediment concentration is 76.0% [7].

Grain Size Screening Results

It can be seen from Tables 3 and 4 that the content of d 15 mm is 8–10%, and the maximum particle size is $D = 18$ mm; the ball mill is about 13 mm; the ball mill is $+ 6$ mm is about 50%; the $d \leqq 0.045$ mm content of the ball mill is about 6%, and the mixing of filling. The content of d 1 mm is between 20 and 25%; the content of $d \leqq 0.074$ mm is between 20 and 25%. From the comparison of two mines −

Table 1 Record of accumulated ore quantity of ball mill

Number	Starting ore volume (t/h)	End of ore volume (t/h)	Accumulated volume (t/h)	Average ore volume (t/h)
1#	15,893.7	16,212.4	318.7	63.7
2#	16,034.2	16,354.6	320.4	64.1

Table 2 Statistics of sample concentration at the sampling points

Sample point	Potency (%)	Sample point	Potency (%)
1# ball mill to feed the ore	94.0	1# classifier overflow	64.7
1# ball mill to drain the ore	71.2	1# grading machine sand return	79.2
2# ball mill to feed the ore	93.7	2# classifier overflow	60.0
2# ball mill to drain the ore	68.5	2# grading machine sand return	78.1
3# ball mill to drain the ore	69.1	Cyclone overflow	52.2
The cyclone feeds the mine	62.8	Torrent sink sand	76.0

0.074 mm, the effect of high grinding concentration is better than that of low grinding concentration within a certain range. The content of d 1 mm is about 7%; the content of $d \leqq 0.074$ mm is about 30%. The content of d 3 mm is about 20%; the content of $d \leqq 0.074$ mm is about 6%.

As can be seen from Table 5, The cyclone feeds the mine + 0.6 mm content is 17.38% and − 0.074 mm content is 25.27%; Cyclone overflow + 0.6 mm content is 10.98% and − 0.074 mm content is 44.43%.

Table 3 1 results of ball mill

Grade (mm)	Productivity (%)			
	Ball mill feed mine	Ball mill drainage	Classifier overflow	Grading machine sand return
+ 15	8.76	–	–	–
− 15 + 10	20.61	–	–	–
− 10 + 6	20.76	–	–	–
− 6 + 3	13.66	7.24	–	22.67
− 3 + 1	9.41	15.09	7.26	41.42
− 1 + 0.25	9.93	29.49	30.40	22.61
− 0.25 + 0.074	8.68	25.27	30.25	8.18
− 0.074 + 0.045	2.11	6.33	8.16	1.06
− 0.045	6.17	16.58	23.93	4.06
Amount to	100	100	100	100

Table 4 2 results of ball mill

Grade (mm)	Productivity (%)			
	Ball mill feed mine	Ball mill drainage	Classifier overflow	Grading machine sand return
+ 15	10.21	–	–	–
− 15 + 10	23.78	–	–	–
− 10 + 6	19.18	–	–	–
− 6 + 3	12.21	8.31	–	20.36
− 3 + 1	8.96	16.69	6.68	30.14
− 1 + 0.25	8.57	31.29	31.25	26.01
− 0.25 + 0.074	8.77	22.32	32.43	15.63
− 0.074 + 0.045	2.05	4.61	7.46	2.1
− 0.045	6.27	16.78	22.18	5.76
Amount to	100	100	100	100

Table 5 Grain size screening results of two-stage grinding grade products

Grade (mm)	Productivity (%)		
	The cyclone feeds the mine	Cyclone overflow	Torrent sink sand
+ 1	5.73	0.85	12.12
− 1 + 0.6	17.38	10.98	27.93
− 0.6 + 0.25	16.61	20.84	24.38
− 0.25 + 0.074	35.01	22.90	24.57
− 0.074 + 0.045	6.11	9.28	3.1
− 0.045	19.16	35.15	7.9
Amount to	100	100	100

4 Process Flow Calculation

4.1 Calculation of Sand Return Ratio

Calculated according to the content of − 0.074 mm in the graded operation product

$$i1 = \frac{c-a}{a-b} \times 100\% = \frac{32.09 - 22.91}{22.91 - 5.12} \times 100\% = 51.6\%$$
$$i2 = \frac{c-a}{a-b} \times 100\% = \frac{29.64 - 21.39}{21.39 - 7.86} \times 100\% = 60.98\%$$
$$i3 = \frac{c-a}{a-b} \times 100\% = \frac{44.43 - 25.27}{25.27 - 11} \times 100\% = 134.27\%$$

4.2 Classification Efficiency Calculation of the Grading Machine

$$E1 = \frac{100(\beta-\alpha)(\alpha-\theta)}{\alpha(100-\alpha)(\beta-\theta)} \times 100\%$$
$$= \frac{100 \times (32.09 - 22.91) \times (22.91 - 5.12)}{22.91 \times (100 - 22.91) \times (32.09 - 5.12)} \times 100\% = 34.29\%$$
$$E2 = \frac{100(\beta-\alpha)(\alpha-\theta)}{\alpha(100-\alpha)(\beta-\theta)} \times 100\%$$
$$= \frac{100 \times (29.64 - 21.39) \times (21.39 - 7.86)}{21.39 \times (100 - 21.39) \times (29.64 - 7.86)} \times 100\% = 30.48\%$$
$$E710 = \frac{100(\beta-\alpha)(\alpha-\theta)}{\alpha(100-\alpha)(\beta-\theta)} \times 100\%$$

$$= \frac{100 \times (44.43 - 25.27) \times (25.27 - 11)}{25.27 \times (100 - 25.27) \times (44.43 - 11)} \times 100\% = 43.31\%$$

4.3 Mill Utilization Coefficient

Calculated according to the newly generated − 0.074 mm content

$$K1 = \frac{\gamma Q}{V} = \frac{(0.2291 - 0.0828) \times 63.7}{18.5} = 0.51\,\text{t/m}^3\,\text{h}$$
$$K2 = \frac{\gamma Q}{V} = \frac{(0.2139 - 0.0832) \times 64.1}{18.5} = 0.45\,\text{t/m}^3\,\text{h}$$
$$K3 = \frac{\gamma Q}{V} = \frac{(0.2411 - 0.11) \times 63.9}{18.5} = 0.45\,\text{t/m}^3\,\text{h}$$

5 Optimization and Adjustment

5.1 Optimization of Process Parameters

According to the results of the process investigation, the operating conditions affecting the grinding grading effect are optimized and adjusted [8–10].

(1) The grinding concentration of 2# ball mill is 68.5%, and the grinding concentration is optimized by reducing the water added to the mine, which is increased to about 75%.
(2) The feed concentration of the cyclone is 62.8%, and the concentration is too high, affecting the grading effect, and the graded overflow concentration is 52.2%. By adding water pipe at the feeding pump tank, increasing the supplementary water quantity, reducing the feed concentration, and controlling the feed concentration of the cyclone at about 55%, so as to optimize the grading effect.

5.2 Optimization of Equipment Parameters

After checking the cyclone, it is found that the cyclone cylinder and cone wear seriously, but the cylinder and cone interior are not smooth, which affects the overflow core size of the cyclone is large, and the size of the settling nozzle is small.

The parameters of 710 cyclone were optimized and the badly worn cylinder and cone were replaced; the size of overflow core was changed from 320 to 260 mm; and the size of sand settling nozzle was changed from 110 to 130 mm to optimize the classification effect.

5.3 Optimize the Application Situation

Through optimization and adjustment, the particle size of the selected materials is significantly thinner without coarse particles. For sampling and screening analysis of the optimized second stage grinding products, the overflow of + 0.6 mm is 0, − 0.074 mm is 53.14%; the composition of the overflow was significantly improved, and the classification efficiency increased to 51.86%.

6 Conclusion

(1) Through the process investigation, the reasons for the coarse size of flotation are found out, and the operation state of the grinding grading system is understood. The problem of coarse grain size is solved through the optimization of process parameters and equipment parameters.
(2) The results of the process investigation show that through the operation concentration detection of each operation point, the grinding concentration of 2# ball mill is low, and the ore concentration of 710 cyclone is too high. Through the particle size screening of each operation product, the grinding mineral material is the crushing final product P80 = 13 mm, the particle size of the selected material is coarse, and the 10.98%, − 0.074 mm content of + 0.6 mm is 44.43% [11].
(3) The calculation results of the process show that the grading efficiency of the graded spiral grader is about 30%; the grading efficiency of the 710 hydrocyclone is 43.31%, and the grading efficiency is low. The utilization coefficient of the ball mill is calculated at 0.5 t/m^3 according to the newly generated -0.074 mm content.
(4) Through the optimization of process parameters and equipment parameters, the cylinder, cone, overflow core, and sand settling nozzle of the cyclone were replaced, the classification overflow content of + 0.6 mm was 0, − 0.074 mm 53.14%, and the classification efficiency was increased from 43.31 to 51.86%.
(5) Through the optimization of grinding efficiency, the grinding fineness is significantly improved, and the fine grain content is increased, and the dissociation degree of coarse grain mineral gangue and pyrite coated with gold is improved. The flotation index improved significantly, and the concentrate enrichment ratio increased from 21.57 to 21.94 by 0.37; the flotation recovery rate increased from 93.17 to 93.41% by 0.24%.

References

1. Duan XX (2012) Mining and grinding. Metallurgical Industry Press
2. Yang JW (2006) Mining and grinding technology. Metallurgical Industry Press
3. Zhao QG, Zhang MX (2003) Hydrocyclone separation technology. The Chemical Industry Press
4. Pang XS (2006) Separation theory and practical application of hydrocyclone. Mining Express
5. Zhou WM (2007) Analysis of the results of the grinding and floating operation process investigation. China Mining
6. Yuan J (2015) Investigation and analysis of the mineral processing process of a gold mine in Henan province. Yunnan Metallurgy
7. Zhang CX, Bai XM, Wang CY (2009) Study on process optimization of a concentrator. Metal Mine
8. Gao LK, Chen Y, Zhou P (2007) Experimental study on the grinding process of an iron ore in Yunnan province. Min Eng
9. Wu JJ, Dai HX (2009) Brief analysis of the influencing factors of the grinding process. Yunnan Metallurgy
10. Xiao QF, Duan XX (2006) Analysis and countermeasures of problems that should be paid attention to in the process of grinding. Comprehensive Utilization of Minerals
11. Liu ZB (2014) Process investigation and analysis and transformation measures of a gold concentrator. Non-ferrous Metals (Ore-Dressing Part)

Detection Method of UAV Operation in Power Transmission and Transformation Engineering Based on Thermal Radiation Technology and Temperature Standard Source

Bin Wang, Shengchao Jiang, Haoze Zhuo, Feifeng Wang, and Yunqing Pei

Abstract Due to the low average accuracy of drone operation detection and recognition, it is necessary to design a new operation detection method for drones in power transmission and transformation engineering based on thermal radiation technology and temperature standard sources. Utilizing thermal radiation technology and temperature standard sources to perform 3D reconstruction and dense image matching for drone operation detection, planning the path for drone operation detection in power transmission and transformation projects, and completing drone operation monitoring in power transmission and transformation projects. The experimental results show that this method has good detection effect, high average accuracy and accuracy of detection and recognition, and has certain application value, making a certain contribution to improving the safety of transmission and transformation engineering.

Keywords Thermal radiation technology · Temperature standard source · Power transmission and transformation · Engineering · UAV · Function · Testing

1 Introduction

In fact, the production process of electric power is complex, and it needs to go through several links, such as power generation and distribution. In the power generation link, various energy sources need to be used as support [1–3]. Transmission needs to be configured with relevant lines, and distribution needs to convert electric energy into usable forms for users. Power transmission and transformation projects pay special attention to power transmission and transformation links. Under the background of industrial production, China's power demand is increasing day by day. The existing small and medium-sized power transmission and distribution projects can no longer

B. Wang (✉) · S. Jiang · H. Zhuo · F. Wang · Y. Pei
Guangxi Key Laboratory of Intelligent Control and Maintenance of Power Equipment, Electric Power Research Institute of Guangxi Power Grid Co., Ltd., Guangxi, Nanning 530023, China
e-mail: cwgbh1@163.com

S. Yadav et al. (eds.), *Energy Power and Automation Engineering*, Lecture Notes in Electrical Engineering 1118, https://doi.org/10.1007/978-981-99-8878-5_27

meet the current power demand. It is urgent to expand the scale of power transmission and transformation projects, and use power systems with high reliability to reduce the power transmission pressure of power transmission and transformation projects. The research shows that China's power transmission and transformation projects mainly include 110, 220, 330 kV, and other levels, and different voltage levels have different requirements for transmission lines. In order to promote the development of various regions, China has paid more and more attention to the construction of power transmission and transformation projects, optimizing the existing communication automation, electrical installation, and other links.

The construction environment of power transmission and transformation projects is complex, and the internal transmission lines are widely distributed. Due to the long-term impact of the external environment, self-loss, and other effects, it is very easy to have operational failures [4]. If the transmission line failure of power transmission and transformation projects cannot be effectively detected, it may lead to the abnormality of the entire power transmission and transformation function, and even lead to some serious safety accidents. UAV is an advanced intelligent patrol equipment for power transmission and transformation projects. It can effectively take the internal line images of power transmission and transformation projects, conduct comprehensive analysis, and obtain effective patrol results [5, 6]. Relevant researchers have designed many related detection methods for the operation of power transmission and transformation projects according to the characteristics of UAVs, but most of the methods have poor image matching effect, which does not meet the current requirements for the operation detection of power transmission and transformation projects. Therefore, a new detection method for the operation of power transmission and transformation projects needs to be designed based on thermal radiation technology and temperature standard source.

2 Design of UAV Operation Detection Method for Power Transmission and Transformation Project Based on Thermal Radiation Technology and Temperature Standard Source

2.1 UAV Operation Detection 3D Reconstruction Dense Image Matching Based on Thermal Radiation Technology and Temperature Standard Source

According to the above 3D reconstruction intensive image matching process, the opposite points and the relative clove shop of the image can be determined, and influence search matching can be carried out in combination with the initial parallax map to achieve gross error filtering and generate relatively dense point clouds [7, 8].

2.2 Planning of UAV Operation Detection Path for Power Transmission and Transformation Project

After the above 3D reconstruction intensive image matching is completed, the UAV operation detection path of the power transmission and transformation project can be planned. This paper carries out path planning based on the two-point method, and sets the expected patrol position. At this time, the distance between the operation detection points is as follows (1).

$$R = h - \frac{x - x_b}{y - y_b} \tag{1}$$

In formula (1), h represents the detection radius of UAV operation, x_b, y_b represents the coordinates of the running test. The SLAM model can be built to obtain the dynamic operation characteristics of UAV based on the above set operation detection point spacing.

Effective UAV operation detection reset door can be set according to the above characteristics R_1, as shown in (2).

$$R_1 = \sigma(x_t W_x + H_t - \mathrm{br}) \tag{2}$$

In formula (2), σ represents the number of hidden detection units, x_t represents the batch of given test time, W_x represents the number of test samples for power transmission and transformation works [9, 10], H_t represents the number of input test samples, br represents the hidden status of reset detection. Update the above reset door to obtain the update door of UAV operation detection Z_1, , as shown in (3).

$$Z_1 = R_1 \backslash \sigma(x_t W_x + H_t - \mathrm{bz}) \tag{3}$$

In formula (3), bz represents the hidden status of detection update. According to the above update door, the hidden detection obstacles in the power transmission and transformation project can be determined to avoid collision between UAV and detection equipment and reduce the risk of operation detection. At this time, an effective UAV operation detection planning parameter can be set M_p, as shown in (4).

$$M_p = m_p K_F K_T \tag{4}$$

In formula (4), m_p represents the health index of UAV detection module, K_F represents the basic state of UAV detection, K_T represents the detection defect coefficient, and the optimal inspection path can be obtained by combining the above UAV operation inspection parameters of the power transmission and transformation project H as shown in (5).

$$H = \sum_{p=1}^{n} M_p K_p \tag{5}$$

In formula (5), K_p represents the standard operation detection path. Utilizing the above optimal patrol path can effectively improve the patrol accuracy and reduce the frequency of patrol failures.

3 Experiment

In order to verify the operation effect of the designed UAV operation detection method based on thermal radiation technology and temperature standard source for power transmission and transformation projects, this paper built an experimental platform, and compared it to the conventional UAV operation detection method for power transmission and transformation projects, and carried out experiments as follows.

3.1 Experiment Preparation

Combined with the operation detection requirements of power transmission and transformation UAV, this paper carried out simulation experiments, that is, preset the reasonable power transmission and transformation engineering state, and carried out experiments in the Matlab2017a experimental platform. The experimental platform has SLAM characteristics. It uses a 2.5 Hz Intel Core u5 processor to process the experimental data. In order to improve the experimental performance, it also needs to carry out simulation drive before the experiment, and set a 64 bit Linux drive system. At the beginning of the experiment, the SLAM data set was mainly used for the experiment. 246 UAV patrol nodes were set to determine the average recognition and detection accuracy of different operational detection methods. In combination with the actual operation detection requirements of the power transmission and transformation project, this experiment has set up a simulation operation detection scenario and planned several different types of UAV operation detection objects for the power transmission and transformation project. The operation detection contents are shown in Table 1.

It can be seen from Table 1 that the operation detection objects and detection contents of the above power transmission and transformation project meet the experimental requirements, and the operation detection space distance can be preset in advance to improve the detection safety. During the experiment, it is necessary to always keep a safe distance between the UAV and the patrol line, and prohibit the UAV from passing through various experimental lines.

The three-dimensional model of the experimental power transmission and transformation project needs to be input according to the experimental requirements, and

Table 1 Objects and contents of UAV operation detection in power transmission and transformation project

Patrol objects	Operation detection content
Tower	Tower inclination, tower material deformation and damage, severe corrosion; Missing tower materials, bolts, and foot nails, and buried tower feet in soil; The concrete pole is not sealed at the top, damaged, cracked, or deformed on the ladder; Bird's Nest, Tower Damage, etc.
Tower foundation	Obvious conveyor damage, cracks, exposed reinforcement, etc. Foundation displacement, insufficient slope protection, etc.
Insulator	The umbrella skirt is damaged, the locking pin is missing, and the insulator string is severely tilted. The iron cap is cracked or broken, the steel feet are severely rusted or corroded, and there are discharge marks and serious pollution
Line fittings	Broken clamps, cracks, wear, pins falling off, severe corrosion: grading rings, shielding rings damaged, bolts loose: anti vibration hammer running, falling off, severe corrosion: spacer loose, deformed or out of position, suspended foreign objects: jumper defect, etc.
Overhead ground wire	Loose strands, broken strands, deformation, wear, wire breakage: lightning damage, foreign objects, icing, etc.
Grounding	Loose bolts, discharge burns, exposed grounding wires, etc.
Stay wire	Bending, relaxation, wear, induced corrosion, loss of fixed devices, etc.

then the operation detection area needs to be set, and reliable operation detection viewpoints need to be selected, so as to generate an effective patrol path. In order to ensure the reliability of the UAV operation detection, smoothing processing is also required before the experiment is carried out. In this paper, SLAM optimization algorithm is used. The smoothing steps are shown in Table 2.

As shown in Table 2, the above smoothing algorithm can be used to effectively determine the operation detection cycle and perform Jacobian sorting,

Table 2 SLAM smoothing algorithm

Serial number	Step
1	Construct Jacobian matrix A and RHS vector b for drone operation detection
2	Set iteration variables, i.e. drone operation path
3	If(Uter% = 0)
4	Reorder experimental data
5	Using QR for Cholesky decomposition to find the optimal value
6	Restore the original optimization solution
7	Solve for the best state estimation vector
8	Add new measurement quantity
9	Update the matrix R–R using the given transformation and update accordingly
10	Solve the most optimal solution
11	Find the optimal estimated state variable

thus completing effective experimental decomposition. Combined with the above smoothing algorithm, the average accuracy of operation detection identification can be selected D as an experimental index, the calculation formula of this index is as follows (6).

$$D = \frac{K}{K_0} \times 100\% \tag{6}$$

In formula (6), K represents the identification coefficient of actual operation detection, K_0 represents the identification coefficient of standard operation detection. The higher the average accuracy of operation detection and identification is, the better the performance of UAV operation detection and identification is. On the contrary, it proves that the performance of UAV operation detection is relatively poor. Combined with the above set experimental indicators, subsequent UAV operation detection experiments for power transmission and transformation projects can be carried out.

3.2 Experimental Results and Discussion

Combined with the above experimental preparation, the operation detection experiment of UAV in power transmission and transformation project can be carried out, that is, 10 abnormal problems in power transmission and transformation project can be randomly combined from the above preset operation detection contents. The UAV operation detection method for power transmission and transformation project based on thermal radiation technology and temperature standard source designed in this paper and the conventional UAV operation detection method for power transmission and transformation project are, respectively, used for operation detection. Formula (6) is used to calculate the detection and identification accuracy of different operation detection areas of power transmission and transformation project. The experimental results are shown in Table 3.

It can be seen from Table 3 that the detection and recognition accuracy of the UAV operation detection method designed in this paper based on thermal radiation technology and temperature standard source in different operation detection areas is high, while the detection and recognition accuracy of the conventional UAV operation detection method in different operation detection areas is relatively low.

Table 3 Experimental results

Drone operation detection area	The detection and recognition accuracy of the unmanned aerial vehicle operation detection method for power transmission and transformation engineering based on thermal radiation technology and temperature standard source designed in this article (%)	The detection and recognition accuracy of conventional unmanned aerial vehicle operation detection methods in power transmission and transformation engineering (%)
South A Run detection recognition block	99.53	66.23
North A Run detection recognition block	95.41	65.81
East A Run detection recognition block	96.58	53.96
North B Run detection recognition block	93.39	62.23
South B Run detection recognition block	99.41	51.14
The West A Run detection recognition block	98.95	66.85
North C Run detection recognition block	94.26	43.39
South C Run detection recognition block	95.45	55.45
North D Run detection recognition block	99.98	64.98
South D Run detection recognition block	98.56	52.56

4 Conclusion

There are a lot of transmission lines in the power transmission and transformation project. Affected by the change of power transmission and transformation load and external environment, it is very easy to lead to abnormal lines and affect the operation of the whole power transmission and transformation project. In order to solve the above problems, this paper designs a completely new method of UAV operation detection for power transmission and transformation project based on thermal radiation technology and temperature standard source. The experiment results show that the designed UAV operation detection method based on thermal radiation technology and temperature standard source for power transmission and transformation project has good detection effect, accuracy, and certain application value, and has made certain contributions to improving the operation safety of power transmission and transformation project.

Acknowledgements The study was supported by "Research and Application on Key Technologies of Intelligent Machine Module Inspection Platform for Digital Power Grid Inspection (Grant No. GXKJXM20210296)".

References

1. Liu S, Wang Y, Zheng S (2022) Photovoltaic reactive power compensation strategy for suppressing DC continuous commutation failure. Comput Simul 39(9):101–107
2. Odzer MN, Brooks A, Whitman ER (2022) Effects of environmental factors on the detection of subsurface green turtles in aerial drone surveys. Wildl Res 49(1):79–88
3. Renugadevi S, Dharshini M, Gayathri K (2021) IoT based detection of bore-well unclosed holes using automated drone operated cameras in a remote area. J Phys Confer Ser 1767(1):012028
4. Chen W, Zou Y, Mo W (2022) Onsite identification and spatial distribution of air pollutants using a drone-based solid-phase microextraction array coupled with portable gas chromatography-mass spectrometry via continuous-airflow sampling. Environ Sci Technol 56(23):17100–17107
5. Flak P (2021) Drone detection sensor with continuous 2.4 GHz ISM band coverage based on cost-effective SDR platform. IEEE Access 44(99):1
6. Lv H, Liu F, Yuan NC (2021) Drone presence detection by the drone's RF communication. J Phys Confer Ser 1738(1):012044
7. Walambe R, Marathe A, Kotecha K (2021) Multiscale object detection from drone imagery using ensemble transfer learning. Drones 5(3):66
8. Kolamunna H, Dahanayaka T, Li J (2021) DronePrint: acoustic signatures for open-set drone detection and identification with online data. Proc ACM Interact Mobile Wearable Ubiquit Technol 5(1):1–31
9. Gumaei A, Al-Rakhami M, Hassan MM (2021) Deep learning and blockchain with edge computing for 5G-enabled drone identification and flight mode detection. IEEE Netw 35(1):94–100
10. Yeh CC, Chang YL, Alkhaleefah M (2021) YOLOv3-based matching approach for roof region detection from drone images. Remote Sens 13(1):127

Investigation on the Ablation Characteristics of Copper–Tungsten Contacts in SF_6 Gas

Xiabo Chen, Xubo He, Hao Sun, Feng Jiang, Zeyu Wang, Mingming Sun, and Dongyang An

Abstract In modern power system, SF_6 circuit breaker undertakes the important tasks of short circuit protection, switching control, and power distribution, which is an important factor to maintain the safe and stable operation of the system. The ablation caused by arc will shorten the electrical life and breaking performance of the contact system. Therefore, it is necessary to study the electrode ablation characteristics in SF_6 gas arc and explore the influence of different factors on the electrode ablation. In this paper, based on the new in-situ optical diagnosis platform, the ablation of copper–tungsten contacts is studied experimentally, which provides theoretical support and basic parameters for the design and optimization of SF_6 circuit breaker contact system.

Keywords Ablation · Copper–tungsten · SF6 gas

1 Introduction

Circuit breaker is one of the most critical components in the power system. It carries important functions, such as fast cutting off the AC and DC main circuit and frequent switching on and off large current. It has been applied in various links of power grid, such as power generation, power transformation, transmission, and distribution [1–3]. In recent years, with the construction of EHV (extra-high voltage) grid, in EHV long distance transmission, the circuit breaker frequent operation is needed to meet the reactive power regulation, so in more than 110 kV EHV substation system in substation, with SF_6 circuit breaker dominant [4]. In SF_6 circuit breaker, the movement of arc contact is one of the most important parts in the circuit breaker, it needs to withstand strong arc in the process of circuit breaker tripping. Due to its excellent abrasion resistance and low thermal expansion coefficient, copper–tungsten composites are widely used in the fabrication of arc contacts of SF_6 circuit breakers.

X. Chen · X. He · H. Sun (✉) · F. Jiang · Z. Wang · M. Sun · D. An
State Key Laboratory of Electrical Insulation and Power Equipment, Xi'an Jiaotong University, Xi'an, China
e-mail: sunhao1031@mail.xjtu.edu.cn

S. Yadav et al. (eds.), *Energy Power and Automation Engineering*, Lecture Notes in Electrical Engineering 1118, https://doi.org/10.1007/978-981-99-8878-5_28

In SF_6 connect and disconnect the circuit breaker frequently current process, the arc of contact between the strong arcing caused by the electric contact loss, deformation and fracture, may be the cause of open circuit failure of circuit breaker. Once the circuit breaker fails to be opened, the huge thermal effect and electric power impact brought by the short-circuit current will lead to permanent damage to the electrical equipment in the system, and even cause major accidents, such as fire and explosion, resulting in huge economic losses and serious threats to personal and property safety [5]. Therefore, improving the service life and reliability of circuit breaker arc contacts has become one of the key problems urgently to be solved in the field of switching appliances [6].

The ablative modes of copper–tungsten electrode in SF_6 circuit breakers are usually divided into three types: evaporation and vaporization ablative, droplet splash ablative, and material stripping ablative [7]. Evaporation ablation means that when the arc energy is injected into the electrode, it will be accompanied by the generation of electrode molten pool and evaporation ablation of the electrode. Vaporization ablation is the ablation that occurs when the temperature of the molten pool on the surface of the arc reaches the boiling point of the material with the continuous injection of arc energy. Droplet splash ablation refers to the phenomenon that the liquid metal in the molten pool breaks away from the electrode surface and forms splash droplets under the action of the arc heat and force. In the actual breaking process, due to the large current, the material loss caused by sputtering ablation is generally much higher than that caused by evaporation and vaporization, which is an important factor causing the deterioration of contact failure and shortening the life of gas switch. Generally, the phenomenon of spalling ablation is not caused by the direct action of electric arc, but is a characteristic reflection of long-term stress fatigue of electrode materials. Generally, it develops from the damage area of stress concentration such as contact cracks and internal cavities, and its appearance often declares the complete failure of the contact system.

The experimental diagnosis methods of electrode ablative characteristics are generally divided into offline measurement and in-situ measurement. Offline measurement method refers to taking out the ablation electrode to be studied after the ablation experiment is completed, and using precision balance weighing method, SEM (electron microscope scanning analysis), EDS (surface energy spectrum analysis), and other methods to obtain the net ablation amount of electrode, electrode ablation morphology and electrode surface composition and content. The in-situ measurement method of electrode ablation refers to the method of online diagnosis of the macro and micro parameters of electrode ablation process by using the measurement principle of optics, such as high-speed imaging method, Townson scattering method, and so on.

On the basis of previous experiments, an in-situ diagnosis system for the ablation of copper–tungsten contacts is proposed innovatively based on the visualization imaging method of laser enhancement combined with narrowband filtering and the data processing method of image edge detection combined with particle tracking matching algorithm. The key ablative characteristics of copper–tungsten electrode such as spatter amount, ablative amount, and arc shape were obtained by using the

diagnostic system under different experimental factors. It provides experimental basis and theoretical support for further improving the performance of breaker contacts.

2 Experimental Introduction

2.1 Experimental Platform

The circuit used in the arc burning experiment is a DC circuit. The circuit is mainly composed of capacitor bank *C*, adjustable resistance *R*, two thyristors, and an arc burning cavity. The maximum charging voltage of capacitor *C* is 500 V and the maximum current it can provide is 500 A. Ignition and arc transfer can be achieved by controlling the opening time of two thyristors. There is an electromagnetic mechanism in the body of the arc cavity, and the experiment of pulling arc is carried out through the absorption of the electromagnetic mechanism.

The optical path used in the experiment is mainly composed of high-speed camera, high-power laser, narrow band filter, and other optical components for in-situ optical diagnosis.

The trigger time sequence of the high-speed camera, thyristor, and electromagnetic mechanism in the experiment system is controlled uniformly by the control signal output of the DG535 delay trigger to ensure the repeatability of the experiment. During the experiment, the arc current waveform is measured by Hall current sensor, and the arc voltage waveform is measured by high voltage probe.

2.2 Experimental Principle

For the traditional in-situ optical observation method, the arc radiation intensity can cover the ablative of the electrode surface, which hinders the observation of droplets and particles. In order to solve the above problems, it is necessary to enhance the reflected light intensity of electrode while attenuating arc light, so as to realize the in-situ diagnosis of electrode ablation during arc burning. When the gas arc is burning, the spectrum emitted by the arc is a complex spectrum composed of atom, ion emission line, and molecular band spectrum. However, the relative intensity of the arc spectral line is mainly distributed in the visible region, and the relative intensity of the arc spectral line decreases rapidly in the infrared region [8]. Therefore, a visualization method of electrode ablation based on high-power laser enhancement combined with narrow band filtering is proposed. Firstly, a high-power laser with wavelength of 808 nm was introduced as the probe laser to directly irradiate the electrode and arc region during arc burning, and effectively enhance the reflected light on the electrode surface. Secondly, a narrow band filter with the central wavelength matching the laser's central wavelength is placed in front of the lens of the high-speed

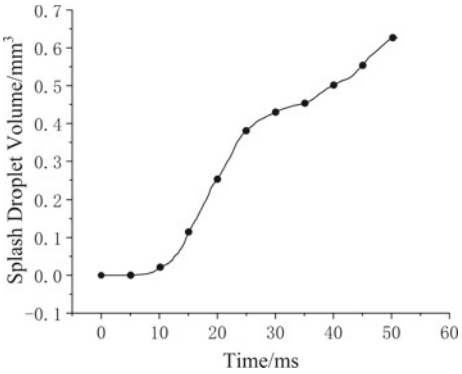

Fig. 1 The ablative volume of splash droplet with time

camera to attenuate the harmful arc noise while preserving the effective reflected signal on the electrode surface. Through this visualization principle, the signal-to-noise ratio of electrode ablation imaging is greatly improved, and in-situ diagnosis of electrode surface ablation morphology and macroscopic ablation products can be realized simultaneously.

2.3 Image Processing and Particle Statistics Algorithm

In order to measure the ablative quality of splash droplets in situ, it is necessary to extract the feature information from the original image of electrode splash. The post-processing method of splash ablative image used in this paper mainly includes edge detection and droplet reconstruction. The image convolution is calculated by the Laplacian edge operator of second-order difference [9]. A dynamic threshold image segmentation method was used to reconstruct the spatter droplets [10]. In this experiment, PTV, a flow field particle tracer velocity measurement algorithm, was used as the tracking algorithm of spray droplets to precisely match the same droplets in the continuous frame sequence. Figure 1 shows the final time-varying spatter ablative volume obtained by the spatter particle measurement algorithm.

2.4 Experimental Arrangement

In this paper, the ablative characteristics of $W_{70}Cu_{30}$ anode in SF_6 DC arc are studied. Steady arc burning experiments are carried out to calculate the ablative amount and spatter amount under different pressure and current conditions, and the key reasons leading to the difference in ablative amount are pointed out.

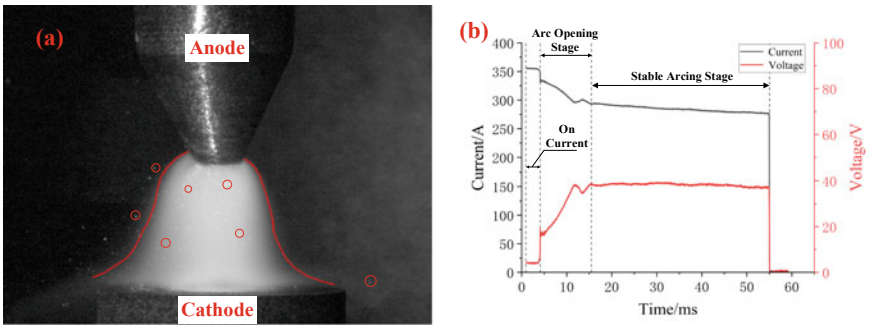

Fig. 2 Arc shape and voltage current waveform of CuW_{70} electrode with arc burning current of 300 A

3 Experimental Conclusion

3.1 Arc Shape and Voltage and Current Waveform

The electrode adopts the shape of "point-plate", which will produce a stable ignition arc, which is conducive to the repeatability of the ablation experiment. As shown in Fig. 2, this is an ablative experiment with CuW_{70} as anode under the experimental conditions of normal pressure SF_6 and arc burning current of 300 A. Figure 2a shows the shape of the arc under stable arc burning. The upper electrode is the anode and the lower electrode is the cathode. The red line marks the shape of the arc, and the arc is a stable "bell-shaped" arc. Figure 2b shows the voltage and current waveform measured in the experiment, which can be divided into three stages: "current passing—arc pulling—stable arc burning". In the stable arc burning stage, the arc voltage is quite stable, indicating that the arc always takes the shape of "bell" arc in the stable arc burning stage. Stable arc shape is helpful to the reliability and repeatability of ablation experiment.

3.2 Ablation Experiments of Copper–Tungsten Contacts Under Different Pressure Conditions

In this experiment, the arc burning current is 200 A, the gas medium is SF_6, the anode contact is CuW_{70} experimental conditions, by changing the gas pressure (pressure range: 0.5–4 atm) to study the amount of ablation and splash ablation. The ablation amount was measured by precision balance, and the splash ablation amount was tracked and counted by visualization imaging method based on laser enhancement combined with narrowband filtering. Curve *a* in Fig. 3 is the ablation quantity curve obtained by weighing the mass difference before and after ablation with precision

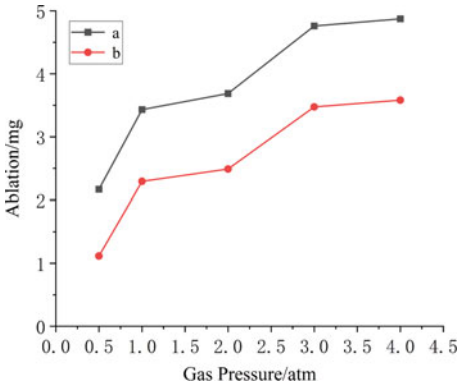

Fig. 3 Weighing ablation and sputtering droplet ablation statistics of CuW_{70} contact under different gas pressure

balance, and curve *b* in Fig. 3 is the ablation quantity of splash droplets obtained by in-situ optical diagnosis. It can be seen from Fig. 3 that the ablation amount of CuW_{70} contact under different pressure is smaller than that obtained by weighing. This is because besides of the ablation amount caused by splashing droplets, the ablation amount of CuW_{70} contact is also caused by the evaporation and vaporization of the contact. With the increase of gas pressure, the ablative amount of weighing and splashing drops will increase, and their upward slopes are similar. This indicates that with the increase of gas pressure, the increase of the ablative amount is mainly caused by the ablative amount of splash drops, and the proportion of the ablative amount of splash drops in the total ablative amount increases with the increase of gas pressure.

3.3 Ablation Experiments of Copper–Tungsten Contacts Under Different Current Conditions

In this experiment, under the experimental conditions that the gas medium is normal pressure SF_6 and the anode contact is CuW_{70}, the ablation amount and splash ablation amount are studied by changing the current (current range: 50–300 A). Curve *a* in Fig. 4 is the statistics of weighing ablative quantities under different arc burning current conditions, and curve *b* in Fig. 4 is the comparison of ablative quantities of splash droplets under different arc burning current conditions obtained by in-situ optical diagnosis. According to Fig. 4, it can be found that the spatter ablation amount of CuW_{70} contact is also smaller than that obtained by weighing under different arc burning current levels. At the same time, it can be found that both the sputtering and weighing ablative quantities increase with the increase of current grade, and the rising slope of weighing ablative quantities is greater than that of sputtering ablative quantities, indicating that with the increase of arc burning current, evaporation and vaporization ablative quantities also increase.

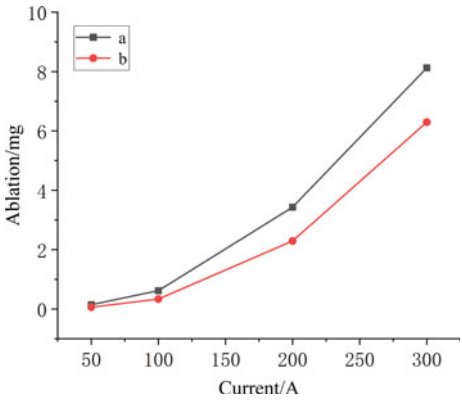

Fig. 4 Weighing ablation and sputtering droplet ablation statistics of CuW_{70} contact under different current

4 Conclusion

In this paper, based on the new in-situ optical diagnosis experiment platform, the ablation of CuW_{70} contacts under SF_6 gas medium was studied by changing the pressure and arc burning current, and the following conclusions were drawn.

For the ablation experiment under different pressure conditions, the ablation amount of CuW_{70} contact will increase with the increase of pressure. This is because with the increase of gas pressure, the arc will receive the beam, resulting in the decrease of arc root radius and the increase of anode surface current density. At this time, the efficiency of arc energy conduction to the anode surface will be improved, which is conducive to the anode phase transformation to produce molten pool. The sputtering droplet ablation is caused by the continuous injection of arc energy into the anode contact, which makes the tungsten skeleton on the surface of the contact melt to form the anode molten pool, and the explosion of a large number of bubbles caused by copper steam gushing from the anode molten pool. Therefore, the anodic molten pool formed in the arc burning process determines the ablation amount of splash droplets. Therefore, the increase of gas pressure will accelerate the formation of anode molten pool and lead to the increase of the ablation amount of splash droplets. In addition, it can be seen from Fig. 3 that the dominant ablative amount is that of splashing droplets, so the ablative amount of CuW_{70} contacts will increase with the increase of gas pressure.

For the ablation experiments under different arc current conditions, the ablation amount of CuW_{70} contact will increase with the increase of current. This is because with the increase of the current, the current density on the anode surface will also increase, and the energy injected by the arc into the anode surface will also increase, which will contribute to the generation of the anode molten pool, and thus improve the ablation amount and total ablation amount of the splash droplets. In addition, the increase of current will lead to the expansion of arc roots, so with the increase of current, the amount of evaporation and vaporization ablation will also increase.

References

1. Rong MZ (2004) Electrical contact theory. China Machine Press, Beijing. https://xueshu.baidu.com/usercenter/paper/show?paperid=8b1abfbfedd51b248b1a81a90a2d6486
2. Wang QP (1991) Electric arc theory. China Machine Press, Beijing. https://www.clcindex.com/book/view/BC43E44A1580A6E99B9EC30AB8E2076E/
3. Chen ZK, Sawa K (1998) Effect of arc behaviour on material transfer: a review. IEEE Trans Compon Packag Manuf Technol A 21(2):310–322. https://doi.org/10.1109/95.705480
4. Ding C, Yu CJ, Yuan Z (2023) Effect of making speed on arc contact erosion of SF_6 circuit breaker. High Volt Apparat 9:1–9
5. Cui YF, Wu Y, Rong MZ, Chang HD, Guan W (2019) Comparative study on the erosion mechanism of $W_{70}Cu_{30}$ anode in DC gaseous arcs. In: Proceedings of the 2019 5th international conference on electric power equipment: switching technology (ICEPE-ST). Kitakyushu, pp 681–684. https://doi.org/10.1109/ICEPE-ST.2019.8928714
6. Liu LZ, Guo XX (2023) Simulation study on contact ablation characteristics under electric arc action. Electr Eng 587(05):1–9
7. Slade PG (2013) Electrical contacts: principles and applications. CRC Press, Boca Raton, p 1311. https://doi.org/10.1201/b15640
8. Ding XZ, Liu ZK, Yan Y, Geng KS (2015) Analysis of characteristics and application for arc spectral components. J Electr Eng 10(05):75–86
9. Cai LM, Wang LJ (2020) Digital image processing: analysis and implementation using MATLAB. Tsinghua University Press, Beijing
10. Sheppard C (1988) Super-resolution in confocal imaging. Opt Int J Light Electr Opt 80(2):53

Comparative Study on International Zero-Carbon Building Certification System Under the Vision of Carbon Neutrality

Yunbo Zhang, Keying Qian, Qiang Wang, Jie Wang, Yingang Feng, and Jingjing Zhang

Abstract Under the background of carbon neutrality and peak carbon dioxide emissions, the concept of zero-carbon building has been paid more and more attention, and the transition to low-carbon and zero-carbon has become the future development trend of China's construction industry. In this paper, five international typical zero-carbon building certification systems with different regions and different development levels are selected as the research objects, and the basic situation of different systems is introduced, and the five zero-carbon building certification systems are compared from three aspects: certification preconditions, evaluation objects, and evaluation contents. Finally, combined with the characteristics of five typical international zero-carbon building certification systems and the current specific situation of zero-carbon building development in China, this paper puts forward suggestions for organizations and enterprises interested in applying for zero-carbon building certification to continuously improve the level of zero-carbon buildings and apply for zero-carbon building certification with different certification difficulties in stages. Relevant organizations and enterprises can give priority to the zero-carbon building certification launched by CAGBC and the building certification jointly launched by TÜV Rhineland and BRE, and then further apply for LEED Zero certification launched by USGBC and other certification systems with stricter requirements on carbon balance.

Keywords Zero-carbon building · Zero-carbon building certification · Certification system comparison

Y. Zhang · K. Qian · Q. Wang · J. Wang · Y. Feng · J. Zhang (✉)
Central University of Finance and Economics, Beijing, China
e-mail: 1546994122@qq.com

S. Yadav et al. (eds.), *Energy Power and Automation Engineering*, Lecture Notes in Electrical Engineering 1118, https://doi.org/10.1007/978-981-99-8878-5_29

1 Introduction

Climate change is one of the non-traditional security faced by the world today, and global climate governance is very important for maintaining global ecological environment security and promoting sustainable development. Adhering to the concept of Community of Shared Future for Mankind, China has put forward the goal of "double carbon" [1]. In this context, low-carbon development of China's energy and related industries has become an important direction of carbon emission reduction.

The construction field is one of the key industries to implement energy conservation and emission reduction. According to "Global Status Report for Buildings and Construction" published by the Global Alliance for Buildings and Construction (GlobalABC), in 2021, the global construction industry will emit about 10 billion tons of carbon dioxide, accounting for 37% of the total global emissions. In recent years, the construction industry has actively explored green building methods and put forward the concepts of green building, low-carbon building, and zero-carbon building [2].

Zero-carbon building, also known as net zero-carbon building, refers to the realization of zero-carbon emission by reducing carbon emissions and increasing carbon sinks during the whole life of the building. Promoting the construction of zero-carbon buildings plays an important role in reducing carbon emissions in the construction sector and helping peak carbon dioxide emissions to be carbon neutral.

Zero-carbon building certification is the key link of zero-carbon building construction, and its certification standard can standardize the building, which is very important for solving the emission problem in the construction field and providing index guidance for emission. This paper will briefly introduce five famous foreign zero-carbon building certification institutions, and make a comparative analysis of their certification systems, aiming at providing some theoretical guidance for the development of zero-carbon building certification system in China through the research and analysis of zero-carbon building certification.

2 Introduction of International Typical Zero-Carbon Building Certification System

This paper selects five international typical zero-carbon building certification systems covering different regions and different levels of development as the research object. The selected zero-carbon building certification standards have been introduced by certification bodies in different countries, which is typical and representative.

On May 29th, 2017, the Canada Green Building Council (CAGBC) launched the country's first zero-carbon building standard, and the new standard represents the next development of green building innovation needed to meet Canada's emission reduction targets. On October 11th, 2017, the Green Building Council South Africa (GBCSA) announced the official launch of its net zero emission plan. In

Table 1 International typical zero-carbon building certification system

Push-out mechanism	Launch time	Applied range	Term of validity
CAGBC	May 2017	New buildings and existing buildings	One-time certification (ZCB-design)/1 year (ZCB-performance)
GBCSA	October 2017	New buildings and existing buildings	3 years
USGBC	November 2018	New buildings and existing buildings	3 years
NZGBC	September 2019	Existing buildings	1 year
TÜV Rhineland and BRE	November 2021	New buildings and existing buildings	3 years

November 2018, the U.S. Green Building Council (USGBC) officially announced the launch of LEED Zero (Leadership in Energy and Environmental Design) certification. On September 24th, 2019, the New Zealand Green Building Council (NZGBC) launched Net Zero Carbon Roadmap for Aotearoa, which introduced a set of tools to allow New Zealanders to benchmark their buildings and certify them as net zero-carbon standards. The certification was developed in cooperation with Toitū Envirocare. On November 7, 2021, Germany TÜV Rhineland Greater China Region (hereinafter referred to as "TÜV Rhineland") and British Building Research Establishment (BRE) jointly launched the "Evaluation and Certification System for Zero Carbon Buildings" at China International Import Expo [3] (Table 1).

3 Comparative Study on International Typical Zero-Carbon Building Certification

This paper selects the typical indicators of zero-carbon building certification system, and makes a comparative study of five international typical zero-carbon building certifications from three aspects: certification preconditions, evaluation objects, and evaluation contents. Certification preconditions mainly compare the preconditions that buildings applying for certification need to meet under different certification systems. The evaluation object explains the types of buildings that can apply for certification under different certification systems. The evaluation content compares the evaluation indexes of different certification systems.

3.1 Certification Prerequisite

In the precondition of certification, LEED zero-carbon certification in the United States is strict, which requires that LEED certification must be passed under BD

+ C or BO + M rating system before zero-carbon certification can be carried out; Other certification standards require one as an extension or independent certification of green building certification, and the other is no special requirements. Relatively speaking, the prerequisites for these two certifications are relatively loose.

The ZCB-Design standard of CAGBC is applicable to all new buildings (except single and multi-family residential buildings that fall under Part 9 of the National Building Code) and the renovation of existing buildings (including HVAC, envelope, and/or interior renovations). ZCB-Performance standards can be used in any existing building [4].

GBCSA certification can be used as a part of Green Star, EDGE, or EWP projects, or as an independent certification.

The LEED Zero certification project launched by USGBC must pass LEED certification under BD + C or BO + M rating system. Core and Shell certification projects meet the minimum occupancy requirements of LEED during the implementation period: the average occupancy rate of buildings in the past 12 months must reach 50% or above [5].

The zero-carbon certification proposed by NZGBC can be used as an extension of the overall Green Star performance rating or as an independent zero-carbon certification.

The zero-carbon building certification issued by TÜV Rhineland and BRE has no specific requirements for preconditions.

3.2 Evaluation Object

In terms of evaluation objects, most of the authentication systems can authenticate new buildings and existing buildings, but there are some differences in specific details. CAGBC certification is aimed at the renovation of new buildings and existing buildings under ZCB-Design standards, and at existing buildings under ZCB-Performance standards; GBCSA certification supports zero-carbon building certification for new buildings, existing buildings, and other buildings; LEED Zero certification introduced by USGBC supports new building certification under BD + C certification and existing building certification under BO + M certification; The certification and evaluation objects launched by TÜV Rhineland and BRE include the embodied carbon emission of buildings, the carbon emission of the whole life cycle of buildings, and the carbon emission of building operations (new buildings and existing buildings) [6]. In addition, NZGBC's certification system is only for existing buildings.

3.2.1 Evaluation Content

In terms of evaluation content, there are differences in the emphasis of different certification systems, and there are also corresponding differences in evaluation content and scope.

While the zero-carbon certification evaluation content introduced by CAGBC requires carbon emissions, there are also certain requirements for energy efficiency, peak demand, and airtightness in energy use. In addition, zero-carbon design certification also needs to meet innovation requirements.

GBCSA shows that the preferred pathway to achieve net zero/net positive carbon emissions are Energy Efficiency, On-site Renewables, Off-site Renewables, Carbon Offsets, respectively. The standard has created five levels. In terms of evaluation content, different levels aim at different emission ranges, and with the increase of levels, the emission ranges increase. At present, only the details of Levels 1 and 2 are explained, but the details of Levels 3–5 are not explained. The evaluation content of the first level is the discharge of infrastructure, that is, the discharge of fixed construction services, excluding the energy use of residents. The evaluation content of Level 2 is related to the emissions of infrastructure and residents' operation energy use.

The LEED Zero certification project launched by USGBC is based on LEED certification. The evaluation content is mainly aimed at carbon emitted from energy delivered and transportation and carbon avoided by renewable energy and carbon offsets, and the calculation formulas of different indicators are given, paying attention to the calculation process and the calculation result of carbon-dioxide equivalent (CO_2E) balance of zero [7].

NZGBC certification aims at greenhouse gas emission and offset, and has certain requirements for building emission management and emission reduction plan.

The application for TÜV Rheinland and BRE certification includes four directions: embodied carbon, operating carbon (new buildings), operating carbon (existing buildings), and life cycle carbon. Certification not only scores carbon emissions corresponding to the certification scope, but also scores personnel management, equipment, and measurement management for different scopes, and determines the final rating according to the final score.

The main evaluation contents of different certification systems are compared in the following Table 2.

4 Conclusion

Through the comparative study of five zero-carbon building certification systems introduced by CAGBC, GBCSA, USGBC, NZGBC, and TÜV Rheinland and BRE, it is found that there are some differences in certification preconditions, evaluation objects, and evaluation contents among different certification systems, but the certification focuses on the carbon emitted and avoided, and the five certification systems all focus on the formulation, recording, and calculation of the carbon emission range.

Part of the certification system evaluation content also includes management, innovation, and so on. Among the certification standards for zero-carbon buildings introduced by CAGBC, ZBC-design standard is used to guide new buildings or transform existing buildings to achieve zero-carbon emission, which is a one-time

Table 2 Comparison of main evaluation contents of zero-carbon building certification

Certification authority	Carbon[a] emitted	Carbon[b] avoided	Energy[c] efficiency	Emission[d] management	Emission[e] reduction plan	Impact and[f] innovation influence
CAGBC	√	√	√			√
GBCSA	√	√	√			
USGBC	√	√				
NZGBC	√	√		√	√	
TÜV Rheinland and BRE	√	√		√		

[a]Carbon emitted in CAGBC certification refers to embodied carbon, refrigerants, RECs and carbon offsets, on-site combustion, etc. In GBCSA, it refers to the emissions related to the residents' operation energy use, embodied emissions, renovation emissions, deconstruction emissions; In USGBC, it refers to the energy delivered and transportation of the project; In NZGBC, it refers to greenhouse gas emissions; In TÜV Rheinland and BRE, it refers to implicit carbon emissions, operational carbon emissions (new buildings and existing buildings), and life cycle carbon emissions

[b]Carbon avoided includes RECs and carbon offsets in CAGBC certification; In GBCSA, it refers to the consumption of renewable energy; In USGBC, it refers to on-site renewable energy generated and exported to grid, off-site renewable energy procured, carbon offsets; In NZGBC, carbon credits offset greenhouse gas emissions; In TÜV Rheinland and BRE, life cycle carbon certification requires that carbon compensation can completely offset carbon emissions, and there is no clear requirement for other scope certification

[c]Energy efficiency in CAGBC refers to energy efficiency, peak demand, and airtightness, and in GBCSA refers to the proportional requirements for renewable energy

[d]Emission management in NZGBC means that demonstrate that building emissions are being managed by achieving a 4 Star NABERSNZ whole building/base building rating, or at least 8 out of 20 points (base building) or 9 out of 23 points (whole building) in the "Greenhouse Gas Emissions" Credit of Green Star Performance; In TÜV Rheinland and BRE, it refers to personnel management, equipment and measurement management, and supplier management

[e]Emission reduction plan in NZGBC indicates that there are plans to further reduce emissions, including phasing out all fossil fuel consumption for space and hot water heating by 2025 and all other fossil fuel consumption by 2030

[f]Impact and innovation in CAGBC refers to the need to use two innovative strategies in zero-carbon building design certification

certification and provides a way to ensure that buildings can achieve zero-carbon emission after being put into operation. The evaluation content has certain requirements for energy efficiency, and the application for certification also needs to pay attention to impact and innovation. ZBC-performance certification requires energy efficiency, but there is no clear requirement for impact and innovation. GBCSA pays more attention to energy efficiency, and thinks that the best practice to achieve net zero/net positive carbon should start with on-site energy efficiency, followed by on-site renewables, and then consider off-site renewables or carbon offsets. The LEED Zero certification issued by USGBC focuses on the calculation process and the calculation result is carbon-dioxide equivalent (CO_2E) balance of zero. NZGBC has certain requirements for building emission management and emission reduction plan. The certification issued by TÜV Rheinland and BRE is based on the International Standard Organization (ISO) and BRE standards, as well as the design and calculation of building carbon emissions in China, covering all building types and life cycle stages.

Under the vision of carbon neutrality in peak carbon dioxide emissions, in September 2021, "Working Guidance For Carbon Dioxide Peaking And Carbon Neutrality In Full And Faithful Implementation Of The New Development Philosophy" mentioned that improving the quality of green and low-carbon development in urban and rural construction, promoting the low-carbon transformation of urban and rural construction and management mode, vigorously developing energy-saving and low-carbon buildings, and accelerating the optimization of building energy structure. In October 2021, the State Council issued "Action Plan for Carbon Dioxide Peaking Before 2030", which mentioned the key tasks of peak carbon dioxide emissions Action in urban and rural construction, promoted the green and low-carbon transformation of urban and rural construction, accelerated the improvement of building energy efficiency, accelerated the optimization of building energy structure, and promoted the low-carbon transformation of rural construction and energy consumption. In March 2022, the Ministry of Housing and Urban–Rural Development issued "14th Five-Year Plan for Building Energy Conservation and Green Building Development", which defined the key tasks of improving the quality of green building development, improving the energy-saving level of new buildings, strengthening the energy-saving green transformation of existing buildings, promoting the application of renewable energy, implementing building electrification projects, promoting new green construction methods, promoting the popularization and application of green building materials, promoting regional building energy coordination, and promoting the construction of green cities during the 14th Five-Year Plan period.

In terms of relevant standard systems, China has promulgated and implemented such standard systems as "Assessment Standard for Green Building" and "Building Carbon Emission Calculation Standard" [8]. The index system of "Assessment Standard for Green Building" consists of five categories: safety, durability, health and comfort, convenience of life, resource conservation, and environmental livability, with improvement and innovation as extra points [9]. "Building Carbon Emission Calculation Standard" divides the calculation of building carbon emission into three

stages: operation stage, construction and demolition stage, building material production and transportation stage, and specifies the calculation method and related details. "Technical Standard for Nearly Zero Energy Building" explains the basic provisions, indoor environmental parameters, energy efficiency indicators, technical parameters, technical measures, and evaluation of net zero energy-consumption buildings, and divides the building types into near-zero energy-consumption buildings, ultra-low energy-consumption buildings, and zero energy-consumption buildings [10]. In September 2021, Tianjin Low-carbon Development Research Center took the lead in formulating the "Guidelines for Identification and Evaluation of Zero-carbon Buildings", which is the first group standard for zero-carbon buildings in China. But at present, there is no national standard related to zero-carbon building certification in China.

From the relevant policy documents, before 2020, the concept of zero-carbon building appeared less frequently in relevant policy documents, and in recent years, zero-carbon building has been mentioned more and more in relevant policy documents [11]. From the perspective of the relevant standard system, the current national standards mainly focus on green buildings and buildings with net zero energy consumption. Besides the carbon emission-related indicators, the standard index system also considers other aspects, such as health, comfort, and convenience of life, while the standard system related to zero-carbon building certification is still being improved. To sum up, the development of zero-carbon buildings in China is in the primary stage, and the construction industry needs to transition from the current stage to low-carbon and zero-carbon. When applying for zero-carbon certification, organizations or enterprises can give priority to applying for certification systems with rich evaluation indexes and different certification levels, so as to reduce the difficulty of certification, increase the success rate of certification applications, and enhance the confidence of organizations or enterprises applying for certification. The zero-carbon building certification issued by CAGBC and the building certification jointly issued by TÜV Rheinland and BRE are more in line with the above conditions. Therefore, organizations or enterprises interested in applying for zero-carbon building certification can consider choosing between them. After that, relevant organizations or enterprises can further apply for LEED Zero and other certification systems with stricter requirements on carbon balance introduced by USGBC.

In addition, individuals or organizations need to pay attention to the requirements of some certifications on the premise and evaluation object of certification and the validity period of certification when conducting zero-carbon certification for buildings. When the authentication object meets the relevant requirements, the authentication goal is determined by considering the difficulty of authentication and the popularity of authentication.

References

1. Dong HR, Liu J, Qin YY, Wu SR, Luo G (2021) Thoughts on moving from green buildings and passive buildings to zero-carbon buildings. Chongqing Architect 10:19–22
2. Chen DY (2021) Revision of German green building evaluation criteria under the vision of carbon neutralization and its enlightenment. South China University of Technology, Beijing
3. Wang S, Huang S (2021) TüV Rheinland: helping China to develop with high quality and build a better world. Import Export Manag 579(12):58–60
4. Guo WZ, Wang QQ, Meng C, Chen YH (2023) Canadian zero-carbon building practice and enlightenment. HVAC 02:57–63
5. Yu F, Feng W, Leng JW (2022) American zero-carbon building policy and development. HVAC 52(04):72–82
6. Hang N, Jiang JD (2021) A preliminary study on the pathways to achieving zero-carbon buildings and communities in the UK: a case study of the Hockerton housing project. In: Proceedings of the 2021 annual conference and first chief engineer forum of the chief engineer working committee of the Chinese civil engineering society, pp 89–92
7. Zhou J (2012) Study on zero-carbon building standard system under the goal of carbon neutrality. China Qual Stand Herald 275(03):21–23
8. Standard N (2021) Technical standard for zero-carbon building was launched. Build Energy Effic 04:135
9. Zhang SC, Wang K, Xu W (2023) Research on carbon emission control indicators of low-carbon, near-zero carbon and zero-carbon public buildings. Build Sci 02:1–35
10. Xia QQ (2022) Thoughts on zero-carbon buildings based on the "dual carbon" goal. Real Estate World 19:23–25
11. Zhang SC, Wang K, Yang XY, Xu W (2023) Research on carbon emission control indicators of low-carbon, near-zero carbon and zero-carbon residential buildings. Build Sci 02:11–57

Mechanical Manufacturing and Electrical Automation Control

Experimental Study on Transient Behavior of Proton Exchange Membrane Electrolytic Cells Under Voltage Fluctuations

Xin Su, LiJun Xu, Bin Hu, Di Zhu, LuXiang Mi, and TianYi Jia

Abstract The transient behavior of proton exchange membrane (PEMEC) under voltage fluctuation conditions is a research focus for hydrogen production from renewable energy sources. This paper conducts an experimental study on the transient response of PEMEC under voltage fluctuation conditions. The transient behavior of PEMEC under different voltage fluctuation conditions is explored. The experimental results show that the voltage fluctuation causes a significant current overshoot. The current overshoot amplitude increases with the voltage step amplitude. The overshoot phenomenon is more pronounced at low voltages, and the overshoot decreases with the overall voltage increase. Voltage regulation at high voltages should reduce the magnitude of voltage changes to prevent excessive transient power from damaging the electrolyzer and creating safety problems. In addition, the current overshoot is larger at the beginning of continuous voltage fluctuation. The current amplitude gradually decreases and stabilizes as the voltage fluctuation time increases. This study elucidates the transient behavior of PEMEC during voltage fluctuations. The study results are expected to provide technical support and data reference for developing control systems for renewable energy hydrogen production systems under fluctuating conditions.

Keywords Proton exchange membrane electrolyzer · Transient response · Overshoot phenomenon · Voltage control · Renewable energy · Hydrogen energy

1 Introduction

Energy is the basis of human social development. In recent years, the increase in energy demand and over-dependence on fossil energy has led to resource, environmental, and energy security problems. Renewable energy is expected to become

X. Su · L. Xu (✉) · B. Hu · D. Zhu · L. Mi · T. Jia
Key Laboratory of Hydrogen Energy Utilization Technology, Xinjiang Institute of Engineering, Urumqi 830023, China
e-mail: false1311817899@qq.com

S. Yadav et al. (eds.), *Energy Power and Automation Engineering*, Lecture Notes in Electrical Engineering 1118, https://doi.org/10.1007/978-981-99-8878-5_30

an alternative to fossil energy. However, the fluctuating and intermittent nature of renewable energy leads to the safety problems of grid-connected renewable energy on a large scale. Using renewable energy for hydrogen production by electrolysis of water can provide a new way of renewable energy consumption [1–4]. Hydrogen production from renewable energy has two advantages: on the one hand, hydrogen production from electrolytic water can be a new way to consume excess renewable energy; on the other hand, the lower cost of residual electricity can significantly reduce the cost of hydrogen production. Therefore, research on renewable energy hydrogen production will promote the development of renewable energy and the hydrogen industry [5, 6].

The proton exchange membrane electrolyzer (PEMEC) is an important device for hydrogen production from electrolytic water. Its adaptive fluctuation characteristics can be well adapted to intermittent renewable energy sources [7]. Göellei et al. [8] modeled hydrogen production electrolyzers for complex energy systems. The results indicate that the hydrogen production system has a good ability to dissipate fluctuating power. The PEMEC has a good fluctuation adaptation, so the effect of voltage fluctuation on the PEMEC should be studied.

In the current study, fluctuating voltages were found to have a shock on the durability of hydrogen production equipment. In the test protocol of Honsho et al. [9], a PEMEC experiment was presented after 160 days of fluctuating voltage shocks. The results of the study showed that fluctuating voltages could cause performance degradation. Similarly, it was noted that fluctuating voltage affects catalyst stability [10]. In addition, there is an effect of voltage fluctuation on electrolysis efficiency. Dobo and Palotas [11] experimentally investigated the behavior of an electrolyzer under fluctuating power conditions and found that voltage fluctuation significantly affects the system efficiency. In addition to electrolysis efficiency, voltage fluctuations also affect power consumption. Zhao et al. [12] found that fluctuating voltage causes an increase in power consumption during high-temperature PEMEC voltage regulation experiments.

Although fluctuating voltage has many effects on PEMEC, the principle of transient behavior is not yet clear. Few articles have studied the transient behavior of PEMEC under voltage fluctuations. Therefore, in this paper, the transient behavior of PEMEC during the voltage step is experimentally investigated. The study results are expected to provide technical support and data reference for developing control systems for renewable energy hydrogen production systems under fluctuating conditions.

2 Experimental Details

The experimental equipment used in the experiment is a customized PEM electrolytic cell. The end plate is made of insulated stainless steel and has good mechanical strength. The current collector is made of a pure titanium plate that has undergone gold plating and mirror treatment and has a low contact resistance. The collector is

inscribed with a 50 mm × 50 mm serpentine flow field. The channel width is 1 mm, the channel depth is 2 mm, and the rib width is 1 mm. Both the anode and cathode adopt a thickness of 450 μm titanium felt as a porous layer. Among them, the anode titanium felt is coated with 0.5 μm Iridium plated coating, and the cathode titanium felt is coated with 0.5 μm Platinum plated coating. The membrane electrode (MEA) uses Nafion 117, and the catalyst uses IrO_2 and Pt. IrO_2 has a loading capacity of 2.0 mg/cm^2, and Pt has a loading capacity of 2.5 mg/cm^2. The size of the membrane electrode is 50 mm × 50 mm × 0.18 mm. The power supply adopts an A-BF SS-K1560SP high-precision regulated power supply with a voltage range of 0–15 V, a current range of 0–60 A, a current resolution accuracy of 1 mm, and set progress of ± 0.03%. The DC-regulated power supply is connected to the computer through an interface and can achieve power control and parameter recording functions through programming. The constant temperature water bath pot adopts the HH-2 model product of Shaoxing Shangyu Xiangda Instrument Manufacturing Company, with a temperature control accuracy of ± 0.5 °C. The peristaltic pump adopts the BT1100S model product of Rongbai Constant Flow Pump Manufacturing Co., Ltd., with a flow rate accuracy of ± 1%, which can meet experimental requirements.

The experimental time was adjusted according to the experimental content, and the data were recorded every 1 s. In order to improve the repeatability and credibility of the experimental data, the data were averaged by repeating the experiment three times. To ensure that the experiment is completed under the same scale, the data of this experiment are measured in the same equipment under continuous operation.

3 Results and Discussion

3.1 The Effect of a Single Step in Voltage Generation

The transient behavior of the voltage step increase is shown in Fig. 1. The experimental results show that the current has an extremely fast response rate for voltage step changes at the millisecond (ms) level. According to Fig. 1a, a significant overshoot of the current occurs when the voltage steps from 1.6 to 2.0 V. At 30 s, the current changes from a stable level to a stable level. The current overshoot reaches 4.8 times the current change value at 30 s when the current jumps from a stable 1.8–7.6 A and then slowly decreases to 2.8 A at 60 s. The current overshoot amplitude reaches 4.8 times the current change value. During the whole process, the device's power jerked up from 2.9 to 15.2 W, then slowly decreased to 5.6 W. To study the effect of voltage step amplitude on the current overshoot phenomenon, the experiment was set to step from 1.6 to 2.5 V. The results are shown in Fig. 1b. At 30 s, the power jumps from the originally stable 1.2 to 17.2 A and slowly decreases to 3.5 A at 60 s. The current overshoot amplitude reaches 6.0 times the current change value. Throughout the process, the device power jerked up from 1.9 to 43.0 W and

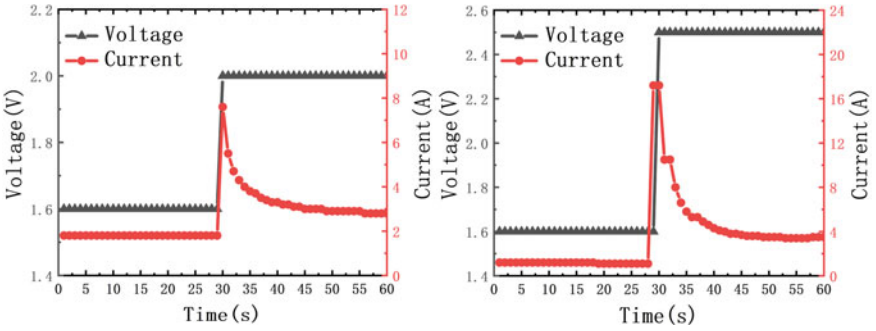

(a)1.6 V-2.0 V (b)1.6 V-2.5 V

Fig. 1 Voltage step-up

then slowly decreased to 8.8 W. Comparative experimental results showed that the current overshoot amplitude increased as the voltage step amplitude increased.

The transient behavior of the voltage step-down is shown in Fig. 2. The experimental results of the voltage step-down from 2.0 to 1.6 V are shown in Fig. 2a. At 30 s, the power decreases sharply from the originally stable 2.9 to 0 A and then rises slowly to 1.8 A at 60 s. The device power decreases sharply from 5.8 to 0 W and then rises slowly to 2.9 W. The current overshoot phenomenon is more obvious when the voltage decreases from 2.5 to 1.6 V (Fig. 2b). In particular, the current is negative from 30 to 45 s due to the large step amplitude. However, since the measurement device only records positive currents, the minimum value of the current can only be recorded as 0 A.

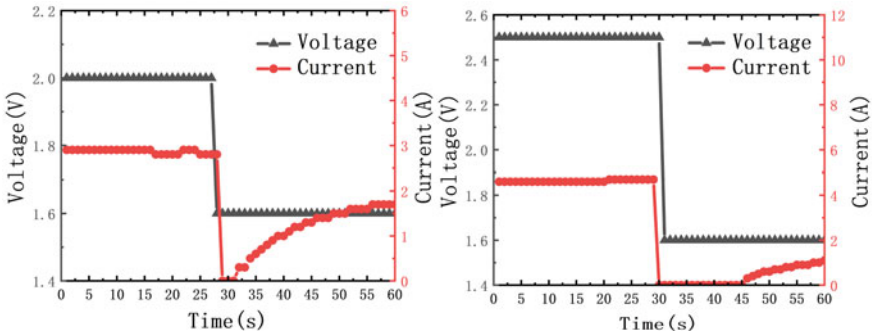

(a)2.0 V-1.6 V (b)2.5 V-1.6 V

Fig. 2 Voltage step-down

3.2 The Effect of Two Steps of Voltage Generation

To investigate the effect of fluctuating power conditions on the electrolyzer, two-step voltages were used in the electrolyzer voltage variation. The experiments were set up with the voltage first rising and then falling, and the results are shown in Fig. 3. The voltage was increased from 1.6 to 2.0 V and then to 1.6 V. The experimental results are shown in Fig. 3a. The current rises sharply from 1.6 to 6.7 A at 30 s and slowly decreases to 2.7 A. The current decreases sharply to 0 A at 60 s, continues for 5 s, and then slowly recovers to 1.6 A. The overshoot generated by the step-up and step-down of the current is 3.6 and 2.5 times the current change, respectively. In order to study the effect of the voltage step on current overshoot under high voltage conditions, the voltage is set from 2.0 to 2.5 V and then stepped down to 2.0 V. The experimental results are shown in Fig. 3b. The overshoot produced by the step-up and step-down of the current is 2.8 and 2.1 times the current change, respectively, which is slightly lower than the overshoot phenomenon in Fig. 3a. The experimental results are shown in Fig. 3c, where the voltage is set from 2.5 to 3.0 V and then stepped down to 2.5 V. The overshoot generated by the step-up and step-down of the current is 2.4 and 1.5 times the current change, respectively. The experimental results show that the overshoot phenomenon is more obvious only when the voltage steps at low voltage conditions, and the amount of overshoot decreases with the increase of the overall voltage.

To explore more fluctuating power effects, the effect of voltage first decreasing and then increasing on its performance is studied here, as shown in Fig. 4. The experimental results are shown in Fig. 4a for a voltage that first steps down from 2 to 1.6 V and then up to 2.0 V. The current decreases sharply from 3.3 to 0 A at 30 s and then rises slowly to 2 A. The current increases sharply to 7.6 A at 63 s and then recovers slowly to 3.1 A. The overshoot generated by the step decrease and increase in current is 1.5 and 4.1 times the current change, respectively. In the second group of experiments with the same overall voltage increase and the same step amplitude (shown in Fig. 4b), the overshoot of the current during the step-down and step-up is 2.1 and 3.6 times the current change, respectively. The results of the experiments where the voltage is set from 3.0 to 3.5 V and then stepped up to 3.0 V are shown in

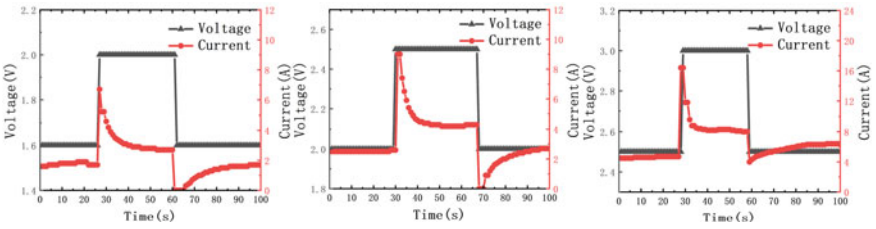

(a)1.6 V-2.0 V-1.6 V (b)2.0 V-2.5 V-2.0 V (c)2.5 V-3.0 V-2.5 V

Fig. 3 Voltage rises and then falls

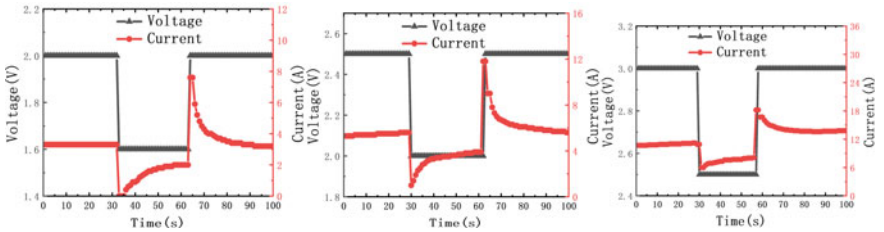

(a)2.0 V-1.6 V-2.0 V (b)2.5 V-2.0 V-2.5 V (c)3 V-2.5 V-3 V

Fig. 4 Voltage drops and then rises

Fig. 4c. The overshoot produced by the step-down and step-up of the current is 0.8 and 0.8 times the current change, respectively. The results are similar for the voltage drop followed by a rise followed by a fall, and the current overshoot decreases with the overall voltage rise.

The experimental results of the continuous voltage rise are shown in Fig. 5. The experiment's voltage steps from 1.6 to 2.0 V at 30 s and from 2.0 to 2.5 V at 60 s. During this process, the current is raised from 1.4 to 5.9 A at 30 s, then slowly falls back to 2.3 A, then rises from 2.3 to 8.3 A at 60 s, then slowly falls back to 3.9 A. The overshoot of the two successive steps of the current rise is 4.0 and 2.8 times the current change, respectively. 4.0 and 2.8 times the current change. The overshoot generated by the current decreases significantly as the voltage increases. However, it is particularly important to note that the maximum instantaneous power during the 2.0 V step to 2.5 V reaches 20.8 W, which is much larger than the steady power at 1.6 V (2.2 W), 2.0 V (4.6 W), and 2.5 V (9.8 W). Therefore, voltage regulation at high voltage should reduce the magnitude of voltage change to prevent the safety problem caused by excessive transient power damaging the electrolytic cell.

Fig. 5 Continuous voltage rise

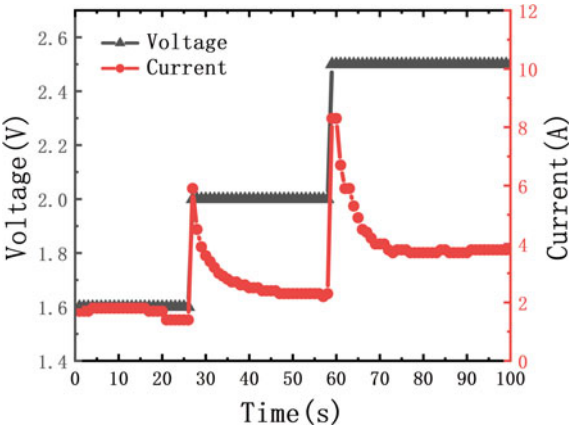

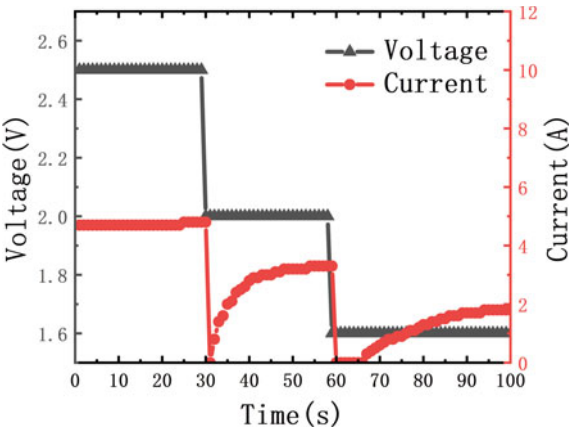

Fig. 6 Continuous voltage drop

The experimental results of the continuous voltage drop are shown in Fig. 6. In this process, the current decreases from 4.8 to 0 A at 30 s, then slowly rises to 3.3 A, then decreases from 3.3 to 0 A at 60 s, then slowly rises to 1.9 A. The overshoot of the two successive step decreases of the current is, respectively, 2.2 and 1.4 times the current change.

3.3 The Effect of Continuous Voltage Fluctuations

The experimental results of the continuous voltage fluctuation are shown in Fig. 7. The experiment was set up with the voltage fluctuating continuously between 2.0 and 2.5 V. At the beginning (within 0–10 s), the current fluctuation amplitude was large (current fluctuated between 1.9 and 15.6 A) due to the continuous voltage fluctuation, and the overshoot generated by the current during the voltage fluctuation was significantly larger. However, with the increase of the voltage fluctuation time, the current fluctuation tends to stabilize, and the current fluctuation amplitude gradually decreases (the current fluctuates between 0 and 8.7 A).

The experimental results show that at the beginning of the continuous fluctuation, the current has an obvious overshoot phenomenon when the current fluctuation amplitude is larger; with the increase of voltage fluctuation time, the current fluctuation amplitude gradually decreases and finally stabilizes.

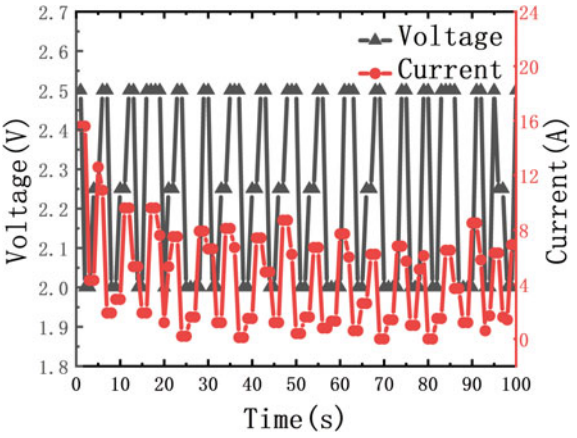

Fig. 7 Continuous voltage fluctuation

4 Conclusion

In this paper, an experimental study of PEMEC transient response under voltage fluctuation conditions is conducted. The experiments are carried out by first visualizing the renewable energy volatility as voltage fluctuation, thus, the transient response characteristics of the PEM electrolyzer under fluctuating power input conditions. The following conclusions were obtained from this experiment:

(1) The input current produces a significant overshoot under fluctuating power conditions. Moreover, the amplitude of the current overshoot increases with the voltage step amplitude in both step-up and step-down conditions.
(2) Overshoot is only more pronounced at low voltage conditions with voltage steps, and the overshoot decreases as the overall voltage increases. Therefore, voltage regulation at high voltage should reduce the magnitude of voltage change to prevent excessive transient power from damaging the electrolyzer and creating safety problems.
(3) When the voltage fluctuates continuously, the current overshoot is obvious at the beginning, and the current fluctuation is large; as the voltage fluctuation time increases, the current fluctuation amplitude gradually decreases and finally becomes stable.

Acknowledgements The project is supported by Foundation project: National Natural Science Foundation of China (Grant No. 51967020); Key R&D projects of Xinjiang Uygur Autonomous Region (China): (Grant No. 2022B01003-1). Xinjiang Uygur Autonomous Region Youth Science and Technology Top Talent Project: (Grant No. 2022TSYCCX0053).

References

1. Hermesmann M, Müller TE (2022) Turquoise, blue, or grey? Environmentally friendly hydrogen production in transforming energy systems. Prog Energy Combust Sci 90:100996
2. Oliveira AM, Beswick RR, Yan YS (2021) A green hydrogen economy for a renewable energy society. Curr Opin Chem Eng 33:100701
3. Hosseini SE, Wahid MA (2016) Hydrogen production from renewable and sustainable energy resources: Promising green energy carrier for clean development. Renew Sustain Energy Rev 57:850–866
4. Salehmin MNL, Husaini T, Goh J (2022) High-pressure PEM water electrolyser: a review on challenges and mitigation strategies towards green and low-cost hydrogen production. Energy Conver Manag 268:115985
5. Dang J, Yang FY, Li YY et al (2022) Transient behaviors and mathematical model of proton exchange membrane electrolyzer. J Power Sour 542:231757
6. Astakhov O, Agbo SN, Welter K et al (2021) Storage batteries in photovoltaic–electrochemical device for solar hydrogen production. J Power Sour 509:230367
7. Carr S, Premier GC, Guwy AJ et al (2014) Hydrogen storage and demand to increase wind power onto electricity distribution networks. Int J Hydr Energy 39(19):10195–10207
8. Göellei A, Goerbe P, Magyar A (2016) Measurement based modeling and simulation of hydrogen generation cell in complex domestic renewable energy systems. J Clean Product 111:17–24
9. Honsho Y, Nagayama M, Matsuda J et al (2023) Durability of PEM water electrolyzer against wind power voltage fluctuation. J Power Sour 564:232826
10. Rheinländer PJ, Durst J (2021) Transformation of the OER-active IrOx species under transient operation conditions in PEM water electrolysis. J Electrochem Soc 168(2):024511
11. Dobo Z, Palotas AB (2016) Impact of the voltage fluctuation of the power supply on the efficiency of alkaline water electrolysis. Int J Hydr Energy 41(28):11849–11856
12. Zhao DQ, He QJ, Yu J et al (2022) A data-driven digital-twin model and control of high temperature proton exchange membrane electrolyzer cells. Int J Hydr Energy 47(14):8687–8699

Mechanical Design of an Intelligent Grass Square Laying Vehicle

Xin Chen, Zige Fan, Yilan Wu, Xiao Qi, Xiaoxuan Luan, Haoyu Qin, Maotou Song, and Yaxi Wang

Abstract At present, desertification management mainly adopts the method of laying grass squares. However, at present, the grass square lattice mainly relies on manual completion, low efficiency, and high cost. Therefore, the author's team has developed a kind of intelligent grass square lattice laying vehicle. The device mainly includes: grass delivery device, laying mechanism, and traveling mechanism. The design of the device realizes the horizontal and vertical simultaneous laying of grass squares, instead of manual reinforcement of grass squares, which greatly improves the working efficiency, reduces the amount of manual labor, and solves the problems existing in the traditional sand fixing vehicle. The prototype test results show that the device can complete the task with higher speed and better laying effect. The intelligent grass lattice laying vehicle proposed in this paper has high practicality and feasibility, which is of great significance to improve the efficiency and quality of grass lattice laying, and at the same time provides a new research idea for other researchers in the field of desertification management.

Keywords Desert management · Grass square sand barrier · Mechanical automation laying car

1 Introduction

Land desertification in the western region of China has been increasing, which seriously affects the local ecological environment and social development. In the work of desert management, grass square grid is proven to be a proven engineering technology means, setting grass square grid sand barriers can increase the roughness of the dune surface, effectively reduce the airflow velocity close to the surface, greatly weaken the scouring of the surface by high winds, and therefore play a role in wind and sand consolidation [1]. At present, the laying of grass squares is still mainly done by hand. Manual laying of grass squares is labor-intensive, and the quality of laying

X. Chen · Z. Fan · Y. Wu · X. Qi · X. Luan · H. Qin · M. Song · Y. Wang (✉)
Wuhan Institute of Technology, Wuhan, China
e-mail: wangyaxi@wit.edu

S. Yadav et al. (eds.), *Energy Power and Automation Engineering*, Lecture Notes in Electrical Engineering 1118, https://doi.org/10.1007/978-981-99-8878-5_31

is unstable, which is inefficient and costly in the task of wind and sand fixation [2]. In contrast, mechanized sand control is more scientific and efficient, which has an important role in environmental protection and ecological construction and is worth promoting in future desert management [3]. In China, sand control and sand management machinery and equipment have not been popularized and promoted. Due to the lack of benefit assessment, the application value of sand fixation equipment cannot be accurately quantified and assessed, and the lack of scientific standard basis for the design and acceptance of mechanized sand fixation afforestation operations has limited the scope of its promotion and application [4].

2 Research Status and Analysis of Existing Products

At present, the research on grass square laying machines at home and abroad is still in the preliminary stage. In 2005, Liu et al. [5] carried out simulation optimization of the laying wheel system to improve the design method of traditional machinery. In 2006, Shu and Liu [6] analyzed the possibility of the WTC-5120 desert vehicle as a traction device through theoretical calculations and vehicle as traction equipment when the robot passes in the desert. In 2007, Wang and Liu [7] designed a mechanical control system with advanced functions and reliable technology based on PLC system. In 2016, Li et al. [8] focused on analyzing the bottlenecks that need to be broken by mechanized sand fixation. In 2022, Kong et al. [9] analyzed that the design and development of sand fixation vehicle based on digital, intelligent technology are of social development and are of great significance.

The large sand fixing equipment currently in use is powered by a truck with a forage box and laying structure, which is laid during the forward movement of the truck, the structure is shown in Fig. 1, but this equipment has more limitations:

(1) Can only be laid in one direction, in the vertical direction to continue laying damage to the paved part.
(2) This equipment presses the grass into the ground by rollers when laying, so it is necessary to use pre-made grass curtains for laying work, but pre-made grass curtains will add extra labor cost.

Fig. 1 Existing grass-squared three-dimensional sand fixation vehicle

Aiming at the shortcomings of the current research situation and the defects of the existing equipment, this paper mainly starts from the structural design of the device: the research of the overall structural design of the vehicle, including the design of the grass delivery device, the laying mechanism, the traveling mechanism, as well as the design of the rotary sand pushing mechanism innovation, in order to enhance the degree of automation of the device.

3 Design Solutions

The author has designed the overall structure of the device, which is shown in Fig. 2. It mainly consists of the grass conveying part and the traveling part, where the traveling part contains the grass square laying mechanism and the traveling mechanism. The straw conveying part arranges and conveys the straw to be laid. The grass square laying mechanism mainly includes longitudinal laying mechanism, transverse laying mechanism, and rotating sand pushing mechanism, while the walking mechanism is powered by crawler.

3.1 Forage Conveying Device

Since the collected grass is stored in the grass box in a loose state, if the grass is directly spread to the ground in this state, not only will the grass fly apart, but also the effect of unorganized grass to prevent wind and sand fixation will be greatly reduced. Therefore, we design the grass conveying device and spread the grass by mechanical flattening.

The straw conveying device is shown in Fig. 3, which mainly contains conveying mechanism, driving mechanism, and overall frame. The conveying mechanism is composed of flattening rollers, and the flattening rollers are equipped with friction

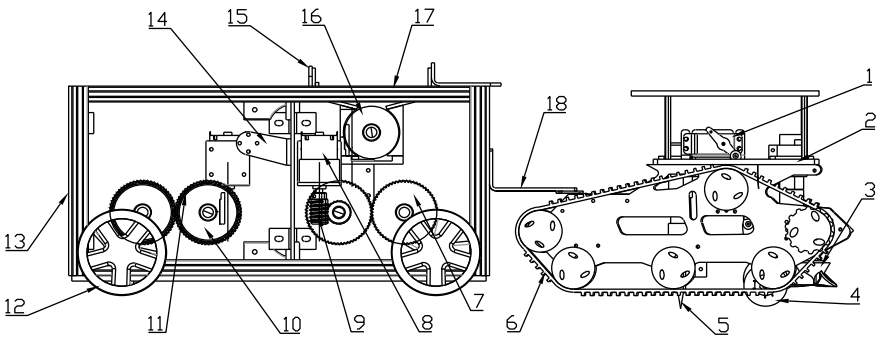

Fig. 2 Overall structure of grass square laying truck

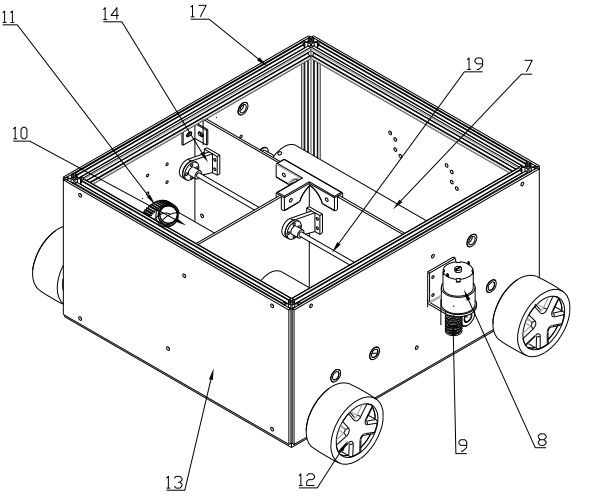

Fig. 3 Forage conveying device

cams to increase the friction between the flattening rollers and the straw, so that the straw can be quickly sorted and conveyed to the discharge port. The driving mechanism is mainly driven by the drive motor through the gear transmission to achieve the function. The front end of the straw conveying device (the forward direction of the vehicle is the reference) is the longitudinal straw conveying part, and the prefabricated straw curtain is placed on the straw curtain support and is laid longitudinally with the forward movement of the device. The rear end of the grass delivery device is the transverse grass delivery section. The transverse laying is carried out by intermittent placement of the grass. The overall frame is constructed from aluminum profiles.

3.2 Forage Longitudinal Spreading Mechanism

The longitudinal laying mechanism is required to press the grass strip into the ground during forward laying of the unit. The longitudinal laying mechanism of grass square is shown in Fig. 4, which mainly consists of longitudinal connecting rod, grass press, rudder, and swing arm connecting rod. According to the characteristics of universal joint, one section is fixed to the base to limit its degree of freedom to 1, and the other end is connected to the longitudinal connecting rod. By controlling the rotation angle of the tiller, the contact between the grass press and the ground can be controlled, so that the flexibility and adjustable range of the device are enhanced.

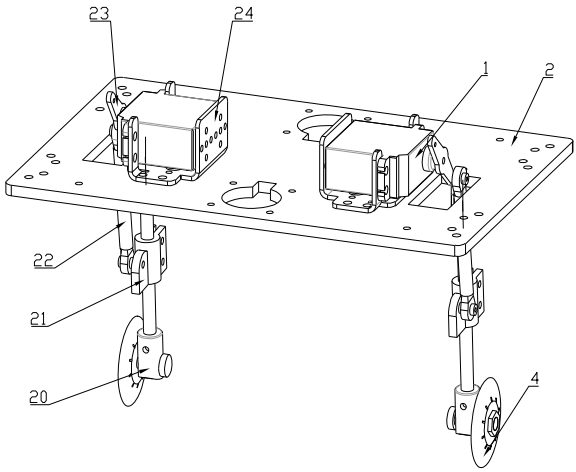

Fig. 4 Grass square longitudinal laying mechanism

3.3 Grass Longitudinal Spreading Mechanism

The transverse spreading mechanism presses the transverse grass into the sand through the inserting knife. As shown in Fig. 5, the telescopic motor is installed on the baseplate through a bracket, controlling the telescopic motor's feed motion and driving the cutting tool to move downward, achieving the function of pressing horizontal forage into the sand. The horizontal forage forms a grid pattern with the vertical grass belt, completing the laying of the grass grid. The device works in a loop, thus achieving continuous laying of the grass grid in both horizontal and vertical directions.

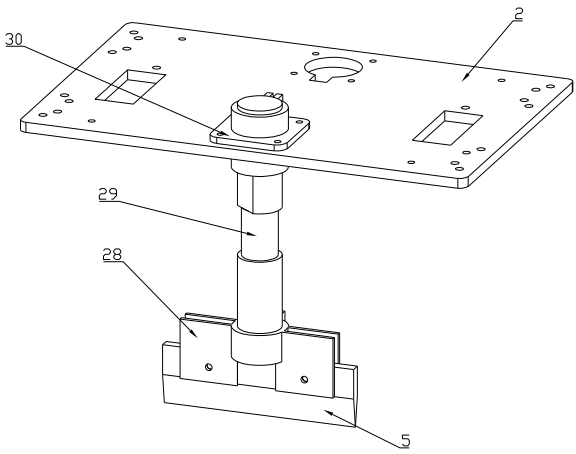

Fig. 5 Grass square horizontal laying mechanism

3.4 Rotating Sand Pushing Mechanism

The rotating sand sweeping mechanism is the main innovative structure of this mechanical device. The main function is to push the sand from the middle of the grass square to the roots of the wheat grass and press down the sand sweeping wheel to compact and strengthen the grass square. The author has made a variety of solutions to design this structure.

Option 1 (Fig. 6) the number of wheel leaves is three, the angle between adjacent wheel leaves is 120°, the angle between the wheel leaf edge pushing sand structure, and the central linkage is also 120°. In the process of rotation, the sand at the center of the lower pressure to push around; the advantage of this structure is simple to make; the mechanism is stable; the disadvantage is that the amount of pushing sand is not easy to control; the accuracy of other control components requires a high degree.

Option 2 (Fig. 7) The number of wheel blades is five, with a curved shape and a thin wall around the edge to prevent dust from being raised in the process of pushing sand. The advantages of this structure are that the curved shape makes the process of pushing sand more smooth, and the number of wheel blades is set appropriately so that the corresponding function can be realized with a small rotation angle.

Fig. 6 Scenario 1

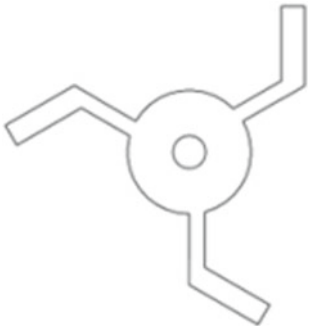

Fig. 7 Scenario 2

Fig. 8 Scenario 3

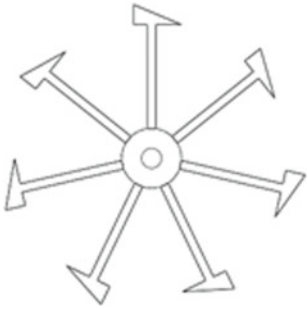

Fig. 9 Scenario 4

Option 3 (Fig. 8) The number of wheel blades is seven, and the edge of the sand pushing structure is a covenant-shaped block; the advantages of this structure is easy to make and reasonable structure; the disadvantage is that the sand pushing effect is not ideal.

Option 4 (Fig. 9) has four blades and a spiral curved shape. The advantage of this structure is that the number of blades is reasonably set and easy to control, and the middle solid part is a tab, with a small cross section near the ground end, which is more helpful to insert into the sand.

Through repeated research and discussion of different options, scheme four has been ultimately chosen as the final design plan.

As shown in Fig. 10, the rotating sand sweeping mechanism mainly consists of a telescopic mechanism, a power device, and a sand sweeping wheel. It can push the sand in the center of the laid grass grid to the surroundings, reinforcing the grass grid and effectively prolonging its service life and sand fixing effect. The rotating sand sweeping mechanism is mainly controlled by a telescopic motor for rotation and pressing.

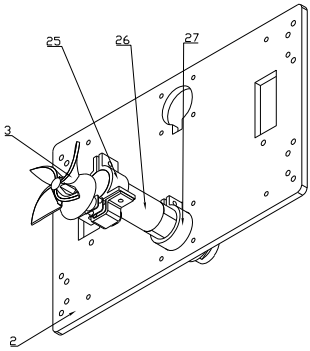

Fig. 10 Rotating sand sweeping mechanism

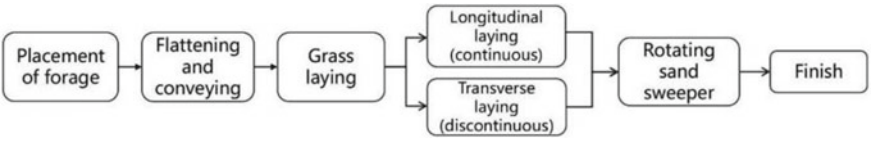

Fig. 11 Workflow diagram of grass square laying truck

4 Working Principle

The specific working principle of the grass square laying car is in Fig. 11: The grass is placed in the grass box, as shown in Fig. 12, and then laid to the ground through the grass outlet by the flattening device. With the forward movement of the grass square laying car, the longitudinal laying device touches the grass belt and presses the grass into the ground; the principle of transverse laying is the same as longitudinal laying; the time of releasing the material is determined according to the movement speed of the grass square laying car; the grass is located under the transverse laying. When the grass is under the transverse laying device, the telescopic motor controls the downward movement of the inserting knife to finish the transverse laying. When the rotary sand sweeping device moves to the middle of the grass square, the telescopic motor controls the rotary sand sweeping wheel to rotate and press down to complete the grass square reinforcement function.

5 Intelligent Control

The intelligent grass square laying vehicle generally uses electricity to control the functions of the traveling device, the grass square laying device, and the rotating sand pushing device. The STM32F103 development board is used to control the mechanical vehicle, as shown in Fig. 13. The STM32F103 series microprocessor

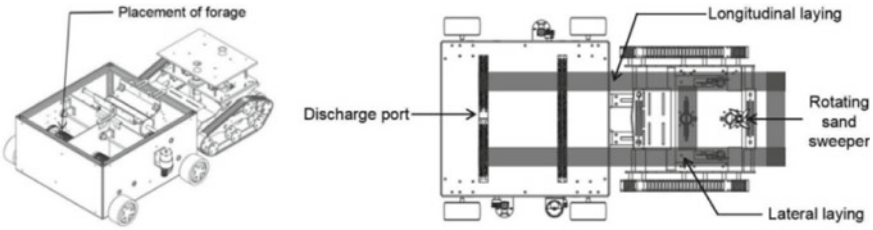

Fig. 12 Schematic diagram of the workflow of the grass square laying truck

Fig. 13 STM32F103 development board

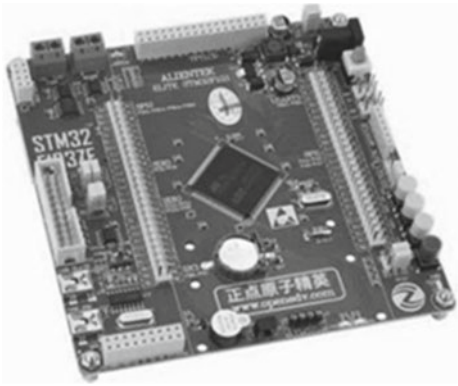

is the first 32-bit standard RISC (compact instruction set) processor based on the ARMv7-M architecture, providing high code efficiency and high control accuracy.

The intelligent grass square laying carriage's functional realizations, such as the flattening roller conveying grass, the rotating pushing sand, and the control of the lateral insertion knife pressing grass all use DC reduction motors. Since closed-loop control of the motor speed is not required, the motor does not come with an encoder, but has the same high control accuracy.

6 Innovation Points

(1) Forage conveying device: Loaded with forage for longitudinal and transverse laying.
(2) Transverse and longitudinal laying mechanism: It is carried out simultaneously with longitudinal laying, and grass squares are laid at once to avoid damage during secondary laying.

(3) Rotating sand pushing mechanism: Automatically pluck the sand in the center of the grass square to the roots of wheat grass around, which makes the grass square more solid and enhances the effect of the grass square in preventing wind and fixing sand.
(4) Traveling mechanism, with good resistance to tipping and traveling stability, but also has a small turning radius of mobility, so to a certain extent can effectively solve the existing sand fixing vehicle long-distance driving cannot maintain a straight line of the problem.

7 Conclusion

The research and application of new science and technology have a prominent role in effective sand control and sand consolidation, curbing the development of land desertification, and controlling and reducing the occurrence of dust storms [10]. Based on the above design, the author's team has designed a fully functional, efficient, and reliable intelligent grass square paving vehicle. According to the prototype test data, the number of grass squares paved in one minute is up to 80, while the paving efficiency of traditional sand fixing vehicle is about 3000 per hour. So, the efficiency of the traditional paving method is increased by nearly 60%. Its design is simple, improves the laying efficiency, saves manpower cost, is easy to operate, has good stability, and has the potential to expand. So, it has innovative and high value of popularization and application.

In the future, the author will conduct in-depth research in the following aspects:

(1) Improve the execution efficiency of the device: At present, the execution efficiency of the intelligent grass square laying vehicle needs to be further improved. The design of the vehicle can be optimized to improve the moving speed and operational flexibility of the vehicle and reduce the laying time.
(2) Designing a more intelligent control system: The current intelligent vehicle for laying grass squares mainly relies on pre-set laying patterns and lacks real-time sensing and decision-making capabilities. Future research could be devoted to designing smarter control systems that enable vehicles to make decisions based on real-time environmental changes, with autonomous planning and path selection capabilities.
(3) Improve the environmental adaptability of the device: There may be differences in the laying effect of the device in different environments. Future research can optimize and improve the intelligent vehicle for different environmental conditions to improve its adaptability and stability.

References

1. Jiang RS (2020) Analysis of the application of grass square sand barriers in wind and sand control. Agric Disaster Res 10(09):126–127+129. https://doi.org/10.19383/j.cnki.nyzhyj.2020.09.051
2. Yuan JC, Chang TL, Zhang YH (2022) Mechanism design of scattered straw square laying robot. Mach Manuf 60(06):15–18. https://kns.cnki.net/kcms2/article/abstract?v=3uoqIhG8C44YLTlOAiTRKibYlV5Vjs7iJTKGjg9uTdeTsOI_ra5_Xe0OYoLHPBrycLpA0wQg8yOUusBCrYZqStITxkemiEGQ&uniplatform=NZKPT&src=copy
3. Li XD, Mou R, Dai M, Qiu JH (2018) A new model of sand control based on mechanization. Temp For Res 1(04):58–62. https://kns.cnki.net/kcms2/article/abstract?v=3uoqIhG8C44YLTlOAiTRKibYlV5Vjs7iLik5jEcCI09uHa3oBxtWoPKZa5iiD8FgWBc9wM03vFowwv0RyJYBZk3F4hjPFAsw&uniplatform=NZKPT&src=copy
4. Xu XY, Zhao P, Tang JN, Ji YF, Ma XB (2020) China's sand control machinery research and development status and prospects. For Grassland Mach 1(02):21–25. https://doi.org/10.13594/j.cnki.mcjgjx.2020.02.006
5. Liu YC, Cao XG, Liu JJ (2005) A preliminary study on the design and experimental research of grass square laying robot laying wheel system. For Mach Woodwork Equip 04:14–16. https://kns.cnki.net/kcms2/article/abstract?v=3uoqIhG8C44YLTlOAiTRKgchrJ08w1e7F1IFNsBV5UuydnAfkZZjeYA_ZlNIwUvr_imyzpJMnTuHk2uo0lMBgRHmYPc7uQ2M&uniplatform=NZKPT&src=copy
6. Shu Q, Liu JH (2007) Robot possibility study for laying grass squares for wind protection and sand fixation. J Agric Mach 07:99–102+120. https://kns.cnki.net/kcms2/article/abstract?v=3uoqIhG8C44YLTlOAiTRKgchrJ08w1e7aLpFYbsPrqGeMWhI2KbO71LTQ7fx9U8hpuzIqGWg9ZTLrUb3U5g0QN5CoQPNkzkL&uniplatform=NZKPT&src=copy
7. Wang GK, Liu YB (2007) Design of an Integrated and efficient control system for a grass square laying robot. Technol Consult Herald 20:11. https://doi.org/10.16660/j.cnki.1674-098x.2007.20.011
8. Li XD, Mou R, Dai M, Qiu JH (2018) A new model of sand control based on mechanization. Temp For Res 1(4):58–62. https://kns.cnki.net/kcms2/article/abstract?v=3uoqIhG8C44YLTlOAiTRKibYlV5Vjs7iLik5jEcCI09uHa3oBxtWoPKZa5iiD8FgWBc9wM03vFowwv0RyJYBZqJC4-c-_J6l&uniplatform=NZKPT&src=copy
9. Kong DR, Sun BG, Zhang KP, Zhang P, Qi Y, Zhang L (2022) China's grass square sand barrier laying machinery research and development status and outlook. For Mach Woodwork Equip 50(11):24–30. https://doi.org/10.13279/j.cnki.fmwe.2022.0161
10. Zhang Y (2022) The "greening of the country" needs to be empowered by science and technology. Ningxia Daily, 2022-03-09(006). https://doi.org/10.28607/n.cnki.nnxrb.2022.000767

Research on the Optimization Model of Time-of-Use Electricity Price Linkage Between Supply and Demand

Dandan Dai, Lili An, Donglin Xie, Jing Liao, and Li Zhang

Abstract After the implementation of time-of-use electricity price on both sides of supply and demand, the system benefits brought by them need to be transmitted and distributed through electricity price. Therefore, this paper uses the game signal transmission theory to construct a dynamic game linkage model of time-of-use electricity price on the supply side and the demand side, which realizes the market-oriented distribution of peak-shaving and valley-filling benefits in each link of the system through dynamic linkage and equilibrium. The simulation shows that the model can objectively distribute the peak-shaving and valley-filling benefits brought by time-of-use electricity price through electricity price signal transmission according to the market force of each link of the system.

Keywords Electricity market · Electricity price linkage · Time-of-use electricity price · Demand-side management

1 Introduction

The implementation of time-of-use electricity price on both sides of supply and demand can guide the reasonable time distribution of electricity load through price signals and improve the efficiency of the entire power system. In order to avoid the risk of implementing time-of-use electricity price on the power grid side and improve the enthusiasm for its implementation, it is necessary to formulate a reasonable time-of-use price linkage mechanism between the power grid side and the demand side, and use the electricity price signal transmission of each link to realize the load guidance function, risk avoidance function, and benefit distribution function.

D. Dai (✉) · J. Liao · L. Zhang
State Grid Hunan Electric Power Co., Ltd. Economic and Technical Research Institute, Changsha, China
e-mail: 1562138622@qq.com

L. An · D. Xie
Financial Assets Department of State Grid Hunan Electric Power Co., Ltd., Changsha, China

S. Yadav et al. (eds.), *Energy Power and Automation Engineering*, Lecture Notes in Electrical Engineering 1118, https://doi.org/10.1007/978-981-99-8878-5_32

In recent years, scholars at home and abroad have done some research on risk avoidance and benefit distribution after the implementation of time-of-use electricity price shaving and valley filling. Literature [1] takes the estimated load considering the price elasticity of user demand as the basis for time period division, divides each time point into three time periods: valley, flat, and peak, and finally makes an example calculation of the time period division of peak-valley time-of-use electricity price in a province. The literature [2] takes the electricity price of industrial users in different transaction modes as the research object, introduces the idea of peak-valley time-of-use electricity price in different trading modes, and studies the optimization model of peak-valley time-of-use electricity price of industrial users. The literature [3] aims to optimize the load curve and reduce the cost of electricity consumption on the user side and constructs the elasticity coefficient matrix of power users, which verifies the role of the model in demand-side management. Literature [4] research constructs a hybrid power demand response management mechanism including power grid companies, electricity sales companies, and large industrial users, that is, power grid companies carry out incentive-type demand response management for electricity sales companies, and electricity sales companies carry out price-type demand response management for large industrial users. Literature [5] in view of the challenges brought by the new situation of current power supply and demand, the regional seasonal peak electricity price mechanism is studied. Starting from the actual demand for short-term peak load, the implementation period and price level of the peak electricity price are scientifically determined, and the case analysis is carried out by taking the power grid of a certain region as an example to reasonably determine the seasonal peak electricity price mechanism in the region. With the help of demand response, literature [6] proposes an independent microgrid supply and demand collaborative optimization method considering time-of-use electricity price to achieve efficient coordination and utilization of resources on both sides of supply and demand. Literature [7] explores the real-time electricity price pricing mechanism after the supply and demand reform, analyzes the relationship between real-time electricity price and user load response under the current background, and establishes the mathematical model relationship between load and electricity price, electricity price, and electricity sales profit.

However, none of the above literature considers the interaction between the time-of-use electricity price on the supply side and the time-of-use electricity price on the demand side. Therefore, this paper uses the game theory signal transmission mechanism to construct a dynamic linkage model of time-of-use electricity price on the supply side and the power grid side, which not only realizes the time-of-use price load guidance goal on the demand side, but also realizes the avoidance of the power price risk on the power grid side through the dynamic game linkage of electricity price, and uses the electricity price signal to realize the reasonable participation of all links in the power system in the sharing of benefits of peak shaving and valley filling.

2 Time-of-Use Price Linkage Model

2.1 Time-of-Use Electricity Price Linkage Mechanism

In the mature electricity market, the time-of-use electricity price setting on the supply side and the demand side is affected by cost, demand, load pattern, etc., and is a dynamic adjustment process. The benefits of time-of-use electricity price shaving and valley filling should be shared by the supply side, the grid side, and the demand side through electricity price transmission.

For the supply side, each power plant calculates the unit power generation cost of each period according to the historical load situation and determines the electricity price level in each period to participate in the bidding with the goal of maximizing its own interests. For the grid side, according to the constraints of its own transmission and distribution capacity and the transmission and distribution price, the time-of-use electricity price quotation on the supply side is transmitted to the demand side. The formulation of demand-side time-of-use electricity price is affected by the joint influence of time-of-use cost, that is, the supply side time-of-use electricity price and the grid side transmission and distribution price, and the quotation of demand-side time-of-use electricity price is determined based on its own electricity consumption behaviour and with the goal of maximizing its own interests.

The demand-side user's own electricity consumption behaviour formulated according to the time-of-use electricity price on the supply side effects the time-of-use power generation cost on the supply side by changing the power load pattern. Changes in the cost of time-of-use power generation have prompted the supply side to reformulate the time-of-use electricity price on the grid. The grid side feeds back the newly formulated time-of-use electricity price to the demand side. Demand-side users change their electricity consumption behaviour through the supply side electricity price signal and reformulate new demand-side quotations. The three stakeholders on the supply side, the grid side, and the demand side respectively influence each other through decision-making on the time-of-use electricity price on the grid, the interests of the power supplier, the electricity consumption behaviour, and the price on the demand side, and finally achieve linkage equilibrium through repeated dynamic games. The electricity price of each link at the time of equilibrium includes load guidance signals, risk avoidance signals, and benefit distribution signals, so as to realize the reasonable sharing of the benefits of time-of-use electricity price determined by the market itself.

2.2 Model Building

Supply Side Model. According to the historical load demand data and the power generation cost of the time period, the power plant on the supply side determines the quotation for each period with the goal of maximizing its own interests, and

then determines the time-of-use electricity price on the supply side through bidding between power plants. Its objective function is:

$$\max R_{\mathrm{f}} = \sum_{i=1}^{3} (P_{\mathrm{f}i} - C_{\mathrm{f}i}) Q_i + B_{\mathrm{f}} - C_{\mathrm{iave}} P_{\mathrm{CO_2}} \tag{1}$$

In the formula, $i = 1, 2, 3$ are valley, flat, and peak periods; $P_{\mathrm{f}i}$ is the time-of-use electricity price on the supply side; $C_{\mathrm{f}i}$ is the unit cost of electricity generation in the i period; Q_i is the transaction electricity in the i period; B_{f} is the benefit of the grid side slow construction power supply after load peak shaving and valley filling due to the time-of-use electricity price; C_{iave} is the CO_2 emissions per unit of power generated by Class I units, respectively; $P_{\mathrm{CO_2}}$ is the unit price of carbon emissions for Class I power supplies. $C_{\mathrm{f}i}$ consists of unit variable costs and fixed costs:

$$C_{\mathrm{f}i} = C_{\mathrm{fd}i} + C_{\mathrm{fr}i} \tag{2}$$

In the formula, $C_{\mathrm{fd}i}$ is the unit variable cost, that is, the variable cost of fuel and labour cost per kWh of electricity, which is the fixed value; $C_{\mathrm{fr}i}$ unit fixed cost, that is, the allocation of fixed costs on the unit of electricity in each period.

The daily apportionment C_1 of the fixed costs of the power plant is:

$$C_1 = \frac{Yy\varphi}{365} \tag{3}$$

In the formula, Y is the installed capacity of the generator set of the power plant; y unit cost; φ is the annuity coefficient during the operating period.

The daily maximum power generation load in the system is calculated to share the daily power generation capacity cost on the unit power generation load, that is, the daily cost per unit of power generation capacity C_2:

$$C_2 = C_1 / N_1 \tag{4}$$

In the formula, N_1 is the maximum daily power generation load, that is, the maximum power generation load during peak hours. Suppose there is only baseload generation Q_{11} during valley hours. Normal hours include baseload and waist load power generation, Q_{21} and Q_{22}, respectively. Peak power is composed of baseload, waist load, and peak-load power generation, Q_{31}, Q_{32}, and Q_{33}, respectively. The base load capacity, waist load new capacity and peak-load new capacity are L_1, L_2, and L_3, respectively. If the daily capacity cost of the baseload is evenly allocated to the baseload electricity, the fixed cost per unit of baseload power generation is apportioned as:

$$C_{\mathrm{j}} = C_2 L_1 / (Q_{11} + Q_{21} + Q_{31}) \tag{5}$$

Similarly, the fixed cost allocation per unit of electricity generated by waist load new capacity and peak-load new capacity is respectively Eqs. (6) and (7):

$$C_{\mathrm{y}} = C_2 L_2 / (Q_{22} + Q_{32}) \tag{6}$$

$$C_{\mathrm{f}} = C_2 L_3 / Q_{33} \tag{7}$$

The electricity in the valley period is all baseload power generation, and the fixed cost of the unit of electricity during the valley period is apportioned as:

$$C_{\mathrm{fr1}} = C_{\mathrm{j}} \tag{8}$$

The fixed cost allocation of unit electricity during peak hours is as follows:

$$C_{\mathrm{fr2}} = \frac{C_{\mathrm{j}} Q_{21} + C_{\mathrm{y}} Q_{22}}{Q_{21} + Q_{22}} \tag{9}$$

$$C_{\mathrm{fr3}} = \frac{C_{\mathrm{j}} Q_{31} + C_{\mathrm{y}} Q_{32} + C_{\mathrm{f}} Q_{33}}{Q_{31} + Q_{32} + Q_{33}} \tag{10}$$

In this way, the unit cost of power generation is obviously timely, the capacity is abundant during the valley period, and the fixed cost per unit of electricity is low. Capacity is scarce during peak hours, and the fixed cost allocation per unit of electricity is high.

B_{f} is a free capacity cost, which refers to the power supply investment cost reduced by power generation enterprises, which can be determined according to the average cost of the peak-shaving unit and its supporting equipment that are built less or slowly:

$$B_{\mathrm{f}} = A_{\mathrm{g}} \times \frac{\Delta Q_{\mathrm{k}}}{365(1 - k_1)(1 - k_2)} \tag{11}$$

In the formula, A_{g} is the unit of electricity cost-free; ΔQ_{k} is the amount of electricity reduced by the implementation of time-of-use electricity price every year; k_1 is the transmission and distribution loss coefficient when considering the power loss of the power grid; k_2 is the electricity consumption rate of the plant.

The supply side includes the following restrictions.

(a) Bidding and quotation constraints

The quotation of each period has a negative correlation with the transaction power of each period, which can be fitted by historical auction data. To simplify the calculation, it is assumed to be linear, which does not affect the discussion of the essence of the problem and avoids cumbersome mathematical derivation:

$$Q_i = \begin{cases} 0 & P_{\mathrm{fi}} > M^n_{i\cdot\max} \\ a - bP_{\mathrm{fi}} & P_{\mathrm{fi}} \le M^n_{i\cdot\max} \end{cases} \tag{12}$$

In the formula, $M^n_{i\cdot\max}$ is the maximum value of the valid quote in the i period in the nth game auction. Generators whose offer is greater than the valid offer will not be able to transact electricity.

(b) Power generation constraints

Ensure that the maximum power generation load of the power generator is within its generating capacity.

$$N_1 \le G_{\max} \tag{13}$$

In the formula, $G_{\max}$ is the maximum power generation capacity of the unit.

Power Grid Side Model. The power grid company on the power grid side calculates its own transmission and distribution revenue according to the time-of-use purchase cost and historical load conditions and provides transmission line constraints for both supply and demand sides. The benefits of the implementation of time-of-use electricity price by power grid companies mainly include the benefits of short-term peak shaving and reducing standby capacity, the benefits of long-term postponement of transmission and distribution line construction, and the improvement of the stability and reliability of the entire power grid, mainly including the cost of free electricity and the cost of free capacity, as shown in the following formula:

$$R_{\mathrm{g}} = B_{\mathrm{r}} - B_{\mathrm{s}} = \left(A \times \frac{\sigma_2}{365} + \frac{\Delta P_{\mathrm{t}}}{1 - k_1} - P_{\mathrm{n}} \times \frac{\Delta Q_{\mathrm{k}}}{1 - k_1} \right) \times T \tag{14}$$

In the formula, R_{g} is the income of the power grid company; B_{r} is the avoidable capacity cost; B_{s} is the transmission and distribution income from less electricity sold; A is the annual avoidable capacity cost of the power grid company; σ_2 is the annuity coefficient of the power grid operation cycle; ΔP_{t} is the peak-load power of the grid reduced by the time-of-use price; P_{n} is the transmission and distribution price.

The constraints on the grid side are mainly the constraints of transmission and distribution lines.

The transmission load of line J is within its transmission capacity:

$$I_j \le I_{j\cdot\max} \tag{15}$$

Demand-Side Model. For users, on the basis of the time-of-use electricity price set on the grid side, they can only consider the transmission and distribution price and transmission and distribution line constraints on the power supply side, choose their own power consumption mode, and ensure that their own average electricity price is the lowest, and their objective function is:

$$\min P = \frac{\sum_{i=1}^{3} P_{gi} Q_i}{\sum_{i=1}^{3} Q_i} \tag{16}$$

The constraints are as follows:

(a) Self-consumption price response

The relationship between the nth demand-side time-of-use electricity price and the nth linkage game optimization before and after the optimization:

$$\begin{bmatrix} Q_1^n \\ Q_2^n \\ Q_3^n \end{bmatrix} = \begin{bmatrix} \partial P_{g1}/P_{g1} \\ \partial P_{g2}/P_{g2} \\ \partial P_{g3}/P_{g3} \end{bmatrix}^{\mathrm{T}} E^{\mathrm{T}} \begin{bmatrix} Q_1^{n-1} & 0 & 0 \\ 0 & Q_2^{n-1} & 0 \\ 0 & 0 & Q_3^{n-1} \end{bmatrix} + \begin{bmatrix} Q_1^{n-1} \\ Q_2^{n-1} \\ Q_3^{n-1} \end{bmatrix} \tag{17}$$

In the formula, E^{T} is the user's own reaction matrix.

(b) The relationship between electricity sales price and electricity is constrained

Considering the power consumption that must be consumed in each period, the psychological threshold of consumption and the limitation of equipment operation capacity, the total electricity consumption in each period will only change with the change of electricity price within a certain range:

$$Q_i = \begin{cases} Q_{i\cdot\min} & P_{gi} \geq P_{gi\cdot\max} \\ C - DP_{gi} & P_{gi\cdot\min} < P_{gi} < P_{gi\cdot\max} \\ Q_{i\cdot\max} & P_{gi} \leq P_{gi\cdot\min} \end{cases} \tag{18}$$

3 Example Analysis

3.1 Underlying Data

The original load data is shown in Fig. 1 based on the actual historical operation data of a regional power supply company and the historical operation data of a typical power plant. The basic data on the supply side are: $Y = 1500$ MW, $y = 8800$ yuan/kW, $\varphi = 0.0333$, $C_{\mathrm{fd}i} = 0.0032$ yuan (kWh). The price elasticity matrix of demand-side users is shown in Table 1.

According to the daily 24 h, it is divided into 8 h each of the peak, flat section, and trough, and the specific time period is divided as follows: peak: 11:00–14:00, 18:00–23:00; flat section: 7:00–11:00, 14:00–18:00; trough: 23:00–7:00 the next day.

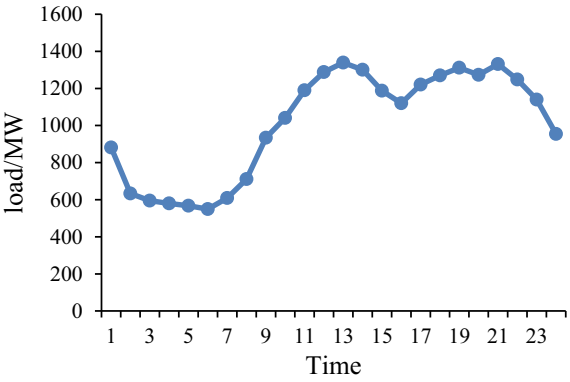

Fig. 1 Original load chart

Table 1 User demand price elasticity

	Valley	Flat	Peak
Valley	− 0.1	0.01	0.012
Flat	0.01	− 0.1	0.016
Peak	0.012	0.016	− 0.1

3.2 Study Results

When the dynamic linkage of time-of-use electricity price reaches equilibrium, the time-of-use electricity price on the supply side and the demand side are shown in Fig. 2.

After the dynamic linkage between the supply side and the demand-side time-of-use electricity price reaches equilibrium, the peak-shaving and valley-filling benefits and the distribution ratio of various stakeholders are shown in Figs. 3 and 4.

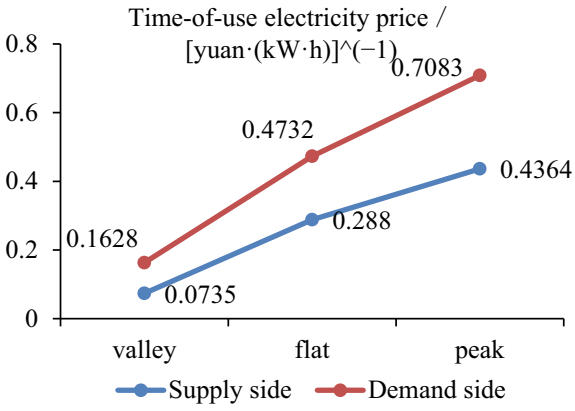

Fig. 2 Time-of-use electricity price at linkage equilibrium

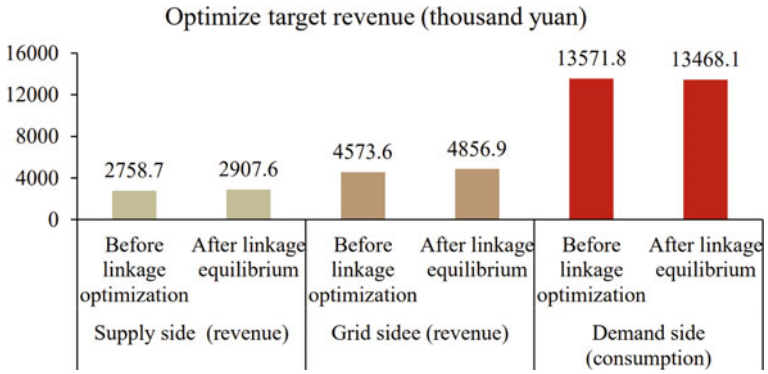

Fig. 3 Optimal target revenues for each entity during balancing

Fig. 4 Equalization of time-of-use price benefit distribution

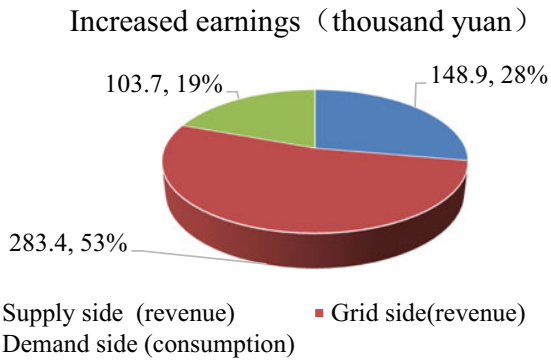

4 Conclusion

Based on game signal transmission, this paper establishes a dynamic game linkage model of time-of-use electricity price on the supply side and the demand side. In the linkage process, the influence of the time-of-use electricity price on the grid side is transmitted to the demand side through the power supply side, and the demand-side user's feedback on the quotation of the optimal time-of-use electricity price on the demand side by changing the electricity consumption behaviour. When the electricity price linkage reaches equilibrium, the model can objectively distribute the peak-shaving and valley-filling benefits brought by the time-of-use electricity price according to the market force of each link of the system, and objectively distribute the peak-shaving and valley-filling benefits brought by the time-of-use electricity price, so as to improve the benefits of the supply side, grid side, and demand-side links.

Acknowledgements This paper is supported by State Grid Hunan Electric Power Co., Ltd. Science and Technology Project Grant (5216A221N005).

References

1. He Y, Ye Z, Wei W (2022) Research on time division of peak-valley TOU tariff considering price elasticity of user demand. Prices Mon 12:1–9. https://doi.org/10.14076/j.issn.1006-2025.2022.12.01
2. Gao Z (2022) Demand-side-management measures of power market based on user characteristics. Guangxi University. https://doi.org/10.27034/d.cnki.ggxiu.2022.001923
3. Xu B, Yue X, Guan Y et al (2022) A hybrid demand response strategy to solve the problem of "peak valley inversion" in power grid. Syst Eng Theory Pract 42(08):2129–2138
4. Zhang C (2017) Study on optimal model of peak and valley time price for industrial users in different transaction modes. North China Electric Power University, Beijing
5. Bai J (2018) Research on real-time electricity price analysis and modeling based on electricity sales side reform. Tianjin University
6. Guo C (2018) The research on power load forecasting and supply-demand benefit optimal dispatch considering demand side response. Shenyang Agricultural University
7. Yang Y (2017) Theoretical research and application on optimized planning of "generation-grid-load-energy storage" for electrical power system. North China Electric Power University, Beijing

Electric Heating Load Prediction Based on TCN-LSTM Hybrid Neural Network

Gaoqiang Qu, Zifa Liu, Bo Gao, Hongxi Zhang, Chengchen Li, Shiqin Wang, Hao Yong, and Xinyi Li

Abstract The traditional load prediction is based on linear modeling, which does not consider the uncertainty of load and has no small errors. Deep learning methods are used for load prediction because of their strong data feature extraction and fitting ability. From the accuracy of electric heating load prediction, an electric heating load prediction model based on TCN-LSTM hybrid neural network is proposed. Several influencing factors with the strongest correlation with electric heating load are selected as input features by Pearson correlation analysis among multiple features, and weakly correlated meteorological features are filtered out; then CEEMDAN decomposition is used to decompose the historical electric heating load time series into multiple eigenfunctions as well as a residual term to obtain the historical input feature time series corresponding to each input feature; finally, the TCN and LSTM hybrid models are finally used for electric heating load prediction. The simulation results show that the electric heating load prediction model based on the TCN-LSTM hybrid neural network can extract effective information from the historical load data, realize the dimensionality reduction processing, and improve the operation rate and accuracy of the artificial network.

Keywords Pearson correlation analysis · CEEMDAN decomposition · TCN · LSTM · Electric heating load

1 Introduction

As electric heating continues to grow and people's requirements for comfort gradually increase [1], the proportion of electric heating load in the total load is gradually increasing, bringing considerable challenges to the safe and smooth operation of power systems. Accurate electric load forecasting is important in ensuring reliable and economic operation of the power system and affects many decisions. Power supply and consumption patterns can be further optimized by more accurate load

G. Qu (✉) · Z. Liu · B. Gao · H. Zhang · C. Li · S. Wang · H. Yong · X. Li
State Grid Ningxia Electric Power Co., Ltd., Yinchuan 750001, China
e-mail: qgq300@163.com

S. Yadav et al. (eds.), *Energy Power and Automation Engineering*, Lecture Notes in Electrical Engineering 1118, https://doi.org/10.1007/978-981-99-8878-5_33

forecasting [2], thus improving the distribution scheme of the system and enabling rational distribution of electrical energy [3]. Therefore, it is essential to improve the accuracy of electric heating load forecasting.

Several studies have been carried out by domestic and foreign scholars in electric heating load forecasting, and the traditional load forecasting mainly includes time series method, pattern recognition method, and regression analysis method [4], which are based on linear modeling and do not take into account the uncertainty of load, and there are no small errors. In recent years, with the prominence of deep learning in dealing with high-latitude, nonlinear problems, the use of artificial intelligence to build load forecasting models has become more and more common. In terms of data extraction, the literature [5] uses Pearson correlation coefficient analysis for feature selection of load for multidimensional nonlinearities in power systems. The literature [6] uses wavelet decomposition to decompose the historical load into a series of smooth subsequences for prediction, and finally, the final prediction is obtained by reconstruction. The literature [7] used a multi-layer clustering method to preprocess the input data and then completed the load prediction using an improved BP neural network. In terms of optimization algorithms, the literature [8] established a BP neural network-based electric heating load prediction model and used a particle swarm optimization of the initial weights and thresholds of the BP neural network based on the fitness function using the particle swarm optimization of parameters. The literature [9] used genetic algorithm to determine the topology of the neural network, which optimized the global search ability and flexibility of the neural network, but the model was easy to fall into local optimum. The literature [10] proposed a joint short-term electric, gas, and thermal load forecasting method based on deep structural multi-task learning, which applies deep learning and multi-task learning to energy demand forecasting. The literature [11] uses attention mechanism and time series decomposition to improve LSTM neural network accuracy; in terms of forecasting models, the literature [12] used a constructing a novel electric heating prediction model and analyzed that the LSTM prediction model has higher accuracy for single-factor prediction. The literature [13] proposed a load forecasting model combining fuzzy processing with deep neural network (DNN), using the affiliation function to fuzzify the meteorological features, so that the forecasting model has a stronger nonlinear expression, but the model lacks the consideration of the factors influencing holidays and electricity prices. In the literature [4], a hybrid model short-term load forecasting method literature based on convolutional neural network (CNN) and long short-term memory (LSTM) network was proposed for the characteristics of load data temporality and nonlinearity. The literature [14] analyzed a variety of features for load prediction and built a prediction model with a better generalization capability SVM, but due to the increase in the uncertainty of the load and the higher dimensionality of the features, the training time of the SVM prediction model became longer and the accuracy became lower.

In the aforementioned literature on electric heating load prediction studies, the single prediction methods based on artificial neural networks all suffer from the disadvantages of easily falling into local optimal solutions, slow convergence, and easy overfitting in their calculations due to the complex data and high dimensionality. The

combined prediction model has higher prediction accuracy than the single prediction model. Therefore, in this paper, firstly, we use Pearson correlation analysis to reduce the dimensionality of multiple variables to avoid the weakly correlated factors and their interference to the prediction results, and realize the dimensionality reduction process; then we use CEEMDAN to decompose the historical electric heating load data into subseries with different frequencies and obtain the historical input feature time series corresponding to each input feature; secondly, we use TCN and LSTM models to derive the load. The results of the prediction are linearly combined by assigning different weights to a single model, and the sum of all the prediction results is used as the preliminary prediction value of the electric heating load at the preset future moment; finally, the analysis is based on the actual data of a region, and the results of the calculation show that the combined model in this paper can reduce the error of a single model in extreme scenarios, and also has a more stable prediction effect compared with other combined models and the prediction. The prediction results are more accurate.

2 Pearson Correlation Analysis

2.1 Input Sequence for Prediction Algorithms

Deep learning algorithms are essentially an attempt to learn the probability distribution of a sample implicitly or explicitly by looking at multiple samples given a sample set. When performing electric heating load prediction, the prediction performance will be greatly improved if all the relevant sequences that may affect it can be fed into the neural network. However, as the length of the input sequences increases, the span of dependencies between the sequences to be captured becomes longer, and the calculation of parameter optimization based on gradient descent becomes more difficult. Pearson correlation analysis is a statistical analysis method that converts multiple variables into a few variables by dimensionality reduction. By doing screening of multivariate time series, selecting a few influential factors as the input features of the model for prediction, eliminating the interference of weakly correlated features on the prediction results, and reducing the dimensionality of the data, the effect of reducing variables and eliminating covariance can be achieved.

2.2 Pearson Correlation Analysis to Extract the Characteristic Components

The Pearson correlation coefficient [15] is used to measure the magnitude of the correlation between the independent variable and the dependent variable, and its value is between -1 and 1. The larger its absolute value, the stronger the correlation.

Pearson correlation coefficient greater than 0 represents positive correlation and less than 0 represents negative correlation, which is shown in Eq. (1).

$$r = \frac{n\sum_{i=1}^{n} x_i y_i - \sum_{i=1}^{n} x_i \sum_{i=1}^{n} y_i}{\sqrt{n\sum_{i=1}^{n} x_i^2 - \left(\sum_{i=1}^{n} x_i\right)^2}\sqrt{n\sum_{i=1}^{n} y_i^2 - \left(\sum_{i=1}^{n} y_i\right)^2}} \tag{1}$$

Pearson coefficient was used to divide all explanatory variables and find out the high, moderate, weak, and irrelevant variables in explanatory variables. Its division is as follows: $0.8 \leq |r| < 1$ is highly correlated; $0.5 \leq |r| < 0.8$ is moderately correlated; $0.3 \leq |r| < 0.5$ is weakly correlated; $|r| < 0.3$ is barely correlated.

3 Fundamentals of CEEMDAN

CEEMDAN is based on EMD decomposition [16], which weakens the modal mixing problem by adaptively adding Gaussian white noise, and the decomposition process is characterized by completeness and almost no reconfigurability error. Let $E_i(\cdot)$ be the ith modal component after EMD and IMF_i be the ith modal component generated by CEEMDAN, the CEEMDAN algorithm is described as follows:

(1) Add the M-dimensional Gaussian white noise sequence $v_j,\ j = 1, 2, \ldots, M$ with mean value 0 to the pre-decomposed signal Y to obtain M sequences to be decomposed $C_j,\ j = 1, 2, \ldots, M$.

(2) The decomposition of C_j is performed using EMD to obtain the first eigenmode component $\mathrm{IMF}_1(t)$ and the residual component $r_1(t)$, as shown in Eqs. (2) and (3).

$$\mathrm{IMF}_1(t) = \frac{1}{M}\sum_{j=1}^{M} \mathrm{IMF}_1^j(t) \tag{2}$$

$$r_1(t) = Y - \mathrm{IMF}_1(t) \tag{3}$$

where $\mathrm{IMF}_1^j(t)$ is the jth IMF component obtained at the 1st EMD.

(3) Continue to add white noise to the ith residual component produced after decomposition and perform EMD decomposition to obtain the $i + 1$st eigenmode component $\mathrm{IMF}_{i+1}(t)$ and the residual component $r_{i+1}(t)$, as shown in Eqs. (4) and (5).

$$\mathrm{IMF}_{i+1}(t) = \frac{1}{M}\sum_{j=1}^{M} E_1\left[r_i(t) + \varepsilon_i E_i\left(v_{j+1}\right)\right] \tag{4}$$

$$r_{i+1}(t) = r_i(t) - \mathrm{IMF}_{i+1}(t) \tag{5}$$

where ε_i is the ith weighting factor.

(4) Repeat step 3 until the residual components obtained are monotonic functions and can no longer be decomposed, at which point the K eigenmodal components are obtained and the original signal is decomposed into Eq. (6).

$$Y = \sum_{k=1}^{K} \mathrm{IMF}_k + r_k(t) \tag{6}$$

where $r_k(t)$ is the kth residual component.

The historical electric heating load time series is obtained, the complete empirical modal decomposition is used to decompose the historical electric heating load time series into a plurality of eigenmodal functions and a residual term, each eigenmodal function and the residual term are each treated as a subsequence, and the historical input feature time series corresponding to each input feature is thus obtained based on said historical data time series information.

4 Electric Heating Load Prediction Based on a Combined TCN-LSTM Model

4.1 Temporal Convolutional Network Prediction Model TCN

The core of a convolutional network is an inner product operation on data and a set of filter matrices with fixed weights. In the field of time series forecasting, the need for more difficult parallel computational improvements to RNN networks has seen convolutional networks being transformed into time series convolutional networks suitable for the needs of time series forecasting. It transforms one-dimensional convolution into a model suitable for time series problems, using a multi-layer network to learn information over longer time spans, with each layer of the network sweeping through all data up to the previous time point using a one-dimensional convolutional kernel. The deeper the network is, the longer the time period of information can be learned, and finally, the prediction result can be obtained. TCN is an optimized and improved model of convolutional neural networks for time series problems [17], and the basic structure is shown in Fig. 1.

TCN incorporates causal convolution extended convolution and residual convolution respectively. Causal convolution makes TCN suitable for sequence modeling, that is, the value of the moment is only determined by the value of the previous layer and the previous one, reflecting the time constraint. Extended convolution enables TCN to obtain longer time sequence information, thus alleviating the problem of incomplete learning of historical information. The residual connection makes the TCN avoid the phenomenon of gradient extinction and makes the network structure more stable. Figure 2 shows the basic unit of the TCN model.

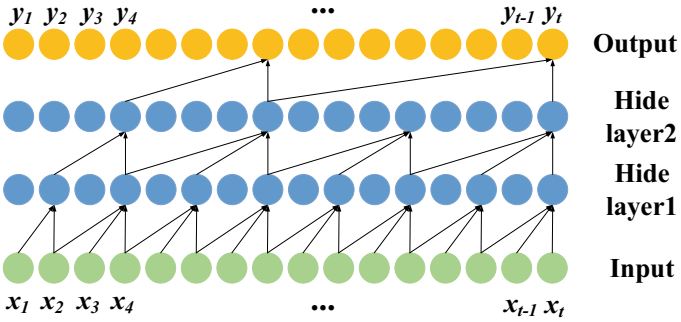

Fig. 1 Basic structure of time convolution network prediction model TCN

Fig. 2 Basic units of TCN model

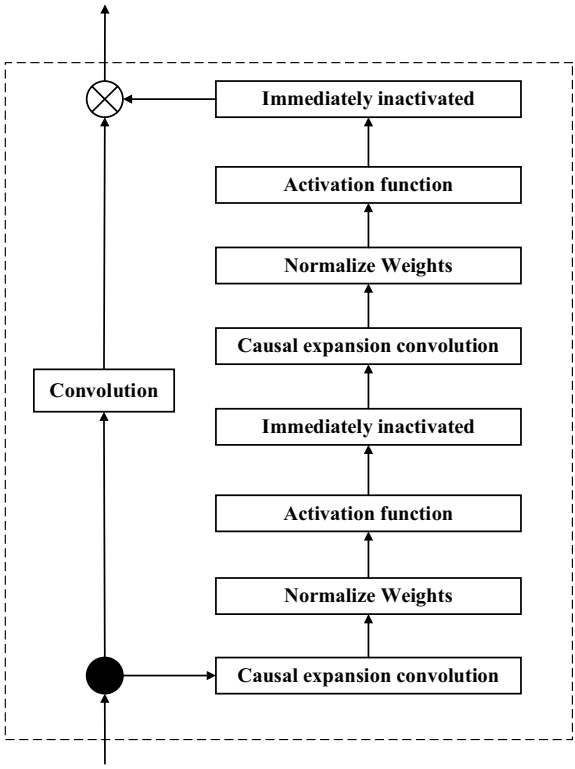

4.2 Long and Short-Term Memory Neural Network Prediction Model LSTM

Long short-term memory neural network prediction model that is LSTM neural network prediction model, LSTM consists of activation function sigmoid to form a network layer [18], plus a multiplication operation together to form a gate structure. LSTM network has three layers: input layer, hidden layer, and output layer, and the basic unit of the network is shown in Fig. 3.

The basic cell contains an input gate, an oblivion gate, and an output gate. In Fig. 3, x_t is the input of the current layer and h_{t-1} is the output result of the previous layer. After they pass the forgetting gate together, any value between 0 and 1 is output to the old cell state S_{t-1}, which determines the forgetting part, with "0" for "all forgetting", "0" means "all forgotten" and "1" means "all passed." The x_t in the input gate is passed through the sigmoid and tanh functions, respectively, and the results are multiplied to produce the new information, plus the S_{t-1} after forgetting, and their sum is the new cell state S_t. The S_t passed through the tanh function together with o_t determines the output h_t. The calculation formula is as in Eqs. (7) to (12).

$$f_t = \sigma\left(\omega_x^{\mathrm{f}} x_t + \omega_h^{\mathrm{f}} h_{t-1} + b_{\mathrm{f}}\right) \tag{7}$$

$$i_t = \sigma\left(\omega_x^{\mathrm{i}} x_t + \omega_h^{\mathrm{i}} h_{t-1} + b_{\mathrm{i}}\right) \tag{8}$$

$$c_t = \sigma\left(\omega_x^{\mathrm{c}} x_t + \omega_h^{\mathrm{c}} h_{t-1} + b_{\mathrm{c}}\right) \tag{9}$$

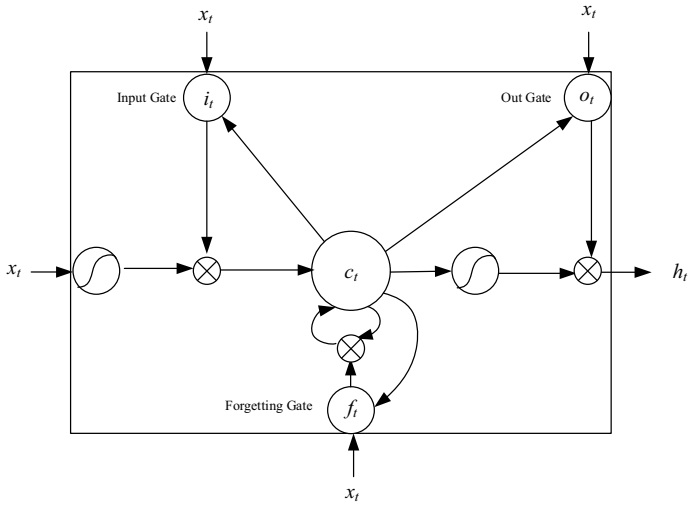

Fig. 3 Basic unit of LSTM neural network

$$o_t = \sigma\left(\omega_x^{\mathrm{o}} x_t + \omega_h^{\mathrm{o}} h_{t-1} + b_{\mathrm{o}}\right) \tag{10}$$

$$S_t = c_t \times i_t + S_{t-1} \times f_t \tag{11}$$

$$h_t = o_t \times \tanh(S_t) \tag{12}$$

where σ is the sigmoid function; ω_x^{f}, ω_x^{i}, ω_x^{c}, ω_x^{o}, ω_h^{f}, ω_h^{i}, ω_h^{c} and ω_h^{o} are the weight matrices of x_t, h_{t-1}, oblivion gate, input gate, metazoan input, and output gate, respectively; b_{f}, b_{i}, b_{c} and b_{o} are the bias vectors of the corresponding parts.

4.3 Combined Prediction Models

Combined TCN and LSTM Model. All the historical input feature time series and the subseries are divided into training set and test set according to a certain ratio, and the selected input feature data are normalized. In the specific embodiment, the first 100 days of data are used as the training set and the last 10 days of data are used as the prediction set, and the input feature data are normalized according to the normalization method. Then the temporal convolutional network prediction model and the long and short-term memory neural network prediction model are trained, and the trained first deep learning model and the trained second deep learning model of the subsequence are used to obtain the target subsequence 1 and the target subsequence 2 of the subsequence corresponding to the predetermined future moment, respectively, and then the optimal weighted combination method is used to give them the corresponding weights and then linearly add them together. So that, the two combined prediction results of the two prediction models are obtained by combining them, and the calculation method is as in Eqs. (13) to (16).

$$\begin{cases} e_i^{\mathrm{TCN}} = F_i^{\mathrm{TCN}} - F_i \\ e_i^{\mathrm{LSTM}} = F_i^{\mathrm{LSTM}} - F_i \end{cases} \tag{13}$$

$$E = \begin{bmatrix} \sum_{i=1}^{S} \left(e_i^{\mathrm{TCN}}\right)^2 & \sum_{i=1}^{S} e_i^{\mathrm{TCN}} e_i^{\mathrm{LSTM}} \\ \sum_{i=1}^{S} e_i^{\mathrm{TCN}} e_i^{\mathrm{LSTM}} & \sum_{i=1}^{S} \left(e_i^{\mathrm{LSTM}}\right)^2 \end{bmatrix} \tag{14}$$

$$[\omega_1, \omega_2]^{\mathrm{T}} = \frac{E^{-1} R}{R^{\mathrm{T}} E^{-1} R} \tag{15}$$

$$Q_i = \omega_1 F_i^{\mathrm{TCN}} + \omega_2 F_i^{\mathrm{TCN}} \tag{16}$$

where F_i^{TCN} and F_i^{LSTM} are the target subsequence 1 and target subsequence 2 of the ith preset future moment, respectively; F_i is the actual subsequence of the ith preset future moment; e_i^{TCN} is the prediction error value of the target subsequence 1 of the ith preset future moment; e_i^{LSTM} is the prediction error value of the target subsequence 2 of the ith preset future moment; E is the deviation matrix; S is the number of multiple preset future moments; ω_1 and ω_2 are the weight coefficients of the TCN model and the LSTM model, respectively; $R = [1, 1]^{\mathrm{T}}$; Q_i is the combined prediction values of the ith preset future moment.

Preset Indicators. The final predicted value of electric heating load and the actual value of electric heating load at multiple preset future moments are obtained, and the error analysis of the final predicted value of electric heating load is carried out by combining multiple preset indicators. Among them, the multiple preset indicators include: mean absolute error MAE, root mean square error RMSE, and mean relative error MAPE, and the error analysis is performed on the final predicted value of electric heating load. The calculation equations are shown in Eqs. (17) to (18).

$$\mathrm{MAE} = \frac{1}{H}|u_i - \overline{u}_i| \tag{17}$$

$$\mathrm{RMSE} = \sqrt{\frac{1}{H}\sum_{i=1}^{H}(u_i - \overline{u}_i)^2} \tag{18}$$

$$\mathrm{MAPE} = \left(\frac{1}{H}\right) \times \sum_{i=1}^{H}\left(\frac{|u_i - \overline{u}_i|}{\overline{u}_i}\right) \times 100\% \tag{19}$$

where u_i and $\overline{u}_i$ are the final predicted value of the ith electric heating load and the corresponding actual value of the electric heating load in the test sample, respectively; H is the capacity of the test sample. The lower the value of the preset indexes indicates the better the prediction effect of the model, and the goodness of the electric heating load prediction model is evaluated by calculating the above three indexes of the final predicted value of electric heating load.

4.4 Forecasting Process

Pearson correlation analysis is used to filter out the weakly correlated meteorological features to avoid their interference with the prediction results and realize the dimensionality reduction process; CEEMDAN algorithm adds adaptive Gaussian white noise at each stage of the original wind power decomposition process and obtains the components of each feature that are different from each other by calculation, with a complete decomposition process and extremely low reconstruction error. It effectively solves the EMD modal mixing problem, while overcoming the

problems of low efficiency of EEMD decomposition and the difficulty of complete noise elimination. Then, using the principle of phase space reconstruction, the IMF components are reconstructed, which can effectively improve the thermal prediction accuracy and prediction efficiency; secondly, the single models of TCN and LSTN have limitations, and the combined model comes into being to predict the electric heating load at predetermined future moments. Thus, a combined prediction model based on Pearson feature extraction and CEEMDAN, TCN-LSTM is established to predict the electric heating load, and the prediction process is shown in Fig. 4.

(1) Pearson correlation coefficient is used for feature extraction. Several factors with the strongest correlation with electric heating load are selected among multiple features, and the weakly correlated features are filtered out to avoid their interference with the prediction results and to achieve dimensionality reduction processing, which reduces the workload of the neural network and improves the operation rate and accuracy.
(2) Component prediction based on data features, modal decomposition of the original data by CEEMDAN to obtain the components of different frequency bands, improve the similarity between the data, and apply the appropriate model to model the prediction of each subseries separately.

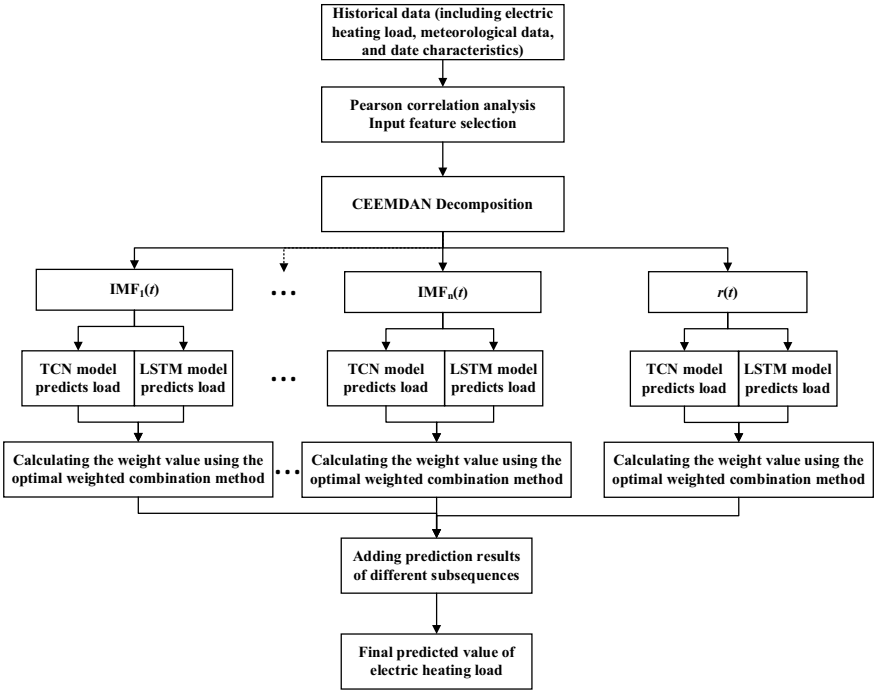

Fig. 4 Flow chart of electric heating load prediction

(3) Combined model is used for electric heating load prediction; two deep neural network prediction models, TCN and LSTM, are built for each subsequence, different weights are assigned to the single model; the prediction results of the two single models are linearly combined to obtain the prediction results corresponding to each subsequence; the sum of all the prediction results is taken as the preliminary prediction value of electric heating load at the preset future moment.

5 Analysis of the Algorithm

In this paper, a single model and a combined model are used in the Matlab platform for simulation and comparison analysis. In the specific example, the first 100 days of data are used as the training set and the last 10 days of data are used as the prediction set.

5.1 Data Sample Selection and Pre-processing

Data Sample Selection. In this paper, the factors affecting electric heating in a region of Ningxia in 2022: temperature, relative humidity, date type, rainfall, wind speed, wind direction, air pressure, and cloudiness, and the results are shown in Table 1.

Before processing, there were 8 meteorological parameters at each moment, while after feature filtering by Pearson correlation coefficients, only 3 meteorological parameters were used as input at each moment. This improves the computational efficiency of the neural network while ensuring accuracy. In addition this method has objectivity and universality, and in the specific example, the input features that were selected to have a strong correlation with the electric heating load were temperature, relative humidity, and date type.

Table 1 Pearson correlation analysis

Parameter	Correlation strength	Pearson correlation coefficient
Temperature	Highly correlated	0.87
Relative humidity	Highly correlated	0.76
Date type	Highly correlated	0.73
Rainfall	Weak correlation	0.56
Wind speed	Weak correlation	0.43
Wind direction	Weak correlation	0.41
Pressure	Almost unrelated	0.13
Cloud amount	Almost unrelated	0.05

Time Series Decomposition Based on CEEMDAN. Based on the historical data time series information, the historical electric heating load time series is obtained, and the complete empirical modal decomposition is used to decompose the historical electric heating load time series into multiple eigenmodal functions as well as a residual term, and each eigenmodal function and residual term are treated as a subsequence respectively, and the historical input feature time series corresponding to each input feature is obtained based on the historical data time series information. CEEMDAN is used to decompose the historical electric heating load data into subseries with different frequencies, and the data are analyzed for smoothness, followed by modal decomposition of the electric heating load time series Y using CEEMDAN. In specific examples, CEEMDAN mode decomposition results of historical electric heating load time series are shown in Fig. 5, which are divided into 10 IMF components, namely $\mathrm{IMF}_1(t) \sim \mathrm{IMF}_n(t)$ and a residual component $r(t)$, at this time, $n = 10$.

Based on the historical data time series information, obtain the historical input feature time series corresponding to each input feature, extract the temperature, relative humidity, and date type time series information every 15 min in chronological order for 110 consecutive days in the historical data time series information, and form the historical input feature time series.

5.2 Combined TCN and LSTM Model Prediction Design

All historical input feature time series and this subsequence are divided into training and test sets according to a certain ratio, and the selected input feature data are normalized, and then the temporal convolutional network prediction model and the long short-term memory neural network prediction model are trained, and the trained first deep learning model and the trained second deep learning model of this subsequence are used to obtain the subsequence corresponding to of the target subsequence 1 and target subsequence 2 of the predefined future moment. The parameter settings of the LSTM neural network are shown in Table 2.

5.3 Analysis of Prediction Results

Comparing the single TCN model, single LSTM model, and modified CEEMDAN-TCN-LSTM model, the results of the error analysis index of each model are shown in Table 3, and the electric heating load prediction results are shown in Fig. 6.

It can be seen from Table 3 that compared with the single TCN model and the single LSTM model, the MAE, RSME, and MAPE values of the model proposed by CEEMDAN-TCN-LSTM model are smaller, which indicates that the accuracy of the electric heating load prediction model proposed in this paper is higher. As can be seen from Fig. 6, compared with other models, the model proposed in this paper

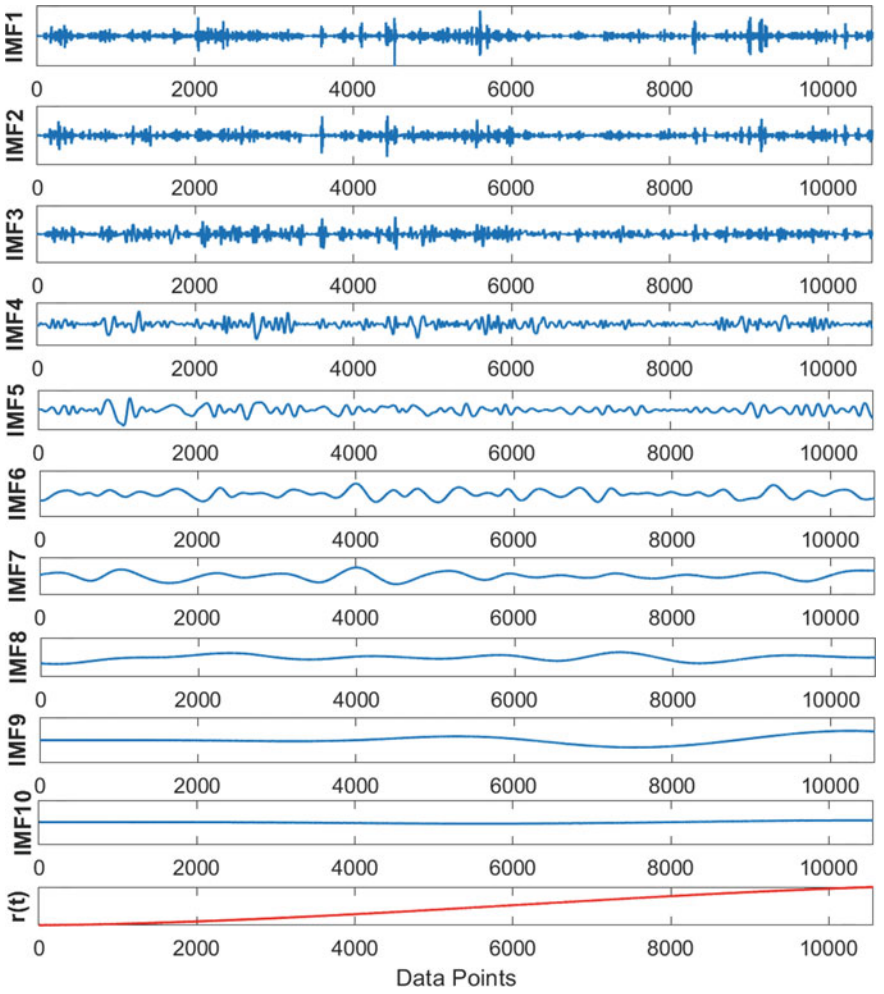

Fig. 5 CEEMDAN modal decomposition results

Table 2 Parameter settings of LSTM neural network

Epoch	Number of neurons		
	First layer	Second layer	Third layer
100	50	160	30

Table 3 Error analysis indicator results for each model

Model	MAE (kW)	RMSE (kW)	MAPE (%)
TCN	17.87	19.33	15.86
LSTM	18.94	21.09	14.39
CEEMDAN-TCN-LSTM	12.66	13.46	9.74

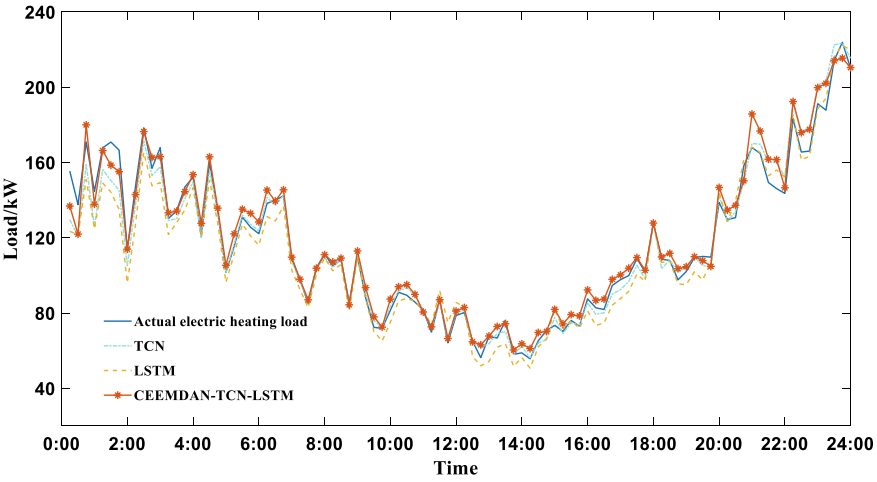

Fig. 6 Prediction results of electric heating load

has good tracking ability for load changes, and the thermal prediction load curve is closer to the actual load curve, which verifies the effectiveness of the model.

6 Conclusion

For the characteristics of large-scale electric heating regional load with strong random volatility and large fluctuation, the single model prediction results are poorly predicted. This paper proposes to select input features by Pearson correlation analysis, then CEEMDAN performs modal decomposition on the original data, and finally adopts TCN-LSTM combined model for electric heating load prediction. The results of the algorithm show that the model achieves dimensionality reduction processing, can extract effective information from historical load data, improves the operation rate and accuracy of artificial network, and has a good effect on improving the accuracy of load prediction model.

Acknowledgements This research is financially supported by Natural Science Foundation of Ningxia under grant 2022AAC03614 and the authors thank the reviewers for their constructive suggestions.

References

1. Huang Y, Zhu Y, Mu G et al (2018) Evaluation of adjustable capacity of household electrical heating load based on temperature forecast. Power Syst Technol 42(8):2487–2493 (in Chinese). https://doi.org/10.13335/j.1000-3673.pst.2018.0547
2. Yan G, Kan T, Yang Y et al (2020) Demand response optimal scheduling for distributed electric heating based on deep reinforcement learning. Power Syst Technol 44(11):4140–4149. https://doi.org/10.13335/j.1000-3673.pst.2020.0252a
3. Wang W, Li F (2020) Study on substitutable value of electric heating instead of coal heating in northern China under carbon constraints. J Clean Prod 260. https://doi.org/10.1016/j.jclepro.2020.121155
4. Lu J, Zhang Q, Yang Z et al (2019) Short-term load forecasting method based on CNN-LSTM hybrid neural network model. Autom Electr Power Syst 43(08):131–137. https://doi.org/10.7500/AEPS20181012004
5. Chen J, Yang J, Lou Z (2019) A new short-term load forecasting model based on XGBoost algorithm. Electr Meas Instrum 56(21):23–29. https://doi.org/10.19753/j.issn1001-1390.2019.021.004
6. Shen C, Qin J, Sheng W et al (2016) Study on short-term forecasting of distribution transformer load using wavelet and clustering method. Power Syst Technol 40(02):521–526. https://doi.org/10.13335/j.1000-3673.pst.2016.02.027
7. Zhao Y, Gao Z, Xiao Y et al (2019) Short-term load forecasting based on multilayer clustering and improved BP neural network. Eng J Wuhan Univ 52(07):622–629. https://doi.org/10.14188/j.1671-8844.2019-07-009
8. Peng X, He H, Yao J et al (2010) Method of bus-load forecasting using BP neural network optimized by PSO. Proc CSU-EPSA 22(05):146–151. https://doi.org/10.3969/j.issn.1003-8930.2010.05.025
9. Wang D, Wang L, Zhang G (2012) Short-term wind speed forecast model based on genetic BP neural network. J Zhejiang Univ (Eng Sci) 46(05):837–841+904. https://doi.org/10.3785/j.issn.1008-973X.2012.05.010
10. Shi J, Tan T, Guo J et al (2018) Multi-task learning based on deep architecture for various types of load forecasting in regional energy system integration. Power Grid Technol 42(03):698–707. https://doi.org/10.13335/j.1000-3673.pst.2017.2368
11. Heidari A, Khovalyg D (2020) Short-term energy use prediction of solar-assisted water heating system: application case of combined attention-based LSTM and time-series decomposition. Sol Energy 207:626–639. https://doi.org/10.1016/j.solener.2020.07.008
12. Chen Z, Liu J, Li C et al (2020) Ultra short-term power load forecasting based on combined LSTM-XGBoost model. Power Syst Technol 44(02):614–620. https://doi.org/10.13335/j.1000-3673.pst.2019.1566
13. Jin S, Xue H, Lin X, Zhang Z (2017) Study of short-term load forecasting of power system based on fuzzy deep neural network. J Qingdao Univ (Eng Technol Ed) 32(04):12–16. https://doi.org/10.13306/j.1006-9798.2017.04.003
14. Gong Y, Teng H (2019) Short-term load forecasting based on GOA-SVM. Electr Meas Instrum 56(14):12–14. https://doi.org/10.19753/j.issn1001-1390.2019.014.003
15. Shun L, Yuan F (2022) Research on stock price prediction based on orthogonal Gaussian basis function expansion and Pearson correlation coefficient weighted LSTM neural network. Adv Comput Signals Syst 6(5). https://doi.org/10.23977/acss.2022.060504
16. Hu C, Zhao Y, Jiang H, Jiang M et al (2022) Prediction of ultra-short-term wind power based on CEEMDAN-LSTM-TCN. Energy Rep 8(S8). https://doi.org/10.1016/j.egyr.2022.09.171
17. Zhang B, Song C, Jiang X et al (2023) Electricity price forecast based on the STL-TCN-NBEATS model. Heliyon 9(1). https://doi.org/10.1016/j.heliyon.2023.e13029
18. Wei J, Wu X, Yang T et al (2023) Ultra-short-term forecasting of wind power based on multi-task learning and LSTM. Int J Electr Power Energy Syst 149. https://doi.org/10.1016/J.IJEPES.2023.109073

Anomaly Data Mining Method of Electric Power Metering Automation System Based on Improved Threshold Algorithm

Chao Liu, Lu Wang, Huiqiong Zhou, Lu Huan, and Yong Ou

Abstract When analyzing abnormal data of electric power metering automation system, because the data itself exists in a dynamic form, the accuracy of the identification results of abnormal data is poor. Therefore, this paper proposes a research method for abnormal data mining of electric power metering automation system based on improved threshold algorithm. Considering that, when the least square method is directly used for analysis, the data of the power metering automation system is processed in a unified way, which is difficult to ensure the adaptation of the mining results to the data state of the real-time power metering automation system. When the threshold algorithm is improved, the weighted mechanism is introduced, and the weighted least square method is used to improve the threshold algorithm. In the abnormal data mining stage, the direct reconstruction method is used to analyze the relationship between the actual data and the norm, and the improved threshold function is used to analyze the difference of the reconstructed data to judge the abnormal data. In the test results, the accuracy of the design method for abnormal data identification reached 77.78%, with high accuracy.

Keywords Improved threshold algorithm · Power metering automation system · Anomaly data mining · Least square method · Weighting mechanism · Direct reconstruction

1 Introduction

During the operation of the power metering automation system, the correct measurement of power related index parameters can provide a reliable basis for the assessment of the economic benefits of power grid enterprises and has important practical

C. Liu (✉) · L. Wang · H. Zhou · L. Huan
State Grid Xinjiang Marketing Service Center, Urumqi 830000, Xinjiang, China
e-mail: liu107720@163.com

Y. Ou
Shenzhen Longyuan Technology Co., Ltd., Shenzhen 518000, China

S. Yadav et al. (eds.), *Energy Power and Automation Engineering*, Lecture Notes in Electrical Engineering 1118, https://doi.org/10.1007/978-981-99-8878-5_34

significance for the fairness and impartiality of power sales. To some extent, the enterprise provides data guarantee for the investigation and treatment of violations of electricity use [1], the prevention of electricity theft, and the handling of electricity disputes. Therefore, it can be considered that the data in the electric power metering automation system plays a role in guiding users to use electric energy to a great extent. By improving the rationality and scientificity of the use of electric energy [2], it helps to comprehensively improve the comprehensive economic benefits of the whole society. However, it is worth noting that in the context of the continuous improvement of the economic level in recent years, the number of power grid enterprises, power customers, and the number of electric energy metering devices are showing a significant growth trend [3], which also puts forward higher requirements for the operation performance of the power metering automation system [4]. This paper analyzes the means to ensure the safe, reliable, and accurate operation of the power metering automation system at the current stage, which mainly focuses on improving the operation and management level. In the specific implementation process, in combination with the requirements of the existing power industry and the grid company [5], it is carried out by sending special personnel to test the device according to the periodic plan. The composition of the power metering automation system is analyzed, and this detection method still has some shortcomings in the face of the current power system. The first is that the periodic calibration method is ineffective for the long-term continuous operation of the power metering automation system. Once the planned time is relatively long [6], the power metering automation system may have faults or hidden troubles outside the calibration period, leading to its failure to be found in time. This may lead to measurement errors or failure to obtain specific and accurate data information [7]. Secondly, it is difficult to control the data error points obtained by manual on-site verification of the power metering automation system. Under different environmental conditions, the corresponding load point range error is large. Combined with the above analysis, it can be seen that it is of great practical significance to further deepen the research on the detection and management methods of power metering automation system. As a common method of data analysis [8], threshold algorithm combines its own characteristics with the characteristics of power metering automation system, and there is huge development space for reasonable integration of the two [9].

Therefore, on the basis of improving the threshold algorithm, this paper proposes an abnormal data mining method of power metering automation system based on the improved threshold algorithm.

2 Design of Abnormal Data Mining Method for Electric Power Metering Automation System

2.1 Improvement of Threshold Algorithm Based on Weighted Least Squares

In order to improve the error analysis under different conditions, the weighted mechanism is introduced, and the weighted least squares method is used to improve the threshold algorithm. The improved objective function can be expressed as

$$\min_x Q(x) = e^h weh \tag{1}$$

Among them, $Q(x)$ represents the objective function of the threshold algorithm, e indicates the error between the data of the power metering automation system and the rated value, w represents a diagonal weighted matrix with positive elements, and h represents the residual. In this way, when the iterative error of the data of the power metering automation system is relatively large, the adaptive control of the threshold can be achieved by appropriately reducing the weighting coefficient. When the iterative error of the data of the power metering automation system is relatively small, the reasonable adjustment of the threshold can also be achieved by appropriately increasing the weighting coefficient [10].

The specific settings and methods can be expressed as

$$\min_x Q(x) = \mathrm{diag}\{r(k)\}e^h weh \tag{2}$$

Among them, $r(k)$ represents the iterative weighting coefficient vector.

According to the way shown above, the threshold algorithm is improved to provide a basis for subsequent abnormal data mining of power metering automation system.

2.2 Abnormal Data Mining of Power Metering Automation System

Combined with the improved threshold algorithm in Sect. 2.1, this paper first uses the direct reconstruction method to analyze the relationship between the actual data and the norm (representing the number of non-zero elements in the vector). The specific calculation method can be expressed as

$$\begin{aligned} &\min_x \| Q(x) \| \text{ s.t.} \\ &y = \Phi x = \Phi \Psi s \end{aligned} \tag{3}$$

Among them, $y = \Phi x$ represents the inverse operation of the data of the electric power metering automation system, y represents actual data, Ψ stands for norm, and s represents a sparse vector. Reconstruct the power metering automation system in the way shown in Formula (3). In the specific calculation process, the norm equivalence problem can be controlled by adjusting the sparse vector to ensure the reliability of the final exception mining results.

Finally, combined with the improved threshold function, the reconstructed data is analyzed, which can be expressed as

$$\varepsilon = y - \min_{x} Q(x) \tag{4}$$

Among them, ε represents the difference between the reconstructed data and the threshold algorithm. According to the improvement of the threshold function in Sect. 2.1, $\min_{x} Q(x)$ it is an adaptive judgment standard for critical state of data. Therefore, when ε if it is greater than 0, it means that the data at the next time is abnormal; otherwise, it means that the data at this time is normal.

3 Application Test

3.1 Test Data Preparation

In this way, the core abnormal data mining in the power metering automation system is comprehensively analyzed. On this basis, the statistics of the data information that the operation status of each node is "normal," among which, the monitored data information such as three-phase voltage and current amplitude, phase to phase angle, and power factor angle of the secondary circuit are shown in Table 1.

The monitored data of three-phase voltage and current amplitude, power factor angle, total active power, split phase active power, etc. of the electric energy meter are shown in Table 2.

The monitored data such as voltage drop error of voltage secondary circuit, error of main and auxiliary energy meters, three-phase ratio difference angle difference of voltage transformer, and three-phase ratio difference angle difference of current transformer are shown in Table 3.

Prepare the test data in the way shown above. In the setting of test methods for the control group, the traditional abnormal data mining method and the abnormal data mining method based on difference analysis are used respectively. By comparing the mining effects of different methods for abnormal data of power metering automation system, the performance of the design method in this paper is analyzed.

Table 1 Secondary circuit data information of power metering automation system

Data item name	Numerical value	
The three-phase voltage amplitude of the monitoring point PO (V)	A-phase	56.3
	B-phase	56.4
	C-phase	56.5
Three-phase voltage amplitude of monitoring point PI (V)	A-phase	56.2
	B-phase	56.3
	C-phase	56.4
The three-phase current amplitude of monitoring point C0 (mA)	508 for all three phases	
Three-phase current amplitude of monitoring point CI (mA)	508 for all three phases	
Power factor angle at junction box (°)	A-phase	9.6
	B-phase	8.51
	C-phase	8.11
The angle between the three-phase voltage phases of the monitoring point PO (°)	AB-phase	120
	BC-phase	119
	CA-phase	118
Phase to phase angle of three-phase voltage at monitoring point P1 (°)	AB-phase	120
	BC-phase	119
	CA-phase	118
The angle between phases of the three-phase current at monitoring point C0 (°)	AB-phase	120
	BC-phase	119
	CA-phase	118
Phase to phase angle of three-phase voltage at monitoring point CI (°)	AB-phase	120
	BC-phase	119
	CA-phase	118

3.2 Test Results and Analysis

On the basis of the above, the missing and false detection of abnormal data by different methods are counted, and the data results are shown in Fig. 1.

Based on the test results shown in Fig. 1, the performance of the three anomaly data mining methods is analyzed respectively. Among the test results of the traditional anomaly data mining methods, the proportion of unidentified anomaly data reaches 22.22%, and the proportion of incorrectly identified anomaly data reaches 44.44%. The overall analysis effect on the anomaly data is not ideal, and the accurate recognition rate is only 66.66%.

Table 2 Data information of electric energy meter of electric power metering automation system

Data item name	Numerical value	
Three-phase voltage amplitude (V)	A-phase	56.1
	B-phase	55.9
	C-phase	56.0
Three-phase current amplitude (mA)	508 for all three phases	
Power factor	A-phase	0.986
	B-phase	0.989
	C-phase	0.990
Phase to phase angle of three-phase voltage at monitoring point P0 (°)	AB-phase	120
	BC-phase	119
	CA-phase	118
Total active power (MW)	84.35	
Split phase active power (MW)	A-phase	28.10
	B-phase	28.08
	C-phase	28.17

Table 3 Error verification data information of power metering automation system

Data item name	Numerical value	
Voltage drop error of secondary circuit (%)	A-phase	0.002
	B-phase	0.004
	C-phase	0.009
Error of main and auxiliary energy meters (%)	Main energy meter	0.06
	Secondary energy meter	0
Three-phase ratio difference of voltage transformer under rated voltage (%)	A-phase	0.152
	B-phase	− 0.157
	C-phase	0.152
Three-phase angle difference of voltage transformer under rated voltage (%)	A-phase	− 0.6
	B-phase	0.8
	C-phase	− 0.3
Three-phase ratio difference of current transformer under rated current (%)	A-phase	− 0045
	B-phase	0.038
	C-phase	− 0.045
Three-phase angle difference of current transformer under rated current (%)	A-phase	2.3
	B-phase	− 0.5
	C-phase	2.3

Fig. 1 Comparison of test results of different methods

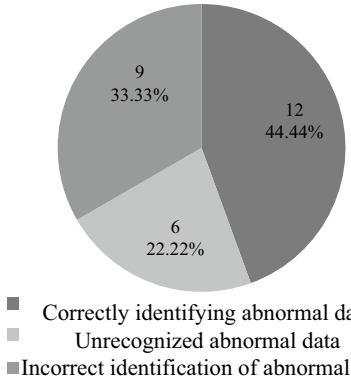

(a) Traditional anomaly data mining methods

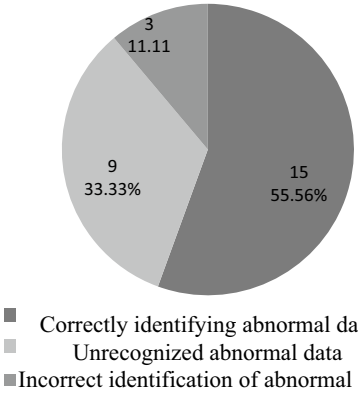

(b) Outlier data mining method of difference analysis

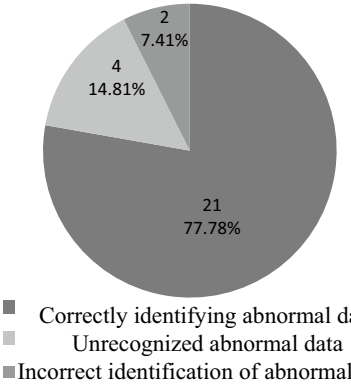

(c) This paper designs an anomaly data mining method

4 Conclusion

Combined with the above analysis, it is easy to see that the accuracy and stability of the operation of the power metering automation system are directly related to the economic interests of both sides of the power resource trade and are an important factor affecting the internal economic benefits of power enterprises. This paper takes the power metering automation system as the research object and designs an abnormal data mining method based on the improved threshold algorithm, which greatly improves the recognition effect of abnormal data. With the help of the design and research of this paper, we hope to provide valuable reference for the stable operation of the power metering automation system and maximize its role and value in the process of power resource trading.

References

1. Zhang R, Qian C (2022) ECG signal denoising algorithm based on RFDA wavelet threshold. Comput Simul 039(008):373–376
2. Lin H, Cui J, Bai X (2021) Feature extraction of marine water pollution based on data mining. Symmetry 13(2):355
3. Xie Y, Wen P, Hou W et al (2021) A knowledge image construction method for effective information filtering and mining from education big data. IEEE Access PP(99):1
4. Wang G, Sun M, Sun H et al (2022) An adaptive threshold of remaining energy based ant colony routing algorithm. J Northwest Polytech Univ 40(2):442–449
5. Li Y, Wei J, Wu B et al (2021) Obfuscating encrypted threshold signature algorithm and its applications in cloud computing. PLoS ONE 16(4):e0250259
6. Qiu Y, Sun C, Tang J (2022) Seismic attribute fusion approach using optimized fastICA-based blind source separation algorithm. Geophys Prospect Petrol 57(5):733–743
7. Khodaverdi A, Erlv T, Hult J et al (2021) An automatic threshold selection algorithm to distinguish a tissue chromophore from the background in photoacoustic imaging. Biomed Opt Express 12(7):3836–3850
8. Pei E, Zhou L, Deng B et al (2021) A Q-learning based energy threshold optimization algorithm in LAA networks. IEEE Trans Veh Technol PP(99):1
9. Tang C, Wang H, Zhao J et al (2021) A method for compressing AIS trajectory data based on the adaptive-threshold Douglas–Peucker algorithm. Ocean Eng 232(4):109041
10. Xu T, Se H, Liu J (2021) A fusion fall detection algorithm combining threshold-based method and convolutional neural network. Microprocess Microsyst 82(12):103828

Hierarchical Control Method of AVC Reactive Power and Voltage in 110 kV Substation Based on Two-Level Reactive Power Optimization

Yang Zhu, Qi Lin, Huiyong Qiu, and Tingying Pan

Abstract The conventional hierarchical control architecture of AVC reactive power and voltage in 110 kV substation is generally single-layer processing, and the control efficiency is low, which leads to the expansion of the fluctuation range of the final AVC reactive power and voltage. Therefore, the design, verification, and analysis of the hierarchical control method of AVC reactive power and voltage in 110 kV substation based on two-level reactive power optimization are proposed. According to the actual control requirements and changes in standards, the voltage stability factor index is determined first. Multi objective method is adopted to improve control efficiency. Multi objective AVC reactive power and voltage hierarchical control framework is designed, and two-level reactive power optimization AVC reactive power and voltage hierarchical control model is constructed. Reactive power compensation processing is used to achieve voltage control. The final test results show that after the comparison of three hierarchical control forms, the secondary reactive power optimization P/V control method controls the fluctuation range of reactive power voltage of G110kV substation to below 40 kV, which indicates that this control method is more flexible, more targeted, and faster, with practical application value.

Keywords Two-level reactive power optimization · 110 kV substation · AVC reactive voltage · Voltage stratification · Hierarchical control · Control method

1 Introduction

110 kV substation generally refers to the directional processing place [1] where the voltage and current at the high voltage side are converted to receive electric energy and distribute electric energy. Different from ordinary substations, in general, the voltage fluctuation of 110 kV substations is relatively small, but it is difficult to adjust in the actual process, especially the control of AVC reactive voltage, which

Y. Zhu (✉) · Q. Lin · H. Qiu · T. Pan
State Grid Linhai Power Supply Company, Linhai 317000, China
e-mail: 441372720@qq.com

S. Yadav et al. (eds.), *Energy Power and Automation Engineering*, Lecture Notes in Electrical Engineering 1118, https://doi.org/10.1007/978-981-99-8878-5_35

requires a variety of equipment and auxiliary devices to deal with, so as to better ensure the stability and safety of substation voltage regulation [2]. At the same time, in the dispatching structure of the substation, capacitors, sensors, reactors, and other devices need to be connected to gradually stabilize the operating state of the substation, gradually realize hierarchical control of reactive power and voltage by adjusting the excitation structure, create a cyclical voltage regulation framework, increase the safety and reliability of the 110 kV substation, minimize the disadvantages of intermittent and fluctuating reactive power and voltage hierarchical control of substation AVC, and promote the related control technology to enter a new development stage [3].

2 AVC Reactive Power Voltage Two-Level Reactive Power Optimization Hierarchical Control Method for 110 kV Substation

2.1 Determination of Voltage Stability Factor Index

In general, the AVC reactive power and voltage adjustment and control of 110 kV substation are more complex, involving more power equipment in the process, and collecting corresponding data and information for later measurement and control [4]. Therefore, in such a background environment, it is necessary to determine the voltage stability factor index first. The change of indicators can help the controller judge whether AVC reactive power and voltage are unstable or fluctuate abnormally faster and more timely [5]. According to the actual control demand and standard changes, the voltage stability factor index can be divided into three parts, namely voltage stability factor index, equivalent optimization model index, and voltage variation characteristic index [6]. The DC bus voltage shall be calculated for the voltage stability factor index, as shown in Formula 1 below:

$$G = \frac{\nu \times \vartheta^2}{f - \sum_{y=1} \nu y + b} + \nu f \tag{1}$$

In Formula 1: G represents the DC bus voltage, f represents a descriptive range, ν represents the unit distance, y indicates the number of disturbances, b indicates the constant value of voltage stability, and ϑ indicates the conversion control value. According to the above settings, the calculation of DC bus voltage is completed. By analyzing the change of DC bus voltage, we can judge whether the total voltage of the substation is within the stable range at this time, and make timely adjustments to avoid the problem of low voltage, which will affect the subsequent power supply and dispatching. The reactive power disturbance variables to be measured in the equivalent optimization model index and voltage variation characteristic index are shown in Formula 2 below:

$$o = \zeta \times \int \frac{x\sigma}{\tau + \sqrt{(1-x)^2}} - (\zeta + \sigma) \tag{2}$$

Equation 2: o represents reactive disturbance variable, ζ indicates the disturbance range, τ is the voltage conversion ratio, x represents the adjustable standard value, and σ indicates the voltage coordination value. According to the above settings, the calculation of reactive power disturbance variables is completed. Through the above calculation, the calculation of basic index values of AVC reactive power and voltage hierarchical control is basically completed, the initial understanding of substation voltage control is made, the stable control environment is established, the voltage and voltage stability factor is calibrated, and the control research objective is defined.

2.2 *Multi Objective AVC Reactive Power and Voltage Hierarchical Control Architecture Design*

After the determination of the voltage stability factor index, the next step is to design a multi-objective AVC reactive power and voltage hierarchical control architecture based on the secondary reactive power optimization requirements. Different from the traditional substation voltage control form, this time, based on the actual measurement demand and standard changes of 110 kV substation, the multi-objective processing form is adopted to further expand the actual holding range and gradually form a more stable and safe control structure. First, an AVC voltage automatic control program needs to be equipped in the control structure. Establish the transformative topological connection control relationship of the power grid, build the control master base station and sub base station based on the 110 kV voltage level, and form a three-layer coordinated multi-objective, multi-level control processing architecture. At this time, design the internal processing structure of the framework, as shown in Fig. 1.

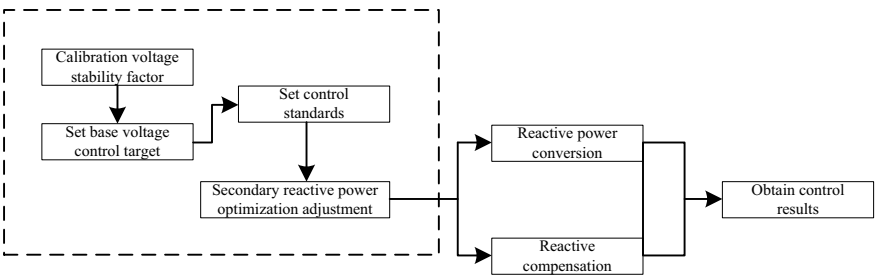

Fig. 1 Structure diagram of multi-target AVC reactive power and voltage hierarchical control architecture

Table 1 Analysis of level II reactive power optimization AVC reactive power and voltage layered control

Name of hierarchical control indicator	Stage 1 control parameter standards	Phase II control parameter standards
Bus voltage (kV)	110	110
Submicrogrid line resistance (Ω)	3.5	2.5
Current distribution ratio	1.06	1.15
Load value	16.34	18.24
Voltage reference value (V)	96.3	98.5

2.3 Build Two-Level Reactive Power Optimization AVC Reactive Power and Voltage Hierarchical Control Model

However, in this part, it should be noted that the resistance setting should be controlled within 1 ~ 5 Ω to minimize the impact on the daily power dispatching and power supply task execution of the substation distribution network. Use the master control base station and sub base station established according to the requirements of secondary reactive power optimization to divide the AVC reactive power and voltage fluctuations at this time, and set the corresponding hierarchical control objectives, as shown in Table 1.

2.4 Reactive Compensation Processing for Voltage Control

Reactive power compensation processing is actually a processing form of correcting and compensating the directional voltage formed by excessive control when the 110 kV substation voltage is controlled hierarchically. The set node can be used to collect the control voltage and current data in multiple directions, and the compensation structure can be set after the specific reactive power compensation position is calibrated, as shown in Fig. 2.

According to Fig. 2, complete the design of reactive power compensation processing structure. Based on this, integrate the requirements of the secondary reactive power optimization control, adjust the initial voltage hierarchical control requirements, transform the fixed control objectives, gradually form a cyclic control system, and become a more flexible 110 kV substation voltage control structure, which can further improve the quality and efficiency of control to a certain extent.

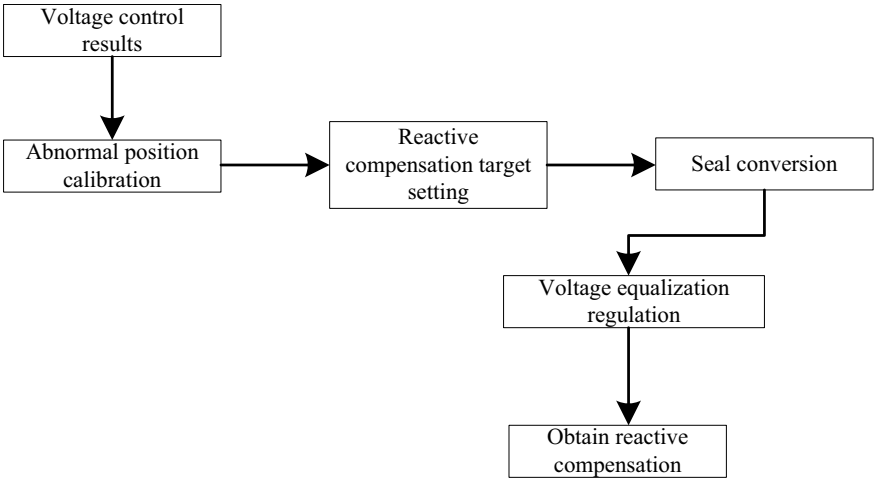

Fig. 2 Structure diagram of reactive compensation processing

3 Method Test

3.1 Test Preparation

Based on the requirements of secondary reactive power optimization, the test environment for the selected hierarchical control method of AVC reactive power and voltage in G110kV substation is tested and analyzed. First, adjust the basic data and information of the substation, determine whether the directional environment of voltage hierarchical control is in a stable state at this time, set the initial step-down control rules, form a cyclical voltage control optimization structure, and connect with the constructed model as the basic test system. At the same time, it is also necessary to integrate specific voltage control requirements to calculate the DC basic voltage of the substation, as shown in Formula 3 below:

$$H = \frac{\alpha\delta}{\chi + (1 - \Im\alpha)^2 \times \delta} + \chi(\delta + \alpha)^2 \tag{3}$$

In Formula 3: H represents the DC basic voltage of the substation, χ indicates the coverage control range, $\Im$ indicates the position of random voltage fluctuation, α indicates the control frequency, and δ indicates the number of short circuits. According to the above measurement, the calculation of the DC basic voltage of the substation is completed. Next, based on this, the comparison items of AVC reactive power and voltage hierarchical control are set, the control program is connected with the main control platform of the substation to form a cyclical voltage hierarchical control framework, and the basic test index parameters are set, as shown in Table 2.

Table 2 Index parameter setting table of AVC reactive power and voltage hierarchical control program

VC reactive voltage hierarchical control index name	Initial control parameter standards	Measured control parameter standards
Maximum delivered power (MW)	5000	5200
Number of flow valves (piece)	16	18
Converter ratio of 500 kV system	3.25	3.45
Short circuit definition	The voltage of the substation is in an unstable state, and the circuit fails, forming a short circuit point	Small short circuit points are associated and extended, resulting in large area substation anomalies, and even causing power equipment failures
Reason for coupling impedance variation	Inconsistent hierarchical control standards	High resistance, creating uncontrollable control obstacles
Rated power (MW)	10,000	13,000
Rated voltage (kV)	110	110

According to Table 2, the setting and analysis of index parameters of AVC reactive power and voltage hierarchical control program are completed, and a dynamic hierarchical control system is built by integrating the requirements of two-level reactive power optimization processing. Use the set node to collect data and information for subsequent use. Complete the construction of the initial test environment for the test. Next, integrate the specific test requirements and standards to conduct specific test verification.

3.2 Test Process and Result Analysis

Each hierarchy needs to set corresponding execution goals according to daily power dispatching and power supply conditions and connect with the basic program. Set four voltage hierarchical control modes, namely, P/E control, C/E control, and two-level reactive power optimization P/V control. The final control results are different for different control modes. Calculate the change of substation voltage at this time, and at the same time, calculate the load value at this time under the environment of micro grid capacitance change, as shown in Formula 4 below:

$$W = \sum_{i=1} \phi i + \varpi \sqrt{(1-k) + \varpi i} \tag{4}$$

In Formula 4: W represents the load value of the substation, ϕ represents the hierarchical control distance, i indicates the control frequency, ϖ is the equilibrium deviation, and k indicates the composite voltage value. According to the above measurement, the load value of the substation is calculated. Set it as the load standard of the foundation. Then, on this basis, in combination with the secondary reactive power optimization requirements, set the real-time value of AVC reactive power and voltage hierarchical control, as shown in Table 3.

Set the real-time parameters of AVC reactive power and voltage hierarchical control according to Table 3. Then, based on this, four voltage hierarchical control modes are adopted, and four regions in G110kV substation are selected for reactive voltage hierarchical control test. The test cycle is set to be 5 h, with a total of 5 cycles. Finally, the voltage fluctuation range is calculated, as shown in Formula 5 below:

$$Y = (1 - N)^2 \times \sum_{t=1} qt + N\omega \tag{5}$$

In Formula 5: Y indicates the fluctuation range of voltage, N represents the initial fluctuation range, q indicates the layered voltage control deviation, t indicates the control times, ω indicates the resistance value. According to the above settings, complete the analysis of the test results, as shown in Fig. 3.

According to Fig. 3, the analysis of the test results is completed: After the comparison of three hierarchical control forms, the secondary reactive power optimization P/V control method controls the fluctuation range of the reactive power voltage of G110kV substation to below 40 kV, which shows that this control method is more flexible, more targeted, faster, and has practical application value.

Table 3 Real-time parameter setting table of AVC reactive power and voltage hierarchical control

Indicator name	Definition description	Specific value
Input voltage	Controllable and adjustable external input voltage	30.5 V
Microgrid capacitance	Total capacitance	1800 uF
Converter line resistance	The directional resistance set in the substation is equivalent to the total resistance	1–5 Ω
Sag coefficient	After hierarchical control, the voltage control difference caused by resistance is also directly related to the operating frequency	30

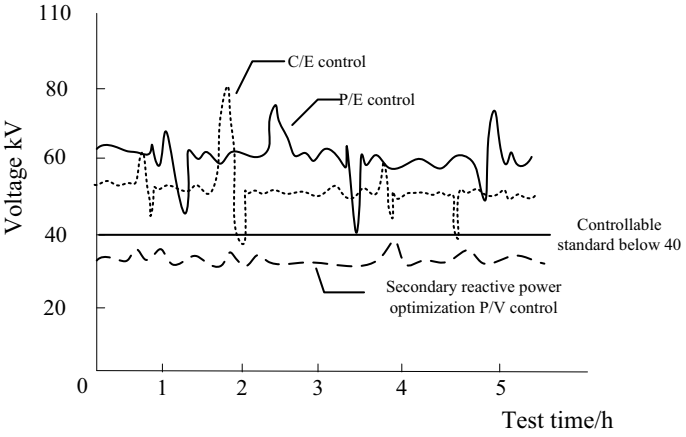

Fig. 3 Comparison and analysis of test results

4 Conclusion

In a word, the above is the design, research, and analysis of the hierarchical control method of AVC reactive power and voltage in 110 kV substation based on two-level reactive power optimization. Compared with the initial voltage hierarchical control form, the built reactive power and voltage hierarchical control is relatively more flexible and multi-source, which can further expand the actual control structure and form a more stable control form under the complex background environment, based on the actual measurement requirements and the constraints of the secondary reactive power optimization conditions.

Acknowledgements The study was supported by the science and technology project of State Grid Zhejiang Electric Power Co. Ltd. (Grant No. 5211TZ23007).

References

1. Han Y, Ning X, Li L et al (2021) Droop coefficient correction control for power sharing and voltage restoration in hierarchical controlled DC microgrids. Int J Electr Power Energy Syst 133(23):107277
2. Sun X, Qiu J (2021) Hierarchical voltage control strategy in distribution networks considering customized charging navigation of electric vehicles. IEEE Trans Smart Grid PP(99):1
3. Zhang Z, Zhang Y, Yue D et al (2022) Economic-driven hierarchical voltage regulation of incremental distribution networks: a cloud-edge collaboration based perspective. IEEE Trans Ind Inform 3:18
4. Fusco G, Russo M, De Santis M (2021) Decentralized voltage control in active distribution systems: features and open issues. Energies 14(9):2563

5. Zhou J, Sun H, Xu Y et al (2021) Distributed power sharing control for islanded single-/three-phase microgrids with admissible voltage and energy storage constraints. IEEE Trans Smart Grid PP(99):1
6. Zhou J, Dong Y (2022) Simulation of voltage correction method for pilot nodes in measurement and control laboratory. Comput Simul 007:039

Multi-source Collaborative Optimal Scheduling Platform for Flexible Interconnected AC/DC Hybrid Distribution Networks

Min Hang, Jiawei Xing, Yan Cheng, and Peng Yu

Abstract Flexible interconnected AC/DC hybrid distribution networks have a large load capacity and cannot achieve the expected collaborative scheduling effect. In order to improve the power supply quality and stability of the distribution network, a multi-source collaborative optimal scheduling platform for flexible interconnected AC/DC hybrid distribution networks is proposed. The platform establishes a multi-objective optimization function with the goal of minimizing the total scheduling cost, power loss, and adjustment amount, and sets constraints to calculate the optimal solution of the function. Search for the optimal scheduling strategy and execute it to build a multi-source collaborative optimal scheduling platform for flexible interconnected AC/DC hybrid distribution networks. The experimental results show that the platform can effectively optimize the scheduling of AC/DC hybrid distribution networks, improve the power supply quality and stability of the distribution network, and under the application of the design method, the load volume of the distribution network is small, and the load fluctuation is relatively gentle.

Keywords Flexible interconnection AC DC hybrid distribution network · Multi-source collaborative optimal scheduling · Dispatching platform · Load capacity

1 Introduction

In recent years, the energy crisis has become increasingly acute, and the development of new energy has become a hot issue of global concern [1]. In the context of increasing requirements for energy development and power grid management, AC/DC hybrid distribution networks have gradually become an important trend in power grid development due to their advantages of efficiency, flexibility, and reliability [2]. However, due to the volatility of power load and new energy output, the

M. Hang (✉) · J. Xing · Y. Cheng · P. Yu
State Grid Shandong Electric Power Research Institute, Jinan 250002, Shandong, China
e-mail: liyongjing0725@163.com

S. Yadav et al. (eds.), *Energy Power and Automation Engineering*, Lecture Notes in Electrical Engineering 1118, https://doi.org/10.1007/978-981-99-8878-5_36

scheduling management of AC/DC hybrid distribution networks has brought new challenges. Therefore, the multi-source collaborative optimal scheduling platform has gradually become a necessary means for the effective management of AC/DC hybrid distribution networks.

Reference [3] proposes coordinated control of power flow controllers and hybrid DC circuit breakers in MVDC distribution networks. By adjusting the polarity and amplitude of the SP-PFC output voltage during a fault, the rising speed of the fault current can be suppressed, thereby reducing the breaking current of hybrid DC circuit breakers. The connection mode and topology of series parallel power factor controllers to the MVDC distribution network are analyzed, and the coordination strategy between series parallel power factor controllers and hybrid DCCC is studied. The mathematical models of series parallel power factor controllers at different fault stages are derived. Using the equivalent model of the series parallel power factor controller, the fault current of the MVDC distribution network can be accurately calculated. Reference [4] proposes a multi-agent based microgrid reconfiguration study for AC/DC hybrid distribution networks, which is used to form microgrids under extreme events. When a severe power outage occurs and the main power grid is disconnected, the proposed optimization model promotes the recovery of critical services by forming nested isolation parts within the HDN. The operational characteristics of isolated HDNs, the droop control nodes of AC and DC parts, and the lack of slack buses in autonomous operation are considered. To reduce the computational burden, a multi-agent soft actor critic approach was developed to solve the proposed reconfiguration problem, in which multiple agents coordinate to control circuit breakers that can be segmented and meet different system states and scales. Simulation tests were conducted in two test systems to verify the effectiveness of the proposed method.

Based on the above research, this paper proposes a multi-source collaborative optimal scheduling platform for flexible interconnected AC/DC hybrid distribution networks. This platform can effectively improve the power supply quality, stability, and reliability of the AC/DC hybrid distribution network, providing important support for the sustainable development of the power system.

2 Multisource Collaborative Optimal Scheduling for Flexible Interconnected AC/DC Hybrid Distribution Networks

2.1 Establishing a Multi-objective Optimization Function

There are multiple objectives, multiple scheduling variables, and multiple dimensions and constraints in the process of flexible interconnected AC/DC hybrid distribution network multi-source collaborative optimal scheduling. Therefore, the power grid multi-source collaborative optimal scheduling problem is transformed into

a multi-objective optimization problem, and a multi-objective optimization function is established based on the economic and stability requirements of distribution network multi-source collaborative optimal scheduling [5]. This time, three sub objective functions are established, with the objective of minimizing the operating cost, power loss, and adjustment of the flexible interconnected AC/DC hybrid distribution network. A multi-objective optimization function is established.

(1) Minimum objective function for operating cost of flexible interconnected AC/DC hybrid distribution networks.

The operating cost of a flexible interconnected AC/DC hybrid distribution network is the sum of controllable scheduling costs, compensation costs for translatable loads, and flexible load scheduling costs. Assuming that the charge/discharge amount of the flexible interconnected AC/DC hybrid distribution network is F at t time, and the unit scheduling time length of the flexible interconnected AC/DC hybrid distribution network is Δt, the controllable scheduling cost is expressed as follows:

$$K_1 = \left(S_{\mathrm{F}} + \frac{W}{365 \times P} \right) \times \Delta t \tag{1}$$

In the formula, K_1 represents the controllable scheduling cost of the flexible interconnected AC/DC hybrid distribution network; S represents the unit operation and maintenance cost of the flexible interconnected AC/DC hybrid distribution network; W represents the installation cost of the flexible interconnected AC/DC hybrid distribution network; P represents the service life of the flexible interconnected AC/DC hybrid distribution network. Assuming that the load dispatching amount of the flexible interconnected AC/DC hybrid distribution network at t time is D, the compensation cost of its translatable load is expressed as follows:

$$K_2 = \sum_{t=1} (\lambda + D) \times K_1 \tag{2}$$

In the formula, K_2 represents the compensation cost for translatable loads in a flexible interconnected AC/DC hybrid distribution network; λ represents the compensation unit price. Assuming that the attenuation of the flexible interconnected AC/DC hybrid distribution network with a level of n is U, the flexible load dispatching cost is expressed as follows:

$$K_3 = \sum_{n=1} Q_n \times U + (U - X) \times K_2 \tag{3}$$

In the formula, K_3 represents the cost of flexible load dispatch for a flexible interconnected AC/DC hybrid distribution network; Q_n represents the compensation cost for the n level reduction; X represents the reduction amount submitted by the flexible interconnected AC/DC hybrid distribution network. According to the above analysis,

the minimum objective function of the operating cost of the flexible interconnected AC/DC hybrid distribution network is expressed by the formula:

$$\min K = K_1 + K_2 + K_3 \tag{4}$$

In the formula, $\min K$ represents the minimum operating cost of a flexible interconnected AC/DC hybrid distribution network.

(2) Minimum objective function of power loss in flexible interconnected AC/DC hybrid distribution network.

With the goal of minimizing power loss in the multi-source collaborative optimal scheduling process of flexible interconnected AC/DC hybrid distribution networks, the objective function is established as follows:

$$\min L = \sum_{t \in T} \left(M_{ij}\right)_t^2 \times \kappa_{ij} \tag{5}$$

In the formula, $\min L$ represents the minimum power loss of the flexible interconnected AC/DC hybrid distribution network; T represents the reactive power optimization cycle; M_{ij} represents the current amplitude flowing from i to node j of the flexible interconnected AC/DC hybrid distribution network branch node at moment t; κ_{ij} represents the resistance from i to j of a branch node in a flexible interconnected AC/DC hybrid distribution network.

(3) Minimum objective function for scheduling of flexible interconnected AC/DC hybrid distribution networks.

$$\min P = \sum_{t=1} (X_t - Y_t) \times \omega \tag{6}$$

In the formula, $\min f_3$ represents the minimum dispatching amount of the flexible interconnected AC/DC hybrid distribution network; X_t represents the planned value of the t time for the multi element coordinated and optimized scheduling in the day ahead; Y_t represents the planned value of the t time of the day's multiple coordinated optimization scheduling; ω represents a penalty factor.

Integrate the objective optimization function established above into a multi-objective optimization function, which is expressed by the formula:

$$D_{\mathrm{MB}} = \min K + \min L + \min P \tag{7}$$

In the formula, D_{MB} represents a multi-objective optimization function for multi-source collaborative optimal scheduling of flexible interconnected AC/DC hybrid distribution networks.

2.2 Set Constraints

Set constraints based on the established multi-objective optimization function and the scheduling requirements of flexible interconnected AC/DC hybrid distribution networks. Firstly, power grid dispatching needs to meet power balance conditions, which are expressed by the formula:

$$Y_{\mathrm{STJ}} = D_{\mathrm{MB}} \times Q \tag{8}$$

In the formula, U represents the network loss power of the flexible interconnected AC/DC hybrid distribution network. Then, for the load constraints of the flexible interconnected AC/DC hybrid distribution network, the formula is expressed as follows:

$$Q_{\min} \leq Q \leq Q_{\max} \tag{9}$$

In the formula, $U_{\min}$ represents the minimum value that a flexible interconnected AC/DC hybrid distribution network can reduce load; $U_{\max}$ represents the maximum value that a flexible interconnected AC/DC hybrid distribution network can reduce load. This constraint condition is used to reduce load constraints on flexible interconnected AC/DC hybrid distribution networks.

2.3 Constructing a Multi-source Collaborative Optimal Scheduling Platform for Distribution Networks

Based on the constraints set above, the established multi-objective optimization function is solved and calculated to obtain the optimal multi-source collaborative optimization scheduling strategy. The possible solution of the multi-objective optimization function is formulated as a function individual, and the set of possible solutions of the function is mapped into a two-dimensional space to generate a search space. Based on the pheromones obtained during each search, the node closest to the target is found, and the optimal solution of the multi-objective optimization function is obtained. Based on the optimal solution result, a distribution network multi-source collaborative optimization scheduling platform is constructed. The specific process is as follows.

Step 1: Parameter initialization. Assume that there are m possible solutions to the multi-objective optimization function, establish a solution set as M, and map all possible solutions in the solution set to a dimension of $x \times y$. Generate search scenarios in two-dimensional space. Initialize parameters such as the number of scene iterations, initial probability, and so on.

Step 2: Path pheromone update. Complete the search task in the search space, update the search path pheromone every time the search is completed, calculate the path pheromone, and select the next access area.

Step 3: Adaptive degree calculation. The fitness function is used to calculate the adaptive degree value of the path. This value can reflect the distance between the access path and the target node, which can be used to determine the degree of compliance with the desired goal of multi-source collaborative optimal scheduling for flexible interconnected AC/DC hybrid distribution networks. The calculation formula is:

$$W_{\mathrm{E}} = \frac{\alpha \times \beta \times (\theta + \rho)}{Q_{\max} - Q_{\min}} \tag{10}$$

In the formula, W_{E} represents the search path adaptability; α represents inertia weight; β represents the node location that has reached the farthest point in historical access; θ represents search speed; ρ represents the individual limit component.

Step 4: Iterative conditional testing. After completing each iteration, check the iteration conditions. If the iteration conditions are not met, return to Step 2 to continue searching. If the iterative requirements are met, the possible solution corresponding to the path with the maximum adaptive degree value is output, which is the optimal solution of a multi-objective optimization function, that is, a multi-source collaborative optimal scheduling strategy for flexible interconnected AC/DC hybrid distribution networks, and it is executed to build a multi-source collaborative optimal scheduling platform for flexible interconnected AC/DC hybrid distribution networks.

3 Experimental Results and Analysis

In order to verify the practicality and effectiveness of the multi-source collaborative optimal scheduling platform for flexible interconnected AC/DC hybrid distribution networks, this paper designed a corresponding experimental environment and set key parameters. According to the actual situation of distributed power sources, network structures, and loads in typical active distribution networks, combined with distribution network operation data, a typical scenario of active distribution networks is designed. Establish a software and hardware simulation environment for collaborative operation of active distribution networks under multiple flexible integration, including but not limited to databases, communication cables, sensors, communication modules, test materials, and monitoring systems. It has front-end display functions and can simulate collaborative operation conditions in different scenarios of distribution networks, meeting the technical verification requirements of the simulation platform. Build an active distribution network collaborative operation simulation platform architecture under multiple flexible fusion, which is divided into control layer, information layer, and physical layer.

Experimental environment: The operating system is Windows 10, the development tools are Matlab2019b, and PowerFactory. The experimental platform uses Lenovo ThinkPad E480. The experimental data uses actual data from a certain area, including power data such as the output of multiple power stations. Experimental parameter setting: The load prediction error is controlled within 5%, and the number of iterations of the co optimal scheduling algorithm is 100. Under the above experimental environment and experimental parameter settings, the multi-source co optimal scheduling platform for flexible interconnected AC/DC hybrid distribution networks designed in this article is used as an experimental group, and the methods in Refs. [3, 4] are used as control groups, and the final experimental results are compared. The qualification rate of distribution network operation status should reach 98%, with the objective function of system load balancing and the need to reduce system energy consumption losses.

Through experimental analysis of a flexible interconnected AC/DC hybrid distribution network in the above environment, the practical application effect of the proposed multi-source collaborative optimization scheduling platform is verified, providing reliable support for the safe and stable operation of the power system. In the experiment, a three-phase balanced node power line network structure is selected, as shown in Fig. 1.

In Fig. 1, DG1–DG3 represents distributed power sources in the network. The maximum active power of each power source is 800 kW, 1200 kW, and 1000 kW, respectively. The dotted line represents the disconnected line, and the solid line represents the connected line. According to the above three-phase balanced node power line network structure, the specific data of power line recovery obtained by this method is shown in Table 1.

According to the results listed in Table 1, it can be seen that under the multi-source collaborative optimal scheduling platform for flexible interconnected AC/DC hybrid distribution networks proposed in this paper, the AC/DC hybrid distribution network was scheduled and the output power of each power source was obtained. The output power of DG1, DG2, and DG3 power sources at different nodes were 200.00, 354.10, and 649.53 kW, 200.00, 323.34, and 649.53 kW, and 500.00, 866.12, and 649.53 kW, respectively. These data reflect the power supply capacity of the power

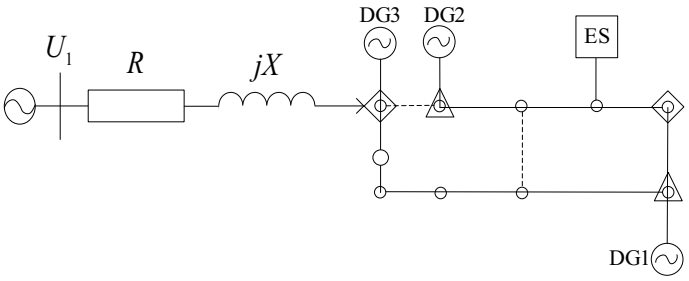

Fig. 1 Network structure diagram of a three-phase balanced node power line

Table 1 Line scheduling results under this method

Node number of the scheduled load	Output power of each power supply (kW)		
	DG1	DG2	DG3
1	200.00	354.10	649.53
2	200.00	323.34	649.53
3	500.00	866.12	649.53
4	500.00	866.12	649.53
5	500.00	866.12	649.53
6	500.00	866.12	649.53
7	500.00	866.12	649.53
8	500.00	866.12	649.53

supply at each node and the load characteristics in the system and can be used as reference data for further optimizing the distribution network. The multi-source collaborative optimization scheduling platform for flexible interconnected AC/DC hybrid distribution networks proposed in this paper can effectively optimize the scheduling of AC/DC hybrid distribution networks and improve the power supply quality and stability of the distribution network.

In order to further verify the applicability of the design method, the load capacity of the distribution network under the application of the three methods is compared. The load generated during the operation of the distribution network is selected for a time period of 0–12 h. Based on the experimental data, the comparison results of the load capacity of the distribution network under the application of the three methods are drawn as shown in Fig. 2.

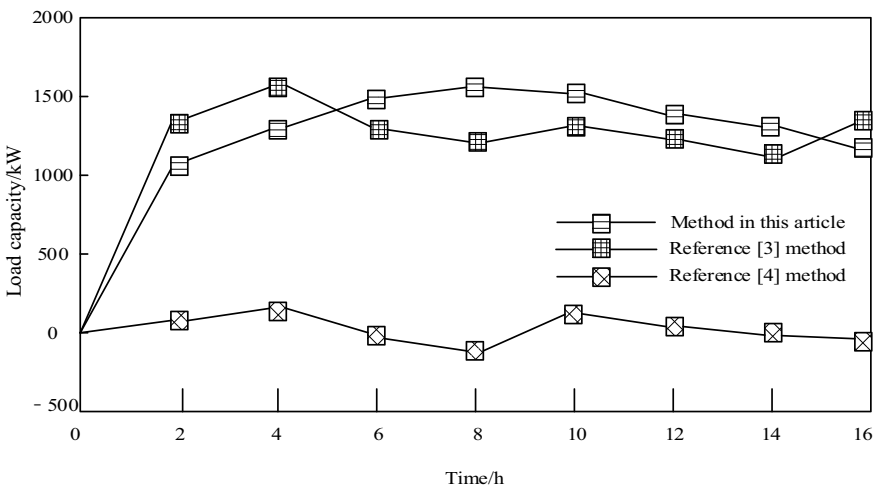

Fig. 2 Comparison results of distribution network load capacity under three methods

As can be seen from Fig. 2, under the application of the design method, the load volume of the distribution network is relatively small, and the load fluctuation is relatively gentle. On a long-term scale, the load capacity of the methods in Refs. [3, 4] is relatively high, and the load fluctuation range of the distribution network is relatively large, with the maximum load capacity of 1523 kW and 1514 kW, respectively. However, the maximum load capacity of the design method is only 124 kW, which is far lower than the methods in Refs. [3, 4], indicating that the proposed method is more stable in the operation of the distribution network and effectively meets the load demand of the distribution network. Therefore, in terms of grid load, the design method shows obvious advantages and is more suitable for multi-source collaborative optimal scheduling of distribution networks compared to the two traditional methods.

4 Conclusion and Outlook

This paper proposes a multi-source collaborative optimal scheduling platform for flexible interconnected AC/DC hybrid distribution networks. Through research, the following conclusions are obtained:

(1) In this paper, the AC/DC hybrid distribution network is scheduled under the scheduling platform, and the output power of each power source is obtained. The output power of DG1, DG2, and DG3 power sources at different nodes are 200.00, 354.10, and 649.53 kW, 200.00, 323.34, and 649.53 kW, and 500.00, 866.12, and 649.53 kW, respectively. This can effectively optimize the scheduling of the AC/DC hybrid distribution network, and improve the power supply quality and stability of the distribution network.
(2) Under the application of design methods, the load of distribution networks is relatively small, and the load fluctuation is relatively gentle.

This article only makes a preliminary study and discussion of the scheduling platform, and further research is needed for future work.

(1) Further in-depth research is needed on the impact of uncertainty in the output power and load volatility of intermittent energy sources such as wind power and photovoltaic on the operation of AC/DC hybrid microgrids with a high proportion of renewable energy.
(2) In the microgrid optimization operation, further research is conducted on the source network load storage coordination and optimization operation, taking into account the spatial distribution of the microgrid while considering the time scale of the microgrid optimization process, making the analysis process more comprehensive.

References

1. Hui HG, Lian Z, Zhang D et al (2022) Orderly charging strategy based on optimal time of use price demand response of electric vehicles in distribution network. Energies 15(5):1–25
2. Bouhouras AS, Kothona D, Gkaidatzis PA et al (2022) Distribution network energy loss reduction under EV charging schedule. Int J Energy Res 46(6):8256–8270
3. Liao J, Zhou N, Qin Z et al (2021) Coordination control of power flow controller and hybrid DC circuit breaker in MVDC distribution networks. J Mod Power Syst Clean Energy 9(6):1257–1268
4. Wu T, Wang J, Lu X et al (2022) AC/DC hybrid distribution network reconfiguration with microgrid formation using multi-agent soft actor-critic. Appl Energy 307(1):1–11
5. Paul S, Sharma A, Padhy NP (2021) Risk constrained energy efficient optimal operation of a converter governed AC/DC hybrid distribution network with distributed energy resources and volt-VAR controlling devices. IEEE Trans Ind Appl 57(4):4263–4277

Multi-objective Voltage Balance Control Method for Distribution Network Based on Active Tabu Search

Qingnan Meng, Jiazhao Zhu, Hongbo Zhu, Hongyin Ding, and Yixiu Jiang

Abstract During the implementation of voltage balance control in the distribution network, due to the lack of analysis of the relationship between parameters during the operation phase of the distribution network, the average voltage deviation is relatively large. Therefore, an active Tabu search based multi-objective voltage balance control method for distribution networks is proposed. Based on the minimization of the ratio of short-circuit voltage to the corresponding switch breaking capacity in the power grid, an objective function stage for voltage balance in the distribution network was constructed, and constraints for the objective function were set from the perspectives of radial topology and power flow. In the voltage balance control phase, the active Tabu search algorithm is introduced to set the distribution network target adjustment parameters as random initialization parameters in the solution space. Analyze the correlation of parameters at different operating stages by using the cost function values of target adjustment parameters in the neighboring distribution network. Finally, use the parameter corresponding to the minimum cost function value as the previous distribution network target adjustment parameter. Control the voltage balance of the distribution network. In the test results, the design method has good voltage control performance under dual objective, three objective, and four objective conditions, and the corresponding average voltage deviation is at a relatively low level.

Keywords Active tabu search · Distribution network · Multi-objective · Voltage balance · Voltage balance objective function · Constraints · Cost function value

1 Introduction

In general, the variable composition of reactive power optimization is divided into two aspects, namely control variable and state variable. The generator terminal voltage, unit reactive power output, and reactive power compensation capacity are control

Q. Meng (✉) · J. Zhu · H. Zhu · H. Ding · Y. Jiang
State Grid Linhai Power Supply Company, Linhai 317000, China
e-mail: 379626099@qq.com

S. Yadav et al. (eds.), *Energy Power and Automation Engineering*, Lecture Notes in Electrical Engineering 1118, https://doi.org/10.1007/978-981-99-8878-5_37

variables, and node voltage and branch power are state variables. This leads to many complex variables to be processed in the process of distribution network control, which is difficult [1, 2]. In view of this, this paper proposes the research of distribution network multi-objective voltage balance control method based on active tabu search, and analyzes and verifies the practical application effect of the designed control method through comparative testing.

2 Design of Multi-objective Voltage Balance Control Method for Distribution Network

2.1 Setting of Distribution Network Voltage Balance Objective Function

In the process of constructing the distribution network voltage balance objective function, based on the minimization of the ratio of the distribution network short-circuit voltage to the corresponding switch breaking capacity [3, 4], the set objective function can be expressed as

$$c(i) = \frac{u_{\mathrm{id}}}{u_{\mathrm{bri}}} \tag{1}$$

Among them, $c(i)$ is the distribution network voltage balance objective function at node i, u_{id} node i three phase short-circuit voltage parameters at, u_{bri} represents the rated interrupting voltage parameter of the bus side circuit breaker. This means that the smaller the voltage threshold, the better the control effect for voltage balance. Then there is

$$\min f(x) = \max c(i) \tag{2}$$

Among them, $f(x)$ indicates the short-circuit point in the distribution network x the maximum parameter of the ratio of the corresponding short-circuit voltage to the breaking voltage. The second is the setting of power flow constraints, which can be expressed as

$$p_i - p_{ni} = I_i \sum I_j \left(G_{ij} \cos\alpha + B_{ij} \cos\alpha\right) \tag{3}$$

$$q_i - q_{ni} = I_i \sum I_j \left(G_{ij} \sin\alpha + B_{ij} \sin\alpha\right) \tag{4}$$

Among them, p_i and p_{ni} represent nodes in distribution network respectively, i the injected active power and the active power of the actual load, q_i and q_{ni} represent nodes in distribution network respectively, i reactive power injected and reactive

power of actual load, I_i and I_j indicates the current parameters of adjacent nodes, G_{ij} represents a node in the distribution network i and nodes j conductance between, B_{ij} represents a node in the distribution network i and nodes j the susceptance between, α represents a node in the distribution network i and nodes j phase angle difference between.

Set the distribution network voltage balance objective function in the way shown above, and provide an implementation basis for subsequent voltage balance control.

2.2 Voltage Balance Control Based on Active Tabu Search

After the algorithm iterates for a fixed number of times or meets the termination condition, that is, after meeting the distribution network voltage balance target function constructed in Sect. 2.1. By putting the historical values of the specific number of the current distribution network target adjustment parameters into the Tabu List, and prohibiting the current distribution network target adjustment parameters from updating to the distribution network target adjustment parameters in the Tabu List [5–7]. The parameter control results can be effectively prevented from falling into a local dead cycle, resulting in the control effect being difficult to achieve the ideal state. The specific calculation method can be expressed as

$$k(n) = n\sigma_{ij}^2 + \mathrm{MAX}\left(\frac{\eta}{M}\sqrt{\gamma c(i)}\right) \tag{5}$$

In combination with formula (4), when using active tabu search algorithm for voltage balance control, the maximum number of algorithm restarts is set based on experience MAX and convergence factor γ is constant, combined with overload factor η and modulation order M the actual state of, and the threshold for comparing the cost function value $k(n)$ make settings [8–10]. When the target adjustment parameters of the distribution network are exactly the same as the target adjustment parameters of the transmission distribution network (correct solution), the cost function value of the target adjustment parameters of the distribution network is output.

Control the voltage balance of the distribution network in the way shown above.

3 Test Analysis

3.1 Test Environment

During the analysis of the actual application effect of the design method proposed in this paper, a distribution network topology based on IEEE 33 bus was chosen as the experimental environment. The details of the result configuration can be found in Fig. 1.

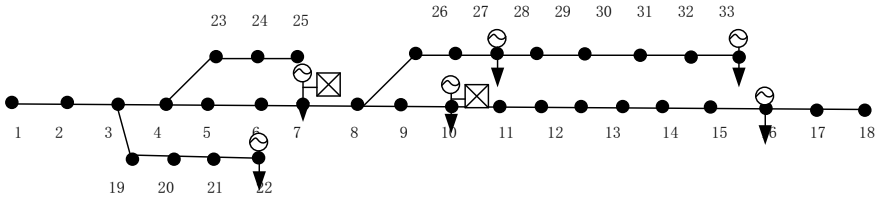

Fig. 1 Test environment structure diagram

Table 1 Test environment parameter settings

Serial number	Index	Parameter
1	Distributed photovoltaic rated power	4.2 MW
2	Rated capacity of distributed photovoltaic inverter	4.2 MVA
3	Upper limit of distribution network node voltage	0.95 p.u
4	Lower limit of distribution network node voltage	1.05 p.u
5	Acceptable safe voltage and voltage deviation	5.0%
6	Rated voltage of static var compensator	1.0 MVar
7	Rated power of energy storage system	1.0 MW
8	Initial network loss of distribution network model	0.04238 p.u

As shown in Fig. 1, the access nodes of the distributed photovoltaic power supply are node 5, node 10, node 16, node 22, node 28, and node 33 respectively. Table 1 shows the specific parameter settings.

On this basis, the voltage of the test distribution network is controlled and managed. In order to ensure the reliability of control effect, the specific parameters of different branches are counted, and the data results are shown in Table 2.

Combined with the data information, test the voltage balance control of the distribution network. In the process of testing, this paper sets up a control group, using the standard droop control method, depth deterministic gradient control method, MAPPO algorithm control method, flexible load voltage regulation method, and the design control method in this paper.

3.2 Effectiveness Analysis

In order to achieve a more objective assessment of the control effect of the designed method, this paper selects ten days' data as the test set and analyzes the specific control effect with the average voltage out of limit value as the indicator.

Firstly, the voltage of different methods is compared when the distributed photovoltaic inverter and static reactive power compensator are taken as the target objects control the effect, and the result is shown in Fig. 2.

Table 2 Specific parameter information of different branches of distribution network

Node branch	Branch resistance (Ω)	Branch reactance (Ω)	Length of branch road (km)	Node branch	Branch resistance (Ω)	Branch reactance (Ω)	Length of branch road (km)
1–2	0.8711	1.6828	4.2286	1–19	0.905	1.7167	4.2625
2–3	2.9057	3.7483	8.8486	19–20	2.9396	3.7822	8.8825
3–4	4.13	5.3242	12.5586	20–21	4.1639	5.3581	12.5925
4–5	2.0112	2.6721	12.1986	21–22	2.0451	2.706	12.2325
5–6	0.2711	0.5372	1.3686	4–23	0.305	0.5711	1.4025
6–7	0.0401	0.0961	0.2686	23–24	0.074	0.13	0.3025
7–8	1.7006	3.2668	8.1786	24–25	1.7345	3.3007	8.2125
8–9	0.3796	6.4106	0.1286	8–26	0.4135	6.4445	0.1625
9–10	0.4736	0.6161	1.4786	26–27	0.5075	0.65	1.5125
10–11	1.2786	1.6535	3.9196	27–28	1.3125	1.6874	3.9535
11–12	2.4509	3.1627	7.4706	28–29	2.4848	3.1966	7.5045
12–13	5.4434	7.0166	16.5386	29–30	5.4773	7.0505	16.5725
13–14	12.3651	15.9306	37.5186	30–31	12.399	15.9645	37.5525
14–15	1.5131	1.9549	4.6286	31–32	1.547	1.9888	4.6625
15–16	2.6516	3.4211	8.0786	32–33	2.6855	3.455	8.1125
16–17	0.3796	6.4106	0.1286				
17–18	3.003	4.0176	30.6586				

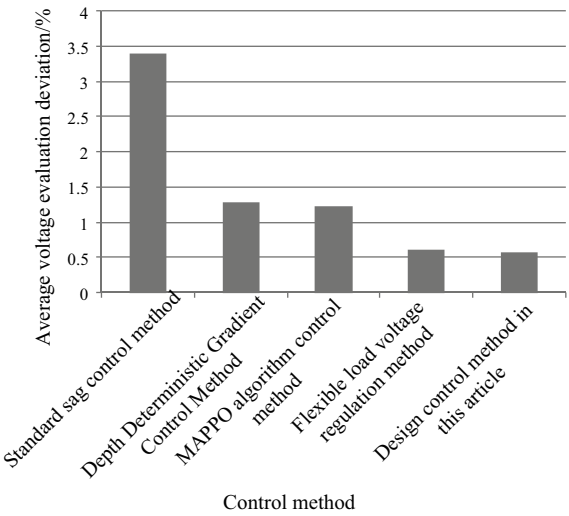

Fig. 2 Comparison of voltage control effects of different methods under double targets

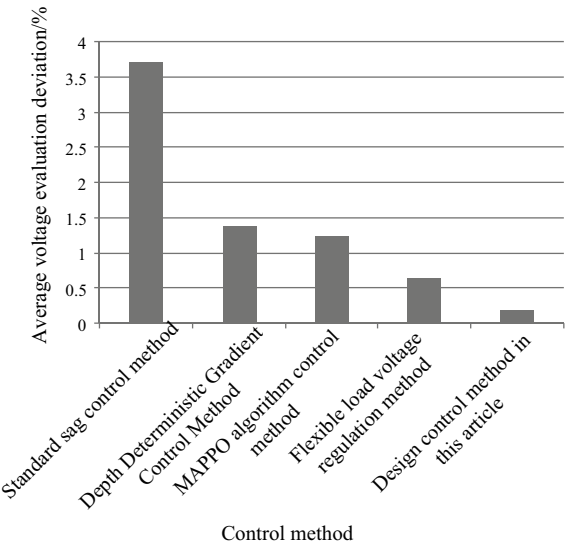

Fig. 3 Comparison of voltage control effects of different methods under three objectives

Figure 2 shows the control method designed in this paper can be controlled within 1%, and the average voltage deviation is 0.67% and 0.64% respectively. The voltage control method proposed in this paper has been deemed optimal based on the average voltage deviation index.

Figure 3 shows the effect of different control methods on the voltage control of the tested distribution network when the distributed photovoltaic inverter, static reactive compensator, and flexible load are taken as the control objectives.

Among them, Fig. 3 shows the control method designed in this paper can control the average voltage deviation within 1%, and the average voltage deviation is 0.588% and 0.147% respectively. Therefore, the control method designed in this paper has the best performance.

Figure 4 shows the voltage control effects of different methods when taking distributed photovoltaic inverter, static reactive power compensator, flexible load, and energy storage system as the target objects.

In Fig. 4, the control method designed in this paper can control the average voltage deviation within 0.5%, whose average voltage deviation is 0.363%, 0.446%, and 0.124% respectively.

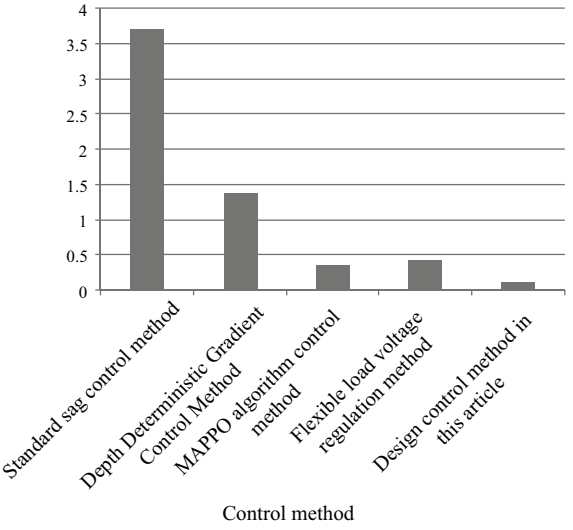

Fig. 4 Comparison of voltage control effects of different methods under four objectives

4 Conclusion

The service life of electrical equipment is affected. In this paper, an active tabu search based multi-objective voltage balance control method for distribution networks is proposed to effectively reduce the average voltage deviation of distribution networks.

Acknowledgements The study was supported by "the science and technology project of State Grid Zhejiang Electric Power Co. Ltd. (Grant No. 5211TZ23007)".

References

1. Zhu YJ, Wu QF, Wu ZS (2022) Reactive power sharing control of battery cell without voltage deviation. Comput Simul 039(003):119–214
2. Lin L, He J, Xu C (2021) Analysis on circulating current and split capacitor voltage balance for modular multilevel converter based three-phase four-wire split capacitor DSTATCOM. J Mod Power Syst Clean Energy 9(3):11
3. Liu J, Li C, Zheng Z (2022) A quasi-two-level medium-voltage SiC MOSFET power module with low loss and voltage self-balance. IEEE Trans Power Electron 37(1):519–533
4. Xiao Z, He Z, Guan R (2022) Analysis and design of a modular self-balance high-voltage input DC–DC topology. IEEE J Emerg Sel Topics Power Electron 10(2):2276–2289
5. Ali M, Tariq M, Lin CH (2021) Operation of a UXE-type 11-level inverter with voltage-balance modulation using NLC and ACO-based SHE. Sustainability 13(16):1–19
6. Jimenez VA, Will A, Lizondo DF (2022) Phase reassignment for load balance in low-voltage distribution networks. Int J Electr Power Energy Syst 137:107691.1–107691.8
7. Muthavarapu AK, Biswas J, Barai M (2022) An efficient sorting algorithm for capacitor voltage balance of modular multilevel converter with space vector pulsewidth modulation. IEEE Trans Power Electron 37(8):9254–9265

8. Rido M, Syahrul RM, Monica T (2021) OR47. Index of cardiac electrophysiological balance (iCEB) in patients with COVID-19. Eur Heart J Suppl 23(Supplement_F)
9. Kawakami T, Yamada K, Umetani K (2022) Design and analysis of power balance mode control using digital control for boost-type DC-DC converter. IEEJ Trans Electr Electron Eng 17(5):739–748
10. Xin Y, Chen C, Sun L (2021) Module selection method with improved capacitor voltage balance for MMC using (2 N + 1) SHEPWM. Int J Electr Power Energy Syst 133:107294.1–107294.11

Research on the Data Monitoring System of Distribution Network Project Based on "Three Rates Combination"

Yueren Zhu, Yixing Gu, Jun Wu, Xuhui Ma, Yifan Ma, and Tao Xiao

Abstract In recent years, the increase in the scale of investment in distribution grid projects and the tightening of investment supervision have made the investment management of distribution grid projects more challenging. To break the traditional monitoring method of distribution network projects, this paper proposed a distribution network project data monitoring system based on "three rates combination". Firstly, obtaining the definition and data sources of distribution network three rate indicators and construct the monitoring and analysis model of distribution network three rate indicators; secondly, formulating the early warning rules based on the distribution network three rate monitoring and analysis system and construct the digital monitoring and early warning system of three rates; finally, the data monitoring software of distribution network project based on "three rates combination" has been developed to solve the problems of distortion of distribution network project statistics, mismatch of cross-sector data and limited space for improving the investment completion rate.

Keywords Three rates combination · Monitoring analysis · Monitoring and warning · Model construction · Software platform

1 Introduction

Distribution network project is an important part of power grid construction, and its role is crucial to the development of power grid, people's life, and social economy [1]. With the reform of transmission and distribution tariff and the deepening of lean management concept within the company, higher requirements are put forward for precise investment strategies and improving the effectiveness of distribution network

Y. Zhu (✉) · J. Wu · X. Ma · Y. Ma · T. Xiao
State Grid Zhejiang Electric Power Co., Ltd. Pinghu Power Supply Company, Pinghu 314200, China
e-mail: tdqiushi@126.com

Y. Gu
Pinghu General Electric Installation Co. Ltd., Pinghu 314200, China

S. Yadav et al. (eds.), *Energy Power and Automation Engineering*, Lecture Notes in Electrical Engineering 1118, https://doi.org/10.1007/978-981-99-8878-5_38

construction. However, the maladaptive nature of traditional distribution network project monitoring and analysis management is becoming more and more prominent. Under the traditional management mode, the data of distribution grid project indicators are scattered in many departments, professional data are managed independently; "empirical" management is still common, data are filled in manually, and data quality varies; there are barriers in the information system, and there is a lack of scientific and effective, multi-source collaborative monitoring methods [2]. The above problems seriously hinder the monitoring and analysis management of distribution network projects, and seriously restrict the healthy, rapid, and sustainable development of power grid enterprises.

The literature [3, 4] both embed grid project control strategies in existing platforms. In the context of strategic alliance, literature [5] analyzes and explores the construction of an information management platform for power engineering EPC projects to achieve automated information management. In the literature [6], the management platform architecture for improving data quality in distribution networks is given. The paper [7] promotes the management mode of distribution network from "empirical judgment and post-event response" to "data-driven and pre-emptive prevention". In order to solve the problem of difficult project management and complex data management in power grid infrastructure, the paper [8] builds a life-cycle index system under the guidance of data management enterprise concept, and comprehensively improves the standardization of data management. The literature [9] proposes a planning model for grid investment projects based on joint monitoring and analysis of the three rates.

In this paper, we analyze the three important indicators of construction progress completion rate (distribution network construction plan execution), investment progress completion rate (development investment plan execution) and booked progress completion rate (project cost execution), build a distribution network project monitoring and analysis and early warning model based on the three rates, and establish a data monitoring platform for the three rates to realize the software curing application, and the practical results show that the application of the software has strengthened the project control and the practical results show that the application of the software has strengthened the control of the project and the accuracy of the investment statistics.

2 Build "Three Rates Combination" Data Monitoring and Analysis Model

2.1 Definition of Three Rate Indicators

Infrastructure, finance, and material, three core indicators of inter-departmental management of power grid infrastructure projects are clarified, namely "construction progress", "investment completion", "recorded cost". "The specific indicators [10] are defined as follows:

Construction progress completion rate: reflecting the actual construction progress of the project, it is the completion of each component work volume expressed as percentage of completion.

Investment progress completion rate: reflecting the proportion of completion of the estimated budget for investment in fixed assets of the project, where the amount of investment in fixed assets is the workload of construction and acquisition of fixed assets expressed in monetary terms.

Accounted progress completion rate: reflects the proportion of project cost completion estimate, where project cost reflects the actual expenditure of various construction costs of the project.

2.2 Analysis of the Relationship Between the Three Rate Indicators and Data Sources

In order to facilitate the analysis of the reasons for the deviation of the three rates of the distribution network, the "construction progress" and "booked progress" are deepened in two dimensions: construction and materials. The specific calculation formula is given in Table 1, using the project tax-inclusive budget as the carrier.

Table 1 Distribution network three rate indicators to take the number of logics

Indicator type	Calculation formula	Source-side data system
Construction progress completion rate	Material image progress × weight + Construction image progress × weight	ERP platform "cji3", "ZFI1402039" command, project budget proposal
Investment progress completion rate	Cumulative number of completed investments ÷ total project investment (estimated budget)	Planning and planning management platform
Credited progress completion rate	Cumulative cost including tax ÷ total project investment (estimated budget)	"ZFI1402039" command in ERP platform

Material image progress = ∑individual material progress × weight.

Material Finance Progress = incurred equipment acquisition costs ÷ proposed budget should be incurred equipment acquisition costs.

Construction image progress = ∑(individual subproject construction progress × weight).

Individual sub-construction progress = actual quantity of work ÷ sub-construction quantity.

Construction Financial progress = incurred (construction project cost + installation project cost) ÷ estimated (construction project cost + installation project cos).

Project construction progress, booked progress can be measured from both construction and materials, based on the project budget proposal, automatically obtain the amount of project process occurring in ERP to obtain the three rate index data.

2.3 Construction of "Three Rates Combination" Data Monitoring and Analysis Model

From the execution plan of infrastructure construction, development investment, and financial budget, the project management of milestone plan execution, physical work volume formation, and financial cost recording is combined with engineering theory, and the "three rates combination" model based on the completion rate of construction progress, completion rate of investment progress, and completion rate of recording progress is established. Based on full research, combined with the above distribution network investment completion calculation method, the process of building the "three rates combination" model for distribution network projects is as follows:

(1) Clarify the model input. Including model source data, required planning plan, PMS2.0, ERP system fields and frequency, data dimension, etc.;
(2) Determine the core calculation logic of the model, including the statistical method of investment completion, data aggregation and summary logic;
(3) Determine the model output, including the display dimension, display mode and report content of key index summary results.

The framework and process of "three rates combination" model construction is shown in Fig. 1.

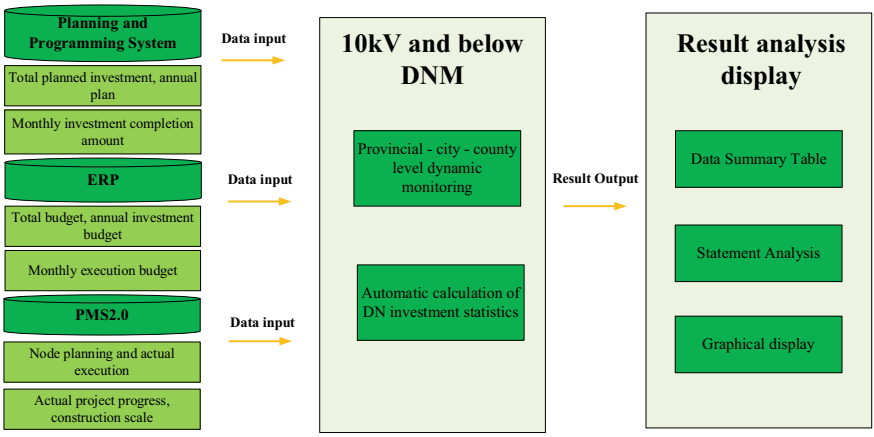

Fig. 1 Schematic diagram of the "three rates combination" model framework for distribution network projects

3 Distribution Network Three Rate Digital Monitoring and Early Warning System

Based on monitoring and analysis of the three rates of distribution network, it deepens the functional application and establishes a rapid response mechanism for the deviation of image progress and financial progress in two dimensions of construction and materials. When the deviation of material image progress and material financial progress is above the specified threshold, an early warning is given; when the deviation of construction image progress and construction financial progress is above the specified threshold, an early warning is given.

The early warning level is mainly divided into the first level and the second level, and only under the condition of triggering the first level of early warning will it be warned in accordance. The logical relationship between the four "material and financial progress" will be analyzed again, thus triggering the second level warning, and presenting the specific reasons for the warning. Early warning mechanism and judgment conditions are given in Table 2.

Table 2 Distribution network three rate warning logic relationship table

Number	Judgment logic	level	Early warning name	Early warning prompt
1	Project|posting progress| > 95%, and project|posting progress-construction progress| > 0%	1	Project management is not standardized	Suspected false production
…	…	…	…	…
18	Project|construction financial progress| ≠ 0%, and project|construction image progress-construction financial progress| > 20%	2	Construction management is not standardized	During the construction, the payment is delayed

4 "Three Rates Combination" Software Curing Application

4.1 Software Function Design

To bring into play the effectiveness of monitoring and analysis of the three rates of the distribution network indicators, the research and development analysis of the three rates curing software. The main functions of the software include four layers of project construction-finance-material data penetration chart display, project management (project basic information maintenance, construction management, material management, fund management), early warning management, data management, personal information maintenance, and authority management as shown in Fig. 2.

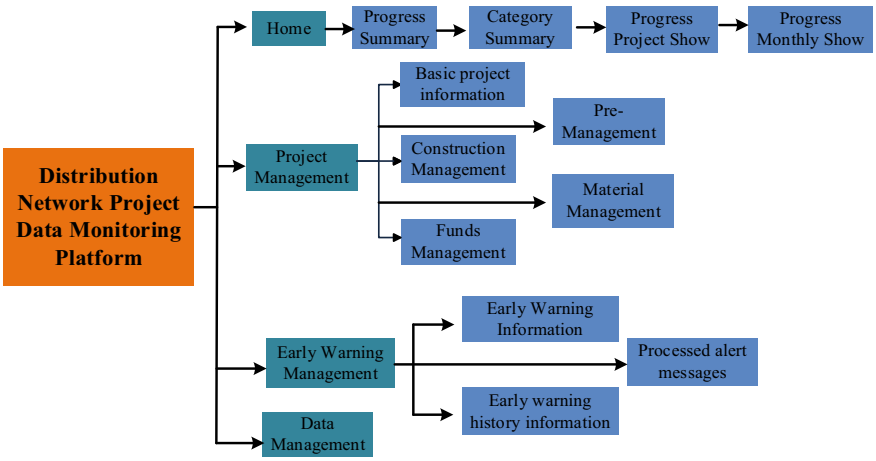

Fig. 2 Functional modules of "three rates combination" software

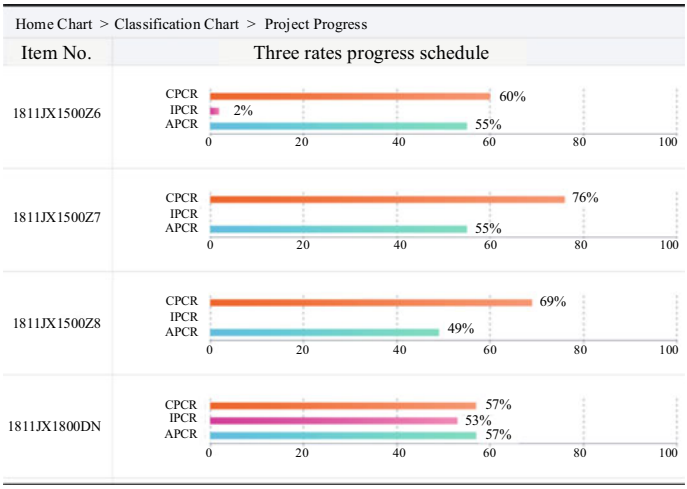

Fig. 3 Project "building-property-material" data four-layer penetration diagram

4.2 Software Application Effect

(1) Data monitoring and analysis results

By 2021, 187 distribution network projects had been entered into the platform. Based on the mathematical model of "construction, finance, and material", the three rates' data monitoring and early warning analysis software analyzes and calculates the construction, finance, and material and progress data of each project as well as the deviation of each data, and visualizes the indicators of the three rates in a penetrating way, as shown in Fig. 3.

(2) Data Alert Management Results

As shown in Fig. 4, the company experienced concentrated start-up and start-up in April and October 2017, respectively, and strengthened the compliance management of start-up and start-up through the software's early warning of such situation.

In Fig. 5, through data analysis, the early warning of material wastage was made in advance, which improved the overall control level of materials.

Since the implementation of the software, 235 warnings were completed and 202 closed-loop treatments were made, of which 43% were for irregularities in material management and 37% were for irregularities in construction management.

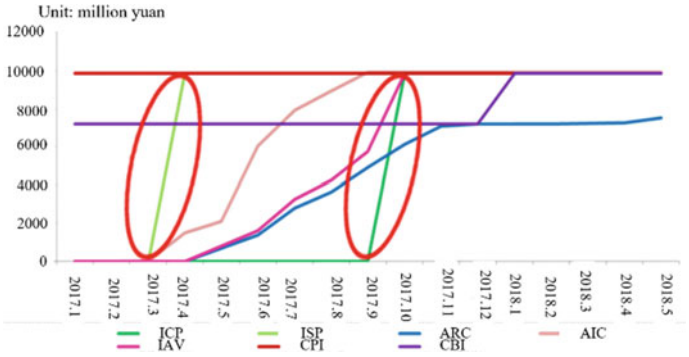

Fig. 4 Project schedule management curve

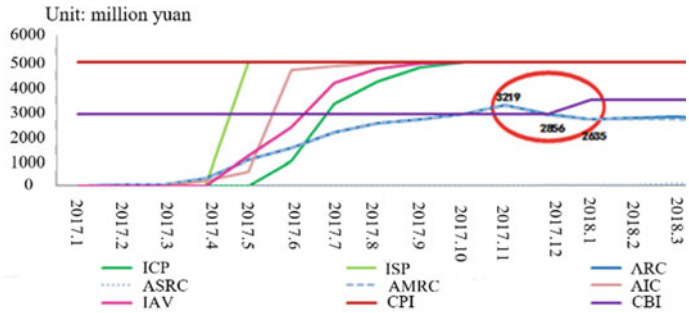

Fig. 5 Project material management curve

5 Conclusion

In this paper, we study to get the definition and data sources of the three rate indicators of grid projects, construct the three rate data monitoring and analysis model, and at the same time, based on monitoring and analysis, develop the three rate distribution network warning rules to locate the problematic projects in time. Finally, the three rate curing application software is developed and practically applied. In Jiaxing Pinghu Company, e.g., the semi-annual distribution network investment completion rate reached 73.08%, an increase of 29.41% year-on-year. The application results show that the distribution network project monitoring system based on "three rates in one" has realized the information recording, visualization, and dynamic tracking of the whole process of the distribution network project, which provides more adequate reference for the investment decision, process control, and analysis and evaluation of the project.

Acknowledgements Supported by State Grid Zhejiang Electric Power Co., Ltd. provincial management of industrial units of science and technology project <<Research on dynamic investment technology of data-driven for distribution network projects>> (2021-KJLH-PH-014).

References

1. Zhang XF (2021) Research on project management mode of distribution network. D. Shandong University, Shandong. https://doi.org/10.27272/d.cnki.gshdu.2021.003150
2. Wang HJ (2022) Research on standardized management of distribution network engineering construction. J Mass Standard 373(14):4–6
3. Shi R, Zhang L, Li YY et al (2020) Research on intelligent statistical algorithm of power grid engineering equipment cost based on physical ID. J Power Syst Clean Energy 36(2):68–74
4. Qi ZB, Zhou YK, Ling S et al (2021) Research on digital management of distribution network engineering based on information platform. J Electr Technol 547(13):156–161
5. Wang W (2019) Information management platform for power engineering EPC projects based on strategic alliance. J Electr World 563(05):82–83
6. Qin LW, Liang S, Gao KL et al (2020) Application analysis of comprehensive data quality management framework in distribution network. J Proc CSU-EPSA 32(04):62–68
7. Wang YD, Niu MZ, Shi C (2019) Big data technology improves distribution network monitoring and analysis management. J Bus Manag 6(S1):268–269
8. Che JC, Wen F, Ma L (2021) Research on whole life cycle data management standards for power grid infrastructure projects. In: The 18th China standardization forum. Fo Shan, pp 915–918. https://doi.org/10.26914/c.cnkihy.2021.024283
9. Chen FE, Liu PP, Mo RQ et al (2020) Power grid investment projects under the joint monitoring and analysis system of three rates planning study. J Power Equip Manag 50(11):152–162
10. Huang H, Yang JY (2022) Statistical research on the deviation of the power grid project plan implementation based on "three-rate combination." J Constr Des Project 473(03):216–218

Design of Fuzzy Variable Frequency Control System for Local Ventilator

Tianyi Jia, Lijun Xu, Zhifeng Chen, Luxiang Mi, Xin Su, and Di Zhu

Abstract Local ventilator frequency conversion control has a certain lag. Because of the failure to control the abrupt gas emission in time, it will lead to the problem of gas exceeding the limit. If the ventilator continues to operate at full frequency, it will be in an under load state during the process of tunneling in coal mines, leading to waste of electrical energy. In response to the above issues, the principle of variable frequency energy-saving control for local ventilator is analyzed based on their ventilation characteristics. A fuzzy variable frequency control system for local ventilator is designed based on fuzzy control theory. A testing platform combining local ventilation devices and signal acquisition devices was established, and frequency conversion testing tests were conducted on the system. The experimental results show that the fuzzy variable frequency control system has certain practicality, which can timely control the real-time emission of gas, control the gas concentration within a safe range, and effectively overcome the hysteresis of ventilation system control.

Keywords Mine ventilation system · Local ventilator · Fuzzy control

1 Introduction

Energy is the foundation and driving force for a country's modernization development. Rich coal, poor oil, and limited gas are the basic national conditions of China. With the application of comprehensive mechanization and automation equipment in coal mining, the production efficiency and safety of coal mining have been continuously improved [1]. However, there are still some safety problems such as gas accumulation in the process of coal mining, which is closely related to the ventilation system of coal mining. In the process of coal mining, coal mining heading face is the coal mine safety accidents, such as gas explosion, coal dust explosion, and so on [2]. About 80% of gas explosion accidents are related to the imperfect

T. Jia · L. Xu (✉) · Z. Chen · L. Mi · X. Su · D. Zhu
Xinjiang Coal Mine Electromechanical Engineering Technology Research Center, Xinjiang Institute of Engineering, Urumqi 830023, China
e-mail: xulijun612@163.com

S. Yadav et al. (eds.), *Energy Power and Automation Engineering*, Lecture Notes in Electrical Engineering 1118, https://doi.org/10.1007/978-981-99-8878-5_39

mine ventilation system. As an important device of mine ventilation, the flexibility and efficiency of mine local ventilator will directly affect the coal mine gas emission [3]. When selecting the local ventilator, the ventilator power is usually selected according to the principle that the maximum driving distance must ensure the normal breathing of underground workers, and the gas concentration does not exceed the limit. In the initial stage of coal mining, if the local ventilator operates at a constant frequency of 50 Hz, it will lead to the waste of air volume and the loss of electric energy when it is running under load [4]. Local ventilator is mainly used for air exchange inside and outside the mine roadway and to reduce the gas concentration in the coal heading face [5], the power consumption accounts for a large proportion of the total power consumption. Therefore, it is necessary to properly adjust the output power of the local ventilator to ensure the efficiency of the ventilator and precisely control the speed of the local ventilator. The application of frequency conversion technology can change the running frequency of the ventilator through the signal size given by the sensor in the heading face to further control the air volume [6]. In the recent years, a lot of improvements and application researches have been made on the variable frequency control system of local ventilator. Zhang [1] reformed the variable frequency speed regulating system of local ventilator based on PLC, which can realize the adjustment of ventilator speed and the control of air volume, so as to achieve the intelligent and automatic delivery of air volume by the ventilator. Du [7] used a particle swarm optimization PID control algorithm to control the speed of local ventilator and improve its output performance.

In this paper, based on fuzzy control theory, a multi-variable coupling nonlinear model of local ventilator speed, gas concentration, air volume, and other factors are established to optimize the mine ventilation network. The system determines the main control mode by logical judgment and adjusts the air volume of local ventilator in time. It can not only effectively control the gas emission in real time, but also maintain the relative balance between air volume and gas concentration, so as to realize on-demand ventilation, energy saving, and consumption reduction, so as to ensure the safety, energy saving, and high efficiency of coal mining.

2 Local Ventilation Arrangement

In the excavation roadway ventilation system, the layout of local ventilator and sensors is illustrated in Fig. 1.

According to the relevant provisions of “Coal Safety Regulations”, the gas sensor T_1 is arranged at the coal mine heading face. In case of $T_1 \geq 1.0\%$, work must be stopped, personnel should be evacuated, and corresponding measures should be taken to deal with it. In case of $T_1 \geq 1.5\%$, gas-electric locking is required. Meanwhile, the “Coal Safety Regulations” stipulate that the wind speed in the coal mine roadway must be maintained at 0.25–4 m/s, and the underground air supply standard is 4 m^3/min.

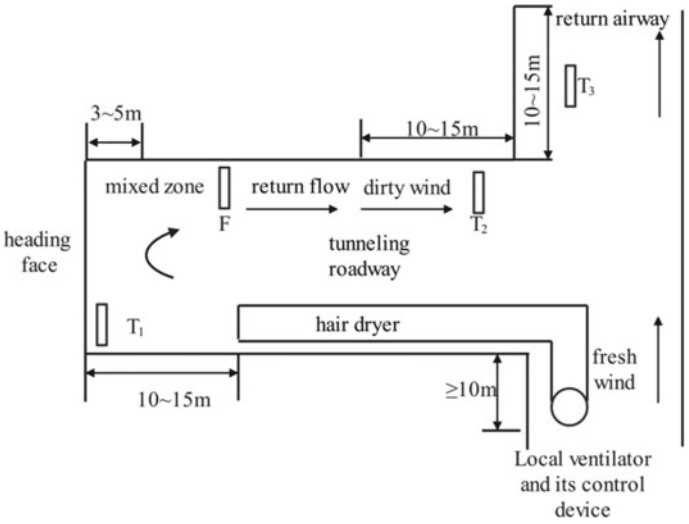

Fig. 1 Layout of local ventilator and sensors

3 Local Ventilator Ventilation Characteristics

In the actual working process, the relationship between air volume Q, air pressure H, ventilator power P, and speed n is as follows: air volume $Q \propto n$, air pressure $H \propto n^2$, and ventilator power $P \propto n^3$. The air volume Q is proportional to the frequency f: $Q \propto f$. When frequency conversion is adopted for local ventilators, the baffle plate is fully open and the ventilation resistance of ventilation pipes basically remains unchanged. H–Q characteristic curve of ventilator is illustrated in Fig. 2. By reducing the frequency of the local ventilator, the air volume of the local ventilator can be reduced, and then the output power can be reduced to achieve frequency conversion energy saving.

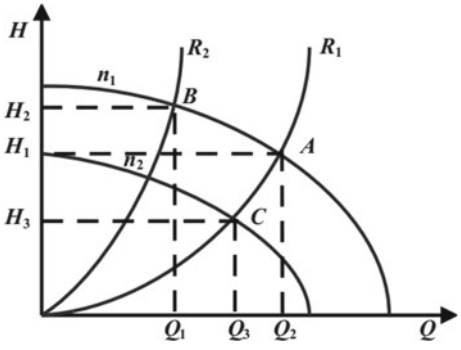

Fig. 2 H–Q characteristic curve of ventilator

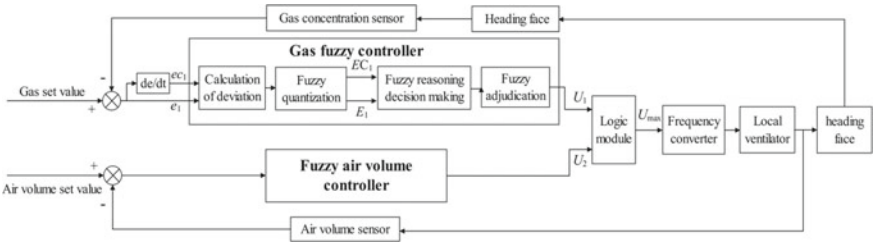

Fig. 3 Principle of control system

4 Design of Control System

4.1 Principle of System Control

The principle of fuzzy variable frequency control system of local ventilator is illustrated in Fig. 3. The control system consists of a gas fuzzy control loop and an air volume fuzzy control loop. In the closed loop of gas fuzzy control, the gas concentration deviation e_1 and deviation change rate ec_1 in the heading face serve as the input of the fuzzy controller, and the output is the signal U_1 that controls the output of the converter, and the air volume is automatically controlled by changing the speed of the ventilator. In the closed loop of air volume fuzzy control, it takes the standard underground air demand per capita of 4 m^3/min as the expected value, collects the air volume signal through the air volume sensor, takes the deviation and deviation change rate of air volume as the controller input, and outputs the signal to control the inverter. Comparing with the traditional control mode, the output of the fuzzy controller is no longer the signal that directly controls the output of the converter, but a control quantity U. Compare the output control quantity U of the gas fuzzy control and the air volume fuzzy control, take the larger value of the two, add a judgment process for the larger control quantity U, take the maximum value of the two, and send it to the voltage input terminal of the mine frequency converter to realize the adjustment of local ventilator speed. When the output control quantity is the same, the gas fuzzy control is the main control.

4.2 Fuzzy Control Approach

Fuzzy Quantization Processing

The expected value of the gas concentration input of the fuzzy controller was set as 0.8%, and the gas concentration range was 0–1.5% according to the ventilation requirements of the heading face. The membership function of gas fuzzy control is illustrated in Fig. 4.

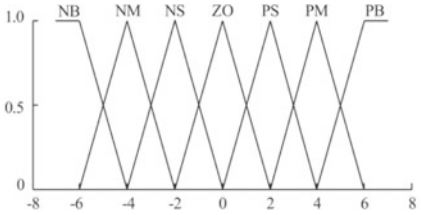

(a) Membership function of deviation E_1

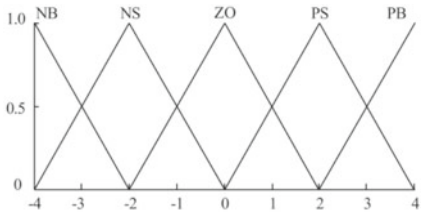

(b) Membership function of deviation rate of change EC_1

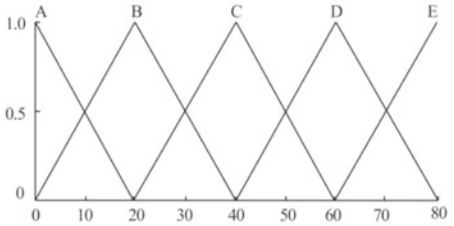

(c) Membership function of the output U_1

Fig. 4 Membership function of gas fuzzy control

The basic theory domain of the gas concentration deviation e_1 was set as [− 0.7, 0.7], and the language variable E_1[− 7, 7] was obtained by scaling the basic theory domain of e_1. The domain of E_1 is divided into seven grades, the fuzzy language set is {NB, NM, NS, ZO, PS, PM, PB}, and the language variable is described as {negative big, negative medium, negative small, zero, positive small, positive median, positive big}. The basic theory domain of the deviation rate ec_1 is set as [− 0.4, 0.4], and the language variable EC_1 [− 4, 4] is obtained by scaling. The theory domain of EC_1 is divided into five grades, the fuzzy language set is {NB, NS, ZO, PS, PB}, and the language variable is described as {negative large, negative small, zero, positive small, positive large}. The basic theory domain of the output quantity U_2 is set as [0, 80], the theory domain of U_2 is divided into five grades, the fuzzy language set is {A, B, C, D, E}, and the language variable is described as {small, smaller, medium, large, and maximum}.

In the fuzzy control of air volume, the expected air supply of the local ventilator is set as the minimum air supply required by the space with the farthest driving distance when the roadway is being driven. The basic theoretical domain of the deviation E_2 between the actual value and the expected air output of the local ventilator is [− 4, 4], the fuzzy language set is {NB, NS, ZO, PS, PB}, and the language variable is described as {negative large, negative small, zero, positive small, positive large}. The basic theoretical domain of deviation change rate EC_2 is [− 2, 2], the fuzzy language set is {NB, NS, ZO, PS, PB}, and the language variables are described as {negative large, negative small, zero, positive small, large}. The basic domain of output U_2

is [0, 80], the fuzzy language set is {A, B, C, D, E}, and the language variable is described as {small, smaller, medium, large, maximum}.

Fuzzy Inference Decision

According to the influence of frequency conversion conditions, gas concentration deviation E_1 and deviation change rate EC_1 on output characteristics combined with the technical knowledge of field technicians and field operation experience, and the gas fuzzy control rule is as follows: the higher the gas concentration, the higher the deviation change rate, the larger the output value; moderate gas concentration, moderate deviation rate, moderate output value; the smaller the gas concentration, the smaller the deviation change rate, and the smaller the output value. Table 1 gives the fuzzy control rules for gas concentration is illustrated in Table 1.

The fuzzy control rule of the air volume is as follows: if the air volume of the local ventilator is less than the minimum air supply volume required by the space at the farthest driving distance of the driving roadway, the smaller the air volume, the smaller the deviation change rate, the smaller the output value, and the air volume of the local ventilator needs to be increased. If the air volume of the local ventilator is equal to the minimum air supply volume required at the farthest driving distance of the roadway, the air volume of the local ventilator can be kept unchanged and the change of gas concentration in the roadway can be monitored continuously. If the air volume of the local ventilator is greater than the minimum air supply volume required for the location at the farthest driving distance of the driving roadway, the greater the air volume, the greater the deviation change rate and the greater the output value, the lower the air volume of the local ventilator.

Fuzzy Adjudication

Fuzzy control rules of MATLAB fuzzy toolbox are applied to clarify the output fuzzy quantity U_1 and U_2, respectively. The output variable surfaces of gas fuzzy control and air volume fuzzy control are shown in Fig. 5.

Table 1 Fuzzy control rules for gas concentration

E_1	EC_1				
	NB	NS	ZO	PS	PB
NB	A	A	B	B	C
NM	B	B	B	C	C
NS	B	C	C	C	D
ZO	C	C	D	D	D
PS	C	D	D	D	E
PM	D	D	E	E	E
PB	D	E	E	E	E

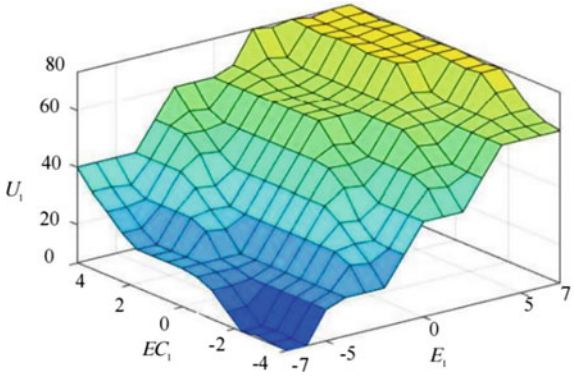

Fig. 5 Gas fuzzy control output variable surface

Hardware Principle

The gas concentration sensor, air volume sensor, and other information acquisition devices are arranged in the coal mine roadway for signal acquisition. The gas concentration of coal mine heading face is taken as the main controlled quantity. The output signal of sensors is used as the input value of fuzzy controllers after f/v conversion, and the information is processed by the fuzzy control algorithm. After converted by D/A and V/I, the output digital signal then drives the frequency converter to adjust the ventilator air volume.

The long-distance transmission of communication information is realized through the drive of amplifier MCP2551, the output of CAN module, and the host computer. The LCD touch screen can locally display the changes of gas concentration and air volume at various positions in the driving roadway, and the paperless recorder can record these data changes. The hardware structure of the system is shown in Fig. 6.

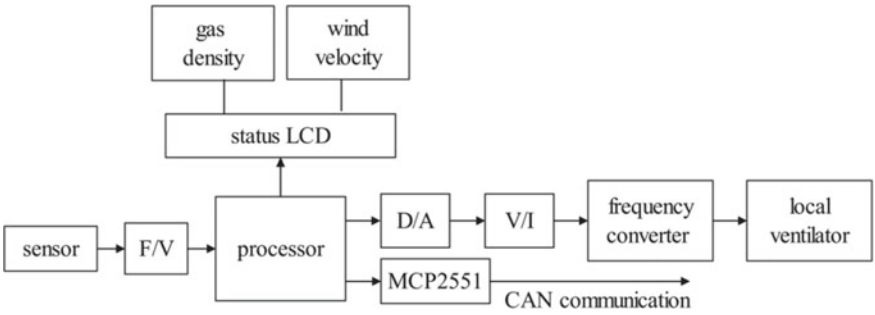

Fig. 6 Hardware structure of the system

Table 2 Main equipment and instruments used in the experiment

Equipment	Specifications and models
Counterrotating axial flow local ventilator	FBDNo_5.0/2 × 7.5
Frequency conversion governor	BPJ-75/690SF
Gas concentration sensor	GJC4
Mine air volume sensor	KGF2
Paperless recorder	MIK-R5000C

5 Test Results and Analysis

5.1 Experiment Platform

The test was carried out by Xinjiang Coal Mine Electromechanical Engineering Technology Research Center. Taking a fully mechanized mining face of coal mine of Xinjiang Coking Coal Group as the research object, combined with the general situation of coal mine roadway and the layout of ventilation devices in coal mine roadway, the relevant provisions of gas concentration, wind speed and air volume of coal mine roadway were tested according to "Coal mine Safety Regulations". In this experiment, the mine flameproof type compressed-in counterrotating axial flow local ventilator FBDNo_5.0/2 × 7.5, BIJ mine frequency conversion governor and signal acquisition devices, and other instruments were used to build a test platform. The main equipment and instruments used in the experiment are given in Table 2.

5.2 Experimenting Result

Experimenting result is given in Table 3. As can be seen from the table, with counter-rotating axial flow local ventilator FBDNo_5.0/2 × 7.5, the input gas concentration is 0.1%–1.0%. Under the local ventilator frequency conversion control system, with the increase of gas concentration, the output active power of the asynchronous motor of the local ventilator will also increase gradually. When the gas concentration is 0.1%, the output power of the frequency converter is 13.15 Hz, and the output power of the local ventilator is 2.15 kW. The frequency conversion control system controls the wind speed as the minimum wind speed 0.25 m/s as required by the "Coal Mine Safety Regulations". As the gas concentration detected by the local ventilation system gradually increases, the output power of the motor of the local ventilator keeps increasing. When the gas concentration reaches 1.0%, the output frequency of the frequency converter reaches 49.5 Hz and the output power of the motor reaches 11.37 kW. The speed of local ventilator will increase with the increase of gas concentration, realizing the automatic regulation of gas concentration by air volume of local ventilator, achieving the purpose of frequency conversion and energy saving.

Table 3 Experimenting result

Serial number	Frequency (Hz)	Active power (kW)	Gas density (%)
1	49.5	11.37	1.0
2	45.9	9.85	0.9
3	41.3	9.25	0.8
4	36.5	7.94	0.7
5	31.5	7.18	0.6
6	27.2	6.15	0.5
7	22.7	5.21	0.4
8	19.65	4.73	0.3
9	13.57	3.23	0.2
10	13.15	2.15	0.1

6 Conclusion

Based on the operation characteristics of local ventilator, the fuzzy variable frequency control system for local ventilator is designed, and it can improve the ventilation capacity of coal mine roadway. When the gas concentration exceeds the limit, the output volume of the ventilator will be automatically increased, which can control the gas concentration within the safe range more quickly, effectively improve the working environment of the coal mine, and greatly improve the safety of coal mine production. According to the gas concentration, the output air volume of the local ventilator can be automatically adjusted to avoid the ventilator from working at full frequency all the time.

Acknowledgements The project is supported by Foundation project: National Natural Science Foundation of China (Grant No. 51967020); Key R&D projects of Xinjiang Uygur Autonomous Region (China): (Grant No. 2022B01003-1). Xinjiang Uygur Autonomous Region Youth Science and Technology Top Talent Project: (Grant No. 2022TSYCCX0053).

References

1. Zhang S, Tang J, Wang M (2022) The challenges and opportunities faced by China's coal industry development under the background of "dual carbon". China Coal 05:1–5
2. Hao H (2018) Analysis of mine gas control and research on outburst prevention measures. Sci Technol Wind 28:120
3. Jing G, Liu M (2022) Statistics and regularity analysis of coal mine gas accidents in China from 2015 to 2019. J Saf Environ 03:1680–1686
4. Bi QP, Li YC, Shen C (2021) Screening of evaluation index and construction of evaluation index system for mine ventilation system. Sustainability 13:11810

5. Yin Z (2019) Stability analysis of coal mine ventilation system. Chin Petrol Chem Stand Qual 02:163–164
6. Yin Y, Yin L (2007) Application of frequency conversion technology and fuzzy control in local ventilation fans in mines. Coal Min Mach 01:139–141
7. Du G, Ma X, Zhang P (2020) Research on speed control algorithm for local ventilation fans in coal mines. Ind Min Automat 09:69–73 + 87

Online Compression Reconfiguration-Based Load Forecasting Method for Distribution Grid Power System

Wenqi Huang, Lingyu Liang, Shang Cao, Xiangyu Zhao, Huanming Zhang, and Hanju Li

Abstract The current conventional power system load forecasting method mainly outputs forecasting results by constructing a time model, which leads to poor forecasting results due to the lack of effective extraction of feature data of load signals. In this regard, an online compression and reconstruction-based load forecasting method for distribution network power systems is proposed. By introducing the concept of particle swarm ensemble, the discrete situation of power load signal data particles is characterized, and data normalization is carried out, and the load signal data is compressed and reconstructed. The maximum information coefficient is calculated and the load data features are extracted by combining the influencing factors, and finally a hybrid prediction model is constructed and the model is solved. In the experiments, the designed method is verified for its prediction effect. The experimental results show that the designed method has a good fit between the prediction results and the actual load curve, and has a good prediction performance.

Keywords Online compressive reconstruction · Power systems · Load forecasting · Sparse dictionaries

1 Introduction

Distribution network power system load forecasting is mainly through the analysis of historical operation data of the distribution network, combined with forecasting algorithms, to achieve the prediction of the expected load situation of the distribution system. By predicting the expected power load of the distribution system, the operating conditions of the power system can be grasped, thus helping the staff to make correct maintenance decisions and realize the effective allocation of power resources [1]. If the upcoming power load can be accurately predicted before the

W. Huang · L. Liang · S. Cao (✉) · X. Zhao · H. Zhang · H. Li
China Southern Power Grid, Digital Grid Research Institute, Guangzhou 510663, China
e-mail: caoshang@csg.cn

S. Yadav et al. (eds.), *Energy Power and Automation Engineering*, Lecture Notes in Electrical Engineering 1118, https://doi.org/10.1007/978-981-99-8878-5_40

power peak period, the power system can be pre-adjusted to meet the power demand at different time periods and ensure the smooth operation of the power system. Distribution system load forecasting can be divided according to the forecasting cycle, with different forecasting objectives and techniques corresponding to different forecasting cycles. It is also susceptible to the influence of variable factors such as weather, which leads to the instability of the prediction results. At the same time, most of the current power systems have a large volume of operational data, and the analysis of historical data is a large amount of engineering work, so the use of conventional methods for load forecasting not only easily leads to deviations in the forecasting results, but also easily affects the forecasting efficiency, which cannot meet the short-term forecasting needs. In this paper, we propose an online compression and reconstruction-based load forecasting method for distribution network power system, which aims to improve the forecasting efficiency and reduce the transmission of edge data by compressing and reconstructing the operational data, so as to improve the operational efficiency of the forecasting algorithm.

2 Online Compression Reconstruction-Based Load Signal Data Preprocessing for Distribution Network Power Systems

The specific expression of the search space is shown as formula (1) [2–4].

$$D(t) = \frac{1}{mL^2} \sum_{i=1}^{m} \sqrt{\sum_{d=1}^{n} (p_{id} - p_d)^2} \tag{1}$$

where m represents the number of power system load signal particles in the search space, L^2 represents the scale of the search space, n represents the three-dimensional vector constant of the search space, p_{id} represents the node coordinate data of the i-th power system load signal particle in the d-th search space, and p_d represents the average of all node coordinate data[5–7]. The above expression of the search space $D(t)$ can characterize the dispersion degree of the power system load signal particles in a certain range. When the dispersion degree of the load signal particles in a certain range is larger, the value of $D(t)$ will be larger; when the load signal particles in a certain range show aggregated distribution, the value of $D(t)$ will be smaller. Therefore, the above formula can determine the distribution of load signal particles in the search space at a certain time, and the optimal solution search can be realized by selecting the most suitable search space, so as to ensure the uniform distribution of load signal particles in the search space of power system. After finishing the above adjustment, all the data in the collection space of load signal particles of power system under uniform distribution are normalized in this paper, and the data fluctuation range is adjusted, and the specific calculation formula is shown formula (2).

$$x^* = \frac{x - x_{\min}}{x_{\max} - x_{\min}} \tag{2}$$

Among them, $x_{\max}$ and $x_{\min}$ represent the maximum and minimum values of the power system load signal particle population under uniform distribution, x represents the original load signal particle data, and x^* represents the particle signal data after processing. After the preprocessing of the power system load signal particle data, the normalized data is obtained, and the particle signal data is compressed online according to the characteristics of the load signal data in the sparse dictionary. In this regard, it is necessary to first select a suitable signal measurement matrix, which is mainly used to measure the signal scale, and also needs to present a mutually independent state with the sparse dictionary. In this paper, the Gaussian random matrix $\Phi_{m\times n}$ is chosen to measure the particle signal scale, which is calculated as formula (3).

$$y_t = \Phi x_t = \Phi DAs = \Theta s \tag{3}$$

where y_t represents the observed signal, D represents the sparse dictionary, A represents the perceptual matrix, and s represents the sparse signal obtained after the mapping process is completed. By using the above formula, the input power system load signal at time t can be projected, thus changing the signal dimension and obtaining the particle signal scale. For the sparse signal s, a constraint expression needs to be constructed to constrain it, and the specific calculation formula is shown formula (4).

$$\min\|s\| s.t. y_t = \Theta s \tag{4}$$

The sparse signal s can be constrained by the above steps, thus converting the constraint problem into a dimensional transformation problem, and then the value of s is calculated by using the regularized matching algorithm, first inputting the training data into the K-SVD sparse dictionary for learning, and then outputting the sparse matrix F. The value of the sparse signal is obtained by mapping it one-by-one with the actual data, thus outputting the mapping result, and then the load signal is online compression and reconstruction, the specific implementation process is shown in Fig. 1.

3 Power System Load Signal Data Feature Extraction

Compared with the mutual information coefficient, the maximum information coefficient can effectively measure the linear relationship between variables and mine the linear relationship between data under different attributes and has a better ability to deal with discrete data. The higher the value of the maximum information coefficient, the higher the similarity of the characteristics between the data. In this regard,

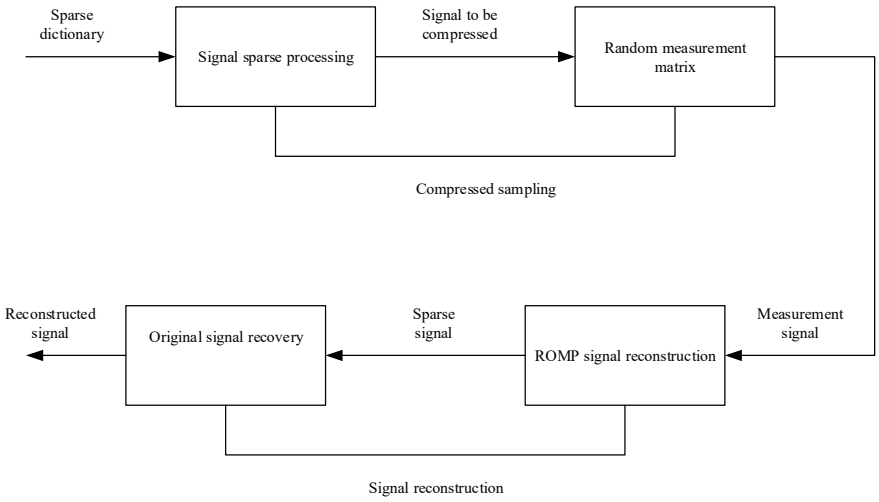

Fig. 1 Online compression and reconstruction process of power system load signal

this paper constructs the maximum information coefficient on the basis of mutual information coefficient, and the specific derivation formula is shown formula (5).

$$I(x, y) = \int p(x, y) \log \frac{p(x, y)}{p(x)p(y)} \tag{5}$$

where $p(x, y)$ represents the probability of joint distribution between load signal data x and load signal data y, $I(x, y)$ represents the mutual information coefficient, and $p(x)$ and $p(y)$ represent the probability of separate distribution of load signal data, respectively. After finding the mutual information coefficient, the value of the maximum information coefficient can be solved according to the construction of the sampling sample function, and the specific formula is shown formula (6).

$$\mathrm{MIC}(x, y) = \max \frac{B(n)I(x, y)\sigma}{\log \min(x, y)} \tag{6}$$

where $B(n)$ represents the load signal sampling sample function and n represents the number of samples. σ represents the correlation coefficient, which characterizes the degree of correlation between two variables and corresponds as given in Table 1.

Considering that the temperature factor in the climatic conditions has a large influence on the load situation of the power system, seven characteristic factors including UV intensity, temperature, and humidity are selected in this paper, and the corresponding maximum information coefficients are calculated to compare the correlation degree between different climatic factors and the load situation of the power system, so that the characteristic factor with the largest correlation degree

Table 1 Correspondence of correlation coefficients

Correlation coefficient	Degree of correlation
0.00–0.19	Very low correlation
0.20–0.39	Low correlation
0.40–0.59	Moderate correlation
0.60–0.79	Highly correlated
0.80–0.99	Extremely high correlation

can be selected. The corresponding characteristic correlation coefficients of specific climatic factors are given in Table 2.

From the Table 2, it can be seen that the characteristic correlation coefficients of the two factors, UV intensity and whole hour, are large, which can be judged to be highly correlated with the load situation of the power system and can be used as the characteristic input variables of the load forecasting model. After the above analysis of the factors influencing the load situation, the maximum information coefficient values of different factors are set as the threshold values, and if the maximum information coefficient value of the factor is higher than the threshold value, it can be seen that the factor has a greater degree of influence on the load situation and can be used as the input value of the model, as formula (7).

$$\varpi = 1/N \sum_{i=1}^{N} \mathrm{MIC}_i(Y) \tag{7}$$

where N represents the number of feature variables of load influencing factors, Y represents the power system load signal data sequence, and MIC_i represents the maximum information coefficient value under the i-th feature factor. The extracted features can not only be used as input data for the load prediction model of the power system, but also can be used to judge the degree of influence of the corresponding correlation coefficients, which can help to adjust the load operation of the power system.

Table 2 Correlation coefficients of characteristics corresponding to climatic factors

Characteristic	Description	Significance test	Maximum information coefficient value
UV	UV intensity	Significant	0.65
Tem	Temperature	Inconspicuous	0.38
Hum	Humidity	Inconspicuous	0.33
Winds	Wind speed	Inconspicuous	0.36
Cloud	Cloud cover	Inconspicuous	0.12
Dew	Dew point temperature	Inconspicuous	0.24
Hour type	Hour	Significant	0.78

4 Power System Load Forecasting Model Construction

Firstly, assume that the active values of neurons representing positive propagation in the BIGRU network structure at moment t and the active values of neurons representing negative propagation, thus obtaining the specific expression of the BIGRU network model as formula (8).

$$\begin{cases} c^{+t} = G(x^t, c^{+t-1}) \\ c^{-t} = G(x^t, c^{-t-1}) \\ h^t = w^{+t}c^{+t} + w^{-t}c^{-t} + \dfrac{b^t}{H} \end{cases} \tag{8}$$

where c^{+t} represents the implied values of neurons for positive propagation at time t, c^{-t} represents the implied values of neurons for negative propagation, x^t represents the input load characteristics data of the model, h^t represents the pooling information at time t, G represents the model output values, w^{+t} and c^{+t} represent the implied weights for positive and negative propagation, b^t represents the implied bias parameters, and H represents the modal confounding function.

5 Experiment and Analysis

5.1 Experimental Preparation

In order to prove that the online compression reconstruction-based distribution grid power system load forecasting method proposed in this paper is better than the conventional distribution grid power system load forecasting method in terms of actual forecasting effect, after the theoretical part of the design is completed, an experimental session is constructed to test the actual forecasting effect of the method in this paper. In order to ensure the experimental effect, two conventional distribution system load forecasting methods are selected for comparison, namely the data mining-based distribution system load forecasting method and the ELM-based distribution system load forecasting method. The specific experimental environment configuration is given in Table 3.

In this experiment, the historical data of power system operation under a large distribution network is retrieved as the dataset for the experiment, and the dataset is divided into two parts, which are used for algorithm training and experimental testing. The data sampling interval is set to 30 min, and a total of 64 load signal data sequences are constructed. The training load results of the model and the test load results are used as the standard to finally output the actual predicted load values. In order to improve the reliability of the experimental results, the load of the power system at different times of the day is selected as the test standard, and three methods

Table 3 Configuration of experimental parameters

Experimental environment parameters	Specific configuration
Simulation platform	MATLAB 2021a
Experimental environment	Intel Core(i) i5-9400f
Software system	Windows 7
Sampling interval	30 min
Sampling time points	4200
Training set data volume	3960
Test set data volume	240

are used to predict it, and the actual prediction performance of the prediction methods is judged by comparing the fit between the prediction curve and the actual load curve.

5.2 Analysis of Test Results

The comparison criterion chosen for this experiment is the degree of fitting between the load prediction curve and the actual load fluctuation curve under different methods, the higher the degree of fitting, the higher the prediction accuracy of the method for electric load, the specific experimental results are shown in Fig. 2. Among them, the thick line part is the actual power system operating load curve.

In contrast, the fit between the predicted load curves and the actual load operation curves under the two conventional methods is smaller, which proves that the load

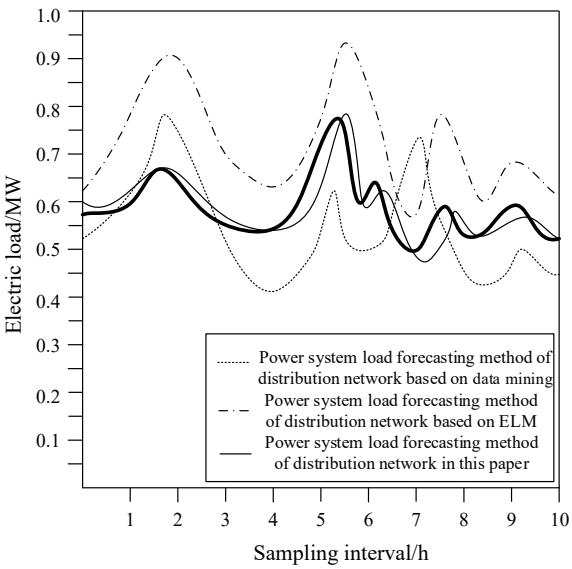

Fig. 2 Comparison of power system load forecast curves

prediction method proposed in this paper is better than the conventional prediction methods in terms of prediction accuracy.

6 Concluding Remarks

This paper addresses the problem of inefficiency of conventional load forecasting methods for power systems, combines online compression and reconstruction technology to process the historical operation data of power systems, and compresses and reconstructs the operation data through online learning compression and sensing methods. The load prediction algorithm constructed on this basis can effectively improve the data transmission efficiency, thus improving the algorithm operation efficiency. The experimental results show that the prediction algorithm proposed in this paper can achieve accurate prediction of the operating load of the power system within the specified time, and it is feasible to ensure the operation efficiency while taking into account the prediction accuracy.

References

1. Li F, Sun M (2021) EMLP: short-term gas load forecasting based on ensemble multilayer perceptron with adaptive weight correction. Math Biosci Eng: MBE 18(2):1590–1608
2. Gomezrosero S, Capretz M, Mir S (2021) Transfer learning by similarity centred architecture evolution for multiple residential load forecasting. Smart Cities 4(1):217–240
3. Chafi ZS, Afrakhte H (2021) Short-term load forecasting using neural network and particle swarm optimization (PSO) algorithm. Math Prob Eng 2021(2):1–10
4. Ngoc TT, Dai LV, Thuyen CM (2021) Support vector regression based on grid search method of hyperparameters for load forecasting. Acta Polytechnica Hungarica 18(2):143–158
5. Envelope Z, Xy A, Fzb C (2022) A two-layer SSA-XGBoost-MLR continuous multi-day peak load forecasting method based on hybrid aggregated two-phase decomposition. Energy Rep 8:12426–12441
6. Panda SK, Ray P (2021) Analysis and evaluation of two short-term load forecasting techniques. Int J Emerg Electr Power Syst 23(2):183–196
7. Sun C, Xu X (2021) Power system transient stability prediction based on deep residual network. Comput Simul 2021(5):77–81

Study on Influencing Factors of Air-Conditioning Loads Participating in Frequency Modulation of Power System

Meiyan Liu and Juanjuan Wang

Abstract Frequency is a crucial parameter to judge the power quality of power system, and also a key factor to maintain the stable operation. Air-conditioning load (ACL) can participate in frequency modulation (FM) of power system, in order to deal with the adverse effect of numbers of renewable energy input power system. Therefore, a cluster load model based on the first-order ETP is established according to the operating characteristic of air-conditioning (AC). In this paper, the influencing factors of its participation in FM are studied. This paper analyzes the influence results of many factors, especially considers the power consumption probability of ACLs under the influence of user's behavior. A power consumption probability model of ACs based on user behavior is proposed, which is incorporated into the cluster model. The validity of the proposed models, which provide a basis for the load side to participate in power system, was verified by simulation.

Keywords Air-conditioning loads · Aggregated model · Load frequency modulation · Probabilistic model

1 Introduction

Compared with the traditional power system that relies on the generation side for FM, as a new type, the FM whit demand side is not only more flexible, rapid and larger capacity, but also more energy-saving and environmental protection, at the same time to meet our country's sustainable development of low-carbon requirements [1, 2].

The proportion of ACLs in demand-side resources is increasing, especially in summer and winter that the rate of ACLs is reaching a peak. By 2050, the International Energy Agency expects ACs to be the second-largest source of global electricity demand growth [3]. In addition, the ACs have the characteristics of fast switching

M. Liu (✉) · J. Wang
School of Automation and Electrical Engineering, Dalian Jiaotong University, Shahekou, Dalian, Liaoning, China
e-mail: lmlmy1103@qq.com

S. Yadav et al. (eds.), *Energy Power and Automation Engineering*, Lecture Notes in Electrical Engineering 1118, https://doi.org/10.1007/978-981-99-8878-5_41

and fast response, which makes it more suitable to participate in the PFM. Therefore, it is of great significance to study the participation of ACLs in FM as a typical representative of demand-side load. Because of the small capacity, large quantity and irregular distribution of AC units, it is necessary to establish an aggregated model of it. The response effect based on ACLs aggregated model is affected by setting temperature, outside temperature, scale load and so on. In [4], a simplified aggregated power model of ACLs based on state queue method is established in this paper. Based on the method of adjusting the setting temperature of AC, the effect of outdoor temperature on the response of aggregated model was studied. In [5], the ACLs are equivalent to a virtual energy storage device. The results show that virtual energy storage capacity and power are greatly affected by outdoor temperature and setting temperature. In [6], the author established an approximate aggregated model of thermostatically controlled loads (TCLs). The effects of ambient temperature and ACs setting temperature on load aggregated response potential were studied. The above-mentioned literatures have established the ACLs aggregated model by different methods. Although the models participating in FM has been verified, the consideration of its influencing factors is not comprehensive.

In view of the above issues and combining with the existing research, Sect. 2 put forwards a TCLs aggregated model represented by ACLs which according to the heat exchange balance principle of the ACs working process. Aggregated power is used as the medium for TCLs to participate in frequency modulation. Section 3 adds an electricity-using probabilistic model of ACs considering user's behavior in the model. Finally through simulation, the multiple influencing factors of aggregated model were analyzed in Sect. 4.

2 TCLs Modeling

2.1 Physical Model of Monomer AC

The physical model of a single TCL, models (1) and (2), usually uses equivalent thermal parameters (ETP). It describes the relationship between indoor and outdoor temperature and the electric power of ACs, which can be simplified to the following first-order ordinary differential equation [7, 8].

$$T_{in}(t+1) = T_o(t+1) - [T_o(t+1) - T_{\text{in}}(t)]e^{-\frac{\Delta t}{RC}} - s(1 - e^{-\frac{\Delta t}{RC}})R\eta P \tag{1}$$

$$s(t) = \begin{cases} 0 & T_{\text{in}}(t) \le T_{\min} \\ 1 & T_{\text{in}}(t) \ge T_{\max} \\ s(t-1) & T_{\min} \le T_{\text{in}}(t) \le T_{\max} \end{cases} \tag{2}$$

Variable $T_{\text{in}}(t)$ is the indoor temperature of the building and outdoor temperature at the time-t. Q is the electrical power of ACs. $s(t)$ is the state of switch: $s(t)$=1 means that the ACs is on, and $s(t)$= 0 means that the ACs is off.

Assume that T_{set} and δ represent the temperature set point and temperature adjustment interval of the ACs, respectively. The boundary of indoor temperature is $[T_{\min}, T_{\max}]$ as (3) and (4).

$$T_{\min}=T_{\text{set}}-\frac{\delta}{2} \tag{3}$$

$$T_{\max}=T_{\text{set}}+\frac{\delta}{2} \tag{4}$$

The starting cycle time of a single AC and standby period time can be expressed as (5) and (6).

$$T_{\text{on}}=\text{CR}\ln\frac{T_{\max}+R\eta P-T_o}{T_{\min}+R\eta P-T_o} \tag{5}$$

$$T_{\text{off}}=\text{CR}\ln\frac{T_{\max}-T_o}{T_{\min}-T_o} \tag{6}$$

So the probability of ACs in working state can be calculated by (7).

$$P_{\text{on}}(t)=\frac{T_{\text{on}}}{T_{\text{on}}+T_{\text{off}}} \tag{7}$$

2.2 Aggregated Model of ACLs

Power of AC unit can be calculated by (8) [9, 10].

$$P^t_{\text{AC},i}=P_i\times S_i(t) \tag{8}$$

The $P^t_{\text{AC},i}$ is the power of AC-i at time-t.

Based on (8), the power response model of ACLs cluster including large-scale users can be established. Aggregated power of ACLs cluster can be calculated by (9).

$$P^t_{\text{ACs}}=\sum_{i=1}^{N}P_i\times S_i(t) \tag{9}$$

3 Aggregated Model of ACLs Which Considering User's Electricity Consumption Behavior

In order to consider the influence of user's behavior factors on aggregated model, two factors are considered: the initial electricity consumption time and the time of continuous electricity use.

3.1 Electricity-Using Probability of ACs

The data comes from [11]. The operation in a day is divided into time period A (9:00–18:00) and period B (18:00–9:00 the next day). The probability density distribution of the user's initial power consumption time and continuous use time in each time period can be approximately regarded as a normal distribution. The probability density of power consumption time at period A and B can be expressed as $f_{A,s}(t)$ and $f_{B,s}(t)$. The probability density of the time of continuous electricity use at period A and B can be expressed as $f_{A,c}(t)$ and $f_{B,c}(t)$ [9, 10], which can be expressed as (10).

The t_{sd} and t_{sn} are the initial electricity consumption time of period A and B. The t_{cd} and t_{cn} are the time of continuous electricity use of period A and B.

$$\begin{cases} f_{A,s}(t) = \frac{1}{\sigma_{sd}\sqrt{\frac{\pi}{2}}} \exp[-2\frac{(t_{sd}-\mu_{sd})^2}{\sigma_{sd}^2}] \\ f_{B,s}(t) = \frac{1}{\sigma_{cn}\sqrt{\frac{\pi}{2}}} \exp[-2\frac{(t_{sn}-\mu_{sn})^2}{\sigma_{sn}^2}] \\ f_{A,c}(t) = \frac{1}{\sigma_{cd}\sqrt{2\pi}} \exp[-\frac{(\ln\frac{t_{cd}}{\mu_{cd}})^2}{2\sigma_{cd}^2}] \\ f_{B,c}(t) = \frac{1}{\sigma_{cn}\sqrt{2\pi}} \exp[-\frac{(\ln\frac{t_{cn}}{\mu_{cn}})^2}{2\sigma_{cn}^2}] \end{cases} \tag{10}$$

$\mu_{sd} = 13.9$; $\sigma_{sd} = 2.9$; $\mu_{sn} = 22.2$; $\sigma_{sn} = 1.9$; $\mu_{cd} = 2.27$; $\sigma_{cd} = 0.85$; $\mu_{cd} = 2.27$; $\mu_{cn} = 6.79$; $\sigma_{cn} = 5.48$.

The probabilistic formula of the ACs is turned on at time-t can be expressed as (11) and (12).

$$\begin{cases} p(\varphi_t = 1) = F_{s,c}(0 \le t_{sn} \le 9, t \le t_{sn} + t_{cn} \le t_{sd}) \\ +F_{s,c}(9 \le t_{sd} \le 18, t \le t_{sd} + t_{cd} \le t_{sn}) \\ +F_{s,c}(18 \le t_{sn} \le 24, t \le t_{sn} + t_{cn} \le t_{sd}) \\ p(\varphi_t = 0) = 1 - p(\varphi_t = 1) \end{cases} \tag{11}$$

$$F_{s,c} = F_s F_c \tag{12}$$

$\varphi(t) = 1$ means the ACs is on, and $\varphi(t) = 0$ means the ACs is off. F_s and F_c are the probability distribution function of the initial electricity consumption time and the continuous use time.

Therefore, the power consumption probability of ACs at time-t can be expressed as (13).

$$p(t) = p(\varphi_t = 1)\, p_{\text{on}}(t) \tag{13}$$

3.2 The Model of ACs Polymerization Power

Suppose there are N ACs participating in the aggregated in a certain area. The aggregated power at time-t can be expressed as (14).

$$P_{\text{acs}}(t) = \sum_{i=1}^{N} p(t) P_i \tag{14}$$

The regulating range of aggregated power is $[P_{\text{low}}, P_{\text{up}}]$. It can be can be expressed as (15).

$$\begin{cases} P_{\text{up}}(t) = \sum\limits_{i=1}^{N} \frac{Q_i P(\varphi=1)[T_o - T_{\max,i}]}{\eta_i (Q_i R_i - \delta_i)} \\ P_{\text{low}}(t) = \sum\limits_{i=1}^{N} \frac{Q_i P(\varphi=1)[T_o - T_{\min,i}]}{\eta_i (Q_i R_i - \delta_i)} \end{cases} \tag{15}$$

Finally, the estimated value of ACs aggregated power at time-t can be expressed as (16).

$$\tilde{P}_{\text{acs}}(t) = 0.5 P_{\text{up}}(t) + 0.5 P_{\text{low}}(t) \tag{16}$$

4 Analysis of Simulation Results

4.1 *Influencing Factors* of Aggregated *Power of Basic ACLs*

The effects of various factors on the response of ACLs' aggregated model are studied without considering the user's behavior. According to the model established in this paper in Sect. 2, the parameters are uniformly distributed within the data range in Table 1.

Experiment 1: Set the number of ACs as $N = 1000$. Suppose the outdoor temperature is maintained to 30 °C for a short time. Adjust the set temperature of the ACs to + 0.2 °C, + 0.4 °C and + 0.6 °C, respectively. Experiment 2: Set the number

Table 1 Parameter of ACLs

Parameters	Values
C	[2, 3]
R	[1.5, 2.5]
P	[1.5, 2]
η	[3, 3.6]
T_{set}	[24]
δ	[1]

of ACs as $N = 800, 1000, 1200$. Suppose the outdoor temperature is maintained to 30 °C for a short time. And the adjustment of temperature is + 0.2 °C. Experiment 3: Set the number of ACs as $N = 800, 1000, 1200$. Suppose the outdoor temperature is maintained to 30 °C for a short time. And the adjustment of temperature is + 0.2 °C.

In Fig. 1, three experiments are simulated, respectively. The results are shown in Fig. 1. Obviously, the response degree, response hysteresis and the time of control increase with the increment of temperature setting. The result is the opposite for the factor of outdoor temperature. The increase of polymerization scale with controlled load has little effect on response speed and control time, but the aggregated power increases in equal proportion with the increase of aggregated scale. Therefore, the ability of adjust frequency can be improved by reasonably selecting the adjustment amount of temperature set point and the aggregated scale of TCLs.

4.2 Aggregated Model ACs Considering User's Behavior

After sampling 10,000 ACs, the startup probability is shown in Fig. 2. According to the user's behavior, the probability model of ACs electricity consumption is more obvious in summer and winter, which fully reflects the randomness of users' use of ACs.

This section studies the application results of the ACLs aggregated model in a day. And the outdoor temperature cannot be constant in a day, so the predicted curve of outdoor temperature in a day is shown in Fig. 3.

After adding the electricity-using probability of ACs, the simulation results of aggregated power are shown in Fig. 4. There are two peaks in the power curve of polymeric ACs. First, the peak at 15:00 is not only related to the high outdoor temperature at that moment, but also influenced by the user's behavior. Secondly, the peak at 24:00 is mostly caused by the continuous use of ACs by users after returning to their homes. The change of ACs aggregated power without considering user behavior is only affected by outdoor temperature. Comparatively speaking, the aggregated model of ACs considering user behavior is more objective, concrete and practical.

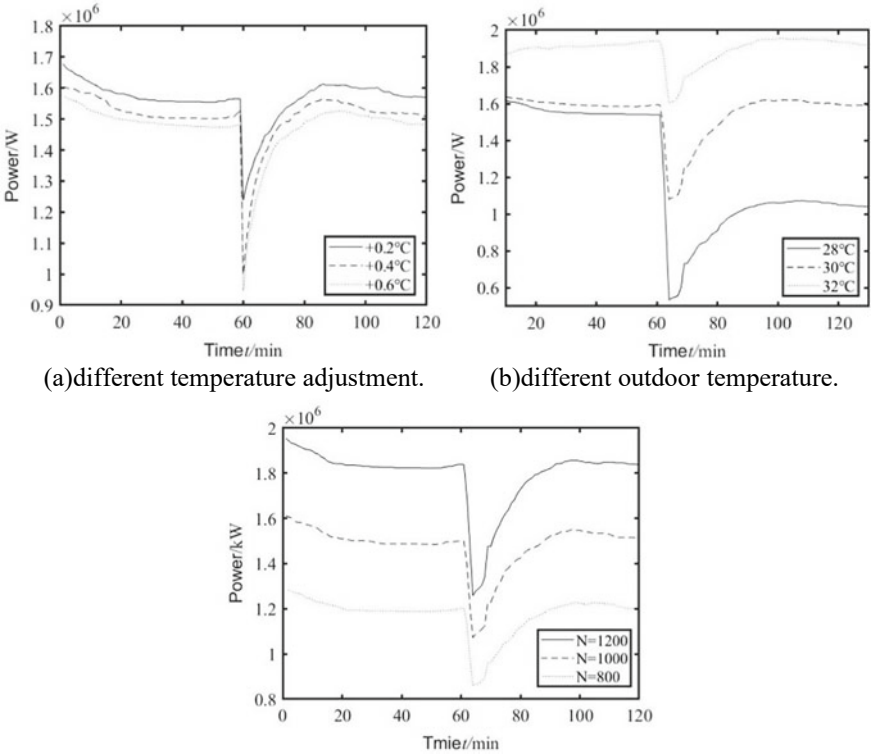

(a)different temperature adjustment. (b)different outdoor temperature.

(c)different scale.

Fig. 1 Simulated graph

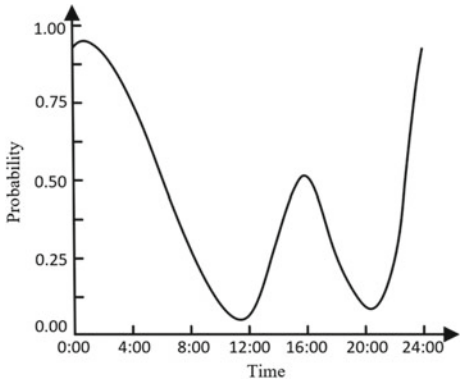

Fig. 2 Starting probability of ACs

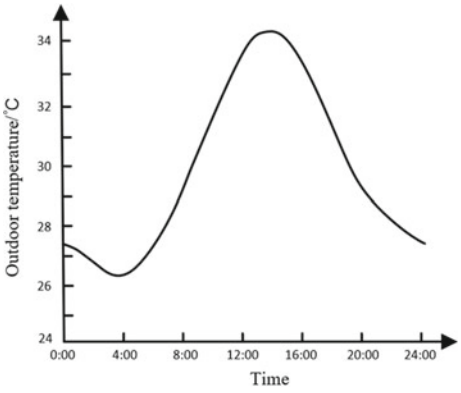

Fig. 3 Prediction curve of outdoor temperature

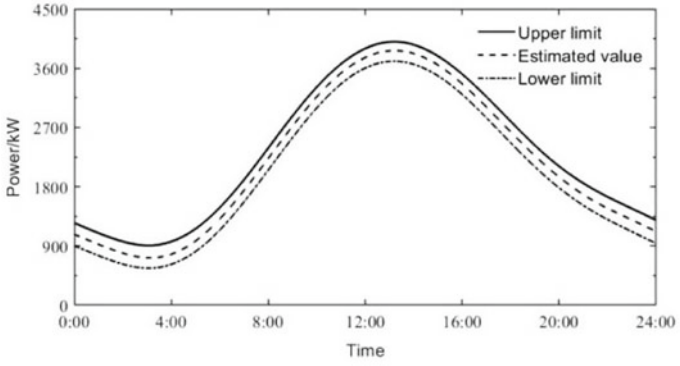

(a) Without considering user's behavior

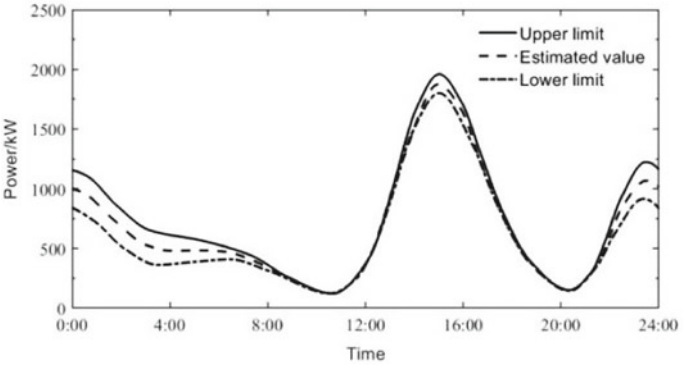

(b) Considering user's behavior

Fig. 4 Comparison of whether to consider the user's behavior

5 Conclusion

From the view of load side of power system, using user's ACLs to participate in FM of power system to achieve stability, based on the advantages of large regulating capacity, good heat (cold) storage effect and fast response speed. The large-scale aggregated mode of ACLs is proposed. We verified the feasibility of the model, and analyzed the influence of multiple factors on the model. Considering the user's behavior, the probabilistic model of electricity-using of ACs is established, and its simulation verifies that the model is more practical than the ordinary model.

The influence results of various factors on the model are studied, which provides reference for the study of stable operation of power system. In the future, effective control methods can be added on this basis in order to get more considerable contrast effect.

References

1. Jiang Y, Li Y, Jiang Y, et al. (2022) Review on key technologies for providing auxiliary services to power system by thermostatically controlled loads. J Autom Electr Power Syst 11(46):191–207.http://www.aeps-info.com
2. Ortega-Vazquez MA, Kirschen DS (2009) Estimating the spinning reserve requirements in systems with significant wind power generation penetration. J IEEE Trans Power Syst 1(24):114–124. https://doi.org/10.1109/tpwrs.2008.2004745
3. Fatih B (2018) International energy agency. In: The future of cooling. IEA Publications, Paris, pp 11–13. https://www.iea.org
4. Jiang T, Ju P, Wang C (2020) Aggregated power model of air-conditioning load considering stochastic adjustment behaviors of consumers. J Autom Electr Power Syst 3(44):105–113. http://www.aeps-info.com
5. Wang Y, Tong Y, Huang M, et al. (2017) Research on virtual energy storage model of air conditioning loads based on demand response. J Power Syst Technol 2(41):394–401. http://www.cnki.net
6. Li Y, Yao J, Yong T, et al. (2017) Estimation approach to aggregated power and response potential of residential thermostatically controlled loads. J Proc CSEE 19(37):5519–5528, 5829. http://www.cnki.net.
7. Nie S, Li T, Chen L, et al. (2022) Primary frequency control strategy of switching thermostatically controlled load and modeling of aggregated model. J Proc CSEE 42:1–11. https://doi.org/10.13334/j.0258-8013.pcsee.221579
8. Wang M, Fan Z, Chen Y, et al. (2022) Quantification and application of cold load pick-up parameters based on temperature-controlled load variation characteristics. J Power Syst Protec Control 21(50):54–64. https://doi.org/10.19783/j.cnki.pspc.211703
9. Yang Z, Ding X, Lu X, et al. (2021) Inverter air conditioner load modeling and operational control for demand response. J Power Syst Protec Control 15(49):132−140. https://doi.org/10.19783/j.cnki.pspc.200548
10. Song M, Gao C, Su W (2016) Modeling and controlling of air-conditioning load for demand response applications. J Autom Electr Power Syst 14(40):158–167. https://doi.org/10.7500/aeps2016030718
11. Jiang T (2019) Study on the usage mode of air conditioners in residential building in summer in Chongqing. D Chongqing Univer Chongqing. http://www.cnki.net

Research on Intelligent Planning of Low-Voltage Distribution Network Based on Adaptive Particle Swarm Algorithm

Min Li, Yigang Tao, Juncheng Zhang, Jing Tan, and Ji Qin

Abstract The current conventional distribution network planning method mainly solves the optimal planning scheme by establishing linear objective function, which is better than the lack of construction for typical scenario set leading to poor planning effect. In this regard, an intelligent planning method of low-voltage distribution network based on adaptive particle swarm algorithm is proposed. The typical scenario dataset is obtained by sampling and extracting the data in the low-voltage distribution network operation dataset and reducing the scenario set. On this basis, the optimization function is constructed with the three parameters of operation cost, power network loss and voltage load as the target parameters, and the function is solved by particle swarm algorithm. In the experiments, the planning performance of the proposed method is verified. The experimental results show that the distribution network intelligent planning method constructed by the proposed method has a high equivalent output of the distribution network and has a better planning performance.

Keywords Particle swarm algorithm · Smart distribution network · Planning methods · Equivalent output

1 Introduction

The rational planning of distribution networks is crucial to the stable operation and power quality of distribution networks. Currently, as the level of distribution network construction continues to improve, customer demand for quality of electricity and project demand for cost also adds more difficulty to the planning process [1]. A good planning of the distribution network must be the result of a comprehensive consideration of operation and maintenance costs, power production quality, power load and voltage. The current lack of planning guidance for conventional distribution network construction projects has led to the following problems: uncoordinated planning and

M. Li · Y. Tao (✉) · J. Zhang · J. Tan · J. Qin
Guangxi Power Grid Corp. Ltd, Nanning 530023, Guangxi, China
e-mail: 418481317@qq.com

S. Yadav et al. (eds.), *Energy Power and Automation Engineering*, Lecture Notes in Electrical Engineering 1118, https://doi.org/10.1007/978-981-99-8878-5_42

construction projects, high planning costs and low-power production quality. Firstly, due to the limitation of investment amount and construction resources, the grid is usually equipped with more construction resources and investment funds for the main grid during the initial planning and construction, which leads to the lack of sufficient financial support during the construction of the distribution grid, thus affecting the construction effect of the distribution grid [2]. At the same time, the lack of reasonable unified planning between the distribution network and the main grid leads to a larger load and lower power output of the distribution network. In addition, the distribution grid is not integrated with the overall planning direction of the city and adjusted during the planning process, resulting in a serious disconnection between the distribution grid project and the surrounding projects, which is not conducive to the surrounding economic development. Due to the lack of effective purification of historical data, the conventional distribution network has a low accuracy of load forecasting, which also affects the electric energy production efficiency of the distribution network and thus cannot meet the electricity demand of customers. To optimize the above problem, firstly, the distribution network project should be coordinated with the main network project and flexibly adjusted according to the overall planning project of the city, so as to plan the distribution network construction project with a better fit with the surrounding projects. In order to improve the overall efficiency of the distribution network planning, we need to combine multi-objective optimization algorithms, select representative objectives as the main objective function and select a high-performance algorithm to solve the objective function iteratively, so as to obtain a more scientific and reasonable planning scheme [3]. In this paper, we first analyze the historical data of the distribution network and construct a typical set of load scenarios by sampling the historical data to provide a reliable data source for the subsequent planning algorithm. By combining with particle swarm algorithm, a multi-objective optimization function with multiple parameters such as planning cost and power quality is constructed and solved to achieve a reasonable planning of the distribution network [4].

2 Low-Voltage Distribution Network Planning Uncertainty Scenario Generation and Analysis

For intelligent planning of low-voltage distribution network, this paper first needs to simulate the uncertainty of the load situation of the generation equipment of low-voltage distribution network, and then generate planning scenarios to provide sufficient datasets for distribution network planning. In the low-voltage distribution network planning work, the so-called scenario refers to the space where the random parameters in the set of uncertainties are located [5]. The analysis of uncertainty scenarios can effectively understand the operation of the LV distribution network, including power parameters, equipment load situation and system operation stability. Therefore, uncertainty scenario generation and analysis are essential for intelligent

planning of low-voltage distribution networks. Conventional distribution network scenario analysis methods usually need to process the historical operation data of distribution network for large planning at the same time, and cluster and analyze different types of scenario data to generate multiple planning scenarios. Although the scenario analysis results obtained by conventional methods are comprehensive, the number of analysis results obtained increases the difficulties in subsequent data processing, which is not conducive to the rapid solution of the planning model [6]. Therefore, in this paper, in order to make the planning effect of the distribution network more rational, after using the stratified sampling method to complete the generation of uncertainty scenarios, the scale of the generated scenarios is reduced to obtain more typical uncertainty scenarios, and the specific implementation process is as follows [7].

The process of scenario generation is also the process of generating a distribution network operation dataset. To obtain a comprehensive and high-quality distribution network operation dataset, the selection of the sampling method is particularly important. By selecting a suitable sampling method, the continuous mathematical model can be effectively discrete to obtain more accurate model calculation results [8]. Therefore, this paper samples Latin hypercubic sampling method to randomly sample the historical operating data of low-voltage distribution network to generate uncertainty scenarios. Since most of the data in the LV distribution network operation dataset are time series data, the use of positive-order sampling method may lead to periodic regular changes in the sampling results. Therefore, to improve the sampling effect of historical operating data of LV distribution network random variables, this paper chooses to use the inverse permutation sampling method to sample them. Firstly, the original dataset of low-voltage distribution network is standardized, and the fluctuation range of the elements in the dataset is adjusted to the interval of 0–1, and then the scale is divided in the interval, and the elements in the interval are equally divided into N equal parts by setting the size of the division scale to obtain N divided subintervals. By using stratified sampling, sampling is performed inside each division subinterval, assuming that the sampling value is l_i, and the corresponding inverse transform value is $x_i = F^{-1}(l_i)$. By using the above sampling method, we can obtain N operating data of power equipment in the low-voltage distribution network, and by substituting this data into the power equation, we can calculate the power output corresponding to different power equipment, thus generating different load output scenarios [9].

Since the power equipment load scenes generated by the above method are large, it is significant to reduce the generated scenes in order to improve the operation efficiency of the subsequent algorithm. In this paper, we adopt the backward reduction method to reduce the above generated power equipment load scenes, and the specific implementation process is as follows.

Firstly, the distribution probability corresponding to each scenario i in the set of N distribution network power equipment load-out scenarios is P_i, then the distance between any two random scenarios can be calculated as shown in the following formula.

$$d(K_{i,j}, K_{t,j}) = \left(\left(K_{i,j} - K_{t,j}\right)^2\right)^{1/2} \tag{1}$$

where $K_{i,j}$ and $K_{t,j}$ represent the coordinates of two random scenes in the scene set, respectively. Then, the minimum value of the distance between any two random scenes can be used as the cut scene, from which the cut target expression can be obtained as follows.

$$p_{ki} = \min d\left((K_{i,j}, K_{t,j}), i \neq j\right) \cdot P_i \tag{2}$$

Assuming that the minimum value corresponding to the cut scenario is p_{km}, the scenario probability can be updated as shown in the following expression.

$$p_{tj} = p_{ki} + p_{km} \tag{3}$$

According to the above scenario update expression, the typical scenarios are eliminated from the total scenarios to obtain a new set of scenarios, thus completing the scenario reduction process. The generation of load scenes for low-voltage distribution network can be completed by the above steps, and the reduction of scenes can be completed by the backward reduction method to obtain the typical load scenes dataset at [10].

3 Construction of Intelligent Planning Objective Function for Low-Voltage Distribution Network Based on Adaptive Particle Swarm Algorithm

For the typical load scenario generated above, this paper constructs a multi-objective optimization function with the three objectives of distribution network operation cost, network power loss and voltage stability margin, and constrains it with the capacity of distribution network power equipment and voltage and current parameters as constraints [11]. After the objective function is constructed, it is solved by particle swarm algorithm to obtain intelligent planning results. The process of constructing the objective function is shown below.

The power source used in low-voltage distribution network is usually distributed power source, and in the process of planning of distribution network, its economic cost and operational efficiency are largely restricted by the condition of distributed power source equipment. Therefore, this paper combines the above analysis and takes the investment cost and operation cost of distributed power supply as the first objective function of intelligent planning of low-voltage distribution network, and the constructed function expression is shown as follows [12].

$$f_{\text{cost}} = \left[\frac{r(1+r)^n}{\left((1+r)^n - 1\right)c_1} + c_2 \right] p_g \tag{4}$$

where p_g represents the electrical capacity of the distributed power supply, n represents the service life of the distributed power supply equipment, c_1 represents the total investment cost of the power supply equipment, c_2 represents the operation and maintenance cost of the power supply equipment in a unit cycle and r represents the cost–benefit conversion rate. Active network loss refers to the value of network power loss due to the operation of the connected power supply in the planning process of low-voltage distribution network. Therefore, in order to improve the overall planning effect of the distribution network, in addition to the operation cost and maintenance cost, it is also necessary to consider the effect of operating power loss.

$$f_{P\text{loss}} = \sum_{k=1}^{k} |i_k|^2 r_k \tag{5}$$

P_{loss} represents the operating power network loss value of the LV distribution network, l and r_k represent the total number of distribution network branches and the corresponding resistance value and i_k represents the current amplitude of distribution network branches. Since the voltage environment of the LV distribution network is susceptible to unstable fluctuations from distributed power sources, it is necessary to take into account the voltage fluctuation interval in addition to the network loss to ensure the effectiveness of the LV distribution network planning. In this regard, this paper introduces an index to describe the degree of change of voltage fluctuation interval, namely voltage stability margin. The voltage stability margin refers to the acceptable variation interval between the actual voltage value and the desired value of the power node. By reasonably limiting the voltage stability margin, the voltage stability of the low-voltage distribution network and the voltage fluctuation of each load node can be effectively ensured. The resulting objective function expression is constructed as shown below.

$$f_U = \sum \left(\frac{U_{\text{load}} - U_e}{U_e} \right)^2 \tag{6}$$

where U_{load} represents the actual voltage value of a load node in the LV distribution network and U_e represents the desired voltage value of the node. The objective planning function of the LV distribution network can be constructed through the above steps. To ensure that the results solved by this function are in a reasonable range, constraints need to be applied to the above objective function. In this paper, three parameters of distributed power supply capacity and current and voltage are selected as the main constraint objects, and the expression of the constraint function is constructed. The specific expressions are shown below.

$$\begin{cases} P_{\min} \le \left| P_{gi} \right| \le P_{\max} \\ |v_i|_{\min} \le |v_i| \le |v_i|_{\max} \\ |I_i|_{\min} \le |I_i| \le |I_i|_{\max} \end{cases} \tag{7}$$

where P_{gi} represents the useful power output from the distributed power sources in the LV distribution network, $P_{\min}$ and $P_{\max}$ represent the maximum and minimum values of the active load in a branch of the distribution network, respectively. $v_i|v_i|_{\min}$ and $|v_i|_{\max}$ represent the maximum and minimum values of voltage fluctuation at the load node of a branch of the distribution network, respectively. I_i The current amplitude at a load node of a branch of the distribution network, $|I_i|_{\min}$ and $|I_i|_{\max}$ represent the maximum and minimum values of current fluctuation at the load node, respectively.

Through the above steps, the construction of the objective function for low-voltage distribution network planning can be completed, and the objective function is constrained by three parameters: capacity, current and voltage, and the objective planning result can be obtained by solving the objective function with the particle swarm algorithm [13].

4 Particle Swarm Algorithm-Based Objective Function Solving

After completing the construction of the objective function, this paper combines the adaptive particle swarm algorithm to solve the objective function of the distribution network intelligent planning constructed above, and the specific algorithm flow is shown in Fig. 1.

According to the above process, it can be seen that the algorithm used in this paper will first input the original dataset, i.e., the dataset of typical scenarios of distribution network completed by the above reduction, which contains important parameters such as current and voltage of each branch node of the distribution network, and the initial population will be generated by judging the type of this parameter. Then, the initial speed of iteration needs to be set, which is set to 0 in this paper, and the maximum number of iterations of the algorithm is set to 100 [14]. Then, the adaptive degree value of each individual is calculated and the particle position is updated according to the power parameters such as tidal network loss in the original typical scene dataset. The coordinates of each particle in the solution space can be output as an output result, but the direct output of the particle coordinates without poor restrictions easily leads to poor accuracy of the algorithm results, and the obtained planning results lack rationality and cannot provide reliable support for the actual planning of the distribution network. Therefore, in order to ensure that the intelligent planning objective function of the distribution network constructed in this paper can output the most reasonable planning scheme, it is also necessary to restrict the output conditions of the particle coordinate output results. Then, the termination condition needs to be set, and the termination condition is set to be the minimum of the

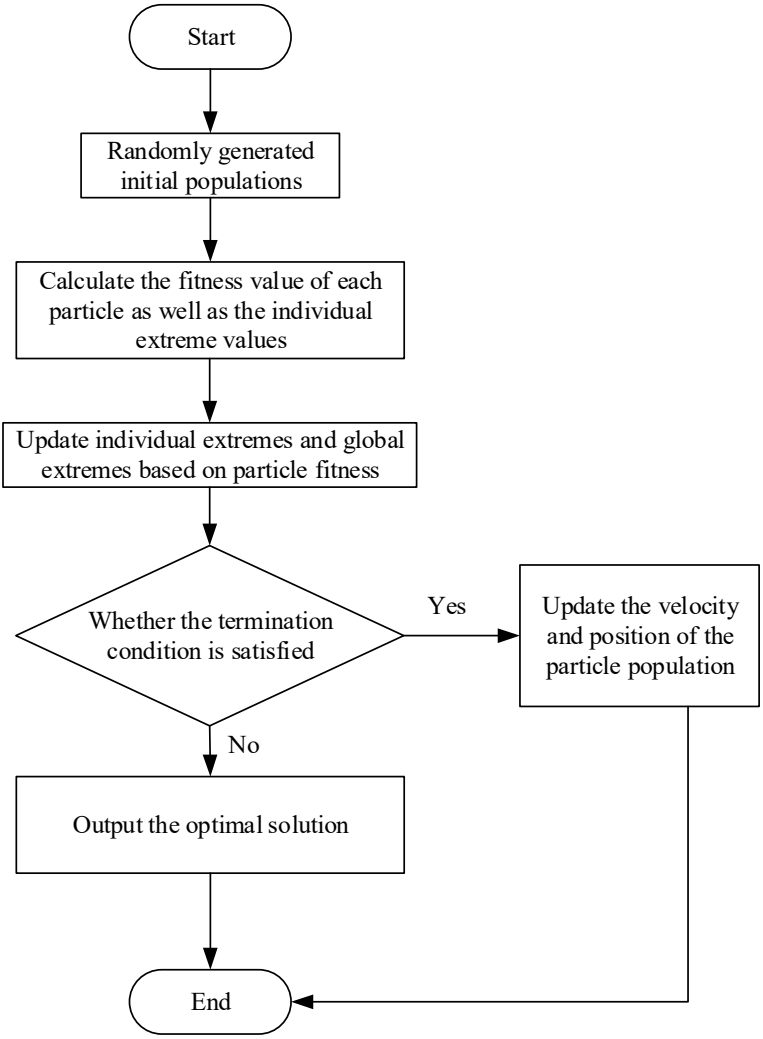

Fig. 1 Algorithm solving process

adaptation value in this paper. By judging whether the updated particle position and particle movement speed satisfy the termination condition, it is determined whether the optimal solution needs to be output. If the updated particle position and moving speed meet the termination condition, the result is the best result and the optimal solution can be output. If the updated value does not meet the termination condition, the above steps need to be repeated to keep updating the particle position until the optimal solution is output [15]. Through the above iterative update process, the accuracy of the optimal solution can be continuously corrected in the process of

optimizing the particle velocity and position, so as to obtain the most suitable global optimal solution.

Through the above steps, the objective function of intelligent planning for low-voltage distribution network can be solved and the optimal planning results can be obtained. By combining the particle swarm algorithm, multiple iterations can be performed to optimize the objective function and the planning results can be more reasonable. By combining this section with the above-mentioned typical scenario set generation and reduction, objective function and constraint construction, the intelligent planning method of low-voltage distribution network based on adaptive particle swarm algorithm is completed.

5 Experiment and Analysis

5.1 Experimental Preparation

To prove that the intelligent planning method of low-voltage distribution network based on adaptive particle swarm algorithm proposed in this paper is better than the conventional intelligent planning method of low-voltage distribution network in terms of practical planning effect, after the design of the theoretical part is completed, an experimental session is constructed to test the practical planning effect of the platform of this paper. In order to ensure the experimental effect, two conventional LV distribution network intelligent planning methods are selected for comparison, namely the grid-based LV distribution network intelligent planning method and the safety boundary-based LV distribution network intelligent planning method.

This experiment uses the historical operational power data of the IEEE-15 distribution network as the experimental raw dataset, which uses distributed power supply as the power supply equipment, with more than 100 power load nodes, of which the nodes to be planned account for more than 60%, which is more suitable to be used as the experimental test set for testing. The data in the original dataset are sampled and reduced by the method in this paper to obtain a typical original data scene collection. This set will be used as the test set as well as the training set for this experiment, and the algorithm will be trained and iterated until the optimal results are output. By analyzing the above typical scenario dataset, four distribution network nodes and 50 electric load nodes are selected as the planning objects of this paper, and the specific planning area is shown in Fig. 2.

The distribution network nodes and electric load nodes in the above region are used as planning objects, and three methods are used to test the planning of the above nodes. In this paper, the number of iterations is set to 100, the initial population size is set to 50, the velocity update parameter is set to 2 and the velocity interval for individual particles is limited to between $[-10, 10]$ and the position of individual particles is limited to between [0, 1450]. Finally, the actual planning effect of the

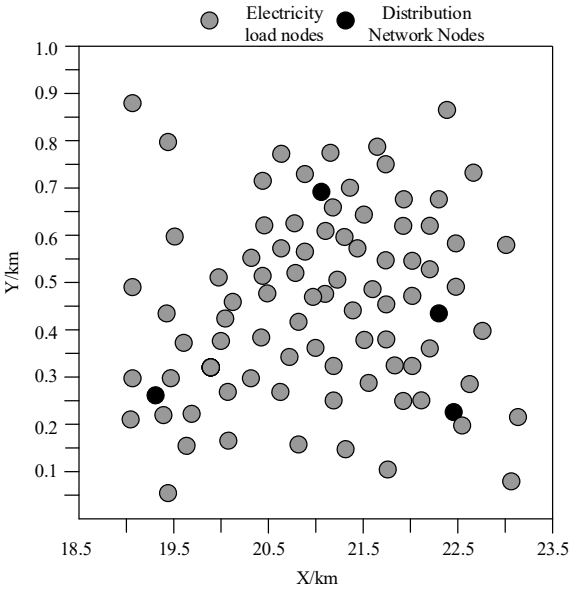

Fig. 2 Schematic diagram of the area to be planned for the low-voltage distribution network

method is determined by comparing the equivalent power output of the distribution network under different planning methods.

5.2 Analysis of Test Results

The comparison standard selected for this experiment is the improvement performance of different planning methods for the output situation, and the specific measurement index is the equivalent output size of the distribution network under different planning methods, and the higher the value represents the better the improvement performance of the method for the processing situation, and the specific experimental results are shown in Fig. 3.

It can be seen from the above experimental results that the equivalent output of each distribution network under different planning methods varies with the changing of sampling time. By observing the equivalent output curve, it is obvious that the equivalent output of the distribution network under the three planning methods shows a trend of decreasing and then increasing. The numerical comparison clearly shows that the adaptive particle swarm algorithm-based planning method proposed in this paper has better planning effect, and the equivalent output of the distribution network after planning is significantly higher than the equivalent output of the two conventional methods. It can be proved that the method proposed in this paper is better than the conventional method in terms of planning effect and has better performance in improving the power output of the distribution network.

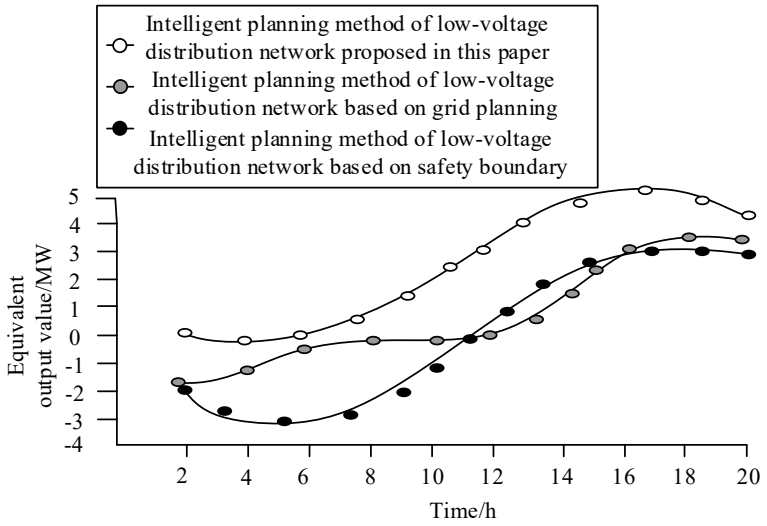

Fig. 3 Comparison results of equivalent power output

6 Conclusion

In this paper, a new intelligent planning method for distribution networks is proposed by combining adaptive particle swarm algorithm to address the problem that conventional distribution network planning methods cannot perform multi-objective planning. By collecting distribution network operation data and performing stratified sampling, so as to obtain a typical scene collection, a more reliable data support can be provided for the subsequent algorithm. The distribution network planning algorithm constructed on this technology adopts a multi-objective planning approach, and the comprehensive performance of its optimization results is better than that of the conventional single-objective planning method, which has a specific certain feasible value.

References

1. Ikechukwu UK, Okechukwu UK, Ngang NB (2021) Improving power system stability in distribution network with intelligent distributed generation scheme. Am J Eng Res (AJER)
2. Rath AK, Parhi DR, Das HC, Kumar PB, Mahto MK (2021) Design of a hybrid controller using genetic algorithm and neural network for path planning of a humanoid robot. Int J Intell Unmanned Syst 9(3):169–177
3. Xu L, Song B, Cao M (2021) An improved particle swarm optimization algorithm with adaptive weighted delay velocity. Syst Sci Control Eng 9(1):188–197
4. Lv Z, Zhou M, Wang Q, Hu W (2021) Small-signal stability analysis for multi-terminal LVDC distribution network based on distributed secondary control strategy. Electronics 10(13):1575

5. Rakhimov OS, Mirzoev DN, Grachieva EI (2021) Experimental study of quality and electricity losses in low voltage rural electric networks. Power Eng Res Equip Technol 23(3):209–222
6. Iqbal MN, Kütt L, Daniel K, Jarkovoi M, Asad B, Shabbir N (2021) Bivariate stochastic model of current harmonic analysis in the low voltage distribution grid. Proc Estonian Acad Sci 70(2)
7. Chawda GS, Kumar P (2022) Mitigation of nonlinear load influence on the power quality of the low-voltage distribution network using DSTATCOM. In: Active electrical distribution network. Academic Press, pp 229–241
8. Tripathi PM, Chatterjee K (2020) Development of improved direct current based saturated core fault current limiter in DFIG system for enhancing the low voltage ride-through capability. IET Gener Transm Distrib 14(1):148–156
9. Li X, Ma R, Gan W, Yan S (2020) Optimal dispatch for battery energy storage station in distribution network considering voltage distribution improvement and peak load shifting. J Modern Power Syst Clean Energy 10(1):131–139
10. Ahmadianfar I, Kheyrandish A, Jamei M, Gharabaghi B (2021) Optimizing operating rules for multi-reservoir hydropower generation systems: an adaptive hybrid differential evolution algorithm. Renew Energy 167:774–790
11. Sahin O, Akay B, Karaboga D (2021) Archive-based multi-criteria artificial bee colony algorithm for whole test suite generation. Eng Sci Technol Int J 24(3):806–817
12. Ranganathan S, Rajkumar S (2021) Self-adaptive firefly-algorithm-based unified power flow controller placement with single objectives. Complexity 2021:1–14
13. Zhou J, Jia W, Liu M, Xu M (2021) Elite adaptive simulated annealing algorithm for maximizing the lifespan in LSWSNs. J Sens 2021:1–11
14. Huang W, Zhang W (2022) Multi-objective optimization based on an adaptive competitive swarm optimizer. Inf Sci 583:266–287
15. Hou S, Gao Q (2011) Review of impact of distributed generation on distribution system. In: 2011 International conference on advanced power system automation and protection, vol 1. IEEE, pp 219–222

Research on Control System of Three-Phase Isolated AC/DC Converter

Xiang Ao and Zhihao Jia

Abstract The isolated AC/DC converter has many advantages such as the ability to convert electricity according to needs, high efficiency, small size, high power density, and the ability to act as a load or power source on demand. The corresponding modulation strategy and control strategy of the topology are analyzed in this paper. Due to the impact of the peak inductance current in its topology on system performance, this paper proposes a control strategy for minimizing the peak value of inductance current to improve system reliability and reduce on-state losses. The optimal algorithm is used to simultaneously change the modulation coefficient and external phase angle to achieve the minimum peak value of inductance current, and the experimental results verify proposed method.

Keywords AC/DC converter · Matrix converter · Control strategy · Peak value of inductance current

1 Introduction

In the recent years, the three-phase isolated AC-DC converter has been proposed as a converter between AC grid and DC power source or load [1–4]. Because of high efficiency, high power density, and bi-directional power transfer ability, the topology has enormous application prospects.

After studying traditional control methods such as direct current control with fixed external phase angle, direct current control with fixed modulation coefficient, and model prediction with fixed modulation coefficient, it was found that the above traditional methods are either constant modulation coefficient or constant phase angle control, which cannot achieve control of the peak value of inductance current.

X. Ao (✉) · Z. Jia
North China University of Technology, Beijing, China
e-mail: 313849963@qq.com

S. Yadav et al. (eds.), *Energy Power and Automation Engineering*, Lecture Notes in Electrical Engineering 1118, https://doi.org/10.1007/978-981-99-8878-5_43

This paper proposed a coordinated optimal control algorithm based on the minimum modulation coefficient and external phase angle of the peak value of inductance current. By changing the modulation coefficient and external phase angle simultaneously through the optimal algorithm, the peak value of inductance current of the isolated AC/DC converter is minimized, the on-state loss of the device is reduced, and the system efficiency and steady-state performance are improved. Based on the above optimal algorithm, this paper proposes two control strategies: the minimum PI control strategy for the peak value of inductance current and the minimum model predictive control strategy for the peak value of inductance current. Finally, the proposed method was validated using MATLAB/Simulink and an experimental platform.

2 System Topological Structure and Working Principle

2.1 System Topology

The circuit topology of the isolated AC/DC matrix converter (IAMC) is shown in Fig. 1, from left to right, consisting of a three-phase AC power supply, grid-side filter, 3–1 matrix converter, high-frequency transformer, rear stage H-bridge circuit, DC side filter, and load [5, 6].

In Fig. 1, u_{sa}, u_{sb}, and u_{sc} are three-phase AC voltages, i_{sa}, i_{sb}, and i_{sc} are grid-side currents, u_a, u_b, and u_c are the three-phase input voltages of the 3–1 matrix converter, and the currents are i_a, i_b, and i_c. The output voltages of the 3–1 matrix converter are u_p, and the current is i_L. The output voltages of the high-frequency transformer are u_s. i_{dc} is the load side current and u_0 is the load side voltage [7].

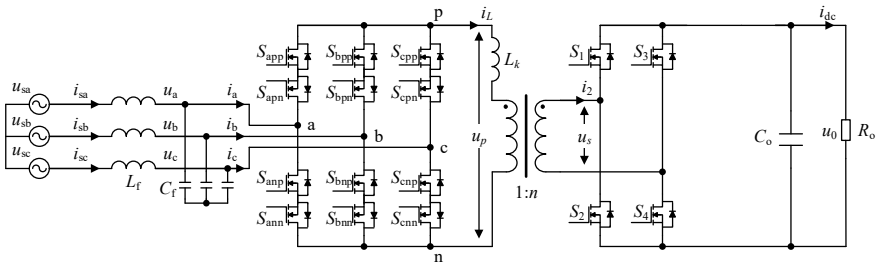

Fig. 1 IAMC main circuit topology

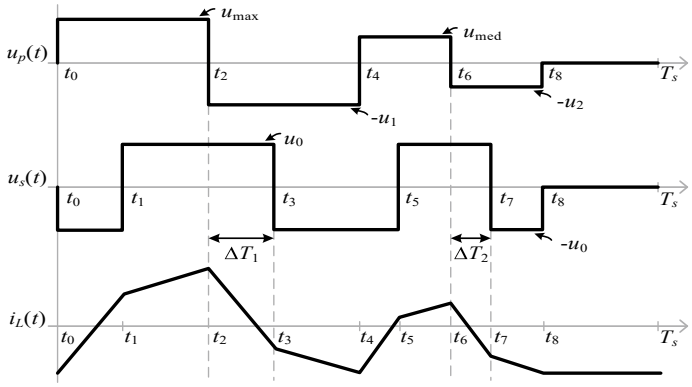

Fig. 2 Waveform of voltage and inductive current at both ends of transformer

2.2 Modulation Strategy of IAMC Circuit

The front stage 3–1 matrix converter adopts a bipolar current space vector modulation strategy. The input of the front stage 3–1 matrix converter is an AC voltage source. During circuit operation, the AC power supply cannot be short circuited, and a free moving path needs to be provided for the inductor L_k. In order to ensure its normal operation, the upper and lower bridge arms of the front stage 3–1 matrix converter can only conduct one bi-directional switch at any time [8–11].

This paper divides a loop into 12 sectors, and the current reference current can be composed of two adjacent fundamental vectors and a zero vector.

To transmit power, a coordinated control method is used, which inserts a phase shift angle between the front stage 3–1 matrix converter and the rear stage H-bridge circuit. The voltage and current waveforms of the output voltage up of the front stage 3–1 matrix converter and the output voltage us of the rear stage H-bridge in one control cycle T_s are shown in Fig. 2.

Starting from t_0, the output voltage up of the previous stage 3–1 matrix converter divides a control cycle T_s into five time periods. The forward maximum line voltage $u_{\max}$ of the previous stage 3–1 matrix converter corresponds to the vector action time t_0–t_2, the forward minor line voltage u_{med} corresponds to the vector action time t_4–t_6, the negative maximum line voltage $u_{\max}$ corresponds to the vector action time t_2–t_4, and the negative minor line voltage u_{med} corresponds to the vector action time t_6–t_8, zero vector action time $t_8 - T_s$.

Divide a control cycle T_s into 9 time periods to obtain the timing of each control period: $t_1 = \Delta T_1$, $t_2 = \frac{d_1}{2}T_s$, $t_3 = \frac{d_1}{2}T_s + \Delta T_1$, $t_4 = d_1 T_s$, $t_5 = d_1 T_s + \Delta T_2$, $t_6 = d_1 T_s + \frac{d_2}{2}T_s$, $t_7 = d_1 T_s + \frac{d_2}{2}T_s + \Delta T_2$ Among them, $T_s = \frac{2\pi}{\omega_s}$, the phase shift time between the front and rear stages is $\Delta T_1 = \frac{\phi d_1 T_s}{2\pi}$, and $\Delta T_2 = \frac{\phi d_2 T_s}{2\pi}$, where ϕ is the external phase shift angle and its value range $0 \le \phi \le \pi/2$.

Table 1 Expressions for d_1, d_2, and d_0 when obtaining 12 sectors

Sector number K	d_1	d_2	d_0
1, 3, 5, 7, 9, 11	$d_1 = m\sqrt{\sin\left(-\theta_i + \frac{\pi}{3}\right)}$	$d_2 = m\sqrt{\sin(\theta_i)}$	$d_0 = 1 - d_1 - d_2$
2, 4, 6, 8, 10, 12	$d_1 = m\sqrt{\sin\left(\theta_i + \frac{\pi}{6}\right)}$	$d_2 = m\sqrt{\sin\left(-\theta_i + \frac{\pi}{6}\right)}$	$d_0 = 1 - d_1 - d_2$

The expressions for $d1$, $d2$, and $d0$ when obtaining 12 sectors are given in Table 1.

The range of modulation coefficient m is $0 \leq m \leq 1/\sqrt{2}$ and the range of sector angle θ_i is $0 \leq \theta_i \leq \frac{\pi}{6}$.

3 Minimum Control of Peak Inductance Current in Isolated AC/DC Converter

The range of voltage regulation in this topology is large. From the grid-side line voltage of the front stage 3–1 matrix converter in Fig. 3, for different load side voltages u_0, the peak inductance current will occur in the following two situations.

When the maximum line voltage $u_{\max}$ is greater than the load side voltage nu_0, the peak of inductance current is obtained at point A and B in the first case. When the maximum line voltage $u_{\max}$ is less than the load side voltage nu_0, the peak of inductance current is obtained at point C and D in the second case.

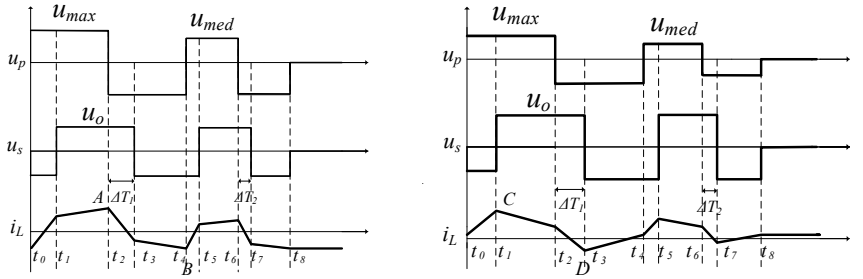

(a)Schematic diagram of inductance current in the first case

(b)Schematic diagram of inductive current in the second case

Fig. 3 Inductance current diagram

Take the first sector as an example, in the first case, the peak inductance current expression is:

$$\mathrm{i_{LAB}} = \frac{\delta d_1 T_s n u_o}{2L} - \frac{d_1 T_s n u_o}{2L} + \frac{d_1 T_s u_{\max}}{2L} \tag{1}$$

Formula for modulation factor m, phase shift angle ϕ, and current I_i as (2):

$$I_i = m^2 \frac{n u_0}{\omega_s L} \phi \left(1 - \frac{|\phi|}{\pi}\right) \tag{2}$$

When the reactive power is 0 and the current $I_\mathrm{i} = I_\mathrm{cd}, \phi = \delta\pi \,/\, 2$ will be substituted into Eq. (2), and then combined with Eq. (1) and Table 1 to obtain the expression (3) for the peak of the inductance current and shift ratio in the first sector:

$$i_{LAB} = -\frac{\sqrt{-\pi\delta n u_0(\delta-2)\omega_s L I_{cd}}\left(\sqrt{3}U_i \cos(\theta_i) + n(\delta-1)u_0\right) T_s \sqrt{\cos\left(\frac{\pi}{6}+\theta_i\right)}}{\pi\delta n u_0(\delta-2)L} \tag{3}$$

Take the derivative of expression (3), make its derivative function zero, and obtain its minimum in Eq. (4):

$$\delta = \frac{\left(\sqrt{3}U_i \cos(\theta_i) - n u_0\right)\sqrt{3}}{3U_i \cos(\theta_i)} \tag{4}$$

Similarly, the optimal shift corresponding to the minimum peak of the inductance current in the other 11 sectors can be obtained in two cases, as given in Table 2.

Table 2 Optimal shift corresponding to the minimum peak of the inductance current

Case	Sector	
	1, 3, 5, 7, 9, 11	2, 4, 6, 8, 10, 12
The first case (A, B)	$\delta = \frac{\left(\sqrt{3}U_i \cos(\theta_i) - n u_0\right)\sqrt{3}}{3U_i \cos(\theta_i)}$	$\delta = \frac{\left(\sqrt{3}U_i \sin\left(\frac{\pi}{3}+\theta_i\right) - n u_0\right)\sqrt{3}}{3U_i \sin\left(\frac{\pi}{3}+\theta_i\right)}$
The second case (C, D)	$\delta = -\frac{\sqrt{3}U_i \cos(\theta_i) - n u_0}{n u_0}$	$\delta = -\frac{\sqrt{3}U_i \sin\left(\frac{\pi}{3}+\theta_i\right) - n u_0}{n u_0}$

4 Simulink Results and Analysis

This paper uses MATLAB/Simulink to build a simulation model of an isolated AC/DC converter. The simulation results of constant modulation coefficient current direct control and model predictive control, inductance current peak minimum PI control, and model predictive control prove the correctness of the proposed control strategy. The main circuit parameters are given in Table 3.

The inductance current waveforms of the four control strategies are shown in Fig. 4.

Table 3 Parameters of IAMC

Description	Value	Description	Value
Input voltage U_i/V	40	Switching frequency f_s/kHz	20
AC side capacitor C_f/μF	92	Output side capacitance C_0/μF	800
AC side inductance L_f/μH	330	Reference voltage u_0^*/V	10
Transformer turn ratio n	1	Load resistance R/Ω	20

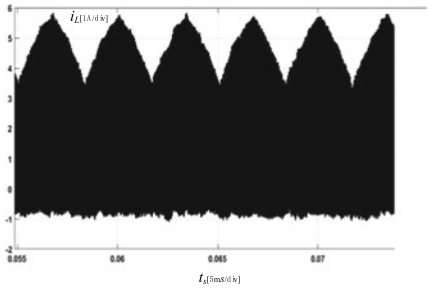

(a)PI control strategy for the minimizing peak inductance current

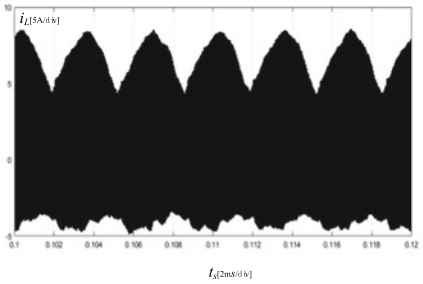

(b)Direct current control strategy with fixed modulation coefficient

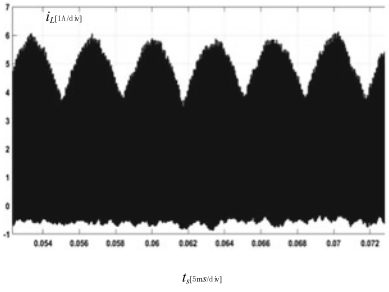

(c)MPC strategy for minimizing the peak inductance current

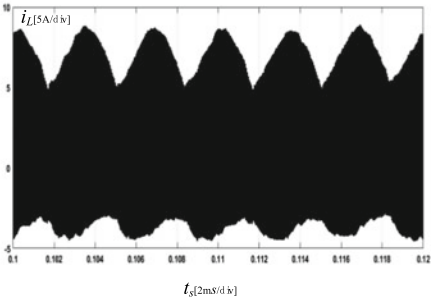

(d)MPC strategy with fixed modulation coefficient

Fig. 4 Inductive current waveform diagram

The simulation results of the relationship between peak inductance current, reference voltage, and load resistance of the four control strategies are shown in Figs. 5 and 6.

From the simulation results of Figs. 4, 5, and 6, the peak value of the inductance current of the proposed control strategy is smaller than that of the fixed modulation coefficient control strategy, which is consistent with theory.

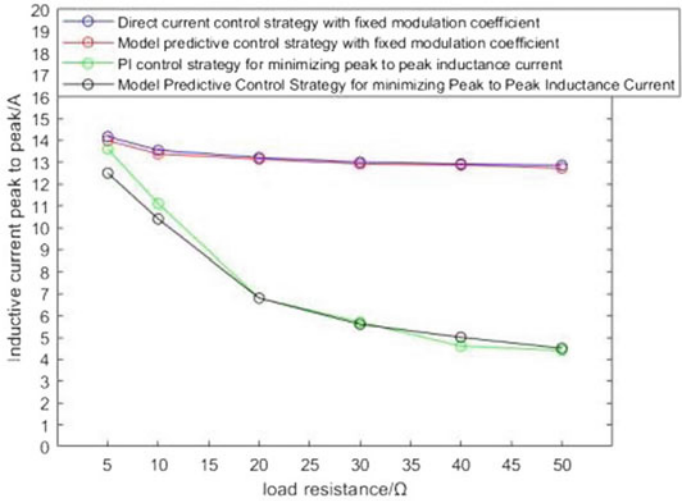

Fig. 5. Relationship between peak inductance current and load resistance

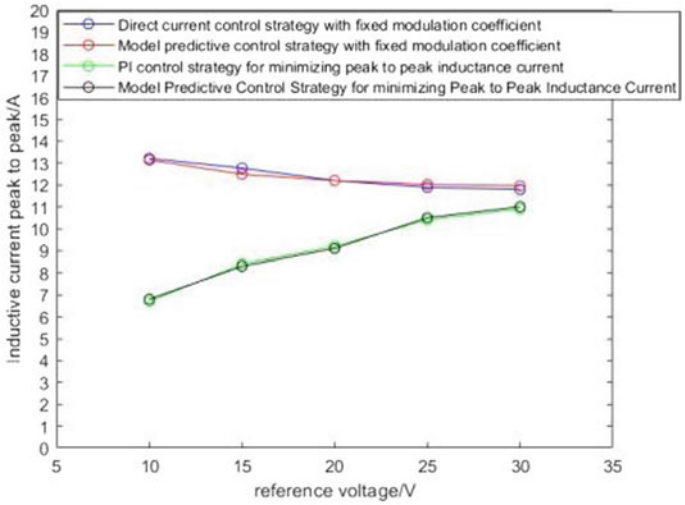

Fig. 6 Relationship between peak value of inductance current and reference voltage

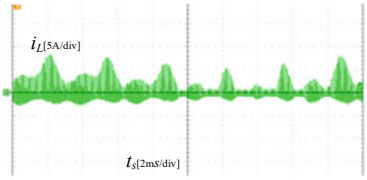

(a)PI control strategy for the minimizing peak inductance current

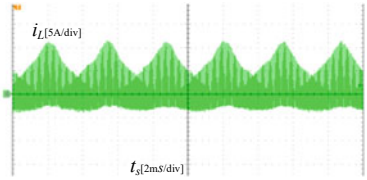

(b)Direct current control strategy with fixed modulation coefficient

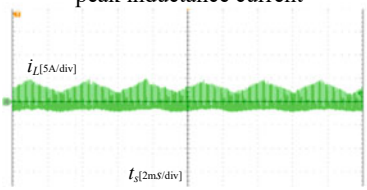

(c)MPC strategy for the minimizing peak inductance current

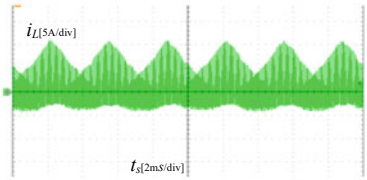

(d)MPC strategy with fixed modulation coefficient

Fig. 7 Inductive current waveform diagram

5 Experimental Results and Analysis

To further validate the effectiveness of this method through experiments, an experimental platform for the IAMC converter was established, and the experimental parameters were the same as the simulation parameters. The inductance current waveforms of the four control strategies are shown in Fig. 7.

The relationship between the peak of inductance current, reference voltage, and load resistance of the four control strategies is shown in Figs. 8 and 9.

From the experimental results in Figs. 7, 8, and 9, it can be observed that the peak value of the inductance current of the proposed control strategy is smaller than that of the fixed modulation coefficient control strategy, which is consistent with theory and simulation.

6 Conclusions

To achieve the minimum peak value of inductance current, this paper proposed a coordinated control method for modulation coefficient and external phase angle. The proposed method was compared with the conventional constant modulation coefficient control method in simulations and experiments. The results show that the proposed control strategy has the smallest peak inductance current with good dynamic performance.

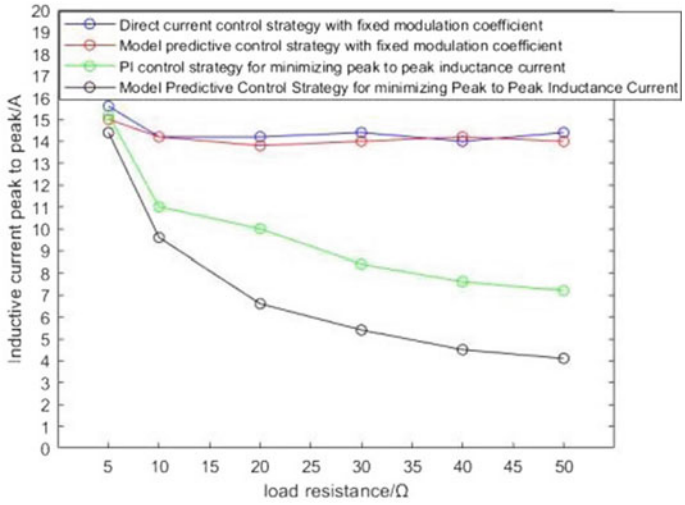

Fig. 8 Relationship between peak inductance current and load resistance

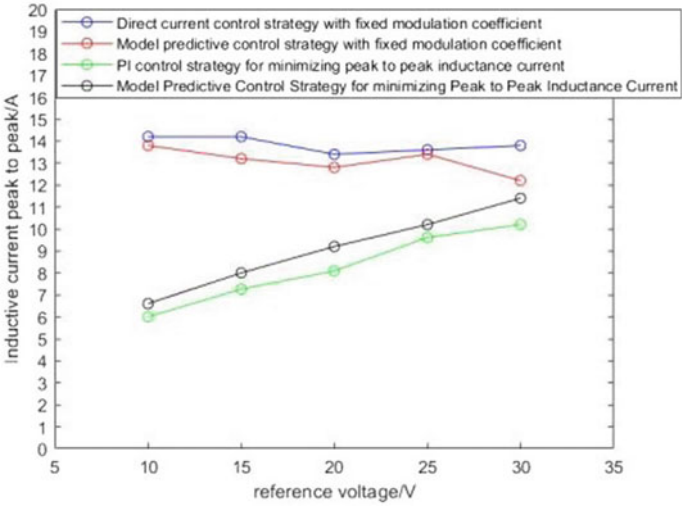

Fig. 9 Relationship between peak value of inductance current and reference voltage

References

1. Williamson SS, Rathore AK, Musavi F (2015) Industrial electronics for electric transportation: current state-of-the-art and future challenges. IEEE Trans Industr Electron 62(5):3021–3032
2. Song J, Zhao R, Kwasinski A (2011) Design considerations for energy storage power electronics interfaces for high penetration of renewable energy sources. ICPE (ISPE)

3. Vazquez S, Lukic SM, Galvan E et al (2010) Energy storage systems for transport and grid applications. IEEE Trans Industr Electron 57(12):3881–3895
4. Yilmaz M, Krein PT (2012) Review of battery charger topologies, charging power levels, and infrastructure for plug-in electric and hybrid vehicles. IEEE Trans Power Electron 28(5):2151–2169
5. Garcia-Gil R, Espi JM (2004) An all-digital controlled AC-DC matrix converter with high-frequency isolation and power factor correction. In: 2004 IEEE international symposium on industrial electronics. Istanbul, Turkey, IEEE, pp 1075–1080
6. García-Gil R, Espí JM, Dede EJ, et al (2005) A bidirectional and isolated three-phase rectifier with soft-switching operation. IEEE Trans Indus Electr 52(3):765–773
7. Singh AK, Das P, Panda SK (2014) Novel switching scheme for matrix based isolated three phase AC to DC conversion. In: IECON 2014-40th annual conference of the IEEE industrial electronics society. IEEE, pp 3324–3329
8. Varajao D, Araujo RE, Miranda LM et al (2018) Modulation strategy for a single-stage bidirectional and isolated AC-DC matrix converter for energy storage systems. IEEE Trans Industr Electron 65(4):3458–3468
9. Fang F, Li YW (2017) ModuLation and control method for bidirectional isolated AC/DC matrixbased converter in hybrid AC/DC microgrid. In: 2017 IEEE energy conversion congress and exposition (ECCE). IEEE
10. Shigeuchi K, Xu J, Shimosato N, Sato Y A new modulation method applying optimal duty cycle and phase shift for bidirectional isolated three-phase AC/DC converter based on matrix converter 3514–3521. https://doi.org/10.23919/IPEC.2018.8507521
11. Abdallah M, Suzuki K, Takeshita T, et al (2017) Soft-switching PWM technique for grid-tie isolated bidirectional DC-AC converter with Si C device. IEEE Trans Indus Appl 1–1

Safety and Reliability Evaluation Method for Intelligent Operation and Maintenance of Converter Station Based on Situation Awareness of Relay Protection Devices

Xi Zhang, Ke Wu, Chuanming Tan, and Weibiao Ye

Abstract When evaluating the operation status of converter stations, due to its dynamic development attribute, the evaluation results are quite different from the actual situation. Therefore, a study on the safety reliability evaluation method of intelligent operation and maintenance of converter stations based on situation awareness of relay protection devices is proposed. After building the converter station control structure model around the outer ring control structure, double dq-PI current control structure and synchronous rotating coordinate transformation structure, combining the dependency between the converter station protection process and the relay protection device, the domain mapping matrix is used to describe the implementation of the protection process of the relay protection device and quantify it according to the healthy state. After the node status of the converter station is divided into infection status and failure status, the safety reliability of the intelligent operation and maintenance of the converter station is evaluated according to the status transfer relationship between relay protection devices. In the test results, the design method has a high accuracy for the evaluation results of the converter station node status and the overall intelligent operation and maintenance security reliability of the converter station.

Keywords Relay protection device · Situational awareness · Converter station · Intelligent operation and maintenance · Reliability assessment · Converter station control structure model

X. Zhang (✉) · K. Wu · C. Tan · W. Ye
Dongguan Power Supply Bureau, Guangdong Power Grid Company, Dongguan 523000, Guangdong, China
e-mail: 190600558@qq.com

S. Yadav et al. (eds.), *Energy Power and Automation Engineering*, Lecture Notes in Electrical Engineering 1118, https://doi.org/10.1007/978-981-99-8878-5_44

1 Introduction

At this stage, the common mode in the power grid operation stage is HVDC based on Voltage Source Converter VSC-HVDC, which is also called flexible DC transmission. Compared with other transmission modes, it has more prominent performance in controllability and flexibility. Because of this, the related research on it has received extensive attention [1, 2]. As one of the important components of voltage source converter HVDC transmission, the level converter (MMC) exists in the form of more modules, so it has more flexible characteristics in structure, and also has obvious advantages in scalability. For HVDC transmission and reactive power compensation equipment, it can limit the output voltage quality control and power fluctuation degree suppression have good effect [3, 4]. In view of this, this paper analyzes the advantages of MMC compared with traditional voltage source converters, which are mainly reflected in the following aspects: first, MMC adopts a modular mechanism in the design phase, so that it has scalable attribute characteristics; secondly, in the specific operation process, the multiple converter stations participating in the utilization of DC bus can be parallel and will not be affected; In addition, in the actual operation stage, MMC has lower operation loss, which realizes the purpose of improving the effective utilization of power resources [5, 6]; finally, with the stable control effect and operation mechanism of MMC, its output voltage waveform also shows a higher stability. In the traditional mode, two-level and three-level HVDC transmission is a common technical means. Compared with this type of transmission mode, MMC also shows obvious advantages in many aspects [7, 8]. Most obviously, the reactive power compensation equipment is a necessary component of the traditional HVDC transmission process, and its main role is to compensate the reactive power absorbed in operation. Combined with the working mode of the converter station, when it is in the rectifier working state, the corresponding reactive power to be absorbed can reach about 50% [9, 10], and when it is in the inverter working state, the corresponding reactive power to be absorbed will continue to increase. In view of this situation, it is necessary to further improve the input of reactive power compensation devices. This not only increases the cost input to a certain extent, but also increases the probability of commutation failure of HVDC transmission. In contrast, MMC can use its own function configuration to control the corresponding active or reactive output bridge, and in the specific control process, the two can be carried out in a relatively independent form, which avoids the dependence on reactive power compensation devices [11, 12]. In addition, MMC can also realize real-time compensation for reactive power and stabilize the output voltage of AC bus in combination with the actual operation conditions at the AC bus.

Combined with the above analysis, it is not difficult to see that MMC plays an extremely important role in the high-voltage DC transmission of voltage source converter, which is related to the final transmission effect. Aiming at the ground, accurate evaluation of its reliability has become one of the issues of concern. In this paper, an intelligent operation and maintenance security reliability evaluation method based on situation awareness of relay protection devices is proposed, which

fully considers the relationship between relay protection devices and the operation status of converter stations and realizes the evaluation research of their operation and maintenance security reliability.

2 Design of Safety Reliability Evaluation Method for Intelligent Operation and Maintenance of Converter Station

2.1 Construction of Converter Station Control Structure Model

In order to accurately evaluate the safety and reliability of the intelligent operation and maintenance of the converter station, it is first necessary to clarify the operation mechanism of the converter station in its own operation phase. For this purpose, this paper first constructs the control structure model of the converter station [13, 14]. The main tasks of converter level control are analyzed. The main implementation basis is the signal transmitted from the system level control, combined with the operating characteristics and mode of the controller itself, and taking each bridge arm as the control target, the corresponding modulation voltage reference value is generated to achieve the regulation of the transmission state [14, 15]. In terms of structure, the core of the whole control system consists of converter level control and two control levels connected with it. On this basis, the converter station control structure model built in this paper is shown in Fig. 1.

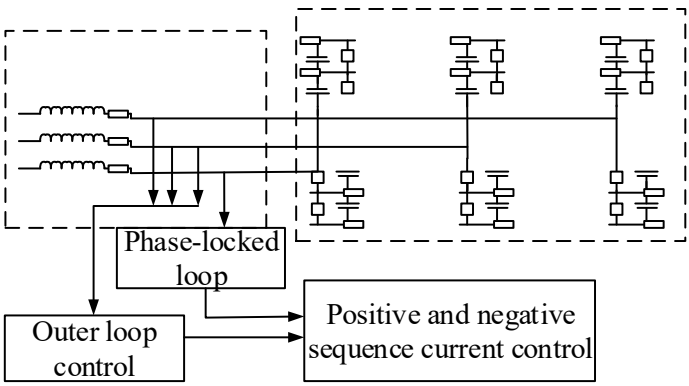

Fig. 1 Control structure model of converter station

It can be seen from Fig. 1 that the converter station control structure model built in this paper is mainly divided into three parts, namely outer loop control structure, double dq-PI current control structure and synchronous rotating coordinate transformation structure. The above three parts are analyzed in detail. Among them, the main function of the outer loop control structure is to accurately control the active and reactive physical quantities of the system in the transmission phase, maintain the system power in a relatively balanced state in this way and provide guarantee for the stable output of the system DC voltage [16, 17]. The specific control objectives of the external loop control structure are analyzed. The main physical quantities of active power are constant DC voltage. In addition, the constant active power and frequency are also included; the main physical quantities of reactive power are constant reactive power and constant AC voltage. In the double dq-PI current control structure, according to the specific implementation, it can be divided into two parts, namely the positive sequence current control link and the negative sequence current control link [18, 19]. During operation, after the positive sequence voltage is extracted by the controller, it is input to the phase-locked loop in the form of an input signal, so as to accurately synchronize the power grid operation state when the MMC AC is asymmetric. For the MMC valve side, after the AC current is locked through park transformation and PLL phase, it needs to be decomposed. The positive sequence component and negative sequence component correspond to the positive sequence current control link and the decomposed component of the negative sequence current control link [20, 21]. In this paper, when the AC side of MMC is asymmetric, the positive sequence component can be expressed as

$$L_1 \frac{di_j^+(t)}{dt} + R_1 i_j^+(t) = e_j^+(t) - u_j^+(t) \tag{1}$$

Among them, L_1 represents the inductance parameter of the bridge arm, R_1 represents bridge arm resistance, $i_j^+(t)$ represents the current parameters of the bridge arm on the positive sequence current control link, $e_j^+(t)$ represents the electromotive force parameter of the positive sequence current control link, $u_j^+(t)$ represents the equivalent voltage parameter of the bridge arm on the positive sequence current control link.

The corresponding negative sequence component can be expressed as

$$L_1 \frac{di_j^-(t)}{dt} + R_1 i_j^-(t) = e_j^-(t) - u_j^-(t) \tag{2}$$

Among them, $i_j^-(t)$ represents the current parameters of the bridge arm under the negative sequence current control link, $e_j^-(t)$ represents the electromotive force parameter of negative sequence current control link, $u_j^-(t)$ represents the equivalent voltage parameter of the bridge arm under the negative sequence current control link. In this way, decoupling AC current of dq axis can be controlled.

The last is the setting of the synchronous rotating coordinate transformation structure, which is based on the three-phase static coordinate system. Considering that the corresponding parameters at the stage are AC flow [22, 23], which is difficult for control, the park transformation method is used to transform the parameters from the original three-phase static coordinate system to the rotating coordinate system, so as to convert the original AC flow, convert to direct flow [24]. At this time, when the proportional integral PI controller is used to control the DC variables of the voltage and current at the MMC valve side, the corresponding control effect will be more ideal.

The control structure model of converter station is constructed in combination with the above mode, which provides a basis for subsequent operation and maintenance safety reliability assessment.

2.2 Safety and Reliability Assessment of Converter Station Operation and Maintenance Based on Situation Awareness of Relay Protection Device

Combined with the above construction structure of the converter station control structure model, this paper fully considers the dependency between the converter station protection process and the relay protection device when evaluating the safety reliability of the converter station operation and maintenance and realizes the evaluation of the safety reliability of the converter station operation and maintenance by sensing the situation of the relay protection device. In the specific operation process, from the perspective of ensuring the reliability, selectivity, quick action and sensitivity of the converter station, devices with different functions can participate in one or more protection processes by establishing information interaction relationships with relay protection devices. The direct impact is that when the action logic is different in the protection process, the corresponding devices participating in the protection process are also different to varying degrees. This paper describes the execution of the protection process of the relay protection device by using the correlation between the relay protection device and the protection process and the domain mapping matrix (DMM). DMM, as a non-square matrix, is mainly used to reflect the corresponding relationship between relay protection device action and converter station operation and maintenance safety. It can be seen from the converter station control structure model library shown in Fig. 1 that it is mainly divided into three core components. In the design phase of relay protection device composition, line protection and bus differential protection process can be completed with the help of five devices. The resulting DMM of relay protection device and protection process is 2×5 matrix, where the row represents the device participating in the execution of the protection process; the list shows the protection process that the device participates in. In order to simplify the protection process, in the process of line protection, this paper takes distance protection and auto reclosing as the core index parameters; in the process

of bus differential protection, this paper takes current differential protection, line unit breaker failure protection and reclosing as the core index parameters. On this basis, combined with the protection action logic, we can realize the classification of all actions of relay protection devices. According to the workload of each relay protection device in different protection processes, the function proportion of the device in each protection process is obtained. Since the completion of the protection process is based on the joint execution of multiple devices, this paper sets the sum between the relay protection device and the protection process as 1. On this basis, the quantitative relay protection device and protection process DMM constructed are given in Table 1.

Combined with the above, the evaluation of the safety and reliability of the intelligent operation and maintenance of the converter station in this paper is based on the node status in the transmission network, and the corresponding evaluation results are divided into three types, namely healthy state, infected state and failed state. Among them, the health state indicates that the device is in normal state without failure risk; the infection status indicates that the device has infected the device with failure risk, and the corresponding failure risk has the ability to spread to related devices. Through maintenance, it can realize the transformation to a healthy state; the failure state indicates that the function of the device participating in the protection process has failed. When the infected device reaches a certain scale, it will become invalid. On this basis, the evaluation results of the safety and reliability of the intelligent operation and maintenance of the T-notch converter station can be expressed as

$$y(t) = \frac{\mathrm{Card}(L_1 \frac{di_j^-(t)}{dt} + R_1 i_j^-(t) \neq L_1 \frac{di_j^+(t)}{dt} + R_1 i_j^+(t))}{n} \tag{3}$$

Table 1 Quantitative relay protection device and protection process DMM

Protection process	Line merging unit	Parent consolidation unit	Line intelligent terminal	Line protection device	Bus differential protection device
Line protection process	0.275362	0	0.166667	0.500725	0.007246
Bus differential protection process	0.210526	0.078947	0.105263	0.052632	0.552632

Among them, $y(t)$ represents the assessment results of the safety and reliability of the intelligent operation and maintenance of the t converter station, $\mathrm{Card}(L_1\frac{di_j^-(t)}{dt} + R_1 i_j^-(t) \neq L_1\frac{di_j^+(t)}{dt} + R_1 i_j^+(t))$ indicates the number of failures of positive and negative sequence current control links and relay protection devices, n represents the total number of relay protection devices participating in the protection process.

The safety and reliability of intelligent operation and maintenance of converter station can be evaluated according to the above mode.

3 Test and Analysis

3.1 Test Environment Settings

In the stage of analyzing the application effect of the evaluation method designed in this paper, the simulation test was carried out. Based on the RT-LAB 5600 real-time online simulation platform, the corresponding test environment was composed of a four terminal 31 level MMC system model as the core. In the specific environmental parameter setting stage, the rated active power is set as 500.0 MW, the corresponding rated DC voltage and rated DC current are 100 kV and 5.0 kA, respectively, and the transformation ratio of the connection transformer is 30/110 kV. On this basis, the relevant parameters of the bridge arm are set, where the equivalent resistance of the bridge arm is 0.3 RvS and the reactance is 15 Ls/mH. In the sub-module setting stage, the specific quantity is 30, and the corresponding capacitance parameter is 8.8 Co/mF. In the specific operation process, four converter stations are used to control the overall operation mechanism. Among them, the control mechanism of No. 1 post-converter station is the integrated control mode of active power and reactive power, the control of No. 2 good converter station is the integrated control mode of DC voltage control and reactive power, and the control mode of No. 3 converter station and No. 4 converter station is the same, both of which are droop control and integrated control mode of reactive power. On this basis, the basic state parameters of the relay protection device in the converter station are set, as given in Table 2.

On this basis, the reliability of converter station under fault condition is evaluated by using the design evaluation method and the conventional method in this paper, and the analysis between them and the actual results is compared, respectively.

3.2 Test Results and Analysis

In the specific analysis process, this paper first counted the number of nodes in the healthy, infected and failed states of the converter station over time, and the data results are shown in Fig. 2.

Table 2 Basic state parameter setting of relay protection device

Status indicators	2018	2019	2020	2021
Number of planning review revisions	87	89	99	109
Number of construction acceptance errors	118	3	3	4
Closed loop data acceptance and modification times	4	5	89	94
Number of power transmission failures	99	114	119	54
Number of production failures	56	61	79	82
Procedure management error rate	59	63	68	81
Equipment defect management error rate	83	0.16	0.15	0.14
Standard operation error-free running time	0.17	0.19	0.46	0.53
Times of system item inspection	0.64	0.73	0.70	1.64
Operation and maintenance work record error times	1.47	1.39	1.32	1.24
Number of safety measure errors	2	2	2	1
Error rate of countermeasures	1	39	43	47
Number of technical innovation design errors	49	57	87	89
Exemption times of technical data	109	113	117	0.3
Number of construction control errors	0.45	0.49	0.65	0.73
Error rate of completion acceptance	2	3	3	3

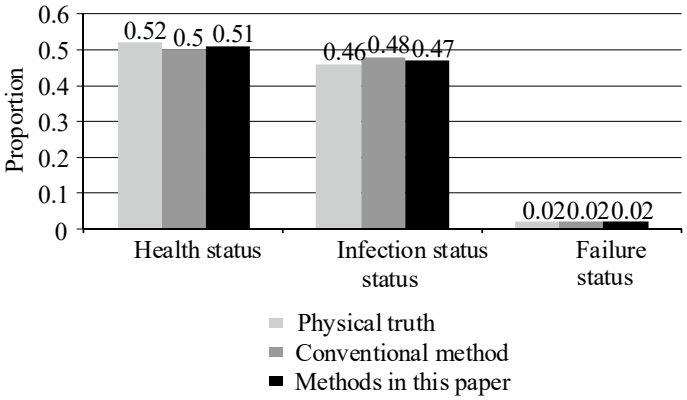

Fig. 2 Statistical table of proportion changes of various nodes

According to the test results in Fig. 2, the method in this paper has a high consistency with the actual situation in terms of the proportion of converter station nodes in different states. The error between the proportion of converter station nodes in the healthy state and the actual proportion is 1.0%, and the error between the proportion of converter station nodes in the infected state and the actual proportion is only 1.0%. The error between the assessment result of the proportion of converter station nodes in the failed state and the actual proportion is 0. Compared with the conventional

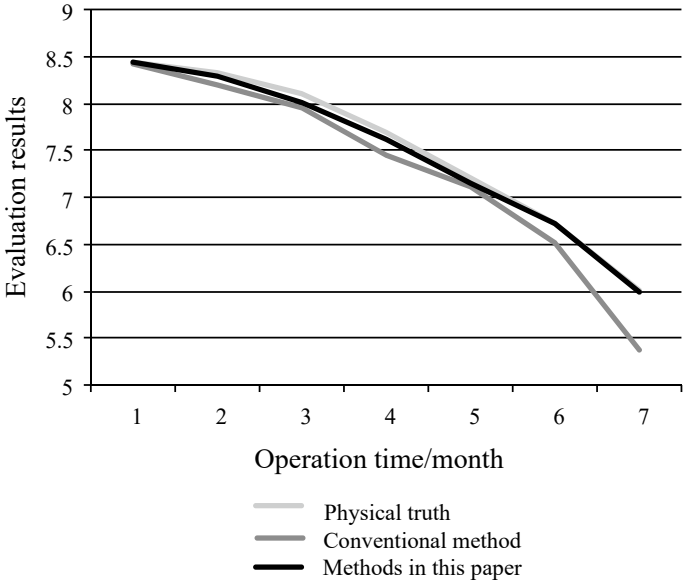

Fig. 3 Safety and reliability of intelligent operation and maintenance of converter station

method, it has obvious advantages in the proportion of converter station nodes in the healthy state and the proportion of converter station nodes in the infected state.

Based on the above basic points, the safety reliability of intelligent operation and maintenance corresponding to converter stations under different operation durations is evaluated, and the data results are shown in Fig. 3.

Combined with the test results in Fig. 3, it can be seen that in the evaluation results of conventional methods, the consistency between the corresponding results and the actual situation has a relatively obvious fluctuation, in which the maximum error is more than 0.5. In the evaluation method designed in this paper, the corresponding evaluation results have a high degree of fit with the actual situation. Moreover, compared with conventional methods, it has obvious advantages in stability and accuracy.

From the above analysis, it can be seen that the intelligent operation and maintenance security reliability assessment method designed in this paper based on the situation awareness of relay protection devices can achieve accurate assessment of the status of converter stations and has good practical application value.

4 Conclusion

For converter stations, the security and reliability of their operation status directly affect the overall transmission effect of the power grid. This paper proposes an intelligent operation and maintenance security and reliability assessment method for converter stations based on the situation awareness of relay protection devices. Combined with the operation structure of converter stations, using the relationship between the situation of relay protection devices and related protection actions, accurate assessment of the status of converter stations is achieved. For the actual transmission management work, it has good practical application value.

Acknowledgements This project is supported by Guangdong Power Grid DC Back-to-Back Dongguan Project (Greater Bay Area Nanyue DC Back-to-Back Project)(031900WS26190001).

References

1. Zhang Y, Yang H, Wang P (2021) The voltage stabilizing control strategy of off-grid microgrid cluster bus based on adaptive genetic fuzzy double closed-loop control. J Electr Comput Eng 2021:1–12
2. Touzon I, Nava V, Gao Z, Petuya V (2021) Frequency domain modelling of a coupled system of floating structure and mooring lines: an application to a wave energy converter. Ocean Eng 220:108498
3. Gladwin SJ, Kumar CV (2021) Read textual features in images and convert to editable form by extended use of artificial neural networks, deep learning and maximally stable extremal region techniques. J Phys Conf Ser 1921(1):012033
4. Wu T, Ji X, Wang G, Liu Y, Yang Q, Bao Z, Peng J (2021) Hydrogen energy storage system for demand forecast error mitigation and voltage stabilization in a fast-charging station. IEEE Trans Ind Appl 58(2):2718–2727
5. Klyuev RV, Bosikov II, Gavrina OA (2021) Improving the efficiency of relay protection at a mining and processing plant. Записки Горного института 248:300–311
6. Kojovic L (1997) Rogowski coils suit relay protection and measurement of power systems. IEEE Comput Appl Power 10(3):47–52
7. Chang CK, Elmashtoly AM (2022) Protection coordination index assessment using fuzzy logic controller. Energies 15(4):1377
8. Man X, Duan F, Piao Y, Tian R, Qiao X, Ji X, Liu Y (2021) Research on simulation ideas of relay protection device on load test based on virtual reality technology. J Phys Conf Ser 2005(1):012196
9. Liu H, Zhang Y, Li W, Zhang X, Wang H (2021) Research on the influence and test of core components on relay protection device. In: IOP conference series: earth and environmental science, vol 631, no 1. IOP Publishing, p 012089
10. Chang C, Wang J, Duan F, Tian R, Liu Y, Ji X, Qiao X (2021) Research on skill training of relay protection device based on virtual reality technology. J Phys Conf Ser 2005(1):012044
11. Zhang H, Liu Z, Fan Z, Song H, Niu Z, Xiong Z, Li X (2022) Failure causes and solutions of relay protection switching power supply. J Phys Conf Ser 2196(1):012039
12. Wang Y, Xu C, Zhu J, Xin M, Zhang L (2021) Research on automatic physical testing method of relay protection equipment through data fusion technology. J Phys Conf Ser 2083(2):022019

13. Sizykh VN, Daneev AV, Vostrikov MV, Menaker KV (2021) The automated system of unified templates as an element of trainability of microprocessor relay protection devices. J Appl Math Phys 9(12):3045–3057
14. Li F, Zhuyuan L (2021) Reliability and dynamic performance simulation based on relay protection summary. J Phys Conf Ser 2074(1):012020
15. Zasypkin AS, Nagay VI (2021) The calculation method of ice melting schemes' relay protection settings and clarification of the ice depositions control method on steel lightning protection wires. J Phys Conf Ser 2096(1):012156
16. Yang L, Sheng L, Yuqiang L, Junwei L, Yuheng C (2021) Technology research on panoramic situation awareness of operation state of smart distribution network. In: IOP conference series: earth and environmental science, vol 645, no 1. IOP Publishing, p 012007
17. Xia Y, Zhang X, Ge H, Hao S, Zou W (2021) Optimal dispatching technology of distributed power generation based on situation awareness. Am J Electr Electr Eng 9(1):7–11
18. Kulkarni AR, Ballal MS (2021) Synergism of synchrophasor measurements and data analytics for enhancing situational awareness of power grid. Comput Electr Eng 93:107231
19. Wang L, Guo W (2022) Nonlinear hydraulic coupling characteristics and energy conversion mechanism of pipeline-surge tank system of hydropower station with super long headrace tunnel. Renew Energy 199:1345–1360
20. Wang Y, Von Krannichfeldt L, Zufferey T, Toubeau JF (2021) Short-term nodal voltage forecasting for power distribution grids: an ensemble learning approach. Appl Energy 304:117880
21. Dong Y, Shan X, Yan Y, Leng X, Wang Y (2022) Architecture, key technologies and applications of load dispatching in China power grid. J Mod Power Syst Clean Energy 10(2):316–327
22. Wang H, Lin P, Hou Z, Sun S (2021) Research on intelligent monitoring and maintenance technology of substation based on digital twin. J Phys Conf Ser 2136(1):012029
23. Liang K, Zhou B, Zhang Y, Li Y, Zhang B, Zhang X (2022) PF2RM: a power fault retrieval and recommendation model based on knowledge graph. Energies 15(5):1810
24. Yang Y, Yao L (2021) Optimization method of power equipment maintenance plan decision-making based on deep reinforcement learning. Math Probl Eng 2021:1–8

Research on Cooperative Optimization Operation of Active Distribution Network Based on Multivariate Flexible Fusion

Jiawei Xing, Yan Cheng, Shumin Sun, Peng Yu, and Yuejiao Wang

Abstract In order to achieve efficient and stable operation of active distribution networks, a study on load storage cooperative operation optimization of active distribution networks based on multiple flexible fusion is proposed. Firstly, according to the distributed power generation coordination control module, the AC/DC hybrid distribution network coordination control module, and the charging load guidance optimization module, the objective function of active distribution network optimization operation is determined; based on the constraints of active distribution network optimization operation, a load storage coordination optimization model of active distribution network source network is constructed. According to this model, disturbances are added to achieve the purpose of searching for optimal results in a small range, and the load storage coordination operation optimization of active distribution network source network is realized. The experimental results show that the current fluctuation can be kept at a relatively low level using the proposed method; after optimized operation, the line power variation range is close to the planned value, achieving effective load storage cooperative operation optimization.

Keywords Multiple flexible fusion · Active distribution network · Source network load storage · Collaborative operation optimization

1 Introduction

With the rapid development of the energy industry and continuous technological updates, active distribution networks, as an important component of the new generation of power systems, have gradually begun to replace traditional passive distribution network systems [1]. Build an active distribution network to address the compatibility of large-scale intermittent renewable energy on the distribution side, and improve the utilization rate of green energy [2, 3]. Active power distribution networks flexibly integrate various energy sources, loads, and energy storage devices through multiple

J. Xing (✉) · Y. Cheng · S. Sun · P. Yu · Y. Wang
State Grid Shandong Electric Power Research Institute, Jinan 250002, China
e-mail: 573602466@qq.com

S. Yadav et al. (eds.), *Energy Power and Automation Engineering*, Lecture Notes in Electrical Engineering 1118, https://doi.org/10.1007/978-981-99-8878-5_45

flexible methods, achieving coordinated operation of source, network, and storage, providing a new solution for the security, economy, and environmental friendliness of power systems. However, with the continuous expansion of the scale of active distribution networks, their operation and optimization issues have become increasingly complex. Therefore, it is particularly important to study the optimization of load storage cooperative operation of active distribution network.

Reference [4] proposes an optimized coordination of directional overcurrent relays in mesh active distribution networks based on the imperial competition algorithm. The optimal setting of directional overcurrent relays ensures that faults are detected and cleared in the shortest possible operating time. In the case of distributed generation, directional protection relays are executed to coordinate relay settings in a mesh network. The main goal of directional overcurrent relay coordination is to find the optimal time scale setting and pickup multiple setting. Due to the complexity of mixed integer nonlinear programming problems, the proposed directional overcurrent relay coordination formula is implemented in three different test cases. Reference [5] proposes using a multi-objective sparrow search algorithm to establish integrated optimization for dynamic reconfiguration of active distribution networks, proposes a multi-objective sparrow search algorithm, and establishes a mathematical model for ADN integrated optimization. A multi-scenario test was conducted in a classical testing system to verify the effectiveness of the proposed method, and the final solution was determined using a similarity ranking technique with ideal solutions.

Although the above research has made some progress, the research on multi-flexible fusion is not sufficient. Therefore, a study on the optimization of active distribution network load storage cooperative operation under multi-flexible fusion is proposed, and its effectiveness is analyzed through simulation.

2 Collaborative Operation Optimization

2.1 Determine the Objective Function of Active Distribution Network Optimization Operation

Under the cooperative operation of active distribution networks under multiple flexible fusion, market-driven distributed power coordination and control modules, AC/DC hybrid distribution network coordination and control modules, and charging load guidance and optimization modules are, respectively, built to coordinate and control the source network load of multiple flexible fusion.

(1) Distributed power coordination control module

Starting from the control and management side of the active distribution network, considering the optimization objective of minimizing the total cost of the active distribution network, the functional expression for minimizing the total cost of the active distribution network by $A_{\min}$ is obtained:

$$A_{\min} = A + \alpha \times |\lambda_r| + \sum_{r=1}^{24} \beta_r - \lambda_{1r} \times C + \beta_{1r} \tag{1}$$

where A represents the transaction cost of active distribution network operation; α represents the distribution coefficient; α_r represents the charging and discharging power at the moment; β_r represents the peak and valley electricity charges of the active distribution network at the r time; λ_{1r} represents the output power generated at moment r; C represents the online cost of active distribution network units; β_{1r} represents the time carbon transaction cost.

(2) AC/DC hybrid distribution network coordination control module

Taking the minimum total cost as the objective function, taking into account various equipment operation constraints and system operation constraints, the AC/DC hybrid distribution network coordination control module can use voltage sensitivity, branch power sensitivity, and line loss sensitivity calculation methods to establish a spatiotemporal coordination function S_{WJ} that expresses the relationship between spatiotemporal regulation costs and regulation effects, expressed as:

$$S_{\mathrm{WJ}} = A_{\min} + (1 - \kappa) \times D_{\min} \tag{2}$$

In the formula, $D_{\min}$ represents the minimum mean square deviation of the load storage cooperative operation of the active distribution network source network; κ represents the weight coefficient. Through the electricity price incentive scheme, the user's charging cost is reduced by utilizing the difference between peak and valley electricity charges. The objective function is expressed as:

$$H_{\mathrm{JK}} = z_1 + \sum_{r=1}^{r} (\eta_r - z_r - y_r) \times S_{\mathrm{WJ}} \tag{3}$$

In the formula, z_1 represents aging maintenance cost; z_r represents the carbon emission benefit cost at the r moment; y_r represents the compensation cost at r time.

(3) Charging load guidance optimization module

The charging load guidance optimization module can establish a charging load guidance model for an electric transportation system under the background of deep interaction of multiple complex networks based on complex network theory. The formula is:

$$\min O = G_e \times (I_{\mathrm{da}} - S_{\mathrm{WF}}) + L \times H_{\mathrm{JK}} \tag{4}$$

In the formula, G_e represents the regulation increment of each unit; I_{da} represents tracking error; L represents the weight coefficient matrix of the control quantity.

2.2 Constructing Constraints for Optimal Operation of Active Distribution Networks

Considering the charging and discharging power balance of the active distribution network, the corresponding charging and discharging current constraints are expressed as follows:

$$\begin{cases} 0 \le C_D \le \dfrac{\varpi}{3} \\ 0 \le F_D \le 2\varpi \end{cases} \tag{5}$$

In the formula, C_D and F_D, respectively, represent the charging and discharging currents of electric vehicles; ϖ represents the active distribution network model. The charge and discharge power constraints are expressed as:

$$\begin{cases} \eta_{r\min} \le \eta_r \le \eta_{r\max} \\ \eta_{r\min} = \max\left(-15, \eta'_{r\min}\right) \\ \eta_{r\max} = \min\left(15, \eta'_{r\max}\right) \end{cases} \tag{6}$$

In the formula, $\eta_{r\min}$ and $\eta_{r\max}$, respectively, represent the minimum and minimum charging and discharging power of the active distribution network; $\eta'_{r\min}$ and $\eta'_{r\max}$ represent the minimum and minimum charge and discharge power at the charging window, respectively.

2.3 Optimization Model for Load Storage Coordination of Active Distribution Network

According to the differentiated requirements of active distribution networks, a single layer source network load storage coordination model is constructed. The differentiated demand of active distribution network users is divided into three types: electricity quantity, frequency, and time. The model is obtained by refining the three types of standards based on the real-time data of active distribution network source network load storage and corresponding standards for different types. The specific content is as follows:

(1) Electricity-type voltage stability standard A_{ij}

After connecting the power load node i of the end user area to the node j, obtain the minimum value of the voltage deviation value A_{ij} from both ends of the line, and define the electricity-type voltage stability standard as the most stable value of the end user area voltage. The formula is used to express the model as follows:

$$A_{ij} = \frac{P_j - Z_j \times R_{ij}}{U_i} \times \eta_{r\min} \tag{7}$$

In the formula, R_{ij} represents the circuit branch impedance; P_j represents the power load of node j, U_i represents the voltage amplitude of node i, and Z_i represents the system power flow direction.

(2) Frequency-type power supply rate standard B_{ij}

The frequency-type power supply rate standard is the maximum value of the standard value of the power supply rate for the end user area:

$$B_{ij} = \frac{P_l(t) - P_d(t)}{P_d(t)} \times A_{ij} \tag{8}$$

In the formula, $P_l(t)$ represents the t hour power of the electrical load; $P_d(t)$ represents the t hour inflow power of the active distribution network. When the frequency-type power supply rate standard is the maximum, the area where the active distribution network is located is not easily affected by other areas, and the self-sufficiency power supply rate is the highest.

(3) Time-type voltage deviation standard C_{ij}

The time-type voltage deviation standard is defined as the voltage difference between power load nodes in the end user area. The formula expression model is as follows:

$$C_{ij} = \frac{\max U - \min U}{B_{ij}} \tag{9}$$

In the formula, U represents the node voltage, $\max U$ represents the maximum value of the node voltage, and $\min U$ represents the minimum value of the node voltage. When the time-type voltage deviation standard is the minimum, the voltage deviation in the active distribution network is the lowest.

Based on the above three types, select the best differentiated demand criteria for end users and build a model as follows:

$$\min F = \zeta A_{ij} + \mu B_{ij} + \gamma C_{ij} \tag{10}$$

In the formula, ω, μ, and γ represent weight factors, and the relationship between weights is set to $\zeta + \mu + \gamma = 1$.

2.4 *Research on Optimization of Load Storage Cooperative Operation of Active Distribution Network Source Network*

According to the active distribution network load storage coordination optimization model, the solution result of the optimization objective function is calculated. In order

to improve the convergence and rapidity in the optimization process of the objective function, a multi-objective solution method that integrates multiple objectives and constraints to obtain the best results is proposed. Assume that the structure of the objective function before collision is $e(s)$, and the structure after collision is $u(s)$. Add perturbation to achieve the purpose of searching for optimal results in a small range. The perturbation P_{YT} calculation is expressed as

$$P_{\mathrm{YT}} = [e(s) + u(s)] \times W_{\mathrm{DF}} \times \min F \tag{11}$$

where W_{DF} represents the dimension of the objective function. The above objective function with perturbation is decomposed, and the constraint conditions for the decomposition process must satisfy that the sum of the kinetic and potential energies of the function molecules before the collision is greater than that after the collision. On this basis, a new objective function structure is generated, and new results are output repeatedly, while the new results are bounced back. According to the above formula, perform cyclic iterative calculation on the rebound function structure to obtain the final calculation result, which is to achieve the research on the optimization of load storage coordinated operation of the active distribution network source network.

3 Experimental Analysis

Define some performance indicators to evaluate the operational effectiveness of active distribution networks, including energy utilization, grid stability, battery life, and other indicators. Through the above simulation experimental environment and parameter settings, it will be possible to better simulate the source network load storage collaborative operation optimization of active distribution networks, providing technical support and reference basis for the operation of actual power grids. Take it as the experimental test group, and select the methods in reference [4] and reference [5] for comparison. Use the experimental test method to compare the application effects of different methods, analyze the collaborative operation optimization ability of the methods, three methods are used to compare the generated power loss, and the results are shown in Fig. 1.

According to Fig. 1, the maximum power loss value of the method in Reference [4] reached 1.65 kW, while the maximum power loss value of the method in Reference [5] was 1.58 kW, while the power loss value generated by the method in this article was the lowest, only 1.24 kW. It can be explained that using the method in this paper to achieve load storage coordinated operation optimization of the source network can maintain current fluctuations at a lower level, improve the quality of current in the branch, and make the entire power allocation process more stable and effective. This is because the method in this paper uses the frequency-type power supply rate standard

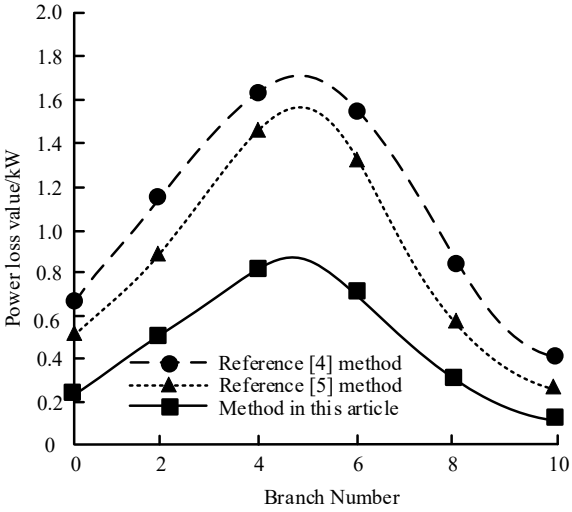

Fig. 1 Power loss comparison results of three methods

as the maximum value of the standard value of the end user area power supply rate, and constructs a model to make the current load in a multi-source distribution network more stable.

Analyze the tie line power before and after the active distribution network load storage cooperative operation optimization using multiple flexible fusion, and compare it with the actual planned value to obtain the power optimization effect of the source network load storage cooperative operation line, as shown in Fig. 2.

According to Fig. 2, before the application of this method, the power of the source network load storage cooperative operation line is unstable, with a large fluctuation range, and cannot ensure the stability and controllability of the active distribution

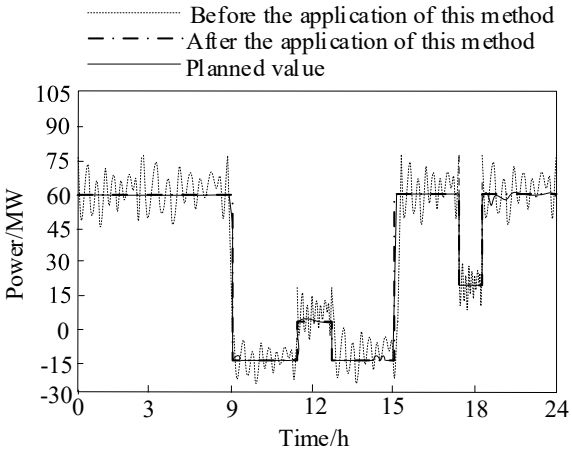

Fig. 2 Comparison of optimization effects of source network load storage cooperative operation route

network. The range of line power variation after optimized operation using this method is close to the planned value, indicating that this method can effectively optimize the load storage cooperative operation of the active distribution network source network.

4 Conclusions

This paper proposes a study on the optimization of load storage cooperative operation of active distribution networks under multiple flexible fusion. Using the method in this paper to optimize the load storage cooperative operation of the source network can maintain current fluctuations at a low level, improve the quality of current in the branch, and make the entire power allocation process more stable and effective. Using this method to optimize the operation, the line power variation range is close to the planned value, which can effectively optimize the load storage cooperative operation of the active distribution network source network.

Acknowledgements Supported by State Grid Corporation of China Headquarters Management Technology Project (medium and low voltage photovoltaic connection throughout the county Research and Application of Hierarchical and Hierarchical Collaborative Regulation Technology for Power Grid, 5400-202216414A-2-0-ZN).

References

1. Raeisinia MR, Javadi S, Jokar MR (2022) Flexibility pricing in the active distribution network including renewable and flexibility sources as a bi-level optimization model. Sustain Energy Technol Assess 52(8):1–10
2. Bansal Y, Sodhi R (2022) A novel frequency estimator for protection applications in active distribution networks. IEEE Trans Ind Appl 58(4):4319–4327
3. Singh PP, Palu I (2021) State coordinated voltage control in an active distribution network with on-load tap changers and photovoltaic systems. Global Energy Interconnect 4(2):117–125
4. Alaee P, Amraee T (2021) Optimal coordination of directional overcurrent relays in meshed active distribution network using imperialistic competition algorithm. J Mod Power Syst Clean Energy 9(2):416–422
5. Li LL, Xiong JL, Tseng ML (2022) Using multi-objective sparrow search algorithm to establish active distribution network dynamic reconfiguration integrated optimization. Exp Syst Appl 193(5):1–18

Intelligent Fault Identification Method for Distribution Network Power Equipment Based on 5G Technology and Association Rules

Zexiong Chen, Xiaodong Liu, Lingli Peng, Ke Tian, Xudong Chen, and Ganlin Mao

Abstract The current conventional distribution network power equipment fault identification method mainly locates the abnormal part in the infrared image to mark the fault node, which leads to poor identification accuracy due to the low degree of image enhancement and denoising processing. In this regard, an intelligent fault identification method for distribution power equipment based on 5G technology and association rules is proposed. By calculating the confidence degree of the sample data, the classification mining process is performed on the power equipment data. The image data is enhanced and denoised by combining grayscale information method and Gaussian filtering algorithm, and the covariance matrix is constructed to analyze the extracted fault feature parameters. In the experiments, the proposed recognition method is verified. The experimental results show that the proposed method has a high recognition accuracy and ideal recognition effect for fault identification of distribution network power equipment.

Keywords Association rules · Distribution networks · Power equipment · Fault identification · Image enhancement

1 Introduction

The operation and maintenance of power equipment in the distribution network is an important part of ensuring the smooth operation of the distribution network, so the detection and identification of power equipment faults is particularly important. In the past, the power inspection work, mainly through the manual way to determine whether the power equipment failure, the method will not only consume labor costs, but also have the problem of low reliability [1]. The conventional human

Z. Chen · X. Liu · L. Peng (✉) · K. Tian · X. Chen · G. Mao
Guangzhou Nansha Power Supply Bureau of GuangDong Power Grid Co., Ltd., Guangzhou 510000, Guangdong, China
e-mail: 398072705@qq.com

S. Yadav et al. (eds.), *Energy Power and Automation Engineering*, Lecture Notes in Electrical Engineering 1118, https://doi.org/10.1007/978-981-99-8878-5_46

inspection method is more dependent on the inspector's familiarity with the electric power equipment and his own professional technical level, which has a greater instability and cannot guarantee that each inspection can perfectly identify all the electric power equipment faults, and there is a certain safety hazard problem. Therefore, in order to improve the accuracy of power equipment fault identification, it is now common to take intelligent power equipment monitoring system to obtain the operating image of the equipment. By combining image recognition technology to analyze the collected infrared images of power equipment. By installing intelligent sensors around the power equipment, the infrared heat of the power equipment can be captured in real time, and the fault nodes can be effectively located according to the infrared heat distribution of the power equipment in the conventional state [2]. The above-mentioned method can complete the identification work for the electric power equipment fault, but there is still some room for improvement in the identification effect. First of all, subject to the limitation of image recognition technology and recognition work equipment and other factors, the infrared image captured by the conventional fault recognition method is often not ideal in terms of clarity, which leads to the later analysis of the infrared image, and will not be able to accurately extract the texture features in the image, which is not conducive to the fault recognition of electric power equipment. In addition, the working environment and transmission environment constraints, infrared image data in the transmission process will usually generate a lot of noise, and these noises will also affect the final recognition effect and are not conducive to the effective extraction of fault features [3]. Therefore, in order to optimize and solve the above problems, the collected infrared image data must be pre-processed to enhance the image in several aspects, such as gray value, clarity, and noise removal effect, which can effectively improve the subsequent extraction effect of the fault features and thus improve the fault recognition accuracy [4].

2 Data Mining of Distribution Network Power Equipment Based on 5G Technology and Association Rules

In order to effectively identify the faults of power equipment in distribution network, this paper firstly combines association rule algorithm to mine the operation data related to power equipment in distribution network and realize the organization of power equipment operation data. In this regard, it is necessary to first construct the frequent item set and then clarify the weight value of each association rule, so as to realize the effective mining of power equipment data, and the specific implementation process is as follows [5].

Firstly, assume that x and y represent the set of attribute values and data types of power equipment operation data in the distribution network, A_{qi} represents a fuzzy association rule corresponding to the attributes of power equipment operation data, R_q represents the association rule, C_{qM} represents the prediction type, and F_{qM}

represents the confidence level of the prediction result. From this, the classifier of power equipment operation data of distribution network can be constructed, and the weights of association rules can be calculated as shown below.

$$w_q = A_{\mathrm{qi}} - C_{\mathrm{qM}} \tag{1}$$

According to the above formula, the weight values corresponding to the fuzzy association rules can be calculated, and the genetic classifier can be used to effectively classify the power equipment operation data in the distribution network database. The confidence rate of the power equipment operation sample data can thus be calculated as shown in the following formula [6].

$$c = \frac{\sum_{n=1}^{i} \mathrm{sw}_p \mu_{\mathrm{aq}}}{\sum \tau_p} \tag{2}$$

where sw_p represents the weight value of the sample data, μ_{aq} represents the label of the classifier when predicting the sample data, and τ_p represents the type of the classifier when predicting the sample data. The confidence rate of each power equipment operation sample data is calculated by the above steps, and the interval with higher confidence rate is the set of frequent items in the distribution network power equipment operation data set. The frequent item sets of the power grid equipment operation data in the data space are locked by the above steps, and the frequency of this item set is the same as the number of occurrences of the maximum confidence [7]. Based on the above planned frequent item set space, the strong association rule is defined, and the association rule is used as the classification criterion for the power equipment operation data of the distribution network. The power equipment operation data that meet the strong association rule are grouped into the same type, and the above steps are repeated until all data samples are classified. By adopting classifier to classify data according to the confidence degree of sample data through the above steps, the problem of poor classification effect caused by unbalanced data density can be effectively reduced, so as to realize effective mining of power equipment operation data of distribution networks [8].

3 Distribution Network Power Equipment Fault Feature Extraction

The distribution network power equipment fault intelligent identification algorithm designed in this paper is mainly through the extraction of fault characteristics and the comparison of real-time monitored power equipment operation data, so as to realize the effective identification of power equipment faults. In the distribution network power equipment monitoring system, it is mainly through image data to achieve the acquisition of power equipment operation status data, and through the

analysis of image data, the real-time operation status of power equipment is judged [9]. Therefore, this paper firstly combines the grayscale gradient information method to unify the infrared image information obtained by the power equipment monitoring system and realize the feature extraction on this basis.

Since the power equipment monitoring images captured by the power equipment monitoring system are infrared images, in order to facilitate the subsequent more effective analysis and processing of the images, it is necessary to first grayscale the image data and normalize the three primary color sensitivity values of each pixel in the image, so as to complete the grayscale processing of the infrared images. The specific grayscale processing formula is shown below.

$$\text{Gray} = R \times 0.299 + G \times 0.587 + B \times 0.114 \tag{3}$$

where R G B represents the pixel size of the infrared image for each of the three primary color channels, and Gray represents the grayscale value of the pixel after processing. In addition to the above steps to complete the grayscale homogenization of infrared images, the power equipment monitoring system in the process of power equipment image data acquisition, usually by the impact of the working environment, will lead to the power equipment operation data in the acquisition and transmission of a large number of noise. These noises will interfere with the subsequent fault identification effect, so as not to get more accurate fault identification results [10]. Therefore, in order to improve the effect of fault identification for electric power equipment, it is also necessary to denoise the image data of equipment operation after processing. In this regard, this paper combines the Gaussian filtering algorithm to denoise the grayscale image filtering process, and the specific calculation formula is shown below [11].

$$G(x, y) = \frac{1}{\sqrt{2\pi}\sigma}\nu \tag{4}$$

where $G(x, y)$ represents the Gaussian filter weights for the aggregated pixel points of the grayscale image, ν represents the filtering scale, and σ represents the distribution bias value. Through the above steps, the weight value of the Gaussian filter can be found, and all the pixels in the grayscale image are processed based on this weight value, thus completing the denoising of the image [12]. Then, the image information matrix of the power equipment operation data after the denoising process is normalized by the following formula.

$$H(x, y) = \frac{h(x, y)}{h_{\max}} N_h \tag{5}$$

Among them, $h(x, y)$ represents the gradient value corresponding to the pixel point of image data, $h_{\max}$ represents the maximum gradient value, and N_h represents the gray value in the sample grayscale image. According to the processing results

Table 1 Parameters for extracting features of power equipment operation data of distribution network

Parameter number	Feature parameter
01	Small gradient advantage of grayscale matrix
02	Unevenness of grayscale distribution
03	Gradient distribution inhomogeneity
04	Energy
05	Grayscale mean
06	Gradient average
07	Grayscale mean square deviation
08	Gradient mean square deviation
09	Correlation
10	Grayscale entropy
11	Gradient entropy
12	Mixture entropy
13	Difference moment

and the main features of the power system monitoring images, 13 image feature parameters are selected as the extracted objects in this paper, as shown in Table 1.

Through the above steps, we can clarify the feature extraction parameters of power equipment operation image data and achieve the effective extraction of operation data features for different parameters to provide reliable help for subsequent fault identification.

4 Distribution Network Power Equipment Fault Intelligent Identification

In order to make an effective judgment on the existence of different types of faults in the distribution network power equipment, this paper combines the principal component analysis method to analyze the different characteristic parameters extracted above, from which the characteristic parameters that can characterize the operation status of the equipment are selected for power equipment fault identification. In this regard, the covariance matrix is firstly constructed, which is mainly changed from the original sample matrix of power equipment operation data, and by combining the extracted feature parameters, the specific formula of covariance matrix can be obtained as shown below.

$$C = \frac{1}{P-1} \sum_{j=1}^{P} \left(X_j - \overline{X}\right)^2 \tag{6}$$

Table 2 Experimental data set

Fault type	Number of training images	Number of test images
High voltage out line	825	253
Poor contact	856	205
Bolt heating	878	229
Local heating of tank wall	782	168
Abnormal cooler temperature	754	248

where X_j represents the original sample space matrix of power equipment operation data of size $p \times q$, and $\overline{X}$ represents the average of the space matrix. After the covariance matrix of the sample space is constructed, the eigenvalues and eigenvectors of the power equipment operation data are calculated. Assuming that the calculated eigenvalues and eigenvectors are and, respectively, a new Eigen transformation matrix can be obtained by arranging the eigenvalues in descending order at. For the newly generated Eigen transformation matrix, the corresponding Eigen parameters Y are expressed as follows

$$Y = XT \tag{7}$$

where T represents the newly generated feature transformation matrix. By calculating the above-mentioned feature values, the contribution rates corresponding to different feature values are obtained, and the cumulative contribution rates are counted.

5 Experiment and Analysis

5.1 Experimental Preparation

A different number of test image data were selected for each fault type, and the specific experimental data set is shown in Table 2.

By using three identification methods to identify different types of faults in the above experimental data set, and recording the identification results, the identification performance of different methods for different fault types is compared.

5.2 Analysis of Test Results

The comparison standard selected for this experiment is the recognition accuracy of different recognition methods for fault types, and the specific experimental results are shown in the following Fig. 1.

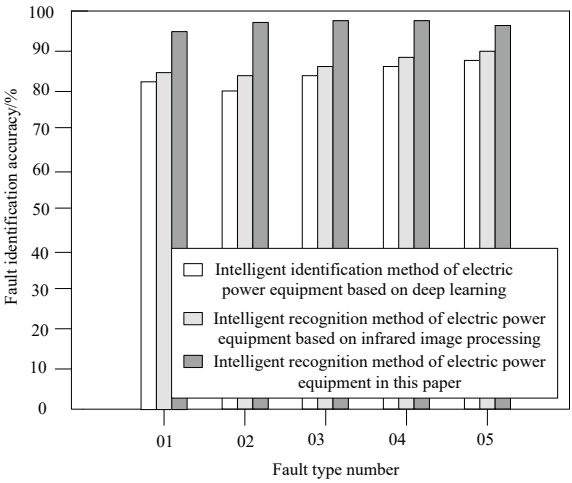

Fig. 1 Fault recognition accuracy comparison results

Through the above experimental results, it can be seen that the recognition performance of different recognition methods also shows a large difference when recognizing different types of fault data. It is obvious from the numerical comparison that the recognition accuracy of the two conventional power equipment fault recognition methods is poor, with the average recognition accuracy ranging from 80 to 90%, and the recognition accuracy fluctuates greatly for different fault types. In contrast, the intelligent fault identification method of power distribution equipment based on 5G technology and association rules proposed in this paper is significantly higher than the two conventional identification methods in terms of recognition accuracy, with an average recognition accuracy of more than 90%, which proves that the proposed identification method is better than the conventional methods in terms of recognition performance.

6 Concluding Remarks

This paper proposes a new fault identification method for power equipment by combining 5G technology and association rule algorithm to address the problem of low recognition accuracy of conventional fault identification methods for power equipment in distribution networks. By using 5G technology to obtain power equipment operation data and combining with association rule algorithm to mine the equipment operation data. Combined with the gray gradient information method to unify the infrared image information obtained by the power equipment monitoring system, the fault identification algorithm built on this basis has higher identification accuracy and can accurately identify for different types of faults.

Acknowledgements The study was supported by China Southern Power Grid Technology Project "5G-based Distribution Network Digital Workload Intelligent Supervision System [086400KK52200003(GZHKJXM2020049)]".

References

1. Li X, Li Q, Wang W et al (2021) An unsupervised multi-shot person re-identification method via mutual normalized sparse representation and stepwise learning. IEEE Trans Intell Transp Syst 44(99):1–15
2. Cheng R, Li Q, Zhang Y et al (2022) Three-phase power cooperative management of distribution network with high distributed energy resources penetration. Energy Rep 8:239–250
3. Mou M, Zhou Y, Zheng W et al (2021) Modeling and control strategy for multi-terminal flexible DC distribution network with echelon utilization power battery. Complexity 2021(25):1–14
4. Mekhilef S, Ahmad S, Alturki Y et al (2022) Hybrid islanding detection technique for distribution network considering the dynamic behavior of power and load. Int J Circ Theory Appl 50(4):1317–1341
5. Yin T, Li J, Cai D et al (2016) Non-contact fault location and identification method for same-tower multi-circuit transmission lines. Energy Rep 2021(7):147–158
6. Wang J, Wang H, Guo L et al (2021) Modeling and fault identification of the gear tooth surface wear failure system. Int J Nonlinear Sci Numer Simul 22(3–4):341–351
7. Xu E, Li Y, Peng L et al (2021) An unknown fault identification method based on PSO-SVDD in the IoT environment. AEJ Alex Eng J 60(4):4047–4056
8. Qu J, Shi C (2021) A multi-sensor data fusion method for intelligent aging condition identification of viscoelastic sandwich structure. IEEE Access 9:63029–63042
9. Zhang J, Zhang Q, Qin X et al (2021) An intelligent fault diagnosis method based on domain adaptation for rolling bearings under variable load conditions. Proc Instit Mech Eng C J Mech Eng Sci 235(24):8025–8038
10. Aly M, Rezk H (2021) An efficient fuzzy logic fault detection and identification method of photovoltaic inverters. Comput Mater Contin 67(2):2283–2299
11. Luo Z, Zhou Y, Li Y et al (2022) Intelligent identification method of sedimentary microfacies based on DMC-BiLSTM. Geophys Prospect Petrol 61(2):253–261
12. Tian Y, Cai F (2022) Fault identification simulation of circuit inspection element based on FR-CNN algorithm. Comput Simul 2022(5):70–84

Rotating Machinery Fault Diagnosis Based on Residual Dense Network with Multi-branch Channel Attention Mechanism

Shuai Wu

Abstract A diagnosis model for rotating machinery faults, called RDB-MBCAM-CNN, based on a residual dense network with a multi-branch channel attention mechanism is proposed to address the poor fault recognition rate on a dataset of ten types of rolling bearing and gear vibration data due to the inability of shallow machine learning models to extract deep features from vibration signal data. This method is based on convolutional neural networks, with a lightweight multi-channel attention mechanism designed to reduce the computation parameter and increase the expression ability of key features. Additionally, it merges deep and shallow features and introduces the idea of a residual dense network by designing residual dense modules to enhance the expression ability of convolutional features. Experimental results show that compared to traditional lightweight CNN and attention mechanism CNN, this model has significantly improved fault recognition accuracy.

Keywords Rolling bearings · Attention mechanism · Residual dense network · Convolutional neural network

1 Introduction

This chapter proposes to apply the backpropagation process of convolutional neural networks (CNN) to fault recognition, highly integrating the entire process of feature extraction, feature processing, and pattern recognition [1]. Feature extraction and processing are achieved through convolutional calculations, and classification is achieved through fully connected layers. Due to the limited sample size of the fault diagnosis dataset and the introduction of parameter and computational complexity with deep CNN network structures, a lightweight CNN is designed to reduce computational and parameter complexity. However, under the condition of limited samples,

S. Wu (✉)
School of Mechanical and Electrical Engineering, Zhengzhou University of Light Industry, Zhengzhou 450002, China
e-mail: 546439793@qq.com

S. Yadav et al. (eds.), *Energy Power and Automation Engineering*, Lecture Notes in Electrical Engineering 1118, https://doi.org/10.1007/978-981-99-8878-5_47

CNN tends to experience feature degradation and poor generalization performance as the network becomes deeper. To enhance the expression ability of convolutional features, this study introduces the calculation concept of residual dense networks and self-attention mechanisms, strengthens the expression of key features, and integrates deep and shallow features [2, 3]. In summary, this chapter designs a multi-branches channel attention mechanism (MBCAM) to achieve key feature attention for rolling bearing fault data, introduces residual dense blocks (RDB) to adaptively integrate deep and shallow features to avoid feature degradation, and proposes a multi-branches channel attention mechanism residual dense block convolutional neural network model (MBCAM-RDB-CNN). Experimental results show that compared with traditional machine learning methods and other deep learning methods, the proposed method has better performance. This method is of practical significance for improving the accuracy and efficiency of rotating machinery fault diagnosis.

2 Network Structure

2.1 Multi-branch Channel Attention Mechanism

The convolutional kernel extracts features from the vibration signals of rolling bearings through the calculation of weight sharing. In the process of calculation, small convolutional kernels can obtain local deep features of the fault data, while large convolutional kernels can obtain global deep features of the fault data. The original form of the fault signal sample is 1×1200. To facilitate convolutional calculation, we convert it into an input form of 30×40 [4]. In order to adaptively obtain deep features of fault data comprehensively, the specific calculation process of MBCAM is as follows:

First, the multi-branch structure is reflected through multiple convolutional kernels. This method cannot only obtain global and local deep information but also adaptively fuse the results of multiple branch calculations. Secondly, attention mechanisms can be applied to capture information that effectively integrates results and improves the expression ability of deep information. Finally, a Softmax attention mechanism is introduced to adaptively allocate weights to different branches and obtain the final calculation results of MBCAM. Figure 1 shows the structural diagram of MBCAM, and the calculation process is as follows:

(1) Multi-branch fusion

Different sizes of convolutional kernels are used to extract features from the vibration signals of rolling bearings. The information input dimension is $H \times W \times C$, where C is the number of channels, H is the height, and W is the width. In this paper, two types of convolution and sizes are 3×3 and 5×5 (the discussion of the optimal combination is presented in Sect. 3). The calculation method based on deep convolution is applied to reduce the number of calculation parameters. The

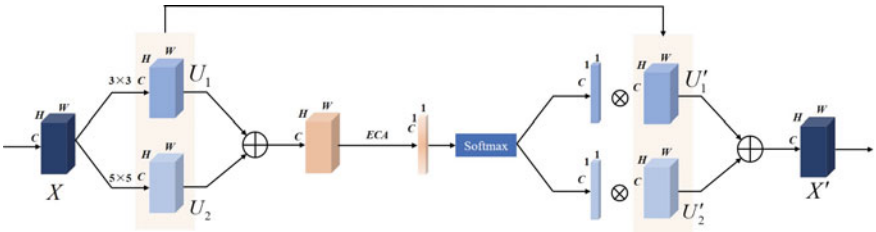

Fig. 1 MBCAM structure

calculation steps of the two convolutions are as follows:

$$\tilde{F} : X \rightarrow U_1 \in R^{H \times W \times C} \tag{1}$$

$$\hat{F} : X \rightarrow U_2 \in R^{H \times W \times C} \tag{2}$$

After completing the deep convolution, batch normalization (BN) is used to maintain the same parameter distribution, and the rectified linear unit (ReLU) function is applied to enhance the nonlinear expression ability of the data. In order to adaptively merge the calculation results of multiple branch convolutions, this is achieved by element-wise addition. The calculation is as follows:

$$U = U_1 + U_2 \tag{3}$$

(2) Lightweight channel attention mechanism

In the squeeze and excitation (SE) method, multi-layer perceptron (MLP) is used to achieve information interaction between channels, and then, a sigmoid function is used to capture the weight of each channel [5]. However, studies have shown that MLP is inefficient and introduces a large number of parameters in the calculation process. In order to streamline the calculation process, this paper introduces efficient channel attention (ECA), which uses a one-dimensional convolution to reduce the attention calculation parameters and enhance the information interaction between channels. Figure 2 shows the structure of ECA, and the specific attention calculation process is as follows.

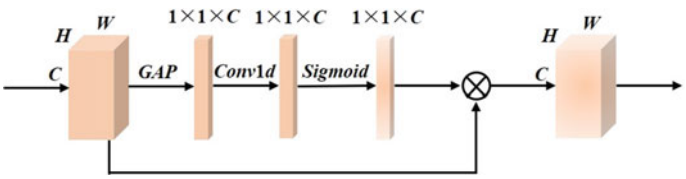

Fig. 2 ECA structure

Using global average pooling (GAP) to obtain feature information of the overall channel:

$$s_{ac} = \frac{1}{H \times W} \sum_{i=1}^{H} \sum_{j=1}^{W} U_c(i, j) \tag{4}$$

After applying GAP, the calculation method of one-dimensional convolution is as follows:

$$w = \text{Sigmoid}(\text{conv1}\, d(s_{\text{ac}}, k)) \tag{5}$$

During the calculation process, the convolution kernel for one-dimensional calculation needs to be determined. In ECA, there needs to be a nonlinear relationship between the one-dimensional convolution kernel size k and the channel C. We use an exponential function with a base of 2 to represent the nonlinear relationship:

$$C = 2^{(\gamma \cdot k - b)} \tag{6}$$

$$k = \psi(C) = \left| \frac{\log_2(C)}{\gamma} + \frac{b}{\gamma} \right|_{\text{odd}} \tag{7}$$

"Odd" represents the nearest odd number. Padding is used before and after one-dimensional convolution to maintain the same number of channels. In this work, "b" is combined with "2".

(3) Soft attention mechanism

To achieve adaptive fusion of different branches, Softmax soft attention operation is applied to allocate weights for different branches, so that the attention mechanism calculation process can adaptively select the emphasis calculation of convolution branches.

$$a_c = \frac{e^{A_c w}}{e^{A_c w} + e^{B_c w}} \tag{8}$$

$$b_c = \frac{e^{B_c w}}{e^{A_c w} + e^{B_c w}} \tag{9}$$

Here, "a" and "b" are attention vectors, A_c is the c-th row of matrix A, and ac is the c-th element of vector "a". Similarly, B_c and b_c. Where $a_c + b_c = 1$, the final feature calculation method is as follows:

$$U_1\prime = a_c \cdot U_1 \tag{10}$$

$$U_2\prime = b_c \cdot U_2 \tag{11}$$

$$X\prime = U_1\prime + U_2\prime \qquad X\prime \in R^{H\times W\times C} \tag{12}$$

2.2 Classification Network for Fault Vibration Signals

In this paper, we use the MBCAM mechanism to obtain effective features that affect the diagnostic classification performance of faults. However, due to the small size of the data samples, deep networks can easily cause feature degradation, resulting in poor recognition ability. In this work, the RDB is introduced, which achieves the fusion of different convolution features through residual connections, effectively avoiding feature degradation. At the same time, the RDB is combined with MBCAM to construct the RDB-MBCAM module, and we use MBCAM instead of convolution calculation in RDB. In order to achieve channel uniformity, we introduce point convolution calculation. In this paper, the network (RDB-MBCAM) applied to rolling bearing fault recognition is calculated as follows:

(1) The original fault vibration signal of size 1×1200 is converted into size 30×40 for convolution processing, and single-channel fault vibration signals are deep extended using point convolution. Due to the small sample size of fault vibration signals, too few convolution kernels cannot fully extract deep features, and too deep convolution kernels will bring huge parameter quantity. In this paper, the convolution kernel channel number is set to 20 and remains unchanged.
(2) The RDB-MBCAM block is applied to achieve deep feature extraction and feature fusion of fault vibration signals.
(3) The maximum pooling calculation method is applied to compress the output dimension, and two fully connected layers are used to establish the mapping relationship between the feature space and the label space. The specific network parameters are shown in Table 1, and the network classification structure diagram is shown in Fig. 3.

2.3 Network Training Hyperparameters

In the training of RDB-MBCAM, after pre-training of hyperparameters, the following detailed settings were made: batch training size of 20, 500 training iterations, cross-entropy loss function for error calculation and backpropagation, and Adam optimizer for optimizing the deep network. Ten different vibration signal categories contain a total of 1000 samples, randomly selecting 800 as the training set and 200 as the test set. Accuracy, precision, and recall are used to evaluate the classification performance of the model [6], and the average of 20 results is taken as the final classification result. The formulas for calculating performance metrics are as follows:

Table 1 Fault diagnosis network-specific parameters (RDB-MBCAM)

No	Calculation type	Kernel number	Kernel stride	Padding	Input size	Output size
1	Point Conv 1	1 × 1	1	0	30 × 40 × 1	30 × 40 × 20
2	MBCAM	3 × 3/5 × 5	1	1/2	30 × 40 × 20	30 × 40 × 20
3	Point Conv 2	1 × 1	1	0	30 × 40 × 40	30 × 40 × 20
4	MBCAM	3 × 3/5 × 5	1	1/2	30 × 40 × 20	30 × 40 × 20
5	Point Conv 3	1 × 1	1	0	30 × 40 × 60	30 × 40 × 20
6	MBCAM	3 × 3/5 × 5	1	1/2	30 × 40 × 20	30 × 40 × 20
7	Point Conv 4	1 × 1	1	0	30 × 40 × 80	30 × 40 × 20
8	MaxPool	2 × 2	2	0	30 × 40 × 20	15 × 20 × 20
9	FC 1	–	–	–	6000 × 1	128 × 1
10	FC 2	–	–	–	128 × 1	10 × 1

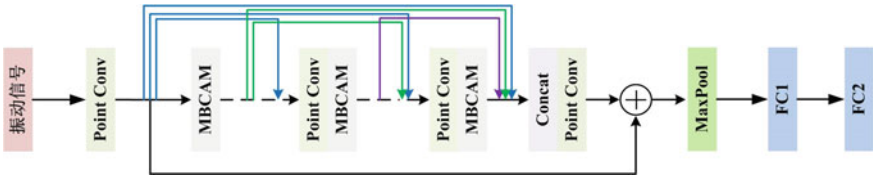

Fig. 3 Network structure diagram for fault vibration signal identification of rolling bearings

$$\text{Accuracy} = \frac{\text{TP} + \text{TN}}{\text{TP} + \text{TN} + \text{FN} + \text{FP}} \tag{13}$$

$$\text{Precision} = \frac{\text{TP}}{\text{TP} + \text{FP}} \tag{14}$$

$$\text{Recall} = \frac{\text{TP}}{\text{TP} + \text{FN}} \tag{15}$$

where TP represents true positive, FP represents false positive, TN represents true negative, and FN represents false negative.

3 Results and Discussion

This article uses the bearing data from Case Western Reserve University (CWRU) to obtain the vibration data of the drive end (DE) and fan end (FE) under ten operating conditions, including ball fault (BF1, BF2, BF3), inner race fault (IRF1, IRF2, IRF3), outer race fault (ORF1, ORF2, ORF3), and normal state (*N*), with a load of 1 hp, a speed of 1772 r/min, and a sampling frequency of 12 kHz, targeting the collection of three types of damage sizes of 0.007–0.021 inches. In order to establish a rolling bearing fault recognition model, we first constructed a dataset, with 1200 sampling points as a fault sample, obtaining 100 samples for each fault category based on the CWRU dataset, and a total of 1000 samples for the data of ten categories.

In order to further demonstrate the effectiveness of the RDB-MBCAM network in recognizing fault vibration signals of rolling bearings, we compared the RDB-MBCAM network with other learning models. Due to the limited amount of fault vibration signal data used in this paper, deep network structures would introduce more parameters and computations, which increases the difficulty of classification. Therefore, we chose lightweight shallow deep learning networks for comparison, including LeNet 5, ShuffleNet V1, ShuffleNet V2, MobileNet V1, MobileNet V2, and AlexNet. We combined the above models with MBCAM, replacing the convolutional calculation process in the model. Table 2 shows the diagnostic results of different classification models. It can be seen that in the lightweight networks, ShuffleNet V1, ShuffleNet V2, MobileNet V1, and MobileNet V2 achieved satisfactory classification performance. Among them, MobileNet V2 achieved 99.30% accuracy, 99.34% precision, and 99.35% recall in the diagnosis of fault vibration signals in the motor end, and 99.10% accuracy, 99.09% precision, and 99.07% recall in the diagnosis of fault vibration signals in the fan end. However, LeNet 5 network had poor classification performance due to its shallow network structure, which could not fully obtain important features that affect classification performance. Furthermore, AlexNet, VGG 11, and ResNet 18, due to their relatively deep network structure, may lead to feature degradation during the extraction process of fault vibration signals in rolling bearings, resulting in a significant decrease in diagnostic accuracy in both motor and fan ends. Finally, in the performance comparison of multiple classification models, RDB-MBCAM achieved the best classification performance.

4 Conclusions

This paper proposes a novel method for rotating machinery fault diagnosis by applying a multi-branch channel attention mechanism (MBCAM) and a residual dense convolutional network (RDB-CNN). The MBCAM-RDB-CNN model successfully achieves accurate fault diagnosis by effectively capturing important features in vibration signals. The proposed method is extensively evaluated on the CWRU fault dataset and compared with other popular fault diagnosis methods.

Table 2 Comparison of diagnostic results of different classification models

Model	Drive end			Fan end		
	Accuracy	Precision	Recall	Accuracy	Precision	Recall
LeNet 5-MBCAM	95.55 ± 2.44	95.83 ± 2.08	96.29 ± 2.14	95.65 ± 1.53	95.73 ± 1.45	96.29 ± 1.40
AlexNet-MBCAM	96.65 ± 1.78	96.84 ± 1.52	97.19 ± 1.45	96.70 ± 1.63	96.73 ± 1.52	97.20 ± 1.40
ShuffleNet V1-MBCAM	99.15 ± 1.09	99.21 ± 1.01	99.22 ± 100	99.30 ± 0.97	99.36 ± 0.87	99.36 ± 0.89
ShuffleNet V2-MBCAM	98.90 ± 0.97	98.99 ± 0.87	98.92 ± 0.94	98.80 ± 1.01	98.89 ± 0.92	98.81 ± 0.99
MobileNet V1-MBCAM	98.90 ± 1.39	98.95 ± 1.24	98.91 ± 1.29	98.90 ± 1.02	99.05 ± 0.86	98.92 ± 1.00
MobileNet V2-MBCAM	99.30 ± 0.92	99.34 ± 0.86	99.35 ± 0.87	99.10 ± 1.30	99.09 ± 1.20	99.07 ± 1.19
RDB-MBCAM	99.90 ± 0.31	99.91 ± 0.27	99.89 ± 0.33	99.85 ± 0.49	99.87 ± 0.41	99.83 ± 0.54

Experimental results demonstrate that the MBCAM-RDB-CNN method outperforms other methods in terms of accuracy and robustness.

References

1. Wang MH, Lu SD, Hsieh CC et al (2022) Fault detection of wind turbine blades using multi-channel CNN. Sustainability 14(3):1781
2. Feng X, Zhao G, Wang Y, Gao D, Ding H (2023) Fault diagnosis method based on the multi-head attention focusing on data positional information. Measur Control 56(3–4):583–595
3. Wang C, Zhu G, Liu T, Xie Y, Zhang D (2023) A sub-domain adaptive transfer learning base on residual network for bearing fault diagnosis. J Vibr Control 29(1–2):105–117
4. Wang T, Chen C, Dong X, Liu H (2023) A novel method of production line bearing fault diagnosis based on 2D image and cross-domain few-shot learning. Appl Sci 13(3):1809
5. Zhong C, Jiang Y, Wang L, Chen J, Zhou J, Hong T, Zheng F (2023) Improved MLP energy meter fault diagnosis method based on DBN. Electronics 12(4):932
6. Mian T, Choudhary A, Fatima S (2023) Vibration and infrared thermography based multiple fault diagnosis of bearing using deep learning. Nondestruct Test Evaluat 38(2):275–296

Automatic Generation and Audit Method of Substation Five-Prevention Logic Based on Typical Interval Graphization

Yanan Zhang, Jie Wang, Xiong Pan, Xiaocong Kan, Shaoping Wang, Chennan Xu, and Pengfei Kou

Abstract The five-prevention logic is crucial for preventing misoperation in substations. The writing and audit of the existing five-prevention logic rely on manual labor, with low efficiency and security risks. Therefore, this paper proposes an automatic generation and audit method of substation five-prevention logic based on typical interval graphization. A database containing device names and circuit information is developed, and two core algorithm modules, topology analysis, and logic generation are established. Moreover, this method is integrated into the anti-misoperation system to achieve standardized and centralized management of the five-prevention ledger and logic for each substation. In addition, it also has the function of intelligent inspection and report output with five-prevention logic. The actual engineering application results show that the system has high accuracy, and the debugging time has been reduced from 6 h manually to 1 min. This method can assist in the intelligent construction of substations.

Keywords Typical interval · Five-prevention logic · Automatic generation · Topological analysis

1 Introduction

The substation anti-misoperation system is one of the important components of power system operation management, which can effectively avoid personnel injury, equipment damage, and even power outage accidents caused by misoperation [1–3]. With the expansion of the power grid scale and the increasing complexity of the power system, the logical formulas in the anti-misoperation system need to be frequently changed and regularly checked and audited to ensure accuracy [4]. The logic formulas

Y. Zhang · J. Wang · X. Pan · X. Kan · S. Wang
Guangzhou Power Supply Bureau of Guangdong Power Grid Co., Ltd, Guangzhou 510000, China

C. Xu (✉) · P. Kou
State Key Laboratory of Power Transmission Equipment and System Security and New Technology, Chongqing University, Chongqing 400044, China
e-mail: xuchennan@cqu.edu.cn

S. Yadav et al. (eds.), *Energy Power and Automation Engineering*, Lecture Notes in Electrical Engineering 1118, https://doi.org/10.1007/978-981-99-8878-5_48

of existing substation anti-misoperation systems are usually manually written, which is inefficient and prone to errors and omissions, posing certain safety hazards [5, 6].

In order to improve the efficiency and accuracy of writing five-prevention logic, researchers have carried out a lot of work. An et al. design a mobile client for anti-misoperation locking, which break through the space and time limitations of the locking system application. Yuanshuai et al. [7] split the formula of the logic to be accepted and the standard anti-error logic in the five-prevention logic of electric power, improving the legibility of the five-prevention logic formula. Yongming [8] proposed and implemented a secondary equipment error prevention technology based on the collaboration of error prevention main and substations, establishing error prevention logical relationships between equipment and between substations. Jinghuai et al. [9] proposed a key technology for integrated error prevention logic formula generation for remote scheduling problems.

To further improve the efficiency and accuracy of writing five-prevention logic, this paper proposes an automatic generation and audit method of substation five-prevention logic based on typical interval graphization. The database is developed based on the device name and circuit information, and the topology analysis algorithm module and logic generation algorithm module are established, which are integrated in the substation anti-misoperation system. In addition, standardized naming rules for defining and managing typical intervals as well as standardized five-prevention rules for defining interval members are created, realizing standardized and centralized management of the five-prevention ledger and logic for each substation. And it has the function of intelligent inspection and output inspection reports for the substation's five-prevention logic.

2 Automatic Generation and Audit of Five-Prevention Logic Based on Typical Interval Graphization

Eliminating misoperation has always been a key task for substations. In the substation, the five-prevention logic management, unlock management, typical operation ticket management, and other measures are used to prevent misoperation [10]. The writing of the five-prevention logic is crucial in the five-prevention logic management of substations. And it needs to meet the following principles: preventing incorrect opening and closing of circuit breakers, preventing on-load opening and closing of isolation switches, preventing live hanging of grounding wires or live closing of grounding isolators, preventing power supply with grounding isolators or ground wires, and preventing accidental entry into the intervals [11].

In the substation, a part composed of the incoming line, the main transformer and the outgoing line, etc., is called an interval. Typical intervals include all possible types of device under the corresponding wiring method. The typical interval model

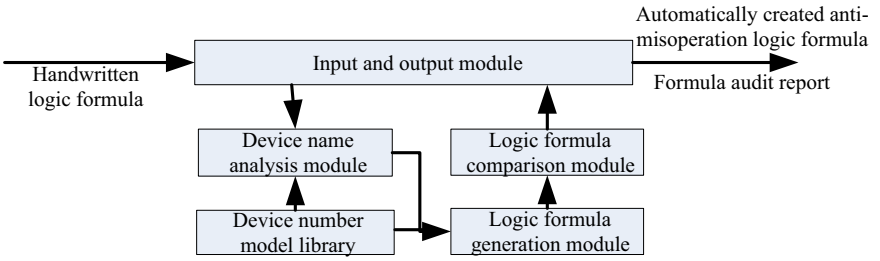

Fig. 1 Five-prevention logic generation and audit process

is an important step in generating the five-prevention logic, which refers to independently modeling the primary and secondary device involved in substation misoperation prevention according to the interval [12]. The generation and audit process of the five-prevention logic is shown in Fig. 1, which mainly includes device number model definition, device name import analysis, model logic formula calculation, logic formula comparison, and necessary input and output.

The device name model in this article is shown in Table 1. The model adopts the table format which is easy to edit and add and can be used for typical and atypical wiring. The two core algorithm modules of the model are the device name analysis module and the logical formula generation module. The device name analysis module analyzes specific device names and matches them with specific members of the model. The logical formula generation module automatically creates error proof logical formulas for device members based on the logical formula definitions of model members and the analysis results of device names.

Taking a typical interval line wiring method consisting of breaker, bus isolator, line isolator, busbar side grounding isolator, outgoing line side grounding isolator, and line grounding isolator as an example, as shown in Fig. 2. In the modeling process, the user first imports the device name ledger, namely 201, 2011, 2013, 2013D, 2011D, and 2015D. Then start the device name analysis module, scan and match the device templates in Table 1 one by one. Such as, the name formula for a breaker is "20?", and the question mark represents any number, which means "3 digits starting with 20". So the 201 device is successfully identified as a breaker. The name formula for the bus isolator is "breaker's number 1", which means "breaker's name formula plus 1". The breaker is known as 201, then the 2011 device successfully recognizes it as the bus isolator. And so on until all devices are successfully matched.

In the logic formula generation module, device logic formulas will be automatically created. For example, the logical formula for opening the bus isolator is " breaker = 0, busbar side grounding isolator = 0, outgoing line side grounding isolator = 0", and it is calculated that the breaker is 201, the busbar side grounding isolator is 2011D, and the outgoing line side grounding isolator is 2013D. The standard logical formula can be obtained by substituting it into the formula: 2011 opening: 201 = 0, 2011D = 0, and 2013D = 0.

Table 1 Example of device name model

Device	Device name formula	Misoperation prevention logic formula
Breaker	20?(number)	Opening: bus isolator = 0, line isolator = 0 + bus isolator = 1, line isolator = 1
		Closing: bus isolator = 0, line isolator = 0 + bus isolator = 1, line isolator = 1
Bus isolator	Breaker's number 1	Opening: breaker = 0, busbar side grounding isolator = 0, outgoing line side grounding isolator = 0
		Closing: breaker = 0, busbar side grounding isolator = 0, outgoing line side grounding isolator = 0, line isolator = 0
Line isolator	Breaker's number 3	Opening: breaker = 0, busbar side grounding isolator = 0, outgoing line side grounding isolator = 0, line grounding isolator = 0
		Closing: breaker = 0, busbar side grounding isolator = 0, outgoing line side grounding isolator = 0, line grounding isolator = 0
Busbar side grounding isolator	Bus isolator's number D	Opening: breaker = 0, bus isolator = 0
		Closing: breaker = 0, bus isolator = 0
Outgoing line side grounding isolator	Line isolator's number D	Opening: breaker = 0, line isolator = 0
		Closing: breaker = 0, line isolator = 0
Line grounding isolator	Breaker's number 5D	Opening: line isolator = 0
		Closing: line isolator = 0

3 Software Implementation

3.1 Topology Analysis

By conducting topology analysis on the wiring diagram, the graphical topology can be obtained. According to the "interval device type table", "backup line device list" and "graph Mod file" in the five-prevention system gradually obtain "bus connection point, starting device", "transformer", "identify bypass bus and corresponding bypass isolator", and "find all intervals" through breadth-first search algorithm. Based on the identification information "interval device type table", identify the intervals and ultimately generate the substation graphical topology as shown in Fig. 3.

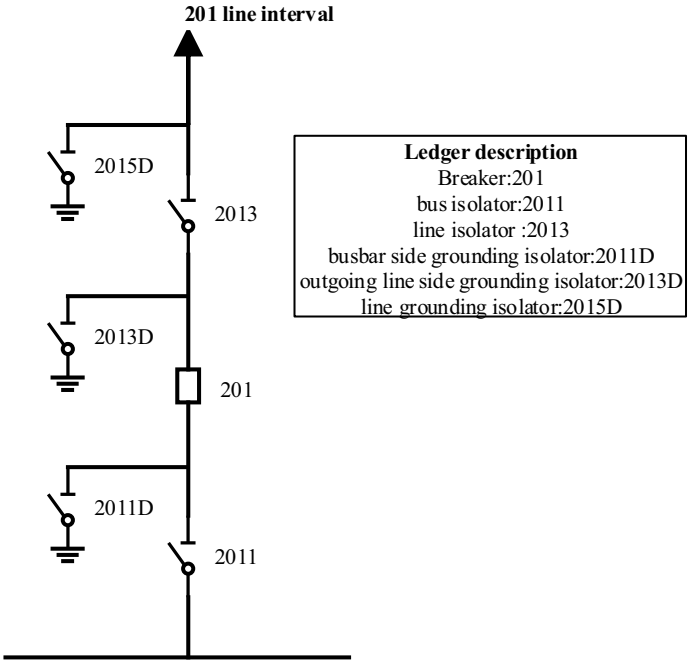

Fig. 2 Typical interval line wiring diagram

3.2 Logic Generation

The logic generation module mainly generates formulas that meet the five-prevention logic, and the objects generated by the logic are isolator, grounding isolator, two state car, and three state car. The logic generation state only has open or closed (0 or 1), only the status bits are judged, and no prompt bits are involved. An example is shown in Fig. 4.

Design implementation of logic generation is divided into two parts, one part using breadth-first search algorithm, the other part using the results of topology analysis for analysis.

3.3 Breadth-First Search Algorithm

During the access process, the breadth-first search algorithm will maintain a sequence Q that is gradually generated and emptied [13]. Taking the topology analysis of the substation as an example, all adjacent nodes that have not been accessed are sequentially accessed from the starting point in a tree structure and marked as accessed. Then add adjacent nodes of the visited node to the end of the sequence until sequence

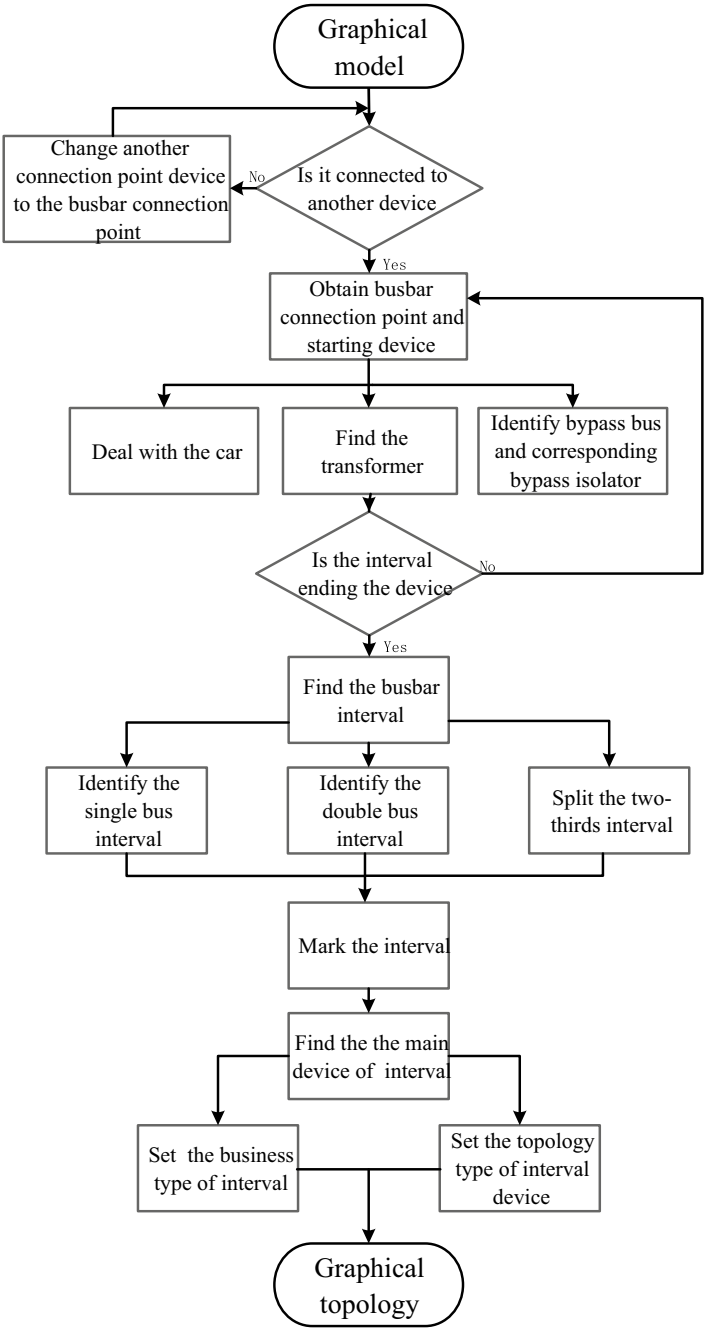

Fig. 3 Topology analysis flowchart

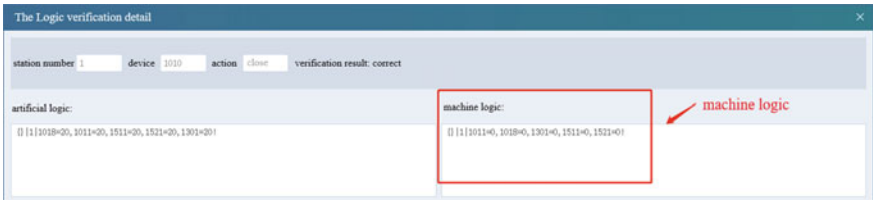

Fig. 4 Example of logical generation

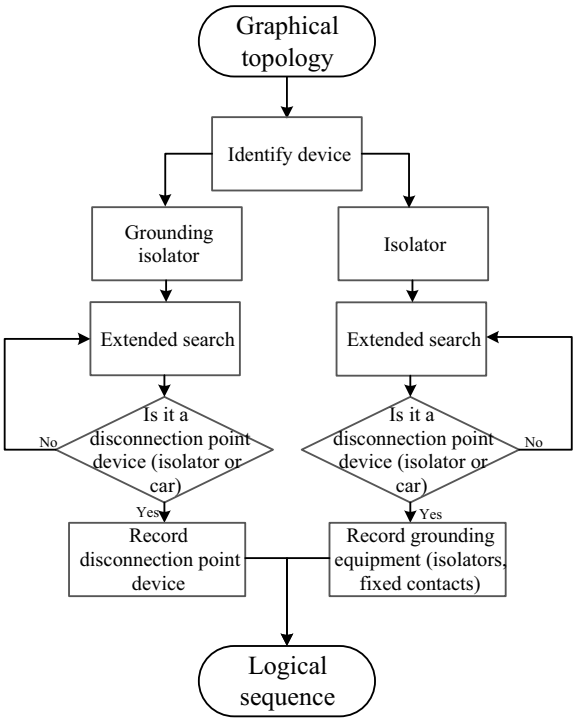

Fig. 5 Example of breadth-first search algorithm flowchart

Q is cleared. When a node that has not been accessed is found, it is used as the starting point to start dividing another topology; when there are no nodes that have not been accessed, the topology analysis is ended. An example is shown in Fig. 5.

3.4 Result Analysis After Topology Analysis

After topology analysis, different types of isolator logic are generated based on the interval type, as shown below.

1. Single *Y* and double *Y* intervals

According to the breakers in the interval, generate the logic for breaker to car.

2. Bypass bus intervals with the side isolator

Other side isolators on the busbar must be in the opening position, and bypass bus interval in the hot standby state. If no bypass bus interval, the logic is empty.

3. Double bus intervals with bus isolator

Operation logic: According to the interval information, get the side of bus isolator, generate logic for opposite side bus isolator and breaker to bus isolator.

Inverted busbar logic: Search whether there is a loop, according to the loop and the opposite side bus isolator generation bus isolator logic. Without the loop, inverted busbar logic cannot be generated.

4. Others

The car: According to the mapping relationship of car and breaker, generate the logic for breaker to car.

The isolator: Within the scope of the integral interval, based on breadth-first search algorithm, when encountering a isolator directly passing through or a breaker stopping, the logic of the breaker to the car is generated.

4 The System Framework

This system is developed using the Qt5.9.3 platform, mainly using C and C++. It is based on the SQLite database and assisted by the Redis database. The system uses B/S and C/S information architecture. The functional architecture of the system includes business layer, logic layer, and data layer, as shown in Fig. 6.

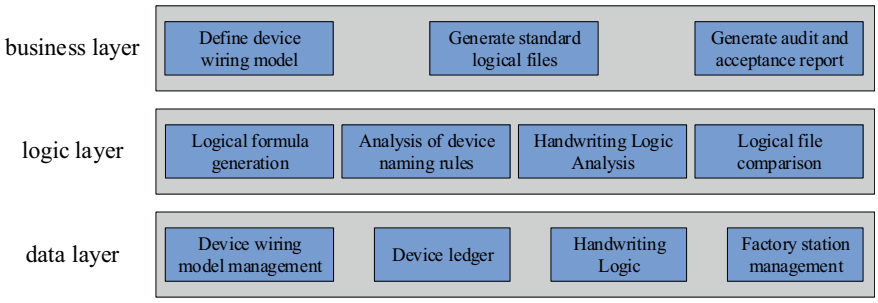

Fig. 6 Functional architecture diagram

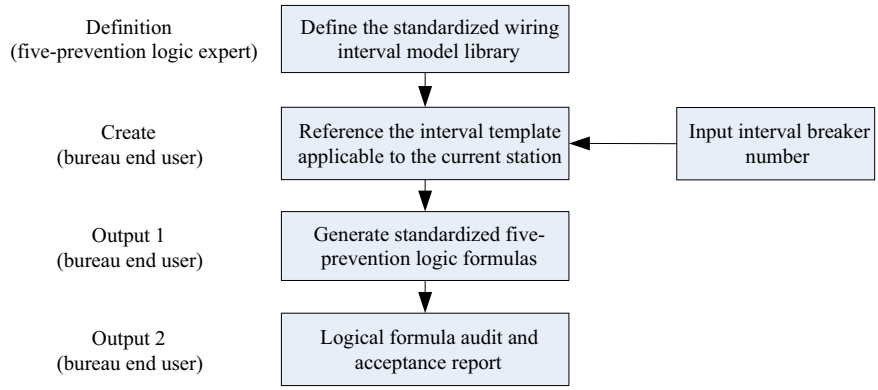

Fig. 7 System interface relations

4.1 The System Interface

The system interface simply supports Windows or LINUX operating system, its interface relations as shown in Fig. 7.

During logical acceptance, the system inputs are interval models and interval data, and outputs are standard logic formulas and acceptance reports. A set of standard wiring mode model base is established inside the system, in which the substation equipment naming rules and logic formula generation rules are defined, and the corresponding model is formulated according to the general wiring mode and equipment naming standard. The model library can be defined manually and does not need to be modified as long as the naming conventions and wiring methods do not change. When used, users only need to click "generate standardized logic" to create a standard logic file and click "start check" to generate a logic check report.

4.2 System Function Realization

The specific functions of the five-prevention logic automatic generation and audit method based on typical interval graphization are as follows:

1. Five-prevention data management for factory stations

Create a "five-prevention data" directory in the running directory. According to the jurisdiction of the operation and maintenance center, create subdirectories named after each substation under this directory. Copy the five-prevention equipment ledger files and primary wiring diagram files of each substation to the corresponding substation subdirectory. After the system starts, it can automatically load the substation data directory list and display it in a tree shape, achieving five-prevention data management for all substations in the jurisdiction area.

2. Define the standard interval model library

The interval error prevention logic model defines a group of related devices as a whole according to their roles and is not constrained by wiring relationships. When non-standard switch intervals occur, redefine the model. At this point, the user can add the roles in the model themselves. The use of roles and models to describe the internal relationships between primary equipment in substations can adapt to any complex wiring.

A standardized management system for five-prevention logic, with device number conventions as the core and interval error prevention logic models as the framework. Standardize error prevention logic model based on station management, and define interval error prevention logic models based on voltage level and interval type according to the wiring diagram of each station. Afterward, based on the wiring method of this station, the corresponding interval model in the model library is referenced, and the breaker number is filled in. The interval error prevention models of different voltage levels in this station are combined to form a complete standardized error prevention logic model.

3. Import device ledger

After adopting this method, the five-prevention system can recognize TXT format and EXCEL format ledger files and read the device numbers and scheduling numbers of all primary equipment in the station from the ledger files. Finally, based on the interval model of this station, automatic identification will be carried out, and equipment data that does not comply with the standardized model will be prompted.

4. Import the handwritten logic

The five-prevention system can import handwritten logic from other manufacturers for audit and acceptance. This system has developed a logical formula parser for each mainstream five defense manufacturer.

5. Generate standard logical file

The five-prevention system can generate standard five-prevention logic files based on the substation model and device ledger files and can be directly used in the microcomputer error prevention system.

6. Generate acceptance audit report

The five-prevention system integrates automatic analysis and verification tools for handwritten logic files. After importing handwritten logic and generating standard logic files, compare them with standardized logic files to generate an acceptance review analysis report for handwritten logic. The report includes situations such as missing, over writing, missing writing, and significant differences.

5 The Engineering Application

5.1 Practical Operation Case Analysis

Taking the logic of 1011 isolator on the side of the #1 main transformer line in Fig. 8 as an example, the typical primary interval corresponding to the 101 interval of #1 main transformer is "single bus line interval", and the device type corresponding to the 1011 isolator is "line side isolator". Then extract the rule of single bus line interval line side cutter latching (line side isolator is in bit), replace the device number, and obtain the logical locking conditions of 1011 isolator as described below.

1011 closing conditions: 10140 in open position, 101B0 in open position, 101T0 in open position, 501T0 in open position, 501 in open position, 51XB in open position, 101 in open position, and 51XBWM in closed position!

1011 opening conditions: 101 in open position!

Taking the closing operation of the 1011 isolator on the side of the # 1 main transformer line as an example, the operation task is analyzed as follows. The type of operation mode conversion is from open to closed, and the actual primary interval involved is 101 interval of # 1 main transformer, while the actual secondary interval involved is 110 kV line protection. # 1 main transformer 101 interval corresponding typical interval to single bus line interval, 110 kV line protection corresponding typical secondary interval of 110 kV line protection class. Using breadth-first search algorithm and topology analysis algorithm to match the corresponding expert database of switch opening/closing rules, the logical judgment result is shown in Fig. 9.

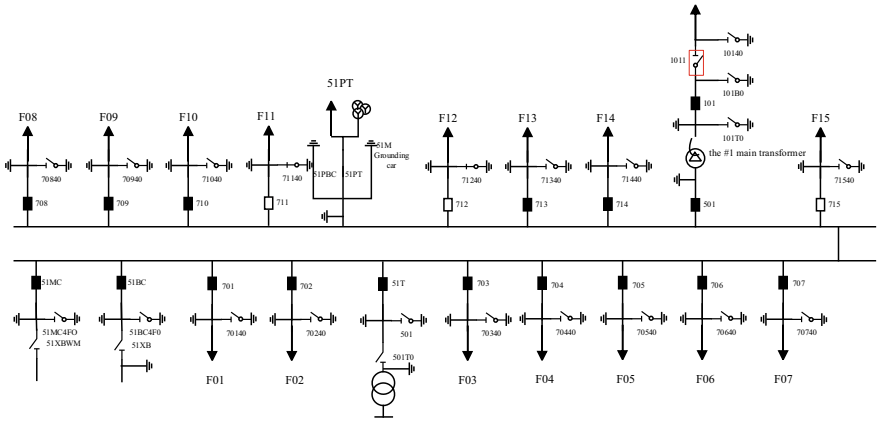

Fig. 8 Typical part wiring of 110 kV station

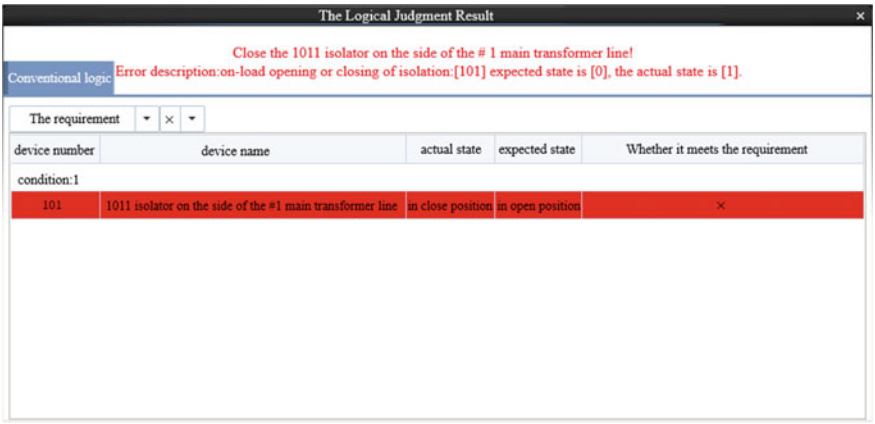

Fig. 9 Logical judgment result

5.2 Engineering Application Advantages

The intelligent substation has adopted this system in practical operation, taking it as an example and conducting practical investigation. The automatic generation and audit system for the five-prevention logic in substations described in this paper has effectively ensured the reliability, safety, and speed of the five-prevention logic generation since its operation and has also avoided the possibility of human error through real-time security constraints. The specific advantages are as follows:

1. Through the model defines the logical rules, model principle is simple to read, acceptance check is very convenient, and automatically generated logic file is credible, readable, and easy to understand.
2. The logical formula generated automatically through the model is concise and without redundancy, without any clerical errors. A correct model is equivalent to a correct logical formula.
3. It saves debugging time for construction personnel in the five-prevention project, saves costs and improves the overall quality of logical files. (The time required to complete the writing of the five-prevention logic for a certain substation by handwriting is about six hours, while the time required to automatically generate the logic using the method described in this paper is less than one minute.)
4. The system constructed by this method can be used to eliminate deep errors and redundancy hidden in handwritten logic for all five-prevention logic files globally.

6 Conclusion

This paper proposes an automatic generation and audit method of substation five-prevention logic based on typical interval graphization, develops a database based on device names and circuit information, and establishes two core algorithm modules: topology analysis and logic generation. Based on the feedback from on-site implementation, the system of this method constructed achieves machine replacing human to write and audit error prevention logic, saving time for error prevention logic writing, improving efficiency, and ensuring accuracy. At the same time, the application results prove the effectiveness of this method in practical engineering.

Acknowledgements Southern Power Grid Corporation Technology Project Funding GZHKJXM20200013 (080042K52200001).

References

1. Lin C, Xu Q (2022) Risk assessment of substation integrated anti-misoperation system considering human reliability. IEEE Trans Power Delivery 38:1462
2. An M, Xu X, Mao L et al (2019) Research and application of mobile online microcomputer anti-misoperation locking system based on ASP. NET web API framework. Proced Comput Sci 155:746–751
3. Xiankang J, Jianwen R, Yue C (2011) Design and implementation of intelligent anti-misoperation integrated operation order system for regional power grid. Electr Power Sci Eng 27(3):13
4. Liu Y, Gao H, Gao W et al (2016) Development of a substation-area backup protective relay for smart substation. IEEE Trans Smart Grid 8(6):2544–2553
5. Yang Y, Jiang HT, McLaughlin K, et al (2015) Cybersecurity test-bed for IEC 61850 based smart substations. In: Proceedings of the 2015 IEEE power and energy society general meeting. IEEE, pp 1–5
6. An M, Xu X, Lin W et al (2019) Research on mobile online microcomputer anti-misoperation locking system based on NFC technology. J Phys Confer Ser 1302(4):042061
7. Yuanshuai D, Jian C, Bin P (2015) A method of automatic generation of diagram-database-rules-order based on bay model. Autom Electr Power Syst 39(3):84–89
8. Yongming W (2020) Anti-misoperation technology of secondary devices for dispatching and control system of smart grid. Autom Electr Power Syst 44(14):94–100
9. Jinghuai L, Weimin M, Zeke L et al (2015) Safety anti-misoperation technology of remote operation of smart grid dispatching and control systems. Autom Electr Power Syst 39(01):60–240
10. Poisson P, Chinniah Y, Jocelyn S (2016) Design of a safety control system to improve the verification step in machinery lockout procedures: a case study. Reliabil Eng Syst Saf 156:266–276
11. Chen Y, Li H, Yang G et al (2023) A full-automatic test system for the intelligent substation based on GOOSE/SV signal simulation. J Phys Confer Ser 2488(1):012049
12. Li G, Huang W, Lin W et al (2019) Research on development and design of maintenance control system based on five-prevention. IOP Confer Ser Earth Environ Sci 252(3):032159
13. Zhang F, Lin H, Zhai J et al (2018) An adaptive breadth-first search algorithm on integrated architectures. J Supercomput 74:6135–6155

Design of a Multi-motor Control System for a Parallel Mechanism

Yanchao Wang, Hongxin Zhang, Liguo Tian, Zikang Xie, and Miao Sun

Abstract In this paper, a motion control system has been designed. The system is used to control twelve motors which drive a parallel mechanism by adjusting pulse width modulation (PWM) with a microcontroller. The motors are selected according to the characteristics of the parallel mechanism. And the dynamic model of the motor is established. Many related control experiments are done, and the control error is analyzed. It is shown that the motion control system designed in this paper can achieve more accurate control of the parallel mechanism experimentally.

Keywords Parallel mechanism · Control system · PWM · Multi-motor control

Y. Wang · H. Zhang (✉) · L. Tian · Z. Xie · M. Sun
Tianjin University of Technology and Education, Tianjin 300222, China
e-mail: zhxlixue@tute.edu.cn

Tianjin Key Laboratory of Information Sensing and Intelligent Control, Tianjin 300222, China

S. Yadav et al. (eds.), *Energy Power and Automation Engineering*, Lecture Notes in Electrical Engineering 1118, https://doi.org/10.1007/978-981-99-8878-5_49

1 Introduction

With the development of science and technology, artificial intelligence, and other related fields, the performance of parallel robots is more and more powerful, and its application is more and more extensive. At present, parallel mechanism is widely used in aerospace, industrial robots, and other related fields due to their advantages of fast running speed, high control accuracy, and high stiffness [1–3]. Parallel mechanisms perform tasks in complex and diverse environments and are faced with complex and dangerous environments. Therefore, the stability and safety of machine-parallel mechanisms perform tasks are crucial [4, 5]. In the complex motion process, how to control the rotation of each joint so that the parallel mechanism moves according to the prescribed trajectory is the key to ensuring that the robotics can run safely and smoothly and guarantee the successful completion of the work [6–8]. Therefore, this paper tries to establish a parallel mechanism model and design a control system according to the model to complete the parallel mechanism motion control.

In this paper, the parallel mechanism is named 3-RRR parallel mechanism, where 3 indicates the number of branches of the mechanism, "*R*" indicates the structure of the branch kinematic chain, and "RRR" means three rotating type joints on each branch chain. A multi-motor control system has been designed for this parallel mechanism.

2 Formatting the Title, Authors, and Affiliations

The 3-RRR parallel mechanism is shown in Fig. 1. The photograph of the parallel mechanism is shown in Fig. 2.

The 3-RRR parallel mechanism consists of a circular static plat pedestal, a top triangular static platform, and three support arms. The motion of the three arms is restrained because of the limitation with the circle and the triangle. In the case of improper control, the three arms will "fight" with each other, resulting in serious damage to the mechanism and motors. A motor is located at the connection between each support arm and the circular static platform. Each arm has three joints, where

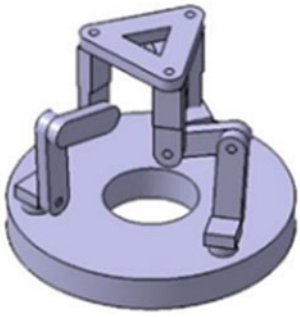

Fig. 1 Schematic of the 3-RRR parallel mechanism

Fig. 2 Photograph of the parallel mechanism

a motor is existed either. Therefore, the mechanism has twelve motors totally. The three support arms of the parallel mechanism are named *a*, *b*, and *c*. From top to bottom, the four motors in the support arm a are named motor *a*1, motor *a*2, motor *a*3, and motor *a*4; motors in the support arm *b* and support arm *c* are named in the same way as for support arm *a* as *b*1, *b*2, *c*1, *c*2, etc.

Take the support arm *a*1 as an example. The detailed structure of the 3-RRR parallel mechanism is shown in Fig. 3.

The parameters of the parallel mechanism are shown in Table 1. The parallel mechanism is constructed by 3D printing.

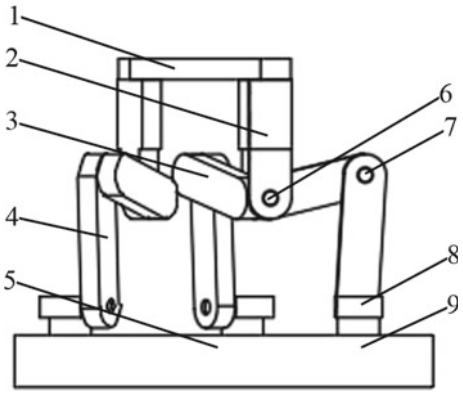

Fig. 3 Structure of the 3-RRR parallel mechanism (1—Top triangular static platform; 2—Support arm *a*; 3—Support arm *b*; 4—Support arm *c*; 5—Circular static plat pedestal; 6—Motor *a*1; 7—Motor *a*2; 8—Motor *a*3; 9—Motor *a*4)

Table 1 Parallel mechanism dimensions

Object	Data
Model weight	4 kg
Top triangle static platform side length	16 cm
The distance between the top triangle and the joint 6	13 cm
The distance between the joint 6 and the joint 7	12 cm
The distance between the joint 7 and the joint 8	15 cm
Circular static plat pedestal	36 cm

Fig. 4 Motor picture

According to parameters, the motor selected for this experiment is SPT55LV-320/35 kg high torque motor, which is shown in Fig. 4. The shape of the motor is cube, with the length is 0.4 cm, width is 0.2 cm, and height is 0.4 cm. The pulse control width is between 0.5 and 2.5 ms, the maximum angle is 300°, and the feedback pulse width is supported.

3 Multi-motor Control System Design

The multi-motor control system is mainly composed of controller, PWM driver, brushless DC motor, reducing gear, and feedback potentiometer to build closed-loop control, as shown in Fig. 5.

The function of brushless DC motor is to convert electrical energy into mechanical energy, and its mathematical model can describe its dynamic characteristics. The mathematical modeling of the brushless DC motor was carried out, and the dynamic model structure of the system was obtained, as shown in Fig. 6.

In the figure, U is the ideal signal instruction; r is armature resistance; L is armature inductance; J_M is the moment of inertia; K_E is the coefficient of back electromotive force: T_L is the torque exerted by load and other factors on the rotating shaft of the motor [9, 10].

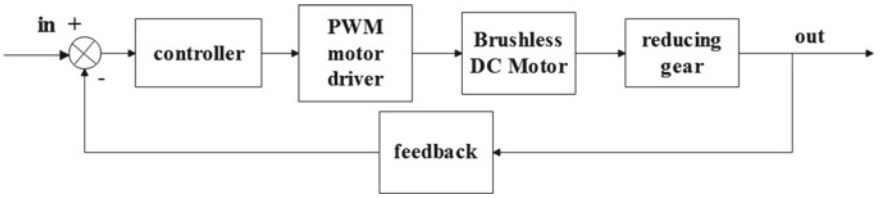

Fig. 5 Multi-motor control system structure

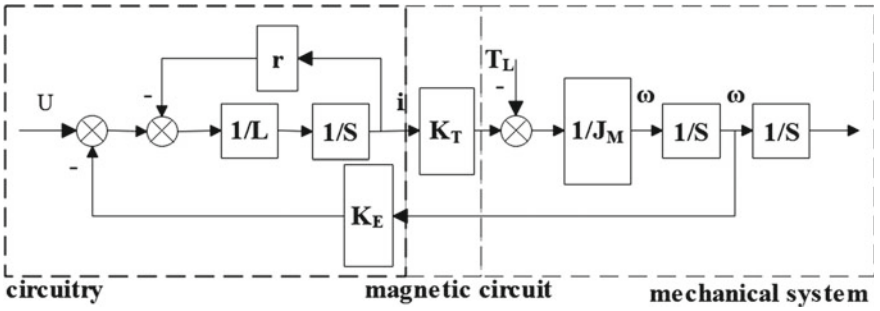

Fig. 6 Brushless DC motor structure

Therefore, the transfer function of a brushless DC motor can be written as follows:

$$\theta(s) = \frac{K_T}{s\left(J_M \mathrm{L}s^2 + J_M \mathrm{r}s + K_T K_E\right)} U(s) - \frac{\mathrm{L}s + r}{s\left(J_M \mathrm{L}s^2 + J_M \mathrm{r}s + K_T K_E\right)} T_L s \quad (1)$$

Because the brushless DC motor has a higher speed and is used with the reduction device, its transfer function is constant, as shown in Eq. (2):

$$\frac{\theta_m}{\theta} = \frac{1}{N} \quad (2)$$

In addition, the unit of rotation degree of the output motor is radian, which is converted into angle, as shown in Formula (3):

$$\delta = \frac{180}{\pi} \theta_m \quad (3)$$

The controller module only needs to change the voltage of the brushless DC motor to control the motor speed. The control strategy adopted in this paper is to change the duty ratio of PWM signal on the driver to realize the control of the motor. STM32F103 is used as the main control chip in this paper. The auto reload value of STM32 MCU clock is set to 2000. The pulse width of the selected motor is between 0.5 and 2.5 ms; therefore, the adjustable range is 2 ms. It is said that the control

accuracy of PWM is 1 μs. Hence, the motor can be controlled with 1 μs unit by PWM signal. The rotation angle of the selected motor is between 0° and 300°, so that the rotation control accuracy of the motor is 0.15°. 2 ms/300° ≈ 6, so the resulting adjusted PWM signal: is 1°/6 μs.

The program writing is mainly divided into two parts: the main program and the interrupt program. The interrupt program part consists of the initialization of general-purpose timer, initialization of PWM output, setting the number of PWM auto-load, the number of clock pre-division, etc. Since there are 12 motors controlled by the parallel mechanism, 12 sets of PWM output timers are needed. Therefore, the PWM control matrix A and angle matrix R are established. The control matrix is as follows:

$$\mathbf{A} = \begin{bmatrix} A_{10} & A_{20} & \cdots & A_{i0} \\ A_{11} & A_{21} & \cdots & A_{20} \\ \vdots & \vdots & \ddots & \vdots \\ A_{1j} & A_{2j} & \cdots & A_{ij} \end{bmatrix} \tag{4}$$

$$\mathbf{R} = \begin{bmatrix} R_{10} & R_{20} & \cdots & R_{i0} \\ R_{11} & R_{21} & \cdots & R_{20} \\ \vdots & \vdots & \ddots & \vdots \\ R_{1j} & R_{2j} & \cdots & R_{ij} \end{bmatrix} \tag{5}$$

where i represents the number of motors, j is the discrete time parameter of PWM signal, A_{ij} represents PWM value, and R_{ij} represents the integer part of the angular displacement of the motor rotation.

The first row of the two matrices is the initial state of the motor. PWM values range between 500 and 2500, corresponding to the range of motor between 0° and 300°.

It is specified here that an increase in PWM value means the motor rotates clockwise and a decrease means the motor rotates anticlockwise. The calculation formula (6) of A_{ij} is as follows:

$$A_{ij} = A_{i0} + 6 \times R_{ij} \tag{6}$$

4 Experiment

Each motor has been turned at initial angle, which is calculated in PWM value $Ai0$, in order to make the motors suit to the parallel mechanism. The relative angle $Ri0$ is set to 0 at the beginning of the parallel mechanism experiment. The initial parameters with $t = 0$ s are shown in Table 2.

Table 2 Parameters at the beginning

	R_{i0}	A_{i0} parameter
Motor a1	0	1638
Motor a2	0	1656
Motor a3	0	2124
Motor a4	0	2220
Motor b1	0	1638
Motor b2	0	1656
Motor b3	0	2124
Motor b4	0	2220
Motor c1	0	1638
Motor c2	0	1656
Motor c3	0	2124
Motor c4	0	2220

A 10-s motion of the parallel mechanism has been simulated. The relative motion angle of each motor is output with sample frequency of 25 Hz, as the simulated solution. In other words, a matrix R with 251 rows and 12 columns can be obtained. Afterward, the matrix A is calculated by using formula (3). As an example, the parameters at 4 and 10 s are shown in Table 3.

Through Tables 2 and 3, the calculated relative angular displacement (R_{ij}) and PWM (A_{ij}) values are integrated into matrix **R** and **A**, and the corresponding motor rotation is controlled by STM32. The results are shown in Fig. 7. The blue curve is the angular displacement data of each motor obtained by simulation. The orange curve

Table 3 Parameters at the time of 4 and 10 s

	Relative angular displacement (°)	R_{ij}	A_{ij}	Relative angular displacement (°)	R_{ij}	A_{ij}
Motor $a1$	0.0088	0	1638	21.8633	21	1512
Motor $a2$	9.7345	9	1602	27.8975	27	1494
Motor $a3$	22.3521	22	1992	7.7065	7	2082
Motor $a4$	32.0866	32	2028	35.604	35	2010
Motor $b1$	− 0.0625	− 1	1644	− 19.1147	− 20	1758
Motor $b2$	9.6037	9	1602	8.3573	8	1608
Motor $b3$	22.537	22	1992	31.2196	31	1938
Motor $b4$	32.1407	32	2028	39.577	39	1986
Motor $c1$	0.0536	0	1638	0.8321	0	1638
Motor $c2$	9.6597	9	1602	− 17.2279	− 18	1764
Motor $c3$	22.4941	22	1992	75.6553	75	1674
Motor $c4$	32.1538	32	2028	58.4274	58	1872

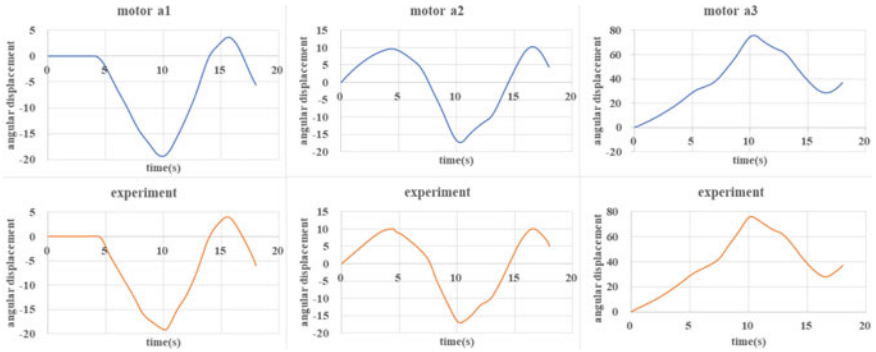

Fig. 7 Comparison of partial motor simulation and experimental results

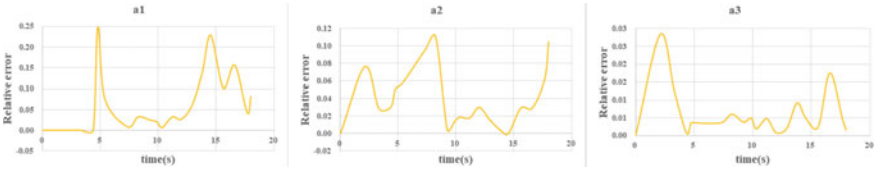

Fig. 8 Relative error of simulation and test

Table 4 Error rate of motor

Motor	$a1$	$a2$	$a3$	$a4$	$a5$	$a6$
Mean error (%)	5.79	2.84	0.44	0.38	0.81	1.09
Motor	$a7$	$a8$	$a9$	$a10$	$a11$	$a12$
Mean error (%)	1.49	0.42	5.40	5.93	0.71	0.28

is the angular displacement change of each motor obtained by the experiment. Due to external disturbance or sometimes unstable system current, there are some errors in the experiment, as shown in Fig. 8. The external load of each motor is different, so the average error rate of each motor is different. Table 4 shows the error rate of the motor.

5 Conclusion

In this paper, a multi-motor control system controlled by twelve motors is designed, the dynamic control model of the motor is built, and the simulation and control experiment are carried out. By calculating the control matrix **A** and **R**, the control of 12 motors is realized on the premise of ensuring the stable motion of the parallel

mechanism. Through error analysis, the control precision of the motor meets the requirements. It is proved that the control system is feasible to control twelve motors of parallel mechanism simultaneously. It lays the foundation for the future research of the multi-motor control method and lays the foundation for the future improvement of the multi-motor control system.

Acknowledgements This work was supported by the National Natural Science Foundation of China (No. 61971312), The Tianjin Natural Science Foundation under Grant (20JCZDJC00150), Tianjin Education Commission Scientific Research Projects (2021KJ010), Initial Scientific Research Projects from Tianjin University of Technology and Education (KYQD202222), and the Research and Innovation Project of Tianjin Graduate Students (No. 2022SKYZ301).

References

1. Sun Y (2022) Of mechanical arm structure design. Autom Mod Manuf Technol Equip 58(7):180–182
2. Hong ZJ (2023) Coal mine mechanical arm slot configuration design and kinematics characteristics of roadway analysis. J Coal Mine Mach 44(3):71–73
3. Zhang X, Zhang XL, He XL, Liu XM (2022) Forging manipulator hydraulic system design and simulation. J Forg Equip Manuf Technol 57(05):52–56
4. Zhang WM, Yang X, Zhao ZHJ, Hu CG, Zeng L (2022) Experiments at the end of the station's robotic arm actuator technology research. J Manned Space Flight 28(6):726–732
5. Sun ZL, Liu JC (2023) All airspace tracking strategy based on six degree of freedom parallel mechanism. J Measur Test Technol 50(02):53–56
6. Xu XJ, Hu ZF, Zhou JY, Cheng JG, Xie Q (2020) Six degrees of freedom parallel mechanism control system based on embedded design. J Electr Technol Appl 46–48(10):110–113
7. Chen QS (2019) Three degrees of freedom parallel mechanism modeling and static stiffness optimal design. Nanjing university of science and technology
8. Zhang FY (2021) Parallel back-to-back three level inverter system control strategy research. Harbin industrial university
9. Chen B (2023) Brushless dc motor double closed-loop control simulation. J Electr 31(6):30–34
10. Xie SH (2020) Brushless dc motor based on fuzzy PI control system modeling and simulation study. J Commun Power Supply Technol 5:72–73

Research on Influencing Factors and Typical Paths of Power Grid Unsafe Behavior

Xin Tian, Xinyang Han, and Xiaoling Jin

Abstract As the reliability and safety of technical systems and equipment continues to improve, the reliability of human–machine systems is increasingly dependent on human reliability. The safe state of objects is affected by the escalation of unsafe human actions, reducing the protective effect of objects. It is necessary to emphasize improving the management system of people's intrinsic safety behavior and comprehensively improve the safety level of the whole system on the basis of improving the intrinsic safety of equipment. Only then can the safety work of power enterprises reach a new level and truly eliminate any unsafe conduct. This paper selects the unsafe behaviors in power grid accidents as the research object. By studying the unsafe behaviors of people in 109 domestic and foreign power grid accidents, the semantic analysis method is used to extract and analyze the unsafe behaviors of people in power grid accidents. The influencing factors of power grid unsafe behavior are obtained, and combined with the logical relationship of the influencing factors, the generation path of power grid unsafe behavior is proposed, which provides a reference for improving the ability of power grid behavior management and control.

Keywords Power grid · Unsafe behaviors · Semantic analysis · Factors · Mechanism

1 Introduction

People are the most active factor in safe production. The "reliable output" of safety behavior can only be guaranteed by fundamentally improving people's safety capability and achieving a controllable, realizable, and efficient safety status. As an important part of the power system, the power grid, similar to other complex industrial systems, has new features such as automation, complexity, opacity, and fault tolerance. Human safety behaviors have a huge impact on the safe operation of the power grid. This paper will study the influencing factors of power grid unsafe behavior,

X. Tian (✉) · X. Han · X. Jin
State Grid Energy Research Institute Co., LTD, Beijing 102209, China
e-mail: 33405024@qq.com

S. Yadav et al. (eds.), *Energy Power and Automation Engineering*, Lecture Notes in Electrical Engineering 1118, https://doi.org/10.1007/978-981-99-8878-5_50

analyze the correlation between influencing factors and safe behavior, and analyze the typical generation path of unsafe behavior from the process of safe behavior, so as to provide theoretical and practical basis for power grid safety behavior control.

2 Unsafety Behaviors Research in Power Grid

The research history of human reliability (HR) and human error (HE) can be traced back to the 1950s. In terms of the development history of the safety discipline, the research of human factors, human reliability, and human error has made great progress in the late twentieth century and early twenty-first century, with constant new beginnings in theorization, basic methods, industrial application, and case analysis. Because of the subjective differences between people and the drastically different interactions with different environments, any small error can have very serious consequences. Despite relatively short history, domestic safety behavior research is developing rapidly. Literature [1] discusses the design of human–machine interaction of energy management system (EMS) in smart grid under the guidance of human factors engineering. It focuses on the analysis of key technologies of human–machine interaction. Literature [2] analyzes the power operation mode in depth and makes improvements from three aspects, namely situational environment evaluation, control mode, and CPC score. Thus, the uncertainty of the model is reduced. Literature [3] analyzes the characteristics of power system safety accidents and human safety characteristics. It provides the concepts of human error and human reliability for power system operation and analyzes the types, mechanisms, and various safety influencing factors of human error for power system operation in combination with the actual situation in power companies. Related literature [4] establishes a human safety influence factor model for power enterprises through literature review at home and abroad. Literature [5] proposes a human factor analysis and classification system suitable for power accidents in combination with the actual situation and characteristics of safe power generation, based on the human factor analysis and classification system of aviation safety accidents. Literature [6] summarizes the research status of electrical malfunction and the influence of people and things in malfunction and related preventive measures. Literature [7] focuses on analyzing the main human factors causing the misoperation of distribution network dispatching and expounding the specific technology and preventive measures of accident handling in distribution network dispatching operation. Literature [8] proposes the 24 model, in which the causes of accidents are divided into internal and external causes of accident organization, and the accident prevention measures are related to the accident mechanism. On the whole, with the focus on the human factors of various problems related to the specific technology of power system, the domestic research lacks the systematic and comprehensive research on the unsafe behavior in power systems.

3 Research on Factors Influencing Unsafety Behaviors in Power Grid

3.1 Text Analysis Method of Grid Operation Accident Report Based on Semantic Analysis

At present, accident case data is mainly stored in the form of accident report text. Semantic analysis technology belongs to the field of artificial intelligence. It is a modern advanced big data technology and a technology for natural language processing, which can effectively improve the quality and effect of work. The goal of semantic analysis is to effectively establish models and systems, achieve automatic semantic analysis of each language unit, and achieve a better understanding of text semantics. In this paper, the semantic analysis method is applied to the extraction of unsafe behavior influencing factors in power grid accident reports.

The natural language processing tool ICTCLAS is used to preprocess the text of the power grid operation accident report. Afterward, part-of-speech analysis is performed on all the terms in the accident report, and business template-driven entity discovery (BT) and entity significant factors (FBC) based on business characteristics are performed on the terms of each text in the power grid operation accident report collection. Method of calculation. The method calculates the formula for each term as follows:

$$\mathrm{BT}-\mathrm{FBC}(t_i) = \mathrm{BT}(t_i) * \mathrm{FBC}(t_i) = \mathrm{NT}_j(t_i) * \log(N/\mathrm{BC}(t_i)) \tag{1}$$

Among them: BT-FBC(t_i) represents the BT-FBC value of the current term t_i, which is equal to the product of the business template-driven entity discovery B$T(t_i)$ of the term t_i and the entity saliency factor IDF(t_i) based on business characteristics. Any term in accident report j can be calculated by entity discovery BT(t_i) and log(N/BC(t_i)). N represents the total number of all texts in the text collection, and BC(t_i) represents how many texts in the text collection have term t_i. Perform the above analysis on each term in the accident report collection to obtain the term BT-FBC value of the entire text. Then, use these BT-FBC values to build a vector space model for each text. After obtaining the feature vector of each accident report, HowNet is used to calculate the semantic similarity of words. HowNet's formula for calculating the semantic similarity between keywords is as follows:

$$\mathrm{Sim}(T_1, T_2) = \beta/(\beta + \mathrm{dist}(T_1, T_2)) \tag{2}$$

Among them: $T1$, $T2$ represent two sememes; dist(T_1, T_2) represents their path length; β is an adjustment parameter, representing the path length when the similarity is 0.5.

Let V_i and V_j be the feature word vectors of two different texts. $V_i = (t_{i1}, t_{i2}, t_{i3},\ldots, t_{im})$, $V_j = (t_{j1}, t_{j2}, t_{j3},\ldots, t_{jm})$, and the formula for calculating the semantic similarity of words between texts is defined as follows:

$$\text{TextSim}(V_i, V_j) = \alpha * \text{VectSim}(V_i, V_j) + (1 - \alpha) * \text{CosSim}(V_i, V_j) \tag{3}$$

Among them: α represents the weighting factor of the similarity between word vectors V_i and V_j, and its value is usually less than 1; VectSim(V_i, V_j) represents the semantic similarity between word vectors V_i and V_j, which is shown by the following formula:

$$\text{VectSim}(V_i, V_j) = \frac{1}{2}\left\{\frac{1}{m}\sum_{k=1}^{m}\max_{1\le l\le n}[\text{sim}(t_{ik}, t_{jl})] + \frac{1}{n}\sum_{l=1}^{n}\max_{1\le k\le m}[\text{sim}(t_{il}, t_{ik})]\right\} \tag{4}$$

Among them, Sim(t_{jl}, t_{ik}) represents the semantic similarity between keywords t_{jl} and t_{ik}, which is calculated by formula (2). Furthermore, CosSim(V_i, V_j) represents the cosine similarity between word vectors V_i and V_j, and the formula is as follows:

$$\text{CosSim}(V_i, V_j) = \left(\sum_{k=1}^{\delta}\text{TFIDF}(t_{ik})*\text{TFIDF}(t_{jk})\right) \Big/ \sqrt{\sum_{k=1}^{m}(\text{TFIDF}(t_{ik}))^2 * \sum_{l=1}^{n}\text{TFIDF}(t_{jk})} \tag{5}$$

Among them: δ refers to the number of occurrences of the same term in the quantities V_i and V_j. Based on the above steps, the similarity matrix of the accident report is obtained. Next, the similarity matrix is used for clustering. The direct K-means method of the CLUTO toolkit is used for text clustering. A similar method is used to analyze the power grid accident report obtained by collecting funds, and the causal factors and related data of the accident are summarized.

This study uses the text similarity measurement method of the vector space model and adopts the business template-driven entity discovery (BT) and the business feature-based entity significant factor (FBC) method to calculate the weight of the term in the vector. And the calculation is further based on the semantic similarity of words, which effectively avoids the inaccurate influence caused by only word frequency statistics. Then K-means clustering is used to determine the influencing factors of power grid human accidents with high similarity.

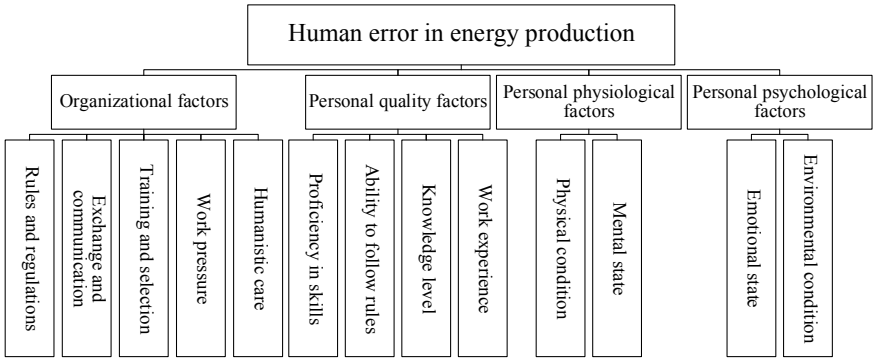

Fig. 1 Classification of factors of unsafe behaviors

3.2 Text Analysis Method of Grid Operation Accident Report Based on Semantic Analysis

This paper studies the 109 domestic and foreign power grid accidents collected by the text analysis method of power grid operation accident report using semantic analysis and extracts the influencing factors of unsafe behavior of the power grid. Factors influencing unsafe behaviors in power grids can be divided into two types: personal and organizational. According to the type, the factors are shown in Fig. 1.

Organizational factors

The factors of organizational unsafe behaviors include rules and regulations, exchange and communication with employees, employee training and selection mode, work pressure brought to employees, and humanistic care for employees.

Rules and regulations refer to safety regulations to be mandatorily followed by operators in energy production and various work instructions, codes, and guiding texts used by professionals. Rules and regulations will influence people's behaviors, and people's safety activities need to learn to adapt to the requirements of rules and regulations. However, "rigid compliance" with complicated and inhuman rules and regulations should be prevented.

Exchange and communication refers to the process of information transmission and exchange inside and outside the organization in oral or written form, formal or informal way. In terms of human factor organization, the key point is the exchange of safety information, two-way and effective communication between management and front-line staff, the management's listening to front-line safety suggestions seriously, unblocked channels, and smooth transfer of work instructions between employees.

The training of safety knowledge and skills will also influence people's behaviors. With regard to training plan, unreasonable time arrangement will bring additional burden to employees. The matching of training content, methods and plans with

needs, and acceptance of employees is of great importance. Because of influence of talent selection on safety behaviors, human resources departments should increase the assessment of safety knowledge and skills according to the talent selection mode, thus increasing the enthusiasm of employees to learn and master safety skills.

Owing to work pressure, people's unsafe behaviors are prone to be caused. Improper working hours and staff arrangements, low management efficiency of organizational factors such as rules and regulations, exchange and communication, and safety training will bring great work pressure to employees, thus giving rise to people's emotional fluctuations, and contributing to people's unsafe behaviors such as reduced attention and tangled mind.

The most fundamental way for organizations to enhance human safety is to improve humanistic care. Specifically, emotional care for employees is very important. The starting point of safety management should be changed from simple accident prevention to caring about and cherishing people and people's safety needs, and self-realization needs can be effectively integrated with corporate objective to reduce the probability of unsafe behaviors fundamentally.

Personal factors

Personal factors of unsafe behaviors include quality factors, physiological factors, and psychological factors.

At present, among human factors for enterprises' safe production, quality factor is of the most concern. The quality factors influencing the probability of personal unsafe behavior include personal skill proficiency, compliance with rules, knowledge level, and working experience. With high skill proficiency and compliance with safety regulations, the probability of personal misoperation can be reduced to a certain degree. With high knowledge level and abundant working experience, personal behavior ability can be improved effectively, avoiding misoperation resulting from nervousness and other emotions.

Human physiological factors can be divided into human physical state and mental state. The physical state of people is the basis of all human behaviors, including physical factors, perceptual ability, and athletic ability of people. The physical state of people depends not only on people's natural quality, but also on external factors, such as whether the person is hungry and whether the person lacks rest. Factors influencing people's mental state include pathological factors and pharmacological factors. On-site operation of power grid enterprises includes special operation such as high-altitude operation and electric welding. Accordingly, operators should not have occupational contraindications. Moreover, after operators take drugs during illness or under some special circumstances, the drug reaction will have an impact on human error as well.

Psychological factors are critical with regard to influence of people's inner activities on their external behaviors. Psychological factors influencing people's behaviors mainly include character traits, attitudes, motivations, and emotions. Character is a relatively stable psychological characteristic of a person. It is found through the comparative study between accident group and non-accident group that operators should have four-high and two-low character traits: high stability, high persistence,

high self-discipline, high constancy, low fantasy, and low tension. Attitude reflects people's views and opinions on things. However, attitude will vary with behaviors. Need generates motivation and motivation dominates behaviors to satisfy needs. A person's emotional change is the most difficult to grasp. People's ability to perceive and judge external signals will be directly influenced by too drastic emotional change.

4 Typical Generation Path of Grid Unsafe Behavior

Currently, similar to other complex industrial systems, the power grid presents new features such as higher automation, complexity, non-transparency, and fault tolerance, bringing about drastic change in causal relationship of accidents. Technical failure and unsafe behaviors are necessary but not sufficient conditions for accidents. Accidents will be caused only by coupling multiple factors in time and space. Unsafe behavior is caused by simultaneous occurrence of a series of loopholes instead of an isolated incident. The mechanism of unsafe behaviors as shown in Fig. 2 is established according to the analysis of factors of unsafe behaviors in power grids. The mechanism of unsafe behaviors is, respectively, lack of safety concept (root cause), lack of safety management system (primary cause), personal factors (indirect cause), unsafe actions and unsafe states (direct cause), accidents, and losses. The causes of unsafe behaviors are all organizational factors, and organizational loopholes may give rise to loopholes in personal factors, resulting in potential safety hazards and unsafe behaviors.

The loopholes at the organizational level include defect/complexity of rules and regulations, unsmooth exchange and communication, insufficient/impractical/

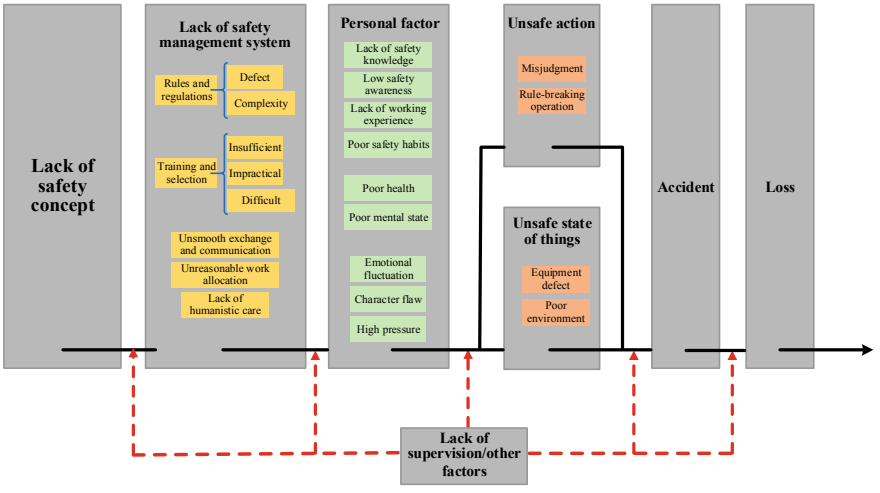

Fig. 2 Mechanism for unsafe behaviors in power grids

difficult training and selection, unreasonable work allocation, and insufficient humanistic care. Because of defect of rules and regulations, the attention paid by employees to rules may be insufficient, thus causing violation of rules. Owing to complexity of rules and regulations, employees may be restrained at work, resulting in high pressure and poor physical, mental, and psychological state. The lack of effective communication will weaken the efficiency and reliability in production. If training and selection methods are unreasonable, the candidates' physical/character flaws may not be effectively screened, bringing potential hazards to safe production. The fairness and reasonability of work allocation will also influence the physical, mental, and psychological state of employees. Moreover, inadequate humanistic care will give rise to negative emotions of employees, influencing the safety of production process.

The lack at personal level includes three aspects, respectively, personal quality factors, personal physiological factors, and personal psychological factors. The lack at personal level of employees during production will bring about mistakes in action and accordingly unsafe behaviors. With insufficient skill proficiency, employees may operate against rules unintentionally. If the degree of compliance with rules is insufficient, employees may have fluke mind and take risk in operating against rules. If the knowledge level and working experience are insufficient, judgment about the key information may be wrong, leading to operation against rules. Poor health may hinder employees from completing operation correctly, causing operation against rules. Under poor mental state or emotional fluctuation, employees cannot work efficiently, resulting in misjudgment and rule-breaking operation. Employees with character flaws may not be suitable for demanding production work, causing misjudgment and rule-breaking operation.

Rule-breaking operation (mistake) and misjudgment (error) are two kinds of unsafe behaviors. Judgment errors are omissions in consciousness, while rule-breaking operations are omissions in body movements. They are both prohibited in production.

On the whole, organizational factors are the root cause and primary cause of human errors. Personal factors are the indirect and direct causes of human errors which give rise to potential safety hazards to further trigger unsafe behaviors and accidents under lack of hierarchical defense (such as inadequate supervision and influence of environmental factors).

Analyzing the generation ways of human error can facilitate exploration of effective control strategies and minimize human errors.

5 Conclusion

The factors and mechanism of unsafe behaviors in power grids were researched in this paper. The factors of unsafe behaviors in power grids include organizational factors and personal factors. The factors of organizational unsafe behaviors include rules and regulations, exchange and communication with employees, employee training

and selection mode, and work pressure brought to employees and humanistic care for employees. Personal factors include quality factors, physiological factors, and psychological factors. The mechanism of unsafe behaviors is that lack of safety concept, safety management system, and other organizational factors lead to personal quality, physiological, and psychological factors, giving rise to unsafe actions and unsafe state of objects, ultimately triggering accidents and losses.

Acknowledgements This paper is sponsored by the State Grid Corporation of China Science and Technology Project "Comprehensive Risk Prevention of Power Supply and Demand Balance in the Electricity Market Environment" (No. 5108-202218280A-2-429-XG).

References

1. Quansheng Z, Yi S, Weidong L (2011) Key Technologies of EMS man-machine interaction in smart grid. Electr Power Autom Equip 31(08):117–121
2. Lu H (2013) Research on human reliability analysis and operation risk in power system. Zhejiang University
3. Tang J (2015) Research on human reliability analysis and accident pre-control of power grid. Zhejiang University.
4. Wu S (2014) Research and application of power enterprise human safety. Beijing Jiaotong University
5. Zhang J (2015) Research on human error of power accidents based on HFACS. Suzhou University
6. Tang J, He D, Guo C (2017) Analysis of human reliability in power grid based on fuzzy synthetic evaluation. J Electr Power Sci Technol 32(03):63–68
7. Jinyuan W, Shaojing Q, Haoxia J, An C (2015) Survey on quantification of human factor risk in electric misoperation. Mech Electr Eng Technol 44(08):13–16
8. Gui F, Yiran C, Surui X, Ping C, Chenhui Y, Yali W (2022) Detailed explanations of 24 model and development of Its 6th version. China Saf Sci J 32(01):12–19. https://doi.org/10.16265/j.cnki.issn1003-3033.2022.01.002

An Optimal Decision Model for Electricity Markets Considering Load Characteristics and Electricity Demand

Guojie Li, Xing Tian, Xue Feng, Pengfei Xu, and Yan Li

Abstract In the current electricity market optimisation decision, the analysis of load characteristics is not comprehensive enough, resulting in low economic efficiency of the optimisation decision results. To this end, an optimisation decision model for the electricity market that considers load characteristics and electricity demand is proposed. Based on the grid operation state, the load characteristics are analysed in three dimensions. Collect historical electricity consumption information and forecast electricity demand. Construct a three-layer model for power market optimisation decision-making. Experiments show that the average economic efficiency of the model's optimisation decision results reaches 95.25%. The economic efficiency of the power market optimisation decision is greatly improved, and it has high practical application value.

Keywords Electricity markets · Optimal decision making · Load characteristics · Electricity demand · Decision models

1 Introduction

Load characteristics are a key element to be considered in decisions about the development of the electricity market [1]. Load characteristics are an important part of the power system. The nature of the load characteristic is a constantly changing law. The variation of this law depends mainly on the active and reactive power of the power system and the variation of the voltage and frequency at the line nodes of the power system. Depending on the cause of the variation of the load characteristics, the load characteristics are divided into different categories. Load characteristics have a great influence on the quality of operation of the power system, and it is important to make optimisation decisions for the power market [2, 3]. The demand for electricity is also a key consideration in making decisions about the optimisation of

G. Li (✉) · X. Tian · X. Feng · P. Xu · Y. Li
Economic and Technological Research Institute, State Grid Ningxia Electric Power Co.Ltd., Yinchuan 750000, Ningxia, China
e-mail: gogojie_123@163.com

S. Yadav et al. (eds.), *Energy Power and Automation Engineering*, Lecture Notes in Electrical Engineering 1118, https://doi.org/10.1007/978-981-99-8878-5_51

the electricity market. The analysis of electricity demand is a key step in achieving a balance between supply and demand. Some areas in Ningxia have a large gap in electricity demand. The main factors affecting electricity demand are analysed, and the subsequent development trends of electricity demand in different regions of Ningxia are summarised and forecast. In particular, an optimisation decision for the electricity market is proposed for the problem of high industrial electricity demand in some regions. Based on such a situation, an electricity market optimisation decision model considering load characteristics and electricity demand is designed. Through this model, more quality construction decisions are proposed for the development planning of Ningxia's electricity market, providing a reliable basis for power grid enterprises to make planning, programming and operational decisions.

2 Analysis of Electrical Load Characteristics Based on Grid Operating Conditions

In this paper, the analysis is carried out on an annual basis. Let the average annual load be P_y, which is calculated by the formula (1):

$$P_y = \frac{\sum Q_d}{N_m} \tag{1}$$

In Eq. (1), Q_d is the average daily electricity consumption in the grid operating status information. Nm the number of months included in the grid operating status information. The peak-to-valley difference is then analysed. The analysis of the peak-valley differential is able to reflect the extent of electricity demand in the region by calculating the difference between the peak load and the trough load. Again, the analysis is carried out on an annual basis. Let the peak-to-valley differential be P_d, which is calculated by the formula (2):

$$P_d = \frac{P_{\max} - P_{\min}}{N_m} \tag{2}$$

In Eq. (2), $P_{\max}$ and $P_{\min}$ represent the peak and trough loads, respectively. Finally, the maximum annual load utilisation hours are analysed. Let the annual maximum load utilisation hours be $T_{\max}$, which is calculated by the formula (3):

$$T_{\max} = \frac{8760\alpha}{N_m} \tag{3}$$

In Eq. (3), α is the annual loading rate. After completing the analysis of the descriptive category indicator dimensions, the analysis of the comparative category indicator dimensions was carried out. The types and content of the comparative category indicator dimensions are shown in Table 1.

Table 1 Content of comparative category indicators

Type of indicator	Indicator content
Load factor	Load fluctuation indicators
Peak-to-valley differential rate	Ratio of peak-to-valley difference to maximum load

The two comparative categories of indicators in the table above are analysed separately. The first is load factor. The load factor is an indicator of fluctuations in the load of electricity data. The load factor is positively proportional to the utilisation rate of the electricity-using equipment. The higher the result of the load factor, the more balanced the load fluctuations in the region and the more stable the operation of the electricity market. In this paper, the analysis of the load factor is carried out on an annual basis, and the load factor is set to be γ, which is calculated as formula (4):

$$\gamma = \frac{P_y}{8760 \times P_{y\max}} \tag{4}$$

In Eq. (4), $P_{y\max}$ is the maximum value of the annual average load. The peak-to-valley differential rate is then calculated. The magnitude of the peak-to-valley differential is mainly influenced by external factors. These external factors mainly include changes in the customer's electricity consumption equipment and climate change. Let the peak-to-valley differential be λ. The formula (5) is

$$\lambda = \frac{P_d}{8760 \times P_{d\max}} \tag{5}$$

In formula (5), $P_{d\max}$ is the maximum value of the annual peak-to-valley difference. After completing the analysis of the dimensions of the comparative class indicators, the analysis of the nature class indicators is carried out. In this paper, the analysis of the nature class indicators is mainly carried out from the perspective of flexible load. The nature class indicators can be divided into two main types, which are transferable load and abatable load. Transferable load is mainly measured for changes in electricity prices in the electricity market. The load shedding is measured for the residential sector. The analysis of each type of load indicator from the above three dimensions completes the process of load characterisation based on the operational state of the grid.

3 Forecasting Electricity Demand Based on Historical Electricity Consumption Information

This paper uses econometrics as a theoretical tool for electricity demand forecasting. The method splits the historical electricity consumption information into different basic units according to time. Each basic unit is a period of the electricity demand forecast. The middle period in each of these basic units is used as a representative of that basic unit. A two-dimensional coordinate system is established to express the electricity demand in the basic units, as shown in the following Fig. 1.

In Fig. 1, the horizontal coordinates indicate the time scale of the electricity consumption information. t_1 indicates the total electricity consumption of the first basic unit in the captured historical electricity consumption information. t_m indicates the total electricity consumption of the basic unit at the middle moment in the captured historical electricity consumption information. t_n indicates the total electricity consumption of the basic unit at the last moment in the captured historical electricity consumption information, i.e. the latest overall electricity market in the region. Electricity demand. $S(t)$ represents the total electricity demand in the region's electricity market at time t. The above schematic diagram of the change in electricity demand is drawn based on the historical customer point information captured. The schematic diagram is then used to make a forecast of future changes in electricity demand in the region's electricity market. Let the forecasted value of electricity demand in this electricity market be y, calculated as

$$y = f[S_1(t_1), S_2(t_2), \cdots, S_m(t_m), \cdots, S_n(t_n)] \tag{6}$$

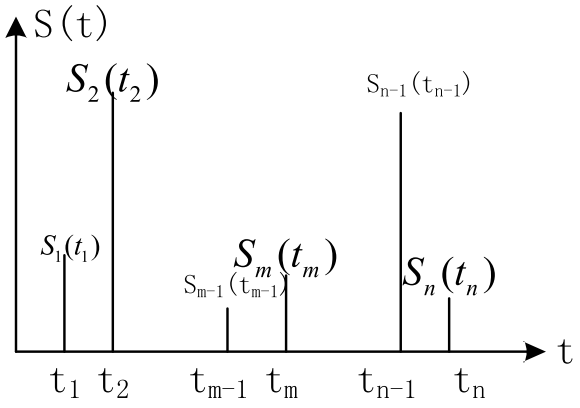

Fig. 1 Schematic diagram of changes in electricity demand

4 Constructing a Three-Layer Model for Optimal Decision-Making in the Electricity Market

Based on the analysis of load characteristics and electricity demand forecasts, a three-layer model is constructed for optimal decision-making in the electricity market. The first two layers of the model access the results of the load characteristic analysis and the electricity demand forecast, respectively. The third layer integrates the data information from the first two layers to make optimisation decisions. The third layer is divided into two main functional modules, namely the profit analysis module and the electricity market clearing module. Firstly, the profit analysis module is constructed. The profit analysis module is divided into two main parts, the profit of the electricity supplier and the profit of the electricity consumer. The market clearing module is divided into regular power market clearing and real-time power market clearing [4, 5]. The contents of the two modules are combined to derive the optimisation decision results for the electricity market together. The three-level model for optimal decision-making in the electricity market designed in this paper is a high-dimensional nonlinear optimal decision-making model. The solution process of the model is shown in Fig. 2.

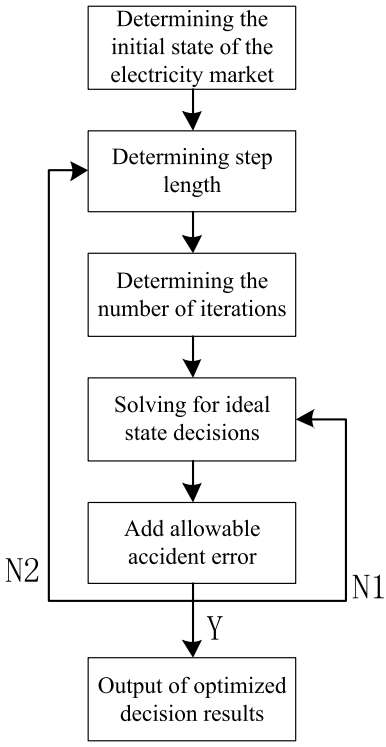

Fig. 2 Electricity market optimisation decision model

The power market optimisation decision model designed in this paper first determines the operating state of the power market. The determination of this state is based on the results of the analysis of the load characteristics above. Based on the different states of operation of the electricity market, the step size of the model is determined. The step size is determined based on the distribution pattern of the different electricity consumption types in the region's electricity market. After the step size is determined, the number of iterations and the error need to be calculated. The maximum number of iterations is $D_{\max}$, given an iteration error of ρ and a number of iterations of D. Based on the results of the iterations in this situation, the electricity market decision in the ideal state is derived. Then add in the error of the type of accident that causes a change in the electricity market [6]. This step entails substitution based on electricity demand forecasts to obtain an optimised electricity market decision. The result of the optimised electricity market decision is then judged. When the case is $N1$, return to step 4 to re-output the result. The judgement formula for $N1$ is formula (7):

$$N1 = \|X_D - X_{D-1}\|_2 < \rho \tag{7}$$

In Eq. (7), XD and XD-1 are the relevant decision variables of the electricity market optimisation decision model when the number of iterations is D and $D-1$, respectively. When the case is $N2$, then return to step 2 to re-output the result. $n2$ is judged by the formula (8):

$$N2 = \|X_D - X_{D-1}\|_2 > \rho \tag{8}$$

If the situation is as shown in the following formula (9):

$$Y = \|X_D - X_{D-1}\|_2 = \rho \tag{9}$$

Then the output result is Y, the final decision result. This completes the construction of an optimal decision model for the electricity market considering load characteristics and electricity demand.

5 Experiment

5.1 Experiment Preparation

This experiment is designed to verify the feasibility of the optimal decision model for the single interest market considering load characteristics and electricity demand proposed in this paper. Set the analysis index for this experiment. This paper incorporates the ratio of customer demand for electricity to electricity supply in the electricity market as the analytical index for this experiment. The results are used to measure the economic benefits resulting from the electricity market optimisation decision. Let

Table 2 Experimental environment parameters

Projects	Parameters
CPU	Intel i7-9700
Memory	32 GB
Solid state drives	1 TB
Operating systems	CentOS 7.4 desktop
Hyperledger fabric operating environment	Docker containers
Running peer nodes	4
Run sorting nodes	1

the customer electricity demand be R and the electricity supply be W. The economic benefit A of the analysis indicator is calculated as formula (10):

$$A = \frac{R}{W} \times 100\% \tag{10}$$

The results of the calculation using formula (10) were used as an indicator to analyse and evaluate the results of this experiment.

To ensure the scientific validity of this experiment, this experiment was designed as a comparison experiment type. Two comparison subjects were set up as the control group. Comparator 1 is an electricity market optimisation decision model that takes into account internal multi-regional interactions. Comparator 2 is a CVaR-based electricity market optimisation decision model.

The data for this experiment uses electricity market data information from a region in Ningxia. The historical electricity consumption information was collected by choosing the recent five-year time period. The setup of this experimental environment is shown in Table 2.

This comparison experiment was conducted in the environment shown in Table 2. Nearly five years' worth of information was entered into the three optimisation decision models separately. One year of historical information was entered into each experiment. The experiment was conducted for a total of five rounds.

5.2 Analysis of Results

The power market optimisation decision model that considers load characteristics and power demand proposed in this paper is named Method 1. The decision model for optimising the electricity market considering the interaction between multiple internal regions is named Method 2. The CVaR-based power market optimisation decision model was named Method 3. After five rounds of experiments, the experimental results were obtained as shown in the following Table 3.

Table 3 Results of different model optimisation decisions

Experimental rounds	Method 1 (%)	Method 2 (%)	Method 3 (%)
1	95.68	85.27	81.54
2	94.26	83.22	84.93
3	94.72	86.17	78.48
4	96.43	79.51	76.88
5	95.16	80.60	79.36
Average economic benefit	95.250	82.954	80.238

From Table 3, it can be seen that the optimisation decision results of the electricity market optimisation decision model proposed in this paper, which takes into account load characteristics and electricity demand, have high economic efficiency. In all five rounds of experiments, the economic efficiency remained above 90%. It can be seen that the optimisation results of the power market optimisation decision model proposed in this paper, which takes into account load characteristics and power demand, can bring higher economic benefits and higher quality power market optimisation decisions and have high practical application value.

6 Conclusion

In response to the problem of low quality of the power market optimisation decision results, the proposed power market optimisation decision model considers load characteristics and power demand. The model analyses the load characteristics of the power system from three dimensions and combines them with the power demand forecasting results based on historical electricity consumption information to jointly construct the power market optimisation decision model, which is able to obtain more economically efficient optimisation decision results and has high practical application value.

References

1. Lavanya M, Kavitha V (2021) A hybrid classical techniques and optimal decision model for iris recognition under variable image quality conditions. J Ambient Intell Humaniz Comput 12(9):8913–8931
2. Wang T, Cao J, Hussain A (2021) Adaptive traffic signal control for large-scale scenario with cooperative group-based multi-agent reinforcement learning. Transp Res Part C Emerg Technol 125:103046.1–103046.27
3. Wu Q, Wu J, Shen J, Du B, Telikani A, Fahmideh M, Liang C (2022) Distributed agent-based deep reinforcement learning for large scale traffic signal control. Knowl-Based Syst 241:108304.1–108304.10

4. Liu Z, Guo A, Liu J, Fang Q (2022) Experimental investigation of loads of coastal bridge deck under the combined action of extreme winds and waves. Ocean Eng 252:111225
5. Fernandes MC, Dias JC, Nunes JPV (2021) Modeling energy prices under energy transition: a novel stochastic-copula approach. Econ Model 105:105671
6. Nahar S, Akter M, Abdul Alim M (2023) Solving multi-objective linear programming problem by statistical averaging method with the help of fuzzy programming method. Am J Oper Res 2:19–32

Simulation Analysis of Voltage Transient Stability Margins in Distribution Networks Under Large-Scale Distributed Power Supply Access Conditions

Tao Zhu, Junfu Liu, Huaipeng Zhang, and Xuepeng Yang

Abstract In the traditional distribution network voltage transient stability margin analysis under the conditions of large-scale distributed power supply access, the processing of the analysis index is not refined enough, resulting in large errors in the analysis results. In this regard, a simulation analysis of the voltage transient stability margin of the distribution network under the conditions of large-scale distributed power supply access is proposed. Extraction of key features. Determine the characteristic parameters of the distributed power supply. Calculation of different index units and orders of magnitude and standardisation of the margin analysis index. Output of margin simulation results. The experiments show that the method has a lower error value than traditional methods in both active and reactive margin analysis and is of high application value.

Keywords Distribution networks · Voltage transient stability margins · Distributed power supplies · Power access · Margin analysis

1 Introduction

The transient stability margin of the distribution network voltage is the allowable voltage fluctuation range of the distribution network [1]. When reactive power is disturbed, the voltage transient stability margin of the distribution network changes. In the construction of a distribution network structure, access to a scaled-up distributed power supply has more advantages than in a traditional distribution network. In this project, access to medium- or low-voltage distributed power sources is usually chosen [2]. Yield analysis can contribute to the quality of practical applications that account for scaled distributed power distribution networks [3]. The access to large-scale distributed power supplies makes the connection between the various areas of the distribution network even closer. In this respect, the distribution network

T. Zhu (✉) · J. Liu · H. Zhang · X. Yang
State Grid Zhongwei Electric Supply Company, Zhongwei 755000, Ningxia, China
e-mail: 413233524@qq.com

S. Yadav et al. (eds.), *Energy Power and Automation Engineering*, Lecture Notes in Electrical Engineering 1118, https://doi.org/10.1007/978-981-99-8878-5_52

under the conditions of access to a scaled distributed power supply is significantly different from the distribution network under the traditional model, changing the performance of the relay protection devices [4]. Based on this change, the voltage transient stability margin of the distribution network under the conditions of scaled distributed power supply access is analysed to test the operational performance of the distribution network.

2 Extraction of Key Characteristics of Distribution Network Voltage Transient Stability

The process of extracting key features of voltage transient stability in distribution networks using principal component analysis in this article is shown in Fig. 1 [5, 6].

After processing all the data information according to the above criteria, the covariance matrix of the standardised data information is created. Set the standardised covariance matrix as R and the calculation process as formula (1):

$$R = \frac{z_i \cdot z_j}{n-1} \cdot xp \tag{1}$$

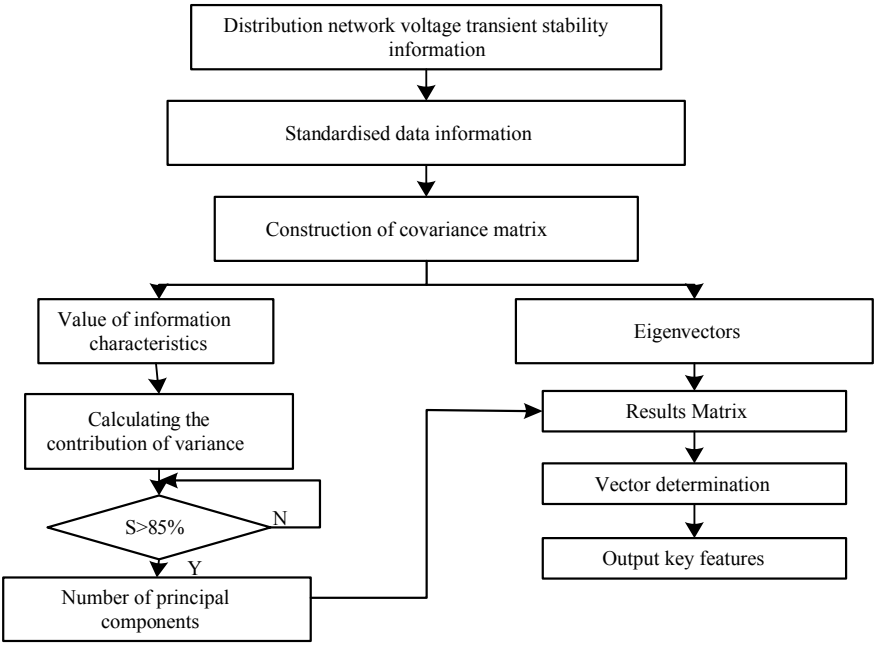

Fig. 1 Distribution network voltage transient stability key features SAR process

In Eq. (1), z_i is the random vector of standardised data information. z_j is the dimension of the standardised data information. n is the amount of distribution network voltage transient stability information. x is the index of the original data information. P is the covariance operation parameter of voltage data. Based on the calculation results of the above equation, the eigenvalues of the covariance matrix correlation coefficients are then calculated. The calculation process is Formula (2):

$$\left|R - \lambda I_p\right| = 0 \tag{2}$$

In Eq. (2), λ is the correlation coefficient of the covariance matrix. I_p is the number of results of the covariance matrix calculation. The eigenvalues are derived from the calculation of Eq. (2). The principal components of the voltage transient stability information of the distribution network are determined from the eigenvalues. The principal components of each information are judged. Assuming the contribution of the principal component as S, the calculation process is shown in formula (3):

$$S = \left|\frac{\lambda m}{\lambda p}\right|^i \tag{3}$$

In Eq. (3), m is the principal component of the voltage transient stability information of the distribution network. i is the random vector. The calculation result of Eq. (3) is judged to determine whether the contribution of this principal component is greater than 85%. If it is greater than, the sequence of principal components is output. If it is not, return and re-run the above calculation process. The number of principal components of the distribution network voltage transient stability information obtained from the output is imported into the result matrix. The number of outputs is m. Using the result matrix, the eigenvectors corresponding to the m principal components are determined. The number of this feature vector is again m. The results obtained are then output to complete the process of extracting key features for voltage transient stability of the distribution network based on principal component analysis.

3 Determine the Parameters of the Distribution Network Access to Scale Up Distributed Power Characteristics

In this paper, a supervised machine learning method is used for the calculation. The irrelevant feature quantities are first removed. A regularisation vector is added to the supervised machine learning model to find the sparse solution. Let the sparse solution of the key feature be Y, calculated as formula (4):

$$Y = \min\left(n^{-1}\|S - x\|^2 + \lambda \sum_{i=1}^{2} R(|\beta i|)\right) \tag{4}$$

In Eq. (4), βi is the penalty term for the voltage transient stability of the distribution network. The calculation of Eq. (4) enables the coefficients of the key characteristics of the voltage transient stability of the distribution network to be reduced continuously. The strength of the coefficient reduction is controlled by the number of iterations of the calculation. Based on the results of the above equation, the nodal voltage magnitude V_{Li} is calculated through the expression of the dynamic load is Eq. 5:

$$V_{\mathrm{Li}}^2 = Q_i \cdot F_i^2 / L_i \cdot Y \tag{5}$$

In Eq. (5), Q_i is the reactive power of the node, F_i is the active power of the node, and L_i is the apparent power of the node. After the calculation of the above equation, the determination of the voltage amplitude of the node of the characteristic parameter of the scaled distributed power supply connected to the distribution network is completed. The phase angle is then calculated. The calculation of the phase angle requires a calculation process based on the variations at the different nodes. The calculation of the phase angle needs to be calibrated at a specific position in the fluctuation cycle of the voltage transient stability signal. Then the scaling is calculated for each node of the distribution network between the peaks and troughs. The phase angle is set to J and is calculated as formula (6):

$$J = \frac{\sqrt{a^2 + b^2}}{Q_i \cdot F_i} \tag{6}$$

In Eq. (6), a is the phase value of the crest in the voltage transient stabilisation signal waveform. b is the phase value of the trough in the voltage transient stabilisation signal waveform. The process of determining the characteristic parameters of the distribution network connected to a large-scale distributed power supply is completed by calculating the nodal voltage amplitude and phase angle of the distribution network connected to a large-scale distributed power supply.

4 Standardised Distribution Network Voltage Transient Stability Margin Indicators

The indicators for margin development analysis are divided into different types, as shown in the following Table 1.

The margin analysis indicators shown in the table above all have a certain degree of influence on the performance of the voltage transient stability of the distribution network. The margin analysis index system established in this paper contains a total of eight indexes. These eight indicators have different calculation units and orders of magnitude. Therefore, this paper chooses to use the efficacy factor method to calculate these eight indicators. All the above indicators were standardised. The standardisation

Table 1 Distribution network voltage transient stability margin analysis indicator types

Type of indicator	Indicator content
Distributed Indicators	Very small indicators Range-based indicators Intermediate indicators
Load margin indicators	Maximum load supply capacity Actual load demand
Branch margin indicators	Branch currents in the distribution network during operation Number of distributed power connections to the distribution network
Equipment margin indicators	Power to discharge or charge energy storage elements

process was carried out using the polar difference method. The extreme value interval of each indicator was processed into a pattern of [0, 1] to obtain the standard indicator k, which was calculated formula (7):

$$k = s + \frac{w - d_{\min}}{d_{\max} - d_{\min}} \times r \tag{7}$$

In Eq. (7), s is the translation of the indicator. r is the number of power connections. $d_{\max}$ and $d_{\min}$ are the maximum and minimum values of the indicator, respectively. r is the amount of rotation of the indicator. Based on the calculation results of the above equation, the standardisation process of the distribution network voltage transient stability margin indicator is completed.

5 Output Voltage Transient Stability Margin Development Analysis Results

In this paper, wavelet neural network is used to carry out the simulation analysis. Let the number of hidden layer nodes be c. The formula is (8):

$$c = 2 \times h + 1 \tag{8}$$

In Eq. (8), h is the number of neuron nodes. The number of nodes in the hidden layer is determined by means of the above equation to ensure that the wavelet neural network presents a high level of fitting and fault tolerance without over-fitting due to insufficient training speed.

First, the R-WNN parameters of the wavelet neural network are iteratively updated. Then the right-hand side weights of this neural network are adjusted. Let the difference of the right-hand side weight adjustment be $E(n)$, which is calculated formula (9):

$$E(n) = \frac{D(n) - O(n)}{h} \tag{9}$$

In Eq. (9), $D(n)$ is the weight value of the desired output. $O(n)$ is the weight value of the actual output. The update learning rate is then calculated. Let the learning rate be T, and its calculation formula is (10):

$$T = \max\{C_1 * E(n)l\}, \text{else} \tag{10}$$

In Eq. (10), C_1 is the empirical value of the wavelet neural network. l is the learning rate of the scale scaling factor. Based on the calculation results of Eq. (10), the indicators are assigned to the standard indicators under the eight base indicators derived above. In this paper, we use the method based on entropy value method to carry out the weighting of indicators. The information entropy value e corresponding to the standard indicator k is first calculated using the formula (11):

$$e = -T|\ln x \cdot k| \tag{11}$$

Based on the calculation results of Eq. (11), the information utility value of the voltage transient stability margin of the distribution network is obtained. The weighting factor B of the standard indicator for this node is then calculated as formula (12):

$$B = \left(\frac{e}{iG}\right)^m \tag{12}$$

In Eq. (12), G is the information utility value of the voltage stability margin of the distribution network. This completes the assignment of indicators to the standard indicators for voltage stability margins in the distribution network. The result of the indicator weighting is judged, and if it does not meet the expectations, the iterative calculation is started again. If the expected value is met, the neural network cycle is exited, and the results of the distribution network voltage transient stability margin simulation are output. This completes the simulation of the voltage stability margin of the distribution network under the conditions of large-scale distributed power supply access.

6 Experiment

6.1 Experiment Preparation

In order to verify the feasibility of the simulation analysis of the voltage transient stability margin of the distribution network under the conditions of scaled distributed power supply access proposed in this paper, this experiment was designed. The

Table 2 Simulated values of basic distribution network parameters

Project	Parameters
Percentage of node distance from the distribution network	50%
Distribution network impedance factor	1
Number of distributed power sources on the distribution network	23
Distribution network mechanical torque	0.25
Distribution network mechanical characteristic load	2
Distribution network stator reactors	0.295
Rotor reactors for distribution networks	0.12
Initial frequency of the distribution network	50

Simulink software was used to carry out the simulation of this experimental data. In this experiment, the basic simulation parameters are shown in the following Table 2.

In this experiment, five nodes were randomly selected for simulation of the voltage transient stability margins in a distribution network with a large-scale distributed power supply. The nodes of the distribution network analysed by different methods are kept consistent.

6.2 Analysis of Results

The simulation and analysis method of voltage transient stability margin of distribution network under the condition of scaled distributed power supply access proposed in this paper is named Method 1. The traditional method of simulating and analysing the voltage transient stability margin of the distribution network under the conditions of scaled distributed power supply access is named Method 2. The results of the experiment were obtained as shown in Tables 3 and 4.

From Tables 3 and 4, it can be seen that the simulation analysis method of voltage transient stability margin of distribution network under the condition of large-scale distributed power supply access proposed in this paper is closer to the real results in the case of active and reactive power. The difference between the analysis results of the proposed method and the real results is 0.001413, while that of the traditional

Table 3 Results of simulation analysis of active margin for different methods

Nodes	Real results	Method 1	Method 2
1	0.410585	0.408466	0.418563
2	0.071025	0.070582	0.072329
3	0.057482	0.058595	0.065284
4	0.235676	0.237307	0.253758
5	0.308761	0.307166	0.314757

Table 4 Results of reactive power margin simulation analysis for different methods

Nodes	Real results	Method 1	Method 2
1	0.188869	0.187166	0.267503
2	0.054361	0.054972	0.056639
3	0.041059	0.041854	0.041891
4	0.118279	0.117638	0.120545
5	0.181479	0.180541	0.185004

method is 0.041162. The average difference between the two methods is 0.0002826 and 0.0082324, respectively. In the analysis of the voltage transient stability margin of the reactive distribution network, the difference between the analysis result of the proposed method and the real result is 0.001876, while the difference of the traditional method is 0.087535. The average difference between the two analysis methods is 0.0003752 and 0.017507, respectively. The results are closer to the real results than those of the traditional method, which can significantly reduce the error of the margin simulation analysis.

7 Conclusion

This paper addresses the problem of large errors in the analysis of the voltage transient stability margins of distribution networks under the conditions of large-scale distributed power supply access. By standardising the margin analysis indexes, the error value of the analysis results is significantly reduced, which is of high practical application value. In future research, it is necessary to solve the unstable balance point in the process of voltage transient stability margin analysis of distribution networks to excise the practical accuracy and further improve the accuracy of the margin simulation analysis results.

References

1. Xu Y, Jiang W, Sun S et al (2022) Quantitative assessment method for transient voltage of distribution network with high-penetration wind power. Electric Power 557:152–162
2. Hou S, Zhang X, Dai Y et al (2022) Distributed power planning for active distribution network considering energy storage coordination and demand side response. Mod Electron Tech 4523:132–137
3. Zhang R, Bie Z (2022) Distributed cluster-level cooperative control of dynamic virtual microgrid cluster for active distribution network. Autom Electr Power Syst 4614:55–62
4. Xu J, Lv F (2022) Reactive failure control of intelligent substation protection information under disturbance excitation. Comput Simul 394:71–75

5. Yang F, Ren W, Shen Y et al (2021) Transient analysis method and identification of arc grounding faults in Petersen coil grounded distribution network. Proceedings of the CSU-EPSA 334:23–31
6. Zhang J, Zhang R, He Y et al (2022) Analysis and verification of small-signal model of Quasi-Z-source network in AC/DC distribution network system. Electr Mach Control Appl 495:94–102

Automatic Planning Method of Pipe-Line Systems by Petri Nets

Jiliang Luo, Zexuan Lin, Xuhang Li, Wei Liu, and Chunrong Pan

Abstract This paper presents an automatic planning method for pipe-line systems under complex logic control rules based on Petri nets. Petri nets are usually modeled manually, which can lead to incomplete models of complex logic control systems. To address this issue, we extend the planning domain definition language (PDDL), which can be automatically translated into Petri nets. For complex logic control pipe-line systems, given a set of tasks, it is difficult to quickly formulate the process execution sequence through manual calculation. This paper designs an automatic pipe-line system planning method based on Petri nets, which can accurately generate Petri nets model and process execution sequences. The beer filtration system is taken as an example to illustrate the method.

Keywords Pipe-line systems · Petri nets · PDDL · Modeling · Automatic planning

J. Luo (✉) · C. Pan
School of Mechanical and Electrical Engineering, Jiangxi University of Science and Technology, Ganzhou 341000, China
e-mail: jlluo@hqu.edu.cn

J. Luo · Z. Lin · X. Li · W. Liu
College of Information Science and Engineering, Huaqiao University, Xiamen 361021, China

Fujian Engineering Research Center of Motor Control and System Optimal Schedule, Xiamen 361021, China

Z. Lin
e-mail: linzexuan@stu.hqu.edu.cn

S. Yadav et al. (eds.), *Energy Power and Automation Engineering*, Lecture Notes in Electrical Engineering 1118, https://doi.org/10.1007/978-981-99-8878-5_53

1 Introduction

In the chemical industry, pipe-line systems are essential [1]. However, it is challenging to model and control these systems with numerous valves in the factory. Additionally, control requirements must be modified dynamically and quickly when transportation tasks change or equipment is damaged. Traditional methods rely on trial-and-error experiments to derive systems models and control diagrams, which can be error-prone and time-consuming. Therefore, researching a reliable method for automatically generating valves models and planning valves controls is crucial for the efficient operation of pipe-line transportation system. Petri nets are mathematical modeling tools for discrete event systems. They can graphically represent concurrency, asynchrony, distribution, parallelism, uncertainty, or randomness. Petri nets are a mathematical tool used to establish state equations representing dynamic behavior [2, 3]. They deduce unknown state information and display dynamic behavior in graphical form. Petri nets are a modeling tool primarily used in computer science, automation, and mechanical engineering [4–7].

The pipe-line system is driven by events such as valves openings or closings, making them amenable to modeling with Petri nets. However, creating a Petri nets model of a pipe-line systems is still challenging. Current modeling approaches often involve modular modeling [8, 9], which is still a manual process. Researchers divide the pipe-line system into multiple operations controlled by valves and create a Petri nets model for each operation. They analyze the relationships between the operations and then connect each operation to the Petri nets through shared places or transitions. However, this approach heavily relies on the researchers' understanding of Petri nets and requires abstraction of the actual system into places and transitions in the Petri nets. Therefore, it is necessary to find a suitable way to ensure the integrity of the Petri nets.

The planning domain definition language (PDDL) is a kind of used to describe the computer automation planning problem of formal languages [10]. PDDL is often used to describe the domain of a planning problem (such as robot navigation, resource scheduling, and so on), including information about the actions, states, and goals available in the domain.

This paper presents an automatic planning method for pipe-line system based on Petri nets, taking a beer filter pipe-line systems as an example. Firstly, PDDL describes the system, and the content of the description is analyzed to design an automatic planning modeling algorithm to convert it into a Petri nets. Then, the operation of the control valves is complex, and the Petri nets model is used to design the automatic planning algorithm of the valves operation. When the given task, the valves operation sequence of the system can be quickly calculated by using the algorithm. Finally, we make various simulation experiments, and the results show that the automatic planning method can ensure the integrity of the model and the feasibility of the systems.

The structure of this paper is as follows: Section II here is not presents basic concepts about ordinary Petri nets and PDDL and modern-day the syntax of PDDL, Section III describes the problem of pipe-line transportation systems. Section IV, automatic planning by PDDL and Petri nets. Section V concludes this work.

2 Problem Statement

The pipe-line system is controlled through a set of valves that transfer fluid from one tank to another tank. In order to make the article more readable, such as the implementation example 1, beer filtration equipment is used to illustrate the proposed concepts and methods.

Example 1. The beer filter device completes filling, filtering, bottling, cleaning, and other tasks, as shown in Fig. 1. It consists of a feedstock tank *Ts*, three filters *MMS*1, *MMS*2, and *MMS*3, two buffer tanks $T1$ and $T2$, a washer *CIP* supply and collection system, and 20 double disk plug valves $v_1 \ldots v_{20}$ [11]. Notice that each valve can be switched to either OPEN or CLOSE position. When the valve is opened, the fluid in the vertical and horizontal pipe-line under its control mixes and then flows out through all outlet pipes, while the fluid in the vertical and horizontal pipes flows separately when the valve is CLOSE. There are 12 operations $o_1, o_2, o_3, o_4, o_5 \ldots o_{12}$ in this plant, which are summarized in Table 1. $o_1 \ldots o_7$ is the operation that controls the valve beer filtration, buffering, and filling, and $o_8 \ldots o_{12}$ is the operation that controls the valve for cleaning the filter and buffer tank. Filters *MMS*1, *MMS*2, and *MMS*3 need to be cleaned after being used once, twice, and three times, respectively; Tank $T1$ and $T2$ need to be cleaned after being used twice, and the cleaning time is 2 *min* each time. In addition, since beer and cleaners are not allowed to mix in this system, the barrier between the two materials should always remain intact.

Relationships between tasks are complex because they can share and compete for resources. This prompted us to construct a PN model, which described the control instructions of these valves through PDDL and converted them into Petri nets, so as to ensure the integrity of the model. The operation of the valve is also complicated, and it is difficult to calculate the operation instructions manually. Therefore, an algorithm needs to be built to automatically calculate the operation instructions.

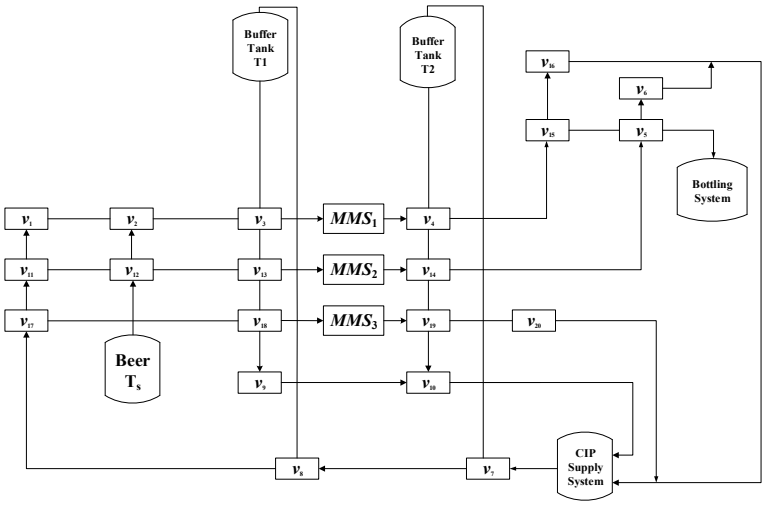

Fig. 1 Process flow diagram of a beer filtration plant

Table 1 Production operations of the beer filtration plant

Operations	Open valves	Closed valves	Tanks	Time
o_1	v_2, v_3	$\overline{v}_8, \overline{v}_9, \overline{v}_{12}, \overline{v}_1$	T_1	4 s
o_2	v_{12}, v_3	$\overline{v}_8, \overline{v}_9, \overline{v}_3, \overline{v}_{11}$	T_1	4 s
o_3	v_3, v_4	$\overline{v}_8, \overline{v}_9, \overline{v}_7, \overline{v}_{10}, \overline{v}_1, \overline{v}_2$	T_1, T_2, M_1	4 s
o_4	v_{13}, v_{14}	$\overline{v}_8, \overline{v}_9, \overline{v}_7, \overline{v}_{10}, \overline{v}_{11}, \overline{v}_{12}, \overline{v}_3, \overline{v}_4$	T_1, T_2, M_2	4 s
o_5	v_{18}, v_{19}	$\overline{v}_8, \overline{v}_9, \overline{v}_7, \overline{v}_{10}, \overline{v}_3, \overline{v}_4, \overline{v}_{13}, \overline{v}_{14}, \overline{v}_{17}$	T_1, T_2, M_3	4 s
o_6	v_4, v_5	$\overline{v}_7, \overline{v}_{10}, \overline{v}_1, \overline{v}_6$	T_2	4 s
o_7	v_{14}, v_{15}	$\overline{v}_7, \overline{v}_{10}, \overline{v}_{11}, \overline{v}_{16}, \overline{v}_5, \overline{v}_4$	T_2	4 s
o_8	v_8, v_9	$\overline{v}_3, \overline{v}_{13}, \overline{v}_{10}, \overline{v}_7$	T_1	2 min
o_9	v_7, v_{10}	$\overline{v}_4, \overline{v}_{14}$	T_2	2 min
o_{10}	v_1, v_6	$\overline{v}_2, \overline{v}_3, \overline{v}_4, \overline{v}_5, \overline{v}_7, \overline{v}_8, \overline{v}_{11}, \overline{v}_{17}$	M_1	2 min
o_{11}	v_{11}, v_{16}	$\overline{v}_{12}, \overline{v}_{13}, \overline{v}_{14}, \overline{v}_{15}, \overline{v}_7, \overline{v}_8, \overline{v}_{17}$	M_2	2 min
o_{12}	v_{17}, v_{20}	$\overline{v}_{18}, \overline{v}_{19}, \overline{v}_7, \overline{v}_8$	M_3	2 min

3 Automatic Planning by PDDL and Petri Nets

Currently PDDL is sufficient to describe the system to be modeled, but it generates a large amount of redundant data when modeling a pipe-line system. For example, when n tasks or device usage is encountered, *n* objects are generated during modeling. The extension of PDDL to *n* tasks is accomplished by designing a singleton type, and

g(x) can be converted to places [12]. So this paper extends the device usage times of PDDL, we define the count type $C = (T, L)$ to be a binary type, and the predicate is not used to describe the state. T represents the number of times the object position is used and is a positive integer. L represents the position of the object and is a positive integer. T is converted to a Petri net position token, representing the number of times an object of this type has been used, and L is also converted to a Petri net position, representing the position of the object type. The conversion function is denoted as *f(x)*. Li [12] designed the function *h(x)* that converts predicates to places and its action to places and the transition function *k(x, y, z)*. Algorithm 1 is further improved on these bases. By placing the PDDL description file of the system into Algorithm 1, Petri net model and valve operation sequence can be automatically generated. Firstly, initialize C^+, C^-, m_0, m_g, T, F, and O to be empty; secondly, we traverse singleton types, degree types, and predicates, respectively, to generate places; thirdly, go through each action and create places, transitions, and two arcs. And then assembled into Petri nets; fourthly, insert the weight of the directed arc (F) of P pointing to T into C^+, and the weight of the directed arc (F) of pointing to P into C^-; finally, the idea of depth-first search is used to find the valve operation and output the valves operation sequences.

Algorithm 1 Automatic planning by PDDL and Petri nets

Input: Entity actions set A, initial states set I, goal states set G, singleton set S, count set C, predicates set P, and object set O;
Output: Sequence of operation set O;

Initialize $C^+ \leftarrow \{\}$, $C^- \leftarrow \{\}$, $m_0 \leftarrow \{\}$, $m_g \leftarrow \{\}$, $T \leftarrow \{\}$, $F \leftarrow \{\}$, $O \leftarrow \{\}$, P $\leftarrow \{\}$;
for all c in C **do**
    Create a place p, Mc(p) $\leftarrow f(c)$, and P $\leftarrow$ P $\cup$ { p};
end for
for all s in S **do**
    Create a place p, Mc(p) $\leftarrow g(s)$, and P $\leftarrow$ P $\cup$ { p};
end for
for all *obj* in O **do**
  for all p in P **do**
    Create a place p, Mc(p) $\leftarrow h(p)$, and P $\leftarrow$ P $\cup$ { p};
  end for
end for
for all a in A **do**
    Create a place p, create two transition t_i, *to*, and create two directed arc f_i, f_o;
    f_i is from t_i point to p, f_o is from p point to t_o;
    Calculate p, t_i, t_o, f_i, f_o into $k(x,y,z)$;
    P $\leftarrow$ P $\cup$ { p}, T $\leftarrow$ T $\cup$ { t_i, t_o}, and F $\leftarrow$ F $\cup$ { f_i, f_o};
end for
P, T, F $\in$ PN

(continued)

(continued)

20: Insert the weight of the directed arc (F) of P pointing to T into C^+, and the weight of the directed arc (F) of T pointing to P into C^-;
21: **for all** i in I **do**
22: Insert i into m_o;
23: **end for**
24: **for all** g in G **do**
25: Insert g into m_g;
26: **end for**
27: $list \leftarrow m_0$;
28: **if** $m_k == m_g$ **then**
29: Insert m_k in $list$;
30: Execution order of places is determined by the post-set places from transitions, which are placed into P;
31: **for all** o in seek the place of mark a in P **do**
32: o insert into O;
33: **end for**
34: Output O;
35: **else**
36: Calculate the sum of transition sets of enabled state under m_k state: $E_k = \{ t \in T \mid m_k \geq C - (. , t);$
37: **if** $E_k = \emptyset$ **then**
38: Exit with failure;
39: **end if**
40: **for all** each transition t in Petri nets **do**
41: **if** t in E_k **then**
42: Fire t to generate a new state m_{k+1},and return to step 33;
43: **end if**
44: **end for**
45: **end if**

4 Conclusion

Describe each operation in the beer filtration system using PDDL and improved PDDL, and convert them into Petri nets for display, as shown in Fig. 2. When the processing plant has a task, it can automatically calculate the operation sequence of the control valves through the automatic planning method. When there are three tasks, the order of operation can be calculated automatically through algorithm calculation, and Gantt chart can be listed through operation sequence, as shown in Fig. 3.

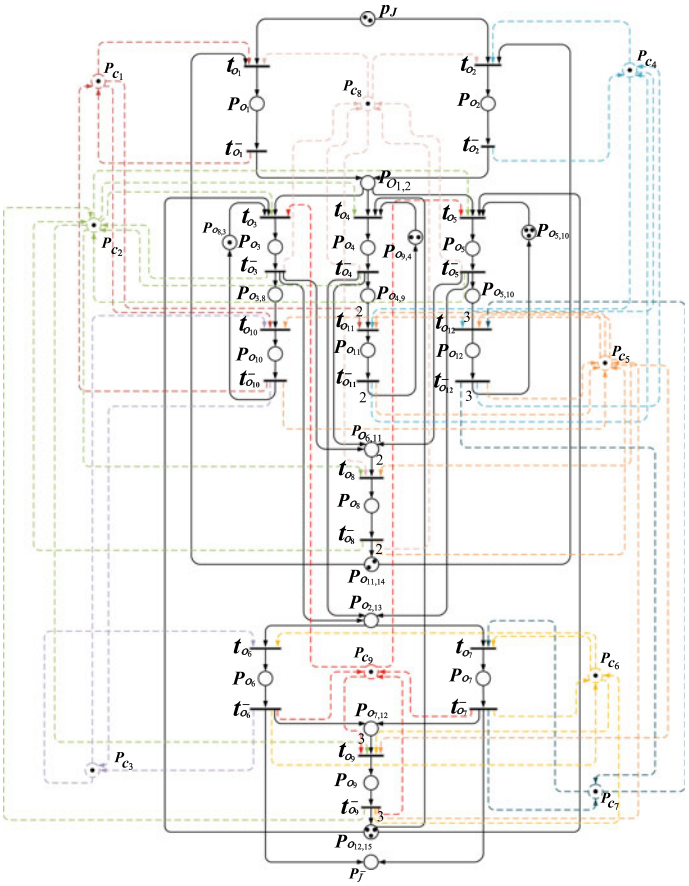

Fig. 2 The process flow diagram of a beer filtration plant

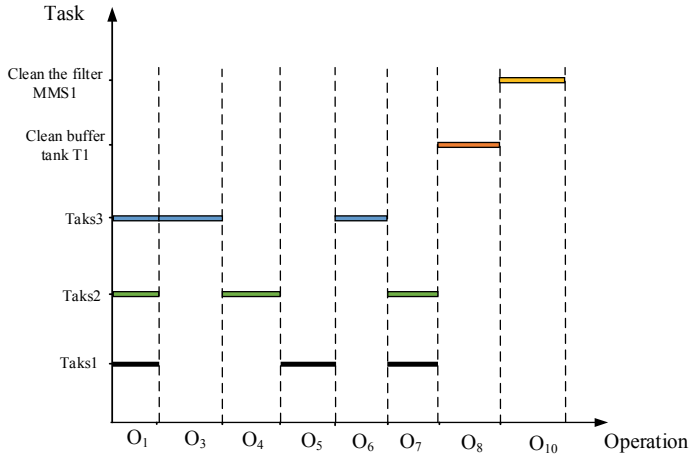

Fig. 3 Beer filtration Gantt chart

Acknowledgements This work was supported in part by National Natural Science Foundation of China under Grants 61973130.

References

1. Fu Y, Luo J, Lin W, Huang Y, Ye J (2018) Petri-net controller for pipe-line transportation system. In: 2018 5th international conference on control, decision and information technologies (CoDIT), pp 809–814
2. Luo J, Huang Y-S, Weng Y-S (2020) Design of variable traffic light control systems for preventing two-way grid network traffic jams using timed petri nets. IEEE Trans Intell Transp Syst 21(7):3117–3127
3. Wang S, Luo J (2018) Synthesis of mobile robot control system on embedded chips via petri nets. J Chin Inst Eng 41(6):442–451
4. Luo J, Tan K, Luo H, Zhou M (2021) Inference approach based on petri nets. Inf Sci 547:1008–1024
5. Boyer M, Diaz M (1999) Non equivalence between time Petri nets and time stream Petri nets. In: Proceedings 8th international workshop on Petri nets and performance models (Cat. No.PR00331), Zaragoza, Spain, pp 198–207. https://doi.org/10.1109/PNPM.1999.796566
6. Zhai Z (2010) Further study on liveness of time Petri net. In: 2010 international conference on mechanic automation and control engineering, Wuhan, China, pp 5508–5511. https://doi.org/10.1109/MACE.2010.5535580
7. Gong M, Song H, Tan J, Xie Y, Song J (2017) Fault diagnosis of motor based on mutative scale back propagation net evolving fuzzy Petri nets. In: 2017 Chinese Automation Congress (CAC), Jinan, China, pp 3826–3829. https://doi.org/10.1109/CAC.2017.8243447
8. Luo J, Ni H, Zhou M (2015) Control program design for automated guided vehicle systems via Petri nets. IEEE Trans Syst Man Cybern Syst 45(1):44–55. https://doi.org/10.1109/TSMC.2014.2342199
9. Davidrajuh R (2019) A new modular petri net for modeling large discrete-event systems: a proposal based on the literature study. Computers 8(4):83

10. McDermott D (1998) PDDL-the planning domain definition language. In: Yale center for computational vision and control. New Haven, CI, USA
11. Yeh M-L, Chang C-T (2012) An automata based method for online synthesis of emergency response procedures in batch processes. Comput Chem Eng 38:151–170
12. Li X, Luo J, Li J, Yi S, Pan C (2022) Parallel Petri nets modeling method of manufacturing system based on the improved PDDL. In: 2022 IEEE international conference on networking, sensing and control (ICNSC), Shanghai, China, pp 1–6. https://doi.org/10.1109/ICNSC55942.2022.10004131

Suitable for the Design of Electric Vehicle Charger LLC Half-Bridge Converter

Bowen Hou, Guangzhui Wei, and Hailong Ma

Abstract The development of new energy vehicles is the only way for China to move from a large automobile country to an automobile power, and it is a strategic measure to address climate change and promote green development. Based on the electric vehicle charger, the design of the half-bridge LLC resonant circuit changer is carried out to improve the charging device of new energy electric vehicles, and the resonant parameter design and resonant frequency gain system design of the half-bridge LLC half-bridge converter of the electric vehicle charger LLC are studied by analyzing the working principle and working characteristics of the half-bridge LLC resonant circuit. Through MATLAB for half-bridge LLC resonant circuit and debugging, observe the waveform and data to obtain the simulation model can effectively ensure the stability of the output, in the full load and heavy load output voltage fluctuation is within the range of change, thus verifying the feasibility of the design of the electric vehicle charger LLC half-bridge resonant converter, therefore, the LLC resonant converter can improve the conversion efficiency of the DC-DC converter, so that the charging efficiency is greatly accelerated, so as to achieve fast charging. It is efficient and fast to apply to the needs of high-power power supplies, thereby promoting the development of new energy vehicles.

Keywords DC-DC converter · EV chargers · Half-bridge LLC resonant converter · MATLAB simulation

B. Hou · G. Wei · H. Ma (✉)
Hechi University, Hechi 5470004, Guangxi, China
e-mail: 1756894073@qq.com

H. Ma
Guangxi University, Nanning 530004, Guangxi, China

S. Yadav et al. (eds.), *Energy Power and Automation Engineering*, Lecture Notes in Electrical Engineering 1118, https://doi.org/10.1007/978-981-99-8878-5_54

1 Introduction

With the continuous consumption of global non-renewable energy and the intensification of environmental pollution problems, the status of electric vehicles that are considered clean and new energy has been continuously improved, and the development of new energy electric vehicles has become the focus of social attention. The development of new energy vehicles is the only way for China to move from a major automobile country to an automobile power, and it is a strategic measure to address climate change and promote green development. However, in the process of promoting the development of new energy vehicles, the charging efficiency of new energy electric vehicles has been questioned, so on the basis of the research status and technical difficulties of high-power on-board chargers of electric vehicles, the research on the resonant converter of the post-stage LLC to improve the conversion efficiency of the post-stage DC-DC converter, so that the charging efficiency is greatly accelerated, so as to achieve fast charging is particularly important. In this paper, a simple and reliable design method is used to study the post-stage LLC resonant converter in depth, and the reliability and stability of this design method are proved through theoretical and simulation observation records [1].

2 LLC Half-Bridge Working Principle and Characteristic Analysis

In this paper, the half-bridge LLC resonant topology is selected, because the excitation source inverter circuit of the LLC resonant converter can also use the full-bridge structure or half-bridge structure, but in the case of the same gain obtained, the half-bridge structure uses fewer components, and the number of turns on the primary side of the transformer is less than half of the full-bridge circuit, which can effectively reduce the weight of the charger and is cost-effective [2]. As shown in Fig. 1, with the dead time ignored, the half-bridge structure consists of switch tubes S1 and S2, and the switch top tube S1 and switch down tube S2 alternately complement each other on and off the drive signal through the half-bridge topology with a fixed duty cycle of 50% [3]. The resonant cavity consists of two resonant inductive elements, namely the excitation inductor Lm and the resonant inductor Lr, which are composed of a resonant capacitor Cr, where Lm is usually the transformer excitation inductor, and the resonant capacitor Cr also plays the role of DC isolation. After the resonant Lm and the load are connected in parallel with Lr and Cr, through the frequency control of the switch tube driving signal, the switching tube working frequency is slightly higher than the resonant frequency, then the resonance produces a current signal similar to a sine wave, and its current phase is slightly lagging behind the voltage phase of the resonant cavity input, so that the entire cavity is inductive, so that ZVS

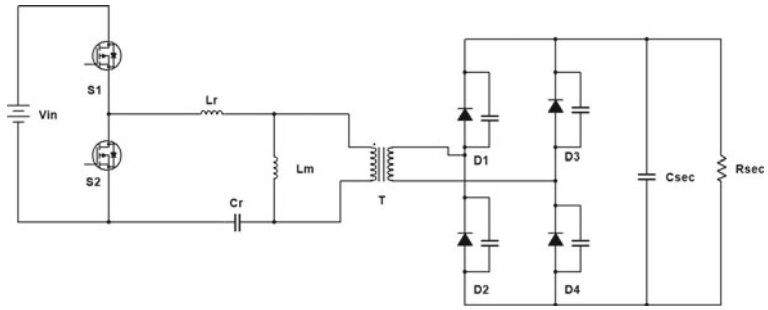

Fig. 1 Schematic diagram of the half-bridge LLC resonant main circuit

can be realized. The secondary side of the transformer is composed of rectifier diodes D1, D2, D3, and D4 to form a full-wave rectifier circuit, the capacitor Csec is the output filter capacitor, and then, we form direct current in the filter part to power the electric vehicle charger [4].

3 Suitable for EV Charger LLC Half-Bridge Converter Parameter Design

The design of EV charger LLC half-bridge converter parameters is the most critical step to improve the conversion efficiency of the post-stage DC-DC converter. Therefore, it is particularly important to design a suitable order of LLC half-bridge resonant transformation parameters and to comply with various rules [5].

The LLC resonant converter operates at two resonant frequencies, namely the series resonant frequency generated by the resonant capacitor C_r and the resonant inductor L_r, and the series–parallel resonance frequency generated by the resonant capacitor C_r, the resonant inductor L_r, and the excitation inductor L_m.

Series resonant frequency generated by resonant capacitor C_r and resonant inductor L_r:

$$f_r = \frac{1}{2\pi\sqrt{L_r C_r}} \tag{1}$$

Series and parallel resonant frequency generated by resonant capacitor C_r, resonant inductor L_r, and excitation inductor L_m:

$$f_m = \frac{1}{2\pi\sqrt{(L_m + L_r)C_r}} \tag{2}$$

3.1 Determine the Transformer Ratio

When designing a half-bridge LLC resonant converter, we first need to determine the input voltage required for our design in this article and the input voltage (V) and set the output voltage (V) for output voltage setting according to the theory of the LLC resonant converter:

$$V_{\text{input}} = 390;\ V_{\text{inputmin}} = 365;\ V_{\text{inputmax}} = 405;\ V_{\text{output}} = 55V$$

The selection of a suitable core model is not only based on theoretical calculations to determine the turns ratio of the transformer, but also the original calculation without considering the resonant gain adjustment, series–parallel resonance frequency F_r.

Turns ratio of transformers:

$$n = \frac{V_{\text{input}}}{2V_{\text{output}}} = 3.7 \tag{3}$$

There into V_{input} is the input voltage, and V_{output} is the output voltage.

3.2 Determine the Maximum and Minimum Gain

First, we first determine the voltage rating of the rectifier diode tube voltage drop and the voltage drop on the secondary side line, because the voltage rating of the diode tube voltage drop and the voltage drop on the secondary side line is an important factor in determining the maximum and minimum gain [6].

Diode tube voltage drop:

$$V_D = 0.7V \tag{4}$$

The rated voltage drop on the secondary line:

$$V_{\text{loss}} = 1.05V \tag{5}$$

Calculate the minimum gain:

$$H_{g\min} = \frac{n(V_{\text{outmin}} + V_D)}{\left(\frac{V_{\text{inputmax}}}{2}\right)} = 1.019 \tag{6}$$

Calculate the maximum gain:

$$H_{g\max} = \frac{n(V_{\text{outmin}} + V_D + V_{\text{loss}})}{\left(\frac{V_{\text{inputmin}}}{2}\right)} = 1.152 \tag{7}$$

The highest gain values are:

$$H_{g\max} = 1.2 \tag{8}$$

3.3 Select the Appropriate Γ and Q Values and Plot the Gain Curve of the LLC Half-Bridge Converter

Characteristic impedance:

$$Z_0 = \sqrt{\frac{L_r}{C_r}} = 2\pi f_r L_r = \frac{1}{2\pi f_r C_r} \tag{9}$$

Factor of merit:

$$Q = \frac{Z_0}{R_{\text{ac}}} = \frac{Z_0}{n^2 R_e} = \frac{\pi^2 Z_0 P_0}{8n^2 V_0^2} \tag{10}$$

Ratio of inductance:

$$L_n = \frac{L_m}{L_r} \tag{11}$$

Normalization frequency:

$$f_n = \frac{f_s}{f_r} \tag{12}$$

Define γ and Q values:

$$\gamma = 3.5,\ Q = 0.27 \tag{13}$$

In an LLC half-bridge converter, the converter gain is mainly determined by the switching frequency, and the LLC gain function is calculated:

$$H(\gamma, Q, f_n) = \frac{1}{\sqrt{\left[1 + \frac{1}{\gamma}\left(1 - \frac{1}{f_n^2}\right)\right]^2 + \left[Q\left(f_n - \frac{1}{f_n}\right)\right]^2}} \tag{14}$$

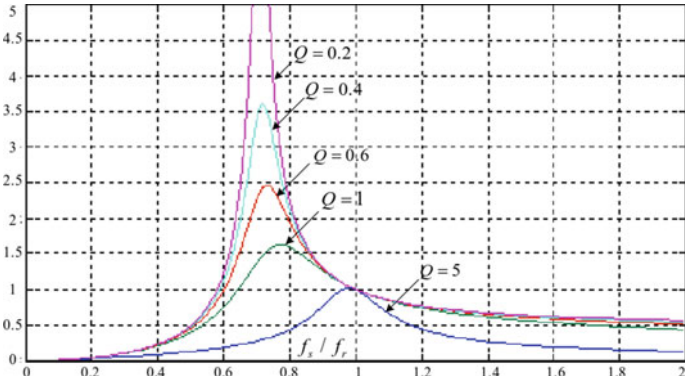

Fig. 2 DC gain curves for different quality factors

Cuse $Q = 0$, that is, the DC voltage gain of the converter in the no-load state is (Fig. 2):

$$M_{\mathrm{OL}}(f_n, \lambda) = \frac{1}{1 + \lambda - \frac{\lambda}{f_n^2}} \tag{15}$$

3.4 Determine the Equivalent Resistance and Calculate the Resonance Parameters

Equivalent load calculation (rated output power rated output voltage): When the output voltage is 55 V and the output current is 11.5 A, then:

$$R_L = \frac{V_{\mathrm{output}}}{I_o} = 4.78\ \Omega \tag{16}$$

$$R_{L\min} = \frac{V_{\mathrm{output}}}{1.1 I_o} = 4.34\ \Omega \tag{17}$$

Equivalent internal resistance:

$$R_e = \frac{8n^2}{\pi^2} R_L = 53.09\ \Omega \tag{18}$$

$$R_{e\min} = \frac{8n^2}{\pi^2} R_{L\min} = 48.20\ \Omega \tag{19}$$

Calculate the resonant capacitance:

$$C_r = \frac{1}{2\pi Q\pi R_e} = 1.12 \times 10^{-7} F \tag{20}$$

Calculate the resonant inductance:

$$L_r = \frac{1}{(2\pi f_r)^2 C_r} = 2.26 \times 10^{-5} H \tag{21}$$

Calculate the excitation inductance:

$$L_m = \gamma L_r = 7.91 \times 10^{-5} H \tag{22}$$

The MOSFET tube is selected as the switching transistor, in order to make the on-resistance small enough, its maximum peak current rating should be 5 ~ 10 times of the peak current of the above equation, which can reduce the on-voltage drop and loss [7].

3.5 Design Resonance Parameters

In summary, the design requirements for the parameter design of the LLC half-bridge converter suitable for electric vehicle chargers are shown in the following Table 1.

By designing the parameters of the LLC half-bridge converter suitable for electric vehicle chargers, we then use the principle of LLC resonant converter and related formulas to calculate the transformer turn ratio, gain range, resonant frequency range,

Table 1 Design indicators and some device parameters of the electric vehicle charger LLC half-bridge converter

Input DC Voltage range	V_{input}	365 ~ 405 V
Rated input DC voltage	V_{rated}	390 V
Rated output voltage	V_{out}	55 V
Rated output current	I_{out}	11.5 A
Rated power	P	600 W
Expect efficiency	*H*	97%
Duty cycle	DT	0.5
Rectifier diodes On-voltage drop	DV	0.7 V

Table 2 Circuit device parameters suitable for EV charger LLC half-bridge converter design

Transformer Turns ratio	N1:N2	3.7:1
Gain range	M min ~ max	0.533 ~ 1.191
Resonant frequency range	Fr min ~ max	80 ~ 130 kHz
Inductance ratio	Ln	3.5
Resonant capacitors	Cr	112nF
Resonant inductance	Lr	22.6μH
Excitation inductance	Lm	7.91μH

inductance ratio, resonant capacitance, resonant inductance, and inspirational inductance. The specific main circuit device parameters of the LLC half-bridge converter design are shown in the following table, that is, the main circuit device parameters of the LLC half-bridge converter design in Table 2 [8].

4 Resonant Gain System Design

After the input 390 V DC is step-down and resonant converted, the output is obtained after rectification and filtering on the secondary side of the transformer to obtain a DC current with an output of about 55 V. Because the characteristics of the LLC circuit are low-frequency filtering, energy is transferred through the fundamental image load, and resonant conversion is required in this process, so we need to design a resonant frequency to control the half-bridge LLC switch, so that the output voltage is more stable and reliable, and the resonant frequency gain system is shown in Fig. 3.

According to the characteristics of the impedance of the resonant element in the resonant network with frequency, the constant voltage output of the resonant converter can be realized, and the control and adjustment of the voltage gain can be realized by adjusting the size of the voltage injected into the resonant network by adjusting the switching frequency injected by the switching network. The system simulation is carried out on the basis of the block diagram of the resonant frequency gain system of the half-bridge LLC in the figure above. The simulation diagram of the resonant frequency gain system of the half-bridge LLC is shown in Fig. 4.

5 MATLAB Simulation and Results Analysis

In order to show the working process of the half-bridge LLC converter more clearly, the Simulink module in MATLAB is used to build a model of the half-bridge LLC resonant converter and simulate it, and replace the load with resistance, and apply the oscilloscope to detect the voltage and current waveforms of various components. The simulation is shown in the figure below, and Fig. 5 is a simulation design for the

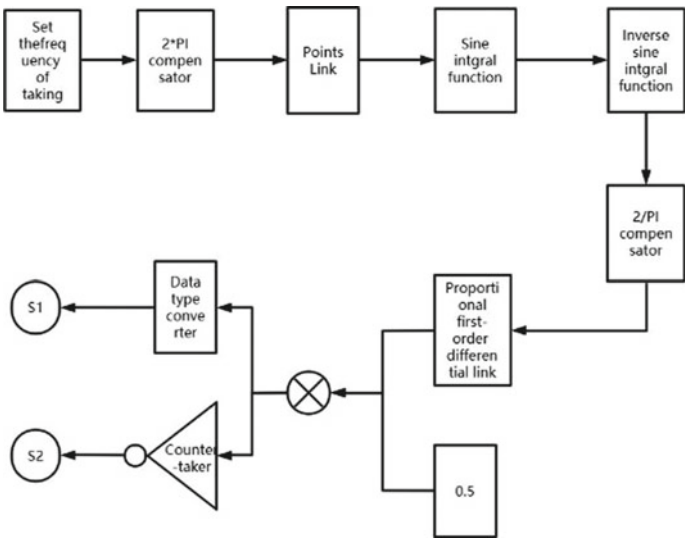

Fig. 3 Resonant frequency gain system diagram of half-bridge LLC

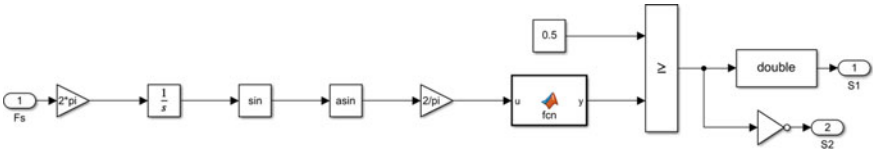

Fig. 4 Simulation diagram of resonant frequency benefit system of half-bridge LLC

LLC half-bridge converter suitable for electric vehicle chargers. The figure consists of the main circuit section, the lower left resonant frequency system section, and the right oscilloscope [9].

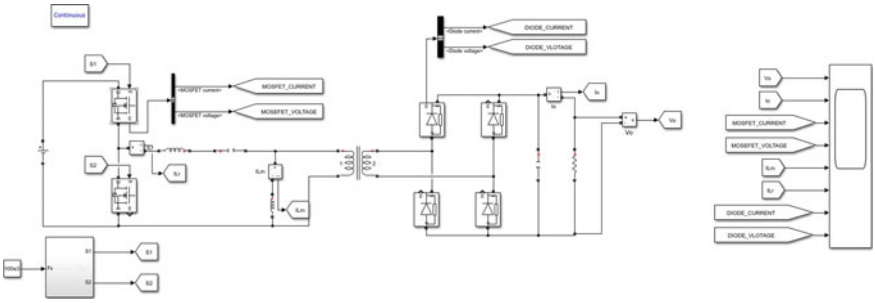

Fig. 5 Simulation design diagram of LLC half-bridge converter suitable for electric vehicle charger

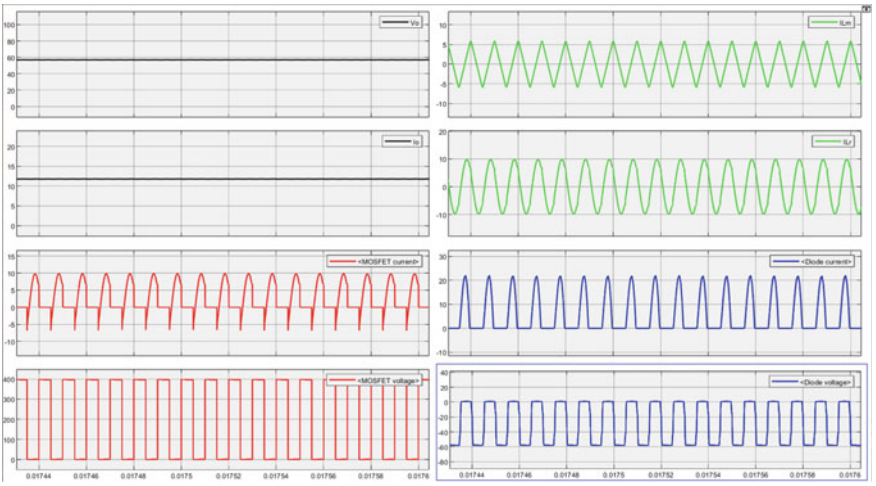

Fig. 6 Waveform diagram of various components suitable for simulation of electric vehicle charger LLC half-bridge converter

The two figures in the lower left corner of Fig. 6 are the current and voltage waveforms of the MOSFET in the LLC half-bridge converter; the two figures in the upper right corner are the current waveform diagram of the excitation inductor Lm and the resonant inductor Lr; the two figures in the lower right corner are the current and voltage waveforms of the rectifier diode [10].

Figures 7 and 8 show 390 V AC input, 55 V output voltage, and 11.5 A output current waveforms. From the above figure, it can be concluded that the output voltage and current are relatively stable, and the output data meets the requirements of theoretical calculation.

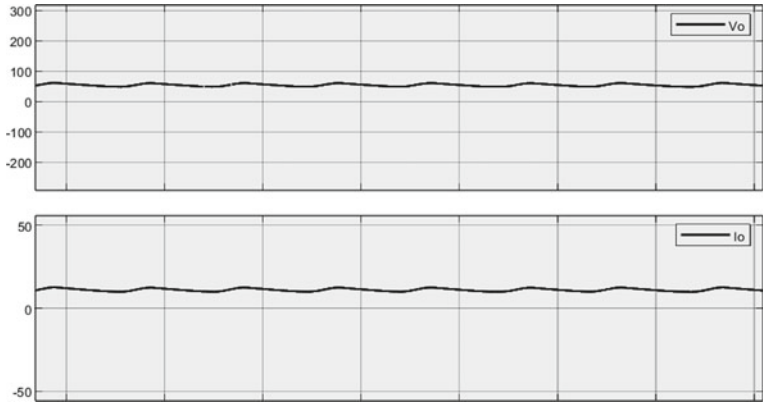

Fig. 7 Output voltage and current waveform diagram

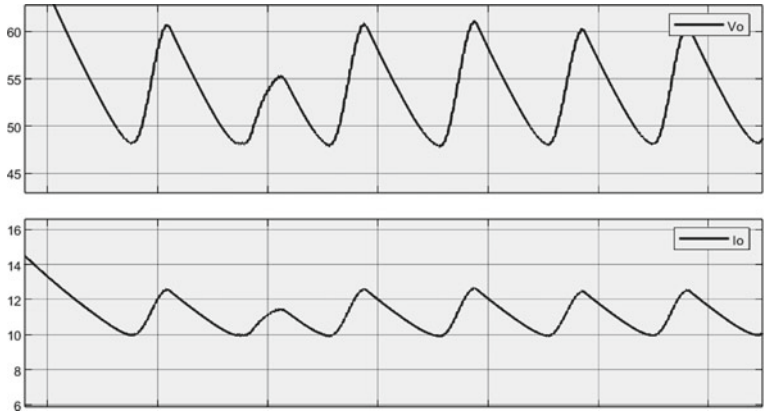

Fig. 8 Output voltage and current waveform diagram

6 MATLAB Simulation and Conclusions

This simulation design is to optimize the post-stage DC/DC circuit part of the electric vehicle charger, design the half-bridge LLC resonant circuit changer, analyze the working principle and working characteristics of the half-bridge LLC resonant circuit, study the resonant parameter design of the electric vehicle charger LLC half-bridge converter, conduct half-bridge LLC resonant circuit and debugging through MATLAB, and observe the waveform and data to obtain the simulation model can effectively ensure the stability of the output. The output voltage fluctuation is within the range of full load and no load, which verifies the feasibility of the resonant parameter design of the electric vehicle charger LLC half-bridge converter, so this design can improve the conversion efficiency of the DC-DC converter, greatly accelerate the charging efficiency, and realize fast charging. Meet the needs of efficient, fast, and high-power power supplies.

Acknowledgements This work was financially supported by 2022 Annual Curriculum Ideological and Political Construction Project of Hechi University (NO.2022KCSZ06); National College Students' Innovation plan Training Project (NO. S202210605005).

References

1. Wang ZA, Liu JJ (2009) Power electronics technology, 5th edn. China Machine Press, Beijing, p 5
2. Zhao D (2015) Design of on-board charger for electric vehicle. Beijing Jiaotong University, p 7
3. Xiaodong W (2018) Design of LLC resonant electric vehicle on-board charger. Beijing Jiaotong University, p 6

4. Junjun D (2015) Research on high-efficiency resonant converter for on-board charger for electric vehicles. Northwestern Polytechnical University, p 11
5. Tao Z, Xiaoping Z (2016) Design of electric vehicle charger based on LLC converter. Zhejiang Communications Vocational and Technical College, p 6
6. Rui S (2022) Research on stable charging technology of lithium battery based on half-bridge LLC resonant converter. Nanjing University of Information Science and Technology, p 6
7. Lihong Z (2006) Design of LLC resonant converter. Zhejiang University, p 5
8. Zhihui W (2016) Research and circuit design of 3.5kW electric vehicle on-board charger. Southwest Jiaotong University, p 4
9. Xin L (2018) Research and design of electric vehicle charging module based on half-bridge LLC resonance. Huashan East University of Science and Technology, p 5
10. Chong Y (2021) Research on two-stage AC/DC converter based on totem pole PFC. Xi'an University of Technology, p 6

Research on Buck Converter Based on Digital Control

Tonglin Wang, Hailong Ma, and Meimei Wu

Abstract With the rapid development of modern power electronics, digital technology is playing an increasingly important role in buck converters. The traditional analog-integrated chip-controlled buck converter requires a large number of components and is too large to meet the needs of power conversion development. The rapid development of digital control technology has led to the development of intelligent and miniaturized power conversion devices. To meet the development needs of miniaturization, digitalization, and efficiency of buck converter, this paper designs and verifies a buck converter based on digital control through the study of digital pulse modulation, signal processing, and PID algorithm. The device is controlled using an integrated chip and can achieve a wide range input of 50 V–240 V, a digitally adjustable output of 12 V–36 V, and a maximum output power of 100 W.

Keywords Buck converter · Digital control · PID algorithm

1 Introduction

With the rapid development of DC voltage generation technologies for renewable energy sources, such as fuel and photovoltaic cells, Buck converters are widely used in the power industry [1], such as DC motor drives, electric vehicles and home appliances [2]. Also buck converters are widely used in battery chargers, microprocessors, and motherboards [3]. With the massive access to various distributed energy sources, buck converters are widely used in DC microgrid systems [4], and as a bridge between DC power loads and DC grid energy exchange, DC converters have important research value due to their advantages such as high efficiency and good dynamic performance [5]. Along with the development of various technology

T. Wang · H. Ma (✉) · M. Wu
Hechi University, Hechi 5470004, Guangxi, China
e-mail: mahailong@hcnu.edu.cn

H. Ma
Guangxi University, Nanning 530004, Guangxi, China

S. Yadav et al. (eds.), *Energy Power and Automation Engineering*, Lecture Notes in Electrical Engineering 1118, https://doi.org/10.1007/978-981-99-8878-5_55

fields to complete the update [6], buck converters are continuously improving their power density, efficiency, and fast dynamic response [7]. The traditional analog integrated chip-controlled buck converter requires a large number of components and is too bulky to meet the needs of power conversion development, so the use of digital control systems is the main area of innovation [8].

2 Digitally Controlled Buck Converter and Control Strategy

2.1 Digitally Controlled Buck Converter

Based on the converter function designed in this paper, the synchronous buck topology is selected as shown in Fig. 1. The synchronous buck converter achieves a lower conduction loss by replacing the diode of the asynchronous buck converter with a switching synchronous device. However, the synchronous buck circuit needs to control two transistors at the same time, and the control is more complicated. With the development of digital control technology, a digital chip with an internally integrated controller and upper and lower transistors can solve these problems very well. Synchronous Buck converter in the transistor Q1 conduction Q2 in the off state, at this time by the input power supply with inductors, capacitors and loads to form a circuit for inductor charging, so that the output voltage began to gradually rise. When the output reaches the required voltage level, transistor Q1 is turned off, and Q2 is in the on state, the circuit composed of the inductor, capacitor, and load, the power supply is not providing energy, but due to the characteristics of the inductor, the current cannot change abruptly, so the circuit does not have a power supply but the inductor continues to output power. The use of fast on and off switching tubes can be achieved on the DC voltage chopper buck.

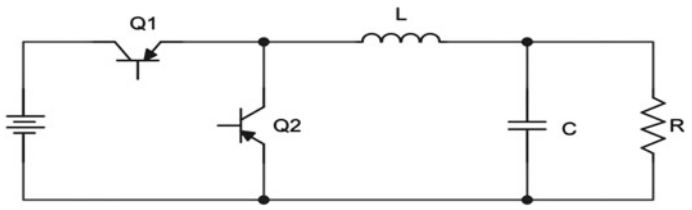

Fig. 1 Synchronous buck circuit

2.2 Control Strategy

PWM is considered as the core of the converter [9], the buck converter designed in this paper is controlled by digital PWM signal, which has better anti-noise performance and faster response to the change of output load when pulse width is adjusted [10], the PWM period is set by using the ARR of MCU timer reload value and the CCR of capture/comparison register value to set the PWM duty cycle, and the counter is set to count up. The control principle is shown in Fig. 2, in t1 time period, the count value is less than the comparison register value, output low; in t1t2 time period, the count value is greater than the comparison register value, output high; at t2, the count value is equal to the reload value, the counter overflows and starts from 0 again, and so on. Using the voltage loop feedback, the output is adjusted by the incremental PID algorithm. The incremental PID algorithm is shown in Fig. 3 to adjust the PWM output by proportional, integral, and differential operations of the error between the ADC detection value and the target value.

3 Main Circuit Component Selection

The main technical specifications of the device designed in this paper are shown in Table 1 design parameters.

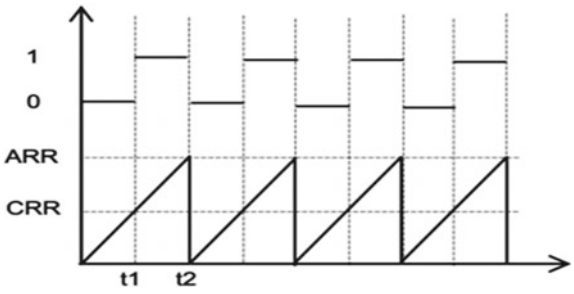

Fig. 2 PWM control principle

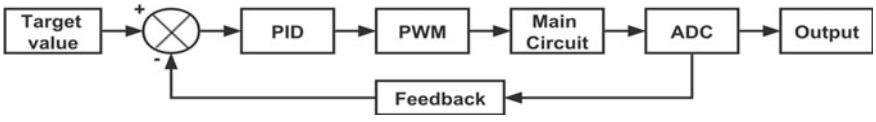

Fig. 3 Incremental PID

Table 1 Circuit design parameters

	Parameters	Numerical values
1	Input voltage range	50 V–240 V
2	Output voltage range	12 V–36 V
3	Switching frequency	13 kHz
4	Output power	100 W

Input and output voltage values versus minimum duty cycle are tried as:

$$D = \frac{U_{\mathrm{OUT}}}{U_{\mathrm{IN}}} = \frac{12}{240} = 0.05 \tag{1}$$

The theoretical maximum output current of the device should be 2.8 A. In the actual design, in order to prevent overload burned device, based on the output voltage IOUT for 10 A to calculate the required components, according to engineering practice, it is known that the general current ripple rate of 0.4, the peak current value formula can be obtained as follows:

$$I_{\mathrm{PP}} = (1 + 0.4) \times I_{\mathrm{OUT}} = 14\ \mathrm{A} \tag{2}$$

The switching frequency FSW is 13 kHz and the minimum inductance value is:

$$L_{\mathrm{MIN}} = \frac{V_{\mathrm{OUT}} \times (1 - D)}{0.4 \times I_{\mathrm{pp}} \times F_{\mathrm{SW}}} = 156\ \mathrm{uH} \tag{3}$$

According to engineering practice, inductance value needs to keep margin and combined with the actual inductor model, and this paper designs inductor selection 220 uH. The output voltage ripple is generally 0.01 of the rated voltage, so the output ripple voltage V_r is:

$$V_r = 0.01 \times (V_{\mathrm{max}} - V_{\mathrm{min}}) = 0.24\ \mathrm{V} \tag{4}$$

The switching tube frequency FSW is 13 kHz, so the on or off time of the switching tube can be approximated as:

$$\Delta t = \frac{1}{F_{\mathrm{SW}}} \times \frac{1}{2} = 38\ \mathrm{uS} \tag{5}$$

According to the formula $V_r = I_{\mathrm{OUT}} \times \frac{\Delta t}{C}$, the minimum capacitance value $C =$ 3.2 mF can be calculated. In order to reduce the voltage fluctuation more effectively and according to the actual capacitor type, two capacitors with a voltage withstand value of 50 V, 4700 uF are connected in parallel, and two more 0.1 uF capacitors are connected in parallel to reduce the high frequency interference.

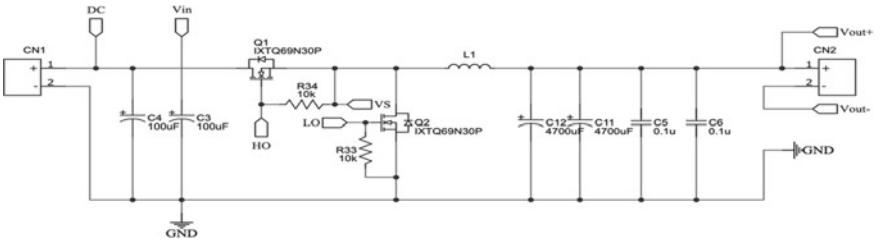

Fig. 4 Buck circuit

4 Converter Design

4.1 Main Circuit Design

The buck circuit design is shown in Fig. 4. The input voltage is filtered by two aluminum electrolytic capacitors with 450 V withstanding voltage and 100 uF capacity to make the input voltage waveform smoother and more stable. The output inductor is 220 uH, and the output capacitor is composed of two aluminum electrolytic capacitors with a voltage tolerance of 50 V and a capacity of 4700 uF in parallel with two 0.1 uF ceramic capacitors. The switching tube is IXTQ69N30P field effect tube, whose VDSS can reach 300 V and current can reach 69 A, with high switching speed and low switching loss. Vout+ and Vout− are the output voltage sampling interfaces, where Vout− is also the output current sampling interface, and HO and LO are controlled by the driver chip to turn on and off.

4.2 Sampling Circuit

The sampling circuit as shown in Fig. 5 is composed of LM358 op-amps, A is the output voltage sampling circuit, the use of differential op-amps can well suppress common mode interference and provide signal-to-noise ratio, and the amplification of the differential input voltage is R4 than R1; B is the output current sampling circuit, by sampling the voltage on R8 and convert it to current value through conversion algorithm; C is the input voltage detection circuit, is a voltage following circuit composed of op-amps, the output voltage value is the voltage value on R12, D is the protection circuit, is a comparator composed of op-amps, by the voltage division of the power supply and the current detection circuit, and the output voltage value is the voltage value on R12. C is the input voltage detection circuit, a voltage following circuit composed of op-amps, the output voltage value is the voltage value on R12, D is the protection circuit, a comparator composed of op-amps, by comparing the op-amp power divider value with the output value of the current detection circuit; when an overload occurs, the output value of the circuit detection circuit is greater

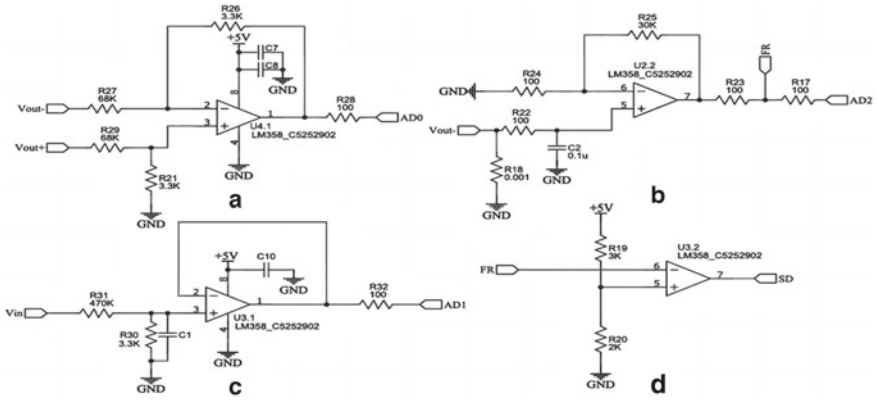

Fig. 5 Sampling circuit

than the op-amp power divider value, and the circuit outputs a low level to disable the driver chip.

4.3 Drive Circuit

The driver circuit design is shown in Fig. 6. The SD port is connected to the main control chip and the overcurrent protection circuit to control whether the chip works or not, and the IN port is connected to the main control chip to control the IR2104 chip to output PWM waves. The two MOS tubes of the synchronous buck converter can be controlled with only one PWM signal. When the MOS tube works, its drain level floats to ground, and the potential is not 0. At this time, it is necessary to place a bootstrap capacitor between VB and VS and charge it with a bootstrap diode to form a voltage difference between HO and VS, which can be used to open the upper bridge arm. In series with the gate resistor to increase the oscillation damping to reduce the sharp oscillation of the PWM waveform to avoid MOS damage, because the MOS tube gate and source input impedance is very high, in order to avoid MOS tube misconductor, so in parallel with a 10 K resistor between the source and the gate.

4.4 Master Control Chip Circuit

The main control chip circuit is shown in Fig. 7. The main control chip used in this paper is an STM32F030F4P6 chip with a maximum frequency of 48 MHz, a built-in 32-bit core, 256 KB of flash memory, 32 KB of static RAM, 20 ports, a 5-channel DMA controller, a 12-bit ADC with up to 16 channels, and six channels

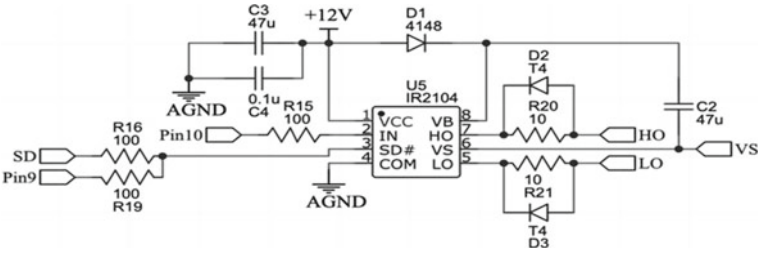

Fig. 6 Drive circuit

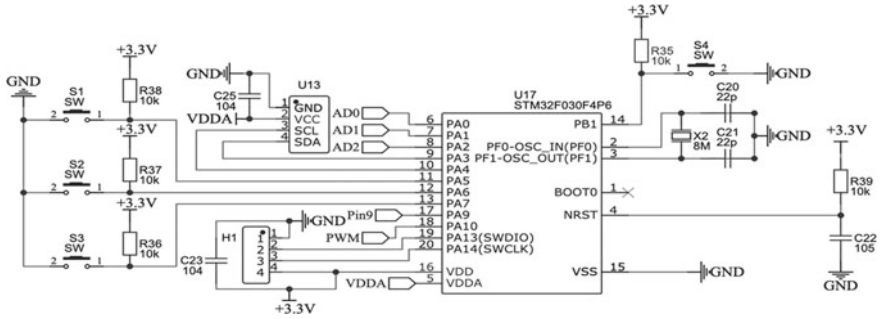

Fig. 7 Main control chip circuit

of PWM output. STM32 chip HSE default is 8 MHz, and using 8 MHz crystal can easily calculate the main clock frequency. When the microcontroller is powered on, the capacitor is charged, and after the capacitor is charged, the reset pin goes from low to high to complete the reset. VDD can effectively filter out the high-frequency components in the voltage by grounding the filter capacitor, which can ensure the stability of the power supply.

4.5 Programming

The main control program is shown in Fig. 8. After system initialization, the ADC subroutine is called for sampling. The ADC subroutine uses three channels to read the input voltage, output voltage, and output current, respectively, and the read values are averaged to reduce the error and converted to actual values by mathematical operations. If the setting mode is selected, the output voltage and output current limit values are set by key and displayed on the OLED; if no regulation mode is selected, the OLED directly displays the system operation parameters. After the output starts, the actual value of output current and voltage collected by ADC is compared with the protection value; if the output exceeds the protection value, the output is stopped immediately; if it does not exceed the protection value, the PID regulation program

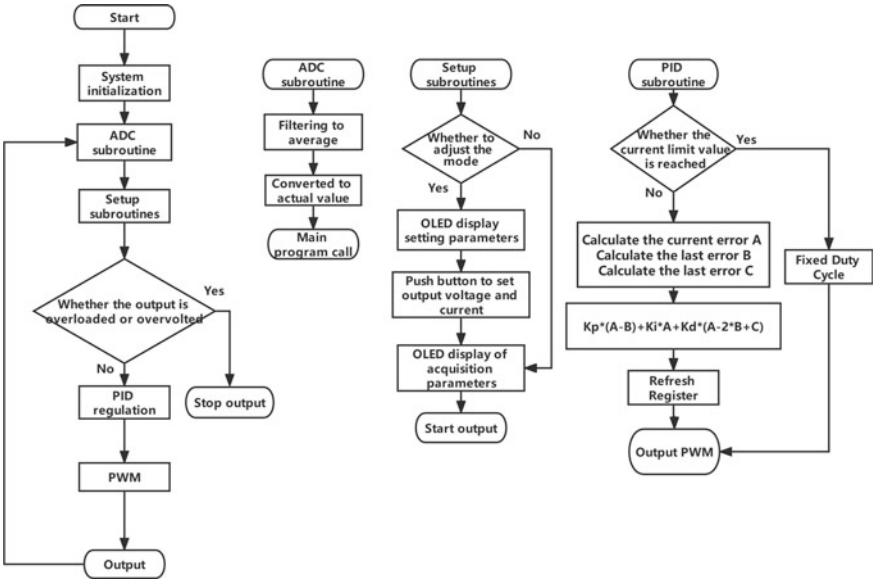

Fig. 8 Master control program

is entered. In the PID program, first judge whether the output current value reaches the set current limit value, if it reaches the limit value, then jump out of the PID program; if it does not reach, then calculate the current error value A, the last error value B, and the last error value C; through the incremental PID formula, update the register value to change the duty cycle.

5 Experimental Tests and Conclusions

5.1 Experimental Testing

The digitally controlled buck converter is physically shown in Fig. 9, using an adjustable DC source as the device input and a cement resistor as the load for testing.

After connecting the experimental device, adjust the input voltage to 50 V, set the output voltage to 12 V, and test its no-load output with MOS tube waveform as shown in Fig. 10.

At an input voltage of 50 V and an output voltage of 12 V no-load, the output is stable with a switching tube duty cycle of 21.8% and a drive voltage peak-to-peak of 12.20 V, which is consistent with the design.

While keeping the output voltage at 12 V, the input voltage is increased to 240 V, and the no-load output and MOS tube waveforms are tested as shown in Fig. 11.

Fig. 9 Physical device

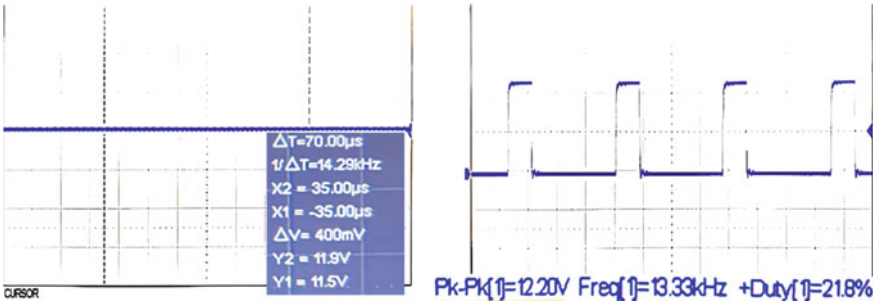

Fig. 10 No-load output and MOS tube waveform at 50 V input and 12 V output

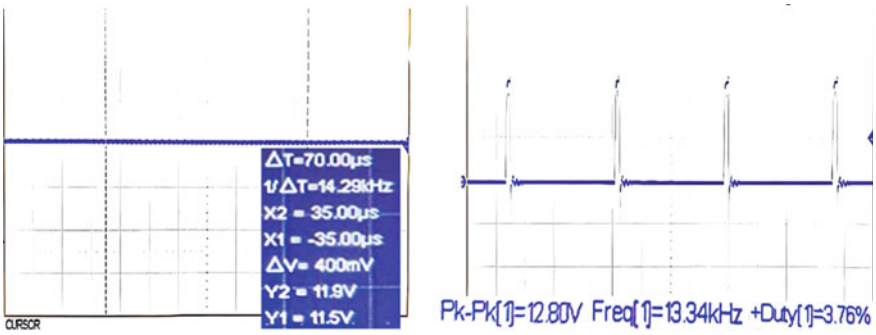

Fig. 11 Input 240 V output 12 V case, no-load output and MOS tube waveform

When the input voltage is raised to 240 V and the output voltage is 12 V no-load, the output remains stable with a switching tube duty cycle of 3.76% and a drive voltage peak-to-peak of 12.80 V, which is consistent with the design.

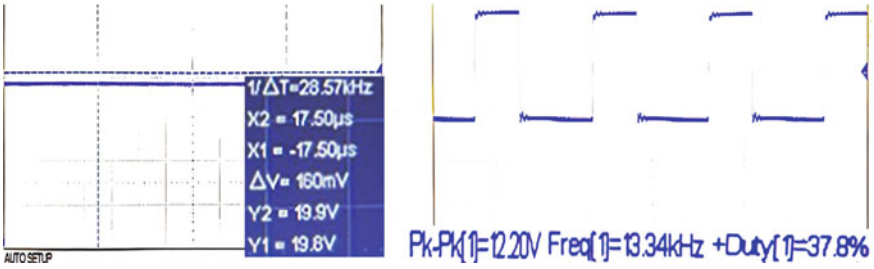

Fig. 12 Input 50 V output 40 W case, the output and MOS tube waveform

Set the input voltage to 50 V, test its 40 W power output, set the output voltage to 20 V, use 10R cement resistor as load, the output and MOS tube waveform as shown in Fig. 12.

At an input voltage of 50 V, output voltage of 20 V, and output power of 40 W, the output is stable, the duty cycle of the switching tube is 37.8%, and the peak-to-peak value of the driving voltage is 12.20 V, which is consistent with the design.

While keeping the output voltage at 20 V, the input voltage was increased to 180 V and the output and MOS tube waveforms were tested as shown in Fig. 13.

When the input voltage is raised to 180 V, the output voltage is 20 V, and the output power is 40 W, the output remains stable, the duty cycle of the switching tube is 10.4%, and the peak-to-peak value of the driving voltage is 13.80 V, which is consistent with the design.

Set the input voltage to 50 V, test its 100 W power output, set the output voltage to 36 V, use 12R cement resistor as load, the output waveform and MOS tube waveform as shown in Fig. 14.

At an input voltage of 50 V, an output voltage of 36 V, and an output power of 100 W, the output remains stable, the duty cycle of the switch is 78.4%, and the peak-to-peak drive voltage is 12.20 V, which is in accordance with the design.

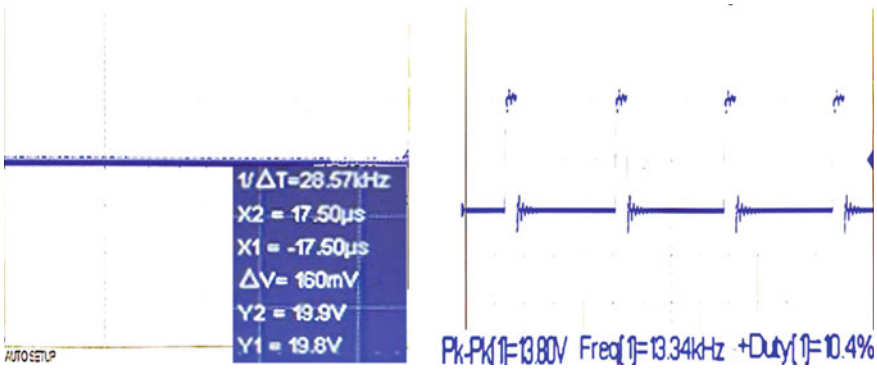

Fig. 13 Input 180 V output 40 W case, the output and MOS tube waveform

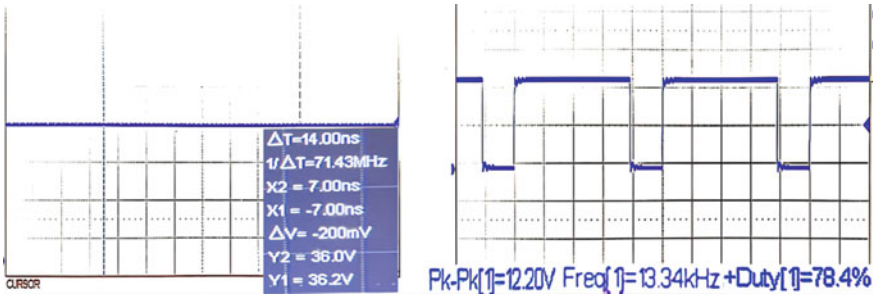

Fig. 14 Input 50 V output 100 W case, the output and MOS tube waveform

Through the test, the output can be stable, and the maximum power can reach 100 W when the input voltage varies in a wide range.

5.2 Conclusion

In this paper, a digitally controlled buck converter is designed by studying the principle of CNC buck converter. The main converter circuit, ADC sampling circuit, and protection circuit are designed by studying the synchronous buck topology. The main control program is designed through the study of digital incremental PID algorithm. Through the experimental demonstration of the real object, the device can realize a wide range of DC 50–240 V input to adapt to various application scenarios with different voltage level requirements and a digitally adjustable output of 12–36 V with a maximum output power of 100 W, which can be applied to the DC output module in the comprehensive training device of power electronics and the power supply device in electrical design.

Later, it can be replaced by components with higher voltage withstand values and more advanced control algorithms to achieve higher levels of accurate voltage conversion, apply it to voltage conversion in new energy electric vehicles, and to meet the need for voltage conversion in large electrical equipment.

Acknowledgements This work was financially supported by National College Students' Innovation plan Training Project (NO.202210605021); 2022 Annual Curriculum Ideological and Political Construction Project of Hechi University (NO.2022KCSZ06).

References

1. Łakomy K et al (2022) Active disturbance rejection control design with suppression of sensor noise effects in application to DC–DC Buck power converter. IEEE Trans Industr Electron 69(1):816–824. https://doi.org/10.1109/TIE.2021.3055187

2. Al-Baidhani H, Salvatierra T, Ordóñez R, Kazimierczuk MK (2021) Simplified nonlinear voltage-mode control of PWM DC-DC Buck converter. IEEE Trans Energy Convers 36(1):431–440. https://doi.org/10.1109/TEC.2020.3007739
3. Aguilar-Ibanez C, Moreno-Valenzuela J, García-Alarcón O, Martinez-Lopez M, Acosta JÁ, Suarez-Castanon MS (2021) PI-type controllers and Σ-Δ modulation for saturated DC-DC Buck power converters. IEEE Access 9:20346–20357. https://doi.org/10.1109/ACCESS.2021.3054600
4. Hao MK, Wang WS, Wu ZQ et al (2022) Multi-mode control study of interleaved parallel Buck-boost converter. Power Electron Technol 56(11):110–112
5. Liu F, Wu ZQ, Wang HD et al (2022) A new three-phase L-shaped dual active bridge Buck-boost converter. Power Electron Technol 56(09):119–121
6. Yang Z, Lei Z (2022) LTC3855-based dual-channel synchronous buck DC/DC converter design. Microprocessor 43(02):16–20
7. Guan Y, Cecati C, Alonso JM, Zhang Z (2021) Review of high-frequency high-voltage-conversion-ratio DC–DC converters. IEEE J Emerg Sel Top Ind Electron 2(4):374–389. https://doi.org/10.1109/JESTIE.2021.3051554
8. Dimitrov V, Hinov N, Genev K (2021) Synthesis and implementation of a digital control system for a Buck DC-DC converter. In: 2021 29th national conference with international participation (TELECOM), Sofia, Bulgaria, pp 161–166. https://doi.org/10.1109/TELECOM53156.2021.9659658
9. Ramkumar MS, Amudha A, Nagaveni P et al (2021) Analysed results of DC-DC converters with softswitching techinques. Materials Today Proc 37:2631–2635
10. Hong Y-W, Chen B-W, Wang Q et al (2021) Optimization method for Type III loop compensation in voltage-mode Buck circuits. Power Tech 45(09):1209–1212, 1226

Research on Improved Droop Control Based on Virtual Impedance Compensation Strategy

Dong Zhao, Bing Hu, Zeyuan Li, Yuefei Xian, Zhenhua Zhao, and Chunwei Shao

Abstract With the application of new power equipment such as hydropower, photovoltaic, and wind power, as well as the promotion of the "oil to electricity" policy for large equipment such as the petroleum, mining, and automotive industries, the demand for megawatt level high-power power sources is becoming increasingly urgent. However, due to hardware limitations such as reactors, transformers, and IGBT, the development of large-capacity individual power supplies is constrained, while multiple power modules can be expanded in series and parallel according to power requirements, providing a new approach for the design of large-capacity power supplies. Focus on the problem of current inequality and bus voltage fluctuations during load disturbances in the parallel operation of high-power DC power sources, an improved droop control algorithm based on a high-pass filter virtual impedance compensation strategy was proposed. The simulation and experimental results show that the improved droop control algorithm achieves current sharing control when high-power DC power sources are operated in parallel, and effectively improves the dynamic characteristics under load disturbances.

Keywords DC power supply · Virtual impedance compensation · Improved droop control

1 Introduction

In recent years, with the accelerated application of new power equipment such as hydropower, photovoltaic power generation, and wind power generation, as well as the promotion of the policy of "oil to electricity" for large equipment such as petroleum equipment and mining equipment, a large number of power electronic devices have been widely used, giving rise to the demand for larger capacity, higher accuracy, and higher stability power supply systems [1]. However, the development

D. Zhao (✉) · B. Hu · Z. Li · Y. Xian · Z. Zhao · C. Shao
CRRC Qingdao Sifang Rolling Stock Research Institute Co., Ltd, Qingdao 266031, Shandong, China
e-mail: 15192635132@163.com

S. Yadav et al. (eds.), *Energy Power and Automation Engineering*, Lecture Notes in Electrical Engineering 1118, https://doi.org/10.1007/978-981-99-8878-5_56

of megawatt level single power supplies is greatly limited by the technological level of IGBT, as well as the limitations of size, weight, and other application environments. The modular and distributed high-power power supply system uses multiple power modules to operate in parallel, greatly improving the power capacity while also having better flexibility, making it the preferred solution for DC microgrids and other applications [2]. However, in the actual manufacturing process, small impedance differences are inevitably generated due to the influence of production technology levels such as internal chopper reactors and switch devices in the power supply. This is manifested in the differences in external characteristics between parallel power supply modules, which cannot achieve ideal current sharing. When operating with load, it leads to a certain power supply working in an overload or light load state for a long time, reducing its service life [3]. Therefore, when designing modular power supplies in parallel, it is necessary to consider how to equalize the current. Sag control achieves current sharing control by adjusting the virtual output impedance of the inverter [4]. It has the characteristics of simple structure, plug and play, and does not rely on line communication, making it a research hot spot in multi-module parallel technology [5].

However, although droop control is widely used, there are two issues that cannot be ignored in the pursuit of higher accuracy and stability: 1. Traditional droop control cannot achieve both higher current distribution accuracy and smaller bus voltage deviation [6, 7]. 2. In the application of a DC microgrid composed of multiple power sources in parallel, sudden disconnection or cut-in of high-power electrical loads, or unstable output voltage of photovoltaic cell modules, can cause a drop or impact in the output parallel bus voltage, leading to shutdown of protection equipment and even lead equipment failure [8].

In order to ensure the accuracy of current sharing while reducing or eliminating the bus voltage deviation existing in traditional droop control, reference [9] adopts an improved droop control method based on dynamic virtual resistance. This control strategy can increase or decrease the value of droop coefficient according to changes in load capacity, reducing the steady-state deviation of output voltage. Reference [10] applies fuzzy algorithms to droop control strategies, enabling real-time adjustment of the droop curve. However, although these two methods can reduce the bus voltage deviation, they cannot improve the dynamic response ability of the DC microgrid.

This article aims to improve the dynamic response ability of bus voltage in parallel power supply systems. Based on the resistive virtual impedance used in traditional droop control, capacitive virtual impedance is added, and a mathematical model for improving droop control with capacitive impedance is established. The gain effect of this capacitive virtual impedance on improving the damping characteristics of parallel power supply is theoretically derived and verified through simulation and prototype experiments.

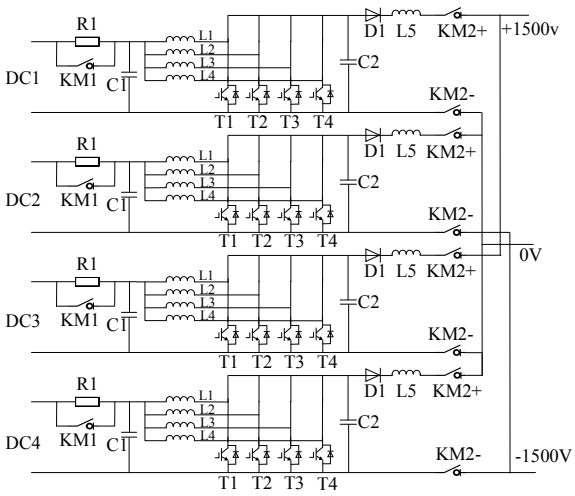

Fig. 1 2 MW DC power supply circuit topology

2 Circuit Principle

As shown in Fig. 1, the 2 MW high-power DC power supply adopts a series parallel circuit topology. The rated capacity of a single power module is 500 kW, and the output voltage is 1500 V. Power 1 and power 3 are connected in parallel, and they serve as the positive pole of the total output bus. Power 2 and power 4 are connected in parallel, and they serve as the negative pole of the output bus. Then, the negative pole of power 1 (3) and the positive pole of power 2 (4) are connected in series as the zero line of the output bus, resulting in an output voltage of ± 1500 V distributed megawatt level power supply with a power of 2 MW. To reduce current stress and reduce current ripple, the single power module adopts a quadruple interleaved parallel boost circuit [11] and controls the conduction and shutdown of switching devices T1, T2, T3, and T4 using four PWM signals with 90-degree phase shifting, achieving a voltage boost on the battery side to 1500 V (Fig. 2).

3 Control Strategy

3.1 Limitations of Traditional Sag Control

Taking the two parallel power sources P1 and P3 in the above 2 MW circuit topology as the research object, the parallel circuit can be simplified in the form of Fig. 3.

The traditional droop control equation can be expressed as:

$$U_{\text{dci\_ref}} = U^* - R_{\text{di}} i_{\text{dci}} \tag{1}$$

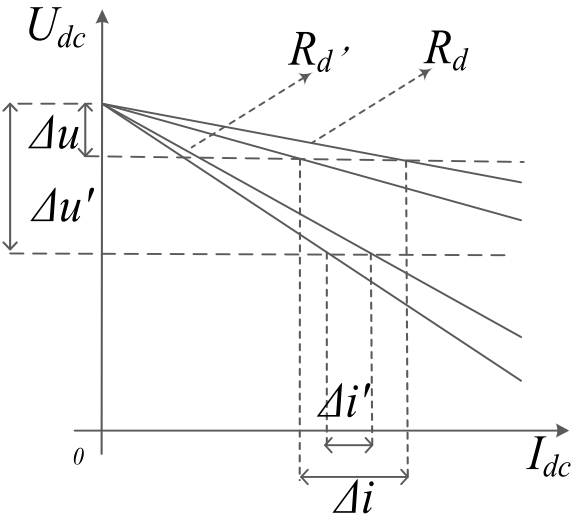

Fig. 2 Limitations of traditional droop control

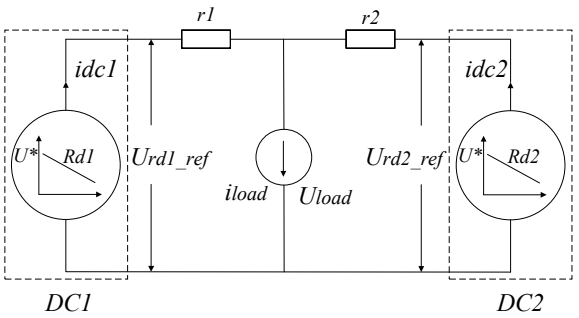

Fig. 3 Simplified block diagram of droop control of two parallel power supplies

In the formula, U^* is the reference value of the output voltage when the DC power supply is unloaded; $U_{\text{dci\_ref}}$ is the reference value of the output voltage of the i-th DC power supply after droop control, $i = 1,2$; i_{dci} is the output current of the i-th DC power supply; R_{di} is the equivalent output impedance of the i-th DC power supply, which is the droop control coefficient. The magnitude of this coefficient depends on the maximum voltage deviation $U_{\max,i} - U_{\min,i}$, and the maximum output current capacity of a single DC power supply allowed by the parallel system. The range of droop coefficient is defined as follows:

$$R_{\text{di}} = \frac{U_{\max,i} - U_{\min,i}}{i_{\max,i}} \tag{2}$$

The traditional droop control equation does not consider the influence of line impedances r_1 and r_2 and assumes that the output current of the DC power supply is inversely proportional to the equivalent output impedance. However, in situations

where the distance between two inverters is long or there is a high demand for power distribution accuracy, the impact of line impedance on droop control cannot be ignored. According to Fig. 3, an equation can be established:

$$\begin{aligned} U_{\text{load}} &= U^* - R_{d1} i_{\text{dc1}} - r_1 i_{\text{dc1}} \\ U_{\text{load}} &= U^* - R_{d2} i_{\text{dc2}} - r_2 i_{\text{dc2}} \end{aligned} \tag{3}$$

According to Eq. (3):

$$\frac{i_{\text{dc1}}}{i_{\text{dc2}}} = \frac{R_{d2} + r_2}{R_{d1} + r_1} \tag{4}$$

It can be seen that in order to achieve complete current sharing of parallel power sources, it is necessary to ensure that the ratio of the droop coefficient of the two power sources is completely consistent with the ratio of the line impedance, or the value of the droop coefficient is much greater than the line impedance. In practical applications, the ratio of the impedance of the two power supply lines cannot be controlled, and increasing the equivalent output impedance, i.e., the droop coefficient, will result in significant voltage deviation.

Figure 2 shows the droop curves of two parallel DC power supplies with droop coefficients R_d and $R_{d'}$ under the traditional droop control strategy, where $R_d < R_{d'}$. It can be seen that when the sag coefficient is taken as a large value, the current sharing deviation of the two DC power supplies decreases and the current sharing ability increases, but the steady-state error of the output voltage leads to a decrease in voltage accuracy. On the contrary, when the droop coefficient is taken as a small value, the steady-state error of the output voltage decreases, but the current sharing accuracy also weakens. Therefore, traditional droop control is contradictory in pursuing current sharing accuracy and voltage accuracy, which is the first limitation that traditional droop control faces.

To get the influence of output current fluctuation on the reference value of output voltage, the small-signal modeling of formula (5) can be established:

$$\Delta U_{\text{dcref}} = -\Delta R_d I_{\text{dc}} - R_d \Delta I_{\text{dc}} \tag{5}$$

In the equation, ΔU_{dcref}, ΔR_d, and ΔI_{dc} refer to the reference value of output voltage, the variation of droop coefficient, and the variation of output current. From Eq. (5), it can be seen that when the droop coefficient is a constant value, the variation of the output voltage reference value ΔU_{dcref} is proportional to the change in output current ΔI_{dc}. It can be seen that when the load of the parallel power supply changes, the reference value of the output voltage will also change proportionally, leading to fluctuations in the output bus voltage, which is the second limitation faced by traditional droop control [12].

3.2 Improve Droop Control Strategy

In order to reduce the impact of load disturbance on the output voltage, this paper adds capacitive virtual impedance instead of traditional pure resistive virtual impedance on the basis of traditional droop control strategy, improving the damping characteristics of the system.

The improved droop control block diagram is shown in Fig. 4.

In Fig. 4, $k_c(s)$ represents the compensation virtual impedance after adding a capacitive link; ΔU_{N}, ΔU_{dc}, and Δi_{dc} refer to the changes in no-load voltage, output voltage, and load current of the converter; C is the output side support capacitor, $G_{PI\_u}(s)$ is the voltage outer loop controller, $G_{\mathrm{PI\_i}}(s)$ is the current inner loop controller, and in general control systems, the bandwidth of the voltage loop is much greater than the bandwidth of the current loop. In this case, the current loop can be equivalent to a first-order inertial link:

$$G_{\mathrm{PI}\_i}(s)=\frac{1}{1+\tau s},\ G_{\mathrm{PI}\_u}(s)=\mathrm{K_{Pu}}+\frac{K_{\mathrm{Iu}}}{s} \tag{6}$$

In the equation, τ is the inertia time constant, K_{pu} and K_{Iu} are the proportional and integral coefficients, respectively.

To obtain the change in output voltage ΔU_{dc}, the quantitative relationship between ΔU_{dc} and load current fluctuation is established according to Fig. 4:

$$\Delta U_{\mathrm{dc}}=\frac{G_{\mathrm{PI}\_u}(s)G_{\mathrm{PI}\_i}(s)}{\mathrm{C}s+G_{\mathrm{PI}\_u}(s)G_{\mathrm{PI}\_i}(s)}\Delta U_N-\frac{1+k_c(s)G_{\mathrm{PI}\_u}(s)G_{\mathrm{PI}\_i}(s)}{\mathrm{C}s+G_{\mathrm{PI}\_u}(s)G_{\mathrm{PI}\_i}(s)}\Delta i_{\mathrm{dc}} \tag{7}$$

From Eq. (7), it can be seen that the change of bus voltage ΔU_{dc} depends on two parts, namely the change of no-load voltage ΔU_{N} and output current variation Δi_{dc}. The influence factor of ΔU_{N} on bus voltage is related to the PI parameters of the voltage and current double closed loop and the capacitance of the filtering capacitor, while the influence factor of Δi_{dc} on bus voltage is not only influenced by PI parameters and capacitance values, but also related to the compensation virtual impedance coefficient $k_c(s)$.

In an ideal situation, to eliminate the impact of load current changes on bus voltage fluctuations, it is necessary to obtain the compensation virtual impedance expression in the above equation:

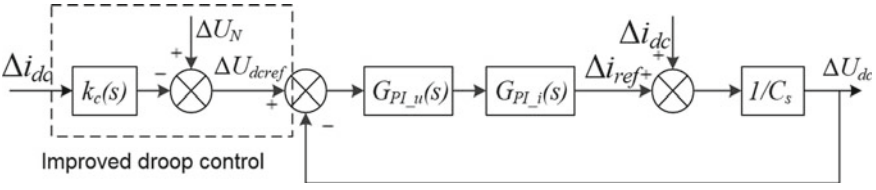

Fig. 4 Improved droop control block diagram

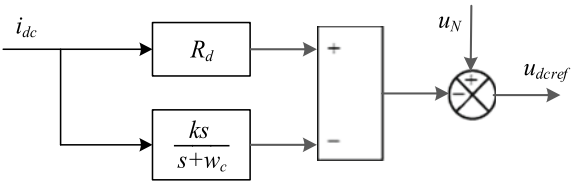

Fig. 5 Improved droop controller

$$k_c(s) = -\frac{1}{G_{\mathrm{PI\_}u}(s)G_{\mathrm{PI\_}i}(s)} \tag{8}$$

Combining Eq. (6), it can be concluded that:

$$k_c(s) = -\frac{\tau s^2 + s}{K_{\mathrm{Pu}}s + K_{\mathrm{Iu}}} \tag{9}$$

If higher-order effects are not considered, further results can be obtained:

$$k_c(s) = -\frac{ks}{s + \omega_c} \tag{10}$$

According to Eq. (10), the compensation virtual impedance can be simplified as a high-pass filter with a cutoff frequency of ω_c, where $\omega_c = K_{\mathrm{Iu}}/K_{\mathrm{Pu}}$, $k = 1/K_{\mathrm{Pu}}$. The block diagram of the droop controller after adding compensation for virtual impedance is shown in Fig. 5.

In this improved droop controller, capacitive virtual impedance and resistive virtual impedance complement each other: In steady-state conditions, resistive virtual impedance Rd plays a dominant role and is used for current sharing between two parallel DC power sources; in load fluctuation conditions, the capacitive virtual impedance *kc*(s) plays a dominant role in obtaining feedforward compensation coefficients related to current changes and reducing output voltage fluctuations.

3.3 Small Signal Modeling of Parallel DC Power Supply

To evaluate the output dynamic characteristics of two parallel DC power supplies, the circuit topology shown in Fig. 1 was simplified. The constant power load was replaced by a constant current source, and a simplified DC–DC power supply circuit was constructed as shown in Fig. 6.

Establish the average model expression for the aforementioned DC–DC power supply:

$$Li_L s = -r_L i_L - du_{\mathrm{dc}} + U_{\mathrm{in}} \tag{11}$$

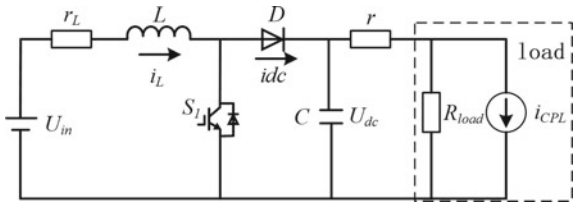

Fig. 6 DC–DC power supply circuit

$$Cu_{\mathrm{dc}}s = di_L - \frac{u_{\mathrm{dc}}}{\frac{P_{\mathrm{load}}}{U_{\mathrm{dc}}} + R_{\mathrm{load}}} \tag{12}$$

In the formula, r_{L} is the internal resistance of inductor L, i_L is the current flowing through the inductor, U_{in} and U_{dc} are the steady-state values of input voltage and output voltage, u_{dc} is the dynamic value of output voltage, P_{load} and R_{load} are constant power loads and pure resistive loads.

Based on the above model, establish a DC power supply control block diagram using a compensating virtual impedance droop controller:

According to Fig. 7, a mathematical model of the controller can be established. The reference value of the DC power bus voltage is obtained by improving droop control:

$$U_{\mathrm{dcref}} = U_N - (R_d + k_c(s))i_{\mathrm{dc}} \tag{13}$$

In the formula, U_{dcref} is the given value of the DC power bus voltage, U_N is the reference value of the output voltage at no load, R_d and $k_c(s)$ are the resistive virtual impedance and the compensating virtual impedance.

Calculate the output current i_{dc} from the inductance current i_L:

$$i_{\mathrm{dc}} = (1 - d)i_L \tag{14}$$

In the formula, d is the duty cycle of the boost circuit switching device.

Construct a voltage–current dual closed-loop controller as shown in Eqs. (15) and (16):

$$i_{\mathrm{Lref}} = (u_{\mathrm{dcref}} - u_{\mathrm{dc}})G_{\mathrm{PI\_}u}(s) \tag{15}$$

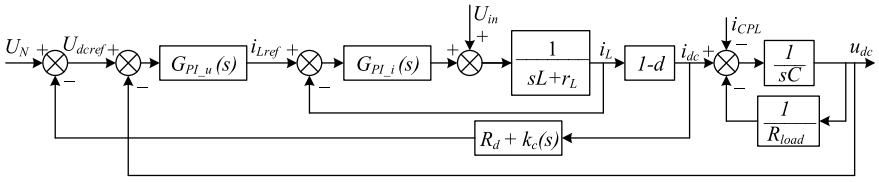

Fig. 7 Control block diagram of DC power supply

$$du_{\mathrm{dc}} = -(i_{\mathrm{Lref}} - i_L)G_{\mathrm{PI\_}i}(s) + U_{\mathrm{in}} \tag{16}$$

In the equation, $G_{\mathrm{PI\_}u}(s)$ and $G_{\mathrm{PI\_}i}(s)$ are PI controllers for the outer voltage loop and the inner current loop, respectively.

Assuming the proportion and integration coefficients of the current loop PI controller are K_{Pi} and K_{Ii}, by combining Eqs. (11), (13), and (16), the expression of the current loop transfer function can be obtained:

$$\frac{i_L}{i_{\mathrm{Lref}}} = -\frac{K_{\mathrm{Pi}}s + K_{\mathrm{Ii}}}{Ls^2 + (r_L + K_{\mathrm{Pi}})s + K_{\mathrm{Ii}}} \tag{17}$$

Similarly, assuming the proportion and integration coefficients of the voltage loop PI controller are K_{Pu} and K_{Iu}, the expression of the voltage loop transfer function can be obtained:

$$\frac{u_{\mathrm{dc}}}{u_{\mathrm{dcref}}} = \frac{D\left(K_{\mathrm{Pu}}K_{\mathrm{Pi}}s^2 + K_{\mathrm{Pu}}K_{\mathrm{Ii}}s + K_{\mathrm{Pi}}K_{\mathrm{Iu}}s + K_{\mathrm{Iu}}K_{\mathrm{Ii}}\right)}{N_1 s^4 + N_2 s^3 + \frac{L}{N_3 s^3 + N_4 s + N_5}K_{\mathrm{Iu}}K_{\mathrm{Ii}}} \tag{18}$$

Among them,

$$N_1 = LC,\ N_2 = (r_L + K_{\mathrm{Pi}})C,\ N_3 = \frac{P_{\mathrm{load}}}{U_{\mathrm{dc}}},$$

$$N_4 = D(K_{\mathrm{Pu}}K_{\mathrm{Ii}} + K_{\mathrm{Pi}}K_{\mathrm{Iu}})\left(1 + \frac{k_d(s)}{R_{\mathrm{load}} + \frac{P_{\mathrm{load}}}{U_{\mathrm{dc}}}}\right),$$

$$N_5 = R_{\mathrm{load}} + \left(CK_{\mathrm{Ii}} + \frac{r_L + K_{\mathrm{Pi}}}{R_{\mathrm{load}} + \frac{P_{\mathrm{load}}}{U_{\mathrm{dc}}}}\right) + D\left(1 + \frac{k_d(s)}{R_{\mathrm{load}} + \frac{P_{\mathrm{load}}}{U_{\mathrm{dc}}}}\right)$$

With the improved droop control strategy, the quantitative relationship between current disturbance and DC bus voltage disturbance can be derived from the small-signal modeling of closed-loop control:

$$\begin{aligned} i_L &= I_L + \Delta i_L \\ u_{\mathrm{dc}} &= U_{\mathrm{dc}} + \Delta u_{\mathrm{dc}} \\ d &= D + \Delta d \end{aligned} \tag{19}$$

In the formula, D is the stable value of the IGBT drive duty cycle, and Δd is the fluctuation value of the duty cycle.

Combining Eqs. (19), (11), (15), and (16), the transfer function of bus voltage fluctuation and current disturbance can be obtained:

$$\frac{\Delta u_{\mathrm{dc}}}{\Delta i_L} = -\frac{R + sL + G_{\mathrm{PIi}}(s)}{G_{\mathrm{PIu}}(s)G_{\mathrm{PIi}}(s)\left(1 + \frac{k_d(s)}{R_{\mathrm{load}}}\right)} \tag{20}$$

The transfer function of bus voltage fluctuation and duty cycle disturbance can be obtained:

$$\frac{\Delta u_{\mathrm{dc}}}{\Delta d} = -\frac{M_1}{M_2 s^4 + M_3 s^3 + M_4 s^2 + M_5 s + M_6} \tag{21}$$

Among them,

$$M_1 = I_L\left(Ls^3 + (r_L + K_{\mathrm{Pi}})s^2 + K_{\mathrm{Ii}}s\right),\ M_2 = LC,\ M_3 = (r_L + K_{\mathrm{Pi}})C + \frac{L}{R_{\mathrm{load}}},$$
$$M_4 = CK_{\mathrm{Ii}} + \frac{r_L + K_{\mathrm{Pi}}}{R_{\mathrm{load}}} + D\left(1 + \frac{k_d(s)}{R_{\mathrm{load}}}\right)K_{\mathrm{Pu}}K_{\mathrm{Pi}} + \frac{K_{\mathrm{Ii}}}{R_{\mathrm{load}}},$$
$$M_5 = D\left(1 + \frac{k_d(s)}{R_{\mathrm{load}}}\right)(K_{\mathrm{Pu}}K_{\mathrm{Ii}} + K_{\mathrm{Pi}}K_{\mathrm{Iu}}),\ M_6 = D\left(1 + \frac{k_d(s)}{R_{\mathrm{load}}}\right)K_{\mathrm{Iu}}K_{\mathrm{Ii}}$$

4 Simulation Analysis

Build a parallel model of two DC boost power supplies as shown in Fig. 3 using MATLAB/Simulink, and compare the dynamic stability of DC bus voltage under two control strategies: traditional droop control and improved droop control based on compensating virtual impedance. The simulation parameters are shown in Table 1.

The switching frequency of both DC power supplies is set to 1.5 kHz, and the output voltage reference value is 1500 V. The load is connected in parallel with a pure resistive load and a constant power load, with a starting load of 120 kW and a sudden increase to 1000 kW at 2 s. Figures 8 and 9 show the output bus voltage and output current waveforms at the time of sudden loading using two control strategies, respectively.

From Fig. 8, it can be seen that before sudden load application, both traditional droop control and improved droop control strategies stabilized the bus voltage at 1480 V. However, after sudden load application, the steady-state value of the bus voltage under both control strategies decreased to 1462 V. This is due to the voltage drop between the sagging resistance and the line resistance, resulting in an output

Table 1 Parameters of parallel simulation model of two DC power supplies

Parameter	Value	Parameter	Value
Single power	500 kW	Inductance	3.2 mH
Total power	2000 kW	Supporting capacitance	3 600 uF
Input voltage	500 ~ 1 000 V	Switching frequency	1500 Hz
Rated input voltage	750	Sag coefficient	0.20
Rated output voltage	1500	Line resistance R_1, R_2	0.10 Ω, 0.12 Ω

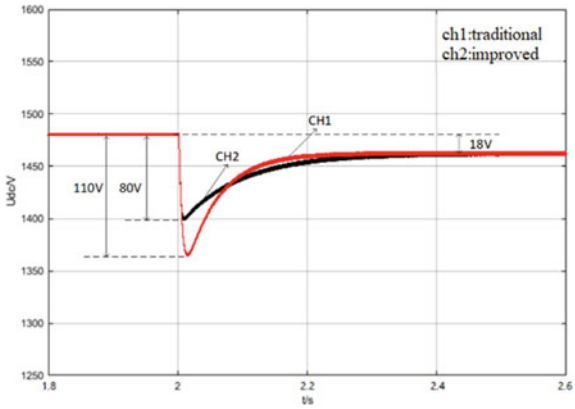

Fig. 8 DC bus voltage waveform

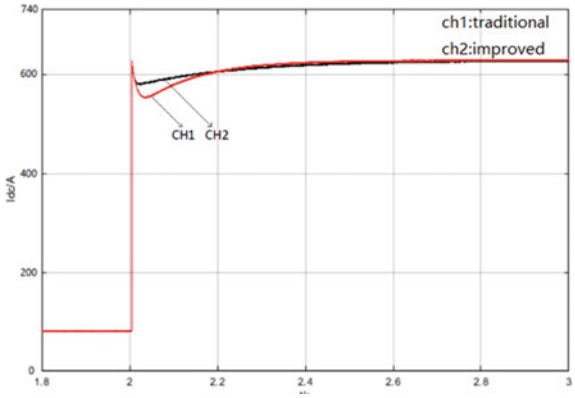

Fig. 9 Output current response curve

voltage slightly lower than the reference voltage of 1500 V, and the larger the load, the greater the voltage deviation. It can be seen that the compensating virtual impedance does not affect the steady-state state.

When sudden load is applied, the DC bus voltage under both control strategies shows a certain degree of decrease; however, the overshoot of the bus voltage under the compensation virtual impedance droop control strategy is 80 V, which is much lower than the 110 V under the traditional droop control strategy. Similarly, as shown in Fig. 9, when suddenly applying a load, the output current overshoot under the compensation virtual impedance droop control strategy is significantly reduced. The simulation results show that adding a capacitive compensation virtual impedance link in the droop control strategy greatly improves the damping characteristics of the control system and enhances the stability of the output voltage.

5 Results

Build a test platform for 500-kW DC–DC converters as shown in Fig. 10. The rated input voltage of a single converter is DC750 V, and the rated output voltage is DC1500 V. Among them, four converters are connected in parallel on the output side to the load box, with a maximum output power of 2 MW. However, considering the limitations of experimental conditions, only two converters are completed in parallel for output testing, with a maximum power limit of 620 kW.

To investigate the effect of adding capacitive compensation virtual impedance on steady-state current sharing performance, the droop control strategy proposed in this article was used to test the inverter. The output current test waveform is shown in Fig. 11.

In Fig. 11, *CH3*, *M*, and *CH4* represent the waveforms of converter 1, converter 2, and total output current, respectively. At 5 s, the output currents of converter 1 and

Fig. 10 500-kW DC/DC converter prototype

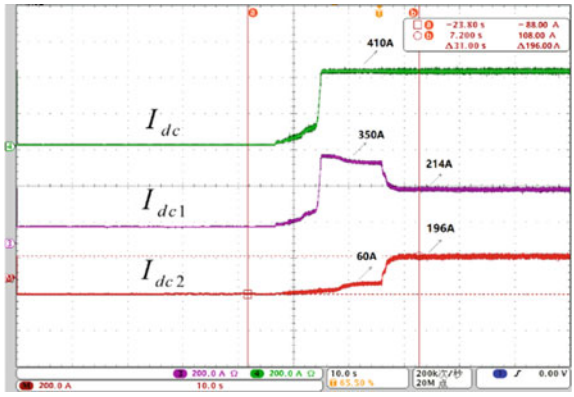

Fig. 11 Output current waveform

converter 2 after soft start are 350 A and 60 A, respectively, indicating significant impedance differences in practical applications; after 5 s, the converter enters the current sharing mode, and the output current of converter 1 drops to 214 A, while the output current of converter 2 increases to 196 A. The current deviation is less than 5% which is the engineering agreed target. The experiment showed that the compensation virtual impedance did not affect the steady-state current sharing effect.

To investigate the impact of improving droop control on the dynamic stability of output voltage, dynamic loading experiments were conducted on two parallel power supplies of DC–DC converters under two versions of program control, traditional droop control and improved droop control, with a sudden loading power of about 250 kW. Figures 12 and 13 show the output voltage waveforms under two control strategies, respectively.

From the experimental results, it can be seen that under sudden load conditions, the output voltage drop value under the improved droop control strategy is about 44 V, which is significantly smaller than the voltage drop value generated by traditional

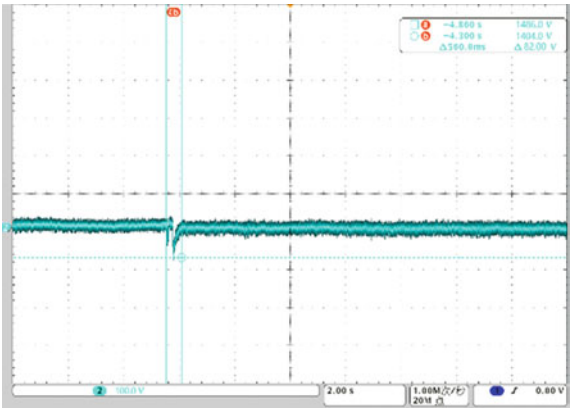

Fig. 12 DC bus voltage waveform based on traditional droop control

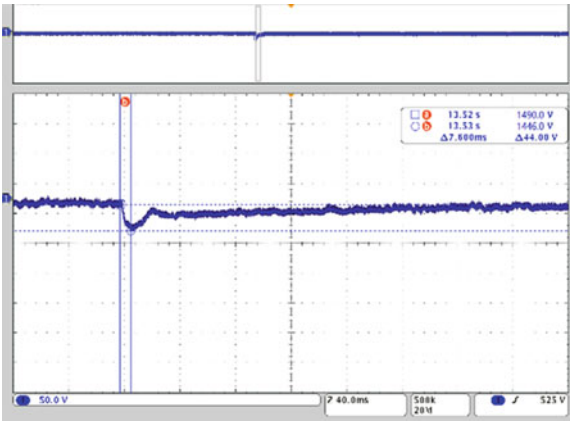

Fig. 13 DC bus voltage waveform based on improved droop control

droop control of 82 V, and the improved droop control strategy eliminates voltage oscillation during sudden load application. The experimental results show that the improved droop control strategy based on compensating virtual impedance improves the dynamic stability of output voltage under load disturbance conditions.

6 Conclusion

This article analyzes the current sharing problem and bus voltage fluctuation problem during parallel operation of megawatt level large-capacity DC power source. Although traditional droop control can achieve steady-state current sharing between parallel power sources, its resistive virtual impedance cannot improve voltage fluctuations during load disturbances. Therefore, this article proposes an improved droop control algorithm based on a high-pass filter virtual impedance compensation strategy. By establishing a small-signal modeling, the transfer function of bus voltage disturbance and current disturbance under the improved droop control strategy is derived. By designing reasonable compensation virtual impedance parameters, the dynamic stability of output voltage during load disturbances can be greatly improved. Finally, based on the MATLAB simulation platform and the current sharing tests of two 500-kW converter prototypes, the superiority of the proposed improvement method was verified, which has guiding significance for the design of distributed systems of high-power DC power sources.

References

1. Maouedj R, Mammeri A, Draou MD et al (2011) Gridconverters for photovoltaic and wind power systems. Energy Procedia 28(11):797–807
2. Boroyevich D, Cvetkovic I, Dong D et al (2010) Future electronic power distribution systems a contemplative view. OPTIM 2010:1369–1380
3. Wang B, Sechilariu M, Locment F (2012) Intelligent DC microgrid with smart grid communications: control strategy consideration and design. IEEE Trans Smart Grid 3(4):2148–2156
4. Luo S, Ye Z, Lin RL et al (1999) A classification and evaluation of paralleling methods for power supply modules. In: Proceeding of 30th annual IEEE power electronics specialists conference, pp 901–908
5. Irving BT, Jovanovic MM (2000) Analysis, design and performance evaluation of droop current-sharing method. In: Proceedings of 15th Annual IEEE applied power electronics conference, pp 235–241
6. Xiaonan L, Guerrero JM, Kai S et al (2014) An improved droop control method for DC microgrids based low bandwidth communication with DC bus voltage restoration and enhanced current sharing accuracy. IEEE Trans Power Electron 29(4):1800–1812
7. Khorsandi A, Ashourloo M, Mokhtari H (2014) An adaptive droop control method for low voltage DC microgrid. PEDSTC, Tehran, pp 201484–201489
8. Kwasinski A, Onwuchekwa CN (2011) Dynamic behavior and stabilization of DC microgrids with instantaneous constant-power loads. IEEE Trans Power Electron 26(3):822–834
9. Huang HH, Hsieh CY, Liao JY et al (2011) Adaptive droop resistance technique for adaptive voltage positioning in boost dc-dc converters. IEEE Trans Power Electron 26(7):1920–1932

10. Kakigano H, Miura Y, Ise T (2013) Distribution voltage control for DC microgrids using fuzzy control and gain-scheduling technique. IEEE Trans Power Electron 28(5):2246–3225
11. Mummadi V, Tomonobu S, Katsumi U (2001) Modeling and analysis of interleaved dual boost converter. In: IEEE international symposium on industrial electronics, pp 718–722
12. Wang JB, Rossi L, Chang JH (2009) Paralleled DC/DC converter via primary current droop current sharing control. In: International conference on power electronics and drive systems, pp 1119–1124

Investigation on Post-arc Recovery Characteristics of SF_6/N_2 Mixed Gas Medium

Xubo He, Xiabo Chen, Hao Sun, Jiayin Fan, Zeyu Wang, Mingming Sun, and Wenzhen Liu

Abstract SF_6 is a strong greenhouse gas with high liquefaction temperature, which limits its application in gas insulation equipment to a large extent. Therefore, the search for a replaceable gas has become a hot topic in electrical field. Although scholars have carried out a lot of research work on SF_6 replacement gas, they have not yet found a gas that can completely replace SF_6. At present, the most cost-effective way is to use SF_6 gas mixture. Therefore, this paper mainly studies the recovery of insulation strength of SF_6/N_2 gas mixture with different proportions after a certain arc-burning time. In this experiment, the RC circuit is used to simulate the arc-burning condition. After the arc current transfer, the high-voltage pulse generator is used to apply pulse to the contact gap, so as to obtain the back-arc recovery characteristic curve of the gas medium, which provides data support for the research and development of the circuit breaker replacing SF_6 gas, and also has important significance for the study of the breakdown problem of the replacement gas circuit breaker.

Keywords SF_6 gas mixture · Post-arc recovery characteristic · Arc

1 Introduction

In the last half century, with the rapid development of the power industry, the voltage level in the process of transmission and distribution is getting higher and higher, which puts forward higher requirements for the electrical equipment in the power system. SF_6 due to its high chemical reliability generally does not produce chemical reactions with other substances; it is not easy to burn and can effectively perform the specified function. Moreover, SF_6 gas has strong arc-extinguishing ability and insulation ability [1, 2]. Therefore, for more than half a century, the power equipment with SF_6 as the insulating medium and arc-extinguishing medium has occupied a

X. He · X. Chen · H. Sun (✉) · J. Fan · Z. Wang · M. Sun · W. Liu
State Key Laboratory of Electrical Insulation and Power Equipment, Xi'an Jiaotong University, Xi'an, China
e-mail: sunhao1031@mail.xjtu.edu.cn

S. Yadav et al. (eds.), *Energy Power and Automation Engineering*, Lecture Notes in Electrical Engineering 1118, https://doi.org/10.1007/978-981-99-8878-5_57

dominant position in medium- and high-voltage power grids [3, 4]. About half of the SF_6 produced in industry is used in the power sector, with about four-fifths in the high-voltage sector. With the development of the power industry in recent years, a large amount of SF_6 is directly leaked or discharged into the atmospheric environment without treatment [5]. However, SF_6 gas also has some defects, among which the most critical is its greenhouse effect. SF_6 gas is a kind of strong greenhouse gas, which has great harm to the atmospheric environment. Its Global Warming Potential (GWP) is about 23,900 times of CO_2 gas. Moreover, SF_6 gas has an extremely long atmospheric life, with a life span of 3400 years [6, 7]. At the third Conference of the Parties to the United Nations Framework Convention on Climate Change held in Tokyo, Japan, in 1997, 149 countries and regions signed the Kyoto Protocol, which listed SF_6 gas as one of the six greenhouse gases with limited emission [8, 9]. Compared with western countries, our country's SF_6 gas emission increases by a large amount every year, and our country's population has a large-scale, vast territory; the demand for electric power is large; therefore, SF_6 gas usage is large, which causes the problem of SF_6 greenhouse gas to be particularly prominent in our country. Moreover, the liquefaction temperature of SF_6 gas is higher, in the north and cold region in our country, and the winter temperature can reach − 30 to − 40 °C. In such an environment, most of the existing SF_6 electrical equipment cannot work normally [10].

In order to solve the problem that SF_6 gas has high greenhouse effect and is easy to liquefy in cold environment, finding alternative gas has always been a hot research topic in the field of electrical. As a replacement gas for SF_6, it should meet the following requirements: First, it should have a low enough greenhouse effect, non-toxic, and do no harm to the environment; secondly, it needs to meet the most basic technical performance requirements, such as low liquefaction temperature, high insulation strength, strong heat dissipation capacity and good arc-extinguishing performance [11]. The current solution is mainly divided into two directions: One is to mix SF_6 gas with some conventional gas of liquefaction temperature to reduce the usage of SF_6 gas; the second is the use of new insulating gas medium, completely replacing SF_6 gas. Scholars have carried out a lot of research work to find SF_6 alternative gases. At present, although there are some new insulating gases, which have the potential to replace SF_6 gas in some aspects, they all have certain defects. The liquefaction temperature of these new gases is low, so they need to be mixed with other buffer gases to reduce the liquefaction temperature [12].

In recent years, some new environmentally friendly gases have attracted much attention, such as c-C_4F_8, C_4F_7N, $C_6F_{12}O$, $C_5F_{10}O$ and CF_3I. The greenhouse effect of these gases is much lower than SF_6, and they have good environmental protection and insulation properties. The insulation properties and GWP values of different gases are shown in Table 1. However, as mentioned above, these gases have a high liquefaction temperature and cannot be used as insulating gases alone. They must be mixed with some buffer gases to meet the ambient temperature requirements of power equipment. At present, the buffer gases mainly include CO_2, N_2 or dry air

[13]. However, at present, the decomposition mechanism of this kind of gas is not clear, and the phenomenon of solid precipitation exists, so the safety of engineering application needs to be further studied [12].

The current research on SF_6 gas mixture mainly focuses on SF_6 mixed with CO_2, N_2, CF_4 and inert gas. The research shows that adding a certain proportion of buffer gas to SF_6 gas can achieve good insulation and arc-extinguishing effect and meet the basic electrical performance requirements of power equipment [14, 15]. In addition, the addition of buffer gas can help to reduce the liquefaction temperature of gas medium, reduce the cost, reduce the impact of SF_6 gas on the environment and improve the greenhouse effect brought by SF_6 gas, which can provide strong support for the realization of the current goal of "carbon peak and carbon neutrality [16]."

Among the above-mentioned buffer gases, N_2 and CO_2 have high content in the air and are the main components of the air, which are relatively easy to obtain. Therefore, these two mixed gases become the preferred targets of alternative gases. Compared with CO_2, N_2 has a lower price and less impact on the environment, so it has become the main research object [17]. At present, circuit breakers with SF_6/N_2 as gas medium have been put into use. In the 1980s, about 160 SF_6 gas-mixed circuit breakers were put into use in Canada. This batch of circuit breakers adopted SF_6/N_2 gas-mixed aeration pressure of 0.5 MPa, of which SF_6 accounted for 40% [18].

SF_6 gas mixture is mainly used as the insulating medium in gas circuit breaker, which plays the role of arc extinguishing and insulation, and is mainly used in medium- and high-voltage circuit breakers. At present, researches on SF_6 gas mixture are in-depth in the aspects of insulation strength and cold breakdown [19], while most researches on insulation strength recovery after arc extinguishing tend to be on the simulation level. In particular, there is a lack of comparative studies on the recovery rate of SF_6 gas mixtures with different mixing ratios after arc ignition. Circuit breaker is an important protection device in power system, and its success affects the normal operation of the whole power system. When gas circuit breaker is normally broken off, it is bound to produce arc. After the arc is extinguished, when it enters the medium recovery stage, whether the gas medium is broken down is the key factor to judge whether the breaking is successful [20].

In this experiment, the RC discharge circuit is used to provide current and simulate arc-burning conditions. After the arc is extinguished for a period of time, the high-voltage pulse device is used to apply pulse voltage between the contacts. By measuring the breakdown voltage in the recovery stage of the gas medium between the contacts after extinguishing the arc, the recovery characteristic curve of the gas medium is obtained. In this paper, the post-arc recovery characteristic curves of

Table 1 Comparison of key characteristics of environmental gases

Characteristic	SF_6	c-C_4F_8	C_4F_7N	$C_6F_{12}O$	$C_5F_{10}O$	CF_3I
GWP	23,500	8700	2100	~ 1	~ 1	0.45
Liquefaction temperature (°C)	− 64	− 8	− 4.7	49	27	− 22.5
Dielectric strength	1.00	1.30	2.00	2.50	1.20	1.20

different proportions of SF_6/N_2 gas mixture are compared, and from the perspective of post-arc medium recovery, which proportion of gas mixture has more potential to replace SF_6 gas.

2 Experimental Setup

The power supply used in this experiment is a high-power capacitor with a stable output voltage of 500 V. The main circuit switch is a three-phase vacuum AC contactor whose action can be controlled by controlling the electrical signal output to the control terminal of the main circuit switch. The current-limiting resistance is a high-power load with adjustable resistance value, which controls the current in the loop by adjusting the resistance value. The high-power diode in the loop is used to protect the equipment in the loop from the influence of the reverse voltage; thyristors VT_1 and VT_2 are controlled by the TTL signal generator. When the main loop switch is closed, the TTL sends an electrical signal to the VT_2 to control its on–off. The function of thyristor VT_2 is transfer current. When VT_2 is switched on, the current flowing through the experimental chamber will be transferred from the branch of VT2. The arc-burning time is controlled by controlling the time difference between VT_1 and VT_2. The function of high-speed camera is to shoot arc image to observe the shape of arc. There is a set of electromagnetic mechanism inside the experimental chamber. The contact mechanism is closed by controlling the current of the closing coil inside the electromagnetic mechanism. The thyristor VT_1 is switched on after the contact mechanism is closed, thus generating current in the loop. Then by controlling the electromagnetic mechanism part of the gate coil current to control the opening of the contact mechanism, generate arc. Trigger signals of thyristor, electromagnetic mechanism and high-speed camera in experimental device are uniformly controlled by TTL signal generator.

3 Experimental Results and Analysis

3.1 Arc Characteristic Analysis

The contact structure is in the shape of "ball–plate," as shown in Fig. 1a. The anode is the ball contact, and the cathode is the plate contact, which is conducive to providing a stable arc during the process of the contact being pulled apart. The material of the two contacts is CuW_{80}. The current of the experiment is 550 A, the current of arc burning is 500 A, the proportion of SF_6 in the gas mixture is 10, 50 and 90%, and the inflation pressure is 2 atm. The arc image taken is shown in Fig. 1b. It can be seen from the shooting results that when the contact reaches the maximum opening distance, the arc presents a stable "bell shape" structure. Figure 2 shows the voltage

and current waveform of the arc in the arc-burning process, which can be divided into three stages from the beginning of the experiment to the current being transferred away. The first stage is the current conduction stage. At this time, the thyristor is switched on, and the contacts are closed. In the second stage, the contact starts to move, and the gap between the upper and lower electrodes gradually increases until the maximum opening distance is reached. The third stage is stable arc-burning stage. Under the condition of 500A current, the arc is stable arc-burning stage. In this stage, the arc form is stable "bell shape."

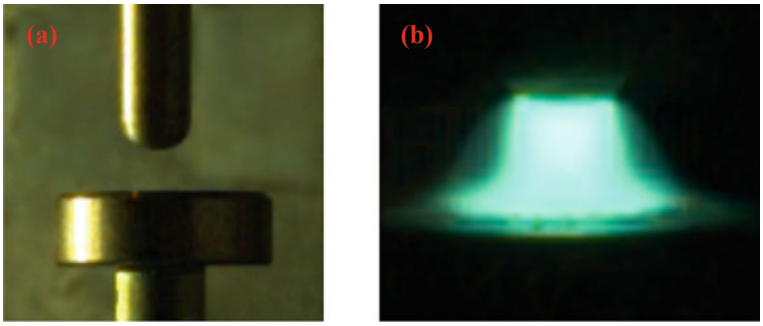

Fig. 1 Electrode shape and arc shape diagram

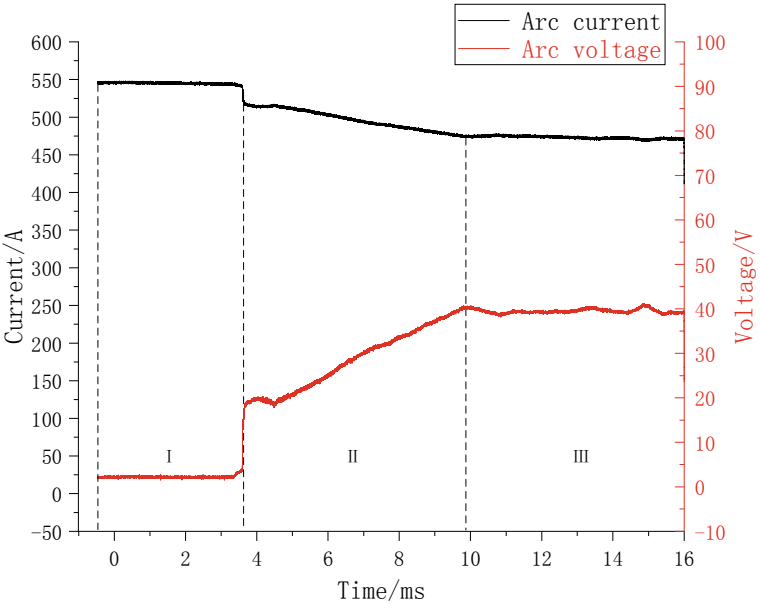

Fig. 2 Arc voltage and current diagram

3.2 *Experiments on Recovery of Back-Arc Medium Under Different Mixing Proportion*

After the arc current is transferred, there are still a large number of charged particles in the area where the arc is generated between the contacts, resulting in low insulation strength of the gas medium between the contacts in a short time. When the pulse voltage is applied to the contacts, the breakdown between the contacts will be caused, forming a breakdown channel. With the diffusion of charged particles between the contacts, the insulating strength of the gaseous medium slowly increases. This process is called electrical recovery process. In the arc-burning process, due to the high temperature of the arc, after the arc current is zero, the gas medium also needs a certain time to recover to the initial temperature, and this process is called the thermal recovery process. Compared to the two processes, electrical recovery is faster than thermal recovery. When the gas medium returns to the initial temperature, then its insulation strength is completely restored and the breakdown channel is no longer formed.

The dielectric insulation recovery test loop built was used to conduct insulation recovery test on SF_6/N_2 mixed gas at different mixing ratios under the condition of 2 atm. The experimental results are shown in Fig. 3. As can be seen from the Fig. 3, as the proportion of SF_6 gas increases, the recovery voltage of the gas mixture rises higher and recovers faster. The recovery rate of the gas mixture with 50% SF_6 is 45.45% faster than that with 10% SF_6, and the recovery rate of the gas mixture with 90% SF_6 is 66.67% faster than that with 10% SF_6. The recovery rate of SF_6/N_2 gas mixture is quite different under the conditions that SF_6 accounts for 50% and 90%, which may be due to the synergistic effect of SF_6 and N_2, leading to a higher saturation ratio.

It can be seen from the above conclusions that, although the higher the SF_6 ratio, the faster the recovery rate of the gas mixture, the higher the SF_6 ratio of the gas mixture will increase the liquefaction temperature of the gas mixture and enhance the greenhouse effect, resulting in the limited application environment and greater harm to the environment. Overall consideration, SF_6 in SF_6 gas mixture should not exceed 50%.

4 Conclusion

In this paper, the insulation recovery test loop of gas medium was built to test the insulation recovery test of SF_6/N_2 mixed gas under the condition of 2 atm, providing certain data reference for the engineering application of SF_6 mixed gas. The experimental results show that the recovery rate of gas mixture increases gradually with the

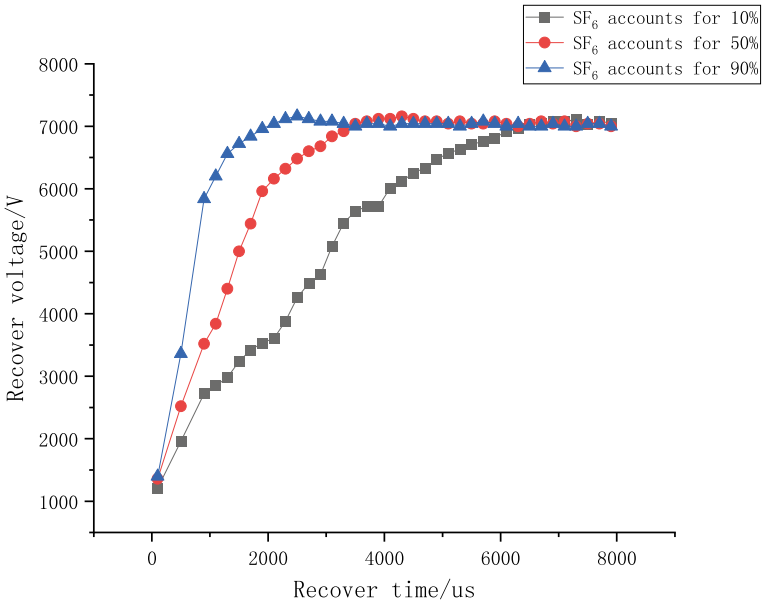

Fig. 3 Post-arc recovery characteristic curve of SF_6/N_2 mixed gas medium

increase of SF_6 proportion. Considering the effects of GWP and liquefaction temperature, SF_6 in the gas mixture should not exceed 50%. Therefore, from the perspective of back-arc recovery, SF_6/N_2 gas mixture with 50% SF_6 has the potential to replace SF_6 gas.

References

1. Xu NF, Jiao L, Chen J, Chen XY, Deng YK (2022) Lightning impulse characteristics of CF_3I–CO_2 gas mixtures in quasi-homogeneous and extremely non-uniform electric field. High Volt Appar 58:158–164. https://doi.org/10.13296/j.1001-1609.hva.2022.10.021.
2. Shi L, Yu T, Fang L, Zhang S (2021) SF_6 discharge decomposition mechanism and its research progress in fault analysis. High Volt Appar 57:1–9. https://doi.org/10.13296/j.1001-1609.hva.2021.08.001
3. Wang GX, Zhao RY (2022) Analysis on application of environmental optimization SF_6 alternative gas in medium and high voltage power equipment. Electr Energy Manag Technol 617:76–80. https://doi.org/10.16628/j.cnki.2095-8188.2022.08.014
4. Lin ZX (2022) Simulation study on partial discharge characteristics of SF_6/N_2 gas mixture. https://doi.org/10.27008/d.cnki.gdbdc.2022.000325
5. Zhang XX, Tian SS, Xiao S, Li W (2018) A review study of SF_6 substitute gases. Trans China Electrotech Soc 33:2883–2893. https://doi.org/10.19595/j.cnki.1000-6753.tces.161253
6. Jia CQ, Xia YL, Ni Y, Xie SJ, Zhang CM (2022) Research on insulation characteristics of SF_6/N_2 gas mixture. Sichuan Electr Power Technol 45:33–37. https://doi.org/10.16527/j.issn.1003-6954.20220207

7. Deng JB, Dong JH, Chen JH (2022) Research advances in interface insulation characteristics of SF_6 alternative gases. High Volt Eng 48:661–673. https://doi.org/10.13336/j.1003-6520.hve.20201603
8. Yan XL, Gao KL, Zheng Y (2018) Progress of gas mixture and alternative gas of SF_6. Power Syst Technol 42:1837–1844. https://doi.org/10.13335/j.1000-3673.pst.2017.2911
9. Zhou AC, Gao LY, Ji XT, Zhang M (2018) Research and application of SF_6/N_2 mixed gas used in GIS bus. Power Syst Technol 42:3429–3435. https://doi.org/10.13335/j.1000-3673.pst.2018.1508
10. Wu JF, Zhang L, Zhong PF (2018) Research of SF_6/N_2 mixture substitution technology for SF_6 insulated current transformer. High Volt Appar 54: 223–229. https://doi.org/10.13296/j.1001-1609.hva.2018.05.035
11. Li XW, Zhao H (2016) Review of research progress in SF_6 substitute gases. High Volt Eng 42:1695–1701. https://doi.org/10.13336/i.1003-6520.hve.20160616003
12. Huang XL, Zhao SW, Wang Y, Su HB, Jia SL (2023) A review of research progress on environment-friendly high-voltage power switchgear. Adv Eng Sci 55:14–29. https://doi.org/10.15961/.jsuese.202200941
13. Lin QM, Deng YK, Zhao S, Xiao DM (2018) Study on the insulation properties of the mixture of SF_6 substitute gas and air. High Volt Appar 54:56–62. https://doi.org/10.13296/j.1001-1609.hva.2018.05.009
14. Li JR, Li J, Liu SX (2023) Study on post arc breakdown characteristics of SF_6/N_2 mixed gas circuit breaker. Electr Energy Manag Technol 625:8–14. https://doi.org/10.16628/i.cnki.2095-8188.2023.04.002
15. Shen TD, Zheng Y, Zhou WJ (2022) Study on synergistic effect of SF_6 mixed gas and its mechanism. Electr Mach Control 26:41–48. https://doi.org/10.15938/j.emc.2022.10.005
16. Cao J, Yuan XF, Ma FX (2022) Study on detection of characteristic decomposition products in SF_6/N_2 mixture gas. Low Temp Spec Gas 40:26–30. https://doi.org/10.3969/i.issn.1007-7804.2022.03.007
17. Zhang JF (2022) Study on arcing and breaking characteristics of SF_6/N_2 gas ring main unit. https://doi.org/10.26991/d.cnki.gdllu.2022.002635
18. Lin X, Li XT, Li LW (2016) Research progress of environmentally friendly SF_6 substitute medium in electrical equipments. High Volt Appar 52:1–7. https://doi.org/10.13296/j.1001-1609.hva.2016.12.001
19. Gu Q, Zhong LL (2022) Evaluation of the interruption capability of SF_6 gas mixtures based on one-dimensional arc model. Electr Power Eng Technol 41:140–146. https://doi.org/10.12158/i.2096-3203.2022.06.017
20. Lin X, Li XT, Wang FM (2014) Dielectric recovery characteristics of SF_6 circuit breaker considering contact burning loss. High Volt Eng 40:3125–3134. https://doi.org/10.13336/j.1003-6520.hve.2014.10.026

Design of Switching Regulated Power Supply Based on Flyback

Binglong Zhu and Hailong Ma

Abstract This article presents the design of a feedback-controlled, variable direct current (DC)-regulated switch-mode power supply suitable for laboratory applications. The design includes optimization of the control loop compensation to ensure stability and responsiveness of the power supply. The hardware circuit design and implementation are described to ensure the power supply operates as intended. Experimental results demonstrate that the designed power supply functions properly within a wide input voltage range (85–265 V) and achieves adjustable DC voltage output (1–36 V). The output voltage deviation is within 1%, and the output ripple is between 1 and 2%, indicating acceptable stability and output quality of the power supply. The design meets the requirements for a variable power supply in laboratory settings, providing a new approach for DC auxiliary power supply in laboratories.

Keywords Flyback switching power supply · Control loop compensation design · DC auxiliary power supply

1 Introduction

The importance of power electronics technology is constantly increasing in various fields. Among them, adjustable switch-mode power supplies are indispensable key elements in automated control systems [1]. They can efficiently convert energy and provide stable outputs, ensuring the normal operation of electronic devices [2]. This power supply technology has several characteristics, including excellent output regulation performance, high efficiency, low noise, and compact size [3]. Therefore, it is widely applied in industries, such as industrial, communication, medical, and provides stable power support to various devices [4].

B. Zhu · H. Ma (✉)
Hechi University, Hechi 546300, Guangxi, China
e-mail: mahailong@hcnu.edu.cn

H. Ma
Guangxi University, Nanning 530004, Guangxi, China

S. Yadav et al. (eds.), *Energy Power and Automation Engineering*, Lecture Notes in Electrical Engineering 1118, https://doi.org/10.1007/978-981-99-8878-5_58

By closely integrating with automation systems, adjustable switch-mode power supplies enable precise automatic control of equipment, thereby improving performance and efficiency while reducing costs [5]. This technology, combined with power electronics and automatic control, has broad application prospects [6]. It is of great significance for technological progress, equipment performance enhancement, and energy consumption reduction.

In previous laboratories, linear power supplies were mainly used as DC power sources. However, linear power supplies are bulky, heavy, and have lower efficiency. Therefore, this paper combines the principles of flyback switch-mode power supplies to design a multi-output adjustable DC-regulated switch-mode power supply. By calculating the theoretical parameters of the power supply and designing and implementing the hardware circuit, the effectiveness of the prototype has been verified.

2 Design Approach

2.1 Operating Principle

The working principle of the flyback topology is shown in Fig. 1. When the input pulse is at a high level, the switch transistor Q1 conducts, and the primary winding outputs voltage to store energy in the transformer [7]. The secondary winding induces an electromotive force with the upper terminal negative and the lower terminal positive. At this time, the diode D1 is cut off, resulting in no output [8]. When the input pulse is at a low level, the switch transistor Q1 is turned off, and the energy in the transformer is released. The induced electromotive force on the secondary side is positive at the upper terminal and negative at the lower terminal. The diode D1 conducts, and the capacitor $C1$ charges while supplying power to the load in parallel with the capacitor [9]. The capacity of capacitor $C1$ should be able to provide the load current and meet the output voltage ripple and voltage drop requirements [10].

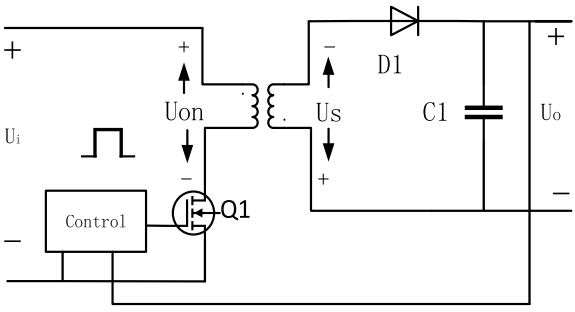

Fig. 1 Working schematic of the converter

The main function of the control part is to adjust the pulse width modulation waveform corresponding to the feedback voltage, so as to quickly reach the specified target output voltage.

2.2 Main Circuit Design of the Adjustable Power Supply

In this design, the input voltage is 85–265 V AC, the output is 1–36 V DC is adjustable, and the output power is 100 W, assuming an efficiency of 80%. Therefore, the rated input power of the transformer is 125 W. The calculation formula for the primary inductance of the high-frequency transformer is as follows:

$$L_p = \frac{\eta * D_{\max} * V_{\text{in\_min}}^2}{2 * f_{sw} * K_{\text{FR}} * P_0} \tag{1}$$

Here, η is the power efficiency, taking 80%; $D_{\max}$ is the maximum duty cycle, taking 50%; $V_{\text{in\_min}}$ is the minimum AC voltage, 85 V; f_{sw} is the operating frequency, and 100 kHz; K_{FR} is the ripple coefficient. In this design, the transformer works in discontinuous mode, so the ripple coefficient is 1. By substituting the data into the upper formula, the original side inductance is 36.125 uH. The peak current of the switch tube obtained $I_{p\max}$ is 5.9A, and the mean $I_{p\text{rms}}$ of the current flowing through the MOS tube is 2.4 A.

According to the AP method, the product of the transformer magnetic core area is 2016 mm^2. Choosing the magnetic core needs to consider a certain margin, and the EE 30 type magnetic core can meet the design requirements. By checking the table, the cross-sectional area of the magnetic core of EE 30 high-frequency transformer Ae is 109 cm^2, and the N_p is 31 turns according to the calculation formula, the ratio of turns N is 3.8, and the N_{sm} of the secondary winding is 8 turns.

2.3 Compensation Loop Design

By conducting theoretical calculations, establish a transfer function model for the power supply and obtain the gain transfer function of the power control loop excluding the compensatory portion:

$$G_{(S)} = \frac{24.4215 - 0.000108\,\text{s}}{1 + 0.01046\,\text{s}} \tag{2}$$

Figure 2 on the left displays the parameters of the Bode plot obtained before power supply compensation. The phase margin is 90°, the crossover frequency is 2.3 kHz, the gain margin is 40 dB, and the slope at the crossover frequency is − 60 dB/dec. The system is unstable.

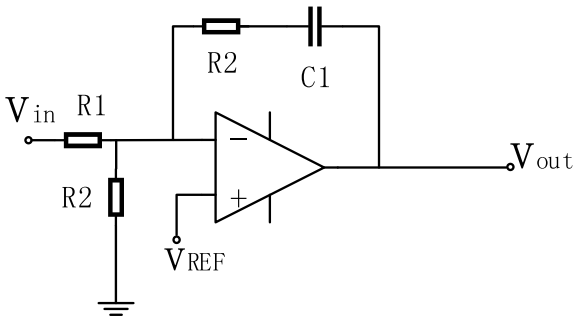

Fig. 2 Schematic diagram of the PI regulator

According to the Bode diagram before the power supply compensation, the compensation zero pole can meet the system stability requirements, and this design uses the PI regulator for compensation.

The PI regulator transfer function is as follows:

$$G(s) = \frac{1 + s * R2 * C1}{s * R1 * C1} \tag{3}$$

The DC gain of the power part is 53.94 dB. It is found that the equivalent inductance of the secondary side of the transformer is 0.1445 mH, the equivalent inductance and the output filter capacitor are at 341 Hz, the zero caused by the output capacitor is at 2467 Hz, the zero point of the compensator is 255.75 Hz, the pole of the compensator is 100 kHz, take $R1 = 13.4$ kΩ, the crossing frequency is 10 kHz, the open loop transfer function gain at the crossing frequency is 0 dB, $R2$ is 65.8 kΩ, and $C1$ is 0.00945 uF. Substitute the data into the PI regulator transfer function to obtain:

$$G(s) = \frac{1 + 0.000622\,\mathrm{s}}{0.000126\,\mathrm{s}} \tag{4}$$

The compensated Bode plot of the power system is shown in the right figure of Fig. 3. In this plot, the phase margin is approximately 80°, the crossover frequency is around 1.06 kHz, the gain margin is 25.9 dB, and the slope at the crossover frequency is − 10 dB/dec.

3 Hardware Circuit Design

The hardware schematic is shown in Fig. 4, which utilizes a common UC3842 flyback switch-mode power supply circuit. The auxiliary power supply uses the VIPER17HN chip to provide stable voltage to the UC3842 and microcontroller in the main circuit. The working principle is as follows: When the input voltage is 220 V, the power supply operates normally and stably outputs a 12 V voltage. The output voltage

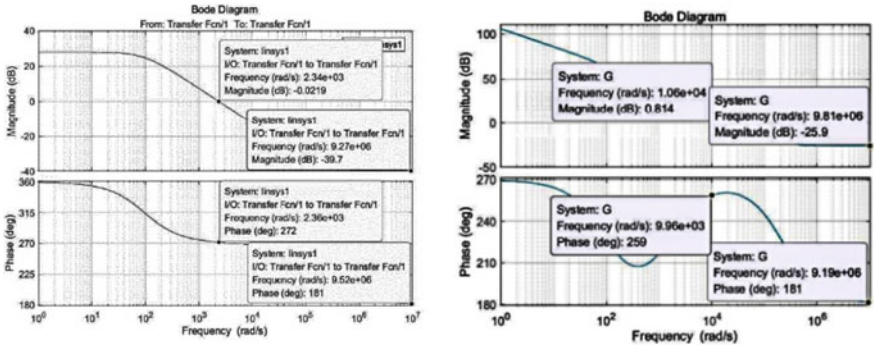

Fig. 3 Bode plots before compensation and after compensation

can be controlled by pressing buttons to control the microcontroller's PWM signal. The PWM signal is filtered by a second-order RC filter to obtain a stable reference voltage. The reference voltage is compared with the sampled output voltage. When the reference voltage is lower than the sampled voltage, the comparator outputs a low level, causing the diode to conduct, pulling down the collector of TL431, turning on the PC817, and reducing the voltage at the point connected to pin 2 of UC3842. UC3842 increases the switch-on time of the switching transistor to raise the output voltage until it reaches the set voltage.

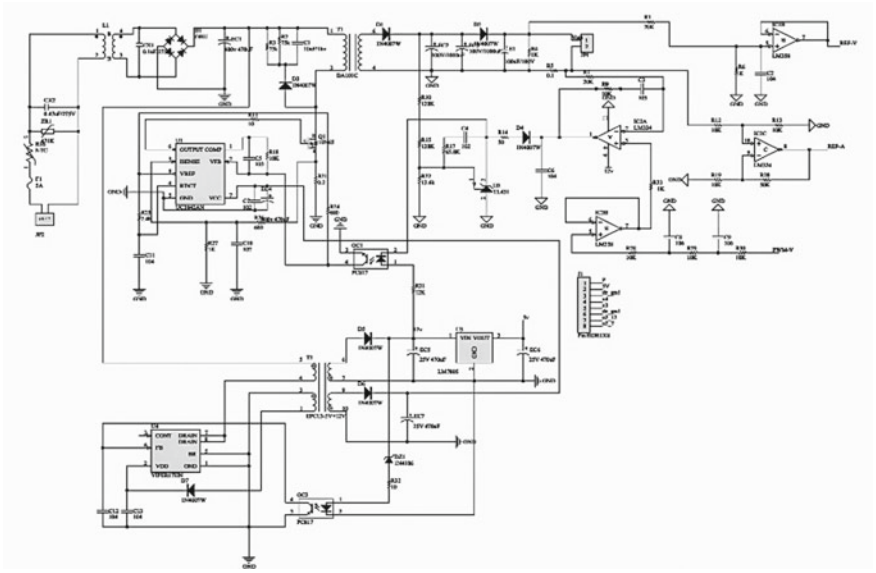

Fig. 4 Schematic diagram of the adjustable power supply

4 Hardware Testing and Analysis

Observe the output waveform with 220 V AC. The output voltage is set to 36 V through the microcontroller button, when the switch is opened, the output voltage is 35.97 V through the multimeter, and the output voltage is within 1% error range. Figure 5 shows the GS terminal waveform of the switch tube at the output voltage 36 V and the voltage ripple at the output voltage 36 V.

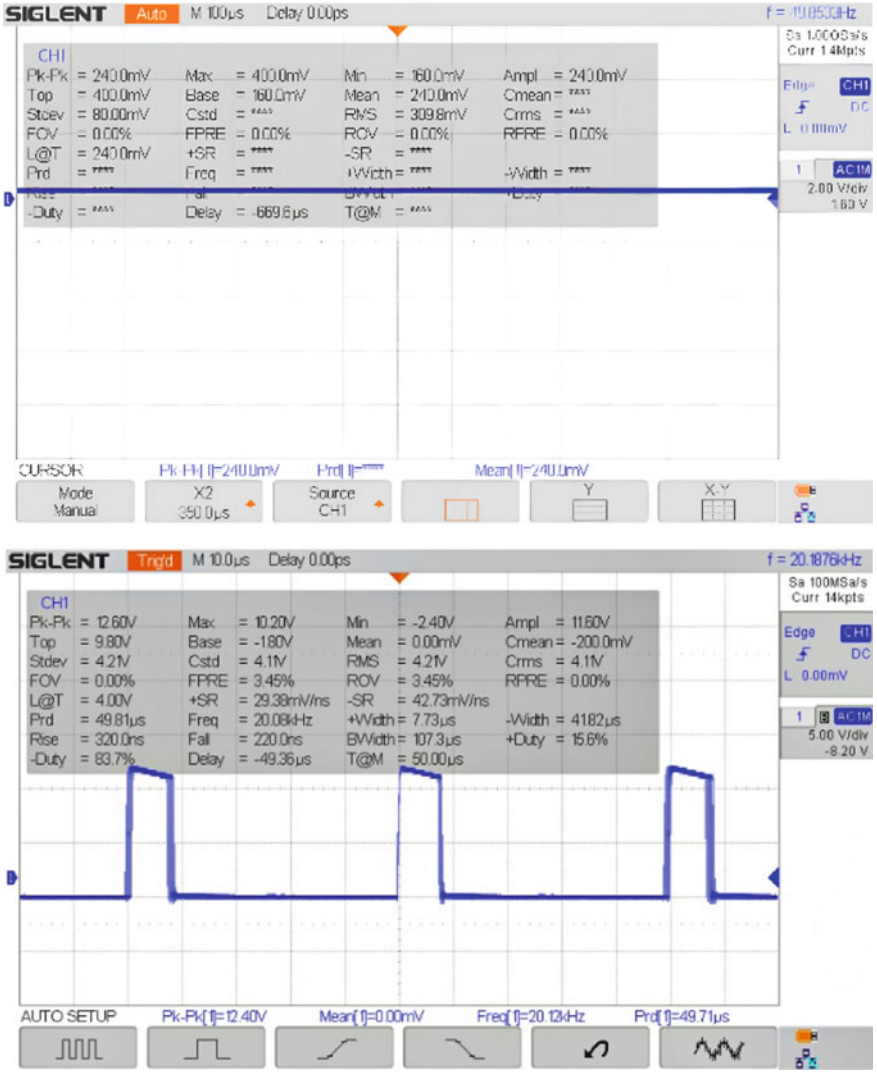

Fig. 5 Output 36 V voltage ripple and switch tube GS waveform

5 Conclusion

In this design, theoretical parameter calculations for the power supply were conducted, followed by the design and implementation of the hardware circuit. Experimental results indicate that the designed power supply can achieve a wide input range of 85–265 V AC and has an adjustable DC output range of 1–36 V. The output voltage deviation rate is within 1%, and the output ripple is between 1 and 2%. Such a design meets the requirements for adjustable power supplies in the laboratory and provides a new choice for DC auxiliary power supply in the laboratory.

Acknowledgements This work was financially supported by National College Students' Innovation plan Training Project (No. 202210605118); 2022 Annual Curriculum Ideological and Political Construction Project of Hechi University (No. 2022KCSZ06).

References

1. Taneri MC, Genc N, Mamizadeh A (2019) Analyzing and comparing of variable and constant switching frequency flyback DC–DC converter. In: 2019 4th international conference on power electronics and their applications (ICPEA). Elazig, Turkey, pp 1–5 (2019). https://doi.org/10.1109/ICPEA1.2019.8911196
2. Patil SP, Patil RR, Mulla AM, Patil SD (2017) Performance analysis of interleaved flyback inverter topology for single phase high power application using MATLAB Simulink. In: 2017 international conference on circuit, power and computing technologies (ICCPCT). Kollam, India, pp 1–5. https://doi.org/10.1109/ICCPCT.2017.8074192
3. Chewale MA, Savakhande VB, Wanjari RA, Sonawane PR (2018) Grid-tied PV inverter based on interleaved flyback converter. In: 2018 international conference on control, power, communication and computing technologies (ICCPCCT). Kannur, India, pp 421–426. https://doi.org/10.1109/ICCPCCT.2018.8574338
4. Wang C-M, Lin C-H, Yang T-C (2011) High-power-factor soft-switched DC power supply system. IEEE Trans Power Electron 26(2):647–654. https://doi.org/10.1109/TPEL.2010.2064336
5. Saved K, Ahmed A, Mohammmed F, Ali I (2020) A high frequency planar transformer isolated DC–DC power converter with secondary-side ZCS active switches and voltage-doubler rectifier. In: 2020 international conference on innovative trends in communication and computer engineering (ITCE). Aswan, Egypt, pp 335–340. https://doi.org/10.1109/ITCE48509.2020.9047805
6. Park J, Roh Y-S, Moon Y-J, Yoo C (2014) A CCM/DCM dual-mode synchronous rectification controller for a high-efficiency flyback converter. IEEE Trans Power Electron 29(2):768–774. https://doi.org/10.1109/TPEL.2013.2256371
7. Li L, Zhang B (2022) Design of buck topology PID compensation network based on Matlab. In: 2022 4th international conference on intelligent control, measurement and signal processing (ICMSP). Hangzhou, China, pp 944–947. https://doi.org/10.1109/ICMSP55950.2022.9858962
8. ElMenshawy M, Massoud A (2019) Multimodule DC–DC converters for high-voltage high-power renewable energy sources. In: 2019 2nd international conference on smart grid and renewable energy (SGRE). Doha, Qatar, pp 1–6. https://doi.org/10.1109/SGRE46976.2019.9020690
9. Gupta H (2022) Topologies of single-input, multiple-output DC–DC converters: design and applications. In: 2022 6th international conference on electronics, communication and

aerospace technology. Coimbatore, India, pp 321–325. https://doi.org/10.1109/ICECA55336.2022.10009405

10. Saadatizadeh Z, Heris PC, Yang Y, Blaabjerg F (2020) High step-up/down switched-capacitor based bidirectional DC–DC converter. In: 2020 IEEE 21st workshop on control and modeling for power electronics (COMPEL). Aalborg, Denmark, pp 1–6. https://doi.org/10.1109/COMPEL49091.2020.9265735

Simulation Study of Arc Characteristics During the Breaking Process of Molded Case Circuit Breaker

Mingming Sun, Xuxu Jiang, Hao Sun, Xiabo Chen, and Xubo He

Abstract With the development and promotion of arc theory and computer technology, arc simulation technology has become an important reference for product development and performance evaluation. Based on the theory of magnetohydrodynamics, an actual molded case circuit breaker model was simulated and studied. Considering the complex multi-physical field coupling characteristics of air arc plasma, ANSYS is used to calculate electromagnetic field, FLUENT to calculate air flow field and thermal field, and the interface program is used to realize data transfer and exchange during the solution process. The analysis of the arc motion during the simulation shows that the grid structure and its spatial distribution affect the arc voltage and the performance of the circuit breaker.

Keywords Magnetohydrodynamics · Molded case circuit breakers · Grid cutting

1 Introduction

Molded case circuit breakers are widely used in low-voltage distribution system and are an indispensable key component in low-voltage electrical appliances. When the line failure in the distribution system occurs, the molded case circuit breakers act and cut off the fault current, which plays a vital role in the safety and reliability of the distribution system [1, 2].

It is of great significance to study the breaking characteristics of circuit breakers to improve the opening capacity of circuit breakers, optimize the design of low-voltage circuit breakers, and ensure the safety of power equipment and staff [3]. If the traditional prototype production and repeated test method is adopted, it lacks economy and timeliness and does not conform to the design concept of modern electrical appliances. Plasma simulation of low-voltage circuit breaker breaking process is an important way to assist circuit breaker design and evaluate circuit breaker breaking

M. Sun · X. Jiang · H. Sun (✉) · X. Chen · X. He
State Key Laboratory of Electrical Insulation and Power Equipment, Xi'an Jiaotong University, Xi'an, China
e-mail: Sunhao1031@mail.xjtu.edu.cn

S. Yadav et al. (eds.), *Energy Power and Automation Engineering*, Lecture Notes in Electrical Engineering 1118, https://doi.org/10.1007/978-981-99-8878-5_59

capacity. With the continuous improvement of arc plasma model and the continuous investment of researchers in arc calculation-related parameters, the theory of arc simulation in the breaking process of circuit breaker has gradually been able to meet the requirements of analysis. The arc-extinguishing method commonly used in molded case circuit breakers is "metal grid arc extinguishing [4, 5]," after the fault current, the circuit breaker moving contact opens, the arc gradually lengthens with the movement of the moving contact, under the action of electromagnetic field and airflow field, to the arc-extinguishing grid movement, under the action of the grid plate, the arc is divided into many short arcs [6], due to the near-pole voltage drop and the cooling effect of the grid, the arc voltage gradually increases, playing a good role in current limiting, and has a very important role in the cutting [7, 8] of the fault arc.

2 Arc Simulation with the Coupling Solution Method

The motion process of arc plasma in the circuit breaker is a complex physical process involving the coupling of multiple physical fields such as thermal field, airflow field, and electromagnetic field. The multiphysics coupling relationship is shown in Fig. 1.

The high-temperature arc column area in the arc-extinguishing chamber is the main channel of current. The temperature and pressure in the arc column area affect the distribution of conductivity. The Joule heat obtained through the electric field calculation as a source term participates in the thermal field calculation. At the same time the heat as a heat source, so that the arc plasma has a high temperature, the arc through heat conduction, radiation, convection to transfer heat to the surroundings, ablating the electrode wall. The metal steam produced by ablation and the steam of other wall materials enter the arc-extinguishing chamber and mix with air to form a mixed gas, and the change of temperature, density, pressure, and other parameters

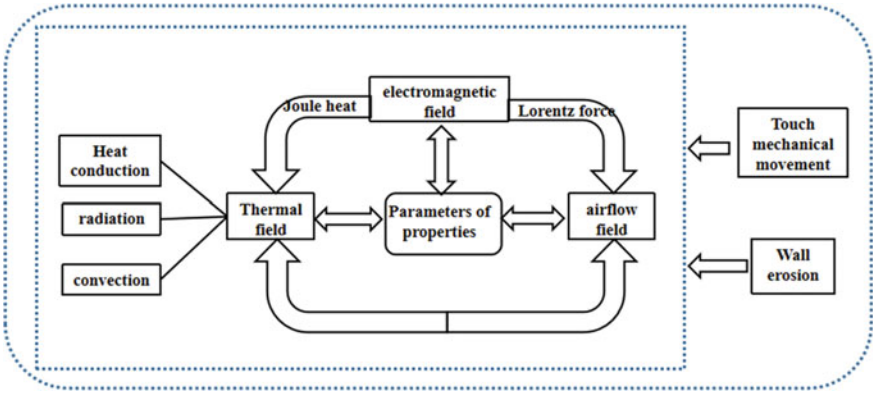

Fig. 1 Multi-physical field coupling relationship of the arc plasma

of the arc plasma in the arc-extinguishing chamber changes the physical parameters of the gas such as conductivity, viscosity coefficient, and radiation absorption coefficient. Moreover, due to the existence of the magnetic field, the arc current will be affected by the Lorentz force, which participates in the calculation of the flow field as the source term.

The air arc plasma has the complex property of multiple physical field coupling, and its governing equations are a set of interrelated nonlinear partial differential equations. This paper is based on magnetohydrodynamics [9]. ANSYS is used to calculate electromagnetic field, and FLUENT is used to calculate thermal field and airflow field. ANSYS and FLUENT are coupled through the interface program to realize the transfer and exchange of data in the solution process, and solving the multiple physics control equations together. Figure 2 shows the flowchart of coupling calculation.

3 Preprocessing of Electric Arc Simulation

3.1 Molded Case Circuit Breaker Geometry Model

In this paper, an arc simulation breaking study was carried out on the actual low-voltage air molded case circuit breaker as shown in Fig. 3. The semi-cylinder is used to replace the rotating shaft connected to the moving contact, and the moving contact is connected with the semi-cylinder. The opening process of the contact during the actual breaking of the circuit breaker is simulated by rotating the contact counterclockwise along the semi-cylindrical surface. The arc-extinguishing chamber contains multiple ferromagnetic grids, and the grids are staggered to cut the arc and increase the arc voltage.

3.2 Boundary Condition Setting

The temperature boundary conditions of the arc-extinguishing chamber wall [10] are set to the one-dimensional thermal conductivity equation:

$$q = q_{\text{rad}} - \frac{\lambda_w (T - T_0)}{d} \tag{1}$$

q is the heat flow density at the wall; q_{rad} is the radiant heat; λ_w is the thermal conductivity of the wall material.

For the electromagnetic field solution [11], the following magnetic vector boundary conditions are satisfied on the solution domain boundary:

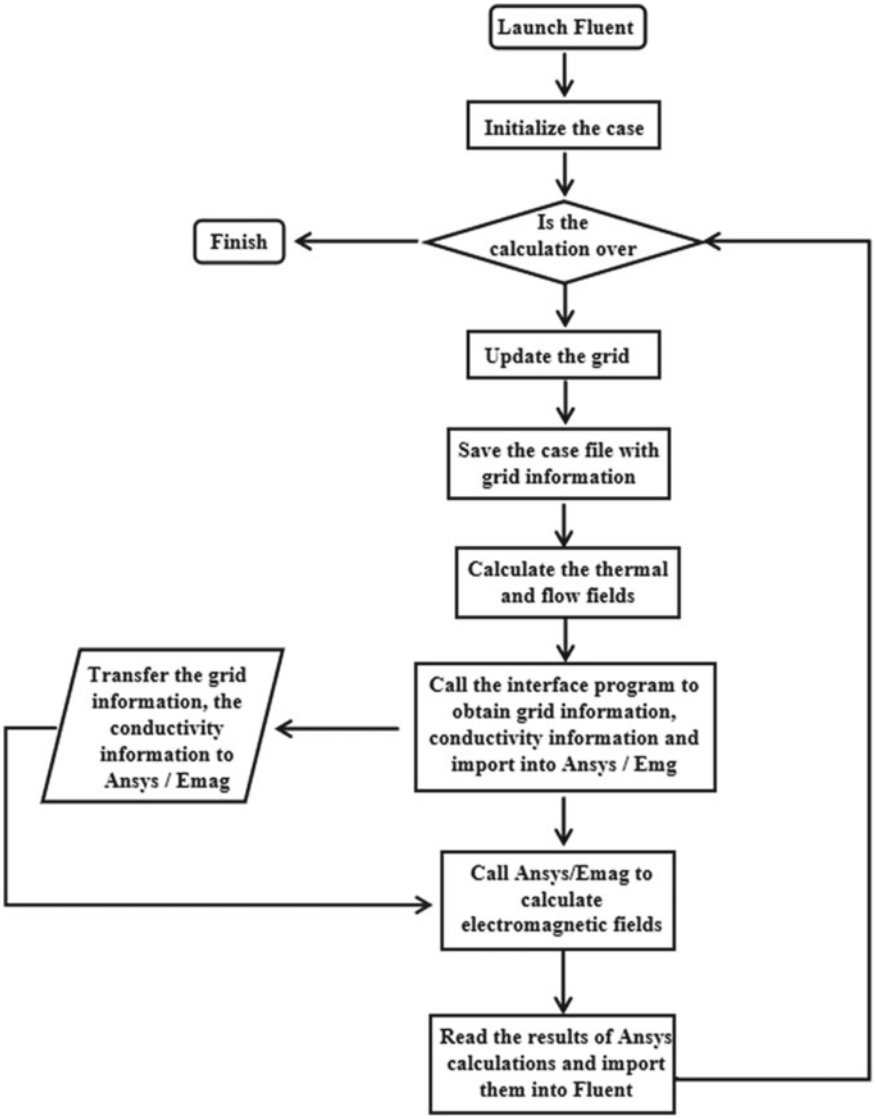

Fig. 2 Flow chart of the coupled calculations

$$\upsilon \nabla \times \vec{A} \times \vec{n} = 0 \tag{2}$$

$$\vec{n} \cdot \vec{A} = 0 \tag{3}$$

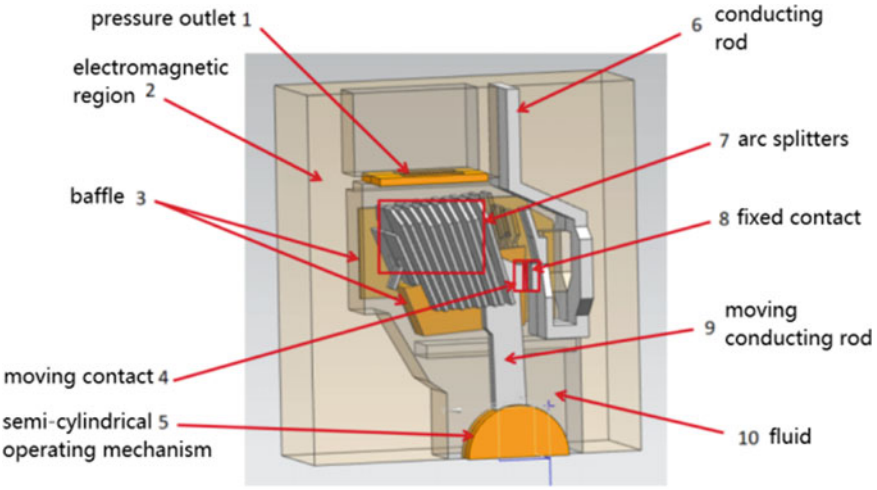

Fig. 3 Simplified circuit breaker geometry model

4 Analysis of Simulation Result

4.1 Analysis of Electric Arc Motion Process in Arc-Extinguishing Chamber

Figures 4 and 5 show the temperature distribution at multiple time points during the entire arc motion.

When the contact is opened, an arc is generated between the contacts, and the arc expands and elongates in a very short time, moves to the arc running channel, and enters the arc-extinguishing grid, and the arc is cut by the grid and is fully expanded in the grid space under the action of the magnetic field and flow field. When the time is 0.00168 s, the arc root of the moving contact is transferred to the back of the moving contact and stays to ablate the back of the moving contact.

When the time is 0.00468 s, the arc root of the moving contact gradually moves toward the front of the moving contact, and the arc moves again to the grid. When the time is 0.0066 s, the arc root of the moving contacts moves from the front to the back and stays on the back. With the gradual opening of the moving contact, the arc is gradually cut by the grid, the temperature of the arc column area rises slowly, with the continuous outflow of high-temperature gas, and the input current gradually decreases; the temperature of the arc area gradually decreases, to 0.008 s, and the arc temperature has dropped to below 15000 K, basically realizing the break.

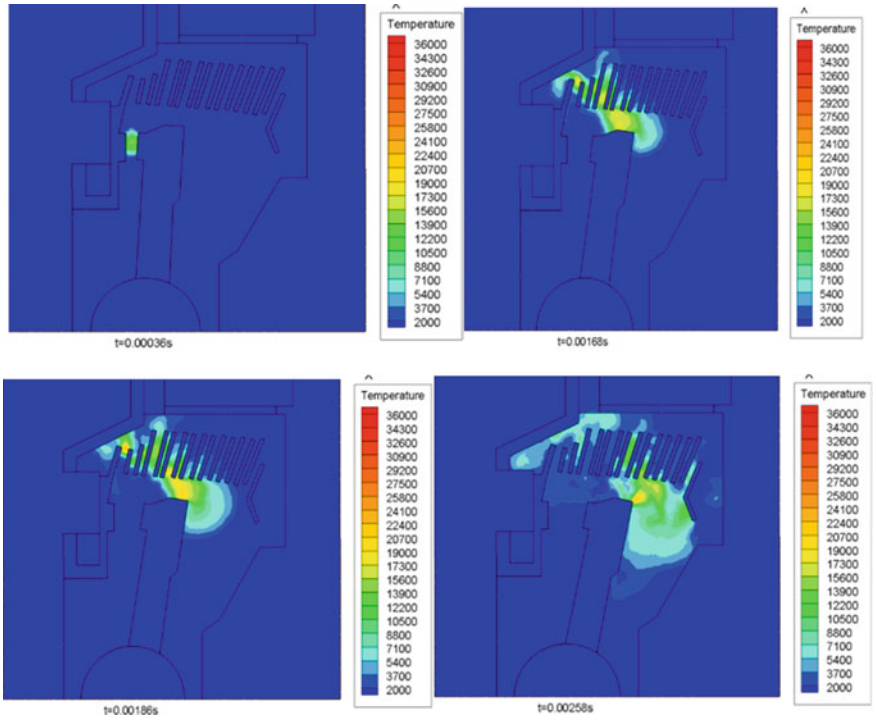

Fig. 4 Temperature distribution at different times during the simulation

4.2 Effect of the Arc Splitters Distribution on the Flow Field

Due to the distribution of the grid, the distribution of the flow field at different grid positions is quite different, and this difference has a great impact on the performance of the arc-extinguishing chamber. Figure 6a shows the distribution of the flow field velocity at 1.8 ms. It can be seen from the figure that the flow field velocity direction near the moving contact is parallel to the grid, while there is a large angle between the flow field velocity direction near the grid where the moving contact is close to the device wall.

Figure 6b shows the details of the flow field velocity distribution near the stationary contacts, which is the local magnification plot near the stationary contacts in Fig. 6a. It can be clearly seen from the figure that the velocity direction of the flow field at this place is parallel to the surface direction of the grid, where the arc column area is subjected to a force perpendicular to the axis of the arc column, because the direction of the velocity of the fluid is parallel to the grid; that is, the arc is very little resistance perpendicular to the axis direction, then the arc is easier to enter the grid, so that the arc is easier to be cut by the grid, easy to achieve the purpose of increasing the arc voltage and limiting the arc current.

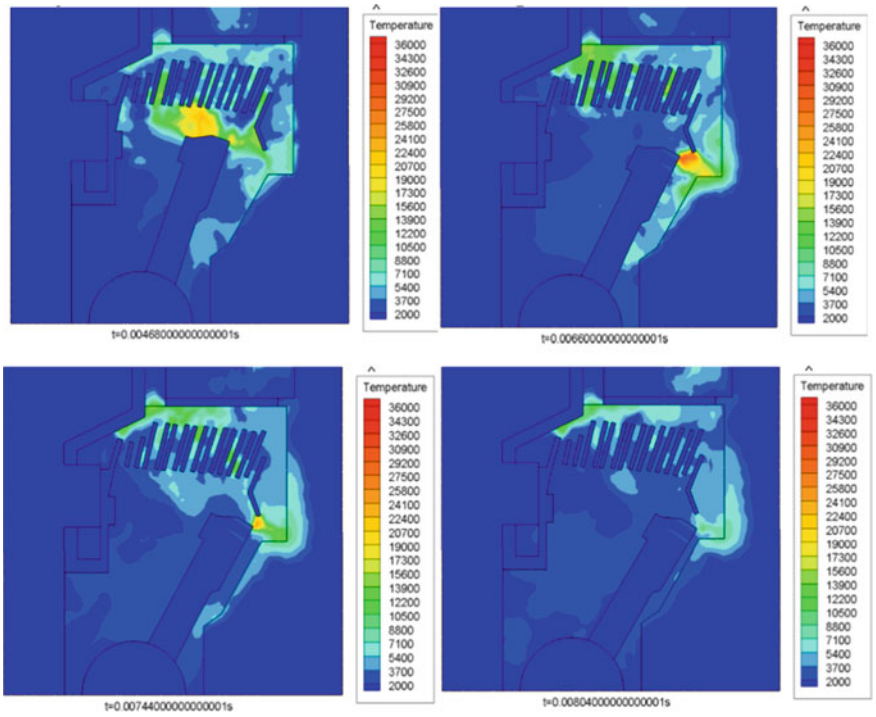

Fig. 5 Temperature distribution at different times during the simulation

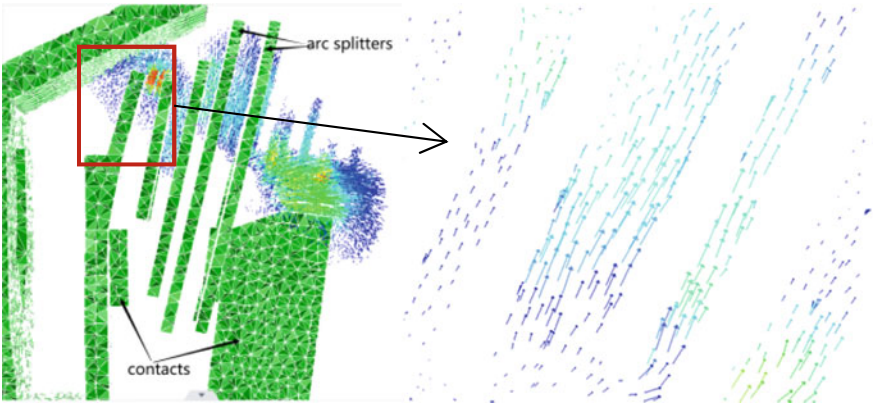

Fig. 6 Flow field velocity distribution diagram

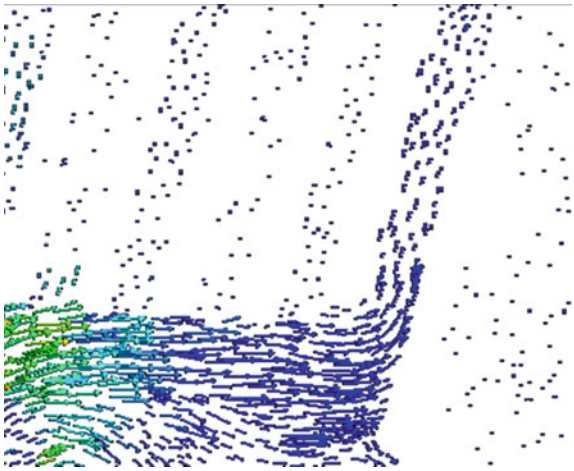

Fig. 7 Flow field velocity distribution diagram

Figure 7 shows the velocity details of the flow field of the grid far away from the static contacts. It is clearly seen that the velocity direction of the main area of the flow field in the arc column area here has a large angle between the direction of the surface of the arc-extinguishing grid. This means that the separation speed of the flow field along the grid surface is relatively small, fluid receives insufficient impetus inside the grid, and the fluid moves along the grid surface and only a small part enters the grid. The arc is barely cut by the arc grid, and the utilization rate of the nearby grid is very low, so the farther away from the resting contact position, the lower the grid utilization rate is.

5 Conclusions

In this paper, the ANSYS–FLUENT coupling simulation method is used to simulate the actual molded case circuit breaker model. The simulation results show that due to the movement of the moving contact, the traction arc stretches longer. Under the action of electromagnetic field and flow field, the arc gradually enters the grid and is cut into multiple short arcs. Due to the uncertainty of the arc motion, the root of the arc is transferred several times during the circuit breaker. In addition, the structure and spatial distribution of the grid have a certain influence on the arc movement and then affect the breaking performance of the molded case circuit breakers.

References

1. Wu G, Zhang S, Shang L (2015) Coupling simulation and measurement method of arc extinguishing efficiency of grid interrupter. J Electr Meas Instrum 29(05):739–747. https://doi.org/10.13382/j.jemi.2015.05.015.
2. Wu J, Wang M (2017) Simulation and experimental study on arc voltage based on MCCB arc extinguishing grid change. Mech Eng 06:28–30
3. Shen P (2021) Analysis and application of arc extinguishing capability of plastic shell circuit breaker. Mod Manuf Technol Equip 057(007):162–164
4. Rong M (2021) Switch electrical computing. Xi'an Jiaotong University, Shaanxi Province
5. Yang F, Rong M, Wu Y et al (2011) Simulation and experimental study of grid-cutting air arc considering grid-ablated metal vapor. J Phys 60(05):502–510
6. Yang Q, Rong M, Wu Y (2006) Simulation and experimental study of air arc motion in low-voltage circuit breaker. Proc CSEE 15:89–94
7. Meunier CG, Mazauric VG, Le Floch Y, Labie P (2004) Eddy-current effects in circuit breakers during arc displacement phase. IEEE Trans Magn 40(2):1358–1361. https://doi.org/10.1109/TMAG.2004.824768
8. Lindmayer M, Marzahn E, Mutzke A, Ruther T, Springstubbe M (2006) The process of arc splitting between metal plates in low voltage arc chutes. IEEE Trans Compon Packag Technol 29(2):310–317. https://doi.org/10.1109/TCAPT.2006.875902
9. Li X, Chen D (2007) Review of mathematical model and characteristics of air switching arc. High Volt Appar 04:269–273
10. Wu Y, Rong M, Yang Q, Hu G (2005) Low voltage breaking arc simulation based on Fluent. Low Volt Electr Appar 05:7–9 + 21. https://doi.org/10.16628/j.cnki.2095-8188.2005.05.002
11. Wu Y, Rong M, Yang Q, Hu G (2005) Simulation and analysis of the dynamic characteristics of low-voltage air arc. Chin J Electr Eng 21:146–151. https://doi.org/10.13334/j.0258-8013.pcsee.2005.21.026

Research and Application of Diversified Load Access Adapting to Distribution Network Planning

Jinxin Yang, Yuanping Huang, Rui Su, and Guobin He

Abstract The distribution network planning method mainly focuses on the division of power supply areas, without predicting the load of the distribution network, which affects the final planning effect. Therefore, this article studies the research and application of diversified load access in distribution network planning. Establish a diversified load access adaptive distribution network planning model, identify the main stakeholders in distribution network planning, and minimize the overall operating cost as the objective function to minimize the cost of distribution network planning, coordinated with its power flow distribution. Through numerical examples, it has been verified that the planning method can meet the needs of practical economic benefits and can be applied in practical life.

Keywords Diversified load access adaptation · distribution network planning method · tidal current distribution

J. Yang (✉) · Y. Huang · R. Su · G. He
Dali Power Supply Bureau of Yunnan Power Grid Co., Ltd., Dali 671000, China
e-mail: astropayment@163.com

S. Yadav et al. (eds.), *Energy Power and Automation Engineering*, Lecture Notes in Electrical Engineering 1118, https://doi.org/10.1007/978-981-99-8878-5_60

1 Introduction

Through flexible dispatching in different planning areas, the loss of distribution network is reduced and the economic benefits of distribution network operation are higher. At present, the distribution network often suffers from line faults, resulting in large-scale blackouts, which seriously affects the living electricity environment of residents [1, 2]. Therefore, this paper designs a diversified load access adaptive distribution network planning method. From the perspective of diversified load access, the planning environment will be more in line with the actual needs of the power grid and provide power security for the surrounding residents.

2 Design of Diversified Load Access Adaptive Distribution Network Planning Method

2.1 Extraction of Diversified Load Output Characteristics of Distribution Network

This paper analyzes the load data of renewable energy generation and reasonably plans the operation mode of distribution network according to the load output. This paper divides the diversified load of the distribution network into photovoltaic output and wind power output to ensure the effectiveness of distribution [3–6]. The output prediction of photovoltaic power generation includes global solar radiation theory and photovoltaic effect [7]. Under the condition of ignoring light scattering and occlusion, the light radiation intensity is as follows:

$$I_t = I_0 \sin \alpha \tag{1}$$

In formula (1), I_t is the light intensity ignoring other conditional factors; I_0 is the light radiation intensity vertically irradiated by the sun; α is the solar altitude angle. Combining I_t by applying photovoltaic effect, the characteristics of photovoltaic power generation output are obtained:

$$P_t = P_s \frac{(R, k, I_t)}{I_0}[1 + \alpha(T - T_t)] \tag{2}$$

In formula (2), R is the state coefficient; P_t is the output of photovoltaic at time t; T is the actual temperature; P_s is the PV rated output; T_t is the standard temperature; k is the clear sky coefficient. Wind power generation is determined according to the relative position of the fan shaft and wind direction, and the speed of air flow directly determines the output of wind power conversion [8–10]. In this paper, Weibull distribution is used to describe the wind speed characteristics, and its probability density function is as follows:

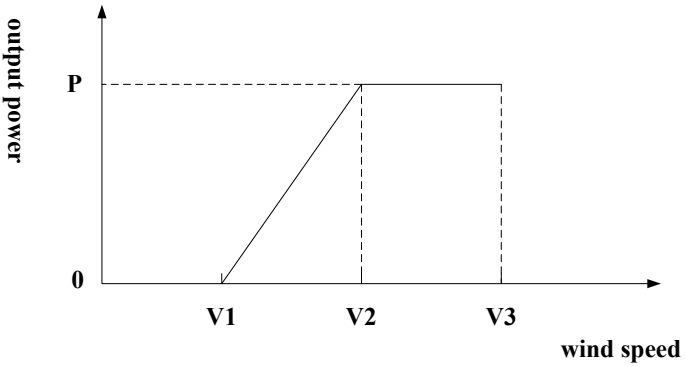

Fig. 1 Output power characteristic curve

$$f(v) = \frac{k}{c}\left(\frac{v}{c}\right)^{k-1} \exp\left[-\left(\frac{v}{c}\right)^{k}\right] \tag{3}$$

In formula (3), $f(v)$ is the complementary function of cumulative distribution function; c is a scaling function; v is the air flow rate on site. According to $f(v)$, the wind power load output is determined as follows:

$$P_v = \begin{cases} 0 \\ (A + Bv + Cv^2)P_r \\ P_r \end{cases} \tag{4}$$

In Eq. (4), P_v is the wind power load output; A, B, and C are the parameters of rated power generation curve; P_r is the maximum power output of a wind turbine under standard operating conditions. According to A, B, and C, characteristic variation relationship between active power of wind turbines and air flow velocity under different air flow velocities is obtained as shown in Fig. 1.

As shown in Fig. 1, P is the maximum power output of a wind turbine under standard operating conditions; $V1$ is the minimum wind speed at which the wind turbine begins to rotate and generate electricity; $V2$ is the wind speed at which the output power of the wind turbine reaches the rated power; $V3$ is the maximum wind speed at which a wind turbine stops operating to protect its own safety. When $V < V1$ or $V \geq V3$, the output power of the distribution network $P = 0$, which cannot ensure the planning benefits. When $V1 \leq V < V2$, the output power increases with the increase of wind speed; When $V2 \leq V < V3$, the output power remains stable, which can ensure the benefits of distribution network planning.

2.2 Build a Diversified Load Access Adaptive Distribution Network Planning Model

Based on the characteristics of diversified load access processing, this paper finds out the main stakeholders of design of power supply system: design and plan the power supply system in an economical and efficient manner by minimizing the cost of power dispatch as the objective function. In the planning process, this paper takes the minimization of comprehensive costs as the objective function of the planning model in terms of coordinating the minimization of comprehensive costs, the maximization of benefits for each entity, operational safety, and reliability assurance, and the expression is as follows:

$$\min\ C_n = C_{n,s} + C_{nJ} + C_{n,o} + C_{n,e} - F_c \tag{5}$$

In formula (5), min C_n is the digital representation of minimized power dispatch costs; $C_{n,s}$ is a long-term construction investment in the power supply system; C_{nJ} is the energy loss expenditure in the process of power transmission and distribution; $C_{n,o}$ ensures the stable operation of the power system and the various costs required for electricity supply; $C_{n,e}$ is the system failure expenses for distribution networks; F_c is the benefit of carbon dioxide emission reduction. The network loss cost is expressed as:

$$C_{nJ} = \sum_{s=1}^{S} T_s \sum_{t=1}^{24} C_{n,s} \Delta t \tag{6}$$

In formula (6), S is a typical planning scenario; T_s is the duration of scenario s; Δt is the unit time interval. Combined with the support conditions of ESS for partial loss of power load in the distribution network, this paper divides the distribution shortage into three cases: First, the power grid is disconnected after fault; second, the fault is power grid disconnection; third, island nodes access ESS. The electrical constraints of the distribution network planning model are added, and the distribution network planning model is built. The model expression is as follows:

$$P_{s,j} = U_{s,j} \sum_{j=1} \min C_n (G_{ij} \cos\theta_{ij} + C_{nJ} \sin\theta_{ij}) \tag{7}$$

In Eq. (7), $P_{s,j}$ is the distribution network planning model expression; $U_{s,j}$ is the voltage of node j in the scene; G_{ij} is the power transmission constraint from node i to node j; θ_{ij} is the line transmission power limit. Staying $P_{s,j}$ under the maximum conditions, the distribution network needs to meet the power flow constraints to ensure the economic benefits of distribution network planning.

2.3 Coordinate Power Flow Distribution of Distribution Network Planning

Under the constraints regarding the overall architecture of the power supply system, this article maximizes its design benefits while ensuring its operational economy because of profits. Thus, the power flow constraint conditions are as follows:

$$S_{s,t,j} = S_{s,t-1,j} - \mu_c \Delta t P_{s,j} \tag{8}$$

In Eq. (8), $S_{s,t,j}$ is the power flow constraint condition of the planning model; $S_{s,t-1,j}$ is the power flow distribution of node j at time $t-1$ in scenario s; μ_c is the charging efficiency. In this paper, diversified load access nodes and capacities that meet various constraints will be transferred to distribution enterprises under different scenarios to optimize the economic benefits of distribution to the greatest extent.

3 Example Analysis

3.1 Experiment Preparation

This experiment simulates the distribution network as a test example. The power node is node 1, the original load node is 2–33, and the new load node is 34–38. The solid line represents the original line and does not need to be upgraded or replaced; dotted lines represent replaceable lines, and dotted lines represent lines to be built. The distribution network structure is shown in Fig. 2.

As shown in Fig. 2, this paper selects the typical operation scenario of distribution network and sets the rated capacity of each DG as 100 kW. Considering the original load size of the distribution network, set the replacement circuit as 5, 6, 7, 16, 18, 19, 25, 26, 27, 31. The new node numbers are 34, 35, 36, 37, 38. Among them, the reactive power is 120 kvar, and the accessible node locations are 25, 26, 27, 28. The accessible node locations are 29, 30, 31, 32, the reactive power is 75 kvar, and the accessible node locations are 6, 7, 8, 22. The active power of node 37 is 100 kW, the reactive power is 60 kvar, and the accessible node locations are 9, 10, 11, 12. The active power of node 38 is 90 kW, and the reactive power is 30 kvar. The accessible node locations are 13, 14, 15, 16. Under this condition, the parameters of the lines to be planned and the replacement lines are set as shown in Table 1.

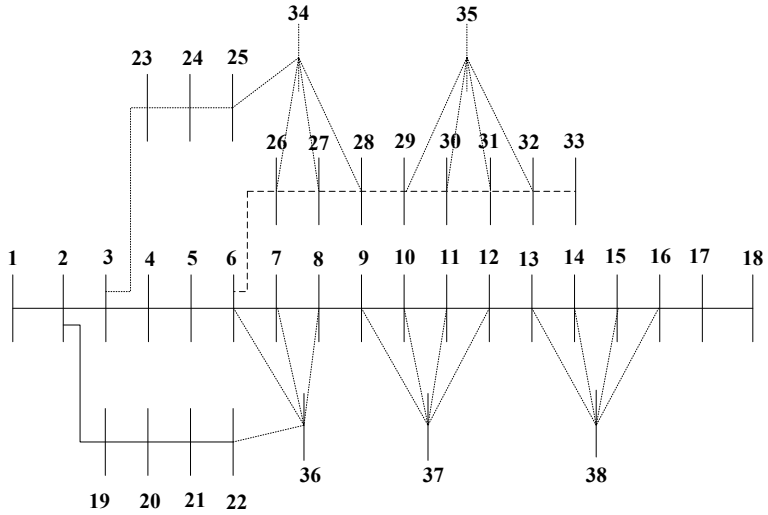

Fig. 2 Schematic diagram of distribution network structure calculation example

As shown in Table 1, 34 nodes replace 26, 27, and 28 nodes; 35 nodes replace 29 and 30; nodes 5, 6, and 7 take over the work of nodes 6, 7, and 8; node 17 takes over the work of node 16. DG configuration is 12 (0,5), 17 (4,2), 29 (0,3), 32 (1,2). The replacement lines are numbered 5, 6, 7, 18, 25, 31, and the new load access positions are 6, 11, 13, 22, 29. In order to ensure the effectiveness of distribution network planning, this experiment carried out distribution network planning under the condition that DG grid connection was considered to ensure the effectiveness of this grid connection collaborative planning.

3.2 Experimental Results

Under the above experimental conditions, this paper randomly selects the locations of multiple load access nodes and analyzes the network loss of distribution network planning in four seasons of a year: the conventional distribution network planning method based on distributed energy access and the conventional distribution network planning method based on source network storage collaboration.

As shown in Table 2, the diversified load access nodes are set as 1–24, 18–33, 23–27, and 9–13 in this paper, the planned capacity of the distribution network after the distribution network planning is different, and the network loss changes accordingly.

Table 1 Parameters of lines to be planned and alternative lines

Line number	Node numbers at both ends		Branch impedance (Ω)		Investment cost (10,000 yuan/km)	Line status
	Extreme point 1	Extreme point 2	R	X		
34	34	26	0.3450	0.1874	10	New line
35	34	27	0.3881	0.2108	10	New line
36	34	28	0.1254	0.0681	10	New line
37	35	29	0.4142	0.2249	10	New line
38	35	30	0.3131	0.1701	10	New line
5	5	6	0.8190	0.7070	5.5	Replaceable circuit
6	6	7	0.1872	0.6188	5.5	Replaceable circuit
7	7	8	0.7114	0.2351	5.5	Replaceable circuit
16	16	17	1.2890	1.7210	5.5	Replaceable circuit
18	2	19	0.1640	0.1565	5.5	Replaceable circuit
19	19	20	1.5042	1.3554	5.5	Replaceable circuit
25	6	26	0.2030	0.1034	5.5	Replaceable circuit
26	26	27	0.2842	0.1447	5.5	Replaceable circuit
27	27	28	1.0590	0.9337	5.5	Replaceable circuit
31	31	32	0.3105	0.3619	5.5	Replaceable circuit

Table 2 Experimental results

Diversified load access node location	Season	Conventional distribution network planning method based on distributed energy access		Conventional distribution network planning method based on source network storage collaboration		The diversified load access adaptive distribution network planning method designed in this article	
		Network losses in distribution network planning (kW)	Distribution network planning capacity (kVA)	Network losses in distribution network planning (kW)	Distribution network planning capacity (kVA)	Network losses in distribution network planning (kW)	Distribution network planning capacity (kVA)
1–24	Spring	808.621	1459.237	632.615	1647.645	321.432	2056.762
	Summer	716.824	1454.492	654.784	1678.155	326.465	2083.311
	Autumn	1074.176	1460.684	732.754	1636.467	345.746	2040.734
	Winter	950.452	1459.816	693.124	1652.682	362.612	2081.908
18–33	Spring	580.826	1712.855	562.154	1979.371	354.154	2146.543
	Summer	1034.351	1719.962	613.546	1980.774	343.746	2154.682
	Autumn	1013.544	1703.111	754.356	1981.862	328.461	2136.688
	Winter	1195.293	1704.005	741.614	1977.862	345.656	2121.966
23–27	Spring	1192.452	1690.381	714.536	1879.947	328.461	2032.697
	Summer	1177.996	1689.214	715.463	1847.700	333.546	2045.669
	Autumn	1196.063	1687.423	815.462	1906.724	312.466	2031.478
	Winter	1198.562	1686.838	854.513	1864.512	325.135	2044.875
9–13	Spring	861.912	1759.702	715.414	1906.666	362.748	2253.457
	Summer	541.011	1758.833	642.545	1903.025	377.546	2245.682
	Autumn	549.093	1757.131	536.754	1907.586	358.346	2216.748
	Winter	971.605	1757.243	647.132	1879.191	372.135	2232.564

4 Conclusion

This article designs a diversified load access adaptive distribution network planning method. From the aspects of load output, planning models, and power flow balance, planning the distribution network is more in line with practical needs.

References

1. Liu X, Wang H, Sun Q et al (2022) Research on fault scenario prediction and resilience enhancement strategy of active distribution network under ice disaster. Int J Electr Power Energy Syst 135(3):107478
2. Aschwanden GD, Wijnands JS, Thompson J et al (2021) Learning to walk: modeling transportation mode choice distribution through neural networks. Environ Plan B Urban Anal City Sci 48(1):186–199
3. Wu F, Zhu Y, Zhu W et al (2021) The spatial distribution characteristics of the centrality advantage stations in Hangzhou metro planning (2005–2022). IOP Conf Ser Ear Environ Sci 634(1):012110 (7pp)
4. Farrag MA, Zahra MG, Omran S (2021) Planning models for optimal routing of radial distribution systems. Int J Appl Power Eng (IJAPE) 10(2):108
5. Liu X (2021) Automatic routing of medium voltage distribution network based on load complementary characteristics and power supply unit division. Int J Electr Power Energy Syst 133(2):106467
6. Dong Z, Lin L, Cao H et al (2022) Distribution network dynamic reconfiguration based on improved fuzzy C-means clustering with time series analysis. IEEJ Trans Electr Electron Eng 17(2):174–182
7. Neelakantan TR, Rohini K (2021) Simplified pressure-driven analysis of water distribution network and resilience estimation. J Water Resour Plan Manag 147(3):06021002
8. Abdel-Mottaleb N, Zhang Q (2021) Quantifying hierarchical indicators of water distribution network structure and identifying their relationships with surrogate indicators of hydraulic performance. J Water Resour Plan Manag 147(4):04021008
9. Ren H, Deng Q, Wen F et al (2021) Joint planning of a distribution system and a charging network for electric vehicles. J Energy Eng 147(1):04020085
10. Yang JJ, Cheng RF, Xu LB (2022) Multi-objective optimization simulation of active distribution network considering new energy access. Comput Simul 39(9):108–113

Orderly Charging and Discharging Control of Electric Vehicle Clusters Considering the Active Participation of Users

Hua Wang, Jing Xu, Lili Wang, Ying Zhou, and Huan Yu

Abstract Electric vehicles are increasingly becoming an important means of transportation for people due to their clean and efficient advantages. The number of electric vehicles continues to rise. Due to the charging behavior of electric vehicle users is random in time and space, a large number of uncontrolled electric vehicle charging loads will have a great impact on the safety and economic operation of the distribution network. The technology of interaction between electric vehicles and the grid enables electric vehicles to participate in grid regulation as both load and mobile energy storage. This paper analyzes the vehicle use of residents. An orderly charging and discharging strategy is proposed that considers the owner's response scheduling willingness and the spatial–temporal characteristics of electric vehicles. The effectiveness of the strategy in this paper is analyzed through simulation verification. The results show that the strategy realizes peak shaving and valley filling, and improves the security of power grid operation.

Keywords Orderly charging · Electric vehicle clusters · Probability model · Active participation

1 Introduction

The demand for long-distance travel residents is increasing, and the supporting facilities for road transportation are gradually improving. Motorized travel tools have become an important choice for residents. It is gradually striding over the fuel vehicle era and entering the era of electric travel. Electric vehicles are an efficient and clean way to travel with good flexibility and energy storage characteristics. Electric vehicles have both the attributes of a vehicle and an electrical load. With the expansion of the number of electric vehicles, their driving behavior and charging habits will have

H. Wang (✉) · J. Xu · L. Wang · Y. Zhou · H. Yu
State Grid Chaoyang Electric Power Supply Company, State Grid Liaoning Electric Power Supply Co., Ltd., Chaoyang, China
e-mail: wanghua_cy@163.com

S. Yadav et al. (eds.), *Energy Power and Automation Engineering*, Lecture Notes in Electrical Engineering 1118, https://doi.org/10.1007/978-981-99-8878-5_61

a certain impact on the traffic flow of the road network and the operation status of the power grid. The technology of interaction between electric vehicles and power grid enables electric vehicles to participate in power grid regulation in the dual roles of load and mobile energy storage [1–3]. Therefore, it is of great significance to make full use of the electric vehicle cluster regulation capability to smooth the power fluctuation of the distribution network [4]. Under a reasonable dispatch strategy, the load pressure in the power grid can be relieved, and peak shaving and valley filling can be realized. Vehicle-to-Grid (V2G) technology is a smart grid technology that is gradually emerging. It can realize the two-way flow of energy between electric vehicles and the grid. Under the premise of satisfying the user's travel, control the electric vehicle to charge from the system during the period of low system load. In the peak load stage, the electric vehicles with sufficient power are controlled to selectively discharge, and the power is reversely input to the grid side. So as to achieve the purpose of reducing the peak load, the peak-valley difference rate and smoothing the fluctuation of the load curve [5, 6].

In order to make full use of the high-quality energy storage resources of a large number of electric vehicles, many scholars use dynamic electricity prices to guide the charging behavior of electric vehicles [7, 8]. Most of them take cities as application scenarios, and consider the station-finding efficiency and fast-charging response strategy of electric vehicles [9, 10]. Some scholars have also proposed a time-of-use pricing strategy that considers the response degree of electric vehicles [11, 12], which improves the satisfaction and participation of vehicle owners. However, when the owner's participation is too high, it will cause the charging peak to form again in the valley, which will endanger the safe operation of the power grid.

In this paper, the use of residents' vehicles, as well as the time and space characteristics of vehicles are analyzed, and a space–time load model for electric vehicles is established. Then, the convenience of user travel and the satisfaction of participating in scheduling are considered. A participation probability model is introduced, and an orderly charging and discharging strategy is proposed that considers the owner's response scheduling willingness and the spatial–temporal characteristics of electric vehicles. Finally, the effectiveness of the strategy in this paper is analyzed through simulation verification. The results show that this strategy realizes peak shaving and valley filling and improves the security of power grid operation.

2 Probability Model for Participating of Electric Vehicles in Dispatching

2.1 Time Characteristics of Electric Vehicles

The travel time characteristics of electric vehicle clusters still conform to a normal distribution, assuming that each electric vehicle participates in dispatching at most once a day. However, whether it performs charging and discharging behavior should

Table1 Vehicle type and destination

Vehicle type	Home (%)	Work (%)	Market (%)	Township or travel (%)
Car	35	30	25	10
Van	25	40	30	5

be judged according to its initial battery capacity E_{EV}. The time when the electric vehicle is connected to the grid at the end of the trip follows a normal distribution.

$$f_s(t) = \frac{1}{\sigma_s\sqrt{2\pi}} \exp\left[-\frac{(t-\mu_s)^2}{2\sigma_s^2}\right] \tag{1}$$

where t is the initial charging time, μ_s is the expectation at the end of the last trip, σ_s is the standard deviation at the end of the last trip and μ_s and σ_s, which vary with the driving characteristics of different types of vehicles.

2.2 Space Characteristics of Electric Vehicles

Residents pay more attention to the economical use of electric vehicles. In addition to daily travel, residents also have special needs such as transportation products. The travel destination is relatively simple, and it is easy to form an obvious traffic travel chain, as given in Table 1. Part of the traffic networks has a slightly simple road condition and a relatively low grade.

Knowing the latitude and longitude coordinates of the vehicle during driving, the mileage of a trip can be calculated by (2).

$$d_i = \sum_{i}^{n} \sqrt{(x_i - x_{i-1})^2 + (y_i - y_{i-1})^2 + (z_i - z_{i-1})^2} \tag{2}$$

where (x_i, y_i, z_i) and $(x_{i-1}, y_{i-1}, z_{i-1})$ are the latitude, longitude and altitude of the electric vehicle at the current moment and the previous moment. d_i is the distance traveled.

2.3 Probability Model of Electric Vehicle Users Participating in Scheduling

The lower the charging cost and the closer the scheduling distance, the greater the willingness of electric vehicle users to respond. The response willingness index D is set as a comprehensive index of the satisfaction degree of electric vehicle users on the dispatch distance and dispatch price, and the formula is as follows.

$$D = \alpha_1 C + \alpha_2 L \tag{3}$$

where C is the charging cost of the vehicle owner and L is the dispatching distance. α_1 and α_2 are weight coefficients, and different values are selected for different types of electric vehicles. According to the response willingness index D, the upper and lower limits of the probability of electric vehicle users participating in scheduling are analyzed, and the formula is as follows.

$$f^{\max} = \begin{cases} 0, & D < -\frac{h_1}{r_1} \\ r_1 D + h_1, & -\frac{h_1}{r_1} \le D \frac{1-h_1}{r_1} \\ 1, & D \ge \frac{1-h_1}{r_1} \end{cases} \tag{4}$$

$$f^{\min} = \begin{cases} 0, & D < -\frac{h_2}{r_2} \\ r_2 D + h_2, & -\frac{h_2}{r_2} \le D \frac{1-h_1}{r_1} \\ 1, & D \ge \frac{1-h_1}{r_1} \end{cases} \tag{5}$$

where f is the response probability of electric vehicle users, r_1 and r_2 are the owners' response willingness coefficients. h_1 and h_2 are the owners' historical response probability coefficients. The probability of electric vehicle users participating in scheduling will be randomly selected from the range between the upper and lower limits as shown in Fig. 1.

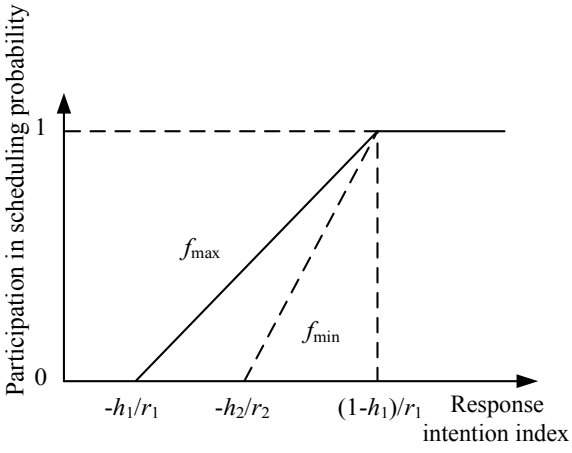

Fig. 1 Vehicle owner participation in dispatching response indicators

3 Model of Orderly Charging and Discharging Strategy for Electric Vehicles

The main function of electric vehicles is to meet people's daily travel needs. The user's travel plan is the first. No matter how the charging strategy changes, the user's travel goal cannot be ignored. In this paper, the least-constrained user agreement is adopted, that is, only the basic travel requirements of electric vehicles and the maintenance requirements of batteries are guaranteed, and the upper limit of the discharge capacity of regional electric vehicle clusters is estimated.

The charging and discharging strategy satisfies the follow constraints.

- Battery constraints. The state of charge (SOC) will not discharge below the guaranteed minimum charge.
- Object constraints. Electric vehicles in non-charging areas do not participate in discharge.
- Time constraints. The time when electric vehicles enter and exit the grid is determined by the user.
- Travel constraints. Ensure that after the electric vehicle leaves the grid, the SOC can complete the travel goal of the next stage.

In the absence of V2G instructions, the electric vehicle will be charged at the first moment when it is connected to the grid. After receiving the V2G instruction, the electric vehicles that meet the policy constraints begin to discharge. The electric vehicles connected to the grid are divided into two types, those that can respond and those that cannot respond. The electric vehicles that cannot respond meet at least any of the following SOC descriptions.

- Battery is lower than $E_j^{\min}$.
- Even if the EV is charged at the fast charge rating, the charge still cannot reach E_j^{need} when leaving.

When the electric vehicle that satisfies the constraint is connected to the power grid, the mathematical description of the upper and lower limits of the response boundary at time t is as follows.

$$E_j^+(t) = \begin{cases} \min\left\{P_j^C(t-t_0) + E_j(t_0), E_j^{\max}\right\}, & t_0 < t \le t_j^L \\ 0, & t > t_j^L \end{cases} \tag{6}$$

$$E_j^-(t) = \begin{cases} \max\left\{\begin{array}{l}(t-t_0)P_j^D + E_j(t_0), \\ E_j^{\text{need}} - P_j^C(t_j^L - t), E_j^{\min}\end{array}\right\}, & t_0 < t \le t_j^L \\ 0, & t > t_j^L \end{cases} \tag{7}$$

where $E_j^+(t)$ is the charging situation when there is no V2G response demand at time t; $E_j^-(t)$ is the charging and discharging situation when V2G response is accepted and started. P_j^C and P_j^D are the maximum charging and discharging power of electric

vehicle j, respectively. t_0 is the current time; $E_j(t_0)$ is the battery power of the electric vehicle at t_0 time. $E_j^{\max}$ is the upper limit of charging of electric vehicle j, which is generally specified as the capacity of the battery; $E_j^{\min}$ is the guaranteed bottom power. t_j^L is the moment when electric vehicle j leaves the charging station. E_j^{need} means that in order to meet the user's demand for car use from time to time, the user's charging expectation is set as the amount of electricity to complete the next trip.

Through the probability model of SOC probability distribution, electric vehicle residence time distribution and charging demand distribution probability model, the discharge subject is determined. Given the response period T^{rsp}, with t_0 as the response starting point, the V2G schedulable capacity model is established.

$$E_i^{\text{rsp}}(t_0, T^{\text{rsp}}) = \begin{cases} E_i^+(t_0 + T^{\text{rsp}}) - E_i(t_0), \text{ Charge} \\ E_i(t_0) - E_i^-(t_0 + T^{\text{rsp}}), \text{ Discharge} \end{cases} \tag{8}$$

where $E_i^{\text{rsp}}(t_0, T^{\text{rsp}})$ is the V2G schedulable capacity within the response period (t_0, T^{rsp}); E_i^+ and E_i^- are the upper and lower boundaries of charge and discharge in the response period, respectively. $E_i(t_0)$ is the initial value of the electric vehicle charging station capacity of t_0 at the start of scheduling.

The V2G dispatchable capacity of an electric vehicle cluster in a region should be the sum of the V2G dispatchable capacity of electric vehicles in all charging stations in the region.

$$E_{\text{sum}}^{\text{rsp}}(t_0, T^{\text{rsp}}) = \sum_i E_i^{\text{rsp}}(t_0, T^{\text{rsp}}) \tag{9}$$

where $E_{\text{sum}}^{\text{rsp}}(t_0, T^{\text{rsp}})$ is the sum of all schedulable capacities in the scheduling period.

The charging and discharging strategy of electric vehicle cluster is shown in Fig. 2.

4 Comparison of Loads in Different Scenarios

In some areas, charging stations have not been popularized on a large scale. They only install ordinary charging piles when purchasing electric vehicles, and do not have fast-charging capabilities.

Therefore, a comparative analysis of two cases is set up. In Scenario 1, there is a charging station in the village that can feed power to the power grid. All electric vehicles are centralized and managed according to their willingness to participate in dispatching. They charge and discharge in an orderly manner. Except for the normal electricity price, no parking fee is charged. In scenario 2, there is no charging station built in the village, and the electric vehicle user's personal charging pile is used for charging, and it can only be charged and cannot be discharged to the power grid. Connected to the grid, there is no parking fee except for charging fees.

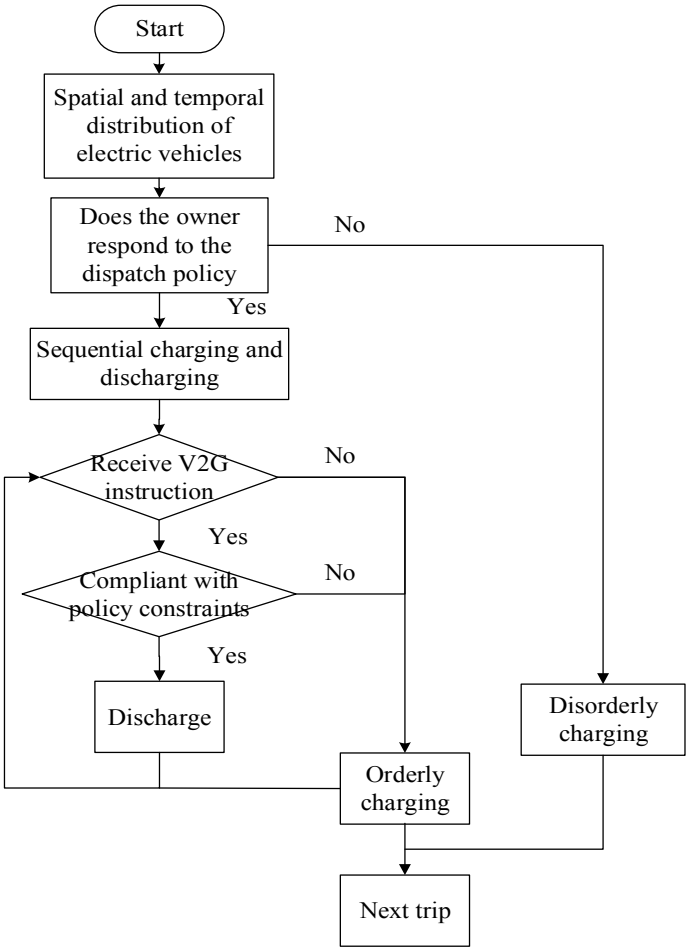

Fig. 2 Orderly charging and discharging strategy of EV cluster

It is assumed that there are 100 electric vehicles in the village, all of which are private vehicles, and 70% of the owners are willing to respond and participate in the scheduling strategy. The battery capacity is 30 kW h, and the cruising range is 250 km. It is fully charged in 1 h under fast charging and 5 h in slow charging.

Figure 3 shows the total load of the power grid under two scenarios. It can be seen that the peak-to-valley difference rate of scenario 1 is 23% lower than that of the disordered charging mode of scenario 2, and the overall curve is relatively smooth. In Scenario 2, the load fluctuation is more serious, which is easy to endanger the safe operation of the power grid. At the same time, it is not difficult to analyze that if there are too many electric vehicle users responding to the dispatch and excessive participation in the discharge, there will be a higher power consumption peak later.

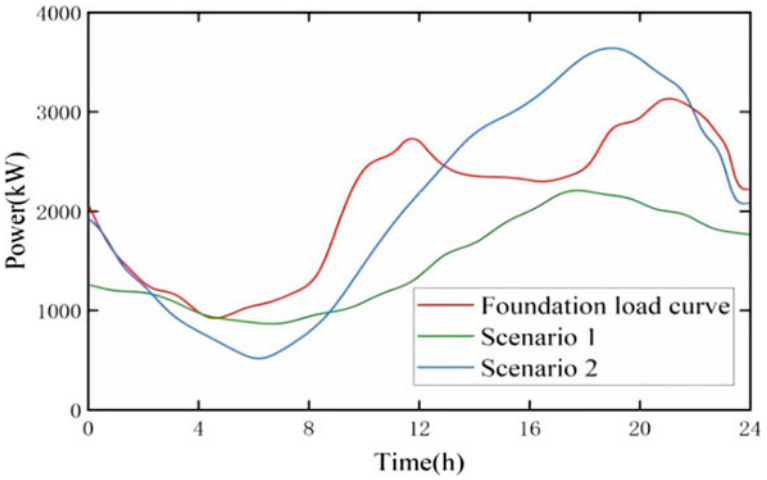

Fig. 3 Comparison of load curves under different conditions

5 Conclusion

This paper analyzes the use of residents' vehicles, as well as the time and space characteristics of vehicles, and establishes a space–time load model for electric vehicles. The convenience of user travel and the satisfaction of participating in scheduling are considered. A participation probability model is introduced, and an orderly charging and discharging strategy is proposed that considers the owner's response scheduling willingness and the spatial–temporal characteristics of electric vehicles. The influence of the user's response willingness on the probability of participating in scheduling is considered among the factors affecting the charging and discharging behavior of electric vehicles, which solves the problem that the vehicle owner's travel convenience is not fully considered in the traditional optimization strategy. From the results, the method in this paper is more suitable for the actual situation and has better scheduling effect.

The orderly charging strategy proposed in this paper has certain practical significance for guiding the orderly charging and discharging of electric vehicles and reducing the negative impact on the power grid. At present, the electric vehicle industry is still in its infancy, and the popularity of electric vehicles is not high. Regarding the user responsiveness, the paper makes a reasonable assumption, but the actual user's response to the dispatching strategy is also affected by the cost of electricity price, travel demand and related subsidy policies.

Acknowledgements This work was financially supported by the Science and Technology Project of State Grid Liaoning Electric Power Co., Ltd. "Research on Key Technologies of Rural Electric Vehicle Positioning and Distribution Network Dispatching Based on Beidou System" (Project No. 2022YF-48).

References

1. Weng G, Zhang Y, Qi J (2014) Evaluation for V2G available capacity of battery groups of electric vehicles as energy storage elements in microgrid. Trans China Electrotech Soc 29:36–45. https://doi.org/10.19595/j.cnki.1000-6753.tces.2014.08.005
2. Song Y, Lin S, Tang Z, He S, Lu Y, Mao T (2020) Temporal and spatial distribution probability modeling of electric vehicle charging load based on dynamic traffic flow. Automat Electr Power Syst 44:47–56. https://doi.org/10.1088/1742-6596/1346/1/012019
3. Wang H, Leng X, Pan Y, Bian J, Yu Z (2022) Orderly charging and discharging strategy of electric vehicle considering spatio-temporal characteristic and time cost. Electr Power Automat Equip 1–13. https://doi.org/10.1109/POWERCON.2014.6993936
4. Liu J, Jiang S, Wang Z, Zhang B, Wang C (2021) Dispatchable capability of eclectic vehicle clusters considering temporal-spatial characteristics. Electr Power Constr 42:83–92. https://doi.org/10.1109/ISGTEurope.2019.8905729
5. Xiao L, Xie Y, Hu H, Luo W, Zhu X, Liu X, Song T, Li M (2022) Two-level optimization scheduling strategy for EV's charging and discharging based on V2G. High Volt Appar 58:164–171. https://doi.org/10.1109/EI247390.2019.9061999
6. Xu L, Xu Y, Wang J, Fang J, Luo S (2014) Research of current-sharing control strategy of parallel PEMFC DC power supply system. Appl Mech Mater 694:173–178. https://doi.org/10.4028/www.scientific.net/AMM.694.173
7. Cheng S, Wei Z, Zhao Z, Wang Y, Zhao M (2021) Decentralized optimization of ordered charging and discharging for charging-storage station considering spatial-temporal access randomness of electric vehicles. Electr Power Automat Equip 41:28–35. https://doi.org/10.1002/er.6272
8. Duan X, Hu Z, Cui Y, Guo Z, Cao X, Ding N, Zhang Y (2018) Orderly charge discharge scheduling of electric vehicles on a long time scale. Power Grid Technol 42:4037–4044. https://doi.org/10.1109/AEEES48850.2020.9121412
9. Ma X, Li Y, Wang H, Wang C, Hong X (2017) Research on demand of charging piles based on stochastic simulation of EV trip chain. Trans China Electrotech Soc 32:190–202. https://doi.org/10.1049/iet-gtd.2015.0995
10. Zheng Y, Li F, Dong J, Luo J, Zhang M, Yang X (2022) Optimal dispatch strategy of spatio-temporal flexibility for electric vehicle charging and discharging in vehicle-road-grid mode. Automat Electr Power Syst 46:88–97. https://doi.org/10.4236/epe.2020.124B007
11. Hou H, Wang Y, Wu X, Chen Y, Huang L, Zhang R (2022) Charging and discharging scheduling strategy for electric vehicles considering psychological effect of mileage anxiety in long-time scale. High Volt Eng 1–12. https://doi.org/10.1109/ISGT-Asia.2015.7387005
12. Yang J, Li Q, Zhang Y, Yao L (2021) Peak shaving optimization modeling for demand response of multiple EV aggregators considering matching degree of power grid demand. Electr Power Automat Equip 41:125–134. https://doi.org/10.1007/s42835-019-00264-0

Mechatronics and Remote Sensing Signal Monitoring

Research on Reserve Capacity Optimization of Power System

Lingyi Li and Shuqiang Zhao

Abstract The rapid development of renewable energy increases the uncertainty in power system and requires the provision of more reserve capacity to ensure the safe operation of the system, and the study of reserve capacity optimization with comprehensive consideration of system operation reliability and economy is of great significance. Based on the analysis of conventional units participating in the provision of reserve in power system, an optimal configuration method of flexible load and energy storage participating in system reserve is proposed, and a source-load-storage multi-type reserve system is constructed to improve the system reserve capacity. The power system reserve optimization model is established and the system reserve capacity constraint based on the chance constraint is set. Finally, the calculation results prove the superiority of the reserve optimization model.

Keywords Reserve optimization · Multi-type reserve system · Flexible load · Chance constrained programming

1 Introduction

The uncertainty brought by the current large-scale renewable energy grid connection brings a great challenge to maintain the stability of power system operation [1], which requires the system to provide more reserve capacity on the original scheduling plan to cope with the uncertainty of renewable energy output and to achieve the balance of power system supply and demand. However, with the increase of the proportion of new energy grid connected, the reserve demand of the system is also rising, and the capacity of conventional units to provide reserve is slightly insufficient [2]. How to cope with the power system source-load dual-side uncertainty, make full use of other flexible resources in the system, and take into account system reliability and

L. Li (✉) · S. Zhao
Department of Electrical Engineering, North China Electric Power University, Baoding 071003, China
e-mail: yl101320@163.com

S. Yadav et al. (eds.), *Energy Power and Automation Engineering*, Lecture Notes in Electrical Engineering 1118, https://doi.org/10.1007/978-981-99-8878-5_62

economy to optimize the configuration of system reserve has become a problem worthy of our attention.

Many research results have been obtained on the optimization of the reserve capacity of new energy power systems. In the literature [3], considering the uncertainty of source load and the random failure of units, an optimization model of system spinning reserve is established. However, the penalty cost of abandoning new energy is not considered in its objective function, which cannot ensure that the system can absorb renewable energy as much as possible. In the literature [4], the collaborative optimization of multi-type power sources such as wind, fire, water, and gas in power system is considered to provide reserve for the system. However, there are few papers that comprehensively consider the source, load, and storage side reserve resources in the power system for coordinated optimization. Based on the existing problems, this paper proposes an optimal configuration method for flexible load and energy storage to participate in system reserve, constructs a source-load-storage multi-type reserve system, establishes a reserve optimization model for power system, and sets reserve chance constraints to balance system reliability and economy. Finally, the calculation results prove the superiority of the proposed reserve optimization model.

2 Source-Load-Storage Multi-type Reserve System

2.1 Flexible Load

According to the different response characteristics of load participating in system regulation, flexible load can be divided into three types: shiftable, transferable, and reducible, and the corresponding different constraints and compensation costs are as follows. Assuming that a dispatching period is 24 h, the unit dispatching period is 1 h, and the shiftable time range of shiftable load $P_{\mathrm{L\_shift}}$ is $\left[T_{\mathrm{s}-}, T_{\mathrm{s}+}\right]$ and the load duration is T_{D}. The optional shiftable start period T_{shift} of shiftable load is as follows:

$$T_{\mathrm{shift}} = \left[T_{\mathrm{s}-}, T_{\mathrm{s}+} - T_{\mathrm{D}} + 1\right] \tag{1}$$

The compensation cost F_{shift} after load shifting is:

$$F_{\mathrm{shift}} = C_{\mathrm{shift}} \sum_{\tau=1}^{T} P_{\tau}^{\mathrm{shift}} \tag{2}$$

where C_{shift} is the unit power compensation coefficient of shiftable load, P_{τ}^{shift} is the shiftable power in the period τ, and T is the total period in the dispatching period, $T = 24$ h. Let the transferable period of transferable load $P_{\mathrm{L\_tran}}$ be $\left[T_{\mathrm{tran}-}, T_{\mathrm{tran}+}\right]$, α represents the load transfer state in a certain period τ, and α is a 0–1 variable. If $\alpha_{\tau} = 1$ means that power transfer occurred in a certain period τ, its power transfer

constraint is:

$$\alpha_t P_{\min}^{\text{tran}} \le P_t^{\text{tran}} \le \alpha_t P_{\max}^{\text{tran}} \tag{3}$$

where $P_{\min}^{\text{tran}}$ is the minimum value of transferable load transfer power; $P_{\max}^{\text{tran}}$ is the maximum transfer power of transferable load.

The running time constraint of the transferable load is as follows:

$$\sum_{\tau=1}^{t+T_{\min}^{\text{tran}}-1} \alpha_t \ge T_{\min}^{\text{tran}}(\alpha_t - \alpha_{t-1}) \tag{4}$$

where $T_{\min}^{\text{tran}}$ is the minimum continuous running time of transferable load.

The compensation cost F_{tran} for calling transferable load is:

$$F_{\text{tran}} = C_{\text{tran}} \sum_{t=T_{\text{tran}-}}^{T_{\text{tran}+}} (\alpha_t P_t^{\text{tran}}) \tag{5}$$

where C_{tran} is the unit power compensation cost of transferable load.

The reduction state of reducible load $P_{\text{L\_cut}}$ in a certain period τ is represented by β, which is a variable of 0–1. The power of the reducible load $P_{\text{L\_cut}}$ in the period τ after participating in the system scheduling is:

$$P_\tau^{\text{cut}} = (1 - \gamma_\tau \beta_\tau) P_\tau^{\text{cut}'} \tag{6}$$

where γ_τ is the load reduction factor of period τ; $\gamma_\tau \in [0, 1]$; $P_\tau^{\text{cut}'}$ is the power of period τ before $P_{\text{L\_cut}}$ participates in system scheduling.

Considering the rationality of load reduction and customer satisfaction, it is necessary to restrict the number of load reduction and continuous reduction time.

$$T_{\min}^{\text{cut}} \le \sum_{\tau=t}^{t+T_{\text{cut}}-1} \beta_t \le T_{\max}^{\text{cut}}, \sum_{t=1}^{24} \beta_t \le N_{\max}^{\text{cut}} \tag{7}$$

$$F_{\text{cut}} = C_{\text{cut}} \sum_{t=1}^{T} \beta_t \left(P_t^{\text{cut}'} - P_t^{\text{cut}} \right) \tag{8}$$

where T_{cut} is the reduction time; $T_{\max}^{\text{cut}}$ and $T_{\min}^{\text{cut}}$ are, respectively, the maximum and minimum time for continuous load reduction; $N_{\max}^{\text{cut}}$ is the maximum number of cuts; C_{cut} is the unit power compensation cost for calling the reducible load.

2.2 Source-Load-Storage Multi-type Reserve System

Considering the three parts of power supply side, load side, and energy storage, the source-load-storage multi-type reserve system in new energy power system is constructed. On the power supply side of the power system, it is mainly considered that the conventional units provide positive and negative reserve for the system. On the load side, the reducible load in the flexible load is mainly considered to provide positive reserve for the system. The energy storage device can provide both positive and negative reserve to the system.

3 Reserve Optimization Model of Power System

3.1 Objective Function

Aiming at the lowest total cost of system operation and dispatching, a reserve optimization model of power system is established, and flexible load and energy storage are considered to participate in system optimal dispatching.

$$F = \min\left(C_{\text{op}} + C_R + C_{\text{wv}}\right) \tag{9}$$

where F represents the total cost of the system; C_{op} represents the operating cost of the system; C_R represents system reserve cost; C_{wv} is the penalty cost for the system to abandon new energy. The specific models of C_{op}, C_R, and C_{wv} are.

The system operation cost includes the cost of power generation and start-stop of thermal power units, the operation cost of energy storage system, and the compensation cost of calling flexible load.

$$\begin{cases} C_{\text{op}} = C_G + C_{\text{QT}} + C_{\text{ST}} + C_{\text{FL}} \\ C_G = \sum_{t=1}^{T} \sum_{i=1}^{N_g} \left(a_i P_{i,t}^2 + b_i P_{i,t} + c_i\right) \\ C_{\text{QT}} = \sum_{t=1}^{T} \sum_{i=1}^{N_G} \left(u_{i,t}\left(1 - u_{i,t-1}\right) S_i\right) \\ C_{\text{ST}} = \sum_{t=1}^{T} \alpha_b P_{\text{ch},t} - \beta_b P_{\text{dis},t} \\ C_{\text{FL}} = F_{\text{shift}} + F_{\text{tran}} + F_{\text{cut}} \end{cases} \tag{10}$$

where C_G is the power generation cost of thermal power units; a_i, b_i, and c_i are the unit output cost coefficient of thermal power unit i; $P_{i,t}$ is the output of thermal

power unit i at time t; C_{QT} is the start-up and shutdown cost of thermal power units; $u_{i,t}$ is the starting state of thermal power unit i at time t, which is a variable of 0–1; S_i is the start-up and shutdown cost of thermal power unit i; C_{ST} is the operating cost of the energy storage system; $P_{ch,t}$ and $P_{dis,t}$ are, respectively, the charging power and discharging power of the battery energy storage system at time t; α_b and β_b are the cost coefficients of charging and discharging of the energy storage system, respectively; C_{FL} represents the compensation cost to be paid for the system call flexible load. Based on the established source-load-storage multi-type reserve system, the reserve cost of the system is as follows:

$$\begin{cases} C_R = C_r + C_{\text{cutr}} + C_b \\ C_r = \sum_{t=1}^{T} \sum_{i=1}^{N_g} \left(e_i H_{i,t}^{+} + f_i H_{i,t}^{-} \right) \\ C_{\text{cutr}} = \sum_{t=1}^{T} f_{\text{cut}} R_{\text{cut},t} \\ C_b = \sum_{t=1}^{T} \left(w_b R_{\text{ch},t} - w_b R_{\text{dis},t} \right) \end{cases} \tag{11}$$

where C_r is the cost of providing reserve for the system by conventional units; e_i and f_i are the positive and negative reserve unit cost coefficients provided by conventional unit i, respectively; $H_{i,t}^{+}$ and $H_{i,t}^{-}$ are the positive and negative reserve provided by conventional unit i at time t; C_{cutr} represents reducible load reserve cost; $R_{\text{cut},t}$ is the positive reserve capacity provided to the system by reducible load at time t; f_{cut} is the unit compensation cost for calling the reducible load; C_b is the reserve cost of energy storage; $R_{\text{dis},t}$ and $R_{\text{ch},t}$ are the positive and negative reserve capacity provided by the energy storage system at time t, respectively; w_b and v_b represent the unit cost coefficients of the energy storage system providing positive and negative reserve capacity for the system, respectively.

The penalty cost of abandoning new energy is:

$$C_{\text{wv}} = \gamma_w \sum_{i=1}^{N_w} \Delta P_{i,t}^{w} + \gamma_v \sum_{i=1}^{N_v} \Delta P_{i,t}^{v} \tag{12}$$

where γ_w and γ_v are the penalty coefficients of unit power for wind abandonment and photovoltaic abandonment, respectively.

3.2 Constraint Conditions

(1) Constraints of thermal power units

$$u_{i.t} P_{i.\min} \le P_{i.t} \le u_{i.t} P_{i.\max} \tag{13}$$

$$\begin{cases} (u_{i.t-1} - u_{i.t})\left(T_{\text{on},i,t-1} - T_{\text{on},i}\right) \ge 0 \\ (u_{i.t} - u_{i.t-1})\left(T_{\text{off},i,t-1} - T_{\text{off},i}\right) \ge 0 \end{cases} \tag{14}$$

$$-P_{i.d} \le P_{i.t} - P_{i.t-1} \le P_{i.u} \tag{15}$$

where $T_{\text{on},i,t-1}$ and $T_{\text{off},i,t-1}$, respectively, refer to the continuous operation and shutdown time of thermal power units at time $t-1$; $T_{\text{on},i}$ and $T_{\text{off},i}$ are the minimum allowable continuous operation and shutdown time of thermal power units, respectively; $P_{i.u}$ and $P_{i.d}$ are the maximum upward and downward climbing power of thermal power units, respectively.

(2) Energy storage system constraint

$$\text{SOC}_{\min} \le \text{SOC}_t \le \text{SOC}_{\max} \tag{16}$$

$$\text{SOC}_0 = \text{SOC}_T \tag{17}$$

where $\text{SOC}_{\max}$ and $\text{SOC}_{\min}$ are the upper and lower limits of the state of charge of the battery of the energy storage system; SOC_0 and SOC_T are the initial state of charge and the end state of charge of the battery of the energy storage system in one cycle, respectively.

(3) Reducible load constraint

$$0 \le P_t^{\text{cut}} + R_{\text{cut},t} \le P_t^{\text{cut}'} \tag{18}$$

where $P_t^{\text{cut}'}$ represents the upper limit of load reduction.

(4) System reserve capacity constraint

$$\begin{cases} \Pr\left(R_{\text{up}.t} + \varepsilon_t \ge R_{\text{res.up}.t}\right) \ge \beta_1 \\ \Pr(R_{down.t} - \varepsilon_t \ge R_{\text{res}.down.t}) \ge \beta_2 \\ \varepsilon_t = \sum_{i=1}^{N_w} \left(\varepsilon_{i,t}^{w}\right) + \sum_{i=1}^{N_{\text{v}}} \left(\varepsilon_{i,t}^{v}\right) - \varepsilon_{\text{load},t} \\ R_{\text{up}.t} = \sum_{i=1}^{N_g} H_{i,t}^{+} + R_{\text{cut},t} - R_{\text{dis},t} \\ R_{down.t} = \sum_{i=1}^{N_g} H_{i,t}^{-} + R_{\text{ch},t} \end{cases} \tag{19}$$

where $R_{\text{up}.t}$ and $R_{down.t}$ are the sum of positive reserve and negative reserve capacities that can be provided by the system at time t; ε_t is a random variable generated by new energy and load forecasting error of the system at time t; $R_{\text{res.up}.t}$ and $R_{\text{res.down}.t}$ are the positive and negative reserve capacity required by the system; β_1 and β_2 are given confidence levels.

3.3 Solution of Model

Based on the sampling method, the reserve chance constraint condition is transformed into a mixed integer constraint condition [5], as follows:

$$\begin{cases} R_{\text{up}.t} + \varepsilon_t\left(\text{floor}\left(N_{\text{sample}}(1-\beta_1)\right)\right) - R_{\text{res.up}.t} \geq 0 \\ R_{down.t} - \varepsilon_t\left(\text{ceil}\left(N_{\text{sample}}\beta_2\right)\right) - R_{\text{res.down}.t} \geq 0 \\ \varepsilon_t = \text{sort}\left(\left[\varepsilon_t^1, \varepsilon_t^2, \cdots, \varepsilon_t^{N_{\text{sample}}}\right]\right) \end{cases} \tag{20}$$

where N_{sample} represents the number of samples; sort(*) is an ascending order function.

4 Example Analysis

The example includes a wind farm, a photovoltaic power station, an energy storage unit, and five thermal power units. Setting the confidence level β_1=β_2=0.96 in the reserve chance constraint, CPLEX is called to solve the optimization problem. The following three scheduling models are selected for comparative analysis: Model 1: Set the reserve demand of the system to 10% of the load capacity, and reserve 25% of the predicted power capacity of wind power and photovoltaic to cope with the uncertainty in the power system. Only the conventional units are considered to provide reserve; Model 2: The reserve constraint is chance constraint, and only the conventional units are considered to provide reserve; Model 3: The reserve constraint is chance constraint, and the source-load-storage multi-type reserve system is adopted in the selection of reserve types.

The scheduling results of the above three models are given in Table 1, the actual output of wind power and photovoltaic power generation is shown in Fig. 1, and the reserve optimization result in Model 3 is shown in Fig. 2.

Table 1 Optimal scheduling results in different models

Model	Total cost/$	Operating cost/$	Reserve cost/$
1	839,062.05	580,103.67	244,877.34
2	803,246.75	573,150.29	222,510.82
3	790,533.91	552,228.58	237,771.03

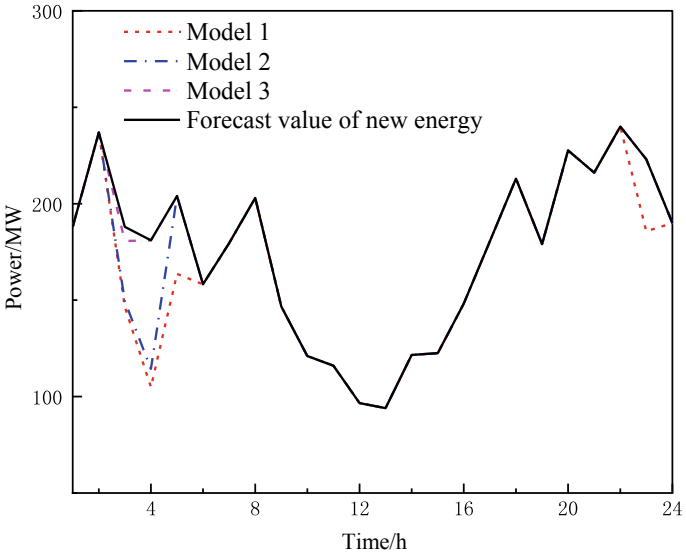

Fig. 1 New energy output

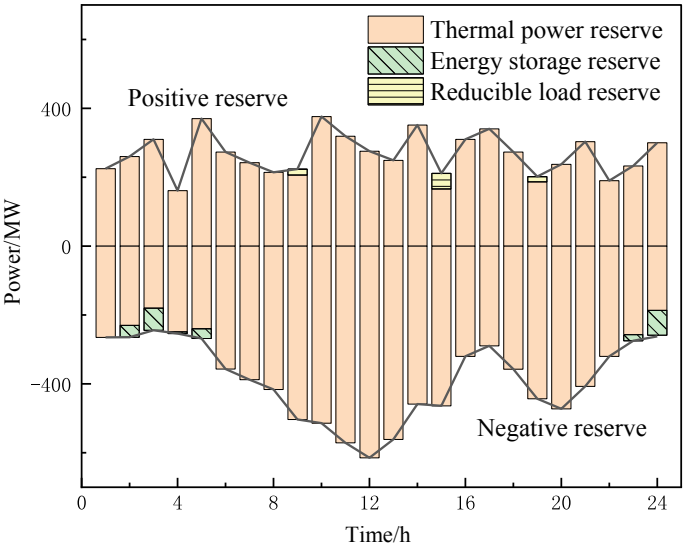

Fig. 2 Reserve optimization result in Model 3

It can be seen from Table 1 that Model 3 proposed in this paper has the lowest total cost and the least amount of wind and photovoltaic abandonment, which is the optimal scheduling scheme. Compared with Model 1 and Model 2, Model 3 has the best flexibility and economy under the premise of ensuring reliable operation of the system, and realizes multi-type energy collaborative reserve optimization.

5 Conclusion

Aiming at the problem of reserve optimization in new energy power system, this paper proposes an optimal configuration method of flexible load and energy storage participating in system reserve, constructs a source-load-storage multi-type reserve system, and establishes a power system reserve optimization model. The comparative analysis results of an example prove that the proposed model can reasonably optimize the reserve capacity in each period, increase the consumption level of new energy and maximize the comprehensive benefits of the power system under the premise of ensuring reliable operation of the power system.

References

1. Wu J, Xue Y, Shu Y et al (2019) Adequacy optimization of power system with large-scale renewable energy access (1) Optimization of spinning reserve. Power Syst Autom 43(8):101–109
2. Nikolaidis P, Poullikkas A (2021) A novel cluster-based spinning reserve dynamic model for wind and PV power reinforcement. Energy 234:121270
3. Zhong H, Lei C (2020) Spinning reserve capacity optimization considering source charge uncertainty of microgrid. Smart Power 48(9):37–42
4. Liang Z, Chen H, Lei J et al (2018) Multi-source coordinated spinning reserve optimization of wind-fire-water-gas-nuclear-pumped storage considering wind power uncertainty. Power Syst Technol 42(7):2111–2119, 2121–2123
5. Zhao S, Wu Y, Li Z et al (2022) Analysis of power system peaking capacity and economy considering the uncertainty of wind and solar output. Power Syst Technol 46(5):1752–1761

Circular Arc Coil Coupling Device for Wireless Charging System of Autonomous Underwater Vehicle

Bin Cai, Menghong Yu, and Haozhou Lu

Abstract In order to improve the poor fault tolerance ability of coupling device of wireless charging system for autonomous underwater vehicles, a magnetic coupling device with strong fault tolerance ability, low internal electromagnetic interference, and good symmetry is proposed in this paper. Firstly, the magnetic field distribution of the proposed magnetic coupling device is studied by ANSYS Maxwell finite element analysis software. Then, using the method of parameter modeling, the coupling coefficient change of the magnetic coupling device under the dislocation state is obtained. Finally, the circuit structure of the wireless charging system using this coupling device is analyzed and calculated.

Keywords Autonomous underwater vehicles · Wireless charging system · Magnetic coupling structure · Coupling coefficient

1 Introduction

Autonomous underwater vehicles (AUVs) are important equipment for marine scientific research, exploration of marine resources, and protection of marine homeland security. They can replace humans in hazardous work in complex aquatic environments [1]. However, AUVs also have obvious and even fatal disadvantages: the onboard battery capacity of AUVs is limited [2]. In the recent years, wireless charging technology has developed rapidly. It has become a research hotspot due to its characteristics of high safety, low operational difficulty, no electrical contact, no underwater leakage, and good isolation, and is also one of the ways to solve the problem of battery energy supply [3, 4].

Although the application of wireless charging technology in underwater field is more difficult than that on land, the underwater wireless charging technology has made some achievements, among which wireless charging technology has been applied in AUV, and electromagnetic wireless charging technology is the most

B. Cai · M. Yu (✉) · H. Lu
School of Automation, Jiangsu University of Science and Technology, Zhenjiang, Jiangsu, China
e-mail: ymhzj2691@163.com

S. Yadav et al. (eds.), *Energy Power and Automation Engineering*, Lecture Notes in Electrical Engineering 1118, https://doi.org/10.1007/978-981-99-8878-5_63

common application in AUV wireless charging [5, 6]. The key problems faced by this technology are as follows: Design of magnetic coupling structure and eddy current loss analysis. In the field of coupling device design, Professor Cai et al. [2, 7, 8] have done a lot of research on the coupling device of arc coil, Yan et al. [9] have done research on the curling coupling device, etc. In the eddy current loss analysis, Professor Zhang et al. [10, 11] analyzed the influence of magnetic field frequency on eddy current loss and obtained the approximate formula of eddy current loss calculation.

This paper has studied the design of the AUV coupling device and the reactive power loss in the circuit and proposed a magnetic coupling device with an arc axial coil structure.

2 Magnetic Coupling Device Design

2.1 Coil Structure Design

The magnetic coupling device is a bridge between the underwater charging platform and the AUV, and it is also the core component of the entire underwater wireless charging system, affecting the power transmission efficiency and power transmission of the AUV wireless charging system. A magnetic coupling device is a device that transmits electrical energy consisting of a transmitting coil and a receiving coil, coupled with magnetic conductive materials. It utilizes the principle of electromagnetic induction to achieve the transmission of electrical energy. Therefore, designing a magnetic coupling device with excellent performance needs to understand the factors that affect the coil coupling coefficient at the transmitter and receiver ends of the magnetic coupling device.

Considering the limited internal space of the AUV and the inability to change the shape of the AUV, it was decided to use a circular arc "rectangular" coil as the receiving coil, which can perfectly fit the inner wall of the AUV, reduce the spacing between the transmitting coil and the receiving coil, and improve the coupling strength between the coils. Considering that the AUV is prone to docking misalignment when operating in an underwater environment, it is decided to design a symmetric transmitting coil structure with respect to the receiving coil. Therefore, this paper proposes a highly symmetrical coil structure with circular arc coils uniformly distributed around the circumference, which includes 12 circular arc "rectangular" transmitting coils and 12 circular arc "rectangular" receiving coils. The receiving coils and transmitting coils correspond to each other one by one. The model is shown in Fig. 1; at the transmitting end, there are 12 circular arc shaped "rectangular" coils installed on the transmitting platform (or rack); at the receiving end, there are 12 circular arc shaped "rectangular" coils installed inside the AUV against the inner shell wall of the AUV, or these coils are embedded in the AUV shell.

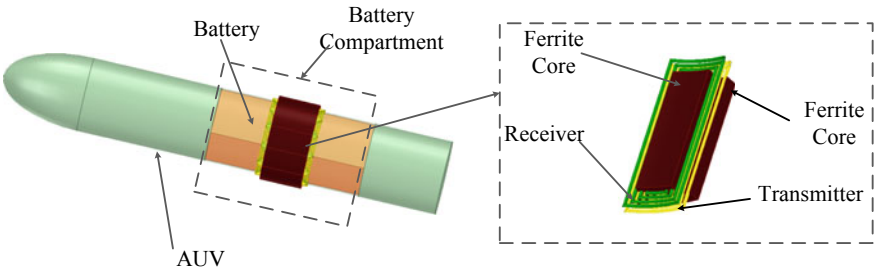

Fig. 1 Circular arc coil structure

2.2 Magnetic Field Analysis of Coil Structure

The key in the design of magnetic coupling device is the magnetic flux pattern design. In order to design a coil structure with large coupling coefficient and strong anti-interference ability, the magnetic flux between coils can be qualitatively analyzed by analyzing the magnetic field between coils. Then, the coil structure is adjusted according to the magnetic field distribution to maximize the coupling coefficient between coils and improve the symmetry of the coil structure. The ANSYS Maxwell finite element analysis tool creates a coil structure model as shown in Fig. 2, which analyzes the magnetic field distribution of the model, as shown in Fig. 3.

From Fig. 3, it can be seen that the magnetic field of the coupling device in this design is mainly concentrated between the transmitter's magnetic conductive material and the receiver's magnetic conductive material, and the magnetic field does not diffuse inside and outside the AUV; at the same time, it can be seen that the magnetic field of the designed magnetic coupling device has symmetry and can well resist rolling misalignment. The conclusion can be drawn as follows: The magnetic coupling device has a high degree of symmetry, has almost no electromagnetic interference inside the AUV, and the rolling misalignment has little impact on the coupling structure.

Fig. 2 Simulation model of coil structure

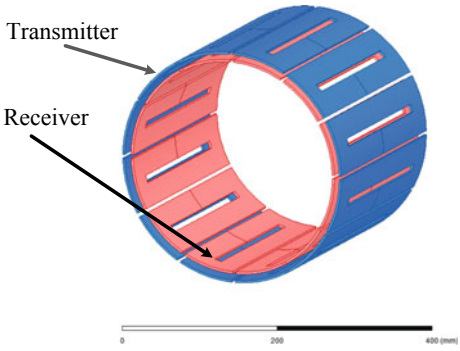

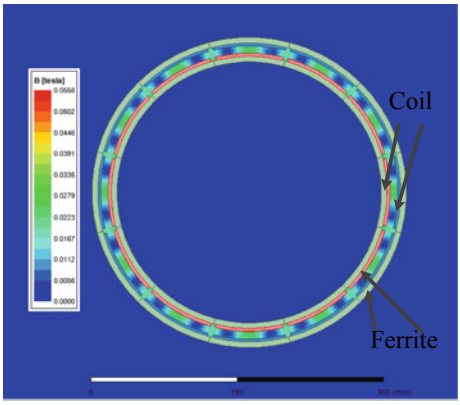

Fig. 3 Magnetic field distribution

2.3 *Misalignment Analysis of Magnetic Coupling Devices*

In order to verify the anti-interference ability of the magnetic coupling device designed in this article, a parameterized model is established using the finite element analysis software ANSYS Maxwell. The coupling coefficient of the rolling dislocation and axial dislocation of the coupling device is analyzed using the parameter scanning method. The anti-interference ability of the coupling device is determined by the fluctuation of the coupling coefficient. The range of the rolling dislocation is − 10° to 10°, and the range of the axial dislocation is − 30 to 30 mm. The simulation results are shown in Fig. 4.

From the analysis of the above figure, it can be seen that within the rolling misalignment range, the coupling coefficient is greater than 0.66, and the coupling coefficient wave is small; within the range of axial misalignment, the coupling coefficient is greater than 0.81, and the fluctuation of the coupling coefficient is very small. According to the simulation results, it can be known that the coupling device model has good coupling effect and strong anti-interference ability.

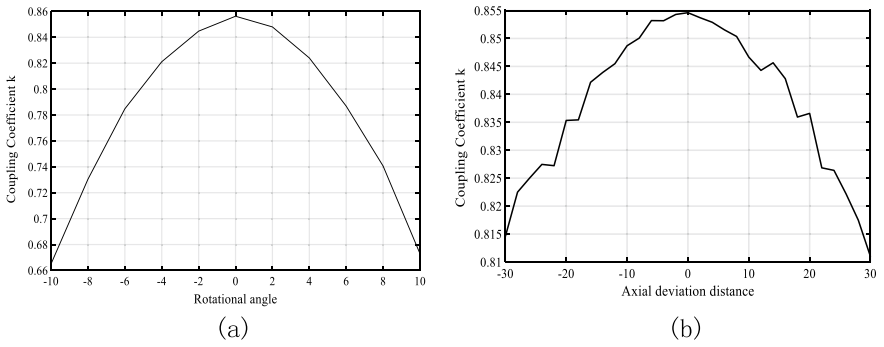

Fig. 4 Change of coupling coefficient under dislocation state

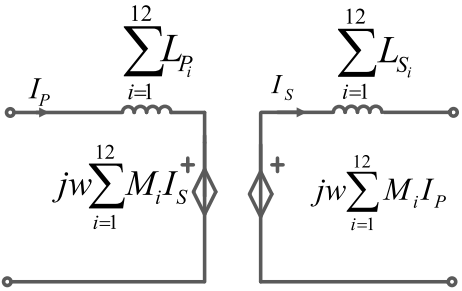

Fig. 5 Inductance equivalent circuit

2.4 Circuit Topology of Coil Structure

The magnetic coupling device designed in this paper has 12 transmitting coils and 12 receiving coils. In circuit analysis, these coils need to be equivalent to a coil to calculate other parameters in the circuit and design a compensation network. The 12 transmitting coils are connected in series for power supply, which can be equivalent to the circuit structure shown in Fig. 5.

Regardless of the inductance internal resistance and mutual inductance in the circuit, the transmitter and receiver inductances of the coil structure can be equivalent calculated as:

$$L_P = \sum_{i=1}^{12} L_{P_i}, \quad L_S = \sum_{i=1}^{12} L_{S_i} \tag{1}$$

3 Circuit Design

3.1 Circuit Structure of Wireless Charging System

In order to verify the performance of the magnetic coupling device designed in this article during the AUV wireless charging process, a corresponding *S*–*S* compensation network circuit structure has been designed for it, as shown in Fig. 6. The circuit structure can be divided into modules: DC power supply module, inverter circuit module, compensation circuit module, magnetic coupling device, rectifier and filter circuit module, and load module. The input voltage of the DC power module is U_{oc}. The inverter circuit module adopts the *H*-bridge inverter mode, and its output voltage and current are U_{IN} and I_{IN}. The output voltage and current of the compensation network are U_{out} and I_S. The rectifier circuit module uses an *H*-bridge rectifier method.

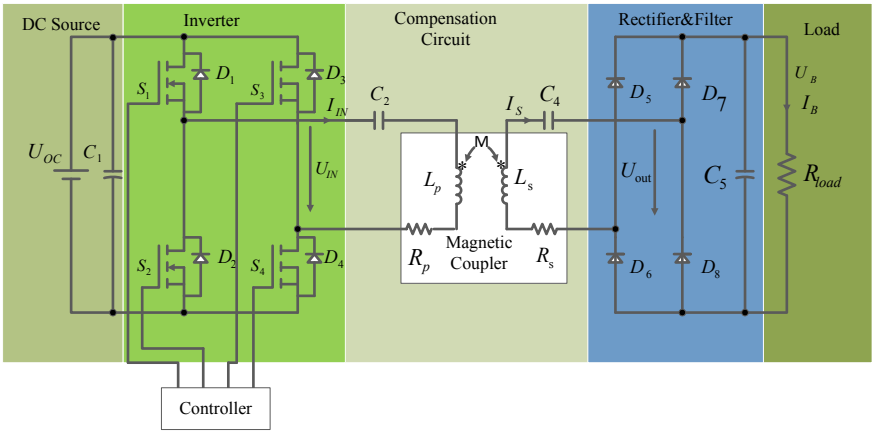

Fig. 6 Wireless charging technology circuit structure

3.2 Circuit Analysis

In order to accurately design circuit related modules, it is necessary to simplify the circuit shown in Fig. 6 and obtain the equivalent circuit structure shown in Fig. 7, in which Z_{IN}, Z_r, and Z_s are included, respectively, which represents the output impedance of the inverter, the reflected impedance of the receiving coil of the magnetic coupling device in the transmitting coil, and the input impedance of the receiver.

Obviously, there are:

$$U_{\mathrm{IN}} = \frac{2\sqrt{2}}{\pi} U_{\mathrm{oc}}, \quad U_B = \frac{2\sqrt{2}}{\pi} U_{\mathrm{out}} \tag{2}$$

Assume:

$$Z_r = R_r + X_r = \frac{(wM)^2}{Z_S}, \quad R_{\mathrm{eq}} = aR_s \tag{3}$$

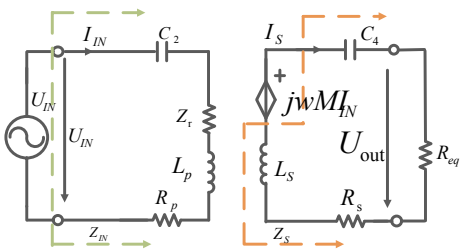

Fig. 7 Equivalent circuit structure of wireless charging system

Ignoring the parasitic resistance of the coil of the magnetic coupling device, there is:

$$Z_{\mathrm{IN}} = jwL_p + \frac{1}{jwC_2} + Z_r \tag{4}$$

$$Z_S = jwL_S + \frac{1}{jwC_4} + R_{\mathrm{eq}} \tag{5}$$

In order to improve the efficiency of the wireless charging system, the coupling strength of the magnetic coupling device can be enhanced, that is, the coupling coefficient of the magnetic coupling device can be improved, and the transmission efficiency of the system can be improved by reducing the reactive power loss in the circuit. According to the principle of maximizing system efficiency, the imaginary parts of Z_{IN} and Z_S are 0, then:

$$|Z_S| = R_{\mathrm{eq}}, \quad Z_r = \frac{(wM)^2}{R_{\mathrm{eq}}}, \quad wL_S = \frac{1}{wC_4}, \quad wL_p = \frac{1}{wC_2} \tag{6}$$

4 Conclusion

This paper proposes a coupling device of a 12 arc rectangular transmitting coil and a 12 arc rectangular receiving coil and conducts theoretical modeling and parameter analysis of the device. The magnetic field distribution of the coupling device and the coupling coefficient under the misaligned state is obtained. The magnetic field distribution of the coupling device between the transmitting end magnetic conductive material and the receiving end magnetic conductive material does not cause interference within the AUV; in the dislocation state, the fluctuation range of the coupling coefficient in the rolling dislocation state is less than 0.2, and the fluctuation range of the axial dislocation is less than 0.04.

References

1. Teeneti CR, Truscott TT, Beal DN, Pantic Z (2021) Review of wireless charging systems for autonomous underwater vehicles. IEEE J Ocean Eng 46(1):68–87. https://doi.org/10.1109/JOE.2019.2953015
2. Cai C, Wu S, Zhang Z, Jiang L, Yang S (2021) Development of a fit-to-surface and lightweight magnetic coupler for autonomous underwater vehicle wireless charging systems. IEEE Trans Power Electron 36(9):9927–9940. https://doi.org/10.1109/TPEL.2021.3064411
3. Kan T, Mai R, Mercier PP, Mi CC (2018) Design and analysis of a three-phase wireless charging system for lightweight autonomous underwater vehicles. IEEE Trans Power Electron 33(8):6622–6632. https://doi.org/10.1109/TPEL.2017.2757015

4. Yan Z, Song B, Zhang Y, Zhang K, Mao Z, Hu Y (2019) A rotation-free wireless power transfer system with stable output power and efficiency for autonomous underwater vehicles. IEEE Trans Power Electron 34(5):4005–4008. https://doi.org/10.1109/TPEL.2018.2871316
5. Zeng Y et al (2022) Misalignment insensitive wireless power transfer system using a hybrid transmitter for autonomous underwater vehicles. IEEE Trans Ind Appl 58(1):1298–1306. https://doi.org/10.1109/TIA.2021.3110496
6. Zhou J, Yao P, Chen Y, Guo K, Hu S, Sun H (2021) Design considerations for a self-latching coupling structure of inductive power transfer for autonomous underwater vehicle. IEEE Trans Ind Appl 57(1):580–587. https://doi.org/10.1109/TIA.2020.3029020
7. Cai C, Zhang Y, Wu S, Liu J, Zhang Z, Jiang L (2020) A circumferential coupled dipole-coil magnetic coupler for autonomous underwater vehicles wireless charging applications. IEEE Access 8:65432–65442. https://doi.org/10.1109/ACCESS.2020.2984530
8. Wu S, Cai C, Wang A, Qin Z, Yang S (2023) Design and implementation of a uniform power and stable efficiency wireless charging system for autonomous underwater vehicles. IEEE Trans Industr Electron 70(6):5674–5684. https://doi.org/10.1109/TIE.2022.3198242
9. Yan Z, Zhang Y, Zhang K, Song B, Mi C (2019) Underwater wireless power transfer system with a curly coil structure for AUVs. IET Power Electron 12(10):2559–2565. https://doi.org/10.1049/iet-pel.2018.6090
10. Zhang K, Ma Y, Yan Z, Di Z, Song B, Hu AP (2020) Eddy current loss and detuning effect of seawater on wireless power transfer. IEEE J Emerg Sel Top Power Electron 8(1):909–917. https://doi.org/10.1109/JESTPE.2018.2888521
11. Zhang K, Zhang X, Zhu Z, Yan Z, Song B, Mi CC (2019) A new coil structure to reduce eddy current loss of WPT systems for underwater vehicles. IEEE Trans Veh Technol 68(1):245–253. https://doi.org/10.1109/TVT.2018.2883473

The Fault Location of Distribution Network Based on Narrowband Communication Technology

Fei Deng, Dong Li, Jing Yu, Yujiao Wang, Wenmin Lu, and Yu Huang

Abstract In this paper, we propose a fault location of distribution network based on narrowband communication technology, which belong to the field fault monitoring and location of distribution network. The whole system consists of master station server, light source module, EDFA optical amplifier module, optical wavelength division multiplexer, optical wave guide magnetic field sensor, photoelectric conversion module, electrical signal filtering and amplification module, analog digital conversion module, electrical signal processing module, narrowband communication module and solar cell module. The optical wave guide magnetic field sensor is installed on the cable, and the other parts are installed on the pole. The fault location system adopts narrowband wireless communication technology for data transmission, which reduces the system cost and power consumption. At the same time, the measured data and historical data are used to obtain the fault point, which improves the accuracy of fault location.

Keywords Narrow band communication · Fault location · Distribution network · Magnetic field

F. Deng · D. Li · J. Yu (✉) · Y. Wang · W. Lu · Y. Huang
College of Information Engineering, Kunming University, Kunming 650214, China
e-mail: 874302545@qq.com

Key Laboratory of Data Governance and Intelligent Decision, Universities of Yunnan, Kunming 650214, China

S. Yadav et al. (eds.), *Energy Power and Automation Engineering*, Lecture Notes in Electrical Engineering 1118, https://doi.org/10.1007/978-981-99-8878-5_64

1 Introduction

With the improvement of people's living standards, the requirements for power supply quality and reliability are also increasing, and they cannot even tolerate the instantaneous interruption of power supply. However, now most of the 10 kV to 35 kV distribution network lines in China are operated in the way that the neutral point is ungrounded. Under the condition of this operation mode, the probability of single-phase grounding in the distribution network is very high. In addition, the diversity and complexity of single-phase grounding faults are extremely difficult to find. Therefore, it is valued that we develop a fault location system to accurately determine the location information of the fault point, which can rapidly response to fault problems and ensure the stable and reliable operation. It is noted that most of the existing distribution network fault location systems use GPRS for communication, which own the characteristics of low utilization, high power consumption, poor flexibility and high cost. It is necessary to use the Internet to solve the problem of distribution network fault [1]. At the same time, it is an effective method for scientific research, combining the data monitored by the system with the data generated by the actual production environment [2–5].

Researchers make a lot of work on fault location of distribution network through monitoring current, monitoring voltage, using neural networks and bionic algorithms. For current monitoring, literature [6] extracts the change characteristics of full current transient quantity with the data of voltage and current. For voltage monitoring [7], this literature uses the correlation between voltage and fault to realize fault discrimination and location. For neural network [8], the literature uses probabilistic neural network to design the model of fault section location of distribution network. The accurate location of fault section can be completed by the analysis of fault transient zero sequence current; For bionic algorithms, there are many pigeon colony algorithms such as ant colony algorithm, whale algorithm and manta ray foraging algorithm [9–13]. These algorithms firstly construct a switching function between fault information and line fault statement, and then use the principle of bionic algorithm to find the global optimal solution. The paper [14] firstly established the fault state expression, which can calculate the theoretical value of fault distance by using multi terminal traveling wave time difference and double terminal traveling wave difference, and substitute it into the expression for obtaining the exact location of the fault. Reference [15] firstly establishes the equivalent model of fault current, then creates the adjacency matrix to monitor the fault, and finds the fault location through comparison. However, all of the above methods have the disadvantages of low utilization rate, high power consumption, poor flexibility and high cost of communication technology.

The technology of narrowband communication is used widely in many fields [16–19], which can reduce the system cost and power consumption. So, for solving the above problems, this technology is used to realize information transmission between sensors and master station server for the final fault location, which depends on converting the magnetic field information of the fault location into digital information.

2 Fault Location System of Distribution Network Based on Narrowband Communication Technology

Narrowband communication technology is mainly used by optical waveguide magnetic field sensor. If the magnetic field at this point changes and a deformed magnetic field is generated, the optical waveguide magnetic field sensor will transmit the discovery to the main server through a series of modules, and then workers will accurately locate the fault point according to the transmitted information, which can greatly save time and improve efficiency. The detailed structure of the system is as follows.

2.1 Components of the System

The distribution network fault detection system based on narrowband communication consists of two parts. The first part is optical waveguide magnetic field supply and the second is named as magnetic field information transmission detection, as shown in Fig. 1.

Firstly, the optical waveguide magnetic field supply is composed of light source module, EDFA optical amplifier module and optical wavelength division multiplexer. Each element is connected by the optical fiber. The structure and function of the entire optical waveguide magnetic field supply are shown in Fig. 2.

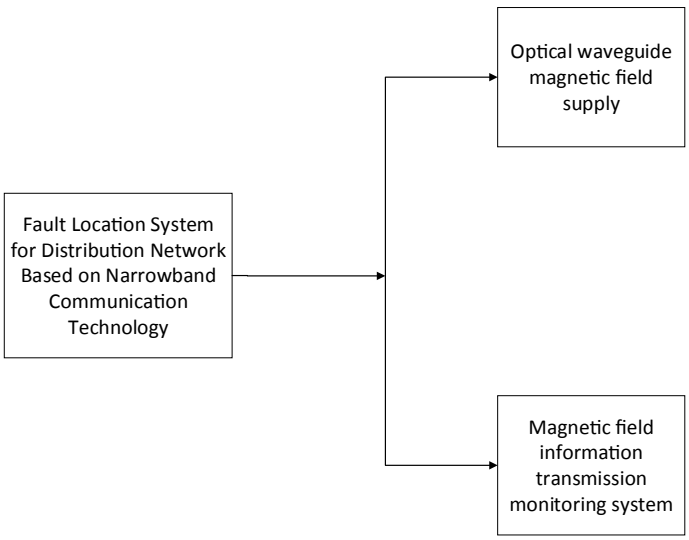

Fig. 1 Two major components of the system

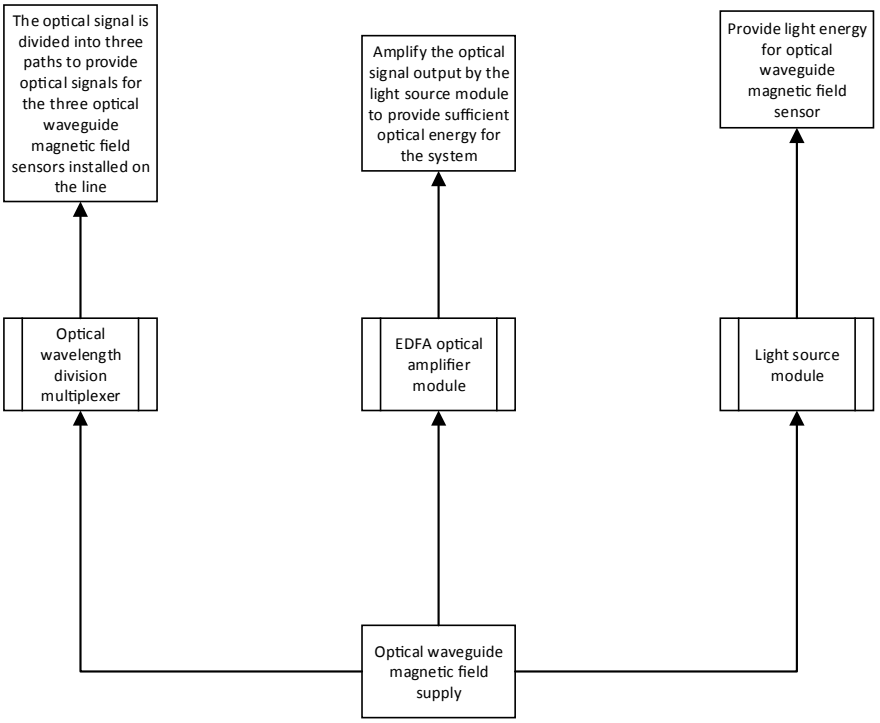

Fig. 2 Structure of optical waveguide magnetic field supply

Secondly, the magnetic field information transmission detection system is mainly composed by optical waveguide magnetic field sensor, photoelectric conversion module, electrical signal filtering and amplification module, analog digital conversion module, electrical signal processing module, narrowband communication module, main server and solar cell module. Each part is connected through electrical signal transmission line, and narrowband communication module and main server are connected through wireless signal. The function of each part is given in Table 1.

2.2 Structure of Whole System

The structure diagram of the whole system is shown in Fig. 3. In Fig. 3, No. 1 is named as cable, No. 2 as optical waveguide magnetic field sensor, No. 3 as light source module, No. 4 as EDFA optical amplifier, No. 5 as optical wavelength division multiplexer, No. 6 as photoelectric conversion module, No. 7 as electrical signal filtering and amplification module, No. 8 as analog digital conversion module, No. 9 as electrical signal processing module, No. 10 as narrowband communication module, No. 11 as solar cell module and No. 12 as master station server.

Table 1 Magnetic field information transmission detection system

Module	Module description
Optical waveguide magnetic field sensor	Used to amplify the optical signal output by the light source module to provide sufficient optical energy for the system
Photoelectric conversion module	Used to convert the optical signal carrying magnetic field information output by the optical waveguide magnetic field sensor into an electrical signal
Electrical signal filtering and amplification module	Used to filter and amplify the output electrical signal of the photoelectric conversion module
Analog-to-digital conversion module	Used to convert the analog signal output by the filtering and amplification module into a digital signal
Electrical signal processing module	Used to process digital electrical signals to obtain magnetic field information around the current line
Narrowband communication module	Used to transmit the currently collected magnetic field information to the master station server through wireless signal transmission
EDFA optical amplifier module	Used to amplify the optical signal output by the light source module to provide sufficient optical energy for the system
Solar module	Used to provide power for light source modules, EDFA optical amplifier modules, photoelectric conversion modules, electrical signal processing modules and narrowband communication modules
Master station server	It is used for information fusion analysis between the received magnetic field information and the historical data stored in the master station server to ultimately determine whether the current magnetic field is distorted, that is, whether there is a fault, and further determine the location of the current fault point based on the installation location of the current sensor

As shown in Fig. 3, the fault location system of distribution network based on narrowband communication technology is included by module 3, module 4, module 5, module 2, module 6, module 7, module 8, module 9, module 10, module 11 and module 12. The module 2 is installed on the cable 1, and the module 3, module 4, module 5, module 6 and module 7, module 8, module 9, module 10 and module 11 are installed on the pole. The module 6, module 7, module 8, module 9 and module 10 are sequentially connected together through the electrical signal transmission line. The module 3, module 4, module 5, sensor 2 and module 6 are connected together through optical fibers in turn.

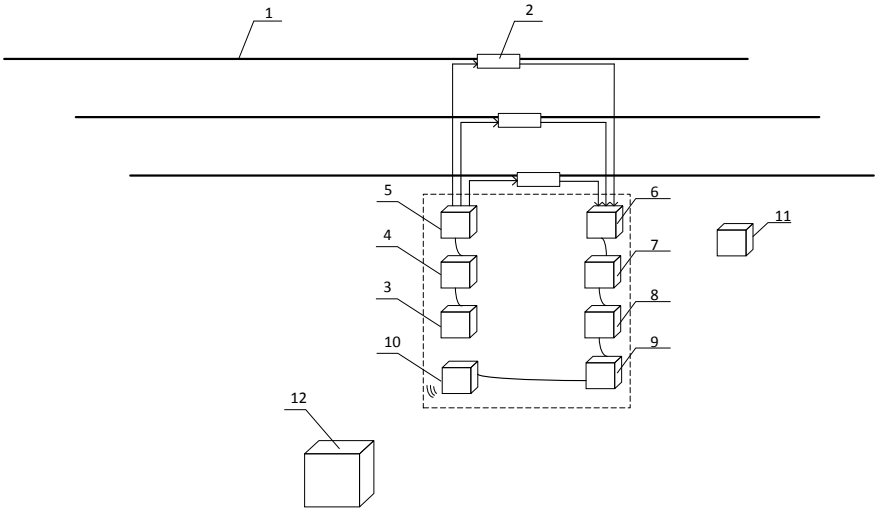

Fig. 3 Structure of whole system

3 Principle of Fault Location

When the distribution network works normally, the current through the power grid line is not be changed dramatically, that is to say, the magnetic field around the line has no obvious change. When the distribution network breaks downs, the current near the fault point will be changed clearly, which the magnetic field around the line will be distorted. The optical waveguide sensor can collect the data of distorted magnetic field around the fault point, obtain the distorted magnetic field information transmitted by the electrical signal, which is transmitted to the main server with wireless signal through the narrowband communication module. The obtained magnetic field information and the stored historical information are combined in main server for finding distorted the magnetic point, which this point is determined as the fault point.

Take a substation as an example, as shown in Fig. 4, where P represents the power supply, No. 1, 2, 3 and 4 represent the optical waveguide sensors installed on the distribution circuit, $f1$ and $f2$ represent the fault points and the arrowheads represent the current direction of the entire circuit respectively.

The specific location of the fault point can be found by monitoring the magnetic field information. The whole algorithm likes this. Firstly, denote $f(i) = \text{Hi}$ as the magnetic field strength information function of the i-th sensor. Secondly, set $g(i)=f(i) - f(i+1)$ represents the magnetic field strength information function in the i-th region. Then, set the threshold value of the magnetic field strength of the sensor as L. If the

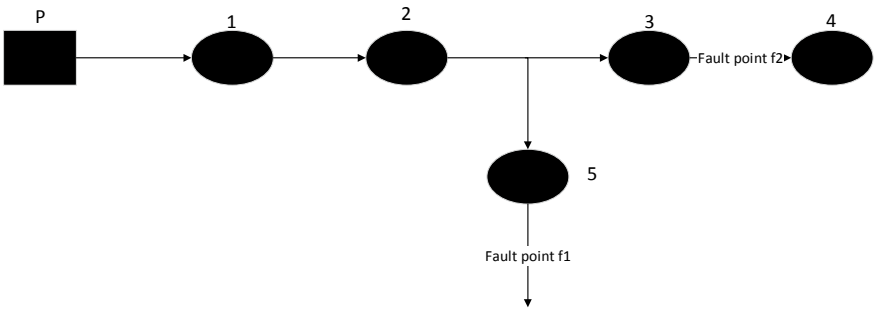

Fig. 4 Topological structure diagram of substation

magnetic field strength between two sensors is distorted, that is to say, the magnetic value exceeds the threshold value, it is determined that the fault location occurs between the two sensors, otherwise no fault occurs. When the distribution network has been judged to have a fault, the fault location can be determined as between the i-th sensor and the i-th+1 sensor.

$$\begin{cases} |g(i)| > L & \text{fault is happend} \\ |g(i)| \leq L & \text{fault is not happend} \end{cases}$$

4 Process of Fault Location

The specific process of fault location method for distribution network based on narrowband communication technology is as follows: Firstly, collect the surrounding magnetic field information through optical waveguide sensors installed on the line. Secondly, convert the magnetic field into optical signals into electrical signals and into digital signals, respectively, which are transmitted to the master station server through narrowband communication technology and compared with historical data. Finally, the fault location is found successfully. The whole flowchart is as shown in Fig. 5.

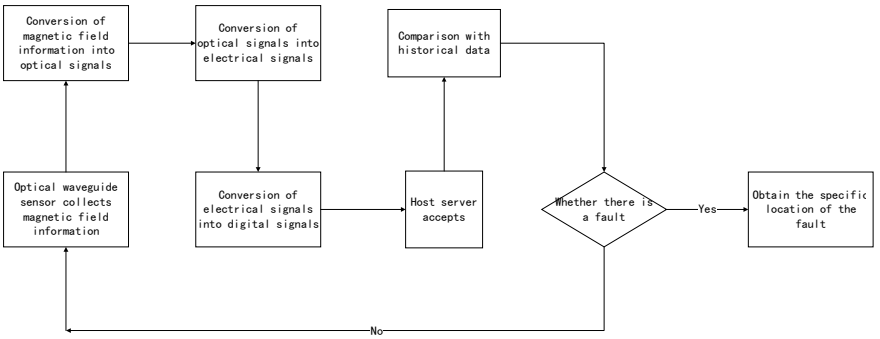

Fig. 5 System flowchart

5 Conclusion

In this paper, a fault location of distribution network based on narrowband communication technology is proposed. The whole system consists of 11 modules. The optical wave guide magnetic field sensor is installed on the cable, and the other parts are installed on the pole. The fault location system adopts narrowband wireless communication technology for data transmission. And the measured data and historical data are used to obtain the fault point. The system can realize monitoring and location of distribution network.

Acknowledgments This work was supported in part by the Special Basic Cooperative Research Programs of Yunnan Provincial Undergraduate Universities Association under Grant No. 202101BA070001-149/ 202101BA070001-150, in part by the National Natural Science Foundation of China under Grant No. 62066023, in part by the Yunnan Students' Innovation and Entrepreneurship Training Program under Grant No. S202211393037.

Reference

1. Zhou XX, Chen SY, Lu ZX, Huang YH, Ma SC, Zhao Q (2018) Technical characteristics of China's new generation power system in energy transformation. J Electr Eng China 38(07):1893–1904, 2205
2. Wu J (2016) Brief analysis of power quality problems in intelligent distribution network. Power Capacit React Compens 37(06):35–39
3. Wen LB, Shan Y, Chang L, Chen SB, Tang ZY (2021) Research on online monitoring and comprehensive diagnosis of short circuit fault in distribution network. Electric Drive 51(14):73–80
4. Yang X (2021) Fine fault location of feeder using monitoring information of distribution transformer. Xi'an University of Technology, p 63
5. Deng F, Liang SB, Tian QS, Chang M (2019) A fault location method for distribution network based on linked list method and time delay. J Kunming Univ Technol (Natural Science Edition) 44(02):63–68

6. Xue YJ, Xu Y, Cheng S (2021) Fault location method for circular dc distribution network based on current change. Smart Power 49(02):76–82, 98
7. Liu KX, Dong WJ, Xiao SW, Wei J, Zhao W (2021) Fault identification and location of active distribution network based on svm classification of voltage data. Power Grid Technol 45(06):2369–2379
8. Xia ZX, Yao CN (2022). Modeling of fault section location in distribution network based on probabilistic neural network. Electron Des Eng 30(19):185–188, 193
9. Ren ZL, Liu WD, Yang L, Wang SA, Luo TY (2022) Fault location of distribution network with distributed generation based on improved pigeon swarm algorithm. J Power Supply 20(04):171–178
10. Zhang RS, Liu LS, Xu H, Ke CY (2022) Distribution network fault location using improved manta ray foraging optimization algorithm. J Fujian Inst Eng 20(03):267–274
11. Xu LL, Yang C, Zeng HR (2023) Fault section location of distribution network with dg based on improved whale algorithm. Electron Sci Technol 36(15–20):27
12. Yang Q (2022) Fault location of distribution network with distributed generation based on sparrow search algorithm. Ningxia University. https://doi.org/10.27257/d.cnki.gnxhc.2022.000150. Wu Tianwei (2022) Application of improved ant colony algorithm in fault location of distribution network. J Lanzhou Univ Arts Sci (Natural Science Edition) 36(02):22–27
13. Wu TW (2022) Application of improved ant colony algorithm in distribution network fault location. J Lanzhou Univ Arts Sci (Natural Science Edition) 36(02):22–27
14. Li LB, Sun TD, Zeng SM, Wang L, Liang JF, Hao YH (2022) Fault location method for distribution network based on multi terminal traveling wave time difference. Power Syst Prot Control 50(03):140–147
15. Yao YF, Wang QZ, Wang HP, Jia J, Xia XB (2021) Fault section location method of low-voltage distribution network based on adjacency matrix. China Power 54(11):91–96, 114
16. QUALCOMM incorporated; patent issued for data multicast or broadcast on control channel for narrowband communication (USPTO 10,498,551). Computers, Networks Communications, 2019
17. Telefonaktiebolaget LM Ericsson (publ); Researchers submit patent application, "narrowband communication system with a standalone carrier", for approval (USPTO 20190349734). Network Weekly News, 2019
18. QUALCOMM incorporated; patent application titled "techniques for allocating time and frequency resources to an uplink channel to carry uplink control information used for narrowband communication" published online (USPTO 20190274134). Computer Weekly News, 2019
19. Stateczny A, Gierlowski K, Hoeft M (2022) Wireless local area network technologies as communication solutions for unmanned surface vehicles. Sensors 22(2):655–655

Carbon Emission Prediction Model of Power Industry Based on CEEMD-SSA-ELM Method

Ling Zhou, Xiong Li, Yuan Ji, Wei Wei, and Fangquan Wu

Abstract When forecasting the carbon emissions of the power industry, due to the lack of analysis on the comprehensive effect of different influencing factors, there is a large deviation between the prediction results and the actual situation. Therefore, a research on the carbon emissions prediction model of the power industry based on CEEMD-SSA-ELM method is proposed. The logarithmic average Dixon index method is used to analyze the factors affecting carbon emissions in the thermal power industry. From the perspective of production and consumption, the composition of specific factors affecting carbon emissions is comprehensively analyzed. With the help of kaya identity, the first decomposition model of carbon emissions is constructed to achieve a comprehensive analysis of the factors affecting carbon emissions in the thermal power industry. In the stage of building the prediction model, CEEMD was used to decompose the original carbon emission influencing factor data, and SSA was used to comprehensively calculate the action intensity of each influencing factor of carbon emissions. Finally, ELM was used to calculate the comprehensive value of carbon emissions. In the test results, the prediction results of the design model for carbon emissions under the baseline scenario, low-carbon scenario and enhanced low-carbon scenario are highly consistent with the measured values, and there is no significant error.

Keywords CEEMD-SSA-ELM method · Power industry · Carbon emission prediction model · Logarithmic mean Dixon index method · Kaya identity · CEEMD decomposition

L. Zhou (✉) · X. Li · Y. Ji · W. Wei · F. Wu
Information Center of Guizhou Power Grid Co., Ltd, Guiyang 550003, Guizhou, China
e-mail: 545008401@qq.com

S. Yadav et al. (eds.), *Energy Power and Automation Engineering*, Lecture Notes in Electrical Engineering 1118, https://doi.org/10.1007/978-981-99-8878-5_65

1 Introduction

Based on the analysis of the environmental status under the background of rapid economic development, as the world's second largest economy, the continuous expansion of its international status also requires that it take more responsibilities in environmental issues [1–4]. In the context of more and more research on carbon emissions, it greatly supports the solution of current environmental problems, and also provides an important theoretical basis and implementation basis for the realization of carbon emission reduction related goals. It is worth noting that only global concern and scientific researchers and the government jointly participate in the research of climate change can effectively solve environmental problems. At this stage, it is the main purpose of researchers to study carbon emissions to make everyone understand the hazards of climate change. Secondly, it is also the fundamental goal of researchers to study carbon emissions [5, 6] to provide a reliable basis for the implementation of relevant energy conservation and emission reduction work plans. Combined with the above analysis, it can be seen that the research on carbon emissions has great significance and long-term development value. The mature carbon emission calculation at this stage is analyzed, which mainly includes four types. First, the carbon emission calculation method based on the carbon emission coefficient is the most widely used method; the second is the carbon emission calculation method based on actual measurement. The calculation result of this method is more accurate, but the related cost input is high; there is also the carbon emission calculation method based on mass balance. The most prominent feature of this method is that it is simple to operate, but the accuracy of the calculation results is relatively low [7, 8]; the last is the carbon emission calculation method based on remote sensing estimation, which realizes the integration of modern technology and improves the efficiency of calculation, but has some limitations in the application phase. For carbon emissions, scientific and reasonable analysis of relevant driving factors is also a key link in the process of calculating them. At present, the index composition analysis (IDA) is one of the widely used decomposition methods for carbon emission influencing factors. Secondly, the structural decomposition analysis (SDA) is also a more common decomposition method [9, 10]. On this basis, more and more attention has been paid to how to combine the current situation and predict the future carbon emissions. This paper proposes a carbon emission prediction model for the power industry based on CEEMD-SSA-ELM method and analyzes and verifies the practical application effect of the designed prediction model through comparative testing.

2 Design of Carbon Emission Prediction Model for Power Industry

2.1 Analysis of Influencing Factors of Carbon Emissions in Thermal Power Industry

In order to accurately predict the carbon emissions of the power industry, it is first necessary to clarify the composition of the factors affecting the carbon emissions of the thermal power industry. For this purpose, this paper uses Logarithmic Mean Division Index (LMDI) to achieve its analysis [5, 11]. Compared with other decomposition methods, the log average Dixon index method has obvious advantages in theoretical basis, and it is not affected by the objective environment in the specific application stage, which makes it have a unique perspective in the interpretation of results. In this paper, when using this method to analyze the influencing factors of carbon emissions in the thermal power industry, the variables are completely decomposed, so that there is no residual item in the corresponding analysis results, so as to ensure the reliability of the analysis of the influencing factors of energy consumption and carbon emissions [12, 13]. In the specific analysis stage, this paper starts from the production end and the consumption end of the power industry, respectively, and makes a comprehensive analysis of the influencing factors affecting the carbon emission of the power industry and the corresponding contribution rate [14]. The specific composition of each factor is analyzed.

Among them, the power supply structure is mainly divided into two aspects. On the one hand, it refers to the proportion of non-renewable energy and clean energy in the power generation structure, and on the other hand, it refers to the proportion of non-renewable energy of thermal power generation in the consumption structure. Coal consumption for power generation mainly refers to the total consumption of fossil energy corresponding to unit power production. This factor largely reflects the carbon emission intensity of the thermal power industry. In general, when the coal consumption for power generation decreases, it means that the energy utilization rate is rising at this time; on the contrary, when the coal consumption for power generation rises, it means that the energy utilization rate is in a declining state at this time. The carbon emission coefficient of energy refers to the total amount of carbon dioxide emitted when the unit of fossil fuel is completely burned. Transmission and distribution loss is an indirect factor affecting carbon emissions. When it affects the actual cost of power loss to the whole society, the corresponding loss directly causes energy waste on the one hand and also causes additional consumption of fossil fuels in the process of making up for the loss. For per capita GDP and population size factors, the development of regional economy is mainly reflected by per capita GDP, which is also one of the important parameters reflecting the contribution of economic development to carbon emissions. The residential power consumption intensity refers to the power demand intensity, which mainly reflects the demand scale of thermal power generation in residential life. Industrial power consumption intensity mainly

refers to the corresponding power consumption when the thermal power industry increases per unit GDP. This index parameter is mainly related to the equipment and technology of the power sector. The higher the equipment perfection, the higher the technical level, and the lower the energy consumption per unit GDP. The last is the industrial structure. Generally, the social industrial structure is mainly divided into three parts: the primary industry, the secondary industry and the tertiary industry. The different proportions of the three also have a significant impact on carbon emissions to a certain extent. Combined with the above analysis, this paper introduces kaya identity when building the primary decomposition model of carbon emissions, and the corresponding analysis results can be expressed as

$$c = \left(\frac{c}{e}\right) * \left(\frac{e}{t_p}\right) * \left(\frac{t_p}{g}\right) * \left(\frac{g}{e_c}\right) * e_c \tag{1}$$

$$m = \frac{c}{e} \tag{2}$$

$$k = \frac{e}{t_p} \tag{3}$$

$$c = m * k * g * p * e_c \tag{4}$$

Among them, represents the total carbon emissions, is the energy emission coefficient, refers to the coal consumption rate of power generation in the process of power production, represents the ratio of fossil fuel power supply to total power production, which is used to reflect the power supply structure, represents the demand for electricity in the whole society, refers to the ratio of power generation to the demand of the whole society, which indicates the structure of power supply and demand, shows the total consumption of fossil fuels in the electric energy stage.

In the way shown above, a comprehensive analysis of the factors affecting carbon emissions in the thermal power industry will be achieved, providing an implementation basis for the subsequent construction of carbon emissions prediction models in the power industry and ensuring the reliability and accuracy of the prediction results.

2.2 Construction of Carbon Emission Prediction Model for Power Industry Based on CEEMD-SSA-ELM Method

On the basis of the above, the carbon emission prediction model of the power industry built in this paper is shown in Fig. 1.

In combination with the CEEMD-SSA-ELM-based carbon emission prediction model of the power industry shown in Fig. 1, in the process of using Comprehensive Ensemble Empirical Mode Decomposition (CEEMD) to decompose the original power data, noise needs to be added to the data first, which can be expressed as

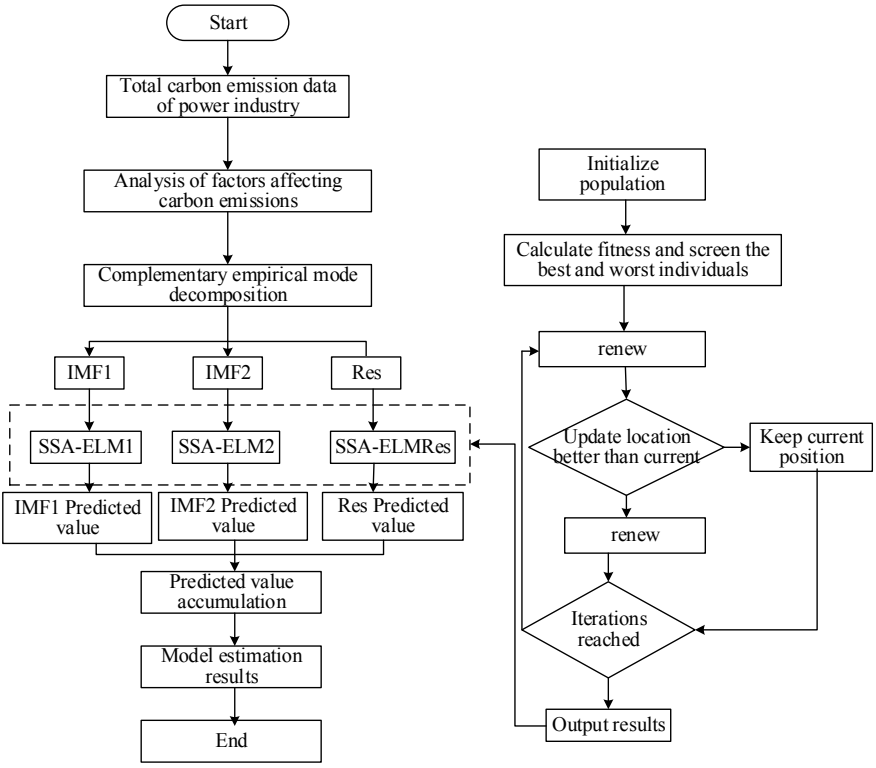

Fig. 1 Carbon emission prediction model of power industry based on CEEMD-SSA-ELM method

$$\begin{bmatrix} M_1 \\ M_2 \end{bmatrix} = \begin{pmatrix} 1 & 1 \\ 1 & -1 \end{pmatrix} \begin{bmatrix} A \\ B \end{bmatrix} \tag{5}$$

Among them, M_1 represents the sum of the original data and the positive Gaussian white noise, M_2 represents the sum of the original data and the negative Gaussian white noise, A represents the data of original carbon emission influencing factors and B represents the added white Gaussian noise. On this basis, the target data is processed in the way of EMD decomposition. Each data has a set of IMF components matching it, and the final average result is

$$\mathrm{imf}_j = \frac{\sum_{i=1}^{n} \mathrm{imf}_{ij}}{n} \tag{6}$$

Among them, imf_j represents the mean value of IMF component of raw data, imf_{ij} represents the ith component of the jth IMF. The corresponding CEEMD decomposition result is

$$x(t) = \sum_{j=1}^{m} \mathrm{imf}_j(t) + \mathrm{res} \tag{7}$$

Among them, $x(t)$ represents CEEMD decomposition results and res represents the mean value.

Based on the above analysis results, Sparrow Search Algorithm (SSA) is used to calculate the action intensity of the factors affecting carbon emissions. The corresponding update method can be expressed as

$$x_{\mathrm{id}}^{t+1} = \begin{cases} x_{\mathrm{id}} e^{-i}, w < W \\ x_{\mathrm{id}} + \mathrm{RL}, w \geq W \end{cases} \tag{8}$$

Among them, x_{id}^{t+1} represents the updated location information, x_{id} indicates the current location information, RL represents the matrix of the function degree of the influencing factor and W represents the early warning value of the SSA. On this basis, when the difference between the updated location parameters and the current location parameters no longer changes, the results at this time will be considered as the final optimization results, which will be used as the output value for the subsequent design of the carbon emission model of the power industry.

Based on this paper, the Extreme Learning Machine, limit learning machine (ELM) is used to calculate the comprehensive optimal value of the degree of effect on carbon emissions, and the corresponding network structure is shown in Fig. 2.

Based on the network mechanism shown in Fig. 2, set the weight of connecting the nodes of the input layer and the ith hidden layer to w, the weight of connecting the nodes of the th hidden layer and the nodes of the output layer to k, and the threshold layer a of the ith node in the hidden layer directly affects the result q of ELM output. In this paper, set the hidden layer output function of ELM to h(*). After training, the weights of the connected hidden layer and the output layer exist in the form of relative

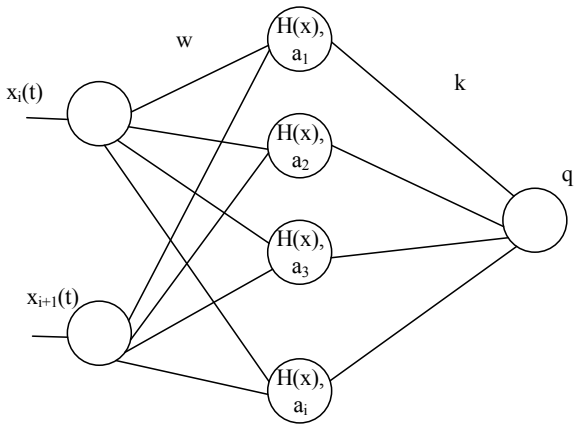

Fig. 2 Extreme learning machine network mechanism

fixed values. With the method of minimizing the approximate square difference, the final ELM output result can be expressed as

$$\sum_{i=1}^{n} k_i h(w_i x_i + a_i) = q_i \sum_{i=1}^{n} k \tag{9}$$

In this way, the carbon emissions of the power industry can be predicted under the combined effect of various influencing factors.

3 Test Analysis

3.1 Design Idea for Carbon Emission Scenario of Thermal Power Industry in a Province

In the process of analyzing the actual application effect of the design method in this paper, this paper uses the scenario analysis method to achieve the construction of the test scenario. In the specific implementation process, it is mainly to set different scenarios and predict the specific carbon emissions on the basis of the research object, on the eve of the future scenarios that are about to happen. This paper fully considered the future development direction of the thermal power industry in a province, combined with the actual situation of the low-carbon route and set each independent variable based on the low-carbon direction. The benchmark scenario, low-carbon scenario and enhanced low-carbon scenario are set, respectively, and three scenarios are used to achieve different corresponding development models. Combined with the analysis results of carbon emission factors in the thermal power industry, this paper analyzes the carbon emission scenarios from four perspectives, namely coal consumption for power generation, power supply structure, GDP per capita and industrial power intensity.

3.2 Parameter Setting for Carbon Emission Scenario of Thermal Power Industry in a Province

In the process of setting the carbon emission scenario parameters of the thermal power industry in a province, this paper first made statistics on the development of the main factors of the thermal power industry in a province during 2005–2020, and the specific data information is given in Table 1.

Combined with the data information in Table 1, it can be seen that during 2005–2020, the growth rate of coal consumption for power generation as a whole showed a downward trend, the growth rate of power supply structure as a whole showed a small

Table 1 Development of main factors of thermal power industry in a province during 2015–2020

Annual/annual	Power generation coal consumption growth rate Power supply/%	Structure growth rate/%	Per capita GDP growth rate Production/%	Industrial power intensity growth rate/%
2005	–	–	–	–
2006	– 2 44	0.42	14.94	– 3. 12
2007	– 3.28	– 0.02	20.00	– 5.14
2008	– 1.34	– 0.87	20.00	3.13
2009	– 1.92	0.37	13.89	4.34
2010	1.07	– 0.80	26.22	– 10.18
2011	– 1.54	1.12	23.67	– 9.00
2012	– 0.42	– 0.40	12.50	– 3.69
2013	– 2 46	0.00	11.46	– 4.65
2014	– 5.26	– 0.50	8.41	– 10.60
2015	– 2.77	– 0.80	5.17	– 7.40
2016	– 2.49	– 1.76	9.29	– 4.45
2017	1.40	– 1.29	11.50	– 0.88
2018	– 0.59	– 1.22	25.56	– 13.85
2019	– 0.87	– 0.12	8.04	– 3.69
2020	– 1.72	– 1.41	4.79	– 11.24

downward trend, the per capita GDP increased significantly and the corresponding growth of industrial power consumption decreased significantly, with the maximum decline reaching 11.24%. Combined with the data given in Table 1 and the relevant requirements of local policies, based on economic growth as the core, this paper sets three different development scenarios, and the corresponding settings of GDP per capita, industrial power intensity, coal consumption rate for power generation and power supply structure rate are given in Table 2.

In the way given in Table 1, different scenarios are constructed as the basis for subsequent carbon emission prediction.

In the specific test process, in order to improve the reliability of the test results, the quality balance method and remote sensing estimation method were used as the control group of the test, and the results of the three different methods were analyzed based on the measured results.

Table 2 Profile settings

Scenario	Influencing	Factor
Benchmark scenario	Power generation coal consumption growth rate power supply/%	– 1.17
	Structure growth rate/%	– 0.50
	GDP growth rate per capita/%	5.50
	Industrial power intensity growth rate/%	– 5.50
Low-carbon scenario	Power generation coal consumption growth rate power supply/%	– 1.65
	Structure growth rate/%	– 1.0
	GDP growth rate per capita/%	5.0
	Industrial power intensity growth rate/%	– 6.0
Strengthen low-carbon scenarios	Power generation coal consumption growth rate power supply/%	– 2.0
	Structure growth rate/%	– 1.5
	GDP growth rate per capita/%	4.50
	Industrial power intensity growth rate/%	– 6.50

3.3 Test Preparation

Firstly, the relationship between the predicted results of carbon emissions and the actual results of different methods under the baseline scenario is compared and analyzed, and the data results obtained are shown in Fig. 3.

Combined with the test results in Fig. 3, it can be seen that in different prediction methods, the prediction results of carbon emissions under the baseline scenario have different degrees of deviation from the actual value. Among them, the prediction results of the mass balance method and the remote sensing estimation method show obvious instability, and the maximum error with the measured value has reached 22,456 tons, in contrast, in the test results of the model designed in this paper, the error between the predicted and measured carbon emissions is always within 10,000

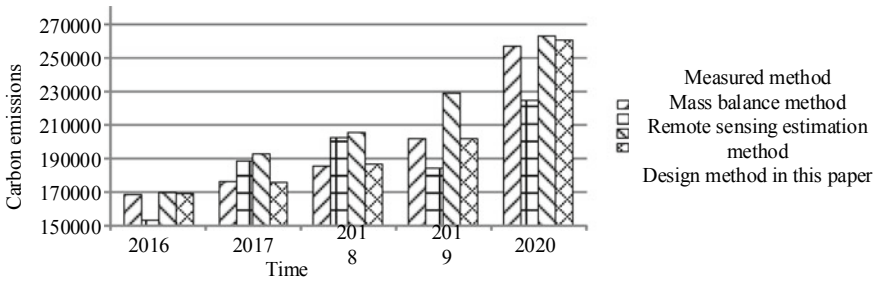

Fig. 3 Comparison diagram of carbon emission prediction results under the baseline scenario

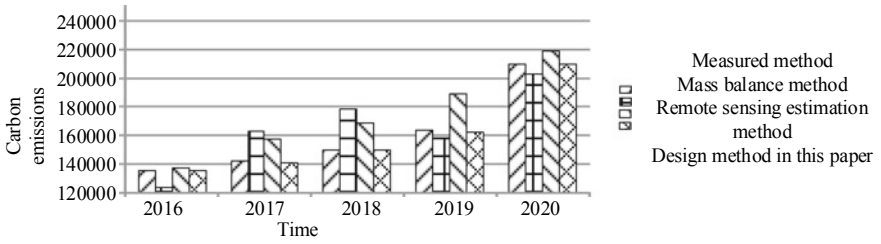

Fig. 4 Comparison diagram of carbon emission prediction results under low-carbon scenario

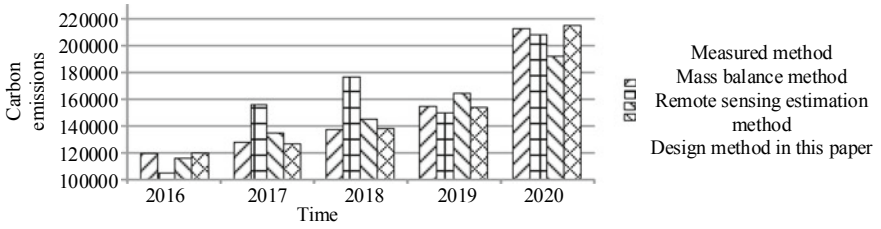

Fig. 5 Comparison diagram of carbon emission prediction results under the enhanced low-carbon scenario

tons, the maximum error is 6635 tons, and the minimum error is only 1326 tons. The test results show that the carbon emission prediction model of the power industry based on CEEMD-SSA-ELM method designed in this paper can accurately predict the carbon emissions under the benchmark scenario.

Figures 4 and 5 show the relationship between the predicted and actual results of carbon emissions under the low-carbon scenario and the enhanced low-carbon scenario, respectively.

Combined with the test results in Figs. 4 and 5, it can be seen that the differences between the predicted results of the three methods and the measured values also show obvious differences when predicting the carbon emissions under the low-carbon scenario and the enhanced low-carbon scenario. But on the whole, the prediction results of the design model in this paper always have high stability and accuracy, without obvious errors, and have obvious advantages compared with the control group.

Based on the above test results, it can be concluded that the carbon emission prediction model of the power industry designed in this paper based on CEEMD-SSA-ELM method can achieve accurate prediction of carbon emissions in different scenarios, which has good practical value for the actual environmental management work and can provide reliable guidance.

4 Conclusion

Based on the analysis of the total amount of greenhouse gases emitted every year in the world, its peak has reached 51 billion tons. In this context, in order to avoid the disasters and negative impacts caused by climate change, reducing greenhouse gas emissions is a policy that countries in the world must resolutely implement. In this regard, relevant requirements have been issued to urge countries around the world to actively participate in and implement actions to reduce carbon emissions, and accelerate the arrival of peak carbon emissions on the basis of low-carbon development. This paper proposes the research on carbon emission prediction model of power industry based on CEEMD-SSA-ELM method, which realizes the accurate prediction of carbon emissions under different scenarios, and has good practical application value.

Acknowledgements This work is supported by Information Center of Guizhou Power Grid Co., Ltd. Research on digital monitoring and prediction technology of carbon emissions in the whole life cycle of power grid and demonstration application of green transformation of electricity substitution in brewing industry project (GZKJXM20210421).

References

1. Liang X, Liu X, Mei L, Zhang D (2021) Multi-objective green multimodal transport path optimization with the participation of high-speed railway. In: 2021 6th international conference on transportation information and safety (ICTIS). IEEE, pp 1072–1077
2. Zhou F, Huang Z, Zhang C (2022) Carbon price forecasting based on CEEMDAN and LSTM. Appl Energy 311:118601
3. Charfeddine L, Kahia M (2021) Do information and communication technology and renewable energy use matter for carbon dioxide emissions reduction? evidence from the Middle East and North Africa region. J Clean Prod 327:129410
4. Chen D, Yang X (2021) Maximum likelihood estimation for uncertain autoregressive model with application to carbon dioxide emissions. J Intell Fuzzy Syst 40(1):1391–1399
5. Wang W, Zhao X, Zhang Q, Fu C, Xie P (2022) Auction mechanism design of the Chinese national carbon market for carbon neutralization. Chin J Popul Resour Environ 20(2):115–124
6. Su Q, Wang H, Shi X, Li G, Sun K (2022) Research on energy supply and demand forecast and carbon neutralization path based on grey-monarch butterfly optimization model. J Phys Conf Ser 2247(1):012008
7. Pistochini T, Dichter M, Chakraborty S, Dichter N, Aboud A (2022) Greenhouse gas emission forecasts for electrification of space heating in residential homes in the US. Energy Policy 163:112813
8. Zeng H, Shao B, Bian G, Dai H, Zhou F (2022) Analysis of influencing factors and trend forecast of CO_2 emission in Chengdu-Chongqing urban agglomeration. Sustainability 14(3):1167
9. Fei X, Long F, Li F, Ling Q (2021) Multi-component fusion temporal networks to predict vehicle exhaust based on remote monitoring data. IEEE Access 9:42358–42369
10. Han J, Kong L, Wang W, Xie J (2022) Motivating individual carbon reduction with saleable carbon credits: policy implications for public emission reduction projects. Ind Manag Data Syst 122(5):1268–1305

11. Wang M, Feng C (2021) How will the greening policy contribute to China's greenhouse gas emission mitigation? a non-parametric forecast. Environ Res 195:110779
12. Yang C, Hao Y, Irfan M (2021) Energy consumption structural adjustment and carbon neutrality in the post-COVID-19 era. Struct Chang Econ Dyn 59:442–453
13. Alao RO, Payaslioglu C, Alhassan A, Alola AA (2022) Accounting for carbon dioxide emission effect of energy use, economic growth, and urbanization in the OPEC member states. Int Soc Sci J 72(243):129–143
14. Xiao-Ding LI, Yun-Huan QU, Li-Hui ZHANG., Yu GONG, Yi-Man DONG, Guang-Hui, LI (2021). Forecast of China's future nuclear energy development and nuclear safety management talents development. IOP Conf Ser Earth Environ Science 691(1):012022

Design of Regional Carbon Emission Monitoring Platform Based on Cloud Edge Collaboration

Zeqi Zhang, Zhe Chen, and Yingjie Li

Abstract Most conventional regional carbon emission monitoring platforms use the NB-IoT principle to upload monitoring data, which is slow, affecting the monitoring efficiency of the monitoring platform, and the accuracy of carbon emissions calculation results is low, leading to a large deviation between the platform monitoring results and the actual carbon emissions. Based on this, a new regional carbon emission monitoring platform is proposed by introducing cloud edge collaboration. On the basis of the completion of the hardware design of the platform, a comprehensive design of the platform software is made. Firstly, based on the sampling control logic, the regional carbon emissions are sampled, monitored and pretreated. Secondly, the emission factor method is used to calculate the regional carbon emissions based on the fuel end. On this basis, the cloud edge collaboration method is used to upload carbon emission monitoring data to improve the efficiency of platform monitoring. The platform test results show that the new platform can significantly improve the accuracy of monitoring results, the carbon emissions monitoring value is closer to the actual value, the deviation of monitoring results is small, and more accurate regional carbon emissions data can be monitored in real time.

Keywords Cloud edge collaboration · Region · Carbon emissions · Platform · Monitor

1 Introduction

Carbon emission refers to a general term of greenhouse gas emissions, in which carbon dioxide is the main greenhouse gas. Any daily activity of people may cause carbon emissions, such as cooking, air conditioning and heating, driving, which will produce carbon dioxide [1] of different concentrations. Daily life produces relatively less carbon dioxide, while industrial production produces more carbon dioxide, especially in thermal power plants, coal-fired power plants and other enterprises. During

Z. Zhang (✉) · Z. Chen · Y. Li
Shenzhen Power Supply Bureau Co, Ltd, Shenzhen 518000, Guangdong, China
e-mail: 18576617356@163.com

S. Yadav et al. (eds.), *Energy Power and Automation Engineering*, Lecture Notes in Electrical Engineering 1118, https://doi.org/10.1007/978-981-99-8878-5_66

the operation of thermal power plants and coal-fired power plants, the main emission source of greenhouse gases is coal combustion. Due to the difference between the amount of fuel and inlet fuel, the types of greenhouse gases generated after combustion are different. Among them, carbon dioxide, nitrous oxide and methane [2] have the highest content and concentration of greenhouse gases. A large amount of greenhouse gas emissions will cause serious damage to the current ecological environment, which may lead to glacier melting, crop production reduction, extinction of various species, climate warming, greenhouse effect, sea level rise, etc. [3].

Therefore, a scientific and reasonable carbon emission monitoring platform is essential to improve the problem of excessive regional carbon emissions and avoid the occurrence of the above problems. Carbon dioxide emission reduction depends on an accurate carbon emission monitoring platform. Based on the global level, the platform's accurate carbon emission data can clearly and intuitively reflect the regional carbon emission reduction progress, which is an important basis for reviewing whether each region has completed the emission reduction task [4]. Based on the level of carbon trading market, credible carbon emission data can serve as the premise and guarantee for the establishment of mutual trust and carbon trading among all parties concerned in the carbon trading market. On the enterprise level, accurate regional carbon emission data can provide important help for technicians to determine greenhouse gas emissions and emission locations, and it is the reference basis for enterprises to develop carbon emission reduction measures and comprehensively manage carbon assets. At this stage, the construction of the traditional regional carbon emission monitoring platform is gradually improved, which can reasonably monitor carbon emissions [5]. However, with the rapid development of current industrial technology, the traditional carbon emission monitoring platform still has some shortcomings in the actual application process. This is mainly reflected in the limited monitoring scope, low efficiency of monitoring task scheduling and the inability to focus on accurate monitoring of carbon emissions in the combustion process in a fast time [6].

Cloud side collaboration can improve the above problems. Through the combination of edge computing and cloud computing, information from each terminal is collected, information is fed back to the cloud, and instructions are issued, so as to achieve the goal of co-existence collaborative carbon emission information collection, monitoring resource scheduling management and comprehensive coverage monitoring [7]. Based on this, this paper introduces the concept of cloud edge collaboration on the basis of the traditional regional carbon emission monitoring platform, and proposes a new monitoring platform, which contributes to the control of regional carbon emissions and the protection of the ecological environment.

2 Hardware Design of Regional Carbon Emission Monitoring Platform

The hardware design of regional carbon emission monitoring platform is the basis of carbon emission data collection and transmission. In order to better design the embedded hardware in the monitoring platform and improve the ability of hardware to find and solve problems, it is necessary to adopt an independent design method to design the embedded hardware module. The schematic diagram of the embedded hardware structure of the regional carbon emission monitoring platform designed in this paper is shown in Fig. 1.

As shown in Fig. 1, the hardware module of the regional carbon emission monitoring platform designed in this paper includes four main parts. Among them, the main control unit module of the monitoring platform is mainly responsible for ensuring the stability and reliability of the operation configuration of the monitoring platform when the platform has no upper application; the monitoring platform power module is responsible for using solar panels to continuously convert solar energy into electrical energy required for platform operation, providing sufficient power for the platform, and ensuring that the platform can meet the demand for long-term power supply for continuous monitoring of regional carbon emissions; the sensor module of the monitoring platform is mainly responsible for collecting monitoring data such as regional carbon emissions and carbon emission characteristics, and selecting specific sensors with high matching degree according to the actual situation of the monitoring target; the monitoring platform wireless communication module is responsible for sending the carbon emission monitoring data transmitted by the platform monitoring master control unit module to the cloud side collaborative data receiving center through the wireless network, and receiving and executing the carbon emission monitoring command [8] issued by the upper computer platform.

On this basis, the hardware equipment in the platform is selected and designed. The gas sensor with model JXBS-3001-MZ is selected. Its precision is $\leq \pm 3\%$ of the reading (25 °C), and its sensitivity is 10PPM alcohol > 0.7 V. The sensor parameters are shown in Table 1.

This type of gas sensor can collect carbon monoxide, oxygen, nitrogen dioxide, methane, hydrogen sulfide, sulfur dioxide, ammonia, hydrogen chloride, Freon, phosphine, nitric oxide, phosphine, ethylene oxide and other gases [9].

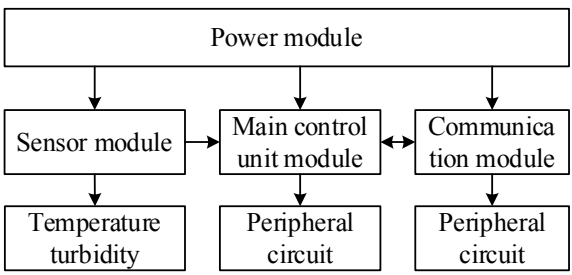

Fig. 1 Schematic diagram of embedded hardware structure of regional carbon emission monitoring platform

Table 1 Parameter settings of JXBS-3001-MZ gas sensor

No	Project	Parameter
1	Sensitivity	0.4 V–0.7 V
2	Warm-up time	$\geq$ 24 h
3	Response time	$\leq$ 30 s
4	Desorption time	$\leq$ 60 s
5	Power waste	230mW

Table 2 Monitor performance parameter settings

No	Project	Parameter
1	Power input	220 AC
2	Working power	35–40 W
3	Accuracy	$\leq \pm$ 3%FS
4	Resolving power	0.01 mg/m3
5	Zero drift	$\leq \pm$ 2%FS/24

The monitor used on the platform is selected as Juyihui 06AMIPJUE-01L monitor with a size of 25 * 32 * 18 mm and a measurement range of 0–10 ppm (customizable range). The performance parameter settings of the monitor are given in Table 2.

Adjust the monitor according to the performance parameters set in Table 2 to ensure its operation quality and monitoring accuracy.

To sum up, complete all the hardware design of the regional carbon emission monitoring platform, build a good hardware operating environment and provide strong hardware support for the platform's high-precision and efficient monitoring.

3 Software Design of Regional Carbon Emission Monitoring Platform

3.1 Regional Carbon Emission Sampling Monitoring and Pretreatment

Regional carbon emission sampling and monitoring requires complete control logic. Through the control logic, the solenoid valve switch in the sampling gas path of the monitoring platform is controlled. Based on the actual demand of carbon emission monitoring, the platform automatically closes the switch to complete sampling and monitoring [10]. During sampling monitoring, it should be noted that since the medium object to be sampled and monitored belongs to a gaseous substance, electromagnetic pneumatic control valves with high matching degree with the gaseous

substance should be used to complete the opening and closing operation of the control loop equipment of the monitoring platform. Carry out regional carbon emission sampling operation [11] according to the control logic process.

On this basis, the sampling monitoring data are preprocessed. Select the sampling pretreatment method suitable for differential absorption spectrometry and combine the sampling monitoring data pretreatment method with the analysis method to control the stability of the platform operation. In the practical carbon emission pretreatment, the concentration of carbon dioxide and sulfur dioxide is measured, and the dynamic change of dust particle concentration in the carbon emission process is recorded [12]. In some cases, the carbon emission value may be close to zero. At this time, the way of rapid condensation of water vapor is used to dehumidify the exhaust gas to prevent carbon dioxide and condensate from contacting, minimize the contact of condensate with dry gas, and avoid dilution of sulfur dioxide in the sampling gas [13]. Through the above carbon emission sampling monitoring and pretreatment, provide basic data support for subsequent carbon emission monitoring.

3.2 Calculation of Regional Carbon Emissions Based on Fuel End

After completing the regional carbon emission sampling monitoring and pretreatment, calculate the regional carbon emissions based on the fuel end. In order to improve the accuracy of the platform monitoring results, in the calculation of regional carbon emissions, the emission factor method is used to combine the activity data (AD) and the emission factor (EF) of the corresponding activity data to calculate the regional greenhouse gas emissions [14]. The formula is:

$$E = \mathrm{AD} \cdot \mathrm{EF} \tag{1}$$

Among them, AD represents regional carbon emission activity data; EF represents the emission factors corresponding to the regional carbon emission activity data. In the accounting of carbon emissions, whether the selected emission factors are representative will affect the accounting results [15]. After the emission factors are determined, they need to be localized to reduce the error of emission calculation results. The fuel end-based emission factor method as the mainstream calculation method mainly considers two aspects [16]. On the one hand, it has strong applicability and can be used for the accounting of greenhouse gas emissions of most enterprises. That is, after the emission factors are measured according to the emission factors provided by the IPCC or a certain measurement parameter, the enterprise can calculate the emissions of the enterprise through the collected corresponding data [17]. On the other hand, the existing emission factors can be used to replace the general

situation of enterprises in a region, and the emission level of emission sources in the region can be obtained, so that the estimation of emissions of emission sources in the region can be completed as a whole [18].

Secondly, based on the principle of material balance method, the regional carbon emission balance calculation formula is obtained:

$$\sum E_a = E_r + E_q \tag{2}$$

Among them, E_a indicates the total amount of various materials entering the system; E_r indicates the total amount of discharged materials; E_q indicates the output material. Through this formula, the input and output of the enterprise production system can be obtained, and the input and consumption of each material involved in production [19] can be mastered. On this basis, use the platform to calculate the carbon dioxide generated by fuel combustion, the formula is:

$$E_c = \sum_{i=1}^{n} (\mathrm{AD}_i \cdot \mathrm{EF}_i) \tag{3}$$

$$\mathrm{AD}_i = \mathrm{NCV}_i \cdot \mathrm{FC}_i \tag{4}$$

$$\mathrm{EF}_i = \mathrm{CC}_i \cdot \mathrm{OF}_i \times \frac{44}{12} \tag{5}$$

Among them, AD_i represents the i activity data of fossil fuels; EF_i represents the i CO_2 emission factors of fossil fuels; NCV represents the i average net calorific value of three fossil fuels; FC_i represents the i consumption of fossil fuels; $\mathrm{CC_i}$ represents the i carbon content per unit calorific value of fossil fuels; OF_i represents the i carbon oxidation rate of fossil fuels; $\frac{44}{12}$ represents the ratio of carbon dioxide to carbon molecular weight. Through the above calculation formula, the regional carbon emissions at the fuel end [20] can be obtained.

3.3 Upload Carbon Emission Monitoring Data Based on Cloud Edge Collaboration

After the above calculation of regional carbon emissions based on the fuel end is completed, the next step is to upload carbon emissions monitoring data using the cloud edge collaboration method to improve the efficiency of platform monitoring.

By using the combination of cloud side collaboration and the path transmission optimization of the layered network structure, the problem of network congestion and transmission delay caused by data upload in large amounts of data can be effectively solved as a whole, and a new solution and idea [21] can be provided to alleviate the

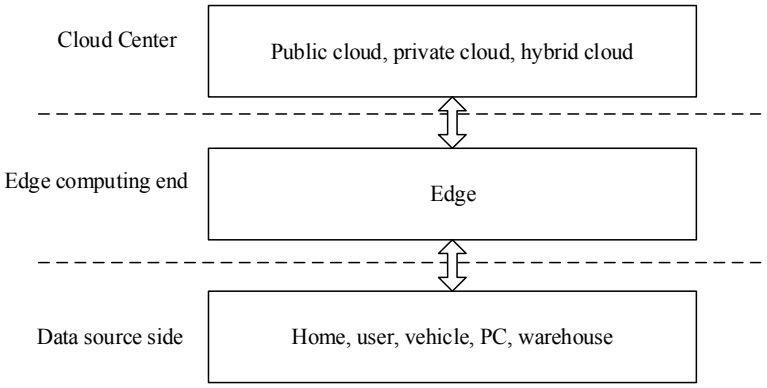

Fig. 2 Schematic diagram of cloud edge collaboration structure

current Internet network resource shortage and information interaction delay. The schematic diagram of cloud edge collaboration structure is shown in Fig. 2.

As shown in Fig. 2, cloud edge collaboration is composed of cloud center, data source end and edge computing end [22]. By using the combination of cloud side collaboration and the path transmission optimization of the layered network structure, the problem of network congestion and transmission delay caused by data upload in large amounts of data can be effectively solved as a whole, providing a new solution and idea for alleviating the current Internet network resource shortage and information interaction delay [23].

In order to simulate the forwarding process of real data streams, it is necessary to consider the situation of mixed uploading of multiple forms of data. The data upload structure is designed as follows: randomly select the data sending end of any edge node as the source end, set the size of the uploaded data packet to represent the size of the cached data stream and simulate the generation process of real data at a certain rate [24]. Set a data cache area on the intermediate forwarding node of the upload path, which is used for the temporary storage area space of data packets after arriving at the node, including a data receiving cache area and a data sending cache area, respectively, representing the cache and forwarding of cached data streams on the node [25].

In the end-to-end multi-path upload of network edge data in the cloud edge collaboration environment, edge nodes near the sending end obtain terminal data and send it back, then receive and upload it to the terminal through edge nodes near the terminal. The corresponding edge server is set in the network edge area near the terminal, and the data upload is realized by relying on the edge server as the edge node agent in the area, which reduces the connection redundancy between nodes and the excessive resource consumption caused by direct upload. Schematic diagram of carbon emission monitoring data uploaded based on cloud edge collaboration, as shown in Fig. 3.

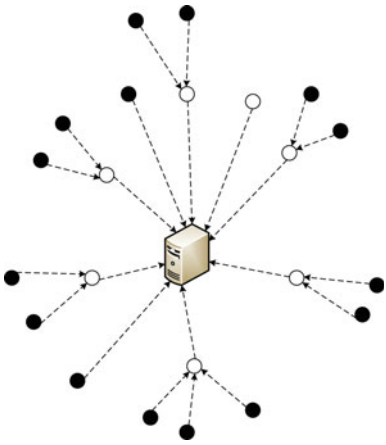

Fig. 3 Schematic diagram of carbon emission monitoring data upload based on cloud edge collaboration

In Fig. 3, the black dot represents the edge node, and the white dot represents the intermediate forwarding node. Not all edge nodes are directly connected to the edge server. Some need to use the edge node as an intermediate forwarding node to forward data to the edge server. For the layered network structure in this paper, based on edge nodes, edge nodes near terminals in a single region are forwarded and uploaded to the regional edge server. Using the layered network structure to manage the data upload process of edge nodes can not only make full use of the advantages of edge nodes, but also meet the data upload needs in the cloud edge collaborative environment.

4 Platform Test

4.1 Test Preparation

First of all, according to the above platform hardware and software design process proposed in this paper, build a regional carbon emission monitoring platform.

The research object of this platform test is two 350 MW units of M thermal power plant in a region, which has strong representativeness and universality, and the test results are more objective. The unit type is condensing steam turbine generator unit, which adopts the front and rear wall opposed combustion mode and uses low sulfur and low ash Indonesian coal as the main fuel. The pollutant emission concentration of the two 350 MW units is near zero. The average emission concentration of nitrogen oxides in the power plant is about 3.62 mg/m3 ~ 3.70 mg/m3, which is far lower than the special emission concentration of 100 mg/m3in industrial standards and specifications; the average concentration of sulfur dioxide is 2.3 mg/m3 ~ 2.4 mg/m3, which is far lower than the special emission concentration of 50 mg/m3specified

in the industrial standard specification; the average concentration of smoke and dust is 0.31 mg/m3 ~ 0.39 mg/m3, which is far lower than the special emission concentration of 20 mg/m3specified in industrial standards.

On this basis, select the instruments and equipment required for carbon emission monitoring in this region. Appropriate carbon emission monitoring sampling points and instruments and equipment have a direct impact on the accuracy of carbon emission monitoring data of the platform. Therefore, this paper believes that before selecting the instruments and equipment required for testing, it is necessary to comprehensively and multi-dimensionally test the on-site situation, and select the platform monitoring sampling point and monitor with the highest fitness according to the actual carbon emissions, carbon emission concentration range and platform testing needs. On this basis, the flue gas analyzer is selected to design the technical parameters of the flue gas analyzer, as given in Table 3.

Set the parameters of the flue gas analyzer according to the technical parameters given in Table 3 to ensure its accuracy in platform testing. After the above test preparation, the regional carbon emission monitoring platform designed in this paper is applied to two 350 MW units to verify the monitoring effect of the platform.

Table 3 Technical parameters of JK90-R flue gas analyzer

No	Project	Parameter
1	Detection method	Fixed and online detection
2	Detection range	0–500 ppm, 1000 ppm, 2000 ppm, 10,000 ppm, 20,000 ppm, 10% vol, 100% vol
3	Resolving power	0.1 ppm, 1 ppm, 0.01% vol
4	Linearity error	± 1.0%
5	Response time	≤ 30 s
6	Recovery time	≤ 40 s
7	Output signal	Users can transfer up to 2000 m according to actual requirements
8	Working power supply	24VDC (12VDC–-30VDC)
9	Working humidity	≤ 95%RH
10	Working pressure	≤ 200 kPa
11	Accuracy	± 3%FS
12	Repeatability	± 1.0%

4.2 Result Analysis

In order to ensure that the functions of the monitoring platform can achieve all-round coordinated operation, the monitoring performance of the platform is comprehensively tested in combination with the regional carbon emission monitoring data management platform. Simulate the operation process of the 350 MW unit in the thermal power plant, complete the comprehensive test of data analysis, transmission and cache and make the prototype run continuously for one week in the thermal power plant simulation environment. In the comprehensive test of platform performance, first, establish high-quality communication of regional carbon emission monitoring controller and monitoring data management platform. In the monitoring controller, the address and port number of the carbon emission monitoring platform shall be configured. According to the actual carbon emission, an interface shall be properly added to receive the carbon emission data. In order to make the platform test results more intuitive and clear, the comparative analysis method is introduced. The regional carbon emission monitoring platform based on cloud edge collaboration proposed in this paper is set as the experimental group, and the conventional carbon emission monitoring platform is set as the control group for comparative analysis. The MATLAB simulation analysis software is used to monitor the dynamic changes of regional carbon emissions of the two platforms, compare the monitoring values of carbon emissions of the two platforms with the actual values and draw a columnar comparison chart as shown in Fig. 4.

It can be seen from the comparison results in Fig. 4 that there are some differences between the carbon emission monitoring results of the two platforms. Among them, after the application of the regional carbon emission monitoring platform based on cloud edge collaboration proposed in this paper, its carbon emission monitoring value is closer to the actual value, and the deviation of the monitoring results is small, while the deviation of the control group's carbon emission monitoring value from the actual

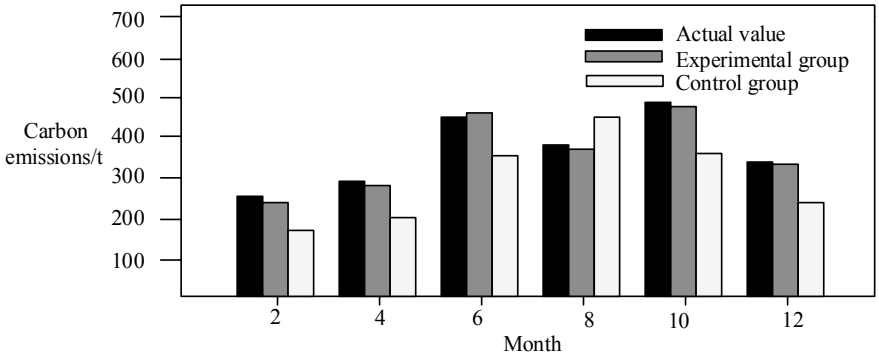

Fig. 4 Comparison results of carbon emission monitoring values and actual values

value is large. It is not difficult to see that the regional carbon emissions monitoring platform based on cloud edge collaboration proposed in this paper is highly feasible and can monitor more accurate regional carbon emissions data in real time.

5 Conclusion

As the main component of greenhouse gases, carbon dioxide emissions have a greater impact on the ecological environment. Carbon dioxide emission reduction depends on an accurate carbon emission monitoring platform. In order to improve the problems and shortcomings in the practical application of the traditional regional carbon emission monitoring platform, this paper introduces the concept of cloud edge collaboration and proposes a new monitoring platform. Through the research in this paper, the accuracy of carbon emission monitoring results of the platform has been effectively improved, and the dynamic changes of regional carbon emissions can be grasped in real time in a fast time. The proposed monitoring platform has a high degree of automation, strong control logic and a complete carbon emission continuous monitoring platform is formed by configuring the upper computer configuration. Through optimization, upgrading and reconstruction, the failure rate of the monitoring platform has been reduced, the stability of the platform's continuous monitoring operation has been comprehensively improved, the monitoring data results will not be affected by external interference during the operation process and the platform construction investment is less, which can achieve the goal of environmental protection monitoring in an all-round way.

References

1. Solikhah B, Wahyuningrum IFS, Yulianto A, Sarwono E, Widiatami AK (2021) Carbon emission report: a review based on environmental performance, company age and corporate governance. In: IOP conference series: earth and environmental science, vol 623, no 1, p 012042. IOP Publishing
2. Guo YE, Shang DG, Zuo LX, Qu LF, Cai D, Jin T, Hou G (2021) Damage mode identification of Carbon fiber/Epoxy composites under fatigue process using acoustic emission monitoring. J Phys Conf Ser 2125(1):012036
3. Basuki I, Budiman A, Netzer M, Safitri R, Maulana R, Nusirhan TSE, Bernal B (2021) Dynamic of groundwater table, peat subsidence and carbon emission impacted from deforestation in tropical peatland, Riau, Indonesia. IOP Conf Ser Earth Environ Sci 648(1):012029
4. Liu Y, Tan Q, Han J, Guo M (2021) Energy-water-carbon nexus optimization for the path of achieving carbon emission peak in China considering multiple uncertainties: A case study in inner Mongolia. Energies 14(4):1067
5. Ahvar E, Ahvar S, Mann ZÁ, Crespi N, Glitho R, Garcia-Alfaro J (2021) DECA: A dynamic energy cost and carbon emission-efficient application placement method for edge clouds. IEEE Access 9:70192–70213
6. Li J, Liu R, Xie Q (2022) The price fluctuation in Chinese carbon emission trading market: new evidence from adaptive Fourier decomposition. Procedia Comput Sci 199:1095–1102

7. Gu G, Zheng H, Tong L, Dai Y (2022) Does carbon financial market as an environmental regulation policy tool promote regional energy conservation and emission reduction? Empirical evidence from China. Energy Policy 163:112826
8. Sun ZH, Luo X, Wu EQ, Zuo TY, Tang ZR, Zhuang ZL (2022) Monitoring scheduling of drones for emission control areas: an ant colony-based approach. IEEE Trans Intell Transp Syst 23:11699–11709
9. Sgobba F, Sampaolo A, Patimisco P, Giglio M, Menduni G, Ranieri AC, Spagnolo V (2022) Compact and portable quartz-enhanced photoacoustic spectroscopy sensor for carbon monoxide environmental monitoring in urban areas. Photoacoustics 25:100318
10. Yang M, Wang H, Liu P, Cheng J (2021) A 3D electrochemical biosensor based on Super-Aligned Carbon NanoTube array for point-of-care uric acid monitoring. Biosens Bioelectron 179:113082
11. Zhou Y, Williams CA, Hasler N, Gu H, Kennedy R (2021) Beyond biomass to carbon fluxes: Application and evaluation of a comprehensive forest carbon monitoring system. Environ Res Lett 16(5):055026
12. Gerasimova OA, Vais AA, Luzina EF, Melnik AI, Mantulina AV (2022) Monitoring of organic carbon in the phytomass of pine stands. IOP Conf Ser Earth Environ Sci 981(3):032081
13. Ageev IM, Rybin YM (2021) Measuring complex for carbon-dioxide monitoring in air. Meas Tech 64:339–343
14. Sardar MR, Faisal M, Ahmed K (2021) Simple hollow core photonic crystal fiber for monitoring carbon dioxide gas with very high accuracy. Sens Bio-Sens Res 31:100401
15. Farr NT, Hughes GM, Rodenburg C (2021) Monitoring carbon in electron and ion beam deposition within FIB-SEM. Materials 14(11):3034
16. Alimuddin A, Arafiyah R, Sirajuddin S, Lady N, Susiono W, Masjudin M (2021) System of monitoring on carbon dioxide of broiler chicken growth in closed house. IOP Conf Ser Mater Sci Eng 1098(4):042016
17. He W, Yoo G, Ryu Y (2021) Evaluation of effective quantum yields of photosystem II for CO_2 leakage monitoring in carbon capture and storage sites. PeerJ 9:e10652
18. Toppi M, Baroni G, Battistoni G, Bisogni MG, Cerello P, Ciocca M, Sarti A (2021) Monitoring carbon ion beams transverse position detecting charged secondary fragments: results from patient treatment performed at CNAO. Front Oncol 11:601784
19. del Río JS, Pascual-Gonzalez C, Martinez V, Jiménez JL, Gonzalez C (2021) 3D-printed resistive carbon-fiber-reinforced sensors for monitoring the resin frontal flow during composite manufacturing. Sens Actuators A Phys 317:112422
20. Honeycutt WT, Kim T, Ley MT, Materer NF (2021) Sensor array for wireless remote monitoring of carbon dioxide and methane near carbon sequestration and oil recovery sites. RSC Adv 11(12):6972–6984
21. Kumar S, Kumar H, Bhatia M (2022) Linking carbon emission and economic growth: case from developing economies of the Asian region. Environ Qual Manag 31(4):449–460
22. Ghosh S, Küfer KH, Roy SK, Weber GW (2022) Carbon mechanism on sustainable multi-objective solid transportation problem for waste management in Pythagorean hesitant fuzzy environment. Complex Intell Syst 8(5):4115–4143
23. Sadiq M, Shinwari R, Usman M, Ozturk I, Maghyereh AI (2022) Linking nuclear energy, human development and carbon emission in BRICS region: do external debt and financial globalization protect the environment? Nucl Eng Technol 54(9):3299–3309
24. Wu H, Fang S, Zhang C, Hu S, Nan D, Yang Y (2022) Exploring the impact of urban form on urban land use efficiency under low-carbon emission constraints: a case study in China's Yellow River Basin. J Environ Manag 311:114866
25. Liang X, Liu X, Mei L, Zhang D (2021) Multi-objective green multimodal transport path optimization with the participation of high-speed railway. In: 2021 6th international conference on transportation information and safety (ICTIS), pp 1072–1077. IEEE

Communication Enhancement Techniques for Intelligent Maintenance and Inspection Devices of Power Systems Based on RIS

Jian Fang, Xiang Lin, Fengxiang Zhou, Yan Tian, Min Zhang, and Yingjie Huang

Abstract Intelligent maintenance and inspection devices are critical for ensuring the safe and reliable operation of power systems. However, these devices require reliable and high-bandwidth communication channels, which can be challenging to achieve in the harsh and dynamic environment of power systems. In this paper, we propose the use of Reconfigurable Intelligent Surfaces (RIS) as a potential solution for communication enhancement in power systems. RIS is a promising technology that can improve communication reliability, reduce interference, and cut power consumption through intelligent reflection and refraction of radio signals. We start from the discussion about the specific communication requirements of intelligent maintenance and inspection devices in power systems, which is followed by the introduction of RIS technology and its benefits for enhancing communication in power systems. Some case studies are also represented in this work to demonstrate the effectiveness of using RIS for communication enhancement in power systems.

Keywords Reconfigurable Intelligent Surfaces · Intelligent maintenance and inspection devices · Power systems · Communication enhancement · Beamforming · Wireless communications

J. Fang · X. Lin · F. Zhou · Y. Tian · M. Zhang
Guangzhou Power Supply Bureau of Guangdong Power Grid Co., Ltd., China Southern Power Grid, Guangzhou 510620, China

Y. Huang (✉)
College of Electrical Engineering, Chongqing University, Chongqing 400044, China
e-mail: ying_jie_huang@163.com

S. Yadav et al. (eds.), *Energy Power and Automation Engineering*, Lecture Notes in Electrical Engineering 1118, https://doi.org/10.1007/978-981-99-8878-5_67

1 Introduction

Power systems are critical infrastructures that require reliable and efficient operation to ensure the continuous supply of electricity to consumers [1]. One of the key challenges in maintaining power systems is the need for regular inspection and maintenance of critical components with some of them are often located in remote and difficult-to-access areas, which makes inspection and maintenance challenging and time-consuming. To address these challenges, intelligent maintenance and inspection devices have been developed to automate and streamline the inspection and maintenance process [2].

However, intelligent maintenance and inspection devices rely heavily on communication channels to transfer data and receive commands from remote control centers. The communication requirements of these devices are demanding, as they require high-bandwidth, low-latency, and reliable communication channels that can withstand the harsh and dynamic environment of power systems [3]. Existing communication technologies such as wireless sensor networks and cellular networks have limitations in meeting the communication requirements of intelligent maintenance and inspection devices in power systems.

In recent years, Reconfigurable Intelligent Surfaces (RIS) have emerged as a potential solution for communication enhancement in various industries and applications, including power systems [4]. RIS is a two-dimensional array of smart elements that can manipulate radio signals by reflecting or refracting them in a programmable manner. By controlling the properties of the reflected and refracted signals, RIS can improve the reliability, range, energy efficiency, and bandwidth of communication channels in power systems [5].

This paper provides a comprehensive overview of the potential benefits of RIS technology for enhancing communication in power systems. We first introduce intelligent maintenance and inspection devices in power systems and discuss the associated specific communication requirements. Then, the RIS technology is introduced, which is followed by the discussion about the potential use cases for RIS in power systems. We also represent case studies that demonstrate the effectiveness of using RIS for improving the communication reliability and performance of intelligent maintenance and inspection devices in power systems.

2 Communication Requirements in Power Systems

2.1 Intelligent Maintenance and Inspection Devices

Intelligent maintenance and inspection devices are becoming more prevalent in power systems to monitor, maintain, and inspect various components and systems of power grids. As shown in Fig. 1, these devices include but not limited to advanced sensors [6], intelligent vehicles [7, 8], and wearables [9], which require communication

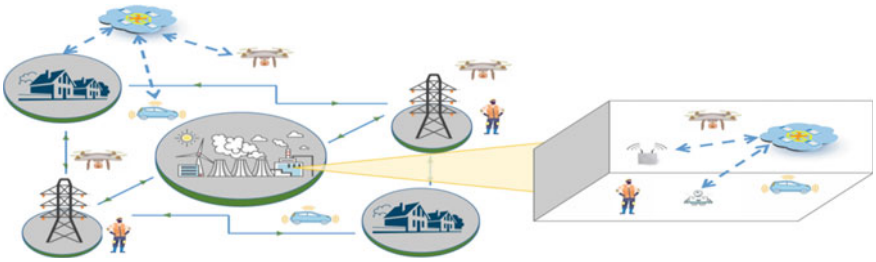

Fig. 1 Intelligent maintenance and inspection devices in power systems

technologies, and data processing capabilities, allowing them to collect and analyze large amounts of data in real-time.

Smart Sensors: In the context of power systems, smart sensors are used for monitoring and measuring various parameters such as temperature, voltage, current, and other environmental conditions. Smart sensors are capable of performing self-diagnosis and self-calibration. They can also communicate with other devices and systems, providing real-time information and enabling better decision-making.

Intelligent Vehicles: As intelligent vehicles, such as drones and robots, can be operated remotely or autonomously, they are increasingly being used to perform inspections and maintenance tasks in power systems, including but not limit to power line inspections, mapping and surveying, and monitoring power plant facilities. Large areas, especially the hard-to-reach areas, such as power lines and towers, can be covered quickly and efficiently, thereby cutting the need for human workers to climb or use specialized equipment and reducing the time and cost of inspections.

Wearables: Wearable devices such as smart glasses and smart helmets can be used to provide remote guidance and support to maintenance workers. The devices can wirelessly transmit images and data to a central control system, where experts can provide real-time guidance and support.

2.2 Communication Requirements

Intelligent maintenance and inspection devices mentioned above typically require reliable, high-speed, and secure communication for effective operation in power systems. In this section, we list some of the necessary communication requirements of these devices.

Real-Time Communication: Many maintenance and inspection devices in power systems require real-time communication to enable advanced and sophisticated applications, such as predictive maintenance, remote control, and autonomous operation. For example, an intelligent drone used for inspecting power lines needs to transmit

high-resolution video in real-time to the operator for analysis. Smart sensors need to provide real-time data and alerts to the control center or maintenance personnel to enable quick responses to any abnormal conditions or changes in the operating parameters.

High Bandwidth: Many intelligent maintenance and inspection devices generate large amounts of data that need to be transmitted to remote locations for analysis. For example, smart drones may require high bandwidth for transmitting real-time video feed or lidar data for obstacle detection. In general, the more data that needs to be transmitted in real time, the higher the bandwidth requirement. Therefore, it is essential to have a communication system with sufficient bandwidth to support the specific requirements of each intelligent maintenance and inspection device in power systems.

Security: The intelligent maintenance and inspection devices used in power systems collect and transmit sensitive information, such as power grid data, inspection data, and maintenance records. Therefore, ensuring the safety and reliability of the communications among devices in power grids is of paramount importance.

3 RIS Technology and its Benefits in Power Systems

RIS, as shown in Fig. 2, is a novel technology that has emerged recently as a promising solution for enhancing wireless communications. RIS is a planar array of low-cost and reflecting elements that can manipulate electromagnetic waves by controlling the reflecting phase and amplitude of each elements. A smart propagation environment that can be constructed to achieve desired communication requirements, such as, enhances the received signal quality, mitigates interference, and improves overall network performance [4, 5]. The use of RIS has been studied in various applications, including indoor and outdoor wireless communications, beyond 5G networks, and satellite communications.

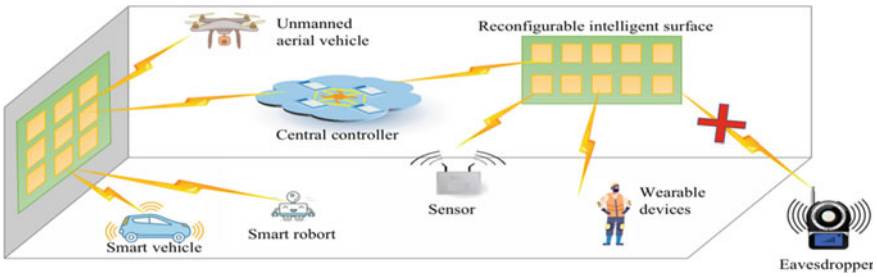

Fig. 2 Applications of RISs to enhance the communication among intelligent maintenance and inspection devices in power systems

In power systems, RIS has the potential to enhance the information exchange among intelligent maintenance and inspection devices, as well as central controllers, which are critical for ensuring the safe and efficient operation of power grids [10]. RIS can be deployed in different locations in power systems, such as on the walls of power plant buildings, substations, and transmission lines, to reflect and manipulate radio waves in order to improve signal strength and coverage.

3.1 RIS-Enabled Real-Time Communications

RIS can be used to realize real-time communication for intelligent maintenance and inspection devices in power systems by enabling better signal propagation and reception. RIS can be placed strategically in the environment where communication takes place, and then be reconfigured to reflect, refract, or diffract the wireless signals. By doing so, RIS can effectively enhance the signal strength, reduce interference, and improve the overall quality of wireless communication.

An critical approach to using RIS for real-time communication is to combine it with beamforming techniques [11], that is, adjusting the phase and amplitude of each reflecting element suitably, to improve the directionality and focus of the wireless signals. Researchers from wireless communication field have already developed and are continuously developing efficient beamforming algorithms based on the wireless channel conditions and the feedback from the RIS.

Therefore, the propagation environment of power systems and the special characteristics of intelligent maintenance and inspection devices should be carefully considered when applying RIS, thereby enabling more effective and efficient monitoring, control, and maintenance of power systems.

3.2 Bandwidth Improvement by RIS

RIS also has an advantage in enhancing the bandwidth of intelligent maintenance and inspection devices in power systems. As shown in Fig. 2, RIS can create a virtual wireless network that provides additional communication channels to improve the bandwidth of communication links [12]. This can be particularly useful in scenarios where the available frequency bands are already congested or where the communication requirements of intelligent maintenance and inspection devices in power systems exceed the capacity of existing communication technologies.

Specifically, a new spectrum sharing approach can be designed by using RIS. In traditional power systems, each devices is assigned a specific and uncorrelated frequency band to avoid interference with others. However, this approach can lead to inefficient use of the spectrum since some bands may be underutilized while others may be congested. With the application of RISs, multiple intelligent maintenance and inspection devices can share the same frequency band by using different phases,

which can effectively increase the spectrum efficiency and provide additional bandwidth for communication. Furthermore, RIS can extend the range and enhance the reliablity of higher frequency bands, such as millimeter-wave and terahertz frequencies, which are highly susceptible to blockage and attenuation. These limitations can be overcome by RIS, thereby offering much wider bandwidths than lower frequency bands.

Overall, RIS has the potential to significantly improve the bandwidth of communication links for intelligent maintenance and inspection devices in power systems, enabling more advanced and data-intensive applications that were previously not possible.

3.3 RIS-Enabled Security Enhancement

RIS can be used to improve the security of intelligent maintenance and inspection operations in power systems by reducing the risk of eavesdropping, jamming, and interception [13]. One critical step is the beamforming design, which directs the signal to intended receivers and limits the signal strength in undesired directions. It thus prevents attackers to intercept or eavesdrop on the communication link. This is especially important for sensitive data that is transmitted between devices in power systems, such as operational data or sensitive information related to the power grid.

Moreover, RIS can also be used to enhance security by mitigating interference generated by nearby devices or attackers. In addition, RIS can provide an extra layer of security by creating a secure communication channel between devices. This can be achieved through the use of encryption and authentication protocols, which ensure that only authorized devices can access the communication channel. Therefore, RIS technology is capable of securing intelligent maintenance and inspection devices in power systems with properly designed beamforming, as well as encryption and authentication schemes.

In summary, the deployment of RIS in strategic locations can help to overcome obstacles that might exist in wireless communication networks and enhance the performance of intelligent maintenance and inspection devices. However, the exact deployment and reflecting parameters of RIS depend on the specific scenarios and the wireless communication requirements of the devices being used.

4 Use Cases

Taking the above-mentioned intelligent maintenance and inspection devices into account, we deploy RIS to assist the communications between these devices and central controller, as given in Fig. 3. To verify the superiority of RIS, we represent the communication performance of the RIS-assisted power system and the one without

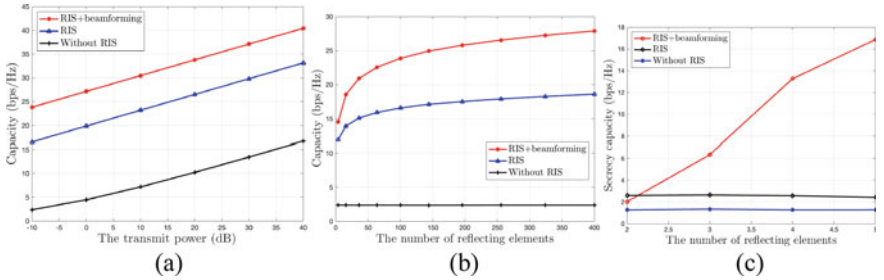

Fig. 3 Simulations: **a** capacity versus transmit power **b** capacity versus the number of reflecting elements **c** secrecy capacity versus the number of reflecting elements

RIS. In the following, the RIS-assisted communications between intelligent maintenance and inspection devices and central controller is referred to as 'RIS', while the one under optimal beamforming scheme is referred to as 'RIS + beamforming'. The conventional communications without RIS are considered as the benchmark, which is referred to as 'Without RIS'.

In the first experiment, we compare the achieved capacity of the considered three scenarios. As we can see from Fig. 3a, the 'RIS + beamforming' always achieves the best performance in terms of capacity, while 'Without RIS' is always the worst choice. 'RIS + beamforming' brings additional around 20 dB and 80 dB gains compared to 'RIS' and 'Without RIS', respectively. Then, we investigate in Fig. 3b the impact of the number of reflecting elements on RIS on the capacity performance. As a result, the power systems assisted by RIS gets improved with the increase in the number of reflecting elements, which is agree with what we expected. To verify the functionalities of RIS in reducing the risk of eavesdropping, the secrecy capacity of all schemes with respect to the number of reflecting elements is simulated in Fig. 3c. It can be observed that the 'RIS + beamforming' still the best option to realize secure communication. It is valuable to note that solely deploying RIS without proposed beamforming design can not enhance the security of information transmission between intelligent maintenance and inspection devices and central controller.

5 Discussions and Conclusions

In conclusion, this paper has proposed the use of RIS for communication enhancement among intelligent maintenance and inspection devices in power systems. We have discussed the specific communication requirements of these devices, including low-latency, real-time, and secure communication. The potential of RIS technology to significantly improve the communication performance in power systems for intelligent maintenance and inspection devices has been illustrated. We also verify the effectiveness of RIS by conducting some simulation experiments.

However, it is important to note that there are still limitations. One is the need for specialized expertise for deployment and maintenance. Another limitation is the difficulties to access accurate channel state information and develop high efficiency but low complexity beamforming schemes, which impact the effectiveness of RIS a lot. Also, RIS technology is still a relatively new and emerging field, and there are currently no standardized interfaces or protocols for communication between RIS and devices in power systems.

Despite these limitations, we believe that RIS technology has the potential to play a significant role in enhancing the communication capabilities of intelligent maintenance and inspection devices in power systems. With further research and development, RIS technology can be optimized for power systems applications, addressing these limitations and providing more reliable and efficient communication for maintenance and inspection tasks in power systems.

Acknowledgements This paper is supported by China Southern Power Grid (GJHKJXM20210068).

References

1. Ahmad T, Zhang D, Huang C, Zhang H, Dai N, Song Y, Chen H (2021) Artificial intelligence in sustainable energy industry: status Quo, challenges and opportunities. J Clean Prod 289:125834. https://doi.org/10.1016/j.jclepro.20
2. Afridi YS, Ahmad K, Hassan L (2022) Artificial intelligence based prognostic maintenance of renewable energy systems: a review of techniques, challenges, and future research directions. Int J Energy Res 46(15):21619–21642. https://doi.org/10.1002/er.7100
3. Aceto G, Persico V, Pescapé A (2019) A survey on information and communication technologies for industry 4.0: state-of-the-art, taxonomies, perspectives, and challenges. IEEE Commun Surv Tutor 21(4):3467–3501. https://doi.org/10.1109/COMST.2019.2938259
4. Pan C, Ren H, Wang K, Kolb JF, Elkashlan M, Chen M, Di Renzo M, Hao Y, Wang J, Swindlehurst AL, You X (2021) Reconfigurable intelligent surfaces for 6G systems: principles, applications, and research directions. IEEE Commun Mag 59(6):14–20. https://doi.org/10.1109/MCOM.001.2001076
5. Liu Y, Liu X, Mu X, Hou T, Xu J, Di Renzo M, Al-Dhahir, N (2021) Reconfigurable intelligent surfaces: principles and opportunities. IEEE Commun Surv Tutor 23(3):1546–1577. https://doi.org/10.1109/COMST.2021.3077737
6. Alonso M, Amaris H, Alcala D, Florez RDM (2020) Smart sensors for smart grid reliability. Sensors 20(8):2187. https://doi.org/10.3390/s20082187
7. Menendez O, Cheein FAA, Perez M, Kouro S (2017) Robotics in power systems: enabling a more reliable and safe grid. IEEE Ind Electron Mag 11(2):22–34. https://doi.org/10.1109/MIE.2017.2686458
8. Aminifar F, Rahmatian F (2020) Unmanned aerial vehicles in modern power systems: technologies, use cases, outlooks, and challenges. IEEE Electrif Mag 8(4):107–116. https://doi.org/10.1109/MELE.2020.3026505
9. Chong YW, Ismail W, Ko K, Lee CY (2019) Energy harvesting for wearable devices: a review. IEEE Sens J 19(20):9047–9062. https://doi.org/10.1109/JSEN.2019.2925638
10. Padhan AK, Sahu HK, Sahu PR, Samantaray SR (2021) RIS assisted dual-hop mixed PLC/RF for smart grid applications. IEEE Commun Lett 25(11):3523–3527. https://doi.org/10.1109/LCOMM.2021.3104630

11. Ye J, Guo S, Alouini MS (2020) Joint reflecting and precoding designs for SER minimization in reconfigurable intelligent surfaces assisted MIMO systems. IEEE Trans Wirel Commun 19(8):5561–5574. https://doi.org/10.1109/TWC.2020.2994455
12. Tian Z, Chen Z, Wang M, Jia Y, Dai L, Jin S (2022) Reconfigurable intelligent surface empowered optimization for spectrum sharing: scenarios and methods. IEEE Veh Technol Mag 17(2):74–82
13. Ye J, Kammoun A, Alouini MS (2022) Reconfigurable intelligent surface enabled interference nulling and signal power maximization in mmWave bands. IEEE Trans Wireless Commun 21(11):9096–9113

Photovoltaic Access Capability Evaluation Algorithm Under Source Load Coordinated Operation of Power Supply and Consumption System

Zhicai Xiang, Sitong Li, Xiaolin Li, Zichao Zhou, Xiaohua An, and Yueming Ding

Abstract Currently, the evaluation of photovoltaic access capacity is mostly based on single-layer processing, resulting in a decrease in evaluation efficiency. Therefore, the design and validation analysis of the photovoltaic access capability evaluation algorithm under the coordinated operation of source and load in the supply and demand system have been proposed. Construct a multi scenario photovoltaic access capacity evaluation and calculation structure, and use fitting processing to design capacity evaluation algorithms under the coordinated operation of source and load in the supply and demand system. The final test results indicate that the difference between the fitted mean values is well controlled 0.5, highly targeted, more accurate and reliable, with controllable errors, and has practical application value.

Keywords Power supply and consumption system · Source load synergy · PV access · Capability assessment · Evaluation algorithm · Power consumption system

1 Introduction

Photovoltaic access is actually a dynamic processing method of energy conversion using photovoltaic power generation technology. Generally, photovoltaic access needs to be associated with a large number of power supply and power consumption equipment. During the design process, there are also very high requirements for the operation status of the power supply and consumption system [1]. Moreover, photovoltaic access can also adjust and deal with the defective positions of the power supply and consumption structure to form a more flexible control program [2]. However, against this background, in recent years, due to the improvement of social power demand and standards, the PV access capacity of some power supply

Z. Xiang · S. Li (✉) · X. Li · Z. Zhou · X. An · Y. Ding
State Grid Rizhao Power Supply Company, State Grid Shandong Electric Power Company, Rizhao 276800, Shandong, China
e-mail: lsitong2010@163.com

S. Yadav et al. (eds.), *Energy Power and Automation Engineering*, Lecture Notes in Electrical Engineering 1118, https://doi.org/10.1007/978-981-99-8878-5_68

and consumption systems has declined, resulting in greater load and pressure on the system operation, which has a negative impact on the implementation of subsequent work [3]. In order to alleviate the above problems, some staff have designed corresponding photovoltaic access capability evaluation algorithms. The traditional evaluation algorithms are mostly one-way processing. Although they can achieve the expected evaluation goals, they are often affected by the external environment and specific factors. In addition, the evaluation tasks are constantly changing and instability is increasing, leading to errors in the final evaluation results [4]. In addition, the access of large-scale distributed photovoltaic is also likely to increase the penetration rate of the power supply and consumption system, bringing about problems such as branch power flow out of limit, voltage quality decline, and many adverse effects. Therefore, the design, verification, and analysis of photovoltaic access capability evaluation algorithm under the source load coordinated operation of the power supply and consumption system are proposed. The so-called source load collaboration of the power supply and consumption system generally refers to the centralized network, electricity, and load collaborative processing in the way of global optimization, and the calculation of equivalent permeability and evaluation indicators to obtain the final benefits [5]. In such a grid environment, the innovation and modification of photovoltaic access assessment forms are carried out from multiple perspectives, and the dynamic comparison processing [6] is carried out in accordance with preset assessment standards. At the same time, under the guidance of source load coordination, a multi-level and multi-objective evaluation structure is designed. In case of overvoltage, three-phase imbalance, large line loss, low energy efficiency, and other problems at the end of the power supply and consumption system caused by low base load in the daytime and large-scale reverse transmission, the equivalent regulation means is formulated in combination with the relevant technology and implementation framework. For the form of large-scale roof distributed photovoltaic system access [7], further ensure the safe and reliable operation of the power supply and consumption system, comprehensively improve the power grid's ability to regulate distributed resources, and provide reference for the design of photovoltaic access assessment algorithm [8].

2 Design Photovoltaic Access Capability Evaluation Algorithm Under Source Load Coordination

Design the evaluation process of photovoltaic access capability evaluation algorithm under the coordinated operation of source and load in the supply and demand system as a whole, as shown in Fig. 1.

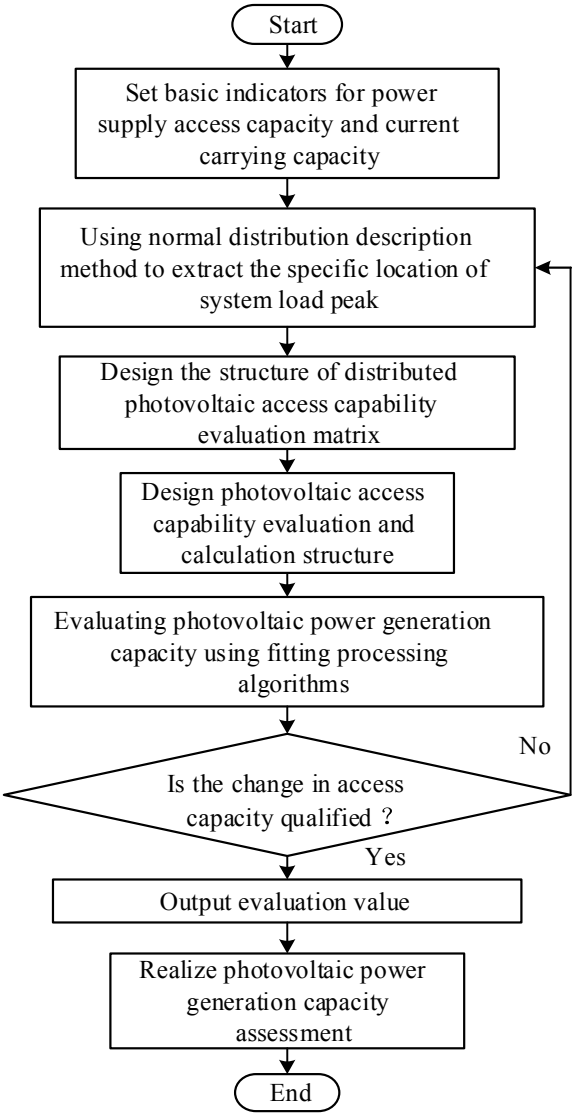

Fig. 1 The evaluation flow of the evaluation algorithm

2.1 Extraction of Power Supply and Line Current Carrying Capacity Evaluation Indicators

In general, the corresponding power supply capacity is different according to the location and scenario of photovoltaic access. The multi-level setting method is adopted and the corresponding power supply capacity standard is formulated according to

the situation, and adjustments are made in time to ensure the improvement of subsequent access capacity [9]. Taking a small photovoltaic power station as an example, the basic setting is 380 V voltage level transmission, and the total built-in capacity should not exceed 25% of the maximum load of transformer power supply [10]. At this time, according to the measured data and information, calculate the maximum allowable PV active output. The details are shown in Formula 1:

$$P = \nu^2 + \frac{(1-c)\nu}{\Im} - \alpha \tag{1}$$

In Formula 1: P represents the maximum value of photovoltaic active output, ν is the base load power, $\Im$ is the power factor, c represents a descriptive range, α indicates the directional access capacity limit. According to the above settings, complete the calculation of the maximum value of photovoltaic active output. According to the change of the maximum value of photovoltaic active power output, the real-time power supply capacity is measured using the initial algorithm. The current carrying capacity of the line is related to the current carrying order, active power, reactive power, and other indicators. Usually, there is a normal variation between these three indicators. The more current carrying orders, the corresponding changes in active power and reactive power will also occur, but there is no specific limit standard for power setting. It needs to be set according to the capacity value of photovoltaic access, with strong convertibility and flexibility. After the value and setting of basic indicators are completed, the next stage of photovoltaic access assessment capability measurement is carried out.

2.2 *Design Distributed Photovoltaic Access Capability Evaluation Matrix*

The specific matrix framework is shown in Fig. 2.

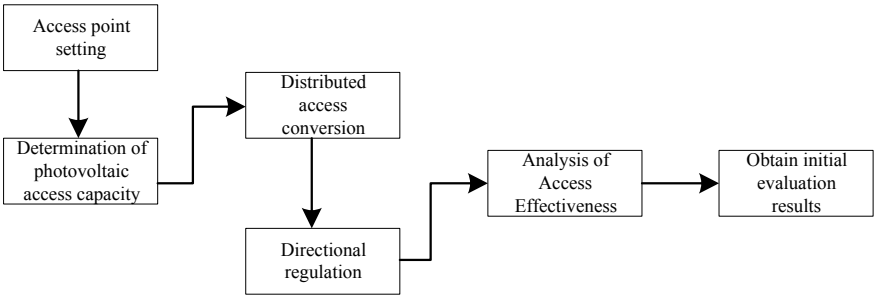

Fig. 2 Structure diagram of distributed photovoltaic access capability evaluation matrix

According to Fig. 2, complete the design and analysis of the structure of the distributed photovoltaic access capability evaluation matrix. Next, build the access route of the distributed photovoltaic construction matrix with the whole county as the promotion scope. The distributed access mode will be more stable and secure, and cover a wider range. The 380 V voltage level is set as the upper limit standard. In the process of photovoltaic access, the fluctuation characteristics of the system load are extracted by using the normal distribution description method, and the specific location of the load peak is marked.

2.3 Build the Evaluation and Calculation Structure of Multi Scenario Photovoltaic Access Capability Under the Source Load Coordinated Operation of the Power Supply and Consumption System

Set the corresponding access capacity, determine the access time consumption of one-way tasks, and calculate the access security boundary limit of the power supply and consumption system for source load coordinated operation according to the set evaluation and calculation structure, as shown in the following Formula 2:

$$W = \sum_{a=1} \gamma a - \sqrt{\varpi + (1 - \varsigma)^2} \tag{2}$$

Equation 2: W indicates the access security boundary limit, γ represents the fitting deviation, a indicates the access frequency, ϖ represents preset permeability, ς indicates the expected value. Based on the above measurements, the calculation of the access security boundary limit is completed, and it is set as the control benchmark for the source load coordinated operation of the power supply and consumption system. In combination with the distributed photovoltaic access scheme, the corresponding access capability evaluation and calculation structure is designed, as shown in Fig. 3.

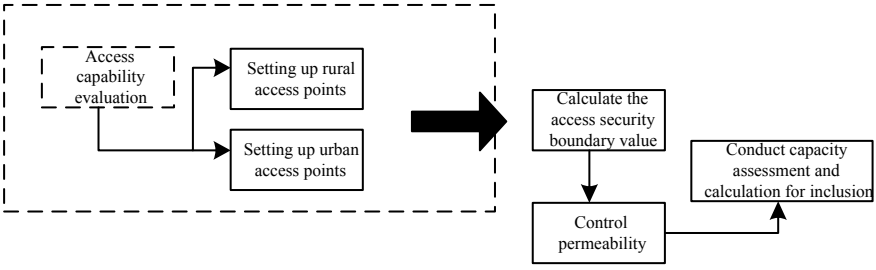

Fig. 3 Photovoltaic access capability evaluation and calculation structure diagram

2.4 Algorithm Design for Evaluation of Fitting Processing Implementation Capability

After completing the construction of the evaluation and calculation structure of multi scene photovoltaic access capability under the source load coordinated operation of the power supply and consumption system, the final evaluation algorithm is designed by fitting. You can first collect the real-time operation status of the photovoltaic power station using the set nodes, collect the corresponding data and information, calculate the change value of the access capacity at this time, and design a fitting processing evaluation framework, as shown in Fig. 4.

3 Experiment

The experimental design is to select three photovoltaic access points in two areas of a certain distribution network, and set and calibrate them as research objects. Adopting a distributed coverage monitoring method, monitoring and verification nodes are set up around the photovoltaic access point. Directional correlation between nodes forms a cyclic control structure. Set basic evaluation indicators and parameters based on actual measurement needs and standards. Based on the background of coordinated operation of power load, measurement research was conducted on the evaluation algorithm of photovoltaic access capacity. Measure and analyze the initial six photovoltaic access points to ensure they are in a stable operating state. Based on actual measurement needs and standards, use monitoring nodes to collect real-time data and information in a targeted manner, and summarize and integrate them. Use MathworksMatlab2020a and IBMCPLEX12.9 solvers to simulate simulation settings and adjust the power system.

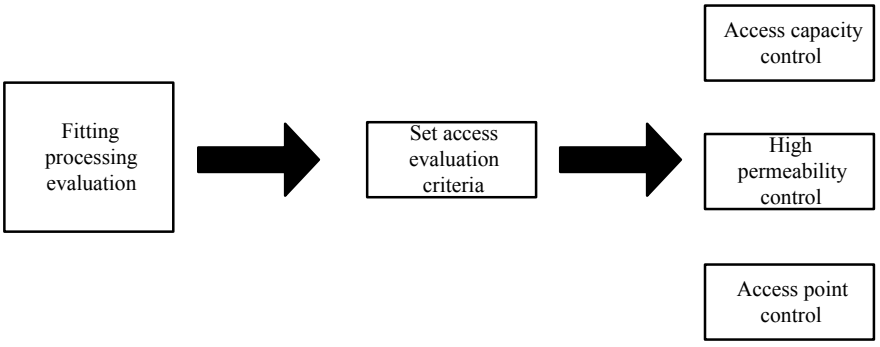

Fig. 4 Diagram of fitting processing evaluation framework

Table 1 Basic evaluation indicators and parameter settings

Photovoltaic access measurement and evaluation indicators	Preset indicator parameter standards	Controllable index parameter standards
Beta distribution description	Access point positioning item, distributed access item, voltage control item	Access point positioning item, distributed access item, voltage control item, power supply capacity control item
Definition of negative volatility assessment	Small range single fluctuation of voltage during photovoltaic connection	Large range and multiple fluctuations in voltage during photovoltaic connection
Normal distribution ratio	1.03	1.12
Take the mean of the evaluation standard deviation	16.05	17.24
Probability of high entropy voltage/%	89.66	92.34
Cumulative distribution function	− 17.62	− 19.05
Fitting evaluation content	Small range single fluctuation of voltage during photovoltaic connection	Minimum voltage, total load control, reference voltage, load reduction
Permeability/%	45.25	48.65

3.1 Experiment Preparation

Select three photovoltaic access points in two areas of a certain distribution network, and set and calibrate them as research objects. This part needs to adopt the distributed coverage monitoring method, mark the corresponding points around the PV access points, set monitoring and verification nodes, conduct directional correlation between nodes, and form a circular control structure, which is convenient for the design and practical application of the access capability evaluation algorithm in the later stage. The basic evaluation indicators and parameters are set according to the actual measurement needs and standards, as shown in Table 1.

3.2 Experimental Process and Result Analysis

In the above built test environment, the measurement research of photovoltaic access capability evaluation algorithm is carried out based on the background of source load coordinated operation. First, the six PV access points initially set are measured and analyzed to ensure that they are in a stable operation state. Next, combined with the actual measurement needs and standards, the monitoring nodes are used to conduct directional collection of real-time data and information, and after summary and

integration, they are ready for subsequent use. At this time, Mathworks Matlab2020a and IBM CPLEX12.9 solver are used to set and adjust the power supply system, and then, based on this, according to the obtained data and initial information, the PV access capacity limit standard is calculated, as shown in Formula 3:

$$G = (1-n)^2 \times \sum_{k=1} \beta k + nm \tag{3}$$

In Formula 3: G indicates the PV access capacity limit standard, n indicates the controllable range, β indicates the directional access distance, β indicates the set access point, m represents the total incoming capacity. According to the above settings, complete the calculation of PV access capacity limit standard, and set it as the initial standard of basic PV access capacity assessment. Next, according to the actual access requirements, the total access capacity of the region is measured at the six points set to obtain the real-time access capacity of the corresponding node. However, because there are differences in the scenarios and access effects between rural and urban areas, the designed capacity evaluation calculation matrix is used to measure the total access capacity of the region, and the final evaluation fitting mean difference is calculated, as shown in Formula 4:

$$L = d - \frac{ad}{a + (1-\varepsilon)^2} \times \varepsilon d^2 \tag{4}$$

In Formula 4: L represents the difference of the mean value of the evaluation fit, d indicates the peak value of directional load, a represents distributed coverage, ε indicates the response time. According to the above settings, comparative analysis of test results is achieved, as shown in Table 2.

Table 2 Comparison and analysis of test results

Photovoltaic access testing points	Photovoltaic access capacity limit standard/MW	Leakage rate/%	Evaluate fit mean difference
Point 1 (rural testing area)	3.651	32.11	0.35
Point 2 (rural testing area)	4.215	31.25	0.41
Point 3 (rural testing area)	3.647	30.16	0.32
Point 4 (urban testing area)	3.021	33.21	0.32
Point 5 (urban testing area)	4.157	30.47	0.25
Point 6 (urban testing area)	4.211	31.69	0.40

According to Table 2, complete the comparative analysis of the test results: through the comprehensive measurement and analysis of six photovoltaic access points set in rural and urban areas, verify and study the access capacity of each point through the change of photovoltaic access capacity, and finally use the design algorithm to get the difference of the evaluation fitting mean value to be better controlled 0.5. It shows that this algorithm has strong pertinence, and in different regions, combined with the background of the source load coordinated operation of the power supply and consumption system, the assessment results are more accurate and reliable, the error is controllable, and has practical application value. The method proposed in this paper can further ensure the safe and reliable operation of the power supply and consumption system, and comprehensively improve the power grid's ability to regulate distributed resources.

4 Conclusion

To sum up, the above is the design and verification evaluation of the photovoltaic access capability evaluation algorithm under the source load coordinated operation of the power supply and consumption system. This time under the background of the source load coordinated operation, the designed algorithm further expanded the actual evaluation scope, gradually forming a more stable and multi-source evaluation structure. In addition, by analyzing the electricity and heat load demand curves, the stability and reliability of the evaluation can be improved, and the evaluation problem can be better solved. The test results show that this method improves the evaluation effect of photovoltaic access capacity, effectively controls the mean difference of fitting, and has clear evaluation objectives, high accuracy, and good reliability. It can provide accurate data reference for solving problems such as high system terminal voltage, three-phase imbalance, high line loss, and low energy efficiency, and has practical application value.

Acknowledgements The study was supported by State Grid Corporation Headquarters Science and Technology Project "Research and demonstration of key technologies for source-load cooperative operation and intelligent operation and maintenance of" (5400-202216167A-1-1-ZN).

References

1. Alaraj M, Kumar A, Alsaidan I et al (2021) Energy production forecasting from solar photovoltaic plants based on meteorological parameters for Qassim Region, Saudi Arabia. IEEE Access 99:1
2. Nawaraj S, Bivek B (2021) Modelling and analysis of decentralized energy systems with photovoltaic, micro-hydro, battery and diesel technology for remote areas of Nepal. Clean Energy 4:4

3. Ma J, Chang J, Wang S et al (2022) Photovoltaic-pyroelectric coupled effect in Ag_2Se/Si heterojunction for broad-band, ultrafast, self-powered, position-sensitive detectors. ACS Photonics 9(6):2160–2169
4. Hwang PC, Ku CY, Chan CC (2021) Detection of malfunctioning photovoltaic modules based on machine learning algorithms. IEEE Access 99:1
5. Alrifaey M, Lim WH, Ang CK et al (2022) Hybrid deep learning model for fault detection and classification of grid-connected photovoltaic system. IEEE Access 10:10
6. Sutikno T, Subrata AC, Elkhateb A (2021) Evaluation of fuzzy membership function effects for maximum power point tracking technique of photovoltaic system. IEEE Access 99:1
7. Ahmed RM, Zakzouk NE, Abdelkader MI et al (2021) Modified partial-shading-tolerant multi-input-single-output photovoltaic string converter. IEEE Access 99:1
8. Soliman MA, Al-Durra A, Hasanien HM (2021) Electrical parameters identification of three-diode photovoltaic model based on equilibrium optimizer algorithm. IEEE Access 99:1
9. Li C, Yao Y, Zhao R et al (2021) Optimization model for time-varying settlement of renewable energy consumption considering accommodation difficulty and supply–demand interaction. Int J Electr Power Energy Syst 125(24):106469
10. Omar B, Savvaris A, Rahil O et al (2021) Saving hydrogen fuel consumption and operating at high efficiency of fuel cell in hybrid system to power UAV. J Earth Energy Eng 10(1):32–42

Mobile Platform Design for Intelligent Maintenance and Inspection of Power Systems Based on Human-Vehicle-Internet Coordination

Jian Fang, Xiang Lin, Fengxiang Zhou, Yan Tian, Min Zhang, and Te Ao

Abstract Recently, there has been a growing focus on the integration of human, vehicle, and internet components to achieve a more streamlined and intelligent approach to power system maintenance and inspection. Within this context, our paper introduces a novel system framework consisting of three essential layers: the terminal layer, network layer, and platform layer. This framework serves as the foundation for effectively coordinating the interactions between human, vehicle, and internet components. While each layer plays a vital role, the significance of the platform layer cannot be overstated. We delve into the intricate specifics of the platform layer, offering comprehensive insights into their roles and interconnections. Furthermore, our research presents practical implementations and detailed experiments that substantiate the efficacy of our proposed design. Through these empirical validations, we establish the tangible benefits of our approach. Our contribution enhances the comprehension of intelligent power system maintenance and inspection driven by the harmonious coordination of human, vehicle, and internet elements.

Keywords Intelligent maintenance inspection · Power systems · Human-vehicle-internet coordination · System framework

1 Introduction

The reliable and safe operation of power systems is essential for the smooth functioning of modern society [1, 2]. However, the maintenance and inspection of power equipment and transmission lines can be challenging and potentially dangerous for personnel. Traditional maintenance and inspection methods rely heavily on manual

J. Fang · X. Lin · F. Zhou · Y. Tian · M. Zhang
Guangzhou Power Supply Bureau of Guangdong Power Grid Co., Ltd., China Southern Power Grid, Guangzhou 510620, China

T. Ao (✉)
College of Electrical Engineering, Chongqing University, Chongqing 400044, China
e-mail: 260774054@qq.com

S. Yadav et al. (eds.), *Energy Power and Automation Engineering*, Lecture Notes in Electrical Engineering 1118, https://doi.org/10.1007/978-981-99-8878-5_69

labor and visual inspection, which can be time-consuming and prone to errors [3]. In addition, the increasing complexity and scale of power systems require more efficient and effective maintenance and inspection approaches.

To address these challenges, an intelligent maintenance and inspection approach based on human-vehicle-internet coordination has emerged recently. The human-vehicle-internet coordination system consists of three key components: the human component, the vehicle component, and the internet component. By leveraging the expertise of human operators, the mobility of vehicles, and the connectivity of the internet, the proposed approach can improve the accuracy and efficiency of maintenance and inspection operations. In this context, the pivotal importance of an appropriate system framework in facilitating the harmonious coordination among human, vehicle, and internet components within the context of power system maintenance and inspection cannot be overstated. In general, the system framework is composed of a terminal layer, network layer, and platform layer. At the core of this visionary approach lies the platform layer, an instrumental component within the associated system framework.

Contributions: In this work, we investigate the strategic design of a system framework composed of the terminal layer, network layer, and platform layer that actively transforms human, vehicle, and internet components into interconnected agents of precision and intelligence. In particular, we embark on an in-depth exploration of the platform design, which empowers power system management with unprecedented precision and reliability. We illustrate the software design supporting the functionalities of the intelligent mobile platform for power system maintenance and inspection. Going beyond theoretical analysis, our research takes a resolutely practical stance by presenting real-world implementations and meticulously designed experiments. Through these carefully orchestrated empirical validations, we not only affirm the robustness of our proposed design but also elucidate its profound impact on power system maintenance and inspection practices.

2 System Framework for Human-Vehicle-Internet Coordination

2.1 Human-Vehicle-Internet Coordination

The concept of human-vehicle-internet coordination in intelligent maintenance and inspection of power systems refers to the use of mobile inspection platforms equipped with a range of sensors, cameras, and other equipment to collect data on power systems, which is then transmitted over the internet to the control center to analysis and to maintenance personnel for operation. As we can expect, the human-vehicle-internet coordination is composed of three main components: the human component, the vehicle component, and the internet component.

The human component refers to the maintenance personnel who carry and operate a series of maintenance equipment and use mobile devices to access and analyze the data collected by the platform. Maintenance personnel are generally equipped with personal protective equipment [4], lighting and infrared cameras, small partial discharge detectors, and ultrasonic receivers for maintenance work. In addition, there are detachable units that can be used flexibly in different situations.

The vehicle component refers to mobile inspection platforms equipped with advanced technology and tools for monitoring, inspecting, and maintaining power systems. The typical vehicles include patrol robots [5], drones [6], and cars. These platforms can be used to inspect power transmission lines, substations, and other critical infrastructure, as well as to perform routine maintenance tasks. They are typically designed to be agile, versatile, and capable of operating in a wide range of conditions and environments.

The internet component refers to the cloud computing and communication infrastructure that is critical to enabling real-time data collection, analysis, and decision-making. The internet component includes a range of technologies and systems, such as a secure and reliable data transmission system, such as wireless networks or cellular networks [7], a fast and accurate data analysis system, such as big data analytics and edge computing [8], and a robust data storage and retrieval system, such as the clouding computing, that work together to ensure that terminal devices can access the data they need quickly and efficiently, and make informed decisions about maintenance activities in real-time.

Overall, the coordination between the human, vehicle, and internet components is critical to the success of the intelligent maintenance and inspection of power systems. Each component plays a unique role in the system, and they must work together seamlessly to ensure that data is collected accurately, transmitted efficiently, and analyzed effectively. This requires careful planning and implementation, as well as monitoring and maintenance to ensure that the system remains reliable and effective over the long term.

2.2 General Network Framework

The coordination of the human-vehicle-internet is essential for the success of intelligent maintenance and inspection of power systems. However, to achieve this coordination, a suitable framework is necessary. The framework should enable data collection, processing, analysis, and decision-making in a seamless manner between the human component, vehicle component, and internet component. In this paper, we propose a three-layer framework consisting of the terminal layer, network layer, and platform layer, as shown in Fig. 1.

The terminal layer is the first layer in the framework, which represents the interface between the physical world and the digital system. In other words, the terminal layer is the interface between the human component and the vehicle and equipment components. The network layer connects the terminal layer and the platform layer,

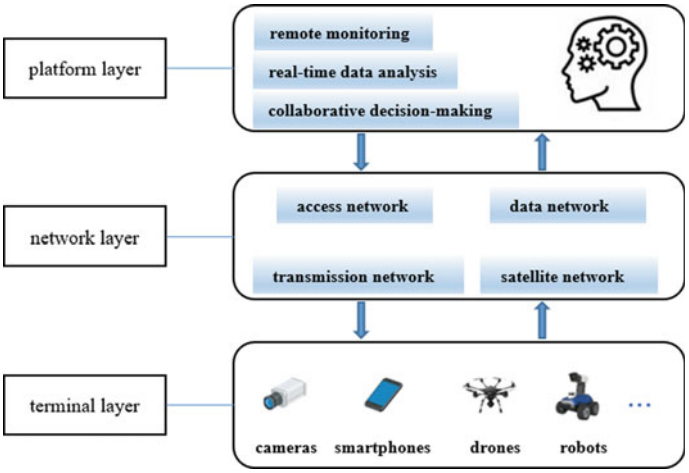

Fig. 1 General network framework

which provides the communication network infrastructure and support for the intelligent maintenance and inspection system. The platform layer is the core component of the framework and it provides a unified management platform for the entire system. This layer processes and analyzes the data collected from the terminal layer through the network layer and performs data cleaning, processing, analysis, and storage to provide insights to decision-makers for making informed decisions about maintenance and inspections. Specifically, the analysis results in the platform layer can generate alarms, reports, and maintenance recommendations, which can be used to guide the maintenance personnel to perform maintenance and inspection tasks. It consists of data analytics tools, machine learning algorithms, and other technologies that can process and analyze large volumes of data quickly and accurately. The platform layer can also provide a graphical user interface (GUI) to display the real-time data and analysis results, and allow the maintenance personnel to operate and control the system. The platform layer plays a crucial role in enabling the human-vehicle-internet coordination and improving the efficiency and accuracy of maintenance and inspection tasks. In the following, we will elaborate on more specific details for the platform layer.

3 Platform Design and Experiments

The practical implementation of the intelligent maintenance and inspection of power systems based on human-vehicle-internet coordination discussed above relies on the deployment of mobile intelligent platforms, the construction of the main control system, and the access of all communication devices. They are capable of data collection, classification, uploading, and historical data inquiry. In the following, we will

give the software design supporting the functionalities of the platforms, which should at least include three modules, that is, the authorization verification module, the equipment ledger module, and the maintenance and inspection management module.

3.1 Software Design Framework

The intelligent maintenance and inspection platform should at least include three modules, that is, the authorization verification module, the equipment ledger module, and the maintenance and inspection management module.

The authorization verification module is designed to ensure that only authorized personnel are able to access and use the software and associated functions, which is composed of two steps as shown in Fig. 2. Firstly, the users display the application code and the device will provide two ways to apply for the software registration file: One is to write the file and obtain the authorization file from the relevant unit by providing the application code file, and another is to obtain the authorization file directly by providing the application code to the relevant unit. Then, the device will authorize the software by selecting the authorization file.

The equipment ledger module refers to a record-keeping system that documents information related to equipment, including equipment ledger information, inspection records, testing records, defect records, and drawing documentation. The interface code implemented by this functional module can be designed accordingly, which is given in the appendix.

The remaining part is the maintenance and inspection module, which is designed for the implementation of core maintenance and inspection operations for the power system. The operation flow chart is given in Fig. 3. According to the specific maintenance and inspection requirements, this module can be designed to include various applications such as status maintenance, inspection management, acceptance management, defect management, and event management. Here, we omit the design details here.

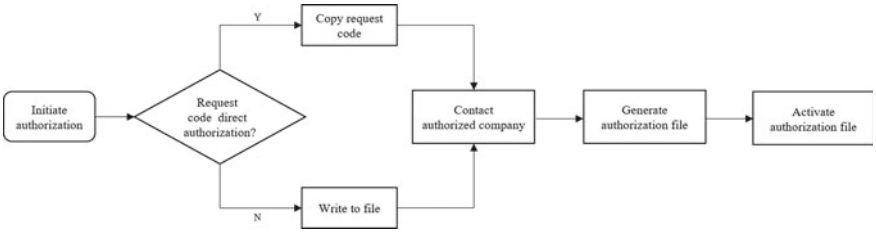

Fig. 2 Authorization verification flow chart

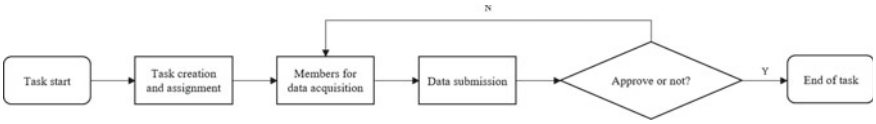

Fig. 3 Maintenance and Inspection flow chart

3.2 Experiments

In this part, we combine the software design with hardware components and implement the developed platform in the practical power systems to perform maintenance and inspection operations. The appearance of the terminal platform is shown in Fig. 4. According to the required functional design, the main functions of the intelligent maintenance system include the following functional modules: the equipment management module, the specialized inspection module, the equipment testing module, the defect management module, the equipment acceptance module, the diagram documentation module, the workstation module, and the regulatory standards module.

After practical field application, the time spent on various tasks in the substation operation and maintenance terminal, both before and after using the mobile intelligent platform, was analyzed as in Fig. 5. It is evident that the implementation of the mobile intelligent platform has significantly reduced on-site work time for operators, leading to a substantial enhancement in work efficiency. Leveraging the substation mobile terminal has enabled end-to-end control over the processes of secondary equipment inspection, testing, and acceptance tasks. Maintenance personnel initiate work orders and push them to the mobile terminals of field workers. On-site, workers use their handheld mobile terminals to scan electronic labels on secondary equipment

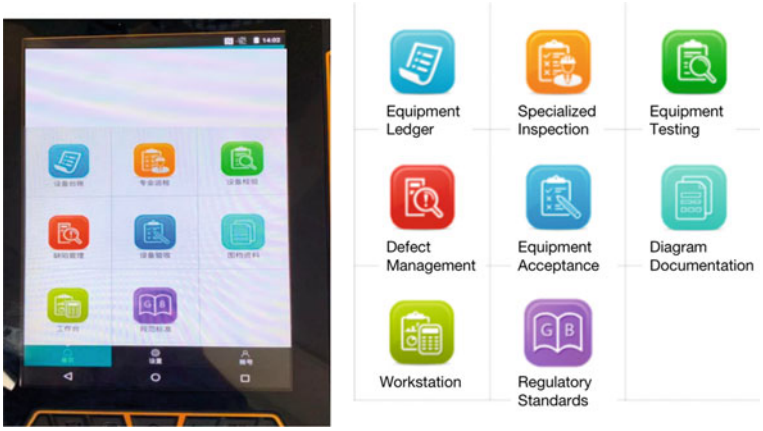

Fig. 4 Appearance and modules of intelligent mobile platform

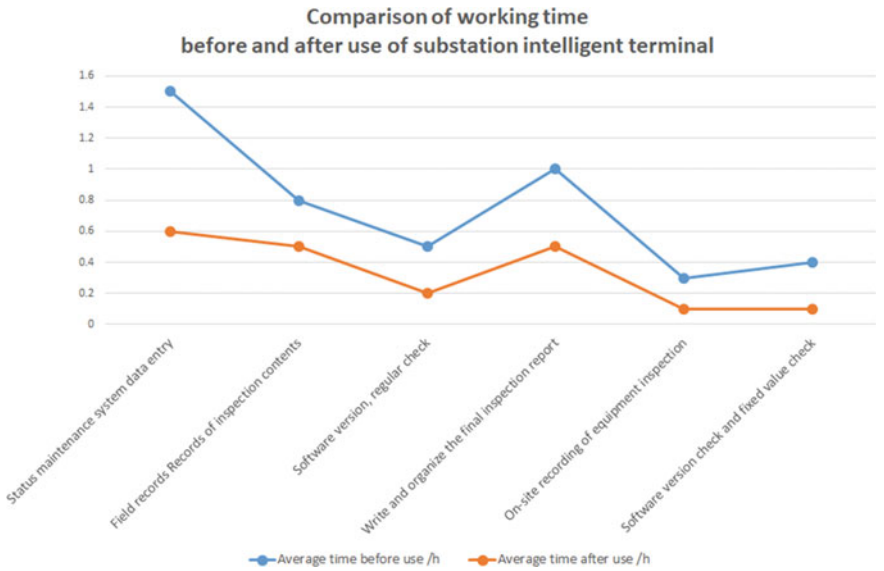

Fig. 5 Comparison before and after using of platform

to confirm the work location. They then proceed with the on-site tasks following standardized workflow processes. Upon task completion, work reports are generated and uploaded to the system's workstation. Management personnel review and approve the reports, completing a closed-loop management cycle. This approach enhances both on-site work safety and efficiency, successfully achieving the set objectives.

4 Discussions and Conclusions

In conclusion, the intelligent mobile platform emerges as a beacon of innovation, ushering in a new era of power system management. The seamless integration of human expertise, vehicle mobility, and internet-driven intelligence within the platform layer epitomizes the essence of the human-vehicle-internet coordination paradigm. Through its dynamic orchestration, the intelligent mobile platform transcends traditional boundaries, amplifying the efficiency, accuracy, and safety of maintenance and inspection processes.

Despite the aforementioned benefits, intelligent maintenance and inspection systems based on human-vehicle-internet coordination face several challenges. One challenge is the need for reliable and low-cost communication infrastructure, which may not be available in some remote areas. Moreover, in any system that involves the transmission of data, security, and privacy are major concerns. In the case of the intelligent maintenance and inspection of power systems based on human-vehicle-internet coordination, it is important to improve data privacy and security [9]. There

is also potential for integrating artificial intelligence and machine learning technologies to improve the accuracy and effectiveness of maintenance and inspection tasks [10]. Overall, human-vehicle-internet coordination has the potential to revolutionize the way maintenance and inspection tasks are conducted in power systems. Further research in this area is highly promising and could lead to significant improvements in the reliability and efficiency of power systems.

Acknowledgements This paper is supported by China Southern Power Grid (GJHKJXM20210068).

References

1. Machowski J, Lubosny Z, Bialek JW, Bumby JR (2020) Power system dynamics: stability and control. Wiley. https://www.wiley.com/en-gb/Power+System+Dynamics:+Stability+and+Control,+3rd+Edition-p-9781119526346
2. Kroposki B, Johnson B, Zhang Y, Gevorgian V, Denholm P, Hodge BM, Hannegan B (2017) Achieving a 100% renewable grid: operating electric power systems with extremely high levels of variable renewable energy. IEEE Power Energy Mag 15(2):61–73. https://doi.org/10.1109/MPE.2016.2637122
3. Babaei M, Shi J, Abdelwahed S (2018) A survey on fault detection, isolation, and reconfiguration methods in electric ship power systems. IEEE Access 6:9430–9441. https://doi.org/10.1109/ACCESS.2018.2798505
4. Hu QR, Shen XY, Qian XM, Huang GY, Yuan MQ (2022) The personal protective equipment (PPE) based on individual combat: a systematic review and trend analysis. Def Technol. https://doi.org/10.1016/j.dt.2022.12.007
5. Zou W, Shu X, Tang Q, Lu S (2019) A survey of the application of robots in power system operation and maintenance management. In: 2019 Chinese Automation Congress (CAC), Hangzhou, China, pp 4614–4619. https://doi.org/10.1109/CAC48633.2019.8996362
6. Siddiqui ZA, Park U (2020) A drone based transmission line components inspection system with deep learning technique. Energies 13(13):3348. https://doi.org/10.3390/en13133348
7. Mahmood A, Javaid N, Razzaq S (2015) A review of wireless communications for smart grid. Renew Sustain Energy Rev 41:248–260. https://doi.org/10.1016/j.rser.2014.08.036
8. Feng C, Wang Y, Chen Q, Ding Y, Strbac G, Kang C (2021) Smart grid encounters edge computing: opportunities and applications. Adv Appl Energy 1:100006. https://doi.org/10.1016/j.adapen.2020.100006
9. Mensi N, Rawat DB, Balti E (2021) Gradient ascent algorithm for enhancing secrecy rate in wireless communications for smart grid. IEEE Trans Green Commun Netw 6(1):107–116. https://doi.org/10.1109/TGCN.2021.3093821
10. Omitaomu OA, Niu H (2021) Artificial intelligence techniques in smart grid: a survey. Smart Cities 4(2):548–568. https://doi.org/10.3390/smartcities4020029

Bypassed On-Chaining: A Highly Secure and Loosely Coupled Data On-Chaining Solution for Electricity Demand Response Systems

Wenqian Jiang, Xiaoming Lin, Kun Zhang, Jianlin Tang, Keying Huang, Mi Zhou, and Yuzhou Zhao

Abstract Using blockchain technology to improve data security, correctness, and trustworthiness of electricity demand response systems is currently a research hotspot in the field of energy IoT. However, the on-chaining process in existing blockchain-based electricity demand response systems often causes problems like poor data correctness and long transaction response time. This paper proposes a novel, secure, and loosely coupled data on-chaining solution called bypassed on-chaining. First, the events occurring in each system terminal are logged into a local database. Subsequently, the independent on-chaining module of each terminal continuously reads the local database to obtain operational data, constructs transactions, and sends them to blockchain nodes. Each terminal only sends requests to the backend services and does not send requests to the blockchain directly, which decouples system operation from the blockchain. The experimental results from our case study show that bypassed on-chaining can ensure the correctness of both system operation data and on-chain data regardless of whether the user client is running normally or not, meanwhile maintaining fast transaction response times, thus significantly improving system reliability and user experience.

Keywords Blockchain · Demand response · Electrical power applications · Bypassed on-chaining · Loosely coupled · On-chaining · Data correctness

W. Jiang · K. Zhang · K. Huang
Guangxi Power Grid Measurement Center, Guangxi, Nanning 530024, China

X. Lin (✉) · J. Tang · M. Zhou · Y. Zhao
Electric Power Research Institute, CSG, Guangzhou 510663, China
e-mail: linxm4@csg.cn

X. Lin · J. Tang · M. Zhou
Guangdong Provincial Key Laboratory of Intelligent Measurement and Advanced Metering of Power Grid, Guangzhou 510663, China

Y. Zhao
Shenzhen Power Supply Bureau Co., Ltd, Shenzhen 518000, China

S. Yadav et al. (eds.), *Energy Power and Automation Engineering*, Lecture Notes in Electrical Engineering 1118, https://doi.org/10.1007/978-981-99-8878-5_70

List of Abbreviations

IoT	Internet of Things
DR	Demand Response
SDK	Software Development Kit
ID	Identity
HASH	A kind of hash function
CPU	Central processing unit

1 Introduction

Demand Response (DR) refers to when a grid company uses economic compensation or incentive mechanism to guide customers to adjust electricity consumption behavior, improving the stability of power system operation. In recent years, demand response has obtained good results in peak-shaving and valley-filling, ensuring power supply, and solving heavy-overload problems of power equipment [1–3]. However, the traditional centralized power demand response system has deficiencies such as insufficient transparency of response power settlement, inflexible market mechanism, and lack of effective market supervision mechanisms [1], which seriously affects the enthusiasm and experience of users' participation in demand response.

Blockchain's decentralized data storage architecture is innately transparent, tamper-proof, traceable, and can flexibly implement different demand response incentive mechanisms [2], offering a fitting solution to the deficiencies of electricity demand response systems. Many electric power companies have already carried out preliminary practices to integrate blockchain technology into electricity demand response systems [1].

2 Results and Discussion

Among previous studies and system designs for blockchain-based electricity demand response systems, You et al. [1] designed a blockchain-based demand response transaction mechanism to achieve real-time control of the demand response transaction process. They also proposed a time-scale pricing model to achieve a balance of interests for all parties in the transaction. Gong et al. [2] analyzed in detail the advantages of combining demand response and blockchain technology and designed a demand response system based on a blockchain combining demand-side main chain and side chain. Li et al. [3] proposed a blockchain application solution based on the demand analysis of the existing automatic demand response systems. They also analyzed the key issues in demand response blockchain systems, including

proof-of-work mechanism, network protocol, smart contract, and information security. Yan et al. [4] proposed a framework for developing a blockchain-based electricity demand response system fitting China's domestic conditions, and development suggestions are given in terms of transaction products, credit management, and platform development.

None of the above studies of blockchain demand response addressed the potential problems that the traditional on-chaining process can cause, nor did they offer any specific on-chaining solutions. Data on-chaining refers to the process in which the terminals or servers send data as transactions from off-chain environments to a blockchain node, which then records the data on the blockchain after the transactions pass consensus. Since the blockchain itself cannot verify the authenticity of the source data [2], the process of data on-chaining is critical in any blockchain-based demand response system. In the existing IoT blockchain applications, the data on-chaining solution either uses the self-on-chaining method or the delegated-on-chaining method [1, 3–8].

As shown in Mode A of Fig. 1, for self-on-chaining, the system operating logic and the on-chain process are closely integrated. Both the user client and backend server can use blockchain SDKs to assemble operational actions into transactions and send them to the blockchain individually. The communication and settlement of operations are both handled by the blockchain, making the operating system highly coupled with the blockchain network. Since all operations are performed based on the state of on-chain data, and the data on-chain is transparent and tamper-proof, the self-on-chaining mode can ensure the correctness of system and transaction operations. However, because the performance of blockchain consensus algorithms, in general, cannot meet the performance requirements of IoT systems [3, 4, 9], the system is prone to problems such as long transaction delays, slow response times, and low response success rate, which damages user experiences. In a worse scenario, the blockchain network may experience large-scale congestion or collapse, when the user clients and backend servers will follow suit and cease functioning.

As shown in Mode B of Fig. 1, for delegated-on-chaining, the user client does not sign the transaction data, but only performs regular system operations and sends requests to the backend servers. All on-chaining actions are executed by the on-chaining module of the backend server. Since the interaction between the user client and the backend server is independent of the blockchain network, the delegated-on-chaining mode can ensure the liveness of the operating system but cannot guarantee the security and correctness of the transaction data. If the backend server fails or commits malicious behavior, the operation or request submitted by the user client may be lost, disordered, or tampered with, and then the wrong transaction data is recorded on the blockchain, resulting in wrong response actions made based on the data on the chain.

The self-on-chaining method has the drawback of high coupling, low transaction speed, and high transaction delay, while the delegated-on-chaining method has the shortcomings of high centralization and poor data security [5, 6]. This paper proposes bypassed on-chaining, a highly secure and loosely coupled data on-chaining solution for electricity demand response systems, which decouples system operation from data

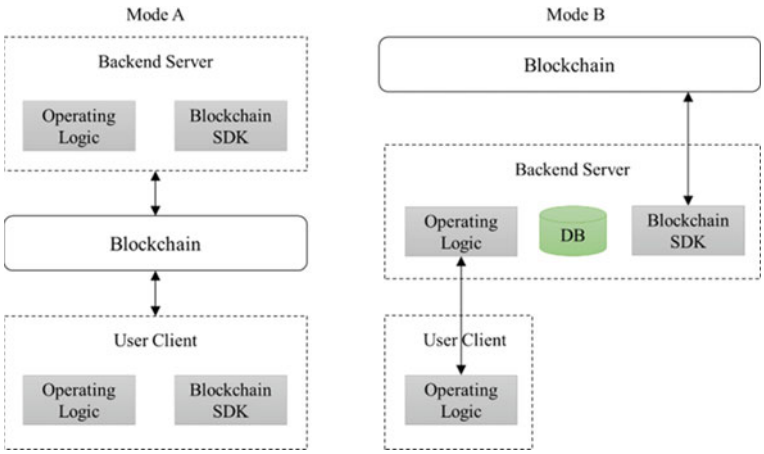

Fig. 1 Existing data on-chaining solutions

on-chaining. It gives each transaction operation a unique ID to ensure data integrity and uses transaction hashing to guarantee the correctness of on-chained data.

3 Bypassed Data On-Chaining for Electricity Demand Response Systems

3.1 Overall Structure

As shown in Fig. 2, the bypassed data on-chaining solution includes four entities: user client, IoT device, backend server, and the blockchain network. The user client directly interacts with users, sends transaction messages to the backend server, receives response messages, and initiates transaction data correctness queries to the blockchain network. The IoT device collects energy data, controls energy usage, and executes demand response actions. The backend server receives requests from the user client, issues and allocates demand transactions, and contacts and controls the IoT terminal. The blockchain network records transaction data and provides correctness proof to queries from each terminal.

The user client, the IoT device, and the backend server each have an independent database and on-chaining module. The database of each terminal is used to cache operation data and record events such as requests and responses occurring in the operating system. The on-chaining module is an independent process that continuously reads the database to obtain operation data, constructs transactions for the data, sends transactions to blockchain nodes, and locates the on-chained cached data and clears them.

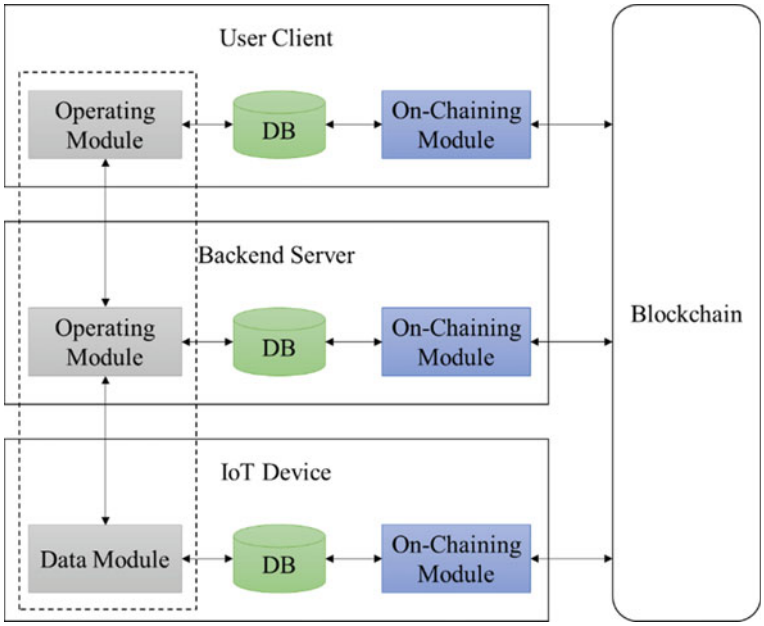

Fig. 2 Bypassed on-chaining structure

Compared with existing on-chaining solutions, bypassed on-chaining keeps the operating systems independent from the blockchain [1, 3–6], which is inside the dashed box on the left in Fig. 2. Each terminal only sends requests to the backend server and does not send requests to the blockchain directly. In this way, if the blockchain network fails or loses connection, the terminals and the backend server will only need to remove the database and the on-chaining module to become a traditional system that can maintain normal operations. In addition, bypassed on-chaining is also free of the issues in the delegated-on-chaining mode by allowing the on-chaining module of each terminal to interact with the blockchain directly, eliminating the potential risk of a malicious backend server and ensuring the correctness of transaction data.

3.2 Design of Key Mechanisms

a. One ID for One Operation

Before sending an operation to the backend server, the user client needs to store it in the local database for later checking with the backend server to prevent the user client from suddenly quitting after the operation has been sent out, thus making it impossible to confirm the execution status of the backend server. For each operation

sent by the user, the backend server will perform a de-duplication check according to the unique ID to prevent it from being executed twice. Then, the backend server will return the same result to the user client for the same ID and store each operation in the local database for future user queries and auditing.

b. One Operation is On-chained Twice

With the design of separating system operation and blockchain, system operations do not depend on the data existing on the blockchain, which is essentially an "occurrence-before-on-chaining" approach. To ensure the integrity of the on-chained data, both the user client and the backend server must separate on-chain records for the same operation [7] to prevent either party from on-chaining after modifying the other's data.

c. Details of an Operation is On-chained Once

Only one copy of the details of an operation needs to be on-chained, and other data records related to this operation can use the digest value of the operation details as a checking value. The user client initiates operation requests and is required to send the operation details to the chain. The backend server is the executor of operations and needs to obtain and on-chain the digest of the operation details. Later, when auditing and verification occur, the essential step is to check whether the digest of the operation details in the user's on-chaining record is the same as the digest value in the backend server's on-chaining record (To check whether HASH (type, parameter, return value) = = digest) [8].

d. Addressing Abnormal System Conditions

User clients will inevitably experience crashes and abnormal exits, usually caused by insufficient memory, long background rest time, etc. Imagine a scenario where a user client sends a request to the background server and abnormally exits before receiving a response from the background server. In this case, if the request was not recorded in advance, then after the program restarts, although the user client can view the execution result of the operation, the user can no longer perform subsequent actions on that operation. We solve this by recording the request in advance and changing its status after receiving the response to ensure the integrity of the request operation. On the other hand, when the on-chaining module sends a transaction to the blockchain network and crashes before it receives a reply from the blockchain node, if the transaction was not marked in advance, after the program restarts, the on-chaining module cannot know whether the operation has been on-chained or not, allowing for the possibility that the transaction is on-chained twice. To address this concern, we record the transaction digest in advance and change the status of the transaction in the database of the on-chaining module after receiving a reply from the blockchain node to ensure the correctness of the on-chaining process.

e. Methods of Maintaining Two Different Cache Databases

The user client and the backend server record operations to the local cache database first, and then the on-chaining module submits the data in the cache database to the

Table 1 Client cache database data structure

Field	Description
UUID	Unique identifier
Type	Data Type. 0: Generic data; 1: Operational data
Paras	Additional parameters
Ret	Return value of the backend server
hash_tx	On-chaining transaction hash value
State	Status. 0: sent to the backend server; 1: Backend server returns success; 2: Sent to blockchain; 3: On-chain successful; 4: Backend server returns error

Table 2 Backend server cache database data structure

Field	Description
UUID	Unique identifier
hash_para	Hash of type, paras, and ret values in client-side data
hash_tx	On-chaining transaction hash value
State	Status. 0: Completed client-side request; 1: Sent to blockchain; 2: On-chain successful

blockchain. Naturally, the size of data in the local cache databases will continuously grow as time goes by and the activity volume keeps increasing [3]. User clients and IoT devices have limited local storage space, so a suitable mechanism to clear up redundant data is needed. We will delete the already-on-chained data records and erroneous records returned by the backend server every time the terminal restarts. For the backend server, since it must allow for the subsequent user client queries, all operational data must be recorded and cannot be deleted. Here we resort to permanent data retention and regular cold backup storage.

3.3 Cache Database Data Structure

Tables 1 and 2 define the data structure of the cache database of user client and the backend server, which standardizes the format of the operations stored to the local database.

3.4 System Workflow Design

Based on the above overall architecture and design, the operating system can be divided into two major parts: user client and backend server, each of which involves operation processing and data on-chaining. The operation processing logic of the backend server is relatively simple, and the on-chaining of the backend server is similar to that of the user client. Therefore, we will focus on introducing the workflow of the user client.

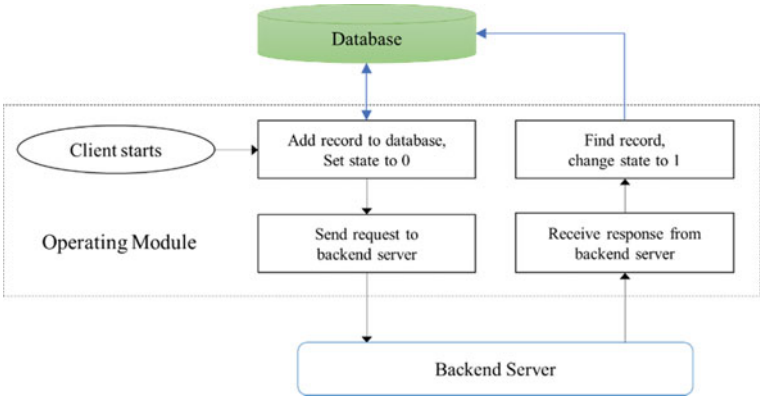

Fig. 3 Operating module workflow

The operating module in the client is responsible for responding to various user operations and handling interactions with the backend server, including functions such as modifying and viewing, while generating the source data to be on-chained and storing them in the local cache database for use by the on-chaining module. The following describes only the processes related to on-chaining.

a. Operation Workflow

As shown in Fig. 3, the detailed steps of module operation workflow are as follows:

(1) The user client starts, adding a database record, and records the local status as 0.
(2) The user client sends a request message to the backend server.
(3) The backend server receives the request and replies with a success response message.
(4) If the user client receives the success response, it finds the request record sent in the first step and changes its local status to 1.

b. Module Initialization Workflow

As shown in Fig. 4, the detailed steps of the module initialization workflow are as follows:

(1) After the user client restarts, find the data record with status 3 and delete it.
(2) Find the data record with status 0 and send it to the backend server.
(3) The backend server receives the request and replies with a response message.
(4) If the user client receives the response, find the request record sent in the second step and change its status to 1.

The client on-chaining module is used for sending the operation data generated by the operating module to the blockchain for recording, and this module needs to ensure that all records are written down on the blockchain in an orderly and correct manner.

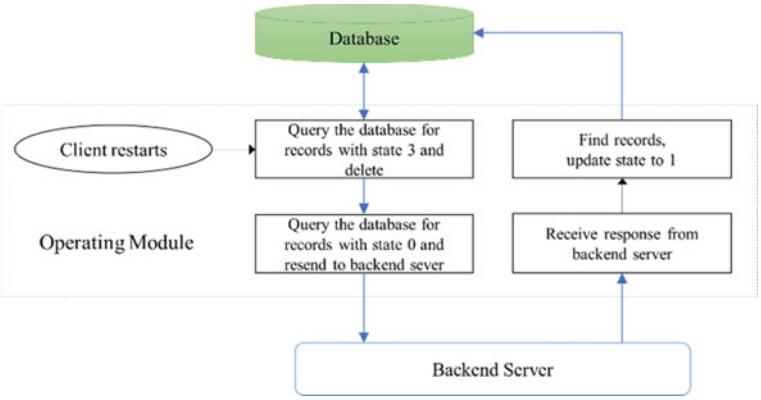

Fig. 4 Operating module initialization workflow

c. On-chaining Workflow

As shown in Fig. 5, the detailed steps of the module initialization workflow are as follows:

(1) The on-chaining module queries the database regularly to find out the data with status 1.
(2) The on-chaining module constructs blockchain transactions of these data.
(3) The on-chaining module obtains the hash of the transaction and records the hash into the database table.
(4) The on-chaining module sends the transaction to the blockchain.
(5) The on-chaining module changes the record status to 3 (i.e., successfully on-chained) if it receives a successful response from the blockchain node.

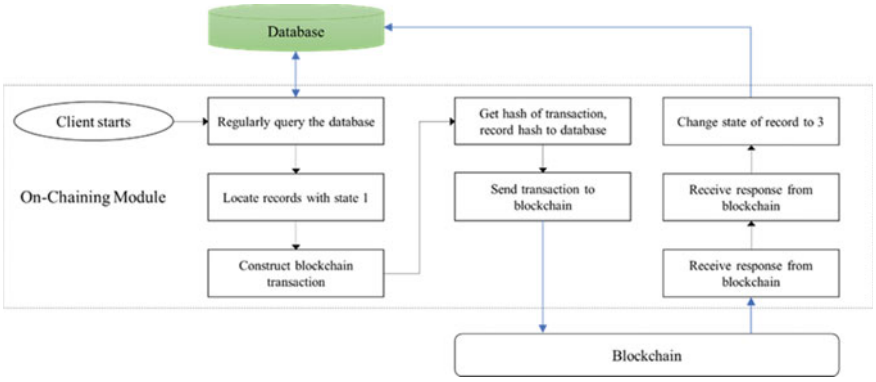

Fig. 5 On-chaining module workflow

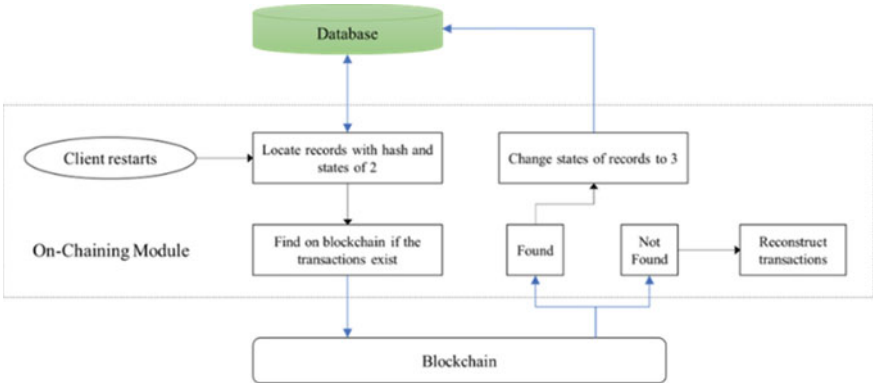

Fig. 6 On-chaining module initialization workflow

d. On-chaining Initialization Workflow

As shown in Fig. 6, the detailed steps of the module initialization workflow are as follows:

(1) Find the data record with status 2 after the client starts.
(2) Go find on the blockchain whether this transaction is already recorded.
(3) If the transaction is already on-chained, change the status to 3; if not, resubmit the transaction to the blockchain.

e. Backend Server

The processing flow of the operating module of the backend server is relatively simple, as it adds a new record to the database after processing the requests from user clients. Since the backed server must allow for the subsequent user client queries, all operational data must be recorded and cannot be deleted, it differs from the user client in that there is no deletion of completed records.

The workflow of the backend server on-chaining module is essentially the same as the workflow of the on-chaining module of the user client.

4 Experimental

To verify the practicality and advancement of the bypassed on-chaining solution proposed in this paper, we conducted simulation tests for our novel solution and the two existing traditional solutions. We also designed normal and abnormal scenarios based on varying user client conditions. The test deployment architectures are shown in Figs. 7 and 8. Among them, the self-on-chaining mode corresponds to mode A

in Fig. 7, the delegated-on-chaining mode corresponds to mode B in Fig. 6, and the bypassed on-chaining mode corresponds to Fig. 8.

The testing equipment includes five cell phone terminals, one backend server, and four blockchain node servers.

The cell phone terminals consist of five Huawei MATE40 cell phones with hardware configuration of 8-core CPU, 16G memory, and 128G storage capacity, using the Android 10 operating system. We deployed on each device a demo demand response

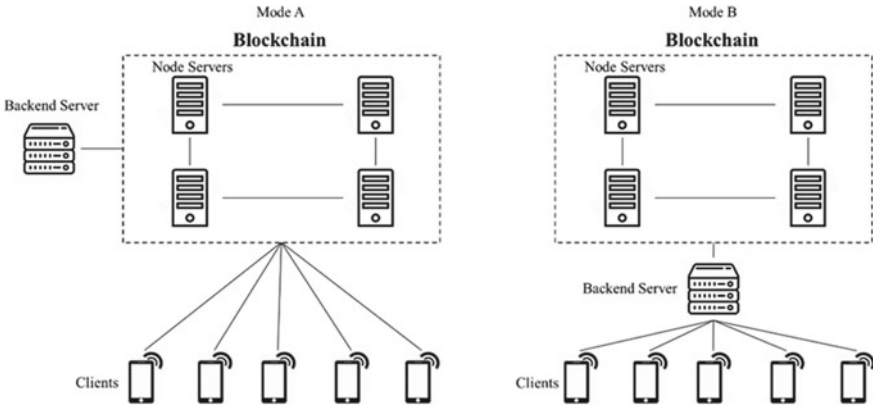

Fig. 7 Traditional on-chaining solutions testing deployment

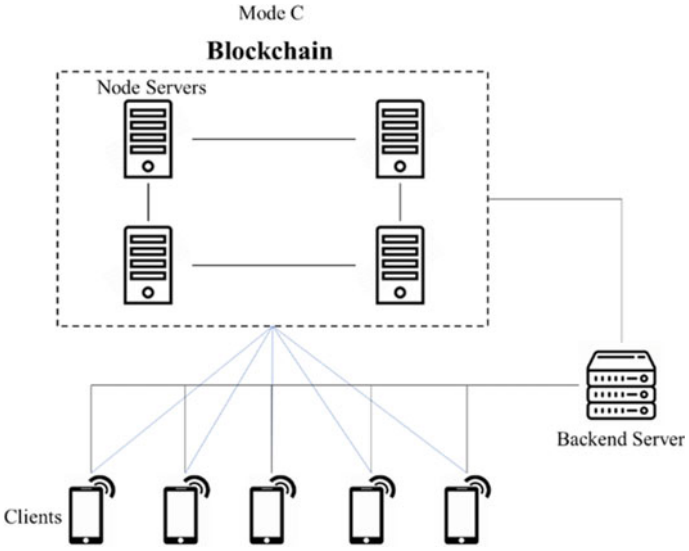

Fig. 8 Bypassed on-chaining testing deployment

application. The demo apps are used for sending requests, answering demands, and viewing result data in this test. The network environment is a 100 M wireless network.

In conjunction with the user-end application, a demo demand response system is deployed on the backend server. The hardware configuration for the backend server is an 8-core CPU, 16G memory, and00201T storage capacity, using Ubuntu18.04 operating system, and the network environment is a 100 M broadband network.

Four blockchain node servers build a blockchain. The hardware configuration of each node is CPU8 core memory 16G, hard disk is 540G, and the network environment is 100 M broadband network, using Ubuntu18.04 operating system.

Testing Items

(1) Total number of demands responded: the sum of the number of demands assigned to each cell phone terminal.
(2) Operation correctness: Check the number of successfully responded demands at each cell phone applications and record them; check at the backend server whether all 1000 demands are assigned and whether the distribution of demands is consistent with the records on the cell phone applications. (Operation correctness% = number of correctly responded demand records/total number of demands published*100%).
(3) On-chaining correctness: Check the distribution of demand response recorded on the blockchain and record it. Compare whether it is consistent with the records of the backend server. (On-chaining correctness% = number of correct on-chained transactions / total number of demands published*100%).
(4) Execution time: the time from request initiation to successful demand response allocation, which is checked on the user application.
(5) On-chain time: the time elapsed between the request initiation and the successful on-chaining of data, which is checked on the user application.

4.1 Case 1—Normal Scenario Testing

Testing Process

(1) The backend server releases 1000 demands.
(2) After the cell phone application listens to the demand being released, it requests the backend server for the demand response qualification. The process is carried out until the backend server indicates that all the demands in this round have been allocated.
(3) Record the data. Then repeat the above steps 3 times.

The results are shown in Table 3.

Table 3 Normal scenario testing results

Mode	Number of demands responded on client	Total number of demands responded	Operating Correctness (%)	Average execution time (ms)	Average on-chain time (ms)	On-chaining correctness (%)
A*	{188,189,209,200,214},{199,208,197,201,195},	1000, 1000,	100	410	620	100
B*	{205,205,188,203,201}	1000	100	120	190	96
C*	{190,216,194,203,197},{156,198,232,214,200},	1000, 1000,	100	100	190	100
	{208,206,203,178,205}	1000				
	{203,182,164,185,266},{212,245,167,188,188},	1000, 1000,				
	{202,195,210,198,195}	1000				

*Mode A—Self-on-chaining. Mode B—Delegated-on-chaining. Mode C—Bypassed on-chaining

4.2 Case 2—Abnormal Scenario Testing

Testing Process

(1) The backend server releases 1000 demands.
(2) After the cell phone application listens to the demand being released, it requests the background service for the demand response qualification. At the user-end, whenever the demand response application finishes sending requests, we immediately terminate the application. Repeat until the mobile terminal shows that all the demands in this round have been allocated.
(3) Record the data. Then repeat the above steps 3 times.

The results are shown in Table 4.

4.3 Result Analysis

In the first round of normal scenario testing, the total number of demands successfully responded to for all three on-chaining modes is 1000, which is consistent with the total number of demands issued by the backend server, and there are no errors or conflicts in demand allocation. As the results show, Mode A has 100% operating correctness and on-chaining correctness, but the average execution time and average on-chain time are significantly longer than those of Modes B and Mode C. Mode B has a faster average execution time and average on-chain time, but its on-chaining correctness is 96%, not 100%. Mode C has 100% operating correctness and on-chaining correctness while having superior execution time and on-chain time.

In the second round of abnormal scenario testing, Mode A and Mode C both have 1000 demands successfully responded, while Mode B has less than 1000 for all three groups of data, and there are errors and conflicts in Mode B's operation execution. Although Mode A maintains 100% correctness, its average execution time and average on-chain time slow down massively, seriously affecting user experience and response timeliness. On the other hand, Mode C still has a fast response time with 100% correctness.

The above test results show that with the bypassed on-chaining solution proposed in this paper, the system can achieve 100% operating and on-chaining correctness even when the user client continues to exit abnormally, which verifies the proposed high-security and loose-coupling features and demonstrates its advancement compared with traditional on-chaining schemes. In addition, the bypassed on-chaining solution can reliably achieve an average execution time of 100 ms and an average on-chain time of 200 ms, which can guarantee user experience in the power demand response scenario [10].

Table 4 Abnormal scenario testing results

Mode	Number of demands responded on client	Total number of demands responded	Operating Correctness (%)	Average execution time (ms)	Average on-chain time (ms)	On-chaining correctness (%)
A*	{198,206,177,217,202},{210,208,213,193,176},	1000, 1000,	100	1340	1560	100
B*	{200,203,180,237,180}	1000	75	130	200	72
C*	{170,143,160,188,179},{132,161,145,155,185}, {183,135,149,190,165} {202,200,200,194,204},{201,203,197,205,194}, {214,205,201,195,185}	840, 778, 822 1000, 1000, 1000	100	100	210	100

*Mode A—Self-on-chaining. Mode B—Delegated-on-chaining. Mode C—Bypassed on-chaining

5 Conclusions

In this paper, we propose a highly secure and loosely coupled data on-chaining solution, bypassed on-chaining, to address the drawbacks of traditional on-chaining schemes used in blockchain-based electricity demand response systems. Its high-security property is achieved by assigning each operation a unique ID to protect the integrity of operations and using transaction hash verification to ensure the correctness of the on-chained data, thus yielding high on-chaining correctness rate and improving integrity of the demand response execution. The loose-coupling feature is achieved by separating the operating system from the on-chaining process and adding a cache database in between, enabling the system to work independently of the blockchain network when necessary. In addition, the status of all transaction operations is recorded on a centralized server database, and all process data is recorded on the blockchain, allowing easy and accurate auditing.

In summary, compared with self-on-chaining and delegated-on-chaining, our bypassed on-chaining solution proposed in this paper has apparent advantages in security, correctness, response time, and flexibility, and therefore has high practical application value [3]. However, several deficiencies exist in our proposed solution, such as having no mechanisms to counter issues caused by data not on-chained in time or low data storage redundancy. We expect further research to expand on our design of bypassed on-chaining and propose improved solutions.

Competing Interests

The authors declare that they have no known competing financial interests or personal relationships that could have appeared to influence the work reported in this paper.

Availability of Data and Material

The data used to support the findings of this study are included in the article.

Authors' Contributions

Conceptualization, J.W. L.X.; methodology, Z.K. T.J.; validation H.K. Z.M. Z.Y.; investigation, H.K.; writing–original draft preparation, J.W. L.X.; writing–review and editing, Z.K. T.J.; project administration, J.W.; All authors have read and agreed to the published version of the manuscript.

Acknowledgements This work was supported by the Science and Technology Project of Guangxi Power Grid Co., Ltd (044400KK52200003).

Credits to every author who contributed to this article.

References

1. Hongliang Y, Zheyuan Z, Jiango L, Xin D, Jianyang Z, Jinsong S, Chengfu S (2022) Research and implementation of blockchain-based electricity demand response trading mechanism[J]. Electr Demand Side Manag 24(01):28–33
2. Feixiang G, Shiming T, Dezhi L, Qiang L, Beng M, Lulu Z, Xun G (2020) Blockchain-based demand response system design. Power Inf Commun Technol
3. Bin L, Chao L et al (2017) A preliminary investigation on the application of automatic demand response system based on blockchain technology. Chin J Electr Eng 37(13):3691–3702
4. Yan Y, Huang J, Chen X, Zhang Z, Tianhan Z, Lin Z (2022) Blockchain-based framework of power demand response in China. IET Renew Power Gener 16(4):781–791. https://doi.org/10.1049/rpg2.12219
5. Ogawa D, Kobayashi K, Yamashita Y (2022) Blockchain-based optimization of distributed energy management systems with real-time demand response. IEICE Trans Fundam Electron Commun Comput Sci. https://doi.org/10.1587/transfun.2021EAP1162
6. Deshpande V (2020) George, Laurent, Badis, Hakim, Desta, Alemayehu. Blockchain Based Decentralized Fram Energy Demand Response Mark. https://doi.org/10.1109/NOMS47738.2020.9110378
7. Bin L, Wangzhang C et al (2018) Multi-level DR bidding security management and technical support based on blockchain in untrusted environment. Proc CSEE 38(8):2272–2283
8. Beibei W, Yachao L, Shengnan Z et al (2019) Key technologies of distributed energy transaction based on blockchain. Autom Electr Power Syst 39(11):198–204
9. Xiaodong Y, Youbing Z et al (2017) Automatic demand response of energy local area network energy storage system based on blockchain technology. Proc CSEE 37(13):3703–3716
10. Ke X, Han Y et al (2019) Design of integrated energy transaction system based on trusted data. Electr Power Inf Commun Technol 17(10):44–48

Design of Off-Grid Wind-Solar Complementary Power Generation System for Alpine Weather Station

Guang-Qing Lin, Xianfeng Yu, Yunxia Luo, and Shubin Yan

Abstract Wind power generation and photovoltaic power generation are one of the most mature ways in respect of the wind and solar energy development and utilization, wind and solar complementary power generation can effectively use space and time. The two forms of power generation can play their respective advantages, replenish each other, and improve the comprehensive utilization of energy through coordination and cooperation, so as to effectively solve the power supply problem of remote areas. This paper describes the design of an off-grid wind-solar complementary power generation system of a 1500m high mountain weather station in Yunhe County, Lishui City. By analyzing the meteorological data and electricity usage of the station, the power of the two independent power generation systems, the number of photovoltaic modules, and the capacity of batteries and inverters are calculated, and a reasonable photovoltaic array is designed and the complementary control module is configured. The system can meet the electricity demand of weather station to the greatest extent, and the output power is stable, the power quality is good, and the structure is reasonable.

Keywords Off-grid type · Complementary scenery · Inverter · Accumulator

G.-Q. Lin · X. Yu (✉) · Y. Luo · S. Yan
College of Electrical Engineering, Zhejiang University of Water Resources and Electric Power, Hangzhou, China
e-mail: yxf@zjweu.edu.cn

S. Yan
e-mail: yansb@zjweu.edu.cn

S. Yan
Zhejiang-Belarus Joint Laboratory of Intelligent Equipment and System for Water Conservancy and Hydropower Safety Monitoring, Zhejiang University of Water Resources and Electric Power, Hangzhou, China

S. Yadav et al. (eds.), *Energy Power and Automation Engineering*, Lecture Notes in Electrical Engineering 1118, https://doi.org/10.1007/978-981-99-8878-5_71

1 Introduction

Nowadays, with the development of society and economy, as well as the increasing population, the consumption of non-renewable resources is increasingly serious [1]. How to research and develop new energy has become a hot topic in the world [2]. Wind energy and solar energy are new, clean, and renewable energy sources. They are naturally complementary in seasonality and time, so they can be combined for complementary development and utilization. In remote areas far from the power grid, such as border guard posts, islands, mountain weather stations, communication base stations, and other places, wind power and photovoltaic power generation is one of the most effective ways to solve the power supply problems in these places, and wind-solar complementary power generation can effectively use space and time. Two kinds of power generation mode can give full play to respective advantages and complement each other. Through coordination and cooperation, the comprehensive utilization rate of energy can be improved. Currently, wind-solar complementary power generation technology has penetrated into People's Daily life and become an indispensable part [3]. This paper takes a 1500 m high mountain weather station in Yunhe County, Lishui City as an example to design a set of off-grid wind-solar complementary power generation system. According to the power load, meteorological data, and natural conditions of the weather station, the modular design idea is adopted to reasonably select and design the electrical equipment of each module, so that the system can meet the power demand of the weather station to the maximum extent. The output power of the system is stable and the electric energy quality is good.

2 System Design Scheme

Based on the analysis of meteorological data and load of alpine weather station, the overall design scheme of the complementary power generation system is proposed.

2.1 The Analysis of Meteorological Data and Load in the Station

Yunhe County of Lishui City is located in the southwest direction of Zhejiang Province, which belongs to the subtropical monsoon climate. The annual average temperature ranges from 15°C to 25°C, the annual average precipitation ranges from 1465 to 1969 mm, the annual average sunshine duration is 1774.4 h, and the annual average wind speed is 0.8 ~ 2.2 m/s. The region has sixteen consecutive days of maximum rainfall, eight consecutive sunny days, and four consecutive days without wind or sunlight.

Table 1 The meteorological data of the weather station in Hangging Jian

Total horizontal radiation (MJ/m^2)	Amount of horizontal scattered radiation (MJ/m^2)	Atmospheric turbidity factor	Relative humidity
4539.6	2694.6	4.761	71.8

Table 2 Load of weather station

Serial number	Load name	Load power (W)	Daily working hours (h)	Daily power consumption (W.h)
1	Telemeter	AC 50	24	1200
2	Microcomputer, printer	AC 400	6	2400
3	Lighting	AC 80	5	400
4	Communication equipment	AC 150	12	1800
Total		AC 680		5800W.h

In this paper, a mountain meteorological station at an altitude of 1500 m in Yunhe County, Lishui City is taken as an example. By using the meteorological database of PVsyst simulation software, the corresponding geographical location is obtained, that is, the latitude is 27°59′49″ and the longitude is 119°29′18″. Then, Meteonorm 8.0 system built in the simulation software is used to import the geographical location of the weather station, so as to obtain the solar radiation amount and other related meteorological data as shown in Table 1.

The electrical load of alpine meteorological stations is characterized by low density and concentration. The electrical equipment mainly includes telemeter (automatic station), microcomputer, printer, lighting and communication equipment, etc. The electrical equipment such as telemeters needs to keep working normally for 24 h. Therefore, continuous and stable power supply must be provided for the electrical equipment to ensure the reliable operation of the meteorological station. Table 2 lists the power and working hours of all the electrical equipment in the weather station.

It can be seen from Table 1 to Table 2, the total power PL of the load inside the weather station is 680W, and the total power consumption QL is 5800W·h.

2.2 Overall Design Scheme

The overall design scheme of the system is: By the control module, the complementary power generation of the photovoltaic array and wind generator can be harmoniously controlled, the charge and discharge management of the battery can be realized, and then the DC-AC conversion can be completed by the inverter, and finally

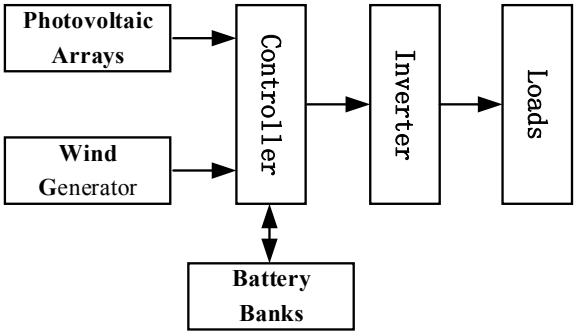

Fig. 1 Structure diagram of off-grid wind-solar complementary power generation system

the power supply to the load can be realized. As shown in Fig. 1, the system can be divided into four modules:

(1) Power generation module: Composed of wind generator and photovoltaic array, it is the energy source of the whole off-grid power generation system.
(2) Energy storage module: It is composed of battery banks, whose function is to balance load and regulate energy, so as to ensure the reliability of power supply to load [4].
(3) Inverter module: The inverter realizes DC-AC energy conversion and has the function of automatic voltage regulation, so as to ensure the power quality of load power supply [4].
(4) Control module: It can respectively realize MPPT control of wind turbine and photovoltaic array, charge and discharge control of battery, complementary and coordinated control of two power generation modes and operation monitoring of system.

Different wind-solar power generation modes can be adopted according to different wind and solar energy resources and different electricity demand in different regions. Theoretically, the best matching method is to use wind power generation as the main and photovoltaic power generation as the auxiliary in design. At present, energy optimization management strategies of wind-solar complementary power generation system are mainly divided into three categories: multi-mode, low-mode, and multi-mode [5]. The design of this system adopts low-mode energy management strategy, which mainly highlights the priority utilization of main energy. Given that the target area has 16 days of maximum continuous rainfall and 8 days of maximum continuous sunny days throughout the year, the wind power generation time and photovoltaic power generation time are designed in a 2:1 ratio.

Off-grid wind-solar complementary power generation system preferentially uses wind energy for power generation at night and in rainy weather. On sunny days without wind, solar energy is preferred for power generation. When it is both windy and sunny, according to the relevant meteorological data and natural environment, compared with the solar radiation and wind energy density as well as the power

generation cost of the two systems, it is determined to choose which power generation mode is preferred. In a windless night or rainy day, the battery banks are used for power supply.

3 Design and Equipment Selection of the Energy Storage Module

In the off-grid wind-solar complementary power generation system, in order to effectively use the wind generator set and solar cell array to generate electricity to meet the load demand of the weather station in windless and no sunlight weather continuously, the energy storage technology is adopted to make the operation of the weather station more stable and reduce the energy loss in the process of energy storage. Energy storage module adopts battery energy storage technology, which is small in size and easy to install [6].

At present, the most widely used batteries in the Chinese market are lead-acid batteries, lithium-ion batteries, nickel-cadmium batteries, nickel-metal hydride batteries, etc. [4]. In terms of cost performance, lead-acid battery is more suitable as an energy storage device for low-power off-grid wind-solar complementary power generation system. The calculation method of battery capacity is generally calculated by formula (1).

$$Q = Q_L d / U \mathrm{KD}_c \tag{1}$$

where, Q—storage battery capacity (A·h); d—Maximum number of consecutive days without wind or sunlight; QL—Total power consumption of all loads in the station (W·h); U—DC voltage (V) of the system; Dc—The loop loss rate, is generally 0.85; K—discharge control coefficient, usually 0.5.

The DC voltage of the system (that is, the voltage of the battery bank) should be selected according to the standard level of the DC voltage (12 V, 24 V, 48 V, etc.). In order to facilitate the selection of components and charging power, the maximum DC voltage should not be greater than 300 V. However, if conditions permit, the voltage of the system should be increased as much as possible, so as to reduce the power loss and the manufacturing cost of the transmission system [7]. As the load power of the weather station is not large, the DC voltage of the system is selected as 48 V. According to the meteorological data and the load of the meteorological station, the storage battery capacity Q can be calculated as 1137.25A·h by Eq. (2–1). Therefore, in practical application, the type of AcmeG 200A·h/12 V lead-acid battery can be used to form a battery bank, which consists of 4 batteries in series into a group, 6 groups in parallel.

4 Design and Equipment Selection of the Power Generation Module

The power generation module is composed of wind generator and photovoltaic array. It obtains electric energy through wind power generation and photovoltaic power generation. It is the energy source of the whole off-grid complementary power generation system.

4.1 Selection of the Wind Generator

Wind generator is a kind of equipment that converts wind energy into electric energy, including wind turbine and generator. Wind turbine is mainly used to convert wind energy into mechanical energy, while generator is used to convert mechanical energy into electric energy [8].

It is known that the average annual wind speed of the mountain meteorological station with an altitude of 1500 m is above 5.5 m/s, the effective wind energy density is 200 ~ 300W/m^ 2, the annual cumulative hours with the wind speed of 3 ~ 20 m/s is more than 5000 h, and the average effective utilization time is 12 h/d. In continuous rainfall, the wind speed and duration are usually greater than the annual average wind speed and time. According to the meteorological data and natural conditions of the meteorological station, the time of Force 4 gale (5.5 ~ 7.9 m/s) was selected as 4 h/d.

According to the optimization and matching of the wind-solar complementary power generation system, it is set that the wind power generator can provide 20 days of electricity for the weather station every month, which can be obtained by Qin = Qout:

$$P_1 \times 20 \times 4 = \mathrm{UQKD}_c + Q_L \times 20 \tag{2}$$

According to the meteorological data and the load of the meteorological station, the wind generator power P1 can be calculated as 1756W by Eq. (2). Therefore, in practical engineering applications, according to the technical requirements of wind generator, as well as the reliability of installation and operation, a FD3.2–2.0/2 kW horizontal axis wind generator can be selected.

4.2 Design of the Photovoltaic Power Generation System

Photovoltaic power generation is a major power generation method that converts solar energy into electric energy by utilizing the photovoltaic effect of semiconductors [4]. At present, photovoltaic power generation is mainly realized by silicon solar cells.

According to the crystal structure of silicon solar cells, they can be divided into three categories: single crystal, polycrystal, and amorphous silicon solar cells [7]. By comparing the cost performance of all kinds of solar cells, this system chooses the photovoltaic array composed of polycrystalline silicon solar cells.

According to the meteorological data of the meteorological station, the average peak sunshine duration on the inclined surface of the photovoltaic array is 3.45 h, and the average annual sunshine duration is selected as 5 h/d. According to the optimization and matching of the wind-solar complementary power generation system, it is set that the photovoltaic power generation system can provide 10 days of electricity for the weather station every month, which can be obtained from Qin = Qout:

$$P_2 \times 10 \times 5 = \mathrm{UQKD}_c + Q_L \times 10 \tag{3}$$

According to the meteorological data of the meteorological station, the total power P_2 of the photovoltaic array can be calculated as 1649.6W by Eq. (3). Therefore, a 70Wp/12 V polycrystalline silicon module is adopted, which consists of 6 modules in series and 5 groups in parallel to form the photovoltaic array. In the photovoltaic power generation system, to match the voltage of the solar cell array with that of the battery, the battery can be in the best charging state only when the voltage of the solar cell array is equal to or slightly greater than the appropriate floating charging voltage [9]. The photovoltaic array output voltage of this system is 72 V, which meets the charging conditions of 48 V battery bank.

The photovoltaic modules of this system are all installed with fixed supports. According to the longitude and latitude data of the weather station, the installation dip Angle of the photovoltaic modules can be determined as 350 and the azimuth Angle as 11,030' by conventional calculation (based on the due south direction).

5 Selection of the Inverter

Since all the electrical equipment in the meteorological station is AC load, the inverter is the key equipment of off-grid wind-solar complementary power generation system. The inverter can convert DC into AC (220 V/50 Hz sine wave) to ensure that the AC load in the weather station can work normally. In addition, the inverter also has the function of automatic voltage stabilization, which can improve the power efficiency and quality of the complementary power generation system [4].

According to the load demand, the capacity of the inverter must be greater than or equal to the total power of the load [9]. In general, the characteristics of the load (resistive load and inductive load) should be considered first, and then the capacity of the inverter should be determined:

$$\text{Inverter capacity} = \text{Resistive load power} * 1.5 + \text{Inductive load power} \tag{4}$$

It is known that the telemeter and communication equipment in the weather station are resistive loads, while the microcomputer, printer, and lighting are inductive loads. The capacity of the inverter can be calculated as 780W by Eq. (4). Therefore, this system chooses 1000VA/48 V sine wave inverter.

6 Design and Equipment Selection of the Control Module

The control module of the complementary power generation system is an intelligent controller integrating wind power generation and photovoltaic power generation. It adopts advanced MPPT power tracking technology to maximize the utilization of wind power and solar energy and also realizes the complementary and coordinated control of wind power and photovoltaic power generation. The control module can be monitored remotely by computer. Controlled by intelligent software, the module can realize the power output of complementary power generation to charge the battery and provide other auxiliary control and protection functions required by the system. The control module is the most important component in wind-solar complementary power generation system. Its performance affects the life and operation stability of the whole system, especially the service life of the battery.

The system adopts the strategy of less mode energy management, which mainly highlights the priority utilization of main energy. According to the change of wind and solar radiation, the control module can realize three operation modes: wind generator supplying power to load independently, photovoltaic power generation system supplying power to load independently, and wind generator and photovoltaic power generation system supplying power to load jointly. According to the running state, the system can be divided into charging state, load state (discharge state), and protection state. The system monitors the running status of each module at the same time and enters the corresponding state under the corresponding conditions. In each state, the system can not only complete the work of its own stage, but also display the corresponding system parameter, and realize the communication between multiple systems and the communication between the system and the upper computer according to the needs of users.

The selection of wind-solar complementary control module should be determined according to the technical indicators of the whole system and the product sample manual provided by the manufacturer. The following technical indicators are generally considered:

(1) Technical parameters of wind turbine: rated total power 2 kW; rated voltage is 48 V; the unloading voltage is 29 V, the charging voltage after unloading is 24.6 V, and the unloading resistance power is 200W.
(2) Technical parameters of photovoltaic modules: rated power of the modules is 70W; the best working voltage is 12 V DC; overcharge protection voltage is 10.5VDC; after charging, the recovery charging voltage is 12.3 V DC; the maximum charging current is 23A. The ambient temperature is $-40°C$ to $+45°C$.

(3) With MPPT power tracking technology, PWM pulse intelligent charging technology, staggered parallel control technology.
(4) With control and protection functions which can prevent battery overcharge, over-discharge, short circuit, overvoltage, undervoltage, and reverse connection.
(5) With man–machine interface, condition monitoring, and remote communication functions.

7 Conclusions

In this paper, the alpine weather station as an example, analyzed all the loads in the station and comprehensively considered the meteorological data and geographical environment of the station on the power generation system, wind power generation and photovoltaic power generation have been realized optimal matching. By completing the design of system modules and the selection of equipment, a complete design of off-grid wind-solar complementary power system suitable for the alpine weather station has been finally realized. The design results of this paper have good reference value for the research and development of similar systems and also can provide an effective solution for the electricity problems in remote villages without electricity, frontier posts, communication bases, and other places.

Acknowledgements This research was funded by 2020 National College Students Innovation and Entrepreneurship Training project: "Three-dimensional Solar complementary power generation system", Zhejiang-Belarus Joint Laboratory of Intelligent Equipment and System for Water Conservancy. The authors would like to thank the editor and the reviewers who provided many valuable comments to improve the paper. Guang-qing Lin would specially like to thank the guidance of Professor Xianfeng Yu, and would also like to thank the help of the supervisors of Yunxia Luo and Shubin Yan.

References

1. Gangqiang F, Yong Y (2021) Design of distributed wind-solar complementary grid-connected automatic power generation system. Mod Electron Tech 44(08):119–122
2. Zhang H (2020) Research on modeling of wind-solar hybrid microgrid and control strategy of maximum power load. IOP Conf Ser Earth Environ Sci 514(4)
3. Maomao L (2019) Analysis of current situation and future development of wind-solar complementary power generation. Mod Econ Inf 16:367
4. Mingzhu Z (2021) Research on capacity allocation optimization of small-scale off-grid wind-power generation system for rural households. Tianjin University of Commerce
5. Jike Z, Shengtie W (2017) Energy optimization management and coordinated control strategy for independent wind-solar complementary power generation system. J Sol Energy 38(10):2894–2903
6. Lin RAN (2021) Research and design of low-power wind-wind complementary power supply. Hubei University for Nationalities

7. Daoqing H, Tao H, Honglin D (2012) Solar photovoltaic power generation system Principle and application technology., Beijing, pp 44–158
8. Daping X, Yibing L, Yuegang L (2011) Wind power Generation Principle. Beijing p 9
9. Huijun C (2016) Application technology of wind-wind complementary power generation. Beijing 56:156–158

Experimental Study on the Performance of Distributors Applied in Flat-Plate Quick-Freezing Machines

Feng Jiao, Jintao Li, Di Liang, Wanfei Cheng, Lin Lou, Hui Jin, Chao Zhang, Chunqiang Si, and Enyuan Gao

Abstract Uneven distribution of the two-phase refrigerant mass flow in the tube-evaporators in flat-plate quick-freezing (FPQF) leads to non-uniform temperature distribution and decreased heat transfer performance. Propose the diversion concept of "Transformed into annular flow pattern + Critical diversion," and a rectifying nozzle type distributor was designed. The distribution performance of the Rectifying nozzle-type critical distributor (RNCD) and the liquid storage distributor (LSD) in the freezer was studied by experiment. The results showed that at an evaporation temperature between − 31 and − 35 °C, the unevenness of the RNCD was lower than that of the LSD. The refrigerating capacity and COP of the freezer were both significantly improved. The maximum increase in refrigerating capacity and COP was 3 and 6.26%, respectively. This study provides basic data for the application of distributors in FPQF.

Keywords Distributor · Plate freezer · Unevenness · Superheat · Refrigerating capacity

F. Jiao (✉) · J. Li · D. Liang
Tianjin Key Laboratory of Refrigeration Technology, Tianjin University of Commerce, Tianjin 300134, China
e-mail: 13752003280@163.com

W. Cheng
CCCC First Harbor Engineering Company Ltd, Tianjin 300134, China

L. Lou · H. Jin
China Construction Third Bureau Group Co., Ltd, No.456 Wuluo Road, Wuhan City 430064, Hubei Province, China

C. Zhang
Moon Environment Technology Co., Ltd, No.1 Binglun Road, Zhifu District, Yantai City 264002, Shandong Province, China

C. Si · E. Gao
Hua Shang International Engineering Co., Ltd, Beijing 100069, China

E. Gao
Chinese Association of Refrigeration, Beijing 100142, China

S. Yadav et al. (eds.), *Energy Power and Automation Engineering*, Lecture Notes in Electrical Engineering 1118, https://doi.org/10.1007/978-981-99-8878-5_72

1 Introduction

The "14th 5-Year Cold Chain Logistics Plan" proposes an important instruction to strengthen the high-quality development of cold chain logistics to reduce the loss and waste of food during transportation and to ensure food quality in China [1, 2]. Various food processing and preservation technologies have been developed domestically and internationally, such as quick-freezing, refrigeration, freezing, and cold-temperature storage technologies. Quick-frozen food uses fresh food ingredients and is processed and frozen at temperatures between − 40 and − 30 °C to form tiny ice crystals inside the food that are distributed similar to the distribution of liquid water within the food [3]. This method causes minimal damage to the cell tissue structure and reduces nutrient loss, thereby ensuring food quality. Quick freezing equipment can be divided into air-circulating, contact, spray, and immersion types based on the freezing method used [4].

FPQF will use the plate-tube as evaporation device, the food will be directly or indirectly applied to the freezing plate placed on the shelf plate-tube evaporator, and evaporation plate-tube direct contact heat exchange, so as to quickly freeze food. It is primarily used for quick-freezing of seafood and meat products, such as various fish, shrimp, shellfish, and packaged meat products. Currently, during freezing in the evaporator tubes, there are issues with uneven distribution of cooling capacity, leading to uneven freezing of food and large temperature differences in frozen products, complex equipment structures, and high energy consumption, among other disadvantages. The uneven cooling capacity in the evaporator tubes is mainly due to unequal distribution of refrigerant flow rate between different lines after throttling, resulting in uneven temperature distribution in the evaporator tubes and uneven freezing of food [5].

Many scholars at home and abroad have studied the optimization methods for the performance of freezers. Liu et al. [6] investigated the impact of different liquid supply methods on the refrigeration system and applied an ejector to replace traditional expansion valves in freezers. Compared with traditional vapor compression refrigeration systems, COP increased by 26%. Shaikh et al. [7] optimized the control of tunnel-type freezers and proposed and tested a zero absolute error (ZAE) model predictive control (MPC) algorithm that can effectively control the freezing temperature and improve the stability of the refrigeration system.

Currently, research on performance optimization of the refrigeration unit in quick-freezing machines mainly focuses on two aspects: refrigerant supply mode and system control optimization. There is little research on the impact of uneven refrigerant mass flow distribution in the various branches of the evaporator on unit performance. While distributors have been applied in refrigeration systems such as air conditioning and cold storage, there is a lack of theoretical research and experimental testing of their application in quick-freezing machines. This paper mainly studies the distribution performance of the RNCD and the LSD when applied to a flat quick-freezing machine through experimental testing, as well as the impact of different distributors on the performance of the quick-freezing machine.

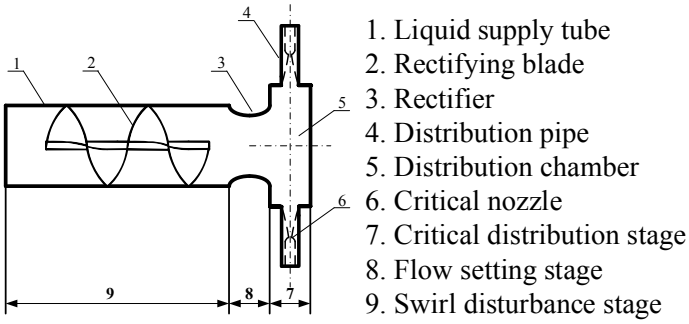

Fig. 1 Structure diagram of RNCD

2 Experimental Test Distributors

2.1 RNCD Shunt Principle and Structure

In refrigeration systems, in order to solve the phase separation problem of two-phase refrigerants during distribution, overcome the flow state of upstream refrigerant, and suppress the pressure wave oscillation caused by non-uniform heat exchange in downstream branches affecting uniform distribution, a new distributor design concept of "rectifying nozzle type distributor + pre-mixing, post-distribution + critical distribution" is proposed [8].

The RNCD is designed based on the new distribution concept. As shown in Fig. 1, the RNCD mainly consists of swirl disturbance stage 9, flow setting stage 8, and critical distribution stage 7. The disturbance stage uses centrifugal force with swirling blades to transform the asymmetric and non-uniform two-phase flow pattern after passing through the throttle device into an annular flow pattern. The shape adjustment stage adjusts the flow pattern to a stable, symmetrical, and uniform annular flow using an arc-shaped rectifier. The critical distribution stage consists of a distribution chamber and sonic nozzles. The distribution chamber evenly distributes the ideal annular flow with equal flow rate and dryness fraction to each branch, and the refrigerant then forms a critical flow through the sonic nozzle, which suppresses pressure oscillations from downstream to upstream feedback, enhances the disturbance and convective heat transfer of downstream heat exchange tubes to refrigerant.

2.2 LSD Distributor

As shown in Fig. 2, the LSD consists of a vertically mounted supply pipe, a hollow cylindrical distribution chamber, and branching channels. The two-phase refrigerant flows through the supply pipe and enters the distribution chamber of the liquid storage

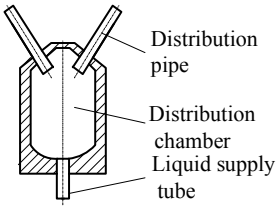

Fig. 2 Structure diagram of LSD

type distributor, where its velocity decreases. Part of the liquid refrigerant deposits at the bottom of the distributor, while the gas refrigerant carries the liquid refrigerant upwards toward the top of the LSD. The two-phase refrigerant gradually mixes evenly in the distribution chamber and is finally distributed to each branch [9].

3 Experimental Instruments and Test Methods

3.1 Experiment Instrument

As shown in Fig. 3, the schematic diagram of the refrigeration system of a FPQF with different distributors is presented. The distributor performance test device mainly consists of the FPQF, parameter measurement and acquisition system, distributor test system, and thermal balance system. During the experimental testing process, to evaluate the distribution performance of different distributors applied to the quick-freezing machine and their impact on the freezing performance, a single machine dual-stage compressor was used to achieve a double compression refrigeration cycle, providing a low-temperature testing environment. The distributors were switched manually by toggling ball valves 7 and 8. The degree of superheat in the refrigeration cycle can be controlled by manual adjustment of the electronic expansion valve. Temperature and pressure parameters at the inlet and outlet of each branch of the distributors and tube-evaporators, as well as the suction port of the compressor, were measured to calculate the degree of superheat in each branch and the pressure drop across the distributor, which allowed for analysis of the performance of different distributors.

3.2 Data Processing Method

(1) Unevenness of superheat degree

To show the diversion performance of different distributors more intuitively, this study evaluated the distributor's diversion performance by the non-uniformity of superheat [10]. The non-uniformity of the average superheat and outlet superheat of

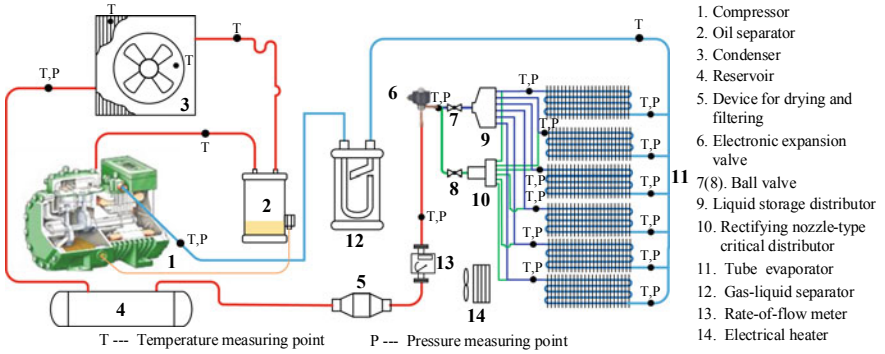

Fig. 3 Schematic diagram of the experimental setup

each branch of the shelf and tube evaporator was calculated as an evaluation index. The smaller the non-uniformity of superheat, the better the diversion performance of the distributor. The calculation of non-uniformity of superheat is as follows (1):

$$S = \sqrt{\frac{1}{n-1}\sum_{i=1}^{n}\left(\frac{T_i}{\overline{T}} - 1\right)^2} \tag{1}$$

where S represents the distribution performance of the distributor; T_i is the superheat of each branch, °C; and $\overline{T}$ is the average superheat of each branch, °C.

(2) Refrigeration capacity

This paper assessed and calculated the refrigeration capacity of the freezer using a heat balance method. The experiment used a heat balance system to adjust the heating power of the electric heater to achieve a balanced state between heating and cooling, allowing the temperature inside the cold storage to reach stability. By calculating the total heat dissipation of all heat dissipating components inside the cold storage, the unit's refrigeration capacity was obtained. The total heating power includes fan power, electric heater heating power, and cold storage leakage, which are calculated as follows (2):

$$Q = K_C(T_2 - T_1) + W_d + W_t \tag{2}$$

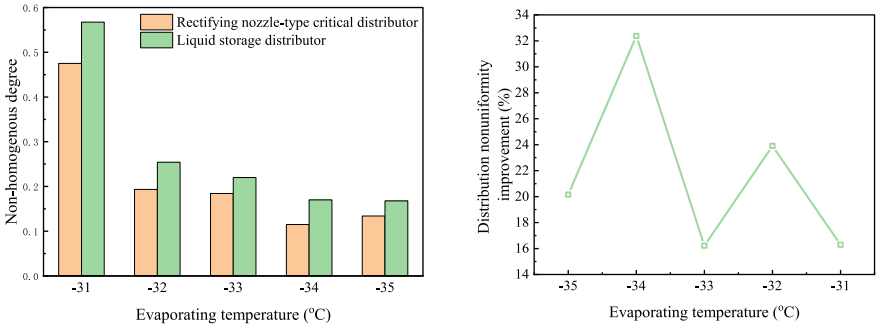

(a) Unevenness of superheat (b) Reduce uneven distribution

Fig. 4 Analysis of shunt inhomogeneity at different evaporating temperatures

4 Experimental Results and Analysis

4.1 Tube Evaporator Branch Outlet Superheat Unevenness Analysis

Figure 4 illustrates the influence of different evaporating temperatures on the distribution performance of the RNCD and LSD under experimental conditions. Figure 4a shows that as the evaporating temperature decreases at − 31, − 32, − 33, − 34, and − 35 °C, the non-uniformity of both distributors' distributions decreases. This is because as the evaporating temperature decreases, the mass flow rate of refrigerant in the refrigeration system also decreases. Under the same experimental conditions, the non-uniformity of the RNCD was lower than that of the LSD. Compared with the LSD, Fig. 4b shows that the non-uniformity of the RNCD decreased by 16.30, 23.91, 16.22, 32.38, and 20.16% as the evaporating temperature decreased. The design of the RNCD effectively improves the uneven distribution of the two-phase refrigerant. Due to the improved structure of the RNCD, the asymmetric and non-uniform flow pattern of the throttled two-phase refrigerant is transformed into an annular flow pattern using swirling blades and a rectifier, achieving equal dryness fraction and flow rate distribution of refrigerant.

4.2 Pressure Drop Analysis of Distributor

Figure 5 shows the effect of different evaporating temperatures on the total pressure drop of the evaporator and distributor. It is shown that the pressure drops of the distributor and the total pressure drop of the evaporator have a small decreasing trend as the evaporating temperature decreases. As the evaporating temperature decreases,

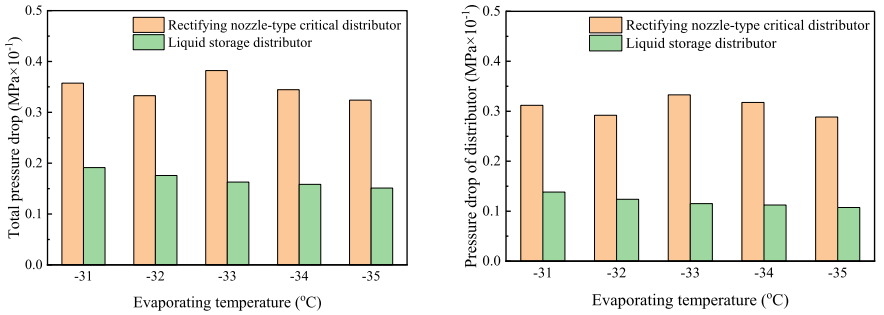

(a) Total pressure drop (b) Distributor pressure drop

Fig. 5 Analysis of pressure drop inhomogeneity of distributor different evaporation temperatures

the opening of the electronic expansion valve decreases, the mass flow rate of refrigerant in the system decreases, and the liquid refrigerant flow rate decreases, resulting in a decrease in the pressure drop of the distributor and the total pressure drop. In actual refrigeration systems, the throttling process is isenthalpic throttling, which has large irreversible losses. The distributor undertakes part of the throttling pressure drop, which can effectively reduce the irreversible losses of the throttling process.

4.3 Performance Analysis of Quick Freezer

Figure 6 shows the influence of different evaporating temperatures on the performance of the quick-freezing machine when using different distributors. Figure 6a expresses that when using both distributors, the system refrigeration capacity decreases as the evaporating temperature decreases, which is in line with the basic principles of refrigeration. Under the same test conditions, the refrigeration capacity and COP of the FPQF using the RNCD were higher than those using the LSD. The experimental results show that the distribution effect of the RNCD is better than that of the LSD under different operating conditions. As shown in Fig. 6, when the evaporating temperature is − 31 °C, the refrigeration capacity of the system using the RNCD is 14.967 kW. As the evaporating temperature decreases, compared with the LSD, the refrigeration capacity of the system using the RNCD can be increased by up to 3%. The COP was improved by 5.07, 3.99, 3.69, 5.83, and 6.26% respectively.

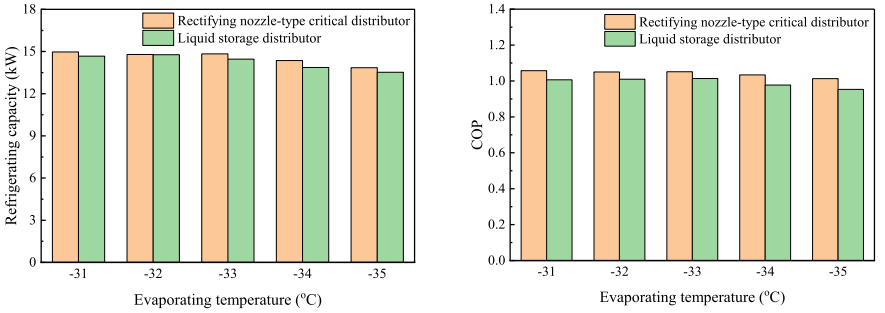

(a)Refrigerating capacity (b) COP

Fig. 6 Analysis of shunt inhomogeneity at different cold storage temperatures

5 Conclusion

This study investigated the distribution performance and the influence on the performance of a FPQF machine using two types of distributors through experiments. The distribution performance of the distributors was analyzed from the perspectives of non-uniformity of superheat, refrigeration capacity, COP, and pressure drop under stable experimental conditions. The non-uniformity of distribution of the RNCD was lower than that of the LSD at evaporating temperatures between − 31 and − 35 °C. The refrigeration capacity and COP of the FPQF were significantly improved, with the maximum increase in refrigeration capacity being 3% and in COP being 6.26%. The results showed that the distribution effect of the RNCD was significantly better than that of the LSD, which can achieve more uniform distribution of two-phase refrigerant and improve the freezing uniformity of the FPQF. The feasibility of the distribution principle of the RNCD has been demonstrated in practical applications, supplying basic support for the application of distributors in FPQF.

Acknowledgements The authors are grateful for the support of the project supplied by Key Technology Research and Application Demonstration of Grape Deep-processing Equipment in Yutian County Science and Technology Assistance and Promotion Major Project of Tianjin Science and Technology Bureau (22ZYCGSN00030), Tianjin Research Innovation Project for Postgraduate Students (22YJSKYCX17), and Key Technology and System of Virus Elimination in Cold Chain Imported Frozen Food (22ZXJBSN00010).

References

1. Aste N, Del Pero C, Leonforte F (2017) Active refrigeration technologies for food preservation in humanitarian context: a review. Sustain Energy Technol Assess 22:150–160. https://doi.org/10.1016/j.seta.2017.02.014

2. Yu H, Mei J, Xie J (2022) New ultrasonic assisted technology of freezing, cooling and thawing in solid food processing: a review. Ultrason Sonochem 12:106185. https://doi.org/10.1016/j.ultsonch.2022.106185
3. Lu R, Yuan Z (2021) Development and research status of quick frozen food. China Food Saf Magaz 10:60–61
4. Singh R, Heldman D (2014) Chapter 7-food freezing. Introduction to food engineering, 5th edn. Food science and technology, Academic Press, San Diego, pp 521–63. https://doi.org/10.1016/B978-0-12-398530-9.00007-3
5. Xiong T, Liu G, Huang S et al (2022) Two-phase flow distribution in parallel flow mini/micro-channel heat exchangers for refrigeration and heat pump systems: a comprehensive review. Appl Therm Eng 201:117820. https://doi.org/10.1016/j.applthermaleng.2021.117820
6. Liu Y, Yu J (2019) Performance evaluation of an ejector subcooling refrigeration cycle with zeotropic mixture R290/R170 for low-temperature freezer applications. Appl Therm Eng 161:114128. https://doi.org/10.1016/j.applthermaleng.2019.114128
7. Shaikh NI, Prabhu V (2007) Model predictive controller for cryogenic tunnel freezers. J Food Eng 80(2):711–718. https://doi.org/10.1016/j.jfoodeng.2006.04.064
8. Sun Z, Wang Q, Liang Y et al (2020) Experimental study on improving the performance of dry evaporator with rectifying nozzle type critical distributor. Int J Refr 111:39–52. https://doi.org/10.1016/j.ijrefrig.2019.11.018
9. Han Q, Zhang C, Xu B et al (2014) Experimental investigation on the distribution performance of refrigerant distributors. J Refr 35(03):1–7
10. Yoshioka S, Kim H, Kasai K (2007) Performance evaluation and optimization of a refrigerant distributor for air conditioner. In: Proceedings of the heat transfer summer conference. https://doi.org/10.1115/HT2007-32664

Organic Rankine Cycle System Variable Condition Analysis

Weiting Jiang, Danyang Song, Hongpeng Jing, and Weiguo Pan

Abstract Organic Rankine Cycle (ORC) power generation systems are one of the most efficient technological means of converting low and medium quality energy sources into mechanical energy at this stage. In this paper, the ORC power generation system is modeled using GREATLAB simulation software, the system input parameters are varied, and the system performance indicators are compared by sensitivity analysis to determine the parameters that have a significant impact on the organic Rankine cycle system.

Keywords Organic Rankine Cycle · Sensitivity analysis · GREATLAB

1 Introduction

Currently, energy consumption accounts for about 70% of total energy consumption, making reducing waste energy in the industry a top priority. The technology for recovering and reusing waste heat at high temperatures is relatively mature, but the technology for recovering and using waste heat is not yet mature at medium and high temperatures.

Several factors influence the operation of medium and low-temperature Organic Rankine Cycles. Among them, the choice of the working fluid has a significant influence on the operating parameters of the system [1]. Organic Rankine Cycles have also been applied to geothermal [2], marine [3], biomass, and automotive [4, 5].

Currently, many studies focus on model optimization [6–10] and few on building experimental platforms for ORC systems; Byung-Sik Park et al. summarized the performance of the most advanced ORC system today, which gave an organic Rankine cycle (mechanical-electric) conversion efficiency of about 70% [11].

W. Jiang (✉) · D. Song · H. Jing · W. Pan
College of Energy and Mechanical Engineering, Shanghai University of Electric Power, Shang Hai 200090, China
e-mail: jiangweiting618@163.com

S. Yadav et al. (eds.), *Energy Power and Automation Engineering*, Lecture Notes in Electrical Engineering 1118, https://doi.org/10.1007/978-981-99-8878-5_73

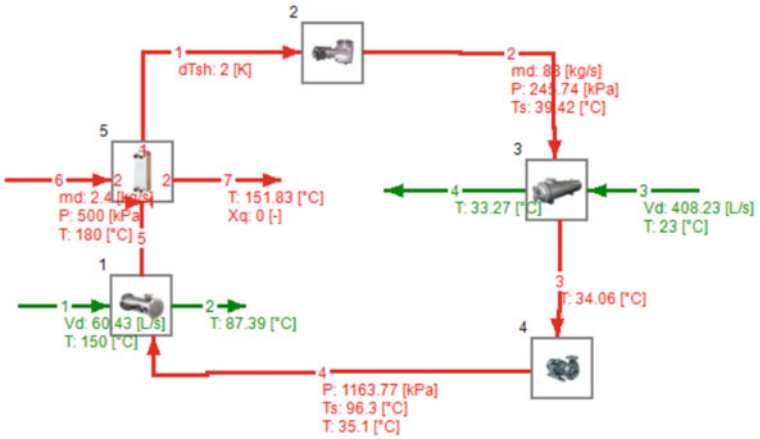

Fig. 1 Organic Rankine Cycle (ORC) system

This study intends to simulate and optimize the off-design operating characteristics of megawatt organic Rankine cycle units, and the specific research contents are as follows.

2 Construction of Organic Rankine Circulation System

2.1 Modeling of Organic Rankine Cycle (ORC) System

To optimize the ORC system, a waste heat recovery system was installed based on the ORC system principle, as shown in Fig. 1. The cooling water source for this system is purified river water. The system comprises 1-evaporator, 5-superheaters, 2-turbines, 3-condensers, and 4-working fluid pumps. The system uses circulating water at 130 °C, 250 t/h, 0.5 MPa as the heat source, and R245fa as the working fluid. At design conditions, the turbine power is 2.66 MW, isentropic efficiency is 80%, and mechanical efficiency is 98%.

2.2 System Accuracy Verification

Using the model library of the GREATLAB platform and some characteristic parameters of the Organic Rankine Cycle system, that can be built and system design conditions can be entered for each part. Once the system is built, the system parameters must be adjusted to achieve a certain degree of accuracy. After continuous adjustment, five data sets with evaporation temperatures between 130 and 135 °C

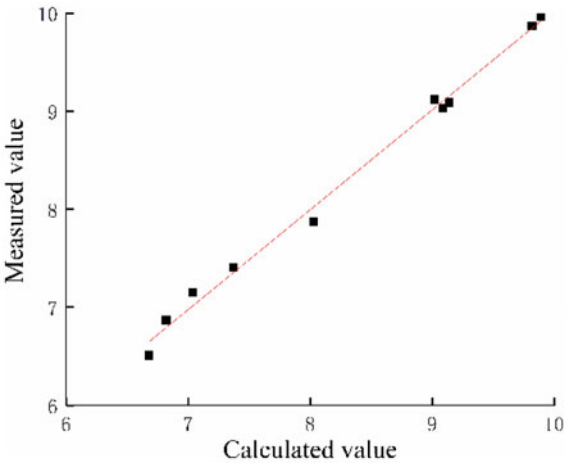

Fig. 2 Comparison of calculated and measured values at heat source temperatures of 130 and 135 °C

were selected, as shown in Fig. 2, to compare the net result and ensure that the error between the calculated system values and the simulated measured values was < 5%. This shows that the model has suitable accuracy and can be used for simulation.

Output power refers to the overall external output power of the system:

$$W_{net} = W_{turb} - W_{pump} \tag{1}$$

In the formula: W_{turb}——Turbine output power, kW;
W_{pump}——Pump power, kW.

2.3 *Effect of Evaporator Heat Source Inlet Temperature on ORC System*

When the evaporating temperature increases, the temperature of the cold source remains the same, so the circulating temperature difference in the system increases, the thermal efficiency of the system will also increase, and the net output power also increases, as shown in Figs. 3 and 4.

2.4 *Effect of Condenser Cold Source Inlet Temperature on ORC System*

When the condensate temperature becomes higher, the heat transfer temperature difference between the organic mass and the condensate in the ORC system decreases,

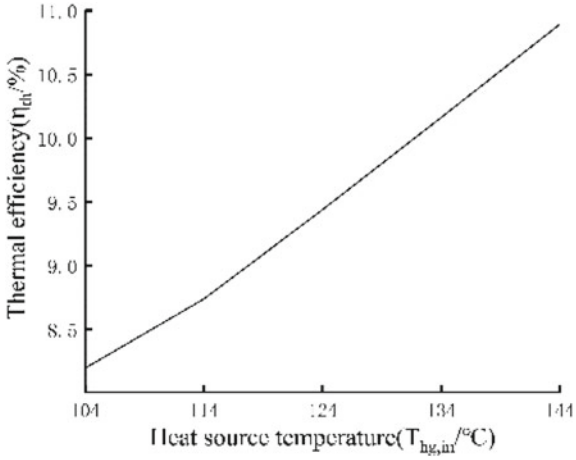

Fig. 3 Thermal efficiency curve

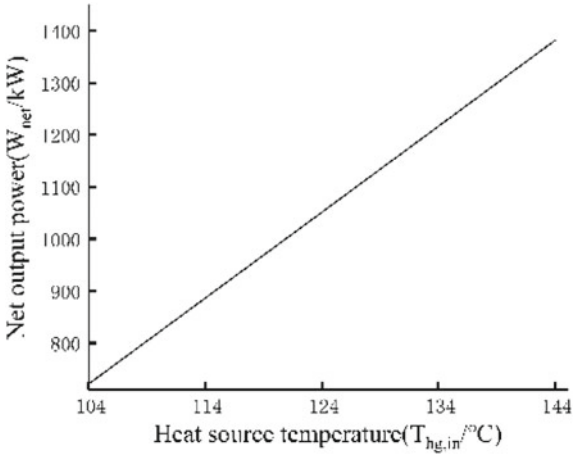

Fig. 4 Net output efficiency curve

resulting in a lower heat exchange, and therefore lower net output power and lower thermal efficiency, as shown in Figs. 5 and 6.

2.5 Effect of Cooling Water Flow on ORC Systems

When the cooling water flow rate increases, the temperature of the organic work mass before entering the evaporator will be lower, and its heat absorption effect in the evaporator heat source will be more significant, that is, the heat absorption increases. Therefore, the work mass entering the turbine to do work will make the net

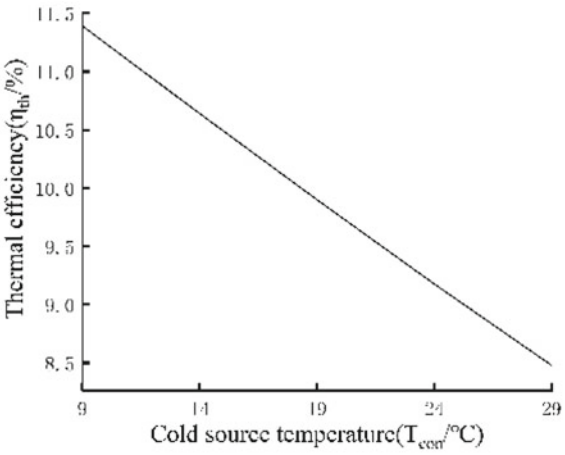

Fig. 5 Thermal efficiency curve

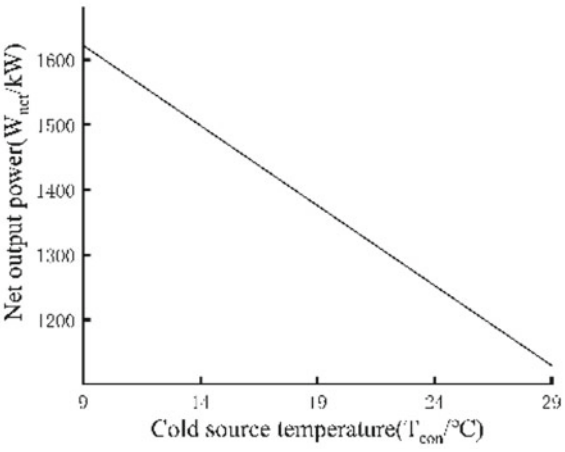

Fig. 6 Net output efficiency curve

output power increase and the cycle thermal efficiency increase, as shown in Figs. 7 and 8.

2.6 Effect of Superheat on ORC Systems

The increase in superheat causes the work mass flow rate to decrease and the thermal efficiency to decrease from 9.6 to 9.2%. The net output power decreases by 7.5 kW for each 1 °C increase in superheat, as shown in Figs. 9 and 10.

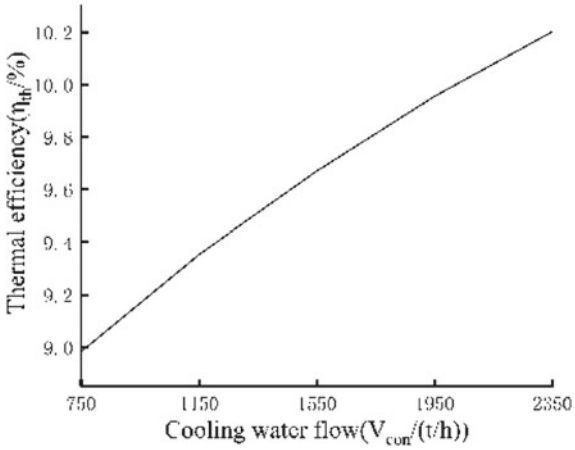

Fig. 7 Thermal efficiency curve

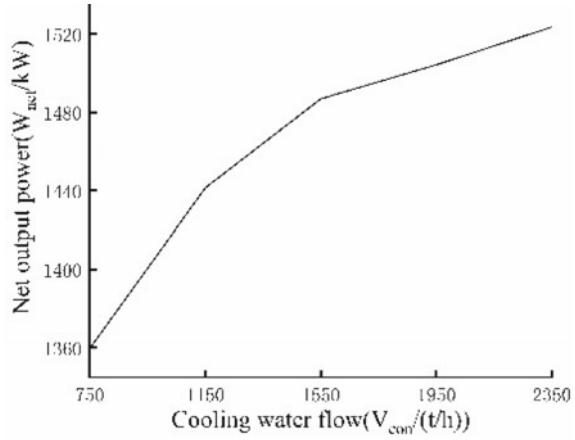

Fig. 8 Net output efficiency curve

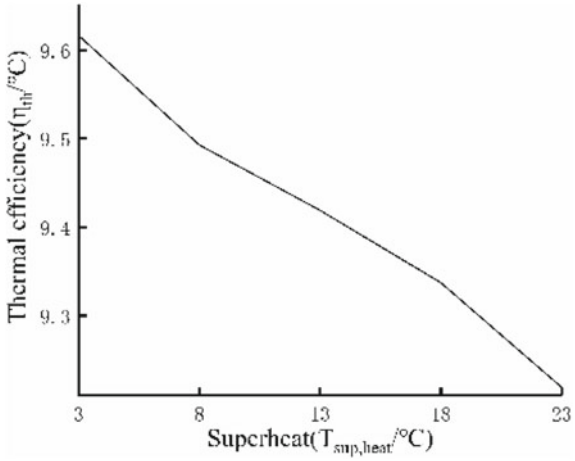

Fig. 9 Thermal efficiency curve

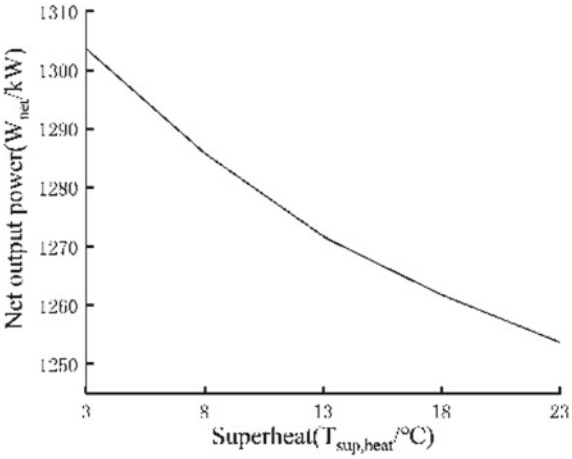

Fig. 10 Net output efficiency curve

3 Sensitivity Analysis

The sensitivity analysis of parameters can indicate the influence of each parameter on the system performance trend. In general, the sensitivity of ORC system operating parameters can be characterized by first-order partial derivative, and its expression is as follows:

$$m = \mathrm{d}y/\mathrm{d}x \tag{2}$$

A sensitivity analysis of the five ORC system parameters (evaporation temperature, cold source temperature, superheat, and cooling water flow) to the system output (net output power, thermal efficiency) is presented in Table 1 below. Taking evaporation temperature as an example, the sensitivity of evaporation temperature to net output is 0.07, meaning that 1 °C increase in evaporation temperature increases net output by 21.56 kW. A positive sensitivity means that the relationship between the parameter and the system output parameter is positive, a negative sensitivity means that the relationship is negative, and a value close to zero means that the parameter has no effect on the system output.

Table 1 Sensitivity analysis results

Parameter	Net output power	Thermal efficiency
	Average value	Average value
Evaporation temperature	0.07	0.0026
Superheat	− 0.005	− 0.00085
Cold source temperature	− 0.009	− 0.00005
Cooling water flow	0.0018	0.0024

The constructed system was analyzed under varying operating conditions and the influence of each parameter was compared on the system performance parameters. The results of the sensitivity analysis show that the parameters that have a significant impact on the system performance parameters are evaporation temperature, cold source temperature, and superheat. On this basis, a multi-parameter optimization of the system is performed.

4 Conclusion

This paper summarizes the current development status and research direction of ORC power generation technology, uses GREATLAB simulation software to establish a model for megawatt organic Rankine cycle system, uses evaporation temperature, cold source temperature, cold source flow rate and superheat degree as system parameter variables, and thermal efficiency and net output power as system performance parameters to simulate the ORC system; the parameters with the greatest influence on system performance parameters are determined by sensitivity analysis as evaporation temperature.

References

1. Wang EH, Zhang HG, Fan BY, Ouyang MG, Zhao Y, Mu QH (2011) Study of working fluid selection of organic Rankine cycle (ORC) for engine waste heat recovery. Energy 36:3406–3418
2. Yang MH, Yeh RH (2014) Analyzing the optimization of an organic Rankine cycle system for recovering waste heat from a large marine engine containing a cooling water system. Energy Conver Manag 88:999–1010
3. Kazemi N, Samadi F (2016) Thermodynamic, economic and thermo-economic optimization of a new proposed organic Rankine cycle for energy production from geothermal resources. Energy Conver Manag 121:391–401
4. Andreasen JG, Meroni A et al (2017) A comparison of organic and steam Rankine Cycle power systems for waste heat recovery on large ships. Energies 10:547
5. Dimitrova Z, Lourdais P et al (2015) Performance and economic optimization of an organic Rankine cycle for a gasoline hybrid pneumatic power train. Energy 86:574–588
6. Zerom MS, Gonca G (2020) Multi-criteria performance analysis of dual miller cycle–Organic Rankine cycle combined power plant. Energy Conver Manag 221:113121
7. Sun J, Li W et al (2011) Operation optimization of an organic Rankine cycle (ORC) heat recovery power plant. Appl Therm Eng 31(11–12):2032–2041
8. Wei DH, Lu XS et al (2008) Dynamic modeling and simulation of an Organic Rankine Cycle (ORC) system for waste heat recovery. Appl Therm Eng 28:1216–1224
9. Wu Q, Ren HB et al (2018) Design and operation optimization of organic Rankine cycle coupled trigeneration systems. Energy 142:666–677
10. Wu XL, Chen JH et al (2018) Integrated operation design and control of Organic Rankine Cycle systems with disturbances. Energy 163:115–129
11. Schuster A, Karellas S et al (2009) Energetic and economic investigation of Organic Rankine Cycle applications. Appl Therm Eng 29:1809–1817

Mechanisms of Air Cathode Pore Structure Parameters and Discharge Regimes on the Performance of Lithium–Air Batteries

Junlong Chen, Biyi Huang, Li Yang, Shan Gu, Zhenzhen Shi, Ru Yang, and Xianfeng Yu

Abstract As the society pays more attention to energy, various kinds of new energy batteries are coming out. Lithium–air battery is a new energy battery that uses lithium metal as the anode and oxygen in air as the positive reactant. Because of its specific energy comparable to that of fuel cells, lithium–air batteries are the most popular research in the direction of new energy batteries in the past few years. However, there are still some disadvantages of Li–air batteries that prevent them from being commercialized well, such as the accumulation of discharge products in the pores of the cathode, which leads to premature termination of the discharge reaction. Therefore, it is necessary to simulate the battery to investigate the existing problems. In this paper, we focus on the effects of lithium-air battery cathode porosity and discharge current density on battery performance and propose certain optimization strategies to address these problems.

Keywords New energy · Lithium–air batteries · Cathode porosity · Discharge current density

1 Introduction

With global warming and the global energy crisis, new energy electric vehicles are receiving more attention in the world. Lithium-air batteries (LABs) have been attracting attention for their high specific energy (11,400 Wh/kg) [1]. Depending on the electrolyte, LABs can be classified into organic system LABs, aqueous electrolyte LABs, organic-water hybrid electrolyte LABs, and all-solid electrolyte LABs, among which organic system LABs have been widely studied due to their simple structure and high energy density. The discharge reaction equation of organic LABs is shown in

J. Chen · B. Huang (✉) · L. Yang · S. Gu · Z. Shi · R. Yang · X. Yu
Zhejiang-Belarus Joint Laboratory of Intelligent Equipment and System for Water Conservancy and Hydropower Safety Monitoring, Zhejiang University of Water Resources and Electric Power, Hangzhou, China
e-mail: huangby@zjweu.edu.cn

S. Yadav et al. (eds.), *Energy Power and Automation Engineering*, Lecture Notes in Electrical Engineering 1118, https://doi.org/10.1007/978-981-99-8878-5_74

Eqs. (1–3), whose anode is generally lithium monomer, which provides the lithium source required for the reaction, and the cathode is a porous material with good reactivity and large specific surface area. Having an open structure is one of the characteristics of LABs, where Li^+ reacts directly with oxygen from the air at the cathode. Li_2O_2 is formed and deposited on the cathode surface during discharge, while Li_2O_2 is oxidized and decomposed during charging [2].

$$\text{Anode reaction}: \quad Li \rightarrow Li^+ + e^- \tag{1}$$

$$\text{Cathode reaction}: \quad 2Li^+ + O_2 + 2e^- \rightarrow Li_2O_2 \tag{2}$$

$$\text{Total reaction}: \quad 2Li + O_2 \rightarrow Li_2O_2 \tag{3}$$

However, the specific capacity of LABs is often much lower than the theoretical value during the actual cycling process, which is due to the insoluble discharge product Li_2O_2 formed at the cathode during the discharge process. With Li_2O_2 continuously generated, the pores in the cathode are gradually blocked, and it is difficult for oxygen in the air to enter the cathode for reaction. In addition, Li_2O_2 has poor electrical conductivity and affects the electron transfer on the electrode surface, which reduces the battery capacity and cycling performance.

Therefore, designing a reasonable air transport path is of great importance to improve the cell performance of LABs [3]. Zhang et al. [4] used KB600 and Super P, materials with different porosity, to make composite electrodes, and the obtained electrodes exhibited higher air transfer capability by mixing KB600 with Super P in a 5:1 weight ratio. Tan et al. [5] prepared a gradient 100–500 μm gradient porous cathode for non-aqueous LABs with extremely high discharge capacity, thus demonstrating that the gradient porous distribution is necessary for the performance enhancement of LABs. In order to further explore the influence of each parameter of the battery on the battery performance, it is necessary to simulate and analyze the mechanism of the internal working process of the battery [6]. Sergeev et al. [7] developed a pore size distribution model for LABs and investigated the relationship between the pore size and the battery performance, concluding that the introduction of larger pore sizes has a significant enhancement of the battery capacity. Li et al. proposed a linear gradient pore structure and demonstrated that the use of linear porous air cathodes resulted in higher specific capacity, more uniform porosity, and more desirable oxygen diffusion coefficients for LABs. In addition, the discharge current density also affects the variation of electrode porosity, which changes the cell capacity [8]. Zhang et al. [9] found that the discharge capacity of LABs decreased sharply with increasing the discharge current density from 0.1 to 0.5 mA/cm^2 at the same electrode thickness. By studying the performance of the porosity LABs at discharge current densities of 0.05 and 0.5 mA/cm^2. Zhang et al. [10] concluded that if the range of the porosity gradient is too large at higher discharge current densities, it will lead to a significant increase in the overpotential of the battery, which will affect the performance of the battery. In summary, the porosity distribution of the

electrode has a very important effect on the performance of LABs, so it is necessary to investigate the effect of the initial porosity distribution and the discharge regime on the performance of LABs. Therefore, this paper constructs an electrochemical model of organic LABs with the help of Comsol software platform to systematically investigate the influence mechanisms of air cathode pore structure parameters and discharge regimes on the battery performance.

2 LABs Moddel

In this paper, a LAB with organic electrolyte is used as the research object, and its schematic diagram is shown in Fig. 1a. When the lithium-air works, the outer air of the cathode diffuses into the pore and reacts with the lithium ions in the electrolyte at the cathode to form lithium peroxide; the lithium monomer at the anode loses electrons to form lithium ions into the cathode. Assuming that the material transport process occurs only in the direction of the cell thickness, the cell can be simplified to a line, so the one-dimensional spatial dimension is chosen to construct the LAB model in this paper (Fig. 1b).

Inside the air cathode, oxygen diffusion, Li^+ diffusion and migration in the electrolyte, electron load transport in the porous carbon skeleton of the air cathode, and discharge product deposition and decomposition phenomena mainly occur. For the above complex physicochemical phenomena, the following assumptions are made:

- the convective transfer phenomena caused by the discharge product generation and decomposition are not considered;
- the initial solubility of oxygen in the electrolyte is saturated during the discharge process, and the solubility of oxygen in the electrolyte is constant;
- the products in the air cathode during the discharge process are all Li_2O_2;

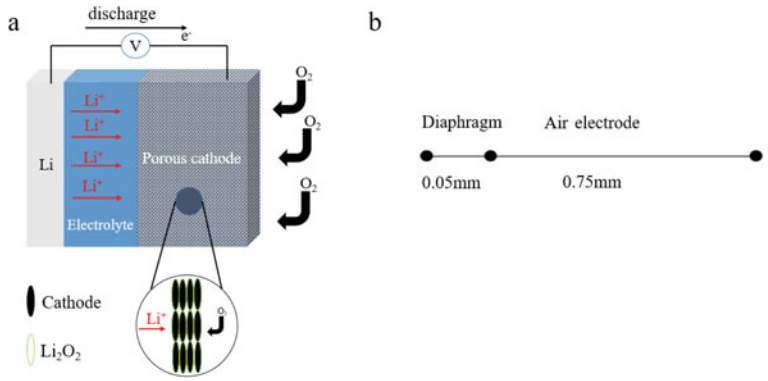

Fig. 1 Model of organic electrolyte LAB

- the electrochemical reactions of both positive and anodes satisfy the Butler-Volmer equation.

The internal control equations and boundary conditions of the non-aqueous LABs during discharge are listed below.

The potential of the cathode can be expressed by Eq. (4):

$$K_{\text{pos}} \nabla \phi_s - a_{\text{pos}} J = 0 \tag{4}$$

K_{pos} is the electrical conductivity and ϕ_s is the potential of the cathode, and the change of ϕ_s represents the change in the output voltage of the cell due to grounding the anode. a_{pos} signifies the specific surface area of the air cathode diaphragm, whose expression is given in Eq. (5). J manifests the current density of the cathode, which can generally be described by the Buster-Volmer equilibrium method, whose expression is given in Eq. (6).

$$a_{\text{pos}} = a_{\text{pos}} \left[1 - \frac{\varepsilon_{\text{Li}_2\text{O}_2}}{\varepsilon_{l0}} \right] \tag{5}$$

$$J = nF \left[K_c (c_{\text{Li}})^2 C_{\text{O}_2} \exp\left(\frac{0.5nF\eta}{\text{RT}} \right) - K_a C_{\text{Li}_2\text{O}_2} \exp\left(\frac{-0.5nF\eta}{\text{RT}} \right) \right] \tag{6}$$

a_{pos0} is the initial active specific surface area of the anode, and the relevant parameters are shown in Table 1. $\varepsilon_{Li_2O_2}$ is the volume fraction of Li_2O_2, and its expression is given in (7), and ε_{l0} indicates the initial porosity. n is the number of electrons transferred, F = 96,487 C/mol, which represents the Faraday constant. η means the overpotential, whose expression is given in (8), K_a represent the reaction rate coefficient of the metal Li, and K_c is the reaction rate coefficient of the cathode. R implies the molar gas constant, which is ~ 8.314472, T represents the temperature.

$$\varepsilon_{\text{Li}_2\text{O}_2} = \left(c_{\text{Li}_2\text{O}_2} - c_{0,\text{Li}_2\text{O}_2} \right) \times \frac{M_{\text{Li}_2\text{O}_2}}{\rho_{\text{Li}_2\text{O}_2}} \tag{7}$$

$$\eta = \phi_s - \phi_l - \Delta\phi_{\text{flim}} - E_{\text{eq}} \tag{8}$$

$c_{Li_2O_2}$ denotes the concentration of Li_2O_2 at any moment, c_{0,Li_2O_2} means the initial Li_2O_2 concentration, $M_{Li_2O_2}$ and $\rho_{Li_2O_2}$ signifies respectively the molecular weight of Li_2O_2 and the density of Li_2O_2, ϕ_l represents the electrolyte potential, E_{eq} is the equilibrium voltage. $\Delta\phi_{flim}$ denotes the membrane resistance voltage, the expression of which is given in (9). R_{flim} represents the membrane resistance of the membrane in Eq. (9).

$$\Delta\phi_{\text{flim}} = \text{J}R_{\text{flim}}\varepsilon_{\text{Li}_2\text{O}_2} \tag{9}$$

Table 1 Model initial values and related parameters

Parameters	Symbol	Value	Parameters	Symbol	Value
The length of the diaphragm [8]	L_{sep}	5×10^{-5} m	Diffusion coefficient of Li^+ in electrolyte [8]	D_{Li}	2.11×10^{-9} m^2/s
Length of air cathode	L_{pos}	7.5×10^{-4} m	Oxygen diffusion coefficient [8]	D_{O_2}	7×10^{-10} m^2/s
Conductivity of cathode [11]	K_{pos}	10 S/m	Conductivity of Li^+ in electrolyte [8]	K_{Li}	1.085 S/m
Initial porosity of air cathode [8]	ε_{l0}	0.73	Transference number of Li^+ in electrolyte [8]	t^+	0.2594
Initial active material solid fraction of cathode	ε_{s0}	0.27	Reaction rate coefficient anodic current [8]	K_a	1.11×10^{-15} m/s
Porosity of separator [8]	ε_{sep}	0.87	Reaction rate coefficient cathodic current	K_c	3.4×10^{-17} $m^7/s/mol^2$
Particle radius in the cathode [8]	r_{pos0}	25×10^{-9} m	Reference exchange current density Li metal	i_{0refLi}	9.65×10^{-1} A/m^2
Initial active specific surface area in cathode	a_{pos0}	3.24×10^7 m^{-1}	Equilibrium potential for oxygen reduction reaction [8]	E_{eq}	2.96 V
Film resistance across Li_2O_2 film [8]	R_{film}	50 Ω*m^2	Number of transferred electrons [8]	N	2
Reference concentration of Li^+ [8]	c_{Li0}	1000 mol/m^3	Density of Li_2O_2 [8]	$\rho_{Li_2O_2}$	2140 kg/m^3
Solubility factor of oxygen in electrolyte [8]	Sol_{O2}	0.4	Molecular weight of Li_2O_2 [7]	$M_{Li_2O_2}$	45.88×10^{-3} kg/mol
External oxygen concentration in air at 1 atm [8]	c_{O_2ext}	9.46 mol/m^3	Density of carbon [7]	ρ_{carbon}	2260 kg/m^3
Initial oxygen concentration in cathode	c_{O_20}	3.784 mol/m^3	Temperature [8]	T	300 K
Solubility limit of Li_2O_2 dissolved in electrolyte [8]	$c_{maxLi_2O_2}$	0.09 mol/m^3	Applied current density	i_{-app}	$-0.05 \times a$ mA/cm^2

The current density J_1 of another lithium metal as the anode can be obtained from the Buster-Volmer equilibrium method, the expression of which is given in (10), where $i_{0\text{refLi}}$ is the negative exchange current density.

$$J_1 = i_{0\text{refLi}}\left(\exp\left(\frac{0.5nF\eta}{\text{RT}}\right) - \exp\left(\frac{-0.5nF\eta}{\text{RT}}\right)\right) \tag{10}$$

As mentioned previously, the effective diffusion coefficients of oxygen and lithium ions are shown in Eqs. (11) and (12) when convection is not considered in the whole model and the Bruggeman model is chosen for the effective diffusion coefficient model.

$$D_{e,\text{O}_2} = \varepsilon^{1.5} D_{\text{O}_2} \tag{11}$$

$$D_{e,\text{Li}^+} = \varepsilon^{1.5} D_{\text{Li}} \tag{12}$$

As the discharge of the LABs proceeds, Li_2O_2 precipitation is produced, and the domain ordinary differential and differential algebraic equations are applied in Comsol to analyze whether Li_2O_2 precipitation occurs in the cell. The relevant expressions are given in (13).

$$d_a \frac{\partial c_{\text{Li}_2\text{O}_2}}{\partial t} = \frac{1}{2F} i_{v\text{tot}}\left(c_{\text{Li}_2\text{O}_2} > c_{\text{max Li}_2\text{O}_2}\right), \tag{13}$$

d_a is the damping or quality factor, taken as 1. i_{vtot} is the electrode reaction source. Equation (13) shows that precipitation occurs when the concentration of Li_2O_2 in the electrolyte exceeds the dissolution limit of dissolved Li_2O_2 in the electrolyte.

The pore utilization rate shows in Eq. (14). S is pore utilization rate, S_0 indicates the integrated area of initial porosity and S_t indicates the integrated area of porosity after a certain time of discharge.

$$S = \frac{(S_0 - S_t)}{S_0} \times 100\% \tag{14}$$

Finally, the system is set up with the cell size of the grid partition for the finer refinement. The initial porosity of the cathode of the cell is 0.73, and the condition of reaction stop in the cell is set at 2.5 V. The initial values of other parameters are detailed in Table 1.

3 Results and Discussion

To investigate the effect of different porosities on the performance of LABs, three pore structures were selected for comparison. Single porosity, i.e., the cathode has a unique porosity $\varepsilon = 0.73$; linearly varying porosity, i.e., the cathode porosity changes linearly with the electrode thickness direction, from the inner side of the cell to the outer side of the air as $\varepsilon = 0.63 \sim 0.83$; gradient porosity, i.e., the cathode porosity is divided into two kinds along the thickness direction, with the inner half as $\varepsilon = 0.63$ and the outer half as $\varepsilon = 0.83$, which is expressed in the text as $\varepsilon = 0.63$–0.83. The oxygen concentrations along the electrode thickness direction for different porosities are given in Fig. 2. All electrodes exhibit higher oxygen concentration on the air side, which gradually decreases with the electrode thickness direction, indicating that there is a resistance to oxygen diffusion into the interior of the electrode. From Fig. 2a, it can be seen that the electrode with gradient porosity has the highest internal oxygen concentration, followed by the linear porosity electrode, and the single porosity electrode has the lowest oxygen concentration, indicating that the gradient porosity is conducive to the diffusion of oxygen to the internal. When the discharge current density increased to 0.5 mA/cm^2 (Fig. 2b), the oxygen concentration on the outer side of the electrode decreased sharply, and very little oxygen could diffuse into the inner part of the electrode to participate in the reaction.

The variation of porosity at different current densities is given in Fig. 3. The pore utilization rate was calculated by Eq. (14) and is shown in Table 2. The difference between the utilization rate of linear porosity and single porosity in the early stage is not significant, which is due to the short time of discharge, and as the discharge time continues, the utilization rate of linear porosity is greater than that of single porosity. At the discharge current density of 0.05 mA/cm^2, the utilization rate of the

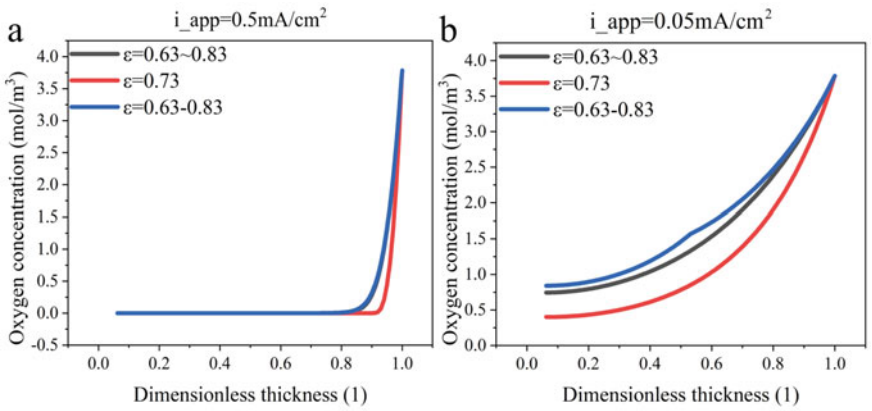

Fig. 2 Oxygen concentration of cathode with different porosities. **a** Discharge time = 3*10^6 s; **b** Discharge time = 4*10^4 s

cathode with the gradient porosity structure increased substantially and more Li_2O_2 was precipitated inside the air cathode with time.

When the discharge current density increases to 0.5 mA/cm^2, a large amount of Li_2O_2 collects on the air side of the electrode, which causes a significant decrease in the utilization rate inside the air cathode. In contrast, the gradient porosity structure has a higher electrode pore utilization, indicating that it is more favorable for the

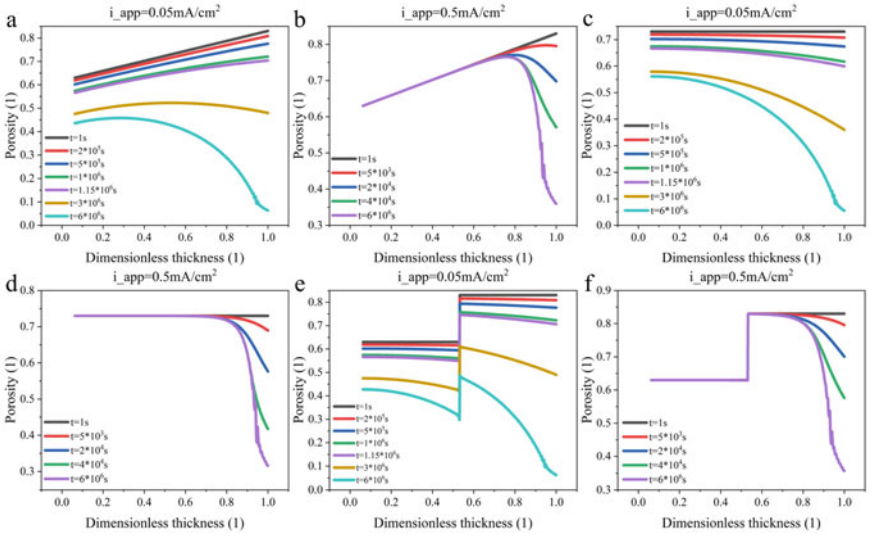

Fig. 3 Porosity variation at different discharge current densities. **a**, **b**: $\varepsilon = 0.63 \sim 0.83$; **c**, **d** $\varepsilon = 0.73$; **e**, **f** $\varepsilon = 0.63$–0.83

Table 2 Electrode pore utilization at different pore gradients

Porosity	0.73	0.63 ~ 0.83	0.63–0.83
Utilization at 0.05 mA/cm^2 ($t = 1$ s)	0%	0%	0%
Utilization at 0.05 mA/cm^2 ($t = 2*10^5$ s)	2.0%	2.0%	4.6%
Utilization at 0.05 mA/cm^2 ($t = 5*10^5$ s)	5.1%	5.1%	7.6%
Utilization at 0.05 mA/cm^2 ($t = 1*10^6$ s)	10.1%	10.1%	12.5%
Utilization at 0.05 mA/cm^2 ($t = 1.15*10^6$ s)	11.6%	11.6%	14.0%
Utilization at 0.05 mA/cm^2 ($t = 3*10^6$ s)	30.4%	30.4%	32.3%
Utilization at 0.05 mA/cm^2 ($t = 6*10^6$ s)	42.1%	49.4%	53.1%
Utilization at 0.5 mA/cm^2 ($t = 1$ s)	0%	0%	0%
Utilization at 0.5 mA/cm^2 ($t = 5*10^3$ s)	0.4%	0.4%	3.1%
Utilization at 0.5 mA/cm^2 ($t = 2*10^4$ s)	2.0%	2.0%	4.6%
Utilization at 0.5 mA/cm^2 ($t = 4*10^4$ s)	4%	4%	6.6%
Utilization at 0.5 mA/cm^2 ($t = 6*10^6$ s)	5%	6.7%	9.3%

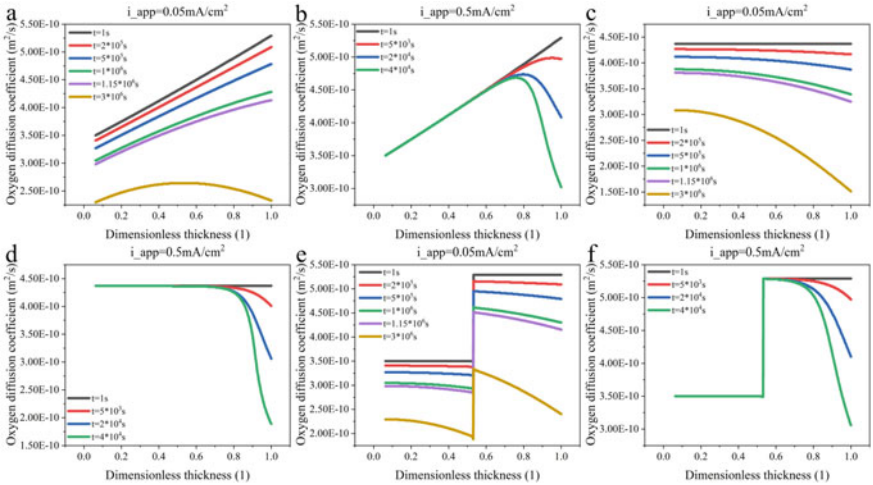

Fig. 4 Effective oxygen diffusion coefficient with different porosities. **a**, **b** $\varepsilon = 0.63 \sim 0.83$; **c**, **d** $\varepsilon = 0.73$; **e**, **f** $\varepsilon = 0.63$–0.83

storage of discharge products at high current densities. Overall, compared with single porosity, gradient or linear porosity can provide more Li_2O_2 storage space on the air side and prevent pores from being blocked prematurely during the discharge process.

Oxygen is an important reactant in the discharge process, and its content and diffusion rate inside the electrode affect the generation of discharge products. The effective diffusion coefficients of oxygen at different porosities are given in Fig. 4. From the figure, it can be obtained that the oxygen diffusion coefficient inside the electrode decreases continuously as the discharge proceeds, and it decreases to a greater extent on the outside of the electrode. Because the outer side possesses more oxygen, Li_2O_2 is more likely to accumulate on the outer side of the electrode, causing the area to be blocked (as shown in Fig. 3).

At a current density of 0.05 mA/cm^2, the oxygen diffusion coefficient inside the electrode decreases gradually with a single porosity, and the decrease is greater at the oxygen inlet. Li_2O_2 accumulates first in the oxygen-rich part of the electrode, so the electrode is more likely to be blocked at the oxygen inlet, resulting in limited oxygen conduction. The above problem can be greatly improved by the linear porosity or gradient porosity electrodes, where the porosity at the oxygen inlet side is larger than at the electrode interior. As can be seen from the figure, the oxygen diffusion coefficients outside the electrodes of two composite porosities are still larger than those inside the electrodes with the reaction at lower discharge current densities, which is favorable to the oxygen transport inside the electrodes. When the discharge current density is 0.5 mA/cm^2, the oxygen diffusion coefficient of each electrode decreases rapidly at the oxygen inlet side, and the decrease is most serious for the electrode with single porosity.

Figure 5 gives the battery discharge curves under different porosities, and it can be seen that the gradient porosity cathode has the largest cell specific capacity. From the previous analysis, it can be seen that the air cathode with gradient porosity has a larger pore structure on the air side, which can store more Li_2O_2 during the discharge process without causing pore blockage, which is conducive to the continuous diffusion of oxygen to the interior of the electrode, increasing the oxygen content inside the electrode and promoting the electrochemical reaction inside the cell. As more substances are involved in the cell reaction, the battery capacity is improved accordingly. The specific capacity and discharge voltage of the cell for each porosity are significantly reduced when the discharge current density is increased to 0.5 mA/cm^2. The high current density leads to the accelerated rate of Li_2O_2 production, the rapid deposition of Li_2O_2 on the air side to block the pores of the electrode, and the low utilization of the active material inside the electrode, which manifests as the decrease of the battery capacity. The decrease in discharge voltage is due to the polarization of the electrode caused by the excessive discharge current density.

However, among the general air cathodes, the porosity of the cathode has a certain randomness along the electrode thickness direction, so it is necessary to explore the effect of random porosity on the battery performance. A new random function rn1 can be added to the definition in Comsol, and the average porosity of the raw composition is at 0.73, and the random porosity distribution of the electrode with a range of 0.2 is shown in Fig. 6a. Figure 6b compares the discharge performance of the two porosity electrodes, the scatter plot indicates the voltage of the cell under single porosity, and the line graph indicates the voltage of the cell under random porosity, and it can be obtained that the specific capacity of the cell in the case of random porosity is slightly larger than that of single porosity.

As can be seen from Fig. 6a, the porosity of the air side of the air cathode with random porosity is higher than the average pore size of 0.73, which provides storage space for insoluble discharge products while also providing a transport channel for oxygen. Therefore, the film thickness of insoluble discharge products in the air cathode with random porosity is no longer smooth along the electrode thickness

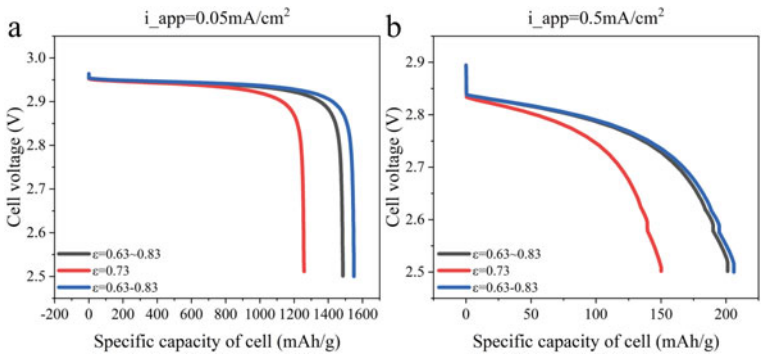

Fig. 5 Cell voltage at different porosities

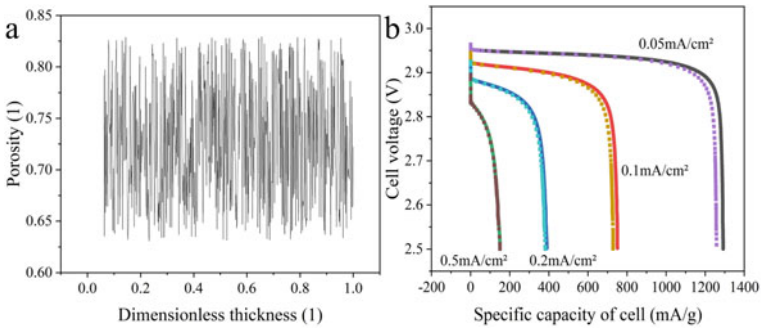

Fig. 6 Random porosity distribution and cell voltage comparison

direction, and the probability of total blockage at the same discharge moment is relatively small compared with that of the air cathode with constant porosity.

4 Conclusion

- The porosity of the cathode largely affects the battery performance, and the use of linear porosity in the cathode provides better performance compared to gradient porosity and single porosity. The role of linear porosity is reflected in various characteristics of LABs, such as optimization of porosity distribution, oxygen concentration, effective oxygen diffusion coefficient, etc. during the discharge process. The adoption of linear porosity in the anode prevents the external pores from being blocked prematurely during discharge, oxygen is fully supplied and diffused inside the electrode, and the utilization rate inside the electrode is improved, which greatly improves the battery performance.
- LABs reaction occurs mainly on one side of the air cathode boundary, and the outer side of the cathode has more oxygen, so Li_2O_2 is more likely to accumulate on the outer side of the electrode. It can be concluded that for battery operation, the larger porosity of should be near the air side to allow more storage space for discharge products.
- In actual preparation, the porosity of the cathode has a certain randomness along the electrode thickness direction. If at random porosity and its average porosity is the same as that of the evidence electrode with a single porosity, the cell has a higher specific capacity compared to that of the cathode with a single porosity.

Acknowledgements The work was supported in part by the National Natural Science Foundation of China under Grant No. 61975189, the Zhejiang Provincial Natural Science Foundation of China under Grant No. LD21F050001 and Grant No. Y21F040001, the Key Research Project by Department of Water Resources of Zhejiang Province under Grant No. RA2101.

References

1. Albertus P et al (2011) Identifying capacity limitations in the Li/oxygen battery using experiments and modeling. J Electrochem Soc 158:A343
2. Peng Z, Freunberger SA, Chen Y, Bruce PG (2012) A reversible and higher-rate Li-O_2 battery. Science 337:563–566
3. Meng J et al (2017) Advances in structure and property optimizations of battery electrode materials. Joule 1:522–547
4. Zhang Y et al (2013) The use of mixed carbon materials with improved oxygen transport in a lithium-air battery. J Power Sour 240:390–396
5. Tan P, Shyy W, An L, Wei Z, Zhao T (2014) A gradient porous cathode for non-aqueous lithium-air batteries leading to a high capacity. Electrochem Commun 46:111–114
6. Elabyouki M, Bahamon D, Khaleel M, Vega LF (2019) Insights into the transport properties of electrolyte solutions in a hierarchical carbon electrode by molecular dynamics simulations. J Phys Chem C 123:27273–27285
7. Sergeev AV, Chertovich AV, Itkis DM (2016) Modeling of the lithium-air battery cathodes with broad pore size distribution. Chem Phys Lett 660:149–154
8. Li J et al (2020) Highly efficient Li–air battery using linear porosity air electrodes. J Electrochem Soc 167:090529
9. Zhang G et al (2010) Lithium–air batteries using SWNT/CNF buckypapers as air electrodes. J Electrochem Soc 157:A953
10. Zhang T et al (2022) Effect of porosity gradient on mass transfer and discharge of hybrid electrolyte lithium-air batteries. J Energy Stor 46:103808
11. Sahapatsombut U, Cheng H, Scott K (2013) Modelling the micro–macro homogeneous cycling behaviour of a lithium–air battery. J Power Sour 227:243–253

Real-Time Acquisition Method of Weak Signal of Distribution Network Terminal Equipment Operation Based on LMS Algorithm

Mingming Zhang, Jin Hu, and Hongwei Guo

Abstract The current distribution network weak signal real-time acquisition node is multiset as the target form, and the acquisition range is greatly limited, resulting in the increase of the final acquisition single point error. Therefore, this paper proposes the design and verification analysis of the LMS algorithm-based distribution network terminal equipment operation weak signal real-time acquisition method. According to the signal acquisition requirements and standards, extract the initial characteristics of signal acquisition, expand the signal acquisition range in the form of multi-target, set multi-target acquisition nodes, and establish a single-end device signal acquisition matrix. Based on this, build a real-time acquisition model for LMS accounting weak signals, and complete real-time acquisition by using compressed signal sensing processing. The final test results show that through three measurements, the single point error of the real-time signal acquisition of the distribution network equipment is better controlled below 0.2, indicating that this method has better signal acquisition speed and efficiency, larger acquisition range, more rigorous comparison, and more controllable error, which has practical application value.

Keywords LMS algorithm · Distribution network terminal · Equipment operation · Weak signal capture · Real-time acquisition · Acquisition method

1 Introduction

The daily operation of distribution network is usually supported by terminal equipment, so the installation and adjustment of equipment and related devices are very important and critical. The weak signal of terminal equipment operation is a common signal form, which mainly means that the signal or optical signal has the characteristics of low strength and is not easy to be received, and is not associated with the

M. Zhang (✉) · J. Hu · H. Guo
Guangdong Grid Co Shaoguan Nanxiong Power Supply Bureau, Shaoguan 512400, Guangdong, China
e-mail: 1282850014@qq.com

S. Yadav et al. (eds.), *Energy Power and Automation Engineering*, Lecture Notes in Electrical Engineering 1118, https://doi.org/10.1007/978-981-99-8878-5_75

equipment and has a high degree of application, and its own instability is also strong, which will also lead to the slow operation of power grid equipment to a certain extent, causing obstacles to the implementation of daily power grid work. Serious or even uncontrollable negative impact [1] will be formed. In order to avoid the above problems, the relevant staff set the limiting conditions. Under the specific power grid environment, they regularly collected the weak signals of the associated devices in real time, analyzed the characteristics of the signals in the same direction according to the change law, and designed equivalent processing measures to avoid the increase of the coverage of weak signals [2]. Traditional real-time signal acquisition methods are mostly unidirectional, and the acquisition area is relatively fixed. Due to the difference of weak signal conditions and states, there is no unified acquisition standard [3]. In addition, the distribution network is often affected by the external environment and specific factors during operation, resulting in inaccurate and unreliable collection results [4].

Moreover, the initial signal acquisition form is highly dependent and needs to be used with professional equipment and auxiliary devices. The efficiency of real-time signal acquisition is low, leading to uncontrollable errors [5] in the final result. For this reason, the design and verification analysis of the real-time acquisition method for weak signals of distribution network terminal equipment operation based on LMS algorithm are proposed. The so-called LMS algorithm mainly refers to a dynamic multi-dimensional calculation method, which generally refers to the minimum mean square calculation form. The signal acquisition target can be optimized and extended by using the rapid decline processing framework in the preset standard to achieve the final calculation purpose [6]. By integrating this algorithm into the real-time acquisition of weak signals in the operation of distribution network terminal equipment, the actual signal acquisition range can be further expanded to a certain extent, the signal transmission channel can be calibrated from multiple angles, and the signal can be captured faster and more timely [7]. At the same time, with the help of LMS algorithm, the measurement of signal transmission path, distance, and other indicators is more accurate, clear, and targeted. To some extent, it can further strengthen the control of real-time signal acquisition error, increase the stability and safety of distribution network equipment operation, gradually form a harmonious and consistent signal acquisition environment, lay the foundation for the daily operation of equipment, and promote the real-time signal acquisition technology to a new development level [8].

2 Construction of Real-Time Acquisition Method for LMS Accounting of Weak Signal of Distribution Network Terminal Equipment Operation

2.1 Initial Feature Extraction of Signal Acquisition

Signal acquisition is a very complex and tedious work, and the final acquisition results can only be obtained by processing multiple links. Therefore, it is necessary to extract the initial characteristics of signal acquisition [9] before integrating LMS algorithm. The signal transmission structure of "terminal master station" is used as the basic processing framework to collect the relevant parameters of the signal according to the signal acquisition requirements and standards set daily and ensure its accuracy and consistency [10]. In order to ensure the normal operation of distribution network equipment, the index values of relevant devices and components can be adjusted and changed to ensure the optimal signal acquisition environment [11]. Set the master station, database, and Web program in the control system of signal acquisition one by one, form a cyclic acquisition environment, and determine the specific acquisition range [12]. At this time, the characteristics of the signal in the transmission process are analyzed, as shown in Fig. 1.

According to Fig. 1, complete the design and analysis of the initial feature extraction structure of signal acquisition. Next, integrate the actual set signal acquisition requirements and standards, expand and calibrate the unit points of the signal acquisition location, and measure the transient difference, as shown in Formula 1:

$$T = \zeta \times \sum_{r=1} \varpi r + \frac{\varpi}{\zeta \aleph - r^2} \times (1 - \aleph)^2 \tag{1}$$

In Formula 1: T represents the transient difference, ζ indicates the load change value, ϖ represents the instantaneous fixed value, r represents the number of acquisition times, and $\aleph$ indicates the acquisition range conversion ratio. According to the above measurement, the calculation of transient difference is completed. It is set as the actual processing standard of signal feature extraction to ensure that the signal will not overlap or distort during the acquisition process, avoid the occurrence of signal acquisition errors as far as possible, gradually form a more controllable transient acquisition structure, design a more stable acquisition framework for the characteristics of the signal, and achieve the extraction of the initial characteristics

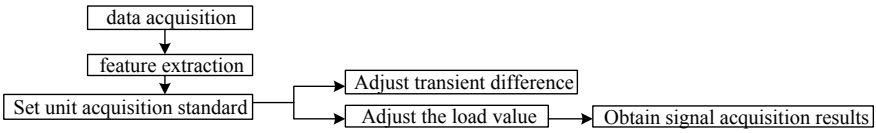

Fig. 1 Structure diagram of signal acquisition initial feature extraction

of signal acquisition. It lays the foundation for the implementation of subsequent real-time signal acquisition [13].

2.2 Setting Multi-Target Acquisition Nodes

After completing the initial feature extraction of signal acquisition, the next step is to integrate the LMS algorithm and set the multi-target acquisition node within the controllable range. Generally, in order to improve the speed and efficiency of signal acquisition, a single target mode is used to set nodes [13]. Although this method can achieve the expected signal acquisition task, it is more vulnerable to the external environment and specific factors, resulting in inaccurate final acquisition results. To avoid the expansion and extension of the above problems, it is necessary to set a multi-target acquisition node form. First, determine the specific range of signal acquisition, measure and calculate the edge value, as shown in Formula 2:

$$S = O + \mu^2 \times \left(\Re + \sigma - \frac{\mu}{X\sigma} \right) \tag{2}$$

Equation 2: S represents the signal acquisition edge value, O indicates the transmission range, μ indicates the signal transmission distance, $\Re$ indicates the preset acquisition time, σ indicates the value of the directional acquisition unit, and X indicates the filtering coverage area. According to the above settings, complete the calculation of the signal acquisition edge value, set it as the basic signal acquisition area standard, divide it into multiple unit independent acquisition areas according to the signal acquisition type, gradually calibrate the corresponding acquisition node positions according to the demand of signal acquisition, and form a complete and cyclic acquisition range.

At the same time, adjust the voltage and current state of the equipment. When the filtered voltage reaches the peak state, the setting position of the node can be appropriately adjusted by means of step input. The acquisition task can be divided into corresponding layers to form multiple acquisition targets. According to the acquisition environment, the core acquisition node and auxiliary acquisition node can be calibrated. The main node is responsible for issuing instructions to the auxiliary node, build a complete acquisition program.

2.3 Establish Signal Acquisition Matrix of Single-End Equipment

After setting the multi-target acquisition node, the next step is to establish a single-end device signal acquisition matrix. In the process of signal acquisition, first set and adjust the frequency of the continuous directional differential signal to ensure

Table 1 Allowable limit difference of signal under different frequency conditions

Signal transmission frequency/MHz	Output time/s	Limit difference
320	1.02	1.32
340	1.06	1.34
360	1.12	1.38
420	1.16	1.45

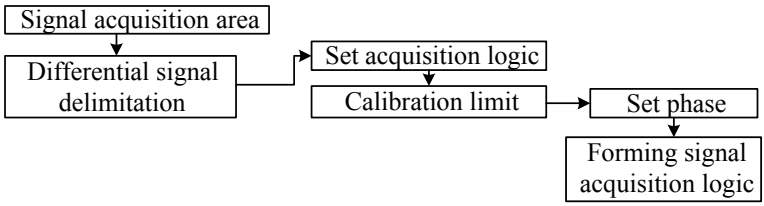

Fig. 2 Structure diagram of signal acquisition directional execution logic matrix

the normal operation of the distribution network equipment and devices, set the acquisition area of the phase, and measure the output time of the subsignal acquisition. Under different frequency conditions, measure the allowable limit difference of the signal, as shown in Table 1.

According to Table 1, complete the setting and analysis of the allowable limit difference of signals under different frequency conditions. Then, based on this, adjust the acquisition area of discontinuous differential signal, and gradually establish the directional acquisition logic, as shown in Fig. 2.

According to Fig. 2, complete the design and analysis of the signal acquisition directional execution logic matrix structure. It should be noted that in the process of signal acquisition, in order to improve the actual acquisition efficiency, the input signal is limited to avoid hysteresis problems in the acquisition process, and the signal acquisition errors and defects at the front end of the matrix are filtered out to further strengthen the signal acquisition capability of the matrix and complete the initial acquisition target.

2.4 Build LMS Accounting Weak Signal Real-Time Acquisition Model

After completing the design of single-end equipment signal acquisition matrix, next, according to the demand of real-time signal acquisition, gradually integrate LMS accounting algorithm to build a distribution network equipment weak signal real-time acquisition model. In general, the equipment needs to be associated and connected with the distribution network to gradually form a stable cyclic signal acquisition

structure. Connect a sensor device in the model program to connect with the initially deployed nodes to obtain the corresponding signal correlation data and information. Then, next, the pulse signal is obtained through the sensing device, and the operating state of the relevant equipment at this time is measured. Use LMS algorithm to measure and calculate the equalization frequency of signal acquisition, as shown in Formula 3:

$$Z = \frac{\pi \varepsilon}{u - \pi \times \sqrt{E}} \times u(1 - E)^2 \tag{3}$$

In Formula 3: Z represents the equalization frequency, u indicates that the signal conversion takes time, π indicates the amount of signal capture, E indicates distortion signal filtering ratio, and ε indicates the dynamic balance difference. Calculate the equalization frequency according to the above measurement. At this time, the signal acquisition has basically formed a fixed processing structure. Set specific unit signal acquisition targets and import them into the matrix to obtain a basic initial signal acquisition result. At the same time, through the constructed signal acquisition framework, the signal types are divided and imported into the corresponding hierarchy of the model again to achieve directional identification and acquisition of signals, to further enhance the quality and efficiency of signal acquisition.

2.5 Compressed Signal Sensing Processing Completes Real-Time Acquisition

After completing the construction of LMS accounting weak signal real-time acquisition model, we need to use compressed signal sensing technology to achieve signal processing and multi-dimensional acquisition. According to the above signal acquisition results, the specific acquisition range can be redefined, the multi-dimensional compression sensing structure can be designed, and the corresponding acquisition target can be formed. According to the different types, the model can be imported into the interior of the model. At the same time, the acquired signals are converted into data packets according to the specific format and transmitted to the internal repository of the main control system. Next, based on this, the signal acquisition matrix is used to recalibrate the corresponding signal position, establish a multi-space, multi-level signal location sensing framework, and design the sensing structure, as shown in Fig. 3.

According to Fig. 3, complete the design and analysis of the compressed signal sensing processing structure. When the acquired signal needs to be relocated, the real-time acquisition of the signal can be processed faster and more timely through compression, reducing the overall error of signal acquisition and improving the execution of subsequent correlation work.

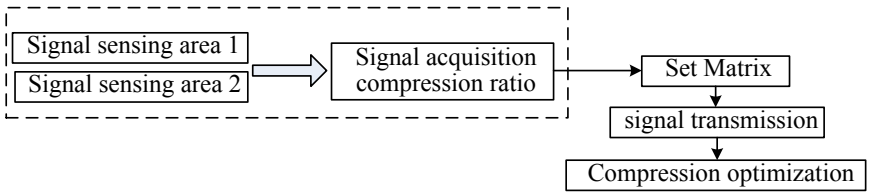

Fig. 3 Structure diagram of compressed signal sensing processing

3 Method Test

This time is mainly to analyze and verify the actual application effect of the real-time acquisition method of weak signals in the operation of distribution network terminal equipment based on LMS algorithm. Considering the authenticity and reliability of the final test results, the analysis is carried out by comparison, and Q distribution network equipment is selected as the main target object of the test. The test equipment is divided into five groups to increase the accuracy of the test results. The equipment and application devices of each group are different. Adjust the basic index parameters of the above equipment, set a unified test standard, and create a stable equipment operating environment. According to the actual real-time signal acquisition requirements and changes in standards, the LMS algorithm is integrated to correlate and build the test environment.

3.1 Test Preparation

Based on the LMS algorithm, in the above built test environment, according to the preset real-time signal acquisition standards and requirements, the test environment for real-time weak signal acquisition method of Q distribution network terminal equipment is built. First of all, it is necessary to clarify the coverage and operation range of the distribution network, as well as the regional dispatching situation. If it is in a normal state and each associated equipment is controllable during operation, the next stage of processing and setting can be carried out. Set a built-in dual signal capture device and function generator in the power grid, and integrate 3D technology to conduct full simulation of the calibrated signal transmission channel. Select one of the channels to filter the initial signal, and the tracking filtering device will form a bipolar sinusoidal vibration signal. Then, set a pulse limiting device at the calibration position of the adjacent channels, collect pulse signals regularly, and obtain the corresponding data and information for subsequent use. At this time, the channel of transmission signal is covered by distribution network dispatching, and the controllable amplitude at this time is calculated, as shown in Formula 4:

$$G = N + \sum_{O=1} \Im O - \frac{ON}{\phi O(1-V)^2} \tag{4}$$

In Formula 4: G represents controllable amplitude, N indicates the coverage of signal acquisition, $\Im$ represents the sine constant value, O indicates the frequency of the liniment, ϕ indicates the signal transmission frequency, and V indicates the biaxial vibration deviation. According to the above measurement, the controllable amplitude is calculated, set as the initial processing standard in the signal acquisition environment, and set the phase angle of the acquisition model. Under the controllable environment of 50, 120, 180, and 240 Hz of the distribution network, the calibrated amplitude phase angles are set to (1 V, 35°), (2 V, 45°), (3 V, 60°), and (4 V, 90°), respectively. Based on this, the setting state of the signal acquisition environment at this time can be measured, and the signal acquisition nodes in each area can be lapped and correlated, basically forming a stable real-time acquisition structure.

According to the change of directional amplitude, the same ground test platform is used to process and filter the initial signal, so as to further improve the fitting accuracy of real-time signal acquisition and delay compensation value. Control the coverage of the ground platform, scan the power of the signal transmission channel through professional equipment, measure the processing status of real-time signal acquisition at this time after comparison and analysis, and calibrate the position of the channel with time delay to achieve balanced adjustment. The index parameters of equipment operation in the distribution network unit area are also quite different under different execution power environments. Therefore, the index parameter standards are set according to the actual measurement needs and standards, as shown in Table 2.

According to Table 2, complete the setting and adjustment analysis of basic indicator parameter standards. Next, LMS algorithm is used to measure and calculate the deviation of real-time signal acquisition in different environments. However, it should be noted that if the characteristics of the signal are very obvious, a unified acquisition standard can be set, which can also improve the speed and efficiency of signal acquisition and complete the construction of the basic test environment. Next, the LMS algorithm is integrated to measure and analyze the subsequent work.

Table 2 Standard setting table of basic test index parameters

Basic test index name	Initial parameter standard	Measured parameter standard
Delay at this time/time	16	24
Shafting error	0.35	0.24
Acquisition directional distance/m	16.35	18.55
Number of channels/piece	18	24
Reconstruction acquisition ratio	1.354	1.247

3.2 Test Process and Result Analysis

Based on the LMS algorithm, the real-time acquisition method of weak signals of Q distribution network terminal equipment operation is measured and studied in the above built test environment. This time, the signal acquisition direction and area can be demarcated first, and the initial data and information can be collected in multiple directions. According to the actual data volume, the data packet is converted to form a unitary transmission method. According to the requirements of signal acquisition, adjust the short-term voltage at this stage, and obtain the bulge signal, interruption signal, fluctuation signal, harmonic signal, and fluctuation signal under the corresponding environment. At this time, calculate the reconstruction ratio during signal acquisition, as shown in Formula 5:

$$Y = \frac{B_2 \times \gamma}{B_1 + \kappa \Im} - \sum_{w=1} \gamma w + B_2^2 \tag{5}$$

In Formula 5: Y represents the signal acquisition reconstruction ratio, B_1 and B_2 represent the initial fluctuation error of signal and the measured fluctuation error, respectively, κ is the root mean square value difference, $\Im$ represents the number of acquisition times, γ represents the one-way acquisition distance, and w indicates the acquisition frequency. Based on the above measurements, the calculation of test reconstruction ratio is completed. Next, the LMS algorithm is integrated to calculate the error between the reconstructed signal and the original signal. Measure the controllable amplitude at this time. If it is within a reasonable range, it indicates that the signal acquisition range is accurate, there is no acquisition distortion or confusion, and the final acquisition results will be more accurate. If it is not within the reasonable range, it is necessary to further describe the acquisition process and structure of the reconstructed signal and calibrate the vibration position during the acquisition process, as shown in Table 3.

Adjust the signal acquisition value according to Table 3. Next, LMS algorithm is used to re-estimate the rationality of controllable amplitude. The standard signal acquisition reconstruction ratio is used to establish dynamic real-time signal acquisition logic. Through the same frequency and same phase conditioning method, the

Table 3 Signal acquisition value adjustment table

Controllable amplitude/V	50 Hz differential frequency ratio	120 Hz differential frequency ratio	180 Hz differential frequency ratio
1.05	15.20	23.45	40.35
2.35	16.33	23.75	42.55
2.55	16.37	25.61	49.67
2.85	17.08	26.67	50.27
3.05	18.15	28.74	52.37

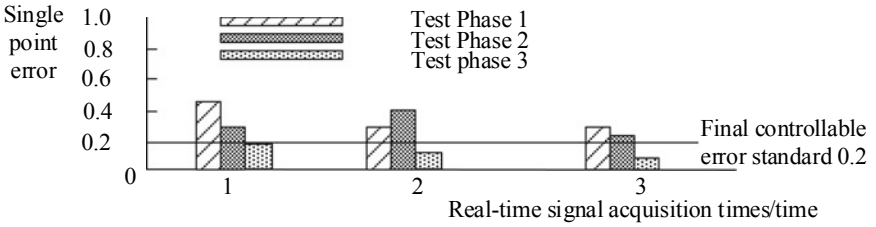

Fig. 4 Comparison and analysis of test results

signal is captured, and real-time acquisition is completed. According to the above measurement and analysis, the single point error of real-time signal acquisition is calculated, as shown in Formula 6:

$$C = \sqrt{\vartheta + \left(F \times \sum_{e=1} \vartheta e - \aleph\right)^2} + \mathrm{Fe} \tag{6}$$

In Formula 6: C represents single point error, ϑ represents the signal acquisition conversion ratio, F indicates the signal transmission rate, e indicates the time consumption of single signal acquisition, and $\aleph$ indicates reconstruction deviation. According to the above settings, the research on the test results was completed, and three collections were conducted. Each collection was divided into two stages. Next, specific tests were conducted, as shown in Fig. 4 below:

According to Fig. 4, the analysis of the test results is completed: Through three measurements, the single point error of the real-time signal acquisition of the distribution network equipment is better controlled below 0.2, indicating that this method has better signal acquisition speed and efficiency, larger acquisition range, more rigorous comparison, and controllable error, which has practical application value.

4 Conclusion

In a word, the above is the analysis and verification research on the practical application effect of the real-time acquisition method of weak signals in the operation of distribution network terminal equipment based on LMS algorithm. This time, the results are explored by comparison. Under the real distribution network background, LMS algorithm can accelerate the speed and quality of real-time signal acquisition and gradually form a more flexible and changeable signal acquisition structure. In addition, in the face of the synchronous operation of the distribution network terminal equipment, the signal transmission shape can be adjusted, and the LMS algorithm can be used to calibrate the relevant index parameters of signal acquisition, strengthen the setting and control of signal frequency and phase, minimize the signal acquisition

error existing in the distribution network dispatching process, and establish a stable support for the daily stable operation of the power grid.

References

1. Lingda K, Feng Z, Yingjie Z, Nan Q, Dashuai L, Shaotang C (2021) Evaluation method of trust degree of distribution IoT terminal equipment based on information entropy. J Phys Conf Ser 1754(1):012108
2. Liu J, Ma C, Gui H, Wang S (2022) A four-terminal-architecture cloud-edge-based digital twin system for thermal error control of key machining equipment in production lines. Mech Syst Sig Process 166:108488
3. Li L, Li Y, You X, Su G, Li S, Yang R (2021) Sensor reliability evaluation index system for main equipment of power distribution IoT. Rec Adv Electr Electr Eng 14(4):473–483
4. Mou M, Zhou Y, Zheng W, Xie Y, Wang S, Liu L, Wei C (2021) Modeling and control strategy for multiterminal flexible DC distribution network with echelon utilization power battery. Complexity 2021:1–14
5. Wang Y, Xi W, Chen J, Chen M, Hu S (2021) Self powered circuit with composite energy storage for monitoring terminal in distribution network. J Phys Confer Ser 1887(1):012041
6. Zhang R, Xiao X, Tian H, Cai Y, Fu Y, He H (2021) Open architecture design of universal terminal for multiple measurement and control scenarios of distribution network. IOP Conf Ser Earth Environ Sci 651(2):022061
7. Chen P, Chen X (2020) Error estimation method of reduced-order small-signal model for multiterminal DC distribution network. IEEE J Emerg Select Top Power Electr 9(6):7212–7222
8. Sun F, Yu M, Wu Q, Wei W (2021) A multi-time scale energy management method for active distribution networks with multiple terminal soft open point. Int J Electr Power Energy Syst 128:106767
9. Li R, Wang G, Dai W, Zan X, Zhang T (2021) Design of distribution equipment monitoring system based on internet of things and multi-agent. J Phys Conf Ser 2093(1):012040
10. van Staden PM, Dang DM, Forsyth PA (2021) On the distribution of terminal wealth under dynamic mean-variance optimal investment strategies. SIAM J Finan Math 12(2):566–603
11. Xu S, Leng X (2021) Design of real-time power quality monitoring system for active distribution network based on computer monitoring. J Phys Conf Ser 1992(3):032127
12. Yang B, Xu Q, Yang S, Chi H (2022) Wideband sparse signal acquisition with ultrahigh sampling compression ratio based on continuous-time photonic time stretch and photonic compressive sampling. Appl Opt 61(6):1344–1348
13. Hao Y, Chen M, Chen W, Zhao Y, Li Y (2021) An active electrode for vital signal acquisition with accurately-tunable sub-Hz high-pass-corner frequency and 164-mV_{pp} linear-input-range. IEEE Trans Circ Syst II Exp Briefs 68(5):1610–1614

Application Research of New Remote Sensing Technology in Tree Obstruction Detection of Power Patrol Line

Lan Lan Liu, Mei Qiu Luo, Jie Huang, Chang Yi Wu, Wen Luo, Xin Chao Liu, Ming Yu Cao, and Pan Liu

Abstract The inspection of transmission line corridor is an important part of power inspection and operation and maintenance, and relying on manual on-site investigation can no longer meet the development needs of modern power grid. This paper mainly studied the airborne LiDAR point cloud technology, drone tilt photography technology in the practice of distance diagnosis, in the analysis of two kinds of new remote sensing technology in the power patrol, and the working principle and process of tree inspection operation, combined with the Hunan transmission maintenance company ± 800 kV Fufeng line, ± 800 kV Jin Su line remote sensing inspection project practical application research. The experimental results show that the application of two remote sensing technologies in the inspection of transmission line trees is effective, and the accuracy of airborne LiDAR point cloud technology is better than that of UAV tilt photography.

Keywords Power line inspection · Airborne LiDAR · UAV tilt photography · 3D reconstruction · Safety distance · Tree obstacle detection · Remote sensing technology · Regular grid segmentation · Buffer zone analysis

L. L. Liu (✉) · J. Huang · C. Y. Wu · X. C. Liu · M. Y. Cao
State Grid Hunan Electric Power Co., Ltd. UHV Power Transmission Company, Changsha 410100, China
e-mail: 249841378@qq.com

L. L. Liu
Hunan Province Key Laboratory of Intelligent Live Working Technology and Gear (Robot), Changsha 410004, China

Live Inspection and Intelligent Operation Technology State Grid Corporation Laboratory, Changsha 410100, China

M. Q. Luo · W. Luo · P. Liu
Hunan Aerospace Zhiyuan Technology Co., LTD., Changsha 410000, China

S. Yadav et al. (eds.), *Energy Power and Automation Engineering*, Lecture Notes in Electrical Engineering 1118, https://doi.org/10.1007/978-981-99-8878-5_76

1 Introduction

Transmission line is the lifeblood of power grid operation, and its safe and reliable operation is of great significance to the stable development of a country's economy and people's livelihood [1]. China's power industry has developed rapidly. In recent decades, there have been a large number of high-voltage and high-voltage transmission lines. These transmission lines have a wide distribution range and a long transmission distance, and the transmission corridors cross the region with complex landforms and diverse types. At present our country power grid of high voltage power line channel inspection is mainly given priority to with artificial inspection way, this way of inspection hard labor intensity, working conditions, inspection efficiency is low, and difficult to manage, already cannot meet the demand of the development of modern and safe operation of power grid, the transmission line along the power operations has been a difficult to solve the problem of [2].

Transmission line corridor in the content safety distance detection is an important part of the power line inspection line work, due to various objective reasons, the kind of safety problems are difficult or find out the low timeliness, tree barrier discharge, line damage by external forces can cause line trip outage, more can cause serious mountain fires such as production safety accident, directly harm the safe and stable operation of the power system, endanger the life of electric power workers and surrounding residents [3, 4].

With the rapid development of remote sensing technology, many emerging technologies have begun to enter the field of power inspection, among which the representative ones are airborne LiDAR point cloud technology and UAV tilt photography technology [5–11], which realize the quantitative inspection of transmission lines of power system. These technologies can quickly and extensively obtain the surface vegetation coverage information in the transmission line corridor area, quantify the risk and classification, determine the high-risk areas of transmission lines, reduce the workload in the process of line operation and maintenance, improve the operation stability of transmission lines, and reduce the operation and maintenance cost. Based on the remote sensing inspection project of ± 800 kV Fufeng line and ± 800 kV Jinsu line of Hunan Transmission Maintenance Company, this paper applied the airborne LiDAR point cloud technology and UAV tilt photography technology to the detection of power patrol tree barriers and successfully extracted 20 tree barrier risk points.

2 Detection Method of Transmission Line Tree Barrier

Through the automatic method to quickly and accurately obtain the distance between the power line and the ground under the ground, and then compare with the safe distance to clean up the hidden terrain below the power line, to ensure that the power line is in a safe state for a long time, which is the main purpose of the power line tree barrier detection. In this paper, the dense forest vegetation areas of the long-distance

transmission line corridor were determined by satellite remote sensing technology, and then the airborne LiDAR point cloud technology and UAV tilt photography technology were used to detect these dense forest vegetation areas to determine the risk points of tree barriers.

2.1 Determine the Vegetation Areas of the Long-Distance Transmission Line Corridor by Using Satellite Remote Sensing Technology

Satellite remote sensing monitoring is a multidisciplinary integrated detection technology, which can obtain the image data of remote target objects. In remote sensing images, various features of surface objects, including spectrum, texture, shape, size, relative position, etc., and its interpretation include identification, differentiation, discrimination, classification, evaluation, evaluation and detection, and identification of some special important phenomena. In order to complete these tasks, it is necessary to draw the outline of remote sensing images according to their attributes and assign attributes. Through these features, the sum of these features is called interpreting the remote sensing image logo. According to the remote sensing monitoring content, the surface information of the transmission corridor of ± 800 kV Fufeng line and ± 800 kV JinSu line can be classified into vegetation area and non-vegetation area, where vegetation is divided into dense forest, sparse forest, farmland, etc., and non-vegetation is divided into building area, water area, bare land, etc., as shown in Fig. 1.

NDVI is the most commonly used to estimate the index of vegetation density and growth status. The NDVI method is used to distinguish the vegetation area in the image, the supervised classification method is used to identify and classify the ground species, and the vegetation area and non-vegetation area can be obtained.

$$N = \frac{\rho_N - \rho_R}{\rho_N + \rho_R}$$

where N represents the value of NDVI, somewhere between -1 and $1{\cdot}\rho_N\rho_R$ The reflectivity of the infrared band and the reflectivity of the red band. 0 represents essentially no vegetation growth in this area; the negative value represents non-vegetation coverage; the larger the number between 0 and 1, the more vegetation coverage. According to the obtained image information of the vegetation area, the object-oriented classification technology is adopted to extract the gray scale features, fractal geometric features, and texture features of the vegetation area image. These three features can describe the physical properties and imaging properties of the vegetation from different angles, so as to achieve the purpose of fine classification.

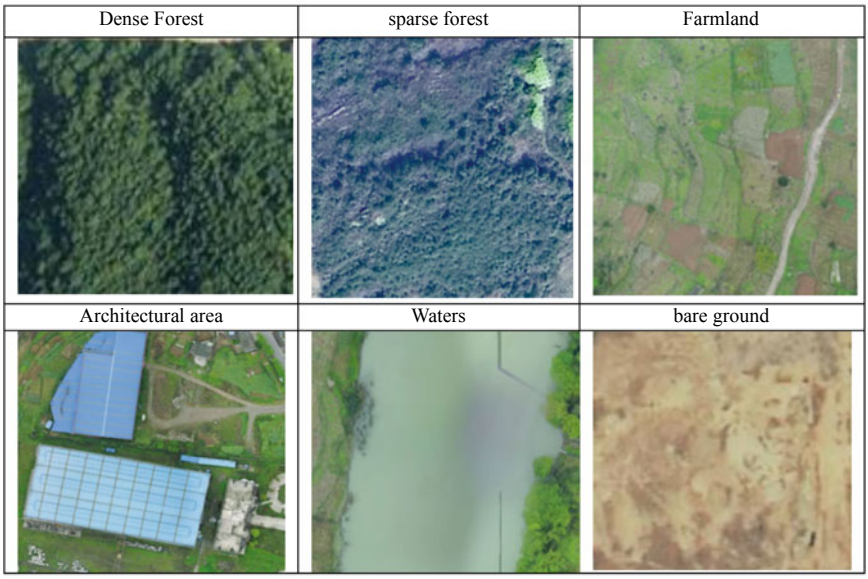

Fig. 1 Interpretation flag

2.2 Onboard LiDAR Point Cloud Technology

The airborne LiDAR system is an active remote sensing technology that can measure objects in three-dimensional space. The ranging principle is to transmit the laser from the airborne platform, then receive the echo, and measure the characteristic information of the target according to the time difference between the transmitting wave and its echo. Onboard LiDAR system is a complex system that integrates various advanced technologies of laser technology, computer technology, high dynamic carrier attitude measurement technology, and high-precision dynamic GPS differential positioning technology. It requires the cooperation of multiple modules to play its effectiveness. With reference to the research idea of reference [12, 13], the airborne LiDAR system detects the safe distance of transmission lines (as shown in Fig. 2): First, the airborne LiDAR original point cloud data is filtered to obtain the laser point cloud data. Then, based on this classification of point clouds, in this paper, the point cloud data is classified into ground points (vegetation points and building points), tower points, and power line points; the HASM-AD surface simulation algorithm obtains the ground object digital surface model (digital surface model, DSM) using K proximity clustering to extract power line data points to obtain some important feature points. Then, the least squares method is simulated to obtain the power line model; finally, the ground digital surface model (DSM) is networked and extracts the highest point. Calculate the distance between the highest point and the power line point to determine whether there is a danger.

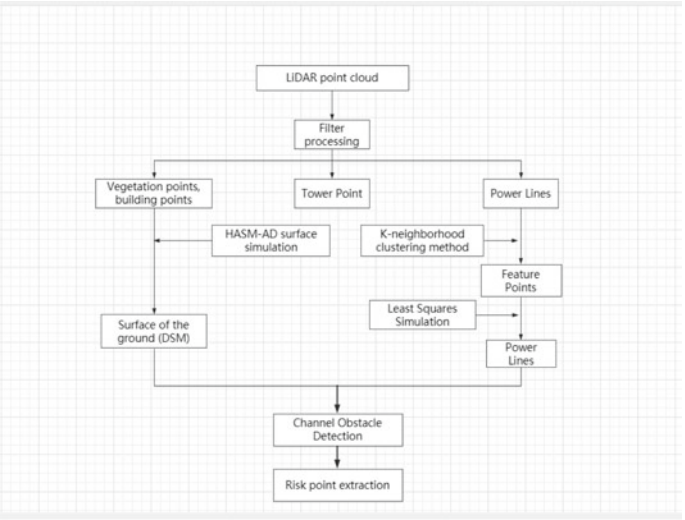

Fig. 2 Basic idea of safe distance detection of transmission lines in the airborne LiDAR system

This paper according to the literature [12] proposed the acquisition of power line point cloud data tree barrier detection method, and the basic principle is: the content point rules grid, extract the highest point, then use the highest point buffer, the buffer power line point, and the highest content point distance calculation, compared with the safe distance, and find the location of the hidden danger. Rule grid segmentation is a spatial index technology. The rule grid segmentation technology is used to divide the map into multiple small map blocks and then index the geographic information data into the scope of the grid, which can reduce the storage and calculation amount in the subsequent data processing. Buffer zone analysis is a unique analysis function in the geographic information discipline. It can analyze the relevant data of the geographic information system by establishing models, and it is a common spatial analysis tool to solve the proximity problem. It is widely used in transportation, forestry, urban planning, and other fields. Buffer analysis is usually based on points, lines, and planes, automatically creating a buffer polygon layer within a certain width around it and then establishing the superposition of the layer and the target layer for analysis to get the desired results. The method adopted in this paper is to draw a two-dimensional buffer parallel to the X-axis and Y-axis with the highest point as the center point and the safety distance (30 m) as the radius and then judge whether the plane coordinates of the fitted power line points (X, Y) are in the buffer zone. If in the buffer, calculate the spatial distance between the power line point in the buffer and the center point, and the resulting distance value is compared with the safe distance, and if the distance value is less than the safe distance, there is a hidden tree barrier; if it is greater than the safe distance, it is safe.

2.3 Drone Vehicle Tilt Photography Technology

UAV tilt photography technology in power line patrol tree obstacle detection refers to the use of fixed-wing or multi-rotor UAV as a flight platform with high-precision positioning device and imaging system to obtain optical images of transmission line channels and recover three-dimensional scenes of transmission line channels with high-precision coordinates using photogrammetry principles to identify and locate obstacle targets in transmission line channels. According to the literature [14, 15] to study the application method of UAV tilt photography technology in tree obstacle detection for power line patrol, the workflow (Fig. 3) is, firstly, aerial photography of the power line channel using UAV with GPS/IMU data; then triangulation method is used to process (extract and correct) the acquired images, GPS/IMU parameters, and other raw data and solve the absolute orientation parameters, generating stereo image pairs (the overlap degree of this paper is 80%); 3D point cloud reconstruction method for the surface of the feature; 3D point cloud reconstruction method for the power line; calculating the spatial distance between the power line and the surface point cloud to detect the obstacle. The PixelGrid UAV aerial image processing platform is selected in this study, which can process the raw UAV images with GPS/IMU data and can accomplish the functions of distortion correction, connection point extraction and leveling, air three encryption, automatic image matching, orthophoto correction, etc. Transmission line channel obstacles hidden danger mainly refers to the spatial distance in the power line channel, and the power line is less than a certain safety threshold of the objects collectively, such as trees, buildings, and so on.

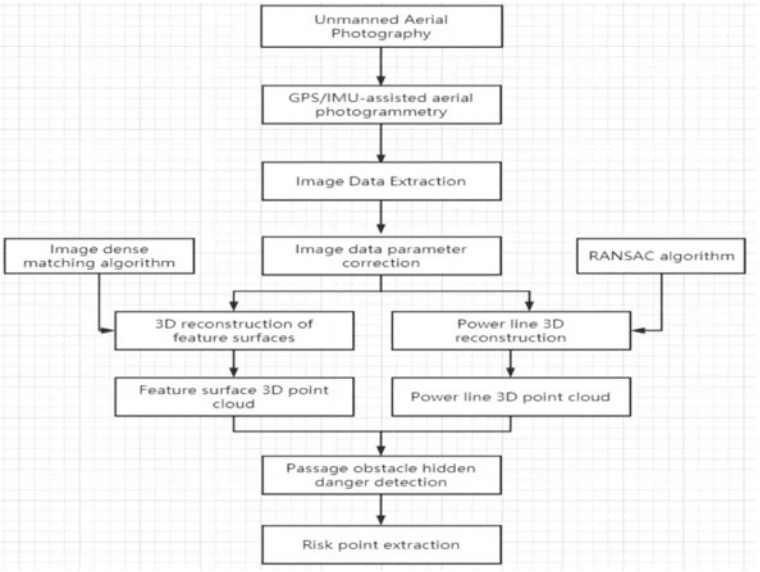

Fig. 3 Workflow of UAV tilt photography technology in power patrol tree barrier detection

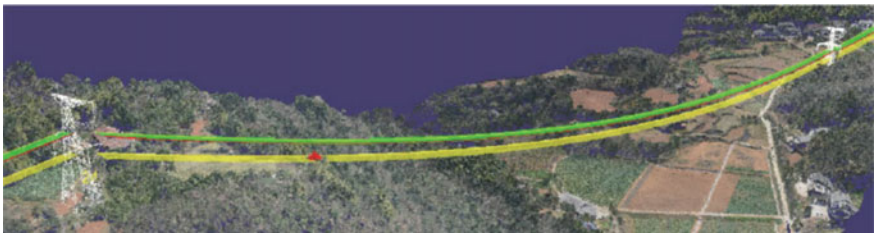

Fig. 4 Green surface is the power line envelope, and the yellow surface is the electrical safety distance envelope

After completing the construction of the three-dimensional point cloud data of the ground surface and the power line, the three-dimensional spatial situation of the transmission line channel can be truly restored to the safety distance between the power line and the ground surface of the power line envelope along the lead hammer line direction down to the electrical safety distance envelope, which reconstructs the safety channel of the conductor, and all the features appearing inside the channel will be regarded as obstacle hidden danger and automatically detected the power line channel. The obstacle detection inside the power line channel is shown in Fig. 4.

3 Experimental Results and Analysis

3.1 Basic Information of the Line

This paper depends on the transmission maintenance company in Hunan Province ± 800 kV Fufeng Line, ± 800 kV JinSu line of remote sensing inspection project, Fufeng line, JinSu line engineering line as shown in Fig. 5, Hunan channel from the Longshan county, Xiangxi autonomous prefecture, the Yongshun County to Zhangjiajie Sangzhi County, Cili County, to Changde city Shimen County, LinLi and Li County three cities seven counties, and transmission corridor through the regional topography complex landform types. The length of JinSu line is 254 km, a total of 561 base towers, the Fufeng line is 255 km, a total of 561 base towers, and the average spacing between the two lines is about 200 m.

3.2 Experimental Results and Analysis

The number of poles and towers on Fufeng line is 125, with numbers from 1431 to 1559. The total number of poles and towers of the JinSu line is 127 bases, with the pole and tower numbers ranging from 2042 to 2170. According to the relevant safety distance standard of DL/T 741-2019, 30 m. By using the onboard LiDAR point cloud

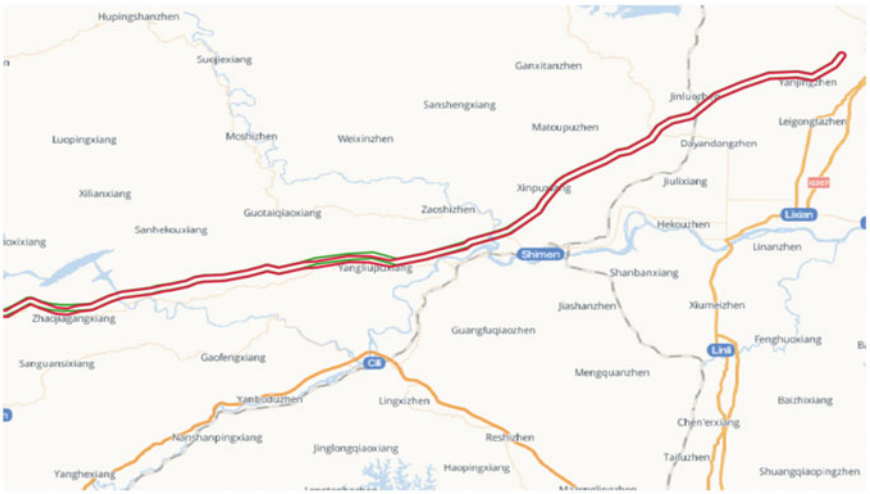

Fig. 5 ± 800 kV Fufeng line and ± 800 kV JinSu line

technology and the UAV tilt photography technology, 20 hidden points were found, including Fu Feng line 7, JinSu line 13, and the distribution is shown in Fig. 6, 1544 to 1545 is shown in Fig. 7. The specific location information of these risk points and the line tree distance measurements are shown in Table 1.

As can be seen from Table 1, compared with the measured near-air data, the line tree distance data measured by LiDAR point cloud technology and UAV tilt photography technology have certain errors, and the data measured by UAV tilt photography technology is greater than the data of LiDAR point cloud technology. In order to better analyze the new type of remote sensing technology measured data and real line tree distance data deviation, this paper uses the following formula to help analyze the LiDAR point cloud technology and drone tilt the precision of online tree ranging, which said LiDAR point cloud technology, line tree range deviation, means LiDAR point cloud technology line tree range average deviation, said drone

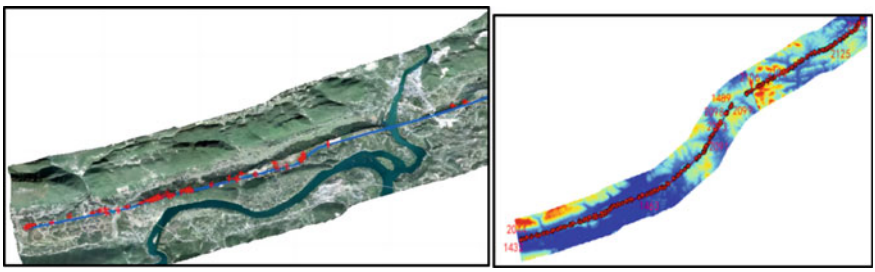

(A) Digital orthophoto DOM (B) Digital surface model DSM

Fig. 6 Distribution of risk points of tree barriers along the line

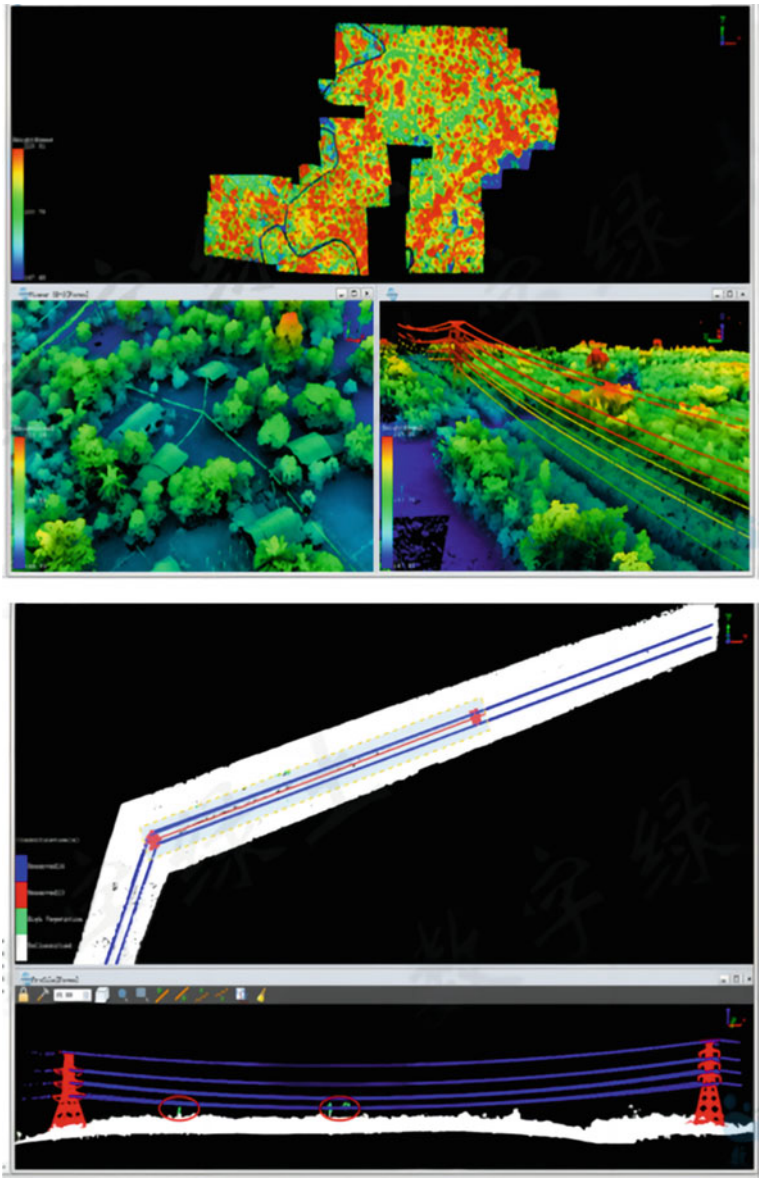

Fig. 7 Image of the hidden problem between Nos. 1544 and 1545 of the tower area of the Fufeng line

Table 1 Specific location information of tree obstruction risk points along the line and the line tree distance measurement

Basic information					Measured near empty distance to D1 (m)	LiDAR point cloud line Tree ranging D2 (m)	Tilt photo line tree ranging D3 (m)
Order number	Line name	Pole tower interval	Longitude	Latitude			
1	Fufeng line	1440–1441	111.20812	29.580623	18	17.71	18.91
2	Fufeng line	1509–1510	111.50586	29.736159	10.5	10.32	11.94
3	Fufeng line	1532–1533	111.58251	29.784214	10.5	10.54	11.15
4	Fufeng line	1535–1536	111.60008	29.788044	16	16.53	18.66
5	Fufeng line	1544–1545	111.63303	29.813998	14	14.86	16.37
6	Fufeng line	1544–1545	111.63825	29.818283	14.5	15.55	16.95
7	Fufeng line	1546–1547	111.63825	29.818281	14.5	15.55	16.67
8	JinSu line	2050–2051	111.21334	29.582891	13.5	14.28	15.36
9	JinSu line	2117–2118	111.48801	29.731195	13.5	12.96	14.65
10	JinSu line	2122–2123	111.50779	29.7373	22	22.03	24.35
11	JinSu line	2139–3140	111.56639	29.778865	23.5	26.69	28.02
12	JinSu line	2140–2141	111.5702	29.781156	21	22.38	24.88
13	JinSu line	2141–2142	111.572683	29.782342	21.5	23.10	24.63
14	JinSu line	2148–2149	111.60791	29.794945	18.5	20.96	21.65
15	JinSu line	2149–2150	111.612835	29.798618	14.5	15.70	17.13
16	JinSu line	2150–2151	111.613567	29.799534	11.5	12.26	12.38
17	JinSu line	2153–2154	111.626993	29.810271	13.5	12.01	14.53
18	JinSu line	2155–2156	111.632999	29.815087	15.5	16.69	17.45
19	JinSu line	2156–2157	111.637048	29.818036	12	12.21	13.92
20	JinSu line	2157–2158	111.637969	29.81876	14.5	15.26	16.32

tilt photography technology line tree range the average deviation Delta_1Delta_2$\overline{\text{Delta_1Delta_2}}$.

$$\text{Delta\_1} = \frac{D2_i - D1_i}{D1_i} * 100\%$$

$$\text{Delta\_2} = \frac{D3_i - D1_i}{D1_i} * 100\%$$

$$\overline{\text{Delta\_1}} = \frac{1}{20}\sum_{i=1}^{20}\left|\frac{D2_i - D1_i}{D1_i}\right| * 100\%$$

$$\overline{\text{Delta\_2}} = \frac{1}{20}\sum_{i=1}^{20}\left|\frac{D3_i - D1_i}{D1_i}\right| * 100\%$$

$D1_{\text{i}}D2_{\text{i}}$ where i is the measurement number; the measured near space distance with the serial number i; the LiDAR point cloud tree ranging with the serial number i; and the oblique line tree ranging with the serial number $i{\cdot}D3_{\text{i}}$.

From Fig. 8, compared with the measured near-air data, Line tree distance data using LiDAR point cloud technology and drone tilt photography. And in most cases it is an upper deviation; the two distance distances are within 20%. The accuracy of the line tree distance data measured by LiDAR point cloud technology is better than that of UAV tilt photography technology; mean deviation of line tree distance data measured using the LiDAR point cloud technique = 0.07. The deviation of the line tree distance data measured using the UAV tilt photography technique = 0.13.$\overline{\text{Delta\_1Delta\_2}}$.

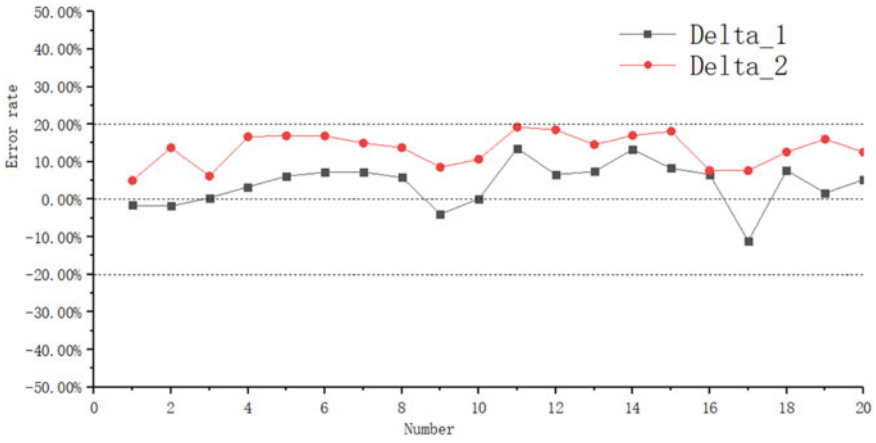

Fig. 8 Deviation in the online tree ranging process of the two remote sensing technologies

4 Conclusion

Transmission line corridor tree barrier distance diagnosis is an important work content of electric power inspection and operation and maintenance. Relying on the remote sensing inspection projects of ± 800 kV Fufeng line and ± 800 kV JinSu line of Hunan Transmission and Maintenance Company, this paper studies the practical applications of airborne LiDAR point cloud technology and UAV tilt photography technology in the diagnosis of tree barrier distance in transmission line corridors, respectively. Different categories of data such as feature surface, towers, and transmission lines are separated from airborne LiDAR point cloud data or UAV image data, and different algorithms are used to reconstruct the feature surface and power lines in three dimensions, determine the transmission line safety channel, and match the tree obstacle hidden points according to relevant safety regulations. The experimental results show that the practical application of the two remote sensing technologies in the tree barrier inspection operation of transmission lines is effective under a certain tolerance range, and the accuracy of the measured data of the airborne LiDAR point cloud technology is better than that of the UAV tilt photography technology.

References

1. Yuan J (2017) Discussion on big data application of Guizhou power grid. Electr Power Big Data 20(12):4–7
2. Chen LQ, Tang HC, Xiao XH (2018) Research on transmission line risk early warning and identification based on deep learning. Electr Power Big Data 21(12):1–5
3. Mu C (2010) Research on the feature extraction method of power line corridor features based on multiple remote sensing data. Wuhan University, Wuhan
4. Zhi X, Zhang J (2017) Detection of surface cover change in transmission corridor and assessment of wildfire susceptibility based on satellite remote sensing. Wuhan University, Wuhan
5. Yin JH, Sun CY, Zheng YC (2007) Research on the application of airborne laser measurement technology in UHV transmission line engineering. Electr Power Constr 28(7):9–13
6. Yang F, Xu ZJ (2009) Application of 3D lidar technology in the operation and maintenance of transmission lines. China South Power Grid Technol 3(2):62–64
7. Yu J, Mu C, Feng TM et al (2011) Research on the extraction method of power lines in onboard LiDAR point cloud data. J Wuhan Univ 36(11):1275–1279
8. Peng XY, Chen C, Rao ZQ et al (2015) Power line safety inspection and intelligent diagnosis based on UAV multi-sensor data collection. High Volt Technol 41(1):159–166
9. Chen C, Peng XY, Shuang S et al (2017) Large UAV power inspection LiDAR point cloud safe distance diagnosis method. Power Grid Technol 41(8):2723–2730
10. Liu Y (2016) Research on tilt photogrammetry image processing and 3D modeling in UAV. East China University of Technology, Nanchang
11. Ma QM (2017) Research on UAV power inspection and 3 D model reconstruction technology. Shandong University, Jinan
12. Zhang G (2015) Power line safe distance detection based on airborne LiDAR point cloud data. Lanzhou Jiaotong University, Lanzhou
13. Wang YF, Yue TX, Zhao MW et al (2014) Tree height identification algorithm and application analysis of onboard LIDAR data. Geogr Inform Sci 16(6):958–964

14. Wang W (2015) UAV image forest information extraction and model research and construction. Beijing Forestry University, Beijing
15. Zhou XH, Li XH, Shi L et al (2019) Research on the practical application of UAV tilt photography technology in the detection of power patrol tree barrier. Electr Power Big Data 22(8):53–59

LCC S2C and Buck–Boost C2C Topology Complementary Method for Hierarchical Battery Energy System

Yihan Liu

Abstract The series connection of batteries is widely used in various scenarios. However, due to the influence of battery imbalance, the performance of the battery pack will be degraded, scrapped in advance, and even cause safety problems. At present, cell-to-cell (C2C) and series-to-cell (S2C) topologies methods have been proposed for hierarchical battery energy system. To combine the advantages of various methods for lower control complexity, high circuit scalability, and high equalization efficiency, a hybrid hierarchical equalizer based on LCC resonant converter and buck–boost unit equalizer is proposed in this paper. This topology applies LCC resonant converter to serial-to-module (S2M) equalization, selects energy transmission path through multiplexing network, and adopts buck–boost equalizer in each module. The simulation results show that the equalizer can reduce the voltage difference of unbalanced batteries by 99.5% within 1 s and that indicates the feasibility of the equalizer. Compared with the existing equalizer, the equalizer proposed in this paper has higher efficiency and lower control complexity. This paper can provide theoretical guidance for the design of new battery equalizer and its application in high efficiency battery equalizer.

Keywords Hierarchical battery energy · LCC S2C and buck–boost C2C · Topology complementary method

1 Introduction

In recent years, with the continuous development of lithium battery production technology, series-connected lithium batteries are widely used in new energy vehicles, electric energy storage, and other emerging fields because of their high efficiency and environmental protection performance [1]. However, due to the production materials or complex time-varying working conditions, there are differences between the single cells of the series battery pack, which will lead to the problem of battery

Y. Liu (✉)
Engineering Institute, Nanjing Agricultural University, Nanjing 211800, Jiangsu, China
e-mail: 2360622093@qq.com

S. Yadav et al. (eds.), *Energy Power and Automation Engineering*, Lecture Notes in Electrical Engineering 1118, https://doi.org/10.1007/978-981-99-8878-5_77

imbalance [2–4]. Furthermore, it will greatly affect the life of the battery and make the battery pack scrapped in advance, and even cause safety problems (such as fire and explosion) [5, 6].

As a tool to solve the problem of battery imbalance, battery equalizer is mainly divided into passive equalization and active equalization. Traditional passive equalization is based on shunt resistance to convert excess energy into heat, which causes energy loss and thermal management issues [7]. Active equalization mainly adopts cell-to-cell (C2C) [2, 8–10], series-to-cell (S2C) [11–16], and hierarchical module equalization (HMB) [21]. Nowadays, active equalization is a more mainstream batteries balancing method with high system efficiency.

At present, the widely used C2C method uses buck–boost equalizer to achieve constant current balance, and C2C method is known as the most basic equalization method in active equalization. In [2], a buck–boost battery equalizer based on the central unit is introduced, which can transfer the energy of overcharged battery to the central unit and re-deliver it to the insufficient battery unit. However, the equalizer of this method is greatly influenced by the control of the central unit, and it is easy to cause the failure of the battery equalizer due to the failure of the central unit. In [3, 4], a bidirectional C2C equalizer is introduced, which uses capacitors to transmit energy, and in [5, 8], an equalizer based on bidirectional buck–boost is introduced, which can balance the energy of adjacent units. However, the series coupling of basic equalization circuits limits the balancing speed. The equalization speed of C2C equalizer is generally low because energy can only be transferred between two units. The S2C method realizes the transmission of energy from the string to the unit and plays a balancing role between them. In [14, 17, 18], the energy transmission path is selected by multiplexing network, but the circuitry is very complex. In [19, 20], multi-winding transformer is introduced to reduce the number of switches, but the design of the transformer is complicated. In [16], the S2C equalizer based on LCC is adopted, which simplifies the constant current balance, reduces the application of special current sensors, and reduces the control complexity. Furthermore, it still needs a multi-switch multiplexing network. Hence, although S2C structure can realize the balance of serial to cell, the circuit complexity is relatively high.

Both C2C and S2C methods belong to single-layer architecture. With the development of battery equalizer, various layered modular architectures combining module equalizer and unit equalizer are born, which effectively improves the equalization speed and the scalability of the circuit. In [21], a multi-layer structure is introduced, but this structure is based on CCM, which cannot achieve the balance of serial to module. In [22–24], how to introduce multi-winding transformer into modular equalizer is introduced, which effectively improves the circuit expansibility. In [25], the hierarchical structure of S2M modular equalizer combined with unit equalizer based on LLC is introduced, but this modular equalizer can only equalize a single module, and the equalization efficiency is not high enough.

To reduce the control complexity and improve the circuit scalability, it is necessary to adopt a layered architecture because of the influence of [21–24] modular structure. As shown in Fig. 1, this paper applies LCC resonant converter to serial-to-module (S2M) equalization, selects energy transmission path through multiplexing network,

and adopts buck–boost equalizer in each module, which combines them to optimize battery equalization. The main contributions of this paper are as follows. First, a design scheme of hybrid hierarchical equalizer based on LCC resonant converter module equalizer and buck–boost unit equalizer is proposed, which effectively improves the circuit expansibility and reduces the control complexity. Second, the working principle of the modular equalizer and the unit equalizer in each module are expounded, and the formulas are derived. Finally, the working effect of the equalizer is verified by simulation.

The structure of this article is as follows. In the second section, the circuit of the designed equalizer is introduced in detail, and the working principles of S2M module equalizer and C2C equalizer are expounded, respectively. The third section puts forward various design factors that need to be considered when designing the circuit. In the third section, the function of the equalization circuit is verified by simulation experiments and compared with other equalization schemes. Finally, the fifth section summarizes this paper.

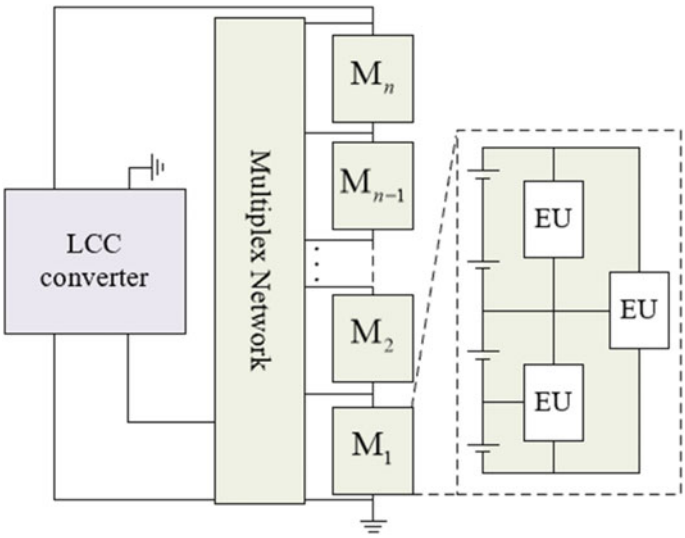

Fig. 1 Mixed equilibrium structure proposed in this paper

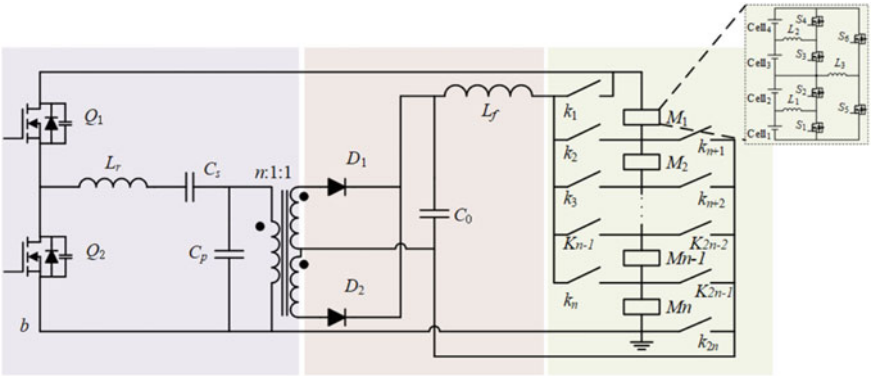

Fig. 2 LCC-based string-to-cell and buck–boost based cell-to-cell hybrid hierarchical battery energy system schematic diagram

2 Operation Principles

2.1 S2M and C2C Mixed Architecture

As shown in Fig. 2, it shows the working principal diagram of the designed hierarchical modular equalizer with two modules (each module contains four units). In the S2M layer, this design adopts the S2M equalizer based on the shared LCC resonant converter, which only needs to be controlled by two signals, and the control complexity is low. Its input is connected to the string, and its output is connected to the switch of the multiplexing network. Multiplexing networks are used to enable each unit to share transformers and modular equalizers. Buck–boost cell equalizer is used in C2C layer to balance a single battery. By combining the modular equalizer based on LCC and the unit equalizer based on buck–boost, the hybrid hierarchical equalization architecture is configured. This hierarchical structure enables more paths to achieve equilibrium. When the voltage of each module is unbalanced, LCC resonant converter provides constant current balance as a constant current source, so that each module can achieve balance. Each module has four separate battery cells. When there is imbalance between two batteries, the bidirectional buck–boost converter transfers charges between the battery cells to achieve C2C layer balance. This hybrid layered structure combines LCC equalizer and buck–boost equalizer, which reduces the control complexity and effectively expands the circuit.

2.2 LCC-Based S2M Module Equalizer

As shown in Fig. 2, the module equalizer is based on the design of shared LCC resonant converter, and the energy flow path from serial to module is selected through the

multiplexing network of $K1$–$K2n$. The left MOS transistor $Q1Q2$ can turn on ZVS, and the transformer secondary diode $D1D2$ can turn off zero-current switch, thus prolonging the switching life and reducing the loss. Multiplexing network can make each module share the transformer, and the filter inductance behind the secondary capacitor of the transformer is used to improve the constant current performance [16]. As shown in Fig. 3, the workflow of S2M module equalizer is shown.

The module equalizer only needs two PWM signals with 50% duty cycle to drive MOSFET $Q1Q2$. On the secondary side of the transformer, two diodes are alternately turned on to establish an energy flow path. In [16], the key steady-state waveform diagram of the equalizer based on LCC is provided.

When there are two modules, that is, eight units, if module 1 is not fully charged, its equivalent circuit is shown in Fig. 4.

When module 1 is under-charged, the module equalization string is activated. At time $T0$, MOSFET $Q1$ is turned on, and ZVS is turned on. At this time, the current on Lr is 0, and the current direction on leakage inductance is left. This circuit partially discharges the battery pack through $Q1$. At time $T1$, the current on Lr gradually rises,

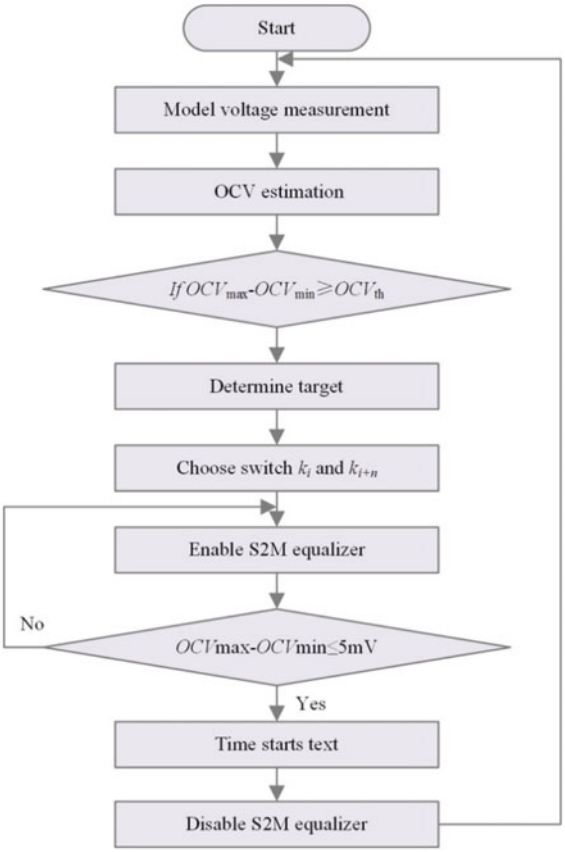

Fig. 3 Work flowchart of S2M equalizer

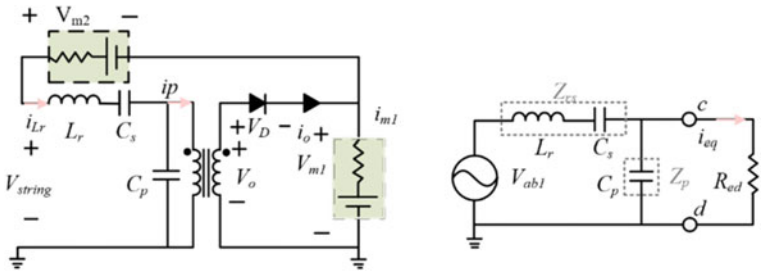

Fig. 4 Equivalent circuit of M1 under-charged

and the terminal voltage of capacitor Cp drops until it reaches 0. At $T2$, Cp starts charging, and the leakage inductance does not participate in resonance, so the two diodes $D1D2$ on the secondary side of the transformer are reversely biased. At $T3$, the current on Lr drops, the current on leakage inductance turns to the right, and $D1$ turns on. At $T4$, $Q1$ is turned off, Coss1 is charged, and Coss2 is discharged. In the dead time, the current on Lr is converted to $Q2$ and flows through the $Q2$ body diode, which means that the body diode is turned on before $Q2$ is turned on, realizing the ZVS condition.

2.3 Buck–boost-based C2C cell equalizer

As shown in Fig. 2, in each module, every two adjacent cells or strings are connected in parallel with the cell equalizer based on buck–boost to provide a bidirectional energy flow path. The following explains the working principle of the unit equalizer based on buck–boost. In [25], the key steady-state waveform in a period is provided.

The source-target cell/string refers to the cell/string with higher voltage and the cell/string with lower voltage respectively. When voltage imbalance occurs, two MOSFET tubes (S_1 and S_2) are complementarily turned on and off according to buck–boost switching mode. The excess charge of the source battery is transferred to the inductor $L1$, and the energy stored in $L1$ is further transferred to the target battery. During commutation, the body diode of the target-side MOSFETS2 provides a freewheeling path for the current on the inductor. Therefore, the body diode can be turned on before the MOS transistor is turned on S_2, thus realizing the ZVS turn-on condition. On the other hand, in order to realize ZVS conduction of source-side MOS transistor $S1$, i_L must be slightly negative before S_2 is turned off. This means that the cell equalizer must be controlled to operate in bipolar continuous conduction mode (CCM). During the dead time after S_2 is turned off, negative i_L discharges and charges the output capacitors (C_{oss}) of S_1 and S_2, respectively. The charge Q transferred from L to these two capacitors can be expressed as:

$$Q = \Delta V C_{\text{oss}} = 2\left(V_{C\text{Source}} + V_{C\text{Target}} + V_d\right)C_{\text{oss}} \tag{1}$$

The minimum charge $q_{\min}$ stored in l can be expressed as:

$$q_{\min} = \frac{1}{2} T_{\text{dead}} i_{L\min} = \frac{1}{2} {T_{\text{dead}}}^2 \frac{V_{C\text{Source}}}{L} \tag{2}$$

In order to realize ZVS conduction and minimum circulating current of S_1, the dead time must be designed. According to Eqs. (1) and (2), it can be deduced that the dead time is expressed as follows:

$$T_{\text{dead}} \geq \sqrt{\frac{4\left(V_{C\text{Source}} + V_{C\text{Target}} + V_d\right)}{V_{C\text{source}}} L C_{\text{oss}}} \tag{3}$$

To ensure that i_L is slightly negative before S_2 is turned off, the constraint condition of duty cycle D can be derived as follows:

$$D \leq \frac{V_{C\text{Target}}}{V_{C\text{source}} + V_{C\text{Target}}} - \frac{V_{C\text{Target}} - V_d}{\left(V_{C\text{Sourse}} + V_{C\text{Target}}\right) T_s} T_{\text{dead,min}} \tag{4}$$

In each module, the C2C unit equalizer can be independently controlled to equalize a single battery, without considering the equalization conditions of the S2M module equalizer. In [21], the design of buck–boost cell equalizer based on bipolar CCM is introduced in detail. The following mainly introduces the design of equalizer in S2M module.

3 Key Design Considerations

3.1 Design Considerations of Hybrid Layered Equalizer

The hybrid layered equalizer proposed in this paper combines the S2M equalizer based on LCC resonant converter with the C2C equalizer based on buck–boost converter. In order to design and realize the overall performance of the hybrid equalizer, the following factors should be considered:

1. How to combine C2C equalizer based on buck–boost with S2M equalizer based on LCC to construct a hybrid hierarchical structure?
2. How to design LCC resonant circuit to realize constant current balance?
3. In order to achieve high conversion efficiency, how to design LCC resonant converter and reduce switching loss to ensure the ZVS conduction condition of MOSFETs?
4. How to compensate the recovery effect of the battery?
5. How to use the cell equalizer to increase the scalability of the circuit?

3.2 Design LCC Resonant Converter in S2M Equalizer to Achieve Constant Current Balance

The circuit uses LCC as the constant current source of the modular equalizer, and the design of this constant current source was put forward by Gilbert et al. According to the curve of current gain relative to normalized frequency under different load conditions and the characteristics of LCC converter, in order to improve the working efficiency of the converter, the module equalizer should be set to work near the resonant frequency. Therefore, the balance current has nothing to do with the load and is determined by the input voltage and the values of the resonant circuit.

In order to obtain a constant balanced current, it is necessary to analyze the parameters of the resonant circuit.

When the voltage of module 1 is unbalanced, the current gain of LCC converter can be deduced as follows:

$$G_I = \frac{Z_p \| R_{\text{eq}}}{Z_{\text{rs}} + Z_p \| R_{\text{eq}}} \times \frac{1}{R_{\text{eq}}} \tag{5}$$

The impedance of each element of the resonant circuit can be expressed as:

$$\begin{cases} Z_{\text{rs}} = j\omega_s L_r + \frac{1}{j\omega_s C_s} \\ Z_p = \frac{1}{j\omega_s C_p} \end{cases} \tag{6}$$

The resonant angular frequency of LCC is:

$$\omega_0 = \sqrt{\frac{C_s + C_p}{L_r C_s C_p}} \tag{7}$$

When $\omega_0 = \omega_s$, the mode of resonance frequency can be deduced as follows:

$$|G_I| = C_n \sqrt{\frac{C_s}{L_r}\left(\frac{1}{C_n} + 1\right)} \tag{8}$$

The fundamental component of V_{ab} is:

$$V_{ab1} = \frac{2V_{\text{string}}}{\pi} \sin(\omega_s t) \tag{9}$$

The output current is:

$$i_{\text{eq1}} = \frac{\pi I_0}{2n} \sin(\omega_s t + \theta) \tag{10}$$

Combined with formulas (7)–(10), the parameters of the resonant circuit are deduced as follows:

$$\begin{cases} L_r = \frac{2nV_{\text{string}}(1+C_n)}{\pi^3 f_s I_0} \\ C_s = \frac{\pi I_0}{8nV_{\text{string}} C_n f_s} \\ C_p = \frac{\pi I_0}{8nV_{\text{string}} f_s} \end{cases} \tag{11}$$

3.3 ZVS Conduction Condition of S2M Equalizer

In order to reduce the switching loss, MOSFETs should be turned on with ZVS. In order to realize the ZVS condition, the body diode needs to be turned on before the MOSFET tube.

Calculate the equivalent impedance and resonant current. When LCC works at resonant frequency, the impedance angle is as follows:

$$\varphi = \arctan\left(\frac{1}{R_{\text{eq}}(1+C_n)}\sqrt{\frac{L_r(1+C_n)}{C_p}}\right) \tag{12}$$

The phase of the output voltage is ahead of the phase of the output current; that is, the impedance angle is greater than zero, which is the condition to realize ZVS conduction. In addition, it is necessary to control the dead time to ensure ZVS conduction and achieve the minimum loop current. Dead time shall meet the following conditions:

$$\frac{1}{\omega_s}\{\arccos[\pi\omega_s C_{\text{oss}}|Z_n| + \cos(\varphi)] - \varphi\} \le t_d \le \frac{\varphi}{2\pi}T_s \tag{13}$$

3.4 Compensating Battery Recovery Effect

Because of the recovery effect of the battery, it takes some time for OCV to reach the steady state, which is caused by the slow diffusion process in the battery, and the changing voltage in this process is the diffusion voltage. In the process of equalization, this situation will affect the judgment of the end time of equalization. Therefore, in order to improve the accuracy of the balance, the recovery effect of the battery needs to be considered in the balance process. That is, the equalization process needs to be extended to compensate for the voltage change after equalization. In the process of compensation, the value of diffusion voltage is equal to the change of OCV. In [16], the extension time is deduced as follows:

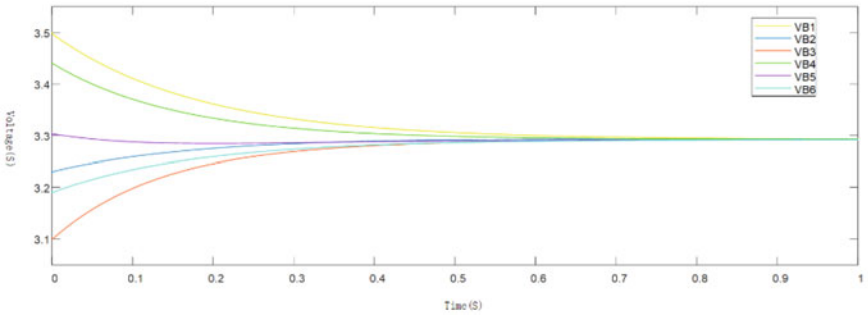

Fig. 5 Simulation waveform of voltage equalization process of six battery packs

$$t_{\text{ext}} = \frac{R_1}{\eta k_{\text{soc}}} \tag{14}$$

where η represents equilibrium efficiency, $k_{\text{soc}} = \frac{\Delta v}{\Delta \text{SOC}}$.

When the balance time is prolonged, OCV converges due to the recovery effect of the battery. In this way, the accuracy of equalization can be improved.

4 Simulation Verification

4.1 Verification of Simulation Effect of Battery Equalizer

In order to verify the analysis of the equalizer, for the battery module with multiple initial voltages, the simulation of balancing six series batteries is carried out, and Fig. 5 shows the voltage balancing process. The first layer is the battery balance of C2C layer inside the module, and the second layer is the battery balance between modules of S2M layer. The initial voltages were set to 3.5, 3.23, 3.1, 3.44, 3.3, and 3.19, respectively, and the difference between the highest voltage and the lowest voltage was 0.4. When the equalizer was activated, the voltages began to converge, and when the equalization ended after 1 s, the voltages almost all converged to 3.29, and the voltage difference was reduced to 0.002, and the equalization effect reached 99.5%, which proved the design feasibility of the battery equalizer, and the equalization effect is good.

4.2 Comparing with Other Equalizers

Because energy can only be transferred between two units, the equalization speed of C2C equalizer is generally low. For S2C battery equalizer, in [14, 17, 18], the

circuit complexity is high. In [19, 20], the design of transformer is complicated, especially when the number of strings is large. In [16], the S2C equalizer based on LCC is adopted, but when only one battery is unbalanced, the equalization speed will be reduced. In [21], a multi-layer structure is introduced, but this structure is based on CCM, which cannot achieve the balance of serial to module. In [22–24], how to introduce multi-winding transformer into modular equalizer is introduced, which effectively improves the circuit expansibility. In [25], the hierarchical structure of S2M modular equalizer combined with unit equalizer based on LLC is introduced, but this modular equalizer can only equalize a single module, and its efficiency is not high enough.

For the equalizer proposed in this paper, the two-layer hierarchical structure design realizes the two-layer equalization of serial to module and unit to unit. At the same time, the LCC structure simplifies the circuit, and the control mode is simple. The simulation results show that the equalization time of this equalizer is shorter and the equalization efficiency is higher than that of LLC module equalizer. At the same time, the equalization effect of the equalizer reaches 99.5%, and the equalization effect is good [26].

5 Conclusion

In this paper, a hybrid hierarchical battery energy system equalization topology is proposed based on S2M and buck–boost of LCC, and its working principle is explained. The equalization method realizes the equalization between different modules and between cell batteries with the virtue of high scalability and simplicity. In addition, we illustrate the principle and design considerations of equalizer, we verify the effectiveness by simulation test, i.e., the voltages of six battery packs with an initial voltage difference of 0.4 are equalized, and the voltage difference is reduced to 0.002, which is reduced by 99.5%, and the time is controlled within 1 s, which proves the good effect of the equalizer and verifies the correctness of the theoretical design.

References

1. Hoque MM, Hannan MA, Mohamed A, Ayob A (2017) Battery charge equalization controller in electric vehicle applications: a review. Renew Sustain Energy Rev 75:1363–1385
2. Kim MY, Kim JH, Moon GW (2014) Center-cell concentration structure of a cell-to-cell balancing circuit with a reduced number of switches. IEEE Trans Power Electron 29(10):5285–5297
3. Baughman AC, Ferdowsi M (2008) Double-tiered switched-capacitor battery charge equalization technique. IEEE Trans Ind Electron 55(6):2277–2285

4. Kim MY, Kim CH, Kim JH, Moon GW (2014) A chain structure of switched capacitor for improved cell balancing speed of lithium-ion batteries. IEEE Trans Ind Electron 61(8):3989–3999
5. Lee YS, Cheng GT (2006) Quasi-resonant zero-current-switching bidirectional converter for battery equalization applications. IEEE Trans Power Electron 21(5):1213–1224
6. Chen Y, Liu X, Cui Y, Zou J, Yang S (2016) A multiwinding transformer cell-to-cell active equalization method for lithium-ion batteries with reduced number of driving circuits. IEEE Trans Power Electron 31(7):4916–4929
7. Gallardo-Lozano J, Romero-Cadaval E, Milanes-Montero MI, Guerrero-Martinez MA (2014) Battery equalization active methods. J Power Sour 246:934–949
8. Phung TH, Collet A, Crebier J-C (2014) An optimized topology for next-to-next balancing of series-connected lithium-ion cells. IEEE Trans Power Electron 29(9):4603–4613
9. Shang Y, Cui N, Duan B, Zhang C (2018) Analysis and optimization of star-structured switched-capacitor equalizers for series-connected battery strings. IEEE Trans Power Electron 33(11):9631–9646
10. Lee KM, Lee SW, Choi YG, Kang B (2017) Active balancing of Li-ion battery cells using transformer as energy carrier. IEEE Trans Ind Electron 64(2):1251–1257
11. Arias M, Sebastián J, Hernando MM, Viscarret U, Gil I (2015) Practical application of the wave-trap concept in battery-cell equalizers. IEEE Trans Power Electron 30(10):5616–5631
12. Uno M, Kukita A (2015) Two-switch voltage equalizer using an LLC resonant inverter and voltage multiplier for partially shaded series-connected photovoltaic modules. IEEE Trans Ind Appl 51(2):1587–1601
13. Kim CH, Kim MY, Park HS, Moon GW (2012) A modularized two-stage charge equalizer with cell selection switches for series-connected lithium-ion battery string in an HEV. IEEE Trans Power Electron 27(8):3764–3774
14. Hannan MA et al (2017) Lithium-ion battery charge equalization algorithm for electric vehicle applications. IEEE Trans Ind Appl 53(1):2541–2549
15. Hua C, Fang Y (2016) A charge equalizer with a combination of APWM and PFM control based on a modified half-bridge converter. IEEE Trans Power Electron 31(4):2970–2979
16. Wei Z, Peng F, Wang H (2022) An LCC-based string-to-cell battery equalizer with simplified constant current control. IEEE Trans Power Electr 37(2):1816–1827
17. Sun J, Zhu C, Lu R, Song K, Wei G (2015) Development of an optimized algorithm for bidirectional equalization in lithium-ion batteries. J Power Electron 15(3):775–785
18. Imtiaz AM, Khan FH (2013) 'Time shared flyback converter' based regenerative cell balancing technique for series connected li-ion battery strings. IEEE Trans Power Electron 28(12):5960–5975
19. Einhorn M, Roessler W, Fleig J (2011) Improved performance of serially connected Li-ion batteries with active cell balancing in electric vehicles. IEEE Trans Veh Technol 60(6):2448–2457
20. Du J, Xu R, Chen X, Li Y, Wu J (2018) A novel solar panel optimizer with self-compensation for partial shadow condition. In: Proceedings of the 28th annual IEEE applied power electronic conference exploration
21. Peng F, Wang H, Yu L (2019) Analysis and design considerations of efficiency enhanced hierarchical battery equalizer based on bipolar CCM buck–boost units. IEEE Trans Ind Appl 55(4):4053–4063
22. Shang Y, Xia B, Zhang C, Cui N, Yang J, Mi C (2017) A modularization method for battery equalizers using multi-winding transformers. IEEE Trans Veh Technol 66(10):8710–8722
23. Shang Y, Cui N, Duan B, Zhang C (2018) A global modular equalizer based on forward conversion for series-connected battery strings. IEEE J Emerg Sel Top Power Electron 6(3):1456–1469
24. Lim CS, Lee KJ, Ku NJ, Hyun DS, Kim RY (2014) A modularized equalization method based on magnetizing energy for a series-connected lithium-ion battery string. IEEE Trans Power Electron 29(4):1791–1799

25. Peng F, Wang H (2020) Wie Z (2020) An LLC-based highly efficient S2M and C2C hybrid hierarchical battery equalizer. IEEE Trans Power Electr 35(6):5928–5937
26. Gilbert AJ, Stone DA, Bingham CM, Foster MP (2007) Design of an LCC current-output resonant converter for use as a constant current source. In: Proceedings of the European conference on power electronics applied, pp 1–6

Study on the Influence of Multiple Faults on the Stability of High and Steep Slopes in Open-Pit Mines

Shuaichuan Rong and Jing Wang

Abstract To study the combined influence of multiple faults on the stability of high and steep slopes in open-pit mines, the finite difference software FLAC^{3D} was applied to analyze the stability of high and steep slopes under the combined influence of four faults in the Tang Ya limestone mine of Gezhouba Xing Shan Cement Co. Combining the current fault development status and the slope instability damage characteristics under the subsequent deep extension mining conditions, the stability of the Tang Ya limestone mine under the combined effect of multiple faults is revealed. The results show that (i) the presence of faults controls the form of slope damage in the Tang Ya open-pit mine, which in turn affects the stability of the slope; (ii) the mechanical cause of slope damage is the fault cutting through the rock mass, resulting in relative slip and extrusion damage due to discontinuous stress transfer between the rock masses; (iii) the impact of mining disturbance on slope damage is small, with the maximum displacement value only increasing from 50.7 to 52 mm, and the plastic zone is never penetrated The maximum displacement value only increased from 50.7 to 52 mm, and the plastic zone was never penetrated.

Keywords Slope stability · Faults · Numerical simulation · High and steep slopes

1 Introduction

Slope stability is a major problem that needs to be faced in the process of open-pit mining [1], which is affected by many aspects. If not handled properly, it is easy to cause great potential safety hazards and economic losses [2]. There are often a large number of structural planes such as faults, joints, and argillized layers in the

S. Rong (✉)
Wuhan Ruixin Special Optical Fiber Co., Ltd., Wuhan 430070, Hubei, China
e-mail: rongshuaichuan@163.com

J. Wang
Hubei Sanjiang Space Wanfeng Science and Technology Development Co., Ltd., Xiaogan 432000, Hubei, China

S. Yadav et al. (eds.), *Energy Power and Automation Engineering*, Lecture Notes in Electrical Engineering 1118, https://doi.org/10.1007/978-981-99-8878-5_78

slope rock mass [3]. The problem of slope failure mechanism under the influence of multiple faults faced by Tangya limestone mine is more complicated [4].

In recent years, many scholars have carried out a series of studies on the influence of faults on slope stability. Wang used FLAC^{3D} software to study the influence of fault location on the slip mode and stability variation of bedding slope [5, 6]. He used FLAC^{3D} strength reduction method and compared it with the slide limit equilibrium method to study the influence of mechanical parameters and geometric parameters on the failure mode and stability of rock slope [7]. Based on the theory of rigid body limit equilibrium and numerical simulation, Tian studied the deformation and failure characteristics, landslide mode, and the influence of different weak layers on slope stability of composite dip slope with multiple weak layers and fault structures [8]. Based on the limit equilibrium theory and numerical simulation method, Lanzhu et al. [9, 10] studied the influence of fault location on the landslide mode and stability of open-pit mine stope and stope-dump composite slope. Kaigan et al. [11] used the Sarma method to calculate and analyze the safety factor of the slope under different structural planes and different sliding surface lengths and analyzed the stability of the high slope with faults. Chuan et al. [12] used 3Dslope slope calculation software to calculate the stability of the northwest slope of Pingzhuang West Open-pit Mine and determined the slope stability coefficient. Jian et al. [13] established a dynamic numerical analysis model of soil slope by FLAC software and studied the dynamic response of slope under near-fault ground motion with forward directivity effect, slip effect, and no velocity pulse. Wandong et al. [14] studied the deformation and failure of the slope and the distribution characteristics of the plastic zone through FLAC^{3D} and revealed the landslide mechanism of the non-working slope of Huajian open-pit mine. Tao et al. [15] studied the instability mechanism of high fill slope by FLAC^{3D} and proved that the local displacement of the calculation area would not lead to the overall instability of the slope. Ye used PLAXIS 3D geotechnical finite element software to establish a slope stability calculation model to analyze the stability of multi-stage loess high slope under the influence of rainfall infiltration [16]. Penghong [17] used FLAC and Geo-Slope software to simulate and analyze the influence of fault location on slope stability.

In summary, the discussion of slope instability mechanism mainly focuses on the influence of changes in rock mass mechanical parameters and slope geometric parameters on slope stability. Specifically, it is the influence of fault occurrence angle and geological structures such as faults and fissures on slope stability. However, there are few studies on the stability of high and steep slopes under the comprehensive influence of multiple faults. Therefore, this paper uses FLAC^{3D} software to establish a high and steep rock slope model and introduces fault point data to study the stability of high and steep rock slopes in Tangya open-pit mines under the influence of multiple faults, so as to guide the prevention and control of landslide areas in Tangya open-pit limestone slopes and ensure the safe production of mines.

2 Analysis of Slope Engineering Geological Conditions

The designed mining elevation of Tangya limestone mine is + 1300 ~ + 880 m. It is mined by the top-down horizontal stratification method. At present, multiple mining platforms have been formed. The highest slope is 170 m, the step slope angle is 64°, the step height is 12 m, the final slope angle above the + 1064 m platform is 39°, the final slope angle from the + 1026 m platform to the + 1062 m platform is 43°, the + 1026 m platform to the lowest mining elevation + 880 m platform, and the final slope angle is 25°. It can be found from engineering practice that the slope of Tangya limestone mine belongs to high and steep rock slope, and the problem of slope deformation and stability is relatively prominent [18]. Many landslide events have occurred since it was put into production, and under the condition of rock mass exposure and unsupported operation for many years, deformation and displacement of rock mass at the surface of many slopes have caused serious economic losses.

Through the surface survey, the fault occurrence and distribution area of Tangya open-pit mine were investigated, and the fault point data were recorded as shown in Table 1. There are four major faults, namely F_1, F_2, F_3, and F_4 in the mine. The properties of the faults are all compressive and torsional reverse faults. The faults are vertical or parallel to the slope surface, which greatly affects the continuity of the slope rock mass. The details of the faults revealed by the survey are as follows:

F_1: Distributed in the northeast of the mining area, extending at both ends. The fault strike is relatively straight, the overall strike is NW–SE (116° ~ 296°), and the dip angle is 70°. Structural breccia is intermittently distributed in the fault zone. The structural breccia is intermittently distributed in the fault zone, containing typical fault gouge and limestone structural lens. The vertical dislocation of the fault is greater than 80 m, and the horizontal dislocation is unclear. Located at the northern end of the slope, it has a general impact on slope stability.

F_2: Located in the southwest of the mining area, the southernmost slope exposed. The width is 2–3 m. The tectonic rock is mainly breccia and cataclastic rock, filled with calcite, with schistosity. The section is wavy, and the interlayer contains debris and argillaceous material.

F_3: It is distributed in the south-central part of the mining area, across the whole mining area, extending for 1160 m, and the northwest end extends to the outside of the map along the Gao (Yang)–Huang (Liang) highway. The overall trend of the fault is northwest–southeast, which is roughly parallel to the stratigraphic trend (130°–310°). The exposed trajectory is a slow wavy, asymmetric '*S*' shape. The dip direction is southwest, and the dip angle is 69°–89°. The fault fracture bandwidth is 1.5–4 m, the structural breccia is developed, and the calcite veins are interspersed. The fault distance is 40 ~ 50 m, and the fault destroys the continuity of the ore body (layer).

F_4: Through the middle of the slope, the tectonic rock is about 1m wide, which is breccia and cataclastic rock, with good cementation and schistosity along the fault surface. There are fissures along the fault, filling calcite.

Table 1 Fault point data statistics table

Fault point	Attitude	Coordinate *X*	Coordinate *Y*	Elevation *H*
DC1	20°∠74°	3457716.536	37481445.198	967.326
DC2	225°∠89°	3457755.749	37481483.695	967.741
DC3	245°∠83°	3457712.088	37481459.168	978.287
DC4	40°∠69°	3457749.845	37481497.277	978.500
DC5	196°∠79°	3457829.976	37481564.345	980.491
DC6	22°∠81°	3457822.435	37481578.835	991.214
DC7	25°∠81°	3457743.772	37481512.727	991.141
DC8	56°∠88°	3457703.888	37481466.001	990.523

3 Numerical Simulation of Slope Stability

Using the finite difference software FLAC^{3D}, the M-C criterion is used as the failure criterion of rock mass, and the penetration of plastic zone is used as the basis of slope instability. The stability of high and steep slope under the influence of F_1–F_4 four faults in Tangya open-pit mine is simulated, and the influence of multiple faults on slope stability is revealed.

3.1 Numerical Model Establishment

In order to study the influence of fault development on the slope stability of Tangya open-pit mine, the point cloud data of the area were collected by UAV [19], shown in Fig. 1. And the coordinates of the fault points in the geological survey (Table 1) were imported into the three-dimensional model of the slope, shown in Fig. 2. The spatial combination relationship between the slope and the fault is shown in Fig. 3.

Considering the boundary problem in numerical calculation, the length of the model along the slope is 200 m, and the height along the gravity direction is 350 m. The boundary conditions of side normal constraint, bottom fixed constraint, and upper surface free are adopted. The numerical model uses tetrahedral elements. In order to fully simulate the influence of faults, the interface command method is used to construct the contact surface, and the fault cutting slope rock mass is simulated to make it discontinuous [20]. The three-dimensional solid model based on FLAC^{3D} is shown in Fig. 4. In the calculation, the slope is regarded as an ideal elastic–plastic body, and the influence of groundwater and other factors on the stability of open-pit slope is ignored. The Mohr–Coulomb model is selected as the constitutive model [21].

The physical and mechanical indexes of rock mass are obtained from rock mechanics test and previous geological data as shown in Table 2.

Fig. 1 UAV top view

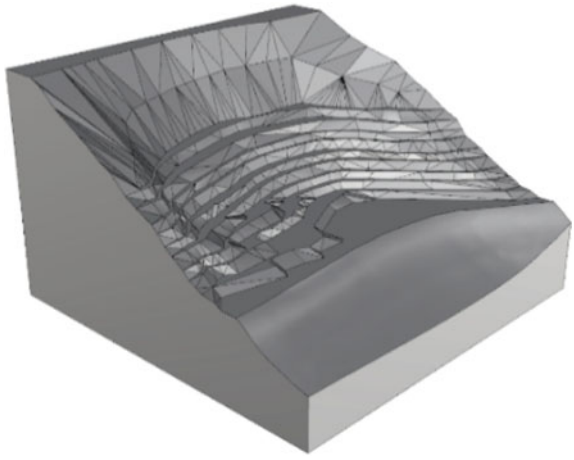

Fig. 2 Three-dimensional model of slope

3.2 Slope Status Simulation Results and Analysis

In order to reveal the influence of faults on slope stability under current conditions, the numerical model is mined to the elevation of + 966 m (the slope height is about 96 m). The obtained displacement distribution and plastic zone distribution are shown in Figs. 5 and 6. It can be found from the cloud map that: (1) The three areas with

Fig. 3 Fault cutting surface

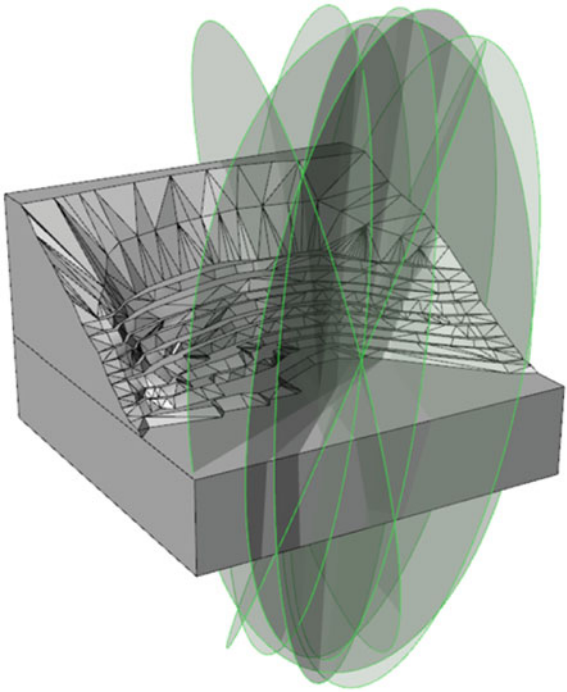

Fig. 4 Three-dimensional solid model

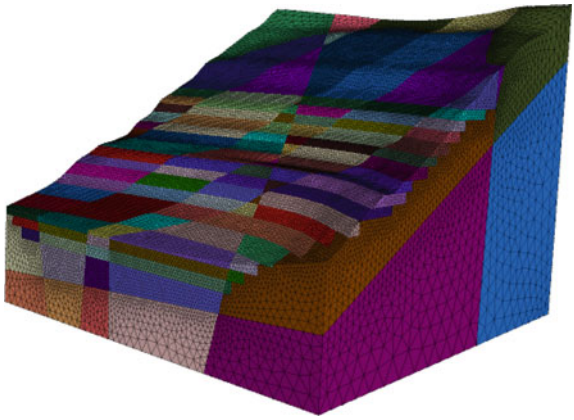

Table 2 Physical and mechanical indexes of rock mass

Parameter	Elastic modulus/ GPa	Poisson ratio	Angle of internal friction/°	Cohesion/ MPa	Density/ $g \cdot cm^{-3}$	Tensile strength/ MPa
Values	8.00	0.25	35.00	2.00	2.60	1.00

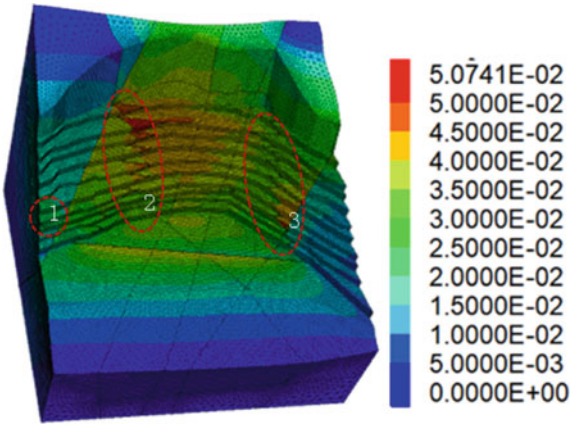

Fig. 5 Overall displacement distribution of the slope after excavation

relatively large displacement are located in the north of the slope (No. 1 area in the figure), the middle of the slope (No. 2 area in the figure), and the south slope (No. 3 area in the figure). Obviously, the areas with large displacement appear near the fault, and the rock displacement between the two fault planes is significantly smaller than the displacement near the fault plane, indicating that the slope near the fault has a greater risk of failure. (2) Compared with No. 3 area and No. 1 area, the range of large overall displacement deformation in No. 2 area is larger, and the maximum displacement value is also larger, reaching 50 mm. According to the survey results, the fault distribution in No. 2 area is also denser. (3) The distribution position of the plastic zone corresponds to the area with large displacement. The location and range of the simulated slope failure are also in good agreement with the actual slope failure (as shown in Figs. 7, 8 and 9). It can be found from Fig. 6 that there are two trends in the development of the plastic zone along the fault and the vertical fault. The position of the plastic zone along the fault is such as the upper part of the No. 2 area, indicating that the slope failure is caused by the mutual slip of the rock mass on both sides of the fault. The position of the plastic zone is similar to the vertical fault development, such as the lower part of the No. 2 area and the No. 3 area, indicating that the slope failure is caused by the relative extrusion of the rock mass on both sides of the fault. In summary, the main reason for the failure of the slope is the relative slip failure and extrusion failure between multiple rock masses. Under the cutting of the fault, the rock mass becomes a discontinuous block. The more faults, the more blocks the slope rock mass is cut, and the more unstable the slope is.

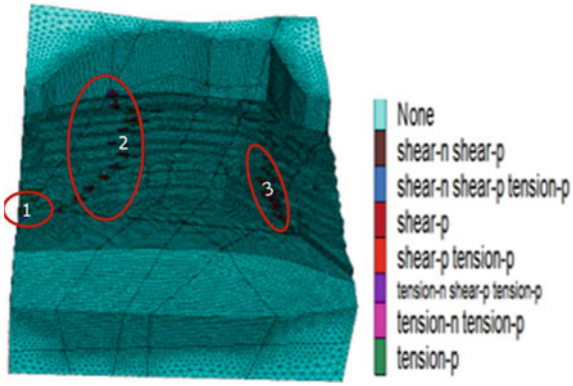

Fig. 6 Plastic zone distribution of slope after excavation

Fig. 7 No. 1 area scene photos

Fig. 8 No. 2 area scene photos

Fig. 9 No. 3 area scene photos

3.3 Slope Deep Mining Simulation Results and Analysis

In order to reveal the influence of fault development state on the slope stability of subsequent deep mining, based on the simulation of current mine production process, according to the design of deep boundary expansion mining, the process of layer-by-layer mining in subsequent mines is simulated, and the slope stability is comprehensively evaluated by two indexes of slope displacement and plastic zone development.

From the slope displacement distribution cloud map and the plastic zone distribution cloud map, it can be seen that from the mining + 954 m platform to the + 880 platform, the maximum displacement of the slope always appears in the No. 2 and No. 3 areas, and the No. 1 area displacement does not increase significantly. The maximum displacement value increased from 50 to 52 mm as shown in Fig. 10. The displacement distribution and the plastic zone distribution for each level is shown in Figs. 11, 12, 13, 14, 15, 16, 17, 18, 19, 20, 21, 22, 23 and 24. It can be seen that the plastic zones in No. 1, No. 2, and No. 3 regions continue to develop along the original development direction, but the extended plastic zone is small and has not been connected in a large range. In general, with the development of deep mining, the maximum displacement value of the slope continues to increase, but the overall growth is small, and the growth effect of the deep mining process on the range of the plastic zone of the slope is also small. Therefore, due to the fact that the fault development attitude does not further extend to the deep area, the fault has little effect on the slope stability in the deep mining process.

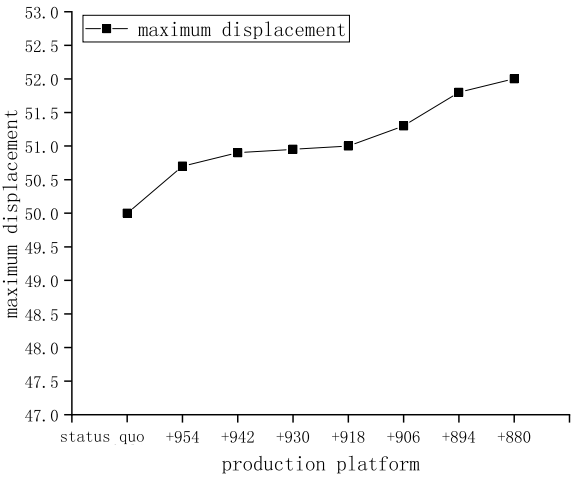

Fig. 10 Maximum displacement change diagram of the mining process

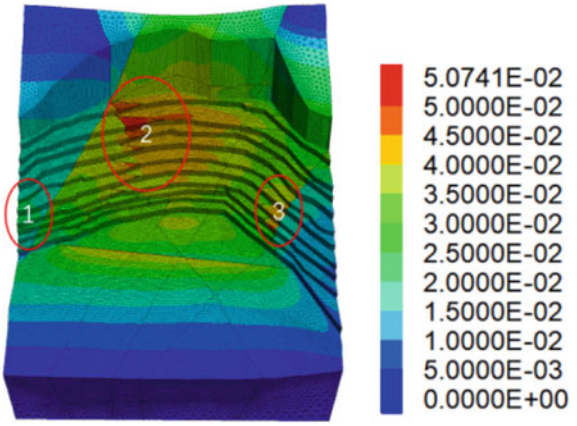

Fig. 11 + 954 m slope overall displacement distribution

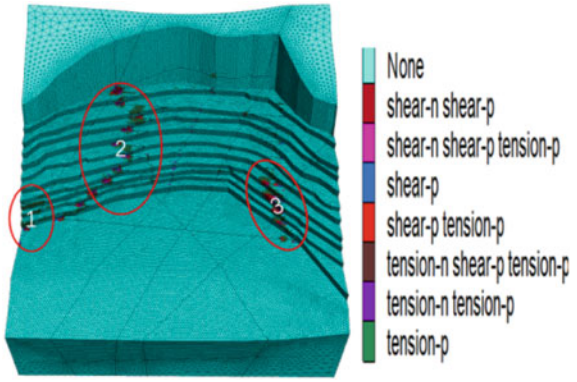

Fig. 12 + 954 m slope plastic zone distribution

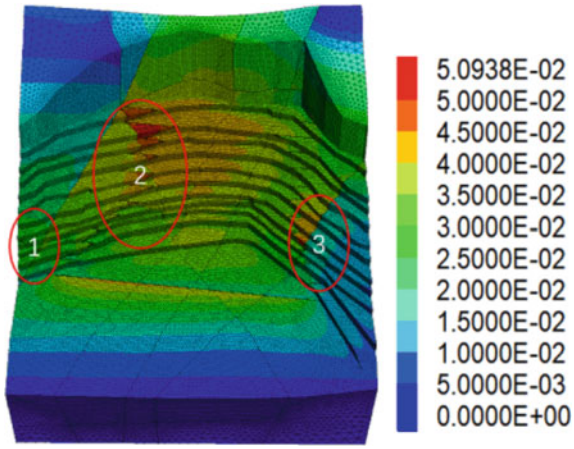

Fig. 13 + 942 m slope overall displacement distribution

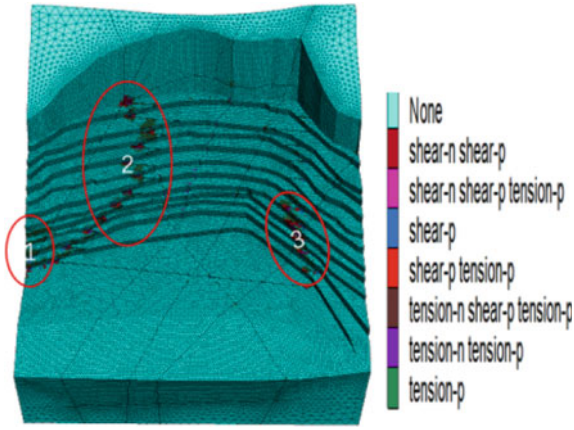

Fig. 14 + 942 m slope plastic zone distribution

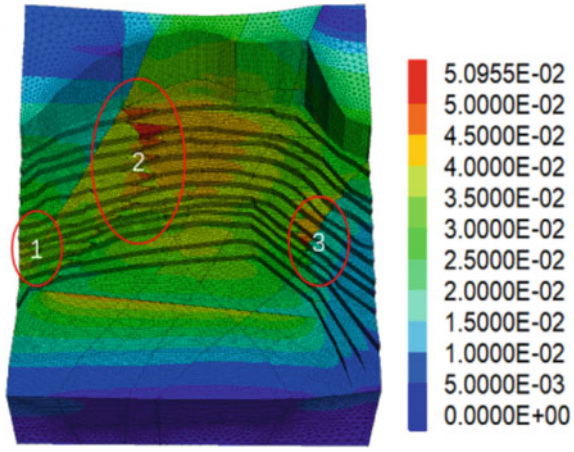

Fig. 15 + 930 m slope overall displacement distribution

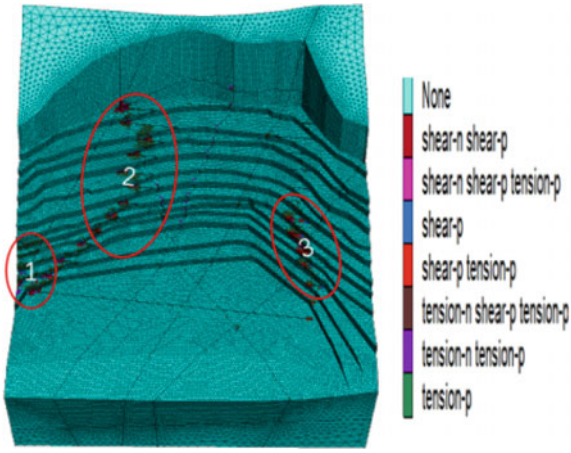

Fig. 16 + 930 m slope plastic zone distribution

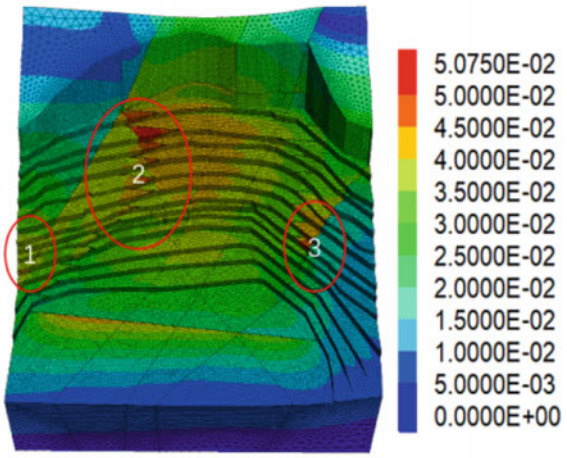

Fig. 17 + 918 m slope overall displacement distribution

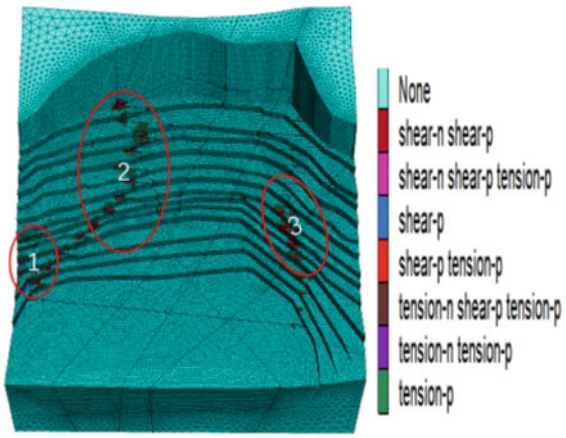

Fig. 18 + 918 m slope plastic zone distribution

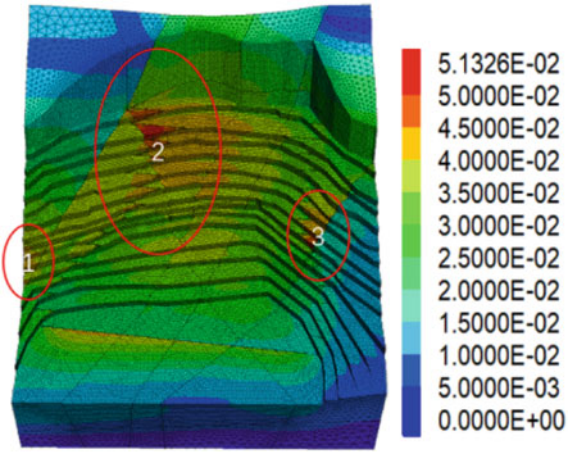

Fig. 19 + 906 m slope overall displacement distribution

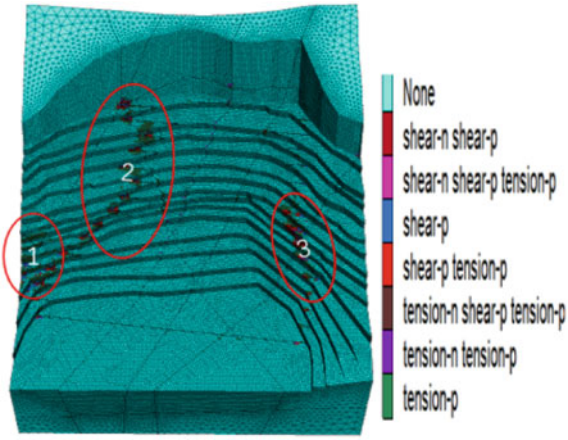

Fig. 20 + 906 m slope plastic zone distribution

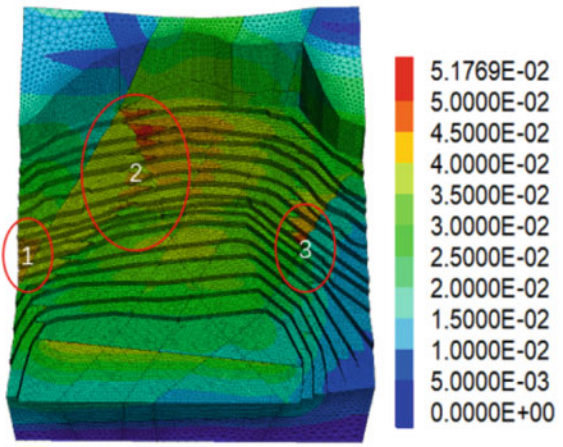

Fig. 21 + 894 m slope overall displacement distribution

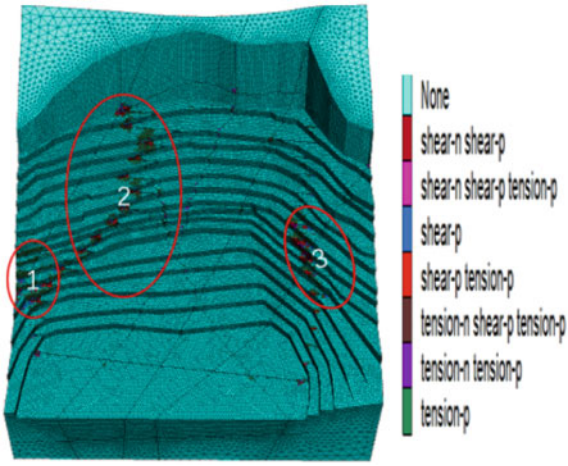

Fig. 22 + 894 m slope plastic zone distribution

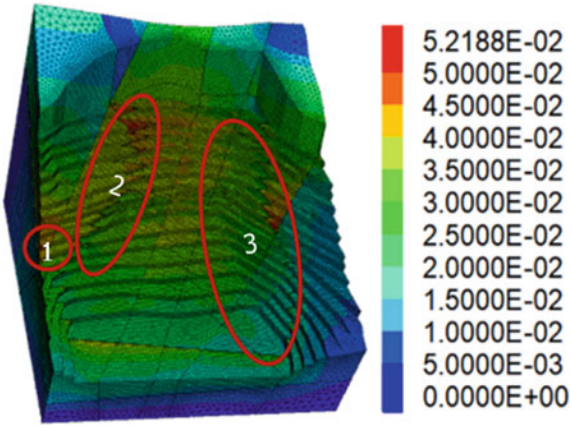

Fig. 23 Overall displacement distribution of the slope after mining

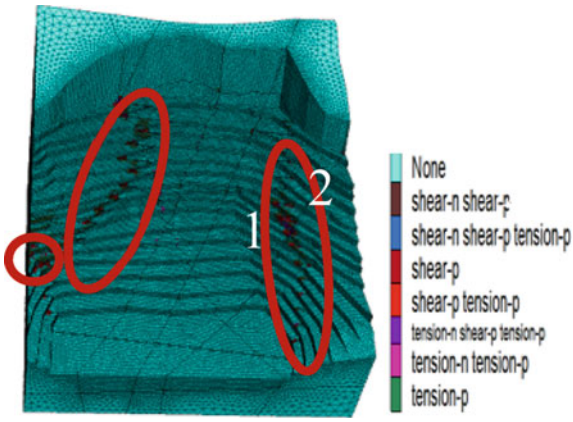

Fig. 24 Distribution of plastic zone of slope after mining

4 Conclusion

FLAC3D is used to simulate the slope stability of Tangya limestone open-pit mine. The failure mechanism of high and steep rock slope under the influence of multiple faults and the influence of mining disturbance on slope safety are revealed. The following conclusions are drawn as follows:

(1) The displacement area of the slope is mainly concentrated near the fault. The range of slope displacement above 4cm in the dense fault area is larger, indicating that the risk of slope failure near the fault is greater, and the denser the fault structural plane is in the local area, the more serious the slope failure is.

(2) Due to the existence of faults, the slope is cut into multiple rock masses. The discontinuity of stress transfer between rock masses leads to the development of plastic zone along faults and vertical faults. The dislocation of rock masses on both sides of faults makes the plastic zone develop and destroy along the fault plane. The relative extrusion of rock masses on both sides of faults makes the vertical fault plane of plastic zone develop and destroy.

(3) Under the continuous influence of faults, with the progress of deep mining, the maximum displacement value of the slope continues to increase, but the overall growth is small, and the maximum displacement value only increases from 50 to 52 mm; the plastic zone continues to develop slightly along the original development direction, but there is no large-scale penetration, indicating that the damage of fault to slope stability has not increased significantly with mining, and the slope safety state is good.

References

1. Bingyin Z, Yanfeng W, Benzhen Z (2016) J Civil Eng 49:1–15
2. Yong L, Changlin L (2011) J Chongqing Jiaotong Univ 30:576–579
3. Liu G, Zhao J, Song HW (2007) J China Univ Min Technol 36(1):17–22
4. Yang JL, Zuo JP, Sun K, Meng BB, Lin X (2011) Chinese J Rock Mech Eng 30(6):1216–1224
5. Dong WA, Zhen WA, Lanzhu CA (2014) China Saf Sci J 28(2):75
6. Zhen W, Lanzhu C (2020) Coal Sci Technol 48:69–74
7. Dazhao H, Bin H, Wenmin Y (2018) Proc Yangtze River Acad Sci 35:128–132
8. Yu T, Bo Z, Bowen L (2021) Coal Sci Technol 49:189–194
9. Lanzhu C, Limin Q, Dong W (2016) J Liaoning Tech Univ 35:804–809
10. Lanzhu C, Xiuping Z, Dong W (2015) Metal Mine 178–182
11. Kaigan X, Shuai W, Ming Z (2020) J Yangtze River Acad Sci 37:119–125
12. Chuan D, Lanzhu C, Lan J (2013) J Liaoning Tech Univ 32:297–300
13. Jian S, Guangyun G, Qingsheng C (2013) Earthq Eng 35:62–68 + 90
14. Wandong H, Mingyu G, Xiaoyun Y (2013) J Liaoning Tech Univ 32:1204–1208
15. Tao Y, Jiahao C, Jian K (2018) Subgrade Eng 2018(05):59–64
16. Shuaihua Y, Yilei S (2018) J Eng Geol 26:1648–1656
17. Penghong D, Hailong W, Dehui Z (2016) Metal Mine 2016(09):53–57
18. Jiliang W, Jing Y, Youhua C (2015) J Water Resour 46:1414–1422
19. Shuguang J, Aibing J, Yiqing Z (2018) Geotech Mech 39:1130–1136
20. Xinyu W, Laishan C, Wen L (2011) Metal Mine 2011(10):58–60
21. Chujian D, Yingren Z, Jiankai Z (2008) Geotech Mech 2008(02):310–314

Application of Edge Computing in S7-1200 Data Acquisition System

Ji Jun, Hai-Jun Zhou, Fei-Fei Xing, and Guan-Hong Cheng

Abstract Through the industrial gateway, real-time collection of analog data humidity and temperature data in S7-1200PLC. First, analyze the requirements according to the needs of the industrial site, then configure the networking mode and IP of the gateway, and perform data filtering and edge computing on the collected data to determine whether there is any abnormality in the equipment. The experimental results show that the edge computing algorithm set in this paper can effectively determine the operating status of the equipment and improve the operating efficiency of the equipment.

Keywords Edge computing · Data collection · PLC

1 Introduction

Edge computing is a new technology to reduce transmission delay and bandwidth limitation, which is to reduce the pressure on cloud computing centers by placing edge servers at the edge of the network close to the side of the IoT device to handle some computing, storage, applications, and other functions [1, 2].

In recent years, the Internet of things technology and cloud computing technology have developed rapidly and are widely used, bringing great convenience to people's production and life [3]. However, with the rapid development of 5G high bandwidth and low latency, new applications such as the Internet of vehicles, virtual reality technology, and industrial control have generated massive data, which has brought great challenges to the traditional cloud computing method, and the traditional cloud computing method has been unable to meet the higher requirements of the current massive data for real-time, offline, security, and other aspects, so scholars have created the concept of edge computing, hoping to solve the current problems [4–6].

J. Jun (✉) · H.-J. Zhou · F.-F. Xing · G.-H. Cheng
Beijing Polytechnic, Beijing, China
e-mail: ji_jun2000@sina.com

S. Yadav et al. (eds.), *Energy Power and Automation Engineering*, Lecture Notes in Electrical Engineering 1118, https://doi.org/10.1007/978-981-99-8878-5_79

2 Industrial Data Collection

Industrial data collection is the use of ubiquitous perception technology to conduct real-time and efficient collection and cloud aggregation of multi-source equipment, heterogeneous system, operation environment, people, and other elements of information. Industrial data collection corresponds to the edge layer in the industrial Internet platform architecture [7–9]. Through various means of communication to access different devices, systems, and products, collect a large range of deep-level industrial data, as well as heterogeneous data protocol conversion and edge processing, to build the data base of industrial Internet platform. Industrial data acquisition is the basis of intelligent manufacturing and industrial Internet, forms the "field bus and industrial Ethernet Fusion, industrial sensor network, industrial wireless, industrial gateway communication protocol and interface" standard, to solve the intelligent manufacturing "data acquisition, data integration, data computing analysis" software problems of [9].

3 System Function Requirements

The functional requirements of this system are: through the industrial data acquisition gateway, collect S7-1200PLC temperature and humidity and other data, after the PLC is powered on, the collected data is refreshed every 5 s, and the collected data is edge-calculated to determine whether the equipment is abnormal.

The system is designed through the following steps: (1) analysis of control requirements, (2) gateway configuration, (3) edge computing design, and (4) system and troubleshooting.

The system flowchart is shown in Fig. 1.

4 System Design Implementation

1. Gateway configuration

In the gateway management software, click the configuration menu, select the networking mode of the industrial data acquisition gateway as Ethernet, and select the gateway to be collected. Parameter configuration. There are three kinds of networking methods, namely "WIFI", "WAN", and "mobile network". WIFI: gateway, the gateway enters the external network by connecting wireless WIFI; WAN: gateway, the gateway enters the external network through direct connection; mobile network: the external network by installing SIM card using the wireless network of corresponding operator. Gateway box state read and access to the external network mode setting. Click the "refresh" button on the right to read the parameters of the current gateway box, select "WAN", and click the "settings" button, as shown in Fig. 2.

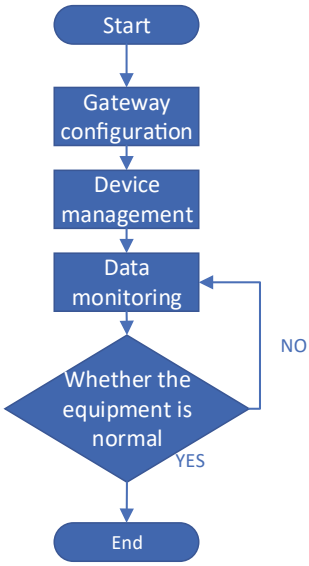

Fig. 1 System flowchart

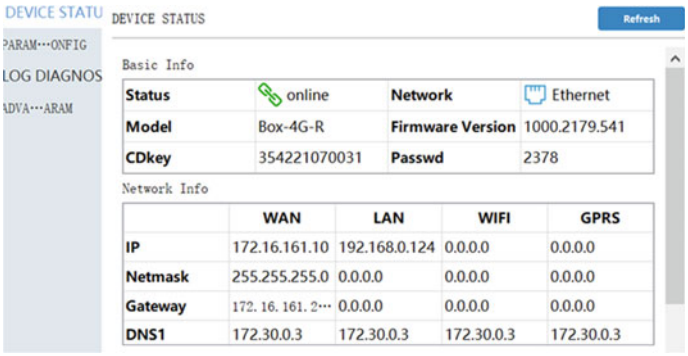

Fig. 2 Parameter configuration

Add the gateway information, the X Edge serial number, and the password to the X Edge: a custom gateway name.

2. Device management

Select “remote download”, click “device management” button, fill in the network PLC setting interface, and then click “ok” button, as shown in Fig. 3.

3. Data monitoring

In the “data monitoring”, click the “new monitoring” button to add the monitoring data, as shown in Fig. 4.

The data monitoring table is shown in Table 1.

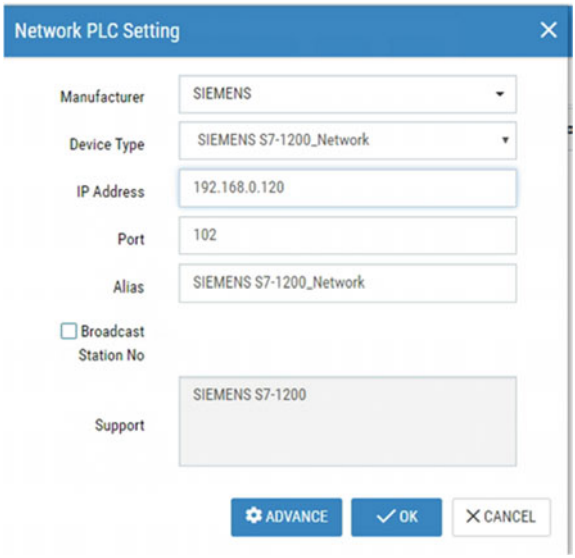

Fig. 3 Network PLC configuration

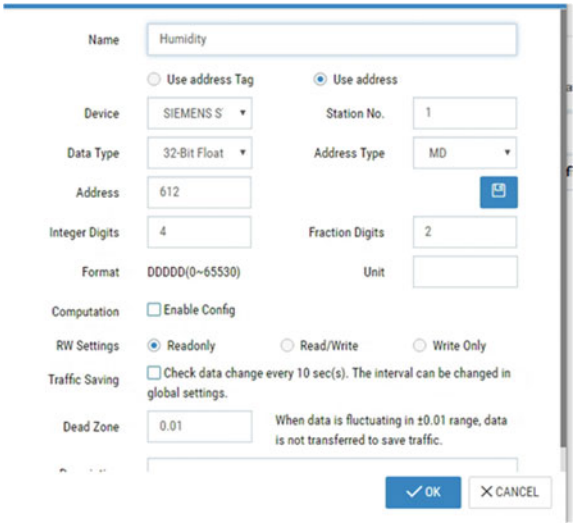

Fig. 4 Monitoring point setting

4. Edge calculation

When the humidity is between 35 and 75%, it means that the production line is in normal condition. When it exceeds 35 ~ 75%, it means that the production line status is abnormal.

(1) First, add a point to the X Edge software data monitoring to represent the judgment result. Click the “new script” button, and on the new script page, click the

Table 1 Data monitoring

Name	Data type	Address
Humidity	Real	%MD612
Start	Bool	%I0.0
Stop	Bool	%I0.1
Reset	Bool	%I0.2
Emergency stop	Bool	%I0.3
Car raw material warehouse 1	Bool	%I1.0
Car raw material warehouse 1	Bool	%I1.1
Bottom feeding cylinder	Bool	%Q2.0
Assembling and testing the cylinder	Bool	%Q2.1
Online time	Real	%MD600
Material quantity	DInt	%MD604
Temperature	Real	%MD608
Equipment downtime	Real	%MD632
Production time	Real	%MD636
Total production quantity	DInt	%MD640
Quantity of qualified products	DInt	%MD644
Total daily power consumption	Real	%MD648

add button to add variables, as shown in Fig. 5. Click the add variable button to add the variable humidity judge.

Complete the script on the right, and then click the "run" button to view the output. If an error occurs, you can view the help. After confirmation, click "save and close".

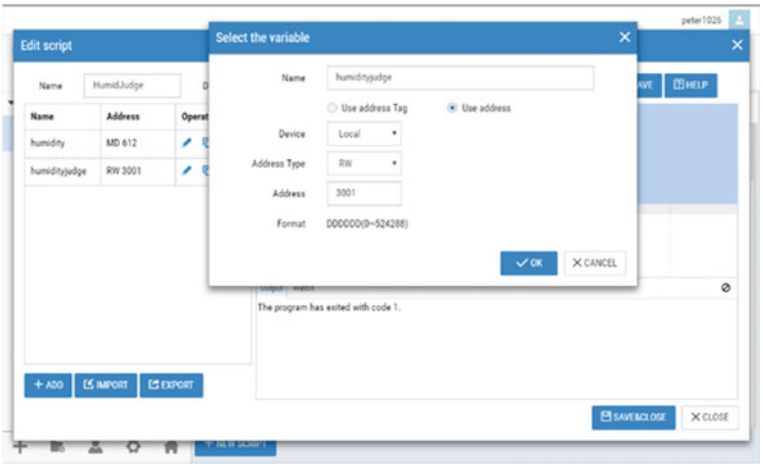

Fig. 5 Edge calculated variables

```
function main ()
{
*********var shidu = getFloat ("shidu", 0);
*********var state = 0;
*********if(shidu < 35).
**********{state = 1;}
*********else if(shidu < = 75).
**********{state = 2;}
*********else
**********{state = 1;}
*********setU16("humidtityJudge", 0, state);
}
```

There are three execution modes, namely X Edge startup execution, cycle execution, and conditional execution. Execution during X Edge startup: execute once after the device is powered up, and take no action later; periodic execution: perform periodically according to the set time; conditional execution: execute the script once when a condition is met. This selection cycle is executed, and the execution cycle is 5 min once. Select the script Humid Judge, and click on the "ok" button. On the data monitoring page, view the values of the data monitoring Humidity and Humidity Judge, as shown in Fig. 6.

Status	Name	Value	Address	Traffic	Description	Operation
●	Humidity	37.80	MD 612	N	MD 612	
●	Temperature	26.80	MD 608	N	MD 608	
●	TemperatureJudge	2	RW 3001	N	Temperature Judge device	
●	HumidityJudge	0	RW 3003	N	HumidityJudge device	
●	Start	0	I.B 0.0	N	Start	
●	Emergency stop	1	I.B 0.3	N	Emergency stop	
●	Car raw material warehouse 1	1	I.B 1.0	N	Car raw material warehouse	
●	Assembling and testing the cylinder	0	Q.B 2.1	N	Assembling and testing the cylinder	

Fig. 6 Computational results

5 Conclusion

In this paper, the data such as S7-1200PLC humidity is collected. The experimental results show that the edge computing algorithm set in this paper can effectively determine the operating status of the equipment and improve the operating efficiency of the equipment.

Acknowledgements This research is supported by the University project of BEIJING POLYTECHNIC (No. 2022X008-KXD).

References

1. Zhijia B (2022) Intelligent building gateway design based on edge computing. Integ Circ Appl 2022(01)
2. Guozheng J (2021) Research on the application of PLC in electrical automation control. Metall Mater 2021(06)
3. Liao CH (2016) S7-300/400 PLC application technology, 4th edn. Machinery Industry Press, Beijing
4. Chen ZP (2018) Siemens S7-300/400 PLC from entry to proficiency. China Electric Power Press, Beijing
5. Siemens AG (2002) Statement list (STL) for S7-300 and S7-400 programming reference manual
6. Siemens AG (2002) Working with STEPT 7 V5.2 getting started
7. Siemens AG (2002) Configuring hardware and communication connections STEPT 7 V5.2 manual
8. Siemens AG (2003) Programming with STEPT 7 V5.2 manual
9. Xiao YJ, Jing Z (2010) The design of tensile testing machine based on MCGS control system. IEEE 3:193–195

Intelligent Perception and Anomaly Information Processing of Power Engineering Smart Construction Site Platform Based on 3DGIS + BIM: A Case Study of Chongming Yangtze River Crossing Project

Binai Li, Fei Lu, Keke Zhang, Hongliang Shi, and Jin Wei

Abstract In order to improve the information management level and platform operation load rate of tower construction in power engineering, it is necessary to introduce a GIS + BIM engine based on B/S architecture to develop a smart construction site platform for power engineering tower construction. The power engineering smart construction site platform based on 3DGIS + BIM integrates 3D geographic information data, oblique photography data, BIM model data flow, and dual-arm monitoring data flow of the tower construction site, realizing real-time monitoring, personnel positioning, and intelligent electronic fence warning, which can improve the level of personnel operation risk control. By introducing an instance database, collecting data information, screening abnormal information, and preprocessing the information before information management through clustering analysis, and the smart construction site platform achieves intelligent processing and clustering of anomalous information in power engineering. Based on the Internet of things and the collaborative mechanism of power engineering projects, a management decision model based on the browser and server is constructed to achieve intelligent decision-making and digital management of risk information in smart construction sites. Comparative experiments demonstrate that the smart construction site platform designed in this paper can avoid platform operation load caused by excessively large data and improve the efficiency and comprehensive management level of platform information management.

B. Li
State Grid Shanghai Municipal Electric Power Company, Shanghai 200122, China

F. Lu · K. Zhang
East China Power Transmission and Transformation Engineering Company, Shanghai, China

H. Shi
Nanjing Ye Dao Date Technology Co., Ltd, Nanjing, China

J. Wei (✉)
Shanghai Blueearth Technology Co., Ltd, Shanghai, China
e-mail: bulkathos24@gmail.com

S. Yadav et al. (eds.), *Energy Power and Automation Engineering*, Lecture Notes in Electrical Engineering 1118, https://doi.org/10.1007/978-981-99-8878-5_80

Keywords 3DGIS + BIM · B/S architecture · Clustering analysis · Information management · Smart construction site

1 Introduction

The Yangtze River crossing line of the Shanghai Chongming 500 kV substation and Transformation Project adopts the "tension-straight-straight-tension" scheme, with a total length of 2894 m for the tension section and a span distance of 1690 m. The height of the crossing tower is 172 m, and the total height is 204 m, making it the highest transmission tower in the Shanghai power grid and the easternmost crossing of the Yangtze River. However, traditional intelligent management platforms are limited in their development due to the constraints of various technologies, and they have problems such as a single structure, incomplete management, and inability to accurately control power site risks. These issues cannot meet the requirements of informationization and digitization development of power enterprises. To solve these problems and deepen management, researchers relied on the Chongming 500 kV Yangtze River crossing tower construction project and developed an intelligent construction site management platform for power engineering based on the B/S architecture of GIS + BIM engine. With the support of the Internet of things, the platform achieves in-depth analysis of information through network interaction and a combination of intelligent perception, intelligent recognition, and multiple computational techniques. This allows for the interaction between people, things, and information. To implement this work, this project has developed an information management platform for power engineering intelligent construction sites based on the B/S architecture of the 3DGIS + BIM engine [1]. The platform integrates three-dimensional geographic information data, oblique photography data, BIM model data flow [2], and dual-arm monitoring data flow of tower installation construction sites. It also provides real-time monitoring, personnel positioning, and electronic fence intelligent early warning. The platform can accurately analyze the information feedback at various stages of power grid engineering implementation, and through digital processing of information, it can achieve the standardized construction of intelligent construction sites, thereby achieving the ultimate goal of intelligent management of the Chongming 500 kV Yangtze River crossing tower construction project.

2 System Components and Architecture Design Title

The intelligent construction site system for electric power engineering focuses on specific factors at the construction site, considering factors such as personnel, materials, and machinery, and establishes corresponding functional units with the support of hardware equipment.

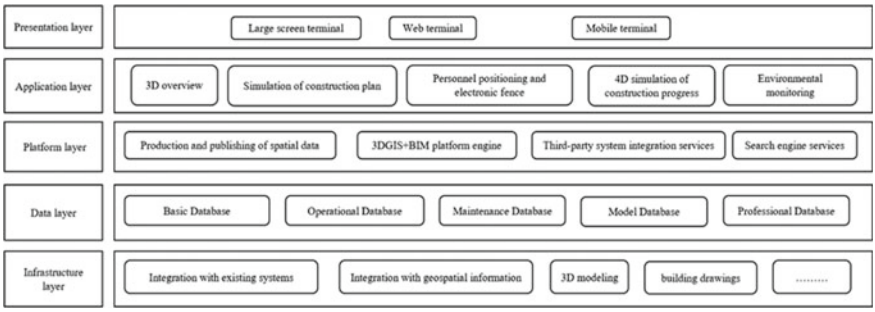

Fig. 1 System architecture diagram

The intelligent construction site management platform for the Chongming 500 kV Yangtze River large-span tower construction project is divided into multiple functional modules, including GIS + BIM overview module, construction progress simulation module, personnel positioning module, electronic fence module, warning module, and other customized modules.

The system adopts a service-oriented technical architecture and the idea and technology of information analysis and application based on a three-dimensional spatial information platform for overall architecture design. The overall architecture of the system platform is shown in Fig. 1.

The system is composed of five layers: the basic layer, data layer, platform layer, application layer, and presentation layer.

The basic layer is mainly responsible for system integration with existing systems and data collection. The spatial data component of data collection includes geographic spatial information, 3D modeling of key areas, and architectural drawing organization.

The data layer is designed as a 5D (3D model + 1D time + 1D content) database, which manages all data information by time through a combination of time and space. Different external systems that interface with the system are supported by abstract design and dynamic data storage methods, with spatial and temporal attributes assigned to them.

The platform layer includes spatial data production, spatial data publishing, 3DGIS + BIM spatial data hosting applications, system interface services, search engine services, etc. This layer uses high-resolution satellite remote sensing data, digital elevation model data, electronic map data, and 3D model data that have undergone fusion processing to create a real 3D digital geographic spatial information platform, supported by 3D digital earth engine software.

The application layer develops specific functional modules based on system needs, supported by data collection, 5D database, system platform, and secondary development interfaces. In the first stage of project implementation, the application layer realizes a comprehensive management application based on BIM. In the next stage, the application layer will gradually expand and deepen its applications.

The presentation layer includes large screen displays, PC-side daily applications, mobile-side daily applications, etc., which are constructed according to the specific needs of the system.

3 Smart Site Exception Information Processing and Clustering for Power Engineering Projects

On the basis of the aforementioned architecture design and functional implementation, to achieve standardized and scientific management of information related to the smart construction site of the Chongming 500 kV extra-high voltage crossing project, it is necessary to introduce an instance database and conduct preprocessing of information management by collecting data, screening abnormal information, and clustering information [3]. In this process, a global search method can be used to select and screen abnormal samples from the historical information stored in the database and platform. Fuzzy analysis method can be used to calculate the similarity between different sample information, with the following formula:

$$r = 1 - \sqrt{\frac{1}{m}\sum_{k>1}^{m}\left(S_{ik} - S_{jk}\right)^2} \tag{1}$$

On the basis of the formula (1): r represents the similarity between different samples of intelligent construction site information in power engineering; m represents the completeness of the information; s_{ik} represents the standard value of the k-th item of the i-th template in the database; s_{ik} represents the standard value of the k-th item of the j-th template in the database. Based on this, the similarity matrix between different sample data is constructed, and the matrix expression is as follows:

$$R = \begin{bmatrix} r_{11} & \cdots & r_{1n} \\ \vdots & & \vdots \\ r_{n1} & \cdots & r_{1n} \end{bmatrix} \tag{2}$$

In formula (2) where R is the similarity relationship matrix between different sample data; n is the number of rows or columns in the matrix; r is the data recombination structure. According to Eq. (2), matrix R satisfies a symmetry relationship in the calculation process. Preliminary clustering of sample data can be achieved by transmitting information in R. In this process, it is necessary to evaluate whether matrix R satisfies the transitivity condition of information. $R \times R$ can be calculated and then compared with R^2 to analyze whether $R \times R$ is equal to R^2. If they are equal, it indicates that matrix R satisfies the information transmission condition.

Based on this, clustering processing is performed on the smart construction site information that meets the conditions. In the processing process, a parameter α is

set, and the intercept matrix of R can be represented as $R_{\alpha(i,j)}$. The following formula can be obtained:

$$R_{a(i,j)} = \begin{cases} 1, r_{ij} \geq \alpha \\ 0, r_{ij} < \alpha \end{cases} \tag{3}$$

In the formula (3), r_{ij} is the statistically processed data flow information. According to formula (3), when $r_{ij} \geq \alpha$, the value of $R_{\alpha(i,j)}$ is 1; otherwise, when $r_{ij} < \alpha$, the value of $R_{\alpha(i,j)}$ is 0. With the above method, the processing and clustering of abnormal information in the smart construction site of power engineering can be realized.

4 The Establishment of a Smart Construction Site Risk Information Decision-Making Model Based on the B/S Architecture

Building upon the aforementioned design, the B/S architecture is introduced to develop the risk information decision-making and corresponding information functional modules for smart construction sites. It is necessary to build a management decision-making model based on a browser and server mechanism through the collaboration between the Internet of things and power engineering projects. Assuming that the digital management platform for power engineering satisfies the following conditions: risk neutrality, all data can be regarded as single discrete variables, and the management decision-making model is based on a single-period binomial distribution model [4, 5]. On this basis, considering the flexibility requirements of data management in the platform and the actual situation of power engineering, the risk probability of engineering data is designed, and the calculation formula is as follows:

$$p = \frac{t_1}{t_2} \times (S + f) \tag{4}$$

In the formula (4), p represents the risk probability of engineering data; t_1 is the adjustment time of the data; t_2 is the time node for dynamic changes in the data; S represents the basic input data quantity; f represents the quantity of data added or reduced by the platform.

Based on the different time periods and stages of the electric power project, establish a smart construction site risk information decision-making model:

$$\lambda = \mathrm{e}^{-k}[p \times (\mu c + \delta) + (1 - p) \times (\mu a + \delta)] \tag{5}$$

In the formula (5), λ represents the smart construction site risk information decision-making model; e represents the risk coefficient; μ represents the fluctuation coefficient in the data entry process; c represents the risk increase rate; δ represents

the risk evaluation index; a represents the risk decrease rate. After establishing the decision-making model, the data characteristics of the engineering information can be mined and analyzed, compared with the actual engineering data characteristics; the relationship between the two can be identified, and a digital management-driven model can be established.

5 Comparative Experiment

After completing the above design, in order to test the practical application effect of the developed information management platform, the researchers conducted a comparative experiment. Taking the Yangtze River large-span line project of Shanghai Chongming 500 kV transmission and transformation project as an example, to ensure the stable operation of the platform, the platform operating environment was designed before the experiment, as shown in Table 1; the smart site information under the platform operating environment was counted and divided into different categories. The specific content is shown in Table 2.

On this basis, the platform developed in the article is used to manage smart construction site information according to specifications. During the management process, it is necessary to concentrate on processing abnormal information of smart construction sites for power engineering and cluster data information according to actual management needs. Then establish a connection between the server side

Table 1 Deployment of smart construction site platform operating environment

No	Item	Parameter
1	Operating system	Windows server 2020/64-bit
2	Main tools	OpenCV 3.0/visual studio 2022
3	Operating environment	Parameters Intel(R) Core(TM) i7
4	CPU frequency	3.58 GHz
5	CPU memory	16 GB
6	Hard drive capacity	1 TB

Table 2 Categories of smart construction site information

Information category	Number	Quantity of information/pieces
On-site risk data	A-01	5000
Employee information	A-02	2000
Engineering equipment information	A-03	10,000
Engineering material information	A-04	8000
Other	A-05	25,000

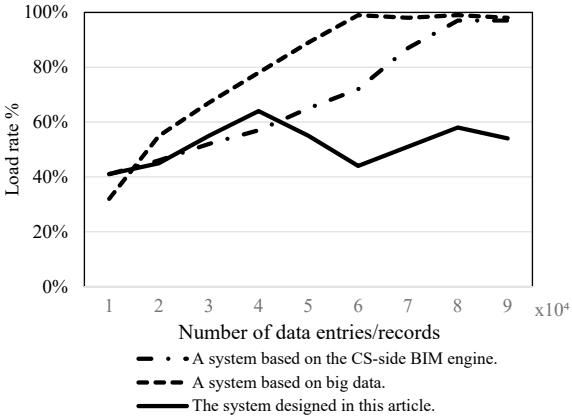

Fig. 2 Platform load rate test results

and the browser side, and implement digital management of information through decision-making on smart construction site risk information.

In order to compare experimental results, a management platform based on CS-end BIM engine technology and a management platform based on big data are introduced as controls [6]. According to specifications, the control group management platform is integrated into the test environment, different data is randomly entered, and the platform backend data is called to calculate the platform load rate during the management process. Generally, as long as the platform does not reach full load during operation (that is, the load rate does not reach 100%), it can manage data normally; once the data volume is large and exceeds the platform load (that is, the platform load rate reaches or exceeds 100%), the platform will experience operational anomalies. Based on this standard, the platform test results are calculated as shown in Fig. 2.

From Fig. 2, it can be seen that the control group platforms reached full load after entering a certain amount of data, while the platform developed in the article had a stable load rate of 40–80% during the management process. The following experimental conclusion can be drawn: Compared with traditional platforms, the management platform based on the B/S architecture GIS + BIM engine designed in this project has good practical application effects, can avoid platform running load problems caused by large amounts of data, and can improve the platform's information management efficiency and comprehensive management level.

6 Conclusion and Outlook

In conclusion, digital and fine-grained construction is an inevitable trend in the management and control of line construction. Currently, it mainly involves the integration of existing achievements. We have made some meaningful new breakthroughs in the pilot application of the Yangtze River crossing project, and some new functions

are still under exploration. The development of low-cost and high-quality supporting technologies such as data collection, transmission, processing, and sharing platforms is needed. Comparative experiments have shown that the platform can improve platform load rate in practical applications and can provide comprehensive technical guidance for the standardized, scientific, and rational development of power enterprises in the market.

References

1. Wang X, Xie M (2022) Integration of 3DGIS and BIM and its application in visual detection of concealed facilities. Geo-spatial Inform Sci 13:1–10
2. Deng Y, Cheng JCP, Anumba C (2016) Mapping between BIM and 3D GIS in different levels of detail using schema mediation and instance comparison. Autom Constr 67:1–21
3. Rodriguez MZ, Comin CH, Casanova D et al (2019) (2019) Clustering algorithms: a comparative approach. PLoS ONE 14(1):e0210236
4. Liu H, Song J, Wang G (2021) A scientometric review of smart construction site in construction engineering and management: analysis and visualization. Sustainability 13(16):8860
5. Wang Y (2022) An improved clustream clustering algorithm for anomaly detection in electric power big data. Eng Intell Syst 30(3):185–193
6. Zhou H, Wang H, Zeng W (2018) Smart construction site in mega construction projects: a case study on island tunneling project of Hong Kong-Zhuhai-Macao bridge. Front Eng 5(1):78–87

Effect of Planar and Cylindrical Coil Structure Parameters on Transmission Efficiency of Magnetic Resonance Wireless Energy Transmission System

Qingyang Chen, Tingrong Zhang, and Yanwen Hu

Abstract The shape and structural parameters of the coil determine the transmission efficiency of the wireless energy transmission system, and it is an important prerequisite to select the best design scheme to clarify the influencing factors of the transmission efficiency of planar and cylindrical coils. This paper compares and analyzes the influence of coil structural parameters on transmission efficiency, such as coil inner radius, coil turns, transmission distance, and coil offset, when the magnetic resonance wireless energy transfer system of cylindrical coil and planar coil is always in a resonant state. Firstly, the Maxwell simulation software is used to calculate the self-inductance and mutual inductance of the coil, and then the compensation capacitor size is determined by HFSS, the resonant frequency of the coil is adjusted to 350 kHz, and finally the transmission efficiency of the wireless energy transmission system is simulated and calculated when the load is 10 Ω. The results show that when the radius in the coil is large and the transmission distance is close, the transmission efficiency of the cylindrical coil is higher than that of the planar coil system. When the inner radius is small or the inner radius is large but the transmission distance is far, the transmission efficiency of the planar coil is higher than that of the cylindrical coil system; cylindrical coil systems are more resistant to deflection than planar coil systems. The results of this paper can provide theoretical support for the design scheme of coil selection.

Keywords Coil shape · Structural parameters · Transfer efficiency

Q. Chen (✉) · T. Zhang · Y. Hu
College of Automation and Electrical Engineering, Lanzhou Jiaotong University, Lanzhou 730070, China
e-mail: 12221565@stu.lzjtu.edu.cn

S. Yadav et al. (eds.), *Energy Power and Automation Engineering*, Lecture Notes in Electrical Engineering 1118, https://doi.org/10.1007/978-981-99-8878-5_81

1 Introduction

For magnetic resonant wireless power transfer (MCR-WPT) technology, transmission efficiency is an eternal topic. In the MCR-WPT system, the shape and parameters of the coil have a direct impact on the transmission efficiency, so the study of the coupling coil is particularly important. When the outer diameter and inductance of the planar spiral coil and the cylindrical spiral coil are the same, the resistance of the former is larger, so the figure of merit of the former is smaller. However, the coupling area of the latter is smaller, which is not conducive to coupling between coils and requires more space [1–3]. In addition, the coupling capacity is best when the inner diameter of the planar spiral coil accounts for about 40% of the outer diameter [4]. The coil radius has a great influence on the transmission distance and transmission efficiency of the coil, and the larger the coil radius, the farther the effective transmission distance, and the higher the transmission efficiency [5–7]. The maximum transmission efficiency generally increases with the increase of the number of turns, but because the optimal value of the coupling coefficient and the optimal value of the quality factor often do not appear at the same number of turns at the same time, but as the number of turns increases, the increase of transmission efficiency will be saturated or even slightly reduced [8]. The quality factor of the coil made of Leeds wire only decreases with the increase of the turn spacing, while the change trend of the coil quality factor of solid wire and tubular conductor is similar to the trend of their coupling coefficient, that is, first rise and then fall, the transmission efficiency will appear a maximum value [9]. In MCR-WPT systems, coil offsets are inevitable, and the offset of transmit coils and receive coils will cause fluctuations in system transmission efficiency and system instability. When the system works in the over coupled state, frequency splitting is prone to occur, and frequency splitting is an important factor that causes system instability and reduced transmission efficiency [10]. The results show that the coupling coefficient is only the main parameter affecting the frequency splitting, not the essential reason, and other parameters may also cause the frequency splitting phenomenon of the WPT system.

Although the study of structural parameters has become relatively common, the comparative analysis of coil systems of different shapes needs further research. In this paper, the two-coil MCR-WPT system is taken as the research object, and the influence of structural parameters such as coil shape, coil offset, coil radius, and turn spacing on transmission efficiency under resonant state is systematically analyzed. Provide theoretical support for coil selection and design.

2 Theoretical Analysis

In this paper, the influence of coil shape and structural parameters on transmission efficiency in a two-coil magnetic resonance wireless power transfer (MCR-WPT) system is studied. Two different shapes, planar coil and cylindrical coil, are considered in the system. The planar coil is shown in Fig. 1, the column coil is shown in Fig. 2, the inner diameter is $r1$, the radius of the litz line is $r2$, the turn spacing is d, the transmission distance is dd, the number of turns of the coil is n, and the coil offset degree is S.

MCR-WPT technology mainly uses the principle of loosely coupled electromagnetic induction to transmit wireless energy through the coupling of magnetic flux inside the magnetic induction coil. Figure 3 shows the MCR-WPT circuit model, which consists mainly of energy transmitting and receiving modules. R_1 and R_2 are the equivalent resistance of the transmitting coil and the receiving coil, R_s is the internal resistance of the power supply, L and C are the equivalent inductance and equivalent capacitance of the coil, respectively, and the system load is regarded as a pure resistive load. I_1 and I_2 are the currents of the primary coil and the secondary coil, respectively, and U_s represents the power supply voltage on the transmitting side. According to Kirchhoff's voltage law:

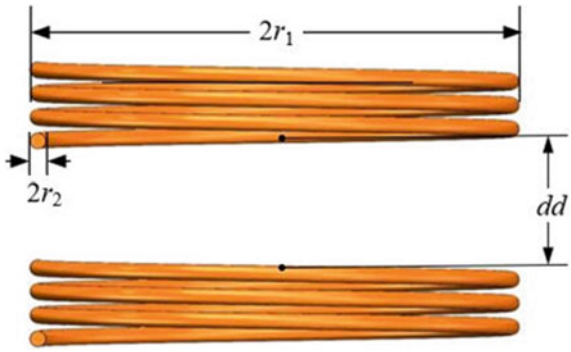

Fig. 1 Cylindrical coil system

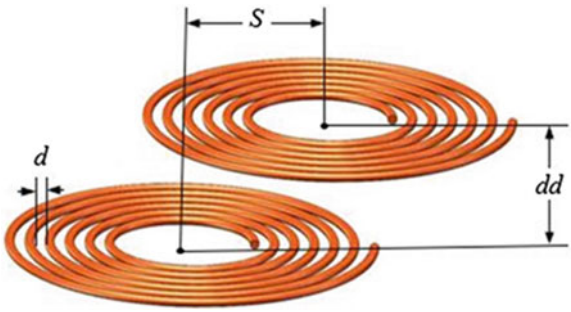

Fig. 2 Planar coil system

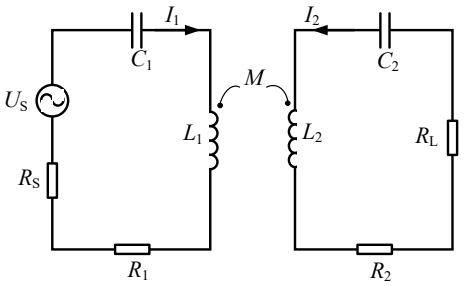

Fig. 3 Magnetic resonant wireless power transfer

$$U_s + j\omega M I_2 = \left(R_S + R_1 + j\omega L_1 + \frac{1}{j\omega C_1}\right) I_1 \tag{1}$$

$$j\omega M I_1 = \left(R_L + R_2 + j\omega L_1 + \frac{1}{j\omega C_1}\right) I_2 \tag{2}$$

When the system is in a resonant state, there are:

$$j\omega L_1 + 1/(j\omega C_1) = j\omega L_2 + 1/(j\omega C_2) = 0 \tag{3}$$

The primary and secondary currents are, respectively:

$$I_1 = \frac{(R_1 + R_2)U_S}{R(R_L + R_2) + (\omega M)^2} \tag{4}$$

$$I_2 = \frac{\omega M U_S}{R_1(R_L + R_2) + (\omega M)^2} \tag{5}$$

The system input power is:

$$P_{\text{in}} = U_S I_1 \cos\theta = \frac{(R_1 + R_2)U_S^2}{R_1(R_L + R_2) + (\omega M)^2} \tag{6}$$

In Eq. (6) is θ the phase angle of current and voltage, when the system is in a resonant state θ. The system output power is:

$$P_{\text{out}} = I_2^2 R_L = \frac{(\omega M U_S)^2 R_L}{\left[R_1(R_L + R_2) + (\omega M)^2\right]^2} \tag{7}$$

Transmission efficiency:

$$\eta = \frac{P_{\text{out}}}{P_{\text{in}}} = \frac{\omega^2 M^2 R_L}{(R_1 + R_2)\left[R_1(R_L + R_2) + (\omega M)^2\right]} \tag{8}$$

It can be seen from the above equation that the parameters affecting the transmission efficiency of the system are mainly angular frequency, coil mutual inductance M, and load $R.L$. In practical applications, the resonant frequency and load are relatively fixed, and the changes of parameters such as coil shape, coil inner diameter, coil turns, transmission distance, and turn spacing of the system have a great impact on the transmission efficiency of the system.

3 The Influence of Coil Shape and Parameters on the Transmission Characteristics of the System

As the core component of electric energy transmission and reception in WPT system, the shape and structural parameters of the coil have a great influence on the self-inductance and mutual inductance of the coil. It can be seen from Eq. (8) that when the load and operating frequency of the WPT system are constant, the mutual inductance between the two coils plays a decisive role in the transmission efficiency, and the factors causing the mutual inductance change mainly include: distance between the two coils, coil shape, coil turns, turn spacing, coil radius, and coil offset degree. Therefore, the influence of the shape and structural parameters of the coil on the transmission efficiency cannot be ignored. Therefore, in this paper, the cylindrical spiral coil and the planar spiral coil are used to analyze the influence of structural parameters on the transmission efficiency at 350 kHz.

4 The Effect of Coil Shape on Self-inductance and Mutual Inductance

In this section, the number of turns of the transmitting side and the receiving side coil is equal $n = 6$ turns; coil inner diameter $r_1 = 70$ mm; the line spacing is $d = 4.7$ mm; multi-stranded litz wire with wire diameter $r_2 = 1.89$ mm; the internal resistance of the coil is $R_1 = R_2 = 0.027(\Omega)$; Maxwell calculates and analyzes the self-inductance and mutual inductance of coils in systems with different coil shapes when the transmission distance changes from 10 to 300 mm.

It can be seen from Fig. 4 that when the transmission distance $dd < 150$ mm, the self-inductance of the plane coil increases rapidly, and when the transmission distance $dd > 150$ mm, the self-inductance growth rate of the planar coil tends to be flat. When the transmission distance $dd < 60$ mm, the self-inductance of the planar coil at the same transmission distance is smaller than that of the cylindrical coil; when $dd > 60$ mm, the self-inductance of the planar coil at the same transmission distance is higher than that of the cylindrical coil. The mutual inductance of planar coils and cylindrical coils gradually decreases with the increase of transmission distance. When the transmission distance is 20 mm $< dd <$ 170 mm, the mutual inductance

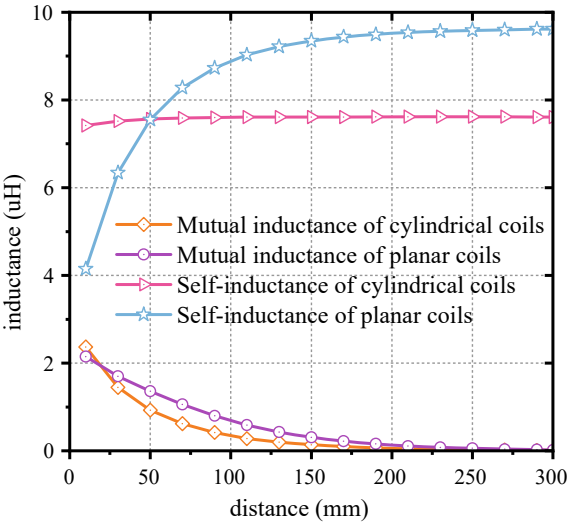

Fig. 4 Self-inductance and mutual inductance change with distance

of the planar coil is higher than that of the cylindrical coil at the same transmission distance. When the transmission distance $dd > 200$ mm, the mutual inductance of the planar coil and the cylindrical coil is basically the same, and the change with the transmission distance is not obvious.

5 The Effect of Distance on Transmission Efficiency

This paper uses $r_1 = 70$ mm; $R_2 = 1.89$; number of turns $n = 6$; turn spacing $d = 4.7$ mm model, transmission distance dd changes from 10 to 300 mm, interval 20 mm take a set of data, and use capacitance compensation method to make the system resonant frequency always 350 kHz. The influence of transmission distance on the transmission efficiency of cylindrical spiral coil system and planar coil spiral system was analyzed.

As shown in Fig. 5, the transmission efficiency of planar coil systems and cylindrical coil systems decreases with the increase of transmission distance. The specific change law is as follows: when the transmission distance $dd = 10$ mm, the transmission efficiency of the cylindrical coil and the planar coil system is equal; when 10 mm $< dd <$ 250 mm, the larger the transmission distance, the lower the transmission efficiency, and the transmission efficiency of the planar spiral coil in this interval is significantly higher than that of the cylindrical spiral coil; when the transmission distance $dd >$ 250 mm, the transmission efficiency of planar coil and cylindrical coil decreases with distance.

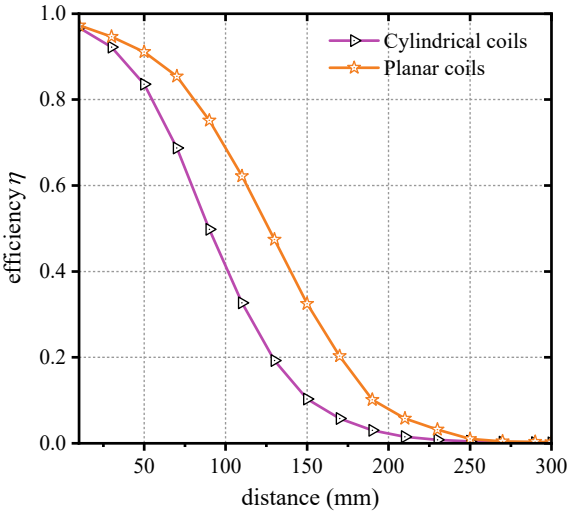

Fig. 5 The effect of distance on transmission efficiency

6 The Effect of the Number of Coil Turns on Transmission Efficiency

In this paper, the MCR-WPT system model of $r_1 = 70$ mm, transmission distance $dd = 100$ mm and $d = 4.7$ mm is used, and a set of data is taken every 3 turns from $n = 6$ to $n = 21$ for cylindrical coils, and $n = 6$, 12, and 18 groups for planar spiral coils to analyze the influence of coil turns on transmission efficiency under resonant state.

As can be seen from Fig. 6, when the number of coil turns $n = 15$, the transmission efficiency reaches the highest, and the number of turns is the optimal number of coil turns. When the transmission distance is 50 mm < dd < 190 mm, the influence of coil turns on transmission efficiency is obvious. For example, when the transmission distance $dd = 190$ mm, when the number of coil turns $n = 6$, the transmission efficiency is 3.03%; When the number of turns of the coil $n = 9$, the transmission efficiency is 80.04%; When the number of coil turns $n = 21$, the transmission efficiency is 71.41%. It can be seen from Fig. 7 that when the transmission distance $dd = 150$ mm, the transmission efficiency of the system increases from 21.34 to 89.38% after the number of coil turns $n = 6$ increases to $n = 18$. It can be seen that within a certain range, the increase in the number of turns of the spiral coil can increase the transmission distance of the system.

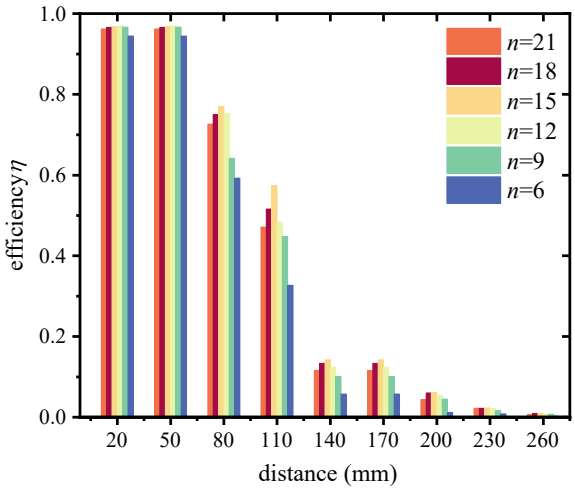

Fig. 6 Effect of the number of turns of cylindrical spiral coil on transmission efficiency

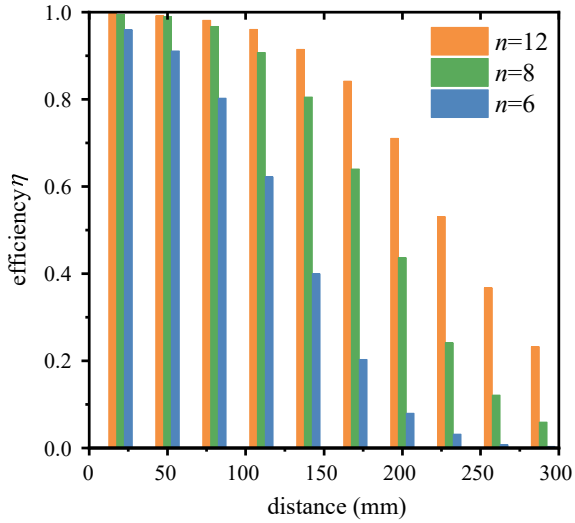

Fig. 7 Effect of the number of turns of planar spiral coil on transmission efficiency

7 The Effect of Coil Offset on Transmission Efficiency

In this section, the coil radius $r_1 = 70$ mm, the transmission distance $dd = 110$ mm, the number of coil turns $n = 6$, the wire diameter $r_2 = 1.89$ mm, and the offset S change from 0 to 100 mm, and the resonant frequency of each point is compensated, and the influence of coil offset on transmission efficiency is analyzed.

It can be seen from Fig. 8 that in the cylindrical spiral coil WPT system, when the offset S of the primary and secondary coils changes from 0 to 100 mm, the transmission efficiency decreases from 41.33 to 9.92%, while the transmission efficiency

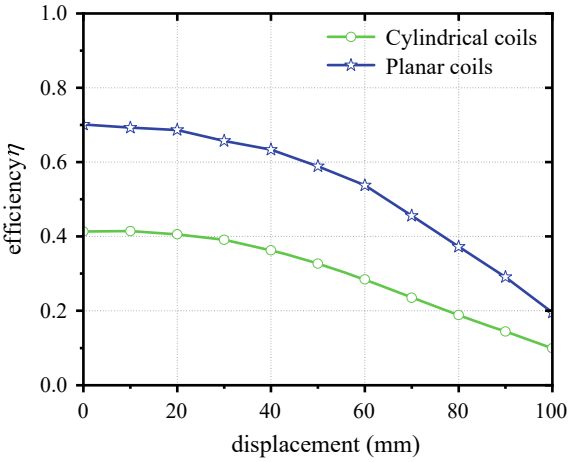

Fig. 8 Effect of coil offset on transmission efficiency

of the planar coil WPT system decreases from 70.12 to 19.53%. With the gradual increase of the offset of the primary and secondary coils, the transmission efficiency gradually decreases. However, under the same degree of offset, the transmission efficiency of the planar coil is much higher than that of the cylindrical coil, and as the coil is offset, the transmission efficiency of the planar coil decreases faster than that of the cylindrical coil. Therefore, the anti-offset characteristics of cylindrical coils are stronger than those of planar coils.

8 The Effect of Coil Radius on Transmission Efficiency

The coil radius is one of the direct factors that affect the transmission efficiency of WPT systems. To this end, Maxwell is used to model the planar coil and cylindrical coil system, respectively, where the number of coil turns $n = 6$ and the transmission distance are 20 mm < dd < 300 mm. Turn spacing $d = 4.7$; primary and secondary coil offset $S = 0$; the coil radius is taken $r_1 = 50$, 70, 90, 110, respectively, and the system is compensated at this point, and the influence of the coil radius on the transmission efficiency is compared and analyzed in the resonant state. The results are shown in Fig. 7.

As shown in Fig. 9, the larger the coil radius of the MCR-WPT system, the higher the transmission efficiency, under the same coil radius, the transmission efficiency of the planar coil system is significantly higher than that of the cylindrical coil system, and the larger the coil radius, the smaller the gap.

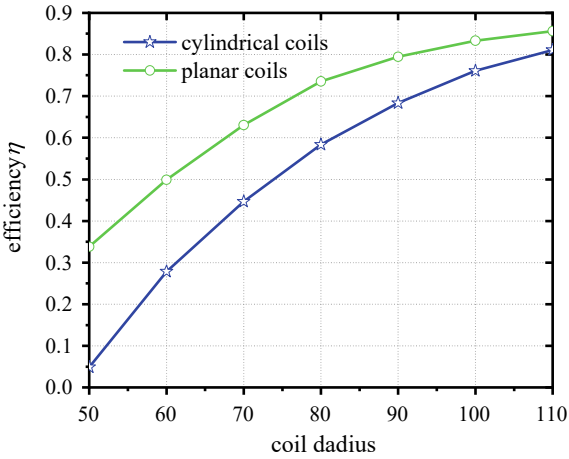

Fig. 9 Effect of coil radius on transmission efficiency

9 Frequency Characteristics

In this paper, the model of coil radius $r_1 = 70$ mm, transmission distance $dd = 20$ mm, and coil offset $S = 0$ is used, and when the number of turns n of the coil changes from 2 to 11, HFSS is used to simulate the plane coil system and the S_{12} of the cylindrical coil system, respectively, and the frequency splitting phenomenon of the system is analyzed, and the results are shown in Figs. 10 and 11.

As shown in Fig. 10, in a planar coil system, the coil has frequency splitting when the coil turns are counted, and the system is in an overcoupled state. When $n > 7$, the frequency splitting phenomenon of the system disappears, and the system is in an undercoupled state. When $n = 7$, the system is in a critically coupled state. As

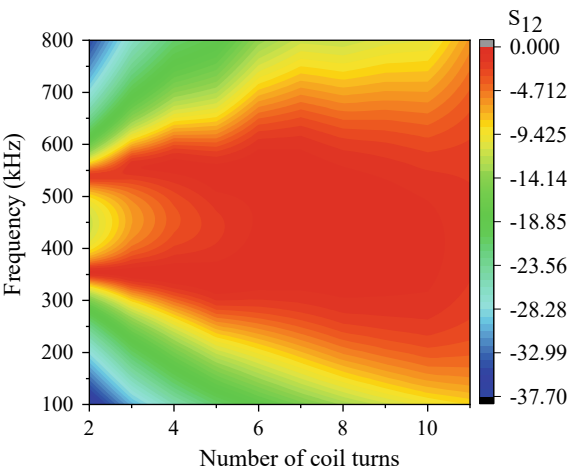

Fig. 10 Effect of the number of turns of the planar coil on frequency splitting

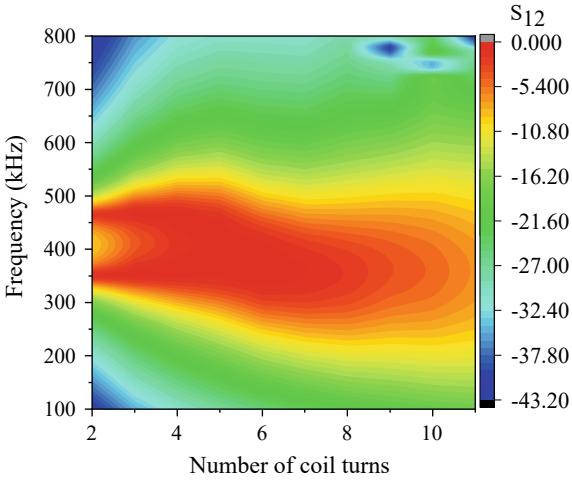

Fig. 11 Effect of the number of turns of the cylindrical coil on frequency splitting

shown in Fig. 11, in a cylindrical coil system, when the coil turns are made, the coil has a frequency splitting phenomenon, and the system is in an overcoupled state. When $n > 6$, the frequency splitting of the system disappears, and the system is in an undercoupled state. When $n = 5$, the system is in a critically coupled state. It can be seen that the more coil turns, the worse the coil coupling state; the fewer the number of turns, the better the coupling state. At the same number of coil turns, the coupling state of the planar coil is better than that of the cylindrical coil system.

10 Conclusion

In this paper, taking the cylindrical spiral coil system and planar spiral coil system as the research object, Maxwell software simulates and analyzes the influence of coil shape and coil parameters on transmission efficiency and coil resonant frequency when the resonant frequency is 350 kHz. It is concluded that when the coil radius is large and the transmission distance is close, the transmission efficiency of the cylindrical coil system is higher than that of the planar coil, and the cylindrical coil system should be selected. When the transmission distance is long or the coil radius is small, the transmission efficiency of the planar coil is higher than that of the cylindrical coil, and the planar coil system should be selected. As the coil offset gradually increases, the transmission efficiency of the bar coil system decreases more slowly than that of the planar coil system, so the anti-offset ability of the cylindrical coil system is stronger than that of the planar coil system.

Acknowledgements This work was supported by the Natural Science Foundation of Gansu Province, China (Grant No. 23JRRA877) and was supported by the Young Scholars Science Foundation of Lanzhou Jiaotong University (Grant No. 1200061169 and No. 1520020821).

References

1. Zhu L, Wang L, Wu X et al (2023) Precise modeling and design of self-resonant helical coils for high-efficiency mid-range wireless power transfer system. IEEE Trans Power Electr 12:1–15. https://doi.org/10.1109/TPEL.2023.3243379
2. Kalina D, Krzysztof G (2022) Wireless power transfer: a review. Energies 15(7236):2–21. https://doi.org/10.3390/en15197236
3. Jung H, Jung S, Young J (2023) Wireless power transfer for variable load, distance, and power division ratio in a loosely-coupled multiple-receiver relay system. IEEE Trans Ind Electr 70(7):6809–6818. https://doi.org/10.1109/TIE.2022.3201302
4. Lan J, Diao Y, Duan X et al (2022) Planar omnidirectional wireless power transfer system based on novel meta-surface. IEEE Trans Electromagn Compat 64(2):551–558. https://doi.org/10.1109/TEMC.2021.3123047
5. Li J, Yu S, Kou N et al (2022) Cylindrical magnetically coupled resonant wireless power transfer system based on flexible PCB coils. IEEE Microw Wireless Compon Lett 32(12):1479–1482. https://doi.org/10.1109/LMWC.2022.3181183
6. Yelzhas Z, Ulrik H, Mehdi A (2023) Single-sided interspiraled inductive impedance matching for magnetic resonance wireless power transfer. IEEE Trans Circ Syst 32:1–12. https://doi.org/10.1109/TCSI.2023.3243924
7. Zeng W, Du G, Yang D et al (2022) Position-independent wireless power transfer system delivering constant power. J Power Electr 22(10):1–12. https://doi.org/10.1007/s43236-022-00478-y
8. Binh D (2022) Power optimization of a magnetoelectric wireless power transfer system with volume constraint. Sens Actuat A Phys 341:3226. https://doi.org/10.1016/j.sna.2021.113226
9. Guo X, Qi Y, Liu L et al (2023) Resonant wireless charging scheme. Energy Rep 9(3):612–621. https://doi.org/10.1016/j.egyr.2022.12.100
10. Ma W, Sun S, Hu Y (2022) Design of a highly integrated wireless power transfer system. Int J RF Microw Comput Aided Eng 32(2):1–9. https://doi.org/10.1016/j.egyr.2022.12.100

Techno-economic Analysis of Supercritical Coal-Fired Power Plant Coupled with Biomass Pyrolysis System

Huiyang Shi, Rui Zhang, and Dong Liu

Abstract An efficient strategy to increase the volume of biomass treatment, reduce coal consumption, and lower carbon dioxide emissions is to co-fire biomass and coal. In this paper, a system model that a 600 MW supercritical coal-fired power plant coupled with biomass fast pyrolysis is established and simulated, using process simulation software. According to the results of process simulation, the energy efficiency, fixed capital investment, internal rate of return, payback period are calculated, which aimed to analyze the thermodynamic and economic performance of the coupling system. The results show that while the coupling technical retrofitting of the system reduces energy efficiency and worsens economic performance, the decrease of energy efficiency is not significant. Additionally, the internal rate of return is higher than the discount rate, and the investment can be returned during the project's life. These findings indicate that the pyrolysis-based co-firing system is technically feasible and economically viable.

Keywords Coupling power generation · Biomass · Pyrolysis · Process simulation

1 Introduction

Due to the low calorific value, harvesting and transportation difficulties, and seasonal fluctuations, biomass power generation in China is mainly based on small-capacity plants, resulting in low efficiency and high costs [1]. In order to solve this issue, a large number of existing coal-fired power plants with high efficiency and complete environmental protection facilities in China can be used to couple with biomass to generate power.

According to the coupling method, there are three types of coal-fired power plant coupling with biomass technology: direct coupling, indirect coupling, and parallel coupling [2, 3]. Direct coupling means that the pretreated biomass is fed into the coal-fired boiler to combust with coal for power generation. In indirect coupling, biomass

H. Shi (✉) · R. Zhang · D. Liu
Nanjing University of Science and Technology, Nanjing 210094, China
e-mail: shihuiyang@njust.edu.cn

S. Yadav et al. (eds.), *Energy Power and Automation Engineering*, Lecture Notes in Electrical Engineering 1118, https://doi.org/10.1007/978-981-99-8878-5_82

is converted into biomass-derived fuels, such as biomass syngas, in a separate furnace from the coal-fired boiler, and then these biomass-derived fuels are passed into the coal-fired boiler to combust with coal. As for parallel coupling, biomass is combusted in the biomass boiler to generate steam, and the steam is fed into the coal-fired boiler for coupling. Direct coupling is the simplest and cheapest coupling method [4]. It requires the least investment and modification, and can be implemented on a large scale with the best cost performance. However, the technology faces some challenges. Firstly, the co-firing can cause slagging and corrosion problems on the surface of heat exchangers [5]. Secondly, the amount of biomass input for co-combustion is constrained by technical and economic constraints. In most cases, the percentage based on input calorific of biomass is around 10% [6]. Finally, the fuel adaptability is poor [7].

In indirect coupling and parallel coupling, the biomass feedstock does not enter the coal-fired boiler directly, thus avoiding the issues associated with direct coupling. However, due to the high investment cost, parallel coupling is less commonly applied. In contrast, gasification-based co-firing is frequently used in indirect coupling, while pyrolysis-based co-firing is less commonly used. Additionally, the characteristics of biomass-derived fuels produced by different thermochemical conversion processes vary and have different influence on the original system's operating performance. Therefore, this paper focuses on investigating the pyrolysis-based co-firing system.

Pyrolysis-based co-firing technology is currently being developed and explored both domestically and internationally. Wornat et al. [8] experimentally found that the existence of alkaline earth metals in the biochar, as well as its porous and disordered carbon structure, contributes to its increased burning reactivity. Kastanaki and Vamvuka [9] concluded that among biochars, lignite coal chars, and hard coal chars, biochars have the highest reactivity. The U.S. Forest Service funded a pilot study at the University of Utah to investigate how well pulverized coal performed when coupled with different forms of wood materials. The results demonstrated that co-combusting with 10% biomass chars causes no operating or feeding problems. Subsequent tests showed that it was also feasible to co-combust with 20% biomass chars. The researchers concluded that biomass chars are a good option for coal-fired power plant coupling with biomass [10]. These findings provide a basis for pyrolysis-based co-firing technology. Kohl et al. [11] conducted simulation to study the feasibility of coupling biomass pyrolysis with a cogeneration system, analyzed the impact of the coupling on the key parameters of the cogeneration plant, and explored different options for the application of pyrolysis oil and pyrolysis char. The results indicated that the coupling was feasible, and the CO_2 emissions of the system decreased. Moreover, it was suggested that pyrolysis oil and pyrolysis char be marketed rather than used internally. Karvonen et al. [12] performed a life cycle evaluation analysis of biomass pyrolysis coupled with combined heat and power (CHP). They found that substituting fossil fuels with bio-oil in CHP system significantly reduced the environmental burden of CO_2 emissions and pollutants. Additionally, the pyrolysis efficiency could be increased by 20%. Chen et al. [13] investigated the co-firing of straw biochar with bituminous coal after different pretreatment using a non-isothermal experiment with a thermogravimetric analyzer. The results showed that the pyrolyzed biochar

exhibited combustion characteristics closer to those of bituminous coal, and the activation energy of the mixture tended to decrease throughout the co-firing process. Additionally, a helpful interplay was observed between the two matters.

In this paper, using Aspen Plus software, a process simulation of the pyrolysis-based co-firing system is conducted, and the thermodynamic and economic performance are analyzed. A typical coal-fired power plant is also modeled and analyzed for comparison's sake. The findings of this paper can be employed as a thorough instruction for designing systems in the future and can provide a techno-economic assessment of the pyrolysis-based co-firing system.

2 Simulation and Analysis Methods

2.1 Description of the System

Figure 1 depicts the flow diagram of the pyrolysis-based co-firing system. The system comprises three units: the fuel conversion unit, which converts the fuel's chemical energy to heat energy; the heat transfer and steam turbine unit, which generates power from the heat energy; and flue gas treatment unit, which removes pollutants. The main equipment in the fuel conversion unit comprises a fluidized bed pyrolysis reactor and a coal-fired boiler. The low energy density biomass is pretreated and introduced into the pyrolysis reactor at about 500 °C, where it undergoes thermochemical decomposition in an oxygen-free atmosphere environment, resulting in the production of bio-oil, biochar, and non-condensable gas. In this paper, the biochar obtained from biomass pyrolysis is used to return to the farmland. Additionally, a fraction of the non-condensable gas is recirculated to the pyrolysis reactor as circulating gas, while the remaining non-condensable gas and bio-oil are burned together with coal in the coal-fired boiler at about 1500 °C. The high-temperature flue gas generated during fuel combustion is utilized for heat exchange with circulating water and air, which makes the circulating water be saturated, evaporated and superheated, the temperature of air increased. The steam, which has been heated to a temperature of 566 °C and pressurized to 22.4 MPa, is directed through the high-pressure (HP) turbine, while the reheated steam at the same temperature and 3.85 MPa is directed through the intermediate-pressure (IP) turbine. And the steam from the IP turbine flows into the low-pressure (LP) turbine, where it is further expanded, before finally entering the condenser. Following heat transfer, the flue gas undergoes denitrification, dust removal, desulfurization, and is eventually discharged into the atmosphere via the chimney.

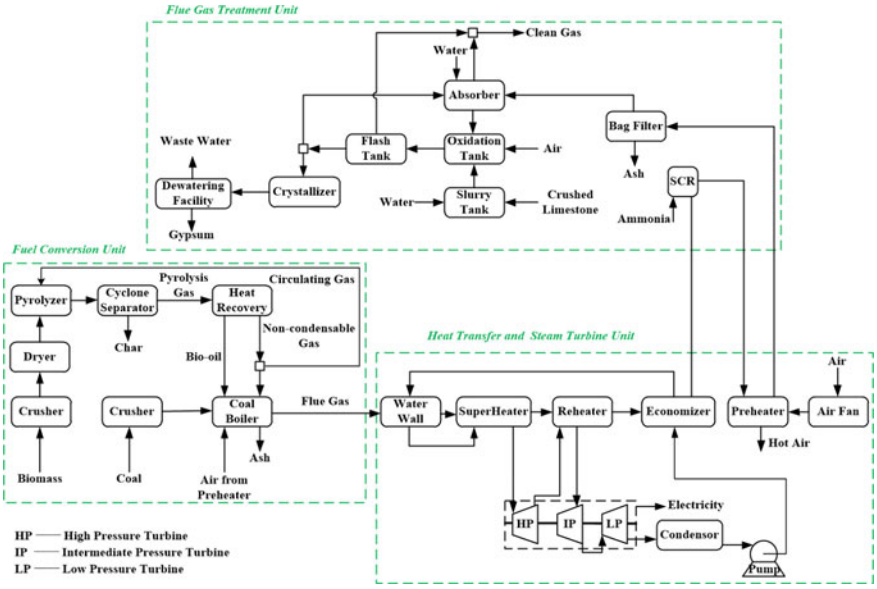

Fig. 1 Flow diagram of the pyrolysis-based co-firing system

2.2 Process Simulation

Figure 2 presents the process simulation of the pyrolysis-based co-firing system. The coal and biomass grinding processes in the fuel conversion unit are simulated by Crusher model. The biomass needs to be dried after grinding since the water content of the biomass entering the pyrolysis reactor is high, which could lead to a reduction in the output of bio-oil. The dryer is simulated using the RStoic and Flash2 models. The dried biomass is then fed into the fluidized bed pyrolysis reactor that is simulated by the RYield reactor. The pyrolytic product yield distributions used in this paper are derived from literature [14]. The gas–solid products are separated by a cyclone, which is simulated by the Cyclone model. The remaining pyrolysis gas is cooled in a Heater model and then passes through a gas–liquid separator simulated by the Flash2 model to separate bio-oil from non-condensable gas. A portion of the non-condensable gas is separated by the Fsplit model and returned to the pyrolysis reactor as circulating gas, while the remaining non-condensable gas and bio-oil enter the coal-fired boiler for combustion. The RYield reactor, Sep model, and RGibbs reactor are selected to simulate the coal-fired boiler. The SOLIDS property method is adopted in simulation of coal and biomass crushers. As the biomass pyrolysis process involves liquid–liquid equilibrium and the bio-oil component is complex, the pyrolysis process is simulated using the NRTL property method. The coal-fired boiler is simulated using the PR-BM property method. Table 1 provides the features of both the coal and biomass used in the simulation.

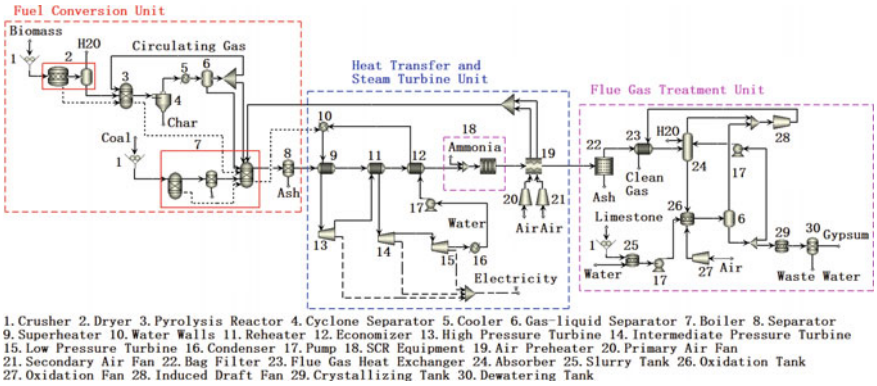

Fig. 2 Process simulation of the pyrolysis-based co-firing power generation system

Table 1 Features of fuels (received basis)

Fuels	Proximate analysis (wt.%)				Ultimate analysis (wt.%)					$Q_{net,ar}$ (kJ/kg)
	M_{ar}	V_{ar}	FC_{ar}	A_{ar}	C_{ar}	H_{ar}	O_{ar}	N_{ar}	S_{ar}	
Coal	7.99	32.68	50.07	9.26	67.77	4.15	8.90	1.01	1.73	26,431.00
Biomass	25.00	56.33	14.00	4.67	33.24	4.30	32.10	0.59	0.10	14,782.50

In the simulation of the heat transfer and steam turbine unit, several models are adopted. The Heatx model is adopted for the simulation of the superheater, reheater, and economizer, while the Mheatx model is chosen for the simulation of the air preheater. The Heater model is used to simulate the water walls and condenser. The Pump model is used to simulate the water pump. The Compr model is used to simulate the fans and steam turbines, the difference is that the fans adopt Compressor model to simulate the process of conveying and compressing air and calculate the power required for the fans to work. The Turbine model is adopted to simulate the expansion of steam and calculate the amount of work done. For the selection of property methods, PR-BM is chosen for the simulation of flue gas side and STEAMNBS is chosen for the simulation of the steam side.

The flue gas treatment unit comprises SCR equipment, bag filter equipment, and FGD equipment. The Mixer and Rplug models are used to simulate the SCR equipment, with the NRTL property method adopted. The ESP model is adopted to simulate the bag filter equipment, and the PR-BM is adopted for calculation of the physical parameters. Several models are adopted to simulate the desulfurization process. Firstly, the ball mill is simulated using the Crusher model, with a limestone outlet size of 45 μm. Subsequently, the limestone slurry tank, oxidation tank, and crystallization tank are modeled adopting the RStoic reactor, with the reactors defined as adiabatic. The absorber is simulated using the RadFrac model, without the condenser and reboiler setting. The Pump model is adopted to simulate the limestone slurry pump and circulating slurry pump, while the Compr model is adopted to simulate

the oxidation fan. The flash tank, which separates surplus nitrogen and oxygen in the air, is simulated by the Flash2 model. The dewatering tank is simulated using the Sep model to separate the gypsum from the waste water. Finally, the Heatx model is adopted to simulate the flue gas heat exchanger, which facilitates heat exchange of flue gas before and after desulfurization. In the simulation, the SOLIDS property method is applied to the ball mill, while the flue gas heat exchanger is modeled using the PR-BM property method. The remaining models are simulated using the ELECNRTL property method.

2.3 Analysis Methods

Energy Efficiency

Energy efficiency is a crucial metric for estimating how much energy is being used in a system. For the pyrolysis-based co-firing system, the energy efficiency can be calculated as

$$\eta = \frac{W_{\text{electricity}}}{R_{\text{coal}} Q_{\text{coal}} + R_{\text{biomass}} Q_{\text{biomass}}} \tag{1}$$

where η denotes the system's energy efficiency (%), $W_{\text{electricity}}$ denotes the net power production (MW), R_{coal} and R_{biomass} denote the quantity of the two fuels being supplied per second, respectively (kg/s), Q_{coal} and Q_{biomass} are the calorific heat of the two fuels, respectively (MJ/kg).

Economic Analysis

The economic analysis of the pyrolysis-based co-firing system includes the calculation of several key indicators, including the fixed and total capital investments (FCI and TCI), internal rate of return (IRR), and discounted payback period (DPP). The FCI can be calculated as [15]

$$\text{FCI} = \sum_{k=0}^{m} C_k = \sum_{k=0}^{m} \left[C_{r,k} \times A_k \times \text{IF}_k \times \left(\frac{S_k}{S_{r,k}} \right)^{b_k} \times E_k \right] \tag{2}$$

where C_k and $C_{r,k}$ are the capital investments of equipment k at the existing scale and reference scale, respectively; A_k is the domestic manufacturing factor. Since the price of equipment in China is much lower than the price in Europe and the United States, if the equipment is from abroad, the correction needs to be made using the domestic manufacturing factor, and A_k takes 0.65, or A_k takes 1 [16]. IF_k, S_k, $S_{r,k}$, and b_k are the installation factor, the existing scale, the reference scale, and the scale factor, respectively. m and E_k are the amount of equipment and economic factor, respectively. Table 2 lists the fundamental information needed to calculate FCI.

Table 2 Initial cost of equipment

Items	$S_{r,k}$	Scale unit	$I_{r,k}/(10^3\$)$	IF_k	b_k	A_k	Year
Biomass preparation [17]	65	t/h	61,774	1.52	0.77	0.65	2008
Coal preparation [17]	273	t/h	15,067	1.67	0.65	0.65	2008
Pyrolysis reactor [16]	1196.91	GJ/h, input	27,864	1.00	0.70	1.00	2011
Boiler [18]	600	MW	89,940	1.00	0.70	1.00	2011
Steam turbines [18]	275	MW	66,700	1.16	0.65	0.65	2007
Pump [16]	250	m^3/h	20	1.995	0.65	0.65	2007
Fans [19]	496.70	m^3/s	91	1.034	0.70	1.00	2010
SCR equipment [18]	2234	NO_x, kg/h	31,810	1.00	0.65	1.00	2015
Bag dust filter [19]	400	MW	4710	1.00	0.65	1.00	2001
FGD equipment [18]	5731.69	SO_2, kg/h	15,948	1.00	0.65	1.00	2004

In addition to calculating FCI, the TCI is also determined, which includes the FCI, the expense associated with process and project contingency (PSC and PJC), and the service fee for the engineering, procurement, and construction contractors (EPC).

The IRR is a measure that is utilized to assess the financial viability of a system, and it can be calculated as

$$\sum_{i=0}^{n} C_i(1+\mathrm{IRR})^{-i} = 0 \tag{3}$$

$$C_i = C_P - \mathrm{FCI} \times (\mathrm{CRF} \times (1+\alpha) + O\&M) - C_F - C_M \tag{4}$$

$$\mathrm{CRF} = \frac{j}{1-(1+j)^{-n}} \tag{5}$$

where n represents the expected lifespan of the plant, C_i represents the annual cash flow, C_P, C_F, and C_M represent the annual revenue from product sales, cost of fuels, and cost of materials, respectively, O&M is the ratio of the annual running and

maintenance expense to the FCI, α denotes the interest rate during construction; CRF is the ratio of annual average investment and j is the discount rate [16].

By accounting for the discount rate over the system's lifetime, the DPP is employed to determine how long it will take for a project to pay for itself. It can be calculated as

$$\mathrm{DPP} = A + \frac{\sum_{i=0}^{A} B_i (1+j)^{-i}}{C} \tag{6}$$

where A represents the last year in which the accumulated cash flow is negative; B_i denotes the net cash flow for year i; and C denotes the annual net cash flow for the year following A.

3 Results and Discussion

3.1 Energy Efficiency

The energy balance results of the pyrolysis-based co-firing system are given in Table 3. When the coal-fired power plant is not modified, the system's net power generation is 567.96 MW, with an energy efficiency of 38.68%.

Table 3 Energy balance of the systems

Items	Unit	Coal-fired power plant	Pyrolysis-based co-firing
Input energy			
Coal input	MW	1468.39	1321.55
Biomass input	MW	0.00	146.84
Output energy			
Turbines	MW	586.29	575.90
Energy consumption			
Crushers	MW	3.13	3.90
Fans	MW	5.06	4.91
Pumps	MW	9.78	9.60
SCR	MW	0.01	0.01
ESP	MW	0.17	0.17
FGD	MW	0.18	0.16
Total			
Net power generation	MW	567.96	557.15
Energy efficiency	%	38.68	37.94

However, after technical retrofitting is implemented, the net power generation and energy efficiency of the system decrease. This is due to the fact that the biochar produced by biomass pyrolysis did not participate in combustion, and the bio-oil has high oxygen and water content, which reduces the heat input from the fuels to the boiler. Additionally, the system's water circulation flow rate is decreased to maintain a constant flue gas temperature at the air preheater's outlet. As a result, less steam is generated through heat exchange, resulting in less work done by the turbines. Moreover, due to the low energy density of biomass, the crushers of the system need to grind more fuels, compared to the original system. Additionally, biomass is more challenging to grind than coal, leading to an increase in energy consumption for the crushers. The bio-oil and non-condensable gas coupling with coal reduces the required air for fuels combustion, leading to a decrease in the energy consumption of fans. And the energy consumption of the pumps is reduced due to the reduction of circulating water. The energy consumption of the flue gas treatment unit is almost unchanged. The internal energy consumption of the pyrolysis-based co-firing system increased by 0.42 MW.

Compared to the coal-fired power plant, the net power generation of the pyrolysis-based co-firing system decreased by 10.81 MW and the energy efficiency decreased by 0.74%. The decrease in energy efficiency is not significant, indicating that the pyrolysis-based co-firing system is technically feasible.

3.2 Economic Analysis

The fundamental economic analysis comprises the evaluation of FCI, IRR, and DPP, and the assumptions regarding basic economic data are provided in Table 4.

The results of the economic analysis of the systems are presented in Table 5. Compared to the original system, the pyrolysis-based co-firing system requires additional investment of biomass pretreatment equipment and pyrolysis reactors, while the investment of coal pretreatment equipment, steam turbines, SCR equipment, FGD equipment, pumps, and fans decreases. This is attributable to the reduction

Table 4 Energy balance of the systems

Price	Value	Items	Value
Coal ($/t)	77.414	Construction period (year) [20]	3
Biomass ($/t)	36.912	Plant lifetime (year) [20]	30
Water ($/t)	0.310	Facility available hours per year (h)	7000
Ammonia ($/t)	461.400	Discount rate (%) [20]	8
Limestone ($/t)	25.377	Overall interest rate during construction (%) [20]	4.9
Electricity ($/t)	0.056	O&M (%) [20]	4
Gypsum ($/t)	9.228		

in the amount of coal and air required for the system, resulting from the non-condensable gas and bio-oil produced by biomass pyrolysis coupling with coal, leading to decreased investment in coal pretreatment equipment and fans. At the same time, the amount of circulating water in the system decreases, which makes the amount of steam decreases, resulting in decreased investment in coal pretreatment equipment and fans. In addition, the low nitrogen and sulfur content in biomass result in reduced NO_x and SO_2 content in the flue gas, leading to decreased investment in flue gas treatment equipment. However, these reductions in investment are not significant enough to offset the increase in fixed capital investment of the pyrolysis-based co-firing system. The FCI rises from 312,903.88 $\times$ 10^3 \$ to 332,910.59 $\times$ 10^3 \$, resulting in a 20,006.71 $\times$ 10^3 \$ increase; the TCI rises from 388,626.62 $\times$ 10^3 \$ to 464,624.35 $\times$ 10^3 \$, a 75,997.73 $\times$ 10^3 \$ increase. These findings suggest that establishing a pyrolysis-based co-firing system within an existing coal-fired power plant would not be overly expensive. But the annual profit of the pyrolysis-based co-firing system is lower than that of coal-fired power plant. Furthermore, the IRR of the system decreases by 8.33%, from 25.97 to 17.64%, the DPP of the system prolongs by 2.13 years, from 9.38 to 11.51 years. It can also be seen that the IRR value of the pyrolysis-based co-firing system is higher than discount rate, indicating that the system is economically feasible.

4 Conclusions

In this paper, a novel co-firing system that couples coal-fired power plant with biomass pyrolysis is presented, which is simulated using Aspen Plus software. Based on the results of the simulation, the thermodynamic and economic performances of the pyrolysis-based co-firing system are contrasted with those of the coal-fired power plant. It is found that the pyrolysis-based co-firing system exhibits lower energy efficiency, higher FCI and TCI investments. As a result, the thermodynamic and economic performances of the pyrolysis-based co-firing system are slightly worse than those of the original system. Compared with the original coal-fired power plant, the net power generation and energy efficiency of the pyrolysis-based co-firing system show little decrease, the IRR is higher than the discount rate, and the DPP only prolongs by 2.13 years.

Table 5 Economic analysis of the systems

Items	Unit	Coal-fired power plant	Pyrolysis-based co-firing
Capital investment			
Biomass preparation	10^3 $	0.00	10,424.49
Coal preparation	10^3 $	60,728.94	56,709.17
Pyrolysis reactor	10^3 $	0.00	17,127.47
Boiler	10^3 $	63,673.28	63,673.28
Steam turbines	10^3 $	101,404.16	100,196.60
Pumps	10^3 $	89.01	87.98
Fans	10^3 $	108.13	105.74
SCR equipment	10^3 $	51,281.66	50,554.82
Bag dust filter	10^3 $	9917.90	9917.90
FGD equipment	10^3 $	25,700.80	24,113.14
FCI	10^3 $	312,903.88	332,910.59
EPC	10^3 $	25,032.31	26,632.85
PSC	10^3 $	0.00	44,477.74
PJC	10^3 $	50,690.43	60,603.18
TCI	10^3 $	388,626.62	464,624.35
Summary			
Fuel and material costs	10^3 $/year	119,956.98	117,974.41
Product sales	10^3 $/year	223,828.37	219,479.84
Annual profit	10^3 $/year	91,046.61	87,911.23
IRR	%	25.97	17.64
DPP	Year	9.38	11.51

Acknowledgements This work was supported by the National Key R&D Program of China (2020YFC1910000).

References

1. Guo H, Cui J, Li J (2022) Biomass power generation in China: status, policies and recommendations. Energy Rep 8:687–696
2. Aviso KB, Sy CL, Tan RR, Ubando AT (2020) Fuzzy optimization of carbon management networks based on direct and indirect biomass co-firing. Renew Sust Energ Rev 132:110035
3. Karampinis E, Grammelis P, Agraniotis M, Violidakis I, Kakaras E (2014) Co-firing of biomass with coal in thermal power plants: technology schemes, impacts, and future perspectives. Wires Energy Environ 3:384–399
4. Xu Y, Yang K, Zhou J, Zhao G (2020) Coal-biomass co-firing power generation technology: current status, challenges and policy implications. Sustain 12:3692

5. Madanayake BN, Gan S, Eastwick C, Ng HK (2017) Biomass as an energy source in coal co-firing and its feasibility enhancement via pre-treatment techniques. Fuel Process Technol 159:287–305
6. Loha C, Chattopadhyay H, Chatterjee PK, Majumdar G (2020) Co-firing of biomass to reduce CO_2 emission. Encycl Renew Sust Mater 3:385–394
7. Roni MS, Chowdhury S, Mamun S, Marufuzzaman M, Lein W, Johnson S (2017) Biomass co-firing technology with policies, challenges, and opportunities: a global review. Renew Sustain Energy Rev 78:1089–1101
8. Wornat MJ, Hurt RH, Yang NYC, Headley TJ (1995) Structural and compositional transformations of biomass chars during combustion. Combust Flame 100:131–143
9. Kastanaki E, Vamvuka D (2006) A comparative reactivity and kinetic study on the combustion of coal-biomass char blends. Fuel 85:1186–1193
10. Eddings EG, Mcavoy D, Coates RL (2017) Co-firing of pulverized coal with Pinion Pine/ Juniper wood in raw, torrefied and pyrolyzed forms. Fuel Process Technol 161:273–282
11. Kohl T, Laukkanen TP, Jarvinen MP (2014) Integration of biomass fast pyrolysis and precedent feedstock steam drying with a municipal combined heat and power plant. Biomass Bioenergy 71:413–430
12. Karvonen J, Kunttu J, Suominen T, Kangas K, Leskinen P, Judl J (2018) Integrating fast pyrolysis reactor with combined heat and power plant improves environmental and energy efficiency in bio-oil production. J Clean Prod 183:143–152
13. Chen L, Wen C, Wang W, Liu T, Liu E, Liu H, Li Z (2020) Combustion behaviour of biochars thermally pretreated via torrefaction, slow pyrolysis, or hydrothermal carbonisation and co-fired with pulverised coal. Renew Energ 161:867–877
14. Heng L, Xiao R, Zhang H (2018) Life cycle assessment of hydrogen production via iron-based chemical-looping process using non-aqueous phase bio-oil as fuel. Int J Greenh Gas Control 76:78–84
15. Zhang R, Chen Y, Lei K, Ye B, Cao J, Liu D (2018) Thermodynamic and economic analyses of a novel coal pyrolysis-gasification-combustion staged conversion utilization polygeneration system. Asia-Pac J Chem Eng 13:e2171
16. Guo Z, Wang Q, Fang M, Luo Z, Cen K (2014) Thermodynamic and economic analysis of polygeneration system integrating atmospheric pressure coal pyrolysis technology with circulating fluidized bed power plant. Appl Energ 113:1301–1314
17. Meerman JC, Ramírez A, Turkenburg WC, Faaij APC (2012) Performance of simulated flexible integrated gasification polygeneration facilities, Part B: economic evaluation. Renew Sust Energ Rev 16:6083–6102
18. Ye B, Zhang R, Cao J, Shi B, Zhou X, Liu D (2020) Thermodynamic and economic analyses of a coal and biomass indirect coupling power generation system. Front Energy 14:590–606
19. Ye B (2020) Process simulation and comprehensive evaluation of a coal and waste coupling incineration system based on circualting flue gas. Nanjing University of Science and Technology, Nanjing
20. Ye B, Shi B, Shi M, Zhang L, Zhang R (2021) Process simulation and comprehensive evaluation of a system of coal power plant coupled with waste incineration. Waste Manag Res 39:828–840

Research and Development of Mobile Unlocking System Based on IoT for Intelligent Substation

Xiong Pan, Jie Wang, Yanan Zhang, Jian Fu, Peng Wu, Kaitao Huang, Zhaoxiao Wu, and Hong Wen

Abstract The effective management of five prevention intelligent keys is vital for the smooth operation of intelligent substations. Addressing the issue of lax key management in substations, this paper proposes a mobile unlocking management system for smart substations based on IoT technology. The system employs a station-side five prevention host, QR codes, and a mobile app to enable remote management and security control of intelligent keys. Leveraging smartphones as mobile carriers, the system grants authorization through RFID technology and QR code scanning. It records information such as the applicant, authorized personnel, time, and reason for access via a cloud server. Moreover, the system offers operation record tracking and traceability functions and can monitor key usage as well as unlocking information in real time. Test results from substations in Guangdong demonstrate that our system effectively controls key access, contributing to the enhanced digitization and intelligence of intelligent substations.

Keywords IoT technology · Substation · Intelligent unlocking · Mobile APP · Remote authorization

1 Introduction

With the continuous improvement of information technology and intelligent operation and maintenance levels in substations, the intelligent unlocking system is gradually replacing the traditional mechanical locking system, providing important support for the five prevention management [1, 2]. The intelligent unlocking system consists of an intelligent unlocking host and unlocking keys. During operation, the five prevention host sends instructions to the unlocking key, and the operator then

X. Pan · J. Wang · Y. Zhang · J. Fu · P. Wu · K. Huang
Guangzhou Power Supply Bureau of Guangdong Power Grid Co., Ltd, Guangzhou, China

Z. Wu (✉) · H. Wen
State Key Laboratory of Power Transmission Equipment & System Security and New Technology, Chongqing University), Chongqing, China
e-mail: 1225459782@qq.com

S. Yadav et al. (eds.), *Energy Power and Automation Engineering*, Lecture Notes in Electrical Engineering 1118, https://doi.org/10.1007/978-981-99-8878-5_83

uses the unlocking key to unlock the designated lock. In addition, the system is also equipped with a universal unlocking key (emergency key), which can unlock all locks in emergencies without affecting normal switching operations. However, since the unlocking key cannot perform logical judgment and does not have any anti-mistake measures, there may be issues during use such as loose key control and casual unlocking, leading to operational accidents [3, 4].

The "Safety Management Regulations for Preventing Electrical Misoperation" issued by State Grid Corporation of China also made clear regulations on the management of unlocking keys. In detail, the authorization password of the anti-mistake device and the unlocking tool (key) should be sealed with a dedicated device. The dedicated device should have an informationized authorization method. The emergency key or unlocking tools (keys) that can unlock all sets of passwords should not be used. In sum, it is required to use the method of "selecting authorized unlocking range" for unlocking. Therefore, there is an urgent need for technical means to meet the above requirements [5, 6].

To address this, this paper developed an intelligent mobile unlocking system for substations. The system is based on the Internet of Things (IoT) technology, connecting the intelligent unlocking host, unlocking keys, and APPs. This system can real time collect and upload the usage of keys and achieve online connections between unlocking keys, APPs as well as cloud servers. By using Radio Frequency Identification (RFID) technology and QR code technology in conjunction, management personnel can remotely authorize the operator's mobile terminal at the control center station, allowing the operator to open the lock of the designated device, ultimately achieving effective control over the unlocking key.

2 System Design

2.1 System Architecture

The intelligent mobile unlocking system for substations employs IoT technology, the Qt ARM Graphics library, and System on Chip (SoC) microchips [7]. The client and server communicate via Restful Http using remote Thrift calls, achieving the informatization, standardization, and intelligence of key management, effectively preventing key abuse.

The system is designed with a layered architecture, making it scalable. The three layers include the data layer, the function layer, and the application layer. The data layer utilizes various object-relational mapping frameworks, such as Dapper, NHibernate, and EF, to enhance data access efficiency. The function layer mainly controls the system's operational processes. The application layer includes the software interface for human–machine interaction and application protocols. As shown in Fig. 1, each layer has specific functions. There is a separation between components in each

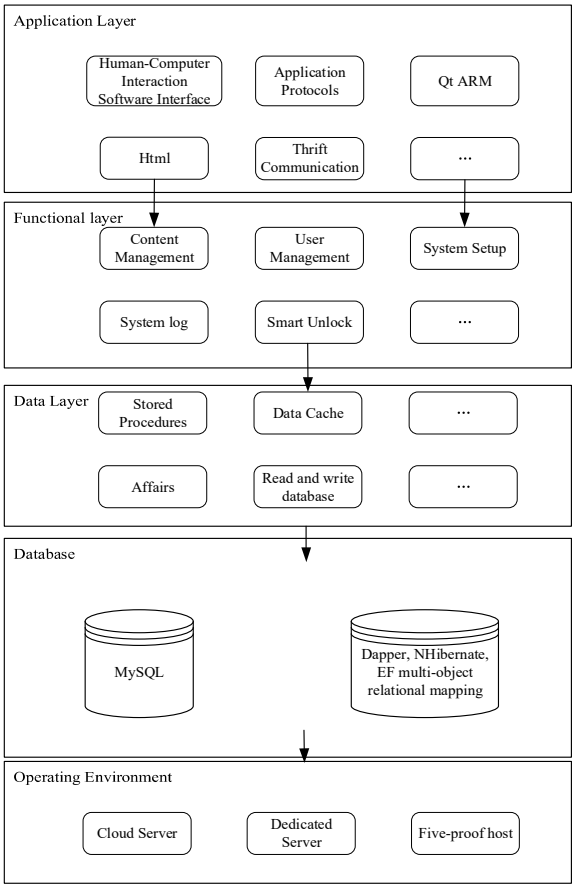

Fig. 1 System layered architecture design

layer, and the components in the layer will only handle the logic of its layer, forming a closed system.

2.2 System Architecture

The intelligent substation mobile unlocking system consists of a mobile unlocking system and a key management system. The mobile unlocking system is composed of a cloud server, an intelligent unlocking host, an intelligent unlocking key, an emergency unlocking key, an application app, and an audit app, as shown in Fig. 2. The cloud server is responsible for running the background services and providing data support for remote applications. The intelligent unlocking host, intelligent unlocking key, and universal unlocking key are deployed at the station for convenient use by maintenance personnel. The application app and audit app are installed by operation and

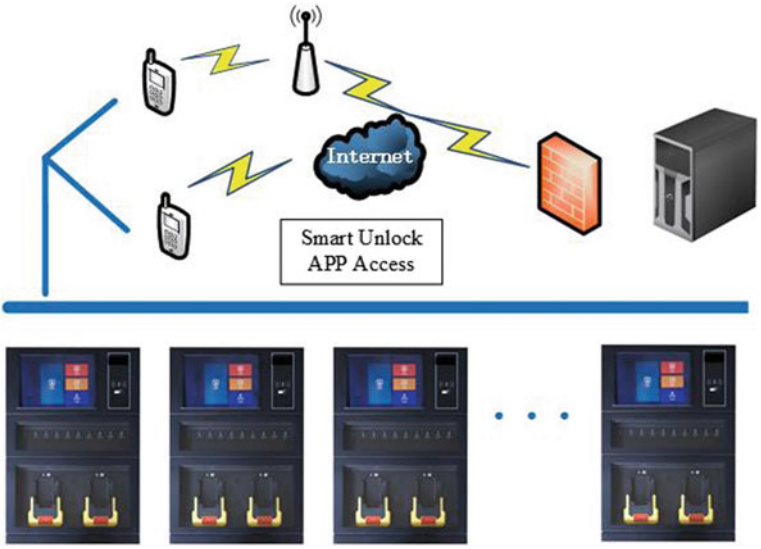

Fig. 2 Structure diagram of intelligent unlocking system

management personnel. Applicants can apply for unlocking through QR codes and dynamic codes. After that, management personnel can authorize remotely through the audit app, thereby achieving functions such as targeted unlocking, emergency unlocking, and management monitoring.

The system management includes a cloud service management system and an audit app. The cloud service management system is a public end for unlocking authorization services, connecting the application app and the audit app. In addition, the cloud records information such as the applicant, auditor, time, and reason. The audit app is used to receive authorization requests submitted by applicants, authorize eligible requests, and view task execution records authorized by the user.

2.3 Unlocking Technology Based on RFID and QR Code Technology

The key management system combines RFID technology [8–10] and QR code technology [11]. The system uses RFID technology to identify and locate keys. It also uses QR code technology to ensure key security and traceability. The system architecture can be divided into three parts: front-end, back-end, and database. The front-end is developed using HTML5, CSS3, JavaScript, and other technologies to realize web-side applications and support users to access the system through browsers. The back-end is developed using Java language, and the Spring Boot framework is used to build the back-end application program to implement the system's business logic

processing. The database uses MySQL to store the data required by the system, including key information, user information, operation logs, etc.

As shown in Fig. 3, the key management system includes four functional modules: key management, user management, log management, and statistical reports. The key management module uses RFID technology to identify and locate keys. It also uses QR code technology to ensure key security and traceability. Administrators can allocate, borrow, and return keys through the system, and then monitor and manage the usage status of keys in real time. In the user management module, administrators can manage and authorize users, and set user permissions and roles to realize the security control of the system. The log management module can record user operation logs and key usage records, which facilitates administrators to view and trace the system's operation history. The statistical report module can generate various statistical reports, such as key borrowing and returning status and user operation status providing data support and a decision-making basis for administrators.

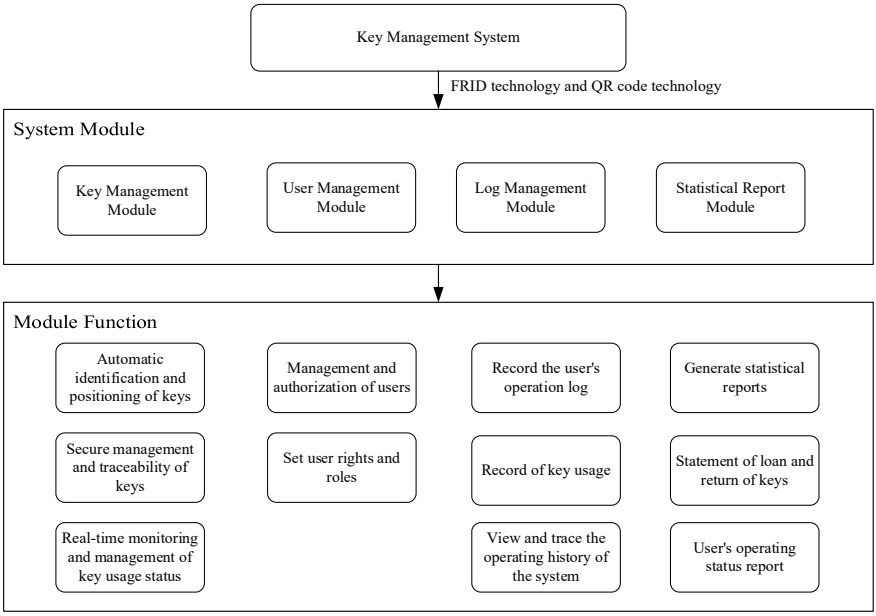

Fig. 3 Key management system module and functional structure

3 System Operation Flow

3.1 Directional Unlocking

When unlocking the five prevention devices in the mobile unlocking system, users can quickly select the scope of authorized devices by clicking on the device list displayed in a tree-like structure on the intelligent unlock host software interface. After confirmation, the system software interface will automatically generate a QR code or dynamic code, as shown in Fig. 4.

Applicants can scan the QR code or enter the dynamic code through the application APP to obtain the application information, access the cloud server via the mobile network, and push the authorization application to the designated account with authorization approval. Authorization personnel can view the application tasks (including the substation, the reason for the application, the applicant, the application time, and the range of the applied devices) and respond to the approval request. The authorization code can only be generated in the applicant's mobile APP after all authorized personnel agree. After the applicant enters the authorization code in the designated box, the system automatically issues an operation task to the intelligent key for the applicant to unlock. If one or more authorized personnel disagree, the applicant can check the dissenting persons and reasons in the APP.

After unlocking is completed, the applicant puts the intelligent key back on the key charging dock and performs the feedback operation. The system automatically generates a feedback QR code when the applicant scans the generated report information through the application APP and uploads it to the authorizer. The authorizer can view the complete information of the unlocking task through the review APP. The above steps realize the closed-loop management of application reporting. The on-site operation range is controlled, as well as the operation information is transparent and traceable.

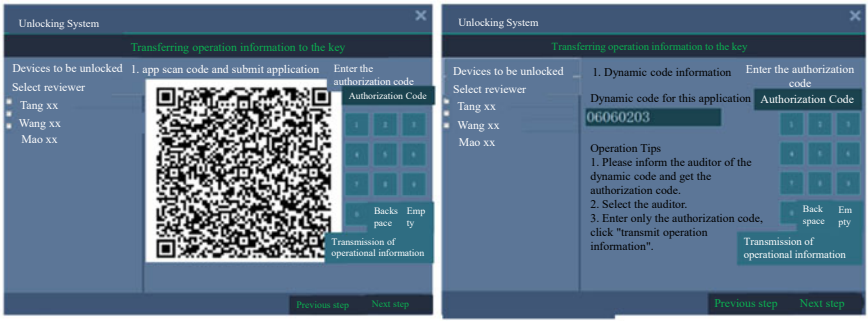

Fig. 4 QR code/dynamic code generation function interface

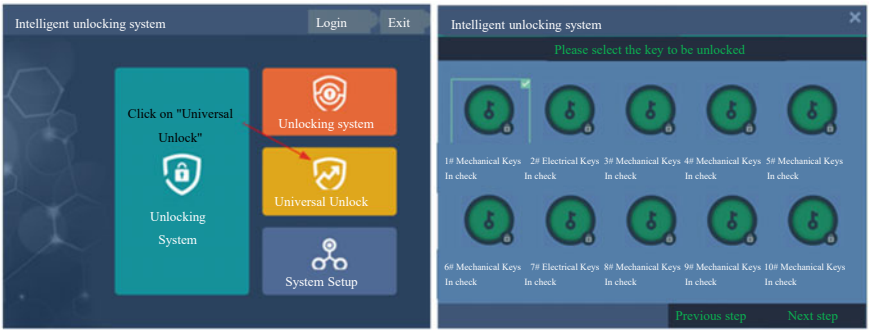

Fig. 5 Emergency unlocking master key interface

3.2 Emergency Unlocking

The mobile unlocking system has a complete function for the use and custody of emergency unlocking keys. Each emergency unlocking key is locked inside the five prevention host through the locking device. During using process, approval and authorization from the leadership are required. Without authorization, even if the five prevention host is open, access to the key cannot be completed.

After approval and authorization, the applicant selects the reason for unlocking, the unlocking key, and the guardian personnel from the universal unlocking list displayed on the intelligent unlocking host software interface. After confirmation, the system software interface automatically generates a QR code and dynamic code, as shown in Fig. 5. The applicant scans the QR code or enters the dynamic code through the mobile app to make the request. In case of an emergency, the system automatically sends a reminder message to the approver's mobile phone for quick approval of the unlocking.

After the applicant completes the operation, they swipe the key column or log in to the intelligent unlocking system, select key return, and perform the key return operation. If the key is returned incorrectly, the red display light of the key seat flashes and the key graphic on the display screen flashes yellow. If the key is returned correctly, the green display light of the key seat flashes and locks, then the key graphic on the display screen flashes green. At the same time, the display screen prompts the number of keys returned and the key number. The system uploads the return information to the approval app and cloud server. The overall process of system unlocking is shown in Fig. 6.

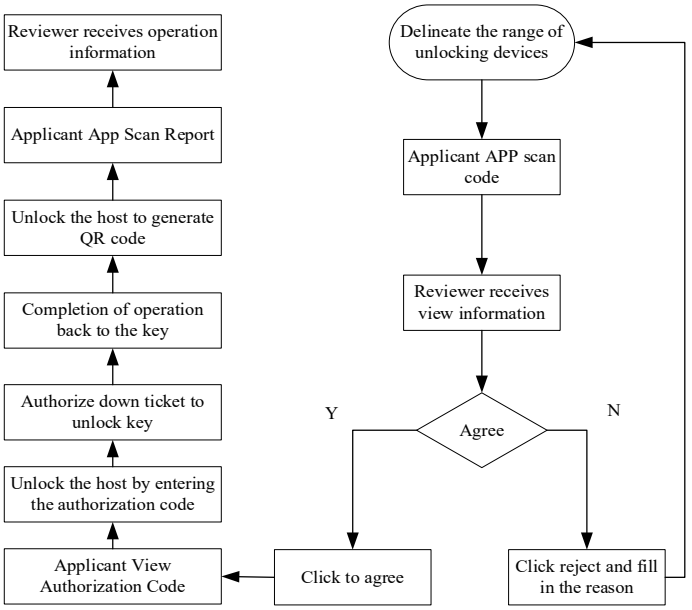

Fig. 6 Overall operation process of the system

4 Conclusions

This paper proposes an intelligent mobile unlocking system for the substation. The system realizes the effective control of intelligent keys and universal keys. It also avoids loose management of the substation's five prevention keys. In addition, this system improves the informatization, standardization, and intelligence of key management within the substation. The specific conclusions are as follows:

(1) By applying/auditing tasks through dynamic codes or scanning QR codes with a mobile app, an efficient and quick mobile office is achieved. This system can improve the work efficiency of the approval personnel and the application personnel within the intelligent substation.
(2) Applicants can choose the equipment and range which needed to be unlocked according to the actual demand. And unlocking operation outside the scope is invalid.
(3) The system supports remote mobile applications as well as authorization operations. And the intelligent unlocking host within the substation is not connected to the network, so any external network attacks cannot affect the actual operations inside the station. In addition, the system uses random QR codes and dynamic codes to ensure the security of remote applications and authorizations.

Acknowledgements Thank our colleagues in Guangzhou Bureau for their help and encouragement, the technical staff of Chongqing University for their support, and the organization for their financial

support. This paper is supported by funding from the technology project GZHKJXM20200013 (080042KK52200001) of Southern Power Grid Company of Guangzhou Power Supply Bureau and technology project (035381KK52220001) of the Southern Power Grid Company of Yunfu Power Supply Bureau.

References

1. Zhao B, Zhai F, Cen W et al (2013) Design and application of a secure chip key issuing system. Appl Mech Mater 365–366:1305–1311. https://doi.org/10.4028/www.scientific.net/AMM.365-366.1305
2. Yu T, Li Z, Zhang W, et al (2020) Anti-error technology of secondary system of intelligent substation based on device state recognition and analysis. In: 5th international conference on advanced intelligent systems and informatics (AISI). Cairo, EGYPT. https://doi.org/10.1007/978-3-030-31129-2_85
3. Cai G, Song T, Wang Z (2012) Analysis of the key technologies and information security of the 220kV digital information substation. In: 2nd international conference on mechatronics and intelligent materials (MIM 2012). Guilin, PEOPLES R CHINA. https://doi.org/10.4028/www.scientific.net/AMR.490-495.100
4. Wang X (2013) Based on network technology new substation error lockout prevention system. China Int Conf Electr Distrib. IEEE. Shanghai, PEOPLES R CHINA. https://www.webofscience.com/wos/alldb/full-record/WOS:000322470200179
5. Li G, Huang W, Lin W, et al (2019) Research on development and design of maintenance control system based on five prevention. IOP Conf Ser: Earth Environ Sci 252(3):032159 (6pp). https://doi.org/10.1088/1755-1315/252/3/032159
6. Ge LJ, Zhang Y, Li H (2012) Analysis on 2nd main transformer trip accident of a certain substation of the west inner mongolia power grid. Adv Mater Res 516–517:1312–1315. https://doi.org/10.4028/www.scientific.net/AMR.516-517.1312
7. Li C, Deng ZW (2020) The embedded modules solution of household internet of things system and the future development. Proc Comput Sci 166:350–356. https://doi.org/10.1016/j.procs.2020.02.086
8. Cheng ZM, Zhu HQ (2012) Designed and development of embedded QR code bar code recognition system. Adv Mater Res 482–484:812–816. https://doi.org/10.4028/www.scientific.net/AMR.482-484.812
9. Ou FC, Jiang W (2013) Research of the QR code based on image preprocessing. Adv Mater Res 850–851:835–838. https://doi.org/10.4028/www.scientific.net/AMR.850-851.835
10. Yi Y (2012) The Design of 2D bar code recognition software on android. Adv Mater Res 442:453–457. https://doi.org/10.4028/www.scientific.net/AMR.442.453
11. Bal E, Bicen H (2016) Computer hardware course application through augmented reality and QR code integration: achievement levels and views of students. Proc Comput Sci 102:267–272. https://doi.org/10.1016/j.procs.2016.09.400

Research on Range of Inertia Simulation and Distribution Ratio of Inertia of Train Braking Test Bench

Yizhou Liu, Jianyong Zuo, and Jingtai Hu

Abstract This paper analyzes the simulation range and inertia distribution ratio of the inertia simulation braking test bench. Perform force analysis of the brake test table built with inertia simulation scheme. Analyze the advantages and disadvantages of different inertia simulation solutions based on the principle of inertia simulation. Propose a suitable simulation solution for rail transit trains. According to the actual vehicle parameters, the parameters of the test bench and the range of inertia simulation are composed. The simulation effect of different inertia simulation distribution ratios is analyzed. The effects of different distribution ratios on inertia simulation and the result of braking test are analyzed. Propose a suitable inertia distribution ratio for rail transit trains.

Keywords Railway · Braking test bench · Inertia simulation · Electro-mechanical mixed solution

1 Introduction

In recent years, our country's railway and urban rail transit are developing rapidly. A large number of new lines and new models have been put into operation, which has spawned the research and development of new technologies related to rail transit vehicles [1]. As an important part of directly guaranteeing the safety of the train operation of the train and the safety of the life of the vehicle, braking system has a very important position in the subsystems of the train. Before the vehicle is put into production, devices and new materials would be tested strictly [2].

At present, for newly developed train or newly developed braking technology, considering costs and safety issues, it is generally not appropriate to directly conduct

Y. Liu · J. Zuo (✉) · J. Hu
Institute of Rail Transit, Tongji University, Shanghai 201804, China
e-mail: zuojy@tongji.edu.cn

J. Zuo
Shanghai Key Laboratory of Rail Infrastructure Durability and System Safety, Shanghai 201804, China

S. Yadav et al. (eds.), *Energy Power and Automation Engineering*, Lecture Notes in Electrical Engineering 1118, https://doi.org/10.1007/978-981-99-8878-5_84

real vehicles and tests running on actual lines during early tests [3]. Rail transportation vehicles have the characteristics of large size, high quality, and high speed [4]. Tests of related new technologies are often difficult. In response to this problem, an inertia simulation idea is generated, and the proportional or small proportion test table is used to use the method of inertia simulation to test the brake system equipment.

This article analyzes the basic principles of inertia simulation and gives an analysis of the simulation effect of the inertia simulation range calculation method of the motor and electrical mixed inertia simulation scheme, and the simulation effect of different simulation inertia distribution ratios.

2 Analysis of Principle of Inertia Simulation

2.1 Fundamental Principle of Inertia Simulation

The essence of the process of relying on friction to produce brake power is the process of turning the flat kinetic energy and rotating kinetic energy of rail transit vehicles into the heat of thermal energy. If we find a physical process that is the same as the essence of the above physical process and energy conversion, but does not require a large size and does not involve the security problem, we can equate the braking process and complete the related test work of the brake system.

According to this, inertia simulation is invented. The braking test bench designed based on inertia simulation ideas uses several large-quality inertia disks to undertake the carrier of kinetic energy or provides an electromagnetic torque equivalent to simulation of the motor. The kinetic energy carried by the rotating system is the same as the flat kinetic energy and rotation energy of the actual simulation vehicle [5], satisfying:

$$\frac{1}{2}mv^2 + \frac{1}{2}J\omega^2 = \frac{1}{2}J_r\omega_r^2 \tag{1}$$

m represents load on axle, v represents speed of running, J represents rotational inertia of one axle, ω represents angular velocity of wheel, J_r represents total rotational inertia of test bench, and ω_r represents angular velocity of test bench.

The coaxial arranging of the wheel pair, brake disk, braking clamping, and other devices used on the actual vehicle can completely equate the kinetic energy, wheel diameter, braking radius, etc. of the actual vehicle, which is convenient for related testing of the braking system. According to different carriers of the equivalent simulation inertia, three solutions are mentioned: mechanical inertia simulation, electrical inertia simulation, and electro-mechanical inertia simulation [6].

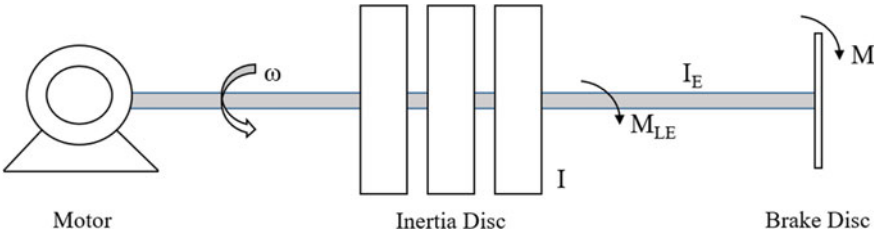

Fig. 1 Force analysis of mechanical inertia simulation solution

2.2 Advantages and Disadvantages of Three Solutions

In the mechanical inertia simulation, several large-quality mechanical inertia disks are set on the main axis system as the carrier of inertia and energy. The inertia of the disks should meet the requirements of the related standards [7, 8]. Disks can be removed by machinery. The force analysis of this solution is shown in Fig. 1.

Taking the direction of the braking torque as the positive direction, the force analysis is as follows:

$$M + M_{\mathrm{LE}} = (I + I_E)\frac{d\omega}{dt} = I_1\frac{d\omega}{dt} \tag{2}$$

M represents braking torque, M_{LE} represents system resistive torque (friction and stray resistive torque). I represents inertia of mechanical inertia disks, I_E represents basic inertia of test bench, I_1 represents total inertia, and ω represents angular velocity.

When the test bench begins to run, the motor will take the entire rotating system to the target speed. Then the motor gets offline. The rotational system simulates the process of braking as the effect of friction of the braking devices. This solution can simulate the whole process of braking and energy conversion completely with a good result, but it costs a lot and is hard to build. The devices need a large range of space. It can only take some certain and discrete inertias. This makes values of inertias which can be simulated limited, adverse to simulation of different vehicle models.

Based on the disadvantages of the mechanical inertia simulation, electrical inertia simulation is invented. This solution uses electromagnetic torque as compensation to simulate the inertia. Electrical inertia simulation solution can take continuous numbers of inertia. But considering the limit of output of motor, the maximum of inertia may be small. This cannot meet the need of characteristics of high speed, big mass, and high energy.

The force analysis of this solution is shown in Fig. 2.

Taking the direction of the braking torque as the positive direction, the force analysis is as follows:

$$M_E = I_2\frac{d\omega}{dt} \tag{3}$$

Fig. 2 Force analysis of electrical inertia simulation solution

$$M + M_{\mathrm{LE}} = M_E + I_E \frac{d\omega}{dt} = (I_2 + I_E)\frac{d\omega}{dt} = I_1 \frac{d\omega}{dt} \tag{4}$$

M_E represents the electromagnetic torque of the motor, I_2 represents the equivalent inertia. I_1 represents total inertia, which is the sum of basic inertia of test bench I_E and electrical inertia I_2. Other physical quantities are the same as (2).

Electrical inertia simulation solution can take continuous numbers of inertia. But considering the limit of output of motor, the maximum of inertia may be small. This cannot meet the need of characteristics of high speed, big mass, and high energy.

To overcome the disadvantages of these two solutions, electro-mechanical mixed solution is invented. This solution applies both the mechanical inertia disks and the motor at the same time. The force analysis of this solution is shown in Fig. 3.

Taking the direction of the braking torque as the positive direction, the force analysis is as follows:

$$M_E = I_2 \frac{d\omega}{dt} \tag{5}$$

$$M + M_{\mathrm{LE}} = M_E + (I + I_E)\frac{d\omega}{dt} = (I_2 + I + I_E)\frac{d\omega}{dt} = I_1 \frac{d\omega}{dt} \tag{6}$$

The physical quantities are the same as (2), (3), and (4).

Electro-mechanical mixed solution can overcome the disadvantages of the others. According to the analysis above, electrical inertia depends on the torque output of

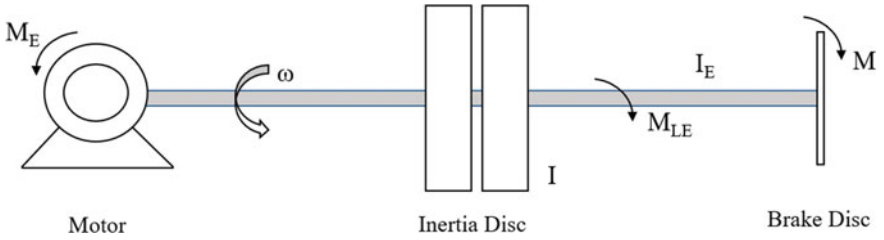

Fig. 3 Force analysis of electro-mechanical mixed inertia simulation solution

the motor and rate of change of angular velocity directly. The control of the output torque of the motor is the key to the success of inertia simulation.

3 Analysis of Range of Inertia Simulation of Electro-Mechanical Mixed Solution

In the process of demonstration above, disadvantages of electrical inertia simulation solution are the limit of the output of motor. It can only carry finite energy and inertia. Electro-mechanical mixed solution also adopts motor to output torque to simulate inertia; the effect and result of simulation are also affected by performance of motor [9].

Taking parameters of typical vehicle model as an example, the parameters are shown in Table 1.

According to the chosen parameters, we can calculate that one single axle carries inertia of 1646 kg·m^2. According to the distribution ratio of 75% mechanical inertia and 25% electrical inertia, mechanical inertia is 1234 kg·m^2, and electrical inertia is 411 kg·m^2. Choose three-phase induction motor. Calculating with a maximum acceleration of 2 m/s^2, the maximum torque output by motor is 1870 N·m. Maximum simulation speed is 400 km/h, corresponding with angular velocity of 2411 rpm, expanding to 2500 rpm. The rated power of the motor is 490 kW.

The purpose of inertia simulation is to simulate the actual physical process of train braking with equal energy. The angular acceleration produced by braking torque is equal to the angular acceleration in (5).

$$\frac{M_b}{I_1} = \frac{M_E}{I_2} = \frac{d\omega}{dt} \tag{7}$$

M_b represents braking torque. Other physical quantities are the same as (5) and (6). According to the force analysis:

$$M_b = |9550\frac{P}{n} \times \frac{I_1}{I_1 - I_0}| = |9550\frac{P}{n} \times (1 + \frac{I_0}{I_1 - I_0})| \tag{8}$$

P represents power of motor, n represents angular velocity of motor, I_1 represents total inertia, I_0 represents total mechanical inertia. It should be pointed out that motor can provide both forward and reverse torque, which means motor can supply both

Table 1 Parameters of actual vehicle

Load on axle	Speed	Wheel diameter	Maximum acceleration	Number of disks on one axle	Total energy
17t	400 km/h	880 mm	2 m/s^2	2	52.5 MJ

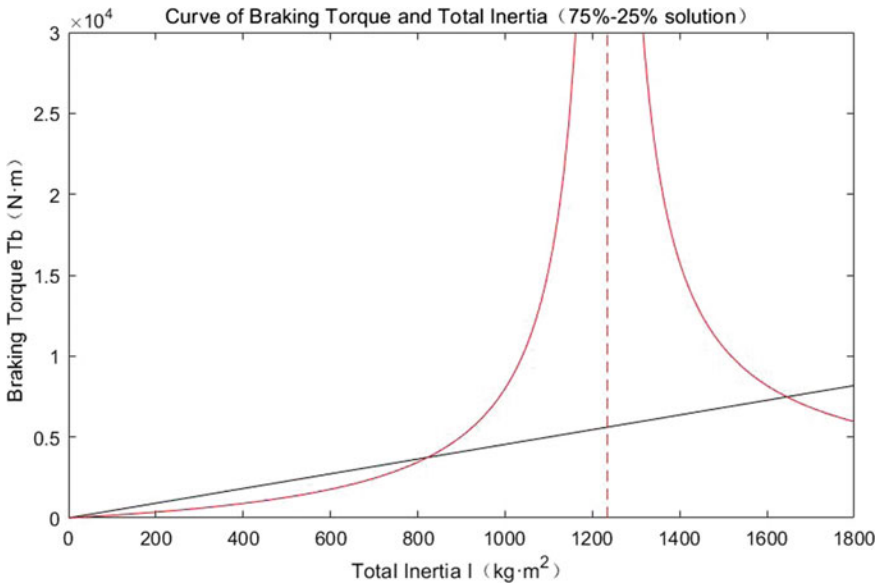

Fig. 4 Curve of braking torque and total inertia for 75–25% solution

positive and negative inertia. The absolute value in (8) refers to different directions of force analysis. The curve of braking torque and total inertia is shown in Fig. 4.

The red dashed line refers to mechanical inertia 1234 kg·m^2. The black line refers to constraint condition of acceleration of 2 m/s^2. The dashed line shows upper limit of motor performance. Area red dashed line is higher than black line shows the output that the motor is able to supply. For a specific braking torque, range of inertia simulation is calculated by (9).

$$\frac{I_0 M_b}{M_b + M_E} \leq I \leq \frac{I_0 M_b}{M_b - M_E} \tag{9}$$

4 Analysis of Distribution Ratio of Inertia of Electro-Mechanical Mixed Solution

The solution above adopts the distribution ratio of 75% mechanical inertia and 25% electrical inertia. Since the output of the motor is adjustable, the distribution ratio could be changed artificially. Different ratios lead to different effects of simulation. According to (8), distribution ratios of 50–50%, 75–25%, 80–20%, and 90–10% are analyzed. Curves of braking torque and total inertia of these four solutions are shown in Fig. 5.

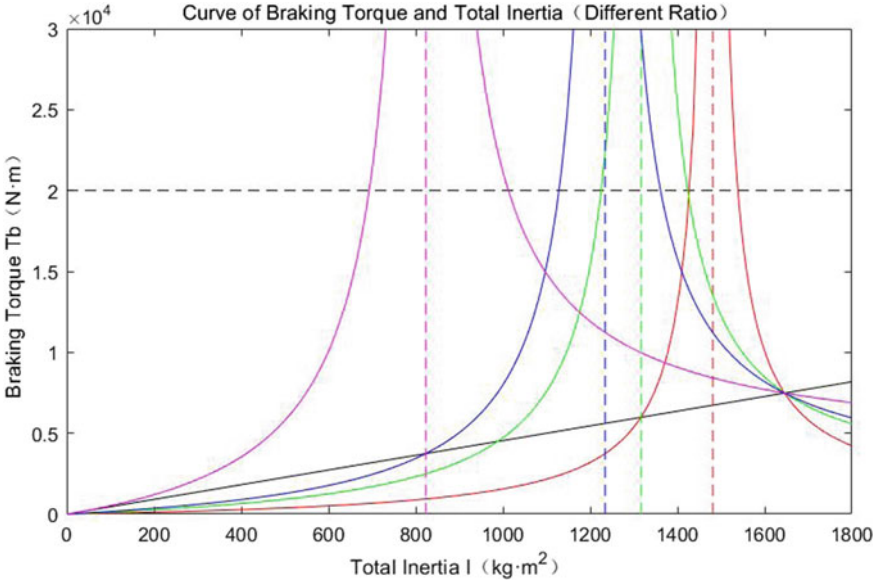

Fig. 5 Curve of braking torque and total inertia for different distribution ratio

As the ratio of mechanical inertia increases, the range of inertia simulation which the system could adjust gets closer. In the actual process of train braking, the frictional coefficient of the points onside the braking disk is not constant. The braking torque is not constant either. When the braking torque increases suddenly, if the ratio of mechanical inertia is higher, then the range of the output of the motor that could be adjusted is smaller. The range of total inertia is narrow. The deviation of total inertia and target inertia may be too large to get a reliable simulation effect and data.

In this electro-mechanical system, considering the high power, the time constant is large. It takes a long time to adjust the output. If the output of torque can't respond in time, it would cause significant deviation in the electrical inertia simulation, which leads to inertia simulation failure. Therefore, the motor should take a quick response control strategy like DTC and the distribution ratio of electrical inertia should not be high [10].

In general, the distribution ratio of 75% mechanical inertia and 25% electrical inertia fits well in the scenario of electro-mechanical mixed solution of inertia simulation test bench of this power level.

5 Conclusion

This paper analyzes the principle of test bench based on inertia simulation and the advantages and disadvantages of different solutions. The parameters of devices in the system are calculated. Range of inertia simulation and effect of distribution ratio of inertia are analyzed.

Electro-mechanical solution can get a balance between range of inertia simulation and distribution ratio of inertia. It has a great advantage compared with the other solutions. For railway transit, the combination of 75% mechanical inertia and 25% electrical inertia is the most suitable.

Acknowledgements The research work is supported by National Key R&D Program of China (2021YFB3703805), Science and Technology Research and Development Programme Topics of China State Railway Group Co., Ltd. (Grant No. N2022J019), and Shanghai Collaborative Innovation Research Center for Multi-network & Multi-modal Rail Transit.

References

1. Chen JF, Tan J, Yu HM (2022) Development of the 1: 1 braking test table of the high-speed EMU. Mech Electr Inf 06:31–33. https://doi.org/10.19514/j.cnki.cn32-1628/tm.2022.06.009
2. Ying ZD, Fan JH, Wu XQ (2021) Experimental study on dynamic braking performance of rail transit train based on vehicle rolling brake test bench. Urban Mass Transit 24(01):26–30. https://doi.org/10.16037/j.1007-869x.2021.01.006
3. Wang H, Pan B (2017) Design of small traction and brake test bench for metro train based on LabVIEW. Urban Mass Transit 20(07):139–141. https://doi.org/10.16037/j.1007-869x.2017.07.033
4. Maulana FR, Supriyo B, Suharjono A (2019) Electronic and GUI development of roller brake tester. J Phys: Conf Ser 1273:1–7. https://doi.org/10.1088/1742-6596/1273/1/012070
5. Tan QX (2016) Electrical resistance due to inertia simulation error compensation method. Indust Control Comput 29(10):125–126. https://doi.org/10.3969/j.issn.1001-182x.2016.10.058
6. Zhao QP, Zhu BL, Cai XX (2016) Simulation research on electrical inertia of the transmission test bench. Automobile Appl Technol (03):149–151+184. https://doi.org/10.16638/j.cnki.1671-7988.2016.03.049
7. UIC 548 Ed. 1 (2015) Brakes-requirements of friction test benches for the international certification of brake pads and brake blocks. https://uic.org
8. UIC 541-3 Ed. 7 (2010) Brakes-disc brakes and their application-general conditions for the approval of brake pads. https://uic.org
9. Shuai ZQ, Gao F, Fu R (2019) Study of electric simulation inertia range for train braking test dynamometer. J Dalian Jiaotong Univ 40(03):114–119. https://doi.org/10.16037/j.1007-869x.2017.07.033
10. Xiong J (2020) Comprehensive experimental technique research of railway transport equipment based on rolling rig. https://doi.org/10.27461/d.cnki.gzjdx.2020.000711

Probabilistic Optimal Energy Flow of Urban Integrated Electrical Systems Considering Low Carbon Operation

Zhongxi Ou, Yuanyuan Lou, Sui Peng, Kun Yang, Xiaoyan Zhao, and Yede Chen

Abstract The transition from coal to gas is a key aspect of the current energy structure adjustment, aimed at mitigating environmental pollution. The introduction of the "energy internet" has further strengthened the interconnection between natural gas networks and power systems. In this context, the authors propose a joint optimal energy flow model that considers the constraints of the natural gas network on power system operation, as well as their impact on the overall operational costs of the interconnected system. The model accounts for the uncertainty of input variables such as wind power output, electrical load, and gas load, and employs Latin hypercube sampling for probabilistic optimal energy flow calculation, enabling low-carbon operation of the electrical-gas interconnection system with wind power generation. The proposed model is evaluated through case studies on the improved IEEE 9-bus system and an 8-node natural gas network, assessing the impacts of different fluctuation levels on system operating characteristics.

Keywords Uncertainty · Low-carbon · Probabilistic optimal energy flow

Z. Ou · K. Yang · X. Zhao
Zhuhai Power Supply Bureau of Guangdong, Power Grid Co., Ltd, Guangdong Power Grid Corporation, CSG, Zhuhai 519000, Guangdong Province, China

Y. Lou
Guangdong Power Grid Corporation, CSG, Guangzhou 510080, Guangdong Province, China

S. Peng
Grid Planning and Research Center, Guangdong Power Grid Corporation, CSG, Guangzhou 510080, Guangdong Province, China

Y. Chen (✉)
School of Information Engineering, Nanchang University, Nanchang 330031, Jiangxi Province, China
e-mail: 416100210452@email.ncu.edu.cn

S. Yadav et al. (eds.), *Energy Power and Automation Engineering*, Lecture Notes in Electrical Engineering 1118, https://doi.org/10.1007/978-981-99-8878-5_85

1 Introduction

Optimal power flow (OPF) is a critical tool for power system operation and planning [1]. However, traditional OPF methods in China typically do not account for the operation of natural gas networks due to the relatively small proportion of gas turbines in the power system. This assumption implies that natural gas supply for gas turbines is sufficient. Nonetheless, the operation of natural gas networks [2, 3] is subject to constraints such as flow and pressure, and can therefore impact the stable operation of the power system to some extent.

Scholars both domestically and internationally have been investigating the optimal energy flow in electrical-gas interconnected systems [4]. Some literature has proposed joint optimal energy flow models that integrate gas network power flow calculations [5]. These models take into account the impacts of operational constraints of the natural gas network on the power system. However, the research has primarily been based on deterministic models and has not considered the uncertainties associated with the integration of new energy sources. Therefore, further research is required in this area. With the large-scale integration of new energy sources, the uncertainty of power systems has increased, and the probability-based optimal energy flow (POEF) considering the impact of stochastic factors has received significant attention from the academic community [6, 7]. Latin Hypercube Sampling is a widely used approximation method for probabilistic power flow and POPF calculations due to its simplicity, low computational requirements, and high accuracy [8, 9].

This article presents a novel probabilistic optimal energy flow (POEF) model for an electrical-gas system, denoted as GEPOEF. To begin with, a steady-state simulation of the natural gas network is conducted to establish the interdependency between the power grid and the natural gas network, which is achieved by means of gas turbines. Subsequently, a GEPOEF mathematical model is developed to account for uncertainties and correlations associated with wind power output, power load, and gas load. To perform GEPOEF calculations, the widely used Latin hypercube sampling method is employed. Finally, practical examples are provided to demonstrate the effectiveness and feasibility of the proposed algorithm.

2 Steady-State Model of the Natural Gas Network

The natural gas network mainly comprises gas wells, pipelines, and compression stations, through which natural gas is transported from gas wells to users. The steady-state flow rate of natural gas can be represented as:

$$f_g^{oij} = k^{oij} \mathrm{sgn}(\pi^i - \pi^j) \sqrt{|\pi^i - \pi^j|} \tag{1}$$

f_g^{oij} represents gas flow between natural gas node i and j, k^{oij} is weismann constant, π^i and π^j are the secondary pressure between natural gas node i and j.

Compressors are required to recover pressure drops in the natural gas network caused by energy losses during gas transportation in pipelines. The electric power consumption of the compressor can be represented as:

$$\psi^c = B^c f_g^{cij} * \left[\left(\frac{\pi^j}{\pi^i}\right)^{\frac{Z^c}{2}} - 1 \right] \forall c \in C \tag{2}$$

β^{cij} is compression ratio of compressor c, B^c represents design parameter of compressor c. Z^c is compression ratio parameter of compressor c. ψ^c is the electric power consumption of the compressor c.

$$\phi^c = x + y\psi^c + z\psi^{c2} \ \forall c \in C \tag{3}$$

x, y, and z represent consumption parameters of gas-fired compressors.

For each node in the natural gas network, the law of conservation of mass must be satisfied, which can be expressed as:

$$\begin{aligned} &\sum_{o \in T_O^k} f_g^{oij} - \sum_{o \in F_O^k} f_g^{oij} + \sum_{c \in T_C^k} f_g^{cij} - \sum_{c \in F_C^k} (f_g^{cij} + \phi^c) \\ &+ \sum_{w \in W^k} g^w - \sum_{t \in T} T^t \sum_{e \in \varepsilon_G^k} (\eta^e p_g^{te}) = \sum_{\delta \in \Sigma} (D_g^{\delta k} - \gamma^{\delta k}) \end{aligned} \tag{4}$$

F_0^k and T_0^k are connected pipelines to node k at side *From* or *To*. F_C^k and T_C^k are connected compressors to node k at side *From* or *To*. $F\ cij\ g$ is gas flow in compressor c, from node i to node j. W^k is gas wells at node k. g^w is gas production at well w. T^t is energy weighting for period t. η^e is thermal efficiency of generator e. p_g^{te} is active power production for generator e at time t. $D_g^{\sigma k}$ is gas demand of type σ at node k. Σ is types (users) of gas demand. $\gamma^{\sigma k}$ is non-supplied gas of type σ at node k.

3 Probabilistic Model for Multi-source Interconnected Systems

3.1 Uncertainty in Wind Speed

Wind power can contribute to the low-carbon operation of the power system. As a clean and renewable energy source, wind energy is inherently random, intermittent, and fluctuating. In most existing literature, the Weibull distribution is commonly used to model wind speed, with its probability density function expressed as:

$$f(\upsilon) = \frac{k}{c}(\frac{\upsilon}{c})^{k-1} \exp(-(\frac{\upsilon}{c})^k) \tag{5}$$

$f(\upsilon)$ represents the probability density function; υ is the wind speed; k is the shape factor; c is the scale coefficient.

Assuming a power factor of 1 for the wind farm and treating it as a load, the active power output of a single wind turbine depends on the wind speed. This relationship can be described by the following formula:

$$P_w(\upsilon) = \begin{cases} 0 \ \upsilon \le \upsilon_{ci} || \upsilon \ge \upsilon_{co} \\ P_r = \frac{\upsilon - \upsilon_{ci}}{\upsilon_r - \upsilon_{ci}} \ \upsilon_{ci} \le \upsilon \le \upsilon_r \\ P_r \ \upsilon_r \le \upsilon \le \upsilon_{co} \end{cases} \tag{6}$$

υ_{ci} denotes the entry wind speed of the wind turbine; υ_r is the rated wind speed of the wind turbine; υ_{co} is the cut-out wind speed of the wind turbine; P_r is the rated output power of the wind turbine.

3.2 The Uncertainty of Electrical and Power Loads

The forecasting of loads is prone to errors, and several prior studies have presumed that load forecasting errors conform to a normal distribution, which can be expressed as follows:

$$f(D_e) = \frac{1}{\sqrt{2\pi}\delta_{D_e}} \exp\left[-\frac{(D_e - \mu_{D_e})^2}{2\delta_{D_e}^2}\right] \tag{7}$$

In the equation, μ_{P_L} and δ_{P_L} represent the expected value and standard deviation of the active power load D_e in the power system.

In addition to the inherent errors in electricity grid load forecasting, the fluctuation of natural gas grid load also necessitates stochastic analysis. This can be represented as:

$$f(D_g) = \frac{1}{\sqrt{2\pi}\delta_{D_g}} \exp\left[-\frac{(D_g - \mu_{D_g})^2}{2\delta_{D_g}^2}\right] \tag{8}$$

μ_{D_g} and δ_{D_g} represent the expected value and standard deviation of the gas load D_g in the natural gas system.

4 Probabilistic Optimal Energy Flow Analysis

4.1 Deterministic Optimal Energy Flow

The Deterministic Optimal Energy Flow (DOEF) calculation provides a basis for the Probabilistic Optimal Energy Flow (POEF) calculation in electric-gas coupled systems. In order to minimize the total operating cost of the electric-gas coupled system, the GEOEF model has been proposed, which involves the introduction of an objective function, constraints, and MPNG to solve the nonlinear optimization model of the electric power system. Herein, we present an overview of the objective function, constraints, and MPNG used in the GEOEF model.

(1) The objective function

$$\begin{aligned} C(x) = & \sum_{\mathrm{w}\in W} C_G^w g^w + \sum_{t\in T} T^t \sum_{e\in\varepsilon} C_E^e p_g^{te} + \sum_{o\in O} C_O^{oij} f_{g+}^{oij} - \sum_{o\in O} C_O^{oij} f_{g-}^{oij} \\ & + \sum_{c\in C} C_C^{cij} f_g^{cij} + \sum_{i\in N} \alpha_{\pi_+}^i \pi_+^i + \sum_{i\in N} \alpha_{\pi_-}^i \pi_-^i + \sum_{i\in N} \sum_{\delta\in\Sigma} \alpha_\gamma^{i\delta} \gamma^{i\delta} \\ & + \alpha_\varphi \sum_{t\in T} T^t \sum_{m\in \mathrm{B}} \varphi^{tm} \end{aligned} \tag{9}$$

C_G^W is gas cost at well w. C_E^e represents power generation cost (excluding gas cost). C_O^{cij} is transport cost of pipeline o, from node i to node j. C_C^{cij} denotes compression cost of compressor c. $\alpha_\gamma^{i\sigma}$ is penalty for non-supplied gas of type σ at node i. φ^{tm} is non-served active power for bus m at time t. α_φ denotes penalty cost for non-supplied electrical power. B is power buses. $f_{g^+}^{oij}$ and $f_{g^-}^{oij}$ are positive and negative gas flow in pipeline o.

(2) Constraints of natural gas system

The constraints of the natural gas system include Eqs. (1)–(4), as well as the requirement that the unfulfilled gas demand σ for a specific user at node k cannot exceed their total demand.

$$0 \le \gamma^{\delta k} \le D_g^{\delta k} \ \forall\delta \in \Sigma \ \forall k \in N \tag{10}$$

N represents gas nodes.

The constraint conditions for overpressure and negative pressure at each node are as follows:

$$\pi^k \le \overline{\pi}^k + \pi_+^k \ 0 \le \pi_+^k \ \forall k \in N \tag{11}$$

$$\underline{\pi}^k - \pi_-^k \le \pi^k \ 0 \le \pi_-^k \ \forall k \in N \tag{12}$$

In the equations, $\overline{\pi}^k$ and $\underline{\pi}^k$ are the upper and lower limits of pressure.
The constraint conditions related to gas well injection are as follows:

$$\underline{g}^w \leq g^w \leq \overline{g}^w \tag{13}$$

$\underline{g}^w$ and $\overline{g}^w$ are gas production limits at well w.
The pipeline constraints are shown as follows:

$$-\overline{f}_g^{oij} \leq f_g^{oij} \leq \overline{f}_g^{oij} \ \forall o \in O \tag{14}$$

$$f_g^{oij} = f_{g+}^{oij} + f_{g-}^{oij} \ \forall o \in O \tag{15}$$

$$0 \leq f_{g+}^{oij} \leq \delta^{0ij} * \overline{f}_g^{oij} \ \forall o \in O \tag{16}$$

$$-\delta^{0ij} * \overline{f}_g^{oij} \leq f_{g-}^{oij} \leq 0 \ \forall o \in O \tag{17}$$

δ^{oij} is gas flow threshold. $\overline{f}_g^{oij}$ denotes the gas flow capacity of pipeline o, from i to j.

Compressor constraints:

$$0 \leq f_g^{cij} \leq \overline{f}_g^{cij} \ \forall c \in C \tag{18}$$

$$\pi^i \leq \pi^j \leq \beta^{cij} \pi^i \ \beta^{cij} \geq 1 \ \forall c \in C \ \forall i, j \in N \tag{19}$$

β^{cij} is the maximum compression ratio of compressor c. B^c is the compressor design parameter of compressor c. Z^c is ratio parameter of compressor c.

(3) Electric power system constraints

$$\begin{aligned} &g_{pm}(\theta^{tm}, V^{tm}, p_g^{te}, \varphi^{te}, \psi^c) = 0 \\ &g_{qm}(\theta^{tm}, V^{tm}, q_g^{te}) = 0 \ \forall m \in B \ \forall t \in T \ \forall c \in C_E \end{aligned} \tag{20}$$

θ^{tm} is voltage angle for bus m at time t. V^{tm} is voltage magnitude for bus m at time t.

$$\theta^{t_{\text{ref}}} = 0 \ \underline{V}^{tm} \leq V^{tm} \leq \overline{V}^{tm} \ \forall m \in B \ \forall t \in T \tag{21}$$

$\theta^{t_{\text{ref}}}$ is the reference angle must be zero for each period. $\underline{V}^{tm}$ and $\overline{V}^{tm}$ are voltage limits for bus m at time t.

$$\begin{aligned} \underline{p}_g^e \le p_g^{te} \le \overline{p}_g^e \\ \underline{q}_g^e \le q_g^{te} \le \overline{q}_g^e \ \forall e \in \varepsilon \ \forall t \in T \end{aligned} \tag{22}$$

$\underline{p}_g^e$ and $\overline{p}_g^e$ are active power generation limits of generator e. $\underline{q}_g^e$ and $\overline{q}_g^e$ are Reactive power generation limits of generator e.

The complex power constraint is given by:

$$|\mathrm{S}_{fl}(\theta, V)| \le \overline{S}_{fl} \ |\mathrm{S}_{tl}(\theta, V)| \le \overline{S}_{tl} \ \forall l \in L \tag{23}$$

$\overline{S}_{fl}$ and $\overline{S}_{tl}$ are the complex power injections at side *from* and *to* of line l, respectively.

The non-electric active power demand at node m cannot exceed the total demand at the node.

$$0 \le \varphi^{tm} \le D_e^{tm} \ \forall m \in B \ \forall t \in T \tag{24}$$

MPNG is an open-source MATLAB simulation package that serves as an optimization tool for studying the interconnections between electrical systems. A detailed description of MPNG can be found in paper [10]. Specifically, in this article, the deterministic optimal power flow model is solved using the MPNG algorithm.

4.2 Probabilistic Optimal Energy Flow Analysis

In the Deterministic Optimal Energy Flow (DOEF) model, wind power output, electric load, and gas load are treated as random variables, transforming the model into a Probabilistic Optimal Energy Flow (POEF) model. In this study, Latin hypercube sampling is employed to sample the uncertainty model, converting the POEF calculation into multiple deterministic optimal energy flow calculations. Through the analysis of the results of these calculations, the final result of the POEF calculation is obtained.

4.3 Latin Hypercube Sampling

Latin hypercube sampling is a hierarchical method for sampling random variables that effectively captures the overall distribution of these variables through sampled values. The objective of this technique is to guarantee complete coverage of all sampling regions with sampling points. The method involves two steps, namely, sampling and permutation. The sampling step involves generating samples for each input random variable to achieve full coverage of the random distribution area

with sampling points. The second step, permutation, entails rearranging the order of sampling values for each random variable to minimize correlations between the sampling values of independent variables. By following this two-step approach, Latin hypercube sampling ensures comprehensive coverage of the distribution of random variables and effectively reduces correlations among independent variables. These features make Latin hypercube sampling a popular technique in scientific research for simulation, optimization, and uncertainty analysis.

5 Example Analysis

This article employs an enhanced interconnected system consisting of a 9-node power system and an 8-node natural gas network. The fundamental parameters of the 9-node power system and 8-node natural gas system were acquired by referring to literature citation [10].

The article is structured around three distinct scenarios: Scenario 1, which considers only the uncertainty associated with wind power; Scenario 2, which incorporates both wind power uncertainty and uncertainty in electricity load; and Scenario 3, which accounts for uncertainty in wind power, electricity load, and gas load.

The Latin hypercube sampling algorithm is utilized in this paper to sample the uncertain variables 1000 times. The uncertain model is then transformed into 1000 deterministic models to obtain the solutions. Additionally, this article investigates the full integration of new energy wind power to accomplish a low-carbon operation of the interconnected electrical system.

5.1 Only Consider Wind Power Uncertainty Scenarios

Node 9 of the electrical system is connected to a wind farm that has a rated power of 20 MW. The wind speeds of both wind farms follow a two-parameter Weibull distribution with a scale coefficient of 5.218 and a shape coefficient of 1.637. The wind farm is characterized by a cut-in wind speed of 3 m/s, a rated wind speed of 13 m/s, and a cut-out wind speed of 25 m/s. Figure 1 displays the probability histogram of wind farm output. The histogram sections are numbered with a dot and separated by a single space:

The system's total operational cost amounts to 922,935 USD/h, while the gas wells produce 41.0341 MMSCFD (Million Standard Cubic Feet Per Day). The results of the power grid are presented in Table 1.

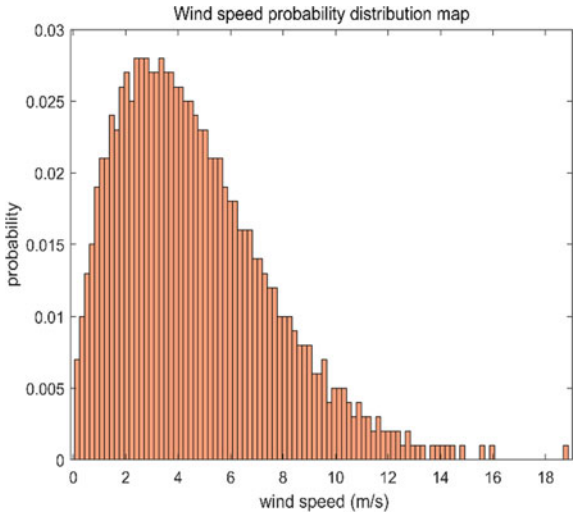

Fig. 1 Wind speed probability distribution

Table 1 Results of power grid

Generator bus number	P/MW	Variance/MW
1	172.5103	14.2711
2	131.8361	1.4005
3	10	0

5.2 Consider Wind Power Uncertainty and Electricity Load Uncertainty Scenarios

Assuming that the standard deviation of power load equals 5% of its expected value, the system's total operational cost is 922949 USD/h, with gas wells producing 41.0341 MMSCFD. The results of the power grid are displayed in Table 2.

Table 2 Results of power grid

Generator bus number	P/MW	Variance/MW
1	172.5152	32.8511
2	131.8371	16.5033
3	10	0

Table 3 Results of power grid

Generator bus number	P/MW	Variance/MW
1	172.8087	20.94
2	131.9345	6.3817
3	10	0

5.3 Consider Wind Power Uncertainty and Electricity Load Uncertainty Scenarios

With a 5% standard deviation of gas load assumed, the power grid results are presented in Tables 1 and 2. The system's total operational cost is 922949 USD/h, and the well gas production is 41.0804 MMSCFD. The results of the power grid are also shown in Table 3.

5.4 Analysis

The examination of Tables 1, 2, and 3 reveals that Scenarios 2 and 3 exhibit an increase in generator output relative to Scenario 1. However, these scenarios also display a larger degree of variance, indicating a higher level of fluctuation in generator output resulting from the uncertainties associated with electricity load and gas load. Therefore, in assessing the electrical interconnection system, it is crucial to not only consider the uncertainty associated with wind power but also take into account the uncertainties associated with electricity load and gas load and their potential impact on the system. It is imperative to recognize the significance of these uncertainties in the evaluation of the system's performance.

The aforementioned results indicate that, in comparison to Scheme 1, both Scheme 2 and Scheme 3 result in increased costs. Consequently, considering the uncertainty of both power and gas loads not only amplifies fluctuations within the electric power system, but also leads to higher overall operational costs. Specifically, in Scheme 3, ignoring the uncertainty of gas loads results in overly optimistic optimization outcomes.

Table 4 displays the node pressures in various scenarios, with the unit of measurement being psia (pounds per square inch).

Table 4 Node pressures in different scenarios

	Node 1	Node 2	Node 3	Node 4	Node 5	Node 6	Node 7	Node 8
Scenario 1	650	581.4172	610.1887	610.1887	586.6037	595.8064	561.7245	464.0001
Scenario 2	650	581.4172	610.1887	610.1887	586.6037	595.8064	561.7245	464.0001
Scenario 3	650	581.1892	605.3698	610.5654	586.9299	596.1571	561.9336	464

Table 5 displays pipeline flow rates for different scenarios, with flow rate measured in MMSCFD.

Analysis of Tables 3, 4, and Fig. 2 reveals that the natural gas system remains stable when considering only uncertainties in wind power and electricity load. However, accounting for uncertainties in gas load, such as a 50 thousand standard cubic feet per day increase in gas production from gas wells, significantly impacts the operation of the interconnected system. The resulting increase in gas load uncertainty leads to instability in the natural gas system, resulting in elevated operating costs for the entire electro-gas interdependent system. This is due to the fact that natural gas serves as a critical fuel that directly affects the energy supply of the electricity system. Inadequate natural gas supply may require the electricity system to adjust its generation output to maintain supply–demand balance, leading to increased output from electricity generation units. Therefore, optimizing these systems jointly requires consideration not only of stochastic variables in power but also of stochastic variables in the natural gas system.

The results of Scenario 2 and Scenario 3 indicate that relying solely on the uncertainty of wind power output may lead to overly optimistic operating outcomes in comparison to Scenario 1. Therefore, it is crucial to incorporate the uncertainty of power system load and the randomness of natural gas networks in the calculation to obtain accurate results. This incorporation of the uncertainty of power and gas loads results in a greater fluctuation of generator output.

Table 5 Optimal natural gas flow rate in different scenarios of pipelines

	Pipeline 1	Pipeline 2	Pipeline 3	Pipeline 4	Pipeline 5	Pipeline 6
Scenario 1	41.0341	20.396	20.6375	− 6.0189	14.6186	26.4149
Scenario 2	41.0341	20.396	20.6375	− 6.0189	14.6186	26.4149
Scenario 3	41.0792	20.4214	20.6573	− 6.0198	14.6375	26.4412

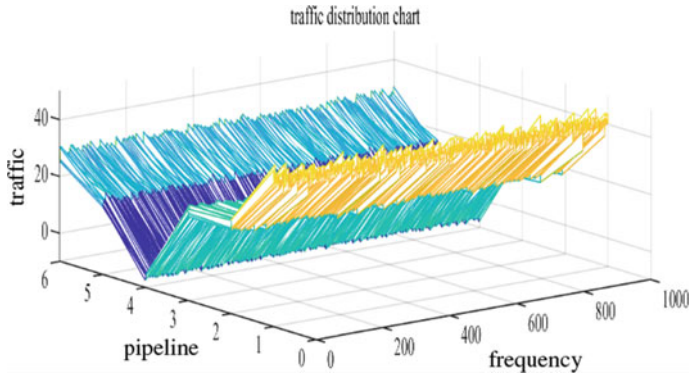

Fig. 2 Pipeline flow

The simulation experiments of Scenario 1 and Scenario 2 demonstrate that the natural gas system remained stable. However, the inclusion of natural gas load randomness, changes in pipeline flow, and node voltage in the natural gas system in Scenario 3 resulted in increased operating costs. These findings reveal that the randomness of the natural gas network has the potential to increase the uncertainty of the power system, and the interaction between the electricity and gas interconnection systems can affect the optimization scheduling plan.

Therefore, when conducting joint optimization of electric-gas interconnection systems, considering the uncertainty of power random variables alone is insufficient. Instead, it is necessary to account for the uncertainty of natural gas system random variables as well to achieve optimal results.

6 Conclusion

This paper presents an optimal energy flow model for an electrical and gas interconnection system, considering the uncertainties of electricity load, gas load, and renewable energy generation. Three scenarios are defined to analyze and compare the impacts on the model. The model is solved using the Latin Hypercube Sampling algorithm. The following conclusions are drawn.

1. Considering only the uncertainty of wind power output in the calculation of operating costs would lead to overly optimistic results. Taking into account the uncertainties of both electricity load and gas load would provide a more realistic estimation. Therefore, it is essential to consider the uncertainty of electricity system load and the randomness of the gas network in the calculation of the Probabilistic Optimal Energy Flow.
2. Taking into account the stochastic nature of gas load, which causes fluctuations in pipeline flow and gas pressure at nodes in the gas system, leads to increased operating costs. The stochastic behavior of the gas network indeed contributes to the uncertainty of the power system, while the interaction between the electrical and gas interconnection systems also impacts the optimization scheduling plan. Therefore, in the joint optimization of the electrical and gas interconnection systems, it is essential to consider the uncertainties of both electricity and gas system random variables. This consideration provides a solid basis for optimizing the system's scheduling and ensuring its optimal operation.

References

1. Dall'Anese E, Simonetto A (2018) Optimal power flow pursuit. IEEE Trans Smart Grid 9(2):942–952. https://doi.org/10.1109/TSG.2016.2571982
2. Zhao B, Conejo AJ, Sioshansi R (2018) Coordinated expansion planning of natural gas and electric power systems. IEEE Trans Power Syst 33(3):3064–3075. https://doi.org/10.1109/TPWRS.2017.2759198
3. He C, Wu L, Liu T, Bie Z (2018) Robust co-optimization planning of interdependent electricity and natural gas systems with a joint n-1 and probabilistic reliability criterion. IEEE Trans Power Syst 33(2):2140–2154. https://doi.org/10.1109/TPWRS.2017.2727859
4. Sun G, Chen S, Wei Z, Li G, Wu L (2017) Multi-period integrated natural gas and electric power system probabilistic optimal power flow incorporating power-to-gas units. J Modern Power Syst Clean Energy 5:412–423. https://doi.org/10.1007/s40565-017-0276-1
5. Shargh S, Khorshid Ghazani B, Mohammadi-Ivatloo B, Seyedi H, Abapour M (2016) Probabilistic multi-objective optimal power flow considering correlated wind power and load uncertainties. Renew Energy 94:10–21. https://doi.org/10.1016/j.renene.2016.02.064
6. Bin L, Feng L, Shengwei M (2015) AC-constrained optimal power flow considering wind power generation uncertainty in radial power networks. In: 34th Chinese control conference (CCC). Hangzhou, China, pp 2797–2801. https://doi.org/10.1109/ChiCC.2015.7260066
7. Attarha A, Amjady N, Conejo AJ (2018) Adaptive robust AC optimal power flow considering load and wind power uncertainties. Int J Electr Power Energy Syst 96:132–142. ISSN 0142-0615
8. Sun W, Zamani M, Zhang HT, Zhou J, Chen Z (2019) Probabilistic optimal power flow with correlated wind power uncertainty via Markov chain quasi-Monte-Carlo sampling. IEEE Trans Industr Inf 15(11):6058–6069
9. Usaola J (2010) Probabilistic load flow with correlated wind power injections. Electr Power Syst Res 80(5):528–536
10. González-Vanegas W, Murillo-Sánchez CE (2022, April) MPNG: matpower natural gas, git. https://github.com/MATPOWER/mpng

Multi-Step Wind Power Prediction Method Based on Bi-GRU and Spatial Attention

Yiwen Cheng and Jing Xu

Abstract Aiming at the prevailing problems in the wind power industry, such as the volatility of wind power and the stability of the power grid system. This paper effectively combines the BI-GRU (Bidirectional Gated Recurrent Unit) algorithm with spatial attention and proposes a multi-step wind power prediction network structure independent of meteorological data. Through the analysis of a large number of experimental data of this model, it is proved that the accuracy of wind power prediction is greatly improved and the response speed is faster, which provides a strong support for the reliability analysis of wind power prediction in actual scenarios.

Keywords BI-GRU · Spatial attention · Wind power · Time series · Power prediction

1 Introduction

In light of State Grid's proposal to "promote energy transformation and adhere to green development in 2023," the task of transforming China's energy and power systems to be clean and low-carbon is significant and critical under the "double carbon" goal. Wind energy, as a clean resource, has the characteristics of being renewable and low-cost. Coupled with China's abundant wind energy resources, wind power generation is undoubtedly a major force in achieving the "double carbon" goal.

In recent years, the cumulative installed capacity of wind power generation in China has exceeded 300 million kW, ranking first in the world for 12 consecutive years. However, due to the characteristics of randomness, volatility, and intermittency of wind energy, the threat to the stability of the power grid system is becoming increasingly prominent. It directly impacts both the safety of wind power grid-connection and the competitiveness of the electricity market. Therefore, in order to make the

Y. Cheng · J. Xu (✉)
School of Physics and Electronic Engineering, Jiangsu University, Zhenjiang 212013, Jiangsu, China
e-mail: xjing@ujs.edu.cn

S. Yadav et al. (eds.), *Energy Power and Automation Engineering*, Lecture Notes in Electrical Engineering 1118, https://doi.org/10.1007/978-981-99-8878-5_86

power grid system more stable and reliable, knowing how to accurately forecast wind power is very important. Predicting the change in wind energy in advance and adjusting the control systems of wind farms in time can reduce wind power abandonment and maximize the utilization of wind energy.

Presently, domestic and foreign researchers have proposed various wind power forecasting methods and models, mainly physical models, statistical models [1], and artificial intelligence methods. The artificial intelligence method is data-driven and makes wind power predictions through the correlation between many data points concentrated by deep learning neural networks [2]. The nonlinear issue of wind power data forecasting curves under particular conditions has been mostly resolved as a result. However, these techniques have a limited processing capacity and are not particularly focused on time series problems. A complete set of meteorological sensors on every wind farm is also not realistically expected in order to acquire the necessary meteorological data in practical scenarios. Based on historical wind power data modeling, this paper organically combines BI-GRU [3] and spatial attention and proposes a multi-step wind power forecasting network structure that does not depend on meteorological data. The calculation requirement of this model is relatively small and solves the problem of forecasting curve lag to a large extent.

2 Materials and Methods

2.1 LSTM

LSTM (Long Short Term Memory) is a neural network with an optimized structure that Jurgen Schmidhuber and Sepp Hochreiter introduced in 1997 [4], which has been extensively utilized in time series data processing and natural language analysis. After a lot of research and practical application, LSTM has been proven to improve the gradient disappearance or gradient explosion issue that occurs during RNN training. LSTM not only inherits the feature of passing state in the hidden layer of RNN, but also adds a new cell state for storing long-distance information, which makes it have better performance. Based on the structure of RNN, LSTM is improved to control the transmission state of information through a gate structure, which mainly includes three "gates," namely the forget gate (f_t), input gate (i_t), and output gate (o_t). The forgetting gate selectively discharges information from the unit's previous state. The input gate regulates how much information is updated at the moment, and the output gate selects which processed information to output. Figure 1 depicts the LSTM's structural layout.

In Fig. 1, the cell state is represented by C, input is represented by x, hidden layer output is represented by h, the output of the LSTM unit at an earlier time is represented by h_{t-1}, the memory of the unit at an earlier time is represented by C_{t-1}. The present network's output is h_t, and the unit's memory is C_t. σ (sigmoid function) and tanh (hyperbolic tangent function) are commonly used activation functions in

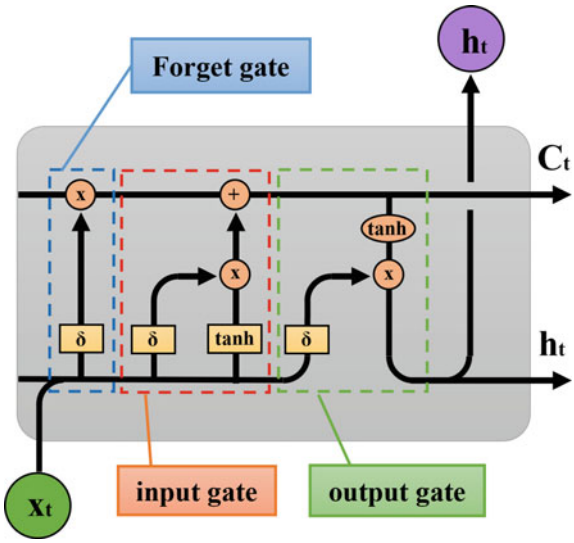

Fig. 1 LSTM neural unit structure

LSTM. The following is the calculation process for LSTM:

$$f_t = \sigma\left(W_f \cdot \left[h_{t-1}, x_t\right] + b_f\right) \tag{1}$$

$$i_t = \sigma\left(W_t \cdot \left[h_{t-1}, x_t\right] + b_i\right) \tag{2}$$

$$\widetilde{C}_t = \tanh\left(W_t \cdot \left[h_{t-1}, x_t\right] + b_c\right) \tag{3}$$

$$C_t = f_t * C_{t-1} + i_t * \widetilde{C}_t \tag{4}$$

2.2 GRU

In 2014, Cho et al. [3] proposed a variant of RNN, GRU (Gate Recurrent Unit), which has a network structure that is less complex than LSTM. Although the GRU has no dedicated memory storage unit, it still uses gate structures to control the retention of information, including resetting and updating gates. Grus can solve the problem of long-distance information dependence well and avoid the problem of gradient disappearance effectively. Therefore, deep learning applications like natural language processing frequently use it.

In Fig. 2, as shown in Fig. 1: x_t is the input vector at time t; h_t, h_{t-1} is the hidden state at time t and time $t-1$. In addition, r_t and z_t are respectively replacement doors

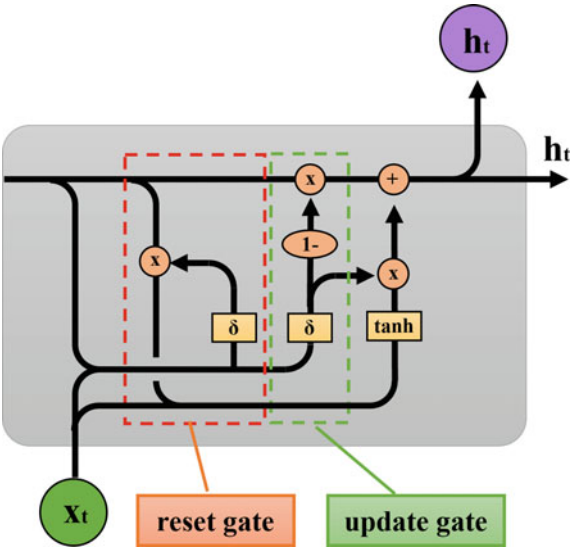

Fig. 2 GRU neural unit structure

and renewal doors. z_t is going to be a number between 0 and 1 after the activation function. The closer z_t is to 1, the more data is "memorized". And the closer z_t gets to zero, the more it forgets. The calculation process for GRUs is as follows:

$$r_t = \sigma\left(W_r \cdot \left[h_{t-1}, x_t\right] + b_r\right) \tag{5}$$

$$z_t = \sigma\left(W_z \cdot \left[h_{t-1}, x_t\right] + b_z\right) \tag{6}$$

$$\widetilde{h_t} = \tanh\left(W_h \cdot \left[r_t * h_{t-1}, x_t\right] + b_h\right) \tag{7}$$

$$h_t = (1 - z_t) * h_{t-1} + z_t * \widetilde{h_t} \tag{8}$$

2.3 *Proposed Method*

Figure 3 displays the proposed method's overall structure. The input data will be sent to the special attention module after passing through the bidirectional GRU network, and then the prediction output will be obtained through the four fully connected layers. The gray area in the figure is the special attention module proposed in this paper. The features extracted through the bidirectional GRU network will pass through an AdaptiveAvgPool1d layer. After passing through this layer, the

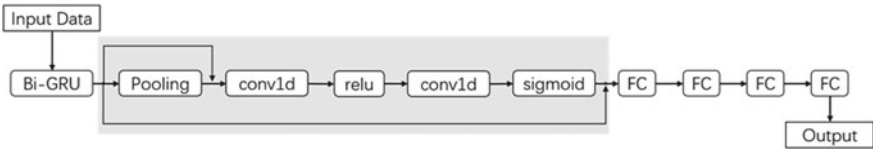

Fig. 3 The structure of the proposed model

features will be compressed, and then the pooled features will be cascaded into one-dimensional convolution. The input channel of this convolution is 128, the output channel is 8, and the convolution kernel and step size are both 1. Then, the features pass through a relu layer, and then pass through a one-dimensional convolutional network with an input channel of 8 and an output channel of 128. Similarly, the convolution kernel size and step size of this one-dimensional convolutional network are both 1. Finally, after passing through the sigmoid layer, the obtained feature is dotted with the feature extracted through the bidirectional GRU network to obtain the final feature. So, the forecasting accuracy of wind power can be greatly improved.

This paper presents a method to predict wind power. The objective of this method is to obtain a relatively accurate predicted value, and to obtain the best parameters through the loss function MSE, to minimize the loss value as much as possible.

$$\mathrm{MSE} = \frac{1}{n}\sum_{i=1}^{n}(\widetilde{y}_i - y_i)^2 \tag{9}$$

In the loss function MSE, the stereotyped data set's entire sample count is represented by n, y_i and $\widetilde{y}_i$ represent the true value and corresponding predicted value of the ith sample respectively.

Generally speaking, feature vector extraction, a data processing technique, is used to transform complex data sets into simple feature vectors so as to analyze and process original data more efficiently. In accordance with the traditional feature vector extraction method, the BI-GRU is utilized in the model given in this paper to generate continuous feature vectors to send a large amount of wind power signal data to the attention module. With this model, we can extract effective wind power features, which can improve the accuracy of wind power prediction.

3 Experience

3.1 Experiment Hardware and Details

We selected the data of a wind farm in East China as a sample, and sampled it between July 10, 2019, and September 28, 2021, which verified the validity of the proposed method in this paper. Based on the deep learning framework of Pytorch,

this paper uses Python3.6.5 in the Ubuntu20.04 environment for experiments. We conducted ten sets of experiments in total: two sets of experiments were conducted under five different window sizes, one based on BI-GRU, and the other based on BI-GRU and spatial attention. In the experiment, we updated the model's parameters using stochastic gradient descent and adopted the learning rate attenuation strategy [5] in deep learning. In addition, we use the Dropout [6] mechanism to effectively avoid the problem of overfitting artificial intelligence neural network algorithms.

3.2 Data Preprocessing and Segmentation

The magnitude difference between different data items may significantly affect the accuracy of the neural network prediction model, so we solve the above problems by normalizing the data. The normalization of data first requires data preprocessing to make the processed data conform to the standard normal distribution, that is, the data is mapped to the interval with the same measurement through different normalization methods. This paper adopts the method of maximum and minimum value normalization to complete the normalization of data and standardizes data items of different magnitude according to the calculation method shown in formula (10).

$$x* = (x - \min)/(\max - \min) \tag{10}$$

In this paper, we segmented the data using the sliding window approach, setting the move size to 1 and the window size to 24, 36, 48, 96, and 144 in turn.

3.3 Evaluation Methods

In deep learning, we often use Root Mean Square Error (RMSE), Mean Absolute Error (MAE), and Mean Absolute Percentage Error (MAPE) to measure the accuracy and feasibility of machine learning model prediction results. MAE and RMSE assess the absolute difference between the actual value and the anticipated value, while MAPE measures the relative deviation. Then, when applied to wind power prediction, if the RMSE, MAE, and MAPE values are smaller, the anticipated value is closer to the actual wind power value, which means that the model has higher wind power prediction accuracy.

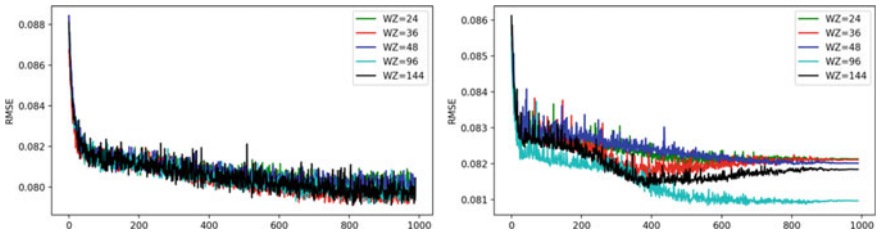

Fig. 4 Train and test set convergence contrast diagram

Table 1 Ability of different models in the training process

GRU	Attention	WZ24	WZ36	WZ48	WZ96	WZ144
		RMSE	RMSE	RMSE	RMSE	RMSE
√		0.081422	0.081308	0.081586	0.081146	0.081333
√	√	0.081938	0.081413	0.081963	0.080839	0.081320

3.4 Training Window Discussions Segmentation

Our experimental data is based on normalized data. During the training process, it has been discovered that as the number of training iterations increases, the training sets of all experiments converge not only quickly but also stably. But as Fig. 4 shows, the test curve is still different compared with the training curve. The test curve under different Windows will have different trends. For example, when the window size is 48, the test curve will always be in a state of decline. When the window size is 144, the test curve will first drop and then rise. When the window size is 96, the test curve will decline gently at first and then continue to decline. Table 1 displays the abilities of different models during training. The experimental findings indicate that when the window size is 96, the RMSE of each model is the smallest. Therefore, when the window size is 96, the method suggested in this paper can be optimized.

3.5 Experiment Results

Figure 5 shows the predicted results of the last 4095 points of the model, where the red line represents the anticipated value of the test set and the blue line represents the actual value. It can be found from the figure that: except for the two points of 553 and 737, the rest of the predicted results are close to the actual power. However, the data of these two points rose suddenly, which we believe is caused by the sudden increase of wind speed. However, there is no such uncertain change in the historical data, so the prediction of these two points is small. The calculation shows that the maximum error in the whole cycle is 7.6%, which is slightly larger. In addition to these two

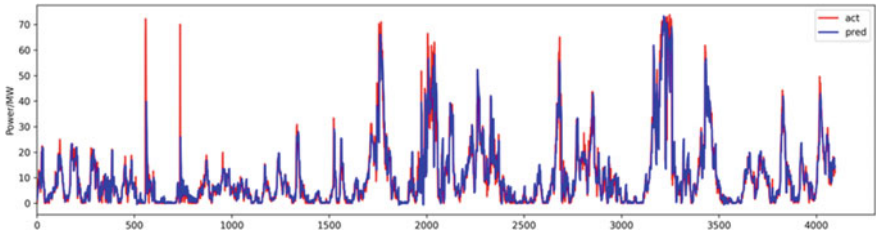

Fig. 5 Comparison diagram of predicted and real values based on the test set

points, the algorithm of this model proposed in this paper has a high precision of wind power prediction and a fast response speed.

4 Conclusions

A new wind power forecasting model independent of meteorological data is proposed to address the issues of wind power volatility and power grid system stability. The model effectively combines the BI-GRU and spatial attention for better expression of data features and improved accuracy of the wind power prediction model.

References

1. Jiang ZY, Jia QS, Guan XH (2019) A review of wind power generation prediction methods at multiple spatio-temporal scales. Acta Automatica Sinica 45(1):51–71
2. Zhou NC, Liao JQ, Wang QG et al (2019) Analysis and prospect of deep learning application in smart grid. Automation Electr Power Syst 43(4):180–197
3. Chung J, Gulcehre C, Cho KH et al (2014) Empirical evaluation of gated recurrent neural networks on sequence modeling. Eprint Arxiv 12:1–9
4. Hochreiter S, Schmidhuber J (1997) Long short-term memory. Neural Comput 9(8):1735–1780
5. Loshchilov, Hutter F (2016) SGDR: stochastic gradient descent with warm restarts
6. Srivastava N, Hinton G, Krizhevsky A, Sutskever I, Salakhutdinov R (2014) Dropout: a simple way to prevent neural networks from overfitting. J Mach Learn Res 15(1):1929–1958

Capacity Detection Method of Uninterrupted Special Transformer Based on Big Data and Pattern Recognition

Wei Cui, Wei Ge, Peng Li, Xun Ma, and Yong Wang

Abstract In order to ensure the normal operation of uninterruptible special transformers and reduce the heavy losses caused by faults, a capacity detection method of uninterruptible special transformers based on big data and pattern recognition is proposed. Under the big data and pattern recognition, the optimal membership degree of capacity detection of uninterruptible special transformer is obtained, and the characteristic parameters of transformer operation state are extracted according to the results. Thus the load model of uninterruptible special transformer is constructed, and the capacity detection of uninterruptible special transformer is realized. The experimental results show that the proposed method can directly reflect the internal operation of the special transformer and detect the capacity problem of the special transformer without power outage.

Keywords Big data · Pattern recognition · No power failure · Special transformer · Capacity detection

1 Introduction

With the increasing social demand, energy supply and distribution equipment have gradually become one of the focuses of social attention. Special transformer is an indispensable part of distribution equipment because of its special properties and wide application fields. However, due to the special operating environment of special transformers, once problems occur, their maintenance costs are high, which will not only affect their safe operation, but also bring huge economic losses [1]. Therefore, it is increasingly urgent to find and solve the problem of insufficient capacity in time

X. Ma · Y. Wang (✉)
Marketing Service Center, State Grid Hebei Electric Power Company, Shijiazhuang 050000, Hebei, China
e-mail: dl_wyo@163.com

W. Cui · W. Ge · P. Li
State Grid Hebei Electric Power Co., Ltd, Shijiazhuang 050000, Hebei, China

S. Yadav et al. (eds.), *Energy Power and Automation Engineering*, Lecture Notes in Electrical Engineering 1118, https://doi.org/10.1007/978-981-99-8878-5_87

during the use of special transformers, ensure their safe and efficient operation, and save energy costs.

At present, the methods commonly used for capacity detection of special transformers are based on Gaussian process [2] and deep learning algorithm [3]. Gaussian process test needs to detect the substation equipment after the transformer is turned off, and the detection result is more accurate, but it will affect the normal work of users. Although the deep learning algorithm detection will not affect the operation of the transformer, it has low accuracy, heavy workload, and high cost. Based on this, it is the key to solve the current capacity detection problem to develop a special transformer capacity detection method without power failure, which can not only meet the accuracy of capacity detection, but also will not affect the daily work of users. At the same time, with the continuous development of big data and artificial intelligence technology, it has become a feasible option to detect the capacity of special transformers based on these technologies. Based on big data and pattern recognition technology, combined with the operating parameters and historical operation data of special transformers, a prediction model for capacity detection of special transformers can be established to monitor the capacity status of special transformers in real time. Therefore, this paper proposes a special transformer capacity detection method based on big data and pattern recognition technology. This method not only solves the problems existing in current capacity detection, but also can comprehensively monitor and analyze the operation of special transformers.

2 Capacity Detection Under Big Data and Pattern Recognition

2.1 Obtaining Optimal Membership Degree Based on Big Data and Pattern Recognition

Big data is a massive, high-dimensional, heterogeneous, and distributed data collection, which contains various data types and formats. In the capacity detection of special transformers without power failure, the application of big data is mainly to determine whether the capacity of transformers is normal by collecting and analyzing a large number of transformer operation data [4]. By analyzing the big data, we can build the operation state model of the uninterrupted special transformer, and then through the big data analysis and modeling technology, we can predict the current state of the transformer and detect whether there is capacity problem. Based on the characteristics of big data, in the capacity detection of special transformers without power failure, data mining technology is used to find the rules and patterns, so as to determine whether its capacity is normal more accurately.

Pattern recognition is an important technology applied in big data analysis. It is to analyze the data, extract some rules and characteristics from it, and then identify it through models or algorithms to achieve the purpose of detecting the data. In the

capacity detection of special transformers without power failure, pattern recognition is mainly used to analyze the characteristics of transformer vibration signals, temperature records, and electrical parameters, so as to establish the relationship between various characteristic indexes, and the capacity detection is carried out by multivariate model analysis, neural network model and other methods. Pattern recognition is commonly used in the capacity detection of uninterruptible special transformers. This paper takes the fuzzy neural network method in pattern recognition technology as the core to obtain the optimal membership degree of uninterruptible special transformers. The detection process is as follows:

Step 1: Sample data

This part of the detection data is a feature vector, and the capacity data of the uninterrupted special transformer is described as $\lambda_{n\times m}$.

Step 2: Data standardization operation

Standardize the operation of pattern recognition for the capacity of uninterrupted special transformer based on the principle of minimum $\lambda_{n\times m}$ usage. The operation method is:

$$\lambda'_{ij} = \frac{\lambda_{ij}}{\lambda_{j\max} - \lambda_{j\min}} \tag{1}$$

In Formula (1), λ'_{ij} represents the capacity characteristic data after standardization operation; $\lambda_{j\max} = \max\limits_{1\le j\le n}\{\lambda_{ij}\}$ represents the maximum value of the characteristic value of the j-th defect; $\lambda_{j\min} = \min\limits_{1\le i\le n}\{\lambda_{ij}\}$ represents the minimum value of the j-th defect characteristic value, and λ_{ij} represents the original data of pattern recognition standardization operation.

Step 3: Set membership function

Set the value range of the capacity characteristic data λ'_{ij} after standardization operation to [0, 1], and calculate the frequency value D_F of the value range by dividing the domain β with variable step size. The Formula is:

$$D_F = \operatorname*{Lin}_{m\to\infty} \frac{\lambda'_{ij} \in \beta}{m} \tag{2}$$

In Formula (2), m represents the total number of data standardization operations.

Using the method of big data and pattern recognition to select the optimal membership function, the Formula is:

$$L_{\mathrm{SD}} = \begin{cases} 0, y < a \\ 1, a \le y \le b \\ D_F, y > b \end{cases} \tag{3}$$

In Formula (3), L_{SD} represents the optimal membership degree; a and b represent fuzzy terms of capacity characteristics of special transformers without power failure.

2.2 Extraction of Characteristic Parameters of Transformer Operation State Based on Big Data and Pattern Recognition

Using big data and pattern recognition to process the collected vibration signal data of uninterrupted special transformer, the specific steps are as follows:

Assuming that the samples contain n data sets, including normal and fault signals, and all samples have m parameters to be selected related to fault signals, the B parameters in the selected A sample are weighted to get W_B^A [5]. If the initial value of W_B^A is equal to 0, practice the parameters to be selected in the sample in order:

$$W_B^A = \left[\frac{S(\eta, \theta)}{n} - \frac{S(\gamma, \theta)}{m} \right] \times L_{\mathrm{SD}} \tag{4}$$

In Formula (4), $S(\eta, \theta)$ represents and selects different types of sets of samples; $S(\gamma, \theta)$ represents the same type of signal set as the selected sample; η represents different types of nearest neighbor points; γ represents the nearest neighbor point of the same type; θ represents the number of neighbors.

In order to reduce the influence of sample classification on the parameters to be selected, they are close to the same type of samples and far away from different types of samples, and the weights calculated according to the Formula are higher. The weights obtained according to sample practice can feed back the relationship between feature parameters and sample types, and feature subsets are constructed by selecting feature parameters according to the weights.

Because some signal parameters are closely related, big data and pattern recognition algorithm are used to obtain the parameter types with large transformer fault weight, and the final feature parameter subset is obtained by removing redundant vectors. For the parameters with relatively large weights, the relationship between them is analyzed, and the correlation coefficient is calculated to determine the relationship size. If the two parameters are highly correlated, the parameters with relatively large weights are saved and the parameters with relatively small weights are discarded, so as to extract the operation state characteristic parameters of the uninterruptible special transformer. The Formula is as follows:

$$R_{\mathrm{FD}} = \frac{\mathrm{cov}(X, Y)}{J_X J_Y} \times W_B^A \tag{5}$$

In Formula (5), $\mathrm{cov}(X, Y)$ represents covariance and $\sigma_X \sigma_Y$ represents the product of mean square error.

2.3 Establish the Load Model of Uninterrupted Special Transformer

In the special transformer without power failure, the cumulative contribution value of transformer load can be directly calculated by Formula (6), and the Formula is:

$$G_X = \frac{\sum_{i=1}^{n} E_i}{\sum_{j=1}^{m} E_j} \times R_{\mathrm{FD}} \tag{6}$$

In Formula (6), E_i represents the i-th feature vector index; E_j represents the total value of index variables of the j matrix. Through the calculation of the above Formula, the load model of the uninterrupted special transformer as shown in Fig. 1 is obtained.

In Fig. 1, if the coordinate is rotated by an angle, the information of the loss variable can be obtained, so that the coordinate in the X_1 axis is transformed to the direction of the short axis, and the transformation equation of the coordinate is:

$$\begin{cases} g_x = x_1 \cos \varepsilon_g + x_2 \sin \varepsilon_g \\ g_y = y_1 \cos \varepsilon_g - y_2 \sin \varepsilon_g \end{cases} \tag{7}$$

In Formula (7), x_1, x_2, y_1 and y_2 are all represented as coordinate axes in the load model of the special transformer without power failure; g_x and g_y respectively represent the rotation components of the circle in the X axis and Y axis of the coordinate system; ε_g represents the direction angle of the circle rotation in the coordinate system.

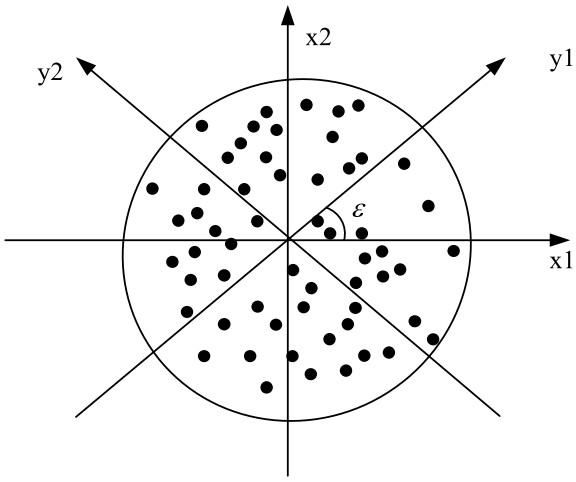

Fig. 1 Load model of special transformer without power failure

2.4 Realize the Capacity Detection of Special Transformer Without Power Failure

The purpose of realizing the capacity detection of the uninterruptible special transformer is to detect whether the actual capacity of the uninterruptible special transformer is consistent with the rated capacity, so as to ensure its normal operation and meet the actual demand. All the recorded data are divided into several standard categories, and the minimum value $L_{c,d}$ is found through the definition of Euclidean distance [6].

$$L_{c,d} = \frac{\sqrt{(h_{c1} - h_{d1})^2 + (h_{c2} - h_{d2})^2 + \cdots + (h_{cn} - h_{dn})^2}}{G_K(g_x, g_y)} \tag{8}$$

In Formula (8), $L_{c,d}$ represents the Euclidean distance from grid c to grid d; G_K represents the dimension from the object to the cluster center. Through Euclidean distance, the distances of different analogies can be directly obtained. The better the clustering effect of the time-domain waveform of the vibration signal of the special transformer without power failure, the smaller the Z_B index, and the Formula for solving the Z_B index is:

$$Z_B = \frac{l_i(e) - l_j(f)}{\max\{l_j, l_i\}} \tag{9}$$

In Formula (9), $l_i(e)$ and $l_j(f)$ respectively represent the average distance between the object e or f and the center vector; $\max\{l_j, l_i\}$ represents the solution of the maximum value in the clustering effect of the special transformer without power failure. Through Formula (9), we can directly get the results of the capacity detection of the uninterruptible special transformer, and with Z_B as the core, we can directly get the load state index of the uninterruptible special transformer, thus completing the research on the capacity detection method of the uninterruptible special transformer based on big data and pattern recognition.

3 Experimental Analysis

In order to verify the validity of the capacity detection method of uninterrupted special transformer based on big data and pattern recognition, experiments are carried out. The experimental data are 500 pieces of sample data provided by an electric power research institute. The sample data include the normal state of the uninterruptible special transformer and two types of failures of the uninterruptible special transformer, namely, overheating failure and energy discharge $S3$. 150 training samples and 30 test samples were randomly selected from the sample data. The data types of experimental samples are shown in Table 1.

Table 1 Failure types of experimental sample data

Fault type	Training sample	Test sample
Normal conditions	50	5
Overheating temperature	55	10
Energy discharge	50	15
Amount to	150	30

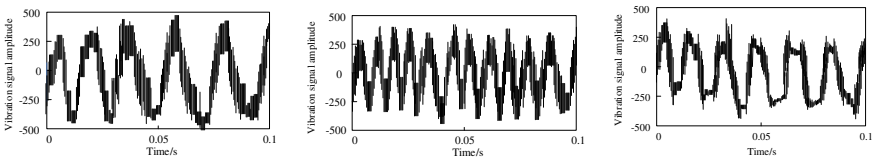

(a) A phase (b) B phase (c) C phase

Fig. 2 Time-domain waveform diagram of vibration signal of uninterrupted special transformer under the proposed method

In order to verify the effectiveness of this method for capacity detection of special transformers without power failure, simulation experiments are carried out. A special transformer that is working but has a fault problem is selected as an experimental sample. The tested transformer is three-phase, assuming that there is a short-circuit fault before phase C, and there is no new winding. The time-domain waveform diagram of vibration signal of special transformer without power failure under the proposed method is shown in Fig. 2.

From Fig. 2, it can be seen that the amplitude of A-phase and B-phase vibration signals is regular, fluctuating up and down, resulting in small errors due to a little noise. Observing phase C, it was found that the vibration signal fluctuated irregularly and was relatively chaotic. At 0.06 s, it began to appear that there was a fault problem in phase C. By analyzing the collected signal data, it was determined that the winding in phase C had a fault problem, thus the amplitude of the vibration signal was determined, which directly reflected the internal operation status of the special transformer, indicating that there was a capacity problem in the special transformer without power failure. To sum up, the proposed method can be used to detect the capacity problem of uninterrupted special transformer.

4 Conclusion

With the increasing demand for electricity in life and production, uninterrupted special transformers occupy an important position in the power system. Transformer capacity detection is one of the key concerns, and the consequences are unimaginable once there is an accident. Therefore, this paper proposes a capacity detection

method for uninterruptible special transformers based on big data and pattern recognition. Through simulation experiments, it is proved that the proposed method can detect the capacity problem of uninterrupted special transformer under big data and pattern recognition. However, this paper does not take into account the influence of weather changes and other factors on the signal of the uninterrupted special transformer. In future research, it is necessary to experiment under various interferences to find a better detection method to improve the universal applicability of the proposed method.

Acknowledgements The study was supported by Science and Technology Project of State Grid Hebei Electric Power Co., Ltd., Project Name: Research and Development of Uninterruptible Special Transformer Capacity Detection Equipment, Project No.: kj2021-036.

References

1. Soni R, Mehta B (2021) Review on asset management of power transformer by diagnosing incipient faults and faults identification using various testing methodologies. Eng Fail Anal 128(2):105634
2. Liu P, Zhao XY (2022) Monitoring of transformer winding micro deformation based on gaussian process. Comput Simul 39(1):86–89
3. Yu X, Dong M, Xing Y (2021) Transformer text recognition with deep learning algorithm. Comput Commun 178(8):153–160
4. Inostroza-Osses MA, López-Santos O, Aldana-Rodríguez YA (2022) Alternative generation of the output voltage waveform in an asymmetric transformer-based cascaded multilevel inverter under fault conditions. Mathematics 10(19):1–15
5. Huerta-Rosales JR, Granados-Lieberman D, Garcia-Perez A (2021) Short-circuited turn fault diagnosis in transformers by using vibration signals, statistical time features, and support vector machines on FPGA. Sensors 21(11):3598
6. Bundak CEA, Abd Rahman MA, Karim MKA (2022) Fuzzy rank cluster top k euclidean distance and triangle based algorithm for magnetic field indoor positioning system. Alex Eng J 61(5):3645–3655

Entropy Weight Detection Technology of Special Transformer Capacity Under Complex Working Conditions Without Power Failure

Zhibo Wang, Guanghua Wu, Anlei Liu, Shujun Ji, and Shifang Hao

Abstract The capacity detection of special transformer under complex working conditions is easily affected by random noise on site, which leads to poor detection effect. In order to solve this problem, the entropy weight method is proposed to detect the capacity of special transformers under complex working conditions without power failure. Constrained variational model is constructed to obtain fault detection information. Detect the connection of transformer winding wires, calculate the power supply voltage on the loop, and detect the defects of transformer insulation winding. By calculating the contact point temperature between the bushing lead and the inner conduit, the defects of transformer insulation bushing are analyzed, and the capacity entropy weight method for special transformer under complex working conditions is realized. The experimental results show that the proposed technology can accurately detect the turn-to-turn short circuit fault of special transformer, and the fitness curve approaches the optimal value with iteration.

Keywords No power failure · Special transformer · Complex working conditions · Capacity entropy weight method · Detection technology

1 Introduction

In modern society, the power system is not only the foundation of social and economic development, but also the necessity of people's life. As an important part of the power system, special transformers bear the important responsibility of ensuring the normal operation of the power system. However, there are many complicated working conditions in the use of special transformers, which poses great challenges to the

G. Wu · A. Liu (✉) · S. Ji · S. Hao
Marketing Service Center, State Grid Hebei Electric Power Company, Shijiazhuang 050000, Hebei, China
e-mail: Liuanlei1201@163.com

Z. Wang
State Grid Hebei Electric Power Co., Ltd, Shijiazhuang 050000, Hebei, China

S. Yadav et al. (eds.), *Energy Power and Automation Engineering*, Lecture Notes in Electrical Engineering 1118, https://doi.org/10.1007/978-981-99-8878-5_88

detection and evaluation of their performance parameters [1]. Traditional detection methods rely on experimental tests under static or partial dynamic conditions, but these methods are affected by working conditions, data quality, and testing methods, and it is difficult to accurately characterize the actual situation of special transformers [2, 3]. In order to solve this problem, entropy weight detection technology came into being. Entropy weight method is a multi-factor evaluation method based on information entropy theory. Its uniqueness lies in that it can consider the correlation between various factors and analyze the influence of various factors on comprehensive evaluation indicators on the basis of maintaining the internal information of the data itself, so as to obtain multi-factor comprehensive evaluation results. In the detection of special transformer, the working condition data is taken as the factor index of entropy weight method, and the entropy weight model is constructed, which can be used to evaluate the capacity of special transformer under complex working conditions and has certain advantages.

Through in-depth research on the capacity entropy weight detection technology of special transformer under complex working conditions without power failure, it can provide strong support and guarantee for power system security and provide new ideas and methods for the application and development of special transformers.

2 Detection of Capacity Entropy Weight Method Without Power Failure

2.1 Insulation Defect Fault Detection of Special Transformer

In order to ensure the stability and safety of special transformer operation without power failure, non-contact detection method is needed. Entropy weight method is a commonly used multi-index decision-making method, which can comprehensively consider various evaluation indexes and make a reasonable decision-making scheme. By calculating the weight of each index, it comprehensively calculates the total score of each index, thus obtaining the final evaluation result [4]. Therefore, using entropy weight method to detect the capacity of special transformer under complex working conditions can effectively improve the detection accuracy and improve the reliability and safety of equipment.

Under the condition of no power failure, the entropy weight method for detecting the capacity of special transformer under complex working conditions needs to decompose multiple modes in the frequency domain of the original signal, and in the process of decomposition, a constrained variational model is constructed, which can be expressed as:

$$\begin{cases} \min \sum\limits_{n} \frac{\{\lambda(t)\}e^{j}}{f_n(t)} \\ \text{s.t.} \sum\limits_{n=1} f_n(t) = a(t) \end{cases} \tag{1}$$

In formula (1), $\lambda(t)$ stands for impulse function; $f_n(t)$ stands for modulus function; $a(t)$ stands for fault signal; j stands for imaginary unit.

The fault types of insulation defects in special transformers can be divided into winding defects and bushing defects according to the fault location. Combined with the constrained variational model of variational modal decomposition, the fault detection information can be obtained in time.

Defect of Insulation Winding of Special Transformer

The defect of insulation winding of special transformer refers to the failure, fracture, and short circuit of transformer winding due to the reasons of insulation structure, material, manufacture, and operation, which affects the normal operation of transformer. Special transformers are mainly used in special fields, such as civil buildings, nuclear power plants, petrochemical, and other industrial fields, so their maintenance and repair have high technical difficulties and risks.

The DC resistance of special transformer has nothing to do with its surface insulation state, but once insulation fault occurs, its DC resistance will be abnormal. The equivalent circuit of inductance and resistance of special transformer winding is simply decomposed into an equivalent circuit. When DC voltage is applied to the winding of special transformer, the induced current will not change sharply at the moment when the circuit is turned on, and the current value is 0. Because there is no current in the resistor, there is no voltage drop across the resistor, so it can be regarded as the supply voltage applied to the inductor [5].

The calculation formula of power supply voltage is:

$$U_H = I_C R_C + \theta \frac{\mathrm{d}I_C}{\mathrm{d}t} \tag{2}$$

In formula (2), θ represents winding inductance; R_C stands for series resistance; t represents time; I_C stands for series current.

The current change rate is positive, indicating that the current value increases. When the current gradually increases, the voltage will also increase. Under the constant total voltage, the voltage at the inductor gradually decreases and the voltage is close to zero. Therefore, the voltage across the resistor is the supply voltage, and the current is stable. In this case, the measured DC resistance is compared with the standard resistance. Test circuit diagram, as shown in Fig. 1.

As can be seen from Fig. 1, when the current in the galvanometer is 0 under the action of the resistor, there is no potential difference between the two terminals connecting the galvanometer, and the line is in a balanced state at this time. In the equilibrium state, the measured DC resistance is compared with the standard resistance value. If the measured DC resistance value is greater than the standard resistance value, then there is a turn-to-turn short circuit in the connection, so the defect of the insulation winding of the special transformer can be determined.

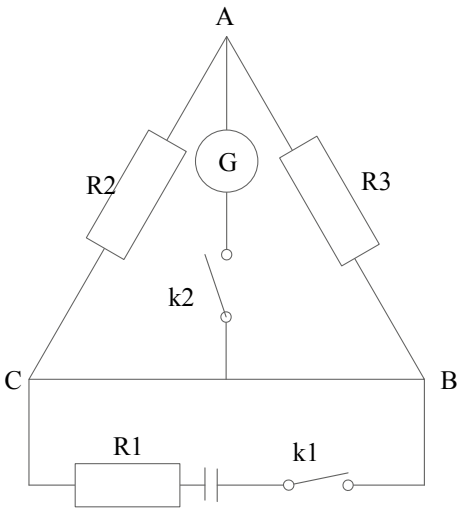

Fig. 1 Structural diagram of detection circuit

Defect of Insulation Bushing of Special Transformer

The defect of insulation bushing of special transformer refers to the problems such as oxidation, aging, and cracking caused by the structure, material, manufacture, and operation of insulation bushing, which affects the winding safety and electrical performance of transformer. Insulating sleeve is one of the important electrical insulation structures in transformer, which is usually wrapped around the winding to protect the winding and isolate it safely.

The working current of the special transformer is realized through the passages such as the wire clamp, the internal thread of the military cap, the lead wire passing through the core, the winding, etc., and the internal pipeline of the high-voltage bushing is used as the bushing support, so that no current can pass through. Due to the influence of voltage, the special transformer in the distribution network has partial discharge, which leads to the decline of insulation level and brings certain safety risks to the equipment.

Calculating the induced voltage of bushing through-core lead after variational mode decomposition can be expressed as:

$$U_G = \ln \frac{R_2 + R_3}{R_1} \times I_Y \tag{3}$$

In formula (3), R_1 represents the lead resistance, and R_2 and R_3 both represent the inner tube resistance; I_Y represents the lead current.

In the conduction loop formed by the contact between the lead wire and the inner conduit, the contact point temperature is calculated according to the following formula:

$$I_J \times R_H = \zeta \times \left(T_1^2 - T_2^2\right) \tag{4}$$

In formula (4), I_J represent that current flowing through the contact point; R_H represents the ring structure resistance; ζ stands for Lorenz constant; T_1 represents the highest temperature of the contact point; T_2 represents the average temperature of the surrounding medium.

If the temperature is too high, the contact point will generate a large amount of heat, and the melting temperature of the lead copper conductor will reach the upper limit of welding at the contact point, resulting in welding phenomenon; if the special transformer produces inrush current or short circuit during charging, it will be overheated for a short time. Because of the high contact temperature, the copper conductor will be welded. In addition, the local high temperature will also burn the lead-white yarn, which will cause carbide to fall off, thus causing the insulation sleeve of the special transformer to fail.

2.2 *Realizing the Detection of Special Transformer Capacity Under Complex Working Conditions by Entropy Weight Method*

In order to ensure the continuity of the production and operation process, the equipment is not shut down, but is maintained, replaced, tested, and troubleshooted while the equipment is running. In this state, the equipment will continue to run without stopping, and it will not affect the normal operation and production of special transformers.

The fitness of special transformer under complex working conditions is calculated by entropy weight method, and the calculation formula is as follows.

$$S = \sum_{j=1}^{n} T_j \times S(\psi) \tag{5}$$

In formula (5), S represents fitness value; T_j indicates the time when the fault occurs; ψ stands for fault cluster; n represents the fault cluster threshold. Quantify the calculated fitness of high-voltage transformer, and define the fitness as any real number between 0 and 100. When the calculation result of S approaches 0, it means that the fitness of the equipment in operation is low, that is, the equipment is in a fault state. When the calculation result of S is the middle value between 0 and 100, it shows that there is a latent fault in the operation of the equipment. When the calculation result of S approaches 100, it shows that the equipment has a high degree of adaptability in operation, that is, the equipment is in normal operation. According to the above method, the entropy weight method is used to detect the capacity of the special transformer under complex working conditions, and the detection results are matched with the operation time sequence of the equipment. Finally, the detection

results such as fault state, type, and location are output in a visual form to realize the entropy weight method detection of the capacity of the special transformer under complex working conditions.

3 Experimental Analysis

In order to verify the practical application effect of entropy weight method for capacity detection technology of special transformer under complex working conditions without power failure, the method designed in this paper is compared and tested by taking a large power enterprise in a certain area as an example. Special transformer equipment of ISO-SE model is selected as the experimental component, and it is connected with GNLV3-12 substation control box by means of transmission wires. Before the experiment, the operation parameters of the special transformer put into use in this enterprise are analyzed, and the specific contents are shown in Table 1.

According to the index values shown in Table 1, the relevant parameters in the current loop of the special transformer are set to ensure that the point charge can be in a stable transmission state. In order to ensure the authenticity of the experimental results, all experimental equipment indicators should be reset to zero before the experiment begins. According to Fig. 2, screen the experimental variable indicators.

According to the screening process of experimental data in Fig. 2, some faults are artificially added to the winding simulating turn-to-turn short circuit fault. Draw the detection frequency response curve of normal running winding and turn-to-turn short circuit fault winding, and the results are shown in Fig. 3.

As can be seen from Fig. 3, the frequency response curve of the faulty winding is generally the same as that of the winding under normal operation, except that the curve with turn-to-turn short circuit fault moves up a little compared with that of the normal winding, and the position of two peak points moves forward and the other moves backward. This is consistent with the artificially added fault, so it can be proved that the proposed technology can accurately detect the turn-to-turn short circuit fault of special transformers.

Table 1 Operating parameters of special transformer

Number	Experimental installation	Parameter
1	Special transformer equipment	ISO-SE
2	Substation control box	GNLV3-12
3	Internal resistance of special transformer	5.8 × 1013 Ω
4	Work efficiency	50–60 Hz
5	Maximum number of iterations	> 90%
6	Internal resistance of special transformer	90

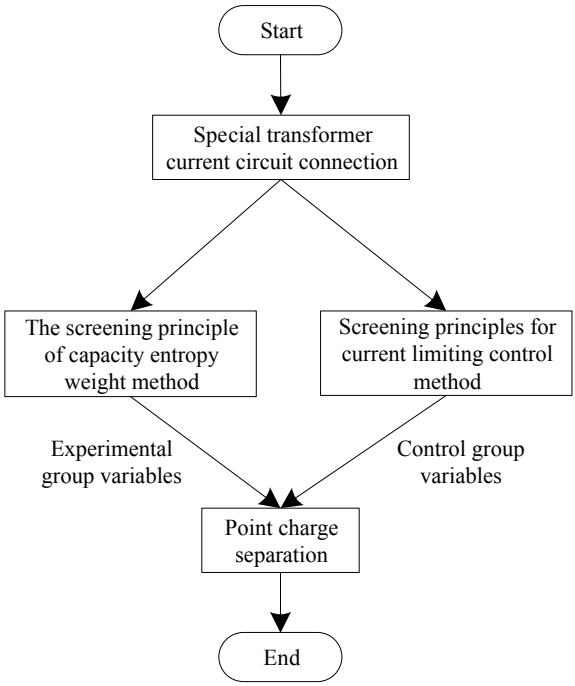

Fig. 2 Experimental data screening process

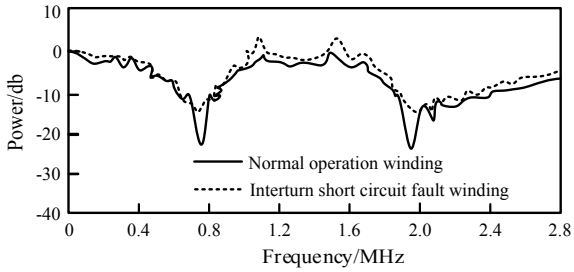

Fig. 3 Comparison of detection results between normal running winding and interturn short circuit fault winding

In order to further verify the effect of the proposed technology, the adaptability of the entropy weight method for detecting the capacity of special transformers under complex working conditions is tested. Under the condition of no power failure, the maximum number of iterations is set to 90 and the optimal fitness is 98, and the obtained results are shown in Fig. 4.

As can be seen from Fig. 4, the fitness curve of the proposed technology approaches the optimal value with the iteration of the experiment. When the number of iterations is 20, the fitness curve is close to the optimal fitness value; when the number of iterations is 30, the fitness curve is in a convergent state. This shows that the proposed technology can quickly converge on the complex working condition

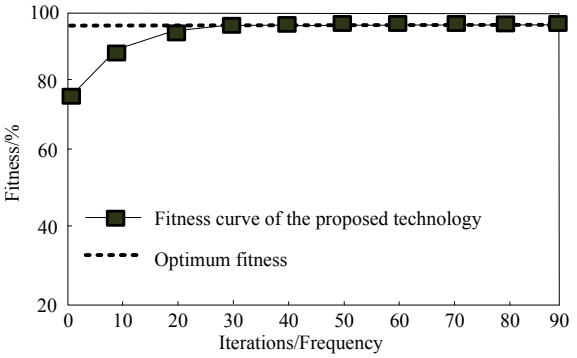

Fig. 4 Detection results of fitness change of special transformer under complex working conditions by entropy weight method

capacity of special transformers without power failure, and the detection effect is good.

4 Conclusion

In this paper, the entropy weight method is proposed to detect the capacity of special transformer under complex working conditions without power failure. Through experiments, the conclusions are as follows: (1) The frequency response curves of faulty windings are generally the same as those of windings under normal operation, and the proposed technology can accurately detect the turn-to-turn short circuit fault of special transformer. (2) The fitness curve of the proposed technology approaches the optimal value with the iteration of the experiment.

Acknowledgements The study was supported by Science and Technology Project of State Grid Hebei Electric Power Co., Ltd., Project Name: Research and Development of Uninterruptible Special Transformer Capacity Detection Equipment, Project No.: kj2021-036.

References

1. Popescu M, Mastorakis NE, Popescu-Perescu LN (2022) New aspects providing transformer models. Perescu 8(1):1–10
2. Chen Q, Wu W, Gao X (2022) Sound absorption performance of aluminum silicate fiber for noise and vibration reduction of distribution transformer. J Phys Confer Ser 2152(1):012037
3. Inostroza-Osses MA, López-Santos O, Aldana-Rodríguez YA (2022) Alternative generation of the output voltage waveform in an asymmetric transformer-based cascaded multilevel inverter under fault conditions. Mathematics 10(19):1–14
4. Satar B, Zhu H, Bresson X (2022) Semantic role aware correlation transformer for text to video retrieval. IEEE 23(8):19–22
5. Huynh PBT, Kim JH, Yun TY (2022) Dual-resistive feedback wideband LNA for noise cancellation and robust linearization. IEEE Trans Microw Theory Techn 70(4):2224–2235

Research on Vehicle-To-Grid Interaction Architecture and Typical Patterns Based on Cloud-Net-Edge-End

Qing Shi, Weizheng Kong, Hongcai Dai, Zhiqiang Zhang, Siyu Zhang, Chunming Wang, Xiaoyu Wu, and Dian Wang

Abstract There are many factors that influence vehicle-to-network interaction, and their interrelationships are complex. In order to systematically analyze the interactions between various stakeholders in the process of electric vehicle and grid interaction under different interaction modes, this article establishes typical architecture patterns based on cloud-edge and different interaction modes and operating scenarios. This provides an effective method for the evolutionary analysis of vehicle-to-network interaction and enables a targeted approach to developing effective interaction strategies based on a clear understanding of the mechanism of the interaction process.

Keywords Electric vehicles · Vehicle-to-grid interaction architecture · Application scenarios · Typical patterns

1 Introduction

Against the background of practicing the dual-carbon target and constructing a new energy system, the energy consumption side has shown an accelerated pace of electricity substitution, and massive, heterogeneous, decentralized, and ubiquitous distributed resources continue to emerge. Electric vehicles (EVs) are a new emerging resource on the energy consumption side in recent years, with the dual characteristics of load and power source [1]. As of the end of 2022, the total number of new energy vehicles in China has reached 13.1 million, accounting for 4.1% of the total number of cars, among which the number of pure electric vehicles is 10.45 million, accounting for 79.78% of the total number of new energy vehicles [2], ranking first

Q. Shi (✉) · W. Kong · H. Dai · S. Zhang · C. Wang · X. Wu · D. Wang
Department of Energy Internet Research, State Grid Energy Research Institute, Beijing, China
e-mail: shiqing@sgeri.sgcc.com.cn

Z. Zhang
School of Electrical Engineering, Southeast University, Nanjing, China

S. Yadav et al. (eds.), *Energy Power and Automation Engineering*, Lecture Notes in Electrical Engineering 1118, https://doi.org/10.1007/978-981-99-8878-5_89

in the world. The large-scale development of EVs has an impact on the load, peak-valley difference, energy structure, and grid stability of the power system. According to a research report by the World Resources Institute, when the penetration rate of private electric vehicles exceeds 50%, most distribution transformers will face overload risks [3]. Therefore, the integration and efficient allocation of a large number of EV resources and their efficient interaction with the power system have become an important technical means to stabilize the distribution grid load fluctuations and promote the development of a new power system [4].

The interaction process between EVs and the power grid involves multiple stakeholders such as users, operators, the grid, and the government, with complex coupling relationships of energy and information. To achieve a good interaction between EVs and the power grid, it is necessary to identify key factors in the interaction process, sort out the relationships among stakeholders, and propose a typical mode of the EV-grid interaction architecture, providing top-level design support for the effective interaction between EVs and the power system.

Currently, research on the EV-grid interaction architecture mainly focuses on the macroscopic analysis of energy and information flow interaction with the power system and the analysis of interaction strategies. One article established a system dynamics analysis model for the EV-grid interaction process, analyzed the causal loop diagram of the EV-grid interaction process, refined the flow relationship between internal factors of the EV and the grid sub-modules, and explored the impact of electricity prices and travel plans on the charging and discharging response of EVs [5]. Another article proposed an EV-grid interaction scheduling strategy using clustering optimization to minimize the total load variance of the schedulable load during the research period, achieving peak shaving and valley filling goals [6]. The article studied the EV control strategy for power system flexibility, designed a flexible scheduling scheme for "maximum available flexibility calculation-power system flexibility demand calculation-EV flexibility control," and proposed an EV-grid interaction scheduling strategy [7–10].

Based on the aforementioned research, this article analyzes in-depth the relationship between energy and information in the interaction process between electric vehicles and the power grid and proposes a cloud-edge-end-based architecture and typical scenarios for the interaction between electric vehicles and the power grid. This article provides an effective method for the evolutionary analysis of the interaction between electric vehicles and the power grid, which provides a basis for understanding the mechanism of the interaction process and proposing targeted and effective interaction strategies.

2 Methodology

The method of combining scenario analysis and stakeholder analysis is used to design the vehicle-grid interaction architecture. The design process is divided into six steps: identifying key issues, identifying influencing factors, scenario construction,

scenario analysis, scenario evaluation, and determining the vehicle-grid interaction architecture.

2.1 Identifying Key Issues

The key issues include the economic, safety, and stable operation problems of the power system caused by the large-scale development of electric vehicles, the insufficient power capacity of the distribution network caused by the large-scale development of electric vehicles, and the need for greater flexibility in the power system demand side to improve the consumption of new energy and reduce carbon emissions.

2.2 Identifying Influencing Factors

The stakeholder analysis method is used to identify the stakeholders of the vehicle-grid interaction, including users, operators, power grid enterprises, social organizations, and the government. Among them, the user is the smallest unit participant of the vehicle-grid interaction and can participate directly or through the operator. The operator is the intermediate organizer of the interaction between electric vehicles and the power grid, and the power grid enterprise provides energy and benefits, while social organizations provide relevant standard guarantees, and the government issues relevant policies to ensure that the relevant subjects can obtain benefits and play their value in the interaction process.

2.3 Scenario Construction

The scenarios of electric vehicle and power grid interaction mainly include residential community personal charging scenarios, public charging station scenarios, and dedicated charging station scenarios. The residential community personal charging scenario can participate directly or through charging operators, while public charging station and dedicated charging station scenarios can participate directly or through operators.

2.4 Scenario Analysis

According to different application scenarios, a multi-level cloud-network-edge-end interactive architecture is applied to analyze the vehicle-grid interaction, analyzing the flow direction and interaction mode of energy flow and information flow in the

information domain, energy domain, subject domain, and capital domain. The main interaction modes include information interaction modes such as ordered charging, power market, demand response, and green energy trading, as well as energy interaction modes such as ordered charging and bidirectional charging and discharging. The subject interaction modes include power grid, operator or aggregator, and user. The capital interaction modes include vehicle owners and operators, vehicle owners and power grid companies, operators and power grid companies, and operators and trading centers.

2.5 Scenario Evaluation

At present, the vehicle-grid interaction is still in the stage of electric vehicle participation in ordered charging, while the vehicle-to-grid (V2G) technology is still in the pilot demonstration and technical verification stage. At this stage, the vehicle-grid interaction needs to adapt to scenarios such as residential community personal charging, public charging station, and dedicated charging station, and provide correct and timely feedback based on specific application scenarios.

2.6 Determining the Vehicle-Grid Interaction Architecture

The flow direction of energy flow and information flow under different interaction modes in the information domain, energy domain, subject domain, and capital domain is systematically designed to reflect the internal connection of the vehicle-grid interaction and determine the vehicle-grid interaction architecture.

3 Results

3.1 Electric Vehicle and Electric Grid Information-Energy Coupling Relationship and Multi-level Interaction Framework Among Multiple Entities

Ordered Electricity Interaction

The power system dispatch center is the initiator of ordered electricity. The power grid puts forward the demand for ordered electricity, and the cloud computing center sends the load regulation capability instruction to the vehicle network platform based on

the available resource pool capacity. The vehicle network platform informs the operators, aggregators, and vehicle owners to directly adjust the charging and discharging power. The orderly electricity consumption interaction process is shown in Fig. 1.

Demand Response Interaction

The marketing department of the power grid company is the initiator of demand response. The power grid puts forward the demand for demand response, and the cloud computing center sends the demand response demand to the vehicle network platform based on the available resource pool capacity. At the same time, the edge computing center sends the demand response demand to the operators, aggregators, and vehicle owners, and settles the transaction after accepting the response. The demand response interaction process is shown in Fig. 2.

Electricity Market Interaction

The electricity trading center is the initiator of the electricity market, which can be further refined into spot market and ancillary service market. The electricity market issues signal for the amount of electricity, power gap, and price. Operators and aggregators offer and respond to the gap amount, and settle the transaction at the trading center. The electricity market interaction process is shown in Fig. 3.

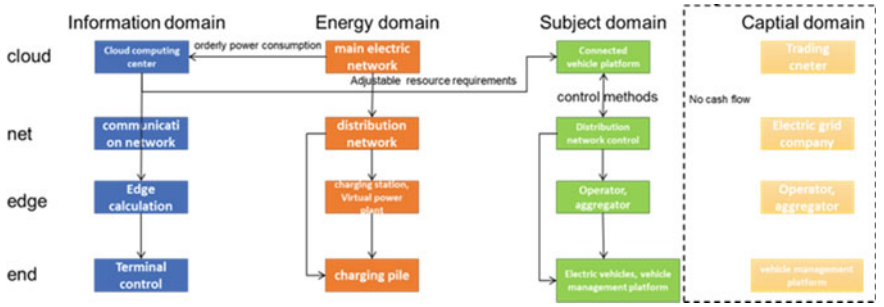

Fig. 1 Ordered electricity interaction

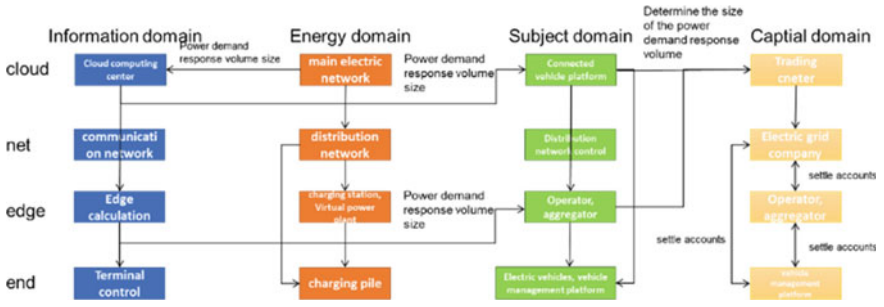

Fig. 2 Demand response interaction

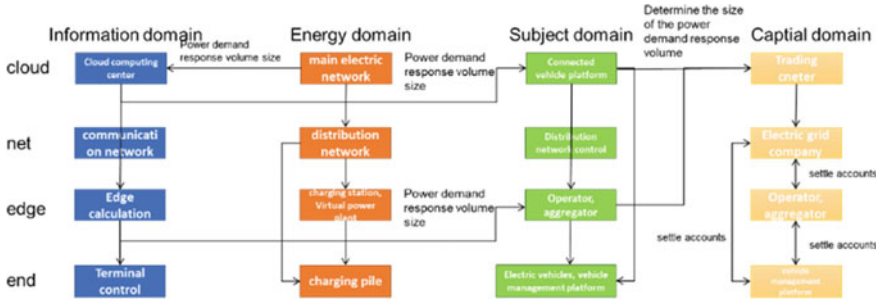

Fig. 3 Electricity market interaction

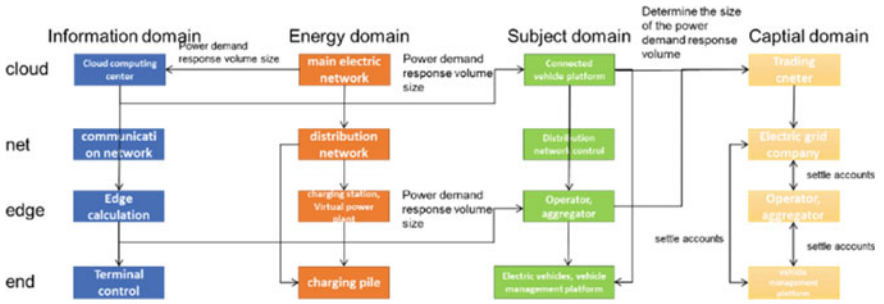

Fig. 4 Green electricity trading interaction

Green Electricity Trading Interaction

Operators, aggregators, and users are the initiators of green electricity trading, and the vehicle network platform is a participating unit. Operators and aggregators propose the green electricity trading amount based on their own and user needs and settle directly at the trading center. The green electricity trading interaction process is shown in Fig. 4.

3.2 Typical Modes of Electric Vehicle Participation in Vehicle-Grid Interactions Under Different Operating Scenarios

Based on the summary of the existing ordered charging demonstration project, three typical connection modes for vehicle-grid interaction systems have been proposed for different types of charging piles and charging pile management systems, providing typical solutions for the implementation of various types of vehicle-grid interaction projects. These three typical connection modes for vehicle-grid interaction systems include: regional charging and discharging management system directly connected

to intelligent charging piles, small-scale operator charging and discharging management system directly connected to intelligent charging piles, and large-scale operator charging and discharging management system connected to intelligent charging piles through the charging station-level monitoring system.

For the regional charging and discharging management system directly connected to intelligent charging piles mode (see Fig. 5), other social information systems such as the power grid dispatching agency's dispatch management system, power grid marketing agency's load management system, and trading agency publish charging and discharging demands and incentive electricity prices, and send this information to the electric vehicle intelligent charging and swapping regional service network operation and monitoring system (including the charging and discharging management system) through communication and control commands to control the input/output power of the charging piles, and provide vehicle-grid interaction services for electric vehicles. At the same time, the operation and monitoring system will issue notifications to the user's APP regarding the charging and discharging status, and users can also customize their participation time and other participation information based on their own needs.

Regarding the small-scale operator charging and discharging management system directly connected to ordered charging piles mode (see Fig. 6), other social information systems such as the power grid dispatching agency's dispatch management system, power grid marketing agency's load management system, and trading agency publish charging and discharging demands and incentive electricity prices, and send

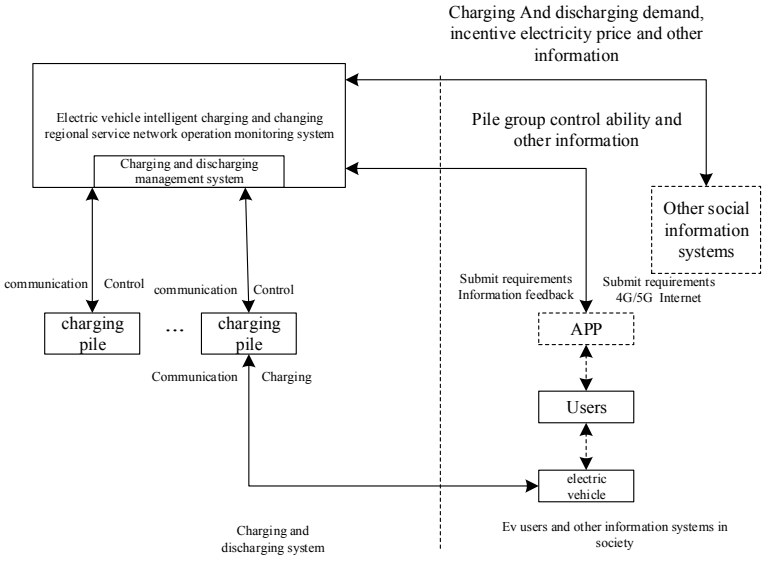

Fig. 5 Regional charging and discharging management system directly connected to intelligent charging piles

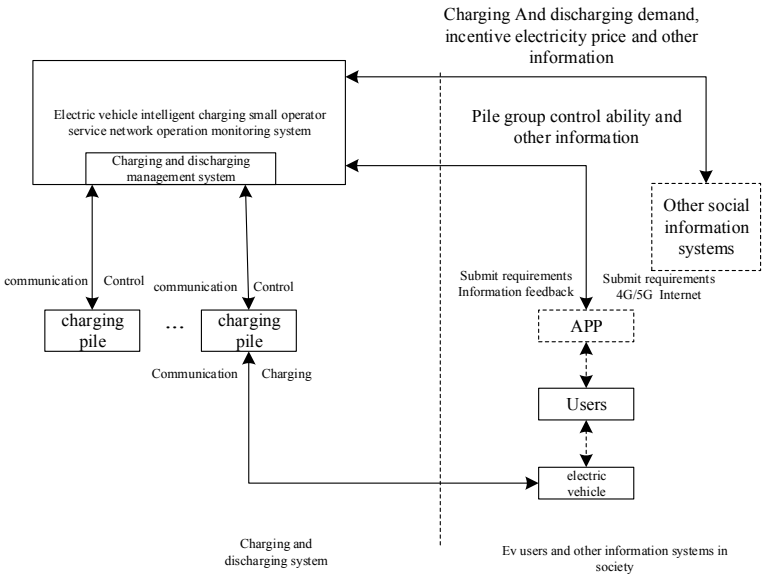

Fig. 6 Small-scale operator charging and discharging management system directly connected to intelligent charging piles

this information to the electric vehicle intelligent charging and swapping small-scale operator service network operation and monitoring system (including the charging and discharging management system) through communication and control commands to control the input/output power of the charging piles, and provide vehicle-grid interaction services for electric vehicles. At the same time, the operation and monitoring system will issue notifications to the user's APP regarding the charging and discharging status, and users can also customize their participation time and other participation information based on their own needs.

Regarding the large-scale operator ordered charging management system connected to intelligent charging piles through the charging station-level monitoring system mode (see Fig. 7), other social information systems such as the power grid dispatching agency's dispatch management system, power grid marketing agency's load management system, and trading agency publish charging and discharging demands and incentive electricity prices, and send this information to the electric vehicle intelligent charging and swapping large-scale operator service network operation and monitoring system (including the charging and discharging management system) through communication and control commands to control the charging station-level monitoring system. The station-level monitoring system controls the input/output power of the charging piles inside the station to provide vehicle-grid interaction services for electric vehicles. At the same time, the operation and monitoring system will issue notifications to the user's APP regarding the charging and

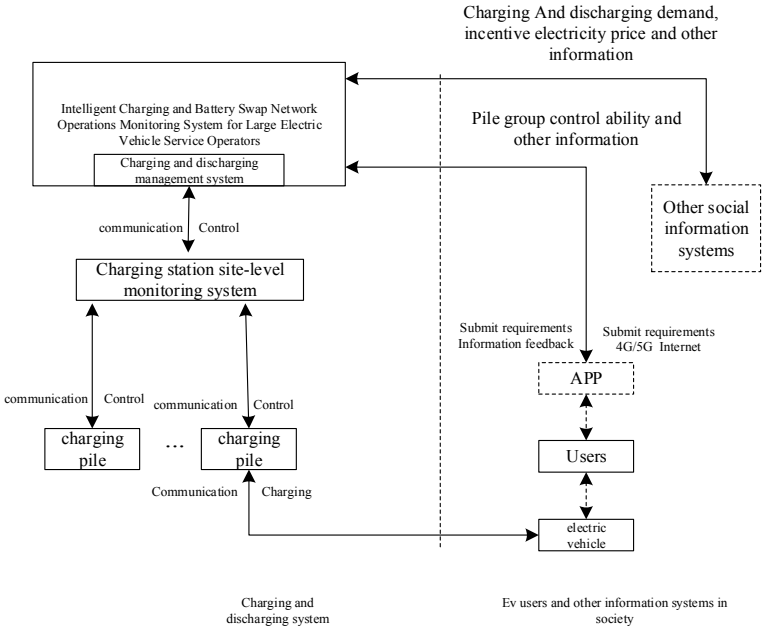

Fig. 7 Large-scale operator charging and discharging management system connected to intelligent charging piles through the charging station-level monitoring system

discharging status, and users can also customize their participation time and other participation information based on their own needs.

4 Conclusion

In response to the non-standard and non-uniform issues of vehicle-grid interaction architecture and typical modes, this paper proposes an electric vehicle and electric grid interaction modeling method based on organizational collaborative behavior identification and systematically explains the flow direction and interaction modes of energy flow and information flow in the information domain, energy domain, subject domain, and capital domain. This solves the standardization and unification of vehicle-grid interaction and provides new ideas for future research on vehicle-grid interaction.

Acknowledgements This paper is supported by a technology project of State Grid Corporation of China, project code: 5400-202112580A-0-5-SF, project name: Research and Demonstration of Key Technologies for Large-Scale Multi-Scenario Electric Vehicle-Grid Intelligent Interaction.

References

1. Kang C, Chen Q, Su J et al (2022) (2022) Scientific problems and research framework of virtual power plant with enormous flexible distributed energy resources in new power system. Autom Electr Power Syst 46(18):3–14
2. The total number of new energy vehicles in China reached 13.1 million, showing rapid growth. http://www.gov.cn/xinwen/2023-01/11/content_5736278.htm
3. Xue L, Xia J, Yu R, et al (2019) How to connect new energy vehicles to electricity more friendly net series 1: roadmap and policy recommendations for the synergy between electric vehicles and power grid in China. World Resources Institute (USA) Beijing Representative Office, Beijing
4. Zhao X, Zhang Y, Li B et al (2022) Effect analysis and development suggestion of domestic and foreign. Electr Power Autom Equip 42(10):280–292
5. Cheng H, Shang Z, Guo Y et al (2021) Research on vehicle-to-grid process based on system dynamics. Power Syst Technol 45(10):4125–4133
6. Wang Y, Chen J, Ma X et al (2020) Interactive scheduling strategy between electric vehicles and power grid based on group optimization. Electr Power Autom Equip 40(05):77–85
7. Yao Y, Zhao R, Li C et al (2022) Control strategy of electric vehicles oriented to power system flexibility. Trans China Electrotech Soc 37(11):2813–2824
8. Lefeng S, Tong L, Yandi W (2019) Vehicle-to-grid service development logic and management formulation. J Mod Power Syst Clean Energy 7(04):935–947
9. Zhou P et al (2019) 2019) Development status and application analysis of vehicle to grid (V2G. J Donghua Univ 36(03):284–292
10. Nuh E, Fatih E, Mithat K (2018) A fast and efficient coordinated vehicle-to-grid discharging control scheme for peak shaving in power distribution system. J Mod Power Syst Clean Energy 6(03):555–566

Research on Drag Reduction Optimization of Offshore Wind Power Installation Vessel Based on Approximate Model

Liu Jie

Abstract The conventional optimization method for drag reduction of offshore wind power installation ships mainly focuses on the optimization of scouring intensity at the bottom. Although the problem of energy consumption has been reduced to a certain extent, the pressure of power load has been increased, which affects the optimization effect of drag reduction. Therefore, an optimization method for drag reduction of offshore wind power installation vessel based on approximate model is designed. Optimize the drag reduction profile parameters of offshore wind power installation ship, and use the cross section area curve instead of the waterline surface curve to constrain the displacement of the wind power installation ship. Based on the approximate model, the drag reduction calculation domain of the wind power installation vessel is established, and the drag reduction conditions are divided to optimize the viscous resistance of the wind power installation vessel and achieve the purpose of drag reduction optimization. The comparison experiment verifies that the optimization effect of the drag reduction optimization method is better and can be applied to real life.

Keywords Approximate model · Offshore wind power installation vessel · Drag reduction optimization method

1 Introduction

Offshore wind power is more abundant and stable than onshore wind power, solving the problem of wind energy shortage. It mainly originates from tropical cyclones in summer and autumn and is concentrated on islands with high wind energy density [1–3]. Offshore wind farms are divided into the transportation and installation of offshore wind turbines, which require the cooperation of two ships, one with transportation and lifting functions, and the other with positioning and positioning functions [4–6].

L. Jie (✉)
Ocean Engineering Fleet, YanTai Salvage, Yantai, China
e-mail: lostwolf2006@163.com

S. Yadav et al. (eds.), *Energy Power and Automation Engineering*, Lecture Notes in Electrical Engineering 1118, https://doi.org/10.1007/978-981-99-8878-5_90

Self-propelled jack up wind power installation ships have the advantages of jack up platforms and floating ships. The working area of the deck is large, and more fans can be loaded to meet the one-time transportation and installation requirements. The offshore wind power installation ship also has self-navigation capability, which can transfer the ship in time during installation to improve the efficiency of wind turbine installation. However, at present, the offshore wind power installation ship is affected by draft, marine environment, etc., and the hull resistance is large, which affects the efficiency of the ship. Therefore, this paper combines the advantages of the approximate model to design an optimization method for drag reduction of offshore wind power installation vessels.

2 Design of Drag Reduction Optimization Method for Offshore Wind Power Installation Vessel

2.1 Optimize Drag Reduction Profile Parameters of Offshore Wind Power Installation Vessel

In the process of drag reduction optimization of offshore wind power installation ship, this paper selects cross section area curve to constrain the displacement of wind power installation ship [7]. The parameters such as displacement, longitudinal center of buoyancy, waterline length, incidence angle, trailing edge angle, stern plate cross-sectional area, maximum sectional area of midship, and its longitudinal position are the drag reduction profile parameters of offshore wind power installation ship. Optimize the above parameters, and the expression of the cross section area curve is:

$$S_a(x) = A_0 + A_1 x + A_2 x^2 + A_3 x^3 + A_4 x^4 \tag{1}$$

In formula (1), $S_a(x)$ is the expression of cross section area curve; A_0 is the sectional area of stern plate; A_1 is the premise curve; A_2 is the tail curve; A_3 is the waterline length; A_4 is the drainage parameter; x is the profile coefficient. According to this expression, the drag reduction profile parameters of offshore wind power installation ship are optimized, and the expression is:

$$S_a\prime(0) = \tan(a_t) \tag{2}$$

In formula (2), $S_a\prime(0)$ is half width of waterline surface; a_t is the length of the waterline. The boundary condition of cross section area curve is expressed as:

$$S_a\prime(t) = B_0(x - x_m) \tag{3}$$

In Eq. (3), $S_a\prime(t)$ is the boundary condition of cross section area curve; B_0 is the initial half width of the waterline surface; x_m is the profile coefficient at m position. The optimized parameters of drainage volume are:

$$\nabla = \int_0^n S_a(x)\mathrm{d}x + \int_0^n S_a\prime(t)\mathrm{d}x \tag{4}$$

In Eq. (4), ∇ is the optimize parameters for drainage; d is the distance parameter of A_1 and A_2. The longitudinal buoyancy center parameters are optimized as follows:

$$L = \int_0^n xS_a(x)\mathrm{d}x + \int_0^n xS_a\prime(t)\mathrm{d}x \tag{5}$$

In formula (5), L is the optimize parameters for longitudinal center of buoyancy. According to the optimized parameters, define the profile curve of the cross section, analyze the profile curve contour, and use the curve contour as the drag reduction calculation space of the wind power installation ship to ensure the drag reduction optimization effect.

2.2 *Establish Drag Reduction Calculation Domain of Wind Power Installation Vessel*

This paper selects an appropriate approximate model for drag reduction optimization of offshore wind power installation ships by combining optimized profile and performance parameters. By establishing a drag reduction calculation domain, the viscous resistance of the ship is optimized to achieve drag reduction [8]. The approximate model adopts parametric optimization, taking displacement, longitudinal center of buoyancy, the maximum cross section area of the midship, the longitudinal position of the maximum cross section area of the midship, waterline length, incidence angle, trailing edge angle, stern plate section area, and other parameters as the main variables of the optimization objective function. Secondly, select the performance parameter variable that reflects the characteristics of the ship type according to the specific ship type. The calculation domain of drag reduction of offshore wind power installation vessel is divided as follows:

$$\begin{aligned} &\min f(x) \\ &\text{s.t.}\begin{cases} g_i(x) \geq 0, & i = 1, 2, \ldots, n \\ h_i(x) = 0, & i = 1, 2, \ldots, m(m \leq n) \end{cases} \end{aligned} \tag{6}$$

In formula (6), $\min f(x)$ is the minimum value of drag reduction calculation domain of offshore wind power installation vessel; $g_i(x)$ is the objective function; $h_i(x)$ is the feasible solution of vector x. When $f(x) = \min f(x)$ is satisfied, then, $h_i(x) = 0$ was established. The displacement, longitudinal center of buoyancy,

maximum cross section area of midship, longitudinal position of maximum cross section area of midship, waterline length, incidence angle, trailing edge angle, stern plate section area, and other parameters are input into the approximate model for drag reduction optimization. The maximum drag reduction value can be obtained in the drag reduction calculation domain, so as to improve the drag reduction optimization effect.

3 Simulation Experiment

In order to verify whether the drag reduction optimization method of offshore wind power installation ship designed in this paper has practical value, this paper has carried out simulation analysis on the above methods. The final experimental results are presented in the form of comparing the conventional optimization methods for drag reduction of offshore wind power installation vessels based on Heston Vasicek model, the conventional optimization methods for drag reduction of offshore wind power installation vessels based on degenerate kernel function and adaptive crossover algorithm, and the optimization methods for drag reduction of offshore wind power installation vessels based on approximate models designed in this paper. The specific experimental preparation process and the final experimental results are shown below.

3.1 Experiment Preparation

In the process of simulation, this paper pays more attention to whether the simulation speed is reasonable. In this paper, according to the actual situation on the sea, the sediment particles with different diameters are selected and the reasonable ship speed is set. Considering the influence of window shape, wave height, current speed, and other parameters of offshore wind power installation vessel on drag reduction optimization, in addition to the relative wind direction angle, current speed, wave height, water depth, engine speed, and other parameters, other calculation quantities involved in the experiment simulation are constant values. Considering the optimization background of this model, the flow velocity of wind power installation ship in the intertidal zone is not very large, and the sand type is mostly fine sand. Therefore, in this experiment, the diameter of the sand particles is set as 0.05 mm, the current is a constant velocity, and the wave height of the current is 0.5 m. The calculated velocity is set as 0.5, 1, 1.5, and 2 m/s based on the sediment velocity and the actual situation. These four velocity variables meet the actual needs of the sea. The real ship speed is set within the range of 6–16kn, and the total resistance of the real ship increases with the increase of the real ship speed, showing a proportional curve. Set the actual ship speed, traction speed, model resistance, model current transformer, model current peak coefficient, actual ship current transformer, actual ship current peak coefficient, and total resistance of the actual ship as the resistance parameters of the wind power

Table 1 Resistance parameters of approximate model of wind power installation vessel

Real ship speed (kn)	Towing speed (m/s)	Model resistance/N	Model Ct ($*10^{-3}$)	Model Cf ($*10^{-3}$)	Real ship Ct ($*10^{-3}$)	Real ship Cf ($*10^{-3}$)	Total resistance of the actual ship/kN
6	0.441	1.895	7.777	4.591	1.735	4.905	154.161
7	0.515	2.562	7.715	4.445	1.692	4.964	213.242
8	0.587	3.336	7.812	4.327	1.665	5.151	281.965
9	0.658	4.084	7.946	4.215	1.644	5.377	344.146
10	0.736	5.325	7.774	4.125	1.626	5.268	467.158
11	0.805	6.256	7.605	4.046	1.601	5.156	547.424
12	0.876	7.497	7.798	3.971	1.585	5.404	664.766
13	0.958	8.568	8.334	3.913	1.568	5.988	864.562
14	0.999	9.405	8.426	3.865	1.548	6.028	912.344
15	1.024	10.321	7.774	3.788	1.529	5.695	1032.786
16	1.145	11.482	7.685	3.669	1.502	5.455	1146.524

installation ship's approximate model. At the same time, these resistance parameters also represent the actual total resistance of the ship. Under the condition that the relationship between the total resistance of the full ship and the speed of the full ship remains unchanged, the resistance parameters of the approximate model of the wind power installation ship are analyzed, as shown in Table 1.

As shown in Table 1, as the ship's speed increases, the resistance parameter values also increase. The actual ship speed of the wind power installation vessel is positively correlated with the total resistance, that is, the real ship speed corresponds to the real ship total resistance and the real ship total resistance curve. In the process of approximate model simulation, there is a large traveling wave near the transition section between the head of offshore wind power installation ship and the balance middle body, where the gradient of profile change is large, which is more suitable for the optimization simulation analysis of drag reduction of offshore wind power installation ship.

3.2 Experimental Results

Under the above experimental conditions, select relative wind direction, water flow velocity, wave height, water depth, and engine speed as simulation parameters, and set 5 different parameter values, five experiments were conducted respectively to ensure the effectiveness of the experiment. In this paper, the windward resistance before and after optimization is taken as the optimization index of the drag reduction optimization method for offshore wind power installation vessels. Before and after

optimization, lower resistance is required to meet the requirements of offshore operation. In the optimization index, the higher the relative drag reduction and the relative fuel saving, the better the drag reduction optimization effect. Under the condition that other conditions are consistent, the optimization index of the conventional Heston Vasicek model based drag reduction optimization method for offshore wind power installation vessels, the optimization index of the conventional degenerate kernel function based and adaptive crossover algorithm based drag reduction optimization method for offshore wind power installation vessels, and the optimization index of the drag reduction optimization method of offshore wind power installation vessel based on the approximate model designed in this paper are compared. The experimental results are shown in Table 2.

As shown in Table 2, the resistance of offshore wind power installation vessels fluctuates greatly due to the impact of the marine environment. After using the conventional drag reduction optimization method for offshore wind power installation vessels based on degenerate kernel function and adaptive cross algorithm, in five experiments, the optimization effect of windward resistance is poor. The larger the simulation parameters such as relative wind direction angle, water velocity, wave height, water depth, and engine speed, the weaker the optimization effect of windward resistance. That is to say, the more complex the offshore environment is, the weaker the drag reduction optimization effect of this method is, which is not conducive to the operation of offshore wind power installation ships, and needs further treatment. However, after using the drag reduction optimization method of offshore wind power installation vessel based on the approximate model designed in this paper, in five experiments, the optimization effect of windward resistance is strong, with the relative drag reduction exceeding 35% and the relative fuel saving exceeding 30%. Moreover, after using this method, there is no problem that the larger the relative wind direction angle, water speed, wave height, water depth, engine speed, and other simulation parameters are, the weaker the optimization effect of windward resistance is. This problem can maintain a more stable optimization effect of drag reduction, better meet the needs of offshore operations, and meet the purpose of this study. This is because the drag reduction optimization method for offshore wind power installation vessels based on approximate models optimizes the drag reduction external parameters of offshore wind power installation vessels and inputs them into the approximate model for drag reduction optimization to obtain the maximum drag reduction value, thereby improving the effectiveness of drag reduction optimization.

4 Conclusion

As a new type of offshore vessel, wind power installation ships can address the challenges of offshore wind turbine transportation and installation, reduce reliance on non-renewable energy, and align with the concept of sustainability. However, these ships are affected by the marine environment, and their large resistance can impact their operational efficiency. Therefore, this paper proposes an optimization method

Table 2 Experimental results

Method	Simulation parameters					Windward resistance/N		Optimization indicators	
	Relative wind direction angle/°	Water flow velocity (m/s)	Wave height/m	Water depth/m	Main engine speed (r/min)	Before optimization	After optimization	Relative drag reduction/%	Relatively fuel-efficient/%
Conventional drag reduction optimization method for offshore wind power installation ships based on Heston Vasicek model	0	0.5	0	50	570	7514.36	5682.32	24.38	19.82
	15	1.0	1	55	600	7041.33	5454.62	22.53	18.26
	30	1.5	2	60	630	6733.65	5306.12	21.20	15.43
	45	2.0	3	65	660	6650.14	5273.11	20.71	14.32
	60	2.5	4	70	690	6543.28	5123.46	21.70	16.17
A conventional drag reduction optimization method for offshore wind power installation ships based on degenerate Kernel function and adaptive cross algorithm	0	0.5	0	50	570	6908.68	4664.64	32.48	28.63
	15	1.0	1	55	600	5758.32	4321.30	24.94	18.54
	30	1.5	2	60	630	5099.07	4156.42	18.49	12.15
	45	2.0	3	65	660	4896.12	4032.11	17.65	11.46
	60	2.5	4	70	690	4532.47	3968.32	12.45	10.32
The drag reduction optimization method for offshore wind power installation vessels designed in this article based on approximate models	0	0.5	0	50	570	4362.52	2436.18	44.16	36.54
	15	1.0	1	55	600	3543.21	2215.46	37.47	34.32
	30	1.5	2	60	630	3046.34	1963.28	35.55	32.18
	45	2.0	3	65	660	2917.88	1632.45	44.05	37.45
	60	2.5	4	70	690	2633.42	1550.27	41.13	36.44

for drag reduction of offshore wind power installation vessels using an approximate model. By considering profile parameters, drag reduction calculation domain, and hydrodynamic calculation, the best optimization scheme is identified to ensure efficient vessel operation. The transition section between the vessel's bow and balance intermediate is selected for analysis of the drag reduction optimization effect. After comparison, it was found that after optimization, the relative drag reduction rate of the approximate model based drag reduction optimization method for offshore wind power installation ships exceeded 35%, and the relative fuel saving rate exceeded 30%. This indicates that the method has good drag reduction optimization effect. By optimizing the drag reduction effect of wind power installation vessels and improving their competitiveness and market share, the development of the wind power industry has been promoted. At the same time, by reducing the resistance of offshore wind power installation vessels, emissions are reduced, playing a role in protecting the environment.

References

1. Yldz HA, Gren-Sümer L (2022) Stabilization of a class of underactuated Euler Lagrange system using an approximate model. Trans Instit Measur Control 44:1569–1578. https://doi.org/10.1177/01423312211058556
2. De SK, Bhattacharya K, Roy B (2021) Solution of a pollution sensitive supply chain model under fuzzy approximate reasoning. Int J Intell Syst 36:5530–5572. https://doi.org/10.1002/int.22522
3. Lazzizzera I (2021) An analytic approximate solution of the SIR model. Appl Math 12:58–73. https://doi.org/10.4236/am.2021.121005
4. Bokes P (2022) Exact and WKB-approximate distributions in a gene expression model with feedback in burst frequency, burst size, and protein stability. Discr Contin Dyn Syst B 27:2129–2145. https://doi.org/10.3934/dcdsb.2021126
5. Liu X, Miao P, Yao Y (2022) VLC nonlinear equalizer based on approximate message passing. Comput Simul 39:197–200. https://doi.org/10.3969/j.issn.1006-9348.2022.10.036
6. Ameen IG, Sweilam NH, Ali HM (2021) A fractional-order model of human liver: analytic-approximate and numerical solutions comparing with clinical data. AEJ Alex Eng J 60:4797–4808. https://doi.org/10.1016/j.aej.2021.03.054
7. Jiang X, Lin Y (2022) Relevant integrals of NURBS and its application in hull line element design. Ocean Eng 251:111147.1-111147.9. https://doi.org/10.1016/j.oceaneng.2022.111147
8. Chiang IY, Wan T (2021) On the drag reduction optimization of the DrivAer fastback model car with digital side mirror. SAE Int J Passen Cars Mech Syst 14:67–84. https://doi.org/10.4271/06-14-01-0005

Feature Extraction and Source Identification for Complex Voltage Sag Based on SAE and Softmax Classifier

Mingming Shi, Xiaodong Yuan, Xian Zheng, Juntao Fei, and Jianhua Zhou

Abstract With the development of power quality monitoring system, the voltage sag monitoring data is becoming larger and larger, which often exist some problems such as incomplete monitoring information and interference signals. This paper proposes an automatic feature extraction and source identification method of complex voltage sag source based on sparse self-encoder (SAE) and softmax classifier. Firstly, the causes of voltage sag are analyzed and summarized. Then the SAE is used to extract the feature of different voltage sag sources, and the depth feature is automatically gotten with the hidden layer of SAE. Finally, the encoder with the softmax classifier and the fine-tune the stacked network outputs the source classification result. The example results show that the proposed method can accurately identify the complex voltage sag source and has good generalization performance and robustness.

Keywords Sparse autoencoder · Complex voltage sag · Source identification · Feature extraction · Softmax classifier

1 Introduction

Voltage sag refers to the RMS value of the supply voltage to 90–10% of the normal value in a short time, and its typical duration is 0.5 ~ 30 cycles [1]. Voltage sag is the most frequent and serious power quality problem. Voltage sag can cause sensitive equipment to stop operation and huge economic losses [2]. Voltage sags are mainly caused short-circuit fault, induction motor starting, and transformer switching. Among them, short-circuit fault is divided into ordinary short-circuit fault and short-circuit fault caused by lightning fault and with the cancelation of the traveling wave detection device [3, 4]. The identification of complex voltage sag sources often relies only on voltage sag monitoring data and has become a meaningful and difficult research content.

M. Shi · X. Yuan · X. Zheng · J. Fei (✉) · J. Zhou
Electric Power Research Institute of State Grid Jiangsu Electric Power Co., Ltd., Nanjing 211103, China
e-mail: 16702324@QQ.com

S. Yadav et al. (eds.), *Energy Power and Automation Engineering*, Lecture Notes in Electrical Engineering 1118, https://doi.org/10.1007/978-981-99-8878-5_91

At present, the identification method of voltage sag source has been studied. Most of these existing methods extract the feature of voltage sag data based on manual experiences, such as S-transform [5, 6], wavelet transform [7, 8], Hilbert yellow transform [9], etc., and then use some data-driven methods, such as support vector machine [10, 11], decision tree [12], and neural network [13], and identify voltage sag sources. However, under the development of power systems, the access of a large number of new type loads and power semiconductors will lead to more interference in the monitoring signal [14], and it will be difficult to extract effective features by traditional manual methods. With the large-scale development of power systems, intelligent voltage sag source identification system has also become a development trend.

Deep learning networks can automatically learn the features of input data and can extract many effective deep features through multi-layer representation learning and nonlinear transformation, which can improve the efficiency and quality of feature extraction [15]. Autoencoder (AE) is an unsupervised learning network, which has been well applied in nontechnical loss detection, load forecasting and fault diagnosis [18]. In this paper, SAE is used to automatically extract the deep feature of complex voltage sag data, and then the softmax classifier is used to identify the voltage sag source. Also, data with errors are used to verify the generalization and robustness of the model.

2 Analysis of Voltage Sag Source

(1) Short-circuit fault. Short-circuit fault is one of the important factors of voltage sag, and its rms waveform is shown in Fig. 1a. Its sag depth of short-circuit fault is deep, generally less than 0.7 p.u, where the sag occurrence and recovery waveform are steep.

(2) Lightning fault. After lightning strikes the transmission line, the lightning current will cause voltage rise fluctuation, the flashover tripping will cause ground fault, and then it will cause and propagate voltage sag in the system. Lightning current is a unipolar shock wave; its model is established according to the double exponential function as $I(t) = \left(I_{\mathrm{L}} / \eta\right) \times \left(\mathrm{e}^{-\alpha t} - \mathrm{e}^{-\beta t}\right)$, where α

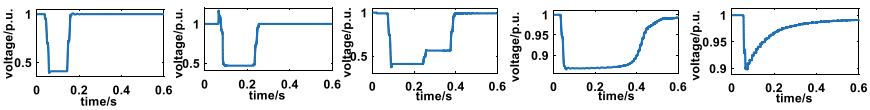

(a) RMS waveform of short circuit fault. (b) RMS waveform of lightning fault. (c) RMS waveform of multi-voltage fault. (d) RMS waveform of induction motor starting. (e) RMS waveform of transformer switching.

Fig. 1 RMS waveform of voltage sag

and β are the wave coefficients, and η is the peak correction factor. Its rms waveform is shown in Fig. 1b. Compared with ordinary short-circuit faults, it shows that the characteristics of rising first and falling due to the voltage waveform containing high-frequency components.

(3) Multi-voltage sag. Multi-voltage sag is one of the short-circuit faults, which is a sag caused by the change of short-circuit fault type, such as after a single-phase grounding fault, the equipment at the fault point burns out and causes a two-phase grounding fault, and its rms waveform is shown in Fig. 1c.

(4) Induction motor starting. When the induction motor starts, it draws 5 ~ 6 times the rated current from the system, resulting in a voltage sag and its rms waveform is shown in Fig. 1d. Its voltage sag depth is generally not less than 0.85 p.u, the temporary descent gradually recovers, and the recovery waveform is relatively flat.

(5) Transformer switching. When the transformer is switched, an excitation surge current of 8 ~ 9 times the rated current will be generated at the sending end, and the system impedance divider will increase, causing a voltage sag, its rms waveform is shown in Fig. 1e. Its voltage sag depth is generally not < 0.85 p.u., the voltage is gradually restored, and the waveform contains harmonics.

3 Voltage Sag Source Feature Extraction and Identification

3.1 SAE-Based Voltage Sag Feature Extraction and Softmax Classifier

AE consists of an encoder and a decoder, and its network structure is shown in Fig. 2. Define the voltage sag data as $\boldsymbol{X} = \{\boldsymbol{x}_1, \boldsymbol{x}_2, \ldots, \boldsymbol{x}_{N_s}\}$, the feature output by the hidden layer is $\boldsymbol{F} = \{\boldsymbol{f}_1, \boldsymbol{f}_2, \ldots, \boldsymbol{f}_{N_s}\}$, the reconstructed voltage sag data is $\boldsymbol{X}' = \{\boldsymbol{x}'_1, \boldsymbol{x}'_2, \ldots, \boldsymbol{x}'_{N_s}\}$. The encoder maps the input layer data $\boldsymbol{x}_i$ to the hidden layer, and then the decoder reconstructs the data $\boldsymbol{x'}_i$ to the output layer. The mathematical expression of the encoder and the decoder is $\boldsymbol{f}_i = S(\boldsymbol{W}_{(1)}\boldsymbol{x}_i + \boldsymbol{b}_{(1)})$ and $\boldsymbol{x}'_i = S(\boldsymbol{W}_{(2)}\boldsymbol{f}_i + \boldsymbol{b}_{(2)})$, where S is the activation function, and the sigmoid function is adopted in this paper.

Network training is to minimize the reconstruction error by optimizing the network parameters $\boldsymbol{W}$, $\boldsymbol{b}$ to make $\boldsymbol{X}$ infinitely close $\boldsymbol{X'}$, and then the output of hidden layer can be used as a depth feature of voltage sag. This paper uses mean squared error (MSE) as the reconstruction error. SAE has the same structure as AE, the difference is that a sparsity constraint E_{sparsity} is added to the hidden layer, so that the hidden layer output is sparsity, and the autoencoder network is prevented from degenerating into a replicator and cannot extract effective features. In addition, to prevent the model from over-fitting, the L2 regular control value size is introduced. The loss function of SAE is

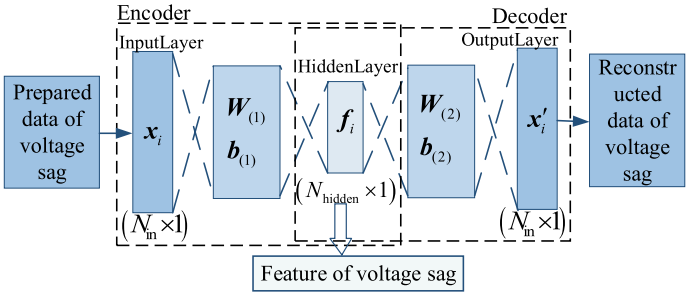

Fig. 2 AE used to extract voltage sag feature

$$E_{\mathrm{SAE}} = (1/2N_s) * \sum_{i=1}^{N_s} \left\| x_i - x_i' \right\|^2 + \lambda * (1/2) * \sum_{l=1}^{2} \left\| W_{(l)} \right\|_F^2 + \beta * E_{\mathrm{sparsity}}$$

$$E_{\mathrm{sparsity}} = \sum_{j=1}^{N_{\mathrm{hidden}}} K_{\mathrm{KL}}(\rho || \widehat{\rho}_j) = \sum_{j=1}^{N_{\mathrm{hidden}}} \rho \ln\left(\rho / \widehat{\rho}_j\right) + (1-\rho) \ln\left(1 - \rho / 1 - \widehat{\rho}_j\right),$$

where λ, β is coefficient of L2 regularizer and sparse regularizer. ρ is the desired activation value for hidden layer neurons, and $\widehat{\rho}_j$ is the average activation value of the jth neuron in the hidden layer.

Softmax classifier is a multi-classifier based on probability model, its input is feature vector, output is the probability that the feature vector belongs to each class, and its network structure is shown in Fig. 3. The input of the softmax classifier is the features extracted by the SAE, the real label is $\boldsymbol{y}_i$, which is one hot encoding, the predicted label is $\boldsymbol{y'}_i$, K is number of categories, and its calculation formula is $\boldsymbol{z}_i = \boldsymbol{W}_{\mathrm{softmax}} \boldsymbol{f}_i + \boldsymbol{b}_{\mathrm{softmax}}$ and $y'_i = e^{z_i} / \sum_{k=1}^{K} e^{z_{i,k}}$.

Fig. 3 Structure of softmax classifier

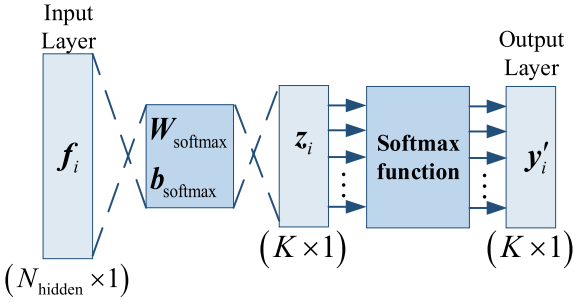

To make the predicting label close to real label, using cross-entropy loss as the loss function of softmax

$$L = -(1/N_s)\sum_{i=1}^{N_s}\sum_{k=1}^{K}\left[y_{i,k} \times \ln\left(y'_{i,k}\right) + \left(1 - y_{i,k}\right) \times \ln\left(1 - y'_{i,k}\right)\right].$$

3.2 *Voltage Sag Source Identification Model*

The voltage sag source identification model is shown in Fig. 4. Its detailed discussion is as follows:

(1) Data preparing. In the actual power grid, different monitoring devices use different sampling frequencies, resulting in inconsistent time scales of data, and these data cannot be directly applied. Therefore, the data should be resampled, and this paper uses linear interpolation to resample the data.

(2) Model training. The training of voltage sag source identification model is divided into three parts. (1) SAE-based unsupervised feature extraction: Input the prepared unlabeled voltage sag data, train SAE according to the process in 3.1, optimize the loss function, and map the original high-dimensional data to the hidden layer. (2) Softmax classifier supervised training: Extract the depth feature of the hidden layer of SAE, and the label data is fed into the softmax classifier for supervised training, and the predicted label is output as the result of classification. (3) Supervised fine-tuning of the stacked network: After SAE and softmax are trained, the encoder is stacked with softmax. Then, the stacked network is fine-tuned with supervision, and the network parameters are further adjusted to improve the performance of the stacked network. Then enter the test data into the trained stacked network to judge the network. Throughout the training process, the scaled conjugate gradient (SCG) algorithm is used to adjust the parameters of the network.

(3) Evaluation index of model. The evaluation indicators of the proposed method are shown in Table 1.

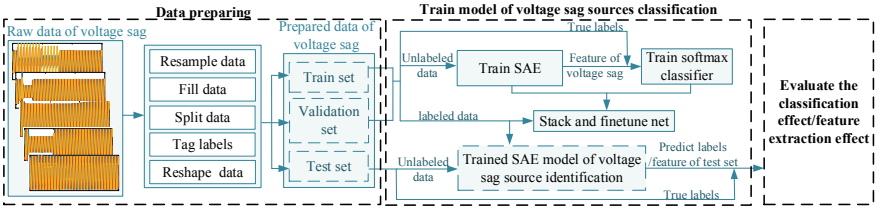

Fig. 4 Voltage sag source identification model

Table 1 Evaluation index of voltage sag source identification

Type of evaluation index	Index	Calculation formula
Evaluation index of classification	ACC	$r_{\mathrm{ACC}} = (N_{\mathrm{TP}} + N_{\mathrm{TN}}) / (N_{\mathrm{TP}} + N_{\mathrm{TN}} + N_{\mathrm{FP}} + N_{\mathrm{FN}})$
	MacroR	$r_{\mathrm{macroR}} = (1/K) \sum_{k=1}^{K} N_{\mathrm{TP},C_k} / (N_{\mathrm{TP},C_k} + N_{\mathrm{FN},C_k})$
	MacroP	$r_{\mathrm{macroP}} = (1/K) \sum_{k=1}^{K} N_{\mathrm{TP},C_k} / (N_{\mathrm{TP},C_k} + N_{\mathrm{FP},C_k})$
	MacroF1	$r_{\mathrm{macroF1}} = (2 \times r_{\mathrm{macroP}} \times r_{\mathrm{macroR}}) / (r_{\mathrm{macroP}} + r_{\mathrm{macroR}})$
Evaluation index of feature extraction	Assessment factor of category separability	$S_{\mathrm{SS}} = S_b / S_w$

4 Simulation and Results

4.1 Data Set

The voltage sag simulation system model is established in MATLAB Simulink, as shown in Fig. 5. The system supply voltage is 110 kV, and the sampling frequency is 25.6 kHz. By changing the location of the fault, the load size, the time of the fault, the type of fault, the size of lightning current, the start time of induction motor, the input time of transformer T2, and the capacity of transformer, eight types of voltage sag source data are obtained. The typical waveforms of these types of sags are shown in Fig. 6. The sample number of each wave collected by simulation is 800, and the total sample size is 6400. The original data is then resampled, changing the sampling frequency from 25.6 to 3.2 kHz. Finally, the resampled data and labels are randomly shuffled, and the data is divided into training set, validation set, and test set according to the ratio of 14:3:3.

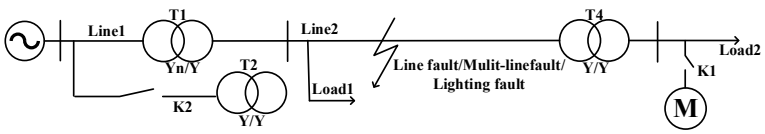

Fig. 5 Voltage sag simulation system model

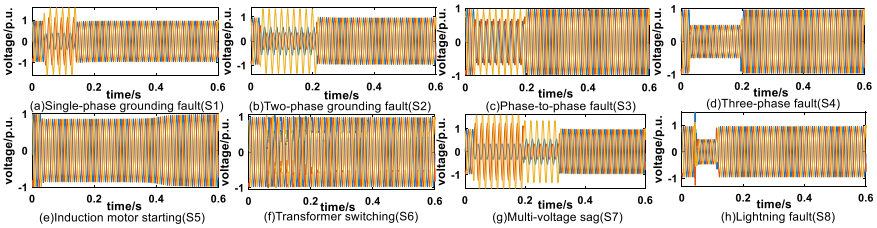

Fig. 6 Typical voltage sag waveform

4.2 Voltage Sag Feature Extraction and Source Classification

The hyperparameters that affect the effectiveness of feature extraction of SAE are ρ and hidden size. Using the model training process proposed in Sect. 3.2 and using the grid search method to find the optimal hyperparameters of the model, the results are shown in Fig. 7. It can be seen that when the hidden size is small (equals 10), the hidden layer is almost completely sparse ($\rho = 1$) and is almost not sparse ($\rho = 0$), and the classification effect of the model is poor. When hidden size is 300 and 500, and ρ is 0.1, the classification effect of the model is the highest. Considering the training time, select the hidden size as 300 and ρ as 0.1. Then the confusion chart is shown in Fig. 8, and ACC is 99.06%, macroF1 is 99.09%, macroP is 99.12%, and macroR is 99.06%.

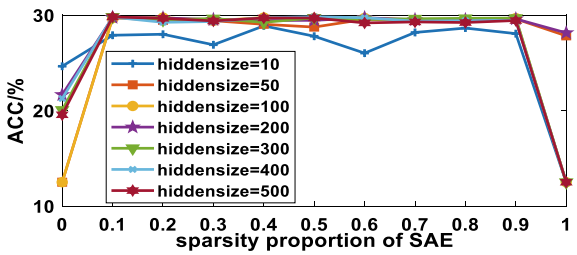

Fig. 7 Method accuracy with different hide sizes

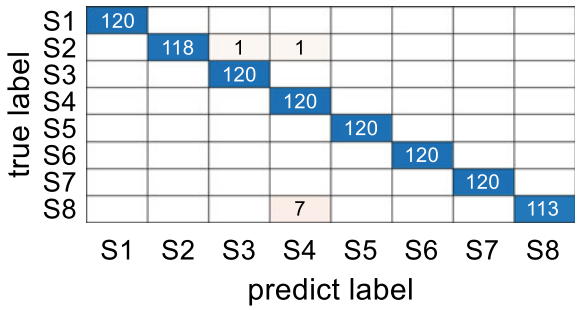

Fig. 8 The confusion chart of test voltage sag data

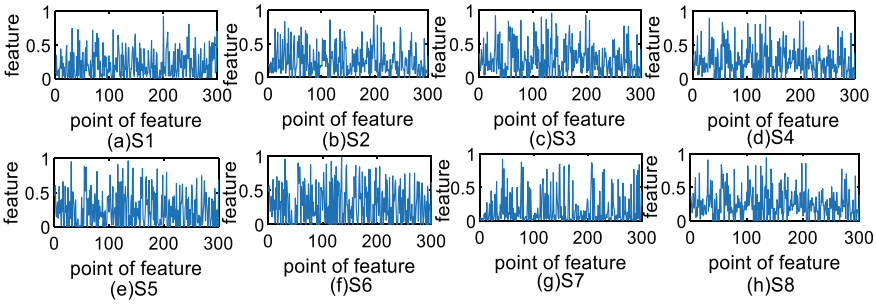

Fig. 9 Average feature vector of voltage sag source

Fig. 10 SS of different feature extraction algorithms

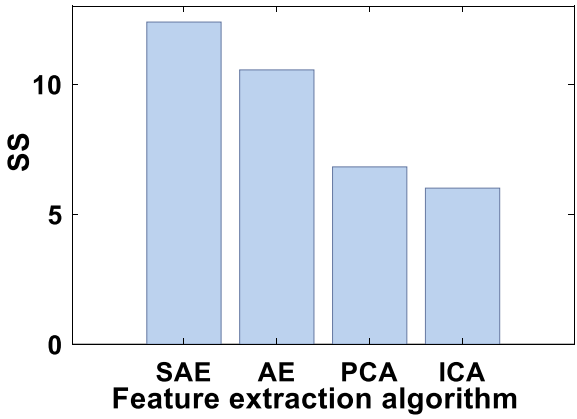

The feature vector of the voltage sag data is extracted from the above model, and the average feature vector is shown in Fig. 9. It is shown that the voltage sag source feature is significantly smaller than the original data dimension, and difference can be seen in Fig. 10.

The evaluation index SS of SAE and other feature extraction algorithms is calculated by the model proposed in 3.3, and the results are shown in Fig. 10. It can be seen that compared with other algorithms, the features proposed by SAE have the largest SS, indicating that the feature set has the largest class separability.

4.3 Robustness Verification of Model

To verify the robustness of the proposed model, a dataset with noise and gross error is used to test the trained model. Noise with signal-to-noise ratio (SNR) of 30 ~ 65 dB is added to the original voltage sag data, and the test results are shown in Fig. 11. It can be seen that the classification effect decreases with the decrease of SNR on the

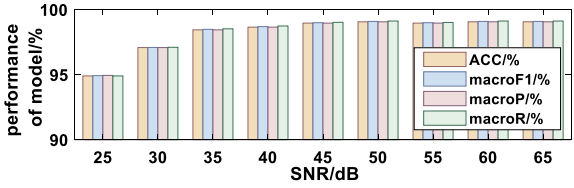

Fig. 11 Test results with noise

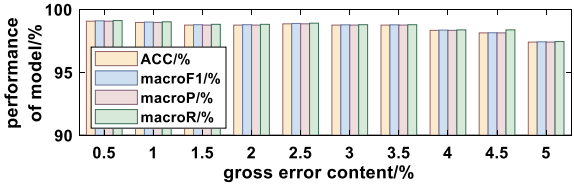

Fig. 12 Test results of data with gross error

whole, but good classification effect can be achieved under each noise level. Add white noise to the original voltage sag data and set the noise intensity as 5–20% of the magnitude of voltage sag, the test results are shown in Fig. 12. It is shown that the classification performance decreases with the increase of the gross error, but good performance of classification can still be achieved under different gross error.

5 Conclusion

In this paper, a feature extraction and identification based on SAE deep learning network and softmax is proposed to realize for identification of complex voltage sag sources with voltage sag data only. The SAE of unsupervised training is used to automatically extract the depth features of voltage sag data, and then the supervised training softmax is used to classify the voltage sag source, and finally, the stacked network is further optimized by supervised fine-tuning. Simulation experiments are given out, and the identification accuracy of complex voltage sag sources including lightning fault and multi-voltage sag is 99.06%, and the accuracy of data with noise and gross error is also high. The results of this paper are only based on simulation verification, and the next step is to apply the proposed method to the actual identification of voltage sag sources.

Acknowledgements This work was financially supported by the Science and Technology Project of Jiangsu Power Testing Research Institute Co., Ltd. (DSY202213).

References

1. IEEE (2019) IEEE recommended practice for monitoring electric power quality. IEEE Std 1159–2019:1–98
2. Zhang Y, Wu Y (2023) Research status of voltage sag risk assessment and prospect under the background of new power system. Electr Power Constr 44(02):15–24
3. Liu K, Liu X, Zhang P et al (2023) Identification method of electricity theft based on long short-term memory autoencoder with load peak features. Autom Electr Power Syst 47(02):96–104
4. Yang Y, Li C, Qin Y et al (2023) Clustering analysis of daily load curve based on convolutional variational autoencoder. Mod Electr Power 18:1–9
5. Liu H, Ye X, Lv G et al (2021) Modified S-transform voltage sag source identification by introducing regulation factor. Electr Drive 51(18):59–64
6. Wang Y, Jing Z (2022) Identification of voltage sag source based on wavelet transform sample entropy and deep kernel extreme learning machine. J Xi'an Univ Technol 38(01):142–150
7. Chu J, Yuan X, Chen B et al (2018) A method for distribution network voltage sag source identification combining wavelet analysis and modified DTW distance. Power Syst Technol 42(2):637–643
8. Li C, Yang J, Xu Y et al (2017) Application of comprehensive fuzzy evaluation method on recognition of voltage sag disturbance sources. Power Syst Technol 41(3):1022–1028
9. Lv G, Jiang X, Hao S et al (2019) Location of voltage sag source based on semi-supervised SVM. Power Syst Protect Control 47(18):76–81
10. Yang X, Zhang T, Pan A et al (2021) Voltage sag source feature identification with S transform and multidimensional fractal. Power Syst Technol 45(02):672–679
11. Wang Y, Xiao X (2021) Heterogeneous stacking integrated learning identification method for voltage sag sources. Power Syst Protect Control 49(15):1–8
12. Ye X, Liu H, Lv G et al (2022) Identification of voltage sag source based on BAS-BP classifier model. Electr Power Eng Technol 41(1):77–83
13. Zhou X, Chen S, Lu Z et al (2018) Technology features of the new generation power system in China. Proceed CSEE 38(7):1893–2205
14. Li D, Mei F, Zhang C et al (2020) Deep belief network based method for feature extraction and source identification of voltage sag. Autom Electr Power Syst 44(04):150–158
15. Wang Y, Liu S, Tang Y et al (2023) Self-learning estimation method for the severity of voltage sags caused by lightning. Electr Power Eng Technol 42(02):188–196

Short-Term Prediction of Wind Power Based on NWP Error Correction with TimeGAN and LSTM-TCN

Shuona Li, Wei Ma, Zhao Liu, Yuge Duan, and Chengwei Tian

Abstract The data quality of numerical weather prediction has a great influence on the accuracy of wind power prediction technology. In order to improve the short-term forecasting effect of wind power, we proposed a combined LSTM-TCN forecasting model based on NWP error correction model with TimeGAN. First, minimal redundancy maximal relevance (mRMR) algorithm is used to extract original NWP features and measured meteorological features, respectively. Then, TimeGAN is used to correct initial NWP data according to the internal hidden associations with the measured weather features. After that, the corrected NWP features combined with historical wind power are applied to establish a wind power short-term prediction hybrid model based on LSTM and TCN network. Finally, the performance of the hybrid model is tested by a wind farm dataset in China, which verified effectiveness of this method.

Keywords Short-term prediction of wind power · TimeGAN · NWP · Measured meteorological data · Error correction · LSTM · TCN

1 Introduction

With the proposal of *carbon peaking and carbon neutrality*, more and more wind power equipments are connected to the grid, whose intermittent and uncertain characteristics have brought challenges to grid security and new energy consumption. Wind power prediction technology is of significance to reduce its random impact on the power system [1].

S. Li (✉) · Z. Liu · Y. Duan · C. Tian
School of Electrical Engineering, Beijing Jiaotong University, Beijing, China
e-mail: 20292014@bjtu.edu.cn

W. Ma
State Key Laboratory of Control and Simulation of Power Systems and Generation Equipments of Electrical Engineering Tsinghua University, Beijing, China

S. Yadav et al. (eds.), *Energy Power and Automation Engineering*, Lecture Notes in Electrical Engineering 1118, https://doi.org/10.1007/978-981-99-8878-5_92

Accurate meteorological information is significantly important for wind power prediction, which is directly weather-related. However, numerical weather prediction system is usually difficult to provide large-scale and high-precise meteorological information due to spatial distance and regional differences between NWP point and wind farm. If initial NWP data are directly used for power prediction, large errors will occur. And fluctuations of NWP data will severely limit forecasting performance [2]. Reference [3] introduced a feature intersection mechanism for feature reconstruction, which uses CNN-LSTM model for error compensation. By minimizing features, the predicting accuracy is improved to some extent, but it does not consider inherent errors in initial meteorological data. Reference [4, 5] considered the effects of inaccurate factors of NWP data, such as internal error and bad data, on wind power prediction error so as to improve short-term wind power prediction performance. Considering the strong mapping uncertainty between NWP error and NWP wind speed, NWP wind speed transfer correction algorithm was to improve the performance of correction model [6].

However, nowadays most studies on short-term wind power prediction consider wind speed and wind direction as inputs of prediction models only. References [7, 8] considered the inaccuracy of wind speed data in the NWP forecasting system and proposed three wind speed correction methods based on multiple linear regression NWP correction method, radial basis function neural network, and Elman neural network. Reference [9] wind farm forecasted wind speed and real wind speed was analyzed by pearson correlation, then GRU based on attention mechanism was adopted to correct the forecasted wind speed in NWP. Reference [10] proposes a method based on time series correlation test and residual channel The wind speed error correction model of the attention network. Reference [11] proposed a method of correcting regional numerical weather forecasts using stacked multi-level denoising autoencoders for NWP data such as wind speed and wind direction in small datasets. However, other meteorological features, such as air pressure, relative humidity, and momentum flux in actual prediction system are also directly related to wind power, and there are few researches on NWP error correction methods considering these meteorological features.

Since the traditional GAN model is limited to capturing the probability distribution of static data, it cannot consider the inherent dynamic temporal correlation of time series data. Reference [12] proposed a TimeGAN model combining unsupervised training and supervised training, which can gradually and accurately capture the dynamic probability distribution of time series, which is conducive to improving the accuracy of time series data generation.

In order to improve the influence of initial NWP data errors on prediction, this work first uses mRMR algorithm to extract the features of NWP features and measured meteorological features respectively by calculating distance correlation between meteorological features and historical wind power, and then TimeGAN is used to generate corrected NWP data to reduce errors among it, and a short-term prediction model combined LSTM and TCN is established to predict wind power. Finally, the effectiveness of the proposed method is verified by using the data of a domestic wind farm.

2 NWP Error Correction Based on TimeGAN

2.1 Error Analysis of NWP Data

Taking the 70-m wind speed and 70-m wind direction in the NWP data and the measured meteorological data as an example, it can be observed that there is a large error between the NWP data and the measured data, and there are obvious under-reporting and hysteresis phenomena, as shown in Figs. 1 and 2.

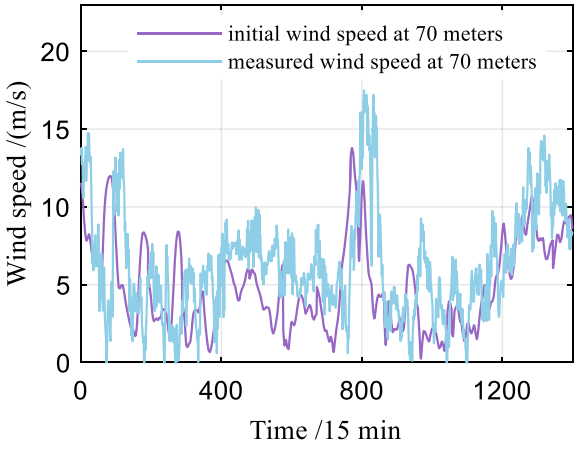

Fig. 1 Comparison of 70-m wind speeds

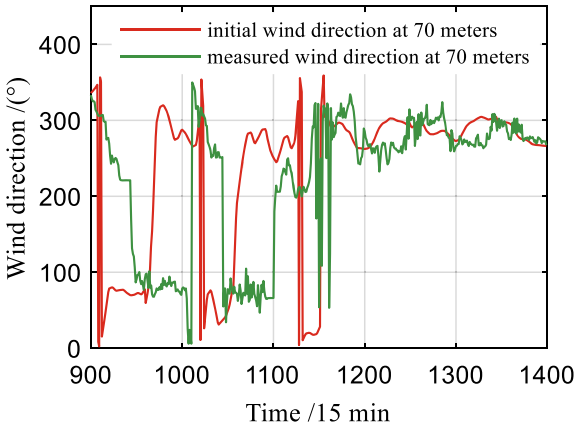

Fig. 2 Comparison of 70-m wind directions in NWP data with those in measured meteorological data

2.2 Error Correction Principle Based on TimeGAN

NWP meteorological data are typical dynamic time series. TimeGAN not only includes unsupervised confrontation network of sequence generator and discriminator but also contains supervised network to learn stepwise conditional distribution of time series [12]. Therefore, TimeGAN can significantly improve the accuracy of NWP data by reconstructing it from initial NWP data.

NWP Feature Reversible Mapping Based on Embedding Function and Recovery Function

Meteorological data are complex high-dimensional data, which usually have deep hidden correlations, and are usually only driven by a few potential factors [12]. If the feature dimension is too large, the generalization ability of the model will deteriorate and is not conducive to the error correction. Therefore, the reversible mapping of embedding and recovery method is used to correct NWP data by mapping it to latent space.

Embedding function is an encoder, which uses a recurrent neural network to map high-dimensional dynamic features of the feature space to a low-dimensional latent space. The value at the next moment is related to the previous, as shown in $h_t = e(h_{t-1}, X_t)$, where h_t is feature vector of measured meteorological data in latent space at time t, X_t is feature vector of measured meteorological data in feature space at time t, and e is embedding function composed of GRU network.

The recovery function is inversion of the embedding function, which uses a recurrent network to map the features of latent space to feature space to reconstruct features, expressed as $\widehat{X}_t = r(h_t)$, $\hat{X}_t$ denotes feature vector of reconstructed NWP data in feature space, and r is recovery function composed of GRU.

The reconstruction loss function L_{er} is defined to train embedding and recovery function by considering stepwise loss of NWP features, expressed as Eq. (1).

$$L_{\text{er}} = \mathbb{E}_{X_{1:L\sim P}}\left[\sum_t \left\| X_t - \hat{X}_t \right\|_2\right]. \tag{1}$$

Unsupervised and Supervised Training of TimeGAN in Latent Space

In TimeGAN model, the sequence generator consists of sub-generator and supervised network, which is defined $\widehat{h}_t = g(\widehat{h}_{t-1}, \tilde{X}_t)$, where $\tilde{X}_t$ is feature vector of NWP data at time t in feature space, $\hat{h}_t$ is feature vector of NWP data from sub-generator at time t, and g is sub-generator composed of GRU. The sequence discriminator compares classification results between generated NWP data and measured meteorological data, expressed as $y_t = d(h_t)$ and $\tilde{y}_t = d(\widehat{h}_t)$ where $\tilde{y}_t$ is the output of generated NWP data at time t, y_t is the output of measured meteorological data at time t, and d is the discriminator composed of GRU network.

The unsupervised loss function L_{gd} for sub-generator and discriminator is shown in Eq. (2).

$$L_{\mathrm{gd}} = \mathbb{E}_{X_{1:L\sim P}}\left[\sum_t \ln y_t\right] + \mathbb{E}_{X_{1:L\sim \hat{P}}}\left[\sum_t \ln(1-\hat{y}_t)\right]. \tag{2}$$

Since L_{gd} only contains an unsupervised loss, it is not enough to motivate the sub-generator to learn a stepwise conditional distribution in NWP data. Supervised network is introduced to train sequence generator using measured meteorological data in latent space so that generated NWP data satisfy the same stepwise conditional distribution. The supervised loss function L_{eg} is shown in Eq. (3). Then sequence generator and discriminator are optimized by cross-training L_{gd} and L_{eg}.

$$L_{\mathrm{eg}} = \mathbb{E}_{X_{1:L\sim P}}\left(\sum_t \left\| h_t - g(h_{t-1}, \tilde{X}_t)\right\|_2\right). \tag{3}$$

Therefore, the global optimization loss functions of TimeGAN are shown in Eq. (4).

$$\begin{cases} \min V(e,r) = \min\limits_{\theta_e,\theta_r}(\lambda L_{eg} + L_{er}) \\ \min\max V(g,d) = \min\limits_{\theta_g}(\eta L_{eg} + \max\limits_{\theta_d} L_{gd}) \end{cases}. \tag{4}$$

In this equation, θ_e, θ_r, θ_g, and θ_d denote parameters of the embedding, recovery, sequence generator, and discriminator network, respectively. λ and η are hyperparameters to balance the two loss functions.

3 LSTM-TCN Hybrid Prediction Model

The TCN model is an improved model for time series data based on one-dimensional convolution. Its unique expansion causal convolution structure can process data in parallel and shorten the operation time. Additionally, the network can obtain a broad receptive field with fewer parameters to capture deep temporal relationship due to a flexible architecture with expansion causal convolution and residual network [13]. In this work, hidden layer number and convolution kernel size are 3, and residual module of the last layer obtains output sequence through a fully connected layer.

Nowadays, LSTM model is widely used in wind power prediction [14]. It has good performance for sequence prediction unaffected by gradient explosion or disappearance on memory. In this case, it is useful for the prediction by correcting multi-dimensional NWP features.

Thus, the LSTM-TCN hybrid forecasting model is used to predict the wind power by using the revised multi-dimensional NWP characteristics and historical power respectively, shown in Fig. 3.

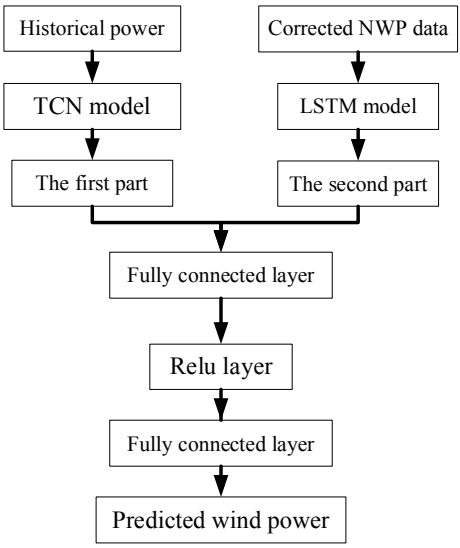

Fig. 3 LSTM-TCN combined power prediction model

4 The Prediction Process of the Model

The model prediction process constructed in this paper is shown in Fig. 4. Due to seasonal distribution of wind power generation, errors between NWP data and measured meteorological data and mapping relationship between meteorological data and wind power are different in different seasons [10]. The initial NWP data, measured meteorological data, and historical measured power are divided into datasets of four seasons: spring, summer, autumn, and winter. After removing the abnormal data among raw dataset including the whole seasons, the training and testing sets of each season of the dataset are divided, after that, Max-Min normalization is employed in eliminating the influence of the difference of different variables on the results.

Distance correlation coefficient of each meteorological feature and each meteorological feature with wind power is computed first. Then the essential feature variables with high distance correlation coefficient are extracted according to the principle of mRMR [15]. Then TimeGAN is used to correct the error of NWP meteorological features and perform unsupervised training and supervised training on the low-dimensional NWP features generated by the latent space and the measured meteorological features mapped to the latent space. Through reversible mapping, the generated NWP data are similar to measured meteorological features. Since the forecast time step in this paper is 24 h, corrected NWP features and historical power are divided into n T-step periods for segmental prediction. Then the multi-dimensional corrected NWP features are input to LSTM, historical power is inputted to TCN, and the outputs of them are spliced using the fully connected layer to obtain the predicted

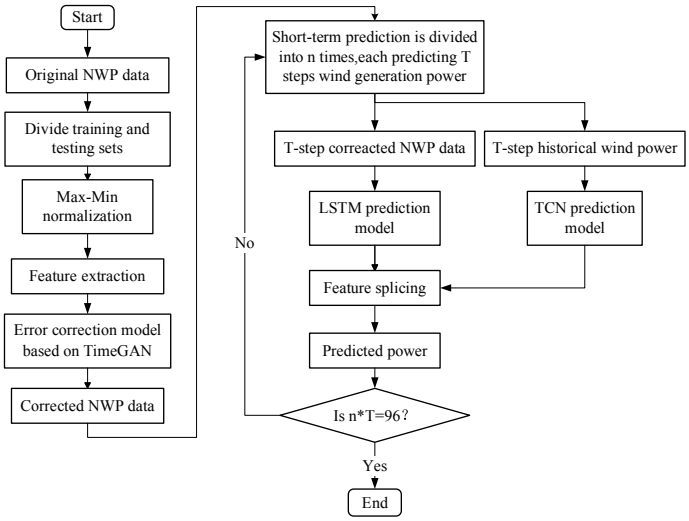

Fig. 4 LSTM-TCN wind power prediction process based on TimeGAN numerical weather prediction error correction

power of T steps. The power series of n segments and perform denormalization to obtain the prediction power are combined.

5 Case Analysis

5.1 Dataset and Environment

This work uses the NWP data, measured meteorological data, and measured wind power of a domestic wind farm from January 1, 2020, to December 31, 2020, for training and testing, with a resolution of 15 min. The prediction task in this work is executed on Pytorch.

5.2 Short-Term Forecast of Wind Power

First, normalize datasets and extract features. Then TimeGAN is used to correct the error of the NWP data. Figure 5 shows corrections by taking the wind speed at 70 m as an example. Then corrected NWP data and historical measured power are input into LSTM-TCN combination model to predict power as shown in Fig. 6 by taking spring as an example. To quantify the effectiveness of model, MAE and RMSE are selected

as evaluations, $\mathrm{MAE} = \frac{1}{C}\sum_{t=1}^{N}\frac{|\hat{p}_t - p_t|}{N}$ and $\mathrm{RMSE} = \frac{1}{C}\sqrt{\frac{1}{N}\sum_{t=1}^{N}(\hat{p}_t - p_t)^2}$ where C is installed capacity of wind farm, N is the length of forecasting sequence, and p_t and $\hat{p}_t$ are the measured and predicted values of wind power, respectively. The evaluation results are shown in Table 1.

According to the experimental results, NWP data and wind power are different for different seasons. The prediction errors in autumn and winter are smaller than those in spring and summer, especially in summer, which shows that wind power in autumn and winter has a stronger correlation with NWP data. Both MAE and RMSE of predicted power by revised NWP data are smaller than those of initial NWP data. Additionally, in spring, autumn, and winter, MAE of predicted power by corrected NWP data is smaller than that of measured meteorological data, which shows that revised NWP features of TimeGAN are less redundant than measured meteorological features. Moreover, fluctuation of power by revised NWP data is significantly reduced, and extreme predicted power is closer to real-time power than initial NWP.

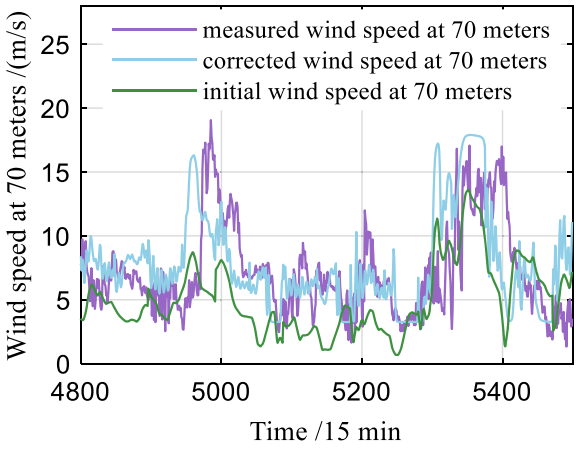

Fig. 5 Comparison of wind speed at 70 m with different meteorological data

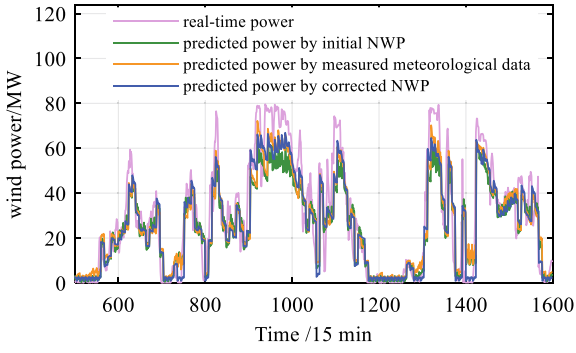

Fig. 6 Comparison of prediction power with different meteorological data

Table 1 Comparison of evaluation indicators of power prediction results

Seasons	Evaluation index	By measured meteorological data	By corrected NWP	By initial NWP
Spring	MAE	0.0974	0.0966	0.1056
	RMSE	0.1367	0.1386	0.1492
Summer	MAE	0.1025	0.1031	0.1073
	RMSE	0.1391	0.1403	0.1441
Autumn	MAE	0.0789	0.0782	0.0794
	RMSE	0.1161	0.1170	0.1172
Winter	MAE	0.0679	0.0672	0.0736
	RMSE	0.1119	0.1142	0.1163

6 Conclusion

In this work, we proposed a TimeGAN and LSTM-TCN-based wind power generation forecasting method with NWP error correction, by which the following conclusions can be drawn:

- Based on the distance correlation coefficient, the mRMR principle can effectively extract meteorological features that are highly correlated with wind power and little redundant with other features from original dataset.
- NWP error correction model based on TimeGAN is conductive to improving inherent errors in NWP data according to the distributions of measured meteorological data for different four seasons, by which their predicted powers are closer to those of measured meteorological data.
- Combining the advantages of the LSTM model for multivariate time series prediction and the TCN model for univariate time series prediction, using the corrected NWP data and historical measured power for segmental forecasting can reduce prediction errors.

Acknowledgements This work is supported by the National Natural Science Foundation of China under Grant No. U52107068.

References

1. Tang X, Gu N, Huang X et al (2022) Progress on short term wind power for echnology. J Mech Eng 58:213
2. Liu Z, Zang Z (2016) Solar forecasting by K-nearest neighbors method with weather classification and physical model. In: North American power symposium (NAPS). Denver, pp 1–6
3. Liu Y, Fan Y, Bai X et al (2022) Short-term wind power prediction based on feature crossover mechanism and error compensation. Trans China Electrotech Soc 57:1–12

4. Couto A, Estanqueiro A (2022) Enhancing wind power forecast accuracy using the weather research and forecasting numerical model-based features and artificial neuronal networks. Renew Energy 201:1076
5. Xu Q, He D, Zhang N et al (2015) A short-term wind power forecasting approach with adjustment of numerical weather prediction input by data mining. IEEE Trans Sustain Energy 6:1283
6. Wang H, Han S, Liu Y et al (2019) Sequence transfer correction algorithm for numerical weather prediction wind speed and its application in a wind power forecasting system. Appl Energy 237:1
7. Liu Y, Wang Y, Li L et al (2016) Numerical weather prediction wind correction methods and its impact on computational fluid dynamics based wind power forecasting. J Renew Sustain Energy 8:033302
8. Khodayar M, Wang J, Manthouri M (2019) Interval deep generative neural network for wind speed forecasting. IEEE Trans Smart Grid 4:3974
9. Yang G, Liu S, Wang D et al (2022) Short-term wind power forecasting based on Attention-GRU wind speed correction and Stacking. Acta Energ Solaris Sin 43:273
10. Andrade JR, Bessa RJ (2017) Improving renewable energy forecasting with a grid of numerical weather predictions. IEEE Trans Sustain Energy C1:1
11. Dong W, Sun H, Tan J et al (2021) Short-term regional wind power forecasting for small datasets with input data correction, hybrid neural network, and error analysis. Energy Rep 7:7675
12. Yoon J, Jarrett D (2019) Van der Schaar M 2019 Time-series generative adversarial networks. Adv Neural Inform Process Syst 32:13514
13. Fu Y, Ren Z, Wei S et al (2022) Ultra-short-term power prediction of offshore wind power based on improved LSTM-TCN model. Proceed CSEE 42:4292
14. Banik A, Behera C, Sarathkumar TV et al (2020) Uncertain wind power forecasting using LSTM-based prediction interval. IET Renew Power Gener 14:2657
15. Liu J, Sun H, Peng C et al (2018) Research of photovoltaic power forecasting based on big data and mRMR feature reduction. In: IEEE power and energy society general meeting (PESGM). IEEE, Portland, pp 1–5

Frequency Converter Topology Research in Flexible Low-Frequency AC Transmission System Applied to Offshore Wind Power Transmission

Wei Ding, Yang Huang, and Qingjian Wang

Abstract Flexible low-frequency AC transmission (LFAC) technology can be used for offshore wind power transmission. Compared with high-voltage alternating current (HVAC) transmission and high-voltage direct current (HVDC) transmission technology solutions, LFAC has its unique advantages. This paper studies three topologies for LFAC inverters, namely BTB-MMC, M3C, and DRU-MMC. And compared and analyzed, M3C is recommended as the topology of the frequency converter in the offshore wind power transmission scene at the present stage. This paper also gives the topology scheme of the transmission system for offshore wind transmission and access to the power grid under the LFAC technology, which provides a reference for subsequent engineering implementation.

Keywords Flexible low-frequency AC transmission system · Modular multilevel matrix converter (M3C) · Offshore wind power transmission · Frequency converter topology

1 Introduction

The overall development of wind power in China is rapid, and the large-scale development of offshore wind power is one of the important measures to achieve the "dual carbon" goal. Offshore wind power has the unique advantage of stable wind energy resources and does not occupy land. The length of China's coastline exceeds 18,000 km, with over 6000 islands and abundant offshore wind energy resources, making the development of offshore wind power relatively advantageous [1]. There are two mature technologies for offshore wind power transmission: high-voltage alternating current (HVAC) transmission and high-voltage direct current (HVDC) transmission.

W. Ding (✉) · Y. Huang · Q. Wang
China Energy Engineering Group Guangdong Electric Power Design Institute CO., LTD, Guangzhou, China
e-mail: dingwei@gedi.com.cn

S. Yadav et al. (eds.), *Energy Power and Automation Engineering*, Lecture Notes in Electrical Engineering 1118, https://doi.org/10.1007/978-981-99-8878-5_93

The power frequency high-voltage AC transmission (HVAC) method has relatively simple structure, mature technology, and rich engineering experience. However, due to the limitation of cable charging current and charging power, the transmission distance is limited, and the higher the voltage level, the greater the charging current [2]. Generally, it is only suitable for offshore 70 km offshore wind farms with a capacity of less than 400 MW. Reactive power compensation at both ends of the cable is one of the effective means to extend the cable transmission distance, but technically, due to the constraints of the current carrying capacity of the cable, the capacity of reactive power compensation is limited.

HVDC transmission technology can avoid the influence of cable capacitance and meet the transmission needs of large-capacity and long-distance offshore wind power. The HVDC transmission technology based on voltage source converter (VSC) is flexible in operation and regulation and can realize fault isolation between offshore wind farms and onshore power grids. At this stage, it is considered to be the best choice for the transmission of deep-sea wind power. HVDC power transmission technology requires the construction of a converter station at sea and on land, and the engineering cost and operation and maintenance costs are relatively high.

How to reduce construction, operation and maintenance costs, and shorten the profit cycle has become a very important topic in the industry. Flexible low-frequency AC transmission (LFAC) technology is a new type of high-efficiency AC transmission technology that uses power electronics technology to flexibly select a suitable frequency in the range of 0–50 Hz to improve the transmission capacity of the power grid and the ability of flexible regulation [3]. It can take into account the advantages of flexible networking, easy realization of voltage level conversion of HVAC; easy long-distance, large-capacity power transmission, and good power flow controllability of the HVDC. Compared with HVAC, LFAC can significantly reduce the capacitive charging current of submarine cables due to the reduction of frequency, thereby increasing the transmission capacity and distance of cables, and providing more options for offshore wind power transmission. Compared with HVDC, LFAC only needs to build a frequency conversion converter station on the land side, which greatly reduces the one-time investment of project construction. At the same time, because the frequency conversion converter station is built on land, it can effectively reduce operation and maintenance costs. In addition, the frequency division offshore power transmission system can use the existing AC circuit breaker, which reduces the technical difficulty of wind power grid connection through frequency division to a certain extent [4].

This paper discusses various topologies and characteristics of frequency converters in LFAC system. And it analyzes and compares the application of various topological structures in the offshore wind power transmission scene. This paper also proposes a grid system topology recommendation scheme applied to wind power transmission scene. This study provides a theoretical basis and reference for the future engineering implementation.

2 Topology Research of Frequency Converter

The AC converter topology is the key to the flexible LFAC system, and it is mainly used to realize the transformation between low frequency and power frequency. In power electronic converter stations with hundreds of kilo volts voltage, the modular multilevel structure is widely considered to be the safest, most efficient, and reliable technical solution.

The current mainstream converter topology schemes based on this technology are as follows:

(1) Back-to-back modular multilevel converter (BTB-MMC).
(2) Modular multilevel matrix converter (M3C) [5].
(3) Diode rectifier unit-modular multilevel converter (DRU-MMC).

2.1 BTB-MMC

The BTB-MMC AC–AC inverter consists of two sets of MMC converters connected on the DC side, as shown in Fig. 1. The MMC converters on both sides are composed of six bridge arms, each bridge arm is composed of *N* half-bridge structure power modules cascaded, and a bridge arm reactor is connected in series in each bridge arm. The whole inverter consists of 12 bridge arms constitute.

In this topology, the power frequency side and low-frequency side of the inverter are naturally decoupled, the control structure is simple, and the technology is mature. It can meet the requirements of different power and voltage levels by increasing or decreasing the number of power modules connected to the inverter. This topology

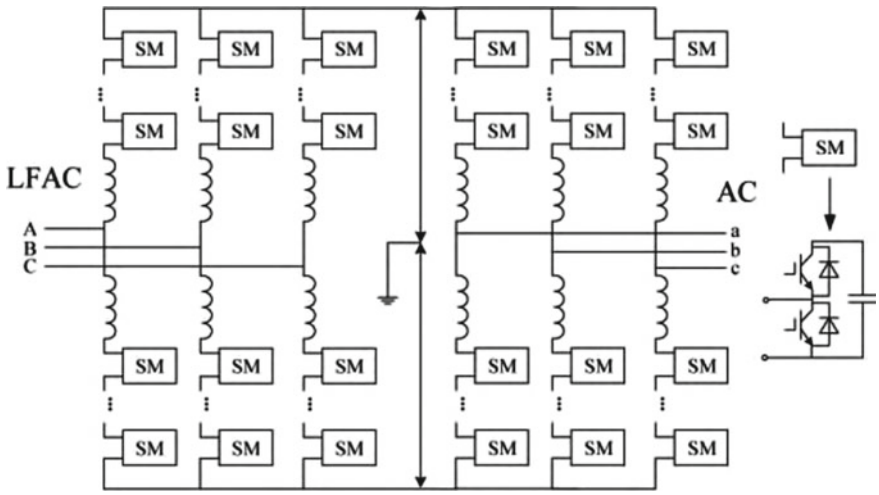

Fig. 1 Typical BTB-MMC inverter topology

has been applied in Guangdong-Hong Kong-Macao Greater Bay Area DC back-to-back and Chongqing-Hubei DC back-to-back projects, and has rich experience in engineering design.

The MMC converter is highly modular and can meet the requirements of different power and voltage levels by increasing or decreasing the number of power modules connected to the converter. It can realize integrated design, shorten the project cycle, and also provide convenience for future system expansion.

However, because this topology divides the frequency conversion process into two links, rectification and inverter, the overall conversion efficiency is reduced. In addition, the frequency converter is composed of two MMCs, the number of bridge arms and power devices is large, and the capacitance of the low-frequency side is large, which reduces the overall economy. In addition, low-frequency operation will lead to longer charging and discharging times of the power module capacitor, increased voltage fluctuations, and increased bridge arm circulation, power module loss, and bridge arm stress.

2.2 M3C

The main circuit topology of the M3C inverter is shown in Fig. 2. The nine full-bridge power module cascaded bridge arms are symmetrically distributed in the three phases (a, b, c) of the AC system on the input side and the three phases (u, v, c) of the AC system on the output side. Between (w), each bridge arm is composed of a bridge arm reactor L and several full-bridge sub-modules connected in series.

M3C inverter has the characteristics of low energy storage, high power density, and multilevel output waveform, can independently control active and reactive power on the AC side, has black start capability, and the capacitor voltage ripple of its sub-modules is smaller. Since the intermediate DC link is omitted, the commutation efficiency is high, and high-voltage DC bus capacitor support is not required. The internal power exchange of the bridge arm branch can solve the problem of large capacitance energy fluctuations under low-frequency conditions, and the AC side has strong fault ride-through capability and high reliability. At present, the State Grid Taizhou 35 kV flexible low-frequency transmission demonstration project and the State Grid Hangzhou 220 kV flexible low-frequency transmission demonstration project both apply this topology.

The converter is composed of nine bridge arms, and each bridge arm is composed of N power modules cascaded sequentially. A bridge arm reactor is connected in series in each bridge arm, and three bridge arms in the same phase form a phase unit. The modular multilevel converter composed of cascaded full-bridge power modules can output negative voltage, while the half-bridge structure can only output positive voltage. In order to output alternating AC voltages with different frequencies on both sides, a full-bridge is required. The structure is a modular multilevel converter type composed of cascaded power modules.

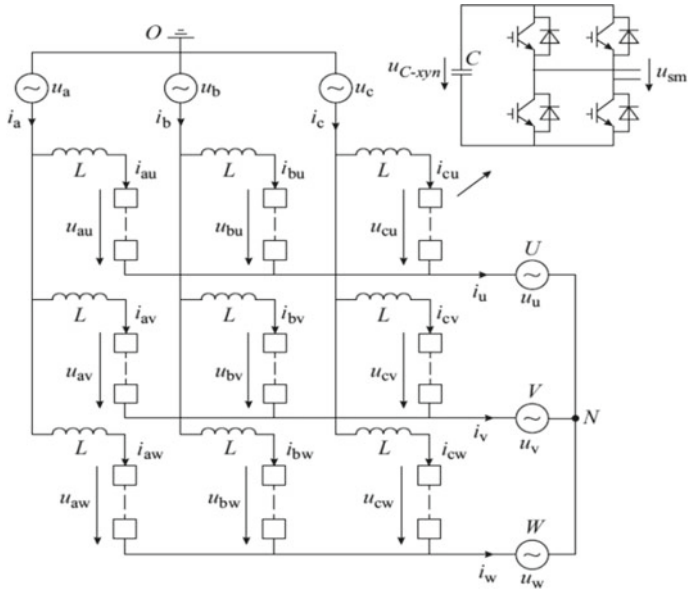

Fig. 2 Typical M3C inverter topology

The M3C inverter still faces problems such as the large number of required sub-modules and complex system control logic, and there is still room for further optimization of the system structure and control strategy. The number and scale of modules of the single-side M3C inverter are larger than those of the DC converter station with the same capacity, which has a certain impact on the overall investment of the inverter station.

2.3 DRU-MMC

Another frequency conversion topology with engineering application prospects is DRU-MMC which is shown in Fig. 3. This structure is equivalent to replacing the converter on one side of the BTB-MMC topology by MMC with DRU, which can give full play to the mature technical advantages of MMC and the cost advantages of DRU's small size, small footprint, and low cost, and build high-efficiency, high-reliability unique, and low-cost LFAC solution.

Due to the lack of passive operation capability of DRU, the DRU side needs voltage support. In the COSCO sea wind power transmission scenario, the "networked wind turbine + DRU-MMC converter" collection and transmission solution was constructed by applying this technology. Grid-structured wind turbines have the ability to connect to weak grids or even passive grids and provide active voltage/frequency support. However, the design and control of grid-type wind turbines and

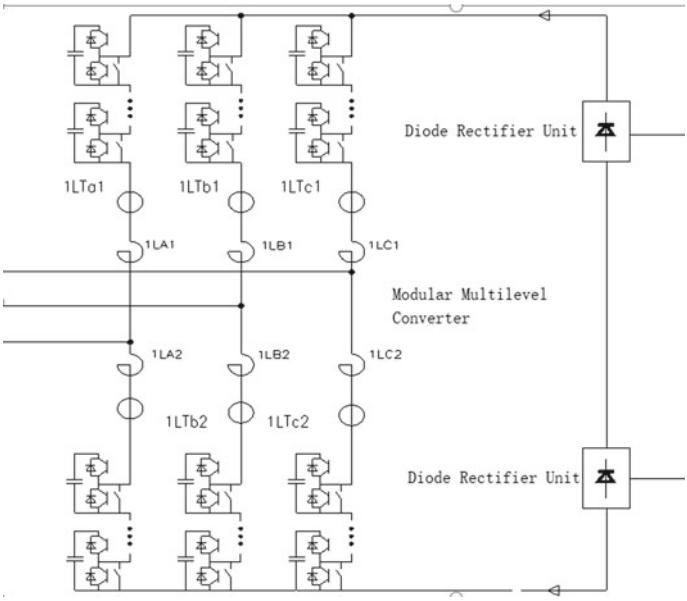

Fig. 3 Typical DRU-MMC inverter topology

converters are relatively complicated. At present, this frequency conversion topology is still in the research stage, and there is no engineering practice yet.

3 Topology Comparison in Offshore Wind Transmission

Overall, the BTB-MMC solution has the lowest economy, while M3C and DRU-MMC are higher, and the industry currently believes that the latter two technical solutions have certain engineering application prospects. The comparison of the three inverter topologies is shown in Table 1.

Due to the limitation of grid-type wind turbines, BTB-MMC and M3C are the topological solutions that can be maturely applied to offshore wind power transmission. However, BTB-MMC is less economical, so this article recommends M3C topology as the first choice for inverter of offshore wind transmission.

4 Grid System Access Topology Recommendation Scheme

The recommended grid connection is shown in Fig. 4. Topology wiring consists of three parts: part A offshore booster station; part B submarine cable; and part C land frequency conversion station. Part C-1 is LFAC side which is equipped with

Table 1 Comparison of the three inverter topologies

No	Items	BTB-MMC	M3C	DRU-MMC
1	Topology type	Half-bridge submodule	Full-bridge submodule	Diode valve + half-bridge submodule
2	Number of bridge arms	12	9	6
3	Ability to access passive systems	Yes	Yes	No
4	Fan starting ability	Yes	Yes	No
5	Fan type	Follow grid type	Follow grid type	Grid-structured type
6	Economy	Bad	Good	Good

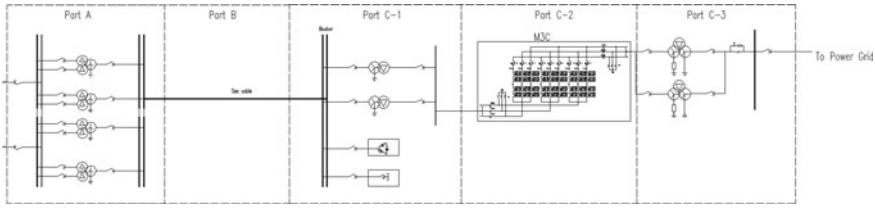

Fig. 4 Typical DRU-MMC inverter topology

isolation transformers, AC energy-consuming devices, and high-voltage reactors to supplement the reactive power of submarine cables. Part C-2 is M3C-type frequency converter. Part C-3 is 50 Hz AC side which is equipped with isolation transformers and a start-up resistor for starting the M3C.

5 Conclusion

Flexible LFAC technology combines some of the advantages of power frequency HVAC transmission technology and flexible HVDC transmission technology, and it can improve the grid transmission capacity and flexible regulation ability to a certain extent. It is a new type of high-efficiency AC transmission technology.

As the key to the flexible LFAC system, the inverter topology has an important impact on the system's operating performance and economy. The network side performance of the three typical topologies in this paper is similar, and they can all meet the technical requirements of the flexible LFAC system for the frequency conversion station. The main technical difference lies in the wind turbine side. Among them, M3C and DRU-MMC are more economical, but DRU-MMC needs to use grid-structured wind turbines. Due to the limitations of grid-structured wind turbines, the recommended topology scheme that can be maturely applied to offshore wind power

transmission is M3C. This paper also gives the complete wiring topology of the sea breeze sending low-frequency scheme that can be applied to actual projects.

With the integrity of the system structure, the improvement of equipment efficiency, and the optimization of control strategies, the advantages of flexible low-frequency AC power transmission will continue to be highlighted.

References

1. Xu QY, Kang CQ, Zhang N, Fan Y, Zhu HJ (2011) A discussion on offshore wind power output characteristics and its accommodation. Autom Electr Power Syst 35(22):54–59
2. Wang XL, Zhang XL, Ning LH, Zhu WP, Wang XF (2017) Application prospects and challenges of fractional frequency transmission system in offshore wind power integration. Electr Power Eng Technol 36(1):15–19
3. Wang XF (1995) Fractional frequency transmission system. Electr Power 1995(1):2–6
4. Huang MH, Wang XL, Liu SQ, Wang XF, Meng QY, Ye R (2019) Technical and economic analysis on fractional frequency transmission system for integration of long distance offshore wind farm. Autom Electr Power Syst 43(5):167–174
5. Zhao GL, Chen WJ, Deng ZF, Yu HY, Xu YF, Zhao ZX (2022) Key technologies and application of flexible low-frequency AC transmission. Autom Electr Power Syst 46(15):1–10